IFMBE Proceedings

Rodrigo Costa-Felix · João Carlos Machado ·
André Victor Alvarenga (Eds.)

Volume 70/1

XXVI Brazilian Congress on Biomedical Engineering

CBEB 2018, Armação de Buzios, RJ, Brazil,
21–25 October 2018 (Vol. 1)

Búzios - RJ
CBEB
2018

Springer

IFMBE Proceedings

Volume 70/1

The International Federation for Medical and Biological Engineering, IFMBE, is a federation of national and transnational organizations representing internationally the interests of medical and biological engineering and sciences. The IFMBE is a non-profit organization fostering the creation, dissemination and application of medical and biological engineering knowledge and the management of technology for improved health and quality of life. Its activities include participation in the formulation of public policy and the dissemination of information through publications and forums. Within the field of medical, clinical, and biological engineering, IFMBE's aims are to encourage research and the application of knowledge, and to disseminate information and promote collaboration. The objectives of the IFMBE are scientific, technological, literary, and educational.

The IFMBE is a WHO accredited NGO covering the full range of biomedical and clinical engineering, healthcare, healthcare technology and management. It is representing through its 60 member societies some 120.000 professionals involved in the various issues of improved health and health care delivery.

IFMBE Officers
President: James Goh, Vice-President: Shankhar M. Krishnan
Past President: Ratko Magjarevic
Treasurer: Marc Nyssen, Secretary-General: Kang Ping LIN
http://www.ifmbe.org

More information about this series at http://www.springer.com/series/7403

Rodrigo Costa-Felix · João Carlos Machado ·
André Victor Alvarenga
Editors

XXVI Brazilian Congress on Biomedical Engineering

CBEB 2018, Armação de Buzios, RJ, Brazil,
21–25 October 2018 (Vol. 1)

Editors
Rodrigo Costa-Felix
INMETRO-Instituto Nacional de Metrologia
Qualidade e Tecnologia
Duque de Caxias, Rio de Janeiro, Brazil

João Carlos Machado
Federal University of Rio de Janeiro
Rio de Janeiro, Brazil

André Victor Alvarenga
INMETRO-Instituto Nacional de Metrologia
Qualidade e Tecnologia
Duque de Caxias, Rio de Janeiro, Brazil

Conference Organization Board

Chair

Rodrigo Costa-Felix, National Institute of Metrology, Science and Technology (Inmetro) and SBEB

Executive Secretary

Thais Medeiros, Brazilian Society of Metrology (SBM)

Members

Financial Chair

Helio Schechtman, Fiocruz and SBEB

Scientific Chair

João Carlos Machado, Federal University of Rio de Janeiro (UFRJ)

Editorial Chair

André Victor Alvarenga, Inmetro

Biomedical Engineering Innovation Camp (DEDEB)

Elyr Teixeira, Senfio

Biomedical Engineering Thematic Challenge (DETEB)

Marcio N. Souza, UFRJ

Monitoring Committee

SBEB President

Adriano O. Andrade, Federal University of Uberlândia (UFU) and SBEB

SBEB Board Chair

Wagner Coelho de Albuquerque Pereira, UFRJ and SBEB

CBEB 2016 Chair

Joaquim Miguel Maia, UTFPR and SBEB

CBEB 2020 Chair

Teodiano F. Bastos, UFES

Scientific Committee

Bioengineering

José Wilson Magalhães Bassani
Rosana A. Bassani

Biomaterials, Tissue Engineering and Artificial Organs

Idágene Aparecida Cestari
Sônia Maria Malmonge

Biomechanics and Rehabilitation

Antonio Augusto Fasolo Quevedo
Liliam Fernandes de Oliveira

Biomedical Devices and Instrumentation

Percy Nohama

Biomedical Robotics, Assistive Technologies and Health Informatics

Alcimar Barbosa Soares
Carlos Julio Tierra Criollo

Biomedical Signal and Image Processing

Antonio Mauricio Ferreira L. Miranda de Sá
Marco Antonio Gutierrez

Clinical Engineering and Health Technology Assessment

Roberto Macoto Ichinose
Rosimary Terezinha Almeida

Metrology, Standardization, Testing and Quality in Health

Adriano de Oliveira Andrade
Antonio Adilton Oliveira Carneiro

Neural Engineering

Antonio Carlos Guimarães de Almeida

Special Topics

Joaquim Miguel Maia

Systems and Technologies for Therapy and Diagnosis

Liliane Ventura
Renato Amaro Zângaro
Renato Evangelista de Araujo

Reviewers

Adalberto Schuck Junior
Adjaci Uchoa Fernandes
Adriana Barrinha Fernandes Moretti
Adriana del Monaco Maria
Adriana Fontes
Adriana Kauati
Adriana Maria Wan Stadnik
Adriane Mara de Souza Muniz
Adriane Muniz
Adriano Almeida Gonçalves Siqueira
Adriano Alves Pereira
Adriano de Oliveira Andrade
Adson Ferreira da Rocha
Agma Traina
Alcimar Barbosa Soares
Alessandro Beda
Alessandro Drena
Alessandro Márcio Hakme Silva
Alessandro Melo de Ana
Alexandre Colello Bruno
Alexandre Henrique Hermini
Alexandre Visintainer Pino
Alfonso Rosales López
Aline do Nascimento
Aluizio d'Affonseca Netto
Alysson Roncally Silva Carvalho
Amauri Amorin Assef
Ana Claudia Patrocinio
Ana Paula Christakis Costa
Ana Paula de Souza
Ana Paula Fontana
Anderson Gabriel Santiago
André Fábio Kohn
Andre Luis Baggio
Andre Salles Cunha Peres
André Thiago Jonathas Alves
André Victor Alvarenga
Andrea Fonseca da Cruz
Andrea Ottoni
Andréa Pereira de Morais
Anselmo Frizera
Antonio Adilton Oliveira Carneiro
Antonio Augusto Fasolo Quevedo
Antonio Balbin Villaverde
Antonio Carlos Gonçalves
Antonio Carlos Shimano
Antonio Giannella Neto
Antônio Márcio Rodrigues
Antonio Mauricio F. L. Miranda de Sá
Antonio Padilha Lanari Bó

Antônio-Carlos G. de Almeida
Arnaldo Fim Neto
Arturo Forner-Cordero
Arturo Rodriguez Cristerna
Beatriz Luci Fernandes
Beatriz Stransky
Bertoldo Schneider Júnior
Bruno Raphael Pastor de Melo
Bruno Vilhena Adorno
Carla Alessandra Scorza
Carlos Alberto Cimini Jr.
Carlos Alexandre Ferri
Carlos Bolli Mota
Carlos Dias Maciel
Carlos Gomes de Oliveira
Carlos José de Lima
Carlos Julio Tierra Criollo
Carlos Marcelo Gurjão de Godoy
Carlos Toshiyuki Matsumi
César Teixeira
Christian Tolentino Dominguez
Christiane Bertachini Lombello
Christiane Ribeiro
Cicero Ferreira Fernandes Costa Filho
Cinthia Itiki
Claudia Cristina Brainer de Oliveira Mota
Claudia Domingues Vargas
Claudia Maria Cabral Moro Barra
Clayton Augusto Benevides
Clayton Moura Belo
Cleudmar Amaral de Araujo
Cleudmar Araujo
Cristine Gusmão
Daniel Castello
Daniel Gustavo Goroso
Danilo Alves Pinto Nagem
Danilo Barbosa Melges
Dario Augusto Borges Oliveira
Denise Zezell
Denny Daniel Collina
Diego Rativa
Diogo Coutinho Soriano
Diogo Wachtel Granado
Ebenézer Silva Cavalcanti
Eddy Krueger
Edgard Afonso Lamounier
Edna Marina de Souza
Edson Antunes
Edson Capello Souza
Eduardo Bock

Preface

The slogan of the XXVI Brazilian Congress on Biomedical Engineering (CBEB 2018) is not a simple compilation of words. It is, in fact, the claiming from an emerging culture regarding the scientific research, technological development, and transfer of technology: "The exact measure of technological development and innovation in health". In its 26th edition, the congress acquires a maturity to take off from the academic ground to a much more prospective aspect in the productive chain. The Biomedical Engineering community in Brazil is highly aware about the social and economic affairs we can accomplish with, and the CBEB 2018 discloses a new open door of opportunities to our colleagues, whatever is the main concern of activity. The Brazilian Society on Biomedical Engineering (SBEB) uses this most preeminent national conference to call the attention of its members about the challengers we are facing nowadays. A bright future is under course, and we all must be well prepared for that.

The event has the tradition of bringing together academic communities, researchers, scientists from several fields, undergraduate and graduate students, as well as representatives from industry, commerce, and governments, so that everyone can discuss and present their ideas on key problems of Biomedical Engineering in the country.

In 5 days, from October 21 to 25, 2018, The Brazilian Congress on Biomedical Engineering, a biennial conference promoted by the Brazilian Society of Biomedical Engineering, received more than 600 participants with different levels of formal education. More than 700 papers were submitted, from which the 500 outstanding ones were approved to be presented in the congress. Among them, 272 full papers are published in this memorable IFMBE Proceedings.

Following a thorough peer-reviewed process, we have finally selected the 272 full papers, and the Scientific Committee would like to thank the reviewers for their outstanding job. The articles found in the proceedings are divided into 11 thematic areas, namely, Clinical Engineering and Health Technology Assessment, Biomaterials, Tissue Engineering and Artificial Organs, Bioengineering, Biomedical Devices and Instrumentation, Biomechanics and Rehabilitation, Neural Engineering, Biomedical Signal and Image Processing, Biomedical Robotics, Assistive Technologies and Health Informatics, Systems and Technologies for Therapy and Diagnosis, Metrology, Standardization, Testing and Quality in Health, and Special Topics, showing how broad is the spectrum of topics in biomedical engineering.

The editors would like to thank all the participants for their high-quality contributions and Springer for publishing the proceedings of the XXVI Brazilian Congress on Biomedical Engineering (CBEB 2018).

Duque de Caxias, Brazil   Rodrigo Costa-Felix
                                                                   President of the Congress

Duque de Caxias, Brazil   André Victor Alvarenga
                                                                          Editor-in-Chief

Rio de Janeiro, Brazil   João Carlos Machado
                                                        President of the Scientific Commission

Acknowledgements

Organizing Society

SBEB

International Society

IFMBE

Supporting Institutions

ABIMO
ASSOCIAÇÃO BRASILEIRA DA INDÚSTRIA DE ARTIGOS E EQUIPAMENTOS
MÉDICOS, ODONTOLÓGICOS, HOSPITALARES E DE LABORATÓRIOS

CAPES

CNPq
Conselho Nacional de Desenvolvimento
Científico e Tecnológico

OPEND'Or

sociedade brasileira de
metrologia

SEBRAE

FIEPA SESI SENAI IEL **SENAI**

Sponsors

EQUIPACARE

SENFIO

Contents

Part IV   Biomedical Devices and Instrumentation

Part VI   Clinical Engineering and Health Technology Assessment

Part VII   Metrology, Standardization, Testing and Quality in Health

Contents

Cell-Tracking System

Fernanda dos Santos Costa Leomil and Pedro Xavier de Oliveira

Abstract

Isolated cells are often chosen for study rather than whole tissues because they can sufficiently represent systems of great complexity. However, conducting experiments with isolated cells is greatly hampered since the available environment is, at first sight, disorganized, due to random cell positioning. Finding a way to improve the performance of the experiments and to enable the organization and selection of an adequate experimental sample population is of great value to researchers. The present work describes a system for tracking isolated cells based on the controlled automation of the *charriot* of a microscope, in order to streamline and simplify this procedure. A microscope was adapted, from non-inverted to inverted, and stepper motors were coupled to its stage so that, by means of toothed belts, their movements were transmitted to the *charriot* axes, which became microcontrolled with the aid of a control system consisting of a joystick and 12 buttons. The new system allowed tracking suitable cells by memorizing their initial positions and later moving the *charriot* back to the stored coordinates. We believe that this is a practical and relatively simple solution that can be easily reproduced in other research laboratories.

Keywords

Cell-tracking • Microcontrolled microscope • Automated microscope charriot

F. dos Santos Costa Leomil (✉) · P. X. de Oliveira
Department of Biomedical Engineering, School of Electrical and Computer Engineering, University of Campinas, Campinas, São Paulo, Brazil
e-mail: fernandascleomil@gmail.com

P. X. de Oliveira
Center for Biomedical Engineering, University of Campinas, Campinas, São Paulo, Brazil

1 Introduction

Several reasons have been motivating researchers to focus their studies on isolated cells rather than whole tissues. In general, cells serve as a way to simplify and represent, subtly but with great credibility, an entire complex system and to reveal mechanisms that are hidden when the whole set is observed. For example, cancer research uses isolated cells to identify structural variants within them in a tissue; neuroscience research uses them to analyze cell functions and mechanisms in order to try do understand more complex phenomena like muscle control and thoughts; in the field of genetics, the whole DNA sequencing is based on the knowledge of individual cells. These are just a few examples, among many other, that use one of the smallest biological structures to seek knowledge and to reveal solutions for various health issues [1–3].

Experiments with isolated cells consist of depositing cell samples in a totally random manner in a cover glass, creating a disorganized experimental environment. However, experimental protocols require the selection of cells with standard characteristics in order to allow comparisons of parameters of interest. For example, parameters such as dimensions and orientation of excitable cells are known to influence the determination of the lethal injury by electric field [4]. Thus, if one's objective is to determine the relationship between lethal injury by electric field and direction, one should seek groups of cells with similar dimensions so that this parameter does not interfere in the investigated relation.

Many technologies have emerged trying to simplify the experimentation processes that will accompany the research [5]. The objective of this work was to develop a system capable of simplifying the process of experimentation with isolated cells, by creating a cell-tracking system through automated control of the *charriot* (and, consequently, the stage) of a microscope, making it possible to organize and select samples of interest more efficiently. The system developed and presented here allows the use of a microscope

to observe samples of isolated cells deposited in glass containers directly in the computer and to move this container (setted up at the stage of the microscope) in a microcontrolled way, also making it possible to store and retrieve cell positions automatically.

2 Methods

The developed system consists of a microscope with a motorized *charriot* (1) and a control system (2).

(1) The base of a Nikon non-inverted microscope was adapted for an inverted microscopy system, i.e., the illumination source was positioned at the top and the objective lens at the bottom. This construct is widely applied for the observation of living cells and organisms. Below the objective was installed a webcam so that the images were observed directly in a computer. A representation of this construction can be seen in Fig. 1.
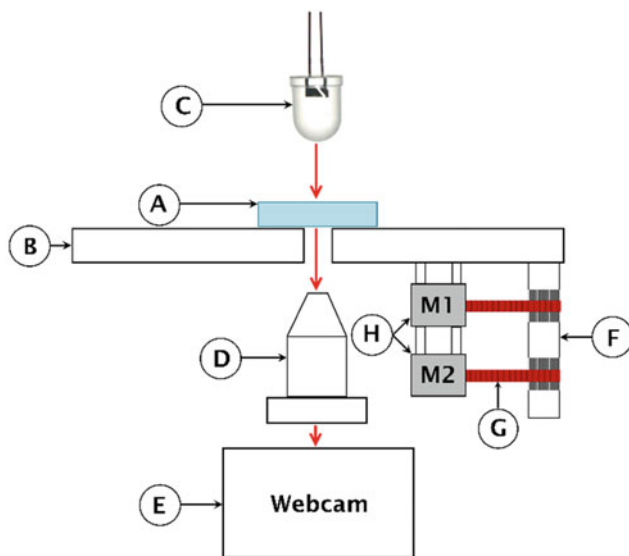
Fig. 1 Representation of the microscopy system. **a** Perfusion/stimulation chamber or slide to be analyzed. **b** XY stage of the microscope. **c** Hight luminance white LED (Super Bright LED, jumbo, 5000 mcd, 1,85 V, 20 mA, Archer, N. Cat. 276–086) powered by a 9 V battery. **d** Objective lens. **e** Webcam. **f** *Charriot*. **g** Toothed belt. **h** Stepper motors (M1 and M2)

Two bipolar stepper motors with an angular displacement of 3.6° per step, running in full step mode, were mechanically adapted to the microscopy system so that its stage control (*charriot*) could be moved by means of microcontroller commands. These motors were driven through drivers (L298N) consisting of two H bridges.

(2) A system to control the stepper motors was constructed in order to facilitate the localization of cells and enable the storage and retrieval of their positions. The panel consists of a joystick, containing two potentiometers and a key, used to select the direction (x or y) in which the *charriot* will be moved, in the horizontal plane; an LCD (liquid-crystal display), model JHD539M with 64 characters, used as a user interface, to inform if the positions of the cells have been stored and, in this case, if the user wants to overwrite some position; 12 buttons used for storing and retrieving up to 12 cell positions. The electronic circuit of the system can be seen in Fig. 2.

The microcontroller used was a PIC18F4550 (Microchip Technology Inc., Chandler, AZ, USA) with a 20 MHz; the software was developed in C in the MPLAB IDE® development environment (Microchip Technology Inc., Chandler, AZ, USA) and compiled by the XC8 compiler (Microchip Technology Inc., Chandler, AZ, USA). The flowchart of the developed software is presented in Fig. 3.

After the beginning of the program, the movement of the joystick is checked by means of the voltage measurement on the analogue ports of the microcontroller associated with each of the two internal potentiometers. First, the program checks whether the two potentiometers are being driven simultaneously, i.e., if the joystick is being moved in any diagonal, and if so, the motors must remain standing. If not, the program checks whether the voltage applied to the potentiometer responsible for driving motor 1 (PotY) is between 2 V and 3 V (potentiometer resting position). If it is negative, indicating that the motor must be activated, the "Move motor 1" subroutine is called, which is responsible for driving the coils of motor 1, described in Fig. 4a, and responsible for moving the *charriot* on the y-axis. If it is positive, the motor 1 should remain stopped so the "Stop motor 1" subroutine is called and the program is continued by checking the voltage in the potentiometer responsible for driving motor 2 (PotX), which operates similarly to the
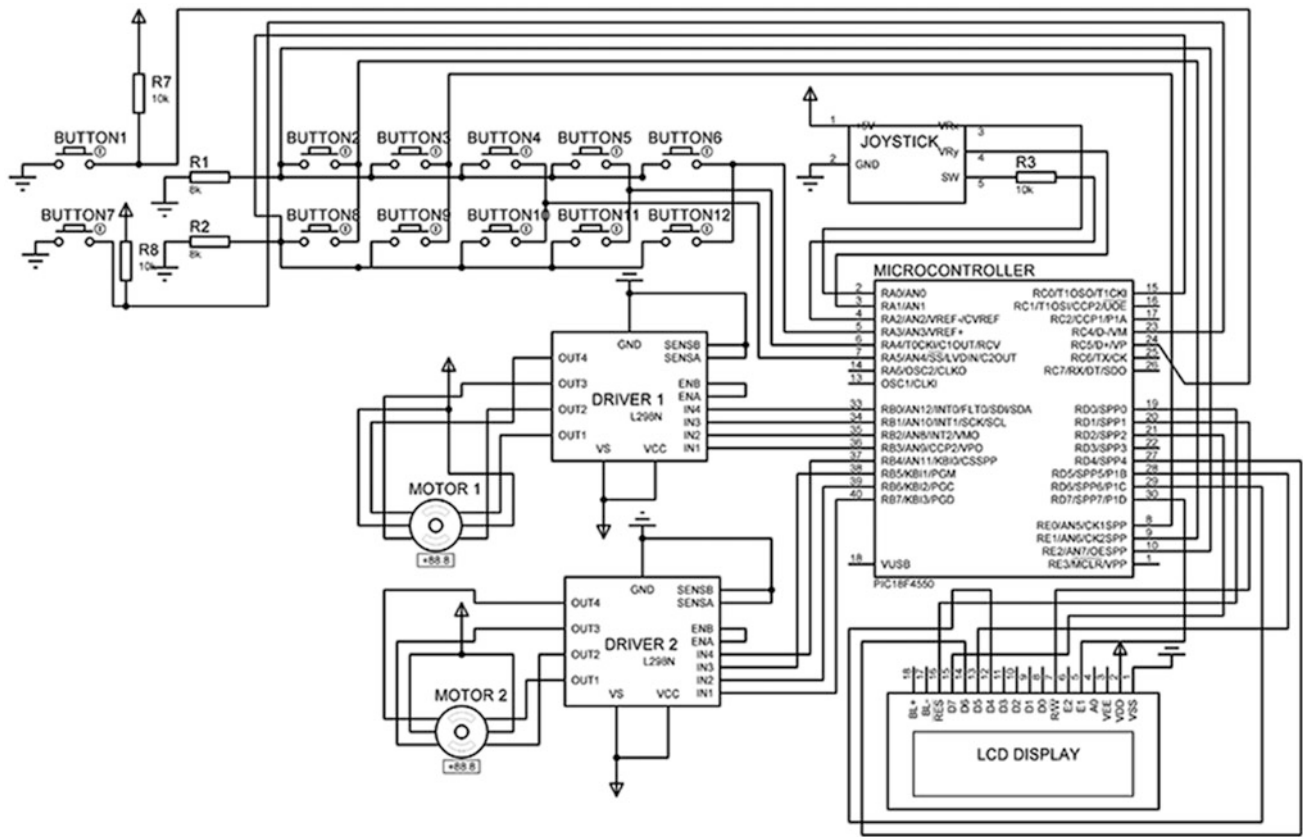
Fig. 2 *Charriot's* movement electronic control circuit

previous one. If it is not in its resting position (2–3 V), the "Move motor 2" subroutine is called (Fig. 4b), moving the *charriot* on the x-axis, and otherwise the "Stop Motor 2" subroutine is called. At each step of the motor there is an increment (if the engine turns clockwise) or decrement (if the engine turns counterclockwise) of the variable that contains the motor's current position (positionY for motor 1 and positionX for motor 2).

Then, the buttons are checked. The subroutine responsible for storing, retrieving or overwriting positions is shown in the flowchart of Fig. 5. If one of the buttons has been pressed, after debounce control, the program checks for how long the button was pressed.

If the button was pressed for more than 4 s, indicating that the user wishes to store a position on that button, the program verifies if it is the first time that button is being pressed, and, if so, the positions of the motors in X and Y at that instant (X position and Y position) are stored in new variables associated to each of the motors and to each of the buttons (finalPositionX and finalPositionY). If it was not the first time the button was pressed, that is, it already has a stored position, the user is prompted to press button 1 within 10 s if he/she wants to overwrite the position on that button. However, if the button was pressed for a time less than 4 s, indicating that the user wants to retrieve a stored position on that button, the program drives motors 1 and 2 until the current positions in X and Y match the positions stored in finalPositionX and finalPositionY.

The "Stop Motor 1" and "Stop Motor 2" subroutines, called in the flowcharts of Figs. 4 and 5, consist of setting zero logic level on the ports of the PIC associated with the motor coils so that the drive of each motor is impossible, since there will be no current flowing through the driver. The motor remains stopped whenever the measured voltage on the joystick potentiometer is between 2 and 3 V, the joystick's rest position.

In order to verify that the recovery of positions was being satisfactorily made, a test was performed with each motor,

Fig. 3 Flowchart of the main routine
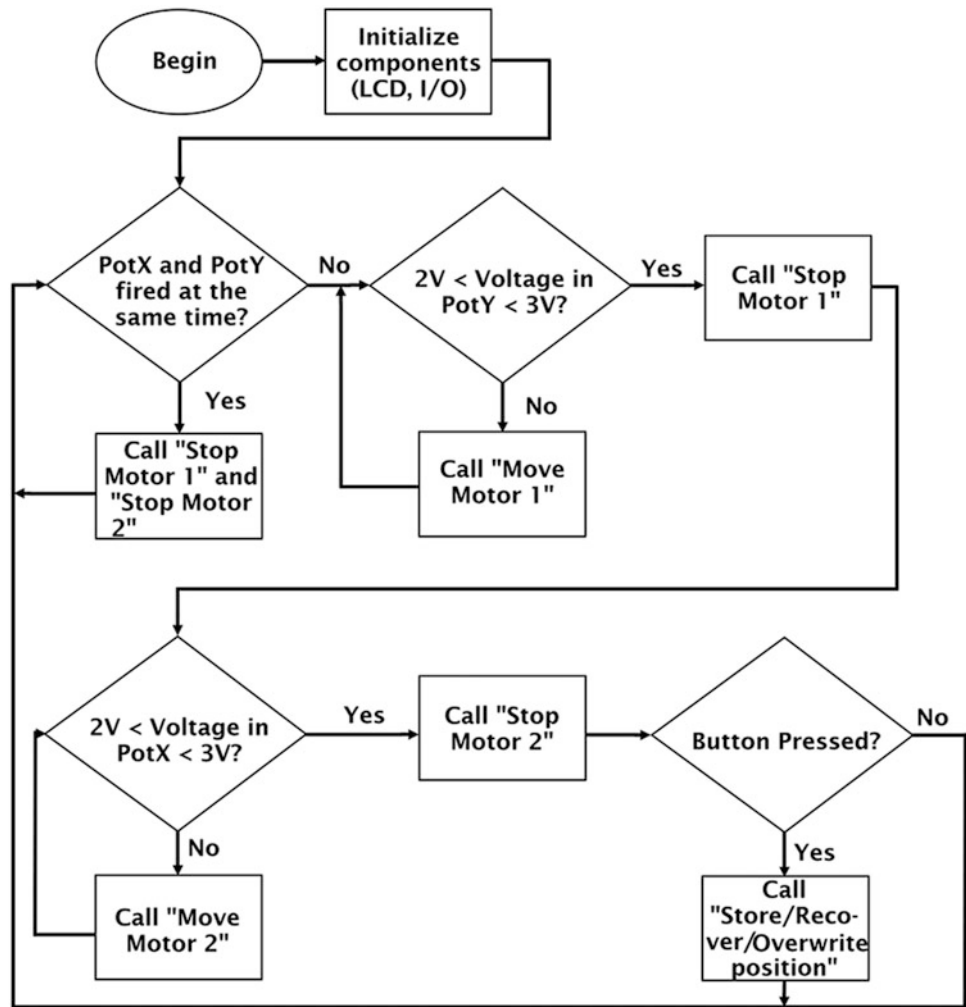
with the aid of a 10 μm precision graticule and the previous known of the displacement in μm per step of each one of the motors. This test always started from the same point in the graticule, where the user determined the number of steps the motor should be driven (10, 50, 100 or 150 steps) and pressed a button. Then, the distance associated with this number in μm was measured using an image editing software.

2.1 Testing with Living Cells

In order to test the effectiveness of the constructed system, it was applied to an experiment with ventricular myocytes isolated from adult male Wistar rats (4–6 months old). In this experiment, we sought to study the relationship between the stimulation threshold (E_T: minimal electric field capable of causing myocyte contraction) and myocytes orientation (myocytes whose major axis was oriented at 0°, 30°, 60° and 90° in relation to the applied electric field (E)).

2.1.1 Myocyte Isolation

Myocytes from the left ventricle were isolated by enzymatic digestion of the heart [6]. After the heart removal, the aorta was cannulated and the heart perfused for 4–5 min with Krebs solution. Type I collagenase (0.4–0.5 mg/ml; Worthington Biochemical Corporation, Lakewood, NJ, USA) was then added to this solution and the heart was perfused for 15–20 min. To stop enzymatic digestion, the heart was perfused with TyrCl containing bovine serum albumin (0.5 mg/ml; Calbiochem, San Diego, CA, USA) for approximately 10 min. Finally, the ventricle, after dissecting, was delicately shaken in cardioplegic solution for dissociation of the cells.

(a) Move Motor 1
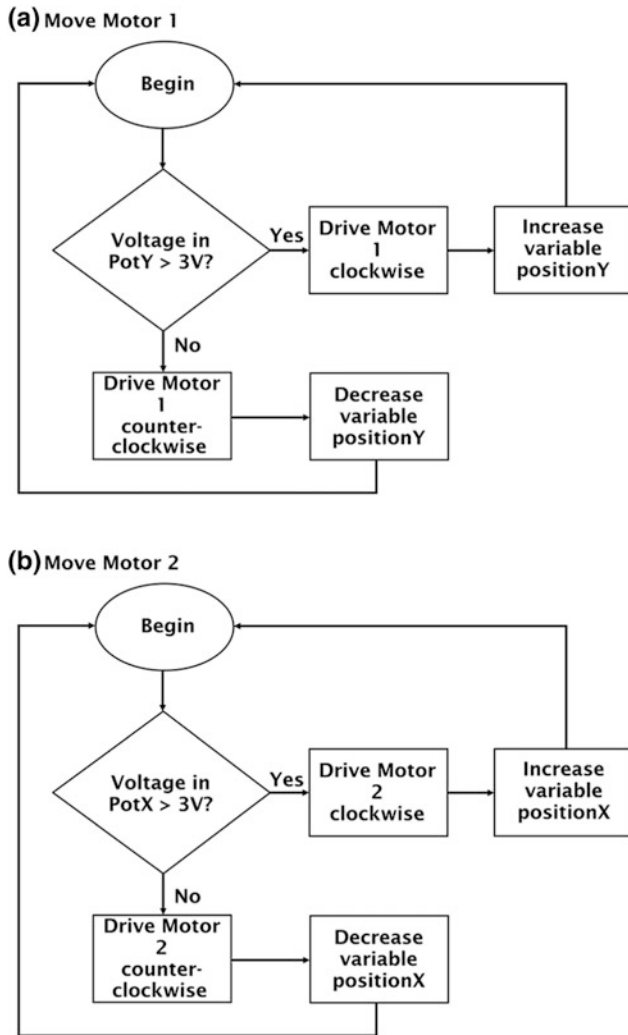
(b) Move Motor 2

Fig. 4 Flowchart of the subroutines used to drive the stepper motors: **a** Move motor 1. **b** Move motor 2

The experimental procedure with animals was approved by the Commission of Ethics in the Use of Animals of the Institute of Biology of UNICAMP (protocol no. 4093-1 (K)) on 12/16/2015.

2.1.2 Experimental Protocol

After the cell isolation process, cells were deposited in a rectangular perfusion/stimulation chamber [7]. Inside the chamber the distribution of E is uniform and the cells are randomly positioned in relation to E. The chamber was then fixed with screwdrivers in the microscope's *charriot*. The electrodes were connected to a low intensity stimulator that produced bipolar electrical voltage pulses with a total

duration of 10 ms at 0.5 Hz (CEB/Unicamp fabrication). The constructed system allowed the study of 12 cells in a single chamber. With its use, cells positioned at 0°, 30°, 60° and 90° with respect to E had their positions stored in each of the buttons arranged in the box panel and could be followed throughout the experiment. For each cell E_T was measured by decreasing the stimulator output voltage until the cell stopped responding to the stimuli by means of contractions which indicated that the stimulation threshold had been reached. At the end of the experiment, it was possible to obtain mean values of E_T for different cell orientations.

This procedure was done once as an exploratory analysis.

3 Results

A picture of the mechanical coupling between the stepper motors and the microscope's *charriot* is shown in Fig. 6. The motors were attached to the lower base of the microscope stage by means of screws (Fig. 6a) and nylon-made gears were attached to the drive shafts X and Y of the *charriot* (Fig. 6b) to transmit, with the aid of toothed belts, the movements from the stepper motors' gearbox.

The displacement of the x-axis was 5.5 ± 0.025 μm per step and, for the y axis, was 9.1 ± 0.026 μm per step (Fig. 7). Such displacements were different for each motor because the gears ratios linked to the two axles of the *charriot* are different. However, as expected, the motors presented a linear behavior and a small variation of the displacement with respect to the number of steps (standard deviation can barely be seen in Fig. 7), which is important to ensure the accurate retrieval of cell positions.

A picture of the complete system is presented in Fig. 8. After the adaptation, the LED-based lighting system was positioned at the top of the microscope (Fig. 8a). One can see the perfusion chamber, where the cells are deposited, positioned on the stage which is mechanically coupled to the stepper motors (Fig. 8b). The control system consists of a joystick positioned at its top (Fig. 8c) and 12 buttons used to store and retrieve cell positions (Fig. 8d).

It can be seen in Fig. 9 a picture obtained during an experiment with isolated cardiac myocytes using the constructed system. One can clearly observe important characteristics of these cells, such as, for example, the presence of striations and their well-defined contour.

Figure 10 presents the mean values of E_T for cells oriented at 0°, 30°, 60° and 90° with respect to E direction. We
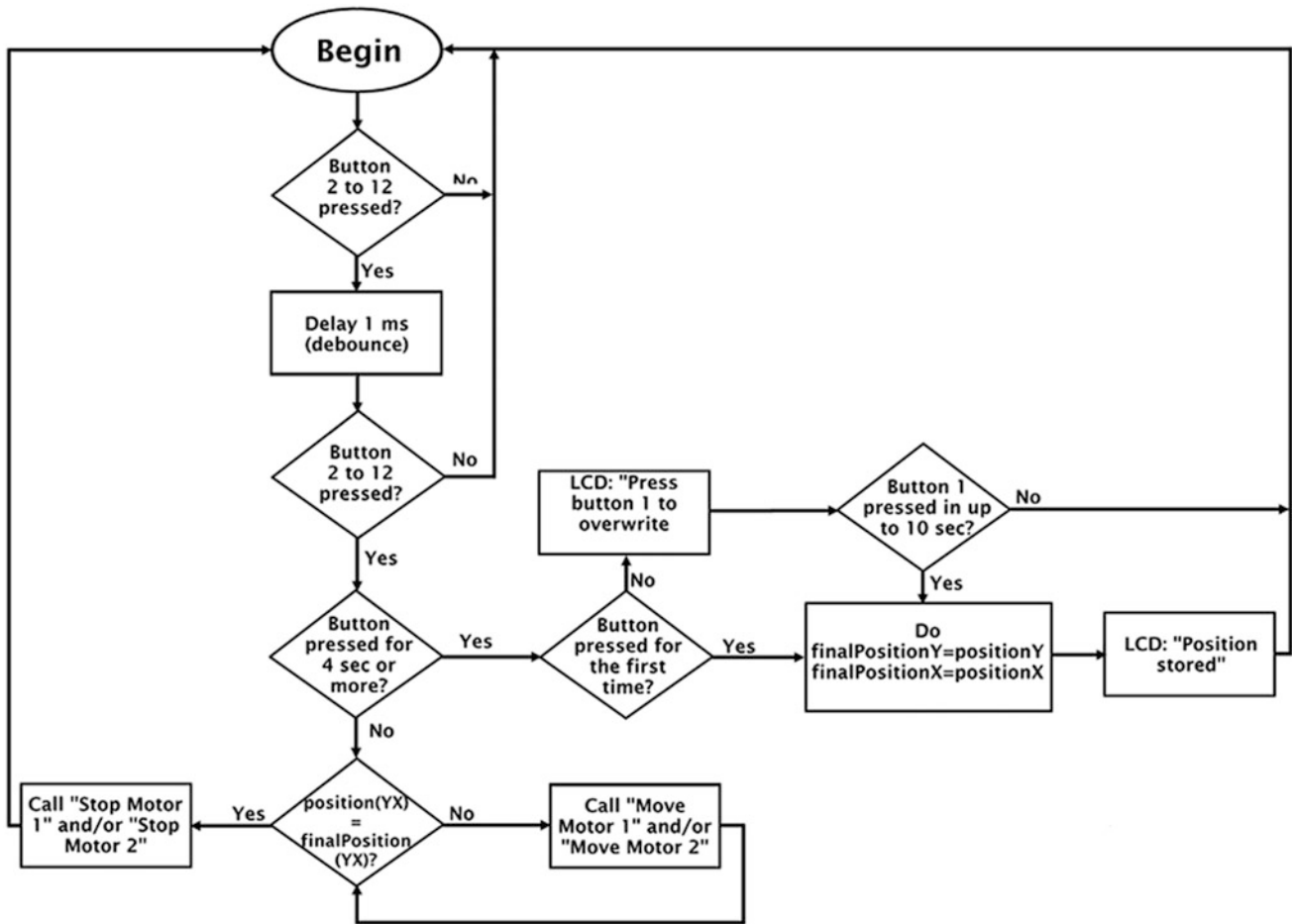
Fig. 5 Flowchart of the button treatment subroutine

were able to analyze 4 cells at 0°, 3 cells at 30°, 3 cells at 60° and 2 cells at 90°. The symbols refer to the mean values and the vertical lines indicate the standard deviation of the mean.

4 Discussion

4.1 The System

The developed system is highly supportive for conducting experiments with isolated cells. The modification performed in the microscope, from non-inverted to inverted with the inclusion of a webcam, allowed the objective to be close to the cell sample so that images with satisfactory quality could be obtained.

The experiments with cells in the system developed in this work were performed with greater speed and precision when compared to experiments in which the *charriot* was manually moved. The microscope's stage shifts were smoother and smaller than in the manual mode.

It was also possible to store and retrieve positions of several cells inside the chamber and, with this, to carry out the experiment always with the most suitable cell, which was dependent on the experimental protocol in question. The retrieval of positions was satisfactory, so that in 100% of cases, the retrieved position showed the cell within the field of view of the camera.

4.2 Testing with Living Cells

The experiment was done with the intention of providing an exploratory analysis. From the obtained result it was possible to study 12 cells in a single chamber and to monitor the
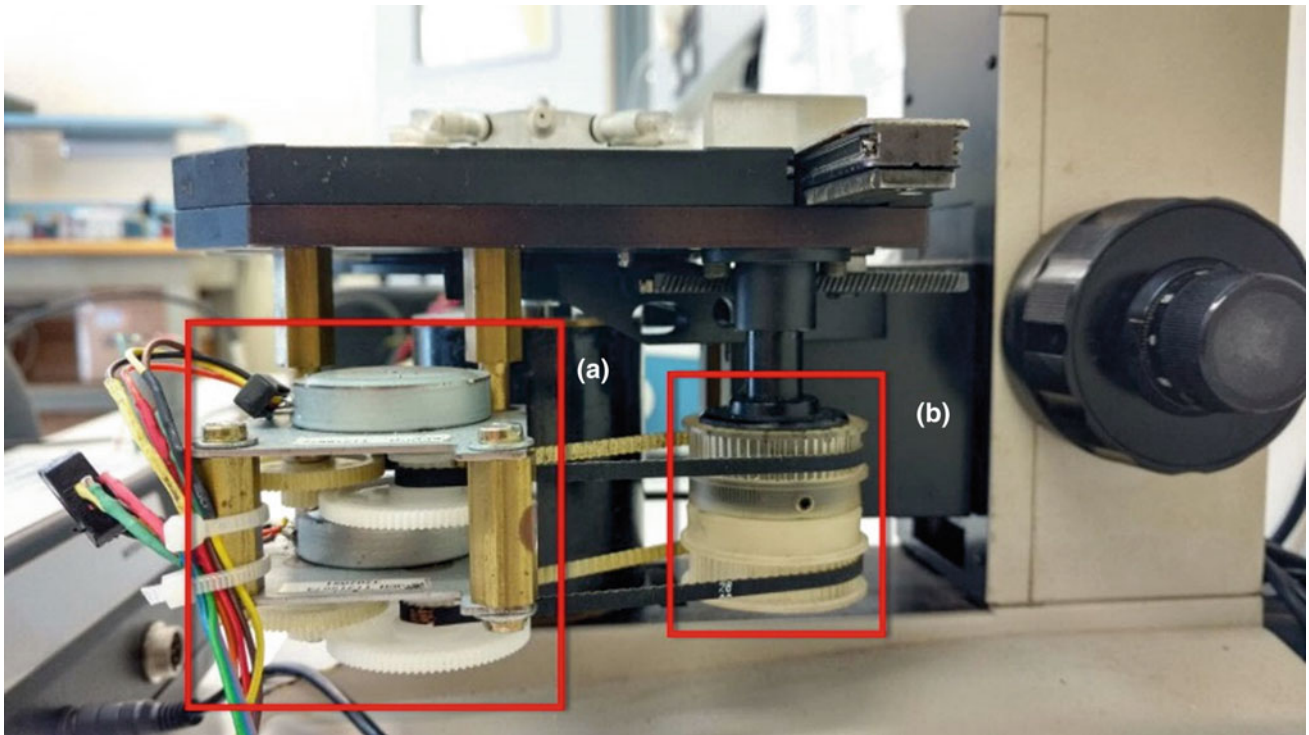
Fig. 6 Picture highlighting the mechanical coupling between the stepper motors and the *charriot*. **a** Stepper motors fixed to the bottom of the microscope's stage with screws. **b** Nylon gears fixed by screws and glue to the axles of the *charriot*
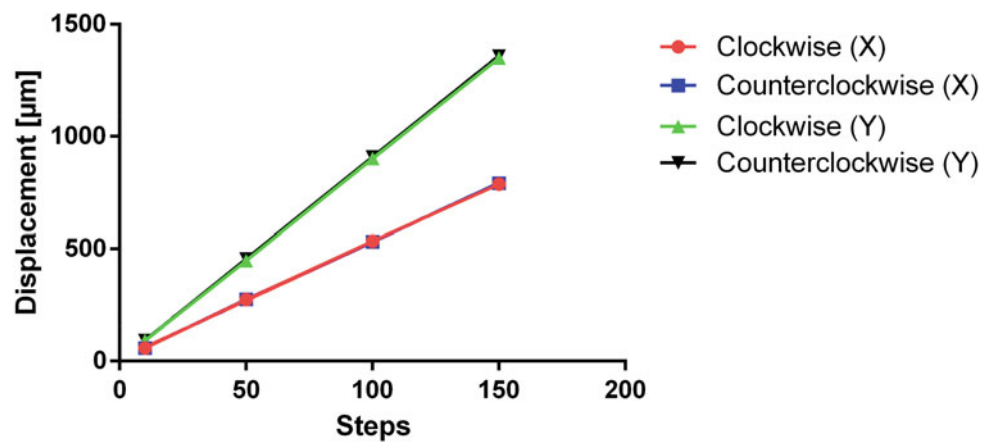
Fig. 7 Relation between the displacement of the *charriot* and the number of steps of the motor. The green and black lines correspond to the displacement of the *charriot* in the positive and negative directions of the horizontal axis (X) and the red and blue lines correspond to the displacement in the positive and negative directions of the vertical axis (Y)

Fig. 9 Picture of a cardiac myocyte obtained with the constructed system using a 40X objective lens. In the image it is possible to observe some characteristics of the cell, such as its dimensions and the presence of striations

Fig. 8 Picture of the developed system. **a** Lighting system positioned at the top of the microscope. **b** Perfusion chamber positioned on the stage of the microscope which is coupled to the stepper motors. **c** Joystick attached to the top of the control system, used to move the *charriot*. **d** 12 buttons used for storage and retrieval of cell positions
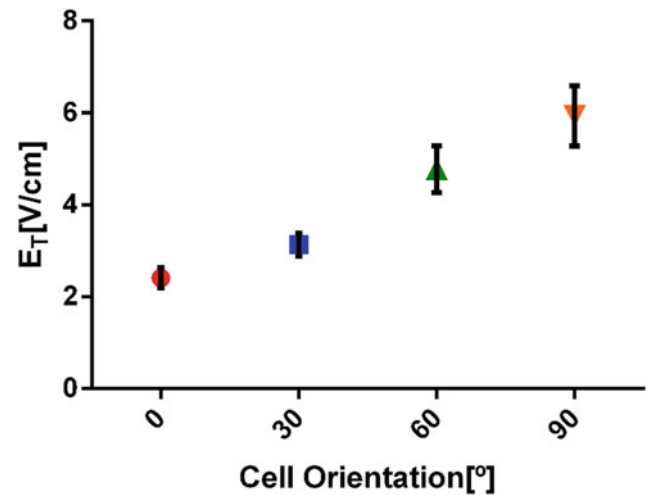
Fig. 10 Mean values and standard deviation of stimulation threshold for cells oriented at 0º, 30º, 60º and 90º with respect to electrical field direction

5   Conclusions

The system developed in this work allowed cell experiments to be performed faster and with greater ease than in the usual mode. Moreover, the system appears as a simple and relatively inexpensive solution when compared to others capable of providing the same solutions presented here, and it can be implemented without major difficulties in laboratories of

behavior of each one in response to a stimulus without their positions being lost.

Figure 10 presented the mean values for E_T for four different cell orientations: 0°, 30°, 60° and 90°. It indicates an increase tendency of E_T as cell orientation with respect to E direction also increases, as it has already been shown in the literature [4].

different research sectors (it is estimated that the approximate cost of the prototype was R$ 500.00, not including labor). Of course, improvements may be included in this system in order to make it even more suitable for researchers in the development of cell-related work.

Conflict of Interest The authors declare that they have no conflict of interest.

References

1. Hjortland, G.O., et al.: Genome wide single cell analysis of chemotherapy resistant metastatic cells in a case of gastroesophageal adenocarcinoma. BMC Cancer **11**, 455 (2011)

2. Why Scientist analyze single cell, Qiagen. https://www.slideshare.net/QIAGENscience/why-scientist-analyze-single-cells. Accessed 30 Mar 2018

3. Gawad, C., Koh, W., Quake, S.R.: Single-Cell genome sequencing: current state of the science. Nat. Rev. Genet. **17**(3), 175 (2016)

4. de Oliveira, P.X., Bassani, R.A., Bassani, J.W.M.: Lethal effect of electric fields on isolated ventricular myocytes. IEEE Trans. Biomed. Eng. **55**(11), 2635–2642 (2008)

5. Resources to single cell analysis, Qiagen. https://www.qiagen.com/nl/resources/knowledge-area/single-cell-resource/. Accessed 30 Mar 2018

6. Penna, L.B., Bassani, R.A.: Increased spontaneous activity and reduced inotropic response to catecholamines in ventricular myocytes from footshock-stressed rats. Stress **13**(1), 73–82 (2010)

7. Gomes, P.A.P.: Aplicação de técnicas de engenharia no estudo de células cardíacas isoladas: medição de [Ca2 +] e limiar de estimulação (Doctoral dissertation) (1997). http://repositorio.unicamp.br/jspui/handle/REPOSIP/260545

Comparison of Three Different Mathematical Models Applied to Respiratory Mechanics During Bronchoconstriction

Amanda N. Barros, Renato de L. Vitorasso, Marcelo H. Valenga,
Fabio Gava Aoki, Thiago Guimarães Rodrigues, Paulo F. G. Cardoso,
Rogério Pazetti, and Henrique T. Moriya

Abstract

The assessment of respiratory mechanics is usually made by mathematical models. The simplest and one of the most known models is the *Linear Single-Compartment Model* (*LSCM*). The main prerogative of LSCM is linearity. However, the respiratory system does not have a linear behavior under several circumstances and the objective of this work is to compare the LSCM with 2 nonlinear models. In order to fulfill these comparisons, 6 male *Wistar* rats were studied during bronchoconstriction. Using a commercial ventilator, the LSCM and two nonlinear variations of this model were applied during mechanical ventilation in basal and during two doses of methacholine (MCh) a bronchoconstrictor. The two nonlinear models were: (1) a volume-dependent single compartment model, which have a nonlinear term related to elastance; (2) a flow-dependent single compartment model, which have a nonlinear term related to resistance. This study evaluated the adjustment of models to the measured pressure value and the evaluation of these models was conducted using the *F*-ratio test, which is based in comparison of variances, and the Akaike criterion, that measures the difference between the model and the sample values. Through of the value of *mean squared residual*, the results indicate improvement at the approximation when we add the nonlinear terms in relation to the linear model, in most cases, mainly the volume-dependent single compartment model. And another result is that the Akaike criterion presented a more effective comparison during the evaluation than the *F*-ratio test.

Keywords

Respiratory mechanics • Mathematical models • Nonlinearity

1 Introduction

The mathematical models are important tools to model systems [1]. Each model presents their own complexity and characteristics. One of the main characteristics that differentiate one model from another is linearity, since there are linear and non-linear models [2]. Another important characteristic is the number of modeled parameters. This characteristic is relevant, since the modeled parameters, in studies of respiratory mechanics, must present physiological meaning [3]. A model with an excellent fit and many parameters with no physiological meaning is not useful to a biomedical study.

In the last years, the assessment of respiratory mechanics using small animal ventilators (SAV) contributed for a better understanding of diseases physiology that affect the respiratory system [4], such as bronchitis and asthma, which caused approximately 5 deaths/day in Brazil in 2013 [5].

Another important feature present in the studies of respiratory mechanics is the challenge of the system. Usually, some challenge is imposed to the system in order to highlight a potential difference and, probably, one common method of challenge the system is the bronchoconstriction induced via methacholine (MCh). The bronchoconstriction is the 'narrowing of air passages of the lungs from smooth muscle contraction, as in asthma' [6].

The evaluation of respiratory mechanics may be done via time or frequency domain modeling. Even the simplest models, i.e. the time domain ones, as the models studied in this work, may or may not present non-linear terms.

In addition, it is known that the lung has a nonlinear mechanical behavior under several circumstances [3], as observed in numerous diseases or, e.g., in a

A. N. Barros (✉)
Institute of Mathematics and Statistics, São Paulo, Brazil
e-mail: manda.n.barros@gmail.com

A. N. Barros · R. de L. Vitorasso · M. H. Valenga · F. G. Aoki ·
T. G. Rodrigues · H. T. Moriya
Laboratory of Biomedical Engineering, Escola Politécnica of the
University of São Paulo, São Paulo, Brazil

P. F. G. Cardoso · R. Pazetti
Thoracic Surgery Research Laboratory (LIM 61), Instituto do
Coração, São Paulo, Brazil

bronchoconstriction caused by MCh [7]. Thus, under some circumstances, it is expected that adding nonlinear terms to linear models would improve the adjustment that will be done through linear regression.

The purpose of this article is to apply three models, one linear and two nonlinear, on data of respiratory mechanics of a group of *Wistar* rats and compare them using *F*-ratio test and the Akaike's Criterion.

2 Materials and Methods

2.1 Animals

Male Wistar rats (n = 6, 10 week old, 314 ± 17 g body weight) non-SPF (non *Specific Pathogen Free*) were used in this study. They came from animal facility of School of Medicine of the University of São Paulo (FMUSP) received ration and water according to their needs and were kept in an environment with lighting cycles of 12 h with artificial light and 12 h without light. All the animals received the care according to the established norms in [8]. The procedures are according to the Brazilian National Law number 11794 from 10/08/2008, which regulates all research activities involving animal use in the country. The experiment with animals was approved by the CEUA—FMUSP (0057/12).

2.2 Experimental Protocol

The animals were anesthetized via intraperitonial with xylazine 1 mg/100 g (xylazine hydrochloride 20 mg/mL, Rompun, Bayer) and ketamine 7.5 mg/100 g (dextroketamine hydrochloride 75 mg/mL, Cristália). They were placed supine for endotracheal intubation, where a polyethylene cannula (ID = 3 mm, L = 85 mm) was introduced. One second cannula was inserted into the right jugular vein for injections of *Phosphate Buffered Saline* (PBS) solution and the doses of MCh. After this preparation, the animals were kept with mechanical ventilation trough the SAV, using a tidal volume of 10 mL/kg, respiratory frequency of 90 bpm and the Positive End Expiratory Pressure (PEEP) of 3 cmH$_2$O, using a water column.

After the calibration of the SAV and the connection of animal to the ventilator the experimental protocol began. The protocol consisted of the application of volumetric disturbances for acquisition of the respiratory signals of pressure (P) and volume (V) at the trachea.

At the beginning of the protocol, ramp insufflation maneuvers were performed (30 cmH$_2$O). Four quasi-sinusoidal volume perturbations of 5 mL/kg and frequency of 90 bpm were applied every 30 s in order to obtain data to calculate the parameters of elastance and resistance of the respiratory system.

In the basal scenario were performed ventilator perturbations without any solution in the venous access. In the second scenario was applied the PBS, followed by four perturbations. In the two following scenarios were performed measurements right after the applications of MCh in the doses of 30 and 300 µg/kg. The first perturbation was performed 5 s after the intravenous injection of MCh [9]. Finally, one last acquisition of the respiratory signals was performed 5 min after the last dose of MCh, that represents the scenario where the drug already would have been metabolized [10].

2.3 Data Collecting

The measurement of the pressure (P) and volume (V) of the respiratory system was performed using a mechanical ventilator (flexiVent FX2, SCIREQ, Canada). One quasi-sinusoidal perturbation (1.5 Hz) of volume was used to apply the models and calculate the mechanical parameters of respiratory system with the sampling frequency of 256 Hz.

2.4 Application of Mathematical Models

The LSCM or model 1 was calculated by regression with the pressure (P) and volume (V) values, as can be seen in Eq. 1 [3].

$$P = EV + R\dot{V} + P_0 \tag{1}$$

where E is the elastance, R is the resistance, $\dot{V}$ is the respiratory flow and finally P_0 is a constant the function of which is to absorb any errors in estimating functional residual capacity.

The second studied model (Model 2) is a volume-dependent single compartment model, one variation of the Model 1 with the addition of one nonlinear E_2 term related to volume as presented in Eq. 2.

$$P = E_1 V + E_2 V^2 + R\dot{V} + P_0 \tag{2}$$

In Eq. 2, we have the same variables and parameters defined for the LSCM with the addition of V^2, the squared lung volume.

The last model (Model 3), a flow-dependent single compartment model, just like the Model 2, also is a variation of LSCM, but with the addition of one nonlinear term (R_2) in relation to airflow, as presented in Eq. 3.

$$P = EV + R_1 \dot{V} + R_2 \dot{V}|\dot{V}| + P_{0P} \qquad (3)$$

In Eq. 3, we have the terms already defined and $|\dot{V}|$ that is the absolute value of the airflow.

2.5 Comparisons

To compare the three models, the *F*-ratio test and the Akaike criterion were used [3]. The *F*-ratio test consists in a statistic test using the *F* of Fisher-Snedecor distribution to compare the equality between two variances [11]. We used this to compare two different mathematical models using the *mean squared residual* (*MSR*), the variance of the residuals between a data set and its model fit [3], that is calculated according to the Eq. 4.

$$MSR = \frac{\sum_{i=1}^{n}\left(P_i - \hat{P}_i\right)^2}{n - m} \qquad (4)$$

In Eq. 4, *n* is the sample size, P_i is the value of measured pressure and $\hat{P}_i$ is the estimated value by the model in sample *i*. We also have *m* that is the number of parameters used in each model. Therefore, for each studied case, there is a *MSR* value related to a different mathematical model. To perform the *F*-ratio test that compares variances, we have to check if the ratio between two different models (with the numerator as the highest value) is in the area between 2.5% and 97.5% of the *F* distribution with $n - 1$ and $n - 1$ degrees of freedom [12], and this calculation were done through a mathematical programming environment (*Matlab, The MathWorks, USA*).

The Akaike criterion is performed through a constant called *Akaike information criterion corrected (AICc)* that is calculated through the Eq. 5.

$$AIC_c = 2m + n[\ln\left(2\pi MSR\right) + 1] + \frac{2m(m+1)}{n - m - 1} \qquad (5)$$

It is possible to calculate this value for all models, and to compare the three studied models simultaneously. According to the Akaike criterion, the best model is the one that presents the lower *AICc* value [13].

3 Results

Figures 1, 2 and 3 shows the graph with all the chosen models applied in data of one animal and the calculated values by linear regression, each graph is based on a different animal from the sample.

Figure 4 shows the *MSR* values at the basal phase of each mathematical model.
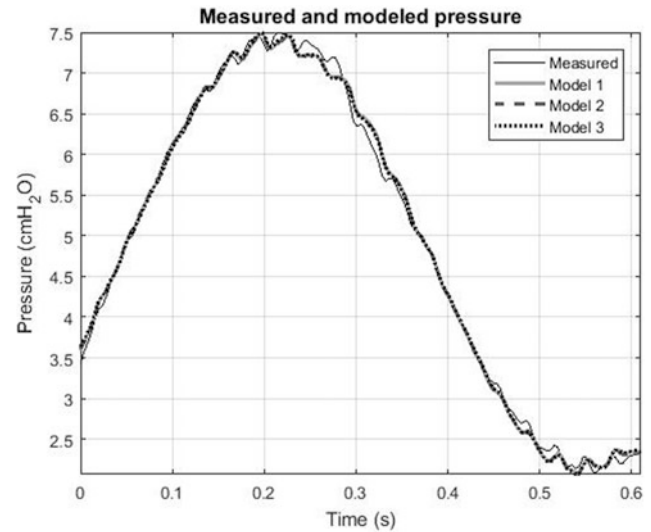
Fig. 1 The measured pressure value (continuous black line) and the pressure modeled by the three models of an example animal in basal
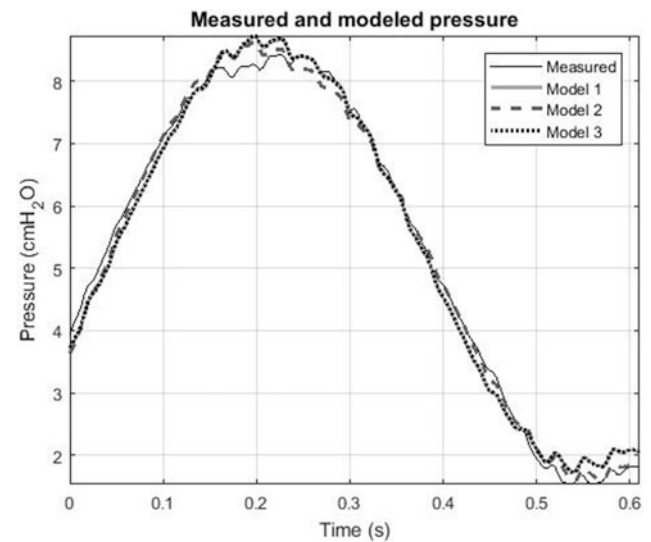
Fig. 2 The measured pressure value (continuous black line) and the pressure modeled by the three models of an example animal in the second dose of MCh (0.3 mg/kg)

Figure 5 shows the *MSR* values at the saline phase of each mathematical model.

Figures 6 and 7 show the *MSR* values of each mathematical model at the 0.03 and 0.3 mg/kg of MCh doses.

Figure 8 shows the *MSR* values at the last phase of the experiment, when MCh was already metabolized.

The Table 1 relates the best mathematical model, according to Akaike criterion, to the studied phases of the experience.
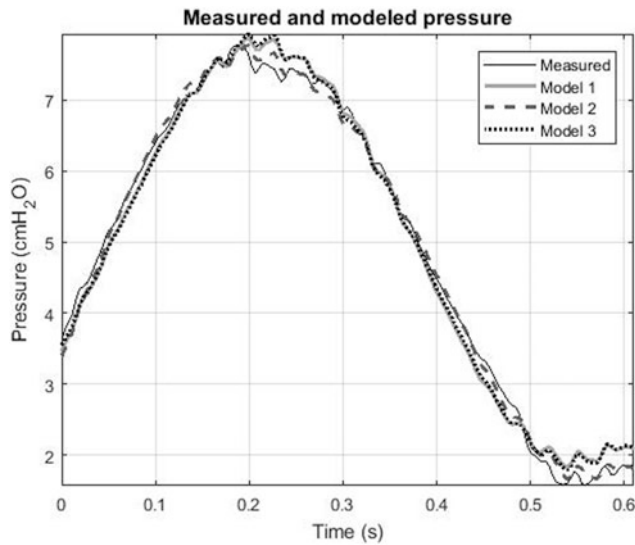
Fig. 3 The measured pressure value (continuous black line) and the pressure modeled by the three models of an example animal in the MCh post-metabolism state

Fig. 5 Boxplot graph with the *MSR* values of the mathematical models at the saline phase

Fig. 4 Boxplot graph with the *MSR* values of the mathematical models at the basal phase
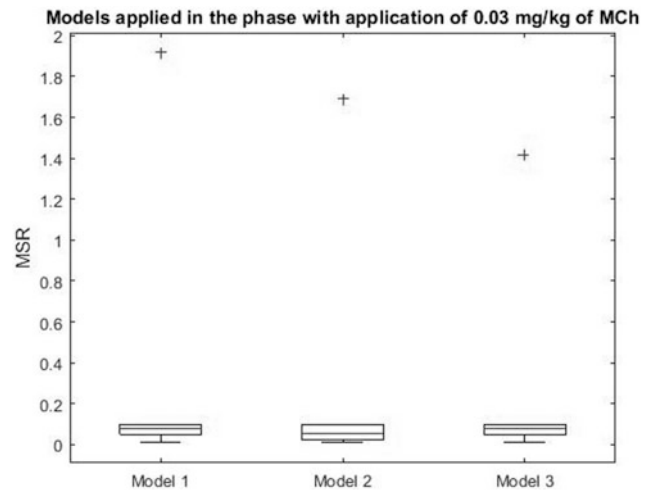
Fig. 6 Boxplot graph with the *MSR* values of the models at the first dose of MCh (0.03 mg/kg)

4 Discussion

There are many forms of assess the adequacy of the models to the measured data. Visually, e.g., in the Fig. 1, the mathematical models were very close to each other and close to the data related to the linear regression too. However, in the Fig. 2, at the highest dose of MCh, there is an example where the selected models do not approach very well to the measured data. Conversely, in the Fig. 3, it is possible to notice that the Model 2 is the closest to the measured data.

Figures 4, 5, 6, 7 and 8 show that in practically every case the *MSR* values of the model 3, with flow-dependent, and *LSCM* presented similar behavior and pattern. In contrast, the model 2 tends to present lower *MSR* values when compared with the other two models; specially in the Fig. 8, i.e. in the post-metabolism phase.

In addition, Table 1 depicts that only at the saline phase all the models presented similar results, as can also be seen in Fig. 5. It is also possible to notice that in the phase where the animal is with the MCh post-metabolized, the best model, according to Akaike criterion, was the Model 2, with nonlinearity at the volume. Also, at all stages, except the saline phase, the nonlinear models were the ones that approached better to the measured data (Table 1).
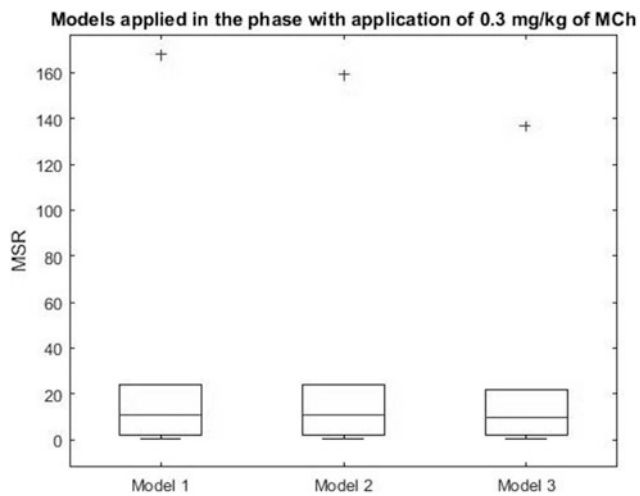
Fig. 7 Boxplot graph with the *MSR* values of the models when we applied the second injection of MCh
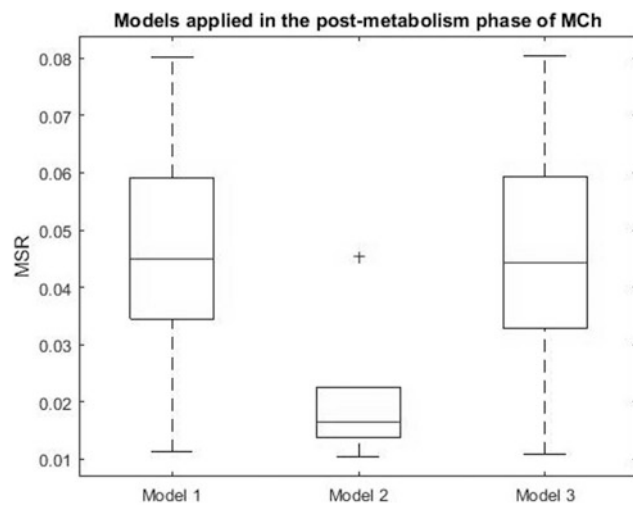
Fig. 8 Boxplot graph with *MSR* values of the models at the post-metabolism phase

Table 1 Number of times in which each model was considered the best, according to Akaike criterion related to each studied phases

	Basal	Saline	0.03 mg/kg of MCh	0.3 mg/kg of MCh	Post-metabolized
Model 1	0	2	0	0	0
Model 2	4	2	4	2	6
Model 3	2	2	2	4	0

About the *F*-ratio test, the results (not shown) indicate that none of the models could be considered superior, in relation to approximation, to the other studied cases. In all cases, the *F*-ratio test showed no significant difference between the approximations made by the models.

Thus, analyzing the comparison forms of models used in this article, it is possible to notice that the *F*-ratio test was not able to select a mathematical model that could be considered better than the other models in any of the cases tested; unlike the Akaike criterion. It is possible that the Akaike criterion has a little more sensitivity than the *F*-ratio to differentiate the result of adapting different mathematical models to the same data. It is important say that the Akaike criterion is an estimate of the expected, the relative distance between the fitted model and the observed data [13]; that is why the criterion always finds the best model even if the selected model do not have a physiology meaning or if the difference between models is small. Therefore, it is important to carefully choose the models to use the Akaike criterion.

It is known that the *F*-ratio test is based on a strong assumption that the distribution of the sample data should follow the Gaussian distribution [9]. This may be one of the reasons to justify the fact that the *F*-ratio test is not able to differentiate the selected models. Even because in this study we not guarantee that the assumption has been respected. On the other hand, the Akaike criterion requires nothing more than the *MSR* values of the models to compare them; therefore, it is much easier to apply.

It is possible to notice that the respiratory mechanics of bronchoconstricted rats are significantly better described by the model including volume-dependent, the Model 2, than by *LSCM* and the model with flow-dependent, as described by literature [14, 15]. The term '*EV*' in the Model 1 assumes that the pressure-volume dynamic relationship of the respiratory system is linear, and then the addition of '$E_2 V^2$' gives to the model a better approach to describe nonlinear pressure-volume behavior. The volume-dependent elastance term represents a progressive stiffening of the lung as it inflates from functional residual capacity up to total lung capacity [3]. The improvement due to the nonlinear volume-dependent term E in this case could be explained for some reasons like the properties of the lung parenchyma may have changed, as seen in pulmonary fibrosis, for example; or the lung parenchyma could have stiffened during bronchoconstriction.

But the addition of $R_2 \dot{V}|\dot{V}|$, in most cases, did not result in a significant improvement, and physiologically speaking the model 3 is better when the flow is turbulent [3], which probably did not occur very frequently in this study.

5 Conclusion

The nonlinear models got superior results, mainly the volume-dependent model, model 2, in relation to the linear one, in the majority of the studied cases, as we initially supposed.

In the matter of mathematical models' comparison, the Akaike criterion selected in each case the best of the three models. However, the F-ratio test could not discriminate the model with the best approximation in any of the cases.

Conflict of Interest The authors have no conflict of interest to declare.

References

1. Edelstein-Keshet, L.: Mathematical Models in Biology, 1st edn. Society for Industrial and Applied Mathematics, New York (2005)
2. Boccara, N.: Modeling Complex Systems, 2nd edn. Springer Science and Business Media, New York (2010)
3. Bates, J.H.T.: Lung Mechanics: An Inverse Modeling Approach, 1st edn. Cambridge University Press, New York (2009)
4. Bates, J.H.T., Rincon, M., Irvin, C.G.: Animal models of asthma. Am. J. Physiol. Lung Cell. Mol. Physiol. **297**, L401–L410 (2009)
5. Cardoso, T.A., et al.: Impacto da asma no Brasil: análise longitudinal de dados extraídos de um banco de dados governamental brasileiro. J. Bras. Pneumol. **43**, 163–168 (2017)
6. Dorland, N.W.A.: Dorland's illustrated medical dictionary, 32nd edn. Elsevier Health Sciences (2011)
7. Peták, F., et al.: Methacholine-induced bronchoconstriction in rats: effects of intravenous vs. aerosol delivery. J. Appl. Physiol. **82**, 1479–1487 (1997)
8. Institute of Laboratory Animal Resources: Guide for the Care and Use of Laboratory Animal, 1st edn. National Academy of Sciences, Washington (1996)
9. Bates, J.H.T., et al.: Temporal dynamics of acute isovolume bronchoconstriction in the rat. J. Appl. Physiol. **82**, 55–62 (1997)
10. Rodriguez, E., et al.: The orl rat is more responsive to methacholine challenge than wild type. Pulm. Pharmacol. **29**(2), 199–208 (2014)
11. Hartley, H.O.: The maximum F-ratio as a short-cut test for heterogeneity of variance, vol. 37, pp. 308–3012. Oxford University Press (1950)
12. Bussab, W.O., Morettin, P.A.: Estatística Básica, 5th edn. Saraiva, São Paulo (2002)
13. Burnham, K.P., Anderson, D.R.: Model Selection and Multimodel Inference: A Practical Information—Theoric Approach, 2nd edn. Springer, New York (2010)
14. Kano, S., et al.: Influence of nonlinearities on estimates of respiratory mechanics using multilinear regression analysis. J. Appl. Physiol. **77**, 1185–1197 (1994)
15. Wagers, S., et al.: Nonlinearity of respiratory mechanics during bronchoconstriction in mice with airway inflammation. J. Appl. Physiol. **92**, 1802–1807 (2002)

Constant Phase Model's Sensitivity to Increasing Doses of Methacholine

Henrique Tomaz Amorim, Renato de Lima Vitorasso,
André Suaiden Schimidt, Maria Aparecida Oliveira,
and Henrique Takachi Moriya

Abstract

The Constant Phase Model is an important approach for assessment of respiratory mechanics as its parameters have important physiological interpretations. As it is used extensively for fitting impedance data for mice and other small animals, particularly under effect of bronchoconstricting drugs, it becomes relevant to analyze how impedance magnitude respond to this stimulation accordingly to the model's parameters. This study intends to evaluate the different behaviors under increasing methacholine (MCh) doses through a sensitivity analysis to measure the model's responsiveness. Also, there is an evaluation of how the sensitivity coefficients change relatively to each MCh dose, in observation of a relation between the doses and the evolution of the impedance's absolute value and the parameters. Results suggests that increasing MCh doses accentuate the dissipative effects, which means that the contribution of conservative parameters to impedance's magnitude is reduced while the dissipative parameters relevance are increased. In addition to it, in observation of the strictly growing behavior of the sensitivity coefficients' deviation from Phosphate Buffered Saline (PBS) coefficients, one can notice how this pattern evolves as the MCh doses changes.

Keywords

Sensitivity • Constant phase model • Methacholine doses

1 Introduction

In assessment of respiratory mechanics, the input impedance measure, defined as the ratio in frequency domain of the tracheal pressure and the airflow in the airways, is a powerful tool to analyze how the respiratory system behaves. Its interpretation becomes valuable to analyze the respiratory system state when there is a link to the system physiology, which is obtained through fitting specific mathematical models to such data. A model largely employed to such purpose is the Constant Phase Model (CPM), whose parameters are airway resistance (R), airway inertance (I), tissue elastance (H), related to energy stored in the tissue and the tissue viscance (G), related to tissue dissipation of energy [1]:

$$Z(\omega) = R + j\omega I + \frac{G - jH}{\omega^{\alpha}} \qquad (1)$$

where, $\alpha = (2/\pi) \cdot atan(H/G)$ and $\omega = 2\pi f$.

This model has been used to fit impedance data in mice, rats and dogs [2]. Often this data is obtained through multiple measures of tracheal pressure under increasing bronchoconstrictor drug doses, i.e. methacholine (MCh). Such a procedure can vary the values obtained, depending on how the drug is applied. The most used approach is the bolus technique, which is a unique drug application that has a maximum response near the moment in which the application is made, but also a responsiveness that decay through time. In contrast, there is the continued infusion technique, used by Thamrin et al. [3], in order to evaluate the CPM's sensitivity coefficients and uncertainty of its parameters.

Considering the relevance of the MCh to the impedance measure, it becomes natural questioning how higher doses of this bronchoconstrictor drug can influence impedance response in contrast to the low doses. However, it is important to emphasize that the difference between the two application methods, as previously discussed, is very relevant to respiratory system response. For the sake of

H. T. Amorim · R. de Lima Vitorasso · H. T. Moriya (✉)
Biomedical Engineering Laboratory, University of São Paulo, São Paulo, Brazil
e-mail: htmoriya@usp.br

A. S. Schimidt · M. A. Oliveira
Department of Pharmacology, Instituto de Ciências Biomédicas, USP, São Paulo, Brazil

comparison, in this study, we will consider the impedance measure under increasing MCh doses using bolus technique in comparison to the results obtained by Thamrin et al. [3].

2 Methods

2.1 Measurement and CPM Parameter Estimation

All experiments involving laboratory animals were evaluated and approved by the 'Ethics Committee for Animal Use' (N° 15 on pgs. 16 of Book 3, 03/27 2014) from the Institute of Biomedical Sciences—University of São Paulo. The procedures are according to the Brazilian National Law number 11794 from 10/08/2008, which regulates all research activities involving animal use in the country.

The experiment was performed in 9-week female Balb/c mice (n = 5) (23.11 ± 1.27 g). The animals were sedated with an intraperitoneal (i.p.) injection of Ketamine (120 mg/kg) and Xylazine (12 mg/kg). The tracheostomy and cannulation were performed with a metal cannula 18G (BD Company, Brazil).

Then, the animal was connected to a small animal ventilator (flexiVent version 5.2, SCIREQ, Canada) and ventilated in quasi-sinusoidal wave form with a tidal volume of 10 mL/kg, PEEP of 3 cmH$_2$O and respiratory frequency of 150 breaths per minute. The right jugular vein was dissected by inserting a needle attached to a flexible PVC tube (Critchley Electrical Products PTY, Australia).

The respiratory muscles were blocked with pancuronium bromide (1 mg/kg i.p.) and two alveolar recruitment maneuvers were performed (up to the value of 30 cmH$_2$O).

After the recruitments, PBS (Phosphate Buffered Saline) was injected through the right jugular vein and 15 perturbations of 3 s each were performed. The perturbations were composed of a sum of 13 sinusoids (Hz): 1, 1.5, 2.5, 3.5, 5.5, 6.5, 8.5, 9.5, 11.5, 14.5, 15.5, 18.5 and 20.5. There was a 2 min interval between the PBS and each new dose.

The same perturbations were performed for all doses of Methacholine (MCh): 30, 100, 300, 1000 μg/kg and the MCh also was injected through the right jugular vein in bolus. Automation routines of the ventilator control program were used to perform the perturbations.

Thus, we took the average between all PBS measurements in order to fit CPM to one average impedance. As we are using bolus technique for applying MCh, we took the average between the second impedance measurement of each animal, which was the highest MCh response among all measurements.

The CPM parameters (R, I, G and H) estimation for the average impedances were made by the minimization of an error function, whose entries are grouped by the vector $\theta = (R, I, G, H)$ [3, 4]:

$$\phi(\theta) = \left[\frac{1}{p} \sum_{i=1}^{p} |Z_d(f_i) - Z_m(f_i)|^2 \right]^{1/2} \quad (2)$$

where p is the quantity of frequencies considered in the study, $Z_d(f_i)$ is the measured impedance and $Z_m(f_i)$ is the model prediction for the impedance, both calculated at frequency f_i.

2.2 Sensitivity Coefficient

As defined by Beck and Arnold [5], it is possible to consider a sensitivity coefficient to evaluate how fast the model changes as the constants (R, I, G and H) change. It also provides important physiological information about the contribution of airways and tissue to the impedance. Here, we considered the pondered partial derivative of $|Z|$ with respect to the parameter θ calculated at the frequency f_i [3]:

$$X_\theta(f_i) = \frac{|\theta|}{|Z|} \frac{\partial |Z|}{\partial \theta}(f_i) \quad (3)$$

As we calculated an analytic expression of the partial derivative for each θ, we were able to calculate the numerical value of this expression for each frequency f_i.

2.3 Model for Sensitivity Coefficients

Considering the Eq. (3), one can get analytic expressions for each one of the sensitivity coefficients. Although, the expressions would get over complicated to compute the distance between the functions. For simplifying, we consider a model containing exponential functions:

$$X_\theta(f) = \beta_1 e^{\beta_2 f} + \beta_3 e^{\beta_4 f} + \beta_5 \quad (4)$$

The function $X_\theta(f)$ is defined for each sensitivity coefficient in terms of the frequency, then the domain of the functions is the closed interval $[1\,\text{Hz}, 20.5\,\text{Hz}]$.

2.4 Parameter Estimation for Sensitivity Model

The sensitivity coefficients are fitted to the model exposed by Eq. (4) through the minimization of the error function,

whose entries are determined by the vector $\beta = (\beta_1, \beta_2, \beta_3, \beta_4, \beta_5)$, which are the model constants:

$$\phi(\beta) = \left[\frac{1}{n-1} \sum_{i=1}^{n} \left(\frac{X_\theta(f_i) - X_\theta^*(f_i)}{X_\theta(f_i)} \right)^2 \right]^{1/2} \quad (5)$$

where $X_\theta(f_i)$ is the sensitivity coefficient magnitude taken by expression (3) and $X_\theta^*(f_i)$ is the prediction of the model, both calculated at frequency f_i, and n is the quantity of frequencies considered in the study. Through the process of the minimization of $\phi(\beta)$, it's possible to determine the constants of the model for each sensitivity coefficient.

2.5 Distance Function Evaluation

As a way to show, numerically, how sensitivity coefficients change as the methacholine infusion rate changes, we will take calculations of the distance between the functions fitted to each sensitivity coefficients using Eq. (4). The distance is a parameter to define how different two functions are, as it can be zero if both functions are the same.

Considering two continuous functions $f(x)$ and $g(x)$, whose domain is the closed interval $[a, b]$, the distance between those two functions is defined as [6]:

$$\|f - g\| = \sqrt{<f - g, f - g>} \quad (6)$$

where the operation $<.,.>$ is defined by:

$$<f, g> = \int_a^b f(x)g(x)dx \quad (7)$$

As we have considered functions for the sensitivity coefficients in the domain of frequency [1 Hz, 20.5 Hz], we get to:

$$\|p(f) - q(f)\| = \left[\int_1^{20.5} (p(f) - q(f))^2 df \right]^{1/2} \quad (8)$$

This number, that consists of a measure of distance between the functions, allows us to evaluate how much of difference exists between them, as if this number approaches zero, the function $p(f)$ approaches $q(f)$. Considering this approach, for the sake of comparison, we will take the distance of each coefficient (relative to 30 μg kg^{-1}, 100 μg kg^{-1}, 300 μg kg^{-1} and 1000 μg kg^{-1} MCh dose, respectively) in relation to the PBS coefficients, which is precisely the deviation from PBS.

3 Results

3.1 Impedance Fit

We took the average between the impedance's measurements of each animal and then obtained an average impedance for each MCh dose. The CPM was then fitted to these values as a way to describe the respiratory system's average parameters for each case. Observing Fig. 1, one can note how MCh contributes for rising Re(Z) and Im(Z), which also contributes to impedance's absolute value (|Z|) gain. It can be interpreted as the bronchoconstriction effect turning the breathing into a more effortful task.
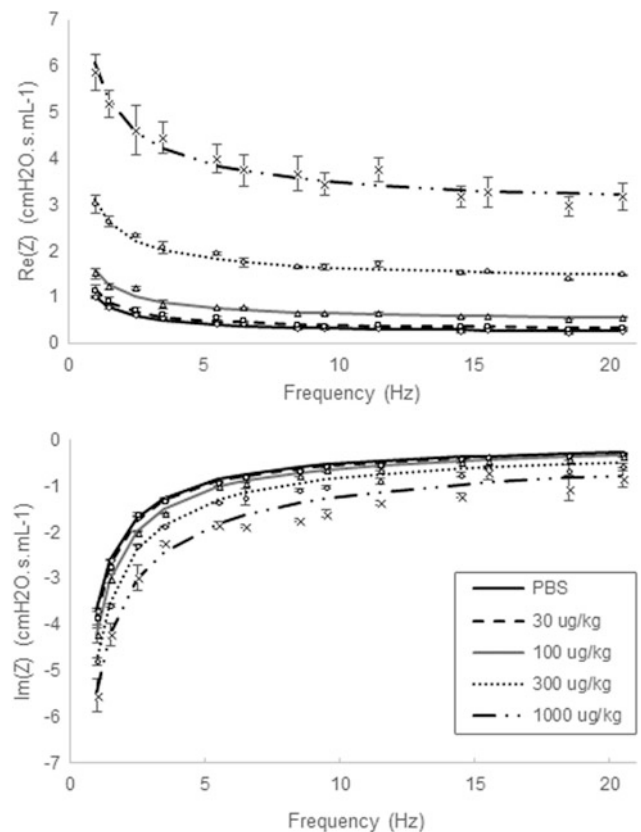
Fig. 1 Typical CPM fit for each MCh dose using the average taken by impedance data versus frequency. The notation Re(Z) and Im(Z) indicates, respectively, the real part and imaginary part of Z. The continuous line indicates the model fit and the open symbols are located specifically at the average of measurements of all mice for the respective frequency at each MCh dose. The bars describe the standard deviation for each point

3.2 Methacholine Pattern

We took calculations for the sensitivity coefficients of the average impedance values. After taking the calculations for the coefficients in the known frequencies, we calculated the constants $\beta = (\beta_1, \beta_2, \beta_3, \beta_4, \beta_5)$ that best suited those points using the minimization of the error defined by Eq. (5). This process allows to evaluate de behavior of the sensitivity

coefficients analytically. The graphic results for the model fit are shown in Fig. 2. The fitting error, in all cases, was less than 5%.

Distinguished patterns can be observed at each case, but the overall behavior is that the sensitivity coefficients related to the R parameter increases with frequency while the I coefficients remains essentially the same. The G coefficient tends to increase slowly with frequency at small MCh doses
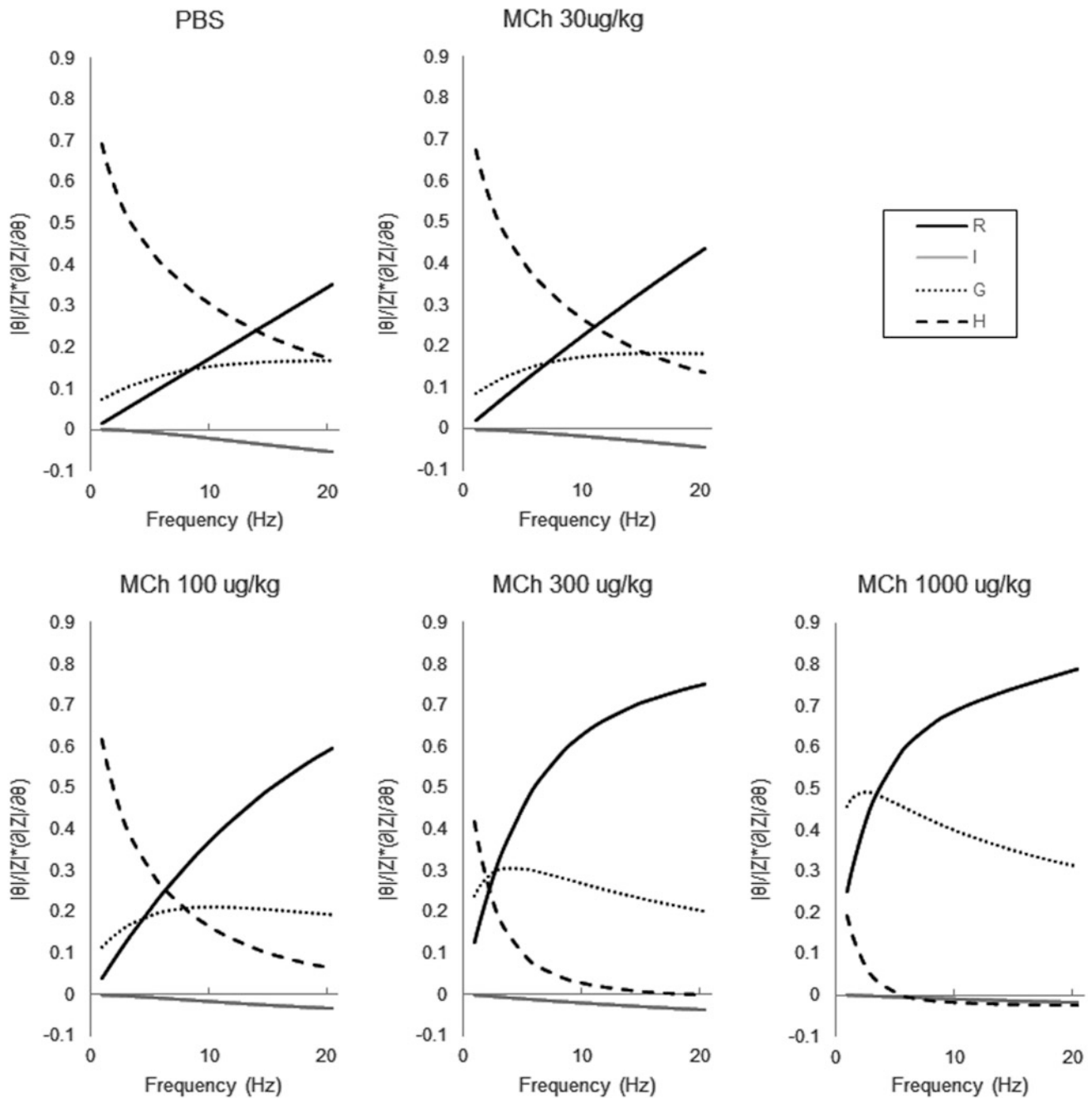
Fig. 2 Plots of sensitivity coefficients with respect to each parameter considering each one of the methacholine doses and the PBS conditions, calculated using the average impedance data, versus frequency
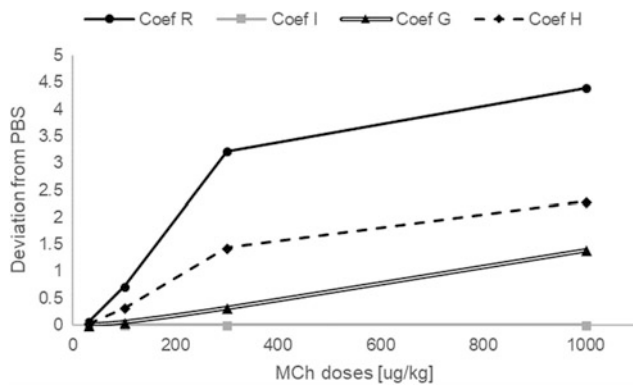
Fig. 3 Evolution of deviation between the sensitivity coefficients for higher MCh doses and the PBS sensitivity coefficients, which are those taken with no MCh influence. On the horizontal axis we dispose MCh doses in μg/kg

and decay slightly at higher frequencies in higher MCh doses while H coefficient decay fast with frequency in all cases.

3.3 Changing Evaluation of the Coefficients

The result of how deviation between the MCh doses' sensitivity coefficients and PBS coefficients evolves according to methacholine's doses is shown by Fig. 3. It is possible to notice that, for all sensitivity coefficients, there is an increasing behavior in the distance. It shows that, as the MCh doses increase, the sensitivity pattern becomes more different than the initial one (PBS). The major gain occurs between the initial doses (100 and 300 μg/kg) and after it the growing rate becomes lower, but still considerable.

4 Discussion

As shown by Fig. 2, the sensitivity coefficients with respect to R and G become more significant as the methacholine dose rises. It shows a correlation between the degree of bronchoconstriction and the susceptibility of the lungs to these parameters, which are both of dissipative nature.

In the specific case of the coefficient R, as MCh dose increases, the rising slope becomes higher at lower frequencies and the magnitude becomes more representative. Considering the coefficient G, in all cases we get a rise until around 4 Hz and then it starts to decline. However, at higher MCh doses, the magnitude becomes more relevant.

Both, R (airway resistance) and G (tissue viscance), are descriptive parameters of the model for dissipative aspects in the lung [1, 2, 7]. The parameter R is proportional the dissipated energy in the airways and G is a constant that is related to the loss of energy through the tissue [1]. This appointment is relevant to see that as the bronchoconstriction rises, the dissipative aspect of the respiratory system starts to prevail, then there is more resistance to the breathing activity, as expected. Then, a bigger energetic effort in the breathing activity, dedicated to conduct the air thorough the airways and to inflate the lungs' tissue, is made.

Analyzing the coefficient H, as the MCh dose increases it becomes less significant in magnitude [3]. In particular, we can highlight the contribution to the sensitivity at lower frequencies [3]. Considering the fact that parameter H (tissue elastance) has a conservative nature and is associated with the energy stored in form of potential elastic energy in the tissue [1], the behavior of this parameter shows that, at a bigger bronchoconstriction degree, the impedance's absolute value becomes less susceptible to elastance at higher frequencies, then it is possible to conclude that the impedance rely less on the conservative aspect of the lungs' tissue at this state.

Through the perspective of Fig. 3, the deviation from PBS grows constantly with the MCh dose, which shows that model's sensitivity pattern varies accordingly to bronchoconstriction degree. In other words, increasing doses of MCh will contribute for the model's sensitivity patterns to be invariably different from patterns of previous doses. These arguments work for sensitivity coefficients related to R, G and H. However, the deviation related to the parameter I keeps constant for all doses. It is due to the fact that the magnitude of I itself is very low while the uncertainty associated is very high [8]. In fact, the sensitivity related to I is small and negligible, as the magnitude of the parameter has influence over it.

In summary, the deviation analysis aspects and the behaviors exposed by Fig. 2, when analyzed together, indicate the accentuation of impedance's sensitivity pattern for each parameter, which means, in general terms, that the impedance value becomes more susceptible to R and G and less sensitive to H as the bronchoconstriction increases at higher frequencies.

Considering that if the sensitivity related to some parameter is low, a higher distortion on this parameter will affect less the impedance. It indicates that in this situation that physiological aspect is less relevant when compared to others. This conclusion, when followed by parameters' error analysis, as proposed by Thamrin et al. [3] and Lutchen [4], allows a deep understanding of how impedance magnitude varies in terms of physiological parameters.

References

1. Bates, J.H.T.: Lung Mechanics: An Inverse Modeling Approach. Cambridge University Press, Nova Iorque (2009)
2. Hantos, Z., Daroczy, B., Suki, B., Nagy, S, Fredberg, J.J.: Input impedance and peripheral inhomogeneity of dog lungs. J. Appl. Phys. **72**, 168–178 (1992)
3. Thamrin, C., Janosi, T., Collins, R., Sly, P.D., Hantos, Z.: Sensitivity analysis of respiratory parameter estimates in the constant-phase model. Ann. Biomed. Eng. **32**, 815–822 (2004)
4. Lutchen, K.R.: Use of sensitivity analysis and optimal experiment design for estimating mechanical parameters in respiratory system models. In: IFAC Modelling and Control in Biomedical Systems. Venice (1988)
5. Beck, J.V., Arnold, K.J.: Parameter Estimation in Engineering Science. Wiley, Nova Iorque (1977)
6. Barone, M.: Álgebra Linear, 3rd edn. Publicações do IME, São Paulo (1988)
7. Vitorasso, R.L.: Análise da aplicação do modelo de fase constante na avaliação mecânica respiratória em animais durante broncoconstrição. São Paulo (2016)
8. Mori, V.: Impedância respiratória de entrada: comparação entre os métodos convencional e de wavetube. São Paulo (2015)

Evaluation and Quantification of Electrode Arrangement Performance for Electrochemotherapy

R. Guedert, G. B. Pintarelli, A. de C. Antonio Jr., and D. O. H. Suzuki

Abstract

Electrochemotherapy is a recognized electroporation-based technique for treatment of cutaneous and subcutaneous tumors. The treatment occurs as function of electrical field amplitude. The electric field distribution can be complex depending on the geometry of the electrodes (e.g., needles electrodes). Complex tumor and electrodes geometries must be subjected to pre-treatment analysis. The electric field distribution can be studied using computer simulation images which can be a laborious process in case of comparison of many electrodes models. Treatment parameters, as type of electrode and amplitude voltage, can be optimized to avoid inadequate electrical field for electrochemotherapy. Quantifying electrode performance (i.e., percentage of the electroporated tumor volume) would facilitate the treatment optimization. In this study, it was described a new metric to analyze electrode performance, the metric is based on three fractions/volumes: non-electroporated, reversible electroporated and irreversible. The metric was tested in a proposed case study which is the European Standard Operating Procedures of Electrochemotherapy type III electrode. The Miklavcic electroporation model was used to describe the electrical properties changes in the tissue as function of electric field. Equivalent performances were possible by varying the number of needles of the type III electrode and the electric field applied.

Keywords

Electrochemotherapy • Electric fields distribution • ECT treatment planning • ESOPE

1 Introduction

Electroporation is a technique of increasing membrane permeability due formation of pores. Pores are consequence of membrane reorganization during sufficiently high electric field external application. There are two electroporation-based technologies for cancer treatment. Firstly, electrochemotherapy (ECT) can take advantage of introducing chemotherapy drugs (e.g. bleomycin) into tumor cells [1–3]. Therefore, the cells die in consequence of the drugs action (reversible electroporation). Secondly, irreversible electroporation (IRE) induce cell membrane destruction. This technique exceeds membrane perturbation in a way the pores created cannot reseal. Therefore, without additional drugs [4, 5].

Both ECT and IRE are high selectivity treatment, in other words, avoid the removal of extended tissue area. Surgical margins range from 10 to 50 mm and may decrease the life quality of patients. High selectivity characteristic is appreciated on head and neck tumor [6, 7]. ECT protocol is defined by European Standard Operating Procedures of Electrochemotherapy (ESOPE) published in 2006 [1, 8]. Currently, ECT is used for treatment of cutaneous and subcutaneous tumors in European clinics [9, 10] and in veterinary clinics in Brazil [3, 11, 12].

ECT effectiveness is a function of the electric field distribution. Electric field distribution changes according to the electrical properties of the tissue. Electroporation cause transient changes in the electrical properties. Distribution of fields can be studied based on models of electrical properties changes (i.e. conductivity) due to electroporation. ECT effectiveness can be predicted by pre-treatment (or treatment planning). Pre-treatment regards applied voltage, electrode geometry and tissues electroporation model to study electric field distribution. Pre-treatment depend on the use of imaging which can be laborious for the user and computational system if analyzing and comparing different electrodes configurations [13–16].

R. Guedert (✉) · G. B. Pintarelli · A. de C. Antonio Jr. · D. O. H. Suzuki
Instituto de Engenharia Biomédica, Universidade Federal de Santa Catarina, Florianópolis, Brazil
e-mail: guilherme.b.pintarelli@gmail.com

Our aim is to propose an electrodes performance metric based on three fractions/volumes: non-electroporated, reversible electroporated and irreversible. A variation of ESOPE electrode arrangement was used as case of study (ESOPE type III). The number of needles (N) in the perimeter of the central electrode was varied. The reduction of needles inserted in the patient facilitates the ECT procedure. Electrode performance was considered positive when the treatment area was affected by sufficient electric field for electroporation.

2 Materials and Methods

Simulations were executed to solve the equation of continuity under assumption of steady state situation (Eq. 1). The tetrahedral elements mesh was assembled in the software COMSOL Multiphysics® version 4.4 (COMSOL Inc., Sweden).

$$\nabla \cdot \boldsymbol{J} = -\nabla \cdot (\sigma \nabla V) = 0 \tag{1}$$

where $\boldsymbol{J}$ is the current density (A/m^2), σ is the tissue electrical conductivity (S/m) and V is the electric potential (V). In Eq. 2, V is used to compute electric field $\boldsymbol{E}$. In Eq. 3 (Ohm's law) $\boldsymbol{E}$ is used to compute current density $\boldsymbol{J}$.

$$\boldsymbol{E} = -\nabla V \tag{2}$$

$$\boldsymbol{J} = \sigma \boldsymbol{E} \tag{3}$$

The boundary conditions were all insulation on the external surfaces (Neumann's boundary condition). The contact between electrode and tissue was modeled as Dirichlet's boundary condition.

Electroporation conductivity change is a function of the applied electric field (E). A suitable model should be used, such as the model of Miklavcic et al., shown in Eq. 4 [17]. This model has already been studied by Suzuki et al. in different circumstances of ECT treatment and a similar approach was used in this study [3, 12, 18].

$$\sigma(E) = \sigma_0 + \frac{\sigma_{Max} - \sigma_0}{1 + D \cdot e^{-\left(\frac{E-A}{B}\right)}} \tag{4}$$

where, $A = \frac{Eirrev + Erev}{2}$, $B = \frac{Eirrev - Erev}{C}$, C = 8 and D = 10.

The *in silico* model is rectangular shape (epidermis to bone) with subcutaneous spherical tumor. The three three-dimensional geometries are according to Fig. 1. Values of geometry dimensions are shown in the figure (in millimeters). The mesh consisted of 310,239–334,270 tetrahedral elements (depending on the electrode number). The required electrical conductivities and electric fields amplitudes for irreversible (*Eirrev*) and reversible electroporation (*Erev*) are shown in Table 1. Electrical conductivities for tissues are obtained from Eq. 4, and the input parameters are set out in Table 1. The spherical tumor has a radius of 2 mm, the distance between periphery electrodes and central electrode was 4 mm. Other geometry parameters are shown in Table 2. Calculations were run on a personal computer (Intel Core i5-2400, 3.10 GHz, 8 GB RAM) with Windows 10 (x64, Microsoft Inc., Redmond, WA, USA) operating system.

The method of electrode performance analysis is based on three volumes: Occurrence of reversible and irreversible
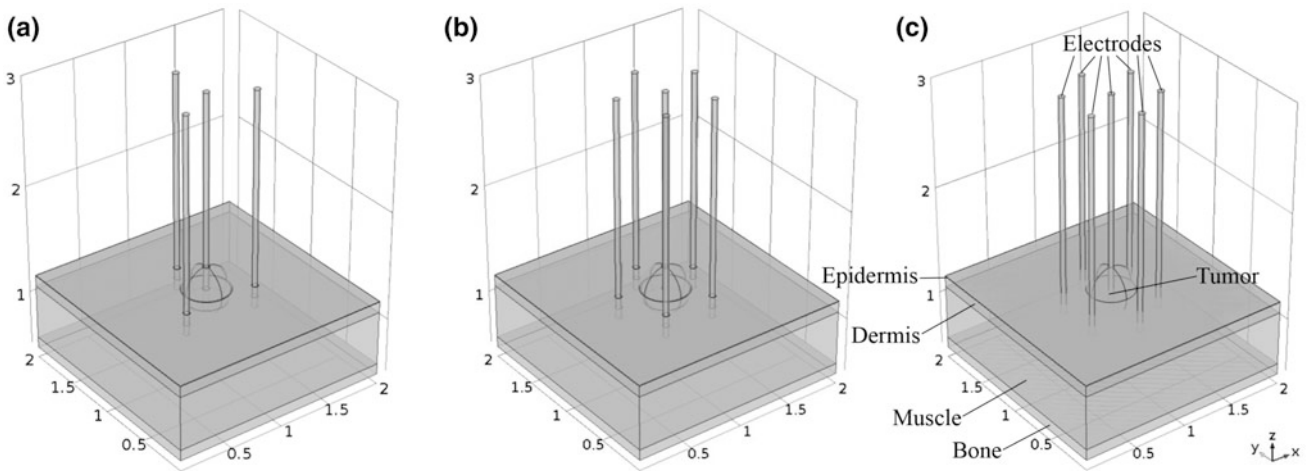
Fig. 1 Demonstration of the studied needles electrodes structures. **a** Three electrodes in the periphery (N = 3). **b** Five electrodes in the periphery (N = 5). **c** Six electrodes in the periphery (N = 6)

Table 1 Parameters used for simulation [3, 19]

Material	Initial electrical conductivity (σ_0) (S/m)	Maximum electrical conductivity (σ_{Max}) (S/m)	Erev (kV/m)	Eirrev (kV/m)
Electrodes	1.74×10^9	1.74×10^9	–	–
Tumor	0.750	0.300	40	80
Epidermis	0.800	0.008	40	120
Dermis	1.000	0.250	30	120
Muscle	0.340	0.135	20	80
Bone	0.01	0.01	–	–

Table 2 Parameters used for simulation [18]

Material	Length (mm)
Electrodes radius	0.03
Epidermis	0.06
Dermis	1
Muscle	5
Bone	1

electroporation and non-occurrence of electroporation. The volume separation is made with thresholds as shown in Table 1 (i.e., *Eirrev* and *Erev*). Electrode performance was defined as percentage of tumor area electroporated (reversible and irreversible). In ECT is not desired areas without suitable electric field for electroporation, those areas are named ECT blind spots. Volume evaluation was calculated using MATLAB software. The developed method was applied considering the radius equal to the tumor (evaluation of the electroporation efficacy in the tumor). In addition, the same method was applied in the regions neighboring the tumor, that is, a radius beyond the volume of the tumor (i.e. safety margin). The safety margin radius can be changed according to the surgeon's preference. In this work the safety margin used was twice the radius of the tumor. A mesh error of 2% was considered. Therefore, results within this range were considered equal.

3 Results

The electric field distribution of the three types of electrodes (N = 3, 5 and 6) for 100 kV/m application were organized in Fig. 2a, b and c respectively (data is not shown for 40, 70 and 130 kV/m). It is observed that inside the volume of the tumor in all situations there are no ECT blind spots.

The compilation of volume method executed for the tumor volume is shown in Fig. 3. That is, distinction of reversible (EP rev) and irreversible (EP irrev) electroporation and non-electroporation (EP null) fractions. The non-occurrence of electroporation is observed in the applications of 40 kV/m. When combining the use of 3 peripheral needles (N = 3) and 40 kV/m the EP null volume is greater

than 25%. Volumes of EP null indicate presence of blind areas this situation is not suitable for ECT.

The safety margin analysis with the developed method is according to Fig. 4. In the tested configurations, the presence of EP null in the safety margins is close to 10% for the best case (N = 6 and 130 kV/m).

4 Discussion

The non-occurrence of electroporation (% EP null) is the worst case in ECT and should be avoided, in this type of situation tumor recurrence may occur [1]. Regarding % EP null in the tumor volume, there is no difference among the number of electrodes and electric field settings if electric field is over 70 kV/m, that is, it has the same performance. Considering safety margin there is growth of % EP null as we decrease the electric field and the number of needles. Exceptionally for application of 130 kV/m the number of electrodes makes no difference for the safety margin % EP null. Equivalent electrodes performance with less number of needles are desirable. The perforation of fewer needles facilitates the clinical procedure.

The separation between reversible (% EP rev) and irreversible (% EP irrev) electroporation volume is more sensitive to the alteration of number of needles. This observation was observed in all study situations. The higher number of electrodes and greater electric field is related to the increase of % EP irrev. EP irrev is prominent for 70 to 130 kV/m independent to the number of needles (disregarding the 70 kV/m and H = 3). Procedures with predominant % EP irrev have risk of thermal damage to surrounding healthy tissue as temperature will increase due to Joule
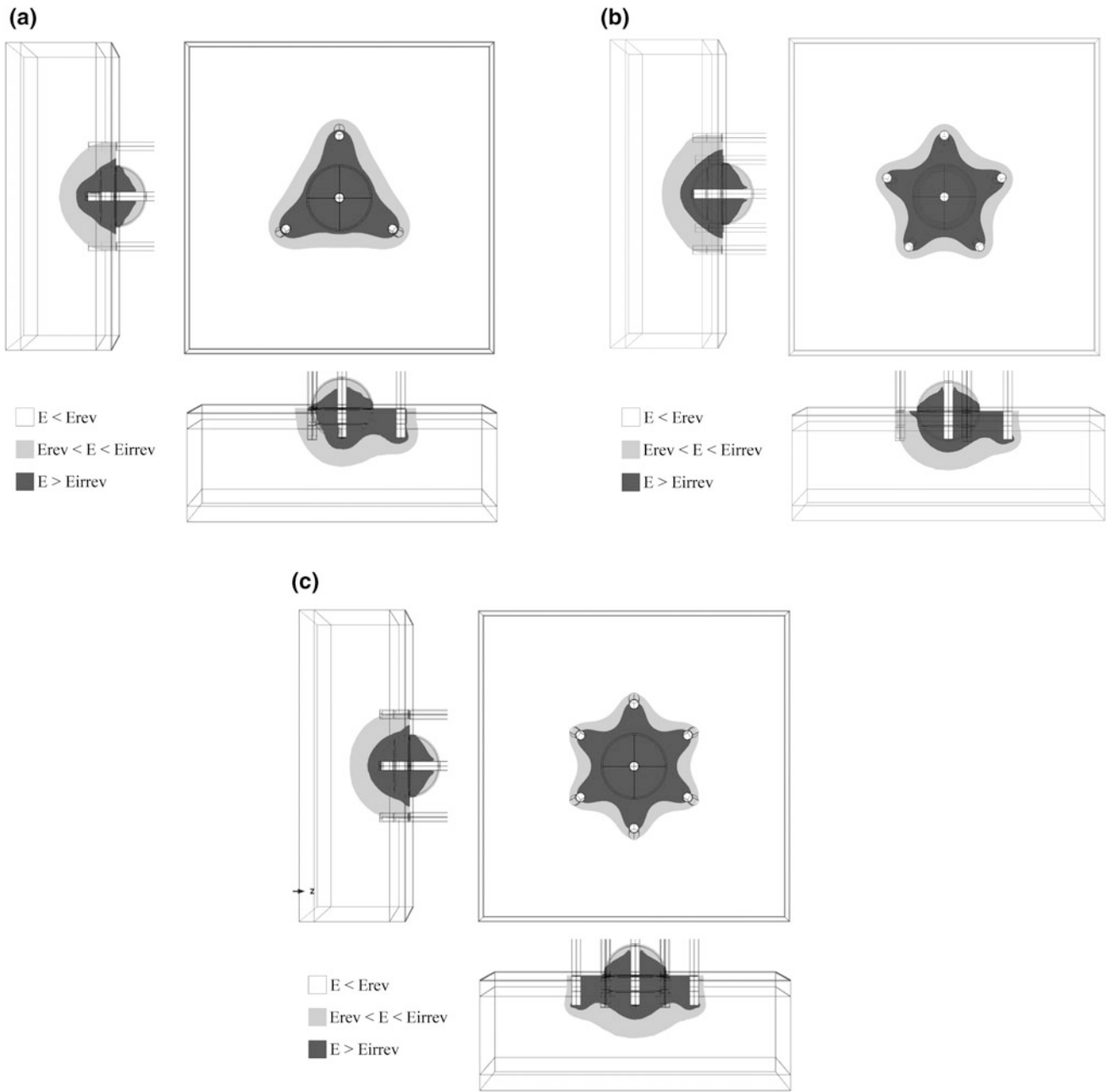
Fig. 2 Demonstration of the electric field distribution of the three studied electrodes, the electric field is observed in three segments of interest: no electroporation (white), reversible electroporation (light grey) and irreversible electroporation (dark grey). **a** Three electrodes in the periphery (N = 3). **b** Five electrodes in the periphery (N = 5). **c** Six electrodes in the periphery (N = 6)

Fig. 3 Distribution of electric field intensity in three segments of interest within tumor volume. N represents the number of peripheral needles of electrode structure as shown in Fig. 1
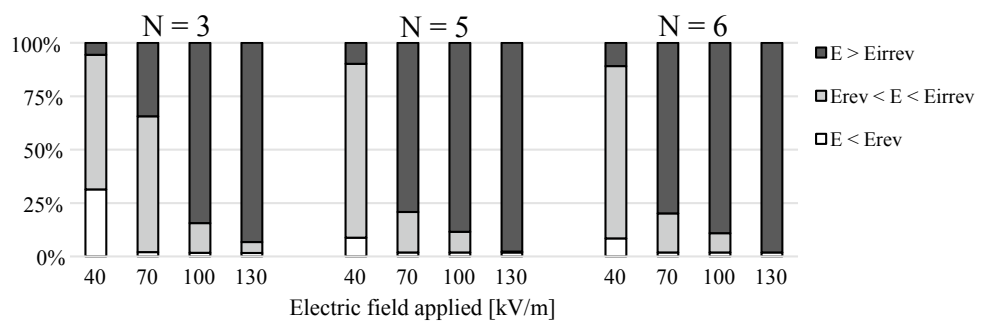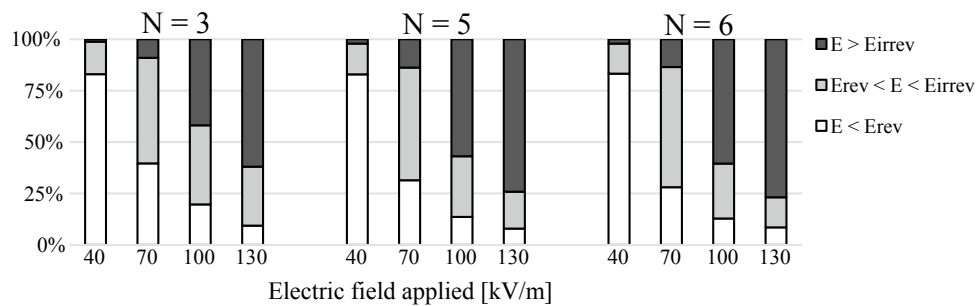
Fig. 4 Distribution of electric field intensity in three segments of interest within safety margin volume. N represents the number of peripheral needles of electrode structure as shown in Fig. 1

heating. Thermal damages are correlated with scar formation and impaired immune response. [4].

It is noted that safety margin on tumor surgery is used to remove primary tumor and tumor cells spread into surrounding tissues. The value of the surgical margin should be based on histological test and according to the clinical procedure of the surgeon. In this work the metric represents a pre-defined value, which could be changed according to the case.

During pre-treatment electrodes and voltage can be optimized aiming electric field for electroporation in desired area. Electric field distribution images may not be easy to understand for oncology professionals. Moreover, blind electric field spots may go unnoticed in complex geometries. The absence of the use of electric field distribution images may be beneficial to the pre-treatment process and convenient for clinical application. The new metric based on three fractions of reversible, irreversible and no occurrence of electroporation quantifies electric field distribution study for ECT. Due to dependencies of the simulations there is no reduction in the computational cost. However, pretreatment is usually done days before the procedure. The recorded simulation time was approximately 20 min. Because of this, computational cost is not considered a limiting factor.

Future work can use this type of metric to compute large numbers of simulations of electrode performance. For instance, number of electrodes, types of electrodes, concatenation of polarity and displacement of the electrodes in larger than electrodes tumors. The metric could be combined by automated software to indicate positioning template to ensure that the entire volume of the tumor is covered by sufficient electric field for electroporation.

Although it simplifies the process of analysis of electrode performance, the metric depends on computational simulations and electrical characterization of tissues. Metric computing may contain errors from these procedures which can be a limiting factor. Computation may differ from a real ECT treatment situation. ECT is in improvement and corrections in the thresholds of the metric so as changes in the model can be incorporated. Despite this, the metric quantifies existing procedures, that is, the traditional electric field image-based analysis also contains these errors.

The pre-treatment method is still under development. Pre-treatment may require tomography imaging for knowledge of tumor geometry [14]. In the future the metrics can also be tested based on percentage of transfection to chemotherapy drugs, as well as introducing active thresholds, or transition zones.

5 Conclusion

The success of electrochemotherapy depends on the distribution of electric fields. Sufficient fields must be imposed on tissues for occurrence of electroporation. The dependence of the study of field distribution images during electroporation can be a laborious process for the user (i.e., various types of electrodes and geometric forms of tumors may be subject to verification). Electrode performance is correlated as percentage of tumor area electroporated and areas without suitable electric field are harmful as tumor recurrence may occur. A new metric which facilitates electrodes performance comparison has been proposed. It describes performance of a given electrode in a tumor based on a percentages value: reversible electroporated, irreversible electroporated and non-electroporated.

The metric test was executed with a case study, which are three different arrangements with variations on the number of electrodes (derivatives from ESOPE type III electrodes). Removal of peripheral electrodes has the objective to facilitate the treatment (less perforation). It was observed that for some voltage values the three electrodes can perform similarly.

References

1. Mir, L.M., Gehl, J., Sersa, G., et al.: Standard operating procedures of the electrochemotherapy: instructions for the use of bleomycin or cisplatin administered either systemically or locally and electric pulses delivered by the CliniporatorTM by means of invasive or non-invasive electrodes. Eur. J. Cancer Suppl. **4**, 14–25 (2006)

2. Calvet, C.Y., Mir, L.M.: The promising alliance of anti-cancer electrochemotherapy with immunotherapy. Cancer Metast. Rev. **35**, 165–177 (2016)

3. Suzuki, D.O.H., Marques, C.M.G., Rangel, M.M.M.: Conductive gel increases the small tumor treatment with electrochemotherapy using needle electrodes. Artif. Organs **40**, 705–711 (2016)

4. Garcia, P.A., Davalos, R.V., Miklavcic, D.: A numerical investigation of the electric and thermal cell kill distributions in electroporation-based therapies in tissue. PLoS ONE **9**, e103083 (2014)

5. Rubinsky, J., Onik, G., Mikus, P., Rubinsky, B.: Optimal parameters for the destruction of prostate cancer using irreversible electroporation. J. Urol. **180**, 2668–2674 (2008)

6. Wheatley, K., Wilson, J.S., Gaunt, P., Marsden, J.R.: Surgical excision margins in primary cutaneous melanoma: a meta-analysis and Bayesian probability evaluation. Cancer Treat. Rev. **42**, 73–81 (2016)

7. Snoj, M., Cemazar, M., Slekovec Kolar, B., Sersa, G.: Effective treatment of multiple unresectable skin melanoma metastases by electrochemotherapy. Croat. Med. J. **48**, 391–395 (2007)

8. Marty, M., Sersa, G., Garbay, J.R., et al.: Electrochemotherapy—an easy, highly effective and safe treatment of cutaneous and subcutaneous metastases: results of ESOPE (European Standard Operating Procedures of Electrochemotherapy) study. Eur. J. Cancer Suppl. **4**, 3–13 (2006)

9. Suárez, C., Soba, A., Maglietti, F., et al.: the role of additional pulses in electropermeabilization protocols. PLoS ONE **9**, e113413 (2014)

10. Pucihar, G., Mir, L., Miklavčič, D.: The effect of pulse repetition frequency on the uptake into electropermeabilized cells in vitro with possible applications in electrochemotherapy. Bioelectrochemistry **57**, 167–172 (2002)

11. Calvet, C.Y., Famin, D., André, F.M., Mir, L.M.: Electrochemotherapy with bleomycin induces hallmarks of immunogenic cell death in murine colon cancer cells. Oncoimmunology **3**, e28131 (2014)

12. Suzuki, D.O.H., Berkenbrock, J.A., de Oliveira, K.D., et al.: Novel application for electrochemotherapy: immersion of nasal cavity in dog. Artif. Organs **41**, 767–773 (2017)

13. Miklavcic, D., Snoj, M., Zupanic, A., et al.: Towards treatment planning and treatment of deep-seated solid tumors by electrochemotherapy. Biomed. Eng. Online **9**, 10 (2010)

14. Zupanic, A., Kos, B., Miklavcic, D.: Treatment planning of electroporation-based medical interventions: electrochemotherapy, gene electrotransfer and irreversible electroporation. Phys. Med. Biol. **57**, 5425–5440 (2012)

15. Groselj, A., Kos, B., Cemazar, M., et al.: Coupling treatment planning with navigation system: a new technological approach in treatment of head and neck tumors by electrochemotherapy. Biomed. Eng. Online **14**, S2 (2015)

16. Vera-Tizatl, A.L., Kos, B., Miklavcic, D., et al.: Investigation of numerical models for planning of electrochemotherapy treatments of invasive ductal carcinoma. In: 2017 Global Medical Engineering Physics Exchanges/Pan American Health Care Exchanges (GMEPE/PAHCE), pp. 1–6. IEEE (2017)

17. Sel, D., Cukjati, D., Batiuskaite, D., et al.: Sequential finite element model of tissue electropermeabilization. IEEE Trans. Biomed. Eng. **52**, 816–827 (2005)

18. Suzuki, D.O.H., Anselmo, J., de Oliveira, K.D., et al.: Numerical model of dog mast cell tumor treated by electrochemotherapy. Artif. Organs **39**, 192–197 (2015)

19. Corovic, S., Lackovic, I., Sustaric, P., et al.: Modeling of electric field distribution in tissues during electroporation. Biomed. Eng. Online **12**, 16 (2013)

Evaluation of Rate of Muscular Force Development in Type 2 Diabetic Individuals with and without Diabetic Peripheral Neuropathy

M. A. Favretto, S. Cossul, F. R. Andreis, and J. L. B. Marques

Abstract

Diabetic peripheral neuropathy (DPN) has been associated with motor dysfunctions, such as reduction in the maximum force of ankle dorsiflexion and muscle atrophy in the lower limbs. These changes contribute to functional limitations, such as changes in gait. The rate of muscular force development (RFD) is derived from the force-time curve obtained during a maximal voluntary isometric contraction (MVIC), performed in a short period of time. RFD seems to be better related to gait changes and neuromuscular dysfunctions than the MVIC. Therefore, the purpose of this study was to evaluate alterations in the RFD in type 2 diabetic individuals with and without DPN. Twenty-two adults participated in the study, divided in three groups: control (n = 8), diabetic without DPN (n = 8) and diabetic with DPN (n = 7). The participants performed three MVIC of the ankle dorsiflexion. To the analysis of the force-time curve, it was selected the highest of the three MVICs obtained. The force-time curve was normalized by the peak value of MVIC. RFD was derived as the slope of the force-time normalized curve over the 0–50% and 0–100% force ranges of the MVIC. The area and time to achieve this ranges were also calculated. The MVIC force was significantly lower ($p < 0.05$) for the group with DPN (187.78 ± 71.70 N) when compared to the control group (275.77 ± 88.13 N). The $RFD_{(0-50\%)}$ was significantly lower ($p < 0.05$) for the group with DPN ($115 \pm 44\%$ MVIC/s) in relation to the control group ($233 \pm 102\%$ MVIC/s). The $RFD_{(0-100\%)}$ was significantly lower ($p < 0.05$) for the groups without DPN ($64 \pm 22\%$ MVIC/s) and with DPN ($61 \pm 24\%$ MVIC/s) when compared to the control group ($114 \pm 45\%$ MVIC/s). We conclude that these alterations may be related to muscle fiber atrophy, and loss of the motor unit caused by diabetes mellitus and DPN.

1 Introduction

According to the World Health Organization, approximately 422 million people in the world have diabetes mellitus (DM), of those, 90% are classified as type 2 DM (DM2) [1]. Recent studies suggest that up to 50% of the diabetic population will develop some sort of neuropathy [2]. The most common type of diabetic neuropathy is the diabetic peripheral neuropathy (DPN), which, due to abnormal glucose metabolism, leads to nutrient reduction and to the accumulation of toxins. DPN affects the sensory and motor nerves, which can lead to muscle weakness, foot ulcers, infections, and even lower limb amputation [3, 4].

DPN has been associated with motor dysfunctions, such as reduction in the maximum force of ankle dorsiflexion and muscle atrophy in the lower limbs [5, 6]. These alterations contribute to functional limitations in patients with DPN during daily activities [7]. These individuals walk more slowly, with a wider stance and with a higher internal plantar flexor moment at the first half of the stance phase [6, 7]. This subjects also presents an increased risk of falls [8]. Furthermore, the alterations in the plantar pressure distribution can generate bone deformity that, with continuous gait, may progress to ulceration [6, 9, 10].

Force evaluation can be a useful tool to assess the progress of DPN. Some studies have reported force reduction of maximal voluntary isometric contraction (MVIC) and also changes in the rate of muscular force development (RFD) of

M. A. Favretto (✉) · S. Cossul · F. R. Andreis · J. L. B. Marques
Department of Electrical and Electronic Engineering, Institute of Biomedical Engineering, Federal University of Santa Catarina, Florianópolis, Santa Catarina, Brazil
e-mail: mateus_favretto@hotmail.com

the ankle and knee joints in diabetic patients with DPN [5, 7, 11]. The RFD is a parameter derived from the force-time curve obtained during a MVIC, performed during a short period of time. The ability to produce a rapid increase of force during the initial phase of a voluntary contraction, which is reflected by a high RFD, is an important characteristic to avoid falls during sudden perturbations in postural balance. In addition, this parameter seems to be better related to gait changes and neuromuscular dysfunctions than the MVIC force [11–13].

Therefore, the objective of this work is to evaluate if type 2 diabetic individuals, with and without DPN, presents alterations in the RFD development in isometric contractions of the ankle dorsiflexion.

2 Materials and Methods

2.1 Participants

Data were collected from adults of both sexes, without type 2 DM (n = 8) and individuals with type 2 DM (n = 15). The individuals with diabetes were divided into two groups, classified according to the score of the questionnaire Neuropathy Total Symptom Score (NTSS-6): without DPN (n = 8) and with DPN (n = 7).

The exclusion criteria were: age above 65 years, presence of partial or total lower limb amputation or other neurological or orthopedic impairments due to stroke, cerebral palsy, poliomyelitis, rheumatoid arthritis, prosthesis, or moderate or severe osteoarthritis; having severe retinopathy, severe nephropathy causing edema or requiring hemodialysis and also absence of plantar ulcer at the time of evaluation.

All procedures performed in this study were approved by the Research Ethics Committee of the Federal University of Santa Catarina (Protocol Number: 2.390.994, approval date 09/12/2016).

All participants of the study were informed and clarified about the details of the experiment and voluntarily signed the consent form.

2.2 Experimental Design

The force data were acquired at a sampling frequency of 80 samples per second (SPS) by a portable dynamometer developed to assess the isometric force of ankle dorsiflexion, however, the system returns the average value of 10 samples, resulting in 8 SPS [14].

During the protocol, participants were instructed to be seated, with the hip and knee flexed at a 90º angle and the ankle in a neutral position at a 90° angle to the leg. The foot of the dominant leg was fixed on a portable dynamometer.

The participants performed three MVICs of the ankle dorsiflexion with a 5-s duration. These tests were separated by a 2-min rest interval. To ensure that MVIC was achieved during the trials, participants were verbally stimulated to produce maximum effort. Real-time visual feedback of the force signal was provided to the participants on a computer screen.

2.3 Data Processing

The data of the force was analyzed offline in the software Matlab (The MathWorks, Inc., USA). The sampling frequency of the system was 8 SPS. Therefore, to increase the precision, the data was interpolated by a factor of eight, increasing the sampling frequency to 64 SPS.

To the analysis of the force-time curve, it was selected the highest of the three MVICs obtained. Only 3 s were used and the starting point was defined as the time in which the force achieved 10% of the MVIC. The force-time curve was normalized by the peak value of MVIC. RFD was derived as the slope of the force-time normalized curve (ΔForce/ΔTime) over the 0–50% and 0–100% force ranges of the MVIC. Similarly, the area under the force-time normalized curve ($\int$Force*dt) force ranges from 0–100% and 0–50% of MVIC. The time to reach each force range was also calculated for each force range (see Fig. 1) [15].

2.4 Statistical Analysis

Statistical analysis was performed using SPSS statistics software (IBM, USA). The data is presented as mean ± standard deviation (SD). The force variables and anthropometric data were tested for normality with the Shapiro-Wilk test. Comparisons of variables with non-normal distribution were performed with the non-parametric Kruskal–Wallis test followed by Dunn-Bonferroni post hoc. The comparisons of normal distributed variables were performed by ANOVA tests followed by a Tukey post hoc test. The statistical significance considered was 0.05.

3 Results

The diabetic groups (with and without DPN) did not present significant differences for age, body mass index and duration of diabetes. However, there was a significant difference between the diabetic group without DPN and the control group, for the following data: age and body mass index (Table 1).

The MVIC of the ankle dorsiflexion was significantly different ($p < 0.05$), showing to be smaller ($p < 0.05$) for the
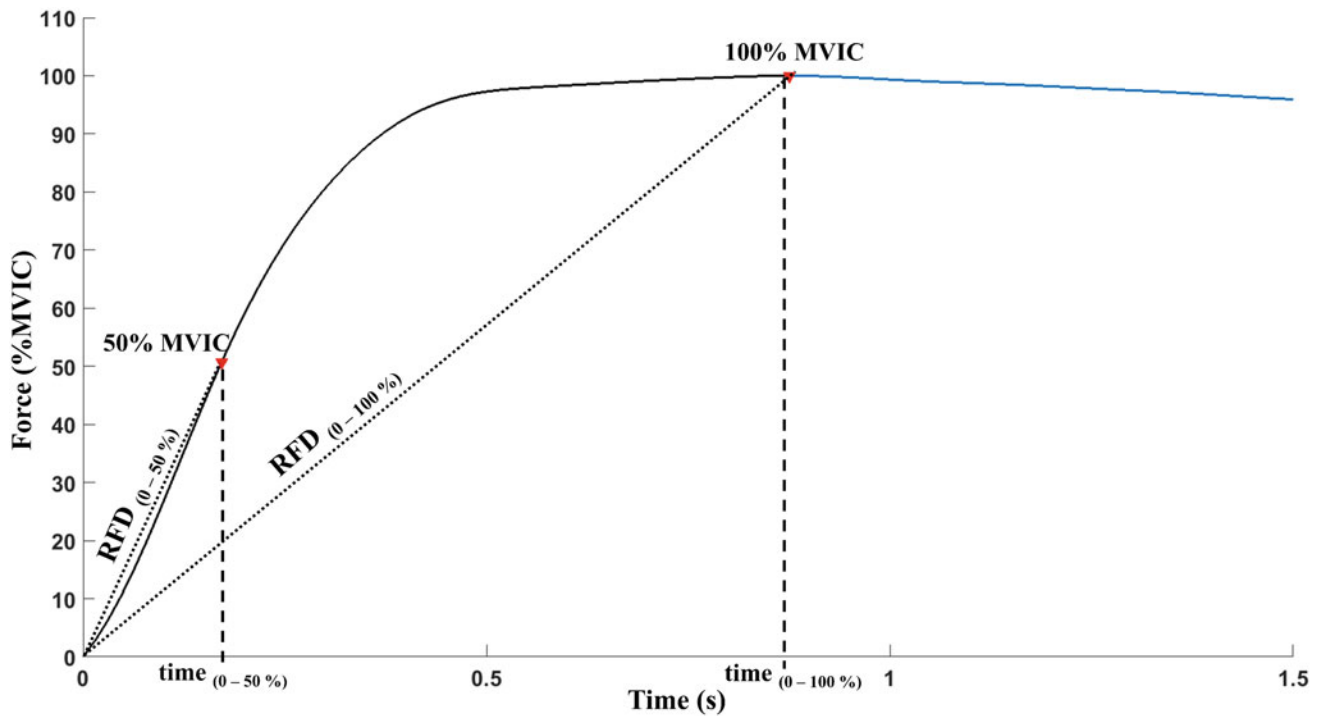
Fig. 1 Normalized force-time curve of a single individual during 3 s normalized by the MVIC. The rate of muscular force development (RFD), the time and area were calculated for the period of 0–50%, and 0–100% of the MVIC

Table 1 Demographic and clinical data (mean ± SD) of the participants

Variables	Control	Diabetic without DPN	Diabetic with DPN
	(n = 8)	(n = 8)	(n = 7)
Age (years)	50.3 ± 5.6*	59.8 ± 5.1*	56.7 ± 5.6
Sex (M/F)	3/5	3/5	2/5
Body mass index (kg/m^2)	25.6 ± 4.8*	31.2 ± 2.1*	29.3 ± 10.4
Diabetes duration (years)	#	7.1 ± 5.7	13.1 ± 10.4
Score NTSS-6	#	1.0 ± 1.1*	9.9 ± 4.6*

*Represent the significantly different between the groups ($p < 0.05$)

group with DPN (187.8 ± 71.7 N) in comparison to the control group (275.8 ± 88.1 N) (see Fig. 2). However, there was no evidence of difference between control and without DPN (215.2 ± 69.3 N).

The time$_{(0–50\%)}$ interval was significantly different ($p < 0.05$), showing to be greater for the group with DPN (0.45 ± 0.12 s) in comparison to the control group (0.24 ± 0.09 s) (see Fig. 3a). Equally, the area$_{(0–50\%)}$ was significantly different ($p < 0.05$), being greater for the group with DPN (9 ± 3% MVIC.s) in comparison to control (5 ± 2% MVIC.s) (see Fig. 3b). Moreover, the RFD$_{(0–50\%)}$ was significantly different ($p < 0.05$), being smaller for the group with DPN (115 ± 44% MVIC/s), also in comparison to control (233 ± 102% MVIC/s) (see Fig. 3c).

The time$_{(0–100\%)}$ was significantly different ($p < 0.05$), being higher for the DM2 groups without NDP
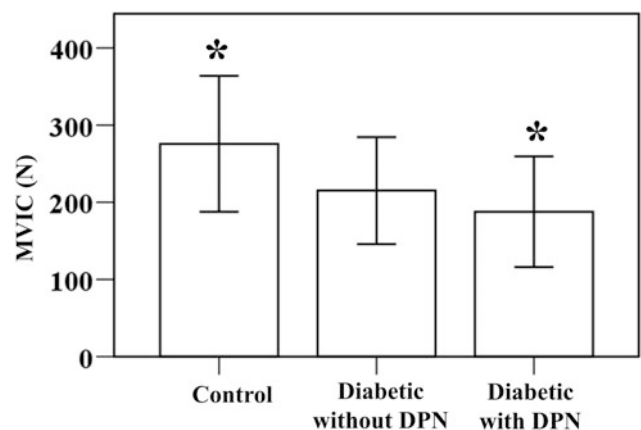
Fig. 2 Mean and standard deviation (SD) for the maximal voluntary isometric contraction (MVIC). *Represents the significantly difference between the groups ($p < 0.05$)
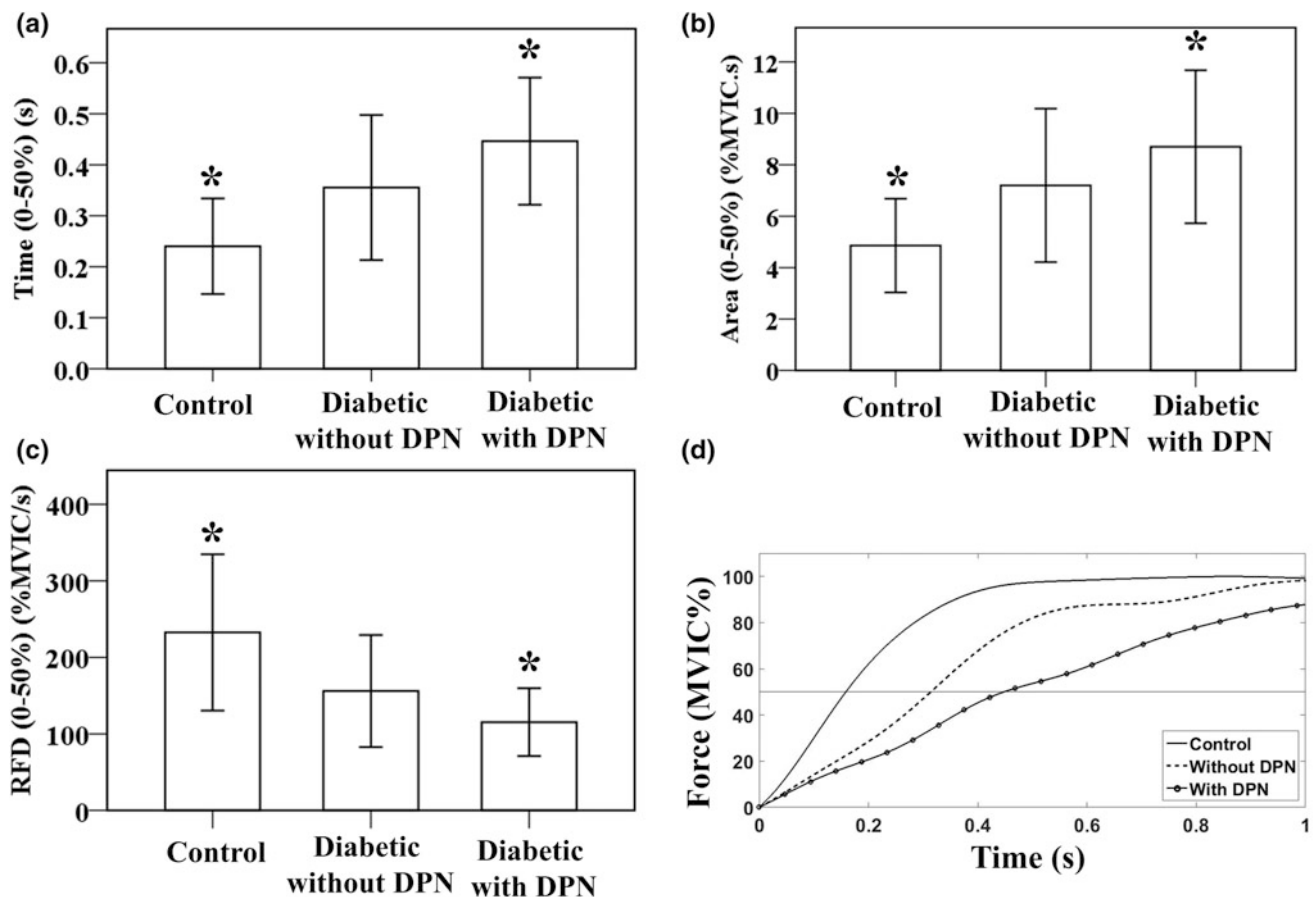
Fig. 3 Mean and standard deviation (SD) of the variables evaluated for the force range 0–50% of maximum voluntary isometric contraction (MVIC). **a** Time. **b** Area. **c** Rate of muscular force development (RFD).

d Example of normalized force-time curve of three individuals. *Represent the significantly difference between the groups ($p < 0.05$)

$(1.63 \pm 0.48$ s) and with DPN $(1.81 \pm 0.60$ s), in comparison to the control group $(0.96 \pm 0.24$ s) (see Fig. 4a). Likewise, the area$_{(0–100\%)}$ of the signal was significantly different ($p < 0.05$), being larger for the DM2 groups without DPN $(121 \pm 38\%$ MVIC.s) and with DPN $(127 \pm 50\%$ MVIC.s) when compared to the control $(68 \pm 18\%$ MVIC.s) (see Fig. 4b). Moreover, the RFD$_{(0–100\%)}$ was significantly different ($p < 0.05$), being smaller for the DM2 groups without DPN $(64 \pm 22\%$ MVIC/s) and with DPN $(61 \pm 24\%$ MVIC/s) when comparing to the control $(114 \pm 45\%$ MVIC/s) (see Fig. 4c).

However, it was not found evidence of difference for any of the variables, when comparing the groups with diabetes, with and without DPN.

4 Discussion

The MVIC force of ankle dorsiflexion was significantly lower only for the group with DPN (see Fig. 2). This result is similar to other work [5] that evaluated the ankle

dorsiflexion force in diabetic individuals with an isokinetic dynamometer. The force reduction in patients with DPN can be explained due to the continuous loss of motor units caused by DPN [16]. Although, along with motor unit loss, a compensatory process occurs that contributes to the proper functioning of the muscle, its role is limited during the course of the disease [5, 7, 17]. Thus, muscle weakness is frequently observed in individuals with DPN, while patients with long-term diabetes without DPN may present normal force [7].

For the group comparisons, individuals with and without DPN presented a higher time to achieve 50 and 100% of the MVIC in comparison to the control group. Consequently, DPN group presented a reduction in RFD (see Figs. 3 and 4). In the same way, these differences can be related to motor unit loss, since the force at a maximal instantaneous contraction directly depends on the recruitment and firing frequency of the motor units [12].

In addition to motor unit loss, the atrophy of the dorsal and plantar flexor muscles of the ankle is recurrent in diabetic individuals with DPN [17]. Furthermore, diabetic
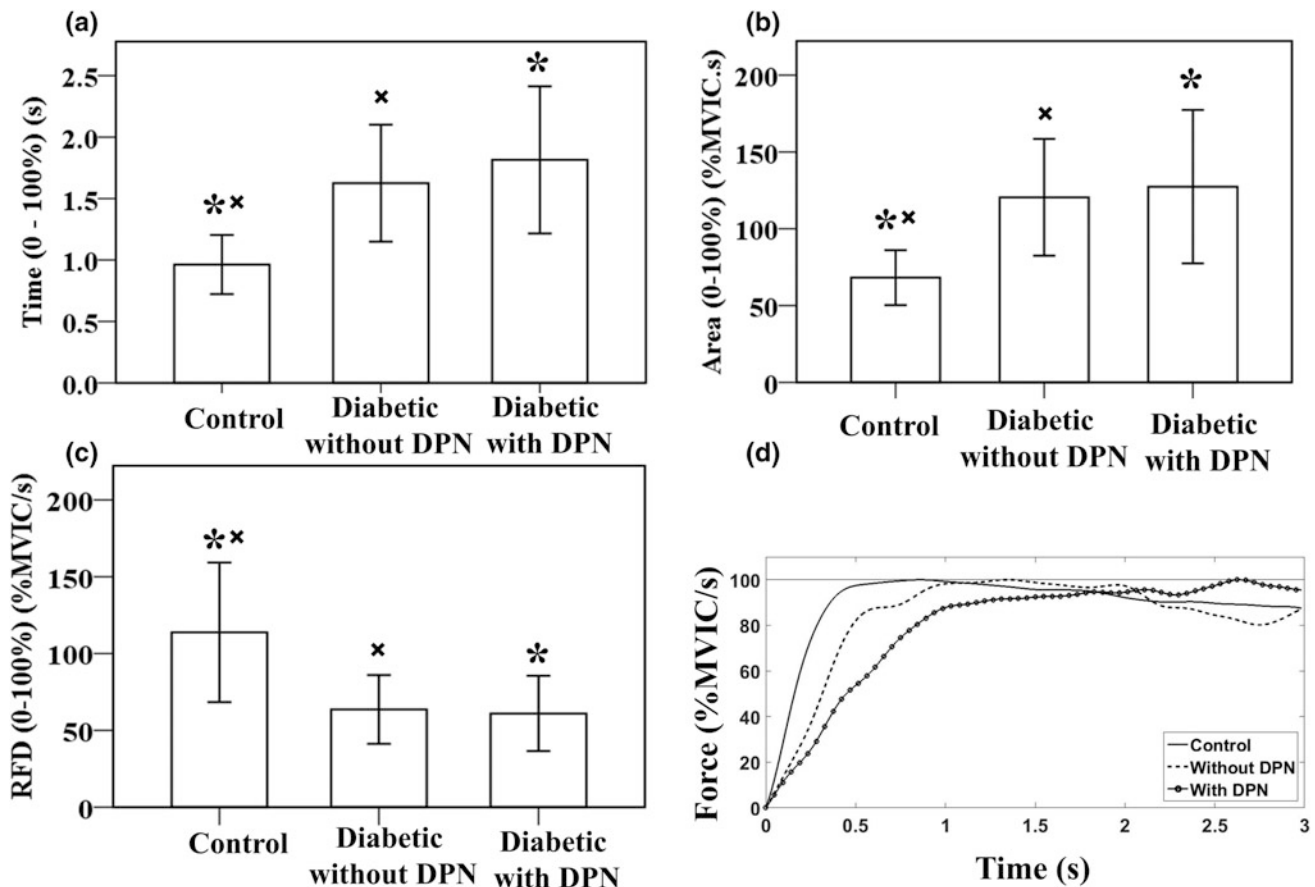
Fig. 4 Mean and standard deviation (SD) of the variables evaluated for the force range 0–100% of maximum voluntary isometric contraction (MVIC). **a** Time. **b** Area. **c** Rate of muscular force development (RFD). **d** Example of normalized force-time curve of three individuals. *Represent the significantly difference between the groups ($p < 0.05$)

individuals with and without DPN show changes in the type of fibers in the skeletal muscles, favoring the presence of type II fibers [3]. Also, both the firing frequency of motor units and the fiber type appear to influence the RFD, especially in the beginning of the force increase [12]. These changes can also have influenced RFD reduction and the increased time to reach MVIC for diabetic groups.

Although the results showed a significant reduction in the parameters analyzed, there is a sex difference between the groups. The number of male participants for each group is 28.6, 37.5 and 37.5% for the DPN group, the control group and the group without DPN, respectively. The sex is an important factor to be considered in studies that involve muscular force [18]. Consequently, further studies should be performed with the same proportion of male/female for each group. In addition, there was a statistically significant difference for age between the control group and the group without DPN. Although this significant age difference was found, this does not affect the parameters analyzed in this work [19, 20].

Finally, the reduced muscle capacity to produce a maximal force in a short time interval, as well as muscle

weakness can represent a higher risk of falls for this population [12]. Besides that, the reduction of muscle force in the ankle dorsiflexion contraction has been associated with plantar ulcers and foot deformity in individuals with DPN [6, 9, 10].

5 Conclusion

Only the diabetic individuals with DPN presented a reduction in MVIC force. However, diabetic individuals with and without DPN require longer time to achieve the maximal isometric force of ankle dorsiflexion, that results in a lower rate of muscular force development. Although patients without DPN showed no significant difference in the MVIC strength, a significant difference was observed in RFD, which may indicate that some type of muscle alteration is already occurring, but not yet sufficiently "severe" to cause changes in maximal force. Therefore, RFD was more sensitive to muscle changes caused by this pathology, compared to the MVIC force. In this way, this parameter can be further analyzed for possible diagnoses.

References

1. WHO Homepage. http://www.who.int/campaigns/world-health-day/2016/en/. Accessed 26 Mar 2018
2. Bansal, V., Kalita, K., Misra, U.: Diabetic neuropathy. Postgrad. Med. J. **82**, 95–100 (2006)
3. Tesfaye, S., Selvarajah, D.: Advances in the epidemiology, pathogenesis and management of diabetic peripheral neuropathy. Diabet. Metab. Res. Rev. **28**, 8–14 (2012)
4. Boulton, A.J.M.: Management of diabetic peripheral neuropathy. Clin. Diabet. **23**, 9–15 (2005)
5. Andersen, H., Jakobsen, J.: A comparative study of isokinetic dinamometry and manual muscle testing of ankle dorsal and plantar flexors and knee extensors and flexors. Eur. Neurol. **37**, 239–242 (1997)
6. Fernando, M., Crowther, R., Lazzarini, P., Sangla, K., Cunningham, M., Buttner, P., Golledge, J.: Biomechanical characteristics of peripheral diabetic neuropathy: a systematic review and meta-analysis of fi endings from the gait cycle, muscle activity and dynamic barefoot plantar pressure. Clin. Biomech. **28**, 831–845 (2013)
7. Andersen, H.: Motor dysfunction in diabetes. Diabet. Metab. **28**, 89–92 (2012)
8. MacGilchrist, C., Paul, L., Ellis, B.M., Howe, T.E., Kennon, B., Godwin, J.: Lower-limb risk factors for falls in people with diabetes mellitus. Diabet. Med. **27**, 162–168 (2010)
9. Armstrong, D.G., Lavery, L.A., Holtz-Neiderer, K., Mohler, M.J., Wendel, C.S., Nixon, B.P., Boulton, A.J.: Variability in activity may precede diabetic foot ulceration. Diabet. Care **27**, 1980–1984 (2004)
10. Van Schie, C.H.M., Vermigli, C., Carrington, A., Boulton, A.: Muscle weakness and foot deformities in diabetes. Diabet. Care **27**, 1668–1673 (2004)
11. Handsaker, J.C., Brown, S.J., Bowling, F.L., Cooper, G., Maganaris, C.N., Boulton, A.J., Reeves, N.D.: Contributory factors to unsteadiness during walking up and down stairs in patients with diabetic peripheral neuropathy. Diabet. Care **37**, 3047–3053 (2014)
12. Maffiuletti, N.A., Aagaard, P., Blazevich, A.J., Folland, J., Tillin, N., Duchateau, J.: Rate of force development: physiological and methodological considerations. Eur. J. Appl. Physiol. **116**, 1091–1116 (2016)
13. Aagaard, P., Simonsen, E.B., Andersen, J.L., Magnusson, P., Dyhre-Poulsen, P.: Increased rate of force development and neural drive of human skeletal muscle following resistance training. Am. Physiol. Soc. **93**, 1318–1326 (2002)
14. Favretto, M.A., Cossul, S., Andreis, F.R., Balotin, A.F., Marques, C.M.F., Marques, J.L.B.: Desenvolvimento de um sistema de avaliação da força isométrica de flexão dorsal do pé. In: V Congresso Brasileiro de Eletromiografia e Cinesiologia e X Simpósio de Engenharia Biomédica, pp. 377–380 (2017)
15. Webber, S.C., Porter, M.M.: Reliability of ankle isometric, isotonic, and isokinetic strength and power testing in older women. Phys. Ther. **90**, 1165–1175 (2010)
16. Ramji, N., Toth, C., Kennedy, J., Zochodne, D.W.: Does diabetes mellitus target motor neurons? Neurobiol. Dis. **26**, 301–311 (2007)
17. Andersen, H., Gadeberg, P.C., Brock, B., Jakobsen, J.: Muscular atrophy in diabetic neuropathy: a stereological magnetic resonance imaging study. Diabetologia 1062–1069 (1997)
18. Cruz-Jentoft, A.J., Baeyens, J.P., Bauer, J.M., Boirie, Y., Cederholm, T., Landi, F., Martin, F.C., Michel, J.P., Rolland, Y., Schneider, S.M., Topinková, E., Vandewoude, M., Zamboni, M.: Sarcopenia: European consensus on definition and diagnosis. Age Ageing **39**, 412–423 (2010)
19. Meldrum, D., Cahalane, E., Conroy, R., Fitzgerald, D., Hardiman, O.: Maximum voluntary isometric contraction: reference values and clinical application. Amyotroph. Later. Scler. **8**, 47–55 (2007)
20. Bemben, M.G., Massey, H.B., Bemben, D.A., Misner, J.E., Boileau, R.A.: Isometric muscle force production as a function of age in healthy 20 to 74 yr old men. Med. Sci. Sports Exerc. **23**, 1302–1310 (1991)

Evaluation of the Forced Oscillation Technique and the Extended RIC Model in the Analysis of Individuals with Work-Related Asthma

Fábio Augusto d'Alegria Tuza, Paula Morisco de Sá,
Agnaldo José Lopes, Hermano Albuquerque de Castro,
and Pedro Lopes de Melo

Abstract

The main objective of this study was to evaluate the performance of the Forced Oscillation Technique (FOT) and the extended RIC (eRIC) model in the analysis of respiratory mechanical alterations in individuals with work-related asthma (WRA). Twenty-nine individuals were evaluated: 17 healthy and 12 with WRA. Considering the resistive properties of the respiratory system, we observed increases in resistance of the peripheral airways (RpeRIC, $p < 0.009$) and a reduction in WRA homogeneity ($p < 0.02$). The use of a bronchodilator resulted in improvement of the total (R0, $p < 0.05$) and mean (Rm, $p < 0.01$) resistance. Regarding reactance, in the WRA group, the mean values were more negative (Xm, $p < 0.03$), while the resonance frequency increased (Fr, $p < 0.0001$), with decreases in dynamic compliance (C, $p < 0.05$, CeRIC, $p < 0.01$) and inertance (IeRIC, $p < 0.02$). We can conclude that FOT associated with the eRIC model may represent an alternative for longitudinal evaluation in WRA patients and can contribute to early disease identification.

F. A. d'Alegria Tuza · P. M. de Sá · P. L. de Melo (✉)
Biomedical Instrumentation Laboratory, Institute of Biology and Faculty of Engineering, State University of Rio de Janeiro, Rio de Janeiro, Brazil
e-mail: plopes@uerj.br

A. J. Lopes
Pulmonary Function Laboratory, Pedro Ernesto University Hospital, Rio de Janeiro, Brazil

H. A. de Castro
National School of Public Health, Oswaldo Cruz Foundation, Rio de Janeiro, Brazil

P. L. de Melo
Laboratory of Clinical and Experimental Research in Vascular Biology, State University of Rio de Janeiro, Rio de Janeiro, Brazil

1 Introduction

Asthma is a chronic treatable disease of the airways that affects all age groups and presents high prevalence, morbidity and mortality worldwide [1]. It is estimated that 10–15% of the asthma cases that begin in adulthood are directly caused by occupational factors, while another 10% result from worsening pre-existing asthma due to working environment conditions [2]. Work-related asthma (WRA) is characterized by obstructed and hyperreactive airways due to the work environment conditions and not to stimuli from outside the workplace [3, 4].

The functional evaluation of asthma, through spirometry, establishes the diagnosis, documents the severity of the airflow obstruction and monitors the course of the disease and the changes resulting from the treatment [5]. However, this technique requires high patient cooperation in the performance of forced respiratory manoeuvres, which may limit its use in children, the elderly or individuals with altered cognition [6]. In addition, the forced manoeuvre puts the bronchi under stress, which can alter the bronchial tone and lead the individual to exhaustion by repetition [7]. Whole-body plethysmography allows the measurement of pulmonary volumes, capacities and resistance [8] but requires high cooperation manoeuvres, much like spirometry.

The Forced Oscillation Technique (FOT), a simple and non-invasive application methodology, has as its main advantages the need for little cooperation and the realization during spontaneous breathing. It can contribute with new parameters for analysis [9]. Recent studies suggest that this technique can be applied in the detection of early respiratory changes in smokers [10], patients with sarcoidosis [11], silicosis [12] and conventional asthma [13]. Thus, it is possible to infer that FOT can contribute to the early diagnosis of patients with occupational diseases [14] and to the longitudinal evaluation of these volunteers. However, we found only one study in the literature that analysed changes

in respiratory mechanics associated with work-related asthma through FOT [15].

2 Objectives

In this context, the objectives of this study were [1] to compare the resistive and reactive properties of the respiratory system of healthy individuals and individuals with work-related asthma, [2] to determine the best parameters to diagnose the mentioned alterations and [3] to analyse the changes resulting from the bronchodilator test in these patients.

3 Materials and Methods

The present study is a controlled observational study developed at the Biomedical Instrumentation Laboratory of the State University of Rio de Janeiro. The study was approved by the Research Ethics Committee of the Pedro Ernesto University Hospital (protocol 456–CEP/HUPE). All individuals signed a consent form. There were no conflicts of interest.

3.1 Volunteers

Twenty-nine individuals were analysed. The control group (CG) consisted of 17 individuals with normal spirometry and no history of previous lung disease. Twelve individuals were included in the WRA asthma group. For both groups, the exclusion criteria were tuberculosis, trauma or thoracic surgery, respiratory infections in the last 30 days, chemotherapeutic and/or radiotherapeutic treatment and inability to perform the tests.

The CG was submitted to spirometry and FOT tests. In the WRA group, the sequence of the tests performed was as follows: interview, Asthma Control Test (ACT) questionnaire and respiratory function tests (FOT, spirometry and plethysmography, in this order).

The use of bronchodilator medication (400 µg salbutamol sulphate spray) was performed immediately after the first set of pulmonary function tests and the second cycle of measurements 15 min later. The WRA group measurements were analysed for two moments: pre-bronchodilator (WRA Pre-BD) and post-bronchodilator (WRA Post-BD). A questionnaire [16] was also applied to evaluate the control of asthma in the 30 days prior to the pulmonary function tests.

3.2 Forced Oscillation Technique

The FOT system applies sinusoidal pressure signals with frequencies that are multiples of 2 Hz in the range of 4–32 Hz, using a device developed in our laboratory [17]. During the examination, the subject remains seated, breathing through a mouthpiece, using a nasal clip and holding their cheeks to reduce the shunt effect of the upper airways. Three consecutive tests of 16 s each are performed, obtaining the mean as the final result. The minimum coherence function considered for acceptance is 0.9.

The results associated with the resistive impedance component were analysed using a linear regression between 4 and 16 Hz to obtain the resistance at the intercept (R0), associated with the total resistance of the respiratory system. The mean resistance between 4 and 16 Hz (Rm), related to the airway resistance, was also assessed, as was the slope of the resistance curve, associated with the non-homogeneity of the respiratory system.

The results related to the reactive component were described by the mean reactance (Xm), associated with the homogeneity of ventilation, the dynamic compliance (Cdin), associated with the elastic properties of the respiratory system, and the impedance modulus of the respiratory system at 4 Hz (Z4), associated with the total mechanical load of the respiratory system.

An electrical model was used to obtain more details about the respiratory mechanics in WRA [18] (Fig. 1). This model employs resistance (R), related to the resistance of the central airways; inertance (I), associated with the inertia associated with the displacement of air mass within the system; dynamic compliance of the respiratory system (C); and peripheral resistance (Rp), describing the resistance presented by the small airways of the respiratory system. The total resistance (Rt), the sum of the values of R and Rp, was also calculated.
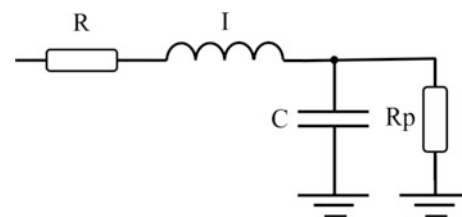
Fig. 1 Electrical representation of a two-compartment model used to analyze respiratory impedance. Resistance, inductance and capacitance are the analogs of mechanical resistance, inertance and compliance, respectively. R is analogous to central airway resistance and Rp describes peripheral resistance, I is associated with lung inertance and C with alveolar compliance

3.3 Data Processing, Presentation and Statistical Analysis

A commercial software package (Origin® 8.0, Microcal Software Inc., Northampton, MA, USA) was used to compare the differences between the groups. First, the Shapiro Wilk test was applied to analyse the distribution of each sample. Considering the non-normal distribution, non-parametric tests were applied. For the comparison of two different groups (control and WRA preDB and control and WRAposBD), the Mann-Whitney test was applied. For the comparison of the same group in different situations (preBd and postBD), the Wilcoxon test was applied.

4 Results

Considering the absence of statistical significance between the biometric parameters analysed, the sample was considered homogeneous (Table 1). The results obtained from the spirometric parameters presented reduced mean values in the presence of asthma. For resistance and TGV measurements, there was improvement after the use of the bronchodilator, with increases in the mean values. Similar results were obtained for Gaw, with improvement of the mean values after bronchodilator use (Table 2). Table 3 shows the sample characteristics according to the disease severity considering Raw measured by plethysmography.

R0 was significantly reduced in the WRA group after use of the bronchodilator (Fig. 2a; $p < 0.05$). A similar result was observed in Rm (Fig. 2b; $p < 0.01$). S showed a reduction in homogeneity in the WRA Pre-BD group ($p < 0.02$) and improvement in the Post-BD group ($p < 0.05$) (Fig. 2c). In the reactive parameters, Xm (Fig. 2d) presented more negative values in the presence of WRA Pre-BD ($p < 0.03$) and Post-BD ($p < 0.01$) and with improved homogeneity in the presence of the bronchodilator ($p < 0.05$). A similar result was observed in Fr (Fig. 2e). Compliance (Fig. 2f) was reduced in the WRA Pre-BD group ($p < 0.05$) and did not show significant change after bronchodilator use.

There were no changes comparing the impedance at 4 Hz between the control group and WRA pre or post bronchodilator. This parameter was reduced after bronchodilator use in the WRA group ($p < 0.02$).

The changes observed from the eRIC model are described in Fig. 3. A significant change in R (Fig. 3a) was observed in the comparison between the Pre-BD and Post-BD groups ($p < 0.005$). For Rp (Fig. 3b), there were increased mean

Table 1 Anthropometric characteristics of the groups studied

	Control (n = 17)	Work-related asthma (n = 12)
Age (years)	48.1 ± 11.6	48.1 ± 12.9
Weight (kg)	72.1 ± 10.2	78.7 ± 14.1
Height (cm)	166.1 ± 6.5	164.5 ± 7.2
BMI (kg/m^2)	26.2 ± 4.1	27.3 ± 6.1

BMI body mass index

Table 2 Spirometric and plethysmographic measurements of the groups studied

	Control (n = 17)	Work-related asthma (n = 12)	
		Pre-BD	Post-BD
FEV$_1$ (L)	3.1 ± 0.7	2.3 ± 0.5	2.4 ± 0.6
FEV$_1$ (%)	99.8 ± 12.6	75.6 ± 16.3	79.6 ± 18.2
FVC (L)	3.8 ± 0.8	3.1 ± 0.7	3.2 ± 0.8
FVC (%)	100.1 ± 13.2	83.1 ± 15.0	84.2 ± 17.9
FEV$_1$/FVC	83.3 ± 4.2	74.9 ± 9.5	77.6 ± 6.9
FEF 25–75%	3.5 ± 0.9	2.1 ± 1.0	2.3 ± 0.8
FEF/CVF	0.8 ± 0.2	0.6 ± 0.3	0.7 ± 0.2
Raw (cmH$_2$O/L/s)		8.0 ± 6.1	5.2 ± 4.4
sGaw (L/s/cmH$_2$O)		0.11 ± 0.09	0.15 ± 0.11
TGV (L)		4.1 ± 5.8	3.5 ± 5.1

FEV$_1$—forced expiratory volume in one second; FVC—forced vital capacity; FEV$_1$/FVC—relation between FEV$_1$ and FVC; FEF 25–75%—forced expiratory flow between 25 and 75%; FEF/CVF—ratio of FEF 25–75% and FVC; Raw—airway resistance; sGaw—specific airway conductance; TGV—thoracic gas volume; n = number of patients evaluated. Pre-BD—pre-bronchodilator; PostBD—post-bronchodilator

Table 3 Classification according to resistance measure

Volunteers	Raw	Severity
4 (34%)	<2.5	Normal
1 (8%)	2.5–4.4	Light
1 (8%)	4.5–8.0	Moderate
6 (50%)	>8.0	Severe

Raw—airway resistance
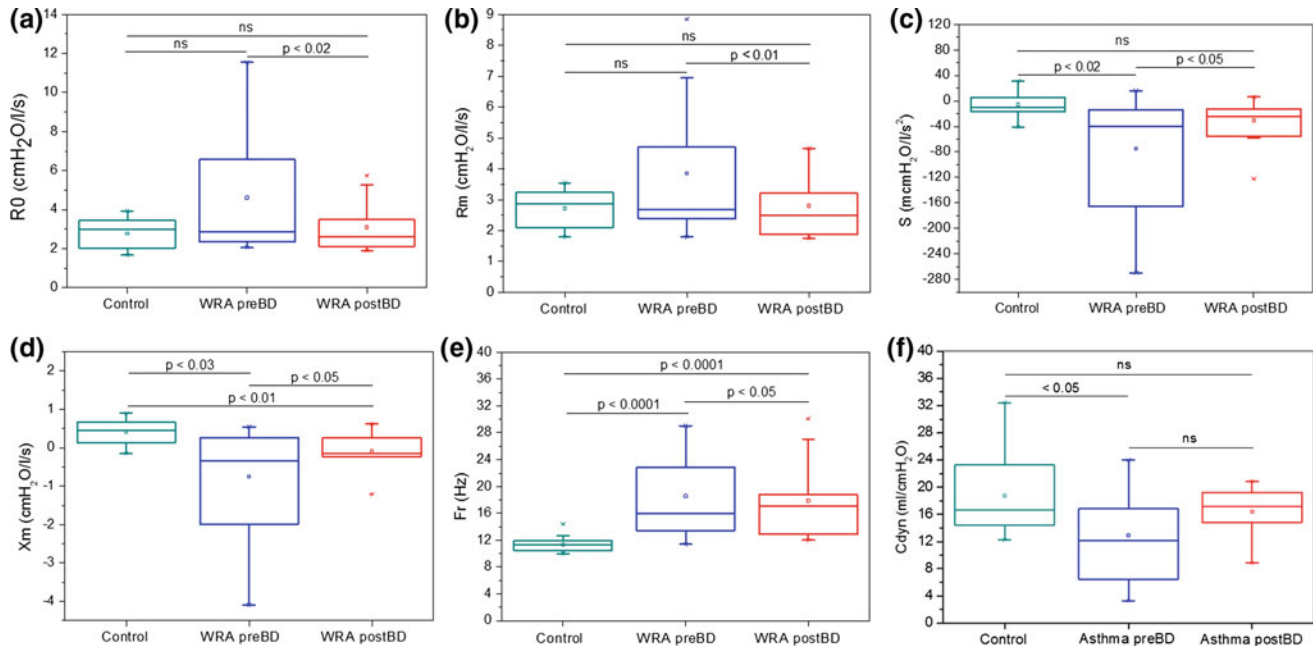
Fig. 2 Comparative analysis of the classical parameters obtained from the control group and worked-related asthma group. Respiratory system resistance (R0; **a**), mean resistance (Rm, **b**) and slope of respiratory resistance (S; **c**), mean respiratory reactance (Xm; **d**), resonant frequency (Fr, **e**) and dynamic compliance (Cdyn; **f**). WRA: work related asthma

values in the Pre-BD ($p < 0.009$) and Post-BD ($p < 0.002$) asthmatics groups. In C (Fig. 3c), the mean values were reduced in the Pre-BD ($p < 0.01$) and Post-BD ($p < 0.02$) WRA groups. Similar behaviour was observed for I (Fig. 3 d), with significant reductions in the Pre-BD ($p < 0.02$) and Post-BD ($p < 0.02$) WRA groups. There were no significant changes in Rt (Fig. 3e).

The Asthma Control Test showed that 50% of the individuals in the WRA group presented score values lower than 18 [16] and therefore were classified as uncontrolled asthma, while 50% were considered as controlled asthma.

5 Discussion

The results from the spirometric and plethysmographic parameters (Table 2) were compatible with the mentioned changes and are in agreement with data previously described in the literature [19].

In the asthmatics group, 50% of the individuals presented values lower than 18 in the ACT and therefore were classified as uncontrolled asthma, while 50% were considered as controlled asthma. This finding can explain the fact that 6 individuals (50%) with WRA presented high Raw and were classified as severe obstruction by plethysmography (Table 3).

R0 is associated with the total resistance of the respiratory system, including airways, the pulmonary parenchyma and the thoracic cage; Rm describes changes in central airways [20]. In the presence of WRA, the airway obstruction and possible irreversible structural changes (airway remodelling) [5, 21] caused by chronic inflammation may lead to deterioration of pulmonary function. However, in the present study, as described in Fig. 2a, b, there were no significant changes in total and mean resistance comparing the CG and the WRA groups, likely due to the great heterogeneity of the asthmatics group studied. In contrast to our results, a previous study [15] showed that R0 was the best parameter to
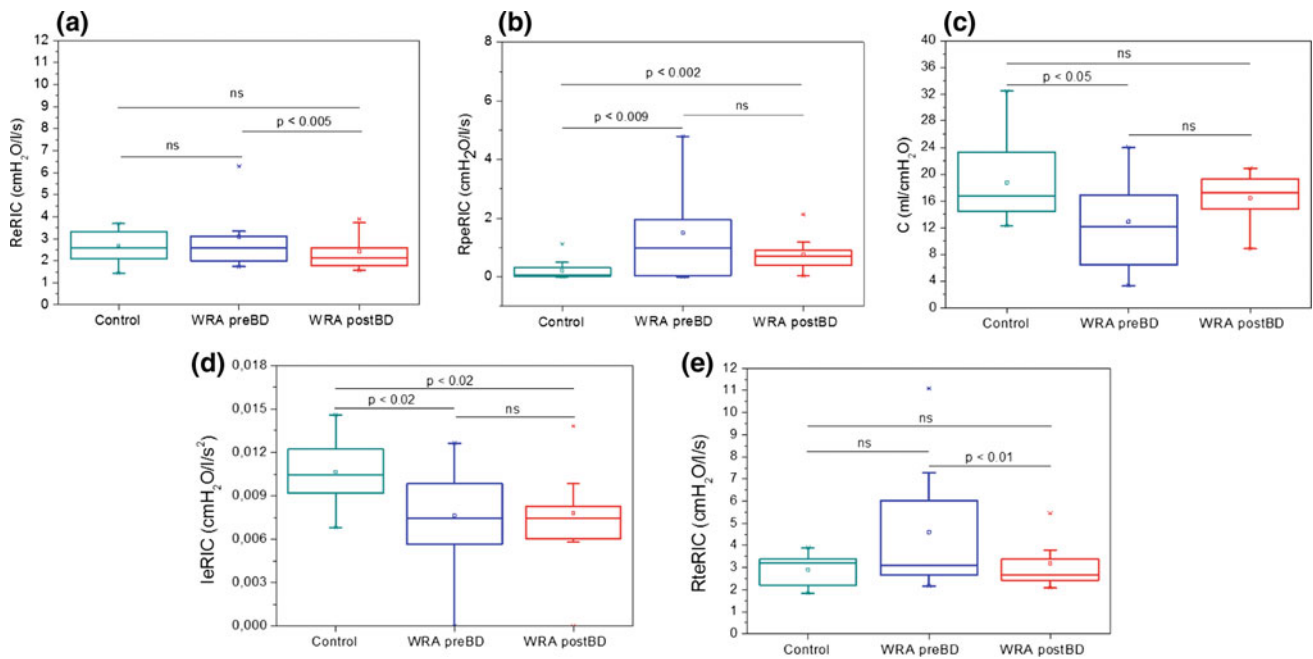
Fig. 3 Influence of work-related asthma and bronchodilator use on parameter values estimated from the compartmental model analysis. Central airway resistance (ReRIC; **a**), peripheral resistance (RpeRIC; **b**), alveolar compliance (CeRIC; **c**), lung inertance (IeRIC; **d**) and total resistance (RteRIC; **e**). WRA: work related asthma

discriminate volunteers with occupational asthma when compared with non-asthmatic patients. However, comparing the pre- and post-BD WRA groups, the FOT was able to identify the improvements in both R0 and Rm after bronchodilator use. Similar results were found in a study with 29 asthmatic adults [7].

The slope of the resistance curve is associated with intrapulmonary gas distribution, and thus, with ventilation homogeneity [22, 23]. In the present study, we observed a decrease in respiratory system homogeneity in the presence of WRA ($p < 0.02$), with a significant improvement after bronchodilator use ($p < 0.05$), in agreement with what was described in previous studies with asthmatics and patients with cystic fibrosis [7, 24, 25]. The alteration of homogeneity may be associated with an inflammatory process with reduction of bronchial lumen either by the presence of bronchospasm or secretion [26]. In agreement with these results, Cavalcanti et al. showed that the use of the bronchodilator led to an increase in the mean values of S in asthmatic volunteers ($p < 0.05$), which may reflect a reduction in respiratory system impedance and an improvement in homogeneity [26].

In normal individuals, the low-frequency reactance is negative due to the system's compliance, showing an increasing value up to zero at approximately 8 Hz (resonance frequency) [9]. More negative values of Xm were observed in the presence of Pre-BD ($p < 0.03$) and post-BD ($p < 0.01$) WRA, with improvements after bronchodilator

use ($p < 0.05$). These results may be related to the increase in the resistance of the peripheral airways that occurs in asthma, as was observed by Souza et al. when studying asthmatic children [27]. More negative values of Xm were reflected in the increase of resonance frequency (Fig. 2e).

There is a much greater influence of upper airway impedance in asthmatic individuals than that observed in normal individuals, in addition to the presence of pulmonary remodelling caused by the frequent inflammatory processes, the increased airway resistance and loss of the elastic support of the pulmonary parenchyma [28]. In our study, the impedance at 4 Hz was reduced after bronchodilator use in the WRA group ($p < 0.02$), reflecting the reduction of the total mechanical load of the respiratory system; however, there was no significant difference in the comparison between the control group and the WRA group.

In a study with asthmatic adults with different levels of obstruction [29], significant changes were observed in all parameters in the eRIC model, in contrast to our findings, where there were no significant changes in ReRIC and RteRIC when comparing the CG and WRA groups (Fig. 3). However, we noticed a reduction in ReRIC ($p < 0.005$) after bronchodilator use in the asthmatic group. RpeRIC was increased in the presence of asthma. This fact is compatible with the pathophysiology of this disease, as it is notorious for causing changes in the peripheral airways resulting from frequent bronchoconstriction reactions [28]. Considering that the disease begins in the peripheral airways, we can

speculate that the modifications found in the RpeRIC may reflect early modifications in the airways. There were significant reductions in IeRIC and CeRIC (p < 0.002 and p < 0.01, respectively), reflecting the pathophysiology of asthma, including intermittent and reversible bronchial narrowing caused by bronchial smooth muscle contraction, mucosal oedema and mucosal hypersecretion [30].

6   Conclusions

This study indicates that FOT may be useful in the identification of respiratory system modifications in volunteers with WRA. Considering that asthma begins in the peripheral airways, the main finding refers to the modifications found in the RpeRIC, which may reflect early modifications in the airways of these individuals. FOT associated with the eRIC model may constitute a simple and easily applied methodology that can be an adequate alternative for both the longitudinal evaluation of these patients and the early identification of the disease.

References

1. Cardoso, T.A., Roncada, C., Silva, E.R.D., Pinto, L.A., Jones, M. H., Stein, R.T., et al.: The impact of asthma in Brazil: a longitudinal analysis of data from a Brazilian national database system. Jornal brasileiro de pneumologia **43**(3), 163–168 (2017)

2. Mendonça, E.M.C.: Asma Relacionada ao Trabalho. In: Santos, U. P. (ed.) Pneumologia Ocupacional Ilustrada—Fotos e Fatos, 1a edn, pp. 59–63. Atheneu, São Paulo (2014)

3. Sarti, W., Voltarelli, J.C., Barbosa, E., Louzada, Jr. P.: Asthma induced by occupational agents Rev. bras. alerg. imunopatol. Rev bras alergimunopatol. **21**(3), 66–74 (1998)

4. Vila-Rigat, R., Panadès Valls, R., Hernandez Huet, E., Sivecas Maristany, J., Blanché Prat, X., Muñoz-Ortiz, L., et al.: Prevalence of work-related asthma and its impact in primary health care. Archivos de Bronconeumología (English Edition) **51**(9), 449–455 (2015)

5. SBPT. Sociedade Brasileira de Pneumologia e Tisiologia. Diretrizes da Sociedade Brasileira de Pneumologia e Tisiologia para o Manejo da Asma—2012. Jornal Brasileiro de Pneumologia **30**(1), S1–S46 (2012)

6. Carvalhaes-Neto, N., Lorino, H., Gallinari, C., Escolano, S., Mallet, A., Zerah, F., et al.: Cognitive function and assessment of lung function in the elderly. Am. J. Respir. Crit. Care Med. **152**(5 Pt 1), 1611–1615 (1995)

7. Cavalcanti, J.V., Lopes, A.J., Jansen, J.M., de Melo, P.L.: Using the forced oscillation technique to evaluate bronchodilator response in healthy volunteers and in asthma patients presenting a verified positive response. J. Bras. Pneumol. **32**(2), 91–98 (2006)

8. de Mir Messa, I., Sardon Prado, O., Larramona, H., Salcedo Posadas, A., Villa Asensi, J.R.: Grupo de Tecnicas de la Sociedad Espanola de Neumologia P. [Body plethysmography (I): Standardisation and quality criteria]. Anales de pediatria **83**(2), 136 e1-7 (2015)

9. Melo, P.L., Werneck, M.M., Gianella-Neto, A.: Avaliação de mecânica ventilatória por oscilações forçadas: fundamentos e aplicações clínicas. Jornal de Pneumologia **26**(4), 194–206 (2000)

10. Faria, A.C., Lopes, A.J., Jansen, J.M., Melo, P.L.: Evaluating the forced oscillation technique in the detection of early smoking-induced respiratory changes. Biomed. Eng. Online **25**(8), 22 (2009)

11. Faria, A.C., Lopes, A.J., Jansen, J.M., Melo, P.L.: Assessment of respiratory mechanics in patients with sarcoidosis using forced oscillation: correlations with spirometric and volumetric measurements and diagnostic accuracy. Respiration **78**(1), 93–104 (2009)

12. Sa, P.M., Faria, A.D., Ferreira, A.S., Lopes, A.J., Jansen, J.M., Melo, P.L.: Validation of the forced oscillation technique in the diagnostic of respiratory changes in patients with silicosis. Conf. Proc. IEEE Eng. Med. Biol. Soc. **2010**, 398–401 (2010)

13. Veiga, J., Lopes, A., Jansen, J., Melo, P.: Within-breath analysis of respiratory mechanics in asthmatic patients by forced oscillation. Clinics **64**(7), 649–656 (2009)

14. Pham, Q.T., Bourgkard, E., Chau, N., Willim, G., Megherbi, S.E., Teculescu, D., et al.: Forced oscillation technique (FOT): a new tool for epidemiology of occupational lung diseases? Eur. Respir. J. **8**(8), 1307–1313 (1995)

15. Descatha, A., Fromageot, C., Ameille, J., Lejaille, M., Falaize, L., Louis, A., et al.: Is forced oscillation technique useful in the diagnosis of occupational asthma? J. Occup. Environ. Med. **47**(8), 847–853 (2005)

16. Roxo, J.P., Ponte, E.V., Ramos, D.C., Pimentel, L., D'Oliveira, Jr. A., Cruz, A.A.: Portuguese-language version of the asthma control test: validation for use in Brazil. J. Bras. Pneumol. **36**(2), 159–166 (2010)

17. de Melo, P.L., Werneck, M.M., Giannella-Neto, A.: New impedance spectrometer for scientific and clinical studies of the respiratory system. Rev. Sci. Instrum. **71**(7), 2867–2872 (2000)

18. Diong, B., Nazeran, H., Nava, P., Goldman, M.: Modeling human respiratory impedance. Comparing the best method with the least estimation errors. IEEE Eng. Med. Biol. Mag. **26**(1), 48–55 (2007). PubMed PMID: 17278772

19. Chan-Yeung, M., Malo, J.L., Tarlo, S.M., Bernstein, L., Gautrin, D., Mapp, C., et al.: Proceedings of the first Jack Pepys occupational asthma symposium. Am. J. Respir. Crit. Care Med. United States **167**, 450–471 (2003)

20. Lorino, A.M., Zerah, F., Mariette, C., Harf, A., Lorino, H.: Respiratory resistive impedance in obstructive patients: linear regression analysis vs viscoelastic modelling. Eur. Respir. J. **10**(1), 150–155 (1997)

21. Pavord, I.D., Green, R.H., Haldar, P.: Diagnosis and management of asthma in adults. In: Spiro, D.G., Silvestri, G.A., Agustí, A. (eds.), Clinical Respiratory Medicine, 4 edn. Philadelphia, Elsevier Saunders, pp. 501–520 (2012)

22. Oostveen, E., Peslin, R., Duvivier, C., Rotger, M., Mead, J.: Airways impedance during single breaths of foreign gases. J. Appl. Physiol. (1985) **71**(5), 1813–1821 (1991)

23. de Melo, P.L., Werneck, M.M., Giannella-Neto, A.: Effect of generator nonlinearities on the accuracy of respiratory impedance measurements by forced oscillation. Med. Biol. Eng. Comput. **38**(1), 102–108 (2000)

24. MacLeod, D., Birch, M.: Respiratory input impedance measurement: forced oscillation methods. Med. Biol. Eng. Comput. **39**(5), 505–516 (2001). PubMed PMID: 11712646. Epub 2001/11/20. eng

25. Lima, A.N., Faria, A.C.D., Lopes, A.J., Jansen, J.M., Melo, P.L.: Forced oscillations and respiratory system modeling in adults with cystic fibrosis. Biomed. Eng. Online 142015

26. Zerah, F., Lorino, A.M., Lorino, H., Harf, A., Macquin-Mavier, I.: Forced oscillation technique vs spirometry to assess bronchodilatation in patients with asthma and COPD. Chest **108**(1), 41–47 (1995)

27. Souza, G.A.F., Faria, A.C.D., Lopes, A.J., Jansen, J.M., Melo, P.L.: Avaliação do Desempenho da Técnica de Oscilações Forçadas na Identificação Precoce das Alterações Respiratórias em Crianças Asmáticas. IV Latin American Congress on Biomedical Engineering; Isla Margarita: Annals of the IV Latin American Congress on Biomedical Engineering, pp. 1005–1009 (2007)

28. Fernandes, A.L.G., Stelmach, R., Algranti, E.: Occupational asthma. J. Bras. Pneumol. **32**, S27–S34 (2006)

29. Faria, A.C.D., Veiga, J., Lopes, A.J., Melo, P.L.: Forced oscillation, integer and fractional-order modeling in asthma. Comput. Methods Programs Biomed. **128**, 12–26 (2016)

30. Cockcroft, D.W.: Direct challenge tests: airway hyperresponsiveness in asthma: its measurement and clinical significance. Chest **138**(2 Suppl), 18s–24s (2010)

Evaluation of the Forced Oscillation Technique in the Differential Diagnosis of Obstructive and Restrictive Respiratory Diseases

Alexandre G. Sancho, Alvaro C. D. Faria, Jorge L. M. Amaral, Agnaldo J. Lopes, and Pedro L. Melo

Abstract

The aim of this study was to investigate the potential of the forced oscillation technique (FOT) in the differential diagnosis of patients with obstructive and restrictive respiratory diseases. A total of 76 individuals was analysed, including moderate obstructive (MO; n = 18), severe obstructive (SO; n = 20), moderate restrictive (MR; n = 18) and severe restrictive (SR; n = 20) patients. The observed changes were consistent with previously published results and the physiological foundations involved. Analyses using receiver operator characteristic curves showed that resistance values provided adequate differentiation between patient groups with more advanced diseases (SO-MR and SO-SR), with diagnostic accuracy ≥ 0.80. The highest accuracy was offered by the respiratory system resonance frequency, which discriminated between the obstructive and restrictive groups accurately (≥ 0.84). Given the ease of performing the test, we can assume that the proposed methodology will provide a significant contribution to the differential diagnosis of obstructive and restrictive respiratory diseases.

Keywords

Oscillatory mechanics • Forced oscillation technique • Differential diagnosis • Respiratory mechanics

1 Introduction

Obstructive and restrictive lung diseases may cause shortness of breath, severe coughing and chest pain. Treatment is different for each condition; therefore, a methodology is required that allows a distinction to be made between these two disease classes [1].

The forced oscillation technique (FOT) is a non-invasive method to evaluate the respiratory system impedance (Zrs) and its two components: respiratory resistance (Rrs) and reactance (Xrs). Due to several recent technical enhancements, FOT currently represents the state of the art in lung function evaluation [2].

The parameters derived from the test allow a more detailed analysis of the respiratory systems of obstructive individuals and patients with restrictive disease. Therefore, FOT presets a great potential in the differential diagnosis of patients with obstructive and restrictive diseases. However, FOT findings that are characteristic of individuals with restrictive diseases have not yet been fully demonstrated [3], and only one study provided evidence that FOT may be able to distinguish between restrictive and obstructive lung disease [4].

Therefore, the objectives of this study were (1) to evaluate the potential of FOT in the differential diagnosis of obstructive and restrictive respiratory changes and (2) to identify the best FOT parameters for this task.

2 Materials and Methods

The experimental phase of this research was developed at the Department of Pulmonology of the Pedro Ernesto University Hospital (HUPE) and at the Biomedical Instrumentation

A. G. Sancho · A. C. D. Faria · P. L. Melo
Biomedical Instrumentation Laboratory, Institute of Biology and Faculty of Engineering, State University of Rio de Janeiro, Rio de Janeiro, Brazil

J. L. M. Amaral
Department of Electronics and Telecommunications Engineering, State University of Rio de Janeiro, Rio de Janeiro, Brazil

A. J. Lopes (✉)
Pulmonary Function Laboratory, State University of Rio de Janeiro, Ernesto University Hospital, Rio de Janeiro, Brazil
e-mail: plopes@uerj.br

P. L. Melo
Laboratory of Clinical and Experimental Research in Vascular Biology, State University of Rio de Janeiro, Rio de Janeiro, Brazil

Laboratory of the State University of Rio de Janeiro. The experimental protocol was approved by the Research Ethics Committee of the HUPE (456-CEP/HUPE) and Informed Consent Form was obtained from all volunteers.

2.1 Respiratory Function Tests

FOT was performed using small amplitude pressure oscillations generated by a speaker applied at the entrance of the individual's airway through the oral cavity during spontaneous breathing. The individual's nostrils were occluded with a nose clip, and the same held her cheeks and chin with her hands to minimise the shunt effect of the upper airways. Three consecutive tests were conducted, each approximately 16 s long, with the mean score being adopted as the final result. The minimum coherence function used for the acceptance of results was 0.9 [5]. The tests were performed at a frequency range between 4 and 32 Hz. The analyses were performed using an *OSCILAB* 2.0 impedance analyser developed at LIB/UERJ.

After FOT, spirometry was performed and interpreted according to the recommendations of the Brazilian Consensus on Spirometry [6] and the American Thoracic Society/European Respiratory Society [7]. The analysed parameters were forced expiratory volume in one second (FEV_1), forced vital capacity (FVC) and FEV_1/FVC ratio and are expressed as absolute values and as percentages of predicted values.

2.2 Analysed Individuals

A total of 76 volunteers were recruited for the study, of whom 38 had bronchial asthma, and 38 had restrictive respiratory disease. Twenty of the asthmatic volunteers had moderate obstruction (MO), and 18 had severe obstruction (SO) [8]. The restrictive disease group included conditions such as idiopathic pulmonary fibrosis, scleroderma, silicosis, sarcoidosis and asbestosis. Eighteen had moderate restrictions (MR) and 20 severe restrictions (SR) [8]. The inclusion criteria for asthmatic volunteers and individuals with restrictive disease were the clinical diagnosis of the disease, exclusion of other cardiovascular and/or respiratory diseases and being over 18 years of age. Asthmatic volunteers experiencing a crisis and/or with a history of smoking were excluded from the study.

2.3 Data Processing, Presentation of Results and Statistical Analysis

The resistive properties were interpreted by means of total or intercept resistance (R0), obtained by linear regression in the resistance curve in the 4–16 Hz range, the angular coefficient of resistance (S) and mean resistance (Rm). R0 is related to the total resistance of the respiratory system, including the airways and resistance of tissue originating from the lung and chest wall, along with the effect of gas redistribution (pendelluft). S describes the resistance change as a frequency and is related to respiratory system inhomogeneities, while Rm is sensitive to the airway calibre and reflects resistance in the central airways. The results associated with reactance were interpreted using three parameters: mean reactance (Xm), resonance frequency and dynamic respiratory system compliance (Cdyn). Mean reactance is generally related to respiratory system inhomogeneity and was calculated using the 4–32 Hz frequency range in this study. The frequency at which Xrs becomes zero is known as the resonance frequency (fr). Cdyn is related to the total compliance of the respiratory system, comprising pulmonary compliance, chest wall compliance and airway compliance. The second component is related to the homogeneity of the respiratory system. Cdyn was calculated based on the reactance at 4 Hz (Cdyn = $1/2\pi fX4$). The 4 Hz impedance module (Z4) was also studied, which reflects the total mechanical load of the respiratory system [5].

The results are presented as the means $\pm$ standard deviations and are described in a table and box graphs. Statistical analysis was performed comparing pairs of groups using the ORIGIN PRO 8.0 program (Microcal Software Inc., Northampton, Massachusetts, United States). Initially, the sample's distribution characteristics were evaluated using the Shapiro-Wilk test. The independent t-test was used when the data exhibited a normal distribution, and a non-parametric test (Mann-Whitney) was used when the data were not normally distributed. Differences were considered statistically significant at $p < 0.05$.

A ROC (receiver operating characteristic) curve analysis was used to evaluate the potential clinical use of FOT indices to discriminate between obstructive and restrictive respiratory changes [9]. Diagnostic accuracy was evaluated using the area under the curve (AUC). According to the literature, ROC curves with a minimum AUC value of 0.80 may be considered useful for clinical use [9]. These analyses were conducted using MedCalc 12 (MedCalc Software, Mariakerke, Belgium).

3 Results

Regarding the biometric characteristics of the studied individuals (Table 1), although slight differences were observed in terms of age and weight between groups, these differences were not significant ($p > 0.05$).

Figure 1 compares the effects of obstruction and restriction on the resistive properties of the respiratory system in the studied patients.

The R0 values (Fig. 1a) in individuals with moderate restrictive changes were not significantly different from those observed in the severe restriction group. The same was observed when comparing moderate obstructive with severe obstructive individuals. Statistically significant differences were observed in all combinations (MO × MR; MO × SR; SO × MR; SO × SR) between the obstructive and restrictive groups.

Figure 1b shows that there were no significant changes in Rm between moderate and severe obstructive individuals; the same behaviour was observed in the moderate and severe restrictive groups. The intergroup (obstructive vs. restrictive) comparison revealed statistically significant differences, except in the comparison between moderate obstructive and moderate restrictive volunteers.

The S of individuals with moderate obstruction was not significantly reduced in comparison with those with severe obstruction (Fig. 1c). The moderate restrictive group showed a significant difference ($p < 0.05$) when compared with the severe restrictive group. Intergroup comparison (obstructive × restrictive) revealed significant changes in all combinations. Figure 2 illustrates the behaviour of the reactive parameters.

Figure 2a shows that no significant changes occurred when comparing the fr values obtained in moderate and severe obstructive volunteers and between moderate and severe restrictive volunteers. Significant changes were observed in all of the restrictive and obstructive group combinations (MO × MR; MO × SR; SO × MR; SO × SR).

Xm had more negative values in severe obstructive than in moderate obstructive volunteers (Fig. 2b), whereas no changes were observed between the restrictive patient groups. This parameter also showed significant changes in all obstructive and restrictive group combinations (MO × MR; MO × SR; SO ×MR; SO × SR).

There were no significant differences between moderate and severe obstructive volunteers or between moderate and severe restrictive volunteers in Cdyn (Fig. 2c). Visually,

Table 1 Biometric and spirometric characteristics of the studied individuals

	Moderate obstruction (n = 20)	Severe obstruction (n = 18)	Moderate restriction (n = 18)	Severe restriction (n = 20)
Age	44.2 ± 17.4	49.6 ± 18.2	57.8 ± 16.1	57.4 ± 16.7
Weight	69.6 ± 13.2	65.1 ± 14.8	65.3 ± 13.5	59.7 ± 15.3
Height	158.1 ± 11.1	159.9 ± 8.99	156.6 ± 6.48	157.3 ± 8.71
FEV_1 (%)	58.9 ± 13.2	39.3 ± 11.6	60.1 ± 5.32	49.8 ± 7.05
FVC (%)	84.4 ± 14.8	69.6 ± 21.1	55.3 ± 3.13	44.5 ± 5.24
FEV_1/FVC	58.4 ± 6.45	46.3 ± 7.42	94.9 ± 15.3	102.1 ± 16.4

FEV_1 = forced expiratory volume in one second, FVC = forced vital capacity
FEV_1/FVC = Tiffeneau index
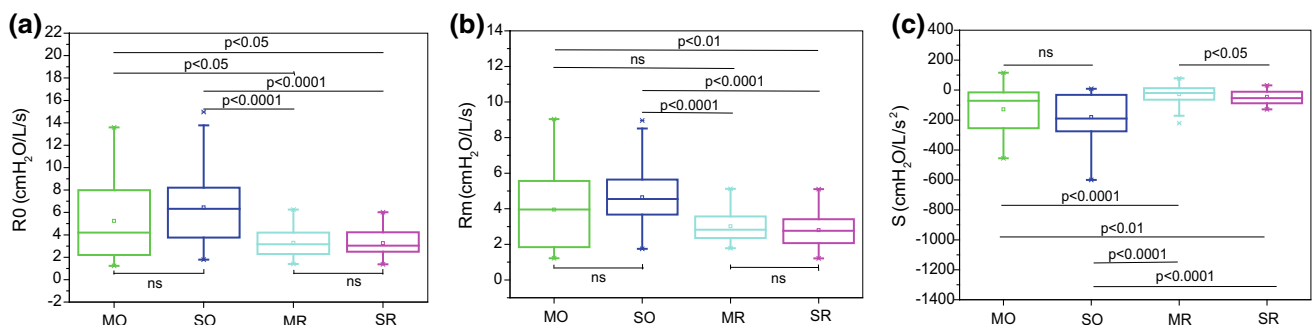
Fig. 1 Comparative analysis of the total resistance (R0, **a**), mean resistance (Rm, **b**) and slope of the resistance values (S, **c**) in moderate obstruction (MO), severe obstruction (SO), moderate restriction (MR) and severe restriction (SR)
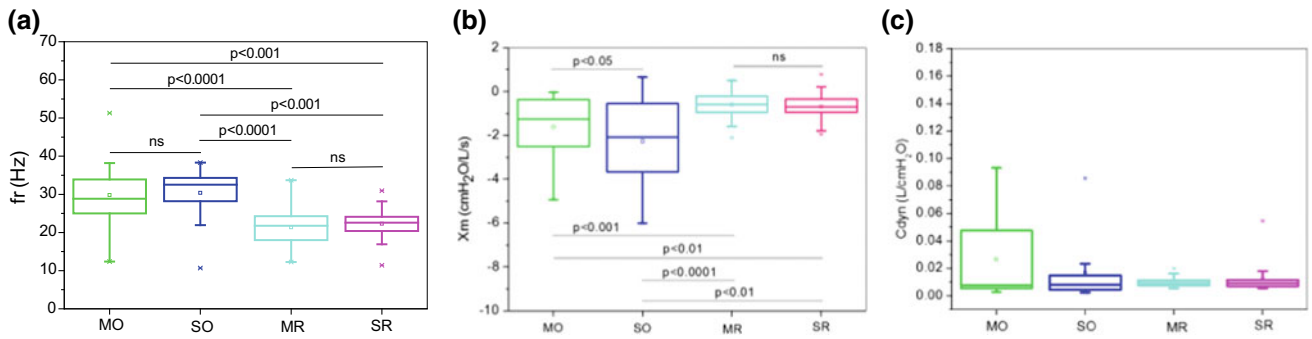
Fig. 2 Comparative analysis of the reactive parameters, resonance frequency (Fr, **a**), mean reactance (Xm, **b**) and dynamic compliance (Cdyn, **c**) in moderate obstruction (MO), severe obstruction (SO), moderate restriction (MR) and severe restriction (SR)
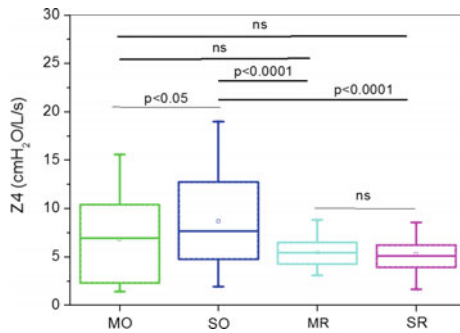
Fig. 3 Comparative analysis of the impedance modulus (Z4) in moderate obstruction (MO), severe obstruction (SO), moderate restriction (MR) and severe restriction (SR)

individuals with restrictive changes had lower Cdyn values. However, intergroup comparisons showed no significant changes in any combination.

Figure 3 shows the behaviour observed in Zrs in comparisons between the obstructive and restrictive groups. There were no significant changes in the moderate obstructive group, but the severe obstructive group had significantly higher values than those of the restrictive groups.

Table 2 shows the evaluation of the diagnostic accuracy of the studied FOT parameters in the discrimination among obstructive and restrictive groups. Fr was able to

discriminate all of the studied groups with adequate diagnostic accuracy (AUC $\geq$ 0.8), while resistive parameters (R0, S and Rm) were adequate in patients with more advanced disease (SO-MR and SO-SR).

4 Discussion

Increased obstruction resulted in greater values of R0 (Fig. 1a), in agreement with other studies [10]. The physiopathology of asthma affects the entire tracheobronchial tree, especially the small calibre airways, and results in progressive degrees of respiratory system and airway time constant impairment. This phenomenon is associated with the disease's inflammatory component effect [10]. Restrictive individuals showed even less visually clear R0 increases (Fig. 1a). The intergroup R0 comparisons showed consistently higher values in the obstructive groups, which is in accordance with the physiopathology of the studied diseases.

The Rm results (Fig. 1b), sensitive to the calibre of the more central airways [5], was consistent with that seen in R0, which reflects total resistance, including the airways, lung tissue and chest wall. The lack of significance in the comparison between moderate obstructive and moderate restrictive groups may be explained by the fact that this class

Table 2 Area under the ROC curve (AUC) and the 95% confidence interval (95% CI) of each studied FOT parameter in the discrimination among the moderate obstructive (MO), severe obstructive (SO), moderate restrictive (MR) and severe restrictive (SR) groups. AUCs $\geq$ 0.8 are described in bold

	MO-MR	MO-SR	SO-MR	SO-SR
R0	0.62 (0.51–0.72)	0.61 (0.51–0.71)	**0.80** (0.72–0.88)	**0.80** (0.72–0.88)
S	0.74 (0.65–0.83)	0.63 (0.54–0.73)	**0.81** (0.74–0.89)	0.75 (0.66–0.84)
Rm	0.59 (0.49–0.69)	0.61 (0.51–0.71)	0.78 (0.70–0.87)	**0.82** (0.74–0.89)
Xm	0.68 (0.58–0.78)	0.62 (0.53–0.73)	0.78 (0.69–0.87)	0.75 (0.66–0.84)
Fr	**0.85** (0.78–0.92)	**0.84** (0.77–0.91)	**0.89** (0.82–0.95)	**0.89** (0.83–0.95)
Cdyn	0.48 (0.38–0.59)	0.50 (0.40–0.60)	0.41 (0.30–0.51)	0.41 (0.31–0.52)
Z4	0.54 (0.44–0.65)	0.55 (0.45–0.65)	0.69 (0.60–0.79)	0.70 (0.60–0.79)

of obstructive patient still does not show a significant reduction in airway calibre.

S describes the redistribution of intrapulmonary gas, which arises from the respiratory system's mechanical non-homogeneities or central airway compliance [10]. The more negative the value of S is, the greater the abnormal pattern of ventilation distribution. In the intergroup comparison, greater changes in homogeneity were observed in obstructive volunteers (Fig. 1c), indicating that these volunteers have a greater impairment in the respiratory system time constants than patients with restrictive diseases. This finding can be explained by the greater level of lower airway impairment usually present in obstructive than in restrictive patients.

Another index that describes ventilation homogeneity is Xm (Fig. 2b). While S describes homogeneity in terms of the distribution of resistive elements in the respiratory system, Xm refers to homogeneity in terms of the respiratory system's elastic and inertial properties. Thus, Xm is related to the compliance and dynamic inertance (Idyn) of the respiratory system [10]. The changes in obstructive individuals were greater than those observed in restrictive individuals (Fig. 2a), indicating that in obstructive individuals, the changes to Idyn and Cdyn are greater than those in restrictive individuals. This result is consistent with those observed in the obstructive parameters (Fig. 1) and shows that the peripheral heterogeneity caused by the obstruction of small airways, characterising the presence of different lung time constants [11], is greater in obstructive patients.

Fr was higher in obstructive than in restrictive volunteers (Fig. 2a), which is in agreement with the more negative Xm values observed in the obstructive groups (Fig. 2b). These changes can be explained by the same factors that are involved in Xm. It should be noted that fr produced the greatest significance in the comparisons between the obstructive and restrictive groups.

Although individuals with restrictive changes visually appeared to have lower Cdyn values, there were no statistically significant differences when comparing the obstructive and restrictive groups (Fig. 2c). Cdyn reflects the distensibility of the respiratory system structures and takes into account the system's capacity to accommodate not only volume but also gas flow. That is, it includes the complications of the lung and bronchial walls, the thoracic/abdominal compartment wall, the upper airways (associated with the soft tissue of the mouth, pharynx and cheek) and thoracic gas compression. Hyatt et al. [12] have suggested that reduced Cdyn values may be associated with decreased compliance or increased airway resistance. Thus, we can assume that the changes associated with the peripheral airways in the presence of obstruction introduced changes to the Cdyn of a similar magnitude to those introduced by reductions in compliance usually found in restrictive diseases, which resulted in the similarity in Cdyn values found between the studied groups.

Z4 is associated with the work done by the respiratory muscles to overcome resistive and elastic loads, promoting the movement of air in the respiratory system [5]. Although it was observed that the increase among obstructive individuals was more significant than that observed in patients with restrictive disease (Fig. 3), this parameter was not adequate to differentiate between obstructive and restrictive patients (Table 2).

5 Conclusions

FOT might be useful in identifying the resistive and reactive changes of the respiratory system in patients with obstructive and restrictive diseases. This methodology showed changes in proportion to the restriction and obstruction according to the physiopathology of the analysed diseases.

The results of this study provide evidence that fr, which is based on a simple and non-invasive technique, was able to distinguish between obstructive and restrictive disease characteristics with adequate diagnostic accuracy. Resistive parameters (R0, S and Rm) proved to be more appropriate for patients with more advanced disease (SO-MR and SO-SR).

References

1. Sahin, D., Ubeyli, E.D., Ilbay, G., Sahin, M., Yasar, A.B.: Diagnosis of airway obstruction or restrictive spirometric patterns by multiclass support vector machines. J. Med. Syst. **34**(5), 967–973 (2010)
2. Bates, J.H., Irvin, C.G., Farre, R., Hantos, Z.: Oscillation mechanics of the respiratory system. Compr. Physiol. **1**(3), 1233–1272 (2011)
3. Oostveen, E., MacLeod, D., Lorino, H., Farre, R., Hantos, Z., Desager, K., et al.: The forced oscillation technique in clinical practice: methodology, recommendations and future developments. Eur. Respir. J. **22**(6), 1026–1041 (2003)
4. Sugiyama, A., Hattori, N., Haruta, Y., Nakamura, I., Nakagawa, M., Miyamoto, S., et al.: Characteristics of inspiratory and expiratory reactance in interstitial lung disease. Respir. Med. **107**(6), 875–882 (2013)
5. de Sa, P.M., Castro, H.A., Lopes, A.J., Melo, P.L.: Early diagnosis of respiratory abnormalities in asbestos-exposed workers by the forced oscillation technique. PLoS ONE **11**(9), e0161981 (2016)
6. SBPT SBdPeT—Diretrizes para Testes de Função Pulmonar. J. Pneumol. **38**(Suppl 3) (2009)
7. Miller, M.R., Hankinson, J., Brusasco, V., Burgos, F., Casaburi, R., Coates, A., et al.: Standardisation of spirometry. Eur. Respir. J. **26**(2), 319–338 (2005)

8. Pereira, C.A.: Espirometria. Jornal de Pneumologia. **28**(3) (2002)
9. Swets, J.A.: Measuring the accuracy of diagnostic systems. Science **240**(4857), 1285–1293 (1988)
10. Cavalcanti, J.V., Lopes, A.J., Jansen, J.M., Melo, P.L.: Detection of changes in respiratory mechanics due to increasing degrees of airway obstruction in asthma by the forced oscillation technique. Respir. Med. **100**(12), 2207–2219 (2006)
11. Lutchen, K.R., Gillis, H.: Relationship between heterogeneous changes in airway morphometry and lung resistance and elastance. J. Appl. Physiol. **83**(4), 1192–1201 (1997)
12. Hyatt, R.E., Scandon, P.D., Nakamura, M.: Interpretation of Pulmonary Function Tests. Lippincott-Raven, Phyladelphia (1997)

Hepatic Fatty Acid Profile in Mice with Nonalcoholic Fatty Liver Disease Using Magnetic Resonance Spectroscopy

Aline Xavier, Flavia Zacconi, Daniel Cabrera, Karen Fuenzalida, and Marcelo Andia

Abstract

Nonalcoholic fatty liver disease (NAFLD) is characterized by the accumulation of intracellular fatty acids in the liver. The only method to confirm the stage of this disease is the biopsy, but it is invasive and risky to patients. The idea of defining a classifier using magnetic resonance spectroscopy (MRS) emerges due to the need to find a way to replace biopsy with a non-invasive method that can classify NAFLD based on the chemical structure of fatty acids stored in the liver. The purpose of this study is to investigate and compare the composition of fatty acids to the metabolites signals in MRS in NAFLD mice liver at 2 time-point during the progression of the disease. A group of C57BL/6 mice was fed with high-fat diet for one month (N = 8) and for three months (N = 6). First, we made a histological analysis to the liver. Then, we analysed the fatty acids with gas chromatography (GC) and MRS. As a result, the histological analysis showed the progression of fat content, and the GC analysis detected a different fatty acid liver composition during the progression of NAFLD along with an increase of the total fat storage in the liver. The differences in the composition fatty acids are also reflected in the MR Spectrum, which could have clinical potential for monitoring the progression of this disease with a non-invasive technique.

Keywords

Magnetic resonance spectroscopy • NAFLD • Fatty acids

1 Introduction

Nonalcoholic fatty liver disease (NAFLD) is characterized by the accumulation of intracellular fatty acids in the liver in the absence of excessive consumption of alcohol. Data from a research performed in 2015 showed that 30% of the total population of South America has steatosis (i.e., fatty liver) [1]. About 30–40% of people with steatosis develop steatohepatitis (cellular inflammation) and about 10–30% of them develop cirrhosis which could progress to hepatocellular carcinoma [2].

Currently, there are no good biomarkers that can predict this "bad progression" of NAFLD. Most of the current available methods are mainly based on the estimation of the total amount of fat storage in the liver, detected by ultrasound (US), computed tomography (CT) and magnetic resonance imaging (MRI). However, those methods have some drawbacks: US does not work properly in obese patients, CT uses ionizing radiation and none of these methods can recognize when there is inflammation. Therefore, the only method to confirm the stage of this disease is biopsy, but it is invasive and risky for patients [3–5].

Recent studies have analyzed the Fatty Acid (FA) composition in liver triglycerides using gas chromatography with mass spectrometer (GC-MS), and they have identified some changes in the FA profile when comparing a healthy liver, to a liver with steatosis and to a liver with steatohepatitis [6–8].

The idea of defining a classifier using Magnetic Resonance Spectroscopy (MRS) emerges due to the need to find a

A. Xavier (✉) · M. Andia
Biomedical Imaging Center, Pontificia Universidad Católica de Chile, Santiago, Chile
e-mail: alinecx90@gmail.com

F. Zacconi
Faculty of Chemistry, Pontificia Universidad Católica de Chile, Santiago, Chile

D. Cabrera
Gastroenterology Department, Pontificia Universidad Católica de Chile, Santiago, Chile

K. Fuenzalida
Instituto de Nutrición y Tecnologías de los Alimentos, Universidad de Chile, Santiago, Chile

M. Andia
Radiology Department, Pontificia Universidad Católica de Chile, Santiago, Chile

way to replace biopsy with a non-invasive method that can classify NAFLD based on the chemical structure of fatty acids stored in the liver. Previous studies have shown that it is possible to associate the results of MRS with those obtained from GC-MS [9, 10].

The purpose of this study is to investigate and compare the composition of Fatty Acids to the metabolites signals in MRS in NAFLD mice liver at 2 time-point during the progression of the disease. The hypothesis is that the composition of the fatty acids changes over time same as the total amount of fat, transformation that could lead to the identification of a biomarker for the progression of the disease.

2 Subjects and Methods

All experiments were approved by the scientific ethics committee for the care of animals and the environment of the Catholic University of Chile (number:170614002).

We fed a group of C57BL/6 female mice with high-fat diet (HFD) for one month (N = 8) and for three months (N = 6). This diet was composed by 60% of fat, 20% of protein, and 20% of carbohydrate. We also fed a group (N = 6) with a chow diet composed by 13% of fat, 30% of protein, and 57% of carbohydrate.

At the end of the diet intervention, the mice were anesthetized with ketamine/xylosine, and the liver was harvested. A portion of the liver was used for histology analysis. We used the remaining liver to extract the Fatty acids methyl esters (FAMEs) using a protocol adapted by Folch et al. [11]. Those FAMEs were analyzed using a 9.4T MRS and GC-MS.

2.1 Histology

Liver sections from mice livers were routinely fixed in 10% of formalin and embedded in paraffin. Then 5 μm tissue sections were stained with hematoxylin and eosin. Histological pictures were obtained using the Aperio Digital Pathology Slide Scanner (Leica Biosystems) and Histopathological analyses were performed by a blinded pathologist who obtained the NAFLD Activity Score (NAS) by using the method proposed by Kleiner et al. [12].

2.2 Gas Chromatography with Mass Spectrometer

Fatty Acid Methyl Esters were analyzed by using gas chromatography with mass spectrometer (GC7890 5975MSD, Agilent, California, USA.) equipped with HP-Innowax capillary column (length 25 m, 0.2 mm internal diameter, 0.2 mm film). Additional configuration of Gas Chromatography with Mass Spectrometer is found in Table 1. Data register was in SCAN mode and peak integration was obtained by the MS ChemStation software.

FAMEs were identified by comparing retention times to known standards and by matching them up with the mass spectra from NIST library (National Institute of Standards and Technology, USA).

The mass of each FAME (in μg) was calculated according to the Integration area of corresponding peak and the relation with the integration area of the internal standard (C19:0) added to the sample (50 μg). Fatty acids composition was defined as the percentage of individual fatty acids in respect of the total fatty acids.

2.3 Magnetic Resonance Spectroscopy

The ^{1}H NMR spectra were obtained in a Bruker Avance spectrometer operating at 9.4T with an acquisition called Zg30 (30° in z axis). The software used to the spectrum analyses was the MestreNova Version 10.0.

We took 10 mg of FAME from each sample and put 70 μl from CDCl3 that has a small proportion of tetramethylsilane as an internal reference; this mixture was introduced into a 5 mm diameter tube. The acquisition parameters were: spectral width 8012.820 Hz, relaxation delay 1 s, number of scans 16, acquisition time 2.045 s, flip angle 30° to avoid T1 relaxation effects and total acquisition time 48.72 s (number of scans × (time between pulses + acquisition time)). The experiment was conducted at 25 °C.

2.4 Correlation Between GC-MS and MRS

The MRS allow us to determine the structure of an organic substance. The spectrum shows the signals in a graph of frequency (ppm) versus intensity in arbitrary units. Each set of chemically equivalent protons originates a signal in such a way that the number of signals in a spectrum indicates the amount of different kinds of protons in a substance. The chemical shift is a measure of how far away the signal is from the reference signal of tetramethylsilane (TMS). The greater the displacement with respect to the TMS (0 ppm), it means that the proton is in an environment where there is electronegative group.

The GC is the gold standard to characterize fatty acids. The mixture containing all the fatty acids methyl esters is introduced in a CG-MS where it is warmed, and the fatty acid starts to separate from each other by their volatility and polarity.

Table 1 Agilent GC7890 5975MSD configuration

Injector temp.	Oven ramp	Sample injection	Electron impact
220 °C	150 °C × 1 min 15 °C/min to 200 °C 200 °C × 5 min 12 °C/min to 260 °C	Split mode (1:20) Helium at 1 ml/min (constant flow)	Ionization potential of 70 eV

Fig. 1 MRS simulation of a FAME with 18 carbons and 2 double bonds. The proton chemically equivalents are grouped by colors. Each different color corresponds to a peak
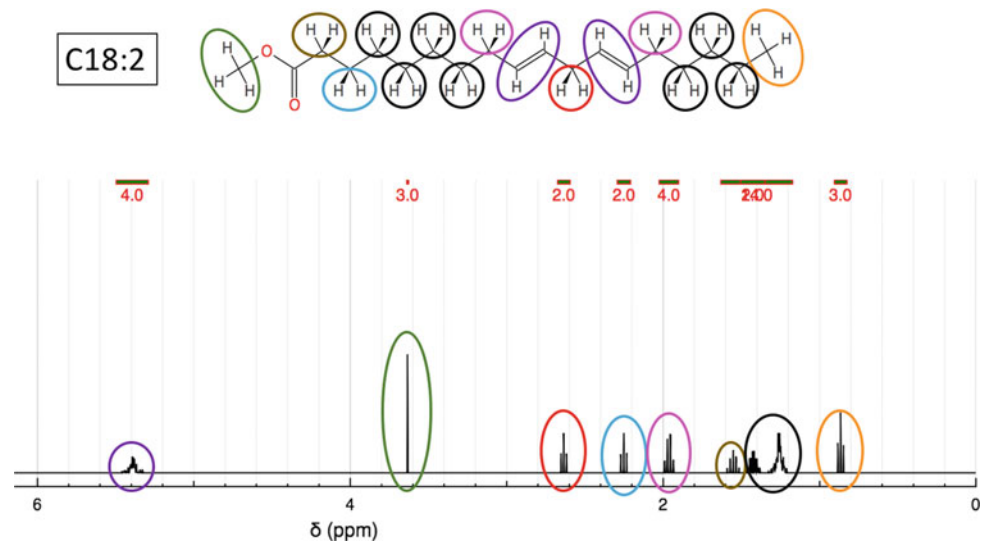
There are many type of FA in the liver of a human being. All of them generate just seven peaks corresponding to the chemical equivalent protons. Figure 1 shows an example of a FAME with 18 carbons and 2 double bonds in the signal of the MR spectroscopy.

To clarify, in MRS we don't detect the quantity of the fatty acids directly, but we can assume that, if we have a change in fatty acids profile, we will have a change in the metabolites detected by MRS.

2.5 Statistical Analyses

We have a small number of data for each group. Therefore, we need a non-parametric method to compare the medians. Kruskal-Wallis was chosen because is the non-parametric test correspondent to ANOVA. The null hypothesis is that the medians are equal. The analysis was performed in Prism 6.

3 Results

The high-fat diet makes the mice increase their weight and accumulates fat in the liver. Table 2 shows the mice weight for each group and the total liver FAME content (weight of FAME/total liver sample).

3.1 Histology Results

The histopathology results showed no steatosis in the chow-diet group; steatosis grade 0, with more focus of fat

Table 2 Mice age, weight and the percentage of FAME in the liver for each group. The first group was fed with a chow diet, the second with a high-fat diet for 1 month and the third one, with a high-fat diet for 3 months

Mice group	Mice age	Mice weight	Weight of FAME/total liver sample (%)
chow-diet	4 months	20.92 ± 0.84	1.76 ± 0.56
1-month-HFD	4 months	23.88 ± 1.48	2.54 ± 0.36
3-month-HFD	6 months	35.07 ± 2.34	3.65 ± 0.30

Fig. 2 Histological results of chow-diet **a** 1-month-HFD, **b**, 3-month-HFD, **c** group
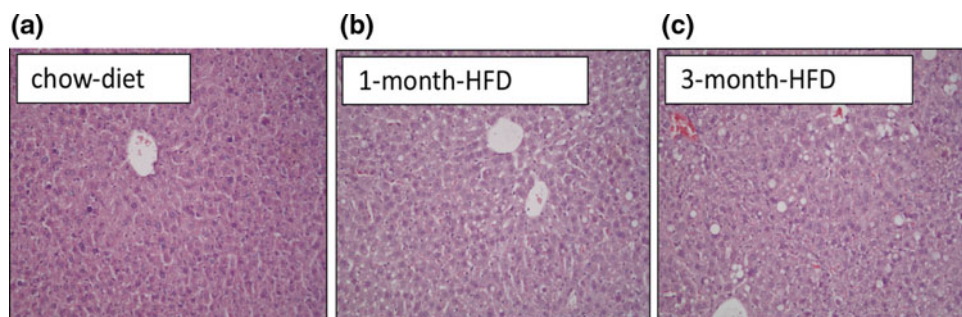
than the chow-diet group, in 1-month-HFD group, and steatosis grade 1 in 3-month-HFD group (Fig. 2).

3.2 Gas Chromatography with Mass Spectrometer Results

We identified 22 fatty acids using the CG-MS. Four of the identified FAs showed significant differences between chow-diet, 1-month-HFD, and 3-month-HFD. Those FAs were oleic (C18:1), palmitic (C16:0), stearic (C18:0), and cervonic (C22:6) acids methyl esters as shown in Fig. 3. Kruskal-Wallis test showed statistical differences between the three groups ($P < 0.05$).

The CG-MS analysis identifies a pattern of fatty acids composition during NAFLD progression. Although the total amount of fatty acids increased during the NAFLD progression, not all the fatty acids progressed in the same way. Compared to chow-diet, 1-month-HFD and 3-month-HFD groups showed an increase of oleic acids methyl esters (C18:1) and a decrease of the palmitic (C16:0), stearic (C18:0), and cervonic (C22:6) acids methyl esters during the NAFLD progression.

All the 22 FAs can be grouped into three categories: Saturated Fatty Acids (SFAs), Monounsaturated Fatty Acids (MUFAs) and Polyunsaturated Fatty Acids (PUFAs). The

Fig. 4 The graphic shows the percentage of SFAs, MUFAs and PUFAs corresponding to the mice with chow-diet, 1-month-HFD and 3-month-HFD

SFAs has no double bonds (example: C14:0, C16:0, C18:0), while the MUFAs has one double bond (example: C16:1, C18:1, C20:1) and the PUFAs has two or more double bonds (example: C18:3, C20:4, C22:6). The graph on Fig. 4 shows that SFAs decreased and the MUFAs increased during the NAFLD progression. These results are concordant with previous studies conducted with human beings by Puri et al. [8].

3.3 Magnetic Resonance Spectroscopy Results

We identified seven metabolite peaks that correspond to the fatty acids by using the MRS. One of the metabolite peaks was used as reference (diallylic methylene at 2.8 ppm) and five of them showed significant differences with the progression of the disease. Figure 5 shows the area under the curve (AUC) of all the metabolites normalized by the AUC of the reference peak. The olefinic peak (5.3 ppm) is not shown in this figure.

In the MRS (Fig. 6), the peaks 0.9 ppm (methyl terminal), 1.2 ppm (Bulk methylene), 1.6 ppm (methylene beta carboxyl), 2.3 ppm (methylene alpha carboxyl), and 5.3

Fig. 3 A box-plot shows the percentage of four FAMEs. Horizontal axis shows the FAME and vertical axis the percentage of participation of each FAME

Fig. 5 Metabolites spectrum with 9.4 T. In black, we have the mice results with chow-diet, in red, the mice result with a high-fat diet for 1 month and in blue, with a high-fat diet for 3 months. Horizontal axis shows the frequency of resonance in ppm and the vertical axis shows the intensity in arbitrary units
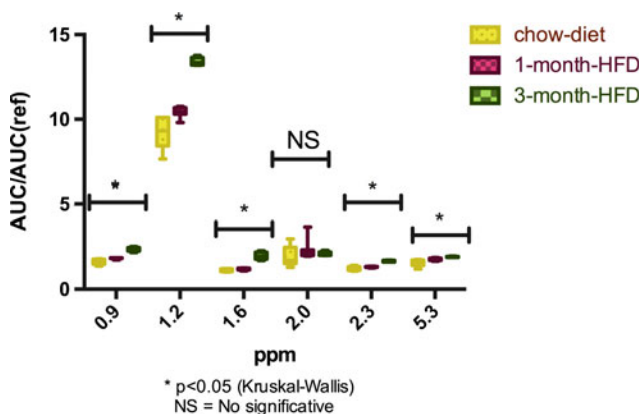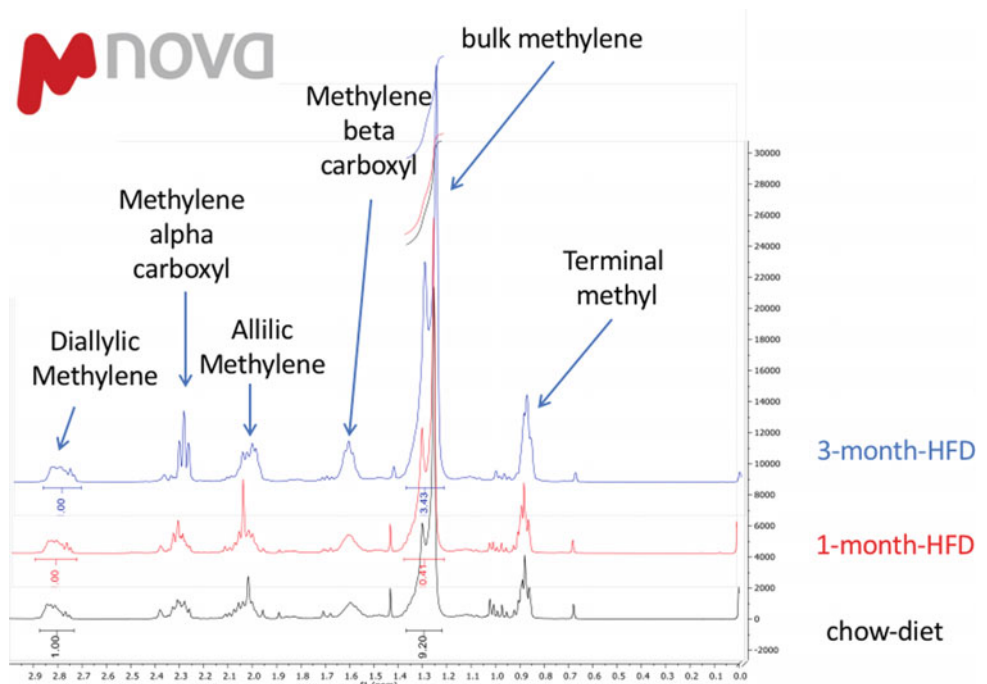
Fig. 6 A box-plot shows the area under the curve (AUC) of 6 metabolites normalized by the AUC of the reference (vertical axis). Horizontal axis shows the frequency of resonance in ppm of each metabolite

(olefinic methylene) showed significant differences during the NAFLD progression.

The diallylic has two double bonds so we will find this metabolite only if we have PUFAs. We used the diallylic as reference and the GC-MS data shows that PUFAs decrease in animals fed for 3 months when compared to the ones fed for 1 month, difference shown in Fig. 6.

4 Conclusion

Mice fed with high-fat diet increase their weights and the amount of fat stored in the hepatocytes. Histological analysis confirmed the progression of fat liver content, therefore the progression of the disease.

GC analysis showed that the fat in the liver is composed of at least 22 different fatty acids, which have different evolution during the NAFLD progression. The difference in the fatty acids composition and evolution is related to the progression of NALFD.

It is possible that those differences could be related to the diet, and therefore they might provide the reason of differences in the NAFLD progression among patients, in which some of them evolve to NASH and cirrhosis whereas others remain in the early stages of NAFLD for a long time.

The differences in the FA composition is also reflected in the MR Spectrum, which could have clinical potential for monitoring the progression of this disease with a non-invasive technique.

As suggestion of future work, we will make the same study with different diets in mice and also, we will study the FA in patients with a 7T MRS. Unfortunately, the 3T and 1.5T don't give us enough resolution and signal-noise ratio (SNR).

References

1. Younossi, Z.M., Koenig, A.B., Abdelatif, D., Fazel, Y., Henry, L., Wymer, M.: Global epidemiology of non-alcoholic fatty liver disease-meta-analytic assessment of prevalence, incidence and outcomes. Hepatology **64**(1), 73–84 (2016)
2. Neumann, M.G., Cohem, L.B.: Biomarkers in nonalcoholic fatty liver disease. Canad. J. Gastroenterol. Hepatol. **28**(11), 607–618 (2014)
3. Ahmed, M.: Non-alcoholic fatty liver disease in 2015. World J. Hepatol. **7**(11), 1450–1459 (2015)
4. Permutt, Z., Le, T.-A., Peterson, M.R., Seki, E., Brenner, D.A., Sirlin, C., Loomba, R.: Correlation between liver histology and novel magnetic resonance imaging in adult patients with non-alcoholic fatty liver disease-MRI accurately quantifies hepatic steatosis in NAFLD. Alimentary Pharmacol. Therap. **36**(1), 22–29 (2012)
5. Reeder, S.B., Cruite, I., Hamilton, G., Sirlin, C.B.: Quantitative assessment of liver fat with magnetic resonance imaging and spectroscopy. J. Mag. Res. Imag. **34**(4), spcone (2011)
6. Yamada, K., Mizukoshi, E., Sunagozaka, H., Arai, K., Yamashita, T., Takeshita, Y., Misu, H., Takamura, T., Kitamura, S., Zen, Y., Nakanuma, Y., Honda, M., Kaneko, S.: Characteristics of hepatic fatty acid compositions in patients with nonalcoholic steatohepatitis. Liver Int. **35**(2), 582–590 (2015)
7. Wang, X., Cao, Y., Fu, Y., Guo, G., Zhang, X.: Liver fatty acid composition in mice with or without nonalcoholic fatty liver disease. Lipids Healthy Dis. **10**, 234 (2011)
8. Puri, P., Baillie, R.A., Wiest, M.M., Mirshahi, F., Choudhury, J., Cheung, O., Sargeant, C., Contos, M.J., Sanyal, A.J.: A lipidomic analysis of nonalcoholic fatty liver disease. Hepatology **46**(4), 1081–1090 (2007)
9. Knote, G., Kenar, J.: Determination of the fatty acid profile by 1H-NMR spectroscopy*. Eur. J. Lipid Sci. Technol. **106**(2), 88–96 (2004)
10. Guillen, M.D., Ruiz, A.: Edible oils: discrimination by ^{1}H nuclear magnetic resonance. J. Food Agric. **83**(4), 338–346 (2003)
11. Folch, J., Lees, M., Sloane Stanley, G.H.: A simple method for the isolation and purification of total lipids from animal tissues. J. Biol. Chem. **226**(1), 497–509 (1957)
12. Kleiner, D.E., Brunt, E.M., Van Natta, M., Behling, C., Contos, M.J., Cummings, O.W., Ferrell, L.D., Liu, Y.C., Torbenson, M.S., Unalp-Arida, A., Yeh, M., McCullough, A.J., Sanyal, A.J.: Design and validation of a histological scoring system for nonalcoholic fatty liver disease. Hepatology **41**(6), 1313–1321 (2005)

Hodgkin-Huxley Model Indicates an Inversion in the Strength-Duration Curves for Mono and Biphasic Stimuli

Pedro Xavier de Oliveira, Jair Trapé Goulart, and Marcelo Zoccoler

Abstract

Action potentials are non-linear variations of the transmembrane potential caused by changes in the membrane conductance. In 1952, Hodgkin and Huxley proposed a set of differential equations that describes mathematically the conductance changes observed during the course of an action potential. Currently, this model is still a good tool for understanding the basic mechanisms involved in the initiation and propagation of the action potentials. The objective of this work was to use a simple application of the Hodgkin-Huxley model to define the relation between the stimulation threshold and variations of the stimulatory waveform, in order to promote cell excitation delivering the lowest energy stimulus. We evaluated the strength-duration curves for mono and biphasic stimuli, giving special attention to short stimuli. This Hodgkin-Huxley implementation allowed the explanation of the mechanisms underlining a curious inversion of the strength-duration curves for mono and biphasic stimuli. Namely, for shorter stimuli (<2.2 ms), the stimulation threshold for monophasic stimuli becomes smaller than for biphasic stimuli. That inversion seems to be a result of the time-dependence of the activation variables of Na^+ and K^+ channels and the inactivation variable of Na^+ channels proposed in the Hodgkin-Huxley model. In addition, we used the model to evaluate the energy of asymmetrical biphasic stimuli in order to find a more energy-efficient waveform, which was shown to be a combination of a 7 ms long hyperpolarizing phase with a depolarizing phase of 6 ms.

1 Introduction

Excitable cells, such as neurons and myocytes, generate and propagate electrical signals called action potentials (AP) in response to certain stimuli. Under resting condition the membrane of these cells is polarized, with a resting potential ranging from −70 to −90 mV with respect to the extracellular medium. If an excitable cell is subjected to a depolarizing stimulus of sufficient amplitude, an AP is triggered, i.e., a nonlinear variation of the transmembrane potential (V_m) occurs as a result of changes in the membrane conductance to different ions [1].

Probably the most important study that established the basis of our knowledge on cellular excitability comes from the fantastic work of Hodgkin Huxley [2]. Studying the squid giant axon, Hodgkin and Huxley were able to describe and to model the basic mechanisms of AP generation. Basically, a depolarizing stimulus promotes a rapid increase in Na^+ membrane conductance which leads V_m to values toward Na^+ equilibrium potential ($\sim$+60 mV), generating a spike of approximately 40 mV. This increase in Na^+ conductance is due to the activation (or opening) of the voltage-dependent Na^+ channels. The same depolarization that promotes the activation of these Na^+ channels also promotes their inactivation, but the inactivation is slower than the activation. Inactivation of the Na^+ channels reduces the rate of rise of V_m during the rising phase of the AP and prevents the spike from reaching the Na^+ equilibrium potential. Also, the depolarization promotes the activation of slow K^+ channels that are important for membrane repolarization, i.e., the activation of these channels brings V_m to values closer to K^+ equilibrium potential ($\sim$−90 mV).

P. X. de Oliveira (✉) · J. T. Goulart · M. Zoccoler
Faculty of Electrical and Computing Engineering (FEEC)/
Department of Biomedical Engineering, University of Campinas
(UNICAMP), Campinas, SP 13083-852, Brazil
e-mail: pedrox@ceb.unicamp.br

P. X. de Oliveira
Center of Biomedical Engineering (CEB), University of Campinas
(UNICAMP), Campinas, SP 13083-881, Brazil

The Hodgkin-Huxley model states that the total current (*I*) through the membrane is given by:

$$I = C_m \cdot \frac{dV_m}{dt} + I_{Na} + I_K + I_L \tag{1}$$

where C_m is the specific membrane capacitance, I_{Na}, I_K and I_L are respectively the Na^+, K^+ and passive leak currents (i.e., a non-specific ionic current). Ionic currents I_{Na}, I_K and I_L are defined by:

$$I_{Na} = \bar{G}_{Na} \cdot m^3 \cdot h \cdot (V_m - V_{Na}) \tag{2}$$

$$I_K = \bar{G}_K \cdot n^4 \cdot (V_m - V_K) \tag{3}$$

$$I_L = \bar{G}_L \cdot (V_m - V_L) \tag{4}$$

where $\bar{G}_{Na}$ and $\bar{G}_K$ are, respectively, the maximum Na^+ and K^+ conductances, V_m is the membrane potential, V_{Na} and V_K are the Na^+ and K^+ equilibrium potential, respectively. m is the activation variable of the Na^+ channels, h is the inactivation variable of the Na^+ channels and n is the activation variable of the K^+ channels. $\bar{G}_L$ and V_L are the leak conductance and leak equilibrium potential, respectively.

In order to trigger an AP it is necessary a stimulus strong enough to promote a critical depolarization required for Na^+ channels activation, promoting a fast and pronounced increase of the Na^+ current due a positive-feedback relationship between V_m and Na^+ conductance. In mammals, the activation threshold of Na^+ channels occurs when V_m reaches ~ -55 mV, representing a critical depolarization of ~ 15 mV [1]. Physiologically, this variation is triggered in pacemaker cells or by neighbouring cells, but it can also be fabricated through electric fields application or current injection. Among the latter, biphasic stimulation is generally considered safer than monophasic because of its charge-balanced nature [3].

The objective of this work was to use a simple application of the Hodgkin- Huxley model to define the relation between the stimulation threshold and variations of the stimulatory waveform, in order to promote cell excitation delivering the lowest energy stimulus.

2 Materials and Methods

2.1 Hodgkin-Huxley Model

The experiments were performed using de Hodgkin-Huxley model [2] implemented on MATLAB R2015a®. We set *I* as the stimulatory current density (I_{ST}) and solved the equation system (Eqs. 1−4 with the activation/inactivation channel differential equations [2]) for V_m. The ordinary differential equations that simulate the squid action potential were numerically solved by the MATLAB software package *ode*45 (fourth order Runge–Kutta method) with a fixed-step size of 0.1 ms. We tested monophasic and biphasic stimuli, in the latter the first phase was always hyperpolarizing.

2.2 Strength-Duration Curve (S × D)

The S × D curves for monophasic and symmetric biphasic stimuli were obtained by varying the depolarizing stimulus duration (for biphasic stimuli, the hyperpolarizing phase duration was increased by the same amount) from 0.6 to 15 ms in steps of 0.1 ms. This way, it is easier to compare the impact of the hyperpolarizing phase. The threshold (I_T) was found by increasing I_{ST} by 0.05 μA/cm^2 until an AP was triggered. Thus, the I_T was the lowest I_{ST} required to trigger an AP.

Using the SxD curve, the gating variables for activation and inactivation and the V_m were estimated for a stimulus starting at 0 ms and having a depolarizing duration of 10 ms, i.e., in a steady-state condition in which the rheobase had been reached. This way, the influence of the hyperpolarizing phase on the model parameters could be assessed.

2.3 Subthreshold Stimulation

The temporal response patterns of the V_m evoked by a subthreshold stimulation were obtained by increasing the stimulus depolarizing duration from 0.6 to 15.1 ms in steps of 0.5 ms and fixed amplitude (0.05 μA/cm^2).

2.4 Asymmetric Biphasic Stimulation

It is well known that the first phase of a biphasic stimulus has an important influence on I_T. In order to quantify its impact, we tested asymmetric biphasic stimulus in which the first phase (negative or hyperpolarizing) was variable both in amplitude and duration while the second phase (positive or depolarizing) was held at constant duration (6 ms). For each pair of amplitude and duration of the first phase, the amplitude of the second phase was increased by 0.05 μA/cm^2 until an AP was elicited and, therefore, I_T was obtained. The first phase had amplitudes ranging from 0 to -4 μA/cm^2, varying by 0.1 μA/cm^2 steps, and duration ranging from 0 (i.e., a monopolar stimulus) to 20 ms with 1 ms steps.

Fig. 1 Strength-duration curve (S × D). I_T: threshold stimulus current density
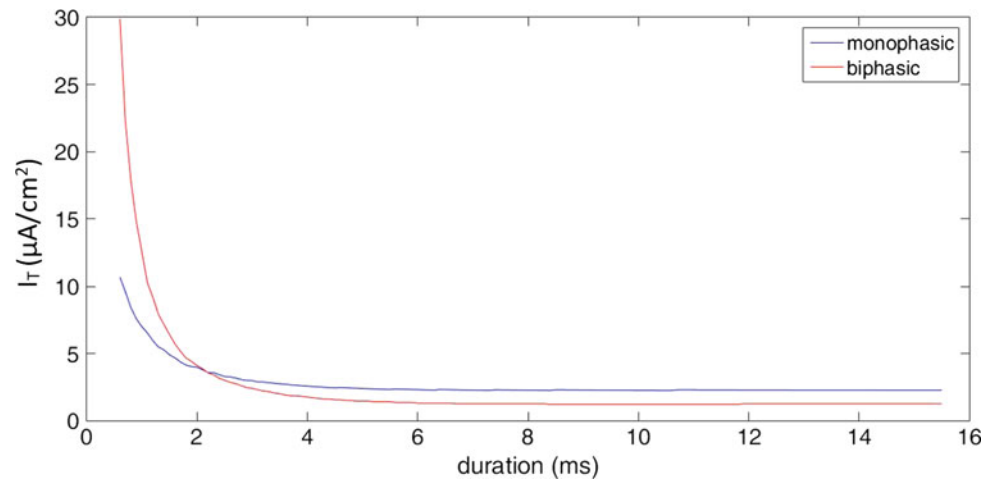
3 Results

3.1 S × D Curve

The simulated S × D curves for monophasic and biphasic stimuli are shown in Fig. 1. The estimated I_T for monophasic stimuli is higher than the biphasic I_T if the stimulus duration is longer than 2.2 ms. However, as seen by the curves intersection, biphasic I_T becomes higher than monophasic for durations shorter than 2.2 ms. Other important information shown in Fig. 1 is that the duration that gives the lowest energy for biphasic stimulation is 6 ms, i.e., the S D curve for biphasic stimuli became asymptotic when the stimulus duration reached 6 ms.

The gating variables for activation and inactivation and the V_m for monophasic and biphasic stimuli of 10 ms are shown in Fig. 2. The first 10 ms of simulation were zoomed in and displayed on the right-side column of Fig. 2. For any steady-state biphasic stimulus longer than 6 ms, in which the rheobase has been reached, the pattern shown in Fig. 2 should be found. The first phase of the biphasic stimulus is hyperpolarizing and lead to a decrease in the activation variables of Na^+ (m) and K^+ (n) channels and an increase in the inactivation variable (h) of Na^+ channels.

3.2 Subthreshold Stimulation

Monophasic and biphasic subthreshold stimulation led to different effect on V_m (Fig. 3). But, for durations shorter
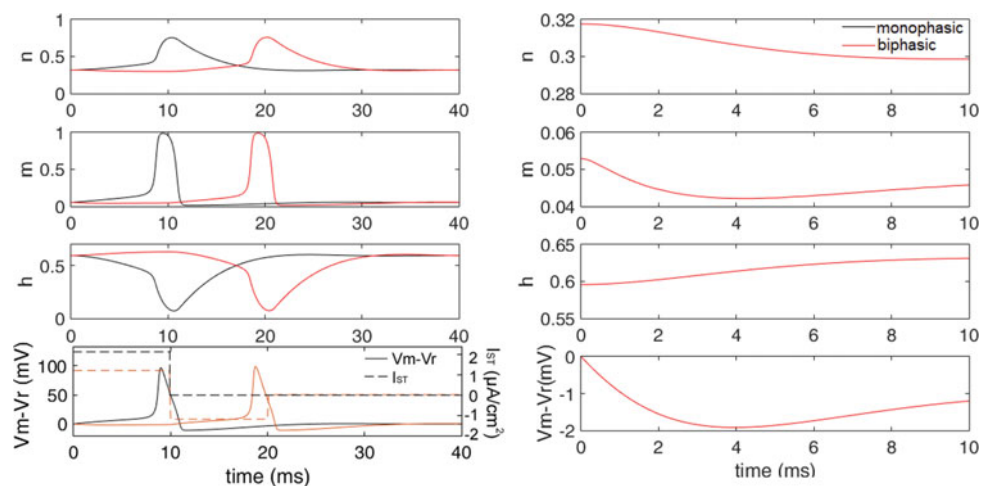
Fig. 2 Curves of the activation variables of K^+ (n, panel **a**) and Na^+ (m, panel **b**) channels, inactivation variable of Na^+ (h, panel **c**) channel and transmembrane potential (Vm) minus resting potential (Vr) evoked by monophasic (black curves) and biphasic (red curves) stimuli (panel **d**). The right column shows a zoom of the first phase of the biphasic stimulus

Fig. 3 Transmembrane potential minus resting potential (Vm − Vr) variation in response to monophasic (**a**) and biphasic (**b**) stimuli. The further to the right is the curve, the longer the stimulus duration
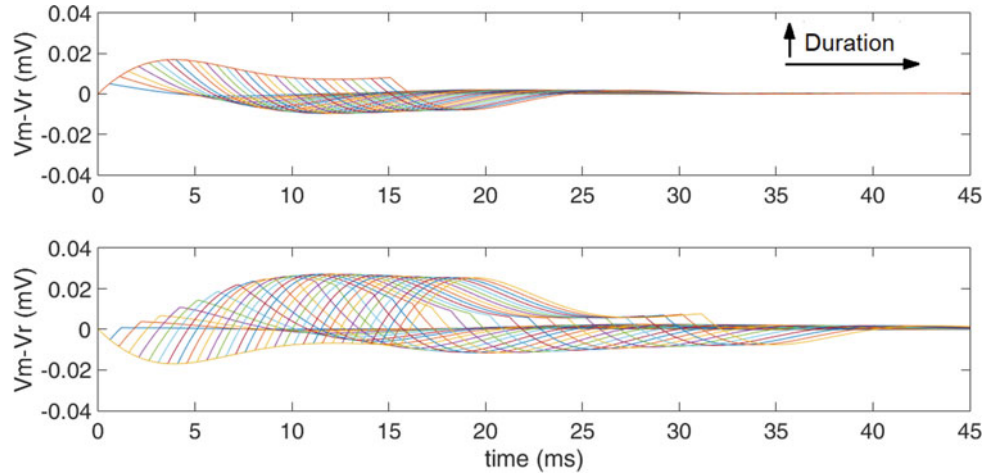
than 2.1 ms, the hyperpolarizing phase of biphasic stimuli caused the same V_m variation in modulus observed when monophasic stimuli were applied. Interestingly, the maximum V_m variation caused by the second phase of the biphasic stimuli is lower than that caused by its first phase for short durations (<2.1 ms), for example, the V_m response to a 0.6 ms long stimulus (Fig. 3b, blue curve close the y-axis) is capable of hyperpolarizing the membrane, but barely depolarizes it afterwards.

3.3 Asymmetric Biphasic Stimulation

Figure 4 shows the I_T as a colored surface and in the z-axis for asymmetric biphasic stimuli. The black dots forming a flat layer represent the I_T for a symmetrical biphasic stimulus (6 ms each phase). As expected, the highest I_T (2.03 µA/cm^2) was found for either a 0 ms first phase biphasic stimulus or a 0 µA/cm^2 first phase biphasic

stimulus (i.e., a monophasic stimulus). The surface region below the black dots plane embraces all sets of asymmetrical biphasic waveforms displaying a lower I_T than a symmetric biphasic waveform with 6 ms each phase. The flat blue base (i.e., $I_T = 0$ µA/cm^2) is caused because the hyperpolarizing phase was intense enough to produce an anode break stimulation [1]. Probably the most important information of this analysis was that the stimulus able to stimulate the neuron with the lowest energy has the following shape: first phase 7 ms long with 1 µA/cm^2 amplitude and second phase 6 ms long with 1.45 µA/cm^2 amplitude.

4 Discussion

4.1 S × D Curve

Our results for the S × D curves show a facilitation in stimulation for biphasic pulses when the duration is above
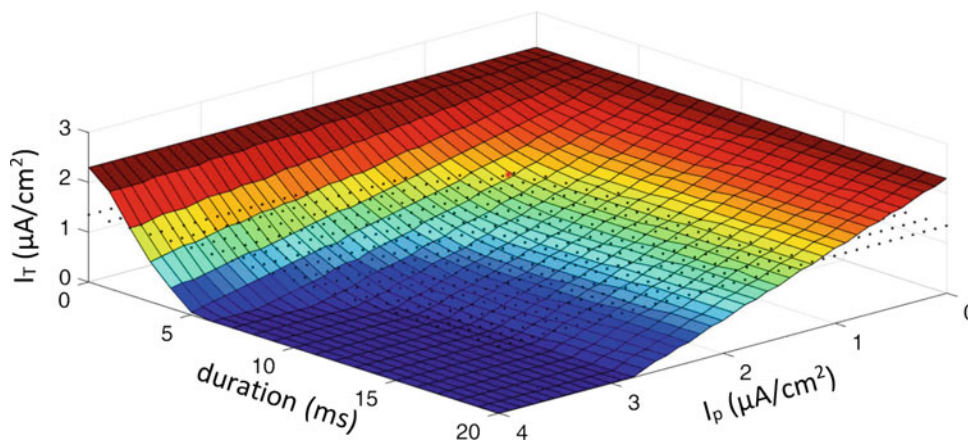
Fig. 4 (I_T) Threshold stimulus current density as a function of the stimulus first phase (hyperpolarizing) duration and amplitude (I_p). The black dots plane corresponds to the I_T for a symmetrical biphasic stimulus with duration of 6 ms each phase. The red asterisk corresponds to the symmetrical pulse (6 ms each phase) threshold

2.2 ms when compared to monophasic. Indeed, cells have shown increased excitability when the membrane is hyperpolarized for very long durations (1.1 s) prior to the depolarizing pulse [4]. Figure 2 right-side shows that, although Na^+ activation variable (m) decreases when the membrane hyperpolarizes, the Na^+ inactivation variable (h) increases (higher values correspond to a lower probability of the inactivated state). This means that even though fewer Na^+ channels are opened at rest, a lower portion of them is inactivated. Therefore, when the depolarizing phase arrives, more channels are available for recruitment, requiring lower current for AP triggering. The membrane hyperpolarization also grants higher Na^+ driving force ($V_m − V_{Na}$), yielding higher I_{Na} when the depolarizing phase starts. Besides that, both K^+ activation variable (n) and its driving force ($V_m − V_K$) decrease during the hyperpolarized phase, which decreases the hyperpolarizing K^+ current, contributing for lower I_T.

Biphasic pulses shorter than 2.2 ms, due to a correspondly shorter hyperpolarizing phase, settle fewer Na^+ channels away from inactivation and supply lower Na^+ driving force. I_K is also less diminished during this phase. This reduced effect on I_{Na} and I_K is caused by the time-dependence of the variables m, h and n, which do not have enough time to change. The very brief biphasic pulses lead to a membrane hyperpolarization without significantly changing those variables, i.e., without the excitability enhancement discussed above. Then, as V_m is mainly changed by the capacitive currents, the hyperpolarizing phase only moves V_m far from the threshold, increasing the stimulus amplitude necessary to reach the threshold (I_T) and consequently causing the intercept between the the S × D curves.

Our simulations contrast with a model from the literature where the Luo-Rudy model [5] was implemented to simulate AP in ventricular cells [6]. In their S × D curve for intracellular current stimulation, biphasic thresholds are always higher than monophasic of same total duration. If instead they had built S × D curves as a function of the depolarizing duration, we would expect a similar behaviour. The authors actually state that they have achieved a 13% lower threshold for a 5–5 ms biphasic pulse against a 5 ms monophasic one, which is in accordance with our results (we obtained a 40% reduction). Interestingly, their extracellular stimulation S D curves display a quite similar curve intersection (for durations <2.5 ms), however, in this case the reason for the loss of biphasic effectiveness for shorter pulses is mostly due to a lack of effective contribution of the Na^+ currents from opposing cell sides when each side receives the depolarizing phase. Another model for extracellular stimulation [7], this time using a two-compartment Hodgkin-Huxley model, yielded the two S × D curves joining rather than just crossing for very short durations (∼<0.3 ms). Here, the main influence is probably the same: lower contributing I_{Na} from opposite ends. The fact that the curves join instead of crossing could be attributed to the fact that, for these very short pulses, the capacitive current is dominant over ionic currents, therefore, the second phase of the biphasic pulse tends just to compensate the V_m variation of the first phase, having little or no influence on the threshold.

4.2 Subthreshold Stimulation

The hyperpolarization phase of the biphasic stimulation is similar, in magnitude, to the monopolar depolarization for pulses shorter than 2.1 ms probably because the dominant current component during this period is the capacitive current. Once the duration is augmented above this point, K^+ deactivation becomes more relevant and hamper further membrane hyperpolarization. At the same time, more Na^+ channels may have left inactivation, explaining the higher depolarizing magnitudes for higher biphasic durations.

On the other hand, the decrease in V_m magnitude for monophasic pulses longer than 4 ms is probably due to an increase in the time-dependent Na^+ channel inactivation as well as K^+ channel activation.

4.3 Asymmetric Biphasic Stimulation

Searching for the lowest energy waveform for stimulation, we used, for the depolarizing phase, the duration of the lowest energy symmetrical biphasic waveform (6 ms) and optimized the hyperpolarizing phase parameters. Therefore, we presented the most energy-efficient asymmetrical squared waveform for intracellular neural stimulation based on Hodgkin-Huxley model (first phase 7 ms long with $−1$ μA/cm^2 amplitude and second phase 6 ms long with 1.45 μA/cm^2 amplitude). Identification of energy-efficient waveforms may be important to help the development of stimulators in which size or battery supply are limiting.

Conflict of Interest The authors declare they have no conflict of interest.

References

1. Weiss, T.F.: Cellular Biophysics: Electrical Properties, vol. 2. A Bradford Book, Cambridge, MA (1997)
2. Hodgkin, A.L., Huxley, A.F.: A quantitative description of membrane current and its application to conduction and excitation in nerve. J. Physiol. **117**, 500–554 (1952)

3. Brocker, D.T., Grill, W.M.: Principles of electrical stimulation of neural tissue. In: Lozano, A.M., Hallett, M. (eds.), Handbook of Clinical Neurology, vol. 116 (3rd series) Brain Stimulation, pp. 3–18. Elsevier, New York, NY (2013)

4. Kavanagh, K.M., Duff, H.J., Clark, R., Robinson, K.V., Giles, W.R., Wyse, D.G.: Monophasic versus biphasic cardiac stimulation: mechanism of decreased energy requirements. PACE **13**, 1268–1276 (1999)

5. Luo, C., Rudy, Y.: A model of the ventricular cardiac electrical potential. Circ. Res. **68**(6), 1501–1526 (1991)

6. Tung, R., Borderies, J.-R.: Analysis of electric field stimulation of single cardiac muscle cells. Biophys. J. **63**, 371–386 (1992)

7. Boinagrov, D., Loudin, J., Palanker, D.: Strength–duration relationship for extracellular neural stimulation: numerical and analytical models. J. Neurophysiol. **104**, 2236–2248 (2010)

Integer and Fractional-Order Modelling in the Early Diagnosis of the Respiratory Abnormalities Associated with Smoking and Chronic Obstructive Pulmonary Disease

Caroline Oliveira Ribeiro, Alvaro Camilo Dias Faria, Agnaldo José Lopes, and Pedro Lopes de Melo

Abstract

The aim of the present study was to evaluate the forced oscillation technique (FOT) associated with fractional-order models in the early diagnosis of the effects of smoking and in patients with early-stage chronic obstructive pulmonary disease (COPD). A total of 79 subjects was analysed: 31 controls, 26 who smoked and 22 with mild COPD. COPD caused significant increases in the inertance (L) and damping factor ($p < 0.001$) and the hysteresivity ($p < 0.001$). L presented high diagnostic accuracy in the identification of the effects of smoking (99.5%) and COPD (99.9%). This model contributed to improving our knowledge about the modifications that occur in the early stage of COPD. Additionally, parameters obtained from this model present great potential for early diagnosis in smokers and in patients with early-stage COPD.

C. O. Ribeiro · A. C. D. Faria (✉) · P. L. de Melo
Biomedical Instrumentation Laboratory, Institute of Biology and Faculty of Engineering, State University of Rio de Janeiro, Rio de Janeiro, Brazil
e-mail: alvaro.camilo@unigranrio.edu.br

P. L. de Melo
e-mail: plopes@uerj.br

A. J. Lopes
Pulmonary Function Laboratory, State University of Rio de Janeiro, Pedro Ernesto University Hospital, Rio de Janeiro, Brazil

P. L. de Melo
Laboratory of Clinical and Experimental Research in Vascular Biology, State University of Rio de Janeiro, Rio de Janeiro, Brazil

1 Introduction

Approximately 80 million people have more severe stages of chronic obstructive pulmonary disease (COPD), accounting for 5% of all deaths worldwide [1]. The spirometry test is typically used to evaluate respiratory obstruction in COPD [1]. Although it is considered the gold standard test, spirometry has the disadvantage of requiring great effort and great cooperation from patients [2], which can result in variation in the quality of the test results [3]. The assessment of respiratory obstruction in the early stages is critically dependent on the sensitivity of pulmonary function tests [4].

There is consensus in the literature on the high importance of early COPD diagnosis [5–7], enabling the establishment of measures that may interfere with disease progression. The forced oscillation technique (FOT) is a non-invasive method that aims to evaluate the respiratory system resistance and reactance during spontaneous ventilation [3]. The method is based on the application of sinusoidal pressure variations in the opening of the airway through a mouthpiece, overlapping spontaneous ventilation.

Fractional-order models (FrOr) in combination with FOT measurements were recently proposed, allowing a more detailed and accurate description of the dynamic behaviour of the respiratory system. These models may provide information associated with resistive properties and on hysteresivity, which reflects the increase in heterogeneity and changes in lung structure. Information on the damping factor, associated with parenchymal deformity, and elastance are also provided [8]. However, there are no studies in the literature describing the use of FrOr models in the early diagnosis of the effects of smoking.

The objectives of this study were [1] to evaluate the potential of the FOT combined with fractional-order models in the early diagnosis of the effects of smoking; [2] to perform similar evaluations in patients with early-stage COPD

and [3] to determine the best parameters for the diagnoses cited.

2 Materials and Methods

The FOT and spirometry assessments were performed at the Biomedical Instrumentation Laboratory of the State University of Rio de Janeiro (LIB/UERJ) and at the Pedro Ernesto University Hospital (Hospital Universitário Pedro Ernesto—HUPE) and were approved by the Research Ethics Committee of HUPE (protocol CEP/HUPE: 2927). Prior to the tests, the individuals signed a free and informed consent form.

2.1 Individuals Analysed

A total of 31 healthy volunteers with no history of smoking or pulmonary disease, characterizing the control group, was studied. The smoking group (n = 26) was composed of individuals over 18 years of age, with no history of cardiovascular or orthopedic diseases, and with no respiratory infections during the last thirty days, clinically stable and with spirometric examination compatible with normality. They present a history of smoking with a smoking load of 5–35 packs a year. The COPD group (n = 22) was composed of patients over 18 years of age, with a previous diagnosis of COPD, in the mild stage of the disease [9]. These patients have no respiratory infections in the last 30 days at the time of the exams and no history of cardiovascular or orthopedic diseases.

2.2 Instrumentation

The tests included FOT and spirometry measurements. The first test was performed using an instrument developed in our laboratory [10, 11] and was characterized by pressure oscillations in the frequency range between 4 and 32 Hz with an amplitude of 1 cm H_2O that were produced by a speaker and transmitted into the respiratory system by a mouthpiece. The resulting flow and pressure signals were measured near the mouth by a pneumotachometer and a pressure transducer, respectively. After amplification, these signals were processed using Fourier transform (F) to estimate the respiratory impedance (Zrs) by the ratio between the pressure (P) and respiratory flow (V′) signals [Zrs = F(P)/F(V′)]. Spirometric measurements [12] allowed us to evaluate the forced expiratory volume in the first second (FEV$_1$), forced vital capacity (FVC) and the FEV$_1$/FVC ratio.
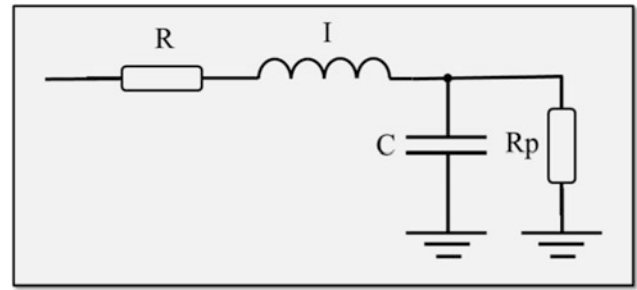
Fig. 1 Two-compartment model used to analyse respiratory impedance. The resistance (R), inductance (I) and capacitance (C) are the analogues of respiratory resistance, inertance and compliance, respectively. Rp represents the peripheral resistance

2.3 Modelling

The model parameters were estimated using the ModeLIB program, also developed in the LIB/UERJ. This program employs the Levenberg-Marquardt algorithm to determine the set of model coefficients that best represents the input data established in terms of least squares. The extended RIC model (eRIC, Fig. 1) was suggested as a model that has improvements compared with the RIC model. In these models, R is the analogue of central airway resistance, Rp describes the peripheral resistance, and I and C are associated with pulmonary inertance and compliance, respectively. The eRIC model can also be used to evaluate the total resistance (Rt = R + Rp) [10].

The fractional-order model proposed for evaluation in this study (Eq. 1) includes a frequency-dependent inertia (If), which takes into account the capacity of the fractional terms to approximate the resistive properties being $0 \leq \alpha \leq 1$, and a component relative to the tissue described as a constant-phase impedance, where $0 \leq \beta \leq 1$, and Cf is fractional compliance.

$$Z_{FrOr}(j\omega) = I_f(j\omega)^{\alpha} + \frac{1}{C_f(j\omega)^{\beta}} \tag{1}$$

These results were interpreted physiologically using the damping (G), elastance (H) and hysteresivity coefficient (η) values, as described by the following:

$$G = \frac{1}{C_f}cos\left(\frac{\pi}{2}\beta\right) \tag{2}$$

$$H = \frac{1}{C_f}sin\left(\frac{\pi}{2}\beta\right) \tag{3}$$

$$\eta = \frac{G}{H} \tag{4}$$

2.4 Statistical Analysis

The results are presented as the means ± SD. The Shapiro-Wilk normality test was performed first. One-way analysis of variance followed by Tukey's test was used when the data exhibited a normal distribution. When the data were not normally distributed, a non-parametric test (Kruskal–Wallis) combined with the Mann–Whitney U test was used. The results were considered significant at $p < 0.05$. The diagnostic accuracy of the studied parameters was evaluated by means of receiver operation characteristic (ROC) analyses [13].

3 Results

The anthropometric and spirometric characteristics of the groups studied are described in Table 1. Table 2 describes the results obtained in the eRIC model.

Examining the parameters obtained with the FrOr model, significant increases in If, damping and hysteresivity were observed. Changes in α and Cf were not significant, and β and elastance showed significant decreases (Fig. 2).

Table 3 shows the results of the area under the ROC curve (AUC) and confidence interval (CI) and describes the diagnostic accuracy of the parameters evaluated.

4 Discussion

R increased comparing the smoking group with the control (Table 2). This parameter is related to increased secretion and changes in the pulmonary parenchyma [14]. Similarly, Rt increased with disease severity. The changes in C may indicate a reduction in compliance and/or an increase in airway resistance [15], providing an adequate description of the changes in the respiratory system of smokers and COPD [9].

The increase in I_f (Fig. 2a) is related with the resistive properties, which are captured in this model from the real part of the inertance. This result is consistent with the pathophysiology because during disease progression, airway resistance increases due to increased secretion and changes in the pulmonary parenchyma [16]. β was significantly reduced in the smoking and COPD groups (Fig. 2d), possibly associated with increased obstruction, a predicted result

Table 1 Anthropometric and spirometric measurements of the groups studied

	Group I control (n = 31)	Group II smokers (n = 26)	Group III mild COPD (n = 22)	ANOVA (p)
Age (years)	59.8 ± 14.2	35.5 ± 10.0*	65.7 ± 11.5	<0.001
Weight (kg)	66.0 ± 11.1	66.0 ± 11.1	63.5 ± 11.8	ns
Height (cm)	163.0 ± 7.9	166.6 ± 7.9	161.5 ± 6.4	ns
BMI (kg/m^2)	24.7 ± 2.7	23.7 ± 2.9	24.3 ± 4.3	ns
FEV$_1$ (L)	2.8 ± 0.8	3.4 ± 0.8***	2.2 ± 0.4**	<0.001
FEV$_1$ (%)	108.7 ± 19.1	104.7 ± 15.4***	87.0 ± 8.6***	<0.001
FVC (L)	3.4 ± 0.9	4.1 ± 0.8**	3.4 ± 0.7	<0.01
FVC (%)	105.6 ± 19.9	105.9 ± 14.8	105.7 ± 10.0	ns
FEV$_1$/FVC	82.9 ± 6.2	99.0 ± 7.2***	65.2 ± 4.7***	<0.001

BMI Body Mass Index; *FEV$_1$* Forced Expiratory Volume in 1 s; *FVC* Forced Vital Capacity; *FEV$_1$/FVC* Tiffeneau Index; n = number of evaluated patients. *ns* Not Significant. *$p < 0.05$, **$p < 0.01$, ***$p < 0.001$, in comparison with the control group

Table 2 Parameters obtained by the eRIC model in the groups studied

	Group I control (n = 31)	Group II smokers (n = 26)	Group III mild COPD (n = 22)	ANOVA (p)
R (cmH$_2$O/L/s)	2.1 ± 0.6	2.9 ± 0.6***	2.4 ± 0.8	<0.001
Rp (cmH$_2$O/L/s)	0.3 ± 0.2	0.3 ± 0.4	1.1 ± 0.6***	<0.001
Rt (cmH$_2$O/L/s)	2.5 ± 0.5	3.2 ± 0.5***	3.5 ± 1.1***	<0.001
I (cmH$_2$O/L/s^2)	0.007 ± 0.004	0.009 ± 0.003	0.009 ± 0.003	ns
C (L/cmH$_2$O)	0.021 ± 0.008	0.015 ± 0.005**	0.018 ± 0.011	<0.05

R Central Resistance; *Rp* Peripheral Resistance; *Rt* Total Resistance; *I* Inertance; *C* Compliance; n = number of evaluated patients. *ns* Not Significant. *$p < 0.05$, **$p < 0.01$, ***$p < 0.001$ in comparison with the control group
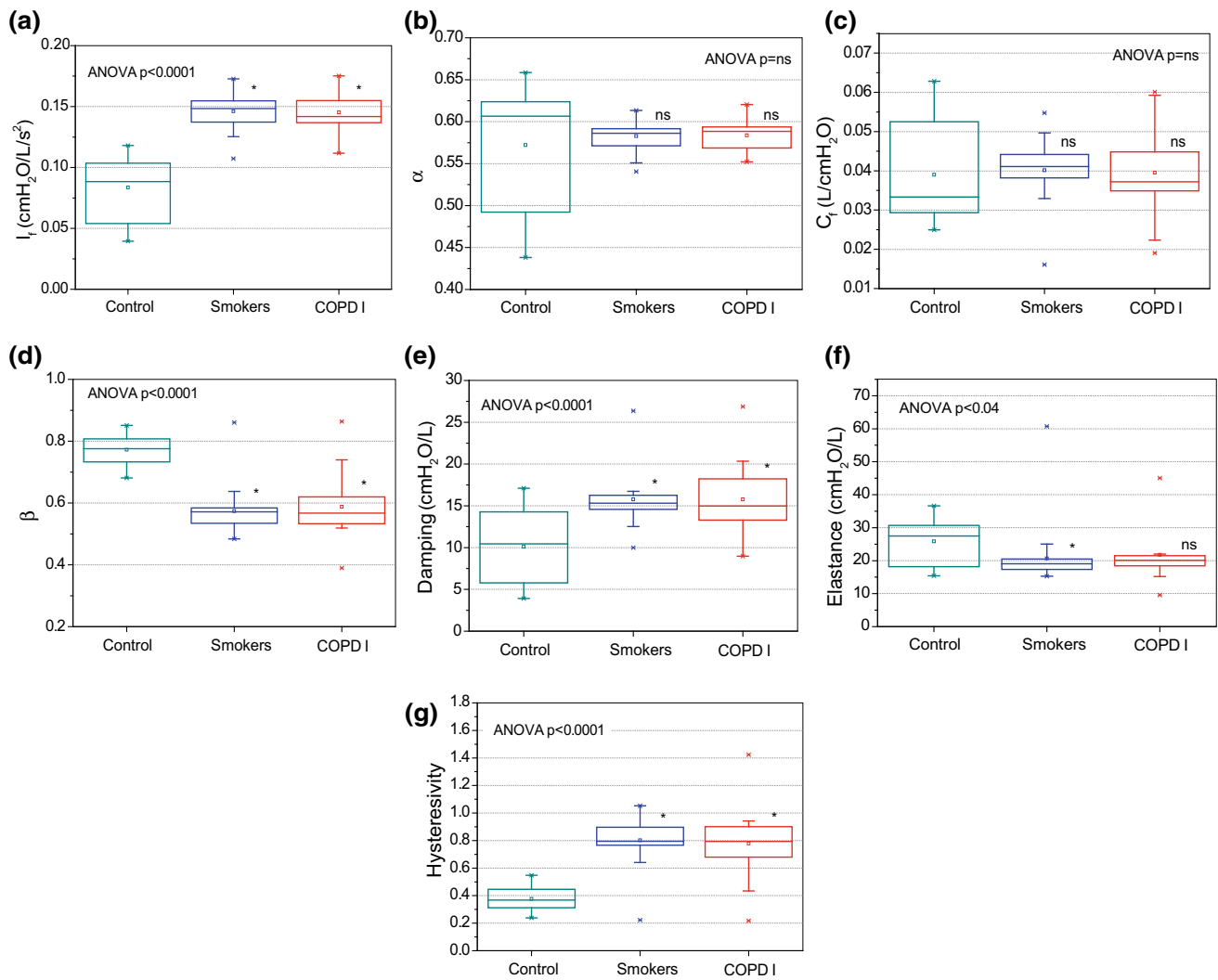
Fig. 2 Behaviour of the fractional-order model parameters in the groups studied. *, $p < 0.05$ relative to control; ns, not significant; If, fractional inductor; α, alpha coefficient; Cf, fractional compliance; β, beta coefficient

of the worsening in respiratory system deformation. This increases the elastance (Fig. 2f). Similar to the β parameter, the significant increase in the damping factor (Fig. 2e) can be explained by the increase in parenchymal deformity [8]. The increase in hysteresivity (Fig. 2g) reflects the increase in heterogeneity and changes in pulmonary structure in the gradual process of disease evolution [2]. The changes observed in alpha and Cf were not significant.

Rt and Rp presented the best diagnostic accuracy among the parameters obtained by the eRIC model in

smokers and COPD patients, respectively (Table 3). In agreement with previous results in mild asthma [8] and in workers exposed to asbestos [17], a higher diagnostic accuracy was obtained through the use of fractional-order parameters. I_f was the best parameter in smokers (AUC > 0.90) and mild COPD (AUC = 0.999). This finding can be explained by the capacity of the FrOr models to adjust to fractional values of 20 dB/dec, in contrast to integer-order models, which are limited to integer multiples of 20 dB/dec. The inclusion of a real part

Table 3 Area under the ROC curve (AUC) and 95% confidence interval (CI) describing the diagnostic accuracy of the evaluated parameters. The best values of AUC are described in bold. eRIC—extended RIC model; R—central resistance; Rp—peripheral resistance; Rt—total resistance; I—inertance; C—compliance; FrOr—fractional-order model; If—fractional inductor, α—alpha coefficient; fractional compliance (Cf); β—beta coefficient; G—damping; H—elastance and η—hysteresivity

	Smokers (n = 26)		Mild COPD (n = 22)	
	AUC	CI	AUC	CI
eRIC				
R	0.820	$0.696 - 0.909$	0.594	$0.450 - 0.727$
Rp	0.504	$0.368 - 0.639$	**0.877**	$0.757 - 0.951$
Rt	**0.850**	$0.731 - 0.931$	0.831	$0.703 - 0.920$
I	0.650	$0.512 - 0.771$	0.574	$0.431 - 0.709$
C	0.744	$0.611 - 0.850$	0.658	$0.515 - 0.783$
FrOr				
I_f	**0.995**	$0.928 - 1.000$	**0.999**	$0.930 - 1.000$
α	0.583	$0.445 - 0.712$	0.588	$0.444 - 0.721$
C_f	0.593	$0.455 - 0.721$	0.577	$0.434 - 0.712$
β	0.962	$0.874 - 0.995$	0.940	$0.839 - 0.987$
G	0.806	$0.680 - 0.899$	0.821	$0.691 - 0.913$
H	0.739	$0.606 - 0.847$	0.660	$0.517 - 0.784$
η	0.962	$0.874 - 0.995$	0.940	$0.839 - 0.987$

that is dependent on frequency may also have contributed to a more accurate description the dynamic response of the respiratory system and to a consequent increase in the diagnostic accuracy in the FrOr model.

5 Conclusion

This study evaluated the use of the FrOr modeling combined with FOT in the diagnosis of early respiratory abnormalities in smokers and mild COPD. FrOr parameters outperformed integer-order models. I_f was the best parameter for this task (AUC = 0.995 and 0.999, respectively), allowing a high diagnostic accuracy, which makes this combination particularly useful for the early diagnosis of the cited conditions. The results of this study are encouraging, and further studies with a higher number of volunteers should be performed to confirm these evidences.

References

1. Silva, K.K., Lopes, A.J., Jansen, J.M., de Melo, P.L.: Total inspiratory and expiratory impedance in patients with severe chronic obstructive pulmonary disease. Clinics **66**(12), 2085–2091 (2011)
2. Amaral, J.L., Lopes, A.J., Jansen, J.M., Faria, A.C., Melo, P.L.: Machine learning algorithms and forced oscillation measurements applied to the automatic identification of chronic obstructive
3. pulmonary disease. Comput. Methods Programs Biomed. **105**(3), 183–193 (2012)
4. Di Mango, A.M.G.T., Lopes, A.J., Jansen, J.M., Melo, P.L.: Changes in respiratory mechanics with increasing degrees of airway obstruction in COPD: detection by forced oscillation technique—ScienceDirect. Respir. Med. **100**(3), 399–410 (2006)
5. Lopes, A.J., de Melo, P.L.: Brazilian studies on pulmonary function in COPD patients: what are the gaps? Int. J. Chronic Obstr. Pulm. Dis. **11**, 1553–1567 (2016)
6. Jones, P.W., Brusselle, G., Dal Negro, R.W., Ferrer, M., Kardos, P., Levy, M.L., et al.: Health-related quality of life in patients by COPD severity within primary care in Europe. Respir. Med. **105**(1), 57–66 (2011)
7. Frantz, S., Nihlen, U., Dencker, M., Engstrom, G., Lofdahl, C.G., Wollmer, P.: Impulse oscillometry may be of value in detecting early manifestations of COPD. Respir. Med. **106**(8), 1116–1123 (2012)
8. Sansores, R.H., Velazquez-Uncal, M., Perez-Bautista, O., Villalba-Caloca, J., Falfan-Valencia, R., Ramirez-Venegas, A.: Prevalence of chronic obstructive pulmonary disease in asymptomatic smokers. Int. J. Chronic Obstr. Pulm. Dis. **10**, 2357–2363 (2015)
9. Faria, A.C.V.J., Lopes, A.J., Melo, P.L.: Forced oscillation, integer and fractional-order modeling in asthma. Comput. Methods Programs Biomed. **128**, 12–26 (2016)
10. Agusti, A., Vogelmeier, C.F.: Global strategy for the diagnosis, management, and prevention of chronic obstructive lung disease 2018 report. GOLD Executive Summary 2018 03/21/2018. http://www.ncbi.nlm.nih.gov/pubmed/28128970
11. Lima, A.N., Faria, A.C.D., Lopes, A.J., Jansen, J.M., Melo, P.L.: Forced oscillations and respiratory system modeling in adults with cystic fibrosis. Biomed. Eng. Online **13**(14), 11 (2015)
12. Miranda, I.A., Dias Faria, A.C., Lopes, A.J., Jansen, J.M., Lopes de Melo, P.: On the respiratory mechanics measured by forced oscillation technique in patients with systemic sclerosis. PLoS One **26, 8**(4), e61657

12. Pereira, C.A.: Espirometria. Jornal de Pneumologia **28**(3), S1–S82 (2002)
13. Swets, J.A.: Measuring the accuracy of diagnostic systems. Science **240**(4857), 1285–1293 (1988)
14. Vogelmeier, C.F., Criner, G.J., Martinez, F.J., Anzueto, A., Barnes, P.J., Bourbeau, J., et al.: Global strategy for the diagnosis, management, and prevention of chronic obstructive lung disease 2017 report. GOLD executive summary. Am. J. Respir. Crit. Care Med. (2017). http://dx.doi.org/10.1164/rccm.201701-0218PP
15. Hyatt, R.E.S., Nakamura, M.: Interpretation of Pulmonary Function Tests. Lippincott-Raven, Phyladelphia (1997)
16. Kaczka, D.W., Dellacá, R.L.: Oscillation mechanics of the respiratory system: applications to lung disease. Crit. Rev. Biomed. Eng. **39**(4), 337–359 (2011)
17. de Sa, P.M., Castro, H.A., Lopes, A.J., Melo, P.L.: Early diagnosis of respiratory abnormalities in asbestos-exposed workers by the forced oscillation technique. PLoS ONE **11**(9), e0161981 (2016)

Analysis of Carbon, Oxygen, Strontium and Lead Isotopes in Human Teeth: Inferences for Forensic Investigation

Ana Claudia Stadler Burak Mehl, Lucilene Yumi Ishida, and Rubens Alexandre de Faria

Abstract

Although numerous techniques can be used to identify human remains, the number of cases that stay unidentified increases each year and is seen as a worldwide problem. Due to the great resistance of dental tissues, even when subjected to extreme conditions, after the failure of traditional techniques of human identification, we can find in teeth our last resources. The teeth, mainly in the enamel, preserve elements as the isotopes, allowing their analysis for forensic purposes. The applications of isotopic analysis have been described in the last decades, however, in recent years, new approaches have been proposed for use in forensic investigations. This study addresses the current research scenario, based on publications, and presents the fundamentals and limitations for the use of carbon, oxygen, strontium and lead isotopes found in the dental structure making inferences about its potential as forensic identification and provenance tool of human remains. The applicability of this resource has been well documented and confirms its immense potential for use in forensic identification and georeferencing.

Keywords

Forensic dentistry • Isotopes • Identification

1 Introduction

The teeth incorporate elements during their formation making them, as well as bones, good indicators of exposure to substances and environments [1, 2].

Isotopes are elements found in the composition of these tissues, which, because they have different rates of growth and renewal, reflect different periods of life. The proportion of isotopes reflects information about the period of its incorporation, such as the place of residence in childhood [2–6]. In this way, the elemental analysis of a tooth constitutes a tool to monitor isotope signals and their origins [2, 3].

The identification of human remains is a worldwide problem. In Europe, around 17% of cases remain unidentified, similar statistics have been found in the USA and other countries [2]. The values of carbon (C), oxygen (O), strontium (Sr) and lead (Pb) isotopes obtained from human skeletal remains can be used to reconstruct facts and habits of ancient populations, as well as to provide place of origin and year of birth [2–4, 7–9]. This information is especially useful when the application of traditional identification methods, such as fingerprints, DNA, dental records and comparability with local databases of missing persons do not provide the required identity [2–4, 7, 10–13].

The purpose of this article is to present the current research scenario, based on publications, involving the analysis of isotopes related to forensic dentistry, the C, O, Sr and Pb isotopic analysis fundamentals in dental elements, their use as origin tracers, the analysis limitations and evaluation of the potential of this resource in forensic science.

2 Materials and Methods

The searches were carried out through the Portal de Periódicos da Capes, in different combinations of the terms "isotopes", "human", "identification", "forensic", "tooth" and the isotopics terms "carbon" isotopes, "oxygen", "strontium" and "lead", due to their relevance in identification and georeferencing studies, published between 2000 and 2018. The results offered by the Web of Science, DOAJ, PubMed/Medline, Scopus and Lilacs bases were chosen.

A. C. S. B. Mehl (✉) · L. Y. Ishida · R. A. de Faria
Federal Technological University of Paraná, Curitiba, Brazil
e-mail: anacsbmehl@gmail.com

2.1 Inclusion and Exclusion Criteria

Studies were included that demonstrated the principles, significance, potential uses and limitations present in the use of the C, O, Sr and Pb isotopes found in dental tissues used in human identification and georeferencing. Were excluded those referring to the evaluation of specific techniques or applications restricted to specific situations or locations.

2.2 Results

The initial search using all terms returned 61 articles, but only 11 showed relevance to this work. Additional manual searches in different combinations of the same terms, without temporal limitation, brought, after an analysis of the summaries, 53 articles, of which after reading, more 20 remained usable, totaling 31 articles in analysis for this study. Another 18 bibliographic references, obtained from isolated searches, were added according to the need for clarification.

2.3 Summary of Obtained Data

The articles information has been entered in Excel® worksheet and sorted by publication date, journal research area, types of used isotopes, sampled biological tissues and objective/application of the study for an overview of the results found.

Of 31 analyzed articles, 17 of them, 55% were published in the last five years.

The journals that published most of these studies were those related to the areas of Health Sciences/Human Biology (55%), as forensic sciences, followed by the Anthropology/Archeology periodicals (26%), although almost all demonstrate some multidisciplinarity, characteristic of isotopic analysis.

Most of these articles, 68%, used combined analysis of different isotopes. Strontium was the most used in these studies, was analyzed in 20 of them, in which 5 was analyzed in isolation. Carbon isotopes were exclusive objects from 2 studies of 18 in which they were used. Oxygen was analyzed in 17 studies, appearing isolated in only 1, and lead analyzed in 11, of which 3 were fully dedicated to its analysis. Nitrogen, sulfur and hydrogen isotopes are analyzed in association with the other isotopes in 11 studies.

Only one of these articles did not use dental enamel in the analyzes, the work of Arora et al. (2014), in which the dentin was used as Pb exposure time biomarker. Dentin was analyzed in combination with enamel in 16 studies. Bones were also analyzed in 16 studies, three of which also included hair and fingernails.

MAIN APPLICATIONS OF STUDIES INVOLVING HUMAN TEETH ISOTOPIC ANALYSIS
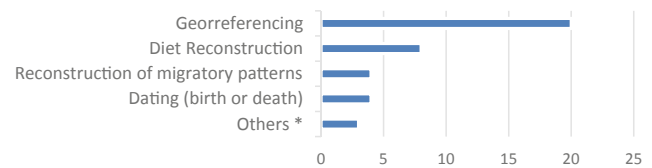
Fig. 1 The graph shows the times number of the study subjects/applications appear among selected articles. *Others describe less frequent goals such as exposure time to Pb, diagenesis study, and description of forensic identification tools

Georeferencing, or provenance identification, motivated most of these studies, being object of 20 them. Nine studies include more than one study object, such as dating, reconstruction of diets and migratory patterns and others (see Fig. 1).

3 Review

3.1 Tooth

The teeth's resistance to temperature and post-mortem degradation establishes them as important information sources for forensic analysis [6–8]. The enamel that recovers it is highly resistant and its position inside the alveoli protects the dentin from micro-organisms attack and infiltrations by exogenous materials (Figs. 2 and 3) [6, 14].
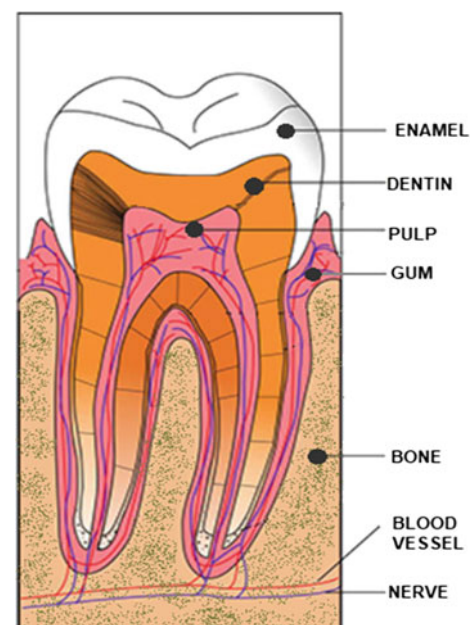
Fig. 2 Schematic drawing of the longitudinal cross-section of a tooth (Adapted from [6])
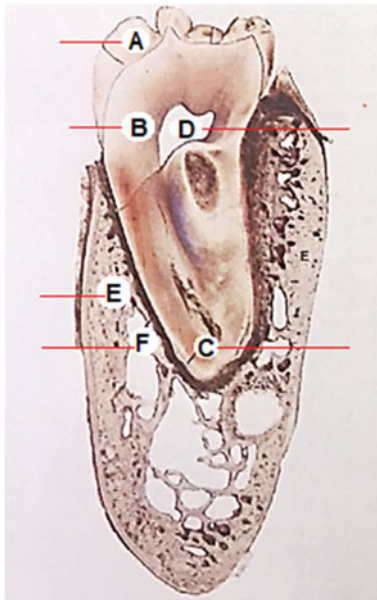
Fig. 3 Cut by wear of a tooth in situ showing the distribution of tissues. A = enamel, B = dentin, C = cement, D = pulp, E = alveolar bone, F = periodontal ligament (Adapted from [15])

Fig. 4 The graps **a** and **b** shows the percentage of components of each tissue by volume and weight (Adapted from [16])

Bones have the property of remodeling throughout life, continuously changing the circulating chemical elements for periods between 5 and 10 years. Therefore, they will provide data on their later years [2, 6, 9, 16]. The dental enamel does not remodel, therefore its isotopic signature represents the diet consumed during its formation, reflecting the biogeochemical environment of this phase [9, 14, 17, 18].

The enamel formation of first permanent molars begins at birth, and is completed up to 3 years [19]. Therefore, the enamel of the first molar will record information about the birthplace and early childhood of an individual. Other teeth will reflect the subsequent phases according to their chronologies of formation. The enamel of the third molars are the last, only completed during adolescence [2, 9, 19].

The enamel is avascular, predominantly inorganic (Fig. 4) and denser than other tissues [6]. The composition mainly by hydroxyapatite, besides conferring high resistance and longevity [20], makes it a safe reservoir for chemical elements and ideal for isotope analysis in forensic investigations of human remains [16].

Dentin constitutes most of the tooth structure, and although it is connected to the blood supply, it is not usually remodeled after its mineralization [2, 21, 22], maintaining isotropic signals for decades [2, 21]. Completed dentinogenesis, process that forms the dentin, a secondary dentin begins to be deposited at a very slow rate throughout life [22], making it possible to obtain informations on both types of dentin.

Ratios of different isotopes are information that can be obtained from dental structures. These values may reveal different information corresponding to the period of time in which the tooth was formed (Fig. 4) [23, 24].

3.2 Isotopes

Carbon Isotopes (δ^{13}C and ^{14}C). δ^{13}C is an isotopic signature, a measure of the stable isotope ratio of ^{13}C^{12}C [25]. The carbon isotopic composition in human bones and teeth is derived from plant nutrition and provides information about the diet of a population in a given region [2, 7, 8, 26] (Fig. 5).

There are regional differences of δ^{13}C values that are reflected in the enamel. Although there are overlapping values in different regions, the range of values found may restrict the probable places of human remains origin. However, as Kamenov and Curtis [2] note, it is safer in georeferencing to use δ^{13}C values combined with values from other isotopes.

Methods for dating by ^{14}C analysis in dental enamel were also developed [8, 27]. By comparing the ^{14}C enamel levels with the atmospheric ^{14}C data, an estimate of the year of birth can be obtained [6].

The study by Alkass et al. [8] emphasizes the importance of combining ^{13}C and ^{14}C dental enamel to identify people in the event of mass disasters, and others in which identification is critical.

Oxygen Isotope (δ^{18}O). δ^{18}O is a measure of the ratio of oxygen stable isotopes ^{18}O and ^{16}O [28]. The δ^{18}O values in
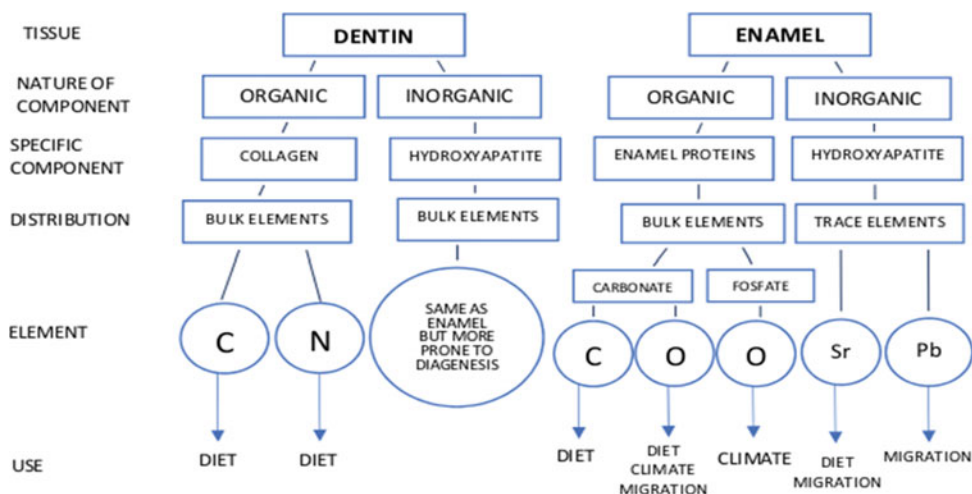
human teeth depend on the isotopic composition of oxygen soaked in water. There is a good correlation between $\delta^{18}O$ of local waters and those found in tooth enamel. The $\delta^{18}O$ is calculated by measurements on the enamel carbonate [2, 7].

The $\delta^{18}O$ is generally calculated by measurements on enamel carbonate [2, 9, 26], but may also be obtained from bone or dentin, being considered important information in the comparative data set [29].

Oxygen isotopes can also present similar values in several regions of the world, thus not identifying a region only in $\delta^{18}O$ values. Therefore, a supposedly "local" individual must first be identified by an independent method. Subsequently, $\delta^{18}O$ values, obtained from local water sources, can provide a more precise georeferencing within the region [2].

Kamenov and Curtis [2] suggest that the combination of data between $\delta^{18}O$ and $\delta^{13}C$ can restrict possible regions of origin for an unidentified individual, and in some cases, adding data from $^{87}Sr^{86}Sr$ to the collected data further limits these regions. This idea is reinforced by Lightfoot e O'Connel [30] when they conclude that the isotope data must be part of a dataset.

Lead Isotope (Pb). Human teeth and bones incorporate lead traces from the local environment during growth and remodeling. Anthropogenic activities cause changes in the natural isotopic background of lead and this is reflected in its composition. Pb is currently one of the most significant pollutants in the environment [26, 31]. Its exposure can be measured in the tooth, since the dentin is its main place of deposition [2, 26, 32].

Contemporary teeth present regional differences due to the use of different types of lead. There are also overlaps of values in various regions of the world, making it difficult to distinguish regions only based on Pb isotopes. Nevertheless, some differences are so pronounced that they become unique

isotopical signatures of Pb [21, 32–34], able to identify their individuals in any region of the world, as in the case of individuals from USA [34]. For Laffoon et al. [35], Pb isotopes serve as a complementary parameter in isotopic analyzes in human teeth offering new variables.

Strontion Isotope ($^{87}Sr/^{86}Sr$). The source of strontium in a region is its geological base, so it is directly related to a geographic location [2]. The ratio of the $^{87}Sr/^{86}Sr$ stable isotopes from geological materials reflects geographic differences according to the age and composition of the material, which makes it a research parameter for geological dating, ancient population studies, food authentication and forensic sciences [5, 14, 36, 37].

Weathering is mainly responsible for the release of strontium from rocks in soils and subsequently to plants, animals and oceans [14].

Strontium and calcium have the same chemical theories, so strontium is an important ingredient in the human system, although in a smaller amount than calcium [9, 14].

The $^{87}Sr/^{86}Sr$ ratio in tissues reflects its original source, consistent with the geo logical area where the individual resided during the formation of the investigated tissues [2, 7, 9, 14]. Plants absorb soil elements through their roots, reflecting this isotopic composition in their final products [7, 14]. Once absorbed by the plants the same value of $^{87}Sr/^{86}Sr$ remains at all trophic levels [14, 35]. Thus the strontium values in the tissues come from the diet and are the same or very close to the bioavailable strontium [35].

Dental enamel is the most characterized matrix in strontium, because it is not influenced by exogenous sources, it is a good marker to determine birthplaces [14]. Bones also incorporate strontium [38], thus reflecting the last 5–10 years of individual's life (depending on the type of bone) [9].

4 Discussion

Alkass et al. [27] state that from a single tooth, it is possible to estimate year of birth, obtain a clue of geographic origin, sex determination, estimate age of person to death and year of death, combining techniques of isotopic analysis, DNA and aspartic acid racemization.

Comparative studies require reference sources to correlate isotopic values of the tissues to their sources. Studies such as that of Kamenov and Curtis [2] that compared high precision Pb isotopes, C, O, and $^{87}Sr/^{86}Sr$ ratio of bulgarian teeth to those of bulgarian mineral sources showed the reference values of these isotopes, providing information directly applicable to contemporaneous cases.

The study by Coelho et al. [2] compiles a database for Sr isotopic analysis and emphasizes the need for new matrix reference materials for future analyzes. The lack of benchmark data for comparative studies is reported in other studies such as Balcaen et al. [4], Rauch et al. [14], Kamenov and Curtis [39] and Font et al. [40].

Values of isotope ratios are rarely unique, so Montgomery [41] states that the isotope analysis is an exclusive technique, since it only excludes unlikely places of origin. Thus, for a reliable georeferencing, the analyzed elements must be isotopically distinct, as reported by Balcaen et al. [4] and Font et al. [40].

The study by Keller et al. [33] describes how the association of Pb, O and C isotopes with the other data initially available in their analyzes improved the possibilities of identification of the individuals studied, reducing the initial options by up to 95% increasing the chances of positive identification.

In addition to the association of isotopes, different analysis and the availability of more data sets can increse the accuracy of the analysis [2].

Ubelaker et al. [27] and Alkass et al. [42] observed that the analysis of different tissues or with different formation times also increase the precision of the data interpretation.

According to Price et al. [43] the high costs and laboratory knowledge required for isotopic analysis are major challenges for less supported projects. Leatherdale [44] also reports the methodological limitations of production and interpretation of isotopic data, since many factors need to be examined simultaneously. An example is the isotopic signatures of C and N, which can be altered by the physiology of the organism itself. Another limitation is to quantify rates of cellular turnover, such as some aspects of bone metabolism, which are not yet fully understood and affect accuracy in chronology establishments.

Another difficulty described by authors such as Kamenov and Curtis [2], Montgomery [17] and Juarez [41] is the study involving modern people, mainly in the West, where it is possible to have a global diet with imported supplies from all over the world hampering a georeferencing based on the dietary isotopes. For Laffoon et al. [35] despite this difficulty, the success of the studies of geographical provenance demonstrates the usefulness of these methods.

Aggarwal et al. [45] consider that identifying a region of origin for an individual may not yet be a positive identification, but is necessary to augment that possibility. According to Radhakrishnan [31], isotopic analysis is a recognized tool and is becoming increasingly important by tracing the origin of human remains in archaeological studies and forensic investigations.

In addition to a forensic identification tool, in recent years, studies based on isotopic analysis of ancient skeletons, such as Killgrove and Montgomery [41], Montgomery [46], Dupras and Tocheri [47], Kinaston et al. [48], Sjogren et al. [49], have been conducted in order to rebuild human history as we know it, reconstructing migrations, customs and diets, generating new theories about past events and allowing the improvement of analysis techniques.

5 Conclusions

Isotopes researches in human tissues has evolved considerably, recent publications demonstrate this, mainly in the health areas, in forensic studies, and anthropology, receiving contributions from a variety of fields such as geology and chemistry.

The teeth, mainly in the enamel, are reservoirs of information in the most preserved way as possible. The treatment of this information by multidisciplinary teams maximizes the possibilities of positive identifications.

The more specific approach to referencing seems to be the $^{87}Sr/^{86}Sr$ ratio. A combined analysis with $\delta^{18}O$, $\delta^{13}C$ and ^{14}C provides additional data that increases the chances of successful research. Pb Isotopes, in specific cases, may be the differential key for solving identification cases.

Even with the limitations reported in the multi-isotope analysis, it should limit geo-referencing options and increase

the number of cases of identified individuals, confirming the great potential that this tool demonstrates through the related studies.

References

1. Bodart, F., Deconninck, G., Martin, L.A.R.N.: A large scale study of tooth enamel. IEEE Trans. Nucl. Sci. NS-28, 1–4 (1981)
2. Kamenov, G.D., Curtis, J.H.: Using carbon, oxygen, strontium, and lead isotopes in modern human teeth for forensic investigations: a critical overview based on data from Bulgaria. J. Forensic Sci. 8 (2017). https://doi.org/10.1111/1556-4029.13462
3. Bartelink, E.J., Mackinnon, A.T., Prince-Buitenhuys, J.R., Tipple, B.J., Chesson, L.A.: Stable Isotope Forensics as an Investigative Tool in Missing Persons Investigations. Springer International Publishing, Cham (2016)
4. Balcaen, L., Moens, L., Vanhaecke, F.: Determination of isotope ratios of metals (and metalloids) by means of inductively coupled plasma-mass spectrometry for provenancing purposes—a review. Spectrochim. Acta Part B At. Spectrosc. 65, 769–786 (2010). https://doi.org/10.1016/j.sab.2010.06.005
5. De Muynck, D., Boyen, S., Delporte, S., Winne, J. De, Vanhaecke, F., Degryse, P.: The Sr87/Sr86 ratio as a powerful tool in forensic investigations. http://adsabs.harvard.edu/abs/2009EGUGA..11.8928D (2009)
6. Hollund, H.I., Jans, M.M.E., Kars, H.: How are teeth better than bone? An investigation of dental tissue diagenesis and state of preservation at a histological scale (with photo catalogue). Internet Archaeol. (2014). https://doi.org/10.11141/ia.36.7
7. Someda, H., Gakuhari, T., Akai, J., Araki, Y., Kodera, T., Tsumatori, G., Kobayashi, Y., Matsunaga, S., Abe, S., Hashimoto, M., Saito, M., Yoneda, M., Ishida, H.: Trial application of oxygen and carbon isotope analysis in tooth enamel for identification of past-war victims for discriminating between Japanese and US soldiers. Forensic Sci. Int. 261(166), e1–166.e5 (2016). https://doi.org/10.1016/j.forsciint.2016.02.010
8. Alkass, K., Buchholz, B., Druid, H., Spalding, K.L.: Analysis of 14 C and 13 C in teeth provides precise birth dating and clues to geographical origin. Forensic Sci. Int. 209, 34–41 (2011). https://doi.org/10.1016/j.forsciint.2010.12.002
9. Beard, B.L., Johnson, C.M.: Strontium isotope composition of skeletal material can determine the birth place and geographic mobility of humans and animals. J. Forensic Sci. 45, 1049–1061 (2000). https://doi.org/10.1520/JFS14829J
10. Malaver, P.C., Yunis, J.J.: Different dental tissues as source of DNA for human identification in forensic cases. Croat. Med. J. 44, 306–309 (2003)
11. Higgins, D., Austin, J.J.: Teeth as a source of DNA for forensic identification of human remains: a review. Sci. Justice 53, 433–441 (2013). https://doi.org/10.1016/j.scijus.2013.06.001
12. Menon, L.M.L., Fernandes, M.M., Paranhos, L.R., Da Silva, R.H.A.: Tanatologia forense e odontologia legal: interface e importância na rotina pericial Forensic thanatology and dentistry: interface and Odonto. 19, 15–23 (2011)
13. Menon, L.M.L., Fernandes, M.M., Paranhos, L.R., Silva, R.H.A.: Tanatologia Forense e Odontologia Legal: Interface e Importância na Rotina Pericial. Odonto. (2011). https://doi.org/10.15603/2176-1000/odonto.v19n37p15-23
14. Coelho, I., Castanheira, I., Bordado, J.M., Donard, O., Silva, J.A.L.: Recent developments and trends in the application of strontium and its isotopes in biological related fields. TrAC Trends Anal. Chem. 90, 45–61 (2017). https://doi.org/10.1016/j.trac.2017.02.005
15. Bhaskar, S.N.: Histologia e embriologia oral de Orban. Editora Artes Medicas Ltda, São Paulo (1998)
16. Pasteris, J.D., Wopenka, B., Valsami-Jones, E.: Bone and tooth mineralization: why apatite? Elements 4, 97–104 (2008). https://doi.org/10.2113/GSELEMENTS.4.2.97
17. Juarez, C.A.: Strontium and geolocation, the pathway to identification for deceased undocumented Mexican border-crossers: a preliminary report. J. Forensic Sci. 53, 46–49 (2008). https://doi.org/10.1111/j.1556-4029.2007.00610.x
18. Bentley, R.A.: Strontium isotopes from the earth to the archaeological skeleton: a review. J. Archaeol. Method Theory. 13, 135–187 (2006). https://doi.org/10.1007/s10816-006-9009-x
19. Reid, D.J., Dean, M.C.: Variation in modern human enamel formation times. J. Hum. Evol. 50, 329–346 (2006). https://doi.org/10.1016/j.jhevol.2005.09.003
20. Rakovan, J.F., Pasteris, J.D.: A technological gem: materials, medical, and environmental mineralogy of apatite. Elements 11, 195–200 (2015). https://doi.org/10.2113/gselements.11.3.195
21. Gulson, B.L., Gillings, B.R.: Lead exchange in teeth and bone—a pilot study using stable lead isotopes. Environ. Health Perspect. 105, 820–824 (1997). https://doi.org/10.1289/ehp.97105820
22. Linde, A., Goldberg, M.: Dentinogenesis. Crit. Rev. Oral. Biol. Med. 4, 679–728 (1993)
23. Ambrose, S.H., Krigbaum, J.: Bone chemistry and bioarchaeology. J. Antropol. Archeol. 22, 193–199 (2003). https://doi.org/10.1016/s0278-4165(03)00033-3
24. Mays, S.: New Directions in the Analysis of Stable Isotopes in Excavated Bones and Teeth. Greenwich Medical Media, London (2000)
25. Panchuk, K., Ridgwell, A., Kump, L.R.: Sedimentary response to Paleocene-Eocene thermal maximum carbon release: a model-data comparison. Geology 36, 315–318 (2008). https://doi.org/10.1130/G24474A.1
26. Adserias-Garriga, J., Thomas, C., Ubelaker, D.H., C. Zapico, S.: When forensic odontology met biochemistry: Multidisciplinary approach in forensic human identification. Arch. Oral Biol. 87, 7–14 (2018). https://doi.org/10.1016/j.archoralbio.2017.12.001
27. Alkass, K., Saitoh, H., Buchholz, B.A., Bernard, S., Holmlund, G., Senn, D.R., Spalding, K.L., Druid, H.: Analysis of radiocarbon, stable isotopes and DNA in teeth to facilitate identification of unknown decedents. PLoS ONE 8, 1–13 (2013). https://doi.org/10.1371/journal.pone.0069597
28. Delta 18 O. https://en.wikipedia.org/wiki/Δ18O
29. France, C.A.M., Owsley, D.W.: Stable carbon and oxygen isotope spacing between bone and tooth collagen and hydroxyapatite in human archaeological remains. Int. J. Osteoarchaeol. 25, 299–312 (2015). https://doi.org/10.1002/oa.2300
30. Lightfoot, E., O'Connell, T.C.: On the use of biomineral oxygen isotope data to identify human migrants in the archaeological record: intra-sample variation, statistical methods and geographical considerations. PLoS ONE 11, e0153850 (2016). https://doi.org/10.1371/journal.pone.0153850
31. Radhakrishnan, R.: Chewing the very teeth because it bites: an anthropological forensics by stable isotope profiling. J. Forensic Dent. Sci. 3 (2011)
32. Arora, M., Austin, C., Sarrafpour, B., Hernández-Ávila, M., Hu, H., Wright, R.O., Tellez-Rojo, M.M.: Determining prenatal, early childhood and cumulative long-term lead exposure using

micro-spatial deciduous dentine levels. PLoS One. **9** (2014). https://doi.org/10.1371/journal.pone.0097805

33. Keller, A.T., Regan, L.A., Lundstrom, C.C., Bower, N.W.: Evaluation of the efficacy of spatiotemporal Pb isoscapes for provenancing of human remains. Forensic Sci. Int. **261**, 83–92 (2016). https://doi.org/10.1016/j.forsciint.2016.02.006

34. Kamenov, G.D., Gulson, B.L.: The Pb isotopic record of historical to modern human lead exposure. Sci. Total Environ. **490**, 861–870 (2014). https://doi.org/10.1016/j.scitotenv.2014.05.085

35. Laffoon, J.E., Sonnemann, T.F., Shafie, T., Hofman, C.L., Brandes, U., Davies, G.R.: Investigating human geographic origins using dual-isotope (87 Sr/86 Sr, ä18 O) assignment approaches. PLoS ONE **12**, 1–17 (2017). https://doi.org/10.1371/journal.pone.0172562

36. Isótopos de Estrôncio. https://en.wikipedia.org/wiki/Isotopes_of_strontium

37. Emery, M.V., Stark, R.J., Murchie, T.J., Elford, S., Schwarcz, H.P., Prowse, T.L.: Mapping the origins of Imperial Roman workers (1st–4th century CE) at Vagnari, Southern Italy, using 87Sr/86Sr and d18O variability. Am. J. Phys. Anthropol. 1–14 (2018). https://doi.org/10.1002/ajpa.23473

38. Hillson, S.: Dental Anthropology. Cambridge University Press, Cambridge (1996)

39. Rauch, E., Rummel, S., Lehn, C., Büttner, A.: Origin assignment of unidentified corpses by use of stable isotope ratios of light (bio-) and heavy (geo-) elements-a case report. Forensic Sci. Int. **168**, 215–218 (2007). https://doi.org/10.1016/j.forsciint.2006.02.011

40. Font, L., Van Der Peijl, G., Van Leuwen, C., Van Wetten, I., Davies, G.R.: Identification of the geographical place of origin of an unidentified individual by multi-isotope analysis. Sci. Justice **55**, 34–42 (2015). https://doi.org/10.1016/j.scijus.2014.06.011

41. Montgomery, J.: Passports from the past: investigating human dispersals using strontium isotope analysis of tooth enamel. Ann. Hum. Biol. **37**, 325–346 (2010). https://doi.org/10.3109/03014461003649297

42. Ubelaker, D.H., Buchholz, B.A., Stewart, J.E.B.: Analysis of artificial radiocarbon in different skeletal and dental tissue types to evaluate date of death. J. Forensic Sci. **51**, 484–488 (2006). https://doi.org/10.1111/j.1556-4029.2006.00125.x

43. Price, T.D., Burton, J.H., Cucina, A., Zabala, P., Frei, R., Tykot, R.H., Tiesler, V.: Isotopic studies of human skeletal remains from a sixteenth to seventeenth century AD Churchyard in Campeche. Mexico Curr. Anthropol. **53**, 396–433 (2012). https://doi.org/10.1086/666492

44. Leatherdale, A.J.: Interpreting stable carbon and nitrogen isotope ratios in archaeological remains: an overview of the processes influencing the δ13C and δ15N values of type I collagen. Totem Univ. West. Ontario J. Anthropol. **21**, Article 5 (2013)

45. Aggarwal, J., Habicht-Mauche, J., Juarez, C.: Application of heavy stable isotopes in forensic isotope geochemistry: a review. Appl. Geochem. **23**, 2658–2666 (2008). https://doi.org/10.1016/j.apgeochem.2008.05.016

46. Killgrove, K., Montgomery, J.: All roads lead to Rome: exploring human migration to the eternal city through biochemistry of skeletons from two imperial-era cemeteries (1st–3rd c AD). PLoS One. **11** (2016). https://doi.org/10.1371/journal.pone.0147585

47. Dupras, T.L., Tocheri, M.W.: Reconstructing infant weaning histories at roman period Kellis, Egypt using stable isotope analysis of dentition. Am. J. Phys. Anthropol. **134**, 63–74 (2007). https://doi.org/10.1002/ajpa.20639

48. Kinaston, R., Bedford, S., Richards, M., Hawkins, S., Gray, A., Jaouen, K., Valentin, F., Buckley, H.: Diet and human mobility from the lapita to the early historic period on Uripiv Island, Northeast Malakula, Vanuatu. PLoS One. **9** (2014). https://doi.org/10.1371/journal.pone.0104071

49. Sjögren, K.-G., Price, T.D., Kristiansen, K.: Diet and mobility in the corded ware of Central Europe. PLoS One. **11** (2016). https://doi.org/10.1371/journal.pone.0155083

Clinical and Thermal Evaluation and Microstructural Characterization of Silicone Gel Used in Newborns Submitted to Non-invasive Ventilation

D. F. C. Ribeiro, F. S. Barros, E. Azevedo, B. L. Fernandes, and P. Nohama

Abstract

This study aimed to evaluate the clinical efficiency and thermal and microstructural characterization of a silicone gel used as nasal protection in newborns (NB) submitted to non-invasive ventilation (NIV). The study was divided into two stages. In the first, a control case study was performed with 11 NBs hospitalized at the Neonatal Intensive Care Units (NICUs) of a public hospital in the South of Brazil, who required NIV with nasal silicone gel protector. The stage of the injury and the need for replacing the nasal protector were evaluated daily until the suspension of NIV. In the second stage, a sample of silicone gel was aged in the neonatal incubator simulating the conditions of use, it was submitted to thermogravimetric analysis (TGA), X-ray diffraction (XRD) and scanning electron microscopy (SEM), and the results were compared to a sample without aging. The incidence of the injury was 72.72%, being 75% of them of stage I, and 25% of stage II. The mean of detachment during use was $1.5 \pm 1,07$ times. As for the TGA, the silicone gel presented thermal stability up to 290 °C. Increased crystallinity and presence of microcracks were observed in the sample that had undergone aging. So, we concluded that the silicone gel is a little effective protector in the prevention of nasal injury in NB submitted to NIV.

Keywords

Silicone gel • Nasal injury • Non-invasive ventilation

D. F. C. Ribeiro (✉) · F. S. Barros · E. Azevedo · P. Nohama
PPGEB - Universidade Tecnológica Federal do Paraná, Curitiba, Brazil
e-mail: debora-camillo@hotmail.com

B. L. Fernandes · P. Nohama
PPGTS - Pontifícia Universidade Católica do Paraná, Curitiba, Brazil

1 Introduction

Prematurity is considered a relevant public health problem due to the high rates of infant mortality [1]. In this period, respiratory system disorders are frequent and, therefore, non-invasive ventilatory support is used in preterm newborns (NBs) [2].

Any technique that uses constant or variable pressure to provide ventilatory support without the need to institute an artificial airway is referenced as NIV [3].

In general, non-invasive ventilation (NIV) devices are made up of a gas source, a pressure generator and the patient interface [3].

The binasal prong is the most common interface used in Neonatology because it is easy to install, has low-cost, provides relatively constant pressure and allows good patient access [4].

Although nasal prongs have advantages and are the most widely used devices, they can cause nasal injury due to the friction between the prong and the sensitive baby skin, an adverse event increasingly present in the NICU [5].

Protectors adhesive as hydrocolloid [6] and silicone gel [7] are applied to the nasal base to avoid direct contact of the prong with the columella and the nasal septum, preventing injuries.

The silicone gel is a dressing designated to prevent hypertrophic and keloid scars [8] also used in pressure ulcers. It is a soft and flexible material [7] composed of an elastomeric membrane and a layer of adhesive composed of polydimethylsiloxane (PDMS) with different levels of crosslinks [9].

Günlemez et al. [7] evaluated the efficacy of silicone gel tape for preventing nasal injury in premature NBs, who were divided into two groups: intervention with RNs who received silicone gel as nasal protection during NIV stay, and a control group that did not receive nasal protection. The nasal injury occurred in 14.9% of the NBs from the control group and in 4.3% belonged to the silicone group. The

authors concluded that silicone gel significantly reduces the incidence and severity of the nasal injury.

In spite of the importance of silicone gel in the protection of the skin of NBs submitted to NIV, the thermal, structural and superficial alterations of the silicone gel that may cause skin irritation or damage to the NB are still little investigated. As the material is composed mostly of water, prolonged exposure to heat and humidity can lead to loss of water and cause cracks and morphological changes in the material, which may result in loss of adhesion or the appearance of dirt accumulation points.

Therefore, the present study aims to evaluate the clinical efficiency as well as the thermal degradation and microstructural characteristics of this material.

2 Method

This study was divided into two stages. The first stage involved a clinical study concerning 11 NBs who needed the NIV support with silicone gel dressing as nasal protector. The infants were admitted to the NICU at Waldemar Monastier Infant Hospital, belonging to the Curitiba metropolitan area, Brazil, from 05/01/2015 to 04/30/2016.

The development of this study respected the national and international standards that govern ethics in research involving human beings and was approved by the Research Ethics Committee involving Human Beings of the Federal Technological University of Paraná—UTFPR (CAAE 42718915.4.0000.5547).

The NBs of both genders were chosen regardless of their race or ethnicity, class or social group, and with less than 38 weeks of gestational age. They were submitted to the NIV support using the short binasal prong as an NIV interface. At least requiring 24 h of NIV support were required to be included in the clinical trial. The exclusion criteria were: NBs with choanal atresia, cleft lip, and cleft palate.

All NBs received NIV via the Inter[®] Neo mechanical ventilator. The interfaces used were short binasal prongs with the same design, but from three different manufacturers: Inca[®], Silmag[®] or Fanem[®], sterilized and reused or new ones selected according to the availability of the material when the NIV was installed.

The NBs were evaluated following a protocol developed specifically for this study, and consisting of neonatal data collection from the medical records and visual inspection. The neonatal data collected were: gender, gestational age, birth weight and length of stay in NIV.

The clinical inspection with the aid of a clinical flashlight revealed the skin injuries in the columella and the nasal septum regions. The injuries were classified regarding the three stages (I, II or III) proposed by Fischer et al. [10],

namely Stage I (intact skin with unbleached erythema), Stage II (partial loss of the dermis thickness presenting a superficial wound with a crustless red bed), and Stage III (necrosis and total tissue loss).

All evaluations were performed before the installation of the NIV and every 24 h until the medical suspension of this support. The injury Stage and the need to exchange the nasal protector were daily recorded.

All NBs received the nasal protector with Mölnlycke Health Care's self-adherent Mepiform[®] dressing, approximately 0.3 mm thick.

The silicone gel used in this study is formed by an outer layer of viscose and polyester and an inner layer of silicone gel with Safetac[®] technology. This technology consists of a silicone blade patented by Mölnlycke Health Care, which provides a selective micro-adhesion, which facilitates the adhesion of the dressing to the skin and reduces trauma to the skin when the dressing is removed [11].

The silicone gel was cut in the nasal base format (Fig. 1) and fixed by a physiotherapist before the installation of the NIV support, protecting the nostrils, columella and the nasal septum.

The silicone gel was replaced only in case of detachment. The neonatal data and evaluation results regarding the injury stage and the need to replace the nasal protector were inserted into a Microsoft Office Excel spreadsheet and submitted to statistical analysis.

The variables were described according to their types: means and standard deviations were determined for the quantitative variables, and the absolute and percentage frequencies were set for the nominal variables.

In the second stage of this study, a square sample of silicone gel with side 3.0 cm was laid on a glass slide with the adherent surface upwards. It was positioned inside a Fanem[®] model 2186 neonatal incubator on a mattress covered by a cloth diaper, distant 11 cm from the proximal border and 20 cm from the lateral door, simulating the environment in which the NB is exposed during the intensive treatment.
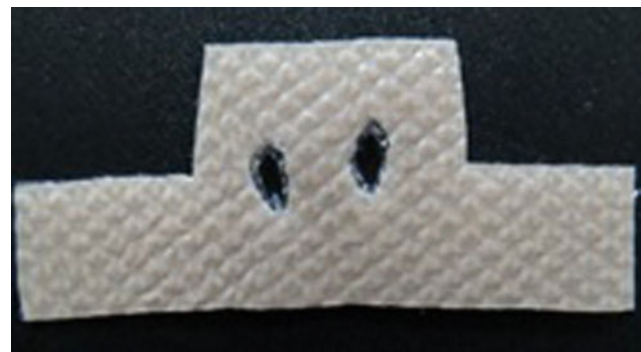
Fig. 1 Silicone gel cut out in the nasal base format

The incubator was in the NICU of HIWM and remained constant for seven consecutive days maintaining constant the parameters: temperature of 36 °C, relative humidity of 90% and effective one ranging from 70 to 90%.

TGA was performed using a Perkin Elmer thermobalance, model STA 6000, following the conditions: 10 mg sample mass; temperature range from 50 to 800 °C, heating rate of 20 °C/min, and atmosphere of N_2 with a rate of 20 ml/min [12].

XRD was performed on the adhesive surface of the silicone gel with a Shimadzu diffractometer, model XRD 7000, Cu Kα radiation, the voltage of 40 kV, a current of 30 mA and speed of the goniometer of 2°/min. All the measurements were made at room temperature with a variation of 2θ between 4° and 70° and time of 3 s.

A baseline was plotted on the diffractogram to separate the region with background radiation to evaluate the crystallinity percentage. The region above this line and below the peaks comprised the amorphous region and the internal area of the peaks corresponded to the crystalline region. The areas of the amorphous and crystalline regions were obtained by integration with the aid of the OriginPro software, obtaining the relative percentage of crystallinity of the samples.

SEM micrographs of the adhesive surface of the silicone gel were obtained using the Zeiss EVO MA15 equipment.

For comparison, in each test, two samples of the silicone gel were analyzed: one without aging (as supplied) and one after aging according to the procedure described previously.

3   Results

In this study, we had evaluated 11 NBs who received NIV using silicone gel as a nasal protector. Five of them (45.45%) were male and 6 (54.55%) female. The mean gestational age was 30.82 ± 4.06 weeks, the mean birth weight was 1377.64 ± 623.55 g, and the mean length of stay in NIV support was 77:12 ± 43:23 h.

The base's nasal injury occurred in 8 NBs (72.72%), being 6 (75%) injuries were of Stage I and 2 (25%) of Stage II. Six of the 8 injuries (75%) occurred within 24 h, and 2 (25%) after 24 h.

Table 1 presents the characteristics of gender, gestational age, birth weight and length of stay in NIV of the NBs with and without injury.

It was found that the average exchange of the silicone gel in case of detachment was 1.50 ± 1.07.

Regarding the TGA, it is possible to observe that both samples (without and with aging) presented thermal stability up to 290 °C (Fig. 2).

Both samples presented three thermal events in the TGA. Table 2 shows the initial temperatures of the said events and the percentage of the residue about the initial mass of the samples with and without aging.

Figure 3 shows the diffractogram of the silicone gel with and without treatment. It is possible to note that both samples had a peak at the angle of 12° and a smaller one at 21°.

Table 3 shows the areas of the amorphous, crystalline regions and the percentage of crystallinity of the silicone gel with and without aging.

In Fig. 4 are shown SEM micrographs of the silicone gel with and without aging. It is possible to observe, in Fig. 4a, the presence of depression and areas of wrinkling and, in Fig. 4b, microcracks and regions of wrinkling.

4   Discussion

In this study, it was found that the incidence of nasal injury in NBs submitted to NIV with silicone gel protection was 72.72%. This incidence was higher than that found by Günlemez et al. [7] which reached only 4.30%. These authors reported a lower incidence even evaluating newborns who remained in NIV for a period longer than the present study. However, in the study realized by Günlemez et al. [7] the silicone gel was used with a thickness of 1.8 mm, while in the present study the silicone gel was used with a thickness of approximately 0.3 mm, suggesting that the difference in thickness of the silicone gel influences the prevention of nasal injury, since thicker protection can reduce the friction between the prong and the skin. Also, it is

Table 1 Characteristics of the NBs with and without nasal injury

Variables	With nasal injury (n = 8)	Without nasal injury (n = 3)
Gender		
Female	4 (50.00%)	2 (66.67%)
Male	4 (50.00%)	1 (33.33%)
Gestacional age (semanas)	32.00 ± 3.69	27.67 ± 3.79
Birth weight (g)	1566.25 ± 636.64	874.67 ± 60.87
Length of stay in NIV (h)	91:34 ± 42:07	38:52 ± 13:01

Mean values ± standard deviation or absolute frequency (percentage) of variables of interest in the 11 NBs studied
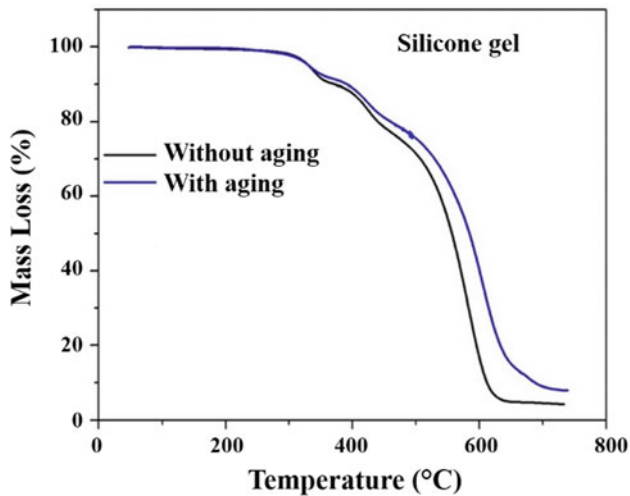
Fig. 2 TGA curves of the silicone gel with and without aging

Fig. 3 Silicone gel diffractograma

Table 2 Initial temperature of the thermal events and percentage of residue of the silicone gel samples without and with aging

Variables	Without aging	With aging
The beginning of the 1st thermal event (°C)	290	290
The beginning of the 2nd thermal event (°C)	350	365
The beginning of the 3rd thermal event (°C)	440	445
End of the 3rd thermal event (°C)	630	660
Residue (%)	5.16	12.99

Table 3 Area of the amorphous, crystalline regions and percentage crystallinity of the silicone gel with and without aging

Variables	Silicone gel without aging	Silicone gel with aging
Amorphous region	738,82	731,78
Crystalline region	268,29	294,41
Percentage crystallinity	26,64	28,69

recommended to leave the prong at least 2 mm away from the columella to prevent nasal injury [13]. In this way, the thicker silicone gel maintains a greater distance between the columella and the skin of the NB reducing the friction between these structures.

In the NICU studied, the official procedure of the institution is the use of the extra thin hydrocolloid tape (0.3 mm) as nasal protection in NBs submitted to NIV. The hydrocolloid dressing consists of a hydrophobic outer layer of polyurethane film and a hydrophilic inner layer made of carboxymethylcellulose, pectin and gelatin [14, 15]. It is a protection that has high adhesiveness to the skin. However, considering that the skin of the premature NB infant is thin and fragile, the functionality as a vital barrier is less effective [16], and the removal of an adhesive nasal protector may cause detachment epidermis slices, resulting in an important inflammatory reaction [17].

In the present study, it was verified that 75% of the injuries were of Stage I, and 25% of Stage II. There were no nasal injuries of Stage III. Sousa et al. [18], when assessing the severity of the nasal injury in 47 premature newborns

who required NIV for a period over than 24 h, observed the occurrence of nasal injury in 32 (68.10%) patients, being 14 (43.70%) injuries of stage I, 16 (50.00%) of stage II and only 2 injuries of stage III (6.30%). The NBs remained on average 72 h in NIV, with use of prong without nasal protection. The non-use of nasal protection could have influenced the occurrence of stage III injuries and the higher incidence of Stage II injuries when compared to the present study.

It was observed that the time of appearance of the injury was 24 h, disagreeing with the results found by Sousa et al. [18] which was 72 h. It is emphasized that that these authors evaluated the presence of nasal injury in premature newborns only at hospital discharge. In the present study, the newborn was evaluated prior to the institution of NIV and every 24 h until the medical suspension of this ventilatory support. In this way, it is verified that the daily evaluation of NBs in NIV implies the early detection of the nasal injury, helping the multi-professional team to develop ways that contribute to minimizing its effects as the application of cold physiological solution and massage in the nostrils.

A factor that could have influenced the high incidence of nasal injury and its early appearance is the detachment of the silicone gel during the stay of the NB in the NIV, which in this study was, on average, 1.5 ± 1.07 times. This event can
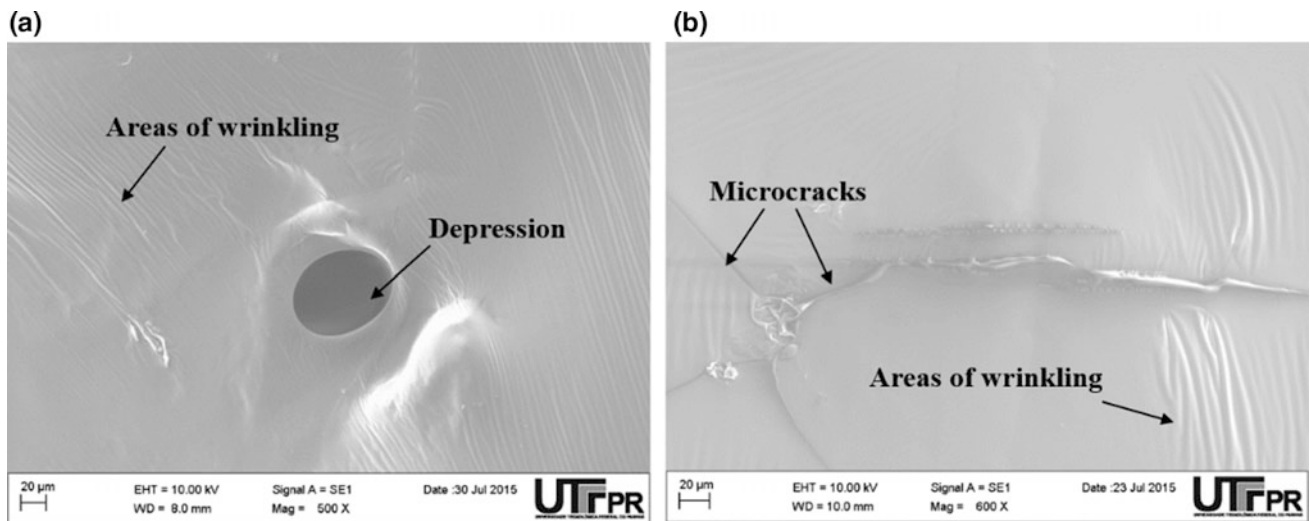
Fig. 4 SEM micrographs of the silicone gel **a** without aging, **b** with aging

be explained by the low initial adhesion characteristic of pressure sensitive silicone adhesives. The detachment of the protection makes the nasal columella more vulnerable to friction with the prong, and consequently, to the development of the nasal injury.

In relation to TGA, it was verified that the silicone gel presents thermal stability up to 290 °C. When considering the temperature at which the nasal protections are exposed when used in the newborns under treatment inside the incubator (below 37 °C), it can be verified that they do not present thermal degradation in this temperature range and in the humidity conditions of the incubator.

It was observed that in the samples with and without aging the first thermal event occurred at approximately 290 °C, the second at 440 °C and the third at 630–660 °C. The thermal degradation of PDMS under inert atmosphere occurs in the temperature range between 400 and 650 °C and is characterized by the breakdown of Si–O bonds and formation of cyclic oligomers at as hexamethyl disiloxane and octamethyl tetrasiloxane. In the presence of oxygen, degradation occurs in two stages, the first one occurs at 339 °C and the second one begins at 400 °C [19].

By Knowing the composition of said the dressing, it is possible to infer that the first thermal event corresponds to the degradation of the viscose lamellar layer since the degradation of regenerated cellulose is 270 °C [20]. The second and third thermal events correspond to the degradation of the silicone.

The samples with and without aging showed two peaks, one in 12° and the other in approximately 21°. The results obtained corroborate with the findings of Silva et al. [21] which, when evaluating membranes of silicone breast implants exposed to different doses and types of radiation, found in the diffractograms of the samples analyzed peaks at 12° and 21°. Such data confirm the silicone as the main constituent of the studied protection.

It has been found that temperature and humidity increase the crystallinity of the silicone gel. This event may have occurred due to the interaction between the oxygen present in the atmosphere and the chemical structure of the silicone gel by the means of dipole-dipole bonds, which could have led to the approximation of the chains and, consequently, the increase of crystallinity.

In the microscopies microscopic images of the samples with and without aging were observed show the presence of wrinkled areas which may be associated with loss of water from the samples to the environment.

In the sample with aging, micro-fissures were visualized in the areas of tensioning that can result from the loss of water, which functioned as a plasticizer. With the loss of water, the polymer chains can approximate more or less depending on their chemical affinity between them and, due to the lack of homogeneity in water loss, some regions lose more of the others causing the appearance of the micro-fissures and regions of wrinkling. The loss of water may also have favored the pairing annealing of the polymer chains, increasing the crystallinity, as observed by the XRD.

In clinical practice, both wrinkling regions and micro-fissures can favor the deposition of dirt and infectious agents that, in the presence of a nasal injury, can cause infection and result in damages to the health of the newborn. Therefore, careful and delicate handling is recommended in the application of these nasal protections in NBs submitted to NIV and intensive care redoubled in the presence of nasal injury due to the risk of infection.

One limitation of the present study was the small sampling group of NBs. It is important to carry out new studies that continue to evaluate the efficiency of the silicone gel in

larger populations of NBs and to correlate their effectiveness with the analysis of the dressing used.

5 Conclusion

This study made possible the evaluation clinical, and thermal and microstructural characterization of a silicone gel used as nasal protection in NBs submitted to NIV.

It was possible to conclude that in the NICU studied the silicone gel is a protection little efficient to prevent nasal injuries, regardless of the stage of this injury, since the nasal injury reached rates higher than 70%.

Based on the TGA results, it was possible to conclude that the silicone gel has thermal stability up to 290 °C, therefore, does not degrade during its use in NBs in the incubator.

The temperature and loss of humidity increased the crystallinity of the silicone gel and caused microcracks, which may favor the deposition of infectious agents.

We believe that the results of this research will help health professionals comprehend the possible effects of the use of silicone gel dressings on NBs under NIV support.

References

1. Oliveira, C.H.T., Moran, C.A.: Estudo descritivo: ventilação mecânica não invasiva em recém-nascidos pré-termo com síndrome do desconforto respiratório. ConScientiae Saúde **8**(3), 485–489 (2009)
2. Nicolau, C.M., Andrade, L.B.: Programa de atualização em Fisioterapia Pediátrica e Neonatal: Cardiorrespiratória e Terapia Intensiva. Artmed/Panamericana, Porto Alegre (2012)
3. Mahmoud, R.A., Roehr, C.C., Schmalisch, G.: Current methods of non-invasive ventilatory support for neonates. Paediatr. Respir. Rev. **12**(3), 196–205 (2011)
4. Kopelman, B.I., Santos, A.M.N., Goulart, A.L., Almeida, M.F.B., Miyosh, M.H., Guinsburg, R.: Diagnóstico e tratamento em neonatologia. Atheneu, São Paulo (2004)
5. McCoskey, L.: Nursing care guidelines for prevention of nasal breakdown in neonates receiving nasal CPAP. Adv. Neonatal. Care **8**(2), 116–124 (2018)
6. Xie, L.H.: Hydrocolloid dressing in preventing nasal trauma secondary to nasal continuous positive airway pressure in preterm infants. World J. Emer. Med. **5**(3), 218–222 (2014)
7. Günlemez, A., Isken, T., Gökalp, A.S., Türker, G., Arisoy, E.A.: Effect of silicone gel sheeting in nasal injury associated with nasal CPAP in preterm infants. Indian Pediatr. **47**(3), 265–267 (2010)
8. Radwanski, H.N., Correa, W.E.M., Refosco, T.J., Junior, A., Pitanguy, I.: Silicone gel em cicatrizes de cirurgia plástica: estudo clínico prospectivo. Revista Brasileira de Cirurgia Plástica **25**(3), 428–433 (2010)
9. Borgognoni, L.: Biological effects of silicone gel sheeting. Wound Repair Regen. **10**(2), 118–121 (2002)
10. Fischer, C., Bertelle, V., Hohlfeld, J., Guex, M.F., Dian, C.S., Tolsa, J.F.: Nasal trauma due to continuous positive airway pressure in neonates. Arch. Dis. Child. Fetal Neonatal Edn. **95**(6), 447–451 (2010)
11. Mölnlycke Health Care Homepage. http://mepiform.pt/mepiform/produto/. Accessed 23 Mar 2017
12. Vasco, M.C., Neto, S.C., Nascimento, E.M., Azevedo, E.: Gamma radiation effect on sisal/ polyurethane composites without coupling agents. Polímeros **27**(2), 165–170 (2017)
13. Squires, A.J., Hyndman, M.: Prevention of nasal injuries secondary to NCPAP application in the ELBW infant. Neonatal Netw. **28**(1), 1–15 (2009)
14. Boateng, J.S., Matthews, K.H., Stevens, H.N.E., Eccleston, G.M.: Wound healing dressings and drug delivery systems: a review. J. Pharm. Sci. **97**(8), 2892–2923 (2008)
15. Ferrari, F., Bertoni, M., Bonferoni, M.C., Rossi, S., Caramella, C., Waring, M.J.: Comparative evaluation of hydrocolloid dressings by means of water uptake and swelling force measurements: II. Int. J. Pharm. **117**(1), 49–55 (1995)
16. Fernandes, J.D., Machado, M.C.R., Oliveira, Z.N.P.: Prevenção e cuidados com a pele da criança e do recém-nascido. Anais Brasileiros de Dermatologia **86**(1), 102–110 (2011)
17. Haynes, J.S.: Skin integrity and silicone: Appeel® 'no-sting' medical adhesive remover. Brit. J. Nurs. **17**(12), 1156–1159 (2008)
18. Sousa, N.F.C., Bonfim, S.F.S.F., Vasconcelos, M.G.L., Bezerra, J. L.O., Silva, D.V.C., Leal, L.P.: Prevalência de lesão do septo nasal em prematuros no uso de prongas nasais. Revista da Escola de Enfermagem da USP **47**(6), 1285–1290 (2013)
19. Camino, G., Lomakin, S.M., Lazzari, M.: Polydimethylsiloxane thermal degradation Part 1. Kinetic aspects. Polymer **42**(6), 2395–2402 (2001)
20. Mano, E.B., Mendes, L.C.: Introdução a polímeros, 2nd edn. Blücher, São Paulo (1999)
21. Silva, J.D.C.B.K.F.: Avaliação da influência da degradação no comportamento, na estrutura e nas propriedades físicas e mecânicas de implantes mamários de silicone. Tese de Doutorado, Instituto Militar de Engenharia (2014)

Design and Hydrodynamic Performance of a Pediatric Pulsatile Pump

I. A. Cestari, M. Mazzetto, H. T. T. Oyama, S. Bacht, M. B. Jatene, I. N. Cestari, and F. B. Jatene

Abstract

We report the design and hydrodynamic performance of a pulsatile blood pump and a pneumatic driver system to treat pediatric patients in need of circulatory support while waiting for a heart transplant. The blood pump consists of a pumping chamber with 15 ml stroke volume separated by a flexible diaphragm from a pneumatic chamber. The blood chamber has two orifices fitted with rings in which tri-leaflet tissue valves are placed to control the inflow and outflow of blood. Blood contacting surfaces are heparin coated. The driving unit allows operation of two pumps to assist the left and right side of the heart, independently or simultaneously in three different modes of operation: full-to-empty, ECG synchronized and asynchronous. The flow generated by the pump increases with preload and application of auxiliary negative pressure during the filling phase reaching approximately 1,6 L/min when the pump is operating in full-to-empty mode. The results suggest the performance of the pediatric VAD designed is compatible with the needs of pediatric patients up to 15 kg body weight.

I. A. Cestari (✉) · M. Mazzetto · H. T. T. Oyama · S. Bacht · I. N. Cestari
Bioengineering, Heart Institute (INCOR), University of São Paulo, São Paulo, SP 05403000, Brazil
e-mail: cestari@incor.usp.br

M. B. Jatene · F. B. Jatene
Surgery Division, Heart Institute (INCOR), University of São Paulo, São Paulo, SP 05403000, Brazil

1 Introduction

1.1 Pediatric Ventricular Assist Devices

The use of ventricular assist devices (VADs) in children as a bridge to transplantation improves survival of patients with congenital or acquired heart disease [1, 2]. Technical challenges still remain for the construction of a pump with reduced size having low risk for thromboembolism, non-hemolytic properties and closely matching the cardiac output of infants and small. The most common form of mechanical support available to pediatric patients is extra-corporeal membrane oxygenation (ECMO) [3]. However, ECMO is mainly recommended for short-term use due to the high incidence of complications during medium and long-term use [4]. Improvements in VAD technology and the FDA approval of the Berlin heart EXCOR device for long-term support for small children in the United States of America resulted in a large increase in the use of VADs [5]. Clinical results from centers in Europe and USA show that the rates of survival of children bridged to transplantation with VADs is estimated to vary from 75 to 96% [6]. Costs associated with this technology, however, are a barrier to its use and dissemination in developing countries. In Brazil, there is no relevant clinical experience with pediatric VADs. Therefore, there is an urgent need for development of devices specific for children. This paper presents the design and hydrodynamic performance of a pulsatile pump for paracorporeal implantation as a bridge to heart transplantation in children.

2 Methods

2.1 Pump Design and Materials

The circulatory assist system developed comprises a pneumatically-actuated VAD and a bedside driver.

The VAD is a pulsatile displacement pump for paracorporeal placement for temporary cardiac support. The pump is made by biocompatible polymer chambers separated by a diaphragm with heparin-coated blood contacting surfaces. Tri-leaflet bovine pericardium valves are mounted on the inlet and outlet titanium connectors of the blood chamber. Figure 1 shows a schematic of the pump (left) and a sagittal section showing the diaphragm separating the chambers (right).

The driving unit allows operation of one or two pumps to assist the left and/or the right ventricle simultaneously and independently in two modes of operation: (a) Full to Empty mode with full filling and emptying of the pump, usually referred to as automatic; (b) Asynchronous mode or fixed pumping rate. In this mode of operation outflow values are adjusted independently. The system allows application of auxiliary negative pressure on the pneumatic chamber in situations of low filling pressures. The system has a console with a monitor which displays the flow generated by the one or two VADs in univentricular or biventricular assistance, respectively.

2.2 VAD Hydrodynamic Performance

A hydraulic simulator of the arterial circulation was developed to simulate hemodynamic conditions considering flow and pressure found in pediatric patients during circulatory support. The simulator was based on the compartment model usually referred in the literature as arterial mock loop [7]. For testing the pediatric device, the simulator was filled with a blood analogue (35% glycerin in 0.9% NaCl salt solution) with a dynamic viscosity of about 3.7×10^{-3} Pa. s at a temperature of 37 °C, maintained with the use of a heat

exchanger inserted in the circuit. The tests were performed with initial compliance and resistance values set at 1 ml mm Hg^{-1} and 1 mm Hg s ml^{-1}, respectively. The simulator was equipped with pressure transducers (TruWave PXMK2051, Edwards Lifescience, USA) and ultrasonic flowmeters (TS-410, ME6PXN219 probes, Transonic Systems, Inc., USA). Signals were recorded for off line analysis (WinDaq DI-720, Dataq Instruments, USA).

3 Results

3.1 Flow and Pressure Curves for the Mock Loop Simulator

Figure 2 shows the pediatric VAD connected to the mock loop simulator (top). In this figure, aortic and atrial pressures are provided by compartments identified by aortic and A, respectively. Aortic compliance is set by adjusting the ratio of air pressure and fluid volume in the Aortic compartment. Hydrostatic pressure in atrial (A) compartment simulates filling preloads between 0 and 20 mm Hg. Systemic resistance is set by a clamp on the tubing connecting the aortic compartment and the atrial compartment, not shown for the sake of simplicity. Representative waveforms of arterial pressure and flow generated by the device are shown (bottom).

3.2 VAD Flow Generation

The performance of the pediatric VAD operating in full-to-empty mode at a constant afterload pressure of 100 mmHg is shown in Fig. 3. The figure shows mean flows (L/min) generated by the pump versus preloads (mmHg)
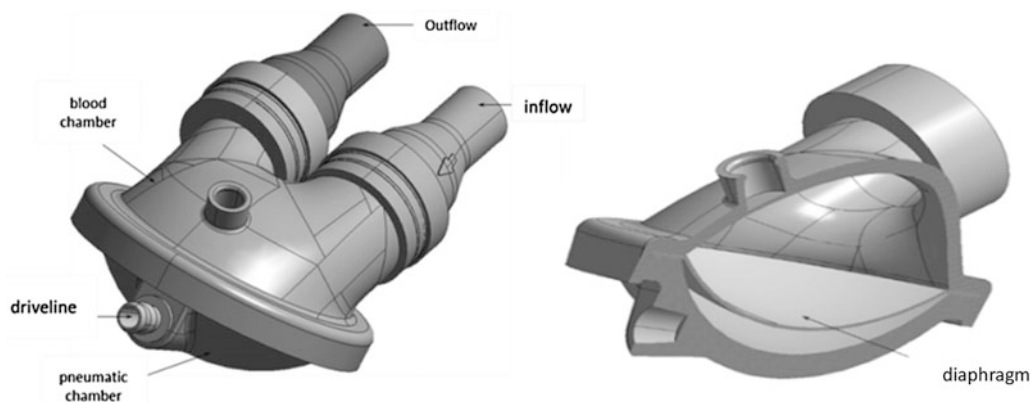
Fig. 1 Illustration of the pump (left) showing the blood chamber with an orifice for de-airing, connectors for directing the flow into and out of the blood chambers and the pneumatic chamber with driveline port. The

figure also illustrates a sagittal section of the blood chamber showing the diaphragm separating both chambers (right)

4 Discussion and Conclusion

The Berlin Heart EXCOR VAD (Berlin Heart AG, Berlin, Germany) and the Medos HIA-VAD (MEDOS Medizin-technik AG, Stolberg, Germany) are the only pulsatile VAD systems commercially available for pediatric patients, including neonates. The design of the pediatric VAD here presented utilizes the same principle of volume displacement utilized in the Berlin Heart EXCOR and MEDOS devices and also utilized in a previously device designed for adult patients used as a bridge to heart transplantation in our institution [8]. The flow patterns in small ventricular assist devices with higher frequency of operation are much more complex and not dynamically similar to that of larger devices. For pulsatile VADs, the risk of hemolysis and thrombus formation are usually inversely proportional to their ejection volume due to the synthetic material interface and frequency of operation. This explains, in part, the scarcity of devices for cardiac assistance of pediatric patients. Previous results from fluid motion studies using particle image velocimetry on a 30 mL ejection volume VAD obtained by our group [9] were incorporated in the design here presented. The geometry of the blood chamber of the VAD was modified with the aim of reducing turbulent motions and removing regions prone to stagnation in order to reduce the incidence of thrombus formation and hemolysis.

Matching of patients to devices can be made based on cardiac output (CO, in L/min) based on weight and body surface area (BSA) [10]. Using the same principle for estimating the range of support offered by the VAD designed and considering its hydrodynamic performance it is possible to predict that it is capable of providing support to neonates and infants up to 15 kg body weight and BSA up to approximately 0.4 m^2.

Clinical application of pediatric VADs is scarce in Brazil where there is no formal funding for long term VADs. In this scenario, the pediatric VAD under development is expected to provide a low cost solution for mechanical circulatory

Fig. 2 Top: VAD connected to the mock loop of the circulation. Aortic and atrial (A) compartments, pressure (P) and flow (F) transducers are connected to record the inflow and the outflow of blood analog. Bottom: Representative waveforms of pressure (dotted line) and flow generated by the device (continuous line) recorded in the loop. Systolic interval (pumping) is indicated by the bold traces above waveforms

with and without application of auxiliary negative pressure during filling. Flow increases with preload and application of auxiliary negative pressure and the pump is capable of generating up to 1.6 L/min.

Fig. 3 Mean flows (L/min) generated by the VAD operating in full-to-empty mode at increasing preloads (mmHg) with and without application of auxiliary negative pressure (mm Hg, legend on the right) during filling of the blood chamber

assistance in children who at present lack any alternative for long term support. The results contribute to the initiative of creating a translational research group for neonatal and pediatric cardiac surgery patients in our institution [11].

References

1. Davies, R.R., Russo, M.J., Hong, K.N., et al.: The use of mechanical circulatory support as a bridge to transplantation in pediatric patients: an analysis of the united network for organ sharing database. J. Thorac. Cardiovasc. Surg. **135**(2), 421–427 (2008)

2. Blume, E.D., Naftel, D.C., Bastardi, H.J., et al.: Outcomes of children bridged to heart transplantation with ventricular assist devices. A multi-institutional study. Circulation. **113**(19), 2313–2319 (2006)

3. The July 2012 Extracorporeal Life Support Organization (ELSO) Extracorporeal Life Support (ECLS) Registry Report International Summary. Ann Arbor, Michigan, Extracorporeal Life Support Organization (2012)

4. Imamura, M., Dossey, A.M., Prodhan, P., et al.: Bridge to cardiac transplant in children: Berlin heart versus extracorporeal membrane oxygenation. Ann. Thorac. Surg. **87**(6), 1894–1901 (2009)

5. Morales, D.L., Almond, C.S., Jaquiss, R.D., et al.: Bridging children of all sizes to cardiac transplantation: the initial multicenter North American experience with the Berlin heart EXCOR ventricular assist device. J. Heart Lung Transp. **30**, 1–8 (2011)

6. Almond, C.S., Morales, D.L., Blackstone, E.H., et al.: Berlin heart EXCOR pediatric ventricular assist device for bridge to heart transplantation in US children. Circulation (127), 1702–119 (2013)

7. Pantalos, G.M., Ionan, C., et al.: Expanded pediatric cardiovascular simulator for research and training. ASAIO J. **56**(1), 67–72 (2010)

8. Moreira, L.F., Galantier, J., Benício, A., Leirner, A.A., Cestari, I. A., Stolf, N.A.: Left ventricular circulatory support as bridge to heart transplantation in Chagas' disease cardiomyopathy. Artif. Organs **31**(4), 253–258 (2007)

9. Ferrara, E., Muramatsu, M., Christensen, K.T., Cestari, I.A.: Particle-image velocimetry study of a pediatric ventricular assist device. J. Biomech. Eng. **132**(7), 1004 (2010)

10. Connell, J.A., Khalapyan, T., Myers, J.L., et al.: Anatomic fit assessment for the Penn state pediatric ventricular assist device. ASAIO J. (53), 687–691 (2007)

11. Wang, S., Caneo, L.F., Jatene, M.B., Jatene, F.B., Cestari, I.A., Kunselman, A.R., Ündar, A.: In vitro evaluation of pediatric hollow-fiber membrane oxygenators on hemodynamic performance and gaseous microemboli handling: an international multicenter/multidisciplinary approach artif organs **41**(9), 865–874 (2017)

Mechanical Evaluation of Poly-ε-Caprolactone and Biosilicate® Composites

A. F. Weber, R. S. Monteiro, S. M. Malmonge, M. T. Souza, O. Petil, and J. K. M. B. Daguano

Abstract

The search for functional materials that repair and/or regenerate of biological tissues in a satisfactory manner has continually risen in the past few years. For such applications, composite materials are each time being better accepted, capable of merge properties from different materials. In this context, the purpose of this study is the development and mechanical characterization of bioactive composite films based on Poly(ε-caprolactone) and Biosilicate®, obtained from two different routes. Route 1 uses the solvent casting technique, and route 2 consists of phase precipitation followed by solvent casting. The mechanical tests show that route 1 presents samples more resistant than route 2, probably due to it high porosity levels. The addition of BS yielded an increase in Young's modulus of around 46%, although the maximum stress and yield strength were reduced. Nevertheless, the mechanical properties of the developed materials are compatible with the biological tissues.

Keywords

Polycaprolactone • Biosilicate • Mechanical properties

1 Introduction

Nowadays, the polymeric materials have a great application, due to their diverse properties and varied types. Therefore, for more specific uses, to improve the properties for targeted uses, the composite materials become interesting, since the properties of the polymers can be improved by adding a new phase [1].

Poly-ε-Caprolactone (PCL) is an aliphatic chain ester polymer which has long-lasting bioabsorbable properties, i.e., takes about 2–3 months for the degradation of that material in the human body. Its use in the biomedical area is usually in suture or systems of drug delivery, where due to its long time of degradation, it is able to carry out its functions by the necessary time [2]. PCL is a polymer approved by the FDA (Food and Drug Administration) and is a material of medium cost, which allows its use in medical applications. In addition to being easily fabricated, it is highly compatible with osteoblasts and therefore may be suitable for long-term implant applications. However, it presents limitations in the applications of bone regeneration due to the low stiffness, hydrophobic nature and absence of bioactivity. One way to overcome these disadvantages is to combine them with bioactive inorganic phases [3], creating a composite.

Biosilicate (BS) is a bioactive glass produced in the Vitreous Materials Laboratory (LaMaV) at Federal University of São Carlos. This material is a glass-ceramic (100% crystalline) based on the composition of Bioglass 45S5. BS has high bioactive properties, which promote an interface of hydroxyapatite with the bone matrix of the human body and a high bonding between them [4]. Because it is a relatively new material, few studies involving the use of BS associated with polymers are found. Among the works already published, it is possible to report the association of BS with alginate [5], PLGA [6], and chitosan [7], which evidence the efficiency of the formed composites. But, there are still no reports of PCL/BS composites.

For years the search for materials to aid and accelerate the recovery of bone tissue, reach new levels in the biomaterials research. A very important factor in this field of research is the mechanical properties. That is an important parameter, because for this application it is necessary to ensure a proper mechanical performance, similar to the human body [8]. In respect of mechanical properties of polymer materials, the

A. F. Weber (✉) · R. S. Monteiro (✉) · S. M. Malmonge · J. K. M. B. Daguano
Engineering, Modeling and Applied Social Sciences Center, Federal University of ABC, Santo André, Brazil
e-mail: rdesouzamonteiro@gmail.com

M. T. Souza · O. Petil
Vitreous Material Laboratory, Federal University of São Carlos, São Carlos, Brazil

ultimate tensile strength it's necessary for polymeric films characterization because this measure represents the load limit that the films resist. Another important parameter is the Yield Strength, which is the maximum tensile that the material holds in elastic behavior [9, 10]. For composite materials, the mechanical properties are even more important, since the addition of a new phase results in different behaviors. Therefore, a study is needed not only of the composite, but also of the matrix [11].

For bone tissue engineering applications, Young's modulus of bone and material to be used should be close so that the effect of stress shielding is avoided [2]. For this purpose, the present study seeks to develop a composite that meets the needs of the tissue repair bone, respecting the natural limits, so that the host environment is not affected.

2 Materials and Methods

2.1 Preparation of PCL/BS Composites

In this study, PCL pellets (molecular weight $\sim 80{,}000$, Sigma Aldrich) was dissolved in chloroform (Synth) in a ratio of 1:10 (%m/v) stirred at room temperature for 3 h. The bioactive glass powder was then produced by milling and sieving the glass. A mean particle size of approximately 20 μm was used. The desired amount of Biosilicate (50%wt relative to the mass of PCL in the solution) was then added to the PCL/chloroform solution, stirred for 30 min [12, 13]. From this, two different routes were adopted. In the first route (R1-PCL/BS), the mixture PCL/BS was ultrasonicated several times at 1 min intervals. The mixture was poured onto a polished glass plate [12]. The second route (R2-PCL/BS) consisted in fast precipitation into excess ethanol. The PCL/BS solution mixture was then precipitated into 5-fold excess of 100% ethanol (v/v). Both routes were air-dried in order to evaporate the solvent [13]. Also, samples without BS were fabricated following the two routes (R1-PCL and R2-PCL).

2.2 Porosity of the Samples

The porosity was calculated using the densities of the dense samples. A total of 5 specimens were used for porosity calculations. The densities of R1-PCL and R2-PCL samples were measured using a pycnometer. The pycnometry technique was used according to the method [14].

2.3 Surface Morphology

The surface morphology of the samples was examined using scanning electron microscopy (SEM) (FEI Quanta 250) after gold sputter-coating (Leica, EM ACE200).

2.4 Mechanical Performance Test

Uniaxial tensile properties were measured with MTS—TrytonTM 250, fitted with a 250 N load cell and 5 mm/min extension rate. The tests were conducting following the ASTM D-882 12 [15]. Samples were randomly cut from the films (n = 5) of R1-PCL, R2-PCl, and R1-PCL/BS and tested, excepted R2-PCL/BS because it's high brittle. After the tensile test, the surfaces of the samples were analyzed by the Physis SZ40—Leica stereomicroscope.

3 Results and Discussion

Figure 1 shows images of the pure PCL and composite films obtained from the two routes. Translucent and more flexible films were formed for the R1 condition, and more rigid and opaque films with spongy appearance and whitish coloration for R2 route. All of them presented Biosilicate particles homogeneously distributed.

The porosity was calculated after determining the densities of the porous samples using a pycnometer, Table 1. For R1-PCL sample, the porosity value was not determined,

Fig. 1 Samples of pure PCL: **a** R1-PCL; **b** R2-PCL, and PCL/BS composite: **c** R1-PCL/BS; **d** R2-PCL/BS
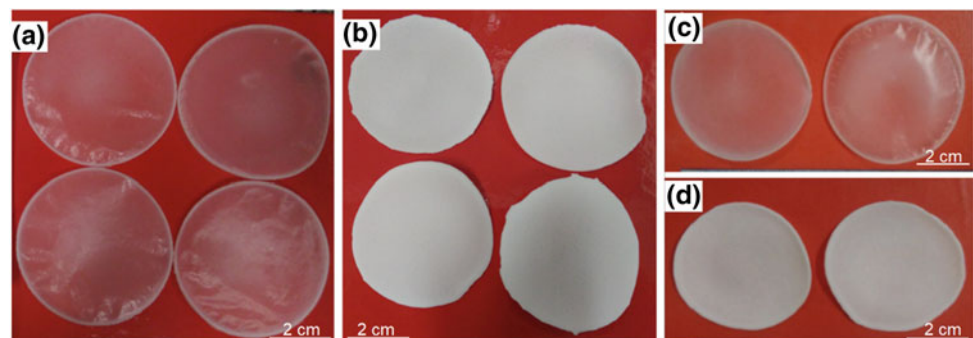
Table 1 Porosity of R1-PCl and R2-PCL samples

Sample	Porosity (%)
R1-PCL	0
R2-PCL	67 ± 4

Table 2 Mechanical properties from tensile testing

Mechanical properties	R1-PCL	R1-PCL/BS	R2-PCL
Ultimate tensile strength (MPa)	10 ± 1	6.4 ± 0.4	2.1 ± 0.5
Yield strength (MPa)	5.2 ± 0.3	4.0 ± 0.3	0.8 ± 0.2
Young's modulus (MPa)	278 ± 40	406 ± 63	41 ± 4

since the films can be considered dense. This is a characteristic of polymer films obtained by the solvent evaporation technique employed in route 1. R2-PCL sample showed a very high porosity. These values are close to those found by composites obtained by route 2 (porosity 78%).

Uniaxial tensile testing was performed to assess the mechanical properties of the composites and to compare the two routes. Ultimate Tensile Strength, Yield Strength and Elastic Modulus were calculated for samples (Table 2).

R1-PCL presented the highest values of ultimate tensile strength, and yield strength. For R2-PCL a significant reduction of these properties was showed, where the mechanical stress corresponds to only 21% and the yield stress to 15%, when compared to R1-PCL.

Comparing the properties for the R1-PCL, which originated dense and homogeneous films, with the other samples, factors such as route of processing and addition of a second phase may interfere with the mechanical properties of the materials. The results for the pure PCL sample were consistent with values found in the literature [16]. In respect of the addition of BS and the change of processing route, ultimate tensile strength, and yield strength decreased with both. This finding is in agreement with the literature [17]. The poor interfacial adhesion between the components of the composite material can result in the reduction of the mechanical properties of the composites and the formation of aggregates [18]. Studies show that additions of up to 5% of a second phase in PCL allow for increases in mechanical properties, relative to pure PCL [19]. However, this increase is not continuous, and for second phase concentrations above 20%, a decrease in properties occurs.

Fig. 2 SEM micrographs of: **a** R1-PCL; **b** R2-PCL; **c** R1-PCL/BS; **d** R2-PCL/BS
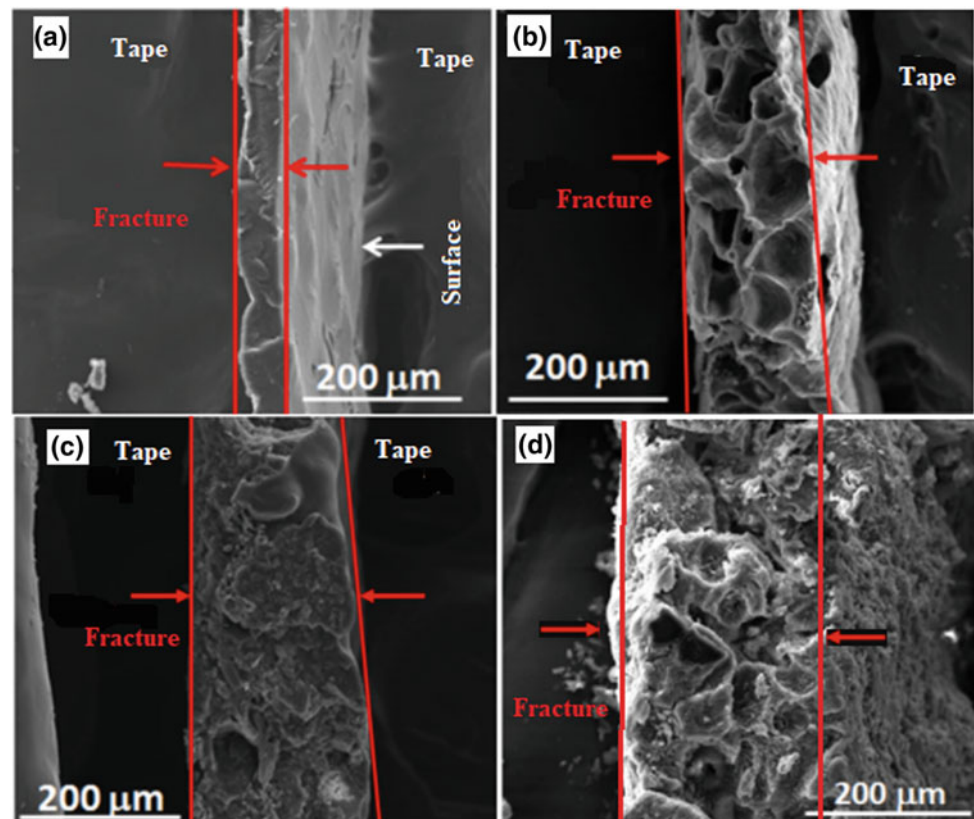
The ultimate tensile strength and Young's modulus values for R1-PCL/BS are quite close to those of spongy bone (7.4 and 400 MPa, respectively). In relation to soft tissues, the maximum tension of R1-PCL is comparable to fibrocartilage (10.4 MPa) and the Young's modulus of R1-PCL presents close to that of ligaments (303 MPa), whereas of R1-PCL/BS is in the range of tendons [16].

Figure 2 shows images of Scanning Electron Microscopy for samples obtained from the two routes.

Figure 2a, c show dense and homogeneous samples, a fact due to its processing, which results in materials with a lower apparent porosity. Since no glass fibers were used, it is believed that the material does not exhibit anisotropy, as can be seen in SEM micrographs. Less porous materials have a larger Young's Modulus since pores are stress concentrators and can behave like material failures. In Fig. 2b, d an apparently more porous material is observed, which results in a material with smaller mechanical properties, as shown in Table 2.

As previously mentioned, R1-PCL/BS composite has values of ultimate tensile strength and Young's modulus close to that of spongy bone, which is interesting since the objective is to obtain a material for bone tissue repair. Such values suggest that if R1-PCl/BS is used for this purpose, it will not cause the effect of stress shielding. Although R2-PCL/BS presents higher apparent porosity, this composite should not be discarded. Its characteristic suggests a more targeted application to scaffolds, since the pores provide conditions for bone cells to proliferate in a bioactive environment due to Biosilicate [13]. However, the high porosity has to be taken into account in a probable development of scaffolds because its mechanical properties are low.

4   Conclusion

In conclusion, for the selection of material for the fabrication of devices intended for bone regeneration applications, the biomaterials' bioactivity is an important consideration as it can affect their effectiveness. Here, we show that the inclusion of 50 wt% of BS into a polymer bulk can improve the composite, allowing obtain devices with a different microstructure as the function of processing route. Despite bioactivity, addition of Biosilicate may compromise its tensile strength compared to a pure PCL. R1-PCL/BS presents mechanical responses close to that of spongy bone, showing promise for an application in bone tissue repair since it will not cause stress shielding. For R2-PCL/BS, an application in making scaffolds is more interesting, since its

high porosity becomes a conducive environment to receive the cells, promoting cellular viability.

References

1. Gibson, R.F.: Principles of Composite Material Mechanics, 4 edn. CRC Press, Florida (2016)
2. Orefice, R.L., et al.: Biomateriais—fundamentos e aplicações, 1 edn. Guanabara Koogan, Belo Horizonte (2006)
3. Dash, T.K., Konkimalla, V.B.: Poly-ε-caprolactone based formulations for drug delivery and tissue engineering: a review. J. Control. Release **158**(1), 15–33 (2012)
4. Crovace, M.C., et al.: Biosilicate®—a multipurpose, highly bioactive glass ceramic. In vitro, in vivo and clinical trials. J. Non-Crystal. Solids **432**(part A), 90–110 (2016)
5. Gabbai-Armelin, P.R., et al.: Injectable composites based on biosilicate® and alginate: handling and in vitro characterization. RSC Adv. **4**(86), 45778–45785 (2014)
6. Kido, H.W., et al.: Porous poly (D, L-lactide-co-glycolide) acid/biosilicate® composite scaffolds for bone tissue engineering. J. Biomed. Mater. Res. B Appl. Biomater. **105**(1), 63–71 (2015)
7. Santos, L.R., et al.: Preliminary in vitro biocompatibility study of chitosan/Biosilicate® composite membranes. In: Workshop de Biomateriais, Engenharia de Tecidos e Orgãos Artificiais 2015, OBI, vol. 1, p. 1. Campina Grande (2015)
8. Abedalwafa, M., et al.: Biodegradable poly-epsilon-caprolactone (PCL) for tissue engineering applications: a review. Rev. Adv. Mater. Sci. **34**, 123–140 (2013)
9. Callister, W.D.: Materials Science and engineering: an introduction. 8 edn. Wiley Inc, Utah (2010)
10. Canevarolo, S.V.: Ciências dos Polímeros, 2nd edn. Artliber, Campinas (2007)
11. Chawla, Krishan Kumar: Composite Materials: Science and Engineering, 2nd edn. Springer, New York (1998)
12. Mohammadkhah, A., et al.: Fabrication and characterization of poly-(ε)-caprolactone and bioative glass composites for tissue engineering applications. Mater. Sci. Eng C **49**, 632–639 (2015)
13. Poh, P.S.P., et al.: In vitro and in vivo bone formation potential of surface calcium phosphate-coated polycaprolactone/bioative glass composite scaffolds. Acta Biomater. **30**, 319–333 (2016)
14. Leblon, C.E., et al.: In vitro comparative biodegradation analysis of salt-leached porous polymer scaffolds. J. Appl. Polym. Sci. **128**(5), 2701–2712 (2013)
15. ASTM-D882-12. Standard test method for tensile properties of thin plastic sheeting. In: Book of Standards: ASTM International, vol. 8, no. 1 (2012)
16. Black, J., Hastings, G.: Handbook of Biomaterial Properties. Chapman & Hall, pp. 135–213. London (1998)
17. Ferreira, F.A, Simbara, M.M.O., Malmonge, S. M.: Estudo in vitro da degradação hidrolítica de polímeros utilizados em engenharia tecidual. In: 8o Congresso Latino Americano de Órgãos Artificiais, Biomateriais e Engenharia Tecidual, 2014, COLAOB. Rosário (2014)
18. Jo, J., et al.: In vitro/in vivo biocompatibility and mechanical properties of bioactive glass nanofiber and poly(ε-caprolactone) composite materials. J. Biomed. Mater. Res. Part B Appl. Biomater. **91**, 231–220 (2009)
19. Liu, J., et al.: Microstructure and properties of polycaprolactone/calcium sulfate particle and whisker composites. Polym. Compos. **33**(4), 501–508 (2012)

Synthesis of Magnetic Nanoparticles and Separation of Impurities

Monalisa Conceição Silva, Elisa Rennó Carneiro Déster, and Francisco Eduardo de Carvalho Costa

Abstract

Nanotechnology is a multidisciplinary field that allows the study of phenomena and properties at nanoscale (10^{-9}). The magnetic nanoparticles (MNPs) have raised interest in biotechnology in recent years. The application of MNPs in the biomedical field is of great importance to cancer treatment, MRI, and other technologies. This paper discusses the production of magnetic nanoparticles and their co-precipitation characteristics in aqueous medium and the study of the yield obtained during the process of obtaining in their pure form. The construction of a magnetic separator is also presented in order to automate the purification of the MNPs. It was observed that the synthesis process is relatively easy to perform, although the removal of residual salts is presented as one of the main obstacles in the process.

Keywords

Nanotechnology • Nanomagnetism • Synthesis

1 Introduction

Nanotechnology is the science that studies particle manipulation at nanoscale (10^{-9}), which is a region that materials present unique features. Feynman (1959) demonstrated the possibility of manufacturing devices by manipulating individual atoms [1]. Since then, this science has gained its place in several fields [2].

M. C. Silva (✉) · E. R. C. Déster · F. E. de Carvalho Costa
Instituto Nacional de Telecomunicações INATEL, João de Camargo 510, Centro, Santa Rita do Sapucaí CEP, Minas Gerais 37540-000, Brazil
e-mail: monalisas@get.inatel.br

E. R. C. Déster
e-mail: elisa.renno@inatel.br

F. E. de Carvalho Costa
e-mail: costafec@inatel.br

In bioengineering, also known as nanobiotechnology and nanomedicine, nanotechnology is prominent in the development of techniques for cancer diagnosis and treatment, for example: magnetic resonance, vectorization of drugs and magnetic hyperthermia. Applications of magnetic nanoparticles (MNPs) in biomedical systems can be used in both in vitro and in vivo diagnostic or therapy [2, 3]. The MNPs allows the possibility of finding cancer cells in their early stages more efficiently [4].

The nanoparticles may show nanomagnetism, which is characterized as the study of MNP's magnetic field. The MNPs have superparamagnetic properties and fluid form. These fluids move along with the particles and move around inside human body [5]. When entering the region heat, MNPs thermal agitation affects atoms, disturbing the alignment of the dipoles, which causes rise in the temperature, and thus, increasing magnetization. One can make use of this temperature change in magnetic hyperthermia therapeutic procedures. The easiness of using the MNPs is easily located in specific target by external magnets, which can also be guided within the body [6, 7].

Thus, further studies play an important role in the development of this technique, making it possible to ease the diseases and other discovery treatments. In this context, this work presents the study of magnetic nanoparticle production and their applications in healthcare as a central focus on the effectiveness of MNPs synthesis using two different process washings, in order to compare their magnetic properties. In addition, it presents the development of a prototype in order to automate the particle washing process.

2 Methodology

The preparation of MNPs is briefly resumed in the coprecipitation method in an aqueous medium, highlighting magnetite (Fe_3O_4) and maghemite ($g\text{-}Fe_2O_3$) and mixed oxides, especially the cubic ferrites (MFe_2O_4) in which M is a divalent metal such as Co Ni, Mn, Cu, Zn and Cd. The

technique consists in the co-precipitation of metal ions in aqueous solutions from the alkaline hydrolysis reactions, and then Condensation Polymerization [8–10]. The hydroxide solution was added to the metal ion one under stirring at a bath temperature at 70 °C.

The coprecipitation reaction in aqueous medium of magnetite was performed according to [3] the following equation:

$$
\begin{aligned}
Fe^{2+}(FeSo_4) + 2Fe^{3+}(FeCl_3) + 8OH^-(NaOH) \\
\rightarrow Fe_3O_4 + 4H_2O
\end{aligned}
\tag{1}
$$
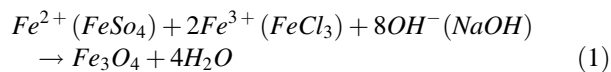
According to the reaction of metal ions in the solution, sodium hydroxide is added at boiling point temperature with constant agitation.

In this study, four substances were prepared by changing the base type. Two substances were synthesized with NaOH and others two with KOH. The whole process is summarized in Fig. 1.

It was added 20 ml FeCl$_3$ and 20 ml FeSO$_4$ and weak bases. To prepare all the mixtures, a beaker was used in a water bath at a temperature of 65–70 °C with vigorous stirring during 5 and 10 min, by using a glass rod (see Fig. 2) [10–12].

After the color changes (turning to black color) (see Fig. 2), the pH of the solutions was measured. The values found varied from 9 to 10. After this, the solutions were transferred to china capsules. Then, the solutions were left in a laboratory stove at 70 °C until they were absolute dry (see Fig. 3).

All MNPs were washed by rinsing with 100 ml of distilled water to remove counter ions (salts). Substances synthesized with KOH were washed four times, since the basic one containing NaOH were washed twice. After the washings, a precipitate of black and brown magnetite nano particles was obtained (see Fig. 4) [2, 10].

After removal of the salts, the four substances were subjected to two more types of washes (distilled water and methanol). In the first, NaOH and KOH were each one washed with 20 ml of distilled water on the magnetic stirrer without heating at 1800 rotation per minute (rpm) at maximum intensity during 2–5 min (see Fig. 5).

The second washing for each type of base was carried out in a magnetic stirrer containing 20 ml on a methanol without heating, at 1800 (rpm), also at maximum intensity during 2 and 5 min (see Fig. 6).

To evaluate the magnetic field after the washing, the MNPs were left to dry in contact with a magnet. The substances washed in distilled water were processed in a laboratory stove at a temperature of 70 °C. For those that were washed with methanol, the drying was performed in a water bath at a temperature of 90 °C [13].

At the end of each step of the synthesis, the weighing of substances was carried out in order to calculate the yield. The yield was calculated from the stoichiometry of Fe$_2$$^+$ and Fe$_3$$^+$ obtained from Eq. 1 with regard to magnetite.
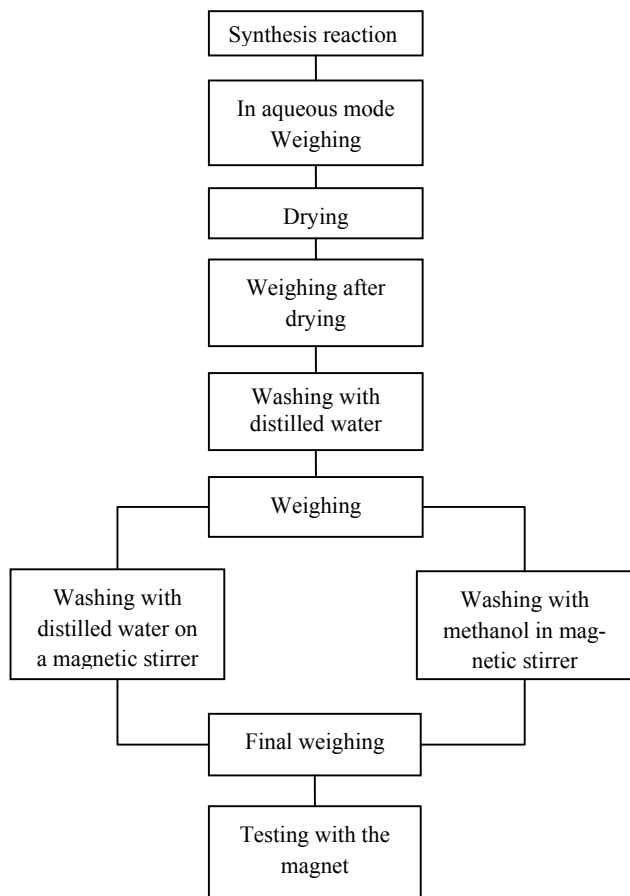
Fig. 1 Representation of the methodology applied for this study
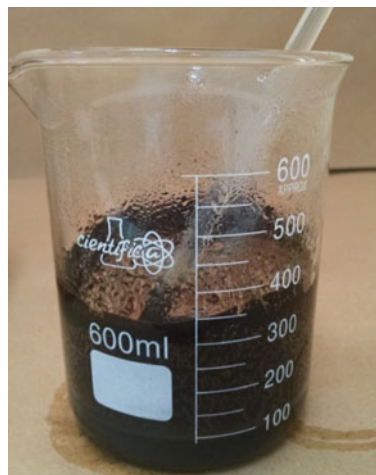
Fig. 2 Example of results after the co-precipitation reaction to obtain the MNPs in a water bath
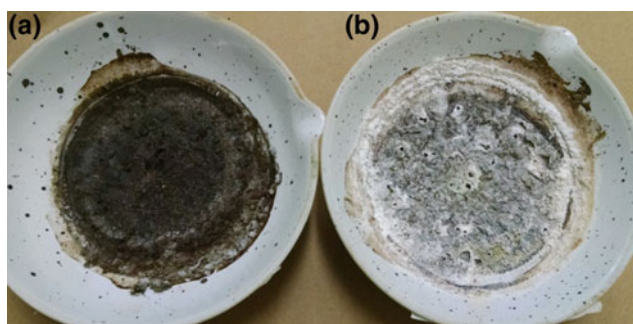
Fig. 3 Visual appearance of MNPs obtained after the first drying, the MNPs being synthesized with NaOH (**a**) and KOH (**b**). Note the presence of salts in both solutions
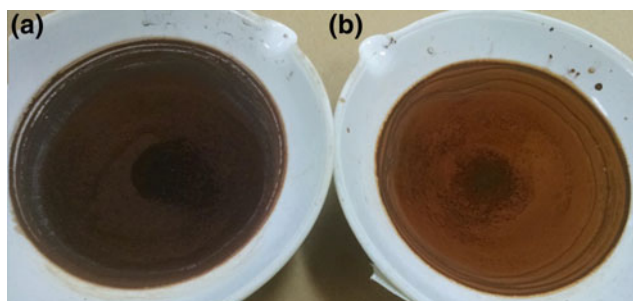
Fig. 4 Appearance of MNPs after washing with distilled water (100 ml each washing). **a** obtained MNPs washed twice with NaOH; **b** obtained by reacting MNPs washed four times with KOH
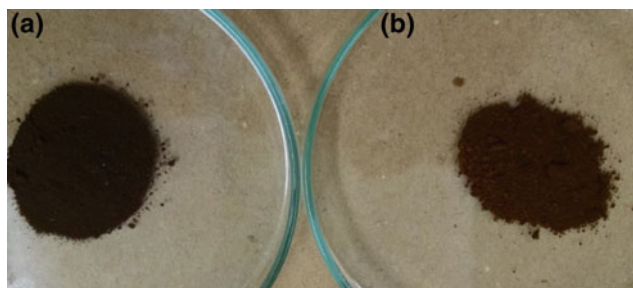
Fig. 5 Appearance of MNPs after washing with 20 ml of distilled water by using a magnetic stirrer. **a** Synthesized with NaOH and **b** synthesized with KOH
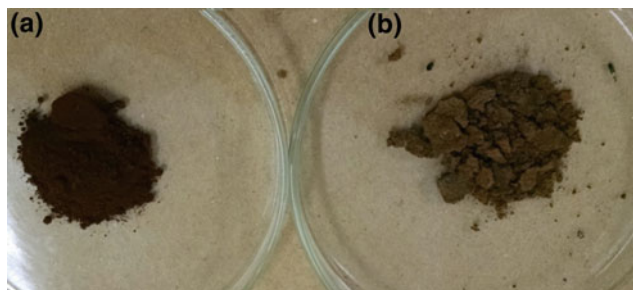
Fig. 6 Aspect of MNPs after washing with 20 ml methanol by using a magnetic stirrer. **a** synthesized with NaOH and **b** synthesized with KOH. Note that MNPs have small clusters visible to the naked eye

3 Results

The metal ions Fe_3^+ and Fe_2^+ were introduced into an alkaline solution to the synthesis of magnetite (Fe_3O_4) and the reaction was proceeded according to the equation:

$$Fe^{2+} + 2Fe^{3+} + 8OH^- \rightarrow Fe(OH)_2 + 2Fe(OH)_3 \\ \rightarrow Fe_3O_4 \downarrow + 4H_2O \quad (2)$$
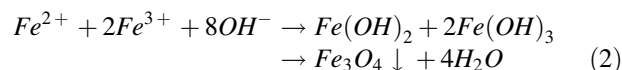
There was a clear presence of salts along with MNPs (Fig. 4). The washing with water and methanol affects the color of the product from the MNP synthesis reaction (see Figs. 5 and 6). They can be noticed through Figs. 7 and 8, the difference between the magnetic behavior of MNPs is the synthesis which use different bases and washings. The MNPs obtained with NaOH presented a stronger magnetic field due to washing by using methanol (see Fig. 8).

The MNPs that were obtained showed high adhesion to the magnet used in mechanical agitation, even preventing the magnetic stirrer from working.

The mass of MNPs in aqueous medium after preparation in a water bath were: 67.57 g/l for NaOH and synthesized with 84.97 g/L to those obtained with KOH (Figs. 9, 10 and 11, Table 1).

The solution designed for efficiency in MNPs washes was the development of a magnetic separator. The separator consists of an electromagnet surrounded by 2000 coils covered with silicone. The electromagnet is powered with a 2 A electric current, which produces a magnetic field that attracts the MNPs. This alternative solution was created to automate the particle washing process.

There are three steps within the separation process. In the first step, the nanoparticles are dissolved in distilled water in a beaker at room temperature. The electromagnet is connected and immersed into the beaker. The magnetic field attracts the particles and salts dissolved in water. To ensure that all the salt was removed, the process is performed again in another beaker containing distilled water, thereby
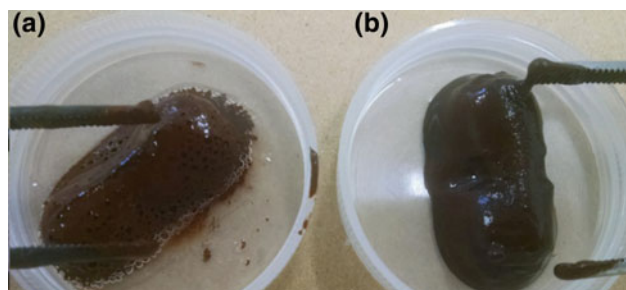
Fig. 7 Test with the magnet after washing the MNPs obtained with KOH. **a** Washing with distilled water and **b** washing with methanol
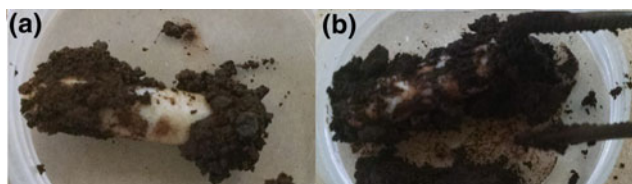
Fig. 8 Test with the magnet after washing MNPs synthesized with KOH. **a** Washing with distilled water and **b** washing with methanol

Fig. 9 Electromagnet prototype covered with silicone
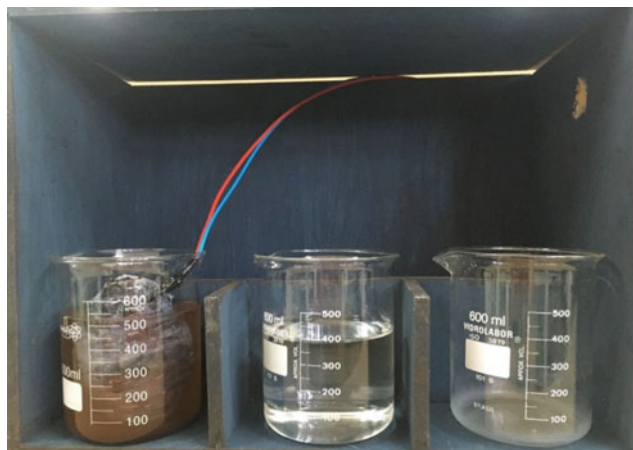
Fig. 10 MNP prototype. Each beaker is a stage in the separation process

Fig. 11 First stage of the process

conducting the second step. Finally, the third step consists of measuring MNPs' magnetic field. The measurement is performed with a Hall sensor programmed by using Arduino microcontroller ATMEGA.

The conductivity of MNPs when put into distilled water was measured before and after the separation. Prior to it, the conductivity was higher compared to the one after the process, which indicates that the salt concentration decreased.

The synthesis of Fe_3O_4 requires that the molar ratio Fe_3^+: Fe_2^+ is equal to two. However, it has proven difficult to achieve and maintain this molar ratio in the oxidizing atmosphere.

The change in color of the substances after washing with methanol indicates a likely change in the MNP oxidation stage (see Figs. 5 and 6).

The washings with distilled water on a magnetic stirrer were not as effective in comparison with methanol when it comes to weight loss. The difference in these values may be due to the presence of residual salts identified by the measured pH values, from 11 to 12. It is possible to visualize the salts also through Fig. 3. Importantly, the purity of the base used has to be considered, since the KOH one is 99.87%, calculated according to their characteristics, compared to the NaOH one, which is 98.27%.

Table 1 Final weighing values after drying with calculated efficiency for different bases and washes

Substance types	Washing type	Final weight (g/mol)	Weight Yield (%)
NaOH	Distilled water	3.54	76.46
	Methanol	4.50	78.40
KOH	Distilled water	3.63	97.20
	Methanol	4.10	88.55

Therefore, the presence of salt in the synthesized magnetic nanoparticles has become a problem to be solved before starting any experiment in vivo. Notice that there were losses of nanoparticles due to the washings.

According to the literature [2, 12, 13] production NPMs, showed good performance in a black color to brown color to KOH and NaOH. With methanol, the washings showed better performance for withdrawing counter ion providing better performance thereof.

This reduction must be analyzed in electron microscopy level on diffraction of X-rays to verify if there was an increase of purity or actual losses in the process.

Transmission electron microscopy and/or scanning electron microscopy associated with X-ray diffraction will be used in a future research, in order to identify the MNPs [2, 10, 13, 14].

4 Conclusions

The structure of MNP is currently known for the diagnosis and treatment of tumors. Its production is simple, taking roughly 30 min for the co-precipitation and 2 h and 30 min to dry. However, MNP's pure form, which is free from salts, is a major obstacle to be overcome without having significant loss on its properties.

According to the different washes presented without the utilization of the constructed prototype, it's possible to conclude that methanol washing presented better performance for both substances produced, besides improving the magnetic field of the particles (see Fig. 7).

The use of the prototype improved the yield in the washes, but not enough to match the yield obtained by washing with methanol.

References

1. Francisquine, E., Schoenmaker, J., Souza, J. A.: Nanopartículas magnéticas e suas aplicações. Química Supramolecular e Nanotecnologia, p. 269 (2014)
2. Duran, N., Mattoso, L.H.C., Morais, P.C.: Nanotechnology: introduction, preparation and characterization of nanomaterials and application examples, pp. 87–92. Editora Artliber, Sao Paulo (2006)
3. Batlle, X., Labarta, A.: Finite-size effects in fine particles: magnetic and transport properties. J. Phys. Condens. Matter **35**, R15–R42 (2002)
4. Goya, G.F., Grazu, V.: Ibarra, MR magnetic nanoparticles for cancer therapy. Current Nanosci. **4**, 1–16 (2008)
5. RIBEIRO, Thatiana Gonçalves Diegues: Synthesis and characterization of magnetic nanoparticles oxides mixed $MnFe_2O_4$ coated with chitosan. the influence of doping with Gd 3+ studies on the structural and magnetic properties. Doctoral Thesis. University of Sao Paulo (2008)
6. Tartaj, P., et al.: The preparation of magnetic nanoparticles for applications in biomedicine. J. Phys. D Appl. Phys. **36**, R182–R197 (2003)
7. Singh, A., et al.: Long circulating lectin conjugated paclitaxel loaded magnetic nanoparticles: a new theranostic avenue for leukemia therapy. PLoS One **6**(11) (2011)
8. Werner, M.E., et al.: Chemotherapy of human tumors: novel approaches from nanomedicine. Current Pham. Des. 2012 (in press)
9. Souza, N.S.: Synthesis and characterization of iron oxide nanoparticles and magnetic fluid graphite (GMF), pp. 42–43. UFSCAR, Sao Paulo (2009)
10. Sun, J., et al.: Synthesis and characterization of biocompatible Fe_3O_4 nanoparticles. J. Biomed. Mater. Res. Part A **80**, 333–341 (2007)
11. Laurent, S., et al.: Magnetic iron oxide nanoparticles: synthesis, stabilization, vectorization, physicochemical characterizations, and biological applications. Chem. Rev. **108**, 2064–2110 (2008)
12. Kawai, N., et al.: Complete regression of experimental prostate cancer in nude mice by repeated hyperthermia using magnetite cationic liposomes and the newly developed solenoid containing ferrite core. Prostate **66**(7), 718–727 (2006)
13. Cherukuri, P., et al.: Targeted hyperthermia using nanoparticles metal. Adv. Drug Deliv. Rev. **62**(3), 339–345 (2010)
14. Hou, C., et al.: The in vivo performance of biomagnetic hydroxyapatite nanoparticles in hyperthermia cancer therapy. Biomaterials **30**(23), 3956–3960 (2009)

Tribological Evaluation of an Optical Fiber Laser Marked Stainless Steel for Biomedical Applications

Eurico Felix Pieretti, Renato Altobelli Antunes, and Maurício David Martins das Neves

Abstract

The effect of laser marking process on the tribological behaviour of ISO 5832-1 austenitic stainless steel (SS) on the friction coefficient and wear volume using ball-cratering wear tests was evaluated in this work. The laser marking process was carried out with a nanosecond optical fiber ytterbium laser at four different pulse frequencies. For comparison reasons, surfaces without laser treatments were also evaluated. A phosphate buffer solution (PBS) was used as lubricant. The wear tests were carried out during 10 min with PBS drip, solid spheres of AISI 316L SS with 1 in. in diameter and of 52–100 chrome steel, with 2 mm in diameter, were used as counter-bodies. The results indicated that the tribological behaviour is influenced by the laser marking process parameters used, and the wear rate is dependent of the normal force and the type of sphere.

Keywords

Orthopaedic implants • Laser • Wear

1 Introduction

Biomaterials, due to corrosion and even friction against implantable components, bones or other body parts can detach particles, which coming into contact with bodily fluids, are able to be placed in locations far from the removed source causing complications to the patients [1].

Detached particles released from the degradation process may move inertly, through tissue and/or circulatory system or can be actively transported [2, 3], compromising the biocompatibility.

The ISO 5832-1 stainless steel (SS) is one of the metallic materials used for implants manufacture, because of its mechanical and electrochemical properties and low cost [4, 5]. The laser technique is commonly used for identification of the metallic implantable medical device [4–7]. This process involved temperatures above 1600 °C, which melts the stainless steel surfaces.

In the biomaterials' field for implantable medical or dental devices, tribological tests are of great value in providing an estimate of the normal, tangential and frictional forces in relation to the volume of material that can be detached from the surface, migration and housing of particles.

The micro-scale abrasion test (or ball-cratering wear test) is a useful method to investigate the wear resistance of various materials [8–10].

The ball-cratering wear test has gained large acceptance at universities and research centers and is widely used in studies focusing on the abrasive wear behavior of dissimilar materials [11–15].

The principle of this wear test consists in a rotating ball that is forced against the specimen being tested and a lubricant, PBS in this case, is supplied between the ball and the specimen during the experiments. The aim of the ball-cratering wear test is to generate "wear craters" on the specimen. The wear volume (V) may be determined as a function of b, using Eq. 1 [11], where R is the radius of the ball.

$$V \approx \frac{\pi d^4}{64R} \qquad (1)$$

Wear tests conducted under the ball-cratering technique present advantages in relation to other types of tests, because it can be performed with normal forces (N) and rotations of

E. F. Pieretti (✉) · M. D. M. das Neves
Nuclear and Energy Research Institute (IPEN-CNEN),
Av. Prof. Lineu Prestes 2242, São Paulo, 05508-000, Brazil
e-mail: efpieretti@usp.br

E. F. Pieretti · R. A. Antunes
Federal University of ABC (UFABC), Av. dos Estados, 5001,
Santo André, 09210-580, Brazil

the sphere (n) relatively low ($N < 0.5$ N and $n < 80$ rpm) [16–20].

The aim of this work was to evaluate the tribological behaviour of the ISO 5832-1 austenitic stainless steel (SS), widely used for biomedical applications, marked via an optical fiber laser process with four different pulse frequencies, using two ball-cratering wear methods.

2 Experimental Procedure

2.1 Ball-Cratering Equipment

A tribometer with free-ball configuration was used for the sliding wear tests. Two load cells were used in the ball-cratering equipment: one load cell to control the normal force (N) and one load cell to measure the tangential force (T) developed during the experiments. "Normal" and "tangential" forces load cells have a maximum capacity of 50 N and an accuracy of 0.001 N. The values of "N" and "T" are read by a readout system.

A nanotribometer, Anton Paar - model NTR^2, was also used mainly to observe friction coefficient evolution. These tests were performed in the air, at 25 °C, with a counter-body of chrome steel 52–100 rotating ball shape, 2 mm in diameter, during 10 min, with normal force of the order of 100 mN, distance equivalent to 2.4 m, and scan speed of 4.0 cm s^{-1}. Surface analyses were conducted using an optical microscope (Olympus, TM).

2.2 Materials

The tested samples were produced by bars of the ISO 5832-1 austenitic stainless steel (SS) biomaterial (chemical composition (wt%): 0.023 C, 0.78 Si, 2.09 Mn, 0.026 P, 0.0003 S, 18.32 Cr, 2.59 Mo, 14.33 Ni and Fe balance) treated with a nanosecond ytterbium optical fiber laser at four different pulse frequencies, as Table 1 shows. Each sample consisted of 5 (SS) specimens.

Spheres made of AISI 316L stainless steel, with diameter of $D = 25.4$ mm were adopted as counter-bodies.

2.3 Micrhardness (HV)

The Vickers microhardness analyses were performed in a Fischerscope HM 2000 microhardness instrument, coupled with an optical microscope. The hardness values refer to the average of 5 measurements at a distance of 50 μm between each indentation for surfaces treated by this laser beam and also for the non treated biomaterial.

Table 2 shows the hardness (H) of the materials used in this work (specimen and balls).

2.4 Wear Tests

As a function of the density (ρ) of the spheres material (AISI 316L SS: $\rho = 8$ g/cm^3) was defined the value of the normal (N) for the wear experiments: $N = 0.25$ N.

The ball rotational speed was $n = 50$ rpm and with the diameter $D = 25.4$ mm of the ball, the tangential sliding velocity of the ball is equal to $v = 0.066$ m/s.

An amount of 25 wear tests (5 per condition) were conducted under $t = 2$ min and with the value of $v = 0.066$ m/s was calculated a value of sliding distance (S) between the specimen and the ball of $S = 8$ m.

All experiments were conducted without interruption and a phosphate buffered saline solution was continuously agitated and fed between the ball and the specimen during the experiments, under a frequency of 1 drop/2 s.

Both the normal force (N) and the tangential force (T) were monitored and registered constantly. Then, the coefficient of friction was determined using the Eq. 2:

$$\mu \approx \frac{T}{N} \qquad (2)$$

3 Results and Discussion

3.1 Analysis of the Volume of Wear—V

Initially are presented images of the specimen submitted to wear tests (Figs. 1 and 2). Surfaces treated by laser technique were analyzed by optical microscopy. For comparison reasons surfaces of this biomaterial without laser was also evaluated. These are relevant results to the biomaterial's field, because when manufacturing an implant one has to choose a suitable area to identification number engravings to avoid wear.

In Fig. 1, the number eight (8) was marked by laser on the ISO 5832-1 stainless steel (SS) surface. At the center of the marked number is shown the wear crater. In Fig. 2 is shown an enlargement of the wear crater presented

Table 1 Frequencies used for laser marking treatment	Sample	1	2	3	4
	Laser frequency (kHz)	80	188	296	350

Table 2 Hardness of the biomaterials used in this work

	Material	Hardness	
Sample	ISO 5832-1 SS	88	HRB
Spheres	AISI 316L SS	25–39	HRC
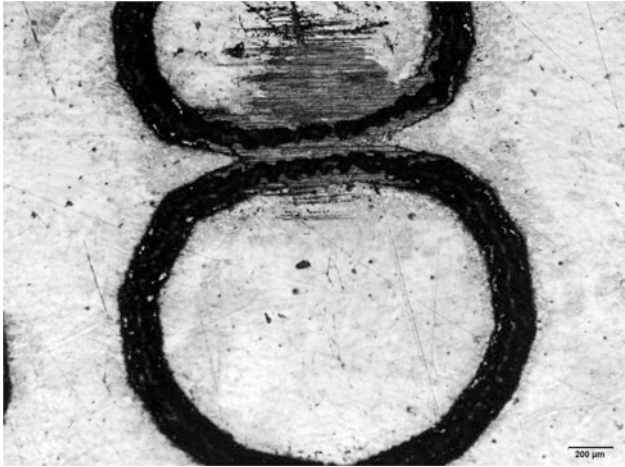
Fig. 1 Wear crater obtained at the center of the laser mark (50x)
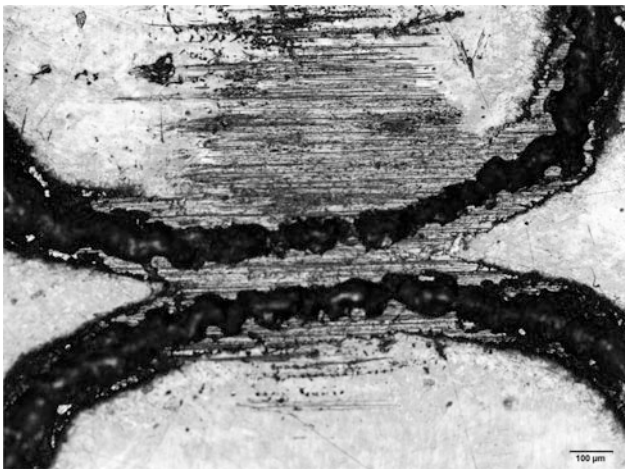
Fig. 2 Wear crater obtained at the center of the laser mark (100x)

previously. This image best exemplifies the surface modification caused by the laser pulses, which melts the surfaces increasing its roughness.

Figure 3 presents the wear volume (*V*) behavior for the conditions marked with laser and blank. It is possible to
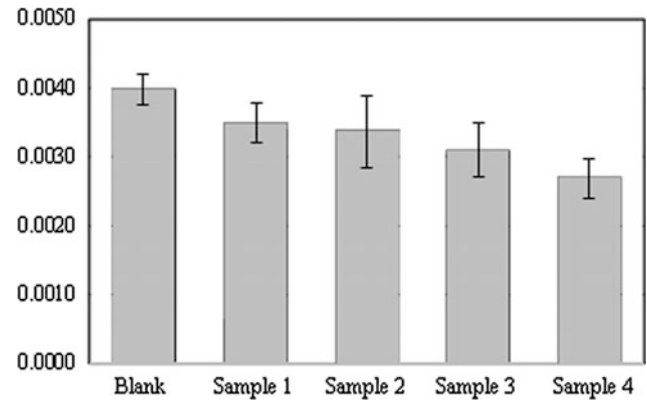
Fig. 3 Wear volume (V) (mm^3) as a function of the surfaces treated by laser

observe that the wear volume decreased when the specimen was treated with laser. This decreasing is associated to a possible increasing of the hardness of the specimen. Table 3 shows the micro hardness measured for every type of sample studied. Each sample was composed of 5 units of laser treated specimens, as well as blank specimens, i.e., without laser beam treatment.

3.2 Analysis of the Coefficient of Friction—μ

Figure 4 shows the behavior of the coefficient of friction (μ) for the conditions which the laser treated and non treated (blank) samples.

The highest values of wear volume were reported for samples without marks. No direct relationship between wear volume and friction coefficient was observed, i.e., the highest value of wear volume was not related to the higher value of coefficient of friction [8, 21–23].

The laser beam affected area is reduced (only the marked algarism). Another important factor is the positioning of the counter body (sphere) over the sample. For the laser marking condition, the obtained coefficient of friction values are closer to those of the sample without laser beam treatment.

Table 3 Micro hardness values for each type of surface finish

Sample	Blank	1	2	3	4
Micro-hardness (HV)	199.3	204.3	215.4	226.1	239.9

Fig. 4 Coefficient of friction as a function of the surfaces treated by laser

4 Conclusions

The tribological behavior was influenced by the type of the laser process used for this biomaterial, and the wear rate was dependent of the normal force. The coefficient of friction shown an increase tendency for all tested conditions. The surface characterization shown modifications due to the high temperatures reached in the laser marking process, which involves the surfaces melting. The results indicated that the wear volume was reduced by the ytterbium optical fiber laser treatment.

Fig. 5 Variation of the friction coefficient as a function of the test time for the laser marked and blank samples

The coefficient of friction values were not constant throughout the tribological test period, as can be imagined. This effect was evaluated and the results of the coefficient of friction variation as a function of the test time are presented in Fig. 5, for the laser marked samples and the blank.

For surfaces with laser marks (Fig. 5), the friction coefficient values are closer to those obtained in the samples without laser treatment.

The friction coefficient values for the untreated samples has shown a rapid increase in the first test periods, and practically stabilize around values close to $\mu = 0.5$, due to the surface being less rough. For all the laser marked samples, there was an increase in the coefficient of friction as a function of the test time; being the highest values obtained for sample 4. Researches have reported magnitudes of these values with the same kind of test under different tribological system [12]. The decrease on the wear volume as a function of the laser pulse frequency rise must be directly associated to the microhardness increase. Hence, for this purpose, the sample treated at the condition 4 presents a better behavior, so that the marked identifications can resist for more time.

References

1. Okasaki, Y.: Effect of friction on anodic polarization properties of metallic biomaterials. Biomaterials **23**, 2071–2077 (2002)
2. Black, J.: Systemic effects of biomaterials. Biomaterials **5**, 11–18 (1984)
3. Anderson, J.M.: Biological response to materials. Mater. Res. **31**, 81–110 (2001)
4. Pieretti, E.F., Costa, I.: Surface characterisation of ASTM F139 stainless steel marked by laser and mechanical techniques. Electrochim. Acta **114**, 838–843 (2013)
5. Pieretti, E.F., Manhabosco, S.M., Dick, L.F.P., Hinder, S., Costa, I.: Localized corrosion evaluation of the ASTM F139 stainless steel marked by laser using scanning vibrating electrode technique, X-ray photoelectron spectroscopy and Mott-Schottky techniques. Electrochim. Acta **124**, 150–155 (2014)
6. Pieretti, E.F., Palatnic, R.P., Leivas, T.P., Costa, I., Neves, M.D.M.: Evaluation of laser marked ASTM F 139 stainless steel in phosphate buffer solution with albumin. Int. J. Electrochem. Sci. **9**, 2435–2444 (2014)
7. Pieretti, E.F., Costa, I., Marques, R.A., Leivas, T.P., Neves, M.D.M.: Electrochemical study of a laser marked biomaterial in albumin solution. Int. J. Electrochem. Sci. **9**, 3828–3836 (2014)
8. Adachi, K., Hutchings, I.M.: Wear-mode mapping for the micro-scale abrasion test. Wear **255**, 23–29 (2003)
9. Stachowiak, G.B., Stachowiak, G.W., Celliers, O.: Ball-cratering abrasion tests of high-Cr white cast irons. Tribol. Int. **38**, 1076–1087 (2005)
10. Stachowiak, G.B., Stachowiak, G.W., Brandt, J.M.: Ball-cratering abrasion tests with large abrasive particles. Tribol. Int. **39**, 1–11 (2006)
11. Rutherford, K.L., Hutchings, I.M.: Theory and application of a micro-scale abrasive wear test. J. Test. Eval. JTEVA **25**(2), 250–260 (1997)
12. Cozza, R.C., Tanaka, D.K., Souza, R.M.: Friction coefficient and abrasive wear modes in ball-cratering tests conducted at constant normal force and constant pressure—preliminary results. Wear **267**, 61–70 (2009)
13. Cozza, R.C., de Mello, J.D.B., Tanaka, D.K., Souza, R.M.: Relationship between test severity and wear mode transition in micro-abrasive wear tests. Wear **263**, 111–116 (2007)
14. Cozza, R.C.: Influence of the normal force, abrasive slurry concentration and abrasive wear modes on the coefficient of friction in ball-cratering wear tests. Tribol. Int. **70**, 52–62 (2014)
15. Trezona, R.I., Allsopp, D.N., Hutchings, I.M.: Transitions between two-body and three-body abrasive wear: influence of test conditions in the microscale abrasive wear test. Wear **225**, 205–214 (1999)

16. Cozza, R.C., Tanaka, D.K., Souza, R.M.: Friction coefficient and wear mode transition in micro-scale abrasion tests. Tribol. Int. **44**, 1878–1889 (2011)
17. Cozza, R.C.: A study on friction coefficient and wear coefficient of coated systems submitted to micro-scale abrasion tests. Surf. Coat. Technol. **215**, 224–233 (2013)
18. Bose, K., Wood, R.J.K.: Optimum tests conditions for attaining uniform rolling abrasion in ball cratering tests on hard coatings. Wear **258**, 322–332 (2005)
19. Axén, N., Jacobson, S., Hogmark, S.: Influence of hardness of the counterbody in three-body abrasive wear—an overlooked hardness effect. Tribol. Int. **27**(4), 233–241 (1994)
20. Gee, M.G., Wicks, M.J.: Ball crater testing for the measurement of the unlubricated sliding wear of wear-resistant coatings. Surf. Coat. Technol. **133–134**, 376–382 (2000)
21. Adachi, K., Hutchings, I.M.: Sensitivity of wear rates in the micro-scale abrasion test to test conditions and material hardness. Wear **258**, 318–321 (2005)
22. Allsopp, D.N., Hutchings, I.M.: Micro-scale abrasion and scratch response of PVD coatings at elevated temperatures. Wear **251**, 1308–1314 (2001)
23. Cozza, R.C.: Effect of the pressure on the abrasive wear modes transitions in micro-abrasive wear tests of WC-Co P20. Tribol. Int. **57**, 266–271 (2013)

A Biomechanics and Gait Analysis Monitored by Accelerometry Inside and Outside the Water

C. C. B. Souza, E. L. Cavalcante, A. V. M. Inocencio, N. A. Cunha,
R. J. R. S. Lucena, M. G. Coriolano, and M. A. B. Rodrigues

Abstract

Human gait is a process of locomotion of the erect body, with at least one foot in contact to the ground, as the locomotion happens. Accelerometry can be used to measure physical activity, or its impact on human body structures, such as gait. The use of accelerometers to analyze human gait has been expanded. We have developed a system composed of four inertial accelerometers. The communication is made by wireless, through Bluetooth protocol. We have placed the accelerometers on the inner calf side and on the medial malleoli. The objective of this work is to analyze and compare walking in and out of the water using accelerometry. For waterproofing the system, we have used liquid glass. We have performed the test in a volunteer undergoing an 8-m walk, in and out of the water. We have acquired accelerometry data in the three dimensions. After data analysis, we could calculate speed, distance traveled and pitch height. The equipment proved to be effective in acquiring and exporting the data. Matlab has calculated other variables.

Keywords

Accelerometry • Gait • Aquatic physiotherapy

1 Introduction

The human gait is a series of coordinated movements that need the interaction of muscular strengths, joint movements and neural motor commands [1]. Walking is a process of erect body locomotion when there is at least a foot in contact to the ground. The gait cycle is divided into two steps: stance and swing. Stance is the period when the foot is in contact with the ground. It corresponds to approximately 60% of the gait cycle. Swing is the period when the foot is removed from the ground. It corresponds to approximately 40% of the gait cycle [2] Gait is considered normal if the observed movement of the body is forward, in an efficient way. Any deflection can produce an abnormal gait pattern. Gait is either considered the most complex human functional activity [3].

The spatiotemporal parameters are frequently used to evaluate gait development and to identify possible disorders. The speed of the gear, the length of the cycle, or of the pass, the length of the step and the cadence are some of the analyzed parameters. The gait cycle is equivalent to one pace. It is formed by one step of one foot, followed by another step of the other foot. Therefore, the length of the gait is the distance between two successive supports of the heel of the same foot. The step is the movement of one foot in front of the other. The length of the step is the distance between feet when both are in contact with the ground. The gait cadence is the number of steps per unit time and the gait speed is the distance traveled by the body per unit time [4].

Accelerometry is a method of kinematic analysis of human motion. Accelerometers can be used to analyze the cycle of movement and possible gait changes. They present as advantages low cost and high resolution [5, 6]. Most of the movements of the human body occur on more than one axis of motion. This way, tri-axial accelerometers are better, since they allow to measure the displacement and acceleration in each of the three orthogonal axes [7].

Aquatic rehabilitation has been used as an additional tool for the treatment of musculoskeletal disorders, due to the physical properties of water, besides physiological and therapeutic effects [8]. The benefits of the activity in the aquatic environment are justified by the physical influences of the water in the immersed body. They generate physiological changes and improvements in the physical condition of the muscle, in the increase of strength, in the resistance in case of muscular weakness and in the facilitation of the gait

C. C. B. Souza (✉) · E. L. Cavalcante · A. V. M. Inocencio ·
N. A. Cunha · R. J. R. S. Lucena · M. G. Coriolano ·
M. A. B. Rodrigues
Federal University of Pernambuco, Recife, Brazil
e-mail: carolinecbsouza@gmail.com

(when allows the gate evolution in certain patients) [9]. The activity in the aquatic environment has increased, both for the practice of physical activity and for rehabilitation. However, there is little information on the biomechanical characteristics of the changes that this environment provides during the specific movement of the gait.

Taking into account that physical therapy evaluation should be based on measurable data, not only on subjective observations, and that there are few studies relating the behavior of walking parameters in the aquatic environment, the present study aimed to analyze the walking of a healthy individual within and outside the water, in order to verify the possible differences between the means, according to the changes of the spatiotemporal parameters. The parameters evaluated are time to perform the test, cadence, length, velocity and pitch height.

2 Materials and Methods

This research was divided into two parts: development and adaption of a device with inertial sensors (accelerometry) in the Human-Machine Interface Laboratory at Federal University of Pernambuco. After this step, this instrument was applied to the main author for tests on the floor and in a specific pool for physiotherapy rehabilitation.

The developed equipment is composed of four inertial sensors to acquire accelerometry integrated into a micro-controller, that makes the communication with a personal computer by the Bluetooth Protocol. The FRDM-KL25Z development board was used for the construction of the equipment prototype. This NXP Technologies development board is a low-cost board that uses the microcontroller (MCU) KL25Z128 with ARM Cortex M0+ core with 128 KB of flash memory and 16 KB of SRAM memory and can operate at 48 MHz. Among the main characteristics of this development board, it is possible to mention the low power consumption, allowing the use of batteries for long periods, and the serial communication interface I2C and SPI in several pins, making possible the integration of the four modules of inertial sensors and of the data transmission module [9].

The wireless data transmission to the computer was done using a Bluetooth 2.0 module. This protocol works with low power consumption and maximum range of 50 m, depending on the power used. Bluetooth devices work in the ISM (Industrial, Scientific, Medical) frequency range, offering relatively high transmission rates (3 Mb/s for 2.0 Bluetooth) and working in pairs with the devices, ensuring the security in the data transmission.

The inertial sensor module chosen to the equipment was the module MPU6050. This module contains an accelerometer integrated with a gyroscope, both tri-axial and based in MEMS (Microelectromechanical Systems), with 6 degrees of freedom (6DOF) in all. The integrated A/D (Analog to Digital) converter has 16-bits and captures the signals for the X, Y and Z axis simultaneously. It a low power consumption module and offers the I2C communication protocol, reducing the number of connected wires to the equipment and making the job easier at the moment of acquisition [9].

Figure 1 shows the block diagram of the system, in which 4 accelerometers were connected to the microcontroller KL25Z128 using I2C communication. From the data, the microcontroller sends the information packet via Bluetooth to a baud rate of 115,200, which leads to 1200 points per second for each axis. In the final stage, the Bluetooth-paired computer receives the data, storing them and plotting in real time a subsampling of 100 packets per second.

For tests with the developed device, we have projected a specific box to the embedded system. This box has outputs to wires of the four channels. The other box, that has the embedded system in which Bluetooth is part of it, stays outside water, inside an exclusive waterproof bag (made with waterproof cloth). This bag has support handles for arms, in a way it stays in back, close to the cervical region.

We have waterproofed the inertial sensor circuit with silicon glue and a waterproof varnish. It stays inside a specifically designed box. We have made the data's acquiring through the previously authorized project by an ethical committee under CAAE 86285418.7.0000.5208.

The test consisted of a walk of 08 m, inside and outside of the water, to analyze the behavior of the accelerometers. In the first moment that walk, out of the water, was performed, then the walk was requested to be made into the water. The walk into the water was carried out with the water close to the individual sternum level. The evaluated parameters were: time to perform the test, rate, length, speed and time step.

Figure 2 illustrates the positioning of the accelerometers, where the accelerometers 1 and 3 are positioned on the inner side of the calf, and the accelerometers 2 and 4 are positioned over the medial malleoli.
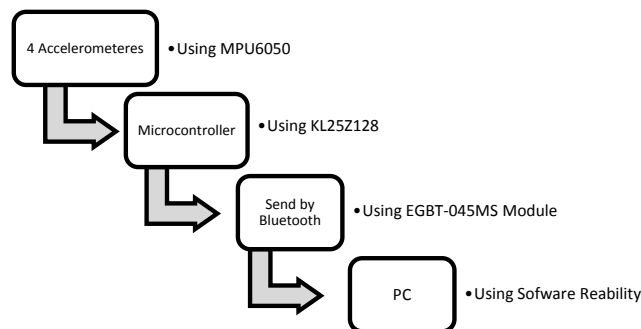
Fig. 1 Block diagram of the system

Fig. 2 Placement of accelerometers

3 Results and Analysis

One of the first challenges of the system has been to run its operation in the water. The first tests showed flaws in the sealing system. To solve the problem, a resin composed of hydrophobic nanostructure was used to protect the hardware. In addition, silicone and a latex compound were used.

After verifying the operation of the system in the water, the next step has been the validation of Bluetooth communication. In it, we have checked the effect of signal attenuation, given the proximity of the antenna to the water. At this stage there was a small loss in the sampling rate, corresponding to 10% of the expected value. In this way, the system was adapted so that this reduction in the sampling rate did not interfere in the desired study.

By analyzing only the data concerning the accelerometry, that we have acquired inside the water, we can note that the swing phase is extended in relation to the stance phase (Fig. 3). This is based on the fact that water offers resistance to sudden movement, what makes this phase of the cycle slower. The buoyancy of the water also helps to reduce imbalances in the Y-axis, facilitating movement execution.

The stance phase of Fig. 3 also shows that there is a variation in acceleration when the foot is fixed. This fact occurs mainly because the foot does not settle very well on the ground while walking on the water.

When we compare the graphs of walking in and out of the water, shown respectively in Fig. 3 and Fig. 4, we note that there is a significant reduction of peak acceleration. The walk in the water becomes necessarily slower because of this fact.

Table 1 presents the data regarding the mean width of the steps in the tests performed in and out of the water, as well as their standard deviation and the number of steps for the right leg. These data confirm what we have expected, where the pitch width within the water is greater than that outside the water.

The system resolution was set in 8 bits because of the low velocity of the body in the walk rhythm. The sample rate applied to the system was 1200 samples per second and a baud rate of 115,200 was chosen to the Bluetooth. This baud rate is enough to organize and send the packages. A test of

Fig. 3 Accelerometry in the X-axis from the right foot in the pool
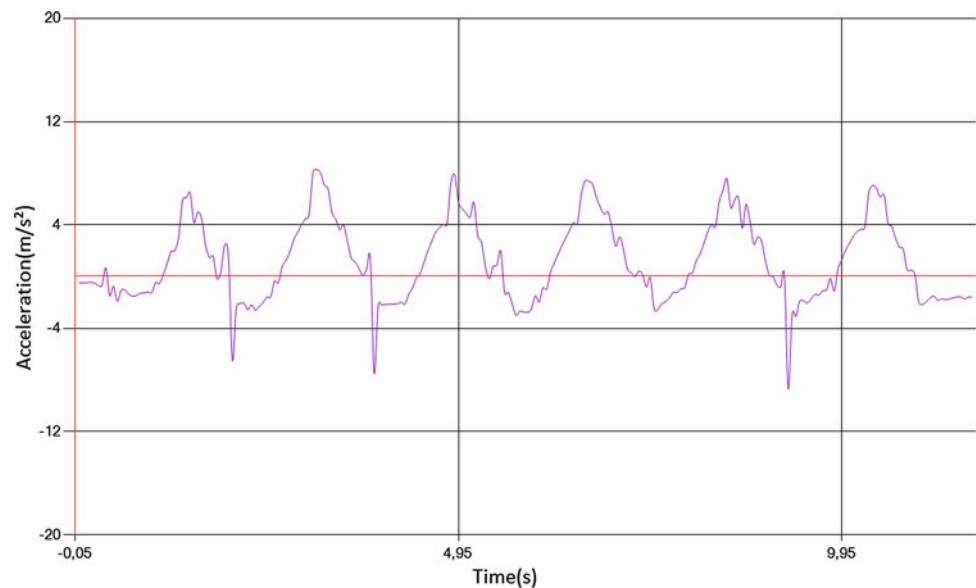
Fig. 4 Accelerometry in the X-axis from the right foot on the floor
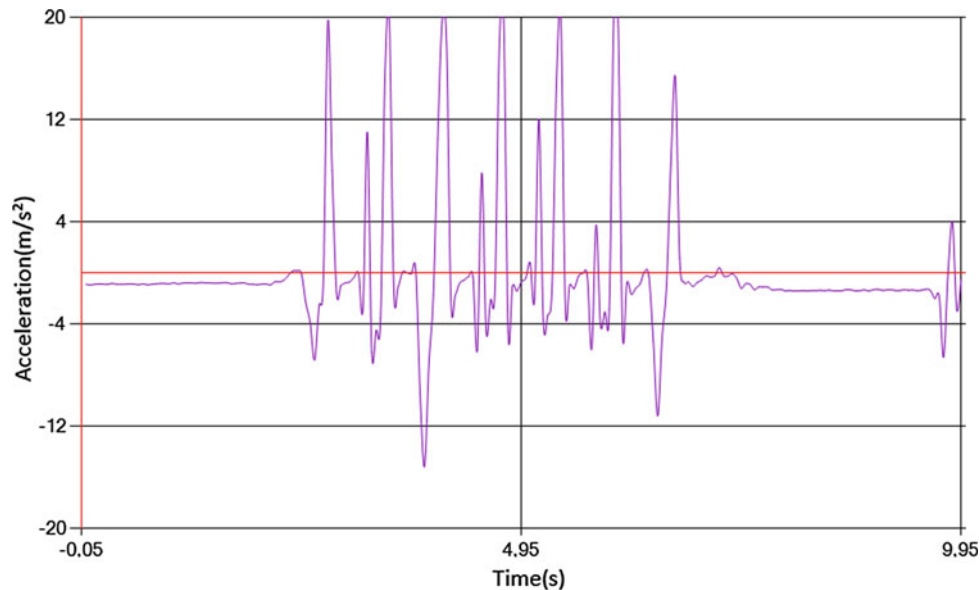
Table 1 Data related to the distance run by the right leg

Samples	Average step width (m)	Standard deviation (m)	Number of steps
Floor 1	1.3498	0.1236	6
Floor 2	1.1284	0.2952	7
Pool 1	1.4651	0.1937	6
Pool 2	1.4289	0.1593	6

Table 2 System properties

System properties	
Resolution	8 bits
Sample rate	1200
Baud rate	115,200
Data loss rate	8.69%
Energy autonomy	1 h

data loss was performed and only 8.69% of the data was missing. According to a performance test realized, the system has 1 h of autonomy (Table 2).

4 Conclusion

Among the difficulties encountered in the project, we can expose the development of the sealing system. This system required studies of waterproofing of electronic circuits that led to the use of nanotechnology.

The attenuation of the Bluetooth communication signal due to water can be neglected with adjustments in the firmware, but we have maintained the sampling rate ratio required for the design.

The developed prototype presented good performance in gait evaluation and stands out because it allows the execution of this type of study inside the water. This particularity allows a series of quantitative studies with regard to aquatic physiotherapy.

Among the future work, it is possible to apply the equipment in the monitoring of the evolution of the patients in the process of rehabilitation through aquatic physiotherapy. In addition, new sensors to capture biological signals are already being evaluated to bring more data to the patient's analysis, allowing a better follow-up of the patient.

References

1. Santos, C.P., Vieira, M.E.M., Sérgio, Stevan, L., Lazendic, J.S.: Sensores inerciais aplicados à marcha humana no esporte. Seminário de Eletrônica e Automação—SEA 2016. Universidade Tec-nológica Federal do Paraná—UTFPR, Curitiba (2016)
2. Sousa, A.S.P.: Análise da Marcha Baseada em Correlação Multifatorial. Master Thesis—Master in Electrical Engineering, Faculdade de Engenharia da Universidade do Porto. Porto (2013)
3. Invensense Homepage. https://store.invensense.com/datasheets/invensense/MPU-6050_DataSheet_V3%204.pdf. Accessed 1 Apr 2018
4. Werneck, A.L.S.: Doença de Parkinson: Etiopatogenia, clínica e terapêutica. Revista Hospital Universitário Pedro Ernesto, UERJ. Rio de Janeiro (2010)
5. Mello, M.P.B., Botelho, A.C.G.: Correlação das escalas de avaliação utilizadas na doença de Parkinson com aplicabilidade na fisioterapia. Fisioterapia do Movimento Journal **23**(1), 121–127 (2010)

6. Massano, J.: Doença de Parkinson actualização clínica. Acta Med. Port. **24**(S4), 827–834 (2011)

7. Keus, Sh: Guidelines for physical therapy in patients with Parkinson's disease. Dutch J. Physio. **114**(3), 1–92 (2004)

8. MBED homepage. https://os.mbed.com/handbook/mbed-FRDM-KL25Z,last. Accessed 15 Apr 2018

9. Invensense Homepage. https://store.invensense.com/datasheets/invensense/MPU-6050_DataSheet_V3%204.pdf. Accessed 18 Apr 2018

Acute Stabilization of Postural Sway After a Cervical Spinal Manipulation

Paulo Toshio Uchiyama, Gustavo Felix Teixeira,
Cristiano Rocha da Silva, and Fernando Henrique Magalhães

Abstract

The present study investigated the effects of a cervical spinal manipulation on postural control of healthy individuals. Seven subjects stood over a foam pad set on a force platform, as quietly as possible, in unipodal stance. The stabilogram area (estimated from center of pressure (COP) signals) was measured before and after a cervical manipulation maneuver. Besides the experimental condition, a placebo condition involving the same procedures (but without effectively applying the manipulation maneuver) was tested. The cervical spinal manipulation generated a transient effect, reducing COP Area during the first and second repetitions of the postural task performed after the intervention (experimental condition). Such an effect was not observed in the placebo condition. Therefore, it is concluded that the cervical spinal manipulation caused an acute stabilization on postural oscillations during the unipodal balance task.

Keywords

Postural control • Neck • Unipodal stance

1 Introduction

It is well known that human postural sway is regulated by mechanisms associated with sensory feedback from the visual, vestibular and somatosensory systems. In this direction, mechanoreceptors and muscle spindles located at the cervical spine are assumed to play an important role in regulating postural sway [1–3]. Mechanoreceptors of the cervical facet joint capsules significantly contribute to proprioception [4], while the muscle spindles of cervical spine intrinsic muscles interact with the vestibular nuclei thereby paying an important role in balance control [5, 6]. Moreover, cervical afferents are involved in reflex mechanisms (e.g. cervico-collic, cervico-ocular and tonic neck reflex) that helps the visual and vestibular systems to stabilize the head, the eyes and keep postural steadiness [7, 8].

Several authors have proposed manual therapy interventions with spinal manipulation for the treatment of dizziness and imbalance of cervical origin [9–12]. However, in a literature review, we have found only 3 studies that addressed the effect of cervical spinal manipulations on measurements directly related to postural control [12–14], all of which were conducted in populations with impaired postural control (i.e. patients with dizziness and/or elderly participants). In addition, these studies were not restricted to a single type of spinal manipulation, but rather used combined interventions such as fast and slow mobilizations, myofascial and joint release, cranial manipulation techniques, trunk and neck exercises, home training programs and ergonomic modifications at work. Thus, it is not possible to draw a conclusion about the effects of a specific cervical spinal manipulation on the performance of the postural control system. Therefore, the aim of the present study was to investigate the effects of a cervical spinal manipulation on postural control of healthy individuals.

2 Methods

2.1 Participants

Seven subjects (4 males, 3 females, 28.1 ± 3.2 years, mean $\pm$ SD) volunteered to participate in this study. All participants were healthy and physically active, with no known musculoskeletal injuries or neurological disorders that could have influenced their balance performance. The experiments were conducted according to the Declaration of

P. T. Uchiyama · G. F. Teixeira · C. R. da Silva ·
F. H. Magalhães (✉)
Biomedical Engineering Laboratory and Neuroscience Program, EPUSP, Universidade de São Paulo, São Paulo, SP, Brazil
e-mail: fhmagalhaes@usp.br; fhmagalhaess@gmail.com

F. H. Magalhães
School of Arts, Sciences and Humanities, University of São Paulo, EACH—USP, São Paulo, Brazil

Helsinki and all procedures were approved by the Human Ethics Committee of the School of Arts, Sciences and Humanities of the University of São Paulo (CAAE 69034717.6.0000.5390) on July 4, 2017. Each participant signed an informed consent document prior to the experimental sessions.

2.2 Center of Pressure (COP) and Foam Pad

A force platform (OR6-7-1000, AMTI Inc., Watertown, MA, USA) was used to assess the COP during quiet stance. A foam rubber pad (Airex balance pad, Alcan-Airex AG, Sins, Swiss) with 49.5 cm length, 40.5 cm width, 66.5 cm height, 0.013 m^3 volume and 58.38 kg/m^3 density was fixed over the force platform during all trials in order to challenge the postural control system. On an unstable support surface, ankle proprioceptive signals are less accurate by decreasing the effectiveness of ankle torque [15]. In the current study, the rationale behind this choice was that the unstable support surface challenges the sensorimotor system and accentuates the need for sources of sensory information other than those from the foot level (such as mechanoreceptors and muscle spindles located at the cervical spine) [16].

2.3 Procedures

Participants were asked to stand over the force platform, as quiet as possible, in unipodal support (i.e. with only the dominant foot touching the ground). Such a challenging posture was chosen as it demands a larger involvement of the vestibular and proprioceptive systems as compared to quiet bipedal stance. Two experimental conditions were tested: before and after a cervical manipulation maneuver (described in the text ahead). Each subject participated in two experimental sessions, on different days: in one of them they performed the balance tests before and after the cervical manipulation maneuver (experimental session, EXP) and in the other they performed the same balance tests before and after a placebo intervention, in which the same procedures of the EXP session were performed, but without effectively applying the manipulation maneuver (control session, CTRL, see details in the text ahead). All participants performed 5 repetitions for each experimental condition; each repetition consisted in keeping the unipodal posture for 60 s over the foam pad. The order of the experimental sessions (EXP and CTRL) was counterbalanced between the participants, that is, 4 of the participants performed the EXP session before the CTRL session and the other 3 performed the CTRL session first. Before the beginning of each experimental session, the participants completed 5 familiarization trials, in order to minimize any practice effect.

2.4 Cervical Manipulation

The cervical manipulation was performed by the same therapist, member certified as a specialist in osteopathy, with more than 10 years of practical experience. It is important to emphasize that the procedure performed by the same therapist is necessary to reduce the variability between interventions [17].

The cervical manipulation consisted of a osteopathic maneuver performed on C7 over T1, as described in [18]. Such a manipulation is commonly used in clinical settings with the objective of correcting restrictions on C7 movements, so as to release structures that are involved in head movements of rotation and flexion. The choice of such a level (C7 over T1) is justified by previous studies that showed the importance of the interaction between the cervical and thoracic vertebrae for the kinematics and sensory function of the neck [19, 20].

During the cervical spinal manipulation, the therapist was standing beside the participant, who remained in prone with the head in neutral position and the neck slightly flexed (with a pillow placed below the sternum of the participant). Then, the therapist performed the following procedures: (1) the therapist's thumb (left or right, depending on the side of the maneuver) was positioned over the side of the spinal apophysis, above the upper border of the trapezius muscle, while the other fingers laid over the participant's clavicle; (2) the therapists forearm was oriented obliquely to the direction of the manipulation, which is inferior-medially oriented (i.e. towards the participant's armpit); (3) the other hand of the therapist was placed over the temporomandibular joint of the participant so as to induce a head inclination, until the therapist realized that the spinous process of C7 made contact with the thumb of his other hand; and (4) from this position, a rapid and vigorous thumb thrust was performed, thereby characterizing the manipulation maneuver in its proper form. Differently from clinical situations, in which it is common to perform manipulation either to the left or to the right side (chosen on the basis of a previous physical evaluation), for the purposes of the present experiments, the participants were submitted to one manipulation at each side (one to the left and one to the right, consecutively performed with the order of the sides being counterbalanced between the participants). In the CTRL sessions, all the procedures described here were repeated, except for item 4.

2.5 Signal Processing

All data were acquired with a sampling frequency of 100 Hz using a 16-bit A/D converter (Optotrak Data Acquisition Unit, Northern Digital Inc, Ontario, CA) controlled by a NDI First Principles software (Northern Digital Inc., Ontario, CA).

Fig. 1 Individual (upper panels) and averaged (lower panels) COP Area measurements (mean ± standard deviation) computed for EXP and CTRL conditions, from the 1st to the 10th repetition of the postural task performed within each experimental session (1st to 5th repetition being before spinal manipulation and 6th to 10th after spinal manipulation). In the upper panels, each color represents a different participant. *depict significant differences ($p < 0.05$) among the indicated repetitions and the remaining ones
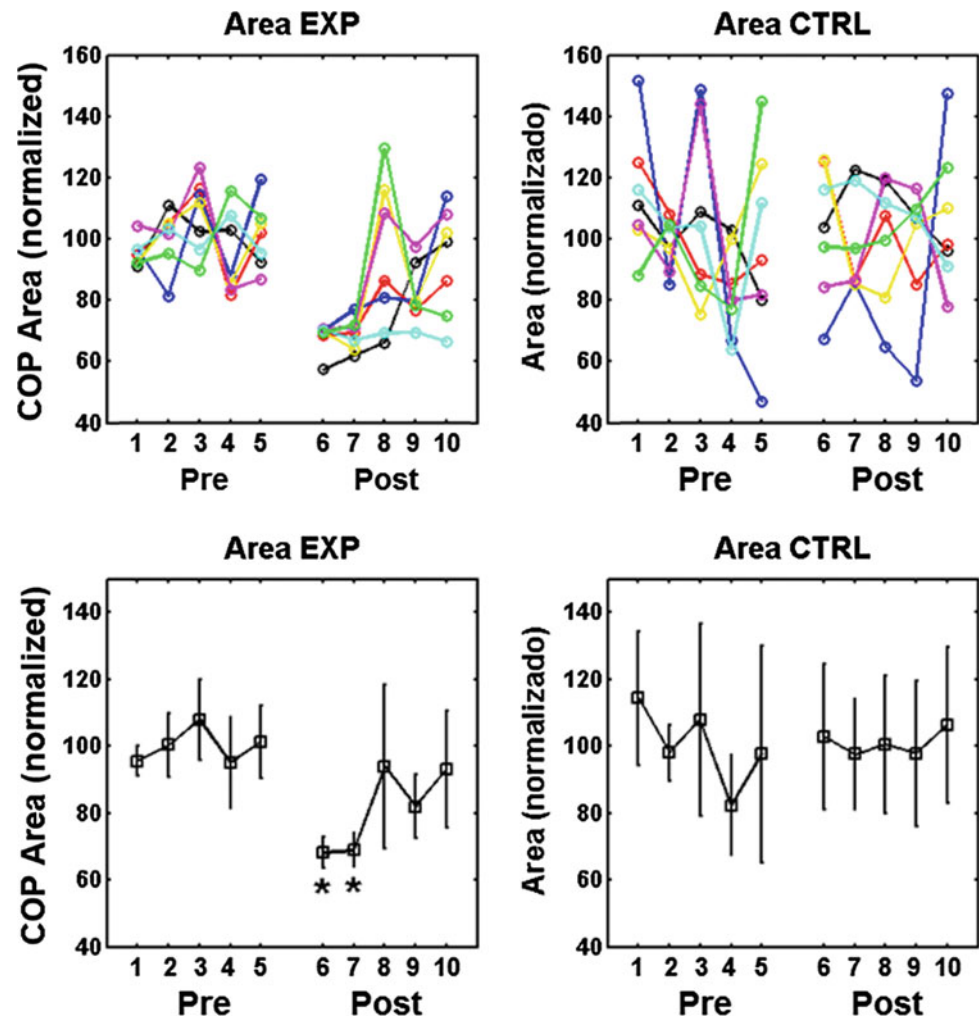
The forces and moments measured by the force plate were used to compute the two components of the center of pressure (COP): in the anterior-posterior axis (AP) and the medio-lateral axis (ML). The COP signals in both directions were passed through a low-pass filter of 10 Hz using a 4th order Butterworth filter. The area of the stabilogram was estimated from the COP data by fitting an ellipse to the AP x ML COP data that encompasses 95% of the data [21]. The area of the COP was computed for each trial. For each subject, measurements of COP Area were normalized with respect to the mean value computed among the 5 repetitions performed before the manipulation (for each experimental session).

2.6 Statistical Analysis

Normality of the data was tested using the Shapiro-Wilk method ($P < 0.05$). As the null hypothesis of Gaussian distribution was not rejected, parametric tests were used for comparisons. A two-way ANOVA with repeated measures was used in order to detect possible differences and interactions between experimental conditions (EXP and CTRL) and number of repetition (1st to 10th repetition within a given experimental session). Bonferroni post hoc comparisons were performed when necessary. All analyses were performed using the statistical package SPSS 22.0 for Windows (SPSS, Inc., Chicago, IL, USA), with an alpha level of 0.05.

3 Results

Figure 1 depicts the individual (upper panels) and mean (lower panels) values of COP Area for EXP and CTRL conditions, from the 1st to the 10th repetition of the postural task performed in each experimental session (1st to 5th repetition being before the cervical spinal manipulation and 6th to 10th after the manipulation). There was a statistically significant interaction between condition and repetition ($F(9, 6) = 2,589$, $P < 0.015$), as well as significant main effects for both

condition (F(1, 6) = 12,882, $P < 0.012$) and repetition (F(9, 6) = 2,672, $P < 0.012$). Post hoc comparisons (with Bonferroni's corrections) indicated that the significant interaction was associated with lower values of COP Area of the 6th and 7th repetitions (corresponding to the first and the second repetitions performed after the cervical manipulation) as compared to the remaining repetitions ($p < 0.05$), which happened for the EXP, but not for the CTRL condition.

4 Discussion

The results of the present study suggest that there was an acute effect of the cervical spinal manipulation on postural control. That is, the manipulation generated a transient effect, benefiting the postural control system during the first and second repetitions of the postural task performed after the intervention. After this period, the effect tends to disappear gradually, as postural sway (as measured by COP Area) became similar to that observed before the manipulation. In the CTRL sessions, in which the subjects underwent a "placebo" intervention, that is, without the manipulation maneuver being completed, the same effect was not observed, as the postural control system was relatively stable throughout the experiment (i.e., with no significant differences among the repetitions).

Transient effects on the postural control system were previously reported in response to vibratory stimuli, muscle fatigue, galvanic vestibular stimulation, among others [22–25]. In the present study, the acute effect is interpreted as a result of transient alterations in the cervical structures resulting from the cervical manipulation maneuver. More specifically, it is speculated that the spinal manipulation caused the release of cervical structures such as soft tissues, bones and blood vessels, thereby favoring the influx of sensory information relevant to the postural control system. Such an effect, however, tends to disappear already from the third post-manipulation attempt (which, in the present experiments, represent a time of approximately 5 min), possibly due to a reorganization of the cervical structures after the manipulation, or due to an adaptation/habituation of the sensory receptors and structures involved. In addition, a direct effect of manipulation on the vestibular apparatus cannot be ruled out, as the rapid perturbation generated by the cervical manipulation may have directly influenced the vestibular structures that have an important influence on balance control.

5 Conclusion

The results showed that the cervical manipulation induced an acute stabilization on postural oscillations during the unipodal balance task. After a period of approximately 5 min, such a stabilizing effect tended to disappear gradually, with the postural control system performing similarly to that observed before the spinal manipulation. Future studies are needed to unravel the specific mechanisms associated with the present results.

References

1. Abrahams, V.C.: The physiology of neck muscles; their role in head movement and maintenance of posture. Can. J. Physiol. Pharmacol. **55**(3), 332–338 (1977)
2. Kulkarni, V., Chandy, M.J., Babu, K.S.: Quantitative study of muscle spindles in suboccipital muscles of human foetuses. Neurol India **49**(4), 355–359 (2001)
3. Boyd-Clark, L.C., Briggs, C.A., Galea, M.P.: Muscle spindle distribution, morphology, and density in longus colli and multifidus muscles of the cervical spine. Spine (Phila Pa 1976) **27**(7), 694–701 (2002)
4. Mclain, R.F.: Mechanoreceptor endings in human cervical facet joints. Spine (Phila Pa 1976) **19**(5), 495–501 (1994)
5. Nitz, A.J., Peck, D.: Comparison of muscle spindle concentrations in large and small human epaxial muscles acting in parallel combinations. Am. Surg. **52**(5), 273–277 (1986)
6. Bolton, P.S.: The somatosensory system of the neck and its effects on the central nervous system. J. Manipulative Physiol. Ther. **21**(8), 553–563 (1998)
7. Treleaven, J.: Sensorimotor disturbances in neck disorders affecting postural stability, head and eye movement control—part 2: case studies. Man. Ther. **13**(3), 266–275 (2008)
8. Magalhaes, F.H., Goroso, D.G.: Preparatory EMG activity reveals a rapid adaptation pattern in humans performing landing movements in blindfolded condition. Percept. Mot. Skills. **109**(2), 500–516 (2009)
9. Galm, R., Rittmeister, M., Schmitt, E.: Vertigo in patients with cervical spine dysfunction. Eur. Spine J. **7**(1), 55–58 (1998)
10. Zhou, W., Jiang, W., Li, X., et al.: Clinical study on manipulative treatment of derangement of the atlantoaxial joint. J. Tradit. Chin. Med. **19**(4), 273–278 (1999)
11. Brandt, T., Bronstein, A.M.: Cervical vertigo. J. Neurol. Neurosurg. Psychiatry. **71**(1), 8–12 (2001)
12. Karlberg, M., Magnusson, M., Malmstrom, E.M., et al.: Postural and symptomatic improvement after physiotherapy in patients with dizziness of suspected cervical origin. Arch. Phys. Med. Rehabil. **77**(9), 874–882 (1996)
13. Fraix, M., Gordon, A., Graham, V., et al.: Use of the SMART balance master to quantify the effects of osteopathic manipulative treatment in patients with dizziness. J. Am. Osteopath. Assoc. **113**(5), 394–403 (2013)
14. Lopez, D., King, H.H., Knebl, J.A., et al.: Effects of comprehensive osteopathic manipulative treatment on balance in elderly patients: a pilot study. J. Am. Osteopath. Assoc. **111**(6), 382–388 (2011)
15. Hatton, A.L., Dixon, J., Martin, D., et al.: The effect of textured surfaces on postural stability and lower limb muscle activity. J. Electromyogr. Kinesiol. **19**(5), 957–964 (2009)
16. Magalhaes, F.H., Kohn, A.F.: Vibration-enhanced posture stabilization achieved by tactile supplementation: may blind individuals get extra benefits? Med. Hypotheses **77**(2), 301–304 (2011)

17. Fraix, M.: Osteopathic manipulative treatment and vertigo: a pilot study. PM R **2**(7), 612–618 (2010)

18. Cueco, R.T.: La columna cervical: evaluación clínica y aproximaciones terapéuticas: principios anatómicos y funcionales, exploración clínica y técnicas de tratemiento. Madrid: Médica Panamericana (2008)

19. Tsang, S.M., Szeto, G.P., Lee, R.Y.: Normal kinematics of the neck: the interplay between the cervical and thoracic spines. Man. Ther. **18**(5), 431–437 (2013)

20. Wassinger, C.A., Rich, D., Cameron, N. et al.: Cervical and thoracic manipulations: acute effects upon pain pressure threshold and self-reported pain in experimentally induced shoulder pain. Man. Ther. (2015)

21. Magalhaes, F.H., Kohn, A.F.: Effectiveness of electrical noise in reducing postural sway: a comparison between imperceptible stimulation applied to the anterior and to the posterior leg muscles. Eur. J. Appl. Physiol. **114**(6), 1129–1141 (2014)

22. Day, B.L., Cauquil, A.S., Bartolomei, L., et al.: Human body-segment tilts induced by galvanic stimulation: a vestibularly driven balance protection mechanism. J. physiol. **500**(Pt 3) 661–672 (1997)

23. Wierzbicka, M.M., Gilhodes, J.C., Roll, J.P.: Vibration-induced postural posteffects. J. Neurophysiol. **79**(1), 143–150 (1998)

24. Eklund, G.: General features of vibration-induced effects on balance. Upsala J. Med. Sci. **77**(2), 112–124 (1972)

25. Paillard, T.: Effects of general and local fatigue on postural control: a review. Neurosci. Biobehav. Rev. **36**(1), 162–176 (2012)

Agreement Between Estimative of Shear Modulus in the Superficial and Deep Layers of the Multifidus

Viviane Bastos de Oliveira, Wagner Coelho de Albuquerque Pereira, and Liliam Fernandes de Oliveira

Abstract

The multifidus is a trunk stabilizer muscle. Superficial fibers are able to generate the extensor torque, while deep fibers stabilize the column for torque generation. Elastography is a technique that allows to evaluate muscular stiffness. The aim of this work is to evaluate the agreement between the shear modulus (G) of superficial and deep layers of the multifidus. Bilateral images were obtained of 26 volunteers in the prone position. Measurements were obtained with the Supersonic Shear Imaging (SSI) technique. Images were taken with the probe guided in longitudinal and transversal directions of the muscle fibers. In longitudinal measurements, G of the superficial and deep layers presented weak correlation in left multifidus ($\rho_s = 0.367$) and right multifidus ($\rho_s = 0.303$). The correlation was also weak in the transversal measurements in left side ($\rho_s = 0.398$) and right side ($\rho_s = 0.342$). Bland-Altman plots showed low agreement between the superficial and deep fascicles. Reliability indicates better results for longitudinal evaluations. Shear modulus measurements of the superficial and deep layers did not show agreement. The acquisitions in the longitudinal showed better reproducibility interdays.

Keywords

Multifidus • Superficial • Deep • Elastography • Shear wave

1 Introduction

In the spinal column model described by Bergmark [1], the stability of the lumbar spine can be subdivided into two systems: Global and local system. The local system has one remarkable role in maintenance of mechanical stability of the lumbar spine, provided by a set of deep muscles, such as multifidus. There are peculiarities of multifidus that must be considered. Its superficial fibers have larger moment arms, with insertions distant from the axis of vertebral rotation, biomechanically better to generate extensor torque in the vertebral column. Directly related to stability, its deep fibers are shorter and closer to the axis of vertebral rotation controlling the movements of vertebrae during the tensile, shear and compression forces [2].

Liu et al. [3] used ultrasound and investigated the reliability of the thickness estimative of the superficial and deep layers of the multifidus in young individuals with and without low back pain, between L3-4 and L4-5 vertebrae. The results of this study showed that ultrasound is a technique capable of differentiating the deep and superficial layers of the multifidus with good reliability. Considering the good reliability of ultrasound measurements, the shear wave elastography is an image technique that allows the estimation of quantitative parameters related to muscle stiffness, and thus, could be used to evaluate differences in stiffness between the superficial and deep layers of the multifidus muscle, by estimating their shear modulus (G). In isotropic medium, G is equivalent one-third of Young's modulus, whose parameter is directly proportional to the elasticity, property that characterizes the ability of an object to deform and return to its initial shape.

Although elastography has been shown to be a promising technique for evaluating the elastic properties of the muscle, few studies have investigated the stiffness of the multifidus using this technique [4–6]. Supersonic Shear Imaging (SSI) is a highly advanced elastography technique, with good reliability in the evaluation of contraction and

V. B. de Oliveira (✉) · W. C. de Albuquerque Pereira · L. F. de Oliveira
Biomedical Engineering Program, COPPE/UFRJ, Rio de Janeiro, Brazil
e-mail: vivi.bastos@peb.ufrj.br

L. F. de Oliveira
Physical Education and Sports School, EEFD/UFRJ, Rio de Janeiro, Brazil

elongation of the multifidus [4]. Nevertheless, there is no studies that has evaluating the stiffness of the multifidus layers separately. Therefore, the objective of the present work is to evaluate the agreement shear modulus from superficial and deep layers of the multifidus. Secondly, the anisotropy was also evaluated.

2   Materials and Methods

2.1   Sample

This study was approved by the Research Ethics Committee of the Hospital Clementino Fraga Filho—HUCFF/UFRJ (no 9760/14, CAAE: 26828914.3.0000.5257) and linked to the university extension project "Musculoskeletal Health Program in public servants", approved in the RUA-UFRJ 2016-2.

The sample was composed of 26 healthy volunteers, with a mean age of 27.10 ± 6.89 years, height of 1.70 ± 0.10 m and mass of 67.74 ± 11.28 kg. All of them signed the document of informed consent agreement.

2.2   Image Acquisition

With the volunteer in the prone position, a support was placed in the abdominal region to minimize lordosis at least 10° [7]. The equipment used to acquire multifidus images was an Aixplorer V.11 (Supersonic Imaging, Aix-en-Provence, FRANCE), in which operates in imaging and pushing modes.

The equipment preset used for imaging mode was as follow: General gain of 58 dB, focus location of 3–4 cm, map of gray scale of 6 and dynamic range of 69 dB [8]. Pushing mode preset was: Penetration mode; smoothing 6; elastogram with range up to 180 kPa, corresponding in the RGB system blue tonality to less tissue shear modulus and red tonality to greater shear modulus, depending on the magnitude of the shear wave; SWE gain of 70%.

The linear probe was Super Linear TM SL10-2 (width 40 mm, 256 elements, frequency band 2–10 MHz, lateral resolution of −6 dB: 0.3 mm) guided at longitudinal orientation of the muscle fascicles, programmed to operate with 6 MHz central excitation frequency. After, images with probe oriented transversally were obtained. Images of the multifidus were obtained bilaterally, at the level of the zygoapophyseal joints of L4-5 and L5-S1, during the expiratory phase, maintenance relaxed paravertebral musculature and minimal pressure with probe.

This system generates a perturbation in the medium by means of an acoustic radiation force (push), fired in successive depths sequentially. The push induces the formation of a shear wave, whose parameters will be used to calculate the G. These successive fires generate a wavefront similar to a Mach cone, creating a quasi-plane wavefront and shifting the tissue in tens of μm at all depths, where knocks move at supersonic speed, spreading and falling less rapidly due to the depth (Fig. 1). So, analyses made in the different depths of the multifidus were acquired in the same image.

The shear wave speed (c_s) is obtained by means of the information from the probe. In order to reach the G value, square of c_s is multiplied by density (ρ), predefined on the system itself as a single for any medium (1000 kg/m^3), assuming anisotropy and the medium as purely elastic (Eq. 1).

$$G = \rho c_s^2 \tag{1}$$

In the acquisition of the images, the mapping area (region in which G analysis can be performed) was previously adjusted to include superficial and deep measurements in the same image.

For each side of this spine (right and left), two images and volunteers participated in two days of collection for each
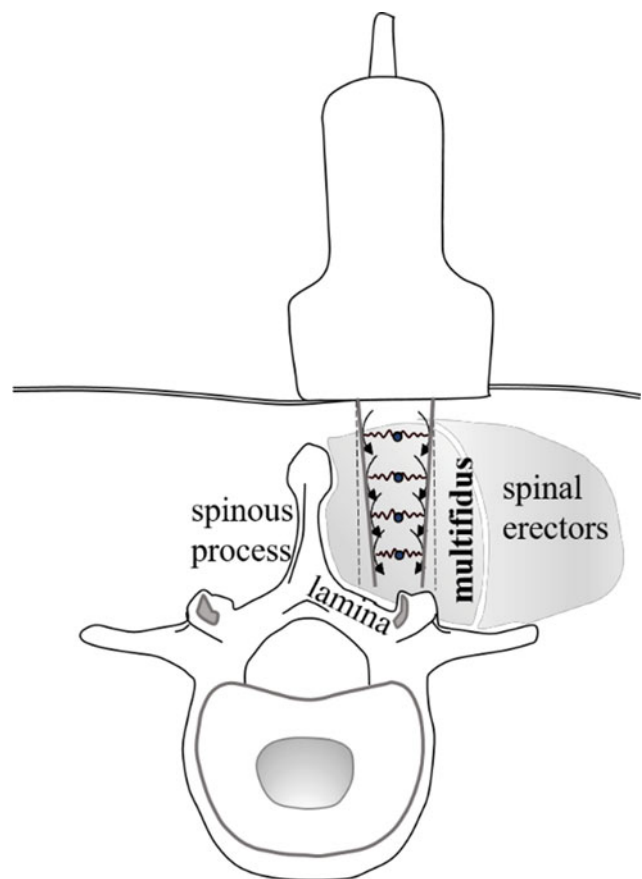
Fig. 1 Transversal images of multifidus acquired with SSI. The technique allows for numerous knocks toward depth at an ultrafast speed, even faster than shear wave propagation, creating a quasi-plane wavefront, which decrease less rapidly as it goes deeper

Fig. 2 Bilateral image acquisition protocol, with the representation of the orientation of the longitudinal probe. Transversal images were taken later
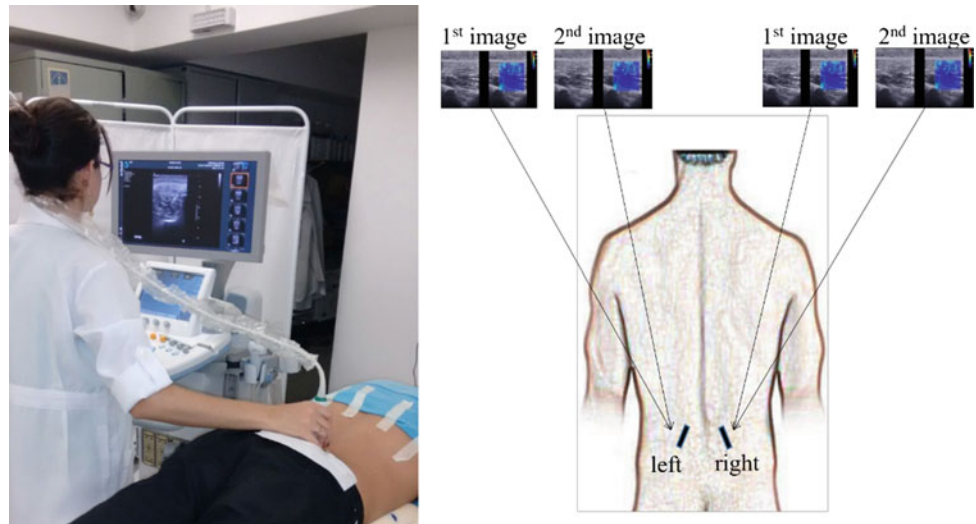
volunteer (Fig. 2), with a 48-h interval between them, in order to determine the measures of repeatability.

2.3　Image Processing

The images were saved in DICOM (Digital Imaging and Communications in Medicine) format for later processing in a routine implemented in MATLAB$^{®}$ (Mathworks, Massachusetts, USA).

In the mapping area, regions of interest (ROI) were drawn in longitudinal images close to the thoracolumbar fascia for superficial layers, and below one imaginary line between the zigoapophyseal joints L4-5 and L5-S1 for the deep layer. In transversal images, the ROI was drawn close to the thoracolumbar fascia to the superficial layer, and close to the vertebral lamina for the deep layer. In these regions, measurements were performed in a circular window with 1 cm of diameter (Figs. 3 and 4).

2.4　Statistical Analyses

Variable analyzed was the G estimated in the two layers of the muscles bilaterally. The descriptive values of the measures were presented with their respective mean ± SD. Subsequently, the data were submitted to exploratory analysis to verify the theoretical normal distribution. The Shapiro-Wilk normality test identified at least a non-normal distribution ($p = 0.008$). Accordingly, non-parametric tests were adopted. Reliability was determined by the calculation of intraclass correlation coefficient (ICC), using ANOVA parameters and Koo and Li classification [9]. The tests were performed in SPSS (SPSS IBM, New York, USA).

Bland-Altman plots were developed in a MATLAB routine for graphical analysis of agreement, distribution of data within the range of agreement (95% interval confidence) and difference found in measurements (bias) of the superficial and deep layers. The correlation between the measurements in the superficial and deep layers was determined by the non-parametric Spearman correlation test (ρ_s).

3　Results

The descriptive values of G are summarized in Table 1 with the values, referring to the 4 images (2 images per day, in 2 days).

Reliability of the transversal measurements ranged from moderate to good (ICC from 0.62 to 0.84) and good for the longitudinal measurements (ICC from 0.77 to 0.86).

Shear modulus of the longitudinal images between the superficial and deep layers presented very weak correlation for the left multifidus ($\rho_s = 0.174$; see Fig. 5) and for the right multifidus ($\rho_s = 0.148$; see Fig. 5). A similar result was found for the transversal images (ρ_s left multifidus = 0.062 and ρ_s right multifidus = 0.063; see Fig. 6). All correlation values were significant ($p < 0.05$). Bland-Altman plots showed biases far from zero for all comparisons. There was no tendency to present negative or positive values, and the points appear randomly distributed.

4　Discussion

The present study aimed to determine the correlation between the shear modulus measurements from superficial and deep multifidus layers. Reliability analysis showed ICC

Fig. 3 Longitudinal images. The circular ROI was traced with 1 cm of diameter superimposed on the mapping area (blue), in the superficial layer (left) and deep (right)
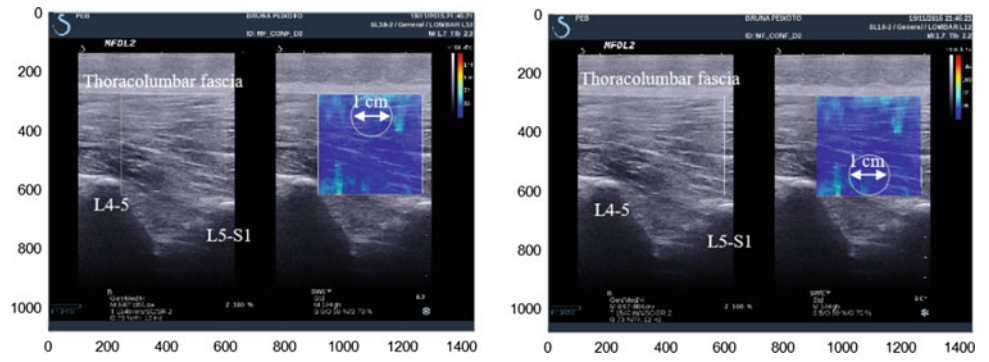
Fig. 4 Transversal images. The circular ROI was traced with 1 cm of diameter superimposed on the mapping area (blue), in the superficial layer (left) and deep (right)
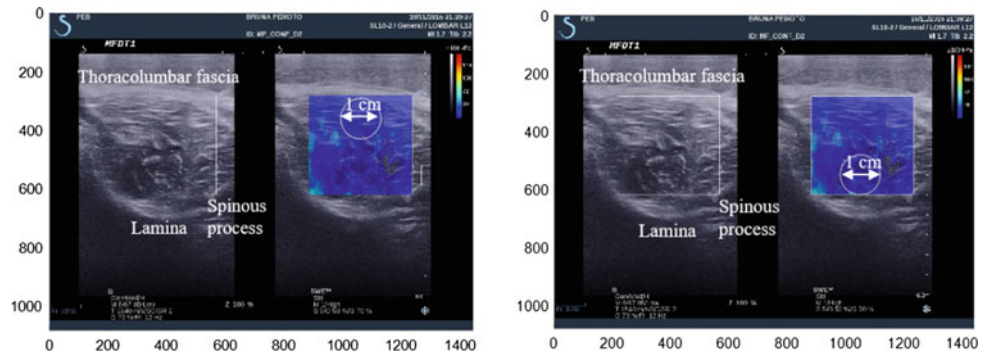
Table 1 Average and standard deviation of the Shear Modulus (kPa) and reliability data

Orientation	Side	Superficial		Deep	
		(kPa)	ICC (interdays)	(kPa)	ICC (interdays)
Longitudinal	Left	7.96 ± 1.67	0.86	6.08 ± 0.89	0.79
	Right	7.68 ± 1.56	0.77	6.27 ± 1.33	0.85
Transversal	Left	7.67 ± 1.87	0.84	5.68 ± 1.37	0.62
	Right	7.38 ± 1.59	0.64	5.84 ± 1.76	0.76
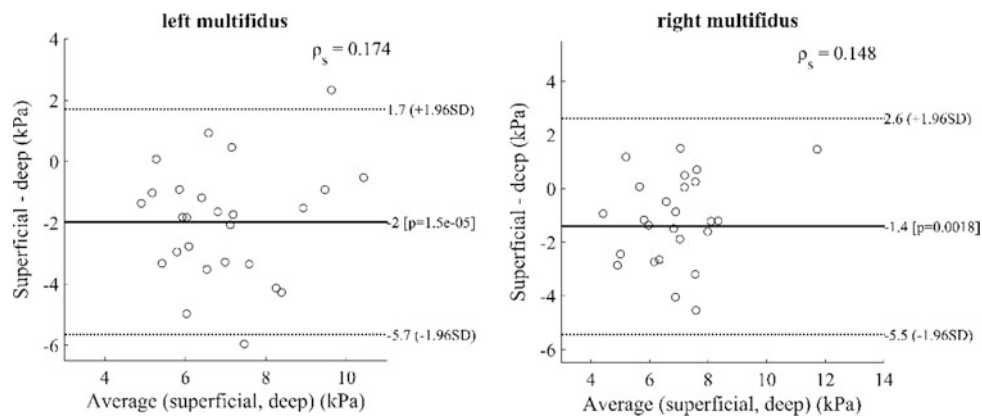
Fig. 5 Bland-Altman plots of the values from images obtained longitudinally. The agreement limit for measurements ranged from −5.7 to 1.7 kPa, with a bias of −2 kPa for left multifidus. For the right multifidus, measurements ranged from −5.5 to 2.6 kPa, with a bias of −1.4 kPa

Fig. 6 Bland-Altman plots of the values from images obtained transversally. The agreement limit for measurements ranged from −5.6 to 1.5 kPa, with a bias of −2.1 kPa for left multifidus. For the right multifidus, measurements ranged from −5 to 1.8 kPa, with a bias of −1.6 kPa
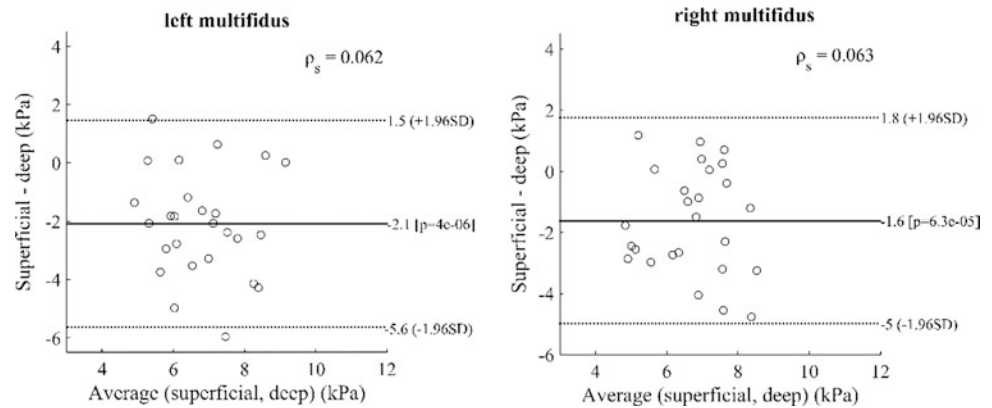
values slightly higher for the longitudinal images. The angle between the transducer and the direction of the fascicles affects the measured shear modulus. In pennation muscles, the probe must be positioned so that the propagation of the shear waves occurs along the directions of the fascicles [10]. The lumbar multifidus is organized into five bands that cross the lumbar spine and are distributed anatomically in multiple fascicles oriented obliquely. Thus, the longitudinal direction corresponds to the direction of the fascicles of the multifidus.

Previous studies with intramuscular electromyography have proven the stabilizing role of deep fibers, because they are activated before the superficial fibers, so that the extensor torque is executed around a stable structure. In people with low back pain, in the side painful there is a delayed recruitment of the fibers when compared to the non-painful side, which indicates that there is a delay in the stability of the lumbar spine [11, 12]. Moseley et al. [13] observed that the deep fibers of the multifidus become phasic in the course of trunk flexion, because the deep fibers must assume an intersegmental control during the rotational and shear forces caused by the compression of the vertebral segments. Kjaer et al. [14] showed that for individuals with low back pain, as the muscle becomes atrophied there is deposition of intra-muscular adipose tissue, which starts from the deepest to the superficial layer. Chan et al. [15] investigated the presence of adipose tissue with magnetic resonance in volunteers with low back pain, besides analyzing elastic properties of the multifidus in vivo with quasi-static elastography system associated with an external source for medium disturbance. Symptomatic individuals had larger areas of adipose tissue and lower values of Young's modulus than asymptomatic individuals (Asymptomatic: 36.43 at 37.37 kPa; symptomatic: 5.79–6.16 kPa).

Moreau et al. [4] published the first study approaching shear waves in multifidus. Participants were evaluated in prone and passive elongation in a massage chair. For the position of passive elongation in the massage chair the average found for the shear modulus was 13.8 ± 2.9 kPa in L2-3 and 22.7 ± 3.8 kPa in L4-5. The values of G found in the pronated position were: 8.5 ± 1.9 kPa in L2-3 and 6.8 ± 1.2 kPa in L4-5. Creze et al. [5] found close to the values of Moreau et al. [4]. They validated the use of the SSI technique for analysis of the multifidus at L3 level. In cadavers, the authors determined that the transducer must be at 9°–22° between multifidus fibers and the spinous process. In vivo, the average value found was 5.4 ± 1.6 kPa and 5.1 ± 1.7 kPa in cadavers. Koppenhaver et al. [6] determined the reliability of G obtained from multifidus in different contractions, with ICC values ranged from 0.44 to 0.66. Reliability of estimative performed in the actual study presented good repeatability interdays.

Present findings corroborate the values of G found in previous studies [4–6]. Measurements performed in groups of asymptomatic volunteers show that the stiffness in the different layers does not present a linear relationship. Bland-Altman plots showed significantly low agreement between the layers. Ewertsen et al. [16] observed in the biceps brachii, quadriceps femoris and gastrocnemius that velocity of the shear waves decreases with depth and closer to a bone structure. For better understanding, an in vitro test should be performed to analyze the effects of depth on shear wave velocity.

In fact, the instrumentation used to estimate the G assumes the density of the medium as homogeneous, in addition to considering the medium as isotropic, when the muscle can be modeled as transverse isotropic medium. Future work is suggested for comparison of the multifidus layers in people with low back pain.

5 Conclusion

The shear modulus measurements of the superficial and deep layers did not show agreement, which suggests that in future studies the analyzes are carried out assuming the differences between the layers. The findings indicate that the analyses have better interdays reproducibility, when performed in the images acquired in longitudinal direction along the muscle

fibers. In addition, the attenuation of the generation of shear waves due to depth should be evaluated.

Conflict of Interest We have no conflict of interest to declare.

References

1. Bergmark, A.: Stability of the lumbar spine: a study in mechanical engineering. Acta Orthop. Scand. **60**(230), 1–54 (1989)
2. Macintosh, J., et al.: The morphology of the human lumbar multifidus. Clin. Biomech. **1**(4), 196–204 (1986)
3. Liu, I.S., et al.: Inter-session reliability of the measurement of the deep and superficial layer of lumbar multifidus in young asymptomatic people and patients with low back pain using ultrasonography. Man. Ther. **18**(6), 481–486 (2013)
4. Moreau, B., et al.: Non-invasive assessment of human multifidus muscle stiffness using ultrasound shear wave elastography: a feasibility study. Proc. Inst. Mech. Eng. Part H J. Eng. Med. **230**(8), 809–814 (2016)
5. Creze, M., et al.: Feasibility assessment of shear wave elastography to lumbar back muscles: a radioanatomic study. Clin. Anat. (2017)
6. Koppenhaver, S., et al.: Reliability of ultrasound shear-wave elastography in assessing low back musculature elasticity in asymptomatic individuals. J. Electromyogr. Kinesiol. **39**, 49–57 (2018)
7. Hides, J., et al.: Multifidus size and symmetry among chronic LBP and healthy asymptomatic subjects. Man. Ther. **13**(1), 43–49 (2008)
8. Masaki, M., et al.: Association of sagittal spinal alignment with thickness and echo intensity of lumbar back muscles in middle-aged and elderly women. Arch. Gerontol. Geriatr. **61**(2), 197–201 (2015)
9. Koo, T., Li, M.: A guideline of selecting and reporting intraclass correlation coefficients for reliability research. J. Chiropr. Med. **15**(2), 155–163 (2016)
10. Miyamoto, N., et al.: Validity of measurement of shear modulus by ultrasound shear wave elastography in human pennate muscle. PLOS One. **10**(4) (2015)
11. Macdonald, D., Moseley, G., Hodges, P.: Why do some patients keep hurting their back? Evidence of ongoing back muscle dysfunction during remission from recurrent back pain. PAIN® **142**(3), 183–188 (2009)
12. Dickx, N., et al.: Differentiation between deep and superficial fibers of the lumbar multifidus by magnetic resonance imaging. Eur. Spine J. **19**(1), 122–128 (2010)
13. Moseley, G., Hodges, P., Gandevia, S.: Deep and superficial fibers of the lumbar multifidus muscle are differentially active during voluntary arm movements. Spine **27**(2), E29–E36 (2002)
14. Kjaer, P., et al.: Are MRI-defined fat infiltrations in the multifidus muscles associated with low back pain? BMC Med. **5**(1), 2 (2007)
15. Chan, S., et al.: Dynamic changes of elasticity, cross-sectional area, and fat infiltration of multifidus at different postures in men with chronic low back pain. Spine J. **12**(5), 381–388 (2012)
16. Ewertsen, C., et al.: Evaluation of healthy muscle tissue by strain and shear wave elastography–dependency on depth and ROI position in relation to underlying bone. Ultrasonics **71**, 127–133 (2016)

Analysis of the 3R15 and C-Leg Knee Prosthesis

C. R. L. Moraes, V. J. B. de Lima, C. C. B. de Souza,
A. V. M. Inocencio, B. Mochel, C. Rodrigues,
and M. A. B. Rodrigues

Abstract

The amputation is a millennial surgical intervention which occurs mainly due to accidents and wars. Actually, considering the greater of people's longevity, there was an increase in the incidence of amputations, especially because of pathologies inherent to age, modern life's habits and urban violence. As the amputation is millennial, the artifices used by the amputated people to gait adaption also are. Today there are many transfemoral prosthesis models and, thinking about that, this research has the objective of compare two prosthesis models, a mechanical (3R15, provided by the Unified Health System-SUS) and a microprocessed (C-Leg). Therefore, was performed a search for volunteers which has been using a mechanical prosthesis for at least 2 years produced by the Associação de Assistência à Criança Deficiente of Pernambuco (AACD-PE). After an initial screening of volunteers, mobility and functionality tests were realized for evaluation of kinematic performance. The tests were realized in linear tracks and tracks with obstacles, based on Ottobock® test protocol. On average, the velocity in linear and square tracks improved of 33.33% and 36.75%, respectively, there was a decrease in the time spent in the obstacle test of 35.96% and an increase in the distance in the slop test of 21, 98%. Based on this and in the reduced number of volunteers, it is concluded, in this first moment, that the C-Leg microprocessed prosthesis is kinetically better than the mechanical prosthesis 3R15, allowing a greater quality of life for the user, but it is necessary increase the number of volunteers to have more robust results.

Keywords

Prosthesis • Comparison • Microprocessed

1 Introduction

The amputation is defined as the removal of a limb from the human body through a surgical or resulting from different etiologies like vascular, traumatic, tumor, congenital or infectious, causing limitations of the individual mobility. The mobility limitation is proportional to the amputation level of the limb [1].

Initially, amputations occurred by traumas occurred during hunting, self-mutilation in religious ceremonies, in the capture of enemies or judicial punishments [2]. In the 21st Century, the two World Wars provoked a considerable number of amputations and motivated the research and development of devices that proposes to replace a lost limb by an artificial or prosthesis [3]. The main objective of this replacement is to increase the amputee's quality of life, ameliorating their self-esteem and providing more autonomy to perform daily tasks.

Inferior limb amputations correspond to about 85% of the amputations; however, accurate epidemiological information is not assured [4]. In 2005, EUA presented between 30 and 40 thousand amputees and the estimation is that, in 2050, approximately 3.6 million people will lose a member [5]. In Brazil, the estimated incidence of amputations is about 13.9 by 100,000 habitants per year. In Pernambuco, the local clinical and epidemiological profile of amputated patients was traced in 2010 by the Associação de Assistência à Criança Deficiente (AACD—Handicapped Children Care Association), when were observed a higher frequency of amputations by vascular cause (55.73%), followed by the traumatic cause (29.18%), in which the transfemoral level (56%) is the most frequent [6].

The purpose of rehabilitation of inferior limb amputees is to recover the limb function and reestablish the gait and

C. R. L. Moraes (✉) · V. J. B. de Lima · C. C. B. de Souza ·
A. V. M. Inocencio · B. Mochel · M. A. B. Rodrigues
Federal University of Pernambuco (UFPE), Recife, PE, Brazil
e-mail: cici2116@gmail.com

C. Rodrigues
University of Porto, Porto, Portugal

other functional activities of the amputated member, reaching the highest level of functionality as possible [7].

People who suffered amputations incorporate alterations in remain muscles, residual limb. Adaptive strategies assure a soft and well-coordinated gait pattern, and the individual adjusts his gait to use the minimal energy the maximum distance possible [8, 9]. For that, the patient uses compensations or increases the movement of non-affected limbs.

In order to analyze these adaptations, this paper aims to present a kinematic comparison between a mechanical and a microprocessed prosthesis through tests realized in linear tracks and tracks with obstacles, based in Ottobock® protocol.

1.1 Human Gait

The walk is a quite complex activity, even being one of the main skills of the individual. It is characterized by smooth, regular and repetitive movements with a surprising efficiency from the neuro-musculoskeletal point of view [10]. The human locomotion is performed in the bipedal posture and is referred in the literature as gait. The main function of this activity is promote the displacement of the body in a soft and efficient way through the space [11].

The gait realization depends on the motor control and the coordination of the neural signals sent to the muscles. The combination of this two factors enables the individual to perform the movement in the joints [11].

This movement is a complex phenomenon which involves the central and peripheral nervous system and the entire skeletal-muscle system. In other words, it's a functional task which requires complex interactions and coordination between some of the most important joints of the body, especially from the inferior limbs [12]. A full gait cycle is defined as the time interval between two successive occurrences of a repetitive event of the walk. It features two phases: stance phase, which corresponds to 60% of the cycle and the swing phase, corresponding to 40% of the cycle (Fig. 1) [13].

The gait of the amputated patient has characteristics that emerge from the absence of a member with some compensations, considering the residual muscle mass, the type of surgery executed and the type of prosthesis used (quality of the material, components and alignment) [15].

The characteristics of the amputee patient gait are: longer prosthetic swing phase, lower intact member balance stage, smaller prosthetic stance phase, a reduced time of single support on the prosthetic side, a longer intact limb stance phase, increase of the width of step (7–16 up to 16–30 cm); and a larger metabolic cost than a normal person gait [16, 17].

2 Materials and Methods

The study was realized at the master degree program of Biomedical Engineering of Federal University of Pernambuco—UFPE, and the second step comprehended the the Handicapped Children Care Association of Pernambuco (AACD), that provides therapeutic and technical support to the patient amputated by the most diverse etiologies.

This research used the following devices: an equipment for measuring foot plantar pressure (baropodometer); an Apple iPad 2.0 Camera, and an Apple 5C iPhone camera. The protocol for training and adaption of the C-leg prosthesis was Rehab from Ottobock® and the adaption from Genium Therapy Protocol. The kinematics evaluation was realized by the Outcome Measurement performance-based tests protocol.

Twenty post-traumatic transfemoral amputation victims attended at the AACD's amputee clinic were selected to compose the population of this study. However, only two of them were electable to the research and then they were invited to become a volunteer and fill a consent form.

The eligibility criteria were that the patients must be victims of post-traumatic transfemoral amputation attended by AACD Pernambuco and uses prosthesis for two years at least. Patients who were victims of transfemoral amputation due to tumors, infections, peripheral vascular diseases, other non-traumatic causes were excluded.

Data collection was performed according to the project approved by Ethics Committee of Federal University of Pernambuco, Brazil platform project number CAAE 47921815.3.0000.5208.

Fig. 1 Steps of the gait cycle [14]
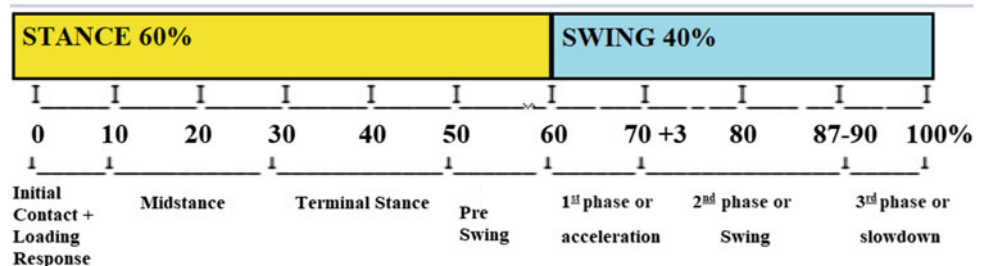
Fig. 2 The obstacle test (left) and the slop test (right), both using the mechanical prosthesis

3 Results

In this research, mobility and functional tests of the prosthesis were performed with kinematic evaluation. The tests were made in linear and obstacle tracks, based on the Ottobock® test protocol.

The kinematic evaluation of the volunteers was performed according to the Outcome Measurement: Performance based tests protocol from the Ottobock, manufacturer of the 3R15 and C-leg prostheses. It was installed a linear track with 6 m long by 0.60 m wide and quadrangular with 1.50 m on each

side with cones in its vertices, and also quadrants with obstacles. In the square track, a fixed time of 60 s was established and the number of repetitions was observed to determine the distance and speed. The images were taken at the same time in facing and in profile. The evaluations were performed 3 times in the linear track, in the obstacle test (Fig. 2, left), in the slope test (Fig. 2, right) and only once in the square test, measuring each execution time. After the tests, it was calculated the velocity for each repetition and the mean of the times and velocities for each volunteer. The kinematic evaluation of the mechanical prosthesis (MP) and of the microprocessed prosthesis (MCP) is presented in Table 1.

Table 1 Kinematic evaluation of mechanical and microprocessed prosthesis

Linear gait test				
Voluntary 1			Voluntary 2	
Average time (s)		Average speed (m/s)	Average time (s)		Average speed (m/s)
MP	7.44	0.81	MP	4.96	1.20
MCP	4.65	1.29	MCP	4.31	1.39
Square gait test				
Distance (m)		Speed (m/s)	Distance (m)		Speed (m/s)
MP	43.00	0.71	MP	57.30	0.95
MCP	55.50	0.92	MCP	81.00	1.35
Obstacle test				
Average time (s)		Touches on the obstacle	Average time (s)		Touches on the obstacle
MP	25.36	0	MP	17.49	2
MCP	14.09	0	MCP	13.35	2
Slop test				
Average distance (cm)			Average distance (cm)		
MP	12.83		MP	11.60	
MCP	15.40		MCP	14.40	

4   Discussion and Conclusion

The analysis of the passive prosthesis was performed without an adaptation period of the prosthesis since the volunteers have been users of this model for more than two years. For a C-Leg knee prosthesis, a period of adaptation of the patients was observed in the AACD amputee clinic, on the supervision and orientation of the doctors and physiotherapists based on the mentioned protocols. This period was 5 (five) days, for 8 h/day divided into two turns of 4 h, totaling 40 h of use and adaptation before the evaluation tests.

Based on this information and on the results obtained it is realized that the knowledge of the human gait is of relevant importance for the analysis of the data. With this experience, it is possible to determine the instants of each stage of the gait and thus observe the behavior of each knee tested.

Analyzing the previous results of the kinematic tests presented in Table 1, it is observed that the linear track performed with the microprocessed prosthesis was executed in a shorter time (on average, 27.74% lower) and a higher speed (on average, 33.33%), or more efficiently. In the test of the square track (on average, 36.75% more velocity), a rapid change of direction is required, thus demanding a greater balance of the patient. In this test, a greater distance was obtained with the microprocessed prosthesis (on average, 36.09%).

In the obstacle and inclination tests, the microprocessed prosthesis offered a greater control and safety to the patient when compared with the mechanical prosthesis. These results make possible for the users to conclude the track with better results than with the mechanical prosthesis. With a shorter time in the obstacle test (on average, 35.96%) and a smaller slope (on average 21.98%), as can be seen in Table 1.

Based on all the evaluations, it can be affirmed in a previous analysis that: (A) the prosthesis provided by the SUS (Health Unic System of Brazil), the mechanical model 3R15, in the first moment, is functional allowing the patient a certain mobility. However, when observing the activities of a person daily, it is perceived that it is limited for some tasks, leading its users to a certain frustration by not performing some activities, decreasing their self-esteem; and (B) the microprocessed knee has a better functionality allowing a greater gait speed and body balance, a better response to spatial changes and obstacles, a better fit and control on the prosthesis and a greater physical safety.

In this first moment, it can be noticed that the use of microprocessed prostheses brings to the user improvement in his quality of life, such as the increase of self-esteem and the accomplishment of activities impossible before. In addition, there is an increase of the efficiency of the movements performed by the user. Although the study was carried out with a low number of volunteers, it obtained satisfactory results and more tests will be performed to obtain more solid statistical data.

Considering the anthropometric aspects of the Brazilian population, it is expected that new researchers will be encouraged and performed in this area since the data available are mostly from the North American population.

Future work indicates the dynamic evaluation of both prostheses with more volunteers in order to obtain a complete comparison with more data. This research intends the development of microprocessed prosthesis with low cost, low consumption and of Brazilian technology, making prostheses microprocessed more accessible to the population.

References

1. Carvalho, J.: Amputações de Membros Inferiores. Em Busca da Plena Reabilitação. 2nd edn. MANOLE, São Paulo (2003)
2. Silva, O.: A epopeia ignorada: a pessoa deficiente na história do mundo de ontem e de hoje. CEDAS, São Paulo (1987)
3. Bowker, H.K., Michael, J.W. (eds.): Atlas of limb prosthetics: surgical and prosthetic principles. 2nd edn. Boston: American Academy of Orthopaedic Surgeons (AAOS) (2002)
4. Fernandes, A.C.: AACD medicina física e reabilitação: princípios e prática. Artes Médicas, São Paulo (2004)
5. Ziegler, G.K.: Estimating the prevalence of limb loss in the United States: 2050. Arch. Phys. Med. Rehabil. **89**(3), 422–429 (2008)
6. Barbosa, D.P.: Perfil clínico e epidemiológico de pacientes amputados na associação de Assistência à Criança Deficiente. Anais Congresso Brasileiro de Fisiatria (2010)
7. Soares, A.S.O.D.C., Yamaguti, E.Y., Mochizuki, L., Amadio, A.C., Serrão, J.C.: Biomechanical parameters of gait among transtibial amputees: a review. Sao Paulo Med. J. **127**(5), 302–309 (2009)
8. Czerniecki, J.M.: Rehabilitation in limb defiency. Gait and Motion analisis. Arch. Phys. Med. Reabil. **77**, S3–S8 (1996)
9. Perry, J.: Análise de marcha: Sistemas de análise de marcha. MANOLE, Baruery-SP (2005)
10. Santos, C.P., Vieira, M.E.M., Sérgio L. Stevan, J.S.L.: Sensores inerciais aplicados à marcha humana no esporte. Seminário de Eletrônica e Automação—SEA 2016—19 a 21 de Setembro de 2016. Universidade Tecnológica Federal do Paraná—UTFPR
11. Sutherland, D.H.: Pediatric gait—normal and anormaldevelopmet. Ravenpress (1992)
12. Cavagna, G., Margaria, R.: Mechanics of walking. J. Appl. Physiol. **21**(1), 271–278 (1966)
13. Rose, J.: Marcha: teoria e prática da locomoção humana. 3rd end. Editorial Guanabara, São Paulo (2007)
14. De Lima, V.J.B.: Modelagem estrutural de joelhos para próteses transfemorais microprocessadas. Dissertação da Universiade Federal de Pernambuco, Recife –PE (2016)
15. Gottschalk, F., Stills, M.: The biomechanics of trans-femoral amputation. Prosthet. Orthot. Int. **18**, 12–17 (1994)
16. Jaegers, S.M.H.J.: Changes in hip muscles after above-knee amputation. Clen. Orthopand Rel. Res. **319**, 276–284 (1995)
17. Orendoff, M.: Gait efficiency using the C-Leg. J. Rehabil. Res. Dev. **43**(2), 239–246 (2006)

On the Load Share Between Nailing and Bone

Paulo P. Kenedi, José R. O. S. Neto, and Rodrigo R. P. Rodarte

Abstract

Intramedullary nailing, which is positioned inside a long bone as a human femur, has been used to fix fractured bones during the healing process, sharing the mechanical loads with bone. To achieve a good fracture consolidation, the available mechanical load has to be sufficient to activate completely the healing process. Thus, the estimation of the level of mechanical load, that is effectively shared between nailing and bone, is an important variable to be accessed. To reach this objective, an analytical model based in mechanics of solids, is presented to describe, at a femur diaphyseal cross section, the load share between bone and nailing. Also, the results of an elastic finite element model is provided as a reference. The results obtained show a good correspondence between models.

Keywords

Intramedullary nailing • Load share • Analytical model

1 Introduction

Intramedullary nailing, for now on called nailing, has been used to stabilize fractured bones and to shorten the patient recovery time, through enabling the load share between bone and nailing. The mechanical load has to be sufficient to activate completely the healing process to obtain an acceptable bone consolidation. Thus, the estimation of the level of mechanical load that is effectively shared between nailing and bone is an important variable to be accessed. In fact, after some weeks of the recovery time it is important that the patient effectively uses the member, where the broken bone is localized, to mechanically induces the activation of the healing process.

Many researchers have been spending efforts to describe aspects of biomechanical performance of skeletal systems, to understand, for instance, how gait patterns can affect the load distribution in human femurs, as Bergmann et al. [1] and Duda et al. [2]. Other researchers, as Cristofolini et al. [3], studied experimentally the bone superficial strains, using a custom designed jig to measure external surface strains at proximal human femur, generated by the load simulation of each thigh muscle. The results show a great variability of strain responses as a function of the muscles or of the selected group of muscles. Duda et al. [4], used a finite-element model to show the influence of muscle forces in human femur strain distribution. They show that the bone loaded with all the thigh muscles experienced a fairly homogeneous strain distribution. Also, Duda et al. [5], in an experimental study, determine that anatomical variability significantly influences the results of biomechanical analyses, particularly the moment arm of the various thigh muscles, and conclude that some muscle moment arms are very sensitive to the anatomical condition, such as gluteus maximus and m. rectus femoris, whereas others are not, such as gluteus medius and m. gastrocnemi.

Other experimental methods were used by Edwards et al. [6] stating that the external muscular loading of long bones is an important factor in determining stress and strain distributions at the external surface of cortical bone, where muscle forces were estimated by the utilization of force platform and motion capture data through static optimization in conjunction with a SIMM musculoskeletal model. Gdoutos et al. [7] did an interesting review of what other

P. P. Kenedi (✉) · J. R. O. S. Neto · R. R. P. Rodarte
Postgraduate Program in Mechanical Engineering and Materials Technology – PPEMM - CEFET/RJ, Rio de Janeiro, Brazil
e-mail: paulo.kenedi@cefet-rj.br

J. R. O. S. Neto
e-mail: netoengemec@yahoo.com.br

R. R. P. Rodarte
e-mail: rrodarte@globo.com

R. R. P. Rodarte
National Institute of Traumatology and Orthopedics – INTO, Rio de Janeiro, Brazil

researchers have already done in stress analysis of human femurs. Raftopoulos and Qassem [8] proposed two interesting analytical models: one with straight and homogeneous beams and other with curved and composite beams. The bone surface strains were measured by Simões et al. [9] who studied the influence of muscle action and a horizontally constrained femoral head on the strain distribution within the intact femur for three loading configurations: joint reaction force only, joint reaction force plus abductors, and joint reaction force plus the abductors, vastus lateralis, and iliopsoas, with the use of uniaxial strain gauges placed on the medial, lateral, anterior, and posterior sides of the proximal femur. Toridis [10] in an early work proposed an analytical model of human femur stress analysis taking into account both cortical and trabecular bones tissues at an arbitrary bone cross section. Also, a more detailed stress analysis for human femur, and also for osteosynthesis systems, were addressed in Kenedi and Riagusoff [11], Kenedi and Vignoli [12] and Taylor et al. [13].

To estimate the load shared by bone with nailing during, and also after, the healing process, the concept of stiffness needs to be used, as in Crandall et al. [14]. In fact, modeling the human femur and the nailing as two springs, in parallel configuration, the mechanical load sharing between them could be accessed through the use of each stiffnesses, with the application of the theory of mechanics of solids. To accomplish this objective many variables has to be available, as: the loads that are acting in proximal femur bone, the bone

and nailing geometry and the bone and nailing material mechanical properties. The proposed analytical model is presented in next section.

2 Analytical Model

To model the relation of external forces acting at proximal human femur and the internal loads acting in a human bone/nailing set, at a diaphyseal cross section, an analytical model is proposed with the utilization of mechanics of solids theory. The analytical formulation is presented and compared with a well-established finite element software, ANSYS. The analytical model supposes that cross sections, for both nailing and bone, are hollow circles. Only the cortical tissue is considered for bone and the nailing is considered to be made of stainless steel. It is supposed that all materials are isotropic and that all generated stresses remain elastic.

2.1 Equivalent Forces and Moments

The initial step of the analytical model consists in rewriting the external forces, shown in Fig. 1a, in an equivalent set of forces and moments at the cross section set 1 centroid (see Fig. 1b):

Fig. 1 **a** External forces and **b** equivalent force and moment at cross section 1
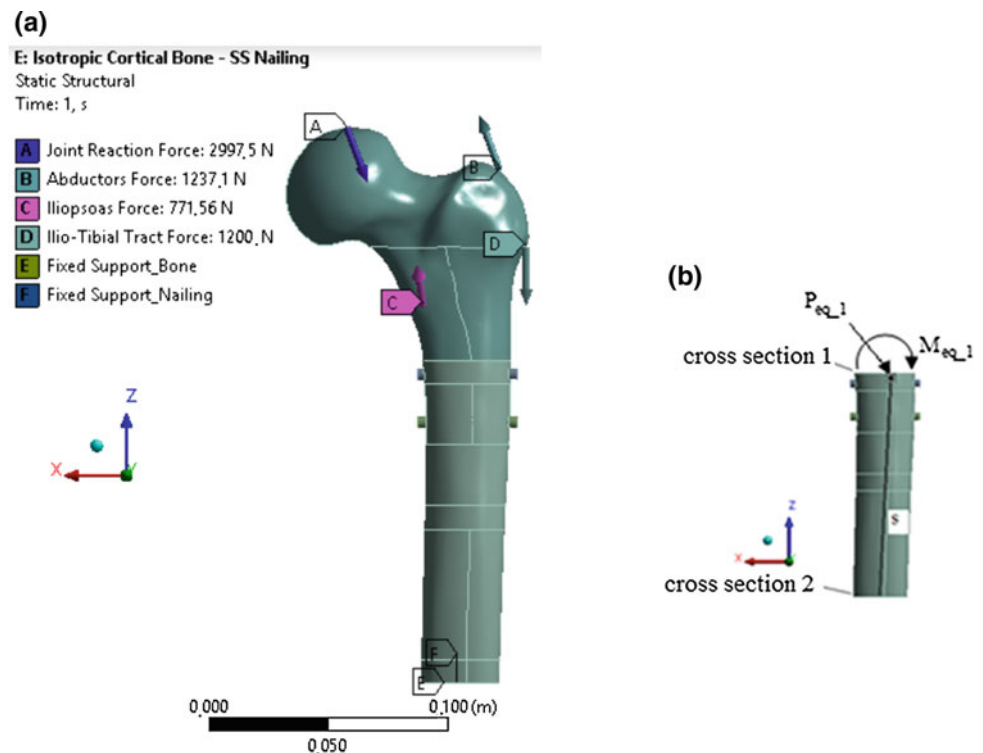
$$P_{\mathrm{i}} = P_i^x \vec{i} + P_i^y \vec{j} + P_i^z \vec{k} \quad d_{\mathrm{i}} = d_i^x \vec{i} + d_i^y \vec{j} + d_i^z \vec{k} \quad (1)$$

$$\begin{pmatrix} V_i^x \\ V_i^y \\ V_i^z \end{pmatrix} = \begin{pmatrix} P_i^x \\ P_i^y \\ P_i^z \end{pmatrix} \quad \begin{pmatrix} M_i^x \\ M_i^y \\ M_i^z \end{pmatrix} = \begin{pmatrix} d_i^y P_i^z - d_i^z P_i^y \\ d_i^z P_i^x - d_i^x P_i^z \\ d_i^x P_i^y - d_i^y P_i^x \end{pmatrix} \quad (2)$$

where, $\vec{i}$, $\vec{j}$ and $\vec{k}$ are unit vectors. The index i ranges from 1 to 4, because the four external forces, as can be seen in Fig. 1a. P_{i} and d_{i} are, respectively, the external forces and the distances between each force application point and the cross section set 1 centroid. The sum of forces ($V_{\mathrm{x\_1}}$, $V_{\mathrm{y\_1}}$, $V_{\mathrm{z\_1}}$) and the sum of moments ($M_{\mathrm{x\_1}}$, $M_{\mathrm{y\_1}}$, $M_{\mathrm{z\_1}}$), shown in Eq. (3), acts at the cross section set 1 centroid, generating the equivalent load $P_{\mathrm{eq\_1}}$ and the equivalent moment $M_{\mathrm{eq\_1}}$.

$$V_{x\_1} = \sum_{n=1}^{4} V_i^x \quad V_{y\_1} = \sum_{n=1}^{4} V_i^y \quad V_{z\_1} = \sum_{n=1}^{4} V_i^z$$
$$M_{x\_1} = \sum_{n=1}^{4} M_i^x \quad M_{y\_1} = \sum_{n=1}^{4} M_i^y \quad M_{z\_1} = \sum_{n=1}^{4} M_i^z \quad (3)$$

$$P_{eq\_1} = V_{x\_1}\vec{i} + V_{y\_1}\vec{j} + V_{z\_1}\vec{k}$$
$$M_{eq\_1} = M_{x\_1}\vec{i} + M_{y\_1}\vec{j} + M_{z\_1}\vec{k} \quad (4)$$

Figure 1a shows, schematically, the loading model configuration with four external static forces applied at femur's head, adapted from the Taylor's fourth load case of human left femur's head, Taylor et al. [13]. The external forces are named: (A) Joint Reaction—P1, (B) Abductors—P2, (C) Ilioopsoas—P3 and (D) Ilio-Tibial Tract—P4 (see Bitsakos et al. [15] for a more complete muscle loading case description). Figure 1b show a reduced version of Fig. 1a, with $P_{\mathrm{eq\_1}}$ and $M_{\mathrm{eq\_1}}$ applied at the cross section set 1 centroid.

Two additional steps have to be taken to estimate the equivalent forces and moments that are acting at bone and nailing cross section set 2, a diaphyseal cross section. First, the stiffness calculations have to be taken with the aid of Sect. 2.2 equations/tables, which are used to estimate the load share between bone and nailing, at cross section set 1. The result of this approach generates the Eq. (5), where the indexes m can be substituted by b for bone and in for nailing. The second step consists in calculate an equivalent force-couple system of cross section set 1 in cross section set 2, using Eqs. (6–7).

$$P_1^m = V_{x\_1}^m \vec{i} + V_{y\_1}^m \vec{j} + V_{z\_1}^m \vec{k}$$
$$M_1^m = M_{x\_1}^m \vec{i} + M_{y\_1}^m \vec{j} + M_{z\_1}^m \vec{k} \quad (5)$$

$$\begin{pmatrix} V_{\mathrm{x}}^m \\ V_{\mathrm{y}}^m \\ V_{\mathrm{z}}^m \\ M_{\mathrm{x}}^m \\ M_{\mathrm{y}}^m \\ M_{\mathrm{z}}^m \end{pmatrix} = \begin{pmatrix} V_{\mathrm{x\_1}}^m \\ V_{\mathrm{y\_1}}^m \\ V_{\mathrm{z\_1}}^m \\ s^y V_{z\_1}^m - s^z V_{y\_1}^m + M_{x\_1}^m \\ s^z V_{x\_1}^m - s^x V_{z\_1}^m + M_{y\_1}^m \\ s^x V_{y\_1}^m - s^y V_{x\_1}^m + M_{z\_1}^m \end{pmatrix} \quad (6)$$

$$P_{eq} = V_{\mathrm{x}}^m\vec{i} + V_{\mathrm{y}}^m\vec{j} + V_{\mathrm{z}}^m\vec{k} \quad M_{eq} = M_{\mathrm{x}}^m\vec{i} + M_{\mathrm{y}}^m\vec{j} + M_{\mathrm{z}}^m\vec{k}$$
$$s = s^x\vec{i} + s^y\vec{j} + s^z\vec{k} \quad (7)$$

where s is the distance between the centroids of cross sections sets 1 and 2. The results of Eq. (7) estimates the loadshare between bone and nailing at cross-section 2. In the next sub-section, the stiffness and loadshare calculations are made explicit.

2.2 Stiffnesses and Load Share Calculations

The stiffnesses calculations use the bone and nailing parts between cross sections sets 1 and 2. Both bone and nailing are modeled as hollow cylinders (see [16] for nailing real dimensions). The bone cross sections modeled as hollow circles is, obviously, a rough approximation of a real bone cross section as can be seen, for instance, in Fig. 3d. This limitation produces, for instance, the same value second moment of area in relation to each cross-section axis (x and y) and null product moment of area. Figure 2a shows a generic cross section at longitudinal coordinate (z axis). Figure 2b shows the lateral view of the set bone/nailing, between cross sections 1 and 2, showing that the bone shaft is also divided in two longitudinal parts, in series configuration, to better adaptation to the cross-section variations. The bone and the nailing are considered to be in parallel configuration, so the transversal displacements and slopes must be the same.

Where the indexes i and o means, respectively, inner and outer, r is a radius and L is a vertical length. Table 1 uses Tables 2 and 3 results, and load components of Eq. (4), through the utilization of a mathematical software, as Mathcad, for accessing the bone/nailing sharing load of cross section set 1, of Eq. (5), as in Crandall et al. [14].

Where each equivalent stiffness k_{eq} is calculated by the sum of bone and nailing stiffnesses (parallel configuration). For instance, the equivalent axial stiffness is calculated as: $k_{a\_eq} = k_a^b + k_a^{in}$. The elastic modulus of the nailing E^{in} is constant, but the elastic modulus of the bone E^{b} is not, but in this analytical model it was used an average value available in technical literature, as Duda et al. [5].

Fig. 2 a Nailing and bone general cross section set and **b** longitudinal cut of bone/nailing set
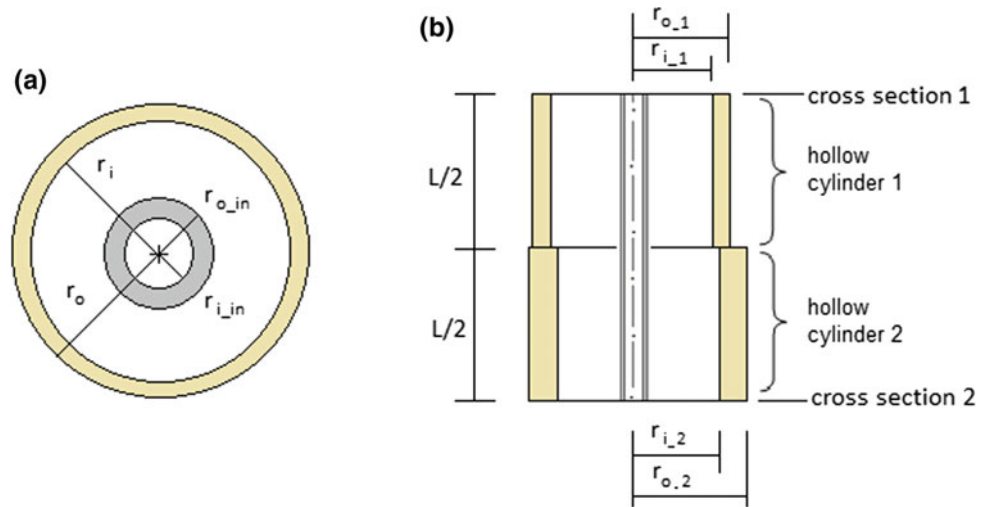
Table 1 Bone/nailing sharing load of cross section set 1

	Bone	Nailing
Shear force x axis[a]	$V_{x\_1}^b = \frac{k_x^b}{k_{x\_eq}} V_{x\_1}$	$V_{x\_1}^{in} = \frac{k_x^{in}}{k_{x\_eq}} V_{x\_1}$
Shear force y axis[a]	$V_{y\_1}^b = \frac{k_y^b}{k_{y\_eq}} V_{y\_1}$	$V_{y\_1}^{in} = \frac{k_y^{in}}{k_{y\_eq}} V_{y\_1}$
Axial	$V_{z\_1}^b = \frac{k_a^b}{k_{a\_eq}} V_{z\_1}$	$V_{z\_1}^{in} = \frac{k_a^{in}}{k_{a\_eq}} V_{z\_1}$
Bend x axis	$M_{x\_1}^b = \frac{k_{bx}^b}{k_{bx\_eq}} M_{x\_1}$	$M_{x\_1}^{in} = \frac{k_{bx}^{in}}{k_{bx\_eq}} M_{x\_1}$
Bend y axis	$M_{y\_1}^b = \frac{k_{by}^b}{k_{by\_eq}} M_{y\_1}$	$M_{y\_1}^{in} = \frac{k_{by}^{in}}{k_{by\_eq}} M_{y\_1}$
Torsion	$M_{z\_1}^b = \frac{k_t^b}{k_{t\_eq}} M_{z\_1}$	$M_{z\_1}^{in} = \frac{k_t^{in}}{k_{t\_eq}} M_{z\_1}$

[a]The shear force is supposed to be resisted only by bending moment stiffness

Note that the transversal sharing load for bone and nailing, for both axis directions x and y, were calculated assuming that both shear forces V_x and V_y are resisted by only bending moment stiffnesses. It was supposed that the transversal concentrated shear forces were acting at a free extremity (section 1) of a vertical beam that was fixed in section 2. Although there are the generation of bending moments and shear forces, it was considered that the bending moment stiffnesses were preponderant in comparison with shear force stiffnesses.

Table 3 Bone/nailing stiffnesses

Load	Bone (two hollow cylinders in series configuration)	Nailing
Shear force x axis[a]	$k_x^b = \frac{24E^b}{L^3} \left(\frac{1}{I_{x\_1}^b} + \frac{7}{I_{x\_2}^b} \right)^{-1}$	$k_x^{in} = \frac{3E^{in}I_x^{in}}{L^3}$
Shear force y axis[a]	$k_y^b = \frac{24E^b}{L^3} \left(\frac{1}{I_{y\_1}^b} + \frac{7}{I_{y\_2}^b} \right)^{-1}$	$k_y^{in} = \frac{3E^{in}I_y^{in}}{L^3}$
Axial	$k_a^b = \frac{2E^b}{L} \left(\frac{1}{A_{x\_1}^b} + \frac{1}{A_{x\_2}^b} \right)^{-1}$	$k_a^{in} = \frac{A^{in}E^{in}}{L}$
Bend x axis	$k_{bx}^b = \frac{2E^b}{L} \left(\frac{1}{I_{x\_1}^b} + \frac{1}{I_{x\_2}^b} \right)^{-1}$	$k_{bx}^{in} = \frac{E^{in}I_x^{in}}{L}$
Bend y axis	$k_{by}^b = \frac{2E^b}{L} \left(\frac{1}{I_{y\_1}^b} + \frac{1}{I_{y\_2}^b} \right)^{-1}$	$k_{by}^{in} = \frac{E^{in}I_y^{in}}{L}$
Torsion	$k_t^b = \frac{2G^b}{L} \left(\frac{1}{J_1^b} + \frac{1}{J_2^b} \right)^{-1}$	$k_t^{in} = \frac{J^{in}G^{in}}{L}$

[a]The shear forces V_x and V_y were only resisted by bending moment stiffnesses

Finally, to obtain the load share, at cross section set 2, the values of Eq. (5), was recalculated, using the distance s between the centroids of cross sections sets 1 and 2, by the utilization of Eqs. (6–7). In next section the application of the numerical model is presented.

Table 2 Cross section variables

	Bone	Nailing
Area	$A_1^b = \pi(r_{o\_1}^2 - r_{i\_1}^2)$ $A_2^b = \pi(r_{o\_2}^2 - r_{i\_2}^2)$	$A^{in} = \pi(r_{o\_in}^2 - r_{o\_in}^2)$
Area moment of inertia	$I_{x\_1}^b = I_{y\_1}^b = \frac{\pi}{4}(r_{o\_1}^4 - r_{i\_1}^4)$ $I_{x\_2}^b = I_{y\_2}^b = \frac{\pi}{4}(r_{o\_2}^4 - r_{i\_2}^4)$	$I_x^{in} = I_y^{in} = \frac{\pi}{4}(r_{o\_in}^4 - r_{i\_in}^4)$
Polar area moment of inertia	$J_1^b = \frac{\pi}{2}(r_{o\_1}^4 - r_{i\_1}^4)$ $J_2^b = \frac{\pi}{2}(r_{o\_2}^4 - r_{i\_2}^4)$	$J^{in} = \frac{\pi}{2}(r_{o\_in}^4 - r_{i\_in}^4)$

Fig. 3 Mesh **a** lateral view
b transversal view at cross section
set 2. Cross sections sets: **c** 1 and
d 2
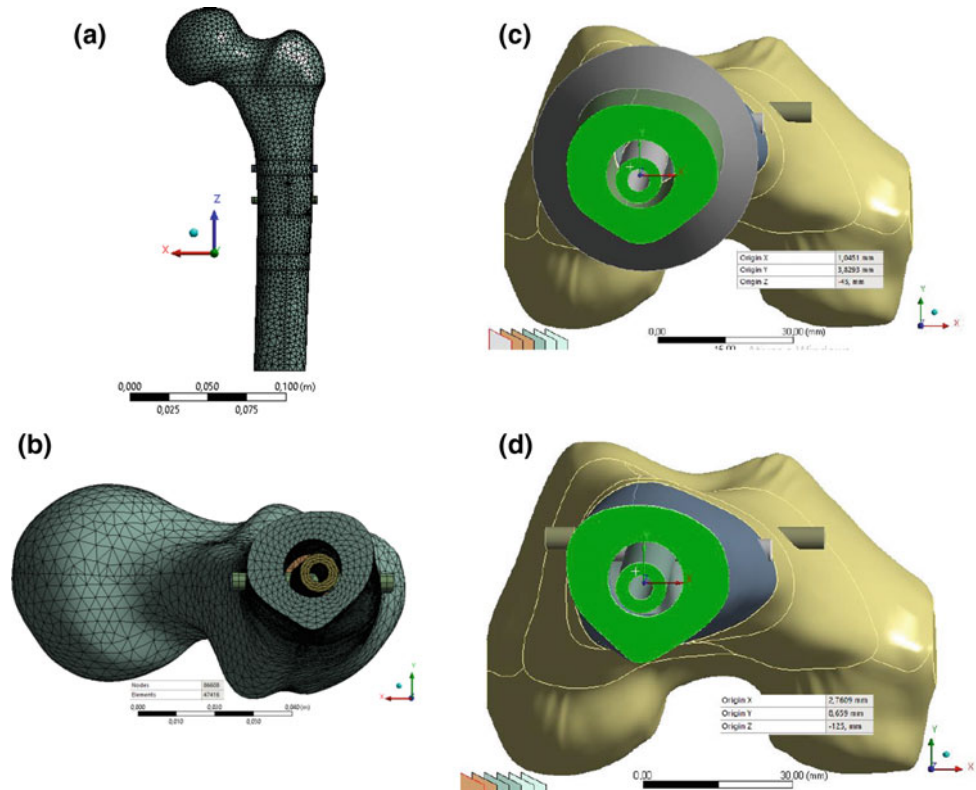
3 Numerical Model

The finite element software ANSYS 16 was used as a reference to evaluate the analytical model performance. The forces applied are shown in Fig. 1a. The bone was modeled as linear, elastic and isotropic, with E^b = 20 GPa, G^b = 8.1 GPa, v^b = 0.236. The nailing was modeled as elastic behavior, with E^{in} = 193 GPa, G^{in} = 73.6 GPa, v^{in} = 0.31, as in Edwards et al. [6]. The four external forces components are (N): P_1 = (−1,062; −130; −2,800), P_2 = (430; 0; 1,160), P_3 = (78; 560; 525) and P_4 = (0; 0; −1,200). The distances between forces point of application and the cross section set 1 centroid are (mm): d_1 = (50; 12; 97.6), d_2 = (−14.2; −26; 76.1), d_3 = (18.1; −25.4; 23.3) and d_4 = (−25.3; −3; 47.6). The vertical distance z between cross sections sets 1 and 2 is 160 mm. The cross-section bone geometry is defined by r_{i_1} = 13.1 mm, r_{o_1} = 14.4 mm, r_{i_2} = 14.7 mm, r_{o_2} = 16.7 mm, and the cross section intramedullary nailing is defined by r_{i_in} = 2.5 mm and r_{o_in} = 5 mm. Figure 3 shows the applied mesh and cross sections sets 1 and 2 geometry.

Note that at the external cross section bone radius are far from be considered circular (for instance, see Fig. 3c, d). Consequently, to establish a representative circular pattern, yellow circles were drawn at bone external positions: one tangent to inner positions (r_{o_inner}) and the other tangent to outer positions (r_{o_outer}), as shown in Fig. 6, at Appendix.

Arbitrarily, it was established that outer radius r_{o_i} occupies an inside position between yellow circles, accessed in function of the mean value between of the area moment of inertia of the yellow circles:

$$r_{o\_i} = \sqrt[4]{4\frac{r_{o_{inner}}^4 + r_{o_{outer}}^4}{2}} \qquad (8)$$

A 2.0 mm mesh was generated for bone and nailing, after a convergence study. 47416 solid elements (SOLID185, SOLID186 and SOLID187) and contact elements (CONTA174 and TARGE170) were used, as well 86608 nodes. All contact surfaces were considered as BONDED, with the use of Model Predictive Control (MPC) formulation.

In next section the results for both, analytical and numerical models, are presented.

4 Results

Both results, for analytical and numeric models, are presented in this section. Figure 4 shows the numeric results from ANSYS 16 software. In Fig. 4, the F.E. numeric model outputs are shown, with the reaction's forces and moments of a diaphyseal region obtained at the cross section set 2.

In Fig. 5 shows a comparison between analytical and numeric results. The sequential numeration below the
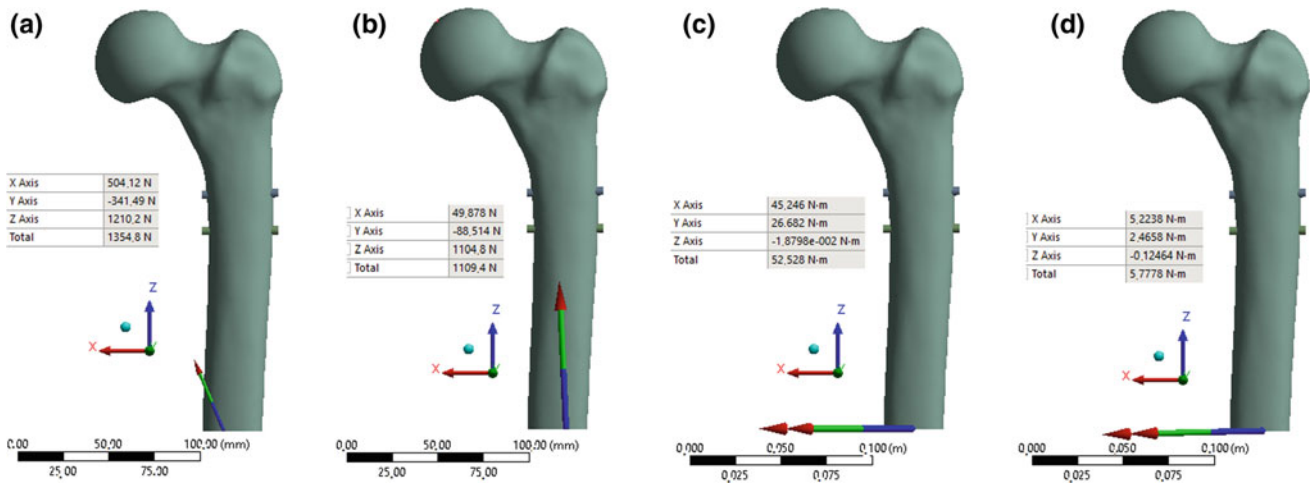
Fig. 4 Finite element results: forces **a** bone and **b** nailing; Moments **c** bone and **d** nailing
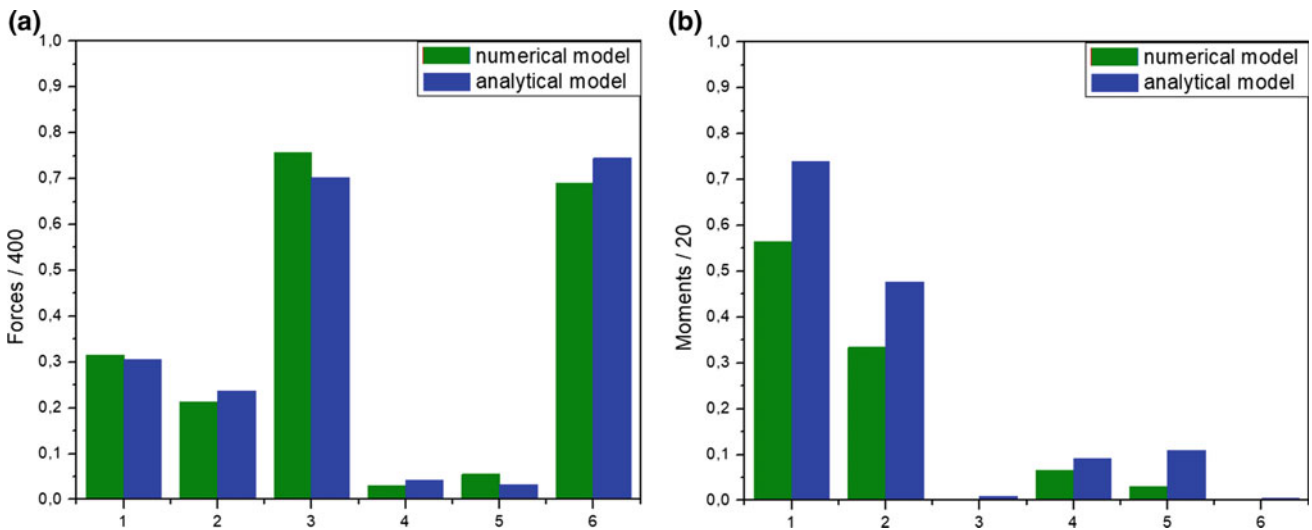
Fig. 5 Models results comparison: **a** forces and **b** moments

horizontal axis, for the Fig. 5a, are: 1: V_x^b, 2: V_y^b, 3: V_z^b, 4: V_x^{in}, 5: V_y^{in} and 6: V_z^{in}; and, for the Fig. 5b, equivalently: 1: M_x^b, 2: M_y^b, 3: M_z^b, 4: M_x^{in}, 5: M_y^{in} and 6: M_z^{in}.

In Fig. 5a shows the force share for transversal forces (V_x and V_y), where the bone parcel is more significative than the nailing one, while for axial force (V_z) the distribution between bone and nailing is quite equitable. The moments share shows, in Fig. 5b, that for cross section moments (M_x and M_y) the bone parcel is more significative than the nailing one, while the torcional moment (M_z) is quite small for both bone and nailing, almost non appearing in Fig. 5b.

Although the analytical model has a quite good performance when compared with numerical model, based in commercial F.E. software, there are some areas that this model can be improved as, for instance, a better description of bone cross section geometry.

5 Conclusions

A solid mechanics approach was used to implement a simplified analytical model to access the load sharing between bone and nailing, considering a diaphyseal cross section set, of a human femur. The analytic model results, when compared to the F.E. numerical model, used as reference, generated results quite close, for major forces and moments, in bone and nailing.

For this bone/nailing model, for the given loading, resulted in larger forces in longitudinal axis for both bone and nail, with comparable values. The transversal forces at bone were around one third of the longitudinal bone force and in turn, at nailing were around one third, or less, of the transversal forces in bone. Bending moments results indicate that for bone were larger than for nailing. The torsional moments were irrelevant for both, bone and nailing.
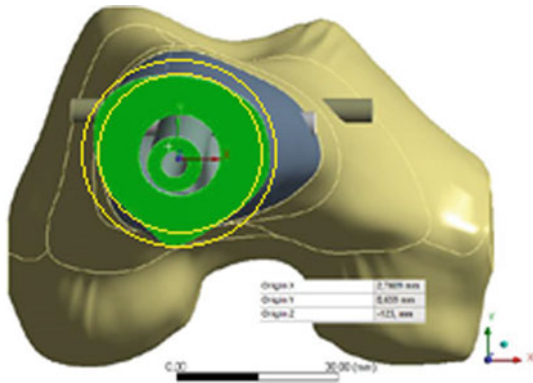
Fig. 6 Yellow circles drawn at bone external positions of the bone cross section 2: one tangent to inner positions and the other tangent to outer positions (Colour figure online)

Appendix

The geometric expressions for both, hollow cylinders for bone and for nailing are explicitated in Table 2. These expressions are used in Table 3.

Note that the cross section geometric parameters of bone as area, area moment of inertia, polar area moment of inertia can be different for each part of L/2 vertical length. Table 3 presents the stiffness calculations, using Castigliano's theorem (see Crandall et al. [14]), which in turn were used in Table 1 (Fig. 6).

Note that the bone and nailing stiffnesses for shear were not calculated, because they were considered not significant.

References

1. Bergmann, G., Deuretzbacher, G., Heller, M., Griachen, F., Rohlmann, A., Strauss, J., Duda, G.N.: Hip contact forces and gait patterns from routine activities. J. Biomech. **34**, 859–871 (2001)
2. Duda, G.N., Schneider, E., Chao, E.Y.S.: Internal forces and moments in the femur during walking. J. Biomech. **30**(9), 933–941 (1997)
3. Cristofolini, L., Viceconti, M., Toni, A., Giunti, A.: Influence of thigh muscles on the axial strains in a proximal femur during early stance in gait. Technical note. J. Biomech. **28**(5), 617–624 (1995)
4. Duda, G.N., Heller, M., Albinger, J., Shulz, O., Schneider, O., Claes, L.: Influence of muscle forces on femoral strain distribution. Technical note. J. Biomech. **31**, 841–846 (1998)
5. Duda, G.N., Brand, D., Freitag, S., Lierse, W., Schneider, E.: Variability of femoral muscle attacments. Technical note. J. Biomech. **29**(9), 1185–1190 (1996)
6. Edwards, W.B., Gillette, J.C., Thomas, J.M., Derrick, T.R.: Internal femoral forces and moments during running: implications for stress fracture development. Clin. Biomech. **23**, 1269–1278 (2008)
7. Gdoutos, E.E., Raftopoulos, D.D, Baril, J.D.: A critical review of the biomechanical stress analysis of the human femur. Biomater. **3**(1), 2–8 (1982). Rev
8. Raftopoulos, D.D., Qassem, W.: Three-dimensional curved beam stress analysis of the human femur. J. Biomed. Eng. **9**, 356–366 (1987)
9. Simões, J.A., Vaz, M.A., Blatcher, S., Taylor, M.: Influence of head constraint and muscle forces on the strain distribution within the intact femur. Med. Eng. Phys. **22**, 453–459 (2000)
10. Toridis, T.G.: Stress analysis of the femur. J. Biomech. **2**, 163–174 (1969)
11. Kenedi, P.P., Riagusoff, I.I.T.: Stress development at human femur by muscle forces. J. Braz. Soc. Mech. Sci. Eng. **37**(1), 31–43 (2015). https://doi.org/10.1007/s40430-014-0164-9
12. Kenedi, P.P., Vignoli, L.L.: An osteosynthesis plate analytical model. J. Braz. Soc. Mech. Sci. Eng. **39**, 645–659 (2017). https://doi.org/10.1007/s40430-016-0598-3
13. Taylor, M.E., Tanner, K.E., Freeman, M.A.R., Yettran, A.R.: Stress and strain distribution within the intact femur: compression or bending? Med. Eng. Phis. **18**(2), 122–131 (1996)
14. Crandall, S.H., Dahl, N.C., Lardner, T.J.: An Introduction to the Mechanics of Solids. Mc Graw Hill Int. Editions, 2nd Edition with SI units (1978)
15. Bitsakos, C., Kerner, J., Fisher, I., Amis, A.A.: The effect of muscle loading on the simulation of bone remodelling in the proximal femur. J. Biomech. **38**, 133–139 (2005)
16. AO Foundation. https://www2.aofoundation.org/ (2013)

Biomechanics of Postural Control in Yoga: A Pilot Study

Dafne Pires Pinto, Pedro Sarmet, Alexandre Visitainer Pino, and Luciano Luporini Menegaldo

Abstract

The purpose of this study is comparing the postural control between practitioners and non-practitioners of Yoga. Four subjects (two practitioners of Yoga) performed quiet standing for 10 s, followed by Vriksasana (tree posture) for 45 s in an eight cameras, four force plate motion capture system. A whole-body OpenSim model was used to calculate by inverse kinematics the body center of mass (COM) and joint angles. The results showed that Yoga practitioners presented smaller and less variable center of pressure (COP) area, lumbar, hips, ankle and subtalar angles, which can be related to better postural control.

Keywords

Postural control • Motor control • Yoga • OpenSim

1 Introduction

Movement is an important aspect of life. It is essential for our ability to walk, run, play and perform other everyday movements [1]. In special, balance maintenance and posture are important for performing these tasks. Maintaining the vertical posture against the gravity field is a complex, due to three main factors [2]. The first is the inherently unstable structure of the human body, usually modeled as an inverted pendulum with multiple joints along its axis, that must be balanced in a relatively small support area [2]. The body's center of mass (COM) is located above the ground, and its projection lie in a small support area with several joints between the COM and the feet. The second factor is the frequent changes in external forces actuating on the body.

And the third factor is the voluntary actions taken by the subject himself that are sources of disturbances.

The main neuromotor phenomena related to these three factors are the postural oscillations, pre-programmed reactions and anticipatory postural adjustments (APAs) [2]. In particular, postural oscillations are studied by observing the deviations of the COM in the horizontal plane; or from the resultant of the vertical forces acting on the body from a support surface, called pressure center (COP). Postural oscillations can be decomposed into two components: rambling and trembling. The rambling corresponds to the migration of the reference point of equilibrium, while the trembling is the oscillation of the COP, around the rambling trajectory [3]. Several studies have been published regarding the movements associated to static and dynamic postures, evaluating bipodal or single leg quiet standing [4], walking [5], jumping [6] and in yoga postures [7].

The benefits of Yoga practice include improved concentration, stress relief, muscle strengthening, what results in improved balance control. Yoga postures require specific motor control strategies, which are acquired by the practitioners by means of mental and physical discipline. The biomechanics of such body postures has not been extensively studied and may reveal new motor control strategies acquired by the practitioners. The present work aims at describing and comparing some aspects of the postural control between a group of Yoga practitioners (YG) and healthy non-practitioner controls (CG), during the performance of the Vriksasana (tree posture). Posturography and kinematical analysis were used for characterizing the postural movements and the main differences between the groups.

2 Materials and Methods

Four subjects, two practitioners and two non-practitioners of Yoga, performed Vriksasana (tree posture) and Natarajasana (Shiva Nataraja posture) (Fig. 1). The non-practitioners of

D. P. Pinto (✉) · P. Sarmet · A. V. Pino · L. L. Menegaldo
Federal University of Rio de Janeiro, Av. Horácio de Macedo, Rio de Janeiro, 2030, Brazil
e-mail: dafnepp@ufrj.br

Fig. 1 a Quiet standing and
b Vriksasana (tree posture)
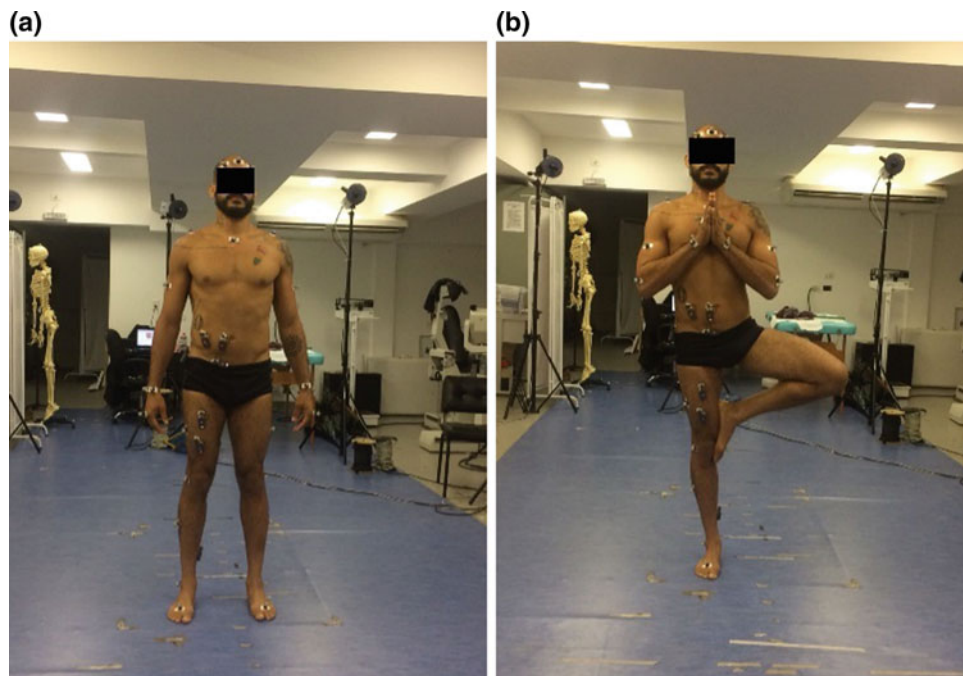
Yoga were labeled as control 1 (male 1.80 m, 82.5 kg, 28 years) and control 2 (female 1.61 m, 60 kg, 32 years), and the practitioners of yoga as Yoga 1 (male, 1.75 m, 74.8 kg, 37 years) and Yoga 2 (female, 1.51 m, 51 kg, 29 years). They agreed to participate in the study and signed a Free and Informed Consent Term. The protocol of this study was approved by the Research Ethics Committee of the University Hospital Clementino Fraga Filho—CEP/HUCFF (71244317300005257). Kinematics, ground reaction force and center of pressure (COP) were captured using a BTS Smart-D (BTS *Bioengineering*, Italy) system, consisting of eight cameras and four force platforms (40 cm × 60 cm) (BTS *Bioengineering*, Italy). Reflective markers were placed on bony prominences (i.e., anatomical points).

A full-body marker-set provided by BTS was used (Table 1). For static acquisition, the subjects remained with each foot over a separated force plate in quiet standing, feet spaced at hip width, for 10 s (Fig. 1). Then, the subjects were asked to change to the tree posture from quiet standing, keeping the dominant leg (right) in the ground, and stay as steady as possible during 45 s. The COP obtained for the right leg was labeled as COP r. The pre-processing was performed with the Smart Tracker and Smart Analyzer software (BTS *Bioengineering*, Italy). OpenSim 3.3 was used to obtain the center of mass (COM) and to solve Inverse Kinematics to estimate the joint angles. OpenSim LaiArnold_2017 model [8] was applied, and anthropometric measurements were taken for model scaling. The

Table 1 Marker-set of anatomical points with respective anatomical description

Symbol	Anatomic description
Head	A central point in the head
r, l head	The sides of the head
Nasion	Nasal bone
r, l zyg pr	Zygomatic processes
C7	Thorny process of the 7th cervical vertebra
T8	Thorny process of the 8th thoracic vertebra
r, l should	Acronyms
Sternum	Sternum
p xiph	Xiphoid process
r, l up arm	Arms
r, l elbow	Humerous epicondyles
r, l radius	Radio styloid processes
r, l ulna	Ulna styloid processes
r, l hand	Third metacarpal
r, l psis	Upper posterior iliac spine
r, l asis	Upper anterior iliac spine
r, l bar 1	Thighs
r, l knee	Femoral epicondyles
r, l bar 2	Shins
r, l mall	Malleoli
r, l heel	Heels
r, l meet	Second metatarsal

post-processing was made in Matlab. The signals from markers and force platforms were filtered using a fourth-order zero lag Buttherworth low pass filter at cutoff frequency of 6 Hz.

3 Results and Discussions

3.1 Posturography

Figures 2, 3, 4, 5 and 6 show the postural biomechanical data obtained from all of the subjects during 20 s of stay in the tree posture after stabilization. The reference system is defined as X-axis pointing forward (anteroposterior direction), Y-axis up and Z-axis (mediolateral direction) to the right. Table 2 shows COP displacement variables.

In general, compared to CG, it is observed that YG presented oscillations of smaller amplitudes in COM and COP, smaller DOT, less variability and less amplitude in trajectory of COP. The statokinesiograms show smaller areas for YG.

3.2 Joint Angles

Figures 7, 8, 9 and 10 show the joint angles obtained for control 1, control 2, Yoga 1 and Yoga 2, respectively, during

Fig. 2 Control 1 in tree posture. Ground reaction forces (GRFx (**a**), GRFy (**b**), GRFz (**c**), center of mass (COM x (**d**), COM y (**e**) and COM z (**f**)) and center of pressure (COP r x and COP r z (red line in (**d**) and (**f**)))
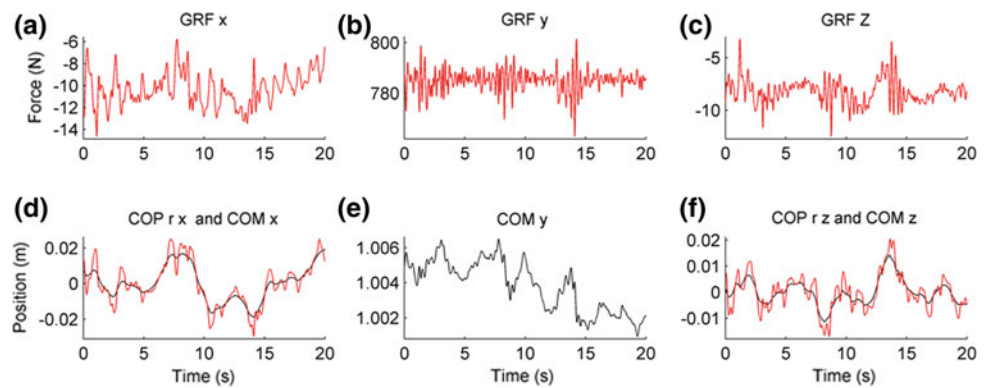
Fig. 3 Control 2 in tree posture. Ground reaction forces (GRFx (**a**), GRFy (**b**), GRFz (**c**), center of mass (COM x (**d**), COM y (**e**) and COM z (**f**)) and center of pressure (COP r x and COP r z (red line in (**d**) and (**f**)))
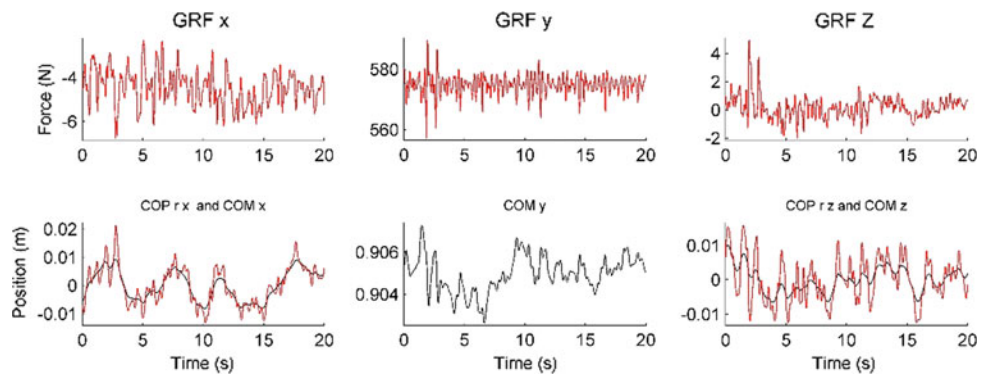
Fig. 4 Yoga 1 in tree posture. Ground reaction forces (GRFx, GRFy, GRFz, center of mass (COM x, COM y, and COM z) and center of pressure (COP r x and COP r z (red line))
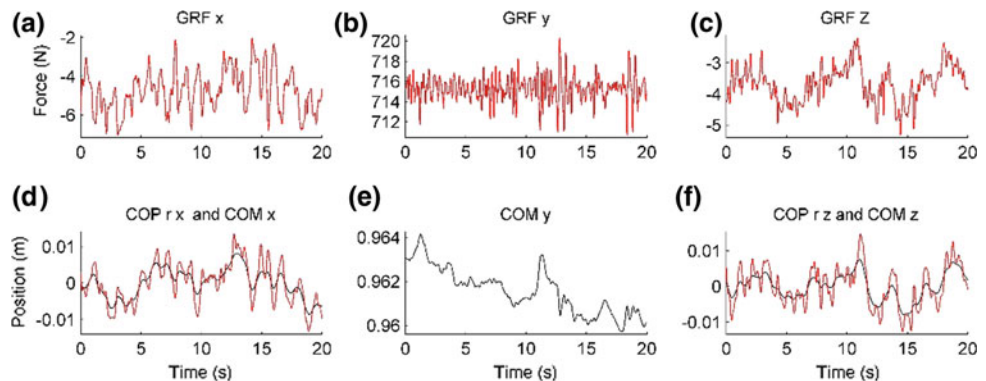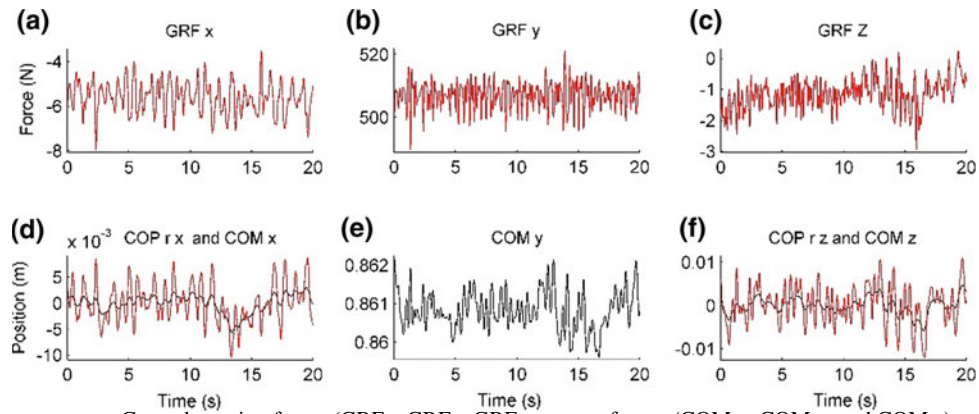
Fig. 5 Yoga 2 in tree posture. Ground reaction forces (GRFx, GRFy, GRFz, center of mass (COM x, COM y, and COM z) and center of pressure (COP r x and COP r z (red line))
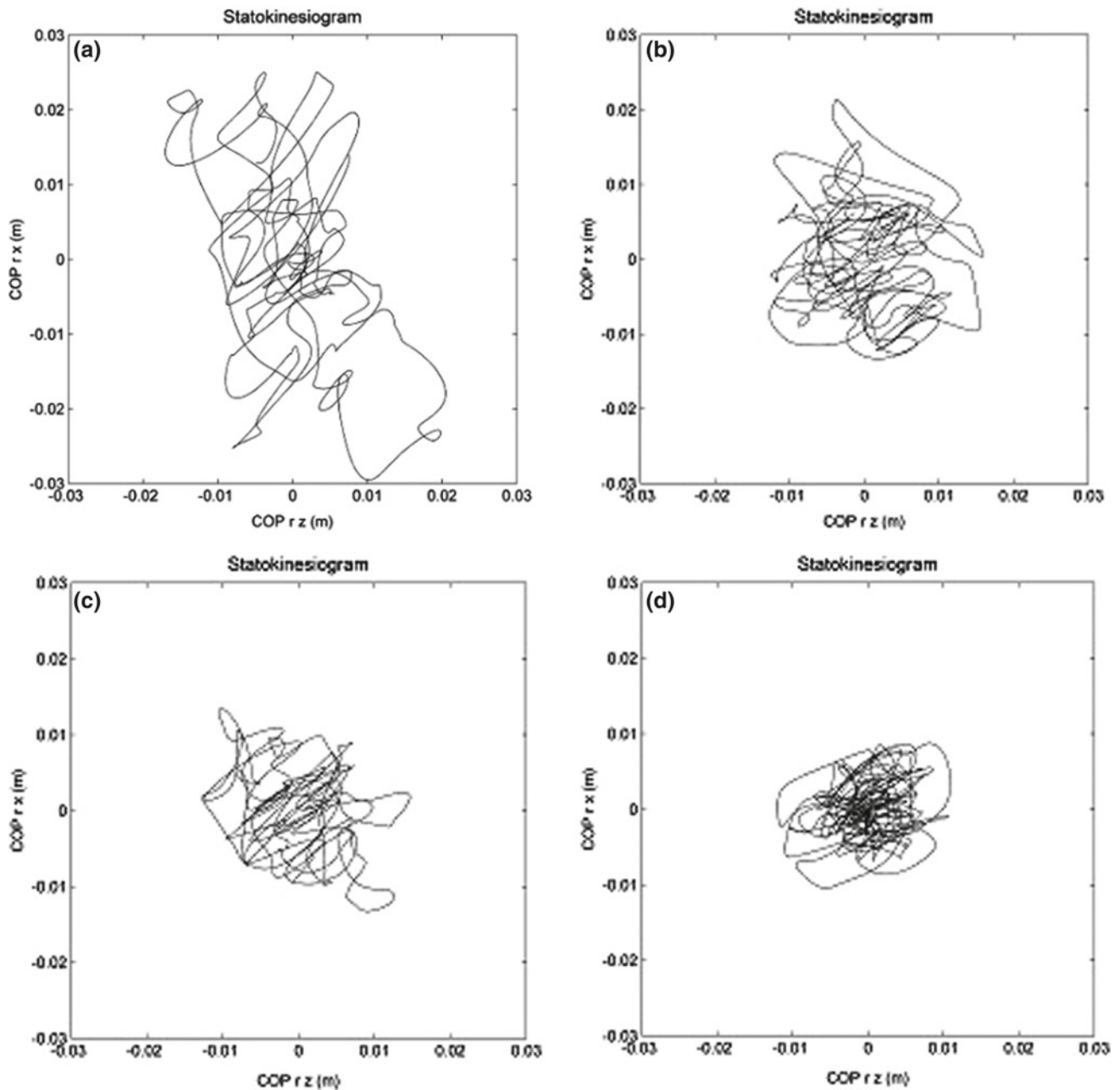
Fig. 6 Statokinesiograms obtained for control 1 (**a**), control 2 (**b**), Yoga 1 (**c**) and Yoga 2 (**d**) during 20 s of performance of tree posture

Table 2 Variables for analysis of COP from tree posture

Variable	Control 1	Control 2	Yoga 1	Yoga 2
Area (m^2)	0.0014	7.9401×10^{-4}	5.6539×10^{-4}	2.929×10^{-4}
Total displacement of COP sway (DOT) (m)	57.1041	42.1583	35.4955	24.9134
Standard deviation of COP displacement in x axis (SDx)	0.0117	0.0067	0.0055	0.0037
Standard deviation of COP displacement in z axis (SDz)	0.0068	0.0064	0.0056	0.0043
Amplitude of COP displacement in x axis (AdCx) (m)	0.0546	0.0347	0.0267	0.0192
Amplitude of COP displacement in z axis (AdCz) (m)	0.0374	0.0286	0.0273	0.0229
Mean velocity of COP in x axis (MVx) (m/s)	0.0265	0.0231	0.0185	0.0237
Mean velocity of COP in z axis (MVz) (m/s)	0.0225	0.0322	0.0211	0.0338
Total mean velocity of COP (TMV) (m/s)	0.0375	0.0430	0.0304	0.0452
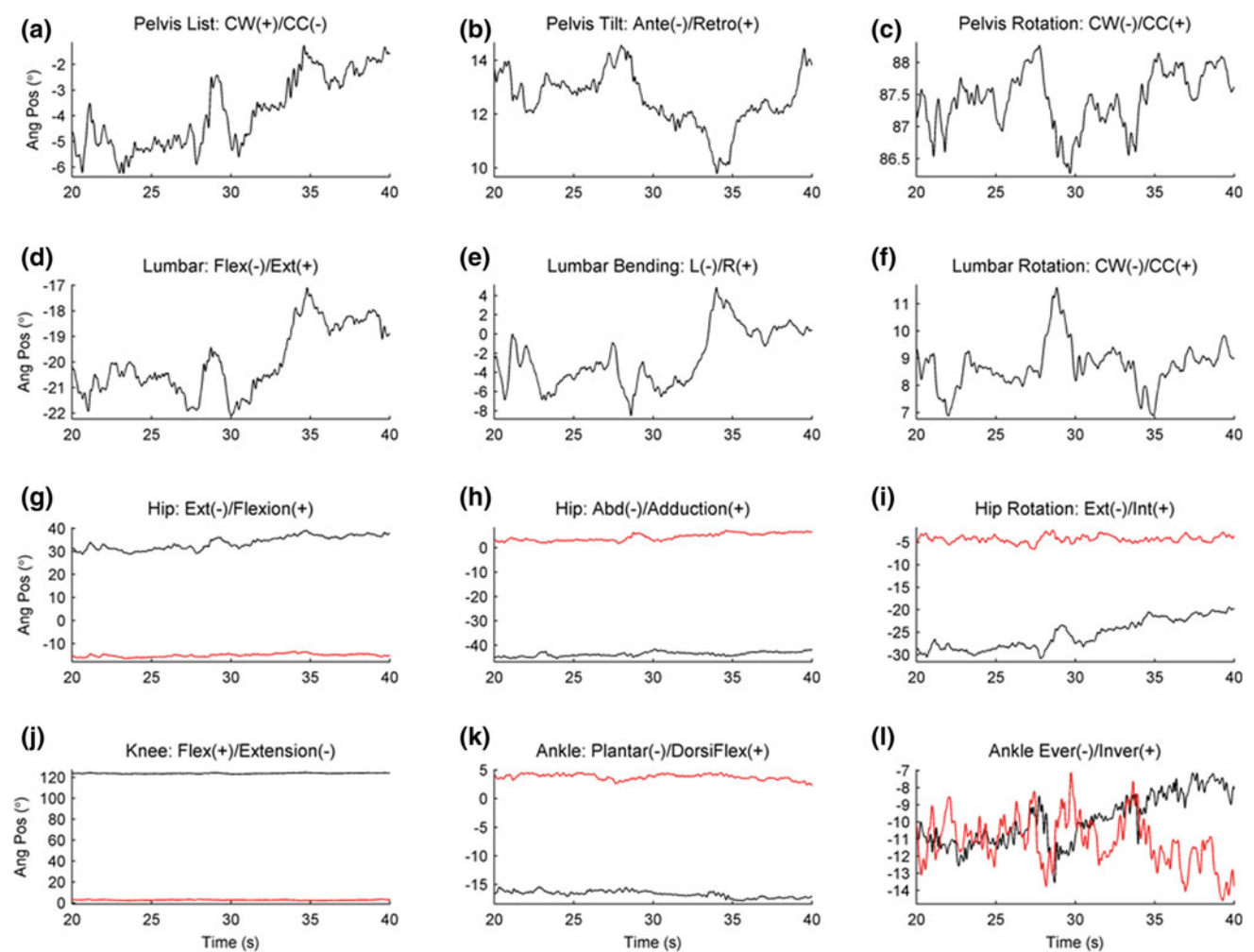
Fig. 7 Control 1 in tree posture. Joint angles obtained for pelvis list (**a**), pelvis tilt (**b**), pelvis rotation (**c**), lumbar flexion/extension (**d**), lumbar bending (**e**), lumbar rotation (**f**), hip extension/flexion (**g**), hip abduction/adduction (**h**), hip rotation (**i**), knee flexion/extension (**j**), angle plantarflexion/dorsiflexion (**l**) and ankle eversion/inversion (**m**). The red line corresponds to right leg
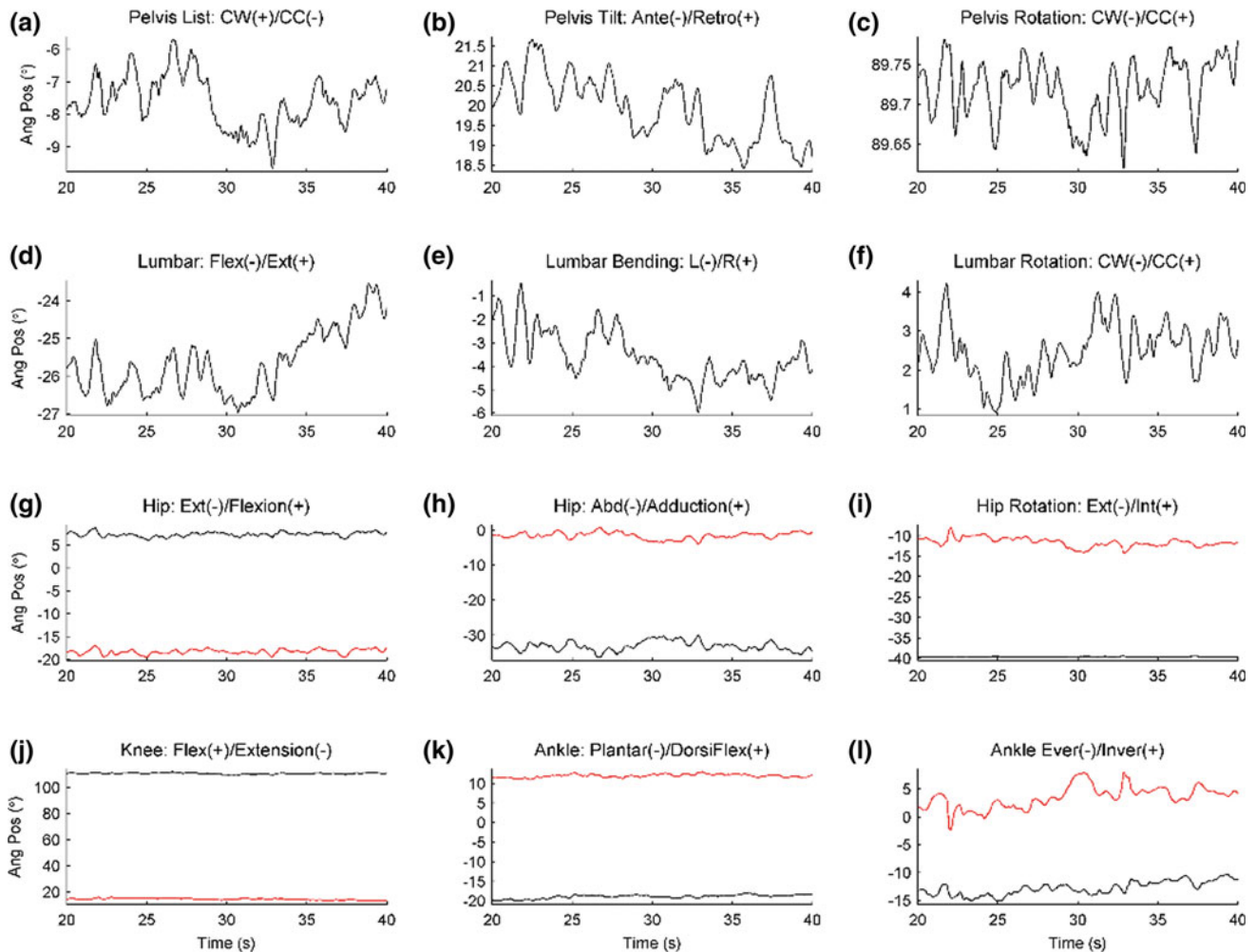
Fig. 8 Control 2 in tree posture. Joint angles obtained for pelvis list (**a**), pelvis tilt (**b**), pelvis rotation (**c**), lumbar flexion/extension (**d**), lumbar bending (**e**), lumbar rotation (**f**), hip extension/flexion (**g**), hip abduction/adduction (**h**), hip rotation (**i**), knee flexion/extension (**j**), angle plantarflexion/dorsiflexion (**l**) and ankle eversion/inversion (**m**). The red line corresponds to right leg

the performance of the tree posture. Tables 3 and 4 show the means, standard deviations and amplitudes obtained for the joint angles.

Yoga practitioners presented greater mean angles of pelvis list, smaller angles of lumbar bending and lumbar rotation, more abduction in both hips, more external rotation in right (support) hip, more flexion in both knees, more dorsiflexion and inversion in the right ankle.

Also, YG showed less variability in pelvis tilt, lumbar extension, lumbar bending, lumbar rotation, hip adduction, left knee, right ankle and right subtalar angles. The amplitudes were smaller for pelvis list, lumbar extension, lumbar bending, lumbar rotation, left hip flexion, hip adduction, left

knee and right subtalar angles. The smaller amplitude may be related to the smaller standard deviation. YG adopts, for the base leg, flexion of knee, dorsiflexion and inversion of subtalar joint, what is possibly related to the smaller displacement of the COP.

4 Conclusions

As expected, trained Yoga practitioners presented better postural control when performing the tree posture, evidenced mainly by a smaller displacement of COP compared to the untrained CG. These preliminary results indicate that better
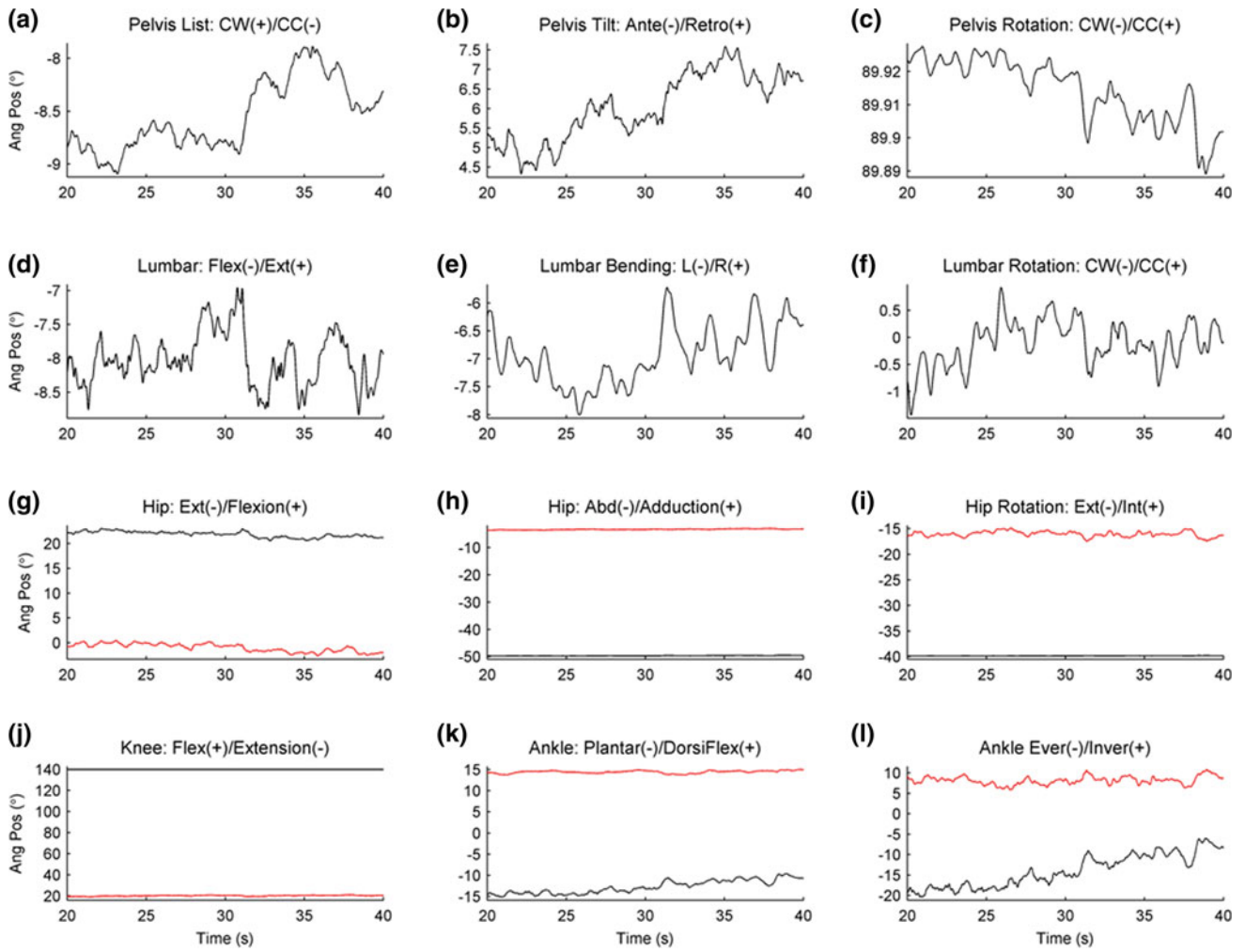
Fig. 9 Yoga 1 practitioner in tree posture. Joint angles obtained for pelvis list (**a**), pelvis tilt (**b**), pelvis rotation (**c**), lumbar flexion/extension (**d**), lumbar bending (**e**), lumbar rotation (**f**), hip extension/flexion (**g**), hip abduction/adduction (**h**), hip rotation (**i**), knee flexion/extension (**j**), angle plantarflexion/dorsiflexion (**l**) and ankle eversion/inversion (**m**). The red line corresponds to right leg
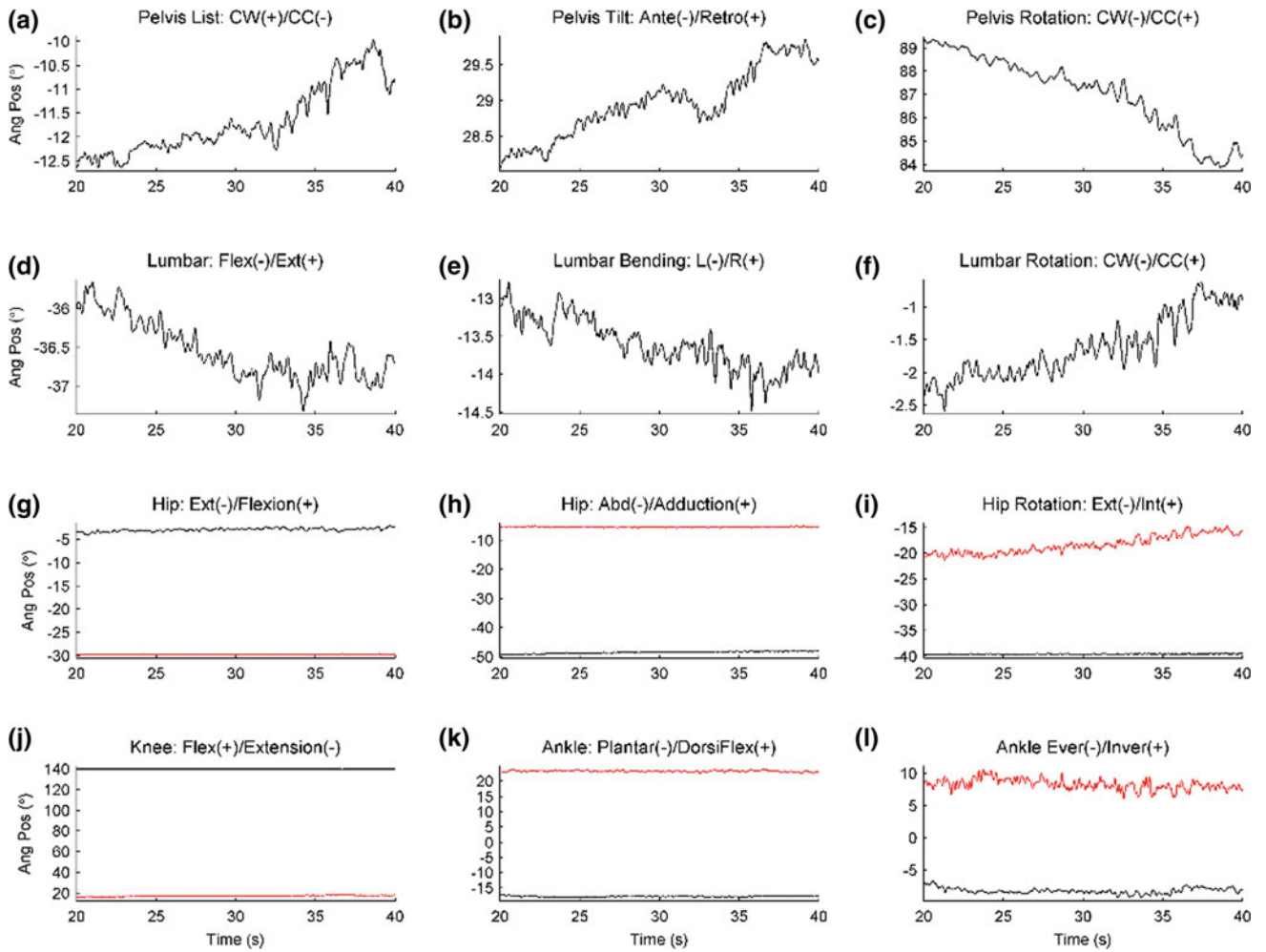
Fig. 10 Yoga 2 in tree posture. Joint angles obtained for pelvis list (**a**), pelvis tilt (**b**), pelvis rotation (**c**), lumbar flexion/extension (**d**), lumbar bending (**e**), lumbar rotation (**f**), hip extension/flexion (**g**), hip abduction/adduction (**h**), hip rotation (**i**), knee flexion/extension (**j**), angle plantarflexion/dorsiflexion (**l**) and ankle eversion/inversion (**m**). The red line corresponds to right leg

Table 3 Mean of joint angles (º)

Joint	Control 1		Control 2		Yoga 1		Yoga 2	
	Average	SD	Average	SD	Average	SD	Average	SD
Pelvis_list	−4.0	1.4	−7.6	0.8	−8.5	0.3	−11.7	0.7
Pelvis_tilt	12.5	1.0	19.9	0.8	6.0	0.9	28.9	0.5
Pelvis_rotation	87.4	0.4	89.7	0.0	89.9	0.0	87.1	1.6
Lumbar_extension	−20	1.3	−25.7	0.8	−8.0	0.4	−36.5	0.4
Lumbar_bending	−2.5	3.0	−3.6	1.1	−6.9	0.5	−13.6	0.3
Lumbar_rotation	8.7	0.8	2.5	0.7	−0.1	0.4	−1.6	0.5
Hip_flexion_r	−15.0	0.6	−18.3	0.5	−1.0	0.8	−29.7	0.0
Hip_flexion_l	33.7	2.8	7.4	0.5	21.9	0.6	−2.9	0.3
Hip_adduction_r	4.4	1.5	−1.5	0.9	−3.3	0.2	−5.6	0.1
Hip_adduction_l	−43.6	0.9	−33.1	1.4	−49.6	0.1	−48.5	0.3
Hip_rotation_r	−4.3	0.7	−11.5	1.1	−16.0	0.5	−18.3	1.7
Hip_rotation_l	−25.5	3.3	−39.6	0.0	−39.8	0.0	−39.6	0.0
Knee_angle_r	2.8	0.3	14.6	0.6	20.1	0.4	17.1	0.5
Knee_angle_l	123.7	0.4	110.7	0.5	139.9	0.0	139.9	0.0
lAnkle_angle_r	3.8	0.5	11.9	0.4	14.5	0.3	23.3	0.3
Ankle_angle_l	−16.7	0.6	−18.9	0.5	−12.7	1.5	−17.8	0.2
Subtalar_angle_r	−11.1	1.4	3.5	2.0	8.2	1.0	8.3	0.8
Subtalar_angle_l	−9.9	1.5	−12.8	1.2	−14.0	4.0	−8.2	0.4

Table 4 Amplitude of joint angles (º)

Joint	Control 1	Control 2	Yoga 1	Yoga 2
Pelvis_list	5.0	4.0	1.2	2.7
Pelvis_tilt	4.7	3.3	3.3	1.8
Pelvis_rotation	2.0	0.2	0.0	5.5
Lumbar_extension	5.0	3.4	1.9	1.7
Lumbar_bending	13.3	5.5	2.3	1.7
Lumbar_rotation	4.7	3.3	2.4	2.0
Hip_flexion_r	3.1	2.5	3.1	0.2
Hip_flexion_l	10.3	2.8	2.5	2.0
Hip_adduction_r	5.3	4.6	0.7	0.6
Hip_adduction_l	3.8	6.3	0.3	1.5
Hip_rotation_r	4.2	6.1	2.5	6.7
Hip_rotation_l	11.4	0.2	0.1	0.3
Knee_angle_r	1.5	3.3	2.0	2.8
Knee-_angle_l	1.6	2.2	0.0	0.1
Ankle_angle_r	2.3	1.9	1.3	1.4
Ankle_angle_l	2.3	2.2	5.5	1.1
Subtalar_angle_r	7.5	10.3	4.9	4.5
Subtalar_angle_l	6.4	4.8	14.3	2.5

postural control in tree posture is due to a mechanism that involves control of body oscillation and alignment of body segments. Further studies with more participants are needed to have a more solid conclusion and to investigate the motor control involved in the postural control of this Yoga posture.

References

1. Shumway-Cook, A., Woollacott, M.H.: In: Lupash, E. (ed.) Motor Control: Translating Research into Clinical Practice, 4th edn. Philadelphia (2012)
2. Latsh, M.L., Zatsiorksy, V.M.: In: Levy, N. (ed.) Biomechanics and Motor Control. Defining Central Concepts. The Boulevard, Langford Lane, Kidlington, Oxford, USA (2016)
3. Danion, F., Latash, M.L.: Motor Control: Theories, Experiments and Applications. Oxford University Press (2011)
4. Bankoff, A.D.P., Ciol, P., Zamai, C.A., Schmidt, A., Barros, D.D.: Estudo do equilíbrio corporal postural através do sistema de baropodometria eletrônica. Revista Conexões **2**(2), 87–104 (2004)
5. Jeong, B., Ko, C.Y., Chang, Y., Ryu, J., Kim, G.: Comparison of segmental analysis and sacral marker methods for determining the center of mass during level and slope walking. Gait Posture **62**, 333–341 (2018)

6. Struzik, A., Pietraszewski, B., Zawadzki, J.: Biomechanical analysis of the jump shot in basketball. J. Hum. Kinet. **42**, 73–79 (2014)

7. Yu, S.S.Y., Wang, M., Samarawickrame, S., Hashish, R., Kazadi, L., Greendale, G.A., Salem, G.J.: The physical demands of the tree (Vriksasana) and one-leg balance (Utthita Hasta Padangusthasana) poses performed by seniors: a biomechanical examination. Evid. Based Complement. Alternat. Med. (2012)

8. Lai, A.K.M., Arnold, A.S., Wakeling J.M.: Why are antagonist muscles co-activated in my simulation? A musculoskeletal model for analysing human locomotor task. Annals Biomed. Eng. (2017)

Blood Flow Restriction Device for Resistance Training

R. D. Santos and C. N. Pai

Abstract

The practice of resistance training minimizes and prevents numerous effects of sarcopenia. Blood flow restriction (BFR) in combination with resistance training acts favorably in the prevention of muscular impairment, besides reducing the risk of injuries and joints overloading. The purpose of this work aims to build an electro-mechanical portable device to control occlusion pressure during resistance training sessions. The internal cuff pressure control, the comfort and the portability were the main requirements imposed for the developing project. The percent variation of the internal cuff pressure, under the action of the implemented control, was lower than 5% during the period that air pump operated; the pressure loss through the valve was 1 mmHg in 3.5 s and the deflating time, strictly related to the comfort constraint, was 4.08 s. The behavior of internal pressure during the experiment suggests that the inflatable cuff associated with a closed loop control system can be satisfactorily applied to control the occlusion pressure of the upper limbs during resistance training sessions. The developed device, using the closed loop control system, was able to control the internal cuff pressure, to achieve the comfort requirement, expressed as maximum deflating time, and its dimensions meet the portability requirements.

R. D. Santos (✉) · C. N. Pai
Universidade de São Paulo, São Paulo, Brazil
e-mail: duarte.renan@outlook.it

1 Introduction

The reduction in the number of motor neurons and muscle fibers units, which occurs during the aging process, limits the skeletal muscle form and function, compromises the muscle control capacity and allows the development of chronic-degenerative diseases [1]. The practice of resistance training can minimize and prevent some of these harmful effects of aging, improving the quality of life of elderly population.

According to the American College of Sports Medicine (ACSM), the practice of resistance training (RT) helps to maintain and to combat the loss of muscle mass by increasing the muscular fitness. The resistance training should be composed of moderate to high intensity strength exercises (>65% of 1 maximum repetition (RM)), with a number of sets ranging from 1 to 3, each composed of 8–12 repetitions [2]. For beginners in RT, the high intensity, recommended by the ACSM, may inhibit the regular practice of this type of training, especially in the cases of elderly with osteoarticular restrictions.

An alternative strategy would be apply low intensity exercise in association with blood flow restriction (BFR). Evidences indicate that BFR combined with low-intensity resistance training, using overloads equivalent to 20–30% 1-RM, results in favourable development of muscular form and fitness [3]. Fatela et al. [4] conducted a study with fourteen young men applying BFR exercise routine. In this study, they found that moderate blood flow restriction on the exercised limb, between 40 and 80% of the total occlusion pressure, associated with low-intensity exercise maximizes the muscular activation without producing the potential negative consequences of the complete occlusion BFR protocols. The findings suggest that BFR may follow the hormesis theory to a certain extent [5, 6]. The vascular occlusion compromises the venous return flow, causing turbulence and reducing blood flow velocity. The induced hypoxia environment causes accumulation of metabolites

and increases the concentration of anabolic hormones, which associated with resistance exercise, promotes a significant increase in strength and muscle hypertrophy [7].

This project aims to construct an electro-mechanical, portable device that actively control the occlusion pressure of the upper limbs, inside the optimal range for muscular activation, during resistance training sessions.

2 Methods

The project was divided into two main phases. First, development and construction, followed by testing and validation. The components used during the construction phase were a double-layer synthetic fabric ("Nylon") with a hook-and-loop fastening ("Velcro"), the tourniquet; an inflatable cuff placed inside the tourniquet; a microcontroller; an air pump for inflation of the cuff; a relief valve and a liquid crystal display (LCD), showing information about the inner pressure of the cuff. During the validation phase, the control system of the device and the pressure were assessed multiple times under different conditions.

2.1 Specifications and Operation

The project was designed using a tourniquet suitable for the upper limbs. For the lower limbs, tourniquets with different width should be used in order to not compromise the pressure measurement [8]. The tourniquet is applied directly at proximal insertion of the exercised limb during the BFR protocol. The inflatable cuff is directly connected to the air pump and to the relief valve, the actuators. During the operation of the device, the air pump is constantly active as well as the pressure sensor. The relief valve, however, is activated only when the internal pressure exceeds a set threshold. The control logic coded in the microcontroller and value of the internal pressure of the cuff determine the closing or the opening of the relief valve. Closing the valve increases the internal pressure of the cuff and consequently the pressure applied on the exercised limb. The opening releases the air and relieves the pressure applied.

Before using the equipment, the user must measure its own value of occlusion pressure, according to the guidelines described in the study by Loenneke et al. [6]. The parameter is used as reference by the device to control occlusion pressure during the exercise.

After the introduction of the initial parameters, the pressure control process can be initiated. The air pump inflates the cuff until the internal pressure is equal to the user-measured occlusion pressure. It is recommended that the exercises start only after this stage is completed.

During the operation of the device, the LCD constantly displays the internal pressure of the cuff registered by the sensor.

2.2 Device Characteristics

The device is designed to be used only on the upper limbs. The maximum pressure is 300 mmHg and the supply voltage is 9 V.

2.3 Requirements

In order to meet the requirements of the American Heart Association (AHA) [9], two dimensional requirements were imposed. The width of the cuff should be less than 100 mm and the cuff length should be greater than 80% of the circumference of the user's arm.

Three other requirements were added to the project based on the field work carried out by professionals from the Escola de Educação Física e Esportes of University of São Paulo (EEFE-USP). The first requirement refers to internal pressure of the cuff, which must be controlled throughout the exercise, within an upper limit of 110% and lower limit equivalent to 90% of the initial occlusion pressure. The second requirement takes into account the deflating time of the cuff. For initial pressures of 300 mmHg, the maximum deflating time must be less than 7 s.

Portability was the last imposed requirement. For this project, portability is defined as the physical characteristic, considering dimensions and weight, which allows the use of the equipment without assistance of a companion during the training session. The references for the developed device portability constraint were the measures of one of the smallest commercial equipment of vascular occlusion, the Kaano Nano Cycle [10].

2.4 Device Architecture

The elements of the device were divided into two main groups: the mechanical and the electrical hardware (see Fig. 1). The mechanical hardware encloses the tourniquet and the cuff, the assembly ensures that pressure is applied regularly around the limb, controlling the occlusion pressure and consequently the blood flow of the limb. The tourniquet (WCS, Cardiomed Comercio de Equipamentos Médicos Ltda, Brazil) is belt-like elongated bag, in vinyl resin, width of 70 mm and length of 250 mm. It is suitable for arms with circumference up to 175 mm, according to the recommendations of the AHA [9].
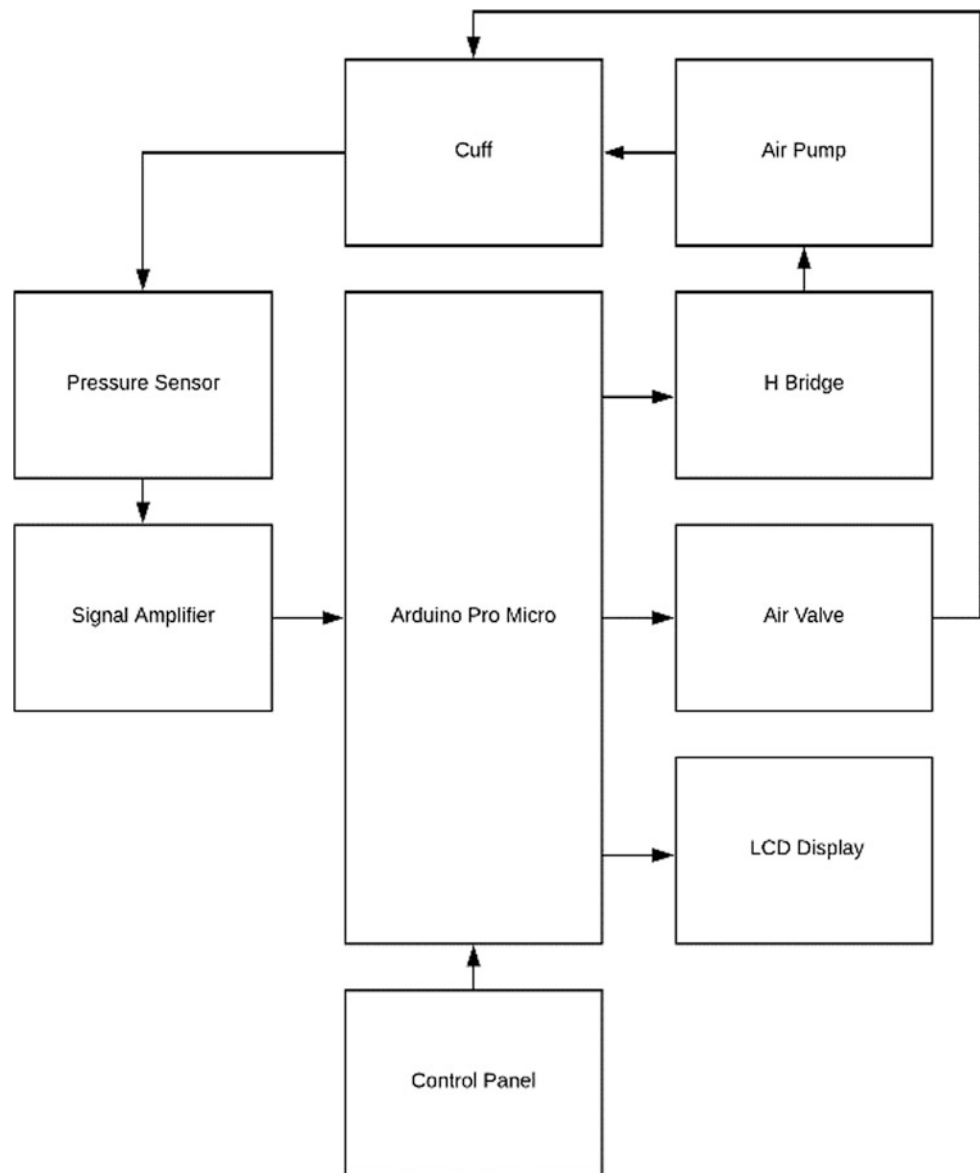
All other components form the electrical hardware. The selected microcontroller uses two analog inputs for communication with the amplifier, two digital outputs for motor driver control (H-Bridge), two Two Wire Interface (TWI) or (I^2C) outputs connect the microcontroller with the LCD display and a digital output controls the relief valve. To ensure a minimum resolution of 1 mmHg, the pressure sensor was calibrated using an analog manometer.

The LCD displays 16 characters per line and uses a standard communication protocol (I^2C). It ensures that the internal pressure of the cuff is displayed in real time, in a clear, simple and user-friendly way.

The relief valve (JMKV1-3A, Jetmaker (Xiamen) Fluid Equipment Co. Ltd, China) controls the internal pressure of the cuff and ensures that the deflating time is less than the design requirement.

The air pump (P54A02R, OKENSEIKO Co. Ltd., Japan) is capable to provide pressures up to 90 kPa (675 mmHg), an air flow of 1800 ml/min and to inflate 500 ml of air, from 0 to 40 kPa (300 mmHg), in 8.5 s. In addition, the reduced dimensions (diameter: 24 mm, length: 71.3 mm) were also another essential factor considered.

The differential pressure sensor (MPS20N0040D-D, Usina Ind. Comércio e Importação, Brazil) provides accurate

analog output signal proportional to the applied pressure, being able to measure pressures ranging from 0 to 40 kPa (300 mmHg) with output ranging from 50 to 100 mV.

The HX711 module (HX711 Amplifier Converter Module, Trade and Import Ind. Plant, Brazil) uses the TTL RS-232 communication protocol and provides a programmable gain amplifier for the sensor output.

3 Results

3.1 Experimental Analysis

A set of four experiments was conducted to verify the adherence of the project to the initial requirements. In all experiments, the microcontroller remained connected to the tourniquet, placed on a flat surface and the occlusion pressure threshold was set at 140 mmHg [3]. Each variable was measured once.

The first experiment, the inflating process started after the positioning of the device on the flat surface and its configuration. After 12 s of operation, the process was interrupted. The internal cuff pressure was measured throughout the operation.

A second experiment was carried out by placing a weight of 1 kg (Oxer, SBF Comércio de Produtos Esportivos LTDA, Brazil) directly over the inflatable cuff, simulating the external force applied by the arm over the walls of the cuff during the concentric movement of the elbow flexion.

The third experiment was performed with an addition of another weight of 1 kg, simulating the increase of the external force applied along the concentric movement of the elbow flexion.

Finally, the device deflating time at 300 mmHg was evaluated. With the relief valve closed, the air pump inflated the cuff until the internal pressure reached the maximum supported value, 300 mmHg. After stabilizing at 300 mmHg, the relief valve was opened through a signal sent by the microcontroller. The deflating time was defined as the time difference between the instant of opening the valve at 300 mmHg and the instant at which the internal pressure of the cuff reached 15 mmHg.

3.2 Pressure Sensor Calibration

During the experiment, a manometer (Premium Manometer, Accumed Produtos Médico Hospitalares, Brazil) and the digital pressure sensor remained connected to the cuff. In this way, the pressure sensor could be calibrated so the digital scale would match the analogic scale of the manometer (see Fig. 2).

Applying a linear regression method, the measurements of the internal pressure of the cuff, in the sensor scale, was approximated by the curve that best fits the internal pressure values measured by the sensor to the values of the real internal pressure.

$$P(x) = 1.62 * \frac{\left(\frac{X}{100} - 83873.6\right)}{300} - 5.85 \qquad (1)$$

3.3 Dimensions

The final dimensions of the project comprise the electronic circuit deposited inside a protective case with opening only for the LCD display and the configuration buttons. A comparison of the Kaatsu Nano Cycle [10] and the developed device, regarding to dimensional aspects, is presented in Table 1.

Fig. 2 Sensor calibration
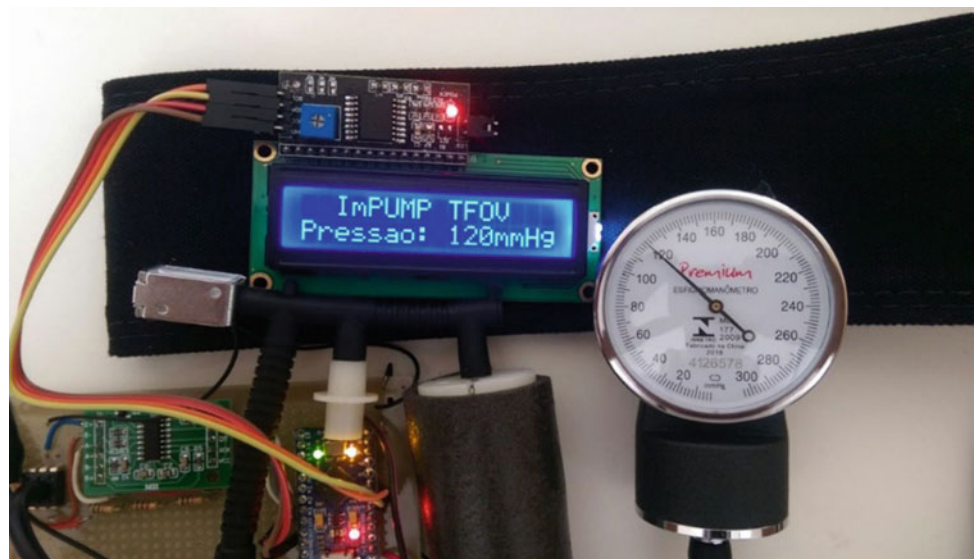
Table 1 Dimensional comparison of the Kaatsu Nano Cycle and the developed device

Item	Kaatsu Nano Cycle	Device
Length (mm)	200	150
Width (mm)	100	100
Height (mm)	50	60
Weight (g)	–	250

3.4 Inflation Capacity and Pressure Maintenance

During the first experiment, the internal pressure presented an oscillatory pattern as consequence of the closed loop control performed by the microcontroller (see Fig. 3). The air pump was active for 12 s and then turned off. The internal pressure control was performed by opening the relief valve while the air pump remained completely active.

The maximum value of the pressure was 140 mmHg and the minimum value of 135 mmHg, under the actuation of the implemented closed loop control. The percentage variation of the internal pressure of the cuff was less than 5% during the period of operation of the air pump.

After turning off the air pump, the pressure loss through the valve could be then evaluated. At the beginning, immediately after turned off, the internal pressure recorded was 137 mmHg. At the final instant, the sensor recorded 136 mmHg inside the cuff. Between the two instants, there was a percentage pressure loss of 0.73% in, approximately, 3.5 s (see Fig. 4).

3.5 Inflation Capacity and Pressure Maintenance in Forced Regimen

The comparison of cuff inflation time for the different regimens was evaluated in the second and third experiments (see Fig. 5). The air pump was kept running for 15 s and then turned off. Internal pressure control was performed by opening the relief valve when the maximum occlusion pressure was reached. In the second and third experiments, external weights were positioned over the cuff representing the external force applied by the arm to the tourniquet.

Comparing the inflation time, it is noticeable that required time for the internal cuff pressure to reach 140 mmHg slightly increases with the increase of the external force applied, since the resistance to air occupancy within the cuff is also increased.

Fig. 3 Internal cuff pressure

Fig. 4 Performance of the control system in the maintenance of pressure

Fig. 5 Comparison of cuff inflation time for different regimens
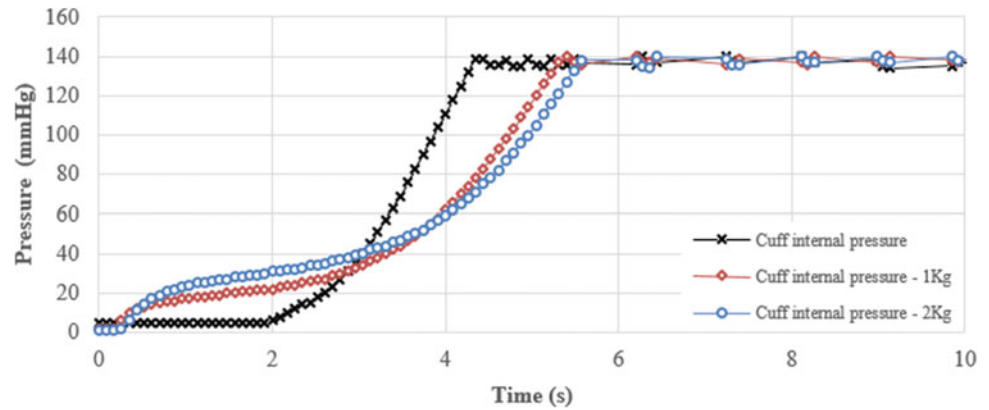
Fig. 6 Deflating time
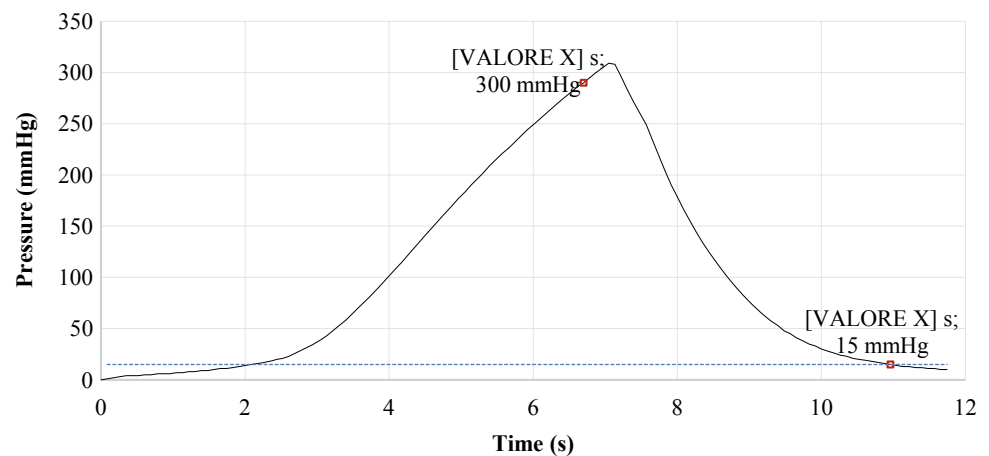
3.6 Exhausting Time

With the device positioned over a flat surface and with no additional weight, the cuff was fully inflated. After 6.87 s from the start of operation of the air pump, the pressure sensor registered 300 mmHg. At this point, the air pump was turned off and the relief valve was opened. At the final instant, 10.95 s, the internal pressure of the cuff reached 15 mmHg and the time counting was interrupted.

Between these two instants, a time difference of 4.08 s was measured (see Fig. 6).

4 Conclusion

The behavior of the pressure inside the cuff in response to the BFR training simulations suggests that an inflatable cuff associated with a closed loop control system can be satisfactorily applied to control occlusion pressure. This behavior was evidenced mainly by the maintenance of the internal pressure within the previously stipulated limits, upper limit

of 110% and lower limit of 90% of the initial occlusion pressure defined by the user.

The experiment conducted to evaluate the deflating time demonstrated that the device, even under high pressures, can rigorously achieve the required comfort condition imposed as maximum deflating time.

Finally, the dimensions of the developed device meet the requirements previously defined for classification within the concept of portability.

One of the limitations of the study was the lack of a data storage system. Thus, although the operation of the device is independent, data collection of variation of internal pressure of the cuff was performed with the device connected to a computer.

The operating time of the device is also another factor of attention for the development of future works that employ this project. The lack of an energy management system limits the uptime of the prototype, given the high consumption.

The aim of the project was to guarantee the precise mechanical and electrical functioning of the device. In the

set of experiments, only in vitro tests were conducted, admitting one measurement of each variable, since the behavior of the device does not change over time. In a near future, in vivo experiments will be conducted and the number of samples of each variable will be chosen depending on the statistical analysis required.

We expect that, in the future, the device will be adopted for studies on muscle hypertrophy and in cases of recovery and rehabilitation of elderly patients.

References

1. Vechin, F.C.: Effects of low load resistance training with partial blood flow restriction in the strength and hypertrophy gains as well as in the muscle satellite cells content in elderly. Dissertation, University of São Paulo (2014)
2. Escho, M.R.: Resistance Training for Health and Fitness. American College of Sports (2013). https://www.acsm.org/docs/brochures/resistance-training.pdf. Accessed 14 Mar 2018
3. Takarada, Y., Takazawa, H., Sato, Y., Takebayashi, S., Tanaka, Y., Ishii, N.: Effects of resistance exercise combined with moderate vascular occlusion on muscular function in humans. J. Appl. Physiol. **88**(6), 2097–2106 (2000)
4. Fatela, P., Reis, J.F., Mendonca, G.V., et al.: Acute effects of exercise under different levels of blood-flow restriction on muscle activation and fatigue. Eur. J. Appl. Physiol. **116**, 985 (2016)
5. Yasuda, T., Brechue, W., Fujita, T., Shirakawa, J., Sato, Y., Abe, T.: Muscle activation during low-intensity muscle contractions with restricted blood flow. J. Sports Sci. **27**(5), 479–489 (2009)
6. Loenneke, J.P., Thiebaud, R.S., Abe, T., Bemben, M.G.: Blood flow restriction pressure recommendations: the hormesis hypothesis. Med. Hypotheses **82**(5), 623–626 (2014)
7. Manini, T.M., Clark, B.C.: Blood flow restricted exercise and skeletal muscle health. Exerc. Sport Sci. Rev. **37**(2), 78–85 (2009)
8. Loenneke, J.P., Fahs, C.A., Rossow, L.M., Thiebaud, R.S., Mattocks, K.T., Abe, T., Bemben, M.G.: Blood flow restriction pressure recommendations: a tale of two cuffs. Front. Physiol. **4**, 249 (2013)
9. Veiga, E., Arcuri, E.M., Cloutier, L., Santos, J.: Medida da pressão arterial: circunferência braquial e disponibilidade de manguitos. Revista Latino-Americana de Enfermagem **17**(4), 455–461 (2009)
10. Kaatsu Global Inc. "Kaatsu Cycle Kit". https://store.kaatsu-global.com/product/kaatsu-cycle-kit/ (2017). Acessed 18 Mar 2018

Comparative Analysis of Ankle Prosthesis Connector Adapters in 3D Printed Using PLA and PETG

A. Silva and Denner Guilhon

Abstract

The high price of adapters of lower limb prostheses and the difficulty for the purchase of this product encouraged us to develop a low-cost version using 3D printing. For printing was chosen two types of filaments: polylactic acid (PLA) and polyethylene terephthalate glycol (PETG). This work had as main objective to evaluate, through simulations and mechanical compression tests, the adapter prototypes' maximum deformations and to identify the best material regarding mechanical resistance. The results obtained through simulations were compared with those obtained from compression tests according to Taguchi orthogonal distribution. A maximum deformation limit of 3 mm was determined, as the average size of the difference in length between the legs of a healthy individual. The maximum deformations found were 0.5976 mm for PETG mate-rial and 0.3103 mm for PLA material. Even tough PLA has shown a lower value of the deformation, PETG was chosen as printing material because no cracks or fractures were found during trials. The results satisfy the imposed maximum deformation limit and are indicators of reliability for use of this component made by 3D printing.

Keywords

3D printer • Adapter • Orthopedic prostheses

1 Introduction

Prostheses are artificial substitutes used to supply the absence of members and their functions [1]. These absences are mostly caused by tumors, injuries, diabetes, and insufficient blood supply or in case of people who are born without the member, congenital amputations [2]. The number of amputations increases annually and the need of prosthesis as an alternative to alleviate its consequences is unavoidable. In the case of amputations of lower limbs, the adoption of prosthesis can mean the full recovery of the locomotion.

The construction of prostheses is usually constituted by modules and may have aluminum, steel or titanium, among others [3]. These components are costly and difficult to access. The use of new technologies can reduce the manufacturing costs in the production of prostheses. As an example of such technology, the 3D printers are, according to [4, 5], capable of producing parts with complex geometry using material deposition.

The proposed prototype consists of developing an ankle-like foot connector (see Fig. 1a), which is responsible for making the connection between the prosthesis foot and the tibia component (see Fig. 1b).

Among numerous available 3D printing techniques, the most widely used is the fused deposition model (FDM), due to the low cost of materials and ease of operation [6]. As this operation has as working principle to melt a polymeric filament on top of a platform according to the part to be printed, it is thus classified as an extrusion process [7].

The use of polymeric materials is due to its wide application, excellent properties, ease of production and low cost. The polymers generally used are Polylactic Acid (PLA) and Acrylonitrile butadiene styrene (ABS) due to their ease of modeling and low glass temperature [8, 9]. Polyethylene Terephthalate Glycol (PETG) according to [10] is a complete material, due to its flexibility, resistance to temperature and im-pact.

The main objective of this work is to evaluate the resistance to compression of the 3D printed prosthesis adapters. We used PLA and PETG to produce the parts. After that, the Taguchi methodology was employed in order to identify the most significant manufacturing parameters of the parts' performance regarding the compression resistance. We also performed simulations using Inventor software to evaluate if

A. Silva (✉) · D. Guilhon
Universidade Estadual do Maranhão, Cidade Universitária Paulo VI, s/n—Tirirical, São Luís, MA, Brazil
e-mail: adira.saffira@gmail.com

Fig. 1 Lower limb prosthesis. **a** Prosthesis foot and tibial component, **b** prosthesis connector
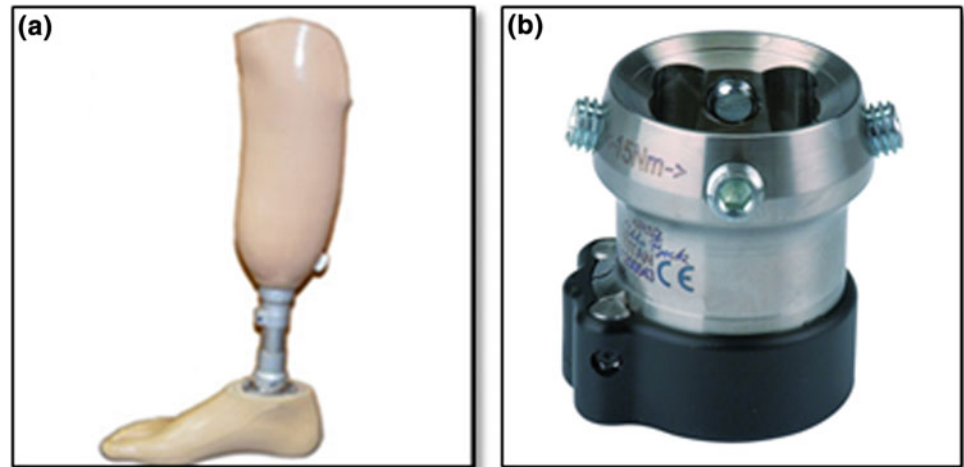
de-formations under previously chosen loads would comply with a maximum limit of 3 mm [12].

2 Experimental Procedure

From Fig. 1a, a similar one was designed and modeled by Macedo [11] in the Inventor software, shown in (see Fig. 2). It presents two entries, the upper one for the prosthesis foot fitting which also uses lateral screws to fixation. The lower one that serves to fix the transfer, which is usually threaded or fixed with clamp-type adapters.

This model is similar to those already available in the market, but uses PETG or PLA polymers as the manufacturing material. Afterwards, we used Inventor software to simulate the behavior of those parts under different loads. The applied load was chosen taking into consideration a healthy person of 60 kg, considering also that the prototype in static position supports half of the weight (distribution in two legs) approximately 300 N. The load was applied according to the Fig. 3.

For security effect, it was preferred to measure beyond the simulation with the application of 300, 1000 and 3000 N. In any case, the deformation should not exceed a 3 mm limit. This limit is the difference in length between the lower limbs considered normal. For values higher than this, there may be discomfort during gait [12].

For the production of the prosthesis, we used a OMNI-ZY3D printer (see Fig. 4) because it is relatively cheaper than the commercial ones and it has open software, allowing to change several parameters.

Three parameters were determined with two variables, as it can be seen in Table 1. The parameters were the material, the fill density, which significantly influence the weight of the prototype, and the fill pattern that was chosen with the purpose of evaluating the variation of the deposition geometry of the material.

Fig. 2 Adapter model for lower limb prosthesis created in inventor software
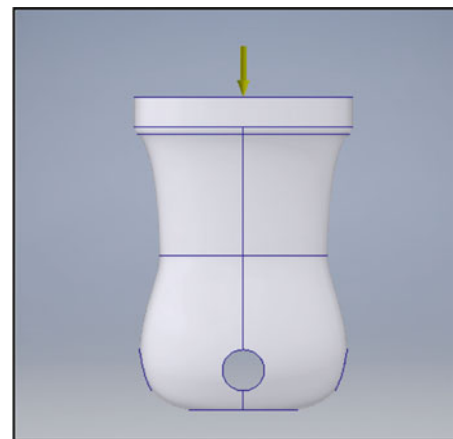
Fig. 3 Schematics for load application used in simulations
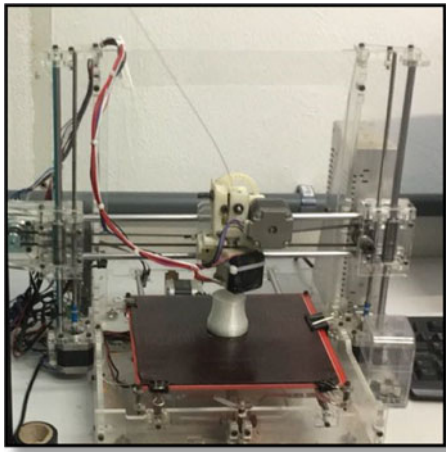
Fig. 4 OMNIZY3D printer

Table 1 Parameters for printed

Settings		
Material	Fill density (%)	Fill pattern
PETG	25	Rectilinear
PLA	50	Octagram spiral

The Taguchi orthogonal method was used in order to determine which of the parameters are the most significant without requiring a large amount of experiment (Table 2). Button [13] explains that Taguchi's methodology suggests evaluating the mean responses for a given set of chosen factors and then assessing the variability through the signal-to-noise ratio (S/N), and the noise described by Taguchi as the interfering causes variability of product functions.

Following the orthogonal distribution of Taguchi, we printed four configurations with three samples each in order to reduce the effects of random data changes. All pieces after printing were subjected to the compression test performed by a universal traction machine of the EMIC line DL1000 (see Fig. 5).

As the stopping criterion of the test, we used a deformation of 4 mm, applied at a speed of 0.5 mm/min. In order to verify the maximum load the adapter would withstand

Table 2 Taguchi orthogonal method

Parameters			
Number of experiments	Material	Fill density	Fill pattern
1	Level 1	Level 1	Level 1
2	Level 1	Level 2	Level 2
3	Level 2	Level 1	Level 2
4	Level 2	Level 2	Level 1
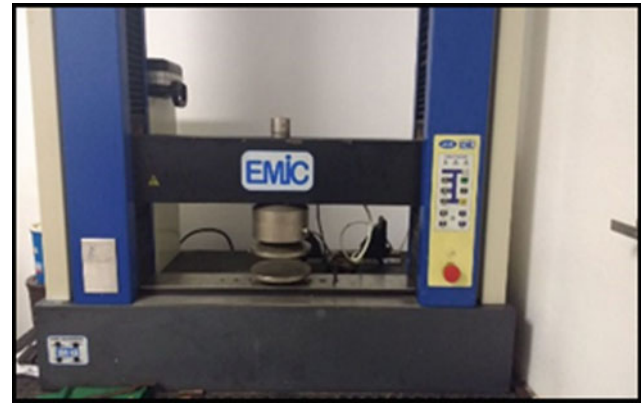
Fig. 5 Universal traction machine of the EMIC line DL1000

until the moment of the fracture, tests were carried out in the adapter and not in standard test bodies.

After the tests and data collection, the efficiency of each parameter was calculated as a function of the deformation. Using the Taguchi method, it was defined that the ideal would be to have a smaller-better deformation, applying then applying the method given by Eq. 1.

$$10 \times \log\left(\frac{1}{n} \times \sum Y^2\right) \qquad (1)$$

where:

- **n-**The number of sample. In this case, it is set three, which is the number of samples for each configuration.
- **Y-**The values to be evaluated. In this case the deformation values found in the compression tests.

3 Results

From the stress analysis simulation performed in the Inventor, we see that the two materials respect the stipulated limit of deformation. The maximum deformations forces for the 300, 1000 and 3000 N are shown in Table 3. The simulations also allow us to visualize the zones of greater deformation (see Fig. 6). We verified that the values of

Table 3 Maximum predicted deformation values in the model using PETG and PLA under loads of 300, 1000 and 3000 N (Software Inventor)

Forces (N)	Distortion (mm)	
	PLA	PETG
300	0.0255	0.0451
1000	0.0852	0.1505
3000	0.2556	0.4514

Fig. 6 Simulated deformation for a 3000 N load, PETG and PLA materials
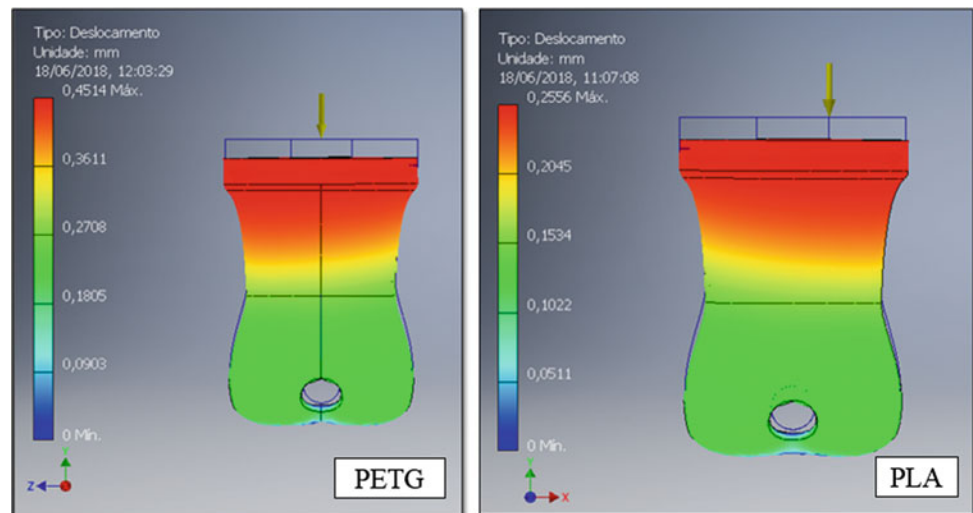
deformation for the two employed materials after application of a 300 N load were within the established limits, being of 0.02 mm for PLA and 0.04 mm for PETG.

In our simulations, we observed that the deformation value is directly proportional to the applied load. Even after raising the applied load to 10 times the value expected in normal conditions (for the purpose of this work, 300 N to each leg), both materials still respect the maximum deformation limit of 3 mm. Moreover, we can see that for all simulations PLA showed lower values of deformation, probably due its greater stiffness when compared to PETG.

The compression tests had as stopping criterion the deformation of 4 mm. After the tests, it was possible to find, through the results, the deformations for the pre-established loads. Since each test have three samples, we performed an arithmetic average of the deformations as shown in Table 4.

Divergences between simulation and compression test results can be explained by the limitations of FDM printers

[8] and the fact that our simulations did not assume empty spaces inside the parts. However, simulation is still valid tool since its results are very similar to the compression tests' (see Fig. 7). We believe that other mechanical properties as tensile strength and fatigue will also be affected by the 3D deposition characteristics.

The average deformation values in Table 3 were inserted in Minitab software, thereby obtaining the Signal Noise Response Table (Table 5) and the graph of the effect on each parameter signal-to-noise ratio (see Fig. 8). The graph and table show the most striking factor was the PLA material with the ratio of 14.016, which showed lower deformations. The parameters of density and fill pattern had almost the same ratios. The configuration that presented less deformation used PLA, 50% fill density and Octagram spiral fill pattern. This setting is not part of the experiments already made, so there is need to perform printing and testing for confirmation.

Table 4 Experimental results of compression tests for PETG and PLA samples

Parameters				Distortion (mm)		
Number of experiments	Material	DP (%)	PP	300 N	1000 N	3000 N
111	PETG	25	Rect	0.0976	0.2413	0.5976
122	PETG	50	Octagonal	0.1321	0.2528	0.4597
212	PLA	25	Octagonal	0.0631	0.1493	0.3045
221	PLA	50	Rect	0.0459	0.1436	0.3103

Fig. 7 Simulation versus compression tests
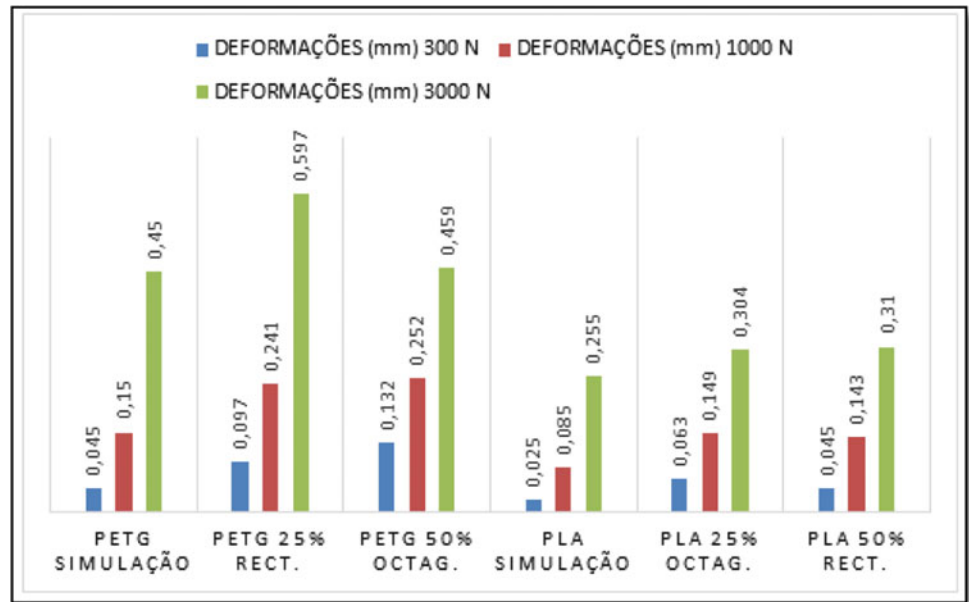
Table 5 Signal noise response table

Level	Response table		
	Material	DP	PD
1	9.322	11.277	11.276
2	14.016	12.061	12.062
DELTA	4.693	0.784	0.785
DESK	1	3	2

4 Discussion

A behavior observed during the tests, for the 4 mm deformation band, was what happened with the beginning of fractures and when there was a possible visual search for the appearance of a barrel model in the parts. Table 6 shows the mean loading values for the beginning of cracks (in PLA samples). These values showed that the applied load must be very high in order that fracture occur. Considering the design needs, all models are reliable.

Another behavior observed during the tests was that in all tests using the PLA material they presented cracking formation and barrel effect deformation mode. In addition, one of the samples fractured upon reaching the 4 mm deformation (see Fig. 9). One of the explanations for this happened is that the pattern of filling the fractured configuration made it more empty than normal.

A positive characteristic for the PETG material was that no tested sample presented cracks, only barrel effect deformation mode. This occurred due to the fact that the material presented greater flexibility and resistance, having thus deformed more, but not arrived at the breakup. (see Fig. 10).

5 Conclusion

The deformations found in the simulations satisfy the maximum limit of 3 mm, in addition to establishing a safety coefficient of 15 for the three loads tested. The results of the simulations and tests showed that the PLA material presented smaller deformations after the application of load. The PETG material, even showing larger deformations, did not present any cracks or fractures. Thus, we showed that the PETG material is suitable for our model, for its greater flexibility and reliability.

Table 6 Average load reached by each configuration at which parts suffered cracks and started to bulge

Parameters				
Number of experiments	Material	DP (%)	PP	Average strength (N)
111	PETG	25	Rect	12130.26
122	PETG	50	Octagonal	13567.87
212	PLA	25	Octagonal	12816.81
221	PLA	50	Rect	32457.61

Fig. 8 Graph of the effect on each parameter signal-to-noise ratio
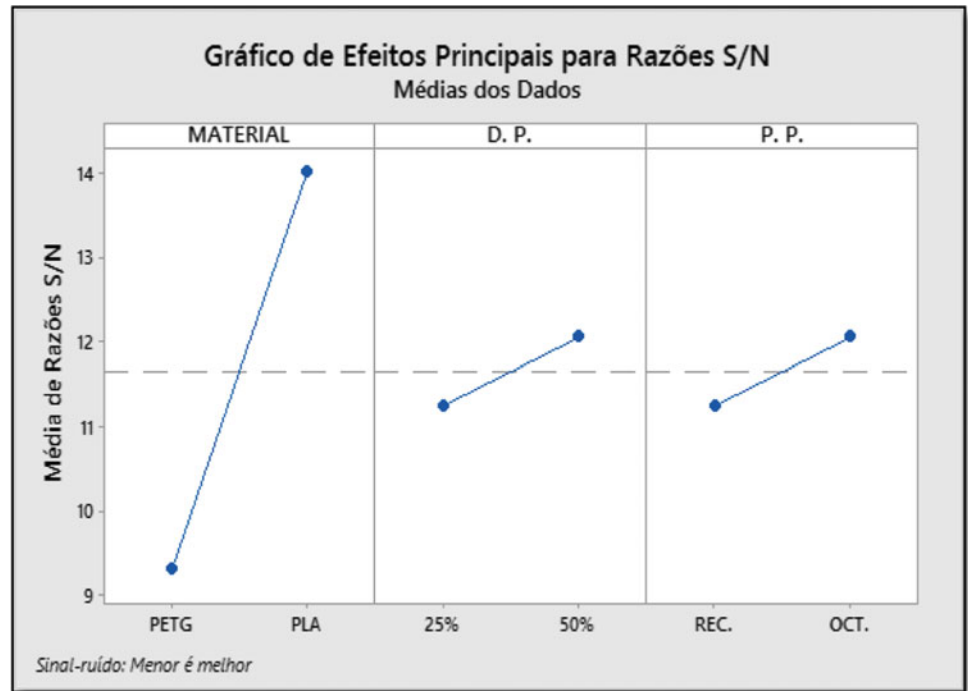
Fig. 9 Adapter models for lower limb prosthesis after compression test

Fig. 10 Adapter models for lower limb in PETG and PLA

The reliability of the models can be attested by the mean values of deformation for the applied loads (Table 3) and by the high load values required for cracking and barrel deformation mode (Table 5). From these values, we can say that any of the tested configurations, when used by a 60 kg person (force applied to each leg of 300 N in a static way), will not deform beyond the stipulated (3 mm) nor suffer cracks.

Despite the positive results with respect to compression results, it will still be necessary to evaluate other mechanical properties to validate the use of this model as an adapter for human prostheses. Nonetheless, we can conclude that due to the low amount of filaments used, low cost in the use of the printer together with the results obtained confirms the initial assumption that 3D printing can be used to make this type of low cost orthosis.

Future work must focus on the adapter's mechanical behavior. One point to be analyzed is the fatigue, since 3D printed prototypes are totally different from its met-al equivalents. Fatigue damage into those prototypes. The fatigue damage in those prototypes will depend on mechanisms such as rupture of the deposition layers and detachment. The combination of these mechanisms may adversely affect some of the properties of these materials, such as strength and stiffness.

References

1. Britannica, E.: Prosthesis. http://www.britannica.com/EBchecked/topic-/479532/prosthesis (2013). Last accessed 14 Nov 2017
2. Britannica, E.: Prosthesis. http://www.britannica.com/EBchecked/topic-/21786/amputation (2013). Last accessed 15 Nov 2017
3. Bernasconi, R., Natale, G., Levi, M., Magagnin, L.: Electroless plating of NiP and Cu on polylactic acid and polyethylene terephthalate glycol-modified for 3D printed flexible substrates. ECS (2016)
4. Lipson, H., Kurman, M.: Fabricated: The New World of 3D Printing. Wiley, Inc., Indianapolis, Indiana (USA) (2013)
5. Yap, J., Renda. G.: Low-cost 3D-printable prosthetic foot. In: Proceedings of the 3rd European conference on design4health, Sheffield. https://goo.gl/v75ttz (2015). Last accessed 15 Dec 2017
6. Chen, Y.H., Ng, C.T.: Integrated reverse engineering and rapid prototyping. Comput. Ind. Eng. **33**(3–4), 481–484 (1997) apoud ULBRICH, Cristiane Brasil Lima et al. Engenharia reversa e prototipagem rapida (2003)
7. Dos Reis, G., Júnior, A.J.C., Da Silveira Campos, R.: Perfil epidemiológico de amputados de membros superiores e inferiores atendidos em um centro de referência (2012)
8. Osejos, J.V.M.: Caracterización de materiales termoplásticos de abs y pla semi-rígido impresos em 3d com cinco mallados internos diferentes. 2016. 196f. Tese (Mestrado em Engenharia Mecânica)—Facultad de Ingeniería Mecánica, Escuela Politécnica Nacional, Quito (2016)
9. Abreu, S.A.C.: Impressão 3D baixo custo versus impressão em equipamentos de elevado custo. 2015. 259f. Dissertação (Mestrado em Engenharia Mecânica)—Faculdade de Engenharia, Universidade do Porto, Porto (2015)
10. Locker, A.: PETG Filament Guide 2018—Explained, Compared and Reviewed. https://all3dp.com/1/petg-filament-3d-printing/ (2017). Last accessed 20 Mar 2018
11. Macedo, P.: Especificações de Projeto para um Adaptador Protético de Tornozelo Impresso em 3D TCC—Universidade Estadual do Maranhão. Engenharia Mecânica, São Luís (2017)
12. Hoppenfeld, S, Quadra, A.A.F., Vizeu, I.M.X.: Propedêutica Ortopédica: coluna e extremidades. Atheneu, São Paulo (2002)
13. Button, S.T.: Metodologia para planejamento experimental e análise de resultados. Programa de pós-graduação em Engenharia Mecânica—Universidade Estadual de Campinas, Campinas (2005)

Comparative Analysis of Anthropometric Variables of Undergraduate Athletes in Different Collective Modalities

Bárbara Silva, Beatriz Menezes, Leandro Fernan-des, and Marco Silva

Abstract

In this study, 33 female athletes from the Basketball, Futsal, Handball and Volleyball teams from Federal University of Uberlandia (UFU) participated, from which 13 athletes were from the Futsal team, 10 athletes were from the Handball team, 6 athletes were from the Basketball team and 4 athletes were from the Volleyball team. Anthropometric measurements were collected at the Biomechanics Laboratory from the Physical Education Faculty (FAEFI) from the Federal University of Uber-landia. After analysis, the results show that body composition is a factor that determines the possibilities to a successful performance, considering each sports modality has its own specificities. Additionally, each function performed by the athlete has its own specificities to provide good performances. A big part of the athletes, among all analysed modalities, is overweight, which compromises the athletes' performances.

Keywords

Anthropometric • Undergraduate athletes • Collective modalities

1 Introduction

Investigations on physical characteristics of athletes led to numerous studies that analyze and search for anthropometric characteristics in different sports modalities [1].

References [2, 3]. These studies are based on what is called "Anthropometry", which is a method that evaluates inertial measurements on athletes bodies using metric tapes, calliper-weighting scale and others instruments to register parameters [4].

Corroborating with the importance of anthropometry in athletes from different sports modalities, works by Dantas and Fernandes [5] and Medina and Fernandes Filho [6], which emphasize the importance of the description of athletes from different sports levels, can be mentioned.

Therefore, presenting the importance of anthropometric knowledge on the most popular sports in Brazil, Basketball, Futsal, Handball and Volleyball modalities are stated as some of the eleven most practiced sports in the country, being four of the five most collective sports practiced by Brazilians [7]. As a result of the big feature these modalities possess in our society, each modality can be characterized.

Basketball had its story initialized in Brazil around 1896 [8], having biomechanical characteristics associated to short distance runs, direction changes, jumps, shoots, agility and balance [9].

One of the versions about the origin of Futsal affirm that the modality was created around 1940, in Brazil [10], with efficient movement velocity being a crucial factor to provide good performance. Also, balance, agility and flexibility are important parameters [11].

Handball is practiced in Brazil since 1928 [12] and is characterized by its considerable amount of ball manipulations and interactions between game partners and rivals [13]. Due to its rich combination of motor abilities, Handball is considered a very complex sport [14].

Volleyball started to be practiced in Brazil around 1915 [15] and requires physical abilities from athletes, such as strength, physical and logical quickness and good resistance, considering the unpredictability of its matches [16]. Differently from the previous modalities, Volleyball is not a contact sport, which means the team does not aim to occupy the opponent's field to score points and only defends its own section [17].

This research aims to analyze and compare anthropometric data such as weight, height, Body Mass Index (BMI), fat percentage and Waist-Hip Ratio (WHR) from the university Basketball, Futsal, Handball and Volleyball female teams, due to the specifications of each sport.

B. Silva (✉) · B. Menezes · L. Fernan-des · M. Silva
Federal University of Uberlandia, Uberlandia, MG, Brazil
e-mail: barbarags.ufu@gmail.com

2 Materials and Methods

In this study, 33 female athletes from the Basketball, Futsal, Handball and Volleyball teams from Federal University of Uberlandia (UFU) participated, from which 13 athletes were from the Futsal team, 10 athletes were from the Handball team, 6 athletes were from the Basketball team and 4 athletes were from the Volleyball team.

Anthropometric measurements were collected at the Biomechanics Laboratory from the Physical Education Faculty (FAEFI) from the Federal University of Uberlandia (UFU), using a inBody 230 (INBODY®) bioelectrical impedance weighting scale and a metric tape. The BMI was calculated according to Eq. (1)

$$BMI = \frac{weight \ [kg]}{height \ [m]} \qquad (1)$$

The bioelectric impedance method, performed according to protocol, is a precise approach to estimate body composition [18]. BMI analysis was made due to its suitable association of Body Mass [19–21]. WHR was calculated due to its high correlation to chronic degenerative dysfunctions, such as cardiovascular diseases and hypertension [22].

This study involving human beings was approved by the Ethics and Research Committee of the Federal University of Uberlândia, protocol n. 337/11 in 05/29/2015, certified according to the guidelines and regulatory standards by the National Healthy Council.

3 Results

Table 1 presents numbers referring to the weight of female athletes of the university Basketball, Futsal, Handball and Volleyball teams.

Table 2 shows height information form the undergraduate players.

Table 3 presents numbers referring to the female athletes BMI from the university Basketball, Futsal, Handball and Volleyball.

According to data from the American College of Sports Medicine (ACSM's) [23], the athletes can be classified, as seen in Table 4.

Table 1 Weight information in kilograms of the athletes

Modality	Mean value	SD	Minimum	Maximum
Basketball	64.6	10.6	49.5	81.3
Futsal	58.6	11.6	45.5	84.3
Handball	64.1	8.9	56.4	88.1
Volleyball	60.35	5.8	55.8	69.7

Table 2 Height information in centimetres of the athletes

Modality	Mean value	SD	Minimum	Maximum
Basketball	166	3.4	162	171.5
Futsal	158.5	6.8	152	171
Handball	164	4.9	154	169
Volleyball	165.5	8.3	154	173

Table 3 BMI information in kg/m^2 of the athletes

Modality	Mean value	SD	Minimum	Maximum
Basketball	23.2	3.6	18	29.3
Futsal	22.3	3.7	19.4	31.9
Handball	24.8	3.5	21.8	32.2
Volleyball	19.5	4.5	19.5	29.4

Table 4 Classification of the university athletes according to ACSM's

Modality	Underweight (%)	Normal (%)	Overweight (%)	Obese 1 (%)
Basketball	16.6	66.6	16.6	0
Futsal	0	69.2	23	7.6
Handball	0	50	40	10
Volleyball	0	75	25	69.7

Table 5 University teams fat percentage data

Modality	Mean value	SD	Minimum	Maximum
Basketball	32.9	9.4	20.3	43.2
Futsal	28.9	5.4	18.8	32
Handball	33.4	5.7	23.2	41.4
Volleyball	27.5	6	19.4	33.9

Table 6 Classification of the university athletes according to body fat percentage according Neiman parameter

Modality	Good (%)	Above Av. (%)	Average (%)	Below Av. (%)	Bad (%)	V. Bad (%)
Basketball	0	33.3	0	16.6	0	50
Futsal	7.6	23	7.6	15.3	30.6	15.3
Handball	0	0	10	10	20	60
Volleyball	0	25	0	25	25	25

Table 5 presents number referring to the fat percentage data of the athletes from the university Basketball, Futsal, Handball and Volleyball teams.

By consulting literature, the Pollock parameter [24] for body fat percentage can be found (Table 6).

4 Discussion

According to the results, after the anthropometric evaluation of the female Basketball team, it was observed a average weight of 64.6 kg. The average of height was 1.66 m. Gentil [25] collected data from the Brazilian National female Basketball team and obtained 182 cm of average height and 70.8 kg of average weight. The average BMI of the Basketball athletes was 23,2, which is considered normal (18, 52) and not far from the National team average value, as alleged by Gentil. It was observed that 66.6% of the team has BMI classified as normal. Values of body fat percentage were between 20.3 and 43.2%, average 32.9%, which is classified as "Very Bad". On the other hand, 33.3% of the Basketball athletes have body fat percentage between 20 and 22% which is close to the average value of 22% from the 2004 Brazilian National team, as stated by Nunes [26]. According to Nunes, the height and the thin body mass influence on the players performances when it comes to rebounds and the best players to accomplish this function would be the centers, due to their bigger height.

According to the Futsal team data, the average body weight was 58.6 kg and the average team height was 158.5 cm, resulting in an average BMI of 22,3. The average body fat percentage was 28.9%. According to Queiroga [3], the average body weight of high-performance athletes vary from 56.8 to 63.9 kg, depending on their position. Also according to Queiroga, the higher body weight, BMI and body fat percentage data come from the goalkeepers, while the team wingmen have the lowest rates for these parameters. Queiroga observed that the average body fat percentage of the goalkeeper was 26.7% while the wingmen had 22% in average.

The Handball team presented 64.1 kg of average weight and 1.64 m of average height, resulting in 24,8 of average BMI. The average body fat percentage was 33.4%. According to Candia [27], in a successful Handball team, a weight above average could be advantageous as it provides better resistance and power for athletes' performances. According to Rodrigues [28], a big part of the athletes show body weight above average and the average body fat of the studied team was 27%. Taborsky [29] studied female athletes from the best european teams in adult categories. It was found a height range between 174 and 177 cm, which is considerably higher to the average value found in this study, 164 cm.

The Volleyball team presented 60.35 kg of average body weight and 165,5 of average height, resulting in 19,5 of average BMI. The average body fat percentage was 27.5%. According to Schultz [30] and Morrow et al. [31], to provide a better physical performance, Volleyball athletes must have a lower body fat percentage, what was not identified in the Federal University of Uberlandia team, as 75% of the team presented body fat from 26 to 33.9%. According to Fleck [32], the optimal body fat percentage for young athletes in Volleyball teams is 19%, which is classified as "Good". The studied sample did not present any athlete in this condition. According to Queiroga [33], the tactic function performed by the athlete is not a crucial factor to create morphological changes in the athletes. However, the lack of specificity according to each athlete position, during practice, could be a problem.

5 Conclusion

After analysis, the results show that body composition is a factor that determines the possibilities of successful performance, considering each sports modality has its own specificities. Additionally, each function performed by the athlete has its own specificities to provide good performances. A big part of the subjects, among all analyzed modalities, is overweight, what compromises the athletes' performances. The only modality in which overweight is a positive factor is Handball. The modality with the biggest body fat percentage variation was Futsal, from which the biggest sample had body fat percentage classified as "good" and "average". This variation might be a good pointer as each tactic function performed in field has a different adequate body profile.

References

1. De Lima, L.R.A., Sigwalt, A.R., Rech, C.R., Petroski, E.L.: Somatotipo e composição corporal de atletas feminino de pólo aquático do Brasil. J. Phys. Educ. **18**(2), 191–198 (2007)
2. Holway, F.E., Garavaglia, R.: Kinanthropometry of group I rugby players in Buenos Aires, Argentina. J. Sports Sci. **27**(11), 1211–1220 (2009)
3. Queiroga, M.R., Ferreira, S.A., Romanzini, M.: Perfil antropométrico de atletas de futsal feminino de alto nível competitivo conforme a função tática desempenhada no jogo. Rev. Bras. Cine. Des. Hum. ISSN **1415**, 8426 (2005)
4. Hebbelinck, M.: Indentificação e desenvolvimento de talentos no esporte. Relatos cineantropométricos. Revista Brasileira de Ciência e Movimento **4**(1), 38–45 (2008)
5. Dantas, P.M.S., Fernandes Filho, J.: Identificação dos perfis, genético, de aptidão física e somatotípico que caracterizam atletas masculinos, de alto rendimento, participantes do futsal adulto, no Brasil. Fit. Perform. J. **1**(1), 28–36 (2002)
6. Medina, M.F., Fernandes Filho, J.: Identificação dos perfis genético e somatotípico que caracterizam atletas de voleibol masculino adulto de alto rendimento no Brasil. Fit. Perform. J. **1**(4), 12–19 (2002)
7. Diagnostico Nacional do Esporte Homepage. http://www.esporte.gov.br/diesporte/2.html, Last accessed 22 Mar 2018
8. Ferreira, A.E.X., de Rose Jr., D.: Basquetebol: técnicas e táticas: uma abordagem didático-pedagógica. EPU (1987)

9. Hippe, M., Flint, A., Lee, R.K.: University basketball injuries: a five-year study of women's and men's varsity teams. Scand. J. Med. Sci. Sports **3**(2), 117–121 (1993)

10. Confederação Brasileira de Futebol de Salão Homepage. http://www.cbfs.com.br/2015/futsal/origem/index.html, Last accessed 22 Mar 2018

11. Masuda, K., Kikuhara, N., Demura, S., Katsuta, S., Yamanaka, K.: Relationship between muscle strength in various isokinetic movements and kick performance among soccer players. J. Sports Med. Phys. Fit. **45**(1), 44 (2005)

12. Hubner, E., Reis, C.: Handebol, pp. 281–284. Lamartine (2005)

13. Eleno, T.G., Barela, J.A., Kokubun, E.: Tipos de esforço e qualidades físicas do handebol. Revista Brasileira de Ciências do Esporte **24**(1) (2002)

14. Martini, K.: Andebol: Técnica, Tática, Metodologia. Publicações Europa-América, Portugal (1980)

15. Matthlesen, S.Q.: Um estudo sobre o voleibol: em busca de elementos para sua compreensão. Revista Brasileira de Ciências do Esporte, Florianópolis: CBCE **15**(2), 194–199 (1994)

16. Borsari, J.R.: Voleibol—Aprendizagem e Treinamento. Um desafio constante. EPU, São Paulo (1996)

17. González, F.J., Darido, S.C., Oliveira, A.A.B.D., Silva, L.C.F.D.: Esportes de invasão: basquetebol-futebol-futsal-handebol-ultimate frisbee (2017)

18. Monteiro, A.B., Fernandes Filho, J.: Análise da composição corporal: uma revisão de métodos. Revista Brasileira de Cineantropometria & Desempenho Humano **4**(1), 80–92 (2002)

19. Dos Anjos, L.A., Denise, O., Serrão, S.A., da Silva, C.V.: Vigilância nutricional em adultos&58; experiência de uma unidade de saúde atendendo população favelada Nutritional surveillance of adults & 58; the experience of a health service for an urban slum population. Cadernos de Saúde Pública **8**(1), 50–56 (1992)

20. Cronk, C.E., Roche, A.F.: Race-and sex-specific reference data for triceps and subscapular skinfolds and weight/stature. Am. J. Clin. Nutr. **35**(2), 347–354 (1982)

21. Micozzi, M.S., Albanes, D., Jones, D.Y., Chumlea, W.C.: Correlations of body mass indices with weight, stature, and body composition in men and women in NHANES I and II. Am. J. Clin. Nutr. **44**(6), 725–731 (1986)

22. De Oliveira Filho, A., Shiromoto, R.N.: Efeitos do exercício físico regular sobre índices preditores de gordura corporal: índice de massa corporal, relação cinturaquadril e dobras cutâneas. J. Phys. Educ. **12**(2), 105–112 (2001)

23. American College of Sports Medicine (ed.): ACSM's Health-Related Physical Fitness Assessment Manual. Lippincott Williams & Wilkins (2013)

24. Pollock, M.L., Wilmore, J.H.: Exercício na saúde e na doença. Medsi, Rio de Janeiro (1993)

25. Gentil, D.A.S., et al.: Avaliação da seleção brasileira feminina de basquete Evaluation of Brazilian female basketball team. Revista Brasileira de Medicina do Esporte **7**(2), 53–56 (2001)

26. Nunes, J.A., et al.: Parâmetros antropométricos e indicadores de desempenho em atletas da seleção brasileira feminina de basquetebol. Rev. Bras. Cineantropom Desempenho Hum. **11**(1), 67–72 (2009)

27. Candia, F.N.P.: Avaliação nutricional esportiva. In: Duarte, A.C. (eds.) Avaliação nutricional: aspectos clínicos e laboratoriais, Atheneu, São Paulo, pp. 213–237 (2007)

28. Rodrigues, C., et al.: Avaliação da composição corporal em atletas de handebol antes e após uma temporada de treinamento. RBNE-Revista Brasileira de Nutrição Esportiva **7**(39) (2013)

29. Taborsky, F.: Game performance in handball. In: Handball Periodical: Periodical for Coaches, Referees and Lectures. EHF, 23–26 May 2002

30. Schutz, L.K.: Volleyball. Phys. Med. Rehabil. Clin. N. Am. **10**, 19–34 (1999)

31. Morrow, J.R., Jackson, A.S., Hosler, W.W., Kachurik, J.K.: The importance of strength, speed and body size for team success in women's intercollegiate volleyball. Res. Q. Exerc. Sport **50**, 429–437 (1979)

32. Fleck, S.J.: Body composition of elite American athletes. Am. J. Sports Med. **11**, S398–403 (1983)

33. Queiroga, Marcos Roberto, et al. Somatotipo como indicador de desempenho em atletas de futsal feminino. Revista Brasileira de Cineantropometria e Desempenho Humano **10**(1), 56–61 (2008)

Design of MATLAB/OpenSim Elbow Flexion Angular Setpoint Controller

Wellington Cássio Pinheiro, Maria Claudia F. de Castro, and Luciano L. Menegaldo

Abstract

Movement simulation is an important tool for better understanding human biomechanics. Associated with appropriate control techniques, mathematical models can simulate physiological responses, such as the closed-loop positioning of a limb. This work aims to design an optimized proportional-integral-derivative (PID), as well as a state feedback controller, using MATLAB to obtain a physiologically plausible elbow position setpoint response. The plant to be controlled is an OpenSim model appropriate for the forward dynamics analysis. Activation and muscle contraction coupled with arm rigid body dynamics were identified by linear models with an accuracy of 74.77% and 93.07% respectively. A MATLAB/OpenSim interface was adapted to run the forward dynamics simulations. PID controller has shown a good robustness, better rise time and zero steady-state error. State feedback controller yielded a smaller overshoot, with good responses for the other design criteria and, conceptually, is a more meaningful representation of the biological controllers than the PID.

Keywords

Forward dynamics • Control theory • MATLAB • OpenSim

W. C. Pinheiro (✉) · L. L. Menegaldo
Biomedical Engineering Department COPPE, Federal University of Rio de Janeiro, Rio de Janeiro, RJ, Brazil
e-mail: wellington@peb.ufrj.br

M. C. F. de Castro
Electrical Engineering Department, University Center of FEI, São Bernardo do Campo, SP, Brazil

1 Introduction

Modeling has been used by biomedical engineers as a bridge between health sciences and engineering for years. It led to better understanding of human body dynamics and paved the way for applying control theory to the development of assistive technologies. According to Grimaldi and Manto [1], there exist two main reasons to develop musculoskeletal models. First, to generate insights about the relationship between neurophysiology and movement control. Second, serve as a plant for the development of assistive technologies. This work focus on the first.

OpenSim is as computational open source software package developed by Delp et al. [2] for simulation of musculoskeletal systems and movement analysis. It contains, among others features, forward and inverse dynamics analysis, inverse kinematics, and static optimization tools, the last for estimating muscle forces. All these functions can be accessed using different programming languages through OpenSim *Application Programming Interface* (API). Associating OpenSim with MATLAB is a very promising way to increase OpenSim applicability to larger neuromuscular systems, allowing the implementation of neural dynamics and closed-loop controllers. Hopefully, this association will allow the faster development of assistive technologies, such as orthosis or electrical stimulators.

This work aims to adapt a MATLAB routine to handle an OpenSim arm model developed by Holzbaur et al. [3] as a plant (Fig. 1a), in the sense of control theory. Here, we have applied a system identification technique to estimate a black-box model able to generate outputs similar to OpenSim plant. Both a proportional-integral-derivative (PID) and a state feedback controller were generated and tested, to produce a setpoint response with physiological characteristics.

Fig. 1 **a** OpenSim arm26 model. **b** Block diagram of arm26 model for identification purposes. Dashed lines show which part of arm26 dynamics will be represented by each transfer function (Color figure online)
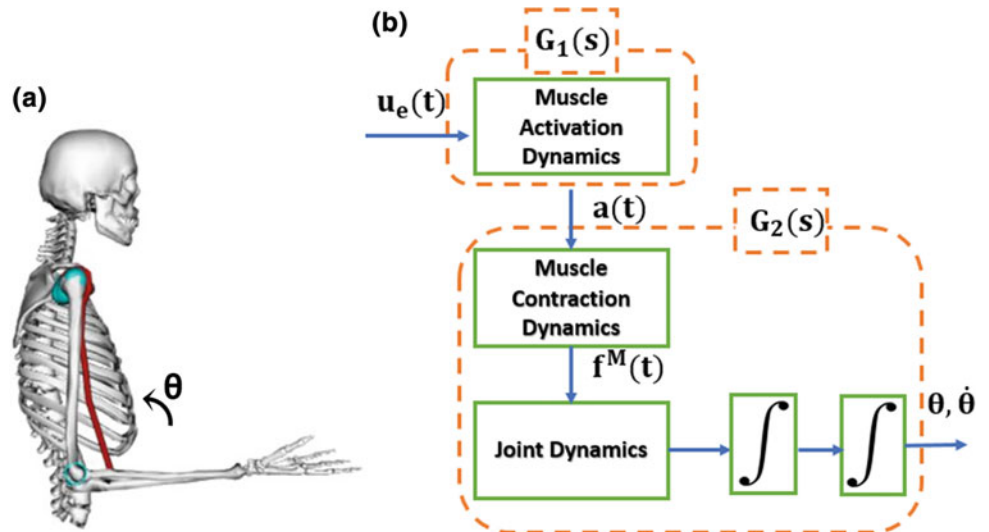
2 Materials and Methods

OpenSim does not offer explicit access to Ordinary Differential Equations (ODEs) which characterize muscle activation, muscle contraction and multibody dynamics. ODEs are extremely helpful for controller design. For the elbow, the simulated OpenSim model returns virtual measurements of the normalized muscle activation $(a(t))$, elbow flexion angle $(\theta(t))$ and velocity $\left(\dot{\theta}(t)\right)$. Neural excitation $u_e(t)$ is the input. A system identification technique called *Recursive Instrumental-Variable Method* (IV) [4, 5] was applied to obtain approximate linear transfer functions $G_1(s)$ and $G_2(s)$ as shown on Fig. 1b and Eqs. (1–2). For the sake of simplicity, at this stage of the project the OpenSim arm26 model developed by Holzbaur et al. [3] had its XML code edited, excluding all muscles but the *Biceps Brachii Long Head* (BIClong).

$$G_1(s) = \frac{a(s)}{u_e(s)} \qquad (1)$$

$$G_2(s) = \frac{\theta(s)}{a(s)} \qquad (2)$$

A MATLAB/OpenSim interface routine was adapted from previous works [6, 7] to handle OpenSim as a plant, and use MATLAB capabilities on control to manipulate model actuators (i.e., muscles). The advantage of using a MATLAB interface with OpenSim is that it contains advanced Control Toolboxes, which can be easily used to design and test candidate control implementations. Forward Dynamics simulations performed on OpenSim and using MATLAB interface, under same conditions, were compared to check interface reliability. At this point, the existence of an equilibrium elbow angle for the arm26 model was also checked. A fixed-step Dormand-Prince 5th order ODE integrator with steps of 0.001 s was used to the MATLAB interface.

A PID controller was designed to obtain the closed-loop stability of the linear identified system and serve as a setpoint controller (Fig. 2), simulating central nervous system (CNS) setpoint regulation. Gains Kp, Ki, and Kd (Eq. 16) were designed based on minimization of *Integral Absolute Error* (IAE), *Integral Time Absolute Error* (ITAE), *Integral Square Error* (ISE) and *Integral Square Time Error* (ISTE) [8, 9]. The formulation of these cost functions is presented on Eqs. (3–6).

Fig. 2 Schematic of PID controller for OpenSim identified plant
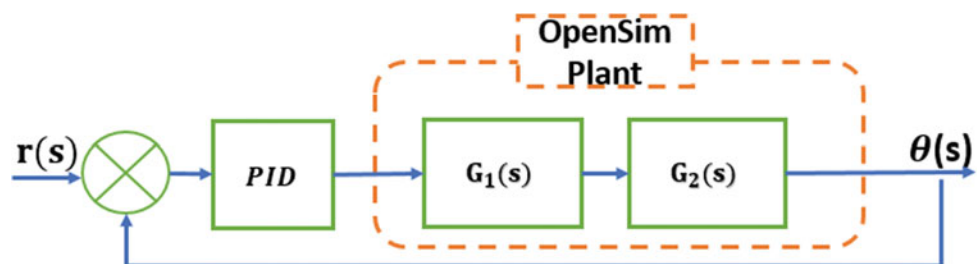
$$IAE = \int_0^\infty |e(t)|dt \qquad (3)$$

$$ITAE = \int_0^\infty t|e(t)|dt \qquad (4)$$

$$ISE = \int_0^\infty e(t)^2 dt \qquad (5)$$

$$ISTE = \int_0^\infty t^2 e(t)^2 dt \qquad (6)$$

$$\begin{cases} \mathbf{z}(\dot{t}) = \mathbf{A_a z}(t) + \mathbf{B_a u_e}(t) \\ \mathbf{a}(t) = \mathbf{C_a z}(t) \end{cases} \qquad (7)$$

$$\begin{cases} \dot{\mathbf{x}}(t) = \mathbf{A_\theta x}(t) + \mathbf{B_\theta a}(t) \\ \boldsymbol{\theta}(t) = \mathbf{C_\theta x}(t) \end{cases} \qquad (8)$$

$$\begin{cases} \begin{bmatrix} \mathbf{x}(\dot{t}) \\ \mathbf{z}(\dot{t}) \end{bmatrix} = \begin{bmatrix} \mathbf{A_\theta} & \mathbf{B_\theta C_a} \\ 0 & \mathbf{A_a} \end{bmatrix} \begin{bmatrix} \mathbf{x}(t) \\ \mathbf{z}(t) \end{bmatrix} + \begin{bmatrix} 0 \\ \mathbf{B_a} \end{bmatrix} \mathbf{u_e}(t) \\ \boldsymbol{\theta}(t) = \begin{bmatrix} \mathbf{C_\theta} & 0 \end{bmatrix} \begin{bmatrix} \mathbf{x}(t) \\ \mathbf{z}(t) \end{bmatrix} \end{cases} \qquad (9)$$

$$\mathbf{K} = \begin{bmatrix} 0 & 0 & \cdots & 1 \end{bmatrix} \mathbf{C}^{-1} \boldsymbol{\phi_d}(\mathbf{A}) \qquad (10)$$

Each of these cost functions was minimized and synthesized a PID controller [8]. The criteria used to choose the controller was minimum overshoot and settling time. The simulations on the OpenSim plant were performed using a fixed-step ODE solver, with a time step of Ts = 0.001 s, and the PID was discretized at the same sampling rate. On the derivative portion, backward differences formula was used, and on the integral part, Tustin's approximation was applied [10]. Due to unmodeled nonlinear effects of the OpenSim plant, manual fine-tuning of PID gains was necessary to find approximate characteristics of a physiologic response (i.e., small rise time and overshoot) on reaching a setpoint.

As a second approach to simulate CNS setpoint regulation, $G_1(s)$ and $G_2(s)$ were converted into a state-space representation (Eqs. 7–8) and associated as a cascade (Fig. 3a) (Eq. 9). After controllability and observability tests, Ackerman's formula [11] (Eq. 10) was used, and poles placed to obtain a physiologically plausible response one on the identified system. Notation used for continuous time (CT) and discrete time (DT) state space representation follows [10, 11].

where $\mathbf{A_a}, \mathbf{B_a}, \mathbf{C_a}$, and $\mathbf{z}(t)$ are muscle activation dynamics matrices and its state vector respectively. And $\mathbf{A_\theta}, \mathbf{B_\theta}, \mathbf{C_\theta}$, and $\mathbf{x}(t)$ are contraction and joint dynamics matrices, and its state space vector respectively. $\mathbf{K}$ is the state feedback gain vector, $\mathbf{C}$ is the controllability matrix, and $\boldsymbol{\phi_d}(\mathbf{A})$ is the characteristic matrix of the system presented on Eq. 9.

Considering that OpenSim plant was simulated with fixed-time steps, a discrete-time control approach was applied. State-space representation was discretized using zero-order hold method (ZOH), and the previously designed state feedback poles were mapped into the unity circle [10].

The obtained states were an abstract mathematical representation of the physical plant states [12]. Available states output by the OpenSim plant were the activation, elbow angle, and velocity. Similarly to PID, a discrete-time state observer was designed. The augmented state vector is presented on Eq. (11), states observer formulation on Eq. (12), and closed loop system form on Eq. (13).

Fig. 3 a Cascade association of identified activation dynamics on CT state-space form, and identified CT muscle contraction/arm rigid body dynamics. **b** Closed-loop schematic of OpenSim plant DT control with state feedback and Luenberger Observer (Color figure online)
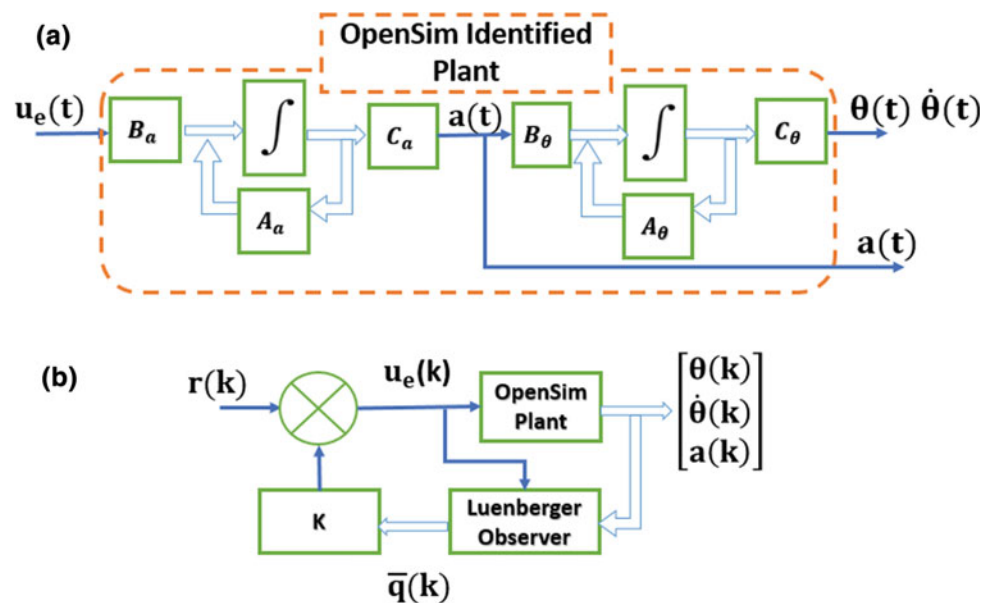
$$\bar{\mathbf{q}} = \begin{bmatrix} \bar{\mathbf{x}} \\ \bar{\mathbf{z}} \end{bmatrix} \qquad (11)$$

$$\bar{\mathbf{q}}(k) = (\mathbf{\Phi} - \mathbf{\Gamma K} - \mathbf{L_p H})\mathbf{q}(k-1) + \mathbf{L_p}\mathbf{\theta}(k-1) \qquad (12)$$

$$\begin{cases} \mathbf{q}(k+1) = \mathbf{\Phi q}(k) + \mathbf{\Gamma u}(k) \\ \mathbf{\theta}(k) = \mathbf{Hq}(k) \end{cases} \text{ such that } \mathbf{u}(k)$$
$$= \mathbf{r}(k) - \mathbf{K\bar{q}}(k) \qquad (13)$$

where $\mathbf{q}$ and $\bar{\mathbf{q}}$ are the discrete-time augmented state vector and augmented estimated states vector respectively, $\mathbf{K}$ is the state feedback gain vector, $\mathbf{r}$ is the reference signal for the targeted angle, and $\mathbf{\Phi}, \mathbf{\Gamma}$ and $\mathbf{H}$ are discrete-time system dynamics matrices.

Discrete-time state observer poles were first designed to be 3 times faster than the closed-loop system poles [10]. However, closed-loop poles, during the fine adjustment stage, were slightly modified to meet physiologic characteristics better, being observer poles kept unchanged. The closed-loop schematic is shown in Fig. 3b.

Finally, a similarity transformation was applied to the estimated states and the result compared with states virtually measured from OpenSim plant. All simulations were performed on a VAIO laptop svf15n26cxb, Windows 10, 8 GB RAM, and an INTEL core i7 processor.

3 Results

3.1 System Identification

First, the *Recursive Instrumental-Variable Method* (IV) was used to identify muscle activation, muscle contraction and arm rigid body dynamics. Transfer functions shown on Eqs. (14–15) were then obtained. $G_1(s)$ approximates activation dynamics with an accuracy of 74.77% (Fig. 4a). $G_2(s)$ approximates muscle contraction/rigid body dynamics with an accuracy of 93.07% (Fig. 4b). Both accuracies were calculated by Eq. (16), where y represents plant output measurement, and $\hat{y}$ is the model output measurement, and "*norm*" represents Euclidean norm operator.

$$G_1(s) = \frac{58.58s + 996.6}{s^2 + 114.5s + 658.2} \qquad (14)$$

$$G_2(s) = \frac{7.165.10^4}{s^4 + 39.73s^3 + 483.8s^2 + 2841s + 5940} \qquad (15)$$

$$\%\text{Fit} = \left[1 - \frac{\text{norm}(y - \hat{y})}{\text{norm}(y - \text{mean}(\hat{y}))}\right] \times 100 \qquad (16)$$
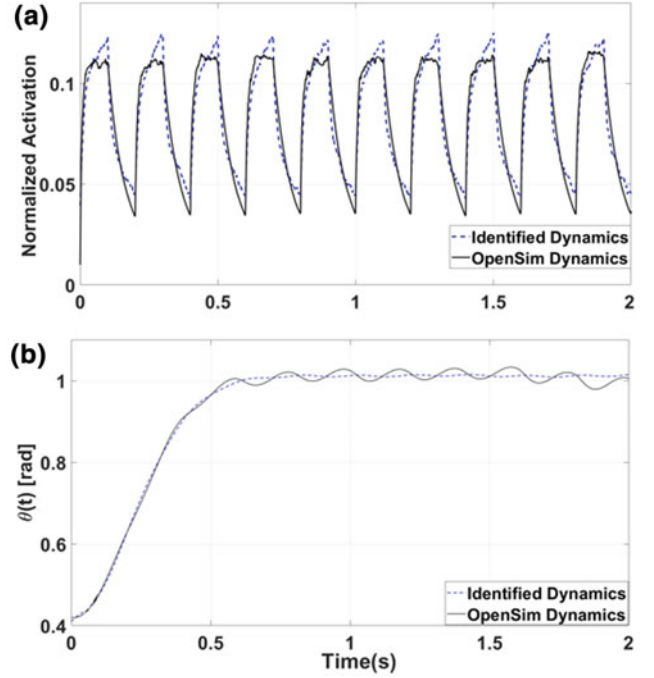
Fig. 4 a Muscle activation virtually measured from OpenSim plant when excitation is applied (solid line), and estimative of muscle activation obtained through $G_1(s)$ (dashed line). **b** Elbow flexion angle virtually measured from OpenSim plant when muscle activation is applied (solid line), and estimative of elbow flexion angle obtained with $G_2(s)$ (dashed line) (Color figure online)

3.2 MATLAB/OpenSim Interface

Based on an application developed by [6, 7] to use MATLAB as OpenSim plant's integrator, control features were implemented to the original code, to simulate the application of different controllers to forward dynamics simulations.

In order to validate the interface, results of forward dynamics simulations were performed with the arm26 model both on OpenSim's forward dynamics tool, and on MATLAB interface, and compared. Curve fitting was calculated with Eq. (16) and mean squared error with Eq. (17). As initial condition, elbow flexion angle was positioned on 30 degrees with zero input on both simulations, and the results are presented in Fig. 5.

$$\overline{\%\text{error}} = \text{mean}\left(\frac{(\theta_{\text{OpenSim}} - \theta_{\text{matlab}})^2}{\theta_{\text{OpenSim}}}\right) * 100 \qquad (17)$$

The curve fitting achieved was 86.52% with $0.4022° \pm 0.482°$ of mean error and standard deviation, respectively. Both simulations converge to an equilibrium point of $24.04°$ caused by the optimal length of BIC.
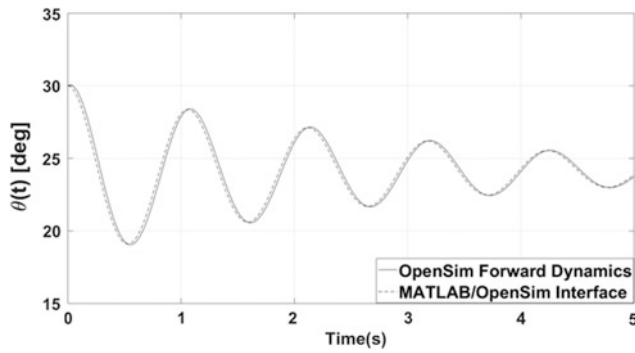
Fig. 5 Comparison between simulation results provided by OpenSim Forward Tool and MATLAB interface

3.3 PID Controller Design

To drive the elbow flexion angle to 90° (Fig. 1a), a PID controller was designed. Hypothetically, healthy physiologic position responses may be characterized by small overshoot (<10%), small rise time (<0.5 s) and small settling time (<1 s) [13]. Therefore, the ideal PID controller would drive the closed-loop plant to the targeted angle within these characteristics. Using PID optimal design criteria of Eqs. (3–6), proportional (K_p), integral (K_i) and derivative (K_d) were calculated (Eq. 18).

$$G_{pid}(s) = K_p + K_i \frac{1}{s} + K_d s \tag{18}$$

Figure 6a shows the corresponding closed-loop elbow flexion responses of the identified linear model. ITAE criterion resulted in smallest overshoot, with acceptable rise and settling time when compared to the hypothesized movement. According to Tan et al. [9], minimization of ITAE synthetizes robust PID controllers, which is a desired characteristic to control nonlinear plants such as an OpenSim model.

The ITAE PID controller transfer function is shown in Eq. (19). It was discretized for applying to the OpenSim plant. The OpenSim plant closed-loop elbow position response with reference angle signal as PID input is shown in Fig. 6b.

$$G_{ITAE-PID}(s) = 0.1234 + \frac{0.1865}{s} + 0.0157s \tag{19}$$

The ITAE PID controller provided a good response with the linearized model. When applied to the OpenSim plant, an unphysiological settling was observed. This effect is possibly due to unmodeled dynamics and nonlinearities of the plant. Thus, the PID gains were manually adjusted, starting from the ITAE solution. The integral gain was decreased to reduce the overshoot and settling time (Fig. 7a) [12]. To improve rise and settling time the proportional gain was
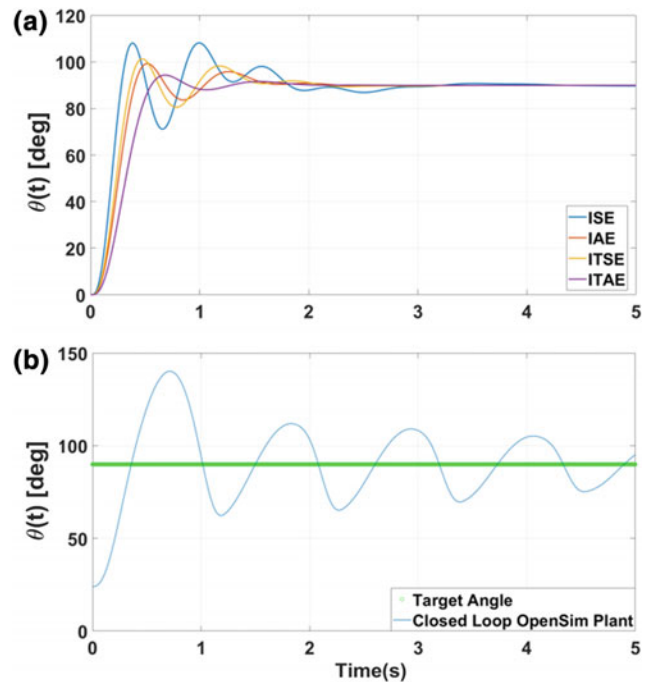
Fig. 6 **a** Elbow flexion angle output on PID synthesis using optimization criteria applied to the linear identified plant. **b** OpenSim plant response to setpoint regulation using PID controller

increased. The effects of both adjustments can be seen in Fig. 7b. As a third step, the derivative gain was increased to diminish the remaining overshoot (Fig. 7c). The fine-tuning tests yielded the recommended gain intervals of Eqs. (20–22). Figure 7d shows the response using gains at half of each interval. After the fine-tuning, overshoot decreased to 2.17%, rise time to 0.291 s and settling time to 0.776 s.

$$0.05 \leq Ki \leq 0.1 \tag{20}$$

$$0.3 \leq Kp \leq 0.35 \tag{21}$$

$$0.08 \leq Kd \leq 0.1 \tag{22}$$

3.4 State Feedback Design

Another approach used to simulate CNS setpoint regulation was state feedback design. $G_1(s)$ and $G_2(s)$ were initially converted into a state-space representation. For the identified plant, using Ackerman's formula, state feedback and state observer closed-loop poles were placed in the complex plane (Fig. 8a). This design provided to the linear and to OpenSim plants a setpoint regulation with small overshoot and rise time. However, approximately 2° of steady-state error was observed (Fig. 8b). This first configuration led OpenSim plant to an overshoot of 5.9%, rise time of 0.335 s and

Fig. 7 **a** PID integral gain decreasing to adjust overshoot and settling time (fixed $K_p = 0.081$ $K_d = 0.012$). **b** PID proportional gain increasing for fine tune (fixed $K_d = 0.012$ $K_i = 0.1$). **c** PID derivative gain increasing (fixed $K_p = 0.3$ $K_i = 0.1$). **d** PID final tuning—physiologic-like setpoint response
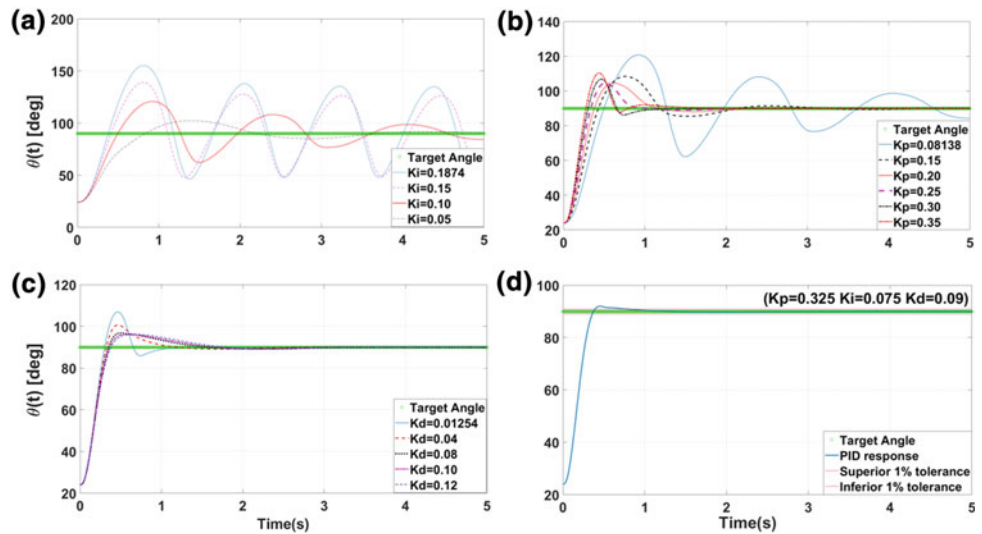
Fig. 8 **a** Pole locations of the linearized system with state feedback and observer 1st adjustment (blue cross), fine adjustment (red star). **b** Comparison of setpoint response between OpenSim Plant (solid line) and linearized model (dashed line) (Color figure online)
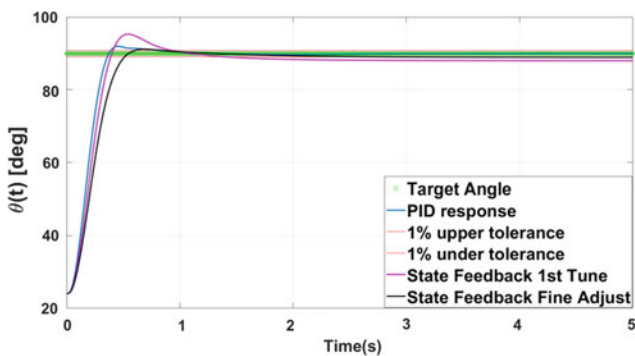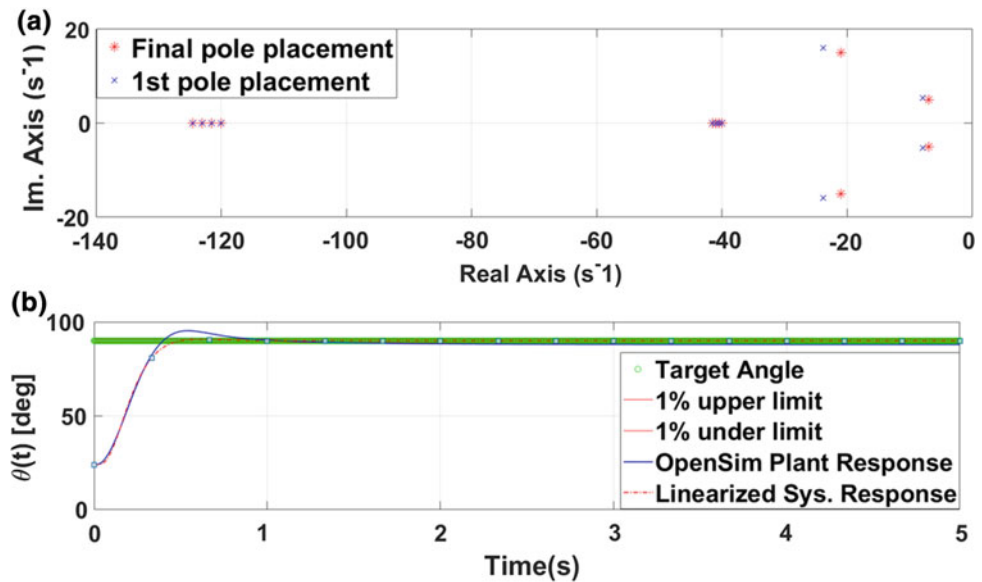
Fig. 9 Comparison of setpoint response of PID final tune and both state feedback designs

settling time of approximately 0.913 s. To decrease overshoot and steady-state error the dominant poles were reduced (real and imaginary parts) to decrease overshoot and keep a good tradeoff with rise and settling time. The reference signal gain was resized in consonance with dominant poles to diminish steady-state error.

After slight changes in dominant poles placement and reference signal gain, overshoot was reduced to 1.28% with a rise time of 0.384 s and approximate settling time of 0.809 s. Results are shown in Fig. 9.

The identified model states hold no physical meaning relatively to OpenSim plant variables [12]. For checking if the identified states hold correct information about plant states, a similarity transformation was applied [14, 15] (Eq. 23, Fig. 10).

Fig. 10 Comparison among virtually measured states from OpenSim plant and estimated ones after similarity transformation
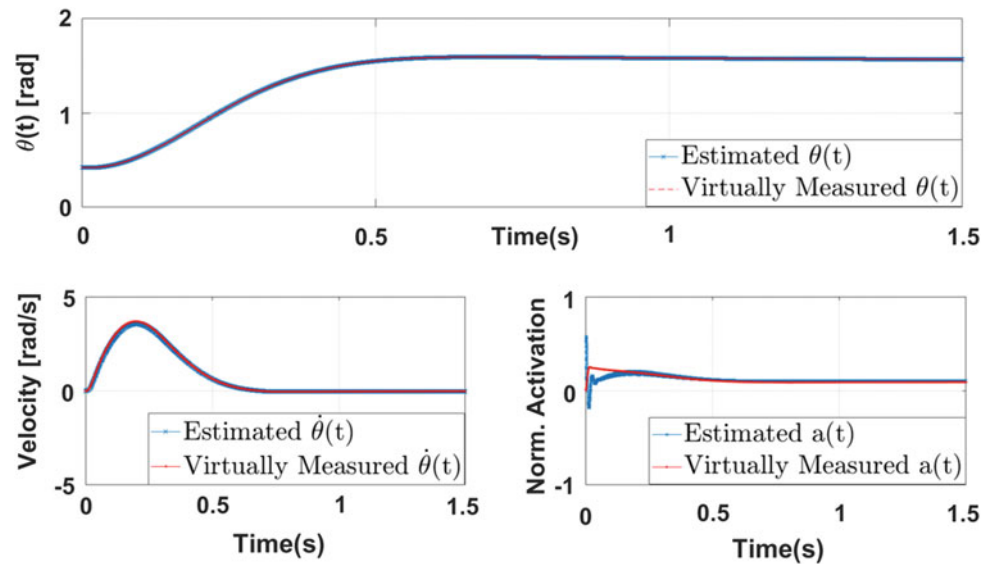
$$\mathbf{p} = \mathbf{Tq} \quad \text{such that } \mathbf{q} = \begin{bmatrix} x_1 \\ x_2 \\ x_3 \\ x_4 \\ z_1 \\ z_2 \end{bmatrix} \text{ and } \mathbf{p} = \begin{bmatrix} \theta \\ \dot{\theta} \\ \ddot{\theta} \\ a \\ x_4 \\ z_1 \end{bmatrix} \quad (23)$$

4 Discussion and Conclusions

This work aimed to design model-based controllers to simulate a CNS setpoint control of a hypothesized elbow flexion. An interface joining MATLAB and OpenSim forward dynamics was used and two different control architectures tested.

Firstly, a PID was designed using ITAE, IAE, ISE and ISTE optimization criteria. ITAE yielded the best PID design. This result is supported by Tan et al. [9] when analyzing different PID design techniques, and evidencing ITAE robustness. Due to unmodeled dynamics and nonlinearities, the fine tune of PID gains was required. Finally, overshoot, rise time, zero steady-state error and settling time expected for natural arm movements.

As a second approach, state feedback associated with a state observer was implemented. The linearized model and OpenSim plant behaved closer to each other compared to the PID. Small relative overshoot, rise time and settling time were obtained, but with a larger steady-state error. After a slight change in dominant poles placement overshoot and steady-state error were greatly diminished.

An important remark is that both controller designs do not behave similarly under unmodeled dynamics and nonlinearities. Even though a formal "μ-analysis" is required [16],

PID seems to be more robust on the vicinities of the targeted elbow angle than state space approach. This is due, among others causes, to the integral effect present on PID and higher sensitivity to uncertainties of state-space techniques [12].

Despite the aforementioned drawbacks on state space approach, according to Menegaldo [17], state feedback and observer relies on a reasonable physiological basis and has been extensively used in the literature for studying cognitive and motor problems. Contrarily, PID is based only on the end-effector position feedback, and we were not able to find a physiologic basis on motor control [17] for an integral term in the controller.

On the observed states (Fig. 10), considerable high-frequency contents were perceived on the activation estimation. As suggested by Franklin et al. [10], some observer poles could be reduced in order to mitigate such undesired effect in the predicted states.

Finally, even considering PID robustness, small rise time, settling time, overshoot and zero steady-state error, state feedback and observer control alternative meets all parameters of hypothesized movement, except zero steady-state error, also relying on the physiologic background. In order to achieve higher robustness levels on the state space approach, robust control theory should be applied on the state space control synthesis, using techniques such as sectorization of nonlinearities and insertion of uncertainty matrices on the model [16, 18]. In conclusion, when the synthesis of the single muscle controller be totally accomplished, additional and redundant musculotendon actuators will be included in the arm simulation model.

References

1. Grimaldi, G., Manto, M.: Mechanisms and Emerging Therapies in Tremor Disorders. Springer Science and Business Media (2012)
2. Delp, S.L., Anderson, F.C., Arnold, A.S., Loan, P., Habib, A., John, C.T., Guendelman, E., Thelen, D.G.: OpenSim: open-source software to create and analyze dynamic simulations of movement. IEEE Trans. Biomed. Eng. **54**, 1940–1950 (2007). https://doi.org/10.1109/TBME.2007.901024
3. Holzbaur, K.R.S., Murray, W.M., Delp, S.L.: A model of the upper extremity for simulating musculoskeletal surgery and analyzing neuromuscular control. Ann. Biomed. Eng. **33**, 829–840 (2005)
4. Ljung, L.: System Identification: Theory for the User. Prentice Hall, Upper Saddle River, NJ (1999)
5. Ljung, L.: System Identification Toolbox^{TM} User's Guide. 1220
6. Seth, A., Sherman, M., Eastman, P., Delp, S.: Minimal formulation of joint motion for biomechanisms. Nonlinear Dyn. **62**, 291–303 (2010). https://doi.org/10.1007/s11071-010-9717-3
7. Millard, M., Uchida, T., Seth, A., Delp, S.L.: Flexing computational muscle: modeling and simulation of musculotendon dynamics. J. Biomech. Eng. **135**, 021005-021005–11 (2013). https://doi.org/10.1115/1.4023390
8. Bolzern, P.G.E., Scattolini, R., Schiavoni, N.L.: Fondamenti di controlli automatici. McGraw-Hill Italia (1998)
9. Tan, W., Liu, J., Chen, T., Marquez, H.J.: Comparison of some well-known PID tuning formulas. Comput. Chem. Eng. **30**, 1416–1423 (2006). https://doi.org/10.1016/j.compchemeng.2006.04.001
10. Franklin, G.F., Workman, M.L., Powell, D.: Digital Control of Dynamic Systems. Addison-Wesley Longman Publishing Co. Inc, Boston, MA, USA (1997)
11. Ogata, K., Severo, B.: Engenharia de Controle Moderno. Prentice Hall do Brasil (2011)
12. Albertos, P., Antonio, S.: Multivariable Control Systems: An Engineering Approach. Springer, London (2004)
13. Winters, J., Woo, S.: Multiple Muscle Systems: Biomechanics and Movement Organization. Springer, New York
14. Chen, C.-T.: Linear System Theory and Design. Oxford University Press Inc, New York, NY, USA (1998)
15. Hespanha, J.: Linear Systems Theory. Princeton University Press (2018)
16. Zhou, K.: Essentials of Robust Control (1997)
17. Menegaldo, L.L.: Real-time muscle state estimation from EMG signals during isometric contractions using Kalman filters. Biol. Cybern. **111**, 335–346 (2017). https://doi.org/10.1007/s00422-017-0724-z
18. Vidyasagar, M.: Nonlinear Systems Analysis. Prentice Hall (1993)

Development of a Power Evaluation System for Combat Sports, Based on Load Cell and Elastic Band

Pedro Vieira Sarmet Moreira and Luciano Luporini Menegaldo

Abstract

The training with elastic bands are very used for training muscle power, however, usually the values of power output are not quantified. This turns totally subjective the process of choice for the rigidity, diameter, length and number of elastics to be used by each athlete. The aim of the present study was to develop a power evaluation system for performance measurements of martial techniques. For this purpose, elastic bands were connected to a load cell, where the elastic constants were properly calibrated through a 2nd order exponential equation with R^2 Adjusted = 1.00 and $p < 0.001$. Following the system was used to evaluate the optimal load for specific power development during taekwondo kicks. As a result this system presented very satisfactory results, since for the valid kicks, the information about the initial strain level of the elastics in which the highest power and force was obtained was quite easy to obtain. In addition, the system demonstrated in this study presents very useful, easy-to-use and fast processing solutions to monitor the performance of athletes at different stages of sports training periodization.

Keywords

Optimal load • Power • Kick speed • Taekwondo

1 Introduction

It is known that strength training composed by movements not specific to the analyzed sports movement can enhance the individual performance of each muscle, however, causing decrement in coordination between different muscles [2, 8]. On the other hand, training with elastic (TE) has been proposed as a training method applicable to the development of strength, muscular power and speed of movement with ecological validity, since it can be adapted so that the movements used for the training are specific to the trained modality [3, 5, 6]. The elastics are lightweight, easy to carry and of practical application, with the possibility of systematically monitoring the load used by controlling the diameter, length and percentage level of elastic stretch [3, 5, 6].

The efficacy of the TE, when carried out for some weeks, in promoting positive adaptations in the speed of combat sport movements, has already been tested by some authors. For example, Dinn and Behn [3] demonstrated that eight weeks of TE specific to the punch movement resulted in an increase in the speed of this technique in 17.6%, with a concomitant increase in the electromyographic activation of the pectoralis major muscle in 65% in relation to the previous values. Meanwhile, during the same training period of isometric contractions, carried out in an explosive manner, there were no changes in movement speed, even with an increase in electromyographic activation levels of the triceps brachii muscle, in 63%. Similarly, Jakubiak and Saunders [6] demonstrated that the application of TE over a period of only four weeks was sufficient to improve taekwondo kicking speed by a significant 7%.

Elastic training also proved to be useful in promoting *post-activation poteniation* (PPA) [1], which is the residual acute increase in strength, speed, or power performance that occurs a few minutes after training, usually attributed to phosphoryation of the myosin regulatory light chains, which makes actin and myosin more sensitive to Ca^{2+} and to an α motoneuron excitability as reflected by changes in H-reflex [4]. Therefore, when PPA is achieved, improvement in the electromyographyc activations are expected. For example, in the study by Aandaal et al. [1], 10 kickboxing athletes and 6 taekwondo athletes obtained significant improvements in kicking velocity of the foot by 3.3% after performing a preconditioning strategy that included performing kicks with elastics. PPA was also observed at the level of neuromuscular recruitment, since increases in the electromyographic

P. V. S. Moreira (✉) · L. L. Menegaldo
Programa de Engenharia Biomédica, COPPE/UFRJ,
Rio de Janeiro, Brazil
e-mail: sarmet_treinamento@hotmail.com

activation of the vastus medialis and rectus femoris muscles were observed in 35.2 and 43.9% in the semi-circular kick, which is the same type of kick performed in the present study by the evaluated athlete.

In spite of the great specificity and effectiveness of the elastic training in promoting adaptations for the performance of martial movements, to date no system was found to analyze performance of strength, power and speed in combat sport movements performed with elastic resistance. The development of this type of system may facilitate the monitoring of the cited physical qualities, as well as be used for the determination of individualized optimum loads, i.e. the diameter, initial deformation and number of elastics in which the maximum power is obtained. In this way, the purpose of this study is to demonstrate the practicality of using elastic equipment developed (in an initial phase) by the authors of the study for the analysis of martial movements.

2 Methods

A load cell (EMG System®), digitally converted by an A/D converter (OT Bioeletronica®, at 1000 fps), and an interface to the MATLAB® (2016a) was initially calibrated by means of linear regression (Fig. 1a) between the weight values measured previously by a scale (Welmy®) and the tension generated by a load cell, during the stabilization of 10 rings of different weights of bodybuilding (from 1 in 1 kg, from 1–10 kg). Next, two elastics with diameters of 14/8 mm were adapted to be attached to, on the one end to a steel cable attached to the load cell and on the other extremity to a strap fixed on the ankle of the volunteer (Fig. 2). Then, the force-strain relationship of each elastic was modeled by a second order exponential regression (Fig. 1b). These regression equations were saved and loaded by a MATLAB algorithm that transforms the measured voltage into force,

deformation, velocity and power applied to the end of the elastic attached to the athlete.

Following, a black belt athlete, Brazilian champion and 3rd placed of Taekwondo Competition of the the Military World Games, with experience in training with elastics, carried out a warm-up of approximately 10 min, followed by 5 min of rest to then carry out the assessment of kick power with elastic resistance. This evaluation was composed by four sets of three repetitions at maximum intensity, with the elastics being of different initial deformation lengths, ranging from 0 cm deformation, progressively increased by 30 cm by 30 cm until either: (a) the athlete found their load of optimum power or (b) the resistance was so high that the technique was visibly compromised, judged by a specialist of the modality. There was 5 min rest between sets and 2 s between repetitions.

All procedures were approved by the Ethical Committee of the Universitary Hospital of Federal University of Rio de Janeiro in 9th December of 2017 (number: 2.421.495).

3 Results

Figure 3 shows the graphical results generated by the system algorithm in response to the series of valid kicks with the elastic resistance that resulted in greater mechanical power produced by the athlete. Table 1 shows the average of each series of 3 repetitions, of the peak of stretch velocity, force and power produced in the elastics during kicks with different elastic resistances caused by different initial deformation.

It is possible to observe that the series in which the highest values of peak power were obtained were those in which the elastics started deformed in 25% (60 cm) and 37.5% (90 cm) of their initial length. However, the subjective evaluation of a specialist in the modality practiced by

Fig. 1 Calibration curves: **a** curve of measured voltage x load cell force; **b** curve of force x stretch produced in the elastic band
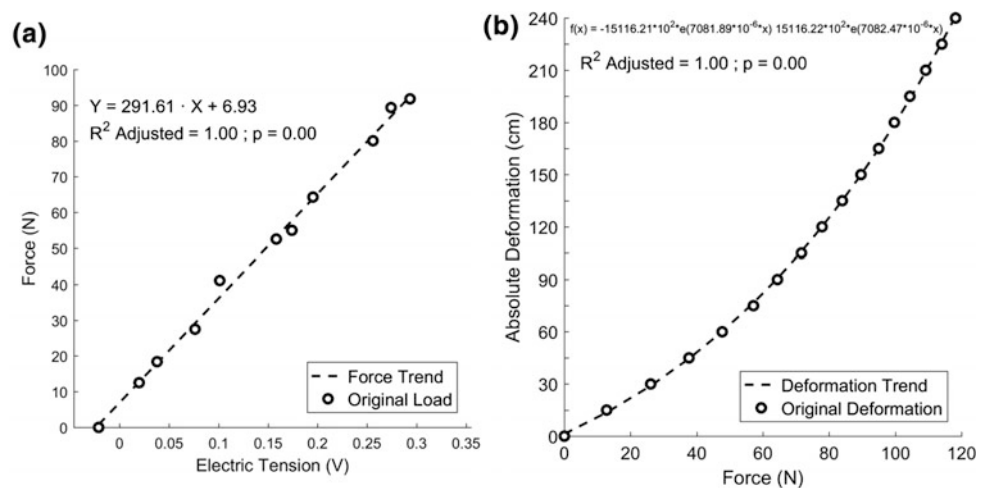
Fig. 2 Elastic power measurement system (bottom) with application (top)
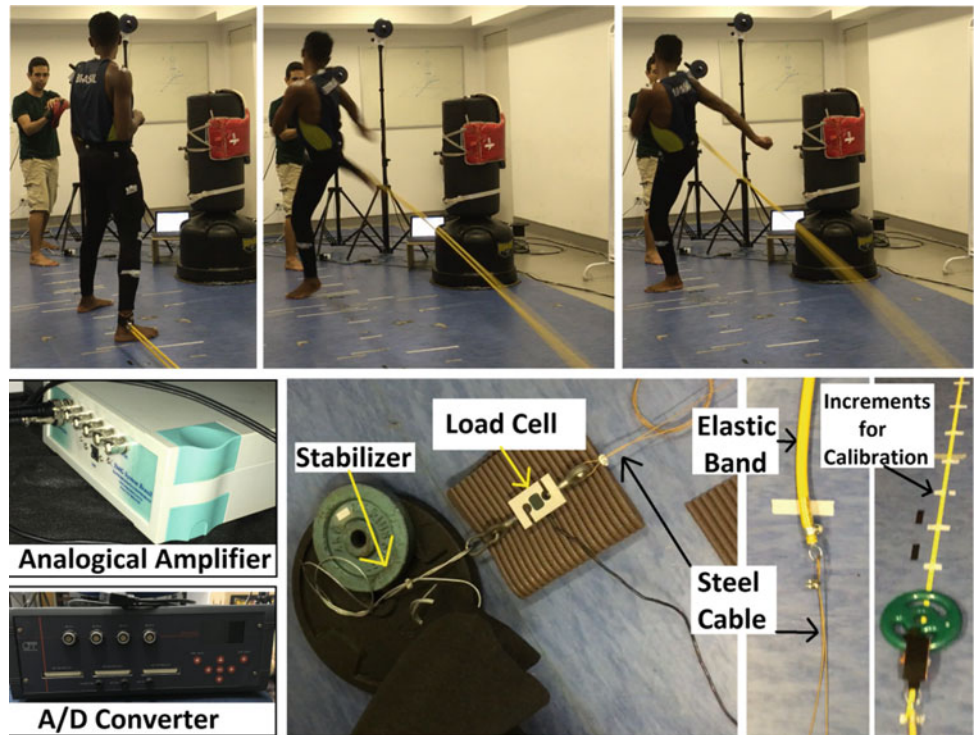
Fig. 3 Curve of strength, deformation, velocity, and power of a series of three kicks load with elastic bands
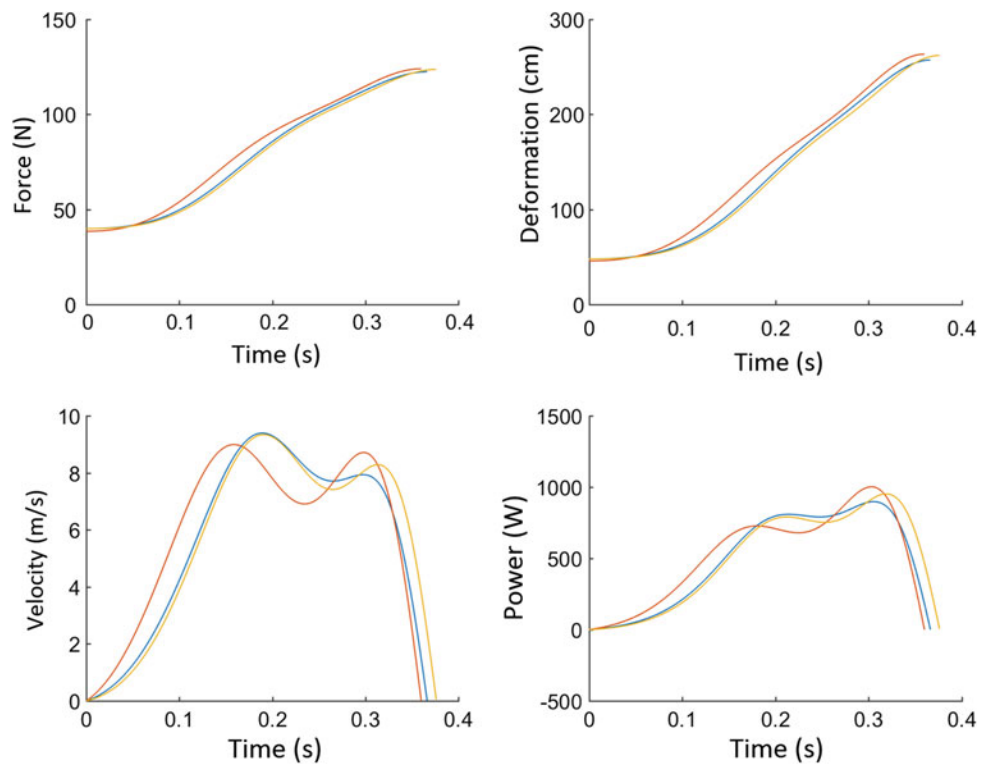
the athlete revealed that the kicks overloaded with the load of greater stretch (90 cm) were performed with insufficient technical level, due to visible changes in hip abduction of the dominant leg, at the beginning of the movement, and by low fluidity in the transition between the flexion phase of the hip and the extension phase of the knee. This difference in transition fluidity could be verified qualitatively by comparing the shape of the speed and power curves of the kicks with initial stretching of 60 cm with those obtained in kicks with initial elastic stretching of 90 cm. In this comparison, it

Table 1 Final results of power, velocity and kicking speed for each initial stretch and strain

Inicial stretch (cm)	Initial strain (%)	Velocity (m/s)	Force (N)	Power (W)	Qualitative validity
00	00.0	8.63	103.3	745	Yes
30	12.5	8.96	114.17	900	Yes
60	25.0	9.24	123.36	951	Yes
90	37.5	9.06	129.48	988	No

was found that the interval between the two peaks (the first, where the hip flexion velocity peak occurs and the second, where the knee extension velocity peak occurs) of each kick had a most prominent drop in speed and power in the series of initial stretch of the elastic equal to 90 cm.

4 Discussion

The main results were: (a) there was a perfect second-order exponential regression adjustment between the force and the elastic stretch level, measured at each calibration stage; and (b) the system was able to clearly demonstrate which initial level of stretching of the elastics is ideal for the evaluated athlete to obtain their optimal performance in muscular power; and (c) the graphs and values generated by the algorithm are quite easy to interpret, which demonstrates the great utility of using such a system for training control, that is, to evaluate an athlete at different stages of training periodization to test the effect of each performed choice of training strategy, as well as in scientific researches on strength, power and speed training for the performance of these variables in the specific technical condition of the sport practiced by the athlete.

There are some studies showing the effectiveness of elastic training for acute residual or chronic increase of power, muscle activation and speed of movement under specific conditions of martial techniques [1, 3, 6] or other ballistic movements [7]. However, none of these studies evaluated muscle velocity and power during the movement execution with elastic load, as was done in the present study. This means that there is no data available to compare the results found in the present study with those performed by other researchers, which shows that, although simple, the system has innovative features.

The presented system has demonstrated great potential in being used to obtain the optimal load and to control training of athletes, however, some limitations must be highlighted: (a) the agreement and other errors (random and systematic errors) of the system for to measure the velocity in comparison with standard gold methods were not evaluated (b) the reproducibility data of the system under standard conditions and in technical sport specific conditions have not yet been measured; (c) with the use of accumulated

repetitions the elastic will suffer natural mechanical fatigue which will imply in reducing the stiffness coefficients, so that, with the current configuration this system should be periodically recalibrated. Based on these limitations, further studies on agreement and reproducibility should be recommended, as well as the continuity in the system improvement work to not depend of frequent systematic recalibrations.

5 Conclusion

The results demonstrate that the developed system is practical and effective to evaluate the performance of martial kicks as well as the optimum power of specific sport movements. Practical applications include monitoring performance of athletes and easily determining the most effective elastic resistance for each athlete.

References

1. Aandahl, H.S., Von Heimburg, E., Van den Tillaar, R.: Effect of postactivation potentiation induced by elastic resistance on kinematics and performance in a roundhouse kick of trained martial arts practitioners. J. Strength Cond. Res. **32**(4), 990–996 (2018)
2. Bobbert, M.F., Van Soest, A.J.: Effects of muscle strengthening on vertical jump height: a simulation study. Med. Sci. Sports Exerc. **26**(8), 1012–1020 (1994)
3. Dinn, N.A., Behm, D.G.: Comparison of ballistic-movement and ballistic intent training on muscle strength and activation. Int. J. Sports Physiol. Perform. **2**, 386–399 (2007)
4. Hodgson, M., Docherty, D., Robbins, D.: Post-activation Potentiation. Sports Med. **35**(7), 585–595 (2005)
5. Hughes, C.J., Hurd, K., Jones, A., Sprigle, S.: Resistance properties of Thera-Band® tubing during shoulder abduction exercise. J. Orthop. Sports Phys. Ther. **29**(7), 413–420 (1999)
6. Jakubiak, N., Saunders, D.H.: The feasibility and efficacy of elastic resistance training for improving the velocity of the Olympic Taekwondo turning kick. J. Strength. Cond. Res. **22**(4), 1194–1197 (2008)
7. Mascarin, N.C., de Lira, C.A.B., Vancini, R.L., de Castro Pochini, A., da Silva, A.C., dos Santos Andrade, M.: Strength training using elastic bands: improvement of muscle power and throwing performance in young female handball players. J. Sport Rehabil. **26**(3), 245–252 (2017)
8. Morriss, C.J., Tolfrey, K., Coppack, R.J.: Effects of short-term isokinetic training on standing long-jump performance in untrained men. J. Strength. Cond. Res. **15**(4), 498–502 (2001)

Development of Multi-sensor System for Dynamic Analysis of Prehension Tasks

Letícia Munhoz Avellar, Natália Rinaldi, Teodiano Bastos, and Anselmo Frizera

Abstract

Prehension involves coordination of two components, reach and grasp. Generally, studies about reach-to-grasp were made in static conditions, in which a person's base of support is wide and stable. When performed combined with gait, the reach-to-grasp movement may be affected by dual task. Recently, hand gesture recognition has attracted a growing interest and can be acquired through a variety of sensors. The Leap Motion Controller introduces a new gesture and position tracking system with sub-millimeter accuracy. However, in a dynamic scenario, such device revealed an inconsistent performance. Therefore, the aim of this study is the improvement of Leap Motion system accuracy in the analysis of reach-to-grasp movements during walking combined with prehension. Two experimental protocols were defined for gait combined with the prehension task. The first one, using one Leap Motion Controller device, whereas the second uses the information obtained from two devices. Five young healthy subjects (24.8 ± 2.96 years) participated of this study. Five tests of each protocol were performed for each participant. The parameters analyzed in this work were the hand grip aperture, through the thumb and index tip positions, the peak grip aperture, the time to peak grip aperture and the stationary hand grip aperture. Results show acquisition failure and low accuracy in the first protocol. In the second, the errors are lower and the tests showed 100% acquisition success. Results show that the use of two Leap Motion Controller decrease the error mean from 47.75 to 18.87% in dynamic tests and reduces acquisition failures.

1 Introduction

Prehension involves the coordination of two components, reach component, moving the hand towards the object to be grasped, and the grasp component, enclosing the object [1]. These two components are integrated and coordinated through neural networks to perform reach-to-grasp successfully [2]. According to Zaal et al. [1], natural prehension is characterized by the hand opening and closing in tune with the movement of the hand toward the target object.

Generally, studies about reach-to-grasp were conducted on static tests, i.e. person's base of support is wide and stable. Other studies show that some modifications are observed in the prehension movement when the base of support is reduced, e.g. in upright stance posture. In a dynamic context, such as gait, the reach-to-grasp movement may be affected by dual task [2].

The act of reaching during walking is a common task in daily activities [3]. Previous studies that combined gait and prehension movements did not usually investigate in detail the reaching and grasping components such as hand grip aperture [2].

In recent years, hand gesture recognition has attracted a growing interest due to its applications in many different fields, such as human-computer interaction, robotics, computer gaming and automatic sign-language interpretation [4]. Hand gestures can be acquired through a variety of sensors, which precisely record every finger's flexion and abduction angles, position and orientation of the wrist [5].

The Leap Motion Controller introduces a new gesture and position tracking system with sub-millimeter accuracy [6].

L. M. Avellar (✉) · N. Rinaldi · T. Bastos · A. Frizera
Federal University of Espírito Santo, Vitória, ES 29075-910, Brazil
e-mail: leticia.avellar@aluno.ufes.br;
leticiamunhozavellar.lm@gmail.com

The controller comprises of a small device that can be connected to a computer through a USB (Universal Serial Bus). Furthermore, it can sense hand movements in the space above this, and these movements are recognized and translated into actions for the computer to perform [7]. Guna et al. [8] showed that the set of measurements in the dynamic scenario revealed an inconsistent performance of the Leap Motion Controller. Its accuracy was evaluated through the deviation of the distance between two moving points with a constant inter-point distance. In this case, the accuracy reduces when the objects move away from the sensor.

The aim of this study is to combine two sensors due to decrease limitations caused by workspace and occlusions, improving the accuracy of the Leap Motion system to analyze the reach-to-grasp movements during walking combined with prehension.

2 Materials and Methods

2.1 Leap Motion Controller

The Leap Motion Controller uses infrared (IR) imaging to determine the position of predefined objects in a limited space in real time. Three separate IR LED emitters are used in conjunction with two CCD cameras [8]. The stereographic camera arrangement complements the IR LEDs to prevent losing track of objects within the field of view and, while, creates a 3D interaction space [9].

The Leap Motion Controller enables to analyze the objects observed in the device's field of view (150°). It recognizes hands, fingers, tools, gestures, and motion[1]. The controller's field of view is an inverted pyramid centered on device's cameras. The effective range of the controller extends from approximately 25–600 mm above the device [8], and, as stated by the manufacturer, the sensor's accuracy in fingertip position detection is approximately 0.01 mm [6].

One difficulty with Leap Motion Controller is to maintain accuracy and fidelity of detection when the hands do not have direct line of sight with the controller [7]. Wachs et al. [5] analyzed that tracking complications arise from occlusions, cluttered environments, and rapid motions that causes motion blur. Addressing these challenges allows good recognition accuracy to be achieved.

2.2 Experimental Protocol

The experimental protocol defined consists of a free gait combined with a prehension task. The aim is to analyze the reach-to-grasp components when executed simultaneously with the gait. This protocol is performed in two different configurations, one using only one Leap Motion Controller and the other using two devices, which results in an increase of the combined field of view of both devices, as well as an increase of the accuracy after the data fusion of both Leap Motion Controller. The participants were five young healthy (24.8 ± 2.96 years), where the participants performed each protocol five times. The distance between the starting point and the object's support was 2.5 m, in order to cancel the first steps and forward at a steady gait. Figure 1 presents the protocol in both configurations.

Figure 2 shows the moment of prehension task and the fingertips positions when grasp the object.

The tests were performed with authorization of the UFES by the ethics committee number CAAE: 64797816.7.0000.5542.

2.3 Data Processing

The Leap Motion Controller devices were integrated with the ROS[2] software platform through a dedicated computer for each device. The ROS leap_motion package was used in the data processing. This package converts data stream into ROS topics by describing direction and normal vectors, position of the center of the palm, the Euler angles of the hand and the bones position of each finger (metacarpal, proximal, intermediate, distal and including the fingertips). To synchronize the machines, NTP (Network Time Procol) protocol was employed [10].

2.4 Data Analysis

The data analyzed in this work were the hand grip aperture, i.e. the distance between the thumb and the index, especially the peak grip aperture, the time to peak wrist and the stationary hand grip aperture, which will be validation basis of the Leap Motion Controller device. These data were analyzed in the Matlab software through the position data of the thumb and index finger tips. Equation 1 was employed to calculate the distance between these positions.

$$d = \sqrt{\left(x_{thumbtip} - x_{indextip}\right)^2 + \left(y_{thumbtip} - y_{indextip}\right)^2 + \left(z_{thumbtip} - z_{indextip}\right)^2}$$
(1)

In Eq. 1, $\left(x_{thumbtip}, y_{thumbtip}, z_{thumbtip}\right)$ represent the coordinates of the thumb tip, $\left(x_{indextip}, y_{indextip}, z_{indextip}\right)$ represent the coordinates of the index tip and d is the distance between

---

Fig. 1 Experimental protocol of gait combined with prehension task using one or two devices
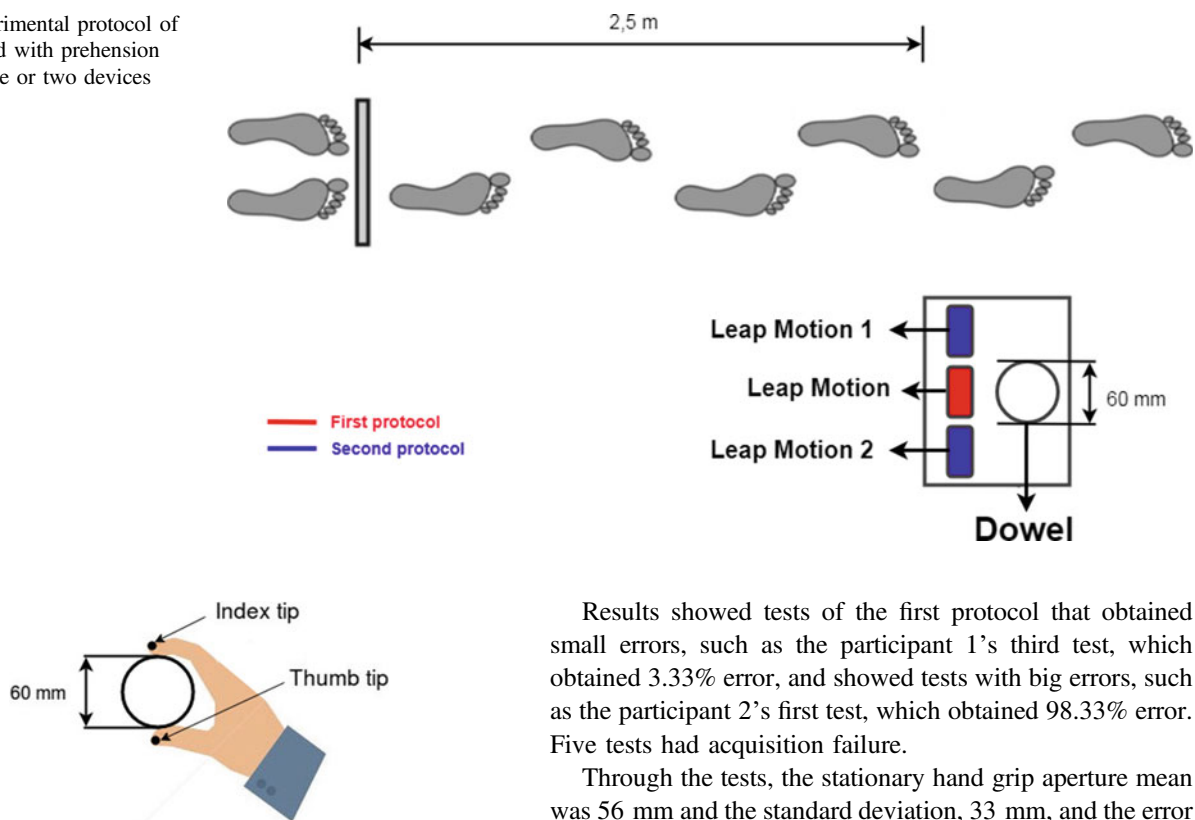
Fig. 2 Fingertips positions when grasp the object

thumb tip and index tip. In addition, a kalman filter was applied to perform the data fusion of both Leap Motion Controller devices [11].

To calculate error module, the obtained stationary hand grip aperture values were compared with the diameter of the object (60 mm), as shown in Eq. 2.

$$error\,module\,(\%) = \frac{|60 - stationary\,hand\,grip\,aperture|}{60} \times 100 \tag{2}$$

3 Results and Discussion

For each experimental protocol, 25 tests were performed (5 tests for each participant). Table 1 shows the prehension parameters obtained during both protocols for each participant.

According Fig. 2, depending on how the person grasp the object, the fingertips positions may be more distant or closer to the object, which influences the stationary hand grip aperture, which leads to lower repeatability of the tests.

Results showed tests of the first protocol that obtained small errors, such as the participant 1's third test, which obtained 3.33% error, and showed tests with big errors, such as the participant 2's first test, which obtained 98.33% error. Five tests had acquisition failure.

Through the tests, the stationary hand grip aperture mean was 56 mm and the standard deviation, 33 mm, and the error module mean was 47.75%.

Figure 3 shows the hand grip aperture curves in three tests for the first protocol. The first curve is the participant 3's second test and has 60% error. The second curve is the participant 4's first test and had acquisition failure. Lastly, the third curve is the participant 5's last test and has 36.67% error.

Results of the first experimental protocol showed acquisition failure in 5 tests and inconsistency of most obtained parameters. Moreover, the obtained standard deviation were high, which is 50% of the mean values presented in Table 1, showing low repeatability, also, the error module mean was high (47.75%), showing limitations of the use of the Leap Motion Controller in dynamic applications such as the one presented in this work.

Results showed 100% acquisition success for the second protocol. Furthermore, results showed tests of the second protocol that obtained small errors, such as the participant 2's last test, which obtained an error of 0%. The biggest error of the second protocol was 56.67%.

Through the tests, the stationary hand grip aperture mean was 65 mm and the standard deviation, 13 mm, and the error module mean was 18,87% for second protocol. The standard deviation and the error module mean of second protocol was much lower than first one, showing greater accuracy and repeatability.

Table 1 Prehension parameters of the experimental protocols tests

Protocols	Tests	Peak grip aperture (mm)		Time to peak wrist velocity (s)		Stationary hand grip aperture (mm)		Error module (%)	
		P1	P2	P1	P2	P1	P2	P1	P2
Participant 1	1	97	85	3.08	4.12	24	57	60.00	5.00
	2	80	76	3.89	4.00	80	65	33.33	8.33
	3	72	78	2.95	3.01	62	65	3.33	8.33
	4	87	80	2.81	3.03	44	52	26.67	13.33
	5	80	64	3.19	4.14	19	46	68.33	23.33
Participant 2	1	120	60	3.00	3.81	119	54	98.33	10.00
	2	92	104	2.66	2.72	88	42	46.67	30.00
	3	117	97	2.37	3.21	42	81	30.00	35.00
	4	119	70	2.28	3.68	20	51	66.67	15.00
	5	118	72	2.67	2.44	24	60	60.00	0
Participant 3	1	98	97	2.58	3.65	84	83	40.00	38.33
	2	35	101	2.00	3.61	24	57	60.00	5.00
	3	92	92	2.36	2.25	82	61	36.67	1.67
	4	101	103	2.92	2.88	86	79	43.33	31.67
	5	84	92	2.57	3.75	77	72	28.33	20.00
Participant 4	1	–	94	–	4.20	–	94	–	56.67
	2	–	86	–	3.06	–	47	–	21.67
	3	–	83	–	3.42	–	61	–	1.67
	4	106	81	1.85	3.33	9	73	85.00	21.67
	5	74	94	1.14	2.90	7	65	88.33	8.33
Participant 5	1	–	119	–	3.00	–	82	–	36.67
	2	–	97	–	3.48	–	78	–	30.00
	3	94	100	3.31	3.13	78	69	30.00	15.00
	4	72	104	3.27	2.49	68	76	13.33	26.67
	5	90	94	2.77	2.87	82	65	36.67	8.33
Mean	–					**56 ± 33**	**65 ± 13**	**47.75**	**18.87**

Figure 4 shows the hand grip aperture curves in three tests for second protocol. The red curve is fused data. The first curve is the participant 3's third test and presents an error of 1,67%. The second curve is the participant 5's fourth test and presents an error of 20%. The third curve is the participant 4's third test and presents an error of 1,67%. In last curve, the Leap Motion Controller 2 failed, however the Leap Motion Controller 1 performed the acquisition and obtained a result with low error.

Results of the second experimental protocol showed no acquisition failure, since when one Leap Motion Controller was not able to detect correctly the hand landmark, the other usually performed the acquisition correctly. Thus, 100% acquisition was ensured. Furthermore, the error mean and
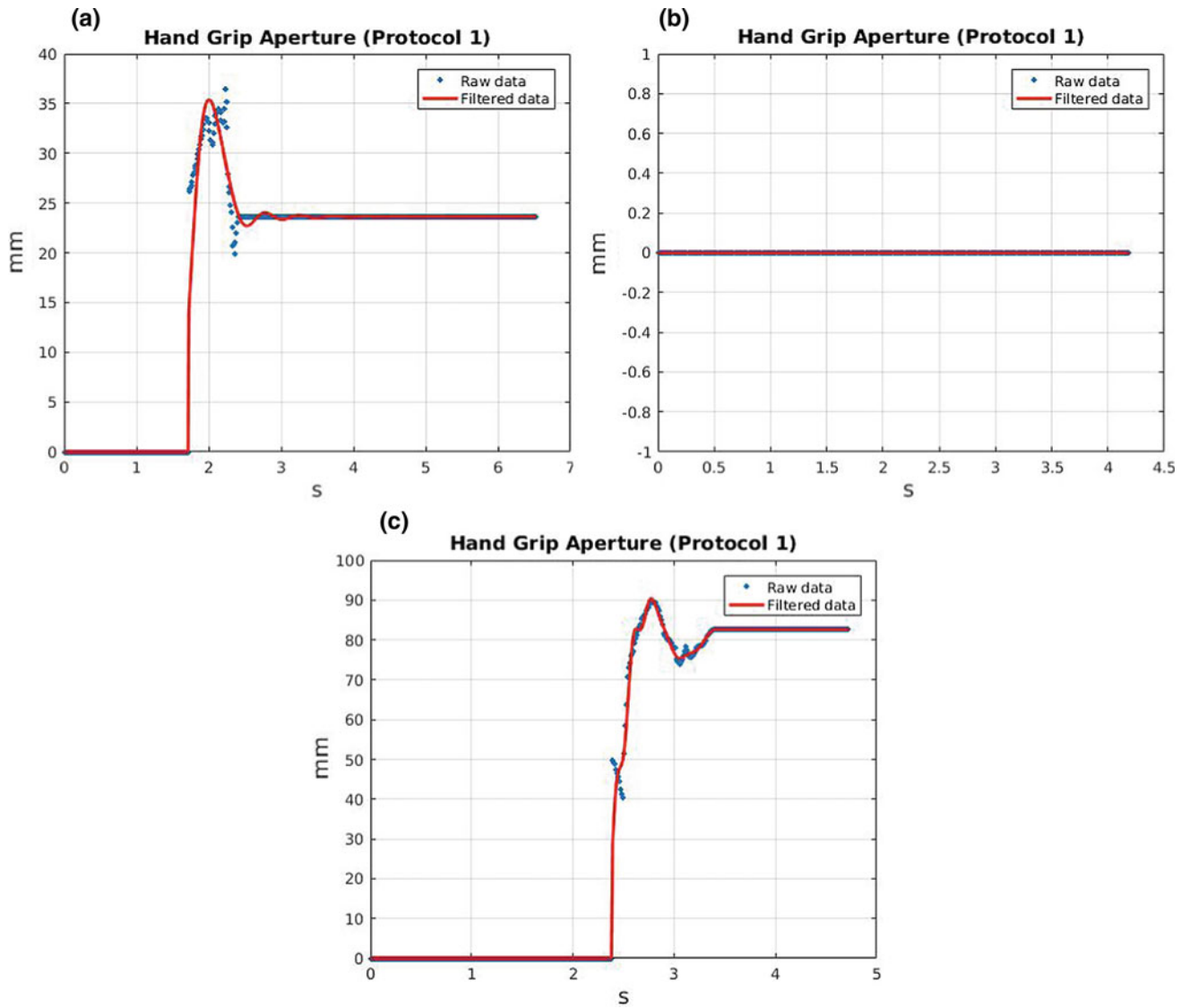
Fig. 3 Hand grip aperture curves in the experimental protocol 1. **a** 60% error curve. **b** Acquisition failure. **c** 36.67% error curve
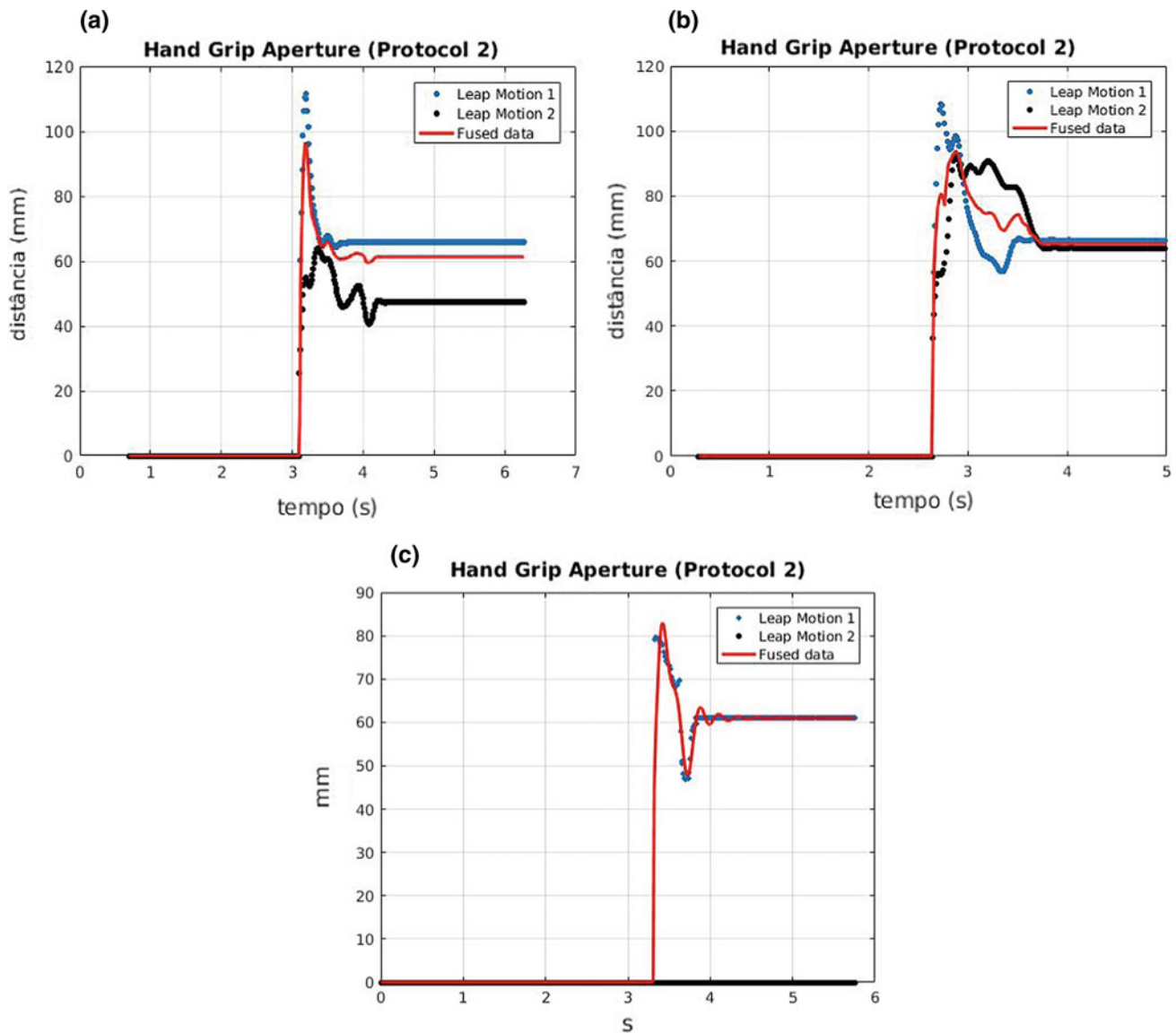
Fig. 4 Hand grip aperture curves in the experimental protocol 2. **a** 1.67% error curve. **b** 26.67% error curve. **c** 1.67% error curve with Leap Motion 2's acquisition failure

standard deviation of the second protocol was smaller than the first protocol, showing that the system is more accurate and presents measures more consistent.

4 Conclusion

This work presented a technique to combine two Leap Motion Controller devices to improve the reliability of data acquisition for dynamic tests. Since one difficulty of the Leap Motion Controller is non-constancy acquisition in the dynamic scenario, two Leap Motion devices are employed for the field of view increase and of the chances of acquiring the data. In addition, the data is fused, which result in an increase of accuracy. Results show that the use of two Leap Motion Controller decrease the acquisition errors in dynamic tests and reduces the chances of acquisition failures. The system architecture also allows the integration of more sensors to expand this application to others scenarios. Future works involve the application of these protocols in elderly

people and the comparison with young adults in order to evaluate task performance and cognitive impairments found on elderly population.

References

1. Zaal, F.T.J.M., Bootsma, R.J., Van Wieringen, P.C.W.: Coordination in prehension. Information-based coupling of reaching and grasping. Exp. Brain Res. **119**(4), 427–435 (1998)
2. Rinaldi, N., Moraes, R.: Gait and reach-to-grasp movements are mutually modified when performed simultaneously. Hum. Mov. Sci. **40**, 38–58 (2015)
3. Carnahan, H., Mcfadyen, B.J., Cockell, D.L., Halverson, A.H.: The combined control of locomotion and prehension. Neurosci. Res. Commun. **19**(2), 91–100 (1996)
4. Marin, G., Dominio, F., Zanuttigh, P.: Hand gesture recognition with leap motion and kinect devices. In: 2014 IEEE International Conference on Image Processing, ICIP. Paris, France, pp. 1565–1569 (2014)
5. Wachs, J.P., Kölsch, M., Stern, H., Edan, Y.: Vision-based hand-gesture applications. Commun. ACM **54**(2), 60–71 (2011)
6. Weichert, F., Bachmann, D., Rudak, B., Fisseler, D.: Analysis of the accuracy and robustness of the Leap Motion Controller. Sensors **13**(5), 6380–6393 (2013)
7. Potter, L.E., Araullo, J., Carter, L.: The Leap Motion controller. In: Proceedings of the 25th Australian Computer-Human Interaction Conference on Augmentation, Application, Innovation, Collaboration, pp. 175–178. Adelaide, Australia (2013)
8. Guna, J., Jakus, G., Pogacnik, M., Tomazic, S., Sodnik, J.: An analysis of the precision and reliability of the leap motion sensor and its suitability for static and dynamic tracking. Sensors **14**(2), 3702–3720 (2014)
9. Curiel-Razo, Y.I., Icasio-Hernández, O., Sepúlveda-Cervantes, G., Hurtado-Ramos, J.B., González-Barbosa, J.J.: Leap motion controller three dimensional verification and polynomial correction. Meas. J. Int. Meas. Confed. **93**, 258–264 (2016)
10. Mills, D.L.: Internet time synchronization: the network time protocol. IEEE Trans. Commun. **39**(10), 1482–1493 (1991)
11. Khaleghi, B., Khamis, A., Karray, F.O., Razavi, S.N.: Multisensor data fusion: a review of the state-of-the-art. Infor. Fus. **14**(1), 28–44 (2013)

Development of New Foot Model for Dynamic Equinus Foot Behavior During Gait

Carlos Gonçalves, Mariana Baccarin, Aline Dalfito, Sheila Denucci,
Carolina Girardi, Marloes Kijzers, Rob Zanders, Monique Berger,
and Lucia Willadino Braga

Abstract

The evaluation of foot deformities in the gait laboratory is still a challenge for many rehabilitation centers. Several models have been proposed in measuring accentuated foot deformities, however there are some limiting factors for the markers placement, the number of markers used, as well as the complexity of their placement which limit the data collection. The aim of this study is to develop a new foot model to measure the dynamic behavior of an equinus foot during gait. Using only four additional markers, our model is built over the original VICON Plug-In-Gait marker protocol, not compromising the time spend to set up the subject for the conventional gait analysis. The outcomes of the measurements are the angle displacements of two regions of both feet: hindfoot and forefoot. It is notable that the values of the angles of the hindfoot and forefoot planes are not zero when the individual is in neutral stance. Therefore compensation is needed using calibration data of unimpaired subjects. The model proposed was tested in an unimpaired subject as well in a patient scheduled for gait exam with right foot equinus. Our results show promising information about the equinus deformity during gait, but further research is needed to indicate the precision of the tool, especially in subjects with stair type equinus.

C. Gonçalves · M. Baccarin (✉) · A. Dalfito · S. Denucci ·
C. Girardi · L. W. Braga
SARAH Network of Rehabilitation Hospitals—Lago Norte Unit,
Brasília, Brazil
e-mail: mabaccarin@hotmail.com

C. Gonçalves
e-mail: cwpg@sarah.br

M. Kijzers · R. Zanders · M. Berger
The Hague University of Applied Sciences, Hague, Netherlands

1 Introduction

The evaluation of foot deformities in gait laboratory is still a challenge for many rehabilitation centers. There are several models that have been used [1–3], however there are some limiting factors for the markers placement when the foot has accentuated deformities, which difficult the data collection.

The most used biomechanical models, notably the Plug-in-Gait model [4], usually represent the foot as a rigid segment, not considering the real foot movements specificity and complexity due to the imminent multi-planar feature of contact surface of the foot joints. In the majority the researches, it is only feasible to measure the angles of foot flexion and dorsiflexion [5, 6]. Such models are insufficient to characterize the foot movements in three dimensions during the support phase of the gait [7]. Therefore, new three dimensional models are necessary to assess the deformities as equinus.

There are two different kinds of equinus deformities, the 'ramp' equinus and the 'stair' equinus. The cause of the 'ramp' equinus is spasticity and/or shortening of the muscle gastrocnemius [8]. In the 'stair' equinus, there is not only the problem with the spasticity and/or shortening of the muscle gastrocnemius, but there is also a deformity in the midfoot, with the consequent lowering of the forefoot. The treatment approach in these two different deformities could be completely different. This is one of the reasons why it is important to measure this kind of deformities during gait.

There are some marker protocols already developed to cope with the cited limitations. Leardini et al. [1] developed a new protocol for gait analysis for children. The main goal in this research was to minimize the marker-set. There are four markers used on the foot to gain data from the feet; dorsiflexion and plantar flexion, inversion and eversion, abduction and adduction. The markers were placed on anatomical landmarks: malleolus lateralis, achilles tendon insertion on the calcaneus and the dorsal margins of the first and fifth metatarsal heads.

Yalamanchili et al. [2] developed and validated a model to calculate parameters (kinetic and kinematic) in the foot during normal gait. The markers were placed on the following anatomical landscapes: malleolus medialis, malleolus lateralis, calcaneal tuberosity, lateral aspect of the calcaneus, base of the second metatarsal, head of the first metatarsal, head of the fifth metatarsal, nail of the first phalanx, nail of the fifth phalanx and the mid-point between 2nd and 3rd metatarsal heads.

From all gathered research, there are some clear steps to create a usable marker protocol to the foot movement. First, the markers should be placed on anatomical landmarks. An anatomical landmark is a place on the surface of the body, and this place can be found by visual inspection or palpation [9]. The best to place a marker is a bone covered only by skin with less displacement during gait. The measurement system registers the markers, so if the markers move a lot, the data of the coordinates won't be correct. Second, there should be planes created by the markers to analyze the angles. At least 3 markers are needed to calculate each segment plane and the markers also shouldn't be in a straight line [10].

The aim of this study is to develop a new foot model to measure the dynamic behavior of an equinus foot during gait.

This research was approved by local ethical committee with the registered CAAE number 90632318.8.0000.0022. All selected subjects that participated in this work have acknowledged the informed consent form.

2 Materials and Methods

Anatomical constraints should be taken care prior the development of the equinus model. Originally the Plug-In-Gait [4] protocol considers the foot as a single block connected to the ankle. For this research, the foot was divided into two articulated pieces: hindfoot and forefoot. This could deal with both equinus cases, and would not compromise the regularly done gait exam in SARAH Network of Rehabilitation Hospitals.

Figure 1 presents the additional markers placed on the foot which represents both hindfoot and forefoot planes. The markers on tuberositas ossis quinti and tuberositas ossis naviculare are easy to place correctly, and both LCS (local coordinate system) created by the markers are a fair representation of the anatomical LCS of both hindfoot and forefoot.

2.1 Equipment

This research used the facilities of the Motion Lab at the Lago Norte unit of the SARAH Network of Rehabilitation Hospitals. The laboratory has 12 VICON MXF40 cameras and uses the software NEXUS 2.5 for data processing. The
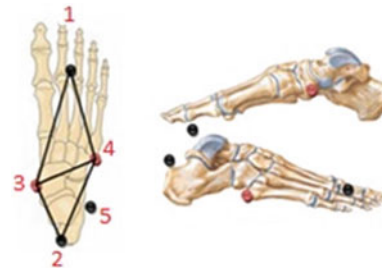
Fig. 1 Marker placement for the equinus model with one plane in the forefoot and one plane in the hindfoot; 1: TOE (marker on mid-point between 2nd and 3rd metatarsal heads), 2: HEE (marker on insertion calcaneus with Achilles tendon), 3: NAV (marker on tuberositas ossis naviculare), 4: TOQ (marker on tuberositas ossis quinti), 5: ANK (marker on malleolus lateralis)

standard Plug-In-Gait marker protocol was followed with additional markers to fulfill our goals. Figure 2 presents the Motion Lab setup for the conventional gait exam.

In order to process the hindfoot and forefoot data, the C3D data exported from VICON NEXUS was load in a Python script with the help from the BTK, Biomechanical Toolkit, library [11].

2.2 LCS Implementation

In order to calculate the angles that will represent plantar flexion and dorsal flexion (around X-axis, α), eversion and

Fig. 2 Motion laboratory set of cameras used in this research

inversion (around Y-axis, β), and abduction and adduction (around Z-axis, γ), the rotation matrix R is obtained from Eq. 1.

$$R = R_{FOOT} \cdot R'_{TIBIA} \qquad (1)$$

R_{FOOT} can be replaced by the rotational matrix created for each one of the hindfoot and forefoot in both legs. R_{TIBIA} is the rotational matrix from the connected tibia. R_{FOOT} and R_{TIBIA} are created from the unit vectors that represents each plane [12]. All the matrices are updated at every new frame capture by the motion capture system. Figure 3 present a representation of LCS of hips, thigh and shank (tibia). Each LCS has its own rotational matrix derived from the real and virtual markers in motion capture system.

However, the neutral position of the foot will result in a non-zero value for all the angles to an unimpaired person. To cope with this situation, a dataset of unimpaired persons was built to store the average value of the angles during normal stance. That value is used to calibrate the data, resulting in angle values that vary around zero when the alignment of tibia and foot is different from neutral.

The resulting calibrated rotational matrix is represented as [12]:

$$R_{CAL} = \left(R'_{C\_FOOT} \cdot R_{FOOT}\right) \cdot \left(R'_{C\_TIBIA} \cdot R_{TIBIA}\right)', \qquad (2)$$

where R_{C_FOOT} is the mean foot orientation from the dataset sample, as well R_{C_TIBIA} is for the tibia.

To keep the standard orientation of biomechanical LCS (Y-axis pointing in the anterior direction), the calculations

for the unit vectors for hindfoot and forefoot planes are described in Table 1.

Additionally to the calibrated rotational matrices, a 95% confidence interval, ci, of this neutral measurement is added to our results. This interval is calculated as:

$$ci = 1.96 \times \frac{\sigma}{\sqrt{n}}, \qquad (3)$$

where n is the sample size of unimpaired subjects of our study ($n = 5$).

2.3 Methodology

The four additional markers were added in VICON conventional protocol for gait analysis in the both subjects analyzed. We collected six trials while the subjects passed over the force plates in the center of the room. The best trial from the 6 set was selected for dynamic equinus analysis.

All trials were performed at the Motion Lab in SARAH Network of Rehabilitation Hospitals, Lago Norte unit.

In order to compare results from the angles of movement from the hindfoot and forefoot, we used the data collected from an unimpaired member of the research team against the data from a patient with equinus foot on the right leg that was already schedule for a gait exam.

The unimpaired dataset for neutral stance calibration was obtained from gait exams of volunteers participating in the research team.

3 Results and Discussion

In Fig. 4 the angles from both hindfoot and forefoot of both legs of the unimpaired subject is presented. Similarities of both legs and also between hindfoot and forefoot can be seen since the feet are unimpaired and the subject has a normal walking pattern.

For normal individuals (Fig. 4), the graphical output obtained with the new markers showed gait events similar to other sets of marks, such as that obtained by the Oxford Foot Model[@], but the great difference was in the number of marks used during the data collection. The possibility of collecting more data with a smaller number of markers allows fewer errors in the placement, greater agility in preparing the patient, and allows placing marks in feet with deformities.

In the frontal plane (Fig. 4a, b), the graphs obtained with the new set of marks show the angular displacement of the ankle between the maximum dorsiflexion (in the terminal support) to the maximum plantar flexion (in the pre-balance and initial balance), being possible the discrimination between the forefoot and hindfoot. The same occurs in the transverse plane (Fig. 4c–f), where it is possible to observe
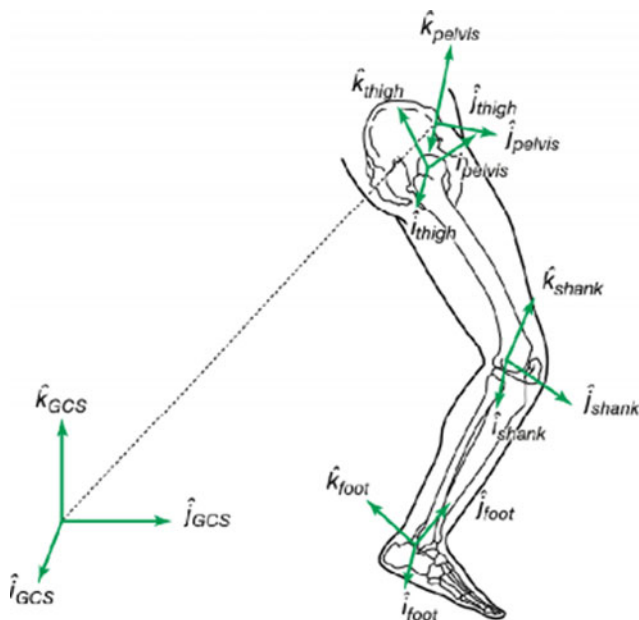
Fig. 3 Example of LCS of hips, thigh and shank of the right lower limb [12]

Table 1 Definitions for unit axis representing hindfoot and forefoot planes

Axis	Direction	Calculation
X (right forefoot)	From RNAV to RTOQ	RTOQ—RNAV
Y (right forefoot)	Perpendicular on the X-axis and Z-axis	Cross product (Z-axis) (X-axis)
Z (right forefoot)	Perpendicular on the triangle (= Normal vector)	Cross product (RTOE-RNAV) (RTOE-RTOQ)
X (left forefoot)	From LTOQ to LNAV	LNAV—LTOQ
Y (left forefoot)	Perpendicular on the X-axis and Z-axis	Cross product (Z-axis) (X-axis)
Z (left forefoot)	Perpendicular on the triangle (= Normal vector)	Cross product (RTOE-RTOQ) (RTOE-RNAV)
X (right hindfoot)	From RNAV to RTOQ	RTOQ—RNAV
Y (right hindfoot)	Perpendicular on the X-axis and Z-axis	Cross product (Z-axis) (X-axis)
Z (right hindfoot)	Perpendicular on the triangle (= Normal vector)	Cross product (RTOQ-RHEE) (RNAV-RHEE)
X (left hindfoot)	From RTOQ to RNAV	LNAV—LTOQ
Y (left foot hindfoot)	Perpendicular on the X-axis and Z-axis	Cross product (Z-axis) (X-axis)
Z (left foot hindfoot)	Perpendicular on the triangle (= Normal vector)	Cross product (LNAV-RHEE) (LTOQ-RHEE)
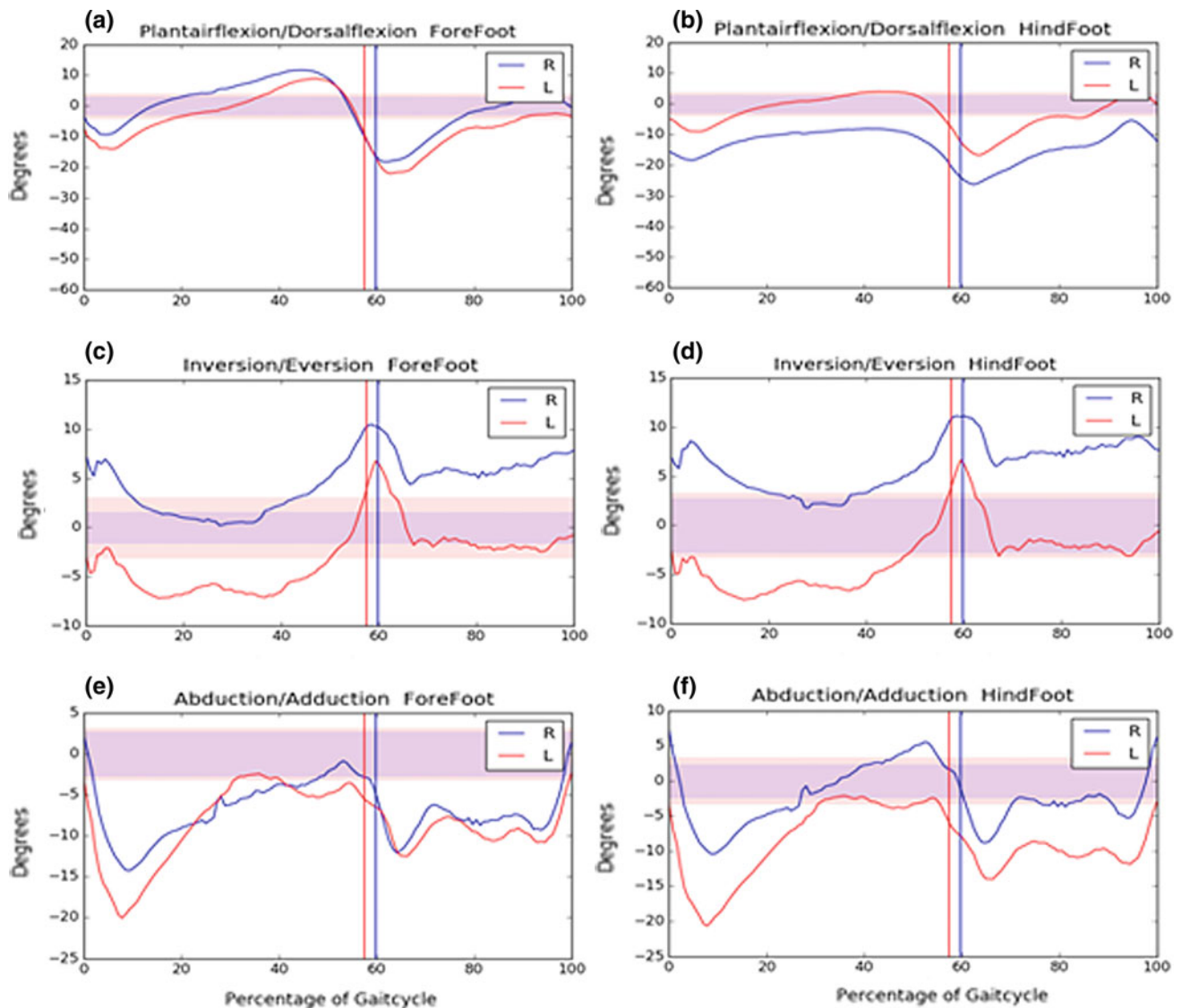
Fig. 4 Angle data (plantar flexion/dorsal flexion (**a** and **b**); inversion/eversion (**c** and **d**); abduction/adduction (**e** and **f**)) from the hindfoot and forefoot of the unpaired subject during the percentage of the gait cycle. Vertical lines indicate the toe-off gait event
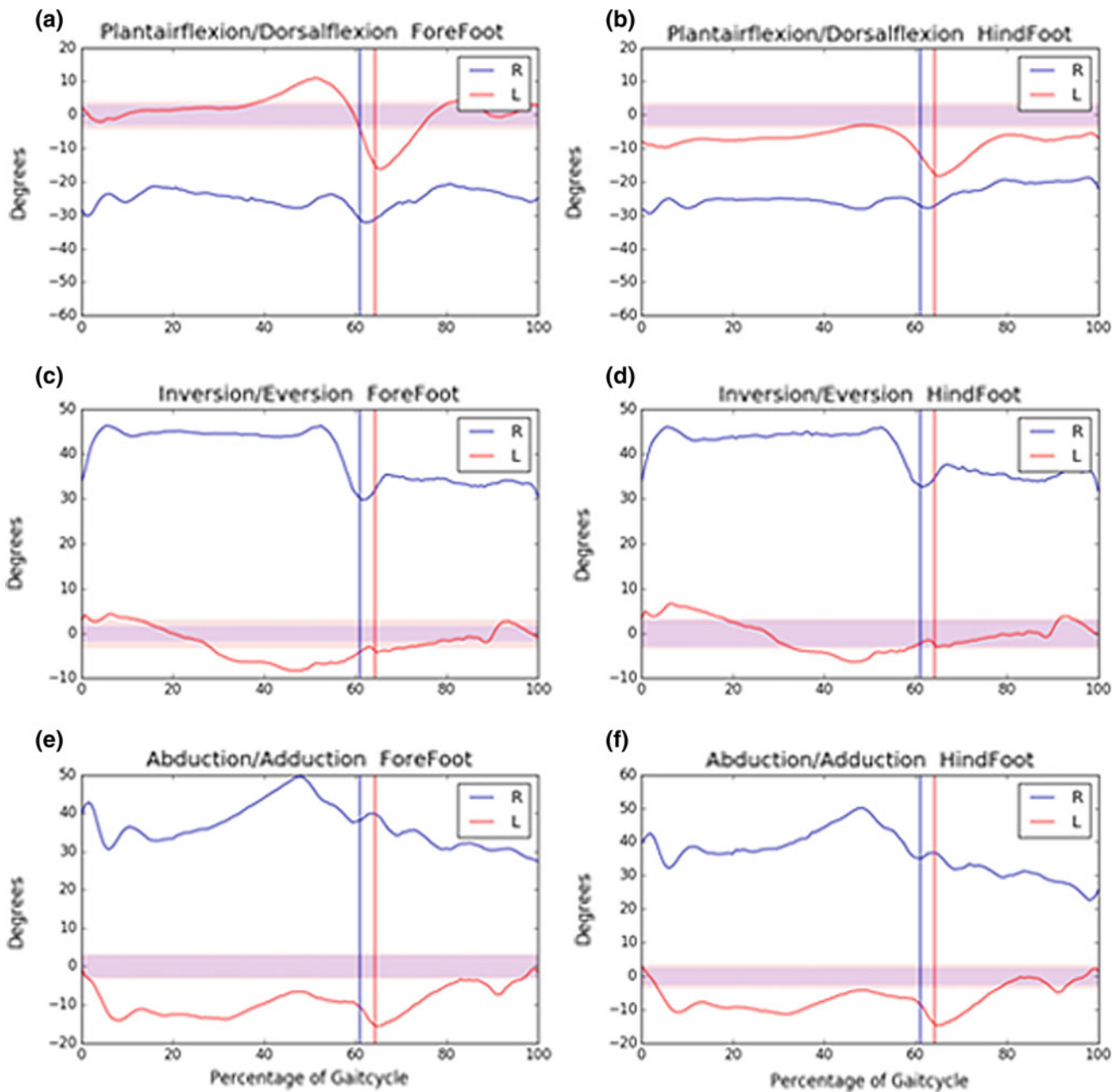
Fig. 5 Angle data from the hindfoot and forefoot of the patient during the percentage of the gait cycle. Vertical lines indicate the toe-off gait event

the angular displacement of the hindfoot and forefoot varying between inversion/eversion and maximum abduction/adduction.

Figure 5 presents the angles from both hindfoot and forefoot of both legs of the patient with the right equinus foot. The difference between values from each leg is very large and the patient has a ramp type equinus, explaining why the difference from right hindfoot and forefoot angles are small.

In Fig. 5a, b, it is possible to verify in the frontal plane graph the presence of equine to the right foot during the whole cycle of the march, with similar degree of equinus between forefoot and hindfoot. On the other hand, the transverse plane graphs (c, d, e and f) show an increase in inversion and adduction of the foot in relation to the presence of right ankle varus. Such data can be used in the routine of a gait laboratory to evaluate feet with equine deformities, equinus varus, varus, valgus, equinus valgus, among others.

4 Conclusion

As a result of our initial tests, it can be concluded that the models can be used to quantify more complexity deformities of the feet during gait. The new model can support the specialist to make best decisions for the patient, considering that different causes can define an equinus foot. The information about the gait analysis added to the information of the physical examination, radiology exam, and professional experience, provides the best decision-making scenario about foot deformities. More research is needed to create reference data and to verify the precision of the representation of the anatomical axis.

References

1. Leardini, A., Sawacha, Z., Paolini, G., Ingrosso, S., Nativo, R., Benedetti, M.G.: A new anatomically based protocol for gait analysis in children. Gait Posture **26**(4), 560–571 (2007)
2. Yalamanchili, S., Abboud, R., Wang, W.: A model to calculate the joint movements and forces in the foot. In: Proceeding of the 9th ICEMI 2009 International Conference on Electronic Measurement and Instruments, pp. 4532–4536 (2009)
3. VICON Oxford foot model
4. (VICON), Plug-in Gait (Product Guide) (2010)
5. Carson, M.C., Harrington, M.E., Thompson, N., O'connor, J.J., Theologis, T.N.: Kinematic analysis of a multi-segment foot model for research and clinical applications: a repeatability analysis. J. Biomech. **34**(10), 1299–1307 (2001)
6. Resende, R.A., Kirkwood, R.N., de Figueiredo, E.M.: Cinemática da marcha de adultos jovens: dados normativos iniciais. Ter Man **8** (39), 370–376 (2010)
7. Scott, S.H., Winter, D.A.: Talocrural and talocalcaneal joint kinematics and kinetics during the stance phase of walking. J. Biomech. **24**(8), 743–752 (1991)
8. Orendurff, M.S., Aiona, M.D., Dorociak, R.D., Pierce, R.A.: Length and force of the gastrocnemius and soleus during gait following tendo Achilles lengthenings in children with equinus. Gait Posture **15**(2), 130–135 (2002)
9. McGraw-Hill, S.P.P.: McGraw-Hill Dictionary of Scientific and Technical Terms (2002)
10. Winter, D.A.: Biomechanics and Motor Control of Human Movement (2009)
11. Barre, A., Armand, S.: Biomechanical ToolKit: open-source framework to visualize and process biomechanical data. Comput. Methods Progr. Biomed. **114**(1), 80–87 (2014)
12. Robertson, G., Caldwell, G., Hamill, J., Kamen, G., Whittlesey, S.: Research Methods in Biomechanics. Human Kinetics (2013)

Dynamical Analysis of Human Gait at Low Speeds

Daniel B. Robbi, João P. C. D. Freire, Antônio P. L. Bó, and Alberto C. G. C. Diniz

Abstract

Within the context of exoskeleton applications for rehabilitation of patients with partial spinal cord injury, there is a degree of actuator variety used to promote and control human gait movements. To study possible actuator alternatives, it is necessary to know the torques acting in the lower limbs joints during the gait cycle. This work's objective is to obtain such required joint torques in a low speed gait scenario, in order to address rehabilitation gait in future works. A non-linear dynamical model capable of describing a simplified human gait dynamics is developed and implemented for simulation. Kinematic data retrieved from both scientific literature and experimental tests conducted by the research team are used as input to an inverse dynamics analysis of gait at the same low speed, allowing the validation and study of the limitations of the proposed model. Simulation results show that the developed model shares the shape and scale of the reference data and remains between its standard deviation limits. Therefore, it can be concluded that even with the data limitations of reference literature, statistical deviation of the experimental tests and modeling simplifications, the developed dynamical model presents satisfactory results. Future works will focus on experimental gait tests at rehabilitation speeds, which are slower than the speed of this paper, to allow a more complete validation of the model for such cases.

Keywords

Inverse dynamics analysis • Human gait • Biomechanics • Rehabilitation

D. B. Robbi (✉) · J. P. C. D. Freire · A. P. L. Bó · A. C. G. C. Diniz
Universidade de Brasília, Brasília, Brazil
e-mail: robbi_brasil@hotmail.com

1 Introduction

The first step in the development of rehabilitation exoskeletons is understanding the dynamics of human gait. The development of a dynamic model is important for the design of both structural part of the orthosis and its actuation system. Such dynamical model expresses the relation between the external forces applied in different parts of the system and the kinematic motion of the limbs. A mistake in modeling can cause physical damage to the patient by exposing the body to excessive or unnatural forces.

The goal of this article is to develop a dynamical model capable of performing the inverse dynamics analysis of the lower limbs for low gait velocities (0.8 m/s), generating torques patterns that will dictate the actuation system design. Those torques are obtained from analysis of the angular trajectories of the leg joints, such as hip, knee and ankle, and the ground reaction force acting in the foot during the stance phase.

Analyzing a low velocity gait is important because it gives the authors the opportunity to validate the developed model, since such type of kinematic and torque data was not find in literature, either for low speeds or rehabilitation gait.

2 Methods

Firstly, a dynamical model based in the biomechanics of the human leg was developed to replicate the human gait. The model is based in a four-link mechanism, representing the trunk, thigh, calf and foot. Additionally, the hip was assumed to have a constant forward speed. Through the implementation of the dynamical model in MATLAB® routines, the model uses as input the kinematic data of gait and the ground reaction forces.

For the second part of this work, the kinematic data used in the dynamical model is the one present in [1] at the speed of 0.8 m/s, considered a low cadence gait. Later, the torques

obtained by the inverse dynamics of the reference data were compared with those found in the reference's same test. Such comparison made possible analyzing the differences and similarities found between the two models and assess the applicability of this paper's model.

Additionally, an experimental gait test was conducted with a healthy subject under the same low speed of 0.8 m/s to obtain the angles of the lower limb joints during that process. The objective of this second approach is to not only analyze the developed dynamical model, but access the capacity of the team to gather experimental data for future works. The retrieved data was analyzed through signal-processing routines alongside the application of the model in MATLAB®. The experimental torque patterns of the lower limb joints were compared qualitatively with both original torques from [1] and the torques determined by inverse kinematics of the reference's data.

2.1 Developed Dynamical Model

The model developed in this study analyzes the movement of the lower limbs by its three leg sections: thigh, calf and foot, and their respective joints: hip, knee and ankle, in the sagittal plane. The trunk was modeled as an extra link connected to the hip. The decision to analyze the dynamics of human gait only in the sagittal plane was done in order to: (1) Reduce the complexity of the model from the tridimensional space to a bidimensional plane; and (2) Neglect the action of the joints in other planes, since the motion of such joints and sections in those planes, even not being null, are greatly reduced in the scenario of low speeds. Additionally, in order to reduce the degrees of freedom of the system, only one leg was modeled for gait analysis.

The model designed for the dynamical analysis of the leg during gait is a four-links robotic manipulator. The different leg-based sections were modeled as rigid elements and the joints as ideal rotational joints, without friction and damping associated. The hip is considered to be an inertial joint, with the sole kinematic property of uniform rectilinear motion with velocity v, hypothesis that is close to reality in low speed gait [2].

The developed model has four rotational degrees of freedom: θ_{CoM}, θ_{HiP}, θ_{Knee}, θ_{Ankle}, as shown in Fig. 1, as well the dimensions of the elements L_{CoM}, L_{Thigh}, L_{Calf} and L_{Foot}, related to the trunk, thigh, calf and foot, respectively.

From [3], the human gait is explained as having two major phases: the stance phase, when the analyzed foot is on the ground; and the swing phase, when the same foot is not in contact with the ground. The stance phase can be divided into three sub-phases: the initial double support, which is between the heel strike of the analyzed leg and the opposite toe off; the single limb stance, that is when only the
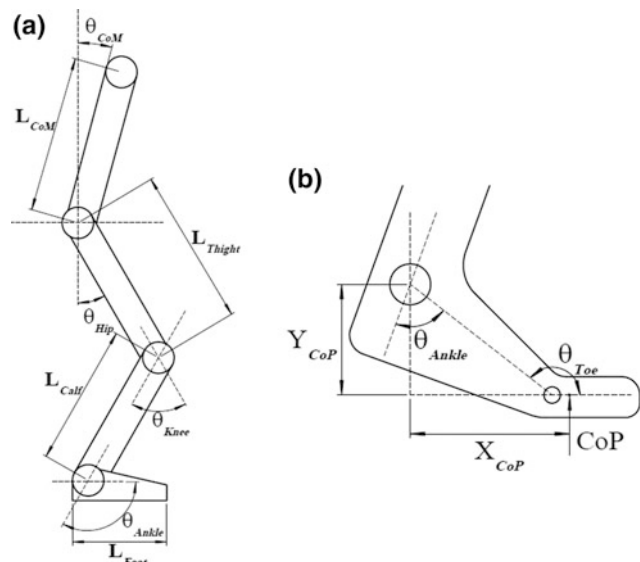
Fig. 1 Dynamical model schematics for **a** lower body and trunk modeling; **b** Extra considerations for foot link with respect to ankle connection and fifth metatarsus

respective foot is on the ground; and the double-support phase, which occurs between opposite heel strike and toe off and both feet are in the ground.

In the swing phase the system is described as the four-links system without any external force applied to the link related to the foot. Applying the Lagrangian formulation in the described dynamical system, its equations of the motion can be determined, and are shown in Eq. (1):

$$D(\theta)\ddot{\theta} + C(\theta,\dot{\theta})\dot{\theta} + g(\theta) = \tau_{din} \qquad (1)$$

where θ is a 4×1 generalized coordinates matrix, $D(\theta)$ is a 4×4 inertial matrix, $C(\theta,\dot{\theta})$ is a 4×4 forces matrix that encompass centripetal and Coriolis terms, $g(\theta)$ is a 4×1 gravitational forces vector and τ_{din} a 4×1 vector of external forces applied in the lower limbs joints.

In the stance phase, a static torque from the ground reaction force must be considered in the model because the analyzed foot is touching the ground. To define the ground reaction force application point in the foot, related to the center of pressure (CoP), and to study its influence on the other joints during the stance phase, new dimensions Y_{CoP} and X_{CoP} were defined as shown in Fig. 1b. There, θ_{Toe} is the angle between the metatarsal joint and the ankle. Therefore, the static torque caused by the ground reaction is given by:

$$\tau_{sta} = \begin{bmatrix} -L_{CoM}F_{Ry}\sin(\theta_{CoM}) + L_{CoM}F_{Rx}\cos(\theta_{CoM}) \\ L_{Thigh}F_{Ry}\sin(\theta_{Hip}) + L_{Thigh}F_{Rx}\cos(\theta_{Hip}) \\ L_{Calf}F_{Rx}\cos(\theta_{Knee} - \theta_{Hip}) - L_{Calf}F_{Ry}\sin(\theta_{Knee} - \theta_{Hip}) \\ X_{CoP}F_{Ry} + Y_{CoP}F_{Rx} \end{bmatrix}$$

$$(2)$$

where F_{Ry} and F_{R_x} are the ground reaction forces in the vertical and in the horizontal directions, respectively.

The equations of motion obtained for the stance phase have the same inertial matrix, Coriolis and centripetal terms matrix and gravitational terms matrix of the swing phase. The difference is precisely the presence of the static torque that does not exist when the foot is not in contact with the ground. The equations of motion are therefore given by the matrix equation represented in Eq. (3).

$$D(\theta)\ddot{\theta} + C(\theta,\dot{\theta})\dot{\theta} + g(\dot{\theta}) = \tau_{din} + \tau_{sta} \qquad (3)$$

2.2 Retrieved Data from Scientific Literature

For the first approach of this paper, the kinematic angles were obtained, alongside with the ground reaction forces, from Winter [1]. Unfortunately, the angular velocity and acceleration of these angles were not provided directly and it was necessary to obtain it numerically through the differentiation of the angles. The position of the center of pressure was assumed linearly dependent with relation to time from the hill to the toe through the stance phase.

The reference torques were also obtained from the same reference along with its uncertainties. It was assumed that these torques follow a normal distribution and all analysis were carried with 95% confiability (coverage factor of 1.96).

2.3 Experimental Gait Trials

This study was approved by an ethical committee (CEP/FS-UnB 129/11, approved in 03/14/2013). Such protocol was approved before the complete implementation of the "Plataforma Brasil" system, therefore, does not possess the 8 digit number used in the national registry of protocols.

To obtain alternative kinematic data for the links and joints, an experiment was conducted in which a person walked naturally at the speed of 0.8 m/s in a JOG FORMA treadmill model from Technogym®, in order to replicate partially the reference experiment conducted by [1].

To retrieve the experimental kinematic data, four samples of 3-Space inertial sensor model from Yost Labs®, with a signal sampling rate of 15 Hz, were used as seen in Fig. 2. The inertial sensors were placed approximately at the half distance of the length of the respective sections in the anteroposterior direction. This way the setup is more practical and it is also easier to see if the sensors are working correctly, by seeing the luminescent pattern emitted by them.

The test was conducted for 30 s after the subject had already reached walking steady-state, eliminating the transitory-state factor. It was also indicated to the experiment

volunteer to walk as far as possible from the treadmill motor so that the electromagnetic field generated by it would not interfere in the inertial sensors placed in the lower limbs.

Due to the absence of an experimental equipment capable of measuring the ground reaction forces on the foot during the stance phase, the respective forces were calculated based in the pattern of low cadence obtained in Winter [1], which presents the horizontal and vertical ground reactions normalized by the mass of the subject. Knowing that the volunteer weighted 90 kg (measured in the experiment day), it was possible to calculate the ground reaction forces based on the data presented in Winter [1]. Also, as explained in Sect. 2.2, the position of the center of pressure was assumed as being linear with relation to time from the hill to the toe during the stance phase.

The kinematic data retrieved from the experimental gait trials was analyzed in MATLAB® routines. In order to get an average gait cycle for each angle, they were firstly isolated and matched with a polynomial-based regression function, distinct for each section. To discard the functions that did not provide a good approximation, an error-based filter was built, deleting the regressions with either a high
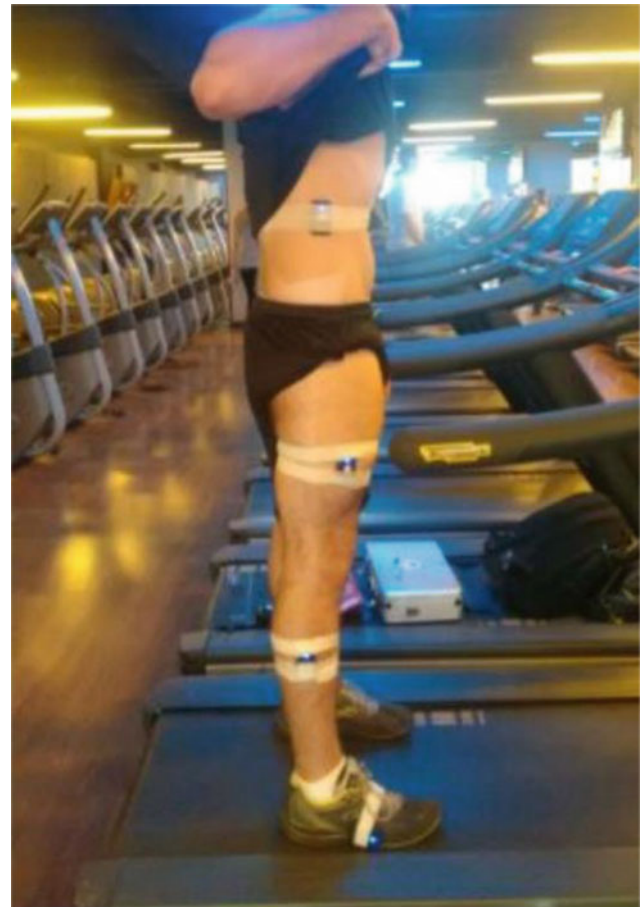
Fig. 2 Experimental setup for the gait trials

cumulative error or highly discrepant individual points. The filtered data was averaged, and a new regression function was created from the average regressed function, giving the final angles for each joint during the gait cycle.

3 Results

3.1 Experimental Gait Trials Results

The gait trials were analyzed and the raw data was treated to convert the angles of the IMU's orientation to the dynamical model orientation. The experimental test originated data of 17 gait cycles that were regressed and averaged, following the methodology presented in Sect. 2.3, to generate the final regressed gait cycle for each angle.

The full raw angles retrieved from the experimental test are displayed in Fig. 3, along with the peaks of the different cycles and the final individual regression functions for each cycle, obtained after the application of the error-based filter. Such remaining functions that will be averaged to generate the final gait cycle for each section.

It can be seen from Fig. 3 the fewer number of filtered regression functions for the trunk and ankle. Such observation is explained by the presence of acute spikes in their respective cycles, what causes a difficulty to generate polynomial functions capable of precisely describe the nature of the cycles. Such situation is caused majorly due the low sampling rate of the IMU's.

The results of both averaged regression function and regressed averaged function for the joint angles are shown in Fig. 4. There, negative angles represent extension and
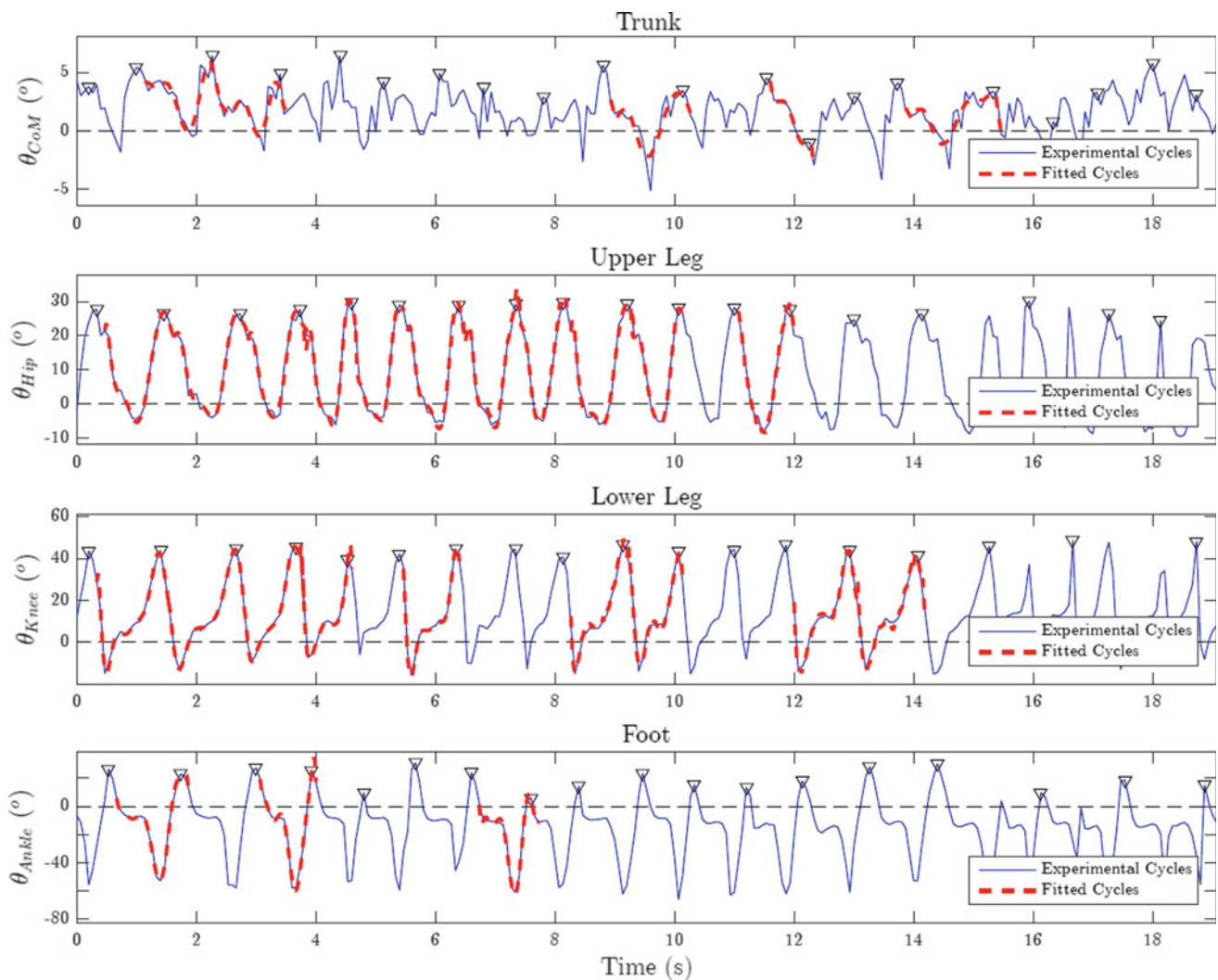
Fig. 3 Joint angles retrieved from experimental trials
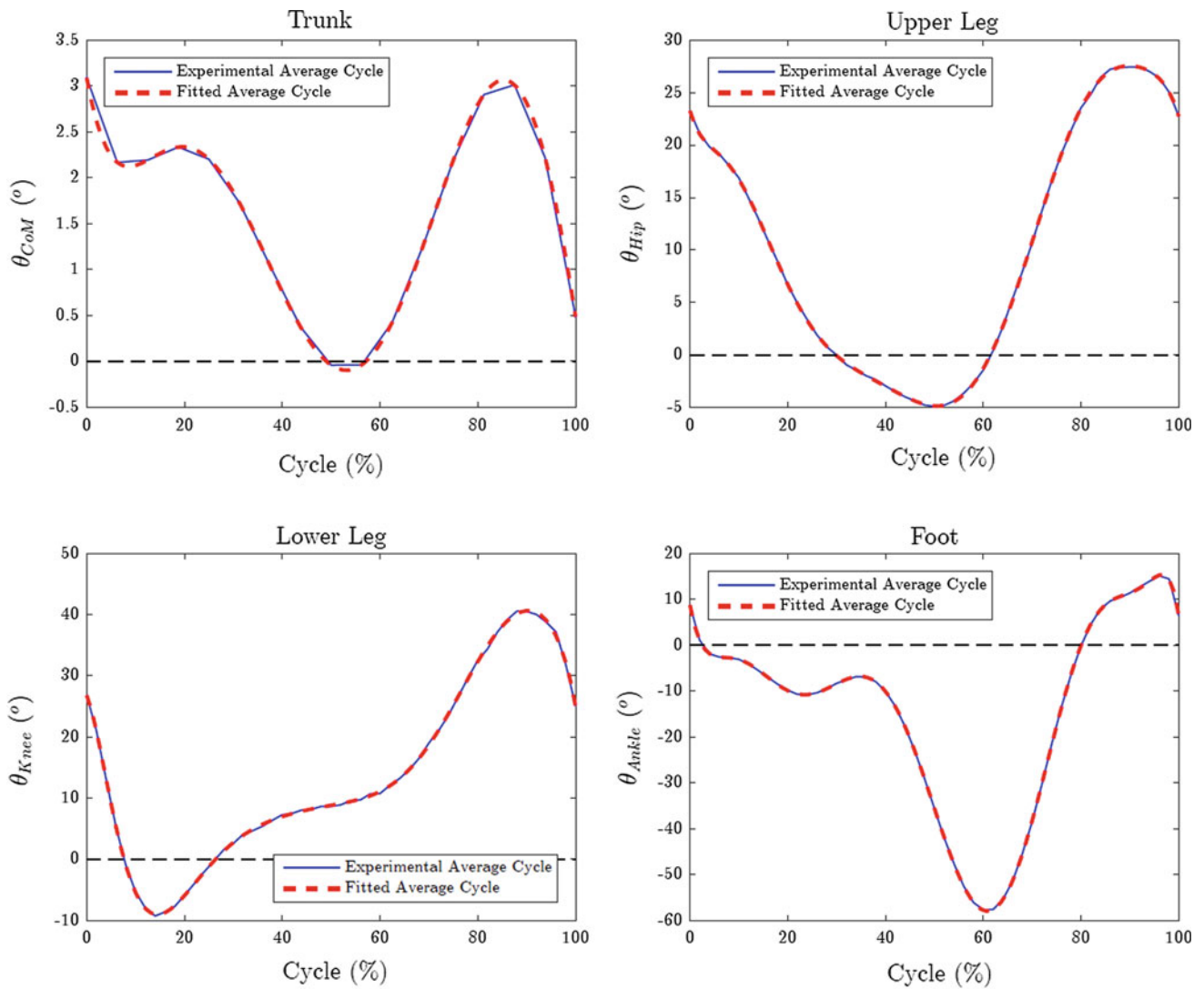
Fig. 4 Final average data of joint angles

positive angles represent flexion of the respective joints. The stance phase occurs from 0 to 60% of the gait cycle.

The results depicted in Fig. 4 show that the experiment was able to generate final averaged functions with smooth patterns that are also within the same scale and shape of gait angles widely known from scientific literature.

It is necessary to declare that the objective of this section is not to compare it with the angular patterns of scientific literature, but access the capabilities of the team to retrieve data from experimental setups. The results from Sect. 3.2 that will show if the angles retrieved in the conducted gait trials are decent for dynamical analysis of gait. Finally, in the view of data acquisition and treatment, this paper's results prove themselves satisfactory and ready for further tests, shown in the next subsection.

3.2 Inverse Dynamical Analysis Results

From the description presented in Sect. 2.1, the dynamical simulations were performed and processed accordingly to the previously mentioned steps. The results for the trunk torques are not presented in this article due to the lack of references trunk torques in literature and because this degree of freedom usually is not actuated in lower-limb exoskeletons. Figure 5 shows the resulting torques in the hip, knee and ankle, where extension moments are negative and flexion moments are positive and the stance phase occurs from 0 to 60% of the gait cycle.

It can be seen that both the torques obtained using the kinematic found in the literature [1] and the experiment are within the uncertainty margin when compared to the
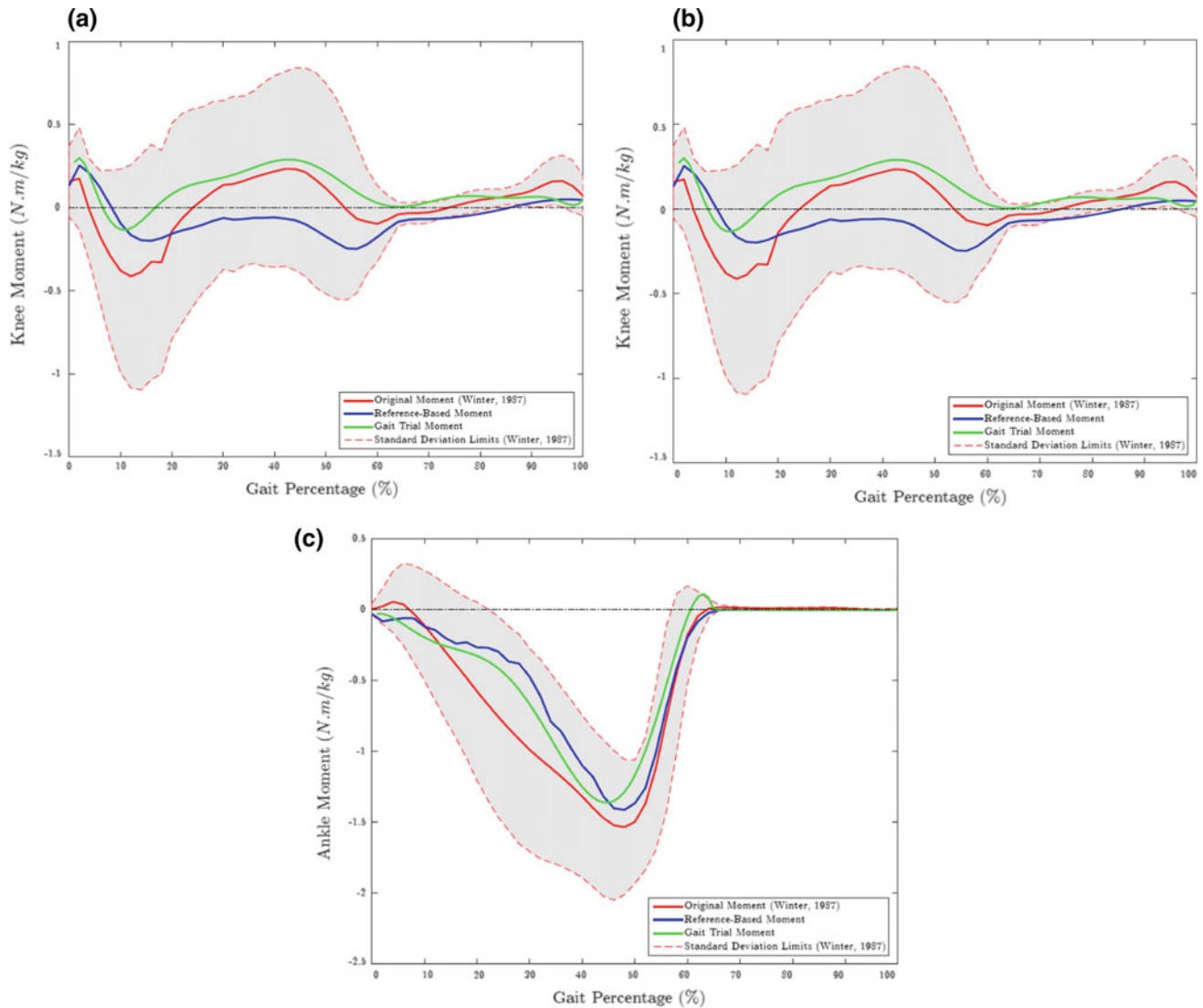
Fig. 5 Low speed gait normalized torques for **a** Hip joint; **b** Knee joint; **c** Ankle joint

references, which validates the developed model for low speeds gaits.

Major differences between the two obtained torques and the references can be justified by the fact that the hip is considered inertial and that the CoP is considered to vary linearly in the foot. Both simplifications may incur in the significant difference found in a non-linear dynamical model such as the one developed in this work.

The differences between the torques obtained using experimental data and the one from [1] are probably due: (1) The angles from the literature are an average from diverse gait trials and the ones from the experiment are from only one dataset; and (2) The subject's profiles, testing conditions and data gathering and analysis of each experiment are highly different. Although the two results have differences, the major trends are similar and both are within

the allowed standard-deviation margin from the reference's values.

4 Conclusions and Future Works

The present study allowed the generation of hip, knee and ankle moments patterns for a low speed gait and validated the four-link based dynamical model developed in the context of inverse dynamics analysis, considering the reference torques and its uncertainties.

The torques obtained from inverse dynamics analysis using the kinematics of the joints obtained experimentally have similar trends to the one obtained using the reference kinematics, and their differences can be explained by the fact that the first is only a dataset and the latter one is an average.

As a future work, the acceleration of the hip during gait will be implemented in the model and its influence in the model dynamics will be quantified properly in order to carry a sensitivity analysis of this term. It will also be conducted an analysis of a rehabilitation gait to quantify all the necessary torques in the joints for an exoskeleton used to rehabilitate those that suffered from a spinal cord injury.

References

1. Winter, D.A.: A Biomechanics and Motor Control of Human Movement, 1st edn, pp. 1–72. University of Waterloo Press (1987)

2. Gard, S.A., Childress, D.S.: What determines the vertical displacement of the body during normal walking? J. Prosthet. Orthot. **13**, 64–67 (2001)

3. Dollar, A.M., Herr, H.: Active orthoses for the lower-limbs: challenges and state of the art. In: IEEE, Proceedings of 10th International Conference in Rehabilitation Robotics. Noordwijk, The Netherlands, vol. 1, pp. 968–977. IEEE (2007)

4. Spong, M., Hutchinson, S., Vidyasagar, M.: Robotic modeling and control, 1st edn, pp. 29–228. Wiley (2006)

5. Wiebren, Z., At, L.H.: Assessment of spatio-temporal gait parameters from trunk accelerations during human walking. Gait Posture **18**, 1–10 (2003)

Effect of Vertebral Mobilizations on Respiratory Pressure

Rafael Victor Ferreira do Bonfim, Gabriel Mauriz de Moura Rocha,
Anna Mércia da Silveira Sousa, Bárbara Fernanda Oliveira Rodrigues,
and Vilson Rosa Almeida

Abstract

Manual therapies have been widely used as a form of treatment for musculoskeletal disorders, such as neck pain, low back pain and respiratory dysfunction, such as chronic obstructive pulmonary disease. One of such techniques is the joint mobilization, which is based on the evaluation and treatment through passive, oscillatory and rhythmic movements. Maximal respiratory pressures and maximal ventilatory ventilation (MVV) are the most commonly used clinical parameters to assess respiratory muscle strength and endurance, and are a practical method of clinical evaluation. The aim of the present study was to analyze the influence of vertebral mobilizations on respiratory pressures. Twenty-eight male individuals, aged 18–30 years old, were randomly assigned to two groups: cervical mobilization (CMG) and thoracolumbar mobilization (TMG). Both groups were evaluated for maximum respiratory pressures by means of a manovacuometer. Cervical mobilization resulted in an improvement in maximal respiratory pressures, while chest mobilization provided a significant improvement only in maximal expiratory pressure. It was observed that the vertebral mobilizations produced physiological effects on the respiratory system and that it can be used as a treatment technique in the dysfunctions of this system.

1 Introduction

Traditional manual therapies have been widely used as a form of treatment for musculoskeletal disorders, such as neck pain, low back pain, upper back pain, upper extremities, and respiratory dysfunctions, such as chronic obstructive pulmonary disease [1, 2].

One of the manual therapies used is the joint mobilization, proposed by Maitland et al. [3], which is based on evaluation and treatment through passive, oscillatory and rhythmic movements. The evaluation is performed through passive movement and palpation of the region to be treated. The passive movements are graded in five levels, according to the amplitude of the accessory movements present in the joints [3, 4].

The maximum respiratory pressures are clinical parameters commonly used to evaluate the strength and the resistance of the respiratory muscles, being a practical method of clinical evaluation [5].

Few studies have evaluated the effect of vertebral joint mobilization with emphasis on respiratory function. Thus, it was verified the necessity of new researches that justify the use or not of these manual techniques in patients affected by pathologies [6].

The aim of this study is to analyze the influence of vertebral mobilizations on respiratory pressures.

2 Materials and Methods

The methodology used in the present work is based on an experimental, explanatory, quantitative, comparative study. Twenty-eight individuals participated on the study; they

R. V. F. do Bonfim (✉) · G. M. de Moura Rocha · V. R. Almeida
Instituto Científico e Tecnológico da Universidade Brasil, Rua
Carolina Fonseca, 235, Itaquera, São Paulo, SP, Brazil
e-mail: ft.rafaelvictor@hotmail.com

R. V. F. do Bonfim · G. M. de Moura Rocha ·
A. M. da Silveira Sousa · B. F. O. Rodrigues
Faculdade Estácio-Teresina Av. dos Expedicionários, 790 - São
João, Teresina, PI, Brazil

were intentionally and non-probabilistically selected. The inclusion criteria were: male participants; and between 18 and 30 years old. The exclusion criteria were: individuals with severe respiratory disorders; individuals with neurological disorders, individuals with malignant diseases, in or near the vertebral column; and individuals who had any facial alterations that prevented the manovacuometry or cognitive alteration.

Data collection was performed in October 2016. Individuals who accepted to participate in the study were submitted to the evaluation to identify possible exclusion factors and to collect identification and anthropometric data.

After the selection, the participants were randomly assigned to two groups: the cervical mobilization group (CMG) and the group submitted to thoracolumbar mobilization (TMG). Both groups were assessed by the researchers for maximal pre and post-mobilization respiratory pressures (Figs. 1 and 2).

For the data collection on maximum respiratory pressures, the individual was initially evaluated using the manovacuometer, where the individual was seated at a 90° hip angle; afterwards, the patient was placed in the supine position and the cervical mobilization was performed at the C3 level, in 3 series of 1 min, with intervals of 1 min between the series, followed by the reassessment of the maximum respiratory pressures by the manovacuometer (Fig. 3).

The same procedure for collecting the maximum respiratory pressures was performed in the other group (GMT),

and soon after the patient was placed in the ventral decubitus for thoracolumbar mobilization (T12), which was followed by the reassessment of the maximum respiratory pressures by the manovacuometer.

The results were showed of comparative way by graphics, which showed the changes in PImax and PEmax before and after the mobilizations using the Student's T-test. The data were also submitted to the D'Agostino normality test (Inserir Referência).

Data from this study were collected after approval by the Research Ethics Committee under CAAE protocol 57843916.8.0000.5209, in accordance with Resolution 466/2012 of the Brazilian National Health Council. All participants signed the Informed Consent Form.

Fig. 2 Thoracolumbar mobilization

Fig. 1 Cervical mobilization

Fig. 3 Manovacuometry

Table 1 Mean values and standard deviations of anthropometric data

	N	Age	Weight	Height	BMI
Mean	28	23.1 ± 2.92	71.5 ± 10	1.73 ± 0.08	23.9 ± 2.9

3 Results

The data of the anthropometric characteristics of the study participants were submitted to the D'Agostino normality test, resulting to be homogeneous (Table 1).

Figures 4, 5, 6 and 7 show the results of the maximum respiratory pressures obtained through the manovacuometry, before and after the mobilizations in the Cervical Mobilization Group (CMG) and the Thoracolumbar Mobilization Group (TMG).

Figures 4 and 5 show the values for maximum respiratory pressures in the CMG group. The comparison between the phases before and after the application of the technique indicates a significant increase in inspiratory ($p = 0.0014$) and maximal expiratory ($p = 0.0357$) pressures.

Figures 6 and 7 show the values for the maximum respiratory pressures in the TMG group. The comparison between the phases before and after the application of the technique evidences a significant increase ($p = 0.0001$) of
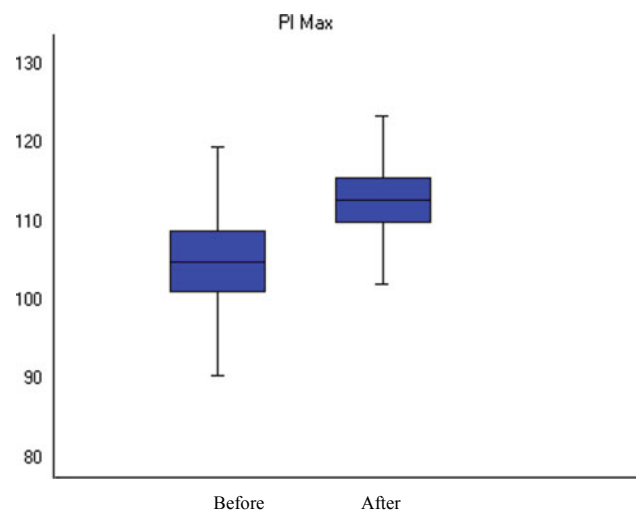
Fig. 5 Boxplot representing the mean and standard error of maximal expiratory pressures, before and after cervical mobilization
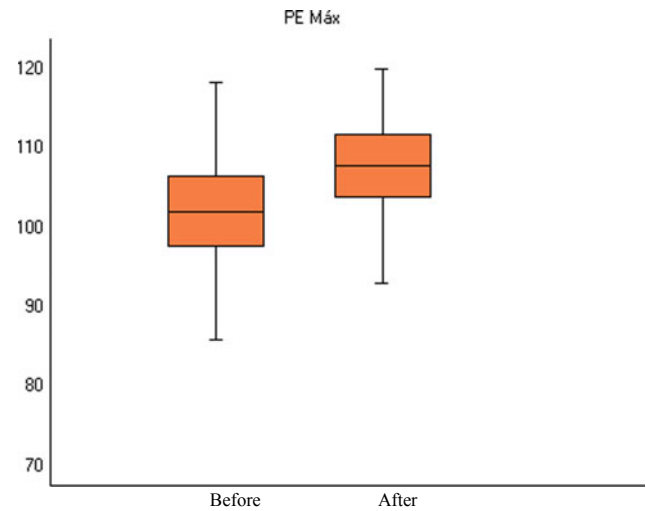
Fig. 4 Boxplot representing the mean and standard error of maximal inspiratory pressures, before and after cervical mobilization
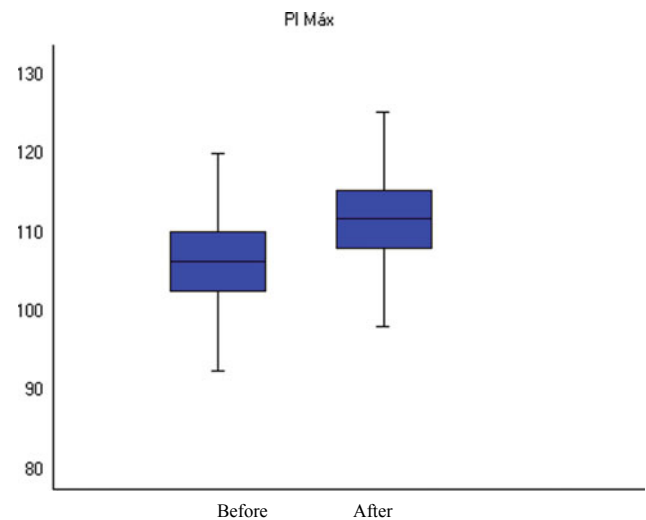
Fig. 6 Boxplot representing the mean and standard error of maximal inspiratory pressures, before and after thoracolumbar mobilization
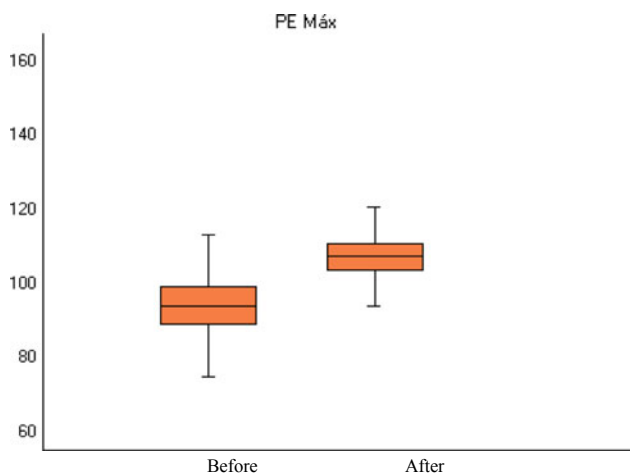
Fig. 7 Boxplot representing the mean and standard error of maximal expiratory pressures, before and after thoracolumbar mobilization

the maximum expiratory pressures, but the same did not occur with the maximum inspiratory pressures.

4   Discussion

The reference values for PImax, which indicate the normal range for males aged 18–65 years, are high, varying from 92 to 121 cm H_2O [7].

In the present study, significant increases were observed in maximal inspiratory and expiratory pressures, in the group submitted to cervical mobilization; on the other hand, in the group submitted to thoracic mobilization, the increase in maximum inspiratory pressures was not significant. This may have occurred because the participants in the TMG group have already had a high inspiratory muscle strength, before the chest mobilization was performed.

Pulmonary volumes and maximal respiratory pressures were evaluated in patients submitted to cervical, thoracic or lumbar spine surgery; Oliveira et al. (2015) suggested that surgery in the thoracic region was associated with greater reductions in vital capacity and maximal inspiratory pressure, as compared to surgery in the cervical and lumbar regions [8]. This is not in agreement with the results found in the present study; it may be explained by the fact that the present work made use of non-invasive techniques.

The value obtained in PEmax is the addition of the expiratory muscles pressure with the elastic retraction of the respiratory system. It is known that manipulation of C3 potentiates the parameters related to total lung capacity or lung volume, there would be a greater lung and chest distension and a greater elastic retraction force, thus influencing

expiratory pressure increase [9]. This would explain the results found related to PEmax in the present research.

Carvalho et al. (2011) concluded that two techniques of manual therapy, a cervical manipulation and a manual diaphragmatic mobilization, increased PImax. And they adopted the hypothesis that spinal manipulation for the third cervical vertebra, one of the source sites of the phrenic nerve motor roots that innervates the diaphragm, could improve the inspiratory power of healthy people. They suggest that the activation of the sympathetic nervous system also had a role in enhancing inspiratory strength [10], corroborating the results of the present study.

Pulmonary function parameters are the most important measures in maintaining quality of life in patients with stroke, they generally have decreased respiratory function due to the reduction of thoracic space caused by altered trunk mobility and muscle impairment on the affected side. Jang and Bang (2016) aimed to determine the effects of thoracic and cervical joint mobilization on the respiratory capacities of patients with stroke [11]. Their work assessed study participants for forced vital capacity (FVC), forced expiratory volume in the first second (FEV1), and peak cough flux. Cervical and thoracic mobilization was applied simultaneously in four sessions and the results demonstrated that all measures collected increased, resulting in improved lung function. Contrary to these results, another study concluded that a single session of manual therapy in the thoracic spine does not provide short-term benefit in the respiratory function of healthy adults [12].

Further studies are needed in order to analyze the effects of long-term manual therapies with a greater number of participants, comparing the efficacy between the techniques and their use in the clinical setting.

5   Conclusion

According to the results, it can be concluded that the cervical mobilization caused an improvement in the maximum respiratory pressures, since the chest mobilization provided a significant improvement only of the maximum expiratory pressure.

Therefore, it is likely that the vertebral mobilizations produce physiological effects on the respiratory system. However, further studies are needed in order to confirm and explain the influence of vertebral mobilizations on the respiratory system and its use in the clinical setting.

References

1. Chu, J., et al.: Peripheral response to cervical or thoracic spinal manual therapy: an evidence-based review with meta analysis. J. Man. Manip. Ther. **22**(4), 220–229 (2014)
2. Wearing, J., et al.: The use of spinal manipulative therapy in the management of chronic obstructive pulmonary disease: a systematic review. J. Altern. Complement. Med. **22**(2), 108–114 (2016)
3. Maitland, G.D., et al.: Manipulação Vertebral – Maitland, 7th edn. Elsevier, Rio de Janeiro (2007)
4. Lin, P., et al.: Prevalence, characteristics, and work-related risk factors of low back pain among hospital nurses in Taiwan: a cross-sectional survey. Int. J. Occup. Med. Environ. Health **25**(1), 41–50 (2012)
5. Fregonezi, G., et al.: Variação diurna de parâmetros de função pulmonar e de força muscular respiratória em pacientes com DPOC. J. Bras. Pneumol. **38**(2), 257–263 (2012)
6. Wang, J.S.: Effect of joint mobilization and stretching on respiratory function and spinal movement in very severe COPD with thoracic kyphosis. J. Phys. Ther. Sci. **27**(10), 3329–3331 (2015)
7. Bessa, E.J.C., Lopes, A.J., Rufino, R.: A importância da medida da força muscular respiratória na prática da pneumologia. Pulmão RJ **24**(1), 37–41 (2015)
8. Oliveira, M.A., et al.: Evaluation of lung volumes, vital capacity and respiratory muscle strength after cervical, thoracic and lumbar spinal surgery. Sao Paulo Med. J. **133**(5), 388–393 (2015)
9. Behne, G.R., et al.: Pressões respiratórias máximas: comparação do efeito imediato da manipulação e da mobilização da terceira vértebra cervical. Arq. ciências saúde UNIPAR **17**(2), 69–76 (2013)
10. Carvalho, A.R., Silva, S.L., Oliveira, A.P.: Efeito imediato de duas técnicas de terapia manual sobre a pressão inspiratória máxima em indivíduos saudáveis: ensaio clínico. Ter. Man. **9**, 143–149 (2011)
11. Jang, S.-H., Bang, H.-S.: Effect of thoracic and cervical joint mobilization on pulmonary function in stroke patients. J. Phys. Ther. Sci. **28**(1), 257 (2016)
12. Wall, B.A., et al.: The effect of manual therapy on pulmonary function in healthy adults. Sci. Rep. **6** (2016)

Exploring Hip and Knee Biomechanical Differences Between Horizontal and Vertical Single Leg Jumps

Henrique Lelis Clemente de Oliveira, Felipe Costa Alvim, and Luciano Luporini Menegaldo

Abstract

Functional tests are used to identify various biomechanical deficits. In some circumstances, more than one test can generate data that are complementary to each other. Two types of single leg jumps were studied: maximum horizontal distance and maximum vertical height. The measurements done in three active women were made using a motion capture system for kinematic analysis, and force platforms to measure the ground reaction forces. The results showed differences in the joint torque profiles and impulse, between the two jumps, possibly revealing different alterations in a clinical condition. Such complementary tests can contribute to a more precise identification of biomechanical deficits and their possible causes.

Keywords

Horizontal jump test • Vertical jump test • Single leg jump • Lower limb kinematics • Functional tests

1 Introduction

Assessments of the physical condition of individuals with biomechanical deficits are described more efficiently when performed dynamically. Such deficits can be associated with increased joint load and impact, decreased muscle strength and reduced range of motion. Dynamic tests allow identifying which structures are acting abnormally in the activities that require motor control skills. Different functional tasks are used to identify such deficits, especially for the lower limbs, such as jump, squats, walking and running tests [1–3]. Eventually, the same assessment of the subject clinical condition can be obtained with different tasks; however, biomechanical variables, such as joint torques, ground reaction forces and muscle activations are likely to be different depending on the test. Is there a specific task, and measured variable, that can provide more meaningful clinical information for specific deficits? The jump test appears in the literature frequently, mainly in the evaluations of knee injury [4, 5].

For an accurate assessment of the physical condition, prevention or in the sports environment, a single task can be not sufficient to predict injury risk or athlete performance. Thus, a detailed study of the different biomechanical variables among the different tests will possible provide insights on how such tests can become complementary [4].

The objective of the present study is to compare biomechanical variables between maximum height and maximum distance single leg jumps. Hip and knee flexion angles will be analyzed, as well as their respective torques, during the propulsion phase of single leg horizontal and vertical jumps. Also, we will analyze the impulse of the reaction forces, as the time integral of the forward and upward force components in time, seeking for an index expressing the subject ability to perform the aimed goal. According to the adopted reference system, the vertical (Y-axis) impulse, which points upwards, is related to the change of linear momentum of the center of gravity in the vertical direction. Similarly, the horizontal (Z-axis) impulse, delivered by the friction of the foot against the ground, corresponds to the horizontal change of linear momentum of the body center of gravity. Being an exploratory study with a few subjects, we will try to identify the most prominent differences between the two types of jumps, as well as possible methodological problems. The results will be used to design a broader study involving a more significant number of patients with knee pathology and healthy controls, with the objective of selecting the most appropriate test and variable of analysis for knee condition assessment.

H. L. C. de Oliveira (✉) · F. Costa Alvim · L. L. Menegaldo
Biomedical Engineering Program, COPPE/UFRJ, Rio de Janeiro,
Brazil
e-mail: henrique.lelis1@gmail.com

2 Methods

The tests were performed according to a project approved by the Research Ethics Committee on 16/01/2014, at the Clementino Fraga Filho University Hospital of the Federal University of Rio de Janeiro (HUCFF/UFRJ), under protocol number 127-13. The tests were performed at the Biomechanics Laboratory of the Biomedical Engineering Program (PEB/COPPE) located at the Federal University of Rio de Janeiro, Brazil. The present study had three female volunteers. An anamnesis was performed by a physical therapist with each volunteer and questions about the level of physical activity and medical diagnosis regarding the orthopedic status were included. Subject 1 (S1) reported practice yoga and walking five times a week and not practiced strength exercises in the last 6 months. Subject 2 (S2) practice running, cycling and strength exercises two times a week in the lest 6 months. Subject 3 (S3) practice climbing 3 time a week and had a chondromalacia patellae diagnosis greater than 6 months. S1 and S2 does not own medical diagnosis. S2 and S3 report knee pain in the tested leg after the tasks. The anthropometric measurements are demonstrated in Table 1.

Two types of single leg jumps were analyzed, using the dominant lower limb. For the horizontal jump, the volunteers were stimulated to jump as far as possible ahead; for the vertical jump, the stimulus was to jump as high as possible. For both jumps, the upper limbs were at the side of the trunk and hands on the iliac crests. Each jump was repeated three times, and the test which had the lowest loss of markers was chose to analyzed. The phase of interest was the propulsion, beginning at the moment in which the ground reaction force starts decreasing and finishes when reaching zero.

A BTS P-6000 force platform (BTS Bioengineering, Milan, Italy) with a sampling frequency of 400 Hz was used to capture ground reaction forces in the three dimensions. For kinematics, a system with eight infrared cameras, (SMART-D BTS®, Milan, Italy) with a sampling frequency of 250 Hz was used. The Helen Hayes simplified protocol with 18 reflexive markers was used as the marker-set. The raw kinematic and force data were reconstructed through the

Smart Tracker Software (BTS®), interpolated and filtered by a Low Pass Butterworth zero-lag 4th order filter at 10 Hz thought the Smart Analyzer (BTS®) software.

Inverse Kinematics and Inverse Dynamics problems were solved to obtain the joint angles and torque data, respectively [6]. Such problems were solved using OpenSim Gait2392_Simbody model. The MATLAB® software was used to calculate the impulse integral with the trapezoidal numerical integration.

3 Results

Figures 1 and 2 show hip and knee flexion angles and torques for the two types of jumps. Positive angles refer to hip flexion and negative angles refer to knee flexion (zero deg are neutral for both). It is possible to observe, for both joints, a higher physical demand for the horizontal jump compared to the vertical jump, evidenced by the larger torques, even with differences in the physical conditions of the volunteers. Nevertheless, no large joint angle profile differences can be recognized.

For both jumps it is necessary a hip, knee and ankle flexion. For the vertical jump the trunk bending forward is smaller than horizontal jump, to increase the body equilibrium control for larger body stability to jump as high as possible. For performing the horizontal jump, it is necessary to bend the body forward mainly by bending the trunk, and this effect reflects on the slightly higher hip peak angles of Fig. 1, at least for the Subjects 2 and 3. Figure 3 shows the ground reaction forces in Y (upward) and Z-axis (forward). In the Y-axis, comparable maximum reaction forces were observed in the two types of jump. However, in this direction, two of the three subjects have shown smaller impulses in the vertical than in the horizontal jump, what is surprising. This can be possible attributed to the greater hip flexion and trunk bending forward. It would require additional vertical force, beyond the propulsion, to maintain the whole body rotational stability, such that the sum of moments about the center of mass is balanced. In the Z-axis, which represents the shear force direction between the foot and the platform, both peak forces and impulse were greater in the horizontal jump.

4 Discussion

Observing the individual subject data, it is possible to infer different patterns and strategies to reach the aimed goal of either jumping higher or farther. These data may provide

Table 1 volunteers anthropometric measurements

	Age	Height (cm)	Weight (kg)
Subject 1	30	153	52
Subject 2	29	152	51
Subject 3	30	161	61

Fig. 1 Hip and knee joint angles in vertical (V) and horizontal (H) single leg jump test. All subjects (S) shown
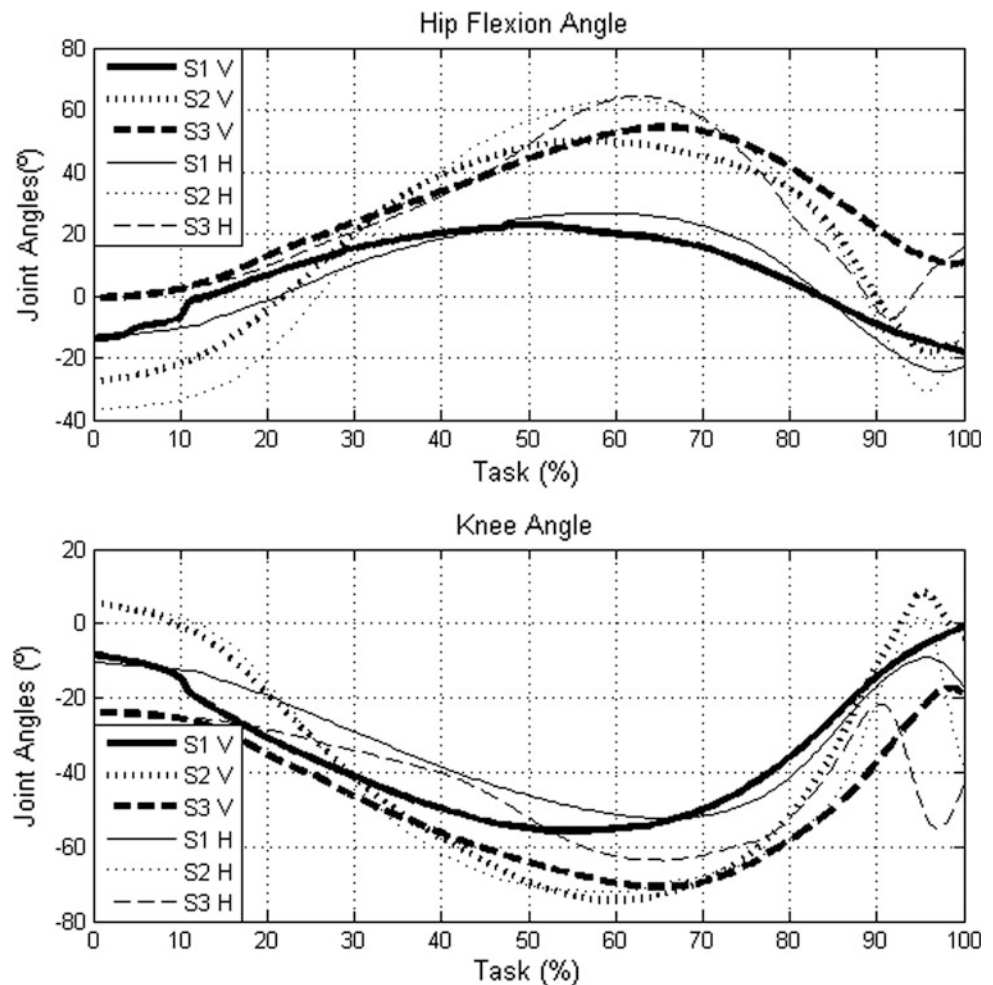
some insights about the expected variability of both jump tests and how to better control secondary variables in the definitive test design. Subject 1 shows a reduced knee and hip flexion amplitude in both tests, as well as joint torques, Z-axis impulse for both tests and Y-axis impulse for the horizontal test. For Subjects 2 and 3, similar kinematics and torque patterns could be observed. However, for Subject 3, knee torque is larger than the others, in a more pronounced way in the horizontal test. The vertical reaction of this Subject is not markedly greater, considering that she weights about 100 N more than the others. However, the Y-axis impulse is higher, reflecting possibly the integral of the additional weight along the task time; simultaneously, the Z-axis force is reduced in both jumps. Although the subject

3 presents chondromalacia patellae, we couldn't, until now, realize if the individual kinematics differences are due to this pathology. New variables and a larger sample are needed to determine the differences. Subject 2 shows a greater Z-axis impulse in both jump types.

Relatively to the jump differences, we observed in all subjects that the horizontal jump required larger knee and hip torques and larger Z-axis reaction forces, for all subjects. Hip presented greater peak torques than the knee in both tasks. These results suggest that hip torque is possibly a sensitive variable for analyzing knee condition based on jump tests. In Table 2 shows the higher Z-direction impulse to the horizontal jump than the vertical jump test. This is evidenced in Fig. 3 by the larger Z-axis shear reaction force
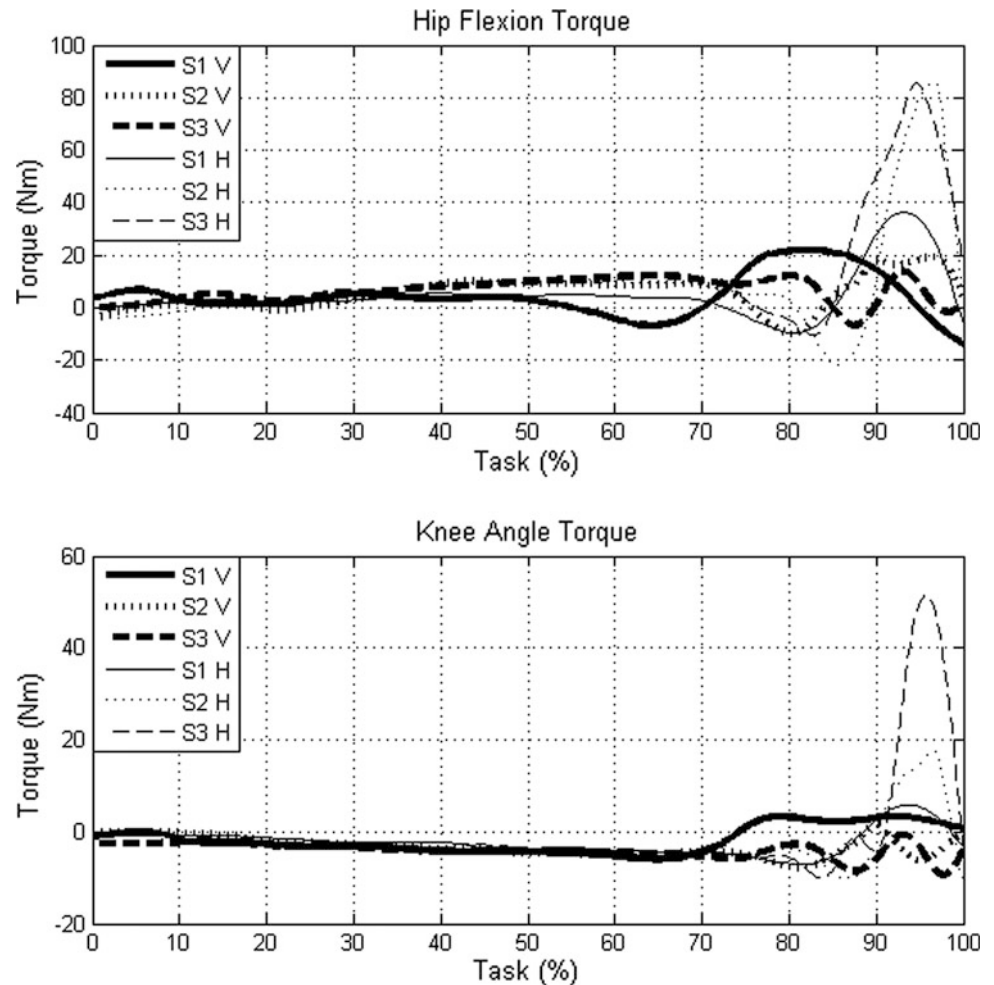
Although these data are not reported here, in the horizontal jump the position of the center of mass and ground reaction vector move towards the tip of the foot, decreasing the body stability margin. This instability may be useful for inducing compensatory strategies of equilibrium control, eventually connected and evidencing the underlying pathologic condition [7–9].

It is known that the more significant is the strength of the quadriceps femoris, the ground reaction force decreases during the propulsion for the jump, and this is directly associated with normal postural stability and motor control, ensuring movements in the sagittal plane more efficient [10]. The jump produces greater ground reaction forces compared to squatting and running. Also, comparing the vertical jump

with the step-down test, it was observed that, when jumping, it is possible to identify if there is an increase in the internal rotation of the hip. This rotation causes an increase in joint impact and the risk of injury [7, 11].

The observed characteristics of each type of jump may be explored in people who have muscular and biomechanical disorders or injury in the lower limbs. Muscle imbalance during femoral quadriceps activation associated with knee flexion increases the compressive reaction forces of the patellofemoral joint. This has been observed in jumping and squatting tests [10, 12].

It has been observed distinct kinematic and dynamic patterns between horizontal and vertical jumps. We believe that the association of their results may contribute to more

Fig. 3 Ground reaction forces (N) of the horizontal and vertical single leg jump in the Y-axis and Z-axis
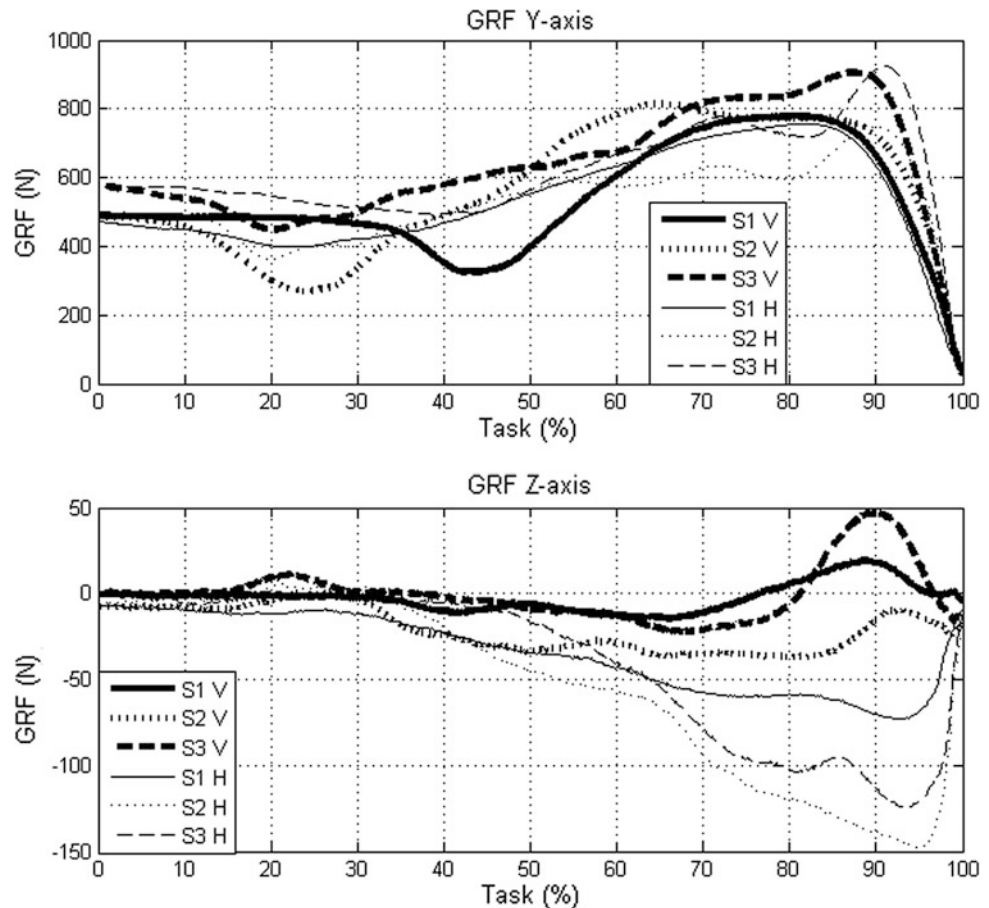
Table 2 Ground reaction force impulse (Ns) for the horizontal and vertical single leg jumps in the Y-axis (upward) and Z-axis (forward)

Impulse	Horizontal Y-axis	Horizontal Z-axis	Vertical Y-axis	Vertical Z-axis
Subject 1	409.84	−26.39	486.06	−2.25
Subject 2	655.81	−65.47	477.85	−17.67
Subject 3	840.61	−54.67	691.53	−0.07

accurate evaluations of underlying causes of biomechanical deficits. This study is in progress as part of a doctorate in the Biomedical Engineering Program.

References

1. Hamner, S.R., Seth, A., Delp, S.L.: Muscle contributions to propulsion and support during running. J. Biomech. **43**, 2709–2716 (2010)
2. Pal, S., Draper, C.E., Fredericson, M., Gold, G.E., Delp, S.L., Beaupre, G.S., Besier, T.F.: Patellar maltracking correlates with vastus medialis activation delay in patellofemoral pain patients. Am. J. Sports Med. **39**, 590–598 (2011)
3. Powers, C.M., Ward, S.R., Fredericson, M., Guillet, M., Shellock, F.G.: Patellofemoral kinematics during weight-bearing and non-weight-bearing knee extension in persons with lateral subluxation of the patella: a preliminary study. J. Orthop. Sports Phys. Ther. **33**, 677–685 (2003)
4. Heebner, N.R., Rafferty, D.M., Wohleber, M.F., Simonson, A.J., Lovalekar, M., Reinert, A., Sell, T.C.: Landing kinematics and kinetics at the knee during different landing tasks. J. Athl. Train. **52**, 1101–1108 (2017)
5. Petschnig, R., Baron, R., Albrecht, M.: The relationship between isokinetic quadriceps strength test and hop tests for distance and one-legged vertical jump test following anterior cruciate ligament reconstruction. J. Orthop. Sports Phys. Ther. **28**, 23–31 (1998)
6. Alvim, F.C., Lucareli, P.R.G., Menegaldo, L.L.: Predicting muscle forces during the propulsion phase of single leg triple hop test. Gait Posture **59**, 298–303 (2018)
7. Willson, J.D., Davis, I.S.: Lower extremity mechanics of females with and without patellofemoral pain across activities with progressively greater task demands. Clin. Biomech. **23**, 203–211 (2008)
8. Bley, A.S., Correa, J.C.F., Dos Reis, A.C., Rabelo, N.D.D.A., Marchetti, P.H., Lucareli, P.R.G.: Propulsion phase of the single leg triple hop test in women with patellofemoral pain syndrome: a biomechanical study. PLoS ONE **9**, e97606 (2014)
9. Petersen, W., Ellermann, A., Gösele-Koppenburg, A., Best, R., Rembitzki, I.V., Brüggemann, G.-P., Liebau, C.: Patellofemoral

pain syndrome. Knee Surg. Sports Traumatol. Arthrosc. **22**, 2264–2274 (2014)

10. Ward, S.H., Blackburn, J.T., Padua, D.A., Stanley, L.E., Harkey, M.S., Luc-Harkey, B.A., Pietrosimone, B.: quadriceps neuromuscular function and jump-landing sagittal-plane knee biomechanics after anterior cruciate ligament reconstruction. J. Athl. Train. **53**, 135–143 (2018)

11. Earl, J.E., Monteiro, S.K., Snyder, K.R.: Differences in lower extremity kinematics between a bilateral drop-vertical jump and a single-leg step-down. J. Orthop. Sports Phys. Ther. **37**, 245–252 (2007)

12. Machado, F.A., Amorim, A.A.: Condromalácia Patelar: aspectos estruturais, moleculares, morfológicos e biomecânicos. Rev. Educ. Física **130**, 29–37 (2005)

Functional Electrical Stimulator
for Treatment of Patients with Foot Drop

Jamile T. D. Alves⊙, Marco A. B. Rodrigues⊙, and André F. P. Aleixo⊙

Abstract

The purpose of the study is to promote tools for the treatment of patients with Foot Drop, who present with gait committed due to the difficulty in flexing the ankle. Functional Electrical Stimulation (FES) for Foot Drop treatment is being diffused because of the efficacy of its application in replacement of the treatment using orthoses. FES is performed through electrical stimulation of the patient's fibular nerve. He receives the electrostimulation during the gait swing phase, which generates the ankle dorsiflexion, correcting the problem of the fallen foot and helping in the quality and symmetry of the gait. Researches show that despite the diverse approaches of FES existing for this type of treatment, fatigue and spasticity problems from this treatment are still observed, which can be minimized depending on the control system applied. This publication presents a device developed for the generation of FES using embedded systems technology, associated to electronic devices for the control of amplitude, frequency and pulse width of the signal. The system forecasts for the future use of some sensor device that indicates the movement of the patient, and so the timing of the electrostimulation is controlled. The experimental results in the laboratory presented the electrical stimulation signals, totally digital controlled, with amplitudes, frequencies and pulse widths according to quantitative parameters applicable to this specific treatment.

Keywords

Foot drop • Functional electrical stimulation • Embedded system

1 Introduction

The Foot Drop syndrome is identified in patients through the difficulty in ankle dorsiflexion, and is usually caused by disturbances in the nervous system, among them, Stroke. When the patient suffers from this syndrome, he presents difficulties to perform the gait efficiently, and is more likely to fall during walking [1].

One of the conventional treatment alternatives is the use of ankle-foot orthosis, a rigid device that is used as a support to keep the ankle in a position that facilitates gait. Currently, the use of FES—Functional Electrical Stimulation is spreading as the main tool for the treatment of Foot-Equine Syndrome. To assist in walking, FES is applied with superficial electrodes for electrostimulation of the fibular nerve, resulting in ankle flexion movement and consequent improvement of gait performance. The use of FES brings several benefits during and after treatment, when compared to the orthosis. It is possible to observe in the patient the improvement in the gait execution in relation to speed, biomechanics, besides helping in the spasticity and other problems caused by the syndrome, resulting in therapeutic advances as the patient uses the FES [1, 2].

The devices used for the application of FES in the treatment of Foot Drop has undergone great advances since its beginning in 1961, and since then the researches on this approach still present different configurations of application and construction [3, 4].

The work developed corresponds to the research and construction of an electrostimulation device, based on information collected about the different modes of construction of FES devices, in order to present a final project to be applied in systems of treatment of Foot Drop Syndrome. This device generates the signal of electrostimulation, and the parameters of frequency, pulse width and amplitude that can be controlled using embedded systems.

J. T. D. Alves (✉) · M. A. B. Rodrigues · A. F. P. Aleixo
Federal University of Pernambuco, Recife, PE 50670-901, Brazil
e-mail: jamile.alves@ufrr.br

2 Materials and Methods

The development of this study was based on the information obtained about functional electrical stimulation for the treatment of Foot Drop patients, on the way it is applied, in addition to the characteristics and types of signs used as stimulus. Through this information and technical specifications obtained from commercial devices, a gathering of requirements for the project was carried out. From there the final device was designed, developed and tested with the objective of generating a FES signal, capable of being digitally controlled and that answer the needs of a high efficiency FES device.

2.1 Project Requirements

The design and implementation of a device for FES, object of this research proposal, was developed considering the trajectory of development of these devices and the technical characteristics of the commercial FES devices. The parameters of the output signal, the type of electrode, the amplitude and the polarity of the signal, among other constructive characteristics will be presented in Table 1, as well as the chosen requirements.

In Table 1, the characteristics observed in FES devices of Walkaide [5] and NESS L300 [6] are considered in commercial specifications. And in review, the specifications observed in literature review on FES [7]. Finally, the same table presents the requirements for this project.

The pulse duration parameter corresponds to the pulse width of the electrostimulation signal. While the burst frequency is the frequency period of active period plus the

inactive period pulse application. This frequency is usually in the order of dozens of Hertz [7].

2.2 Construction and Application of the Device

The FES device is composed of a set of electro-electronic components, resulting in the electrostimulator circuit, that is, the signal-generating circuit of electrostimulation. The system was developed in accordance with the design requirements presented and also built in such a way that it had low energy consumption and small dimensions to facilitate its future practical application. The components chosen for the project were selected so that they met the objectives of the project, and that they were accessible for acquiring and obtaining application information. A general scheme of the device can be seen in Fig. 1.

For general device control, embedded systems using microcontrollers interface with other devices. A microcontroller from the MSP430 family (Texas Instruments) was applied to control the system steps, as well as good performance, good accessibility and low power consumption. For the application phase and system tests, the work was developed in a development kit that applies this microcontroller.

The system performs the adjustment of the electrical stimulation parameters, which correspond to the signal amplitude (in Volts), the burst frequency (in Hz) and the pulse width (in microseconds). This adjustment is done in a totally digital way. Push buttons were used to control these parameters and to trigger electrostimulation. For a final application these buttons can be replaced by control

Table 1 Device specifications and FES design requirements for Foot Drop treatment [5–7]

Criteria	Specifications	Project requirements
Power	Batteries	Batteries with voltage compatible with the other components will be considered
Duration of pulses	Commercial: Between 25 and 450 μs Revision: around 300 μs	Range from 200 to 400 μs
Burst	Commercial: Between 17 and 45 Hz Review: around 50 Hz	Range from 20 to 50 Hz
Current intensity	Commercial: Up to 30 mA depending on load impedance Revision: 30 mA	It should provide a maximum current of 75 mA at a resistance of 1 kΩ
Electrodes	Commercial: transcutaneous Revision: transcutaneous	Transcutaneous
Amplitude of the pulses	Commercial: Up to 120 V	Adjustable range up to 75 V
Signal polarity	Revision: monopolar (unipolar)	Monopolar (unipolar)

Fig. 1 FES device operating scheme
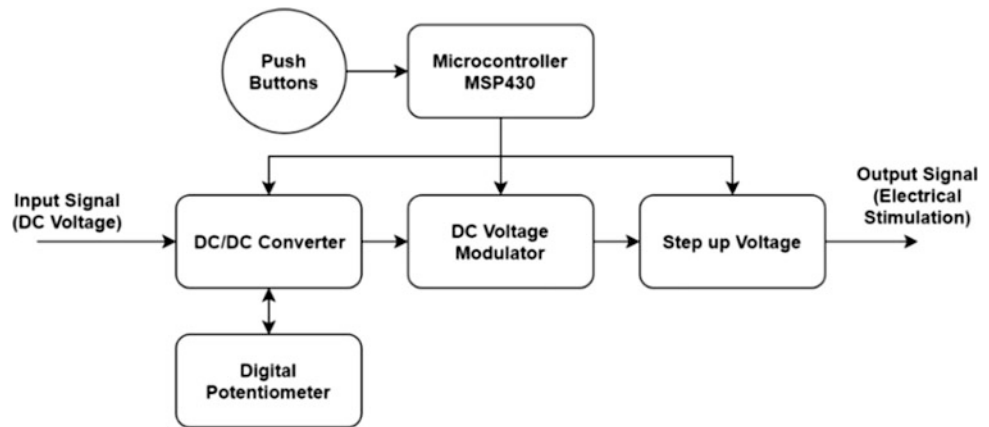
commands, having as reference information from external sensors of the system.

The developed FES device uses a DC voltage input, connected to a DC/DC converter, which provides higher voltage values to control the amplitude of the output signal by digital means, a digital potentiometer was introduced in the circuit, which can be adjusted by the microcontroller, controlling the output signal of the converter.

A signal modulator was connected to the output of the DC/DC converter to enable generation of pulses of the electrostimulation signal. The microcontroller is responsible for controlling the pulse width and burst frequency through the voltage modulator, resulting in a monopolar signal at the output. Thereafter, the modulated signal is raised to amplitudes sufficient to generate functional electrical stimulation.

The burst frequency can be set to three different values, 20, 35 and 50 Hz, the pulse width in three values, 200, 300 and 400 μs, while the output signal can assume voltages with the peak values of 35, 50 and 75 V peak. The duration of time in which the electrostimulation takes place may vary according to the gait times, and to simulate this situation it was provided in the device software that the application of the stimulus lasts one second, a range that can be adjusted subsequently.

To control the entire electrical stimulation process, a firmware was developed to be implemented in the microcontroller. This firmware is shown in the flow chart of Fig. 2. After setting up the microcontroller and its interface with the other devices, the system checks if the power button has been pressed, and if so, gives sequence in the flowchart. For adjustment of the electrical stimulation parameters, the system checks if the adjustment buttons have been pressed. In the event that one or more buttons are pressed, the flow proceeds to the settings and then to the electrostimulation.

Otherwise, it starts electrostimulation. To adjust the pulse width and frequency, the system adjusts the voltage modulator, and in the case of amplitude, the system configures the digital potentiometer, which interferes with the output of the

DC/DC converter. During electrical stimulation, a time interrupt is enabled to count up to half the burst frequency period, and during this time the system toggles the output between on and off, each with time interval of the adjusted pulse width. The interrupt is then re-enabled and counts the remainder of the period. The interrupt routine also has the function of establishing this routine of electrostimulation during the chosen time of one second. After one second without electrostimulation, it resumes the electrical stimulation while the on/off button continues to operate.

It is observed that the system implemented in this research provides a device capable of generating electrical stimulation signals from an electric power source, with adjustment of the parameters of the signal: amplitude, burst frequency, pulse width and duration of the electrostimulation. These parameters can be adjusted directly, in order to test the operation of the electrostimulator circuit. For automatic control of these parameters and direct application of the device, it is expected, using the microcontroller features chosen, the application of sensors that provide this system with the input information, and a firmware capable of processing this information in order to control this device.

3 Results

The FES device studied and developed generated electrical stimulation signals, according to the requirements presented, where the electrical stimulation parameters could be adjusted for future application in the patient. The output signal enablement can be controlled with the main power button, and the signal parameters were adjusted with amplitudes of 30, 50 and 75 V, 200, 300 and 400 μs pulse widths and burst frequencies at 20, 35 and 50 Hz, so that the system could be evaluated with all adjustment options.

Graphs with pulse widths of 300 μs, amplitude of 29.75 V and frequency of 51.02 Hz can be seen in Fig. 3a. In Fig. 3b, the graphs present the parameters: pulse width of
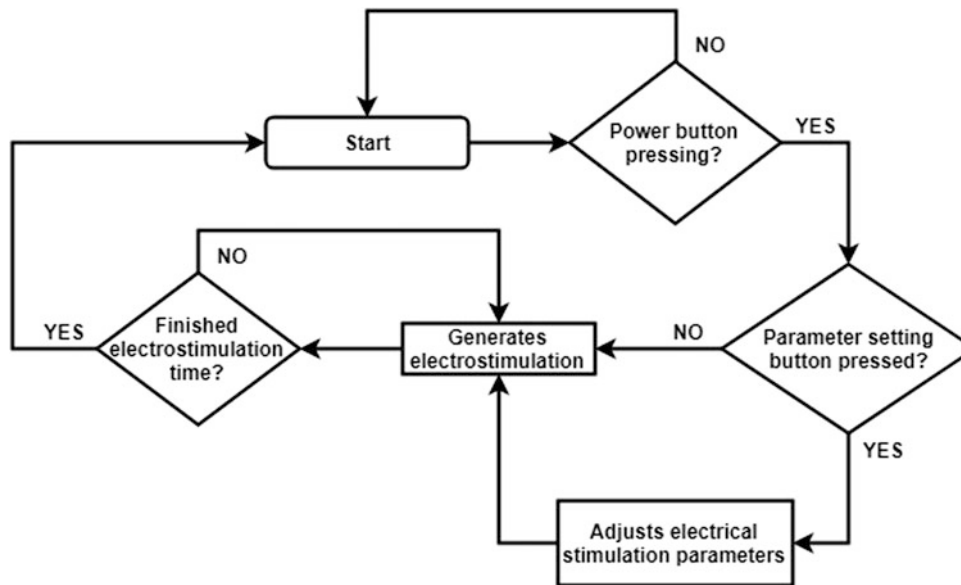
Fig. 2 Firmware flowchart for the FES device

Fig. 3 Electrical stimulation signal with pulse width, amplitude and burst frequency, respectively, **a** 300 μs, 29.75 V and 51.02 Hz; **b** 200 μs, 50.62 V and 35.79 Hz; **c** 400 μs, 75 V and 20.45 Hz
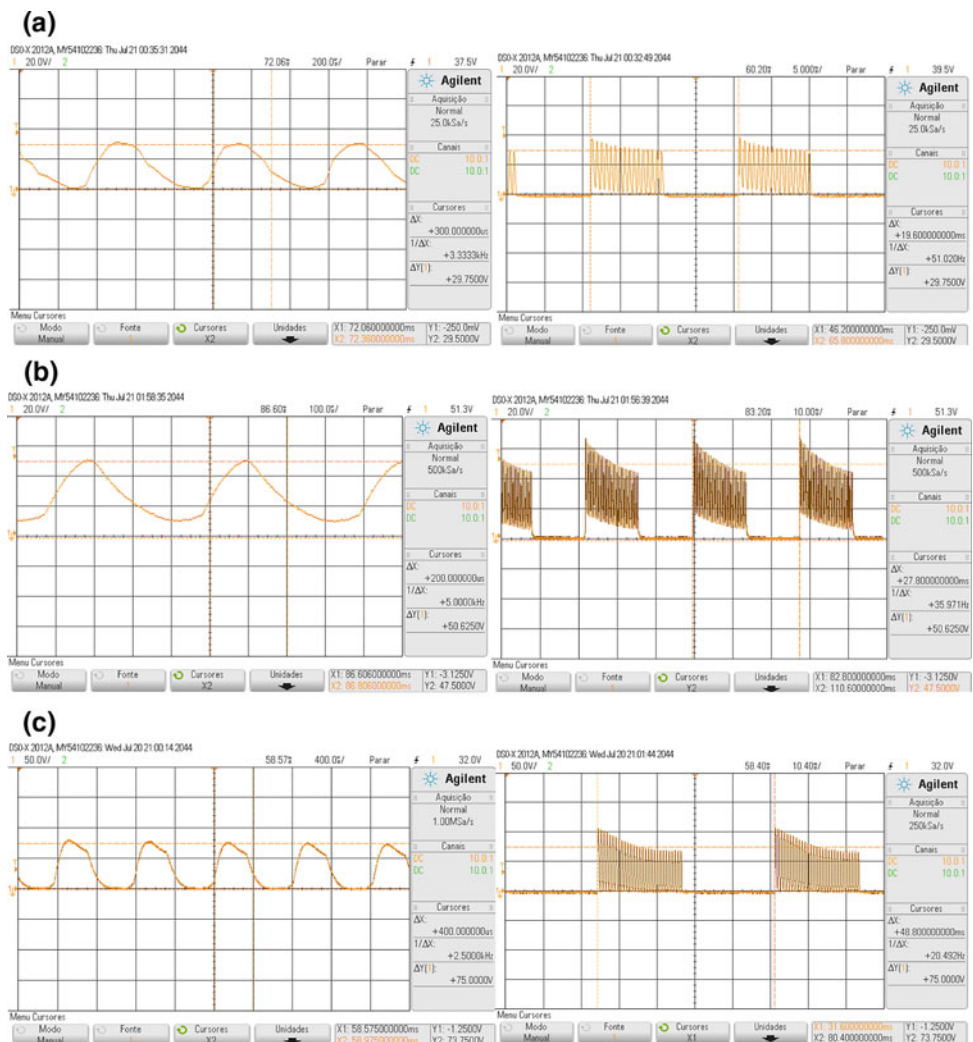
200 μs, amplitude of 50.62 V and frequency of 35.79 Hz. Figure 3c exemplify the electrostimulation output with the parameters of 20.45 Hz of frequency, 75 V of amplitude and 400 μs of pulse width.

4 Conclusion

The use of FES as a treatment is considered complex, since the electrical pulses must be applied as accurately as possible, close to the tissue to be stimulated and selectively. To be classified as functional, the electrical stimulation must result in a movement that reproduces some function of the patient's body [8].

The modulation and intensity of the electrostimulation signal are responsible for the intensity of the movement generated during the treatment application. This movement, in the case of the application in patients with Foot Drop syndrome, corresponds to ankle flexion due to the torque generated by the electrical stimulation of the muscle [9]. The application of the signal occurs in short electrical pulses. Normally, the closed control loop of the electrostimulation system is used, where sensors provide patient movement data so that the system controls the parameters and timing of the electrostimulation [9, 10].

FES devices for the treatment of Foot Drop syndrome show some variations in the number of channels, the moment of electrostimulation, the types of signals applied and the sensors used in the system. These devices have become smaller and more comfortable. They can use multiple channels, or apply only one stimulation channel, where sensors take readings related to the movement and indicate the firing moment of the FES, corresponding, in the latter case, to the gait balance stage [3, 4]. Table 2 presents some types of signal used in FES over the years and the details of its applications [3].

A new trend is observed for the types of stimulations applied in the FES, in which the application of different waveforms and different intensities is considered, resulting in a stimulus that is as close as possible to the natural one [4].

The proposed generation of functional electrical stimulation signals was fulfilled, with respect to the design requirements. The system generates a signal at the output with adjustable burst frequency, pulse width and amplitude

parameters that can be used in a more complete system that is capable of promoting the gait correction of patients with Foot Drop syndrome.

The system can be configured for a digital adjustment of the duration range of the electrostimulation, which was initially fixed in one second. This is one of the characteristics of a stimulation applied to the control of the movement of the gait, primordial for its effectiveness.

For this research, characteristics of the main parameters to be met in this type of treatment (specifications and requirements presented in Table 1) were taken as a basis, aiming also for improvements that meet the needs of these patients, such as comfort and efficiency.

When comparing the operation and application of the Walkaid commercial device with the FES device of this study, it was observed that: (1) In the commercial device, the amplitude adjustment of the electrostimulation signal is manual and analog; the device of this study has digital setting of this parameter; (2) In the commercial device, the adjustments of duration of the electrical stimulation, of burst frequency and of pulse width happen with the use of a software installed in the computer, which must be connected to a device of link with the electrical stimulator so that happens the adjustment of these parameters, taking into account the characteristics of each patient; the device of this study allows access to adjustment of these parameters by digital means, allowing a fully automated control with the future application of a sensorized control system, which meets the needs of the patient simultaneously with the use of the equipment.

During the selection of the components and the assembly of the electrostimulator circuit, one of the points where it was verified the need for an adaptations was in the power supply. In order for the system to not consume unnecessary power in more than one voltage regulator, the components must operate with the same input DC voltage value.

The current applied to FES varies according to the applied voltage and the impending load of the patient. As a protection system, a current intensity measurement should be used as information for the microcontroller to generate a safety shutdown of the device.

And finally, the system makes it possible to advance the research on FES for gait correction in patients with Foot Drop. When a controlled electrostimulation device is

Table 2 Some electrical stimulus of FES for Foot Drop treatment [3]	Stimulus	Details
	Trapezoidal	Uses foot switches; constant pulse width, frequency and amplitude parameters
	Modulated	Uses foot switches; the intensity of the electrostimulation increases at the moment before the heel impulse
	Based on EMG signals	Stimulation similar to natural; greater dorsiflexion of the ankle; less spastic reaction

obtained, tests should be performed to improve the system so that it is autonomous with respect to adjustments of electrical stimulation parameters, according to the needs of the patient.

An important observation about the electro-stimulation circuit is that the way it was formed allows the configuration and application of different types of electrostimulation. The microcontroller can provide the generation of different types of signals, and other frequencies and pulse widths can be obtained up to the limits of the modulator, meeting the specifications of the signals of functional stimulation.

References

1. Everaert, D.G., Stein, R.B., Abrams, G.M., Dromerick, A.W., Francisco, G.E., Hafner, B.J., Huskey, T.N., Munin, M.C., Nolan, K.J., Kufta, C.V.: Effect of a foot-drop stimulator and ankle-foot orthosis on walking performance after stroke: a multicenter randomized controlled trial. Neurorehabil. Neural Repair **27**(7), 579–591 (2013)
2. Morone, G., Fusco, A., Di Capua, P., Coiro, P., Pratesi, L.: Walking training with foot drop stimulator controlled by a tilt sensor to improve walking outcomes: a randomized controlled pilot study in patients with stroke in subacute phase. Stroke Res. Treat. 523–564 (2012)
3. Melo, P.L., Silva, M.T., Martins, J.M., Newman, D.J.: Technical developments of functional electrical stimulation to correct drop foot: sensing. Actuation Control Strateg. Clin. Biomech. **30**(2), 101–113 (2015)
4. Sabut, S.K., Bhattacharya, S.D., Manjunatha, M.: Functional electrical stimulation on improving foot drop gait in poststroke rehabilitation: a review of its technology and clinical efficacy. Crit. Rev. Biomed. Eng. **41**(2), 149–160 (2013)
5. INNOVATIVE NEUROTRONICS. The WalkAide System Clinician Manual Homepage. http://www.walkaide.com/support/Documents/ClinicianManual.pdf. Last accessed 05 April 2018
6. BIONESS. Technical and Specifications Homepage. https://www.bioness.com/Products/L300_for_Foot_Drop.php. Last accessed 24 Aug 2016
7. Krueger-Beck, E., Scheeren, E.M., Neto, G.N.N., Button, V.L.S.N., Nohama, P.: Efeitos da estimulação elétrica funcional no controle neuromuscular artificial. Rev. Neurocienc **19**(3), 530–541 (2011)
8. Bronzino, J.D.: The Biomedical Engineering Handbook, 2nd ed. CRC Press, LLC (2000)
9. Lynch, C.L., Popovic, M.R.: Functional electrical stimulation. IEEE Control Syst. Mag. (2008)
10. Dunning, K., O'dell, M.W., Kluding, P., Mcbride, K.: Peroneal stimulation for foot drop after stroke: a systematic review. Am. J. Phys. Med. Rehabil. **94**(8), 649–664(2015)

Gait Analysis of Foot Drop in the Anatomic Plan Using the Walkaide® Device

F. M. F. B. M. Aragão, A. V. M. Inocêncio, E. M. Aragão Junior, J. C. Vieira, C. Rodrigues, C. S. Silveira, and M. A. B. Rodrigues

Abstract

The human gait shows the single efficiency and functionality and can be considered the most complex functional activity of the human being. Foot drop can be defined as a significant weakness in the dorsal flexion of the foot. The functional electrical orthosis (FEO) are devices that use electrical stimulation to promote functional movements. Besides the FEO promotes the improvement of muscular tropism, this mechanism can be a source of relearning, because all events are interpreted by the body as his owns. This research sought to analyze the impact of the electrostimulation through the Walkaide® system in the angular movement of individuals with foot drop. The data were collected from seven patients and the focus of the evaluation of this research was the subtalar joint angle. After analyze the results, it could be seen that the Walkaide® promoted a significant gait improvement, meanly about the compensatory movements.

Keywords

Rehabilitation • Drop foot • Functional electrical stimulation

1 Introduction

One of the determining characteristic of the human being is the ability of walk erect, in a rhythmic way and, theoretically, without effort or with minimum energy expediture. The act of walk is a continuous event that consists in transfer the weight of one lower limb to the other, with the goal of advance the body forward at the same time that successful imbalances happens [1].

The reduced ability to walk is one of the functional problems frequently related in patients with lower palsy. Some of the source of complains presented by them are correlated with the changes of voluntary control of the limb, integrity of proprioception and of the movement [2].

Foot drop is not characterized as a disease, but a temporary or perpetual sequel due a stroke, cerebral palsy, incomplete spinal injury, neuropathy, diabetes or any type of cerebral trauma. In these cases, the patient presents the incapacity of stand up the frontal part of the foot, dragging their fingers on the floor. Trying to walk in this condition, the patients end up elevating more the knee and the hip, interfering the achievement of a correct gait.

The functional electrical stimulation (FES) can be defined as a controlled nerve activation, using a lower frequency current to promote a contraction in some inactive muscles. This technic can be an alternative to rehabilitation in patients with foot drop, because the stimulus of the peripheral nervous system can restore the elevation of the frontal part of the foot [3, 4].

This paper sought to analyze the use of electrostimulation through the Walkaide® system in the angular movement of the ankle in the swing phase of the gait on individuals with foot drop. This research aims the future development of electrostimulation equipment with Brazilian technology and low cost.

2 Background

2.1 Human Gait

The gait is a succession of alternate and rhythmic movements of the limbs and the body, raising an anterior displacement of the body gravity center [5]. Each individual presents a peculiar gait pattern to move in the environment with the minimum possible effort, besides the habitual and

F. M. F. B. M. Aragão (✉) · A. V. M. Inocêncio · E. M. Aragão Junior · J. C. Vieira · C. S. Silveira · M. A. B. Rodrigues
Federal University of Pernambuco (UFPE), Recife, Brazil
e-mail: flavia.barbosa.1@hotmail.com

C. Rodrigues
University of Porto, Porto, Portugal

selective control to presents proper stability and acceptable appearance [1]. The act of many muscles is involved in the gait, and many combinations of different muscle forces can result in the same model f movement [5].

The human gait is carefully distributed in a cycle and subdivided in phases. The gait cycle phases compose the activities that occurs since the initial touch point of the foot in the floor to the point that the same foot touches the floor again [6].

Each extremity goes through two phases during the cycle, a phase of support and a phase of oscillation. The stance phase begins with the movement that one extremity goes in contact with the floor and continues while the foot keeps in contact. This phase corresponds to 60% of the gait cycle. The swing phase begins when the foot drops out the floor and end right before his contact with the soil. The phase corresponds about 40% of the gait cycle (walking rhythm) [7].

2.2 Foot Drop

The pathology gravity determines the difficulty degree to execute the movement and usually the patient uses the remains functions to complete the movement. The result gait pattern is a combination of deviations caused by the primary dysfunction and by the movement established by the remain function [8].

The drop foot is defined by a significant weakness in the dorsal flexion of the foot. The more affected muscles are the anterior tibial, longus extender of the hallux and the longus extender of the fingers, because they realize the dorsiflexion of the foot during gait [3].

The patient that presents hemiparetic gait has angular restrictions in the ankle, knee and hip because of the tonus increase of the extensor musculature of the lower limbs. The gait becomes misaligned, because requires the realization of the lateral movement of the lower limb during the oscillation phase, characterizing an abnormal gait. Thus, the gait restoration acts essentially in rehabilitation, turning the movement more independent and facilitating his cares [9].

2.3 Functional Electrical Orthesis: Functional Electrostimulation and Walkaide

The Functional Electrical Stimulation (FES) is used in a tentative of reconstruct the neuro muscle function lost or injured, through the application of electrical pulses. The FES is a category of electrotherapy used in muscles with lesion in the motor superior neuron, always with the goal of realize functional movements. This technique is largely applied in patients with foot drop, because it can improve the force, reduce the spasticity, correct the gait and its velocity.

The FES uses an electrical current applied by electrodes on the skin surface to produce depolarization of the motor nerve, resulting in a muscle contraction capable to product functional movements [10].

The functional electrical orthesis (FEO) is a device that uses functional electrical stimulation to promote functional movement. The current profiles used in these devices causes a stimulus that arrives in the central nervous system and product active movement in the patient. Besides promote improvement in the muscle tropism, this mechanism serves also as a relearning, because all events are understood as their own [11].

The Walkaide® is a non-invasive and autonomous device projected specific to provide transcutaneous electrical stimulation comfortable to the patient. The stimulation affects directly the common fibular nerve and the anterior tibial muscle, with the goal of improve the dorsiflexion during the swing phase of the gait. The Walkaide® system fits inside of a support surrounded in the patient leg, below the knee. The device includes slope sensors, with accelerometers and inclinometers to measure the position and velocity of the leg to provide the stimulation in the correct moment [12].

The generated impulses are delivered to the transcutaneous self-adhesive electrodes positioned on the fibular common nerve and in the tibial anterior muscle belly. The stimuli are offered through electric current pulses with low intensity, with duration and amplitude enough to produce action potentials in peripheral nerves. The slope sensors activate the dorsiflexion in all swing phase, reducing or eliminating completely the drop of the foot and turning the gait normal [12].

The Walkainde system parameters are adjusted using software walkAnalist provided by the manufacturer website. The system communicates with the software through the

Fig. 1 The Walkaide® system. Adopted from clinician manual [13]

Bluetooth communication protocol when the system is connected with another device called Walklink (Fig. 1).

3 Materials and Methods

This research consists in a pilot study. It is a qualitative and quantitative cross-sectional study and was realized after the approval of the research ethics committee of UFPE with the CAAE protocol 55850616.1.0000.5208.

In this study were included adult people with age between 18 and 75 years old in both genders that presented unilateral foot drop, prevenient of a central nerve lesion, independent of the etiology but not carrier of a dysfunction in the neuromuscular peripheral complex. Also, the volunteers also had no important limitation of the active or passive movement amplitude of the ankle joint to the dorsiflexion and of the knee joint to the flexion. The sample was composed of seven (7) volunteers. Two volunteers were female (28.6%) and five were male (71.4%).

In this research, the participants were excluded if they needed a support exclusive to walk, like a crutch, a walking stick or an orthosis. Another criterion was if the patient had cognitive problems that turned incapable to understand the directions for the data acquisition. The patients with level greater than 2 in the modified Ashworth scale were also excluded.

The data acquisition was obtained in the Laboratory Kinesiology and Functional Evaluation (LACAF), in the Department of Physiotherapy of the UFPE, between May/2017 and June/2017. The patient visited the laboratory just one time and the procedure were divided in three steps:

(1st) After a clinical evaluation, a static acquisition was acquired with the Qualisys Pró-Reflex system. In this step, the volunteer stayed in an orthostatic position with the two feet on the floor and the crossed arms for a period of 5 s in the system begin. The sample rate of the system acquisition was set in 81 Hz in the Qualisys software.

(2nd) A dynamic acquisition in which the volunteer walked a 5 m distance in a medium period of 10 s three times.

(3rd) In this step, the Walkaide system was settled based in the clinical manual. The volunteer walked also three times the same trajectory of the 2nd step using the Walkaide system adapted to him.

For the data acquisition, it was used the Qualisys Pro-reflex system, Fig. 2. This system is considered a golden pattern by several authors like Kirkwood et al. [14] that had the goal in his study to develop and test the reliability and validity of the GaitGrabber system in obtaining kinematic data from the sagittal plan during the gait. Araújo et al. [15] conducted a similar study to develop a observational gait scale and characterize paralyzed brain children using this same system.

The Qualisys system used is composed of 6 infrared cameras disposed in a room with 40 m^2. Those cameras catch the position of passive reflexive markers that are positioned in specific places. In the beginning of the capture, the system was calibrated as recommended by the manufacturer's manual.

The Visual 3D software was used to create a biomechanical model and process the kinematic data. To identify correctly the parts of the body, markers were mainly placed

Fig. 2 Qualisys system interface with the capture model in the frontal plan. *Source* personal archive
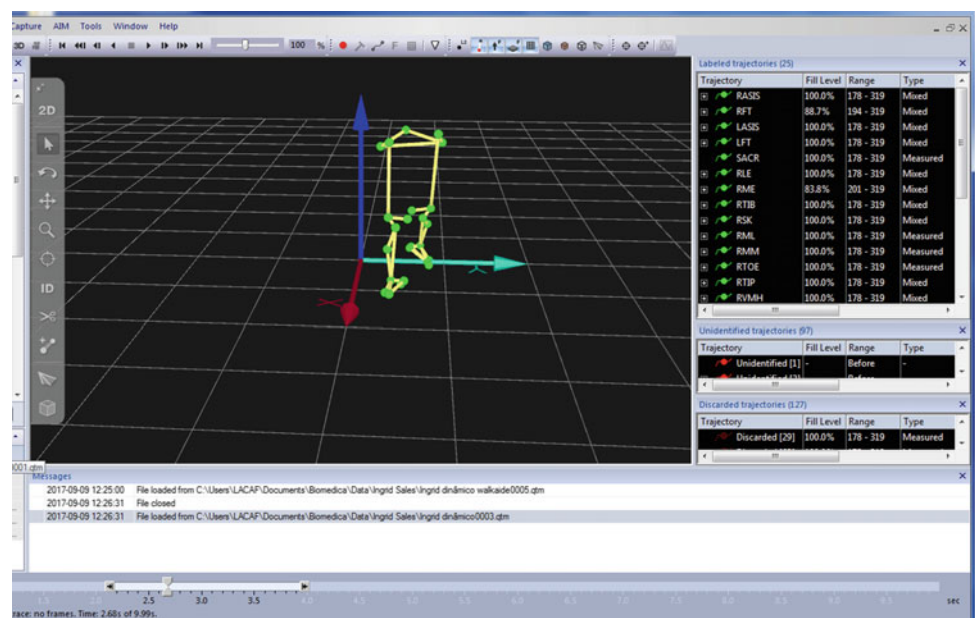
Fig. 3 Biomechanical model vision in Visual 3D in the frontal plan
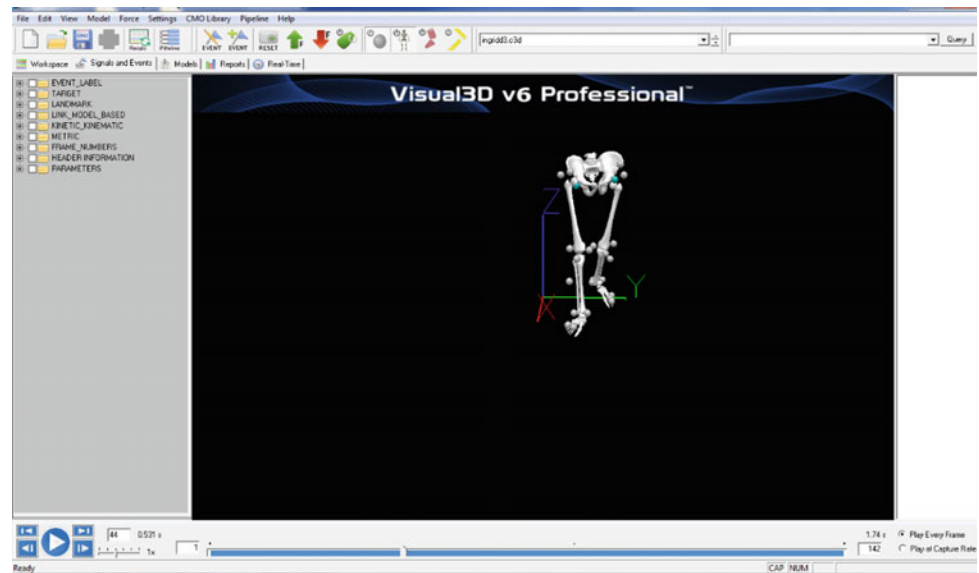
on: Ilium Anterior Superior, Sacrum, Femur greater Trochanter, Femur Lateral Epicondyle, Femur Medial Epicondyle, Head of Tibia, Fibula Apex of Lateral Malleolus, Tibia Apex of Medial Malleolus, Posterior Surface of Calcaneus, Head of 5th Metatarsus and Head of 2nd Metatarsus. The choice of marker's places was based in the segment definitions in C-Motion tutorial [16].

After the acquisition, the markers were labelled and the file was exported to the Visual 3D software, to do the analysis of the movement. A pipeline was created to calculate the ankle angle during gait in the frontal plan, as see in Fig. 3. The angle variation in X-axis represents the flexion/extension, in Y-axis represents the abduction/adduction and in Z-axis represents the longitudinal rotation. The neuter angle for dorsiflexion is 90º according the American Academy of Orthopaedic Surgeons.

The statistical analysis was made in the Biostat 5.3 software, in which the Kolmogorov-Smirnov normality test was applied. The null hypothesis tested was there was normal distribution between the categories and this hypothesis was rejected.

4 Results

The data processed by the Visual 3D software for the subtalar ankle's joint in the Y-axis from the Cartesian plan and the anatomic frontal plan. The executed movement shows the lateral and medial deviation of the foot. The Table 1 describes the ankle angle for each patient.

After the realization of the Komogorov Smirnov normality test in all samples, it was noticed that the graph curve was not normal. For that reason, the analysis was made with the non-parametric test of Wilcoxon for the dependent data

from each patient and with the Mann Whitney's test to the independent samples to do a comparation between all patients in the subtalar joint angle of Y-axis in the frontal plan. All tests were run with the null hypothesis that there is no difference between the groups, with p-value < 0.05.

According to Table 1, the acquired data, obtained from the variation of the foot arch movement in the frontal plan during gait had a significant difference in 6 of 7 volunteers (85.7% of the patients). Various researches report that the use of this angle reveals the foot alignment with the tibia bone during gait [5, 17, 18]. This angle should be about zero when the person is stopped and his variation represents a gait pattern. Otherwise, when the averages of each patient are compared, there is no significant statistical variation, as described in Table 2. This result represents the impact of the use of the device in the volunteer's gait pattern when observed separately.

Comparing the angle variation between the movement range of the foot in the frontal plan, it can be noticed, in

Table 1 Patient's results

Patients	Variation of the foot arch movement in the frontal plan during gait (°)		
	With Walkaide®	Without Walkaide®	p-value
1	0.70 ± 2.11	1.65 ± 1.84	0.000*
2	−6.06 ± 8.64	−9.36 ± 7.40	0.001*
3	−5.76 ± 5.64	−6.97 ± 5.10	0.094*
4	20.23 ± 3.75	19.95 ± 2.63	0.003*
5	−0.02 ± 6.47	3.32 ± 5.99	0.000*
6	−2.73 ± 4.77	−9.34 ± 6.24	0.000*
7	−2.98 ± 2.40	−3.82 ± 2.48	0.000*

Wilcoxon test, with significant level to $p < 0.05$

Table 2 Average (± standard deviation) and *p*-value of the angle variation in frontal plans for all patients

Variation of the foot arch movement in the frontal plan during gait (°)		
With Walkaide®	Without Walkaide®	*p*-value
0.08 ± 2.11	−0.31 ± 1.84	0.952*

*Mann Whitnet test, with significant level to $p < 0.05$

absolute numbers, that the average with the Walkaide system represents an adduction movement, leaving the foot closer to the medial line. With this improvement, there is a reduce of the foot deviations during the gait. Statistically, there were no significant difference. These results can be a reflex of the absence of the training and adaptation phase of the equipment.

After an analysis, it was observed that the patients use compensations to adjust the deviation caused by the primary dysfunction to adept gait with foot drop. In this context, important findings could be observed like the improvement of the compensatory movements of the ankle, where was observed a positive variation of the angle in the frontal plan in 5 of 7 volunteers (Table 1).

With the improvement of adduction because of the device, there were the reduction of abrupt movements in the swing phase of the patients. These movements are realized to avoid the foot to touch the floor. Otherwise, when compared the angle variation of all patients there was no statistical significance ($p = 0.952$), with average without the device being 0.08 ± 2.11, and the average with the device −0.31 ± 1.84.

In Fig. 4, it is possible evaluate the blue variable that corresponds to the gait without the Walkaide system. There is a positive variation from the subtalar joint angle, more evident between 1–1.5 s and 2.5–3 s. This variation implies in a lateral detour during gait. This result reflects the gait from the foot drop patients and can corresponds to an instable gait with drop risks. The behavior of the subtalar joint angle in the frontal plan (Y-axis) contains a greater variation when compared with the red trace, the gait with the Wakaide system. Even with a negative variation in the beginning, probably because of the adaptation, it is possible
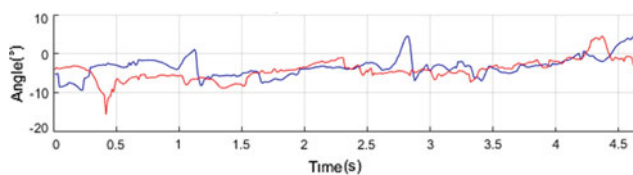
Fig. 4 Comparation between the subtalar joint's angle of the patient in the frontal plan Y-axis with Walkaide (red) and without Walkaide (blue) (Color figure online)

to notice that after 0.5 s, the gait is more regular, showing a stability in the gait pattern with the device.

5 Conclusion

During the Qualisys capture and visual 3D analysis, it was possible to notice that patients with foot drop use compensatory movements to adjust the deviations caused by the primary dysfunction. In this context, it was possible to improve the compensatory movements from the lateral and medial deviations from the foot during 85.6% of the captured sample, corroborating with the research of Sheffler and Chae [19] and Nolan et al. [20].

These findings can be identified because of the stimulation form, promoting a gait close to the normal pattern and helping the patient to reduce the compensatory movements and to maintain the subtalar joint angle without abnormal variations. This condition produces a foot alignment and promotes a stable gait with voluntary motor control.

After analyze the results, it was possible conclude that the Walkaide® device promoted a significant gait improvement related to the physiological movements and also to the compensatory movements. This was found when the results were analyzed individually, but in the comparison of all patients, there were no significant variation. This research raises thoughts on some advances in the use of this portable electrical stimulation technique to correct some difficulties encountered in the data collection with the use of Walkaide® device. This technique corrects the gait of patients with foot drop to become closer to normal gait.

References

1. Ribas, D.I.R., et al.: Estudo comparativo dos parâmetros angulares da marcha humana em ambiente aquático e terrestre em indivíduos hígidos adultos jovens. Rev. Bras. Med. Esporte **13**(6), 371–375 (2007)
2. Ovando, A.C.: Acidente vascular encefálico: comprometimento motor dos membros inferiores e alterações na marcha. Rev. Digit. B. Aires ANO **14**(132) (2009)
3. de Resende, G.P.: Equipamento de Biofeedback para Tratamento Fisioterápico em Pacientes Portadores de Pé Equino. Universidade Tecnológica Federal do Paraná, Curitiba, Dissertação de Mestrado - Programa de Pós-Graduação em Engenharia Biomédica (2014)
4. Calhau, A., et al.: Análise cinemática da marcha. Disciplina de biomecânica do movimento. Mestrado integrado em engenharia Biomédica. Instituto Superior Técnico—Departamento de Física, 4o Ano, 1o Semestre 2007/08
5. Rose, J., Gamble, J.G.: Marcha Humana, 2nd ed. São Paulo, Premier (1998)
6. de Sousa, A.S.P.: Análise da Marcha Baseada em Correlação Multifatorial. Dissertação de Mestrado– Mestrado em Engenharia Biomédica, Faculdade de Engenharia da Universidade do Porto (2013)

7. Brandalize, D., Brandalize, M.: Efeitos da toxina botulínica no tratamento do pé equíno em indivíduos com sequelas de acidente vascular encefálico. Voos Rev. Polidisciplinar Eletrônica Fac. Guairacá **2**(2) (2011)

8. Zuge, R.W., Manffra, E.F.: Efeitos de uma intervenção cinesioterapêutica e eletroterapêutica na cinemática da marcha de indivíduos hemiparéticos. Fisioter. Mov. **22**(4), 547–556 (2009)

9. Agne, J.E.: Eletrotermoterapia: teoria e prática. Orium, Santa Maria (2005)

10. Robbins, S.M., et al.: The therapeutic effect of functional and transcutaneous electric stimulation on improving gait speed in stroke patients: a meta-analysis. Arch. Phys. Med. Rehabil. **87**(6), 853–859 (2006)

11. Gonçalves, B.A., Francisco, N.P.F.: Órteses: orientações e cuidados. In: XIV Encontro Latino Americano de Iniciação Científica e X Encontro Latino Americano de Pós-Graduação—Universidade do Vale do Paraíba (2011)

12. Cameron, M.H.: The walkaide® functional electrical stimulation system—A novel therapeutic approach for foot drop in central nervous system disorders. US Neurol. **6**(2), 112–114 (2010)

13. Walkaide Homepage. http://www.walkaide.com/support/documents/clinicianmanual_lm06_rev2.pdf. Last accessed 21 March 2018

14. Kirkwood, R.N., et al.: Sistema gait grabber na captação de dados cinemáticos durante a marcha. Motriz Rev. Educ. Fis. **18**(3), 505–514 (2012)

15. Araújo, P.A., Kirkwood, R.N., Figueiredo, E.M.: Validity and intra- and inter-rater reliability of the observational gait scale for children with spastic cerebral palsy. Revi. Bras. Fisioterapia São Carlos **13**(3), 267–273 (2009)

16. C-motion Homepage. http://www.c-motion.com/v3dwiki/index.php?title = Marker_Set_Guidelines. Last accessed 19 March 2018

17. Calais-Germain, B.: Anatomia para o movimento: introdução à análise das técnicas corporais, Vol. 1. São Paulo, Manole (1991)

18. Hall, S.J.: Biomecânica Básica. 4ª edição, Rio de Janeiro, Guanabara Koogan (2005)

19. Sheffler, L.R., Chae, J.: Technological advances in interventions to enhance post-stroke gait. Phys. Med. Rehabil. Clin. N. Am. **24**(2), 305 (2013)

20. Nolan, K.J., Yarossi, M., McLaughlin, P.: Changes in center of pressure displacement with the use of a foot drop stimulator in individuals with stroke. Clin. Biomech. **30**(7), 755–761 (2015)

Gait Initiation Process: Comparing Force and Pressure Platforms Data

Fernanda Grazielle da Silva Azevedo Nora⊙, Michelle Bazilio Milan⊙,
Franciele Paiva⊙, Nilva Pessoa de Souza⊙, Alfredo de Oliveira Assis⊙,
Fábio Barbosa Rodrigues⊙, and Marcus Fraga Vieira⊙

Abstract

Gait initiation is the transition from standing to cyclic posture and it is challenging for both typical and pathological subject. Force and pressure platforms are often used to compute the center of pressure (COP) displacement and force or pressure, since these are ways to evaluate gait initiation kinetics. Thus, the aim of this study is to compare kinetic data of gait initiation between one double force platform and one pressure platform. Ten healthy adults performed gait initiation on a AMTI double platform and Tekscan pressure platform. The average data of three successful trials were used for analysis. The duration of anticipatory period (Time_COP_1) and the duration of the first step period (Time_COP_2) were computed by a custom-written Matlab code. Wilcoxon tests were used compare AMTI and Tekscan results. The duration of period 1 (Anticipatory) presented statistically significant differences, where the execution in the plantar pressure platform presented a shorter duration when compared with the force platform (p = 0.003). Both platforms had similar duration time for the period 2 duration (Execution of the first step), therefore did not present statistically significant differences, showing that the two systems present the same information. Therefore, despite the technological differences, it is safe to analyze the COP variables with any of the tested instruments.

Keywords

Gait initiation • Healthy adults • Center of pressure • Force platform • Pressure platform

F. G. da Silva Azevedo Nora (✉) · M. B. Milan · F. Paiva ·
N. P. de Souza · A. de Oliveira Assis · F. B. Rodrigues ·
M. F. Vieira
Bioengineering and Biomechanics Laboratory (Labioeng),
Physical Education and Dance College, Federal University
of Goias, Goiânia, Goiás, Brazil
e-mail: fgnora@gmail.com

1 Introduction

The transition from the standing position to gait, traditionally called gait initiation, requires anticipatory postural adjustments (APAs) appropriate to achieve the intended goal [1–3]. The role of APAs in initiating gait is ambiguous: on the one hand, it aims to preserve balance, minimizing postural disturbances generated by movement. On the other hand, it creates the necessary imbalance to start the forwarding movement by moving the COM forward [1–3]. Gait initiation is the task used to understand such adjustments.

Most of studies have analyzed the behavior of kinetic and kinematic variables in the gait initiation process in adult populations, aiming to understand the postural limitations in pathologies and aging, predominantly Parkinson's disease, amputations and neurological diseases [1, 4–9], as well as gait with typical children, without neuromuscular or orthopedic disorders [10, 11].

The main parameter to be measured in studies that address gait initiation with the use of force platforms and plantar pressure platform is the pressure center (COP), which is considered as the point of application of the resultant of the vertical forces acting on the surface [12] and the main variables studied are the bi-dimensional paths, displacements and speeds of the COP.

The behavior the center of pressure represents the collective result of the postural control system and the force of gravity, the neuromotor response to the center-mass oscillation [12]. This variable is totally independent of the center of mass or gravity. If is foot in contact with the ground, the center of pressure is within the area of that foot. If both feet are in contact with the ground, the center of pressure liquid is located between the two feet, depending on the relative load placed on each foot.

Plantar pressure platforms produce maps with anatomical resolution of the pressures that affect specific areas of the plantar surface. The center of pressure is considered the point of application of the resultant of the vertical forces of

ground reaction force. The magnitudes of the pressures in plantar regions anatomical (the patterns of the spatial distribution of these pressures), as well as the vertical ground reaction forces [13] and other derived variables are quantified. Force platforms, plantar pressure forces provide a COP calculated only from the vertical component of the ground reaction force but have the advantage of providing an anatomical resolution of the position of the COP relative to the plantar surface.

In force platform, the COP is considered as the point of application of the resultant of the ground reaction forces, having as reference the platform's spatial coordinate system, based on three orthogonal axes, which is fixed and defined by the manufacturer, and not the anatomy of the supporting foot. There is no way to know the actual position of the feet by the data obtained unless it is standardized by the experimenter.

You can study gait initiation using one or two force platforms. When using force platform, the main concern is to understand the behavior of the COP during each step of initiating the step, and it is not assumed that there are asymmetries between the right and left members of the research subject. On the other hand, when asymmetries are expected between limbs caused by orthopedic, neurological, or other diseases, two force platforms can be used to assess the contribution of each limb during the step anticipation process and understand the organization of this neuromotor process.

The aim of the study is to compare the kinetic data of gait initiation between a dual force platform and a plantar pressure platform.

2   Methods

2.1   Participants

Ten young adults of both gender participated in this study (aged 22.5 years, body mass of 72.5 kg). All subjects were informed about the purpose and procedures of the study and were instructed to sign the informed consent form before the beginning of the experimental protocol. The study was approved the Ethics and Research Committee of the Federal University of Goias, on April, 17, 2017, having approval number: 2.016.980.

2.2   Experimental Protocol

The COP displacement and duration was divided in three periods [10, 14–16] as shown in Fig. 1:
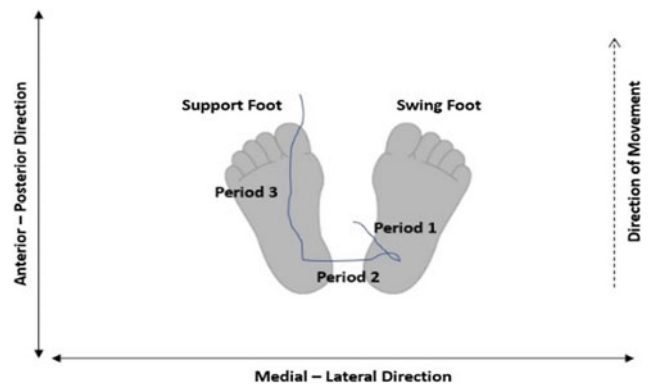
Fig. 1 COP displacement during gait initiation. Period 1—Anticipatory; Period 2—First step; Period 3—Second step

Period 1—Antecipatory: from the begining of the movement until the most lateral position of the COP in the direction of the swing foot (COPAP_1 and COPML_1);

Period 2—First step: from the end of the period 1 to the most medial COP position in the direction of the support foot (COPAP_2 and COPML_2);

Period 3—Second step—from the end of period 2 to the end of the movement, when the COP moves forward (COPAP_3 and COPML_3).

The time duration anticipatory period (Time_COP_1) and time duration first step period (Time_COP_2) were measured with one double force platform (AMTI dual–force platform) and pressure platform (Tekscan—HRMAT) during the gait initiation. The Kinetic data of the force platform and pressure platform were sampled at 100 Hz and 180 Hz respectively. Data processing were performed with Matlab (The MathWorks Inc, USA).

The participants performed three trials to gait initiation on the plantar pressure platform and the force platform.

2.3   Statistical Analysis

Using the Shapiro-Wilk method to test the normality of the data with a sensitivity of p = 0.05, and for the comparison of the duration times of the respective steps in the two platforms a test of the signed posts of Wilcoxon and Statistica 10.0 software (TIBCO) was used.

3   Results

Figure 2 and Table 1 presents time duration the anticipatory period (Time_COP_1) and first step period (Time_COP_2) during of gait initiation, performed on the force and plantar pressure platforms.

Fig. 2 Time duration the periods during of gait initiation + Significant Wilcoxon test (p < 0.05)
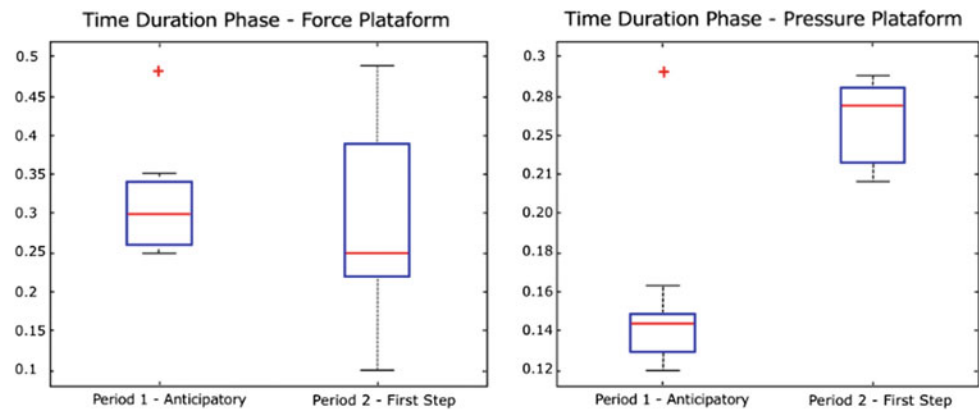
Table 1 Time duration the periods during of gait initiation

	Force platform	Pressure platform	P value
Time_COP_1 (s)	0.32 (±0.03)	0.14 (±0.02)	0.03*
Time_COP_2 (s)	0.28 (±0.10)	0.27 (±0.03)	0.07

Data are expressed as mean ± standard deviation
*Significant post Dunn's test (p < 0.05)

4 Discussion

The force platform and plantar pressure platform data are generally sampled at a frequency of 100 Hz per channel, satisfying the Nyquist criterion in which the minimum sampling frequency should be twice the natural frequency of the system, since in tasks like the quasi-static or static position most of the signal power is between 0.1 and 5.0 Hz [12, 17]. Thus, in this study, the AMTI double strength platform at the 100 Hz frequency was used and the Tekscan plantar pressure platform at 180 Hz with high sensor resolution per cm^2.

The different sampling frequencies presented by the two equipment's used did not affect the results in period 1 (anticipatory) and period 2 (execution of the first step), since the kinetic signals of the human movement are signals of low frequency and occupy mainly the six band [12, 18], so that a sampling frequency of 100 Hz is sufficient to sample the signal without any loss of information.

The duration of period 1 (anticipatory) presented statistically significant differences, where the execution in the plantar pressure platform presented a shorter duration when compared to the force platform (p = 0.003). This can be explained because there is still no apparent movement of the foot in the anticipatory phase. Since the plantar pressure platform presents high resolution in its sensors per cm^2 positioned in the plantar region, they are able to detect the execution time of this phase more quickly when compared to the platform force.

In the force platform, the instantaneous position of the COP is calculated considering the components of the ground reaction force, the moments around the anteroposterior or mediolateral axes, and the data on the actual origin of the force platform, as reported by the manufacturer, having considered that this origin does not always coincide with the geometric origin due to limitations in the manufacturing process [12]. On the other hand, in the plantar pressure platform the instantaneous position of the COP is calculated considering the maps of plantar pressures and the point of application resulting from the vertical force relative to the positioning of the feet on the platform [13].

Both platforms acquired similar duration for period 2 (Execution of the first step), therefore did not present statistically significant differences. This result suggests that when performing the first step the dynamic behavior of the COP presented in the execution time of this phase are similar in the two kinetic systems used, showing that although different information is used to obtain the same variable the behavior of the same showed similarity in both systems.

5 Conclusion

The phenomenon of anticipatory postural adjustments has been studied through the task of gait initiation in different populations, using a plantar pressure platform and force platform, thus presenting a methodological diversity, which does not affect the comparison between the results presented by these two equipment. Therefore, the understanding of the motor strategy during the execution of the anticipatory phase (period 1) the platform of plantar pressure showed more sensitivity for this variable where the duration of this phase was shorter in this equipment when compared with the force

platform. However, for the execution of the first step (period 2) the platforms did not show differences, presenting statistically the same duration for this phase. In spite of the methodological differences presented by these two platforms in the evaluation of the behavior of the cop during gait initiation, it is reliable to use any of both equipment, since they present similar results. Therefore, what should determine the use of each one would be availability, the movement analyzed and the studied population.

References

1. Halliday, S.E., Winter, D.A., Frank, J.S., Patla, A.E., Prince, F.: The initiation of gait in young, elderly, and Parkinson's disease subjects. Gait Posture **8**(8), 8–14 (1998)

2. Couillandre, A., Breniere, Y., Maton, B.: Is human gait initiation program affected by a reduction of the postural basis? Neurosci. Lett. **285**, 150–154 (2000)

3. Wolf, S.L., Barnhart, H.X., Kutner, N.G., McNeely, E., Coogler, C., Xu, T.: Reducing frailty and falls in older persons: an investigation of Tai Chi and computerized balance training. Atlanta FICSIT Group, Frailty and Injuries: Cooperative Studies of Intervention Techniques. J. Am. Geriatr. Soc. **44**, 489–497 (1996)

4. Jian, Y., Winter, D.A., Ishac, M.G., Gilchrist, L.: Trajectory of the body COG and COP during initiation and termination of gait. Gait Posture **1**, 9–22 (1993)

5. Sasaki, O., Asawa, S., Katsuno, S., Usami, S., Taguchi, K.: Gait initiation in bilateral vestibular loss. Auris Nasus Larynx **28**(4), 295–304 (2001)

6. Dibble, L.E., Nicholson, D.E., Shultz, B., Macwilliams, B.A., Marcus, R.L., Moncur, C.: Sensory cueing effects on maximal speed gait initiation in persons with Parkinson's disease and healthy elders. Gait Posture **19**, 215–225 (2004)

7. Jones, S.F., Twigg, P.C., Scally, A.J., Buckley, J.G.: The gait initiation process in unilateral lower-limb amputees when stepping up and stepping down to a new level. Clin. Biomech. **20**, 405–418 (2005)

8. Jacobs, J.V., Lou, J.S., Kraakevik, J.A., Horak, F.B.: The supplementary motor area contributes to the timing of the anticipatory postural adjustment during step initiation in participants with and without Parkinson's disease. Neuroscience **164**, 877–885 (2009)

9. Vrieling, A.H., van Keeken, H.G., Schoppen, T., Otten, E., Halbertsma, J.P.K., Hof, A.L., et al.: Gait initiation in lower limb amputees. Gait Posture **27**, 423–430 (2008)

10. Malouin, F., Richards, C.L.: Preparatory adjustments during gait initiation in 4–6-year-old children. Gait Posture **11**, 239–253 (2000)

11. Ledebt, A., Bril, B., Breniere, Y.: The build-up of anticipatory behaviour. An analysis of the development of gait initiation in children. Exper. Brain Res. (120), 9–17 (1998)

12. Winter, D.A.: Human balance posture control during standing walking. Gait Posture **3**, 193–214 (1995)

13. Orlin, M.N., McPoil, T.G.: Plantar pressure assessment. Phys. Ther. **80**, 399–409 (2000)

14. Crenna, P., Frigo, C.: A motor program for the initiation of forward-oriented movements in humans. J. Physiol. **437**, 635–653 (1991)

15. Hass, C.J., Buckley, T.A., Pitsikoulis, C., Barthelemy, E.J.: Progressive resistance training improves gait initiation in individuals with Parkinson's disease. Gait Posture **35**, 669–673 (2012)

16. Vieira, M.F., De Camargo Neves Sacco, I., Da Silva Azevedo Nora, F.G., Rosenbaum, D., Lobo Da Costa, P.H.: Footwear and foam surface alter gait initiation of typical subjects. PLoS ONE, **10** (8), 1–20 (2015)

17. Haykin, S.S., Van Veen, B.: Signals and Systems. Wiley (1998)

18. Winter, D.A.: A.B.C. (Anatomy, Biomechanics and Control) of Balance during Standing and Walking. Published by Waterloo Biomechanics (1995)

High-Frequency Transcranial Magnetic Stimulation Improves Motor Performance in Individuals with Incomplete Spinal Cord Injury

Amanda Vitória Lacerda de Araújo,
Valéria Ribeiro Nogueira Barbosa, Gilma Serra Galdino,
Felipe Fregni, Thais Massetti, Sara Lynn Fontes,
Danilo de Oliveira Silva, Talita Dias da Silva,
Carlos Bandeira de Mello Monteiro, James Tonks,
and Fernando Henrique Magalhães

Abstract

The aim of the present study was to investigate the effects of high-frequency rTMS on motor function in individuals with iSCI, so as to explore the clinical utility of rTMS in this population. This prospective trial enrolled 15 individuals who were at least six months post incomplete SCI (aged 18–60 years), recruited through referral by medical practitioners or therapists. The study design involved both rTMS-sham and rTMS-active protocols. The protocol included five sessions (one session daily) of high-frequency rTMS (5 Hz) over the bilateral lower limb motor area positioned at the primary motor cortex (M1). In the sham condition, the coil was disconnected from the rTMS device so as to ensure the interruption of the magnetic field. American Spinal Injury Association Impairment Scale (ASIA) motor scores were assessed at baseline (before intervention), after rTMS-sham and after rTMS-active, and the changes from baseline motor values provided by the ASIA score were used to assess the effects of both rTMS-sham and rTMS-active on the motor performance of individuals with iSCI. rTMS active was associated with significantly larger changes in ASIA motor scores as compared to rTMS-sham (T(1, 14) = 5,359, P < 0.001, ES = 0.67). We conclude that rTMS has produced positive results in improving participants' motor function, thereby indicating that rTMS might be used as an effective clinical tool in the rehabilitation of individuals with SCI.

A. V. L. de Araújo · T. Massetti · T. D. da Silva ·
C. B. de Mello Monteiro
School of Arts, Sciences and Humanities, EACH – USP,
University of São Paulo, São Paulo, Brazil

V. R. N. Barbosa · G. S. Galdino · F. H. Magalhães (✉)
Department of Physiotherapy – UEPB, Paraíba State University,
Campina Grande, Brazil
e-mail: fhmagalhaes@usp.br

F. Fregni
Harvard Medical School, Harvard Center for Noninvasive Brain
Stimulation, Boston, USA

S. L. Fontes
Faculty of Medicine, University of British Columbia, Vancouver,
Canada

D. de Oliveira Silva
Physical Therapy Program – UNESP, State University of São
Paulo, São Paulo, Brazil

J. Tonks
University of Exeter Medical School, Exeter, UK

J. Tonks
University of Lincoln, Lincoln, UK

J. Tonks
Haven Clinical Psychology Practice, Cornwall, UK

1 Introduction

Transcranial Magnetic Stimulation (rTMS) involves repetitively delivering biphasic magnetic pulses over a specific cortical site [1, 2] to provide stimulation of the corticospinal tract (CST), primary motor cortex (M1) and spinal cord, so as to induce neuronal reorganization, which can be largely involved in the control of voluntary movements [3]. In this vein, rTMS rehabilitation techniques have been found to be effective in enhancing neurological recovery thereby leading to improved functional abilities [4]. Therefore, rTMS is

emerging as a promising technique in improving neurophysiological outcomes and voluntary motor output in patients with sensorimotor disorders [5–7]. Indeed, studies indicate that motor improvements may be due to modification of corticospinal projections by increasing motor cortical excitability [8–10] and, consequently, promote plasticity associated with functional recovery [7].

Some studies have used rTMS as a noninvasive and painless method to induce long-lasting changes in the excitability of cortical and corticospinal pathways after incomplete spinal cord injury (iSCI). In this scenario, rTMS has been found effective in enhancing corticospinal synaptic transmission [11], reducing spasticity [8, 10, 12] and improving sensorimotor function after iSCI [8–10]. However, other studies report less positive findings, including unchanged sensorimotor function [13], as well as unaltered cortical excitability and level of spasticity [14] in response to rTMS. The lack of consistent results is likely associated with differences in stimulation parameters (e.g. intensity, frequency, number of pulses), number of sessions, relative location of M1, chronicity and levels of injury, and outcome measurements used in previous studies [3].

Therefore, the literature regarding the efficacy of rTMS on sensorimotor function of individuals with iSCI is inconsistent, as the few studies that have addressed this issue yielded contrasting results [3]. Thus, a new prospective study is necessary to provide evidence of the clinical utility of rTMS in individuals with iSCI. Due to the positive effects of rTMS in inducing long-lasting changes in spinal and supraspinal circuits, we hypothesized that rTMS applied over the lower limb motor area would improve motor function in individuals with iSCI. Therefore, our aim was to investigate the effects of high-frequency rTMS on motor function in individuals with iSCI.

2 Methods

2.1 Participants

Fifteen volunteers (all males, 35.3 ± 7.9 years, mean ± SD) with iSCI participated in this study. All participants were clinically diagnosed with iSCI of nonprogressive etiology, which is characterized by spinal, vascular and infectious trauma. Neuroimaging examinations, such as computed tomography and nuclear magnetic resonance were used to exclude spinal cord injuries due to progressive worsening conditions such as neurodegenerative, tumor and demyelinating pathologies. The participants were at least six months post-iSCI, clinically stable, aged between 18–60 years, and were receiving conventional physiotherapy (to a maximum of three times per week) at the time the study was performed. The experiments were conducted according

to the Declaration of Helsinki and all procedures were approved by the Ethical Committee of Paraíba State University, under the number CAEE: 18753713.0.0000.5187 (approved on June 22, 2013). Each participant signed an informed consent document prior to the experimental sessions.

2.2 rTMS

The rTMS was applied using Neurosoft—Neuro-MS 5 (Neurosoft Ltd®, Ivanovo, Russia), a commercially available transcranial magnetic stimulator equipped with an angulated figure-eight shaped coil (AFEC—01-100). rTMS was applied with an angulated figure-eight coil over the lower limb motor area localized in M1 (in order to stimulate both lower limbs), with the handle of the coil parallel to the interhemispheric midline (pointing occipitally), based on the vertex position of the International 10–20 system EEG. The vertex point (Cz) was chosen because the sensorimotor impairment of subjects with iSCI occurs bilaterally, although the degree of involvement varies from one side to the other. Therefore, both cortical sides were stimulated simultaneously, as the vertex point is equidistant between the left and right hemispheres. Standardized caps were used, in accordance with the International 10–20 system EEG to find the motor threshold of the abductor pollicis brevis, a point which corresponds to the motor area, and thus represents the point corresponding to Cz.

2.3 Procedures

The participants were positioned comfortably in either a normal chair or a wheelchair, depending on the level of motor commitment of each patient. The feet were positioned flat on the floor, and the hands rested on the thigh, in the supine position. Each session was held at the Neuromodulation Laboratory of the State University of Paraíba, using the same equipment during the same time of the day.

All participants attended rTMS interventions during two weeks: the first week with rTMS-sham (five sessions) and the second week with rTMS-active (five sessions), which were separated by one week of washout period. The same researcher administered both rTMS-sham and active interventions. The rTMS-sham was performed over five consecutive sessions per week (one session daily). In the sham condition, the coil was disconnected from the rTMS device so as to ensure the interruption of the magnetic field while appearing to be the same shape of the active coil [15]. In addition, the tactile contact of the coil with the skull was maintained. Similarly, the rTMS-active was performed over five consecutive sessions per week (one session daily), with

the stimulation intensity was set at 100% of the motor threshold of the area corresponding to the abductor pollicis brevis (defined as the lowest stimulation intensity that, within ten trials, induced at least five motor evoked potentials assessed on the first dorsal interosseous muscle of the dominant hand in the resting state). The stimulation target was the area associated with the bilateral lower limb motor area (i.e. vertex, Cz) of the M1. The parameters of rTMS were chosen based on safety parameters of the National Institute of Neurological Disorders and Stroke (NINDS). Each session consisted of 12 trains of 50 magnetic pulses at 5 Hz on each train (resulting in 10 s of stimulation for each train). A resting period of 10-s intervals between each train was applied.

2.4 Outcome Measures and Analyses

The International Standards for Neurological Classification of Spinal Cord Injury (ISNCSI) is a medical examination from which part of the American Spinal Injury Association Impairment Scale (ASIA) motor score is derived [16]. It uses a test of the strength of ten key muscles on each side of the body (e.g. elbow flexors, wrist extensors, hip flexors, quadriceps, dorsiflexors). The score ranges from 0 (no contraction) to 5 (normal resistance) through a full range of motion. A total possible score of 50 for the upper extremities (UE) and 50 for the lower extremities (LE) may be obtained [16]. Therefore, the ASIA (motor score) was used to evaluate the motor effects of the high-frequency rTMS. More specifically, the ASIA (motor score) was assessed at baseline (before intervention), after rTMS-sham and after rTMS-active, and the changes from baseline motor values provided by the ASIA score (i.e. data were normalized by subtracting the baseline value) were used to assess the effects of both rTMS-sham and rTMS-active on the motor performance of individuals with iSCI.

The normality and homogeneity of the data was assumed after tested with the Shapiro-Wilk and Levene's test, respectively. Therefore, changes from baseline motor values provided by the ASIA score were compared between rTMS-sham and rTMS-active using a t-test for repeated measures. Effect size (ES, also known as "strength of association") was calculated using the eta-squared indices. ES was considered large if >0.14 [17].
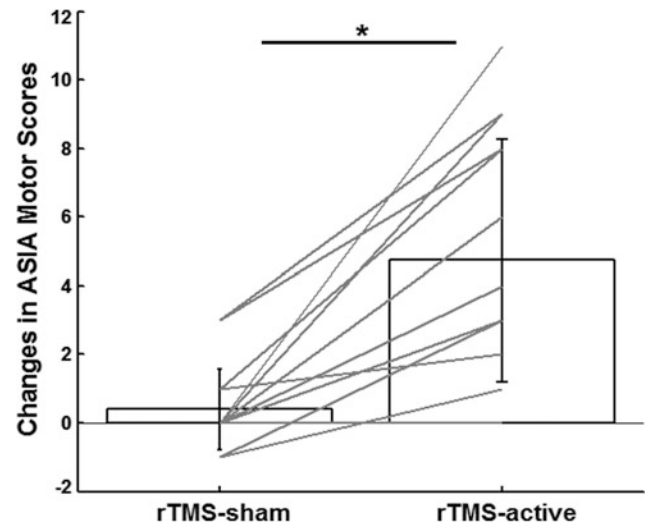
Fig. 1 Changes in ASIA motor scores (with respect to the baseline), for rTMS-sham and rTMS-active conditions. Bars depict mean and standard deviation (n = 15), while gray lines depict individual values. *Indicates statistically significant differences (P < 0.001) between rTMS-sham and rTMS-active conditions

3 Results

Figure 1 depicts the mean ± standard deviation (bars and error bars) and individual values (gray lines) of changes in ASIA motor scores (from baseline) for rTMS-sham and rTMS-active conditions. There was a statistically significant difference (T(1, 14) = 5,359, P < 0.001, ES = 0.67) between conditions, indicating that rTMS active was associated with larger changes from ASIA baseline as compared to rTMS-sham.

4 Discussion

Subjects with iSCI show clinical symptoms which are associated with reduced quality of life and functional independence. The CNS may be able to recover naturally after injury due to plasticity mechanisms and reorganization of residual neural pathways [18]. However, natural recovery is limited and cannot be relied upon [19]. Therefore, it is plausible that rTMS represents an emerging rehabilitation technique to improve sensorimotor performance in individuals with iSCI. The present results confirms our hypotheses, as rTMS-active was associated with larger changes in ASIA motor scores (from baseline) as compared to rTMS-sham, thereby indicating that rTMS was effective in improving motor performance of participants with iSCI.

High-frequency rTMS has emerged as a promising technique in stimulating neural reorganization and synaptic plasticity in cortical and subcortical networks, thereby affecting the descending control of spinal excitability [5, 8, 11, 20, 21]. These mechanisms might accelerate the development of neural connectivity responsible for sensorimotor function improvement [7, 8, 11, 13, 22]. Although an adaptive reorganization involves the formation of new connections and restoration of pre-existing connections, studies that directly address quantitative parameters associated with neuronal repair are limited. This is because most of the outcome measures are not able to assess the neurophysiological substrates that directly contribute to functional recovery, such as specific mechanisms within the brain and spinal cord that influence the generation of the motor command to the affected limbs [22].

In considering three particular studies that have examined the effects of rTMS in individuals with iSCI, interesting results may be pointed out from a functional performance perspective. Belci et al. [9] delivered double pulses of rTMS over the M1 representation of thenar muscles (360 10-Hz doublets, with 10 s between each doublet and stimulus intensity corresponding to 90% of resting motor threshold) for five days in a group of four subjects with iSCI. Results indicated that active rTMS improved somatosensory and motor function at three weeks following stimulation, as assessed by the ASIA, 9-hole peg test and electrical perceptual threshold measurements. Additionally, Benito et al. [8] applied fifteen sessions of sham or rTMS over the leg representation of M1 (20 trains of 40 pulses at 20 Hz with an intensity of 90% of resting motor threshold) in 17 individuals with iSCI. This study found significant improvements in motor function for at least two weeks, as assessed by the ASIA scale for lower limbs and gait function. Contrary to the findings noted above, ASIA scores were unaltered in Kuppuswamy et al. [13]. The protocol had five days of active or sham rTMS (900 pulses at 5 Hz in 2 s trains separated by 80-s intervals, at 80% of active motor threshold) applied to M1 representations of either the hand or forearm muscles in 15 individuals with iSCI. Therefore, the present study provides additional clinical evidence of the potential benefits of high-frequency rTMS applied to the lower limb motor area to improve sensorimotor recovery in patients with iSCI, thereby indicating that rTMS might be used as a clinical tool in the rehabilitation of individuals with SCI.

## 5	Conclusion

The present study found consistent changes in motor function (as measured by ASIA motor scores) in individuals with iSCI after rTMS (as indicated by significant differences between rTMS-sham and rTMS-active conditions). Therefore, rTMS might be used as an effective tool in sensorimotor rehabilitation of individuals with SCI.

References

1. Kobayashi, M., Pascual-Leone, A.: Transcranial magnetic stimulation in neurology. Lancet Neurol. **2**(3), 145–156 (2003)
2. Rossi, S., Hallett, M., Rossini, P.M., et al.: Safety, ethical considerations, and application guidelines for the use of transcranial magnetic stimulation in clinical practice and research. Clin. Neurophysiol. **120**(12), 2008–2039 (2009)
3. Tazoe, T., Perez, M.A.: Effects of repetitive transcranial magnetic stimulation on recovery of function after spinal cord injury. Arch. Phys. Med. Rehabil. **96**(4 Suppl), S145–S155 (2015)
4. Oudega, M., Perez, M.A.: Corticospinal reorganization after spinal cord injury. J. Physiol. **590**(16), 3647–3663 (2012)
5. Ridding, M.C., Rothwell, J.C.: Is there a future for therapeutic use of transcranial magnetic stimulation? Nat. Rev. **8**(7), 559–567 (2007)
6. Ridding, M.C., Ziemann, U.: Determinants of the induction of cortical plasticity by non-invasive brain stimulation in healthy subjects. J. Physiol. **588**(Pt 13), 2291–2304 (2010)
7. Ellaway, P.H., Vasquez, N., Craggs, M.: Induction of central nervous system plasticity by repetitive transcranial magnetic stimulation to promote sensorimotor recovery in incomplete spinal cord injury. Front Integr. Neurosci. **8**(42) (2014)
8. Benito, J., Kumru, H., Murillo, N., et al.: Motor and gait improvement in patients with incomplete spinal cord injury induced by high-frequency repetitive transcranial magnetic stimulation. Top. Spinal Cord Inj. Rehabil. **18**(2), 106–112 (2012)
9. Belci, M., Catley, M., Husain, M., et al.: Magnetic brain stimulation can improve clinical outcome in incomplete spinal cord injured patients. Spinal Cord **42**(7), 417–419 (2004)
10. Kumru, H., Murillo, N., Samso, J.V., et al.: Reduction of spasticity with repetitive transcranial magnetic stimulation in patients with spinal cord injury. Neurorehabil. Neural Repair **24**(5), 435–441 (2010)
11. Bunday, K.L., Perez, M.A.: Motor recovery after spinal cord injury enhanced by strengthening corticospinal synaptic transmission. Curr. Biol. **22**(24), 2355–2361 (2012)
12. Nardone, R., Holler, Y., Thomschewski, A., et al.: rTMS modulates reciprocal inhibition in patients with traumatic spinal cord injury. Spinal Cord **52**(11), 831–835 (2014)
13. Kuppuswamy, A., Balasubramaniam, A.V., Maksimovic, R., et al.: Action of 5 Hz repetitive transcranial magnetic stimulation on sensory, motor and autonomic function in human spinal cord injury. Clin. Neurophysiol. **122**(12), 2452–2461 (2011)

14. Kumru, H., Benito-Penalva, J., Valls-Sole, J., et al.: Placebo-controlled study of rTMS combined with Lokomat((R)) gait training for treatment in subjects with motor incomplete spinal cord injury. Exper. Brain Res. (Experimentelle Hirnforschung) 234 (12), 3447–3455 (2016)

15. Duecker, F., Sack, A.T.: Rethinking the role of sham TMS. Front Psychol. 6(210) (2015)

16. Kirshblum, S.C., Burns, S.P., Biering-Sorensen, F., et al.: International standards for neurological classification of spinal cord injury (revised 2011). J. Spinal Cord Med. 34(6), 535–546 (2011)

17. Cohen, J.: Statistical Power Analysis for the Behavioral Sciences. Lawerence Erlbaum Associates, Hillsdale, NJ (1988)

18. Raineteau, O., Schwab, M.E.: Plasticity of motor systems after incomplete spinal cord injury. Nat. Rev. 2(4), 263–273 (2001)

19. Fawcett, J.W., Curt, A., Steeves, J.D., et al.: Guidelines for the conduct of clinical trials for spinal cord injury as developed by the ICCP panel: spontaneous recovery after spinal cord injury and statistical power needed for therapeutic clinical trials. Spinal Cord 45(3), 190–205 (2007)

20. Lefaucheur, J.P., Andre-Obadia, N., Antal, A., et al.: Evidence-based guidelines on the therapeutic use of repetitive transcranial magnetic stimulation (rTMS). Clin. Neurophysiol. 125 (11), 2150–2206 (2014)

21. Valero-Cabre, A., Oliveri, M., Gangitano, M., et al.: Modulation of spinal cord excitability by subthreshold repetitive transcranial magnetic stimulation of the primary motor cortex in humans. NeuroReport 12(17), 3845–3848 (2001)

22. Potter-Baker, K.A., Janini, D.P., Frost, F.S., et al.: Reliability of TMS metrics in patients with chronic incomplete spinal cord injury. Spinal Cord 54(11), 980–990 (2016)

Human Gait Assessment Using the Qualisys Track Manager (QTM): Determining the Points of the Reflective Markers

Gabriela Oliveira, Gilmar Lucena, Walter Calheiros, Roberto Lima, Lourdes Brasil, and Vera Marães

Abstract

Amputation is defined as the loss of part of an individual's limb. Its high incidence makes that the researches and search for the improvement of the devices that help it during the accomplishment of the activities of daily life can be each day more improved. Therefore, the aim of the research is to determine the best placement of reflexive markers on the individual's skin. The research method was supported by Qualisys Track Manager (QTM) along with the support of several other software that aided in analyzing the data (Anaconda, Juper, Open Gait Analytics). This protocol was thought and referenced by authors who were dedicated to understanding the best points of reflexive markers in the patient's body, where these authors studied the important anatomical points for the collection and better capture of the images. The sites of placement of the markers determined after due analysis of the studies of these authors were in the hip, thigh, knee, leg, and ankle. The protocol was tested and validated by the researchers and in this way was continued in the analysis. The result evidenced the angles found during the process of ambulation of the individual. It is hoped that with this research it will be possible to complete all the proposed objectives so that in the end one can propose improvements in the quality of life of the amputees.

Keywords

Gait analysis • QTM • Markers

G. Oliveira · G. Lucena (✉) · W. Calheiros · R. Lima · L. Brasil · V. Marães
University of Brasília, Gama, DF, Brazil
e-mail: gilmarlucena@gmail.com

G. Oliveira
e-mail: gabiataides@hotmail.com

1 Introduction

Amputations of limbs are practices performed long ago, perhaps being the oldest surgeries performed in the history of medicine [1].

1.1 Concept and Types of Lower Member Amputations

The word amputation is derived from Latin and has the following meaning: *ambi* = around/around and *putation* = prune/withdraw. It is possible to define amputation as the total or partial withdrawal of a limb through a surgical procedure [1, 2].

Transfemoral amputation is performed between knee and hip disarticulation, and can be divided into three sub-levels, that is, in the proximal, middle and distal third. This level of amputation can be caused by vascular pathologies, traumatic, infectious and neoplastic processes or by congenital anomalies [1]. Although this level of amputation is relatively common, the patient who lives with the loss of a limb at the transfemoral level faces several challenges, such as the demands to increase energy, problems of balance and stability [3].

Transtibial amputation, on the other hand, occurs in the leg region and is the very frequent amputation level in relation to transfemoral amputation. The fact of preserving the knee joint will bring many benefits for rehabilitation and a good future for the individual [4].

Because of this, one of the focuses of rehabilitation of an amputated patient is the improvement of the phases of the independent and functional gait. For this purpose, prostheses are used to achieve this goal and reduce functional losses as much as possible. The focus is on orthostatism and the ability to wander with the use of prostheses and sockets [5, 6]. Studies of the movement analysis of a patient using a prosthesis aim to elucidate the mechanisms of movement

control and strategies, as well as to analyze the behavior of the prosthesis and socket reaction forces in relation to the ground [7].

1.2 Analysis of Gait

The analysis of gait is one of the main points of the physiotherapeutic evaluation to identify the kinetic and kinematic alterations of an individual [8]. It provides information on the mechanics of the musculoskeletal system during the execution of motor tasks, on the joints, the forces exchanged with the environment, the loads transmitted through the body segments or through individual body tissues (muscles, tendons, fascias) and the muscular work [9].

In order to evaluate the function of both the muscles and joints involved in the movement of the body, it is necessary to also involve the clinical and physiological context of the individual in order to analyze the forces that are transmitted by all the structures involved. of the muscle and its position and instant orientation in a three-dimensional (3D) view [10].

1.3 Data Acquisition Equipment

A camcorder-based method with the aid of Qualisys Track Manager 1.6.0.x (QTM), which calculates the position of each mark in three dimensions, can be used to capture the walking signals. Some authors like [11] elucidate the advantages of the system of optical cameras that use surface markers to obtain the capture of the movement. This method allows the visualization of the spatial position of the markers, and only then can the velocities, accelerations, angles and angular velocities be calculated during the gait cycle [12].

In order for the gait analysis to occur with the equipment mentioned above, it is necessary to determine the points where the reflexive markers will be coupled in the body of the individual. In the literature there is much controversy about the anatomical points that are used to perform the QTM collection and some scholars do not use a standard model for these collections. However, some authors make a study about this subject and find specific points of coupling of the markers and justify their motive. Based on these authors, the protocol was developed.

The anatomical points are located in the pelvis, thigh, leg and foot. They are easy to locate and this is done by inspecting and palpating the site based on the information presented by [13, 14]. The importance of the ideal location of these points occurs when the researcher is to analyze the articular axes and to make a realistic graphical representation of the bones. In addition, with the use of the ideal [10], the

angles presented during the entire displacement of the individual and if this movement presents a value that fits the parameters of normality already elucidated in the reflexive markers, the investigator can calculate and estimate the linear displacement of the joints [9]. In addition to QTM, there are other ways of analyzing gait in amputated and non-amputated patients and the present article aims to verify this analysis and identify the main points of reflexive markers that are used by researchers to analyze gait.

2 Materials and Methods

This is an experimental study carried out at the University of Brasília—UnB, in the Laboratory of Movement Analysis and Signal Processing located at the Center of High School 04 of Ceilândia—DF. The research is linked to the Faculty of Ceilândia, UnB's (FCE) campus in the satellite cities of Brasília.

2.1 Data Acquisition

It has been approved by the Ethics Committee of the Faculty of Health Sciences of the University of Brasília and is registered in opinion number: 1446986/16. In order to carry out the collections in each individual, all of them must sign the Free and Informed Consent Term (TCLE).

Inclusion criteria that was used for research was individual with transfemoral or transtibial unilateral amputation, aged between 20 and 50 years and accustomed to the use of a prosthesis. Exclusion factors were considered as individual with musculoskeletal problems that would make data collection unfeasible; associated metabolic changes, such as diabetes, rheumatoid arthritis, and others that made it impossible to attend the research site and contribute to data collection.

2.2 Preparation for Data Acquisition

The equipment used is the Qualisys Track Manager (QTM) which contains a software responsible for capturing the images and signals that indicate the movement and angulation acquired by the joints during the whole movement of the body. Then the markers are placed in the individual. The sites where the markers will be coupled: Foot (Calcaneus, 1st metatarsus and 5th metatarsus), Leg (medial portion of the fibula, fibula head, lateral fibula malleolus and medial malleolus of the tibia), Knee (medial portion and lateral portion), Femur (proximal portion of the femur, major trochanter), Hip (EIAS, EIPS), Column (Penultimate lumbar vertebra).

Fig. 1 Placement of reflexive markers Source of authors

Reflexive markers are the instruments used to capture the QTM signal and to identify the gait during the individual's ambulation. The places where the markers are placed should be specific and may subsequently provide data for analysis and formation of the angles that identify the movement of the lower limb.

For the collection of data and verification of the anatomical points previously identified in the articles by [10, 14–16] it was necessary to perform an inspection and palpation of the sites where the anatomical points are sought to place the markers and perform their placement. The markers were secured with a double-sided adhesive tape.

For the collection the individual used bathing suits, according to Fig. 1, which allowed that the visualization of the member and placement of the markers occurred in a more reliable way to the one proposed by the mentioned authors. It is important to point out that always at the beginning of the collection the placement of the markers was done systematically by the same person in order to reduce the variability of their location among the individuals of the research.

We used 08 Oqus MRI cameras that will capture the movement of the markers coupled to the subject's skin and, in addition, will be filmed through a specific camera, called Oqus Video, which will record the whole walking process. Figure 2 illustrates the location where the data was collected.

The second step was to instruct the volunteer to walk barefoot at a predetermined speed and to be comfortable for him and enable him to perform his usual gait with speed and cadence used daily [17]. This will happen on a wooden platform of rubber and approximately 2.5 m. It was also guided a period of practice for the individual to become familiar with the environment and walk as natural as

Fig. 2 Laboratory of analysis of gait and signal processing—FCE Source of authors

possible. At the sign of the researcher, the individual will begin to wander without interruption during the five laps, which corresponds to 1 min approximately.

2.3 Experimental Design

The collected data were stored in MatLab and later analyzed to find the angles and axes that will illustrate the gait process of the individual.

After the data collection will be done the statistical treatment of the same. A descriptive analysis of the collected data was carried out, evidencing mainly the standard deviation and the variance. The collection was performed three times and all these data were reported in the descriptive table. After the three collections, data from the best collection were considered for the results.

2.4 Results

The protocol has already been defined and according to the results found and after analysis it will be necessary to better define the marker points initially stipulated in the protocol and better reposition the cameras so that the next collections

occur with the least possible noise. The delimitations found were the following: positioning of the cameras and the markers. It is expected that changes in this point of the methodology will imply in an improvement of the protocol for the continuation of data collection and analysis of gait data. Figures 3, 4, 5, 6 and 7 show data acquisition of the knee where it can be observed much noise in the signal and failures in the processing of the same ones. Some signs have already been satisfactory, such as in the metatarsus, calcaneus, but it was not possible to analyze more than one pass, which would also make it impossible to proceed with the protocol (Figs. 3, 4, 5, 6 and 7 generated after using Open Gait Analytics software).

You can see changes in plotted graphs. The records present distortions and noise, and the authors have identified some problems that involve the reasons for the noises occurring. One of them is the proximity of the markers that causes the signals to have interferences between the points collected; poorly positioned cameras that do not capture the markers on the subject's body; blockage of the signal due to the positioning of the marker in front of the marker (it may be the individual's own body or even the walking aid instrument such as the walking stick).

According to [12] a noise is an event that disturbs the correct transmission of the messages and information that

Fig. 3 Progression of the fifth metatarsal left and right head with percent of gait cycle
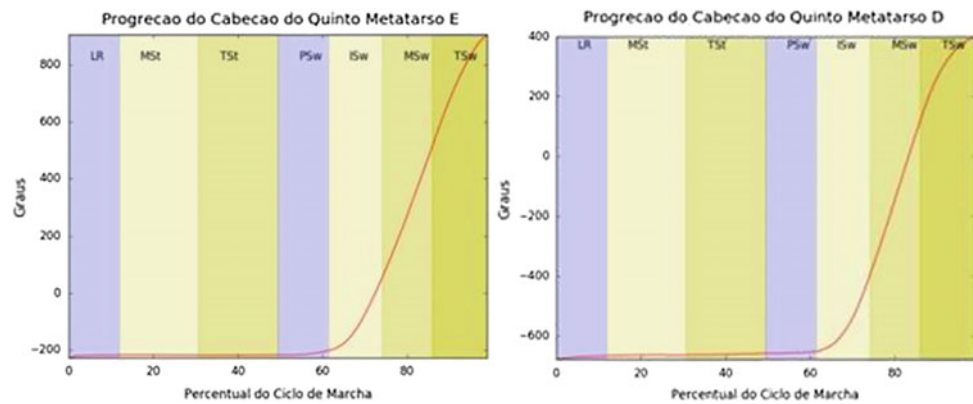
Fig. 4 Angles of the left knee with percentage of the gait cycle
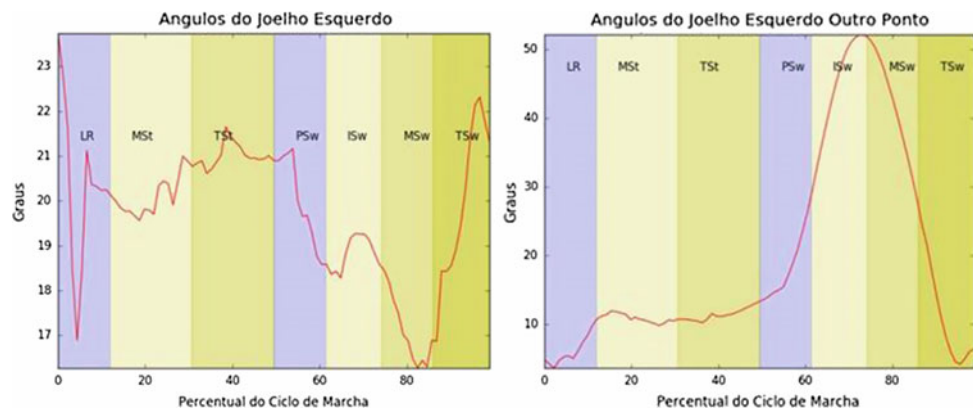
Fig. 5 Angles of the right knee with percentage of the gait cycle
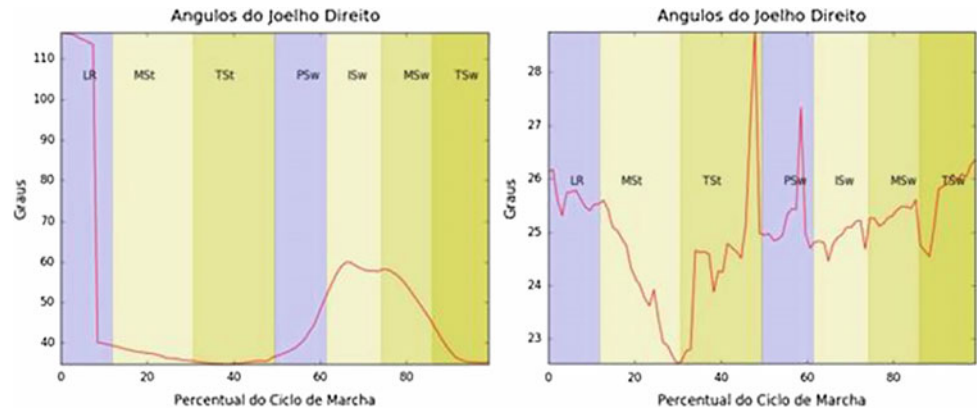
Fig. 6 Head of the fifth left and right metatarsal
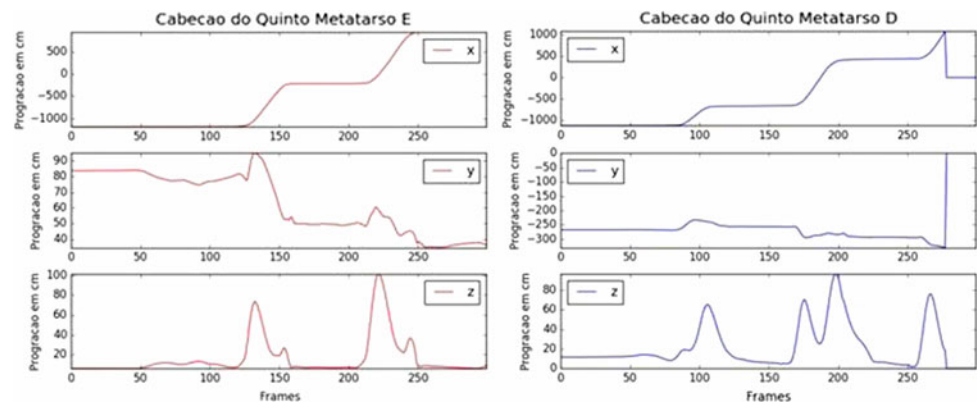
Fig. 7 Head first metatarsal right and left
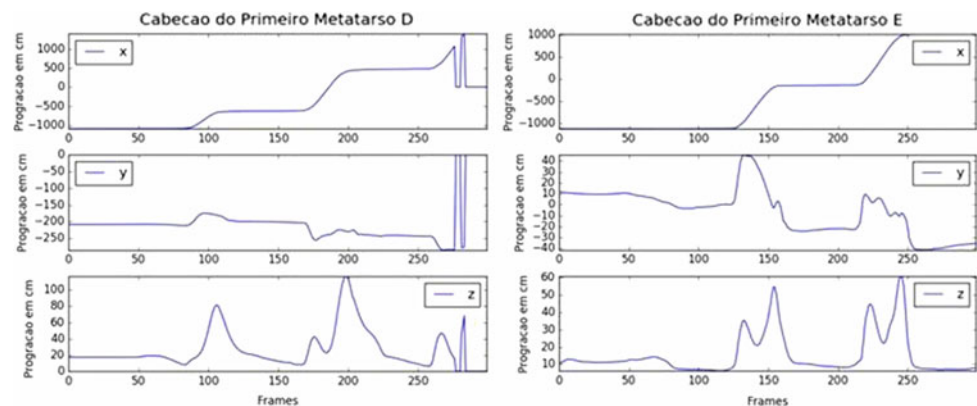
need to be transmitted and the researchers need to eliminate to the maximum to obtain a good result in the collection. The signals receive some classifications, being able to be of the thermal type, induced, impulsive crosstalk. Noises are caused by external or internal factors. And external factors are those that most need to be avoided and eliminated to the maximum. In this way, avoid the transmission of lost signals and information.

In this way, for [18–20], the objective of the gait analysis is to relate in a database information that can characterize the human gait and with the aid of statistical tools all this is possible. The consequence is the definition and standardization of the various types of human march through the aid of these statistical tools and the inclusion of their own spaces, spatio-temporal information, time series and silhouettes during gait analysis.

3 Conclusion

Determining the points where the reflexive markers will be coupled for use in the collection of gait analysis was the initial proposal of the article. After the research in pioneering studies and references that clearly and lucidly showed the anatomical aspects and the positioning of each point it was possible to reproduce which was as-simulated from the articles researched as a basis, to create and adapt to a protocol idealized by the authors of the research.

The study became feasible and ideal for future collections and analyzes that will encourage researchers of these articles. Many others to work on this protocol and analyze not only the human gait, but several other movements performed by the lower limbs, such as sports gesture. The study was also positive so that future researchers who are interested in identifying the ideal points of the MMSS can use the same theoretical framework and the analyzes used in this study.

Conflict of Interests The authors declare that there is no conflict of interests with this paper.

References

1. Carvalho, A.: Amputações de membros inferiores: em busca da plena reabilitação. Manole, São Paulo (2003)
2. Barbosa, M.P.: Amputação transfemoral e desarticulação do joelho. In: Pedrinelli, A. (eds.) Tratamento do paciente com Amputação, Chap. 14, pp. 113–119. São Paulo, Roca (2004)
3. Teixeira, M.F.: A atuação da fisioterapia no paciente com amputação transfemoral unilateral. Trabalho de conclusão de curso, Rio de Janeiro (2008)
4. Matsumura, A.D., Resende, J.M., Chamilian, T.R.: Avaliação pré e pós protética da circumetria dos cotos de amputados transtibiais. Acta Fisiátrica **20**(04) (2013)
5. Blumentritt, S., Schmalz, T., Jarasch, R.: Significance of static prosthesis alignment for standing and walking of patients with lower limb amputation. Orthopade **30**(3), 161–168 (2001)
6. Culham, E.G., Peat, M., Newell, E.: Below-knee amputation: a comparison of the effect of the SACH foot and single axis foot on electromyographic patterns during locomotion. Prosthet. Orthot. Int. **10**(1), 15–22 (1986)
7. Soares, A.S.O.C., Serrão, J.C., Amadio, A.C.: Características eletromiográficas e dinâmicas da marcha de amputados transtibiais com a utilização de calçados esportivos. Braz. J. Biomech. **4**(1), 55–61 (2003)
8. Toro, B., Nester, C.J., Farren, P.C.: The status of gait assessment among physiotherapists in the United Kingdom. Arch. Phys. Med. Rehabil. **84**, 1878–1884 (2003)
9. Capozzo, A., La Croce, U., Leardini, A., Chiari, L.: Human movement analysis using stereophotogrammetry: Part 1: theoretical background. Gait Posture **21**(2), 186–196 (2005)
10. Capozzo, A., Catani, F., Croce, U., Leardini, A.: Position and orientation in space of bones during movement: anatomical frame definition and determination. Clin. Biomech. **10**(4), 171–178 (1995)
11. Grip, H., Hager, C.: A new approach to measure functional stability of the knee based on changes in knee axis orientation. J. Biomech. **46**(5), 855–862 (2013)
12. Lima, R.A.: Implementando um software como serviço para análise e simulação de marcha humana. Dissertação de mestrado. Universidade de Brasília – UnB. Brasília (2015)
13. Hoppenfeld, S.: Physical Examination of the Spine and Extremities. Appleton Century Crofts, East Norwalk, CT, USA (1976)
14. Benedetti M.G., Cappozzo A., Catani F., Leardini, A.: Anatomical Landmark Definition and Identification. CAMARC II Internal Report (1994)
15. Collins, T.D., Ghoussayni, S.N., Ewins, D.J., Kent, J.A.: A six degrees-of freedom marker set for gait analysis: repeatability and comparison with a modified Helen Hayes set. Gait Posture **30**, 173–180 (2009)
16. Kadaba, M.P., Ramakrishnan, H.K., Wootten, M.E.: Measurement of lower extremity kinematics during level walking. J. Orthop. Res. Raven Press, Ltd., New York, 8383–8392 (1990)
17. Hubley-Kozey, C.L., Deluzio, K.J., Landry, S.C., Mcnutt, J.S., Stanish, W.D.: Neuromuscular alterations during walking in persons with moderate knee osteoarthritis. J. Electromyogr. Kinesiol. (2005)
18. Mafra, N.R.: Processamento de Sinal na Avaliação Clínica da Marcha Humana. Faculdade de Engenharia da Universidade do Porto, Dissertação de Mestrado (2012)
19. Carvalho, J.A.: Avaliação funcional dos pacientes amputados. Amputações de membros inferiores: em busca da plena reabilitação, 2nd ed, Chap. 10. pp. 143–164. São Paulo, Manole (2003)
20. Benedetti, M.G., Catani, F., Leardini, A., Pignotti, E., Giannini, S.: Data management in gait analysis for clinical applications. Clin. Biornech. **13**(3), 204–215, 1008 (1998)

Human Gait Cycle Analysis Using an Adapted Mechanical Prosthesis

C. R. L. Moraes , E. M. Aragão Junior, R. J. R. S. Lucena ,
É. L. Cavalcanti , and M. A. B. Rodrigues

Abstract

The knee is a joint that acts in the process of locomotion of the human being. When a person, for some reason, loses this joint starts a slow and expensive process of rehabilitation for the reintegration of this person in society. With this mindset, this project aimed to compare normal gait and gait using an adapted mechanical knee prosthesis, in order to list parameters that in the future a dynamic control system can be used to act on a low cost knee prosthesis, capable of facilitating the process of rehabilitation, making it less traumatic. The tests were performed in healthy people using a device that had two accelerometers and two channels of electromyographic signal acquisition. After the tests, the data were analyzed and the following conclusions were observed: (a) gait with the prosthesis has a higher balance phase and is tiring and slow when compared to normal gait, and (b) there is the possibility of development of a control system for electronic knee prostheses using inertial sensors and electromyography only.

Keywords

Mechanical prosthesis • Accelerometry •
Electromyography

1 Introduction

The knee is one of the joints of the human body most important for performing the movement, allowing humans to move at small distances. When a person loses this joint, being amputated or for congenital defect, in addition to being a traumatic situation physically and mentally is also the beginning of a cycle of adaptations, which will require

patient willpower, patience, dedication and above all a multiprofessional qualified team to follow this process.

The Brazilian Institute of Geography and Statistics (IBGE) reported in its 2010 Census report that about 23.92% of the Brazilian population has at least one type of disability (auditory, visual, motor or intellectual), and that among those 29.09% has a motor deficiency. Still according to the Census, in the state of Pernambuco, little more than 22% of its resident population has some degree of motor deficiency [1]. However the IBGE does not report how much of these motor deficiencies are due to amputation, nor the level of these amputations. Thus the data on this subject are imprecise and only estimated in the literature.

It is estimated by the literature that 85% of the amputations are lower limbs [2]. Of these, approximately 80% of amputations occur due to vascular diseases and/or diabetes. The second major cause of amputation occurs due to trauma (20% of amputations, with 75% of these occurring with men), being the main reasons automobile accidents and wounds of gunshot [3].

Considering the difficulties faced by people who do not have the knee joint, such as the reduction of mobility in space, this study intends to compare the normal gait with gait using an adapted knee mechanical prosthesis 3R15 Ottobock. The purpose of this comparison is that from this information can be developed a control system for an electronic knee prosthesis. In the data collection, we used inertial sensors and an equipment of acquisition of electromyography (EMG).

1.1 Analysis of the Gait Cycle

The gait is considered normal when a person can perform a sequence of synchronized movements of the lower limbs that in turn moves the body forward without losing the stable posture. This process is commonly called gait cycle, being divided in the stance phase, 60% of the cycle, and the swing phase, 40% of the cycle (Fig. 1) [4–6].

C. R. L. Moraes (✉) · E. M. Aragão Junior · R. J. R. S. Lucena ·
É. L. Cavalcanti · M. A. B. Rodrigues
Federal University of Pernambuco (UFPE), Recife, PE, Brazil
e-mail: cici2116@gmail.com
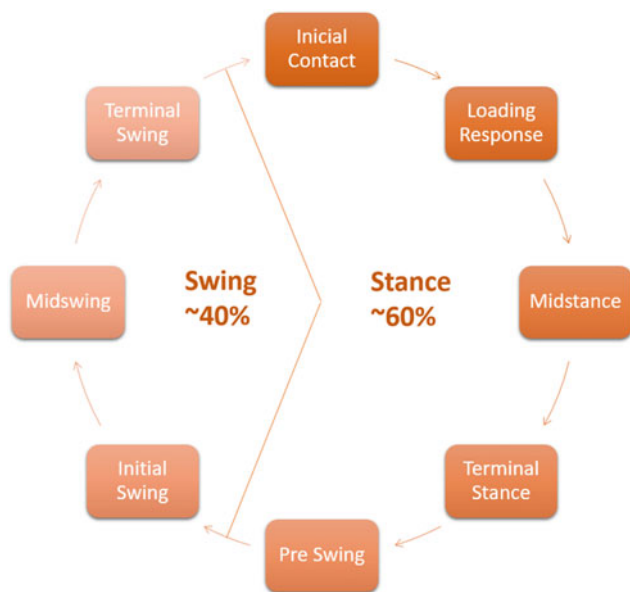
Fig. 1 Phases of gait observing [4]

Fig. 2 Components of the adapted mechanical prosthesis. Adapted fitting in L shape, fastened to the user by Velcro straps, mechanical knee 3R15, Ottobock adapter tube and Ottobock SACH foot

The stance phase corresponds to the period during which the foot is in contact with the ground. This phase is divided into five subphases: initial contact, load response, midstance, terminal stance and pre-swing. The swing phase represents the remainder of the cycle and refers to the period when the foot is raised above the surface. This phase is divided into three sub-phases: initial swing, midswing and terminal swing. The precise duration of these intervals varies with the individual's walking speed [5, 6].

2 Materials and Methods

The study was carried out in the Post-Graduate Program in Electrical Engineering in conjunction with the Post-Graduation in Biomedical Engineering of the Federal University of Pernambuco—UFPE. The following equipment and software are used: Microsoft Kinect, notebook, adapted socket, 3R15 knee mechanical prosthesis and Ottobock SACH foot, equipment developed by GPEB/UFPE, silver chloride surface electrode with saline gel and Reability software for analysis of the data.

As it is a study for the development of a prototype that in this first moment will not be used volunteers with amputations above the knee but the researchers themselves, being used the Ethics Committee with CAAE 2,695,690. Later, when the process is already consolidated and does not present any type of risk to the patient will be used amputated patients, which is not scope of this work.

In order to solve the problem of the lack of amputated individuals, the prosthesis received an adapted socket (Fig. 2), thus enabling the use by the researchers.

The GPEB/UFPE developed equipment consists of two inertial sensors model MPU-6050, an EMG acquisition sensor, a bluetooth HC-05, a microcontroller with low power consumption MSP430G2553, a battery charging system and a 9 V battery (Fig. 3) [7]. Currently this device supports up to four EMG channels and two inertial sensors. However, in this work, only one EMG channel and two inertial sensors were used, since it is intended to use the minimum of sensors, in order to obtain the lowest possible cost.

For the data analysis, the software Reability was developed, developed by GPEB/UFPE. This interface is intuitive and easy to use (Fig. 4). This software allows the real-time visualization of the signals and the possibility of recording and saving the data in the computer for later analysis, together with the video during acquisition [7].

Like Cavalcante et al. [7], it was decided to use Microsoft Kinect in the acquisition of images, since it is an equipment capable of detecting when a person exists in their field of action and of identifying when there is a movement. The synchronization of the video is done automatically with the acquisition of the data and the identification of the gait phases was performed with the aid of a physiotherapist.

The signs were acquired in the laboratory, first without the use of the adapted prosthesis and then with it. The purpose of these tests is to analyze the walk, with and without prosthesis. The protocol was based on the individual walking by nine meters, aiming to enter into a cyclical regime, and recording is only done during the last three meters. This exercise was repeated three times without the prosthesis and three times with the prosthesis.

Before the beginning of the tests, there was more than 40-h training with the adapted prothesis, assisted by
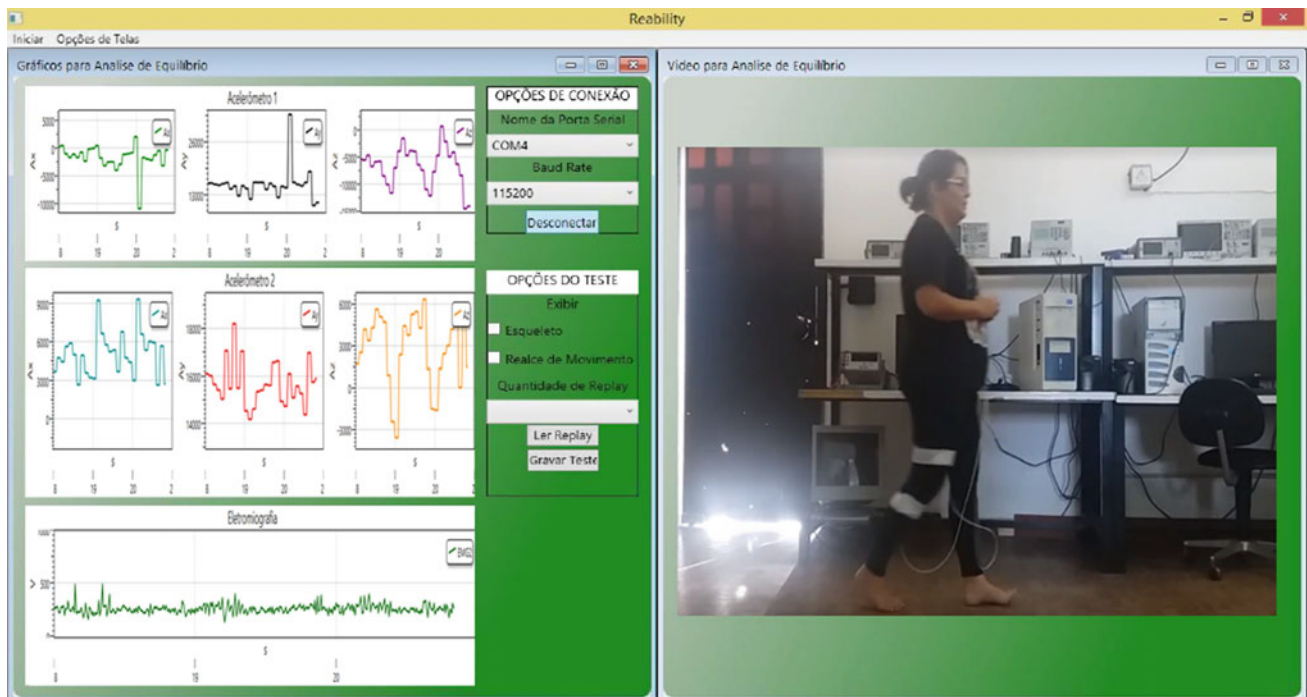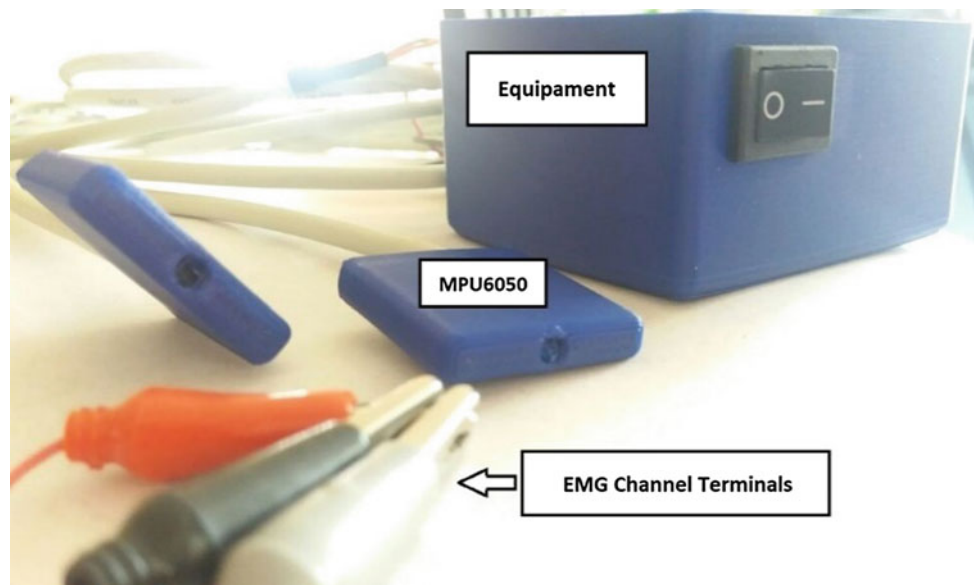
Fig. 4 Platform Reability. On the left side the graphs are visualized. In the first row the graphs of the first accelerometer are shown, in the second line the graphs of the second accelerometer and in the third row the graph of the electromyography; and on the right side the video

physiotherapists at the AACD (Association of Assistance to the Disabled Child), in Recife-PE, as the amputee needs to train during the rehabilitation, researchers need to relearn to walk, understanding their difficulties and limitations imposed due to lack of a member.

The position of the electrodes followed the SENIAM (Surface Eletromiograph for the Non-Invasive Assessment of Muscles) protocol for the lateral quadriceps femoris muscle of the left leg located in the anterior region of the thigh and the accelerometers were positioned in the right leg

with the X axis facing for horizontal with positive direction to the right side, vertical Y axis with positive upward direction and Z axis facing the user. Accelerometer 1 should be centralized at the thigh 10 cm above the knee and accelerometer 2 centered at the leg 10 cm below the knee.

3 Results

The first test performed, without the use of the prosthesis, is intended to make a brief analysis of the gait of a person without disability. Three tests were performed. Table 1 shows the time and speed of each test and in Fig. 5 a representative figure of the test performed.

The EMG and accelerometry data are shown in Fig. 6. The muscle activation signal is highlighted within the red rectangles in the first line. The yellow and purple rectangles were used to highlight two more phases of gait, obtained through the observation of the footage made in conjunction with the presented graphics. The data within the yellow rectangles are in the period from the initial contact to the midstance, in the purple rectangles of the midstance to the pre-swing, in the reds the swing phase and the black rectangle represents that at the end of the gait the user remained standing and resting on both feet.

The acquisition of the signs with the mechanical prosthesis 3R15 were performed in a similar way to the test performed without the use of prosthesis, having the same
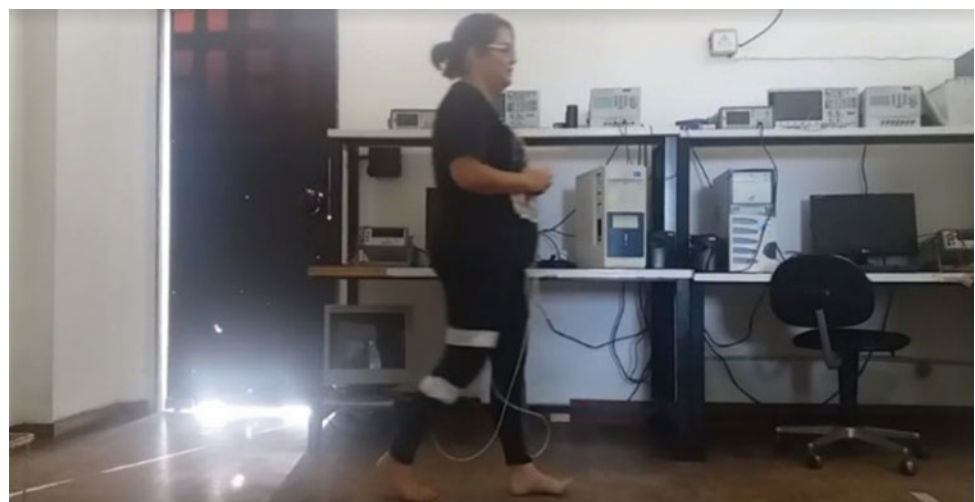
intention as the previous test. However, this analysis is used to make a comparison between the two gears and for the subsequent design of a control system for an electronic knee prosthesis. The time and speed data are presented in Table 2 and in Fig. 7 a representative figure of the test is presented.

The EMG and accelerometry data are shown in Fig. 8. As in the previous test, the muscle activation signal is inside the red rectangles on the first line. The green and yellow rectangles were used to define two more stages of gait and were done observing the footage made in conjunction with the presented graphics. Since the data within the yellow rectangles are in the period from the initial contact to the midstance, the purple rectangles of the midstance to the pre-swing and the red ones in the swing phase.

4 Discussion and Conclusion

This research, although it is not a new topic in the scientific community, is part of a larger work that seeks the development of a low cost equipment for monitoring and control of the gait of people transfemorally amputated. Therefore, it was decided at the first moment to not use people who had above-the-knee amputations to perform the tests with the prosthesis, given that it is difficult for researchers to understand the difficulty that users in the first stage of rehabilitation suffer, and how they face daily difficulties after the rehabilitation phase.

This stage of understanding for the researcher is of fundamental importance, because as the researcher deeply understands the difficulties and problems that arise for the users of knee prosthetics, they are able to propose solutions that will improve the quality of life of these users.

During this training phase it was noticed that one of the main limitations of this model of mechanical prosthesis is that when initiating the initial contact phase the knee of the

Table 1 Data acquired during the tests without the prosthesis

Tests	Time (s)	Speed (m/s)
Test 1	5	0.60
Test 2	5	0.60
Test 3	4	0.75

Fig. 5 Test without the adapted prosthesis
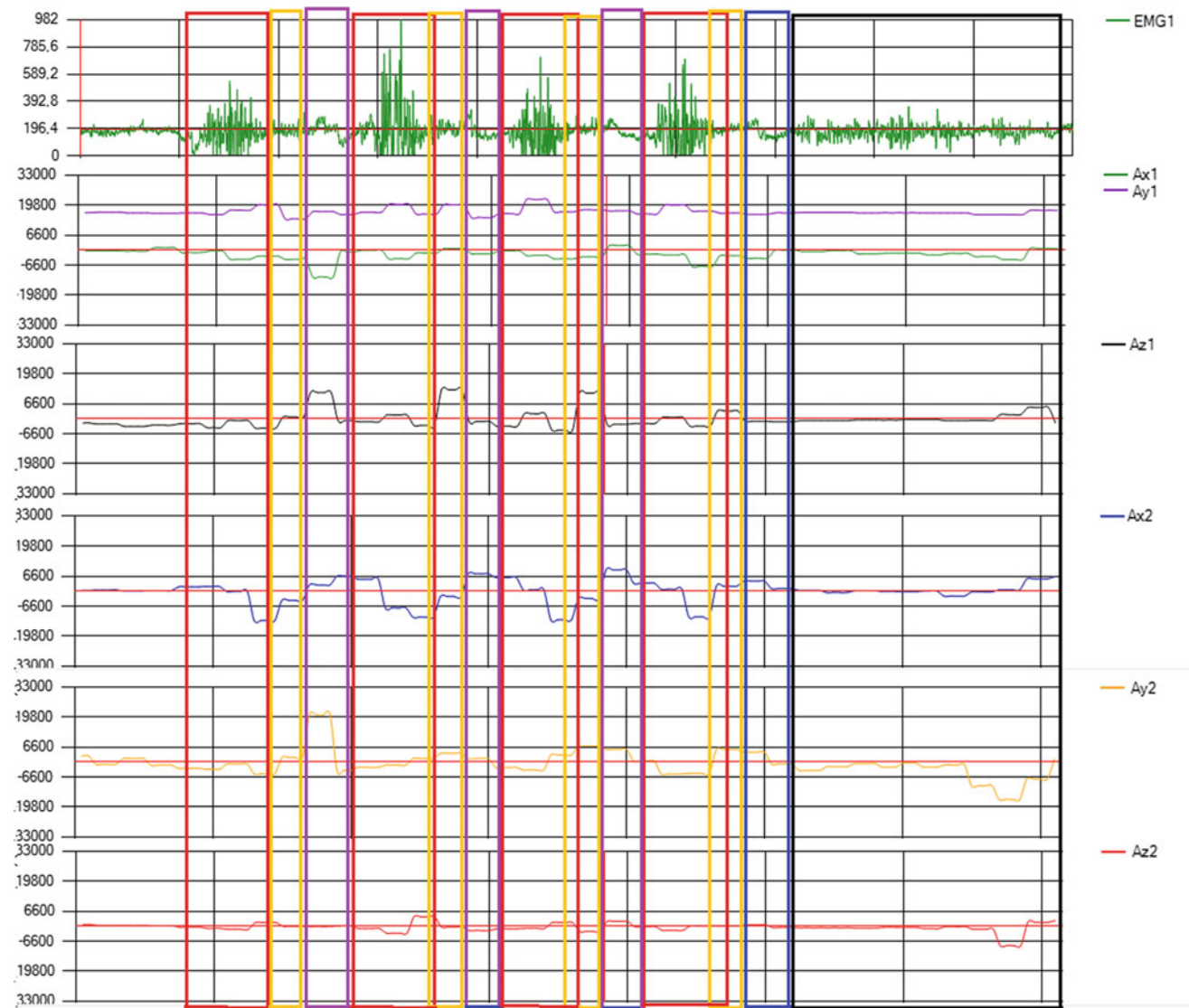
Fig. 6 Graph of the data. First line EMG signal. The second, third and fourth lines are respectively the X, Y and Z axes of the first accelerometer. The fifth, sixth and seventh lines are respectively the data of the X, Y and Z axes of the second accelerometer

Table 2 Dados adquiridos durante os testes com a utilização de prótese adaptada

Tests	Time (s)	Speed (m/s)
Test 1	12	0.25
Test 2	12	0.25
Test 3	11	0.27

prosthesis must be fully extended, because in case there is minimal flexion when the weight of the user is transferred in the phase of response to the load, it will flex at once, which can cause fall.

For the acquisition of the electromyography signals, electrodes were used that were placed in the quadriceps lateral femoralis muscle, using the SENIAM protocol,

positioned contralaterally to the leg that was amputed. This was necessary because the quadriceps femoral muscle of the thigh that was with the adapted prosthesis was always in the relaxed state, due to its positioning (Flexed to 90°). However, it is believed that in people who have amputation above the knee and who were protected immediately after amputation, they have electromyographic signals that are sufficient to be used as classifiers in a control system of an electronic knee prosthesis [8–10].

During the normal gait tests (Fig. 6), it was found that the Y and Z axis graphs on both accelerometer 1 and accelerometer 2 were not stabilized and were not cyclical in all tests performed. These graphs were expected, with rotation on the Y axis indicating a slight external rotation of the knee whereas rotation on the Z axis indicates a slight lateralization of the

Fig. 7 Test with the adapted prosthesis

movement (abduction/adduction movement). This phenomenon was also observed in gait with the adapted prosthesis (Fig. 8), however its variations were greater in accelerometer 2, which is explained by being more distant from the hip.

The rotation on the X axis has the purpose of extending and flexing the knee and is the only axis that has cyclic movement and standard in both gears, being thus like in the other axes more intense in the accelerometer 2. This is explained, therefore when observing the gait it is noticed that the leg executes movements with amplitudes greater than the thigh.

Regarding the data in Tables 1 and 2, it is possible to notice that gait with the prosthesis is slower than normal, and this result was already expected. When using the prosthesis the researcher, spent more energy and made more effort in carrying out the walk and this was perceived with the increase of the amplitude of the EMG signal when the muscle should be relaxed, prolonging the time of the stance phase. The EMG signal, as shown in Fig. 8, has a longer activation time than the signal shown in Fig. 6, indicating that the leg stance phase is larger than that of the leg with the prosthesis, i.e., that the swing phase of the prosthesis is smaller. This phenomenon is explained by the literature, since the user does not have total confidence in the prosthesis leg [2, 11].

Based on all the data acquired during the tests, it is concluded that it is possible to create a control system for an electronic knee prosthesis, using the same equipment that was apply in the gait analysis phase. The equipment used is portable and has bluetooth communication, which allows in the future the creation of a mobile application that will receive signals coming from the prosthesis.
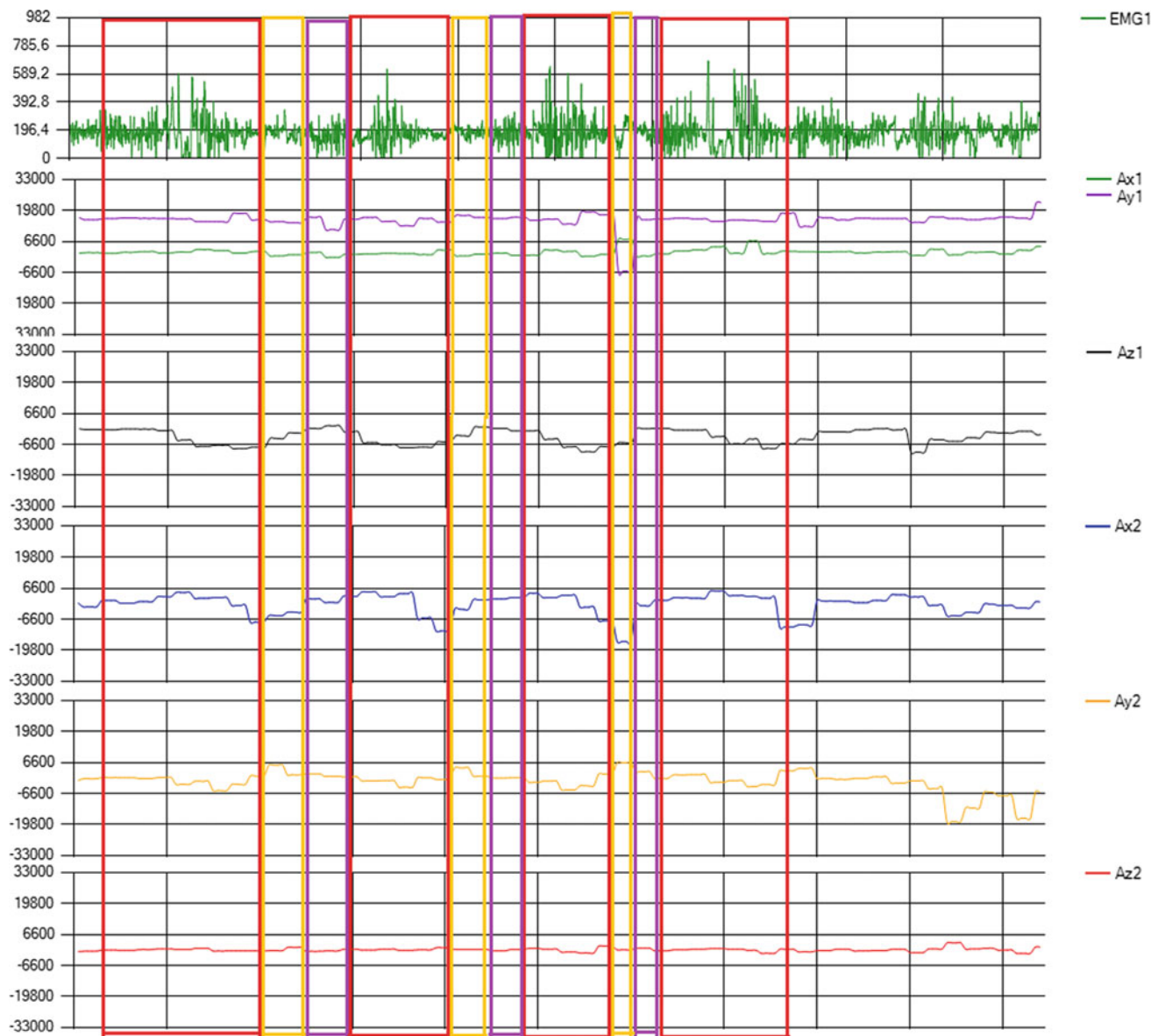
Fig. 8 Graph of the data. First line EMG signal. The second, third and fourth lines are respectively the X, Y and Z axes of the first accelerometer. The fifth, sixth and seventh lines are respectively the data of the X, Y and Z axes of the second accelerometer

References

1. Censo IBGE 2010. Fonte: https://censo2010.ibge.gov.br/resultados.html. Last accessed 2 Aug 2017
2. Carvalho, J.A.: Amputações de Membros Inferiores: Em busca da Plena Reabilitação, 2nd ed., Brasil (2003)
3. da Saúde, M.: Diretrizes de Atenção a pessoas amputadas. Distrito Federal, Brasil (2012)
4. Alves, J.T.D., Cavalcante, E.L., Inocêncio, A.V.M., Lima, E.G., Santos, E.A.B., Moraes, C.R.L., Rodrigues, M.A.B.: Análise das Fases da Marcha Utilizando Sensores Inerciais. In: XXV Congresso Brasileiro de Engenharia Biomédica–CBEB (2016)
5. Perry, J.: Análise de Marcha: Marcha Normal, vol. 1, Brasil (2005)
6. Vaughan, C.L., Davis, B.L., O'connor, J.C.: Dynamics of Human Gait. Estados Unidos da América (1992)
7. Cavalcanti, E.L., Morais, P.A. de O., da Silva, M.G.N.M., Lessa, P.S., Rodrigues, M.A.B.: Sistema de Avaliação Cinesiofuncional

com Sensores de Movimento. In: XXV Congresso Brasileiro de Engenharia Biomédica—CBEB (2016)

8. Young, A.J., Kuiken, T.A., Hargrover, L.J.: Analysis of using EMG and mechanical sensors to enhance intent recognition in powered lower limb prostheses. J. Neural Eng. **11** (2014)

9. Spanias, J.A., Simon, A.M., Ingraham, K.A., Hargrove, L.J.: Effect of additional mechanical sensor data on an EMG-based pattern recognition system for a powered leg prothesis. In: IEEE Conference on Neural Engineering (2015)

10. Spanias, J.A., Simon, A.M., Perreault, E.J., Hargrove, L.J.: Online adaptive neural control of robotic lower limb prosthesis. J. Neural Eng. (2017)

11. de Lima, V.J.B.: Modelagem Estrutural de Joelho para Próteses Transfemorais Microprocessadas, Dissertação –Universidade Federal de Pernambuco. Pernambuco, Brasil (2016)

12. Ottobock, 3R15 Satinless Stell Monocentric, 3R49 Titanium Modular Knee Joints – Instructions for User. Homepage: https://professionals.ottobockus.com/Prosthetics/Lower-Limb-Prosthetics/Knees–Mechanical/Single-Axis-Knee-Joint-Brake/p/3R15. Last accessed 17 Oct 2017

13. SENIAM homepage: http://seniam.org/quadricepsfemorisrectusfemoris.html. Last accessed 15 Jan 2018

Hybrid Solution for Motion Capture with Kinect v2 to Different Biotypes Recognition

Thiago Buarque de Gusmão Lafayette,
João Marcelo Xavier Natario Teixeira, and Alana Elza Fontes Da Gama

Abstract

Motion capture (MOCAP) systems are powerful tools for the health field; they enable kinematic analysis applicable to various rehabilitation purposes. Within the MOCAP technologies, Microsoft Kinect stands out for its advantages as cost, portability, and markerless characteristic. However, its tracking algorithm is modeled from machine learning, so Kinect is conditioned to identify the human body based on a certain pattern and bodies that depart from this pattern are not properly recognized. Thus, Kinect is not feasible for the kinematic analysis of individuals with different biotypes, such as member discrepancy or amputees. Based on the exposed, this work aims to create a tool which uses Kinect as a hybrid optical MOCAP system in which color markers will be positioned on the joints of interest to add extra information through colored passive markers to the standard Kinect skeleton tracking. A case study was conducted with an individual with lower limb discrepancy. The tests of the tool occurred with the numerical analysis of a sequence of movements made by the same. The analysis was made in MATLAB to quantify the angular variation of limbs and length of limb sections. The data was treated by comparing the hybrid method with the standard Kinect method and indicated the viability of the tool to capture movement of the tested biotype even when light variation conditions common to RGB systems are present.

1 Introduction

Motion Capture Systems (MOCAP) are technologies which convert body pose into a 3D representation to work as an input to computer software enabling movement recognition [1]. This technology is already widely used on the entertainment industry, such as movies and games, and, due to their diversity, it is now possible to make interactive games and more realistic animations [2]. In the health research field, these advances make possible obtaining better kinematic analysis, which has a wide application, for example, in sports and rehabilitation [1, 3].

For rehabilitation applications, some requirements are important, such as correct joint estimation, kinematic measures, and cost. The Kinematic measures will be a reference to patients' prognostic, treatment efficacy evaluation and its planning. To be used at clinical environments, these technologies need to be low cost and easy to carry and store. Due to that, the emergence of RGB-D cameras, such as the Microsoft Kinect, promoted a quick grown on MOCAP systems rehabilitation applications [3, 4].

Kinect presents some advantages such as the low cost, portability and markers independence, however, its skeletal tracking is trained to recognize pre-established body patterns. Bodies with different biotypes, which do not match these patterns, present inconsistencies in their skeletal representations. For example, for an individual with lower limb discrepancy Kinect uses one of the lower limbs (LL) as a

T. B. de G. Lafayette (✉)
Rehabilitation Engineering Research Group, at Biomedical Engineering Department, Universidade Federal de Pernambuco and Mechanics Department, Universidade Federal de Pernambuco, Recife, Brazil
e-mail: thiagobuarque@ufpe.com.br

J. M. X. N. Teixeira
Voxar Labs, from informatics center of Universidade Federal de Pernambuco and Eletronic and Systems Department, Universidade Federal de Pernambuco, Recife, Brazil
e-mail: jmxnt@ufpe.com.br

A. E. F. Da Gama
Rehabilitation Engineering Research Group, Biomedical Engineering Department, Universidade Federal de Pernambuco and Voxar Labs, Informatics Center, Universidade Federal de Pernambuco, Recife, Brazil
e-mail: alana.elza@ufpe.com.br

reference and applies the same pattern to the other limb. Thus, any analysis of the biomechanical movement of the LL is imprecise.

Based on that, this work proposes a hybrid solution to enable Kinect to recognize different biotypes correctly. This way this paper aims to make possible to use Kinect as a hybrid MOCAP tool to biomechanics analyses [5], rehabilitation treatment [6] and orthotic modeling [7] for users with different biotypes. This paper will focus on describing how lower limb additional information was added to Kinect to recognize a user with member discrepancy. The proposed method and a case study will be presented.

2   Literature Review

MOCAP systems can be classified as mechanical, magnetic or optical, and it is not possible to affirm which kind is better since all have advantages and disadvantages depending on their purpose [2]. When the aspect is tracked body quality of movement and degrees of freedom, optical systems can be considered the state-of-art [1]. Such technology has been used in sports to analyze biomechanical parameters such as stride length in baseball [8], trunk rotation in golf [9], foot strike patterns in runners and improve technical executions [10]. This technology also presents a high potential for clinical applications [4, 11]. Optical MOCAP systems can be active or passive marker-based or even markerless. This review will focus on the passive markers and markerless ones since these comprise the technology used in this study.

2.1   Passive Markers

This method has two elements: one is the equipment attached to the subject to reflect light in order to provide information from the subject; the other is the equipment set around the subject that receives the information [12].

This method is the most commonly used one for full body capture. There are infrared (IR) model features which require specific setup, space, and retroflexive markers and presents high accuracy level, however, accompanied by a high cost. These characteristics make this technology not adequate to be used in clinical settings [11]. On the other hand, RGB systems can use commercial simple cameras, being portable, low cost and easy to use. However, they can be influenced by the environment characteristics such as light variations, which can lead to false data capture or marker temporary loss [2, 12].

2.2   Markerless

These technologies commonly perform their recognition based on the human body pose estimation. Currently, RGB-D cameras are the most popular technology to perform such task, since using a light pattern they can provide a depth information with only one point of view. Kinect v2, used in this study, has two light sensors: a regular RGB camera and a depth camera with an IR emitter and sensor [4]. The emitter shoots infrared light beams and the IR sensor reads its reflection, which is converted into depth information measuring the distance between an object and the sensor [13, 14].

Kinect v2 offers several advantages over traditional intensity sensors: works in low light levels, gives a calibrated scale estimate, is color and texture invariant, and resolves silhouette ambiguities in the pose. The Kinect's skeleton algorithm is trained to recognize templates of bodies in depth images [13]. For this the software divides a depth image into several spatial regions likely to be joints, then the points are subjected to a deep randomized decision forest classifier containing hundreds of thousands of training images to determine points of interest close to the joints [13].

The Kinect technology was successfully applied to several rehabilitation cases, as for example posture, lower limb kinematics [5]; equine-assisted therapy [6]; stroke rehabilitation therapy [11]. However, all these studies included individuals with standard biotype, which is easily recognized by Kinect. Cases in which this technology could not be applied, such as the aforementioned works, did not discuss different biotypes.

3   Methodology

This paper conducted a case study with an individual with LL discrepancy whose different biotype is not correctly recognized by Kinect's standards for skeleton tracking. It motivated this paper's hybrid tracking method development, using Kinect as a passive capture system (with color markers) along with its original active infrared tracking operation. The color markers provided additional joints to the MOCAP system. This way, the Kinect incorrect skeleton estimation could be collected separately through the color markers, making possible different biotypes kinematics analyses. This work was performed in three stages: Hybrid method for MOCAP tool; case study and data analysis.

3.1   Hybrid MOCAP Tool

The hybrid MOCAP tool was developed in C++ language using Microsoft's Kinect for Windows SDK 2.0, which provides Kinect-specific command functions along with the OpenCV library [15] for the RGB image processing.

The algorithm captures the joints provided by Kinect through basic skeleton functions. In order to add custom joints selected by the user, the algorithm merges RGB and depth information. Firstly, the color of interest is used to

segment the RGB image, so that any pixel that has similar (up to a threshold distance) RGB information will be considered as part of the marker and will be highlighted as a pixel set. After segmenting the marker, the code calculates the centroid of each highlighted area, acquiring the marker's X and Y coordinates and salving them as a struct vector for each frame. For the depth, a specific Kinect interface (ICoordinateMapper) overlaps the color and depth images by correlating each pixel of the images. This way, the centroid calculated in the color image is related to the depth image. Thus, the XY coordinates are bound to a specific Z coordinate for all segmented pixels in Skeleton's coordinate system. Finally, the marker's 3D coordinate is obtained by the mean (centroid) of all 3D coordinates found regarding the selected color.

3.2 Case Study

The study comprised an individual with unequal limb length (ICD-M217) presenting 6 cm lower limb discrepancy, being left femur 10 cm shorter and left tibia 4 cm cirurgically longer to compensate.

Preliminary tests were performed to analyze Kinect skeleton tracking behavior with the discrepancy member user. Six color fabric strips markers were used to identify LL joins. Color markers were placed directly over the knees, ankles, and forefoot at each limb. Each joint received a distinct color to differentiate and allow an isolated analysis of each element. The subject wore black legging pants to increase markers contrast and enable a better silhouette of LL. Figure 1 shows Kinect skeleton tracking and the color markers.

Fig. 1 Six color markers and black legging pants. Green dots indicate joints captured by Kinect standard method (Color figure online)

Experiments were performed using the Hybrid MOCAP tool. Kinect v2 was connected to a Dell Inspiron 15R i5-4210CPU Notebook with 2.4 GHz, 8 GB RAM, AMD Radeon R7 M265 2 GB GPU. When the tool starts, user and Kinect's original skeleton tracking appear on the screen. Color markers could be selected in a previously defined order to work as input to replace incorrect joints. The respective color centroid will represent the correspondent joint.

To test the Hybrid MOCAP tool some movements were performed by the user: (i) Hip abduction and adduction; (ii) Hip and knee flexion; (iii) Step Forward; (iv) Step Back; (v) Free squatting. Joints extracted from the system were recorded to work as input to Motion Visualization, described next.

3.3 Motion Visualization

The tool gives as output a file containing a list of spatial coordinates of the Kinect skeleton joints plus the joints of the colored markers, in a total of 31 joints (25 from Kinect and 6 markers) To analyze this output a MATLAB script was developed. It received the values of the spatial position of the joints (X, Y and Z coordinates) and created a static representation for each frame. The code generated vectors by joining the respective joints thus forming the limb. Such vectors function as a representation of the bone structure. With the bone structure represented in each frame of the recording, the angles between the limb structures were calculated for studying angular variation.

In addition, a motion animation was generated to compare the motion captured with the actual motion of the recording. This way, it is possible to have two forms of analysis, a qualitative and a quantitative for the judgment of the developed tool.

3.4 Data Analysis

The data analysis was done by the same MATLAB script of Motion Visualization. The vectors calculated in the three-dimensional space were projected in the Sagittal plane to calculate the angles of each joint along the motion. The plots were performed showing the angle of each joint separately containing both legs, quantifying the movement of each joint.

The MATLAB routine also estimated the bone size of the limbs analyzed (femur and tibia), by the standard Kinect method and by the developed method as shown and as reference, the size of each member segment was measured with a scale. This way it is possible to check the oscillation of the reference member by Kinect's tracking.

3.5 Ethical Aspect

This work was motivated by personal scope, where the author himself presents the limb discrepancy since 3 years old and was the case of study of this paper. Since this research is based on the author's own deficiency it does not require ethics committee approval.

4 Results and Discussion

The preliminary tests showed that Kinect skeleton tracking presented LL as equals, taking one of the legs as a reference for the other one. Besides that, the leg that worked as a reference for the tracking varied during movement's execution resulting in joint estimation repositioning, mainly in the squat movements as shown in Fig. 2. These observations indicated that using such technology is not adequate to correctly measure biomechanical parameters from individuals with member's discrepancy. To solve this problem we used color markers in the joints where the user presented discrepancy as shown in Fig. 1. For the trunk and upper limbs the software presented satisfactory skeletal estimates for the studied biotype, what was expected since the user does not have a discrepancy of upper limbs.

During hybrid tracking motion visualization, it was possible to observe that movement was detected constantly without losing the marker and LL discrepancy was visible as shown in Fig. 3.

Femur and tibia size variation during tracking at different movements can be observed in Fig. 4 and Fig. 5 respectively. Box Plot display average size, the standard deviation, the first and the third quartile of the members during the different movements. Analyzing these graphs it is possible to note a good precision for the hybrid method since their average values showed few variation during tracking at the different movements. On the other hand, Kinect tracking showed high member size oscillation. Since their mean values varied randomly from one test to another, their first and third quartiles were also more spaced. In some tests the

Fig. 2 Joint reference variation during squat movement during Kinect tracking **a** Knee estimation following the right knee; **b** Knee tracking following the left knee
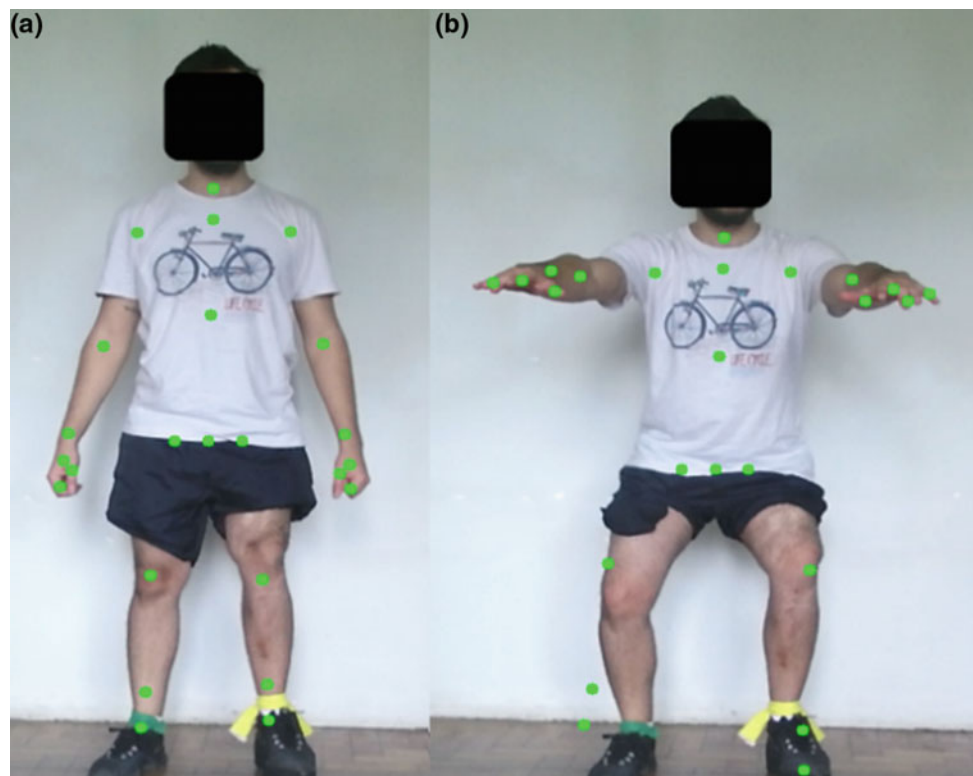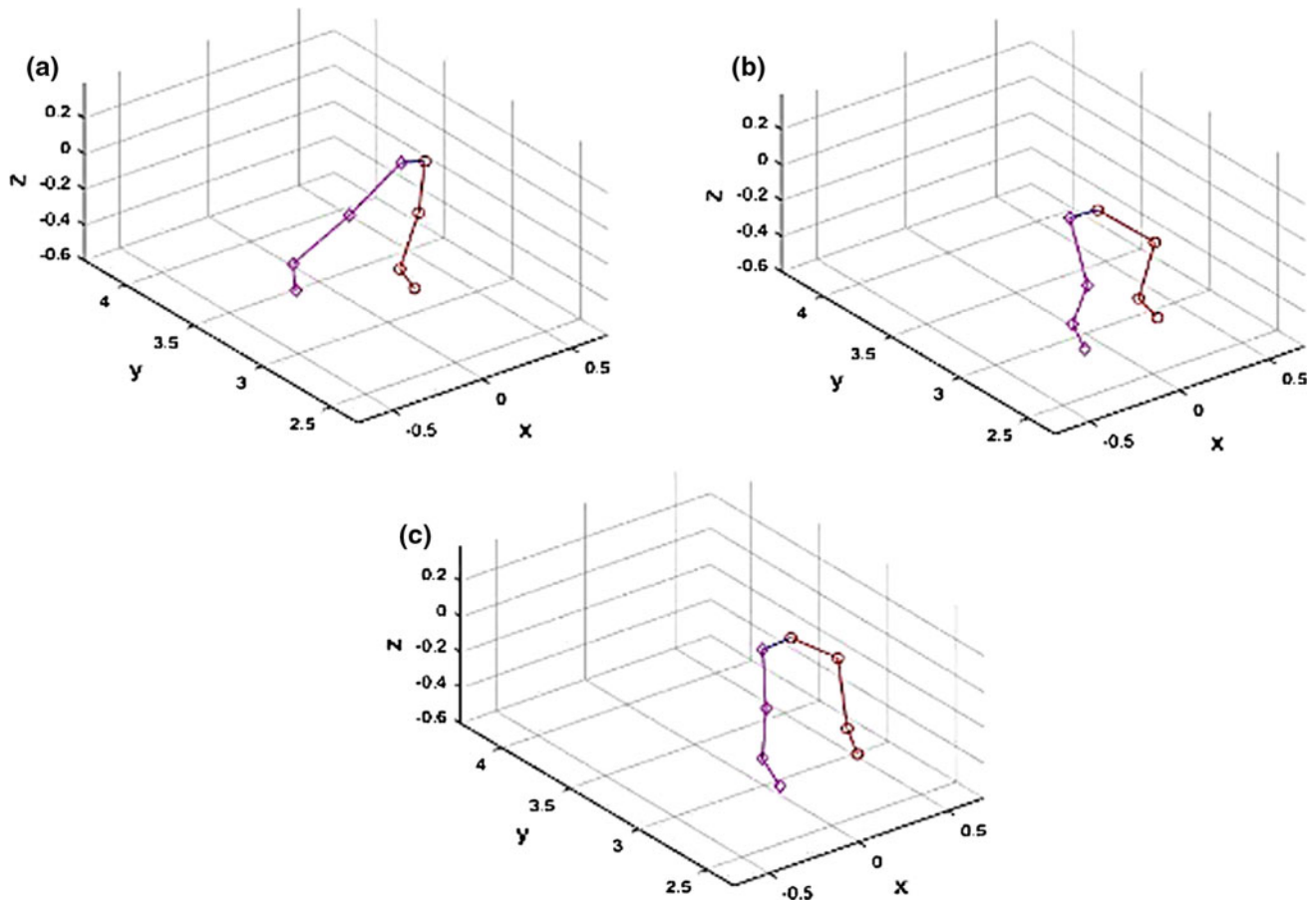
Fig. 3 MATLAB LL 3D hybrid tracking representation. **a** Hip abduction and adduction. **b** Free squatting. **c** Leg combined flexion

representation in box plot is not visualized leaving an empty space in the graph, this occurs in the data which does not varymeaning that they always presented the same value during the tracing. Difference between tracking member size and real member size (anatomic one) can also be observed with the dashed line at the Figs. 4 and 5. Hybrid tracking brings a more accurate measure compared with the Kinect tracking. An accuracy study should be performed in the future to validate this fact.

To better observe this variation behavior Fig. 6 and Fig. 7 shows Kinect and Hybrid tracking, respectively, at each frame when user was performing the abduction movement. It is possible to notice that Kinect tracking

(Fig. 6) presents high variation, probably due to its attempt to guess which knee was the correct reference based on the standard biotype with two similar limbs. On the other hand, the hybrid technique (Fig. 7) presents a more constant line, showing higher tracking stability. The ideal tracking should constantly follow the actual limb size (dashed line). It is also possible to notice that hybrid technique presents better results in this aspect with member size estimation closer to the real measurement.

Angle computation followed biomechanical reference [16] at the sagittal plane, as shown in Fig. 8. The values calculated by MATLAB based on hybrid MOCAP data were coherent since their measured values were within the range
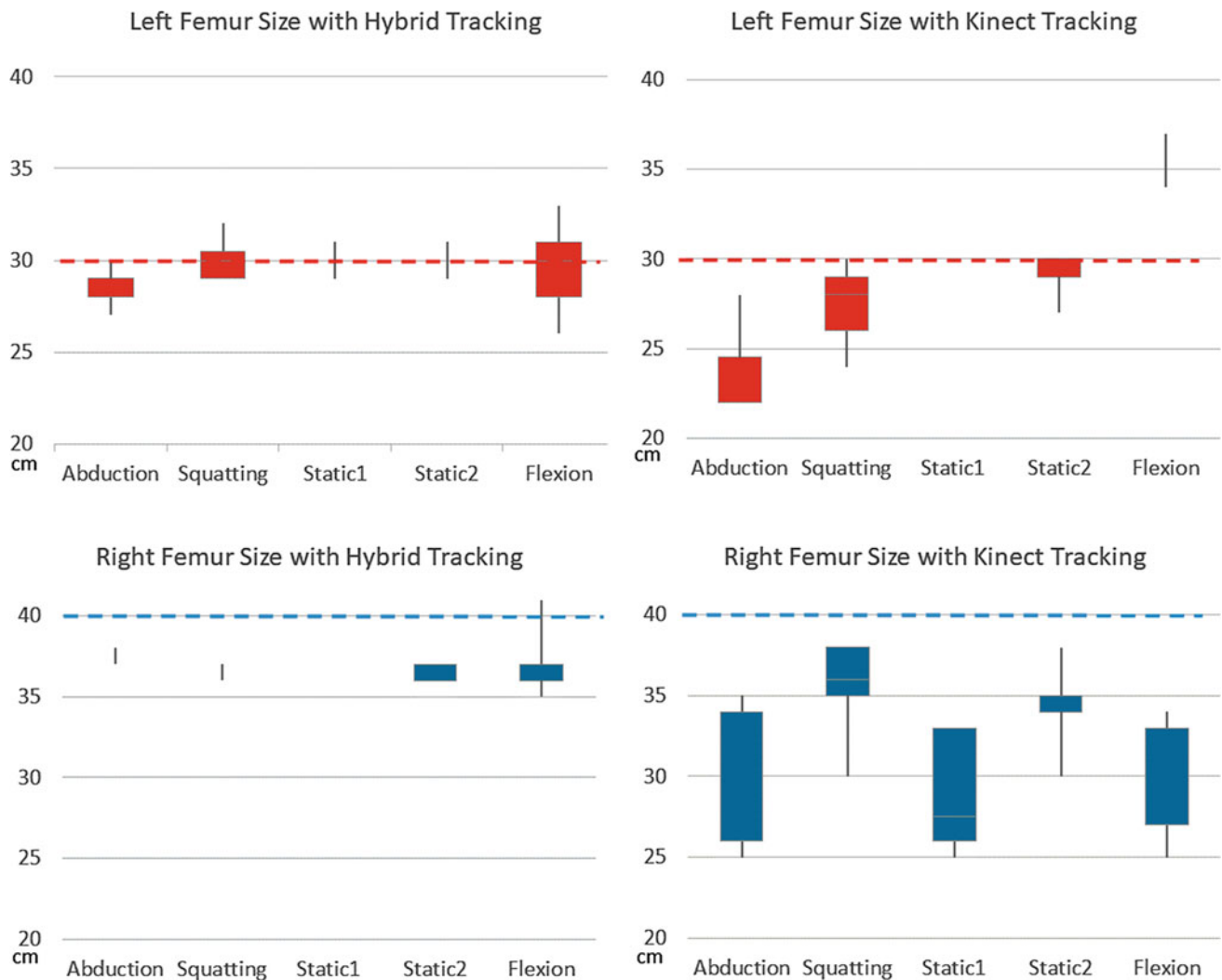
Fig. 4 Femur size variation during hybrid and Kinect tracking at different movement's performance

of performed movement and presented a continuous behavior without the presence of value gap. Figure 9 shows measured values during squat and combined flexion of hip and knee movements, respectively.

During experiments, problems regarding data loss were noticed at feet markers. The inconstant angular variation at ankle angles as evidenced in Fig. 9 during the squat movement indicated an anomalous displacement of this joint, possibly caused by partial recognition of the marker due to color saturation change with the presence of shadows on the marker, generating a centroid displaced relative to the actual

position. The markers of the tips of the feet presented significant fail in its recognition, as exemplified in Fig. 10. This may be due markers location (a horizontal plane in relation to camera), as well as the non-constant illumination that created occlusion zones. It is important to notice, due to the segmentation process used, the higher is the number of artificial markers, heavier the capture tool gets regarding its processing load.

It was evidenced that standard Kinect tracking is a viable MOCAP tool for biomechanical analysis and rehabilitation treatments compared to other commercial MOCAP systems
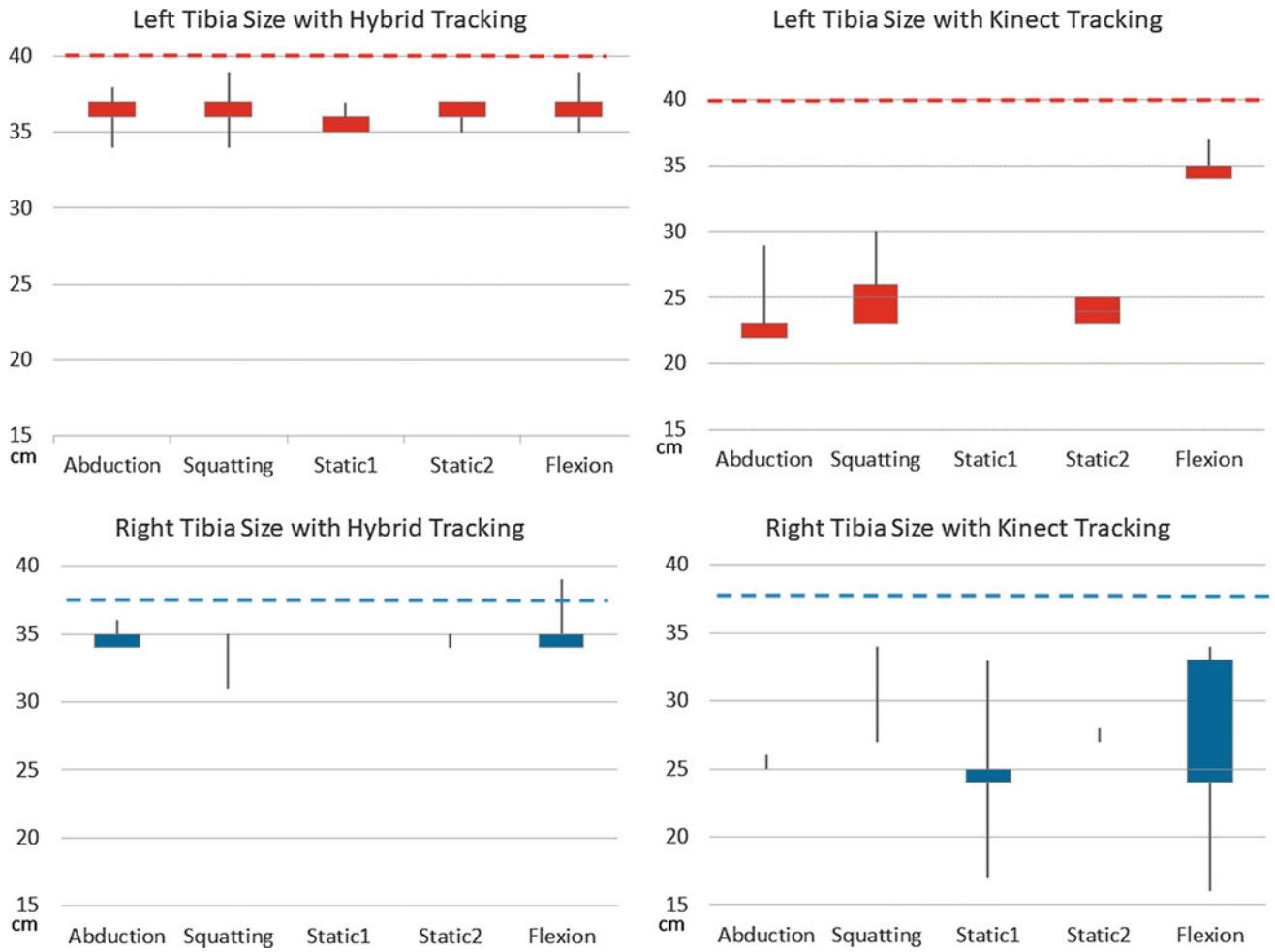
Fig. 5 Tibia size variation during hybrid and Kinect tracking at different movement's performance
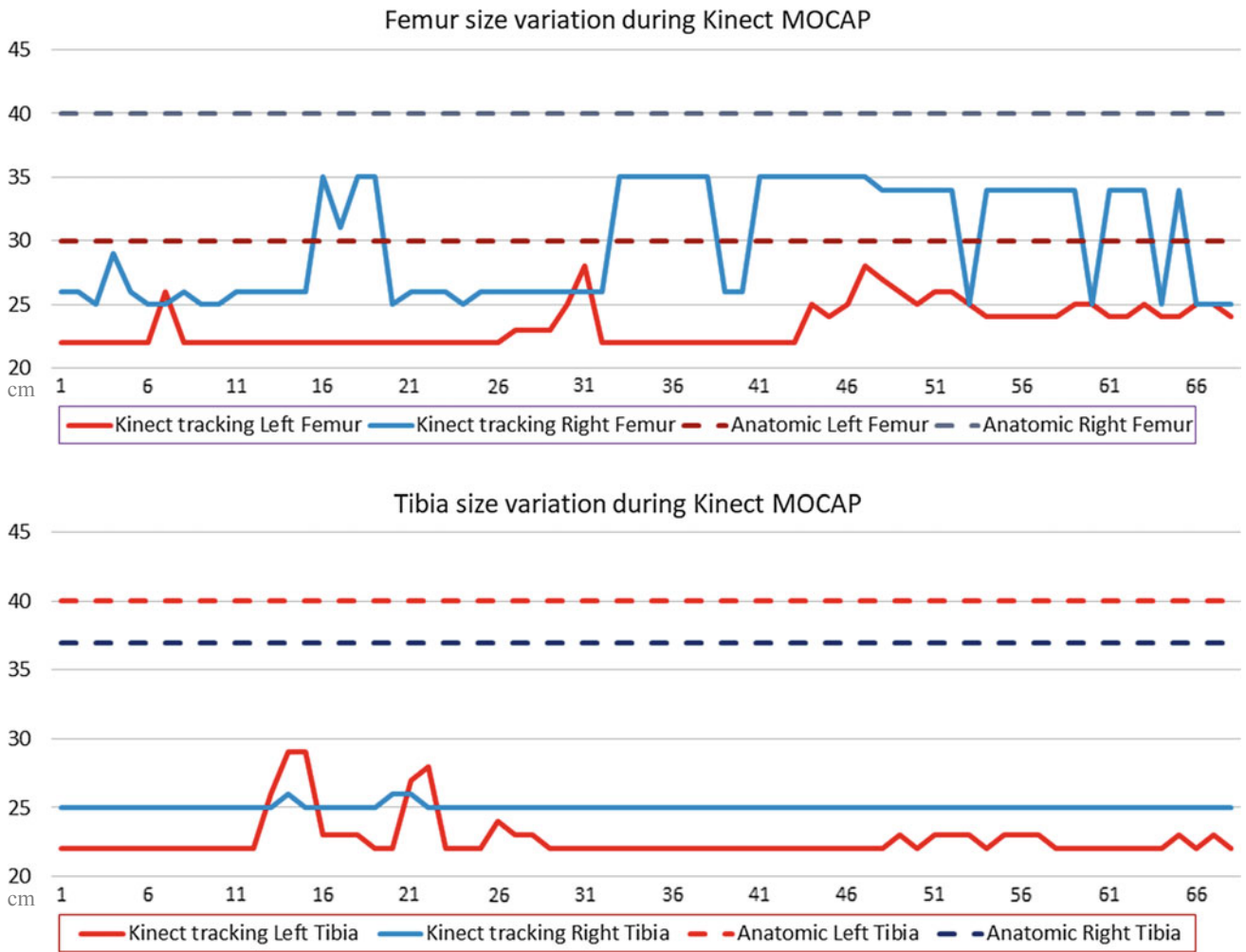
Fig. 6 Femur and Tibia size variation at each frame during Kinect tracking
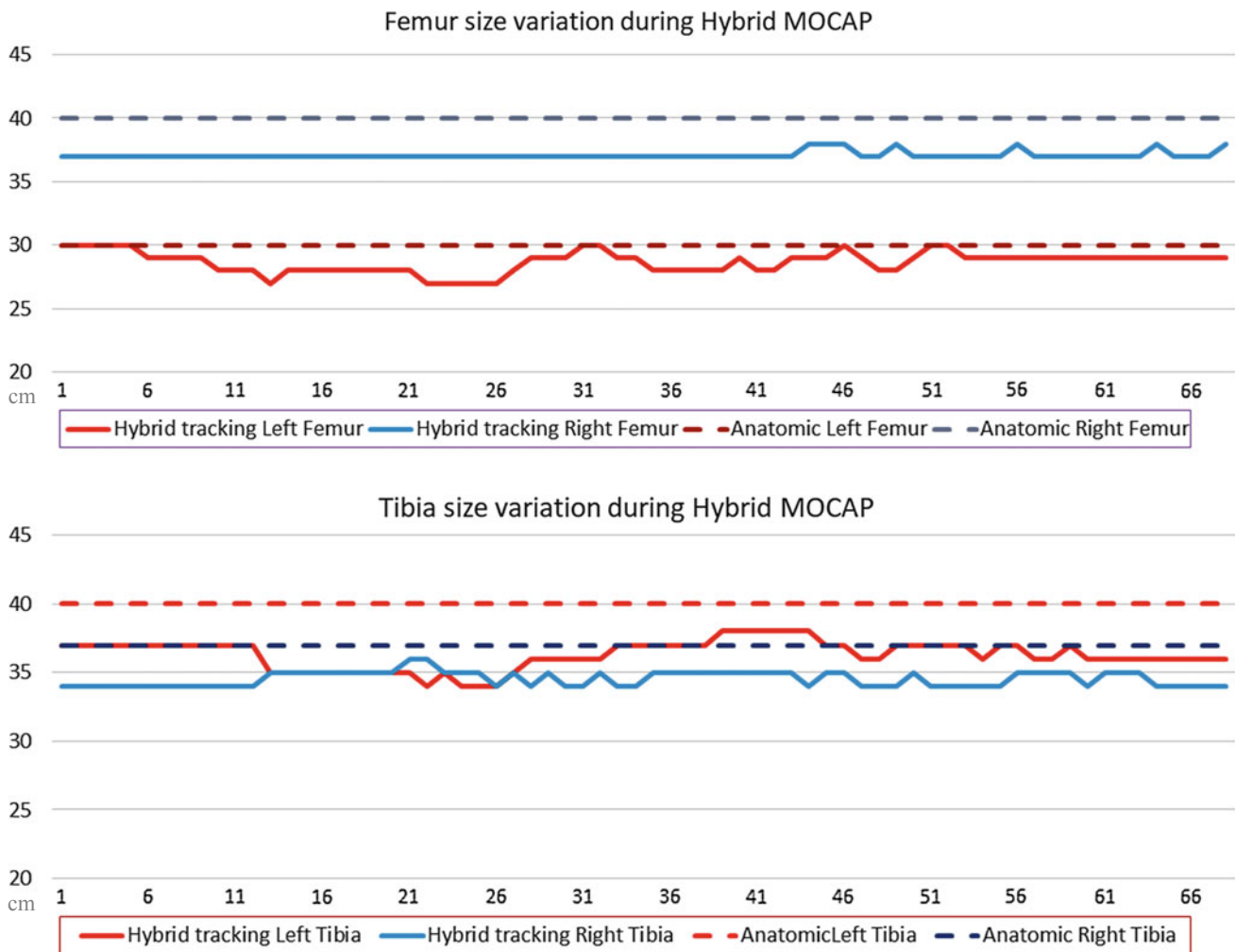
Fig. 7 Femur and Tibia size variation at each frame during hybrid tracking
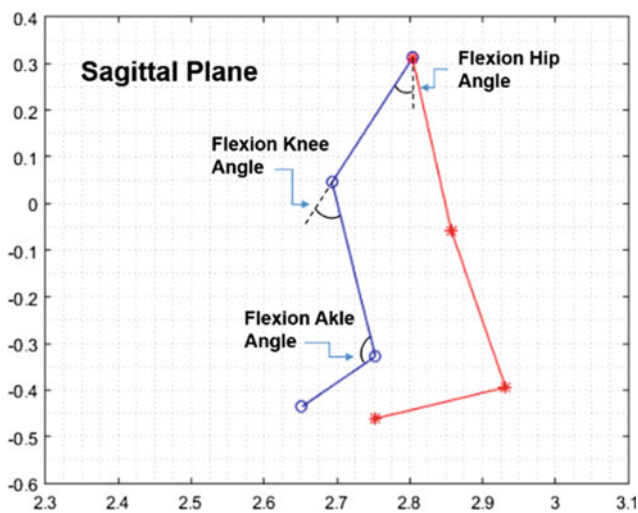
Fig. 8 Biomechanical reference to angular measurement

for the biotypes standards [4, 5]. In the case study, the hybrid method was able to determine the required joints while the standard Kinect method did not.

5 Conclusion

The proposed hybrid method showed itself viable to complement Kinect's tracking, allowing the correct capture of subjects with different biotypes. The implementation of capturing more joints from the RGB camera did not affect the operation of the standard Kinect capture system (depth camera). The two methods presented a complementary interaction in the tests performed. The caught and the measured angular variations represented well the actual movements. Future work shall focus on improving the capture tool to reduce data loss and light influence, such as replacing the
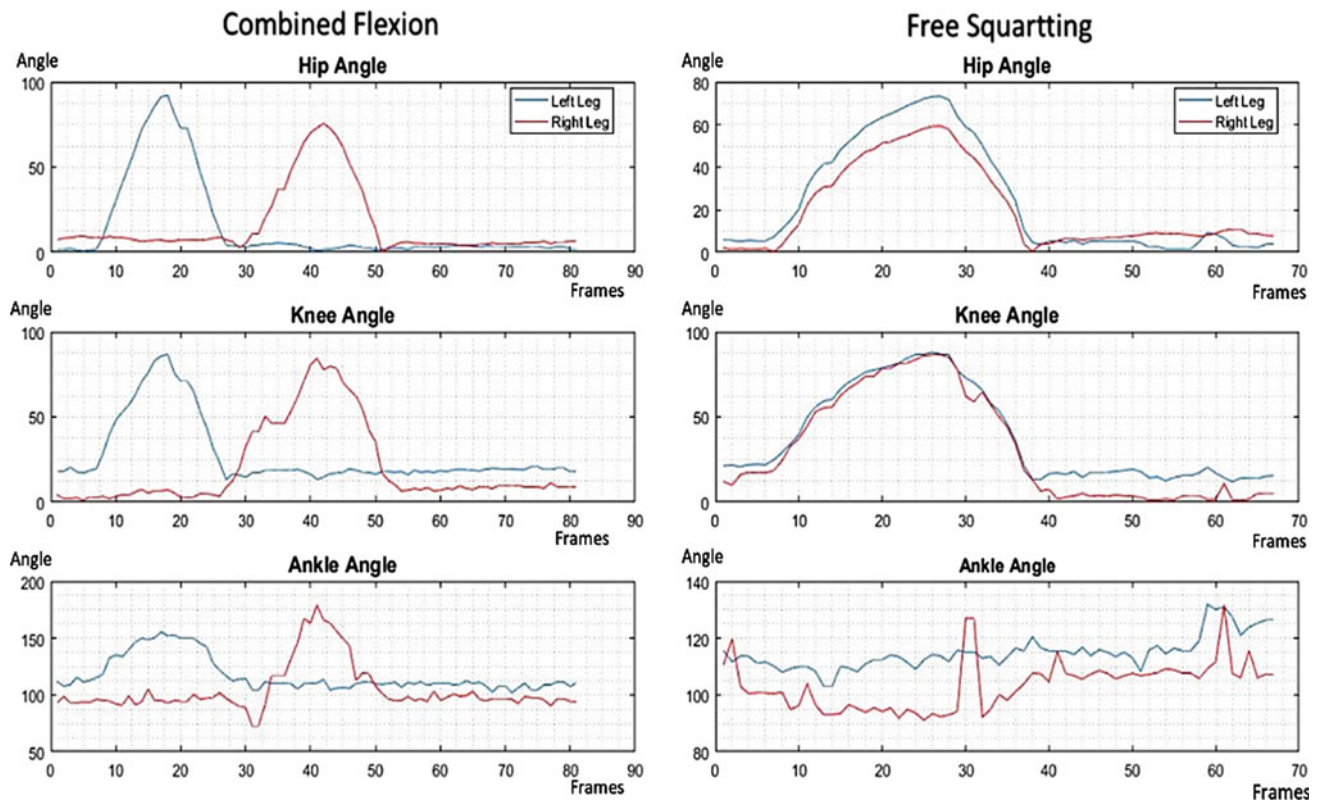
Fig. 9 Angle variation during motion
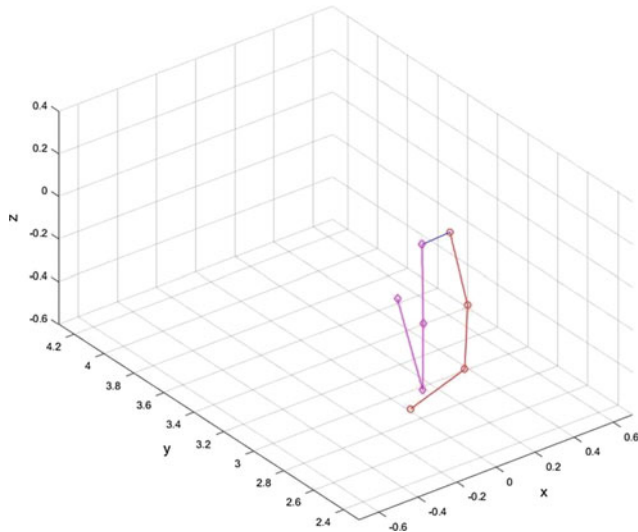
Fig. 10 Loss of the actual location of the toes during the forward movement

RGB color space with HSV to improve the identification of color markers. This work also intends to make the capture tool freely available for public use in a near future.

References

1. Menache, A.: Understanding motion capture for computer animation. Morgan Kaufmann (2011)
2. Victor, J., Gomide, B., Flam, D.L., Queiroz, D.P. De, Empresariais, F.D.C., Fumec, U., Ciência, D. De: Captura de Movimento e Animação de Personagens em Jogos. In: VIII Brazilian Symposium on Games and Digital Entertainment, pp. 1–15 (2009)
3. Fernández-Baena, A., Susín, A., Lligadas, X.: Biomechanical validation of upper-body and lower-body joint movements of kinect motion capture data for rehabilitation treatments. In: Proceedings of the 2012 4th International Conference Intelligence Network Collaboration Systems INCoS 2012, pp. 656–661 (2012)
4. Lun, R., Zhao, W.: A Survey of Applications and Human Motion Recognition with Microsoft Kinect (2015)
5. Eltoukhy, M., Kuenze, C., Oh, J., Wooten, S., Signorile, J.: Kinect-based assessment of lower limb kinematics and dynamic postural control during the star excursion balance test. Gait Posture **58**, 421–427 (2017)
6. Nasyuha, H., Ismail, L.H., As, M.A., Zakaria, N.A., Mahmood, N. H.: Evaluation of Kinect sensor in mechanical horse simulator for equine-assisted therapy. J. Telecommun. Electron. Comput. Eng. **9**, 59–63
7. Hegarty, A.K., Petrella, A.J., Kurz, M.J., Silverman, A.K.: Evaluating the effects of ankle-foot orthosis mechanical property assumptions on gait simulation muscle force results. J. Biomech. Eng. **139**, 031009 (2017)

8. Hansen, C., Rezzoug, N., Gorce, P., Venture, G., Isableu, B.: Sequence-dependent rotation axis changes and interaction torque use in overarm throwing. J. Sports Sci. **34**, 878–885 (2016)

9. Beak, S.H., Choi, A., Choi, S.W., Oh, S.E., Mun, J.H., Yang, H., Sim, T., Song, H.R.: Upper torso and pelvis linear velocity during the downswing of elite golfers. Biomed. Eng. Online **12**, 1–12 (2013)

10. Manuel, J., Pueo, B., Jimenez-olmedo, J.M.: El uso de la tecnología de captura de movimiento para el análisis del rendimiento deportivo (2017)

11. Dolatabadi, E., Zhi, Y.X., Ye, B., Coahran, M., Lupinacci, G., Mihailidis, A., Wang, R., Taati, B.: Elham Dolatabadi (2017)

12. Kurihara, K., Hoshino, S., Yamane, K., Nakamura, Y.: Optical motion capture system with pan-tilt camera tracking and real time

data processing. In: Proceedings of the 2002 IEEE International Conference on Robotics and Automation, (Cat. No. 02CH37292), vol. 2, pp. 1241–1248 (2002)

13. Shotton, J., Fitzgibbon, A., Cook, M., Sharp, T., Finocchio, M., Moore, R., Kipman, A., Blake, A.: Real-time human pose recognition in parts from single depth images. Stud. Comput. Intell. **411**, 119–135 (2013)

14. Kinect for Windows Sensor Components and Specifications. https://msdn.microsoft.com/en-us/library/jj131033.aspx

15. OpenCV library. https://opencv.org/

16. Da Gama, A.E.F., Chaves, T.M., Figueiredo, L., Teichrieb, V.: Markerless gesture recognition according to biomechanical convention. In: XXIV Brazilian Congress on Biomedical Engineering, pp. 2033–2036 (2014)

Identification of Kinematic Parameters of Stroke Gait Using Accelerometer

Flávia A. Loterio, Vivianne F. Cardoso, Alexandre Pomer-Escher,
Teodiano F. Bastos-Filho, Anselmo Frizera-Neto, and Sridhar Krishnan

Abstract

Gait analysis is an important method to evaluate individuals with motor disabilities. Accelerometer and inertial sensors have been an alternative for kinematic gait parameters detection, since they are easy-to-use, affordable, and low-cost. The objective of this study is to verify the possibility of using accelerometer to identify kinematic gait parameters of healthy and stroke individuals. Fourteen volunteers (average age 29 ± 4 years) participated of the first experiment, using one biaxial accelerometer placed on the lateral malleolus, and 5 volunteers (average age 26 ± 3 years) of the second experiment, using the accelerometer located on L2 vertebrae. One stroke individual (48 years) participated in both experiments. The accelerometer placed on the ankle identifies two gait phases of a single leg, and when placed on the lower back, data from both legs can be obtained. Some pathologic gaits, such as stroke, present kinematic asymmetry, which requires both limbs to be analyzed. In those cases, the lower back placement can provide greater amount of data using the same sensor and processing.

Keywords

Accelerometer • Kinematic parameters • Gait

F. A. Loterio (✉) · A. Pomer-Escher · T. F. Bastos-Filho
Doctorate RENORBIO, Federal University of Espirito Santo
(UFES), Vitoria, Brazil
e-mail: loteriofa.ufes@gmail.com

V. F. Cardoso · T. F. Bastos-Filho
Postgraduate Program in Biotechnology, UFES, Vitoria, Brazil

T. F. Bastos-Filho · A. Frizera-Neto
Postgraduate Program in Electrical Engineer, UFES, Vitoria,
Brazil

S. Krishnan
Department of Electrical and Computer Engineering, Ryerson
University, Toronto, Canada

1 Introduction

Human gait is a periodic action with repetitive motions that requires the synchronization of the central, peripheral nervous system and muscles to perform fast and complex movements [1].

The analysis of the human gait pattern by phases allows identifying more directly the functional meaning of the different movements generated in the individual joints and segments, making it possible to determine the kinematic and kinetic parameters and muscular activation by comparing them in different phases [2].

The gait cycle begins, conventionally, when there is foot contact with the ground, and ends when there is the next ground contact with the same foot. It consists of two sequential and distinct phases called stance swing phases (Fig. 1). The stance phase, when the foot is in contact with the ground, can be divided into five sub-phases: initial contact, load response, mid stance, terminal stance and pre-swing. On the other hand, the swing phase, when the foot is advancing, is divided into three sub-phases: initial swing, mid swing and terminal swing [3].

Kinematics describes motion based to position, velocity, and acceleration. It can be measured through photogrammetry, cinematography, footswitches, goniometers and inertial sensors units (accelerometers, gyroscope and magnetometer). Generally, the kinematic parameters of the gait are analyzed by video capture through multi-camera systems, which identify body segments and joint movements. The limitations related to the use of this system of analysis involve the need to be installed in closed environments, preventing its use in outpatient monitoring, and also, implementation costs are quite high when compared to other analysis tools [4].

In the last two decades, portable sensors, which are cheaper and can be applied outside the laboratory environment, have been used and presented excellent results [2]. For instance, Inertial Measurement Unit (IMU), composed of
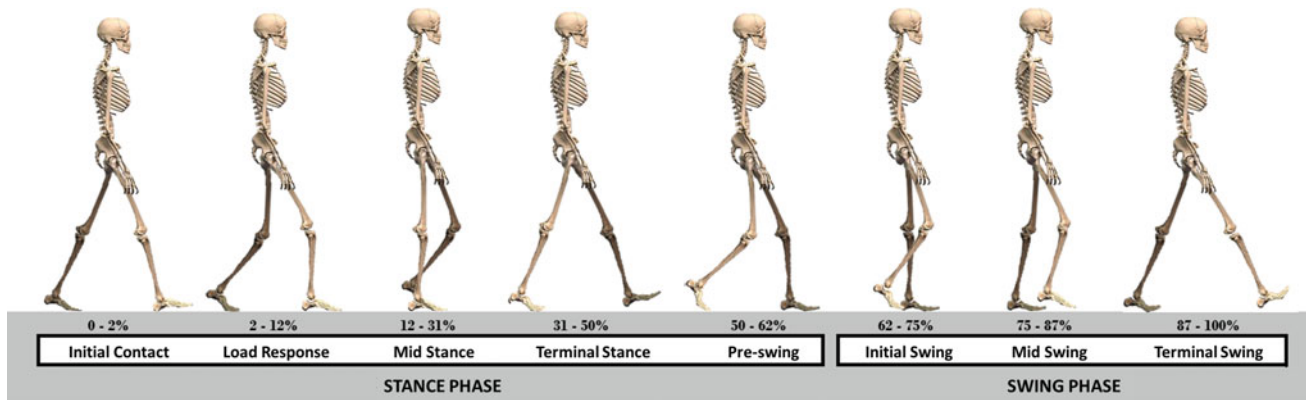
Fig. 1 Gait phases. There are two main phases (stance and swing) and eight sub-phases. The figure shows the values of each phase for the healthy gait, according to Perry [3]

accelerometer, gyroscope, and magnetometer, can be used flexibly and there is no concern about the visibility of the sensors, as it can be used under clothing, objects or body parts without direct interference [5]. In addition, there is less interference with individuals' natural gait, due to their size and weight. IMUs are useful in detecting spatiotemporal parameters, measuring joint angles and providing continuous information during gait. With the technological advance, IMUs have become smaller, lighter and with lower costs, more applicable in external environments [6].

In locomotion activities, the measurement of the acceleration allows the evaluation of the balance, as well as the transmission of the impact on the body segments. In fact, most of the studies in this area uses accelerometers as sensors to measure physical activity or the impact on human body structure in certain movements [7]. For this reason, the accelerometer has been studied as an alternative in the detection of kinematic gait parameters. The accelerometer is a type of inertial sensor that measures the acceleration along its axes, using the physical shifts of displacement [2, 8, 9]. Accelerometers are small and light, which are important features to reduce interference in gait pattern. Two other important points to highlight are the fact they are low-cost and easy-to-use devices.

Some studies evaluated the use of a setup of accelerometers: placed on waist, wrist and both ankles [10]; two accelerometers attached to the shoes, one at the level of the heel and one at the level of the forefoot of each foot [11]; upper chest, each anterior thigh, and under each medial forefoot [12]. In these studies, the accelerometry system provided reliable and valid kinematic measurements of the gait.

However, the acquisition of kinematic parameters can be facilitated by using only an accelerometer, which reduces the discomfort of the subject, besides the time and cost of the process. The use of a single accelerometer on the ankle in healthy subjects allowed estimating the kinematic gait parameters [4, 8]. On the other hand, the curve shape from accelerometer has characteristic peaks, where is possible to divide the gait in four phases: first double support (A–B), single support (B–C), second double support (C–D), and swing phase (D–A) [10], as shown in Fig. 2. However, the points B and C are difficult to identify (it is necessary the use of another sensor, such as footswitch). In addition, other studies used only a single accelerometer in the lower back in healthy subjects and older adults with knee osteoarthritis [13, 14].

For people with motor disabilities, such as stroke victims, outpatient gait analysis is an important step in their recovery process, in order to verify if the course of treatment of the patient is being adequate and identify gait parameters that provide an evaluation of the functional use of the affected lower limb. Thus, gait analysis is a way to provide convenient and low-cost rehabilitation monitoring [2]. There are few studies that use an accelerometer to analyze kinematic parameters and, to our knowledge, no studies were found that use accelerometer placed on lower back in stroke individuals. The objective of this study is to verify the possibility of using only one accelerometer to identify kinematic gait parameters in healthy and stroke individuals.

2 Methodology

2.1 Experimental Protocol and Data Acquisition

- First experiment: one biaxial accelerometer (with the y-axis pointing cranially and x-axis pointing anteriorly) was placed on the lateral malleolus of the subjects. Accelerometer data were recorded using an acquisition equipment EMG 830C (EMG System do Brasil Ltda®) with sampling frequency of 1000 Hz.
  Fourteen healthy volunteers were asked to perform gait on a treadmill at 1.0 m/s for 3 min. One stroke volunteer
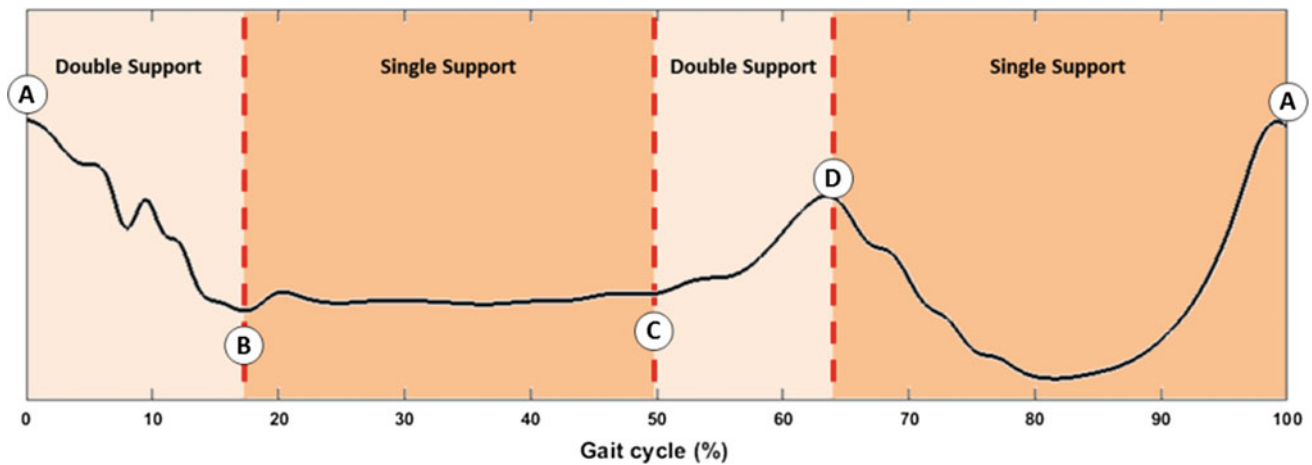
Fig. 2 Curve shape and gait phases obtained using an accelerometer on the ankle. The peaks A and D represent the heel strike and toe-off, respectively. The points B (contralateral toe-off) and C (contralateral heel strike) were obtained by the identification of the points A and D of the other leg. Figure based on [8]

walked on the ground at a comfortable speed for her, 3 times (with 2 min of interval to rest) in a straight line (10 m) without obstacles.

- Second experiment: one biaxial accelerometer was placed on the L2 vertebrae (using an adjustable belt) and the signal was recorded similarly to the first experiment. Five healthy and one stroke volunteers walked on the ground at a comfortable speed for them, 3 times (with 2 min of interval to rest) in a straight line (10 m) without obstacles. In all experiments, the volunteers walked barefoot.

2.2 Volunteers

Fourteen volunteers participated of the first experiment and their characteristics are presented in Table 1. Five volunteers were recruited to the second experiment (Table 2) of this study. As inclusion criteria the individuals should present normal gait. The exclusion criteria were individuals who did not present independent walking or have pain that disturbed the walking.

The stroke subject (female; 48 years old; 165 cm in height; 68 kg in weight; BMI = 24.9 kg/m^2; eight months after stroke; right side paretic) participated of both experiments. As inclusion criteria, the subject should have had one stroke resulting in hemiparetic gait and walk independently.

The research was previously approved by the Ethical Committee of Federal University of Espirito Santo—UFES/Brazil (CAAE: 64797816.7.0000.5542), and all the volunteers signed the Free and Informed Consent Form.

2.3 Data Analysis

- First experiment: the vector module of the x and y axis of the accelerometer was calculated and used to divide the gait cycle in two phases: stance (when the foot was touching the ground and sustaining the body weight) and swing phase (when there was not the foot support and the limb advances). At least 30 cycles of each volunteer were acquired. The results were presented as mean and standard deviation (σ), followed by coefficient of variation (CV), which is calculated as (σ/mean) $\times$ 100, and shows the extent of variation in relation to the mean of the sample. Samples with CV values lower than 15% are considered to have low dispersion, from 15 to 30% moderate dispersion and higher than 30% high dispersion.
- Second experiment: the accelerometer signal was submitted to the same processing in the first experiment. However, in this case it was possible identify five points (see Fig. 4): the positive peak "a" indicates the right initial contact, the positive peak "b" indicates the left one, and the positive peak "c" indicates the right initial contact again, which completes the stride cycle. The negative peak "d" indicates the left toe-off (removal of toes on the ground) and the negative peak "e" indicates the right one. The times "a"–"d" and "b"–"e" indicate double support, and the times "d"–"b" and "e"–"c" indicate single support.

From the collected acceleration signals, the following typical spatial-temporal gait parameters were obtained: speed (m/s), cadence (strides/min), stride length (m), gait

Table 1 First experiment—volunteers' characteristics (M: male; F: female; BMI: body mass index)

Volunteer	Gender	Weight (kg)	Height (cm)	Age (years)	BMI (kg/m^2)
P1	M	85	187	26	24.3
P2	M	95	178	31	29.9
P3	F	65	170	22	22.5
P4	M	65	172	25	22.4
P5	M	66	163	30	24.8
P6	M	73	184	37	21.6
P7	M	90	171	26	30.8
P8	F	56	160	33	21.8
P9	F	46	158	31	18.4
P10	F	57	163	25	21.5
P11	M	70	183	26	20.9
P12	F	58	156	29	23.8
P13	F	46	150	34	20.4
P14	M	73	170	27	25.3
Mean $\pm$ σ	8 M/6F	68 $\pm$ 15	169 $\pm$ 11	29 $\pm$ 4	23.5 $\pm$ 3.5

Table 2 Second experiment—volunteers' characteristics

	Age (years)	Gender	Height (cm)	Weight (kg)	BMI (kg/m^2)
V1	26	F	165	57	20.9
V2	22	F	167	67	24.0
V3	24	M	163	62	23.3
V4	30	M	173	76	25.4
V5	29	M	178	60	18.9
Mean $\pm$ σ	26 $\pm$ 3	3 M/2F	169 $\pm$ 6	64 $\pm$ 7	22.5 $\pm$ 2.6

cycle duration (s), stance phase duration (% of the gait cycle), swing phase duration (% of the gait cycle), double support duration (% of the gait cycle), and single support duration (% of the gait cycle), duration of the phase in which only one foot is in stance position.

3 Results and Discussion

Fourteen subjects participated of the first experiments, using an accelerometer on the ankle. By analyzing the signal peaks, it is possible to identify two gait phases: stance phase and swing. The identification of these phases is important to know how much each lower limb contributes to support the body weight, and, consequently, verify the gait symmetry. In this case, it would be necessary to use an accelerometer on each ankle (right and left).

Figure 3 shows the average curves and percentages of the stance phase (toe-off time) for each participant. The overall average of the stance phase was 60.93%, as expected for healthy gait based on literature [3, 15]. The average toe-off and the CV was calculated (toe-off mean for all volunteers: 60.93% $\pm$ 1.52; and CV = 2.56%), and the variation from the mean had a low dispersion (below 3%). In addition, the characteristic peaks were easily identifiable and presented low variation.

For the second experiment, five subjects walked at different speeds (the most comfortable to each one) using the accelerometer on the L2 vertebrae. Spatio-temporal parameters were calculated (Table 3) showing the contribution of each lower limb during the mean gait cycle, stance and swing phase of each leg, and double and single support (Fig. 4).

Using this sensor placement, it is possible to analyze both lower limbs simultaneously, identifying stance and swing phase, from which it is possible to obtain information on double and single support, as well as symmetry. In the hemiparetic gait of post-stroke individuals, an important parameter that indicates gait improvement is the reduction of asymmetry. For these individuals, the gait analysis using
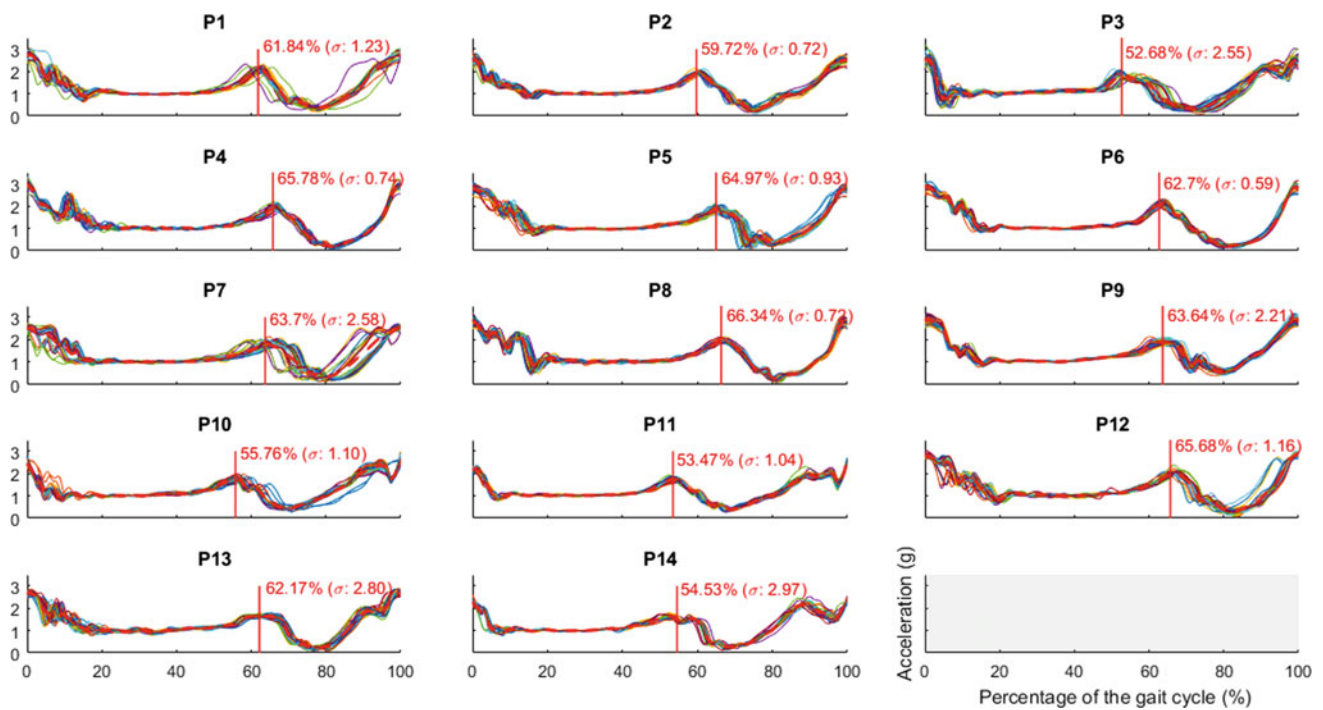
Fig. 3 Average curves and toe-off for each volunteer individually during the first experiment

Table 3 Mean of spatio-temporal parameters from all 5 volunteers in the second experiment

Parameters	Mean	σ	Measurement unity
Speed	0.99	0.10	m/s
Cadence	46.99	2.54	strides/min
Stride length	1.28	0.13	m
Gait cycle duration	1.28	0.07	s
Stance phase duration [% of gait cycle]	62.04	1.50	%
Left stance duration [% of gait cycle]	*62.10*	*1.40*	%
Right stance duration [% of gait cycle]	*61.97*	*1.64*	%
Swing phase duration [% of gait cycle]	37.96	1.50	%
Left swing duration [% of gait cycle]	*37.90*	*1.43*	%
Right swing duration [% of gait cycle]	*38.03*	*1.67*	%
Double support duration [% of gait cycle]	24.08	2.26	%
Single support duration [% of gait cycle]	75.92	2.27	%

only one sensor would be done on the lower back, making the analysis more practical and allowing the analysis of both legs at the same time.

Figure 5 presents the graphic obtained in both experiments for the stroke individual, and Table 4 shows the kinematic parameters from these tests.

In the first experiment, the accelerometer was placed on the ankle of the right leg (paretic side). We can compare the stance phase duration of the right side obtained in first and second experiments (61.73% ± 3.83 and 61.74% ± 0.96, respectively), which were very similar. The stance phase of left leg has higher duration (67.50% ± 2.69), which is expected because the non-paretic side needs to provide more support during stance phase. Furthermore, it can be observed higher duration of double support in the stroke gait (29.24% ± 1.95) than healthy gait (24.08% ± 2.26), results that are in accordance with the literature. Using the accelerometer in lower back, it was possible to analyze both right and left sides, verifying asymmetry and acquiring information about double and single support.
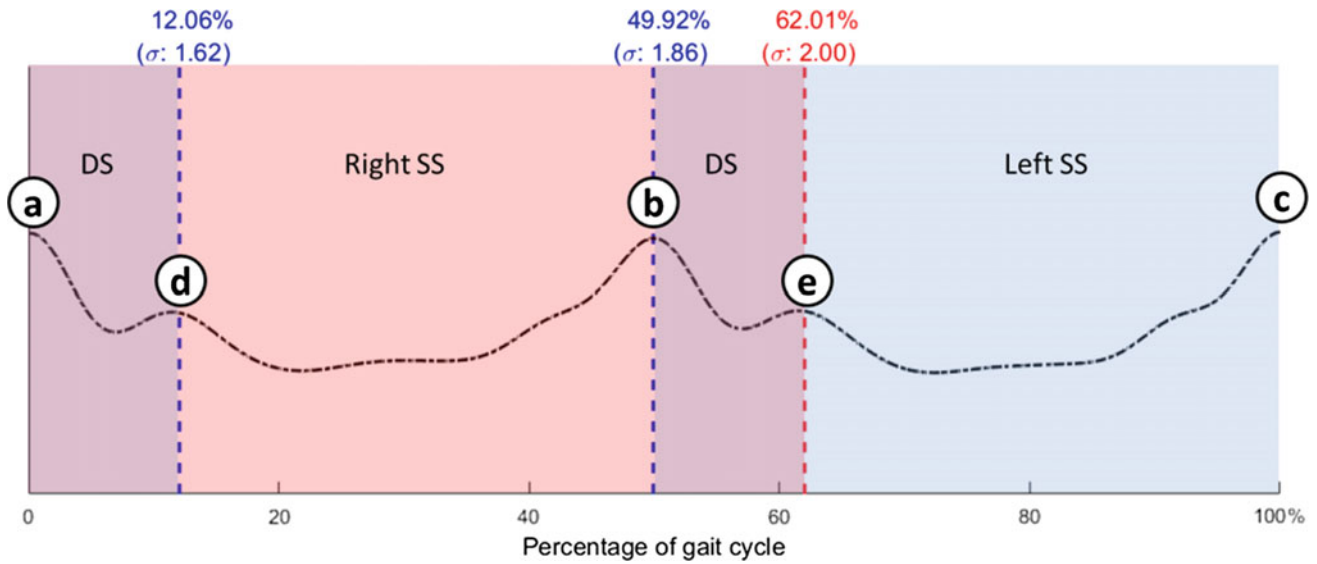
Fig. 4 Mean of the gait cycle from all 5 volunteers in the second experiment. The points a, b and c indicate the initial contact of the feet, and the points d and e indicate the toe-off. The red rectangle indicated the stance phase of the right leg and the blue one indicated the stance phase of the left leg. SS: Single support; DS: double support (Color figure online)
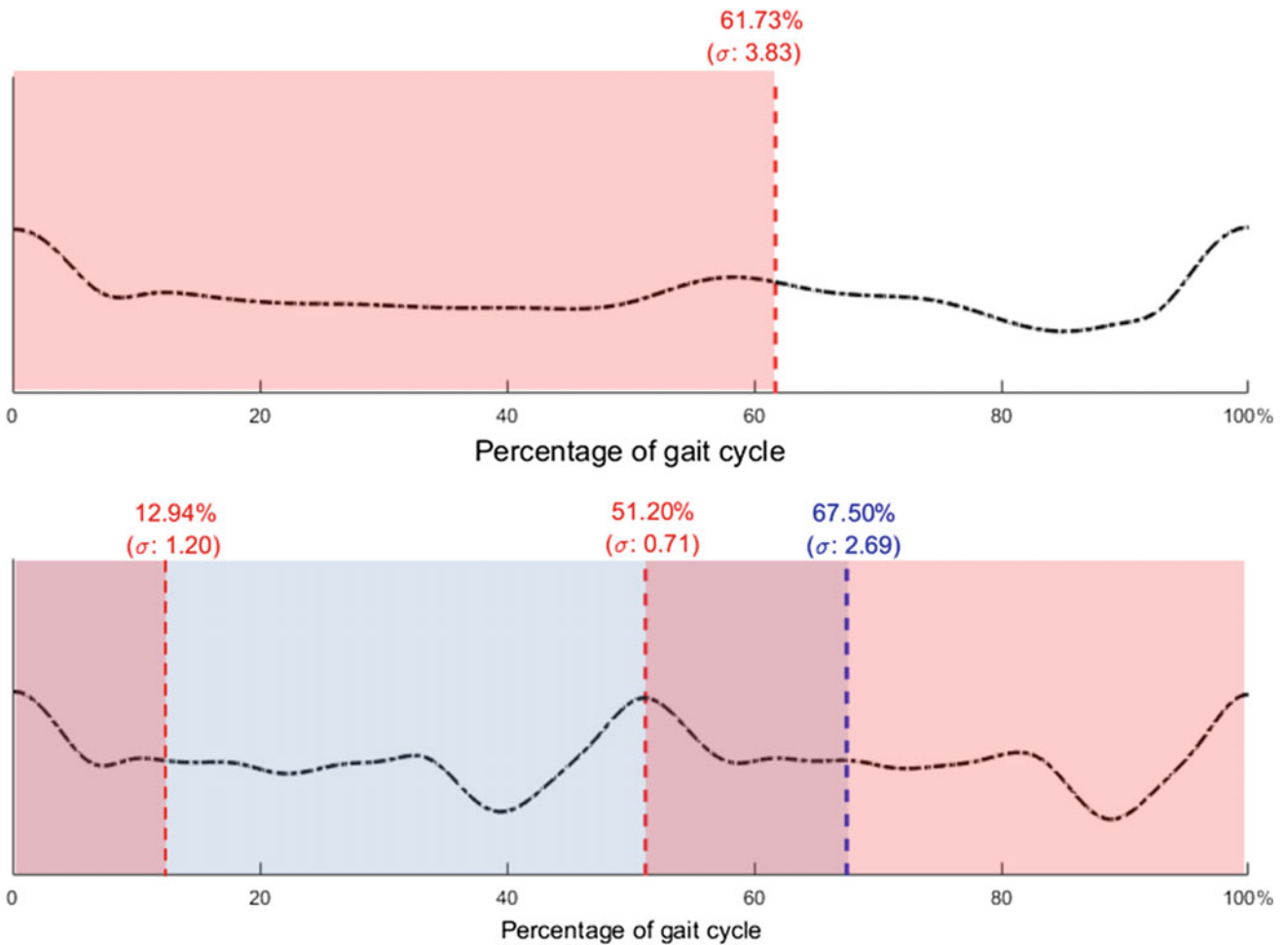
Fig. 5 Mean gait cycle from the stroke individual. The top graph shows the cycle obtained with the accelerometer positioned on the ankle, while the bottom graphic was obtained with the accelerometer positioned on the lower back. The red rectangle indicates the stance phase of the right leg (paretic side) (Color figure online)

Table 4 Mean of spatio-temporal parameters from stroke individual comparing both first and second experiments

Parameters	Accelerometer on the ankle		Accelerometer on the L2		
	Mean	σ	Mean	σ	Unity
Speed	0.46	0.01	0.47	0.03	m/s
Cadence	31.39	1.36	29.09	0.79	strides/min
Stride length	0.88	0.04	0.87	0.25	m
Gait cycle duration	1.91	0.08	1.98	0.06	s
Stance phase duration [% of gait cycle]	–	–	64.62	1.53	%
Left stance duration [% of gait cycle]	–	–	67.50	2.69	%
Right stance duration [% of gait cycle]	*61.73*	*3.83*	*61.74*	*0.96*	%
Swing phase duration [% of gait cycle]	–	–	35.38	1.83	%
Left swing duration [% of gait cycle]	–	–	*32.50*	*2.69*	%
Right swing duration [% of gait cycle]	*38.27*	*3.83*	*38.26*	*0.96*	%
Double support duration [% of gait cycle]	–	–	29.24	1.95	%
Single support duration [% of gait cycle]	–	–	70.76	1.95	%

4 Conclusions

Gait analysis has been used in clinical trials to investigate characteristics of the pathological gait and to evaluate the gait patterns improvement during rehabilitation monitoring. Therefore, portable, small, easy-to-handle, and small-number sensors facilitate the signal capture process in patients.

Both accelerometer placement (on the ankle and lower back) can be used to identify some kinematic parameters of the gait. On the ankle, it is possible identify peaks, which indicate heel strike (initial contact) and toe-off (pre-swing) of one leg, dividing the gait in two phases. On the lower back, data about heel strike and toe-off of both legs can be obtained. Therefore the second placement provides more information, using the same type of sensor and processing. Some pathologic gaits present kinematic parameters asymmetry, which need having both lower limbs analyzed. Thus, the accelerometer can be a practical alternative to healthy and stroke gait analysis in clinical environment.

References

1. Mishra, A.K., Srivastava, A., Tewari, R.P., Mathur, R.: EMG analysis of lower limb muscles for developing robotic exoskeleton orthotic device. Procedia Eng. **41**, 32–36 (2012)
2. Tao, W., Liu, T., Zheng, R., Feng, H.: Gait analysis using wearable sensors. Sensors (Basel) **12**, 2255–2283 (2012)
3. Perry, J., Burnfield, J.M.: Gait Analysis—Normal and Pathological Function, 2nd ed. (2010)
4. Han, J., Seon, Æ.H., Won, J.Æ., Yi, J.: Adaptive windowing for gait phase discrimination in Parkinsonian gait using 3-axis acceleration signals. 1155–1164 (2009)
5. Altun, K., Barshan, B., Tunçel, O.: Comparative study on classifying human activities with miniature inertial and magnetic sensors. Pattern Recognit. (2010)
6. Catalfamo, P., Ghoussayni, S., Ewins, D.: Gait event detection on level ground and incline walking using a rate gyroscope. Sensors (2010)
7. Lima, J.J., Martins, M.R., Okida, S., Stevan, S.L., Schleder, J.C.: Dispositivo para análise dinâmica da marcha humana utilizando sensores inerciais MEMS. Rev. Eng. E Tecnol. **5**, 122–131 (2013)
8. Lee, J.-A., Cho, S.-H., Lee, Y.-J., Yang, H.-K., Lee, J.-W.: Portable activity monitoring system for temporal parameters of gait cycles. J. Med. Syst. **34**, 959–966 (2010)
9. Zijlstra, W., Aminian, K.: Mobility assessment in older people: new possibilities and challenges. Eur. J. Ageing **4**, 3–12 (2007)
10. Khandelwal, S., Wickström, N.: Evaluation of the performance of accelerometer-based gait event detection algorithms in different real-world scenarios using the MAREA gait database. Gait Posture (2017)
11. Boutaayamou, M., Schwartz, C., Stamatakis, J., et al.: Development and validation of an accelerometer-based method for quantifying gait events. Med. Eng. Phys. (2015)
12. Saremi, K., Marehbian, J., Yan, X., Regnaux, J., Elashoff, R., Bussel, B., Dobkin, B.: Reliability and validity of bilateral thigh and foot accelerometry measures of walking in healthy and hemiparetic subjects. Neurorehabil. Neural Repair. **20**, 297–305 (2006)
13. Clermont, C.A., Barden, J.M.: Accelerometer-based determination of gait variability in older adults with knee osteoarthritis. Gait Posture (2016)
14. Godfrey, A., Del Din, S., Barry, G., et al.: Instrumenting gait with an accelerometer: a system and algorithm examination. Med. Eng. Phys. (2015)
15. Whittle, M.W.: Gait Analysis—An Introduction, 4th ed. (2007)

Influence of Knee Abductor Moment on Patellofemoral Joint Stress and Self-reported Pain of Women with Patellofemoral Pain

Marina Waiteman, Bianca Taborda, Ronaldo Briani,
Danilo de Oliveira Silva, Amanda Schenatto, Marcella Pazzinatto,
Fernando Magalhães, and Fabio de Azevedo

Abstract

Increased knee abductor moment (KAM) is thought to be related with elevated patellofemoral joint (PFJ) stress, a major contributor to patellofemoral pain (PFP). Knowing which parameter of the KAM relates with PFJ stress and self-reported pain is important as interventions can vary depending on the altered KAM parameter. This study aimed to compare peak, rate of moment development and impulse of KAM and PFJ stress of women with PFP and pain-free controls during stair descent; and to investigate the relationship among these variables with self-reported pain. Sixty-four women aged 18–35 years were recruited. A three-dimensional motion analysis system with link-segment models and inverse-dynamics equations was used to obtain kinetic data during a stair descent task. A previously reported algorithmic model was used to determine patellofemoral contact force (PCF) and patellofemoral contact pressure (PCP), indicatives of PFJ stress. Self-reported pain was assessed using a visual analogue scale (VAS). Women with PFP presented higher peak, rate of moment development and impulse of the KAM, PCF and PCP during stair descent than pain-free controls, suggesting women with PFP experience higher levels of PFJ stress while descending stairs. Only KAM impulse presented positive moderate correlations with self-reported pain, PCF and PCP. These findings indicate that strategies aimed at decreasing KAM impulse could reduce the load over the PFJ and improve pain of women with PFP.

1 Introduction

Patellofemoral pain (PFP) is a common knee disorder, aggravated by repetitive activities loading the patellofemoral joint (PFJ) such as stair negotiation, squatting and running [1]. PFP has an annual prevalence of 22.7% in the general population [2], from which women are 2.23 times more likely to develop PFP than men [3]. Individuals with PFP present a poor prognosis with 56.7% reporting unfavorable outcomes 5–8 years after treatment [4]. Furthermore, its suggested that PFP can progress to osteoarthritis in the long term [5].

Increased knee abductor moment (KAM) has been proposed as a risk factor to the development of PFP [6]. The KAM is thought to be a measure of lateral knee load distribution and, theoretically, its increase seems to related with the increase in the stress of the lateral facet of the PFJ [7, 8]. Since elevated PFJ stress has been recently proposed as one of the main contributor factors to PFP [9], changes in KAM may be related with PFJ stress and, consequently, with pain symptoms in individuals with PFP. However, no study has been conducted to investigate the relation between KAM parameters with PFJ stress and self-reported pain of individuals with PFP. Knowing which parameter (i.e. peak, rate of moment development or impulse) of the KAM relates the most with PFJ stress and self-reported pain is clinically important as interventions can vary depending on the altered KAM parameter [10–12].

The aims of this study were: (1) to compare KAM parameters (peak, rate of moment development and impulse)

M. Waiteman (✉) · B. Taborda · R. Briani · D. de Oliveira Silva · A. Schenatto · F. de Azevedo
School of Science and Technology, Physical Therapy Department, São Paulo State University, Presidente Prudente, Brazil
e-mail: mariwaiteman@hotmail.com

D. de Oliveira Silva · M. Pazzinatto
La Trobe Sports and Exercise Medicine Research Centre, School of Allied Health, La Trobe University, Bundoora, VIC, Australia

F. Magalhães
School of Arts, Sciences, and Humanities, University of Sao Paulo, Sao Paulo, Brazil

and PFJ stress of women with PFP and sex-matched pain-free controls during stair descent; (2) to investigate the relationship between peak, rate of moment development and impulse of the KAM with PFJ stress and self-reported pain in women with PFP.

2 Methods

2.1 Participants

Sixty-four women aged 18–35 years were recruited via advertisements at universities, public places for physical activity practice, gyms and social media. Participants were divided into two groups: PFP group (n = 32) and pain-free group (n = 32). Prior to data collection, all participants provided written informed consent and the experimental protocol was approved by the Institutional Review Board of the University's Human Ethics Committee (1.484.129).

Diagnosis of PFP was confirmed by a clinician (>five years' experience) based on definitions used in previous studies [13]. The following inclusion criteria for PFP participants were considered: (1) anterior knee pain when performing at least two of the following activities: sitting for prolonged time, squatting, kneeling, running, ascending and descending stairs, jumping and landing; (2) insidious onset symptoms lasting at least 4 months; (3) the worst pain level in the previous month corresponding to at least 3 cm in the visual analogue pain scale (VAS). Women were included in the pain-free group if they had no signs or symptoms of PFP or other neurological or musculoskeletal condition. Exclusion criteria for both PFP and pain-free groups were as follow: sign or symptoms of any other knee dysfunction, history of surgery in any lower limb joint, history of patellar subluxation or clinical evidence of meniscal injury or ligament instability, and referred pain coming from the lumbar spine.

2.2 Instrumentation

Data collection included lower-limb kinetic and kinematic evaluation, during stair descent, of each participant's symptomatic limb (those with unilateral symptoms) or most symptomatic limb (in those with bilateral symptoms) for PFP group, and dominant limb for pain-free group [14]. Kinetic data were collected using a force plate (Bertec Corporation, Columbus, OH, model FP4060) at a sampling frequency of 4000 Hz. A three-dimensional motion analysis system (Vicon Motion Systems Inc. Denver EUA) combined with 9 cameras (type Bonita®B10) operating at a sampling frequency of 100 Hz was used to obtain kinematic data. The force plate and motion system were synchronized by the Vicon Lock® device. The experimental design included a seven step staircase, each step being 28 cm deep and 18 cm high [14]. To ensure a natural stair descent pattern, participants were not made aware of the force plate, which was covered by a rubberized fabric [14].

Participants' worst pain in the last month was evaluated using a 10 cm VAS. Participants drew a perpendicular line on the scale at the position that most likely described their pain. This scale has been validated and it is reliable for assessing women with PFP [13]. Additionally, duration of knee-related symptoms (months) and self-reported knee function (anterior knee pain scale—AKPS) were obtained.

2.3 Procedure

Demographic data were collected prior to testing, including age, body mass, height, length of the lower limbs (distance from the anterior superior iliac spine to the inferior surface of the medial malleolus), width of the ankle and knee joints (through a universal pachymeter −150 to 0.02 mm—Digimess®). Afterwards, the biomechanical model (combination of oxford-foot-model with plug-in gait—PiG to lower limbs) with 29 markers (9 mm of diameter) was positioned by the same investigator in specific anatomic points [15]. Markers placed on the right and left side were: anterior superior iliac spine, posterior superior iliac spine, lateral aspect of the femur, estimated average axis of rotation of the knee joint, lateral aspect of tibia, lateral malleolus, heel posterior face and over the second metatarsal head. Markers placed only on the tested limb were: head of fibula, tibial tuberosity, anterior aspect of the shin, posterior end of the calcaneus, lateral aspect of the calcaneus, sustentaculum tali, base of first metatarsal, head of fifth metatarsal, base of fifth metatarsal and hallux. Medial malleolus, posterior calcaneus proximal and head of first metatarsal were used for static calibration only.

After positioning the markers, a relaxed standing calibration trial was then captured. Then, participants performed three practice stair descent trials to allow familiarization with the instrumentation and environment; the participants were not able to use handrails. Five successful trials were collected for each participant and the mean value of these five trials was used for data analyses in order to attenuate the influence of speed, intra-subject variability, and other external factors [16]. A trial was considered successful when the tested limb touched the fourth step (where force plate was allocated) and the participant had performed the stair descent at their natural comfortable speed [17]. If the trial was not considered valid, an additional trial was performed. Just the kinematic and kinetic data of the fourth step was considered in the analyses.

2.4 Data Analysis

Link-segment models and inverse-dynamics equations were used (Vicon Nexus 2.0® Software) to obtain kinetic data of the lower limbs [16]. For calculations of joint moments, kinetic data was filtered with a fourth-order Butterworth low-pass filter with a cutoff frequency of 12 Hz [16]. The calculation of KAM was performed using the software (Vicon Nexus 2.0® Software). Afterwards, peak, rate of moment development and impulse of the KAM were obtained by custom-written codes in MATLAB® (The Math Works, Inc, Natick, MA). Peak KAM was determined by the maximum value reached during the stance phase and was normalized by the body weight of each participant [6]. The stance phase was defined as time while the foot was in contact with the force plate (fourth step) [14]. The initial and the end of the stance phase were determined when the vertical ground reaction force exceeded 10 N up and down, respectively [14]. The rate of moment development of the KAM was calculated as the change between each point of the KAM and time signals from the foot initial contact until the peak KAM. Then, the change in the KAM was divided by the respective change in time and the mean was calculated [10]. KAM impulse (total area under the curve) was quantified by integrating the moment-time curve, it represents the cumulative twisting load during the entire stance phase [11]. In addition, cadence was calculated based on the time of one entire gait cycle: single leg stance between toe-off of the opposite leg from the fifth step until foot contact on the third step [18].

A previously reported algorithmic model was used to determine patellofemoral contact force (PCF) and patellofemoral contact pressure (PCP) [19], indicatives of PFJ stress. This algorithm has already been used to detect differences in PCF and PCP between individuals with PFP and pain-free controls during stair descent [20]. The detailed description of the algorithm can be found in Appendix.

2.5 Statistics Analysis

All analyses were conducted using Statistical Software for the Social Sciences 18.0 program (SPSS Inc., Chicago, IL). Based on calculations made in sample-power with data from Sinclair et al. [19], a sample size of 28 individuals per group was indicated to evaluate differences in PCP with a statistical power of 85%, observing a minimum difference of 1.31 MPa between means, a standard deviation of 1.36 MPa and a significance level of 5%. PCP was chosen for sample-power calculation because it was the kinetic parameter with the highest standard deviation and the smallest difference between groups [21].

The data were analyzed with respect to their distribution, and homogeneity using the Shapiro-Wilk and Levene's tests, respectively. As all variables were found to be normally distributed, demographics data were compared between groups with independent t-tests. To account for the possible influence of speed on kinetic parameters [17], analyses of covariance were performed to provide between-group comparisons adjusted for the cadence of the participants. The Bonferroni post hoc test was performed for pairwise comparisons. Effect sizes were calculated for pairwise comparisons according to equations previously described, and the guidelines for interpreting the Cohen's d are: 0–0.40 small effect, 0.41–0.70 moderate effect, 0.71 or higher large effect [21]. A Pearson correlation matrix was used to investigate relationships among peak, rate of moment development and impulse of the KAM with the self-reported pain, PCF and PCP in women with PFP. For these analyses, the magnitude of correlation were interpreted as: 0.00–0.25 L or no correlation; 0.25–0.50 fair correlation; 0.50–0.75 moderate to good correlation; and more than 0.75 excellent correlation [22].

3 Results

Independent t-tests revealed no differences between groups for age, height, body mass and BMI (Table 1). Symptoms duration and self-reported knee function of women with PFP are described in Table 1. Also, the results of KAM parameters, PCF and PCF were presented in Table 2 and correlations in Figs. 1 and 2.

4 Discussion

Our findings demonstrated that women with PFP present higher peak, rate of moment development and impulse of the KAM compared to pain-free controls. Moreover, women with PFP presented higher PCF and PCP than pain-free controls, suggesting women with PFP experience higher levels of PFJ stress while descending stairs. Only higher KAM impulse was related with variables indicative of PFJ stress and self-reported pain, that is, the higher the KAM impulse, the higher the PFJ stress and self-reported pain of women with PFP.

Increasingly, studies have been showing important relationship between PFP and knee frontal plane alterations [11, 23, 24] Dynamic KAM has been suggested to contribute to the onset of PFP [23]. A recent prospective study reported that women who demonstrated higher than 15 Nm of KAM during landing may be at increased risk of developing PFP [6]. In accordance with these findings, our results

Table 1 Demographic characteristics of the participants

Variable	PFPG mean (SD)	Pain-free controls mean (SD)	p-value
Age (y)	21.6 (2.9)	21.8 (3.0)	0.88
Height (m)	1.6 (0.5)	1.6 (0.5)	0.71
Body mass (kg)	59.9 (8.8)	60.6 (9.6)	0.74
BMI (kg/m^2)	22.5 (3.7)	23.4 (3.0)	0.82
Worst pain level in the last month (VAS)	5.2 (2.9)	NA	NA
Symptoms duration (months)	58.4 (54.1)	NA	NA
Self-reported function (AKPS)	71.3 (12.5)	NA	NA

Abbreviations PFPG patellofemoral pain group; *SD* standard deviation; *BMI* body mass index; *VAS* visual analogue scale (0–10 cm); *AKPS* anterior knee pain scale (0–100); *NA* not applicable

Table 2 Knee abductor moment parameters and patellofemoral joint stress of women with PFP and pain-free controls during stair descent

Variable	PFPG mean (SD)	Pain-free controls mean (SD)	Mean difference (95% CI)
Peak knee abductor moment (Nm Kg^{-1})	0.57 (0.18)	0.47 (0.15)	0.10 (0.17–0.09)*
Rate of moment development of the knee abductor moment (Nm Kg^{-1}/s)	2.41 (1.7)	1.20 (1.1)	1.21 (1.84–0.45)*
Impulse of the knee abductor moment (Nm Kg^{-1} s)	30.7 (9.0)	22.6 (7.7)	8.1 (12.1–4.01)*
Patellofemoral contact force (N/Kg)	3.84 (2.1)	2.75 (2.0)	1.08 (2.12–0.5)*
Patellofemoral contact pressure (MPa)	12.5 (5.1)	9.2 (3.8)	3.31 (5.50–1.11)*

Abbreviations PFPG patellofemoral pain group; *SD* standard deviation; *CI* confidential interval
*Represents significant differences between groups ($p < 0.05$)
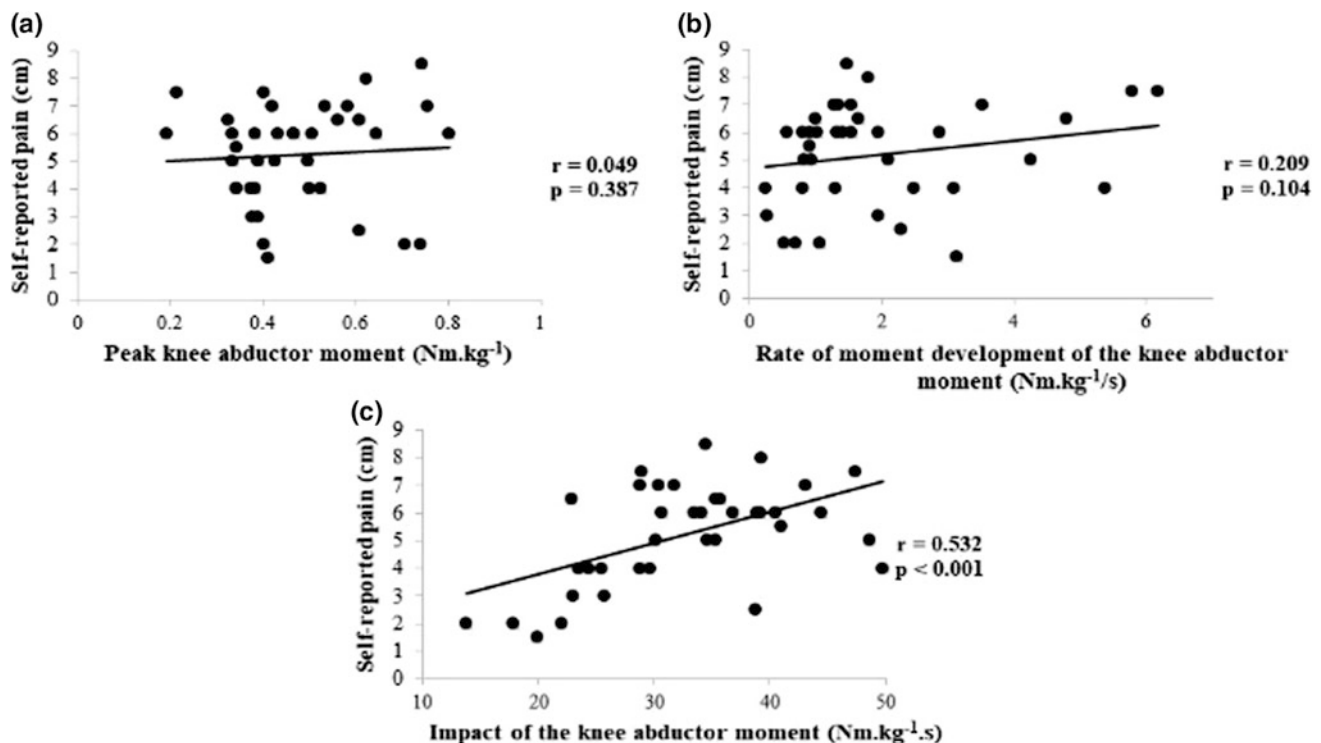
Fig. 1 Correlation between peak, rate of moment development and impulse of the KAM with self-reported pain of women with PFP. *Abbreviations KAM* knee abductor moment; *PFP* patellofemoral pain
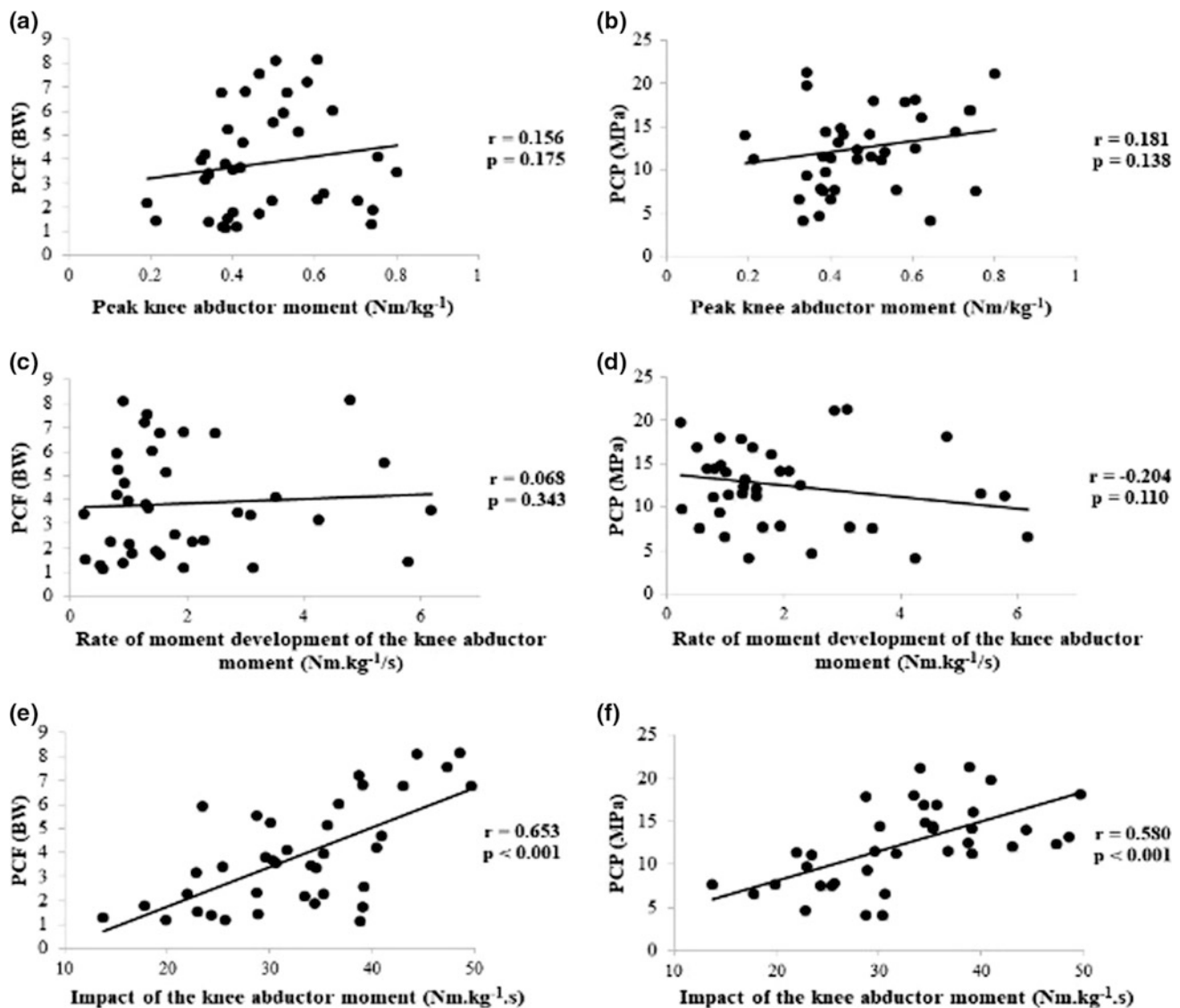
Fig. 2 Correlation between peak, rate of moment development and impulse of the KAM with PCF and PCP of women with PFP. *Abbreviations KAM* knee abductor moment; *PFP* patellofemoral pain; *PCF* patellofemoral contact force; *PCP* patellofemoral contact pressure

demonstrated that women with PFP present higher KAM (peak, rate of moment development and impulse) during stair descent than pain-free controls. Such pattern is particularly important once a previous study [25] reported that a higher than normal abduction moment at the knee joint may be related to progressive degenerative changes at the knee joint. In addition, another study [26] found that the abduction moment during walking was the best predictor of knee joint bone mineral content measured by radiograph absorptiometry. These findings suggest that an increase in the KAM may lead to an increase in knee joint load and may have important implications for the progression of degenerative joint disease [11].

There seems to be a direct relation between tibiofemoral joint kinematics and kinetics with PFJ contact pressures [7].

Studies suggest that a valgus knee orientation and moment may increase the lateral forces acting on the patella, which would be expected to elevate the lateral pressures within the patellofemoral joint [27, 28]. The high knee valgus presented by individuals with PFP during weight-bearing activities [28] influences more lateral transmission of the vector of vertical ground reaction force (VGRF) in relation to the knee joint center, creating a high external KAM [6, 28]. A knee valgus orientation may also reduce the PFJ contact area [29, 30] and increase PFJ stress [28, 30]. In this way, as stress is thought to be the factor responsible for articular cartilage degeneration and wear [31] knowing which parameter (i.e. peak, rate of moment development or impulse) of the KAM relates the most with PFJ stress and self-reported pain is a significant concern in PFP clinical and biomechanical context.

Our results corroborate with the theory that alterations in the frontal plane during dynamic tasks are related with higher PFJ stress [7]. The elevated KAM impulse in women with PFP was positively related with PFJ stress. In a simulated knee valgus position, a 10° change in frontal plane alignment increased the PFJ stress by 45% [27], which supports our findings. As increased PFJ stress has been shown to result in higher subchondral bone strain and pain [32], and our results showed a relationship between KAM impulse and PFJ stress, it is not surprising that the elevated KAM impulse found in women with PFP was also related with higher reports of pain. Interestingly, all parameters of the KAM were higher in women with PFP, but only KAM impulse was related to PFJ stress and self-reported pain. Probably this happened because the impulse represents the cumulative twisting load during the entire stance phase and is more representative of the loading in the knee joint than the other variables [11]. Therefore, treatments aimed at decreasing KAM impulse may have positive effects in managing PFJ stress and pain in women with PFP.

4.1 Clinical Implications

The findings of this study highlight that clinicians should consider interventions aiming to reduce KAM impulse during functional gestures as it is related with PFJ stress and self-reported pain. For instance, flat flexible shoes have also been indicated to minimize increased knee impulse in the frontal plane [33]. In addition to footwear usage, strategies to reduce the knee valgus position and, consequently the KAM impulse and PFJ stress, of women with PFP may be indicated such as general hip abductors and external rotators strengthening, verbal and visual feedback [28]. Strengthening of the knee flexors and extensors may provide balanced co-contraction, compress the joint and potentially limit high KAM impulse during dynamic tasks [6]. Therefore, adequate programs with strengthening, verbal and visual feedback and changes in footwear may be effective in reducing KAM impulse and could be applied in women with PFP, if efficacy is proved in further randomized controlled trials (RCTs).

5 Conclusion

Women with PFP presented higher peak, rate of moment development and impulse of the KAM. Moreover, women with PFP presented higher patellofemoral contact force and patellofemoral contact pressure than pain-free controls, suggesting they experience higher levels of PFJ stress while descending stairs. However, only the KAM impulse was positively correlated with PFJ stress and self-reported pain. Therefore, strategies aimed at decreasing KAM impulse

could be important for reducing the load over the PFJ and improving pain of women with PFP.

Conflict of Interest Statement No author has any financial or personal relationship with people or organizations that could inappropriately influence this work.

Appendix: Algorithm Description for Calculation Patellofemoral Joint Contact Force and Pressure

Patellofemoral joint contact force during stair descent was estimated as a function of knee flexion angle (fa) and knee extensor moment (Em) according to the biomechanical model described by [20]. Firstly, an effective moment arm of the quadriceps muscle (mq) was calculated as a function of knee flexion angle based on cadaveric data presented by [30]:

$$mq = 0.00008fa^3 - 0.013fa^2 + 0.28fa + 0.046 \quad (1)$$

Quadriceps force (QF) was then calculated using the following formula:

$$QF = Em/mq \quad (2)$$

PCF was estimated using the QF and a constant (K):

$$PCF = QF\,K \quad (3)$$

The constant was calculated in relation to the fa using a curve fitting technique described by van Eijden et al. [34]:

$$K = \left(0.462 + 0.00147fa^2 - 0.0000384fa^2\right) / \left(1 - 0.0162fa + 0.000155fa^2 - 0.000000698fa^3\right) \quad (4)$$

PCP (MPa) was calculated as a function of the PCF divided by the patellofemoral contact area. The contact area was described in accordance with Powers et al. [35] who documented patellofemoral contact areas at varying levels of knee flexion (83 mm^2 at 0°, 140 mm^2 at 15°, 227 mm^2 at 30°, 236 mm^2 at 45°, 235 mm^2 at 60°, and 211 mm^2 at 75° of knee flexion).

$$PCP = PCF/contact\ area \quad (5)$$

References

1. Crossley, K.M., et al.: Part 1: Terminology, definitions, clinical examination, natural history, patellofemoral osteoarthritis and

patient-reported outcome. In: 2016 Patellofemoral Pain Consensus Statement from the 4th International Patellofemoral Pain Research Retreat, pp. 839–843. Br. J. Sports Med. Manchester (2016)

2. Smith, B., et al.: Incidence and prevalence of patellofemoral pain: a systematic review and meta-analysis. PLoS One. 13(1) (2018)

3. Boling, M., et al.: Gender differences in the incidence and prevalence of patellofemoral pain syndrome. Scand. J. Med. Sci. Sport. 20, 725–730 (2010)

4. Lankhorst, N.E., et al.: Factors that predict a poor outcome 5–8 years after the diagnosis of patellofemoral pain: a multicentre observational analysis. Br. J. Sports Med. 50, 881–886 (2015)

5. Thomas, M.J., et al.: Anterior knee pain in younger adults as a precursor to subsequent patellofemoral osteoarthritis: a systematic review. BMC Musculoskelet. Disord. 11(201) (2010)

6. Myer, G.D., et al.: High knee abduction moments are common risk factors for patellofemoral pain (PFP) and anterior cruciate ligament (ACL) injury in girls: is PFP itself a predictor for subsequent ACL injury? Br. J. Sports Med. 49, 118–122 (2015)

7. Li, G., et al.: The effect of tibiofemoral joint kinematics on patellofemoral contact pressures under simulated muscle loads. J. Orthop. Res. 22, 801–806 (2004)

8. Scott, S.H., Winter, D.A.: Internal forces of chronic running injury sites. Med. Sci. Sports Exerc. 22, 357–369 (1990)

9. Powers, C.M., et al.: Evidence-based framework for a pathomechanical model of patellofemoral pain. In: 2017 Patellofemoral Pain Consensus Statement from the 4th International Patellofemoral Pain Research Retreat: Part 3, pp. 1713–1723. Br. J. Sports Med., Manchester, UK (2017)

10. Morgenroth, D.C., et al.: The relationship between knee joint loading rate during walking and degenerative changes on magnetic resonance imaging. Clin. Biomech. (Bristol, Avon). 29, 664–670 (2014)

11. Stefanyshyn, D.J., et al.: Knee angular impulse as a predictor of patellofemoral pain in runners. Am. J. Sports Med. 34, 1844–1851 (2006)

12. Atkins, L.T., et al.: Changes in patellofemoral pain resulting from repetitive impact landings are associated with the magnitude and rate of patellofemoral joint loading. Clin. Biomech. 53, 31–36 (2018)

13. Crossley, K.M., et al.: Analysis of outcome measures for persons with patellofemoral pain: which are reliable and valid? Arch. Phys. Med. Rehabil. 85, 815–822 (2004)

14. De Oliveira Silva, D., et al.: Proximal mechanics during stair ascent are more discriminate of females with patellofemoral pain than distal mechanics. Clin. Biomech. 35, 56–61 (2016)

15. De Oliveira Silva, D., et al.: Contribution of altered hip, knee and foot kinematics to dynamic postural impairments in females with patellofemoral pain during stair ascent, Knee. 23, 376–381 (2016)

16. Winter, D.: Biomechanics and Motor Control of Human Movement, 4th ed. New Jersey (2009)

17. Jordan, K., et al.: Walking speed influences on gait cycle variability. Gait Posture 26, 128–134 (2007)

18. Bonacci, J., et al.: The influence of cadence and shoes on patellofemoral joint kinetics in runners with patellofemoral pain. J. Sci. Med., Sport (2017)

19. Sinclair, J., et al.: Sex differences in knee loading in recreational runners. J. Biomech. 48, 2171–2175 (2015)

20. Brechter, J.H., et al.: Patellofemoral joint stress during stair ascent and descent in persons with and without patellofemoral pain. Gait Posture 16, 115–123 (2002)

21. Field, A.: Discovering statistics using IBM SPSS statistics. Sage, London (2013)

22. Portney, L., et al.: Foundations of clinical research: applications to practice. Pearson Prentice Hall, New Jersey (2009)

23. Myer, G.D., et al.: The incidence and potential pathomechanics of patellofemoral pain in female athletes. Clin. Biomech. 25, 700–707 (2010)

24. Sakaguchi, M., et al.: Hip rotation angle is associated with frontal plane knee joint mechanics during running. Gait Posture 41, 557–561 (2015)

25. Andriacchi, T.: Functional analysis of pre and post-knee surgery: total knee arthroplasty and ACL reconstruction. J. Biomech. Eng. 115, 575–581 (1993)

26. Hurwitz, D.E., et al.: Dynamic knee loads during gait predict proximal tibial bone distribution. J. Biomech. 31, 423–430 (1998)

27. Huberti, H.H., et al.: Patellofemoral contact pressures: the influence of Q-angle and tendofemoral contact. J. Bone Jt. Surg. 66, 715–724 (1984)

28. Powers, C.M.: The influence of abnormal hip mechanics on knee injury: a biomechanical perspective. J. Orthop. Sports Phys. Ther. 40, 42–51 (2010)

29. Liao, T.-C., et al.: Runners with patellofemoral pain exhibit greater peak patella cartilage stress compared to pain-free runners. J. Appl. Biomech. 27, 1–26 (2018)

30. Davis, I., et al.: A tale of two treatments for patellofemoral pain. PM & R 9, 1283–1289 (2017)

31. Maquet, P.: Mechanics and osteoarthritis of the patellofemoral joint. Clin. Orthop. Relat. Res. 144, 70–73 (1979)

32. Ho, K.Y., et al.: Comparison of patella bone strain between females with and without patellofemoral pain: a finite element analysis study. J. Biomech. 47, 230–236 (2014)

33. Paterson, K.L., et al.: Effects of footwear on the knee adduction moment in medial knee osteoarthritis: classification criteria for flat flexible vs stable supportive shoes. Osteoarthr. Cartil. 25, 234–241 (2017)

34. van Eijden, T.M., et al.: A mathematical model of the patellofemoral joint. J. Biomech. 19, 219–229 (1986)

35. Powers, C.M., et al.: The effects of axial and multi-plane loading of the extensor mechanism on the patellofemoral joint. Clin. Biomech. 13, 616–624 (1998)

Influence of Visual and Proprioceptive Systems in the Postural Balance of Young Adults

Camille Marques Alves, Eder Manoel Santana, and Eduardo Lázaro Martins Naves

Abstract

The maintenance of postural balance is very important for the performance of daily activities. In order to maintain a perfect integration of the body in space, intrinsic factors such as visual and proprioceptive systems, and extrinsic factors to the individual, are necessary. The absence of the visual system can exert a great influence on the individual body stability. This study identified the possible variables that have statistically differences in postural balance, by subjecting 20 volunteers to open and closed eye tests using a force platform and verified if there are differences in the balance between the genders. The parameters of medial-lateral displacement (cm), anteroposterior displacement (cm), medial lateral displacement velocity (cm/s) and anteroposterior displacement velocity (cm/s) were analyzed. It was concluded that there are statistically significant differences in the anteroposterior velocity when comparing the static equilibrium data of the volunteers in the upright position on the platform under the conditions of open and closed eyes, men also presented greater variability in COP displacement between the two conditions, compared to the women. In this sense, it is possible to identify the importance and influence of the visual and proprioceptive systems in the maintenance of postural balance and the differences between men and women for COP parameters.

Keywords

Balance • Force platform • Eye open • Eye closed • Displacement

1 Introduction

The correct functioning of the visual and proprioceptive systems is very important to guarantee the execution of daily activities [1, 2]. To maintain the equilibrium stable, the ability to control posture without changing the support base is made through the possibility of keeping the center of mass within stability limits [3]. To maintain the postural balance, it is necessary to combine the stimuli coming from the environment with correct response of principal systems to integrate the body with space [4].

For the recognition of the body position is necessary the integrity of the Central Nervous System (CNS), also, to maintain an adequate postural balance, the CNS depends on the afferent information of the visual and proprioceptive systems, which promote the interaction of body with space [5]. The lack or diminution of visual stimuli can generate conflicts with the proprioceptive system causing interference for both locomotion and maintenance of balance [6, 7]. The visual system has great influence on the maintenance of balance, and in its absence can generate events such as imbalance, as well as the loss of sense of location of the individual in the environment [7].

A lot of clinical and laboratory methods have been developed to evaluate the different dimensions of postural control to improve decisions regarding balance deficit and fall prevention [8]. Typically, measurements, like single task performance is often used to evaluates aspects of postural maintenance, however as any single domain measure, critical information about balance could be lost [9]. The parameters of a force platform can reveal with precision the degree of balance deficit associated with biomechanical and neuromuscular control strategies for maintaining the postural balance. Parameters of equilibrium stability such as Center of Pressure (COP) displacements generally used to measure the strategies of balance among different populations [10].

Studies based on healthy populations have been widely used to generate scientific bases of study to aid in the

C. M. Alves (✉) · E. M. Santana · E. L. M. Naves
Federal University of Uberlandia, Uberlandia, MG, Brazil
e-mail: malves.camille@gmail.com

Table 1 Average of weight, height and BMI of all participants		Weight	Height	BMI
	Average	66.055 ± 9.9919	1.707 ± 0.0831	22.675 ± 3.1244

development of new researches with individuals with some involvement [11]. However, even with these results, for [12], there are still many difficulties to interpret these data more closely, since the number of research involving balance with healthy individuals is still relatively low. There is a great need for research in this area involving such population.

Among the postural sway measures yielded from COP, the COP velocity and displacement has been suggested to be most sensitive for detecting changes in balance abilities [13]. In addition, there are few previous studies examining the gender difference in postural stability among young adults, using the parameters velocity and displacement. Thus, the objective of the present study is to verify if there are statistically significant differences for the parameters of displacement and velocity when mapping the stabilometry, for the conditions in which the participant would be in an upright position with the eyes open and eyes closed, and to investigate whether gender influences in COP parameters.

2 Methods

2.1 Participants

To perform the experiments a convenience sample was used, where 20 young people with a 23 ± 3 years age group were selected, which 11 was female and 9 male, all of them were able to perform the task. A questionnaire was applied to obtain information from participants and the role experimental procedure was explained in detail for each subject following ethics approvals by the Ethics Committee of the Federal University of Uberlandia (CAAE 414/10). None of the volunteers has history of lower limb injuries and neuropsychomotor alterations or use controlled drugs that influence in balance. According to this questionnaire, 85% of the participants had right side dominance in the lower limbs, while 15% had left side dominance. Table 1 shows the average values of weight, height and Body Mass Index (BMI) of the volunteers.

2.2 Experimental Procedure

To obtain more assertive results, the questionnaire, applied to volunteers, had important elements to the research, such as measures, calculation of Body Mass Index—BMI (kg/m^2), dominance in the lower limb, history of pathologies, history of physical activities, history of pathologies in some lower limb ligament and use of some type of protection in lower limb joints during physical activity.

A force platform (see Fig. 1), model BIOMEC400 from EMG System® was used for the upright posture analysis. This platform provides the following parameters for analysis: anteroposterior displacement (cm), medial-lateral

Fig. 1 Force platform BIOMEC 400

displacement (cm), anteroposterior displacement velocity (cm/s) and medial-lateral displacement velocity (cm/s). All these parameters were used in future comparisons between the two conditions adopted by the research. The sampling frequency during the experiments was 1000 Hz. Data processing was provided by the force platform software.

During the tasks the participants had to be barefoot and position themselves on the force platform, remaining in the upright posture with their arms along their body. The feet position was standardized throughout the experiment, in both conditions they had to place their feet apart at 25 cm in a marked position on the platform. The balance was recorded for 30 s in two different conditions: bipodal with open eyes and bipodal with closed eyes.

2.3 Data Analyze

The data were filtered and processed by the force platform software, EmgLab. Statistical analysis was performed using Action Stat software version 3.4, where the Shapiro-Wilk normality test was performed, which was verified the non-normality of the data, and then the Wilcoxon test for paired samples to find the significant differences between the parameters in the two conditions.

3 Results

The values of COPx, which represent the mean displacement of the center of pressure antero-posterior was normalized and compared in the two conditions for all participants (see Fig. 2). The coefficient of variation of the COP was analyzed, in order to analyze if its displacement differs between open eyes and closed eyes, Table 2.

The Box-plot was used to represent data of displacement parameters, anteroposterior displacement (cm), medial-lateral displacement (cm), anteroposterior displacement velocity (cm/s), medial-lateral displacement velocity (cm/s) and total area displacement, in eyes open and closed conditions for all participants (Figs. 3 and 4).

To verify the existence of statistically significant differences, a normality test was performed using Shapiro-Wilk, resulting in that most of the data did not follow a normal distribution. Therefore, the paired Wilcoxon test was used for dependent samples. The results can be seen in Table 3, where $p \leq 0.05$ is statistically significant.

Thus, for a level of significance of 5%, there are statistically significant differences for the parameter of antero-posterior displacement. The variability of COP displacement was greater in people of the masculine gender.

Fig. 2 Values of COPx for the two conditions, eyes open and eyes closed
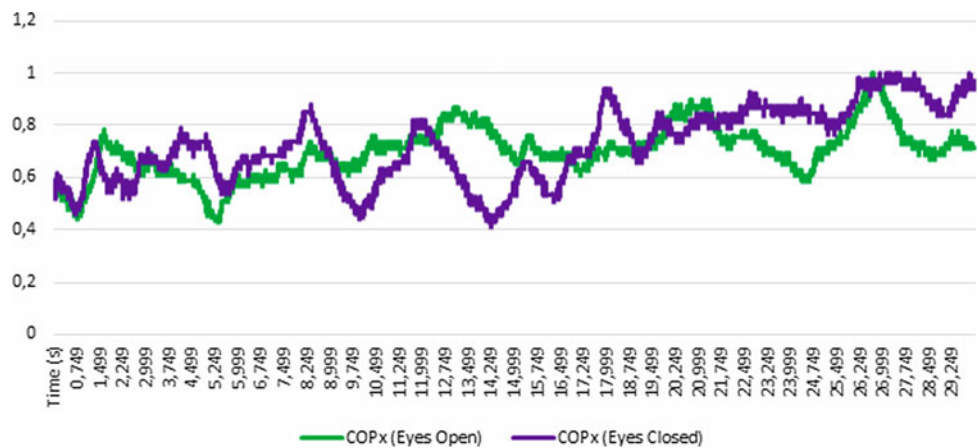
Table 2 Coefficient of variation of COP displacement

	Eyes open (%)	Eyes closed (%)
All participants	35.99	45.33
Female participants	30.13	32.81
Male participants	43.59	61.08

Fig. 3 Box-plot distribution for all parameters in eyes open condition
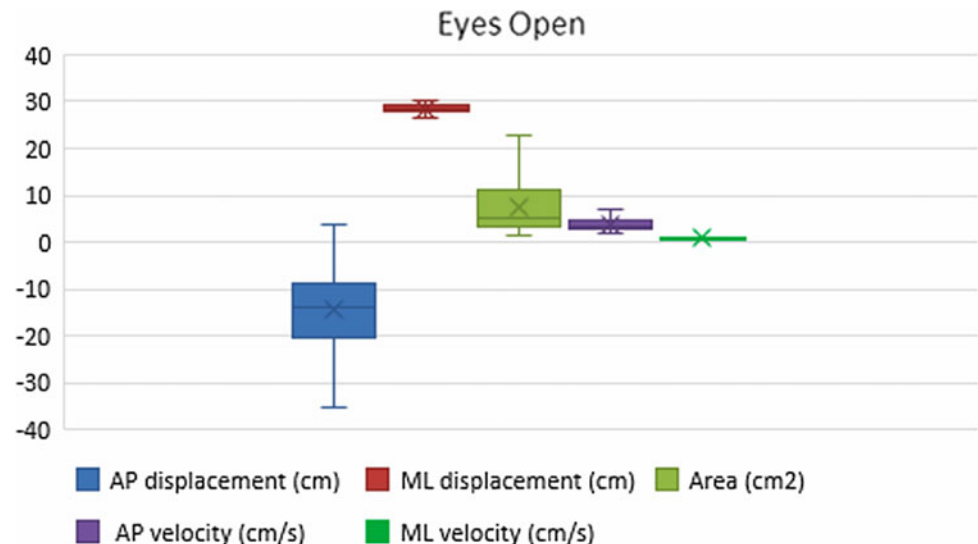
Fig. 4 Box-plot distribution for all parameters in eyes closed condition
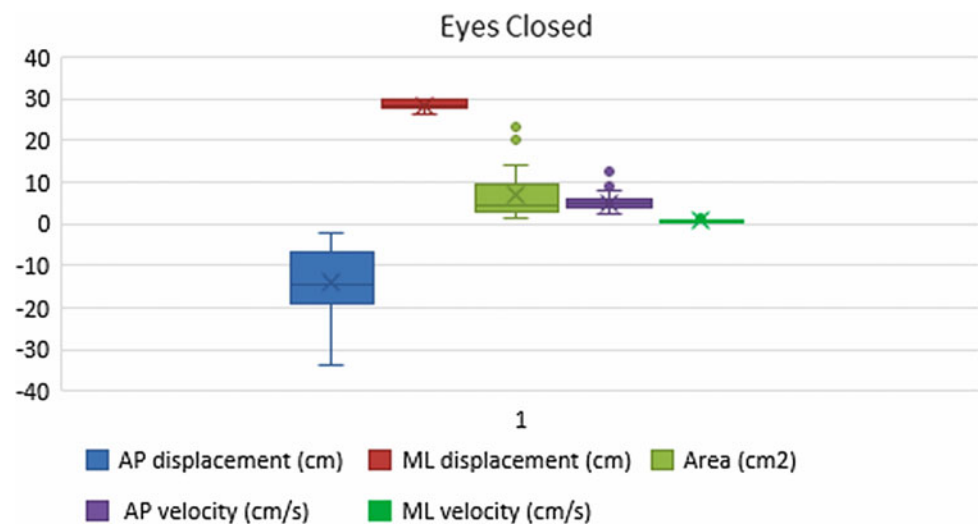
Table 3 *p*-value of analyzed parameters

Parameter	*p*-value
Anteroposterior displacement	0.8983
Medial lateral displacement	0.7228
Anteroposterior velocity	0.0042*
Medial lateral velocity	0.2043

* Statistically significant difference

4 Discussion

The aim of this study was to compare the postural balance of healthy young adults in two conditions, eyes open and eyes closed and to investigate whether gender influences in COP parameters. Analyzing the parameters of anteroposterior and medial lateral displacement and anteroposterior and medial lateral displacement velocity, on a force platform.

A statistically significant difference was found in the anteroposterior displacement velocity. When they were positioned on the platform with their eyes closed, they presented a greater anteroposterior displacement velocity (mean of 5.1 cm/s) than when they had their eyes open (mean of 3.8 cm/s). For [14], at least two of the three sensory systems (visual, vestibular and somatosensory) are necessary to ensure the maintenance of balance. The authors of [14] further state that visual information is a critical factor for balance control.

Analyzing the parameters between the genders it was possible to perceive a greater variability of COP displacement in males. The same was found by [15] where in a study on the effects of gender and physical activity on the postural balance, it was verified that mainly women with closed eyes presented greater anteroposterior displacement velocity. Another study [16] found gender differences in balance tasks, which found better development of female children in tasks which demand high motor coordination and need proprioceptive information.

Although there was no statistical difference in anteroposterior displacement, it was possible to observe that there was a greater displacement in the condition of closed eyes (mean of −14.26 cm), while for the open eyes the mean of anteroposterior displacement was lower (mean of −13.91 cm). The graphic of COPx also shows that was a greater variation for the eyes closed position, when compared to eyes open condition, over time. The same was observed by [17], where blind individuals obtained greater anteroposterior displacement than individuals without visual impairment, and reinforced the hypothesis that vision plays a very important role in controlling balance.

Studies performed by [18] also obtained similar responses, where the anteroposterior displacement velocity and the displacement itself had statistically significant differences between volunteers with their eyes open and closed in the dark. This research has important clinical implications regarding postural balance for rehabilitation, since the variation found in the balance of eyes closed may lead to changes in other motor skills that depend on postural control, such as changes in gait and possible difficulties in the musculoskeletal process of rehabilitation of possible lesions of these young adults.

5   Conclusion

It was concluded that there are statistically significant differences in the velocity of anteroposterior displacement when comparing the static equilibrium of a person standing upright on a force platform with eyes open and closed. Evidencing the importance of the visual system in the maintenance of postural balance in the evaluated group. Differences were also found in the displacement of the COP between genders, there is a trend and evidence in the literature that women have a better equilibrium than men. Future studies will focus on determinate different aspects of postural control and examine its effects on functional balance.

References

1. Duarte, M., Freitas, S.M.: Revision of posturography based on force plate for balance evaluation. Rev. Bras. Fisioter. **14**(3), 183–192 (2010)
2. Samuel, A.J., Solomon, J., Mohan, D.: A critical review on the normal postural control. Physiother. Occup. Ther. J. **8**(2), 71 (2015)
3. da Silva, A., Almeida, G.J., Cassilhas, R.C., Cohen, M., Peccin, M.S., Tufik, S., de Mello, M.T.: Balance, coordination and agility of older individuals submitted to physical resisted exercises practice. Rev. Bras. Med. Esporte **14**(2), 88–93 (2008)
4. Carneiro, J.A.O., Santos-Pontelli, T.E.G., Colafêmina, J.F., Carneiro, A.A.O., Ferriolli, E.: Analysisofstatic postural balance using a 3d electromagnetic system. Braz. J. Otorhinolaryngol. **76**(6), 783–788 (2010)
5. Visser, J.E., Carpenter, M.G., van der Kooij, H., Bloem, B.R.: The clinical utility of posturography. Clin. Neurophysiol. **119**(11), 2424–2436 (2008)
6. Kleiner, A.F.R., De Camargo Schlittler, D.X., Del Rosário Sánchez-Arias, M.: O papel dos sistemas visual, vestibular, somatossensorial e auditivo para o controle postural. Rev. Neurocienc. 349–357 (2011)
7. Gaerlan, M.G.: The role of visual, vestibular, and somatosensory systems in postural balance. Doctoral dissertation, University of Nevada, Las Vegas (2010)
8. Gil, A.W., Oliveira, M.R., Coelho, V.A., Carvalho, C.E., Teixeira, D.C., Silva Jr., R.A.D.: Relationship between force platform and two functional tests for measuring balance in the elderly. Braz. J. Phys. Ther. **15**(6), 429–435 (2011)
9. Persad, C.C., Cook, S., Giordani, B.: Assessing falls in the elderly: should we use simple screening tests or a comprehensive fall risk evaluation? Eur. J. Phys. Rehabil. Med. **46**(2), 249–259 (2010)
10. Nardone, A., Schieppati, M.: The role of instrumental assessment of balance in clinical decision making. Eur. J. Phys. Rehabil. Med. **46**(2), 221–237 (2010)
11. Lessa de Castro, M., Megliorini Godinho, M., Fernandes de Oliveira, L.A., Oliveira Santos, C., CollangeGrecco, L.A., Pasin Neto, H.: Influência de tarefas cognitivas sobre o equilíbrio estático de indivíduos saudáveis. ConScientiae Saúde **15**(2) (2016)
12. Kümmel, J., Kramer, A., Giboin, L.S., Gruber, M.: Specificity of balance training in healthy individuals: a systematic review and meta-analysis. Sports Med. **46**(9), 1261–1271 (2016)
13. Masani, K., et al.: Center of pressure velocity reflects body acceleration rather than body velocity during quiet standing. Gait Posture **39**(3), 946–952 (2014)
14. Simeonov, P., Hsiao, H.: Height, surface firmness, and visual reference effects on balance control. Inj. Prev. **7**(Suppl 1), i50–i53 (2001)
15. Torres, S.F., Reis, J.G., Abreu, D.C.C.D.: Influence of gender and physical exercise on balance of healthy young adults. Fisioter. Mov. **27**(3), 399–406 (2014)

16. Alves, R.F., Rossi, A.G., Pranke, G.I., Lemos, L.F.C.: Influence of gender in postural balance of school age children. Rev. CEFAC **15** (3), 528–537 (2013)
17. Schmid, M., Nardone, A., De Nunzio, A.M., Schmid, M., Schieppati, M.: Equilibrium during static and dynamic tasks in blind subjects: no evidence of cross-modal plasticity. Brain **130**(8), 2097–2107 (2007)
18. Chong, R.K., Gibson, B., Horton, S., Lee, A., Mellinger, J., Lee, K.H.: Spatial orientation during eyes closed versus open in the dark: are they the same? World **2**, 126–132 (2012)

Instrumentation of Pedals of a Road Bicycle as a Proposal for Analysis of Applied Force

Maurício Hüsken and Alexandre Balbinot

Abstract

Cycling has grown as a leisure activity, means of transport and mainly as a professional sport. Therefore, deeper studies and research aiming at maximizing the performance of high-level athletes have been made necessary. Additionally to such studies, the area of instrumentation schemes has developed seeking to make possible the measuring and characterization of several parameters for researchers interested in cycling. Regarding the vibrant surging of systems that allow the measuring of magnitudes such as the force and mechanical power generated by the cyclist, the present research aims at implementing and characterizing the measuring of the forces and mechanical power deriving from pedals and crankset for a road bicycle so as to analyze the results with appropriate statistic methods. The purpose is to compare and verify if that the measurements made on the pedal are equivalent or not to the measurements taken on the crank. Considering the mechanical limitations inherent to the bicycle—the movement of pedals and crankset—independent electrical systems charged by batteries were created, as well as the synchronization for the beginning of acquisitions through *ZigBee* modules. Ten volunteers participated on the practices. They generated twenty sprints of data each. Such data served to statistically evaluate and conclude, based on variance analysis, that the power applied by the cyclists are significantly different for one of the load cell.

Keywords

Load cell • Extensometer • Cycling

M. Hüsken (✉) · A. Balbinot
Electro-Electronic Instrumentation Laboratory (IEE), Electric Engineering Department of Rio Grande do Sul University – UFRGS, 103 Av. Osvaldo Aranha, Bom Fim, CEP: 90031-190, Porto Alegre, RS, Brazil
e-mail: mauricio_husken@hotmail.com

A. Balbinot
e-mail: alexandre.balbinot@ufrgs.com

1 Introduction

Cycling is a sport that has been attracting new adopters for varied reasons. While some use it as a means of transport due to its convenience and/or reduced cost, others practice it for recreational purposes, health, and well-being [1, 2]. The increase in popularity and number of adopters is reflected in the increasing number of professionals seeking for more expressive results, which demand great amount of training and improved strategies. However, since performance is not only associated to the athlete's physical fitness, but also to a better choice of strategy and existent technics, detailed knowledge of technical aspects aiming at searching the highest possible characterization of the movements is necessary [3]. According to [4], there are many ways to measure force, power, cadence, among others. Each of them utilizes a specific location and technology defined by the manufacturers.

Such commercial systems evaluate a specific part of the structure and determine data through absolute values that are then used by their athletes and coaches. Thus, this work aims at measuring data used to calculate force and mechanical power on two main focuses—pedals and crank—and match them in order to verify if they are statistically different. The cranks were machined and instrumented by [5], and the pedals were defined based on commercial models available. The virtual model of the combination pedal-crank was created in the software SolidWorks 2015 as in Fig. 1.

Loads were applied in the lateral directions (a), parallel (b) and perpendicular (c) aiming at defining the point of major mechanic deformation (best location for measure) and realize the cementation of the extensometers. A printed circuit board (PCB) containing the signal conditioning circuit was positioned at the bottom of the pedal. The extensometers are connected to the PCB by wires and the variations of electrical resistance are converted into voltage and amplified.

Fig. 1 Virtualization of the load cell used in the experiments
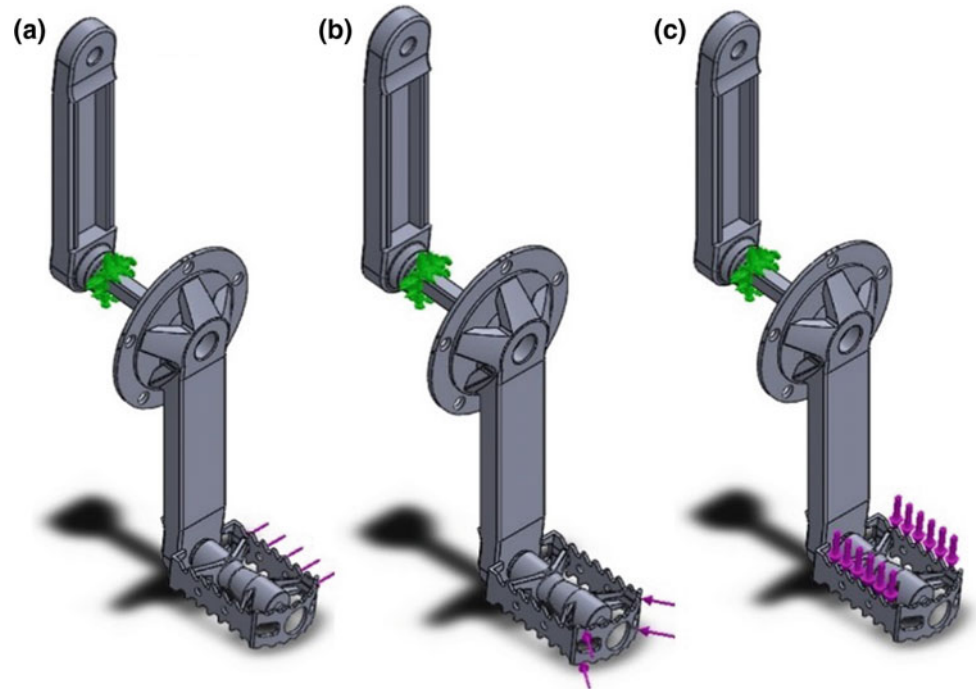
With the circuit positioned at the bottom of the pedal, in a specific case made in ABS, the cyclist is able to pedaling normally through the top face. An acquisition and signal conditioning board designed to be used in the Extensometry Area, model NI 9237, from *National Instruments*, was used in experiments, where 100 samples were collected in a frequency of 1 kHz for each interest point of analysis. After having the load cells done, the calibration was carried out to adjust the scale in relation to the A/D converter. In such case, charges ranging from 0 to 735.75 N in lateral and perpendicular and 0 to 343.35 N in parallel were applied. All of them had a resolution of 49.05 N. At the end of this stage, data were statistically tabulated and evaluated through the Analysis of Variance according to what is suggested in [6–8].

2 Methodology and Hardware Description

2.1 Proposed System

The synchronism to start data collecting is determined by the communication between the ZigBee modules, which received information in broadcast coming from the central module connected to a computer placed at a distance of one meter from the local of training. The commands designed to start and stop the acquisitions of data were managed by a software created in C# language (Visual Studio 2015), which aims at managing and guaranteeing the integrity of transmitted data. The packages are collected and stored in

memory cards each 20 ms (50 Hz) and the statistical analysis is carried out later offline through *software's* Matlab 2013 and Minitab 17. Figure 2 presents the diagram of the proposed system.

A single ZigBee module was used for the crank since the load cells have only one electronic board for processing and store data. Other two ZigBee modules were used for the pedals. The communication between the modules and their respective microcontrollers is carried out through a UART
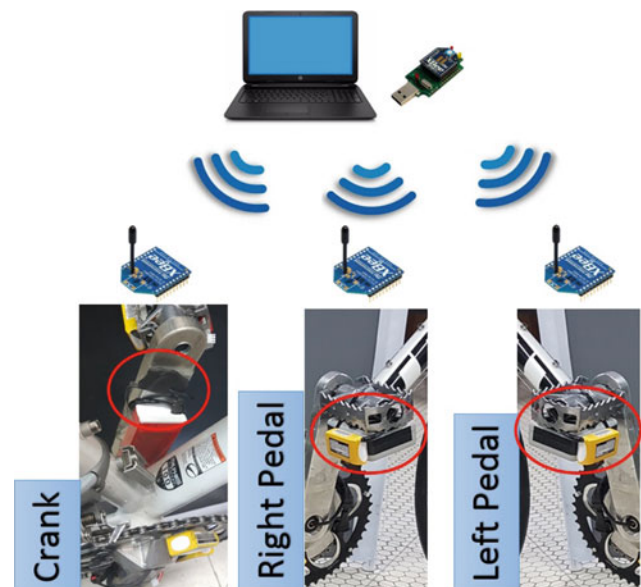
Fig. 2 Diagram of the proposed system
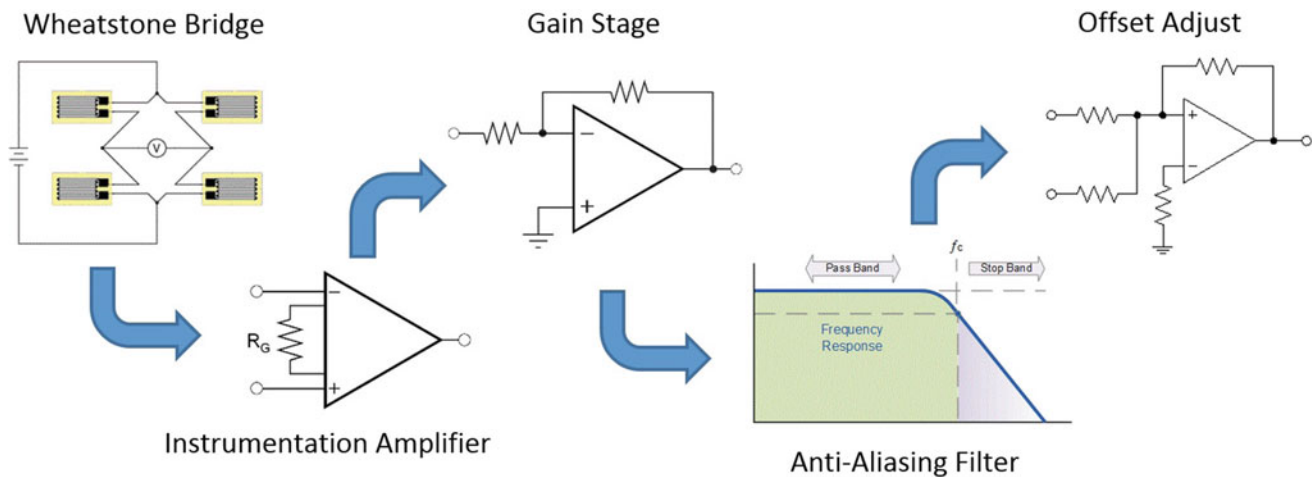
Fig. 3 Block diagram of the conditioning system

(*Universal Asynchronous Receiver-Transmitter*) communication peripheral, which sends bytes of control serially. The *firmware* that manages all the data acquisition process was developed in C language for ARM Cortex M0+ microcontrollers by using Keil µVision5 software whose code is unique and is present in all load cells, including cranks.

2.2 Signal Conditioning Circuits

Four active extensometers (HBM 1-LY13-0.6/120) were used in the Wheatstone bridges to measure mechanic deformation, and 12 extensometers were used in three complete bridges for each pedal. The analog signals were amplified in five stages of gain. Two of them make a fourth-order Butterworth filter [9, 10], which is responsible for eliminating undesirable frequencies above 20 Hz and the fifth stage adds an offset of electrical voltage to adjust entry levels of A/D converter. The power supply of circuits is assured by LiPo rechargeable batteries (two cells, 7.4 V/850 mAh), whose autonomy is estimated in 5 h. Figure 3 presents the block diagram proposed for conditioning circuit.

2.3 Calibration and Experimental Procedure

Before building the bicycle load cells, static calibration procedures were made, which consisted in applications of loads in three axis of interest. Having the extensometers connected to the conditioning circuit and a fixed gain being applied, a fine adjustment was carried out to get the desired amplitude of the electric voltage in relation to the proposed full scale. With the help of a compression machine, loads of 49.05 N ranging from 0 to 735.75 N were applied for lateral and perpendicular axis, and 343.35 N for parallel axis. The

procedure for making the rehearsals considered pedaling in an indoor controlled environment—a laboratory—where the bike was fixed in a training roller with magnetic breaks in such a way that the volunteer would need to put force along all the sprint. Ten healthy amateur volunteers between 28.90 ± 6.21 years old, height 1.79 ± 0.075 m and body mass of 73.40 ± 9.98 kg made 20 sprints each, with 10 repetitions in gear 1 and another 10 in gear 2, taking a minute in each sprint. Data collection were made in a frequency of 50 Hz (period of 20 ms) in a simultaneous way between load cells. Each sprint generated a total of 3001 acquisitions. Figure 4 presents the setup used in the data collection.
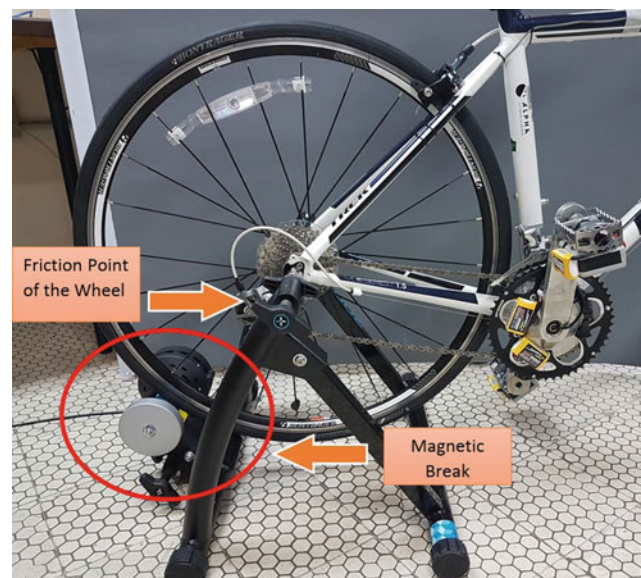
Fig. 4 Block diagram of the conditioning system

2.4 Data Analysis

It was possible to calculate resultant forces for each load cell through the information collected according to Eq. (1).

$$F_R = \sqrt{F_L^2 + F_P^2 + F_{PAR}^2} \qquad (1)$$

where F_R is the resultant force, and F_L, F_P and F_{PAR} presents the components of lateral, perpendicular and parallel forces respectively. In order to calculate power, an applied torque regarding the length of the crank and the cadence of each pedaling cycle was considered according to [5, 10–12] and presented in (2).

$$P = \frac{2\pi}{60} \cdot F_{EFF} \cdot L(m) \cdot CAD(RPM) \qquad (2)$$

where F_{EFF} is the effective force, L is the length of the crank and CAD is the cadence of the pedaling. All these parameters were considered when calculating average values that could be used in response variables in a hypothesis test. Although the best method would have been the Complete Factorial Design, the Sequential Experiment Design was elaborated due to the availability of volunteers and the impossibility to randomize all controllable factors beyond existent limitations in the storage procedures and organization of collected data in memory cards.

Analyzed Factors:	Volunteers	$\rightarrow$ 10 fixed levels (i $= 10$)
	Gear	$\rightarrow$ 02 fixed levels (j $= 2$)
	Load Cell	$\rightarrow$ 04 fixed levels (k $= 4$)
		$nijk = 10$
Response Variables:	Effective Force Resultant Force Mechanical Power	

Hypothesis Test:

H_0: Response Variable is not altered in a significant way by the Analyzed Factor. H_1: Response Variable is altered in a significant way by the Analyzed Factor.

The normality of data was verified through histograms. The Tukey method for Multiple Comparisons was used to assess the occurrence of interactions between the average of factors. These statistic data served as a base to assess the existence or nonexistence of relations between measured data in the cranks with measured data in the pedals.

3 Results

3.1 Analysis of Mechanic Deformation

While the virtual model presented a maximum range of mechanical deformation of 475 $\mu\varepsilon$, the experimental model obtained 425 $\mu\varepsilon$, both in the parallel axis. Results of the same magnitude were found in [13]. The differences between virtual model created and simulated in SolidWorks and the real models can be explained through structural analysis used and the dimensions of load cell which was measured with pachymeter and can add an error.

3.2 Static Calibration of Load Cells

The calibration of load cells was carried out aiming at adjusting the scale according to A/D converter voltage. Figure 5 presents an example of the Linear Regression for the perpendicular axis of left pedal.

The experimental transference functions for remaining axis are presented in Table 1.

As presented in Table 1, the maximum errors of linearity were of 1.56% and 1.12% in perpendicular axis of left and

Fig. 5 Experimental transference function from perpendicular axis to left pedal

Table 1 Load cell output voltage characteristics

Axis	Transference function (mV)	Linearity error (%)
Left pedal—Lateral	y = 2.0425 * load + 1702	0.31
Left pedal—Parallel	y = 2.2822 * load + 1637	0.61
Left pedal—Perpendicular	y = 2.0939 * load + 1680	1.56
Right pedal—Lateral	y = 2.1334 * load + 1616	0.78
Right pedal—Parallel	y = 2.3445 * load + 1600	0.54
Right pedal—Perpendicular	y = 2.1152 * load + 1688	1.12

Fig. 6 Analysis of residues for verifying the use of model for effective force
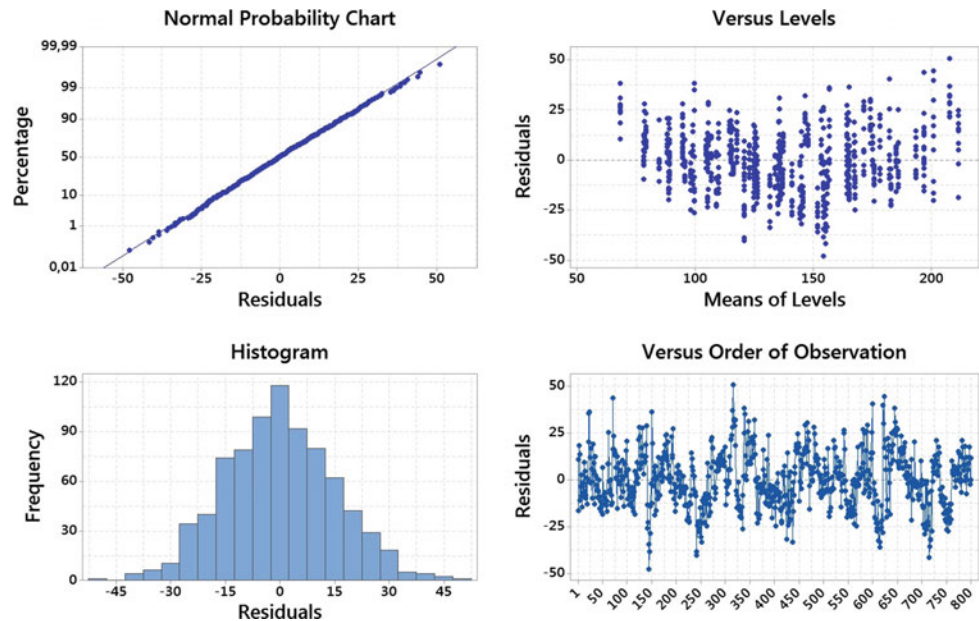
right pedals respectively. This is due to the variability of calibration process that used standard weights positioned with steel cables whose variation directly affects obtained results. The sensibility average was 2.14 mV/N for the left pedal and 2.19 mV/N for the right pedal. Sensibility is how voltage are changing or increase by applied force (in Newton).

3.3 Experimental Evaluation

Experimental evaluation was carried out considering three response variables: c Force; Resultant Force and Power. Evaluations of both residues and the normality of data of Effective Force is presented in Fig. 6.

Through residues analysis and histograms from Fig. 6, the behavior of a normal disturbance was verified for effective force data besides being nonrelated and obvious, i.e. having no apparent structure. Thus, the hypothesis of randomness of errors related to effective force was confirmed, besides the variation to be considered constant for all levels of analyzed factor. The same analysis was considered for Resultant Force and Power since obtained results were similar, i.e. the normality of data and nonrelation between variables. By verifying basic premises, it was possible to carry out Variance Analysis not considering the interaction between analyzed factors as presented in Table 2.

By the analysis of variance, value-p (0.000) provides enough evidence that the effective force applied is different for at least one of the controlled factors in relation to others, when $\alpha = 0.05$, i.e. the effective force depends on the volunteer, the load cell, and the gear. Considering that the three analyzed factors were made in blocks, it is important to mention that interactions between factors were not considered. In order to have a better comprehension of the results, Fig. 7 presents the graphic with the analysis of factors analyzed.

It is noticed by the graphic of main effects that each load cell has a different effective force. Two load cells on the right side of the bicycle had higher average than the effective force of the left side. It is evident that even load cells that are on the same side of the bicycle present significant differences

Table 2 Variance analysis

Analysis of variance—effective force						
Analyzed factors	Degrees of liberty	Quad. sum	Quad. mean	F-value	P-value	Hypothesis
Volunteer	9	260,517	28,946	125.45	0	H1 (Significant)
Load Cell	3	679,714	226,571	981.97	0	H1 (Significant)
Gear	1	23,316	23,316	101.05	0	H1 (Significant)
Error	786	181,354	231			
Total	799	1,144,902				
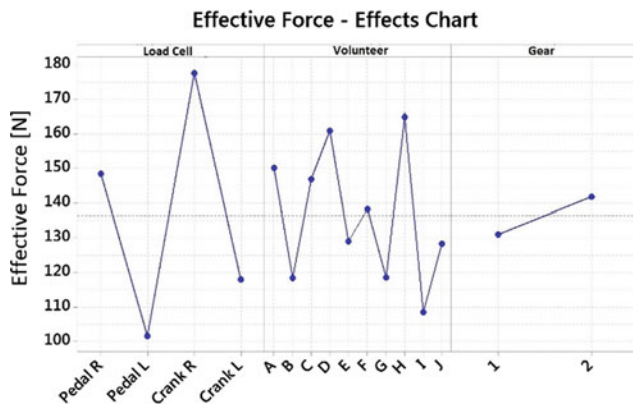
Fig. 7 Analysis of means for effective force

in their forces measured. On average, the cranks present effective forces around 20% higher than the pedals. One of the main causes is linked to the calibration procedure, which requires a distributed positioning of the loads and that can be compared to the force applied by the cyclist during pedaling. Small variations in load position reflect considerable changes in the values measured by the system. The differences between right and left side characterize bilateral asymmetry, which is caused by the way volunteers pedal and distribute force between inferior limbs. The results presented by [5, 14, 15] show that average bilateral asymmetry can reach values up to 60%, which is related to the practice of pedaling and training of each person. Therefore, professional cyclists tend to produce a minor bilateral asymmetry, considering the training for improving movements that directly affects performance. It was also noticed that volunteers applied distinct average forces throughout sprints. Volunteer H applied the highest average force, while Volunteer I applied the lowest average force. Finally, it was also verified that gear also affected significantly the effective force applied. On average, higher module forces were measured in gear 2, which imposes higher friction in pedaling.

References

1. Bini, R.R., Carpes, F.P.: Biomechanics of Cycling, 1st ed. Springer International Publishing (2012)
2. Jensen, S.U.: How to obtain a healthy journey to school. Trans. Res. Part A Policy Pract. **42**(3), 475–486 (2008)
3. Sovndal, S.: Cycling Anatomy. Human Kinetics Publishers, Champaign, IL (2009)
4. Glaskin, M.: Cycling Science: How Rider and Machine Work Together. Ivy Press Limited, United Kingdom (2012)
5. Pigatto, A., Moura, K., Favieiro, G., Balbinot, A.: A new crank arm based load cell, with built-in conditioning circuit and strain gages, to measure the components of the force applied by a cyclist, pp. 1983–1986. IEEE (2016)
6. Sacchetti, M., Lenti, M., Di Palumbo, A.S., Vito, G.D.: Different effect of cadence on cycling efficiency between young and older cyclists. Med. Sci. Sports Exerc. **42**, 2128–2133 (2010)
7. Barratt, P.R., Korff, T., Elmer, S.J., Martin, J.C.: Effect of crank length on joint-specific power during maximal cycling. Med. Sci. Sports Exerc. **43**, 1689–1697 (2011)
8. Casas, V.O., Dalazen, R., Balbinot, A.: Complete factorial design experiment for 3D load cell instrumented crank validation. In: IEEE Engineering in Medicine and Biology Society, Milan, Italy, pp. 3655–3658 (2015)
9. Balbinot, A., Brusamarello, V.J.: Instrumentation and Measurement Fundaments, 2nd edn. LTC, Rio de Janeiro, Brazil (2011)
10. Franco, S.: Design with Operational Amplifiers and Analog Integrated Circuits. McGraw-Hill Educ, NY (2015)
11. Balbinot, A., Lazzari, C.D.: Wireless crankarm dynamometer for cycling. Sens. Trans. J. **128** 39–54 (2011)
12. Balbinot, A., Milani, C., Nascimento, J.S.B.: A new crank arm-based load cell for the 3D analysis of the force applied by a cyclist. Sensors **14**, 22921–22939 (2014)
13. Manolova, A., Crequy, S., Lestriez, P., Debraux, P., Bertucci, W.: Relationship between the pedaling biomechanics and strain of bicycle frame during submaximal tests. Sports **3**(2), 87–102 (2015)
14. Carpes, F.P., Rossato, M., Faria, I.E., Mota, C.B.: During an incremental exercise cyclists improve bilateral pedaling symmetry. Braz. J. Biomotr. **2**(3), 155–159 (2008)
15. Hull, M.L., Neptune, R.R., Smak, W.: The influence of pedaling rate on bilateral asymmetry in cycling. J. Biomech. **32**(9), 899–906 (1999)

Linearization of an OpenSim Arm Model for Feedback Control Design

Wellington Cássio Pinheiro, Maria Claudia F. de Castro, and Luciano L. Menegaldo

Abstract

One of the challenges of Biomechanics science is simulating the physiological or artificial feedback control of human joints. OpenSim is an opensource software package for simulation of musculoskeletal systems and movement analysis that provides highly detailed models suitable for forward dynamics simulations. However, the lack of access to model's Ordinary Differential Equations explicitly hampers the design of feedback controllers based on local linear approximations of system dynamics. System identification techniques can be applied to obtain such linear model approximations and allow model-based control design. This paper aims to apply Recursive Instrumental-Variable Method (IV) as an identification technique to approximate muscle activation and contraction/joint dynamics of the biceps brachialis in an OpenSim arm model. As a result, activation dynamics and contraction/joint dynamics were identified and modeled by transfer function models with 71.91% and 97.35% of accuracy, respectively, to the nonlinear OpenSim model. It was also possible to observe how nonlinear effects should be taken into account when designing the controllers.

Keywords

System identification • Muscle biomechanics • OpenSim

1 Introduction

An undeniably popular approach to better understand a dynamic system behavior is the mathematical modeling. Even though most of the real systems have nonlinear characteristics, a reasonably identified linear time-invariant (LTI) approximation of a system may lead to the design of controllers with a good tradeoff between robustness and performance. OpenSim [1] is a powerful computational environment to model and simulate musculoskeletal systems. However, through OpenSim GUI there is no path to access explicitly the ordinary differential equations which drive the musculoskeletal system model dynamics. The knowledge of system dynamics is essential to design physiological or artificial feedback controllers, such as for Functional Electrical Stimulations, for either isolated human joints or the whole body; system identification techniques may take place filling this gap. For feedback control systems design a linear representation of the system is usually necessary.

To identify a linear model of a system, several approaches are available, such as *Recursive Instrumental-Variable Method* (IV), *Generalized Poisson Moment Functions* (N4SID) or *Subspace State-Space Estimation* (GPMF) [2, 3]. MATLAB System Identification Toolbox [2] presents a user-friendly interface, which permits importing experimental data directly from plant input and output, generate transfer functions to represent system's dynamics, and finally import a different input/output dataset to validate a model. Being those the three necessary steps on identification process [3].

This work aims to present a reliable way to identify a linear representation of an upper limb Arm26 OpenSim model [4] dynamics using classic control theory and MATLAB System Identification Toolbox. This work also aims to serve as first step guide into use OpenSim as a plant for simulation of control strategies applied to assistive technologies and rehabilitation.

W. C. Pinheiro (✉) · L. L. Menegaldo
Biomedical Engineering Department, COPPE, Federal University of Rio de Janeiro, Rio de Janeiro, RJ, Brazil
e-mail: wellington@peb.ufrj.br

M. C. F. de Castro
Electrical Engineering Department, University Center of FEI, São Bernardo do Campo, SP, Brazil

2 Materials and Methods

Firstly, a MATLAB/OpenSim interface routine was adapted from [5]. The interface handles OpenSim model as a plant, and allows the use of MATLAB to manipulate model actuators, simulate inputs and measure states. An OpenSim upper limb model developed by [4] named arm26.osim was used.

Arm26 is a model which comprises *Biceps Brachii Long Head* (BIClong), *Biceps Brachii Short Head* (BICshort), *Brachialis* (BRA), *Triceps Brachii Lateral* (TRIlat), *Triceps Brachii Long Head* (TRIlong), *Triceps Brachii Medial* (TRImed) [4]. For the sake of simplicity, on this paper all muscles other than BIClong were removed. Arm26 model is hereby denoted as plant. Thus, the plant has one actuator (BIClong) and three relevant measurable states: elbow angle (θ) (Fig. 1a), its derivative ($\dot{\theta}$) (Fig. 1b) and muscle activation (a) (Fig. 1b). Model input is the BIClong neuromuscular excitation.

For identification purposes, dynamics were divided as presented in Fig. 1b. Thus, $G_1(s)$ represents muscle activation dynamics, while $G_2(s)$ represents both, muscle contraction dynamics and arm rigid body dynamics.

$$G_1(s) = \frac{a(s)}{u_e(s)} \tag{1}$$

and

$$G_2(s) = \frac{\theta(s)}{a(s)} \tag{2}$$

Next, an excitation (3) was applied to the open-loop plant input to obtain synthetic measurements of a(t) and θ(t). According to [6] to better represent system dynamics, the excitation signal should have a broad spectrum of frequency components. Thus, a square wave was chosen as excitation

signal. The input signal amplitude is relatively small compared to the excitation range (u(t), a(t) $\in$ [0, 1]). This is due of being the target task to keep the elbow angle at 90° with no other load than the arm own weight. Otherwise, the elbow angle would saturate at its maximum physiological range of flexion.

$$u_e = 0.05(1 + \text{square}(2\pi 5t)) \tag{3}$$

After that, u_e(t), a(t) and θ(t) were imported into MATLAB System Identification Toolbox. The option "transfer function model" was selected and the number of poles and zeros were set, looking for the best fit of each dynamics. The algorithm chosen to estimate $G_1(s)$ and $G_2(s)$ was the *IV* method, which is based on Exogeneous Autoregressive modeling (ARX) [3].

After $G_1(s)$ and $G_2(s)$ were estimated, for validation purposes, other excitation (4)–(9) signals were injected into the plant. Then a(t) and θ(t) were measured and stored for the model validation step.

The identified model was validated comparing model and OpenSim plant responses as different parameters on excitation input were varied. First and second (Eqs. 4–5) excitation signals amplitude variations are used to evaluate that. Third and fourth (Eqs. 6–7) excitation signals evaluate deterioration using frequency disturbances. The fifth excitation signal (Eq. 8) is meant to evaluate effects of high frequency on model response deterioration. Sixth excitation (Eq. 9) is a white gaussian noise, represented by N(t), and was add to excitation with SNR = 50 dB to evaluate if model response was robust, in the sense of disturbance rejection.

$$u_e = 0.06(1 + \text{square}(2\pi 5t)) \tag{4}$$

$$u_e = 0.09(1 + \text{square}(2\pi 5t)) \tag{5}$$

$$u_e = 0.05(1 + \text{square}(2\pi 2t)) \tag{6}$$

$$u_e = 0.05(1 + \text{square}(2\pi 12t)) \tag{7}$$

$$u_e = 0.05(1 + \text{square}(2\pi 100t)) \tag{8}$$

$$u_e = 0.05(1 + \text{square}(2\pi 5t)) + N(t) \tag{9}$$

Finally, the validation process consisted of verifying how modeled dynamics performed under excitations (4)–(9) and compare with those measured and stored from the plant. Fitting comparison was based on Eq. (10), known as Normalized Root Mean Squared Error (NRMSE), where y is the plant output measurement, and $\hat{y}$ represents model output measurement, and *norm* represents Euclidean norm operator. Such goodness of fit measurement was used as a system identification quality indicator by [2, 3]. Ease of interpretation and wide use in biomedical engineering modeling [6–9]
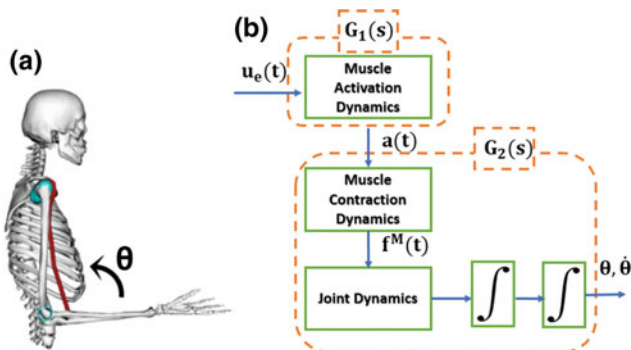
Fig. 1 **a** OpenSim Arm26 model. **b** Segmented system block diagram for identification purposes

were taken into account at NRMSE choice. The fitness percentile may vary between negative infinity and 100, which indicates bad fit and perfect fit respectively. In case of fitness percentile equal to zero, the model does not produce better fit than a straight line equal to the mean of the data [2, 3].

$$\%\text{Fit} = \left[1 - \frac{\text{norm}(y - \hat{y})}{\text{norm}(y - \text{mean}(\hat{y}))}\right] \times 100 \qquad (10)$$

All simulations were performed on a laptop VAIO svf15n26cxb, Windows 10, 8 GB RAM, and an INTEL core i7 processor.

3 Results

The obtained results are presented in following order. First, identified activation and contraction/joint dynamics transfer functions are shown. Secondly, identified activation dynamics is validated and fitness percentile for the validation excitation signal set is presented. Finally, identified contraction/joint dynamics is validated and fitness percentile for the validation excitation signal set is presented as well.

3.1 Activation and Contraction/Joint Dynamics Identification

System identification procedure began by applying to the plant the input $u_e(t)$, according to (3). Simulation was performed using a MATLAB/OpenSim API. The resulting activation $a(t)$ and angular position $\theta(t)$ were recorded and
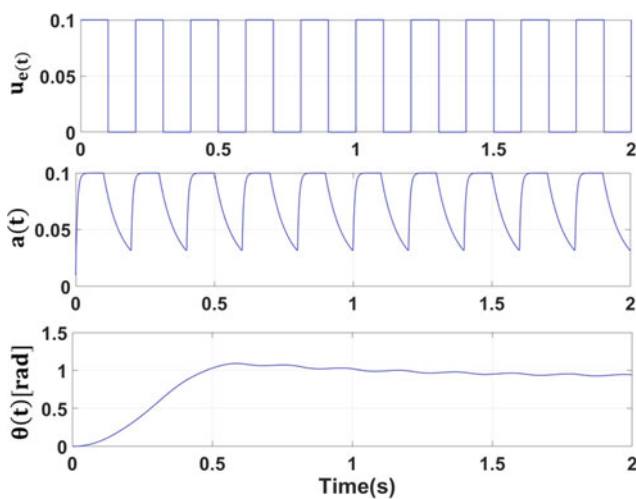
Fig. 2 From top to the bottom excitation signal (Eq. 3) applied to the open-loop OpenSim plant input, normalized activation dynamics virtually measured from plant and contraction/joint dynamics virtually measured from plant as well

regarded as synthetic measurements (Fig. 2), and imported into MATLAB System Identification Toolbox.

Using the IV recursive method, $G_1(s)$ and $G_2(s)$ were estimated as the transfer functions shown in Eqs. (12) and (13). The respective fitting agreement between the plant and identified responses were 71.91% and 97.35%.

$$G_1(s) = \frac{68.88s + 1194}{s^2 + 152.7s + 789.4} \qquad (12)$$

$$G_2(s) = \frac{6046s + 1.539\text{e}04}{s^4 + 16.07s^3 + 175.2 + 775s + 1254} \qquad (13)$$

3.2 Identified Activation Dynamics Validation

To evaluate model accuracy with other inputs than the identification set, excitation signals from Eqs. (4)–(9) were applied to the OpenSim original plant and to $G_1(s)$. The comparison between OpenSim and identified linear model activation results, for the several input signals, are shown in Figs. 3, 4 and 5.

These validation tests permit to evaluate the model under conditions of amplitude variation, frequency variation, and noise contamination. These conditions may be relevant to evaluate the robustness in future feedback control design. Activation dynamics fitting results obtained are presented in Table 1.
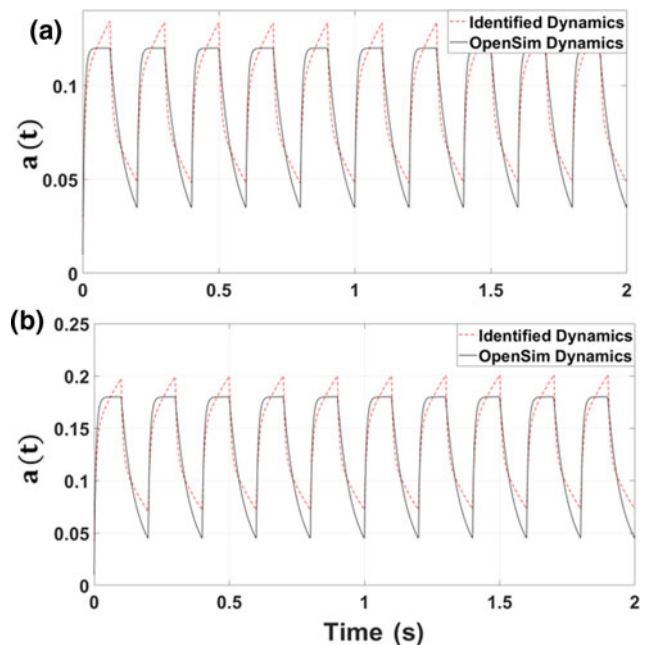
Fig. 3 Comparison of normalized activation dynamics—Excitation amplitude change at same frequency of modeling dataset. **a** Excitation signal follows Eq. 4. **b** Excitation signal follows Eq. 5
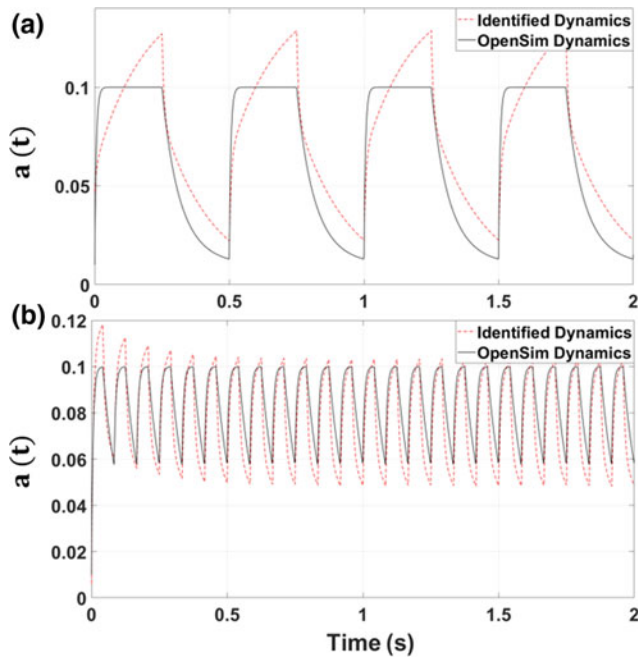
Fig. 4 Comparison of normalized activation dynamics—Excitation frequency change at same amplitude of modeling dataset. **a** Excitation signal follows Eq. 6. **b** Excitation signal follows Eq. 7

Fig. 5 Comparison of normalized activation dynamics. **a** Excitation frequency increased following Eq. 8. **b** Excitation signal with additive Gaussian noise as Eq. 9

3.3 Identified Contraction/Joint Dynamics Validation

A similar procedure was then adopted to the contraction/joint dynamics and its identified linear dynamics $G_2(s)$. The set of excitation signals were inputted on the plant to simulate the six proposed conditions. After that, elbow flexion angle and activation obtained from the plant were stored. Next, activation obtained from the plant was used as input of $G_2(s)$, and its output was compared with elbow flexion angle stored from the plant. Results are presented on Figs. 6, 7 and 8.

The validation of contraction/joint dynamics was also performed and the model fitting parameters (Eq. 10) for different excitations are presented on Table 2.

4 Discussion and Conclusions

On OpenSim, the lack of access to the system's Ordinary Differential Equations explicitly is a natural limitation associated to the complexity of the models and the way they are implemented computationally. The use of physiologically plausible representations, such as Thelen's muscle model, would lead to much harder feedback design due to conditional clauses and nonlinearities present on its dynamics implementation. Therefore, system identification techniques can be useful for designing feedback controllers based on system's model, alternatively to heuristc approaches such as the PID.

Table 1 Fit percentile for different conditions of amplitude, frequency and noise for activation dynamics

# test	Excitation input	%Fit
1	$u_e = 0.06(1 + square(2\pi 5t))$	72.17
2	$u_e = 0.09(1 + square(2\pi 5t))$	70.68
3	$u_e = 0.05(1 + square(2\pi 2t))$	55.08
4	$u_e = 0.05(1 + square(2\pi 12t))$	23.26
5	$u_e = 0.05(1 + square(2\pi 100t))$	−187.6
6	$u_e = 0.05(1 + square(2\pi 5t)) + N(t)$	72.5
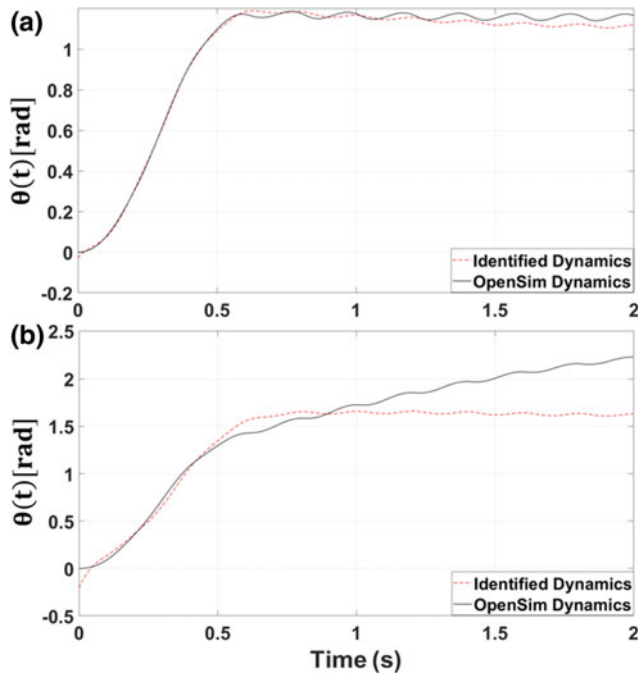
Fig. 6 Comparison of elbow angular dynamics. **a** Small increase on amplitude and same frequency of modeling dataset (Eq. 4). **b** Larger increase on amplitude and same frequency of modeling dataset (Eq. 5)

Fig. 7 Comparison of elbow angular dynamics. **a** Decrease on frequency and same amplitude of the modeling dataset (Eq. 6). **b** Increase on frequency and same amplitude of modeling dataset (Eq. 7)

Regarding activation dynamics, a second order linear model was used to approximate the behavior of a first order nonlinear equation (bilinear equation). Observing the figures and the fitting scores, the identified model does not behave appropriately under large variations on excitation frequency; nonetheless, it behaves robustly to variations on amplitude and to additive noise. Negative fitness percentile indicates poor representation of the identified dynamics; all validation set but one presented highly positive percentiles, indicating good adjustment between OpenSim plant and its identified transfer function. The reason hypothesized for the fitness score to decrease under some validation signals remains on the fact that the identified linear transfer function may impoverish the representation of some frequencies of the spectrum. Also, unmodeled nonlinear dynamics may contribute to fitness diminishment. For designing a feedback controller, these effects must be taken into account.

For the contraction/rigid body dynamics, a linear fourth order model was used to approximate its behavior, which is essentially a 3rd order nonlinear model with states: joint angle, joint velocity and tendon force. Time response and fitting scores suggest that the modelled linear dynamics was most of the time a good approximation to the nonlinear plant. However, contrarily to activation dynamics, it has shown to be more sensitive to amplitude variations, what can be associated to the unmodeled muscular and rigid-body nonlinearities.

As a conclusion, the use of classic feedback control techniques for obtaining physiologically plausible or artificial controllers from linearized models based on OpenSim musculoskeletal models should consider the nonlinearities and its effects on system's response. Although nonlinear controllers can be used to address such issue, they may be harder to design, implement, and computationally expensive when controlling more than one muscle. Therefore, robust control is a promising theory for this and multivariable applications, by treating nonlinearities as plant uncertainties
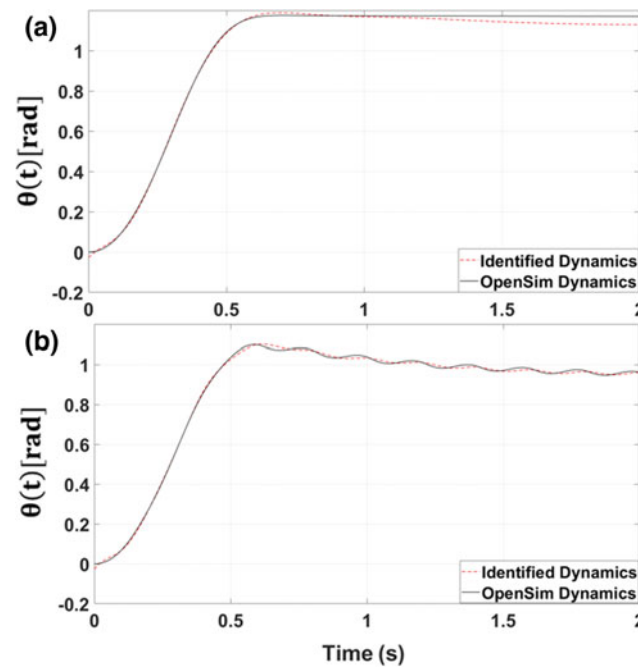
Fig. 8 Comparison of elbow angular dynamics. **a** Extreme increase on frequency of excitation and same amplitude of modeling dataset (Eq. 8). **b** Excitation signal of modeling dataset added to white Gaussian noise with SNR = 50 dB (Eq. 9)

Table 2 Fit percentile for different conditions of amplitude, frequency and noise for contraction/joint dynamics

# test	Excitation input	%Fit
1	$u_e = 0.06(1 + \text{square}(2\pi 5t))$	92.64
2	$u_e = 0.09(1 + \text{square}(2\pi 5t))$	54.72
3	$u_e = 0.05(1 + \text{square}(2\pi 2t))$	53.87
4	$u_e = 0.05(1 + \text{square}(2\pi 12t))$	96.72
5	$u_e = 0.05(1 + \text{square}(2\pi 100t))$	94.15
6	$u_e = 0.05(1 + \text{square}(2\pi 5t)) + N(t)$	97.25

and sectorizing them, as shown in [10], to synthetize a coherent and stable controller.

References

1. Delp, S.L., Anderson, F.C., Arnold, A.S., Loan, P., Habib, A., John, C.T., Guendelman, E., Thelen, D.G.: OpenSim: open-source software to create and analyze dynamic simulations of movement. IEEE Trans. Biomed. Eng. **54**, 1940–1950 (2007). https://doi.org/10.1109/TBME.2007.901024
2. Ljung, L.: System Identification Toolbox™ User's Guide (1220)
3. Ljung, L.: System Identification: Theory for the User. Prentice Hall, Upper Saddle River, NJ (1999)
4. Holzbaur, K.R.S., Murray, W.M., Delp, S.L.: A model of the upper extremity for simulating musculoskeletal surgery and analyzing neuromuscular control. Ann. Biomed. Eng. **33**, 829–840 (2005)
5. Seth, A., Sherman, M., Eastman, P., Delp, S.: Minimal formulation of joint motion for biomechanisms. Nonlinear Dyn. **62**, 291–303 (2010). https://doi.org/10.1007/s11071-010-9717-3
6. Menegaldo, L.L.: Real-time muscle state estimation from EMG signals during isometric contractions using Kalman filters. Biol. Cybern. **111**, 335–346 (2017). https://doi.org/10.1007/s00422-017-0724-z
7. Closed-loop identification of a multivariable dynamic knee rig. https://biblio.ugent.be/publication/6978836
8. Hunt, K.J., Fankhauser, S.E., Saengsuwan, J.: Identification of heart rate dynamics during moderate-to-vigorous treadmill exercise. Biomed. Eng. OnLine. **14** (2015). https://doi.org/10.1186/s12938-015-0112-7
9. Murthy, I.S., Sita, G.: Digital models for arterial pressure and respiratory waveforms. IEEE Trans. Biomed. Eng. **40**, 717–726 (1993)
10. Vidyasagar, M.: Nonlinear Systems Analysis. Prentice Hall (1993)

Monitoring Gait System to Patients with Parkinson's Disease

A. V. M. Inocêncio, E. L. Cavalcante, C. C. B. Souza,
R. J. R. S. Lucena, D. R. R. Freitas, M. G. Coriolano,
I. Gondim, and M. A. B. Rodrigues

Abstract

Gait is a functional task that requires coordination between the major articulations of the body, especially the lower extremity of the human body. The analysis of this activity allows the measurement and evaluation of gait biomechanics, which facilitates the identification of abnormal features and the recommendation of alternative treatments. Parkinson disease (PD) is a neurodegenerative disease, directly resulted from dysfunctions in basal nuclei, located in the brain, and with impact in the automatic motricity control. The use of accelerometers to analyze human gait has grown and set them in various parts of the body can help to identify the phases of the human gait cycle. The main objective of this work was to develop an accelerometry system for gait monitoring in people with Parkinson's disease. We used an equipment developed by the authors to acquire the signal and the data was sent using the Bluetooth protocol for a modular software platform developed for this purpose. Four tri-axial accelerometers were implemented, which also perform the gyroscope function. The data collected correspond to the same patient performing the 10 m distance in three times. The equipment showed robustly in acquiring and exporting the data. Calculations of variables were possible through the use of Matlab® software. After the data analysis, it was possible to map the stance and swing phases, besides calculating important parameters such as average speed, distance travelled, width and height step.

Keywords

Accelerometry • Gait monitoring • Parkinson's disease

A. V. M. Inocêncio (✉) · E. L. Cavalcante · C. C. B. Souza ·
R. J. R. S. Lucena · D. R. R. Freitas · M. G. Coriolano ·
I. Gondim · M. A. B. Rodrigues
Federal University of Pernambuco, Recife, Brazil
e-mail: anavitoriam@gmail.com

1 Introduction

The gait is one of the main abilities of the individual and a natural mechanism characterized by smooth, regular and repetitive movements, with surprising efficiency from the neuro-skeletal-muscle point of view [1].

The gait cycle phases occur from the moment that the foot heel strikes the floor and ends when the same foot heel strikes again. Each lower limb passes through two phases during each cycle: a stance phase and a swing phase. The stance phase is characterized by foot contact with the ground and is responsible for 60% of the overall movement of the cycle. The swing phase occurs from the moment the foot is withdrawn from the ground to the moment the heel touches the ground for the second time. This phase corresponds about 40% of the gait cycle [2].

Gait analysis evaluations are being widely used to identify parameters associated with normal and abnormal gait pattern, as well as to evaluate possible changes after a rehabilitation process [1].

Accelerometers and gyroscopes are used to analyze the movement cycle and possible abnormalities in the gait pattern. Inertial sensors have been popularizing because of his low cost and high resolution. MEMS (Microelectromechanical Systems) technology measures a given magnitude using microelectromechanical systems, processing the data obtained and sending through a communication protocol [3].

Parkinson's disease (PD), the second most common neurodegenerative disorder, was originally described in 1817 by James Parkinson [4]. It is a chronic progressive neurodegenerative disease of the central nervous system, which affects the basal ganglia. It is characterized by the decreasing of dopamine in the nigrostriatal pathway, resulted from the death of black brain neurons. Specifically, the cause is not yet known, but hereditary, infectious, toxic, genetic and environmental factors have been considered [5].

Parkinson's disease is clinically characterized by akinesia, resting tremor, hypertonia, postural reflex disorders and

balance, presenting gait with decreased speed and arm swing and stride length. The gait of people with PD may also present feasting and freezing that usually arise in the attempt to walk, through a curve and through narrow spaces [6]. Festination occurs in an attempt to maintain the gravity center and to prevent falls forward, characterized by the progressive increase in speed and shortening of the step [7].

In this way, the proposed work developed a system for the acquisition and transmission of biomedical data to monitor the locomotion of patients with Parkinson's disease. The parameters evaluated will be time to gait perform the test, width and height step.

2　Materials and Methods

The project aimed to implement a system to monitor gait in people with PD. For the development of this work, was used a NXP development board, capable of acquiring the data from the inertial sensors. The communication protocol implemented was the Bluetooth protocol and a software were developed to display and record the data.

2.1　Development Board

In order to make a portable and low-cost circuit, the NXP Freedom development board FRDM-KL25Z was chosen to the application. This board is capable to arrange the data in packages and send through the Bluetooth® protocol. Free-scale's Freedom development platform features 16-bit analog ports and various power options, such as USB and battery, designed to be a low-cost system. The FRDM-KL25Z hardware has a Cortex MO + processor from the KL2 family of the Kinetis L series.

The board, with the KL25Z128VLK microcontroller, works with a maximum operating frequency of 48 MHz, 128 KB of flash, a USB controller and 16-bits analog to digital converters (A/D). For communication, the card has two 8-bit Serial Peripheral Interface (SPI), Universal Serial Bus (USB), two I2C (Inter-Integrated Circuit) modules, and three Asynchronous Receiver/Transmitter (UART) modules [8].

To communicate with the Human-Computer Interface, it was decided to perform wireless data transmission using the Bluetooth 2.0 protocol. This type of protocol was developed to work with low power consumption and low range, and it can reach up to 50 m depending on the frequency used. In addition, Bluetooth devices work in the ISM (Industrial, Scientific, Medical) frequency range, offer relatively high transmission rates (3 Mbits/s for Bluetooth 2.0), and work

through pairing with devices, enabling secure data transmission.

2.2　Inertial Sensors

For this system, four tri-axial accelerometers were implemented, which also perform the gyroscope function. The position of the inertial sensor modules at strategic points in the body generates signals that represent the necessary parameters for the gait movement analysis in patients with PD, such as length and height steps and velocity. There are already articles in the literature that use commercial systems for gait studies in patients with this disease [9].

The MPU6050 module from InvenSense [5] was used in the development of this system. In a single module there is an accelerometer and a gyroscope, both tri-axial and using MEMS (Microelectromechanical Systems) technology, with 6 degrees of freedom (6 DOF) at all. It has a high resolution because of his 16-bit AD converter and captures the signals for the X, Y, and Z axes simultaneously. In addition, it is a low power device and offers I2C serial communication, reducing the number of wires connected to the device and making the job easier at the time of acquisition.

The inertial sensors need a calibration before the beginning of the acquisition, because there is an offset value attached to the sensor related to the action of the gravity force. This value is very small in the X-axis and in the Y-axis because the gravity axis is perpendicular.

The block diagram of the developed system can be seen in Fig. 1.

2.3　Software Development

The Reability platform [10], in Fig. 1, was developed in Microsoft Visual Studio in the C# programming language. It was make in modules with the aim to simplify its construction and make easy future adjustments. For data plot of the inertial sensors to can be visible and in real time, it was decide only display the accelerometry graphs of the sensors that positioned on the side of each foot. However, the data of the four sensors is record for further analysis.

2.4　Data Collect and Processing

The data collect was performed at the Clinical Hospital of the Federal University of Pernambuco through the project previously authorized by the ethics committee under CAAE 81445817.0.0000.5208. Three samples were collected from
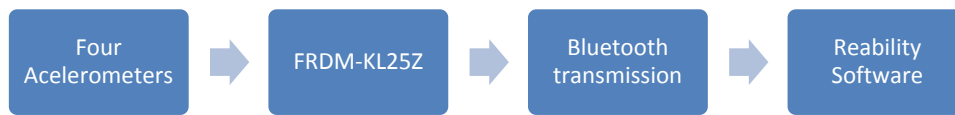
Fig. 1 Block diagram of the project

Fig. 2 Placement of accelerometers

a single patient with a soft degree of PD in March of 2018. The route was 10 m in normal rhythm. The inertial sensors were positioned on the side of the foot (inner face of foot, under medial malleolus) and leg (middle third of the leg) with adhesive tape, as shown in Fig. 2. The positions of the inertial sensors were chosen based in articles in the literature [11, 12]. Tests were executed and the inertial sensors did not bounced. The X-axis corresponds to the direction of the movement; the Z-axis is parallel to the gravity action direction and the Y-axis is perpendicular to the sagittal plan.

After the acquisition of the signals, the data were exported and processed in the Matlab software. From the accelerometry data, the velocity and space data were obtained through the X-axis data. The Z axis of the accelerometer was essential to define the step height. The analysis of the Y-axis presents the imbalances that happened during the progression of the gait.

The distance calculus was made based on the mathematical integration. The velocity is the rate of change of the position of an object and we can obtain the position if a double integration of the acceleration is applied [13]. To avoid noise, a low pass filtering was applied in the signal to remove the noise from electrical and mechanical causes.

3 Results and Discussion

The data were collected through four inertial sensors. The modules situated in the lateral of the feet were more significant to the analysis of the gait phases, because the variation of the inertial sensors were more visible. The accelerometers placed in the lateral of the feet are used to calculate the travelled distance and the step height. Besides that, the Y-axis of this accelerometer show disturbance in the balance of the patient with Parkinson's disease.

The graph in Fig. 3 shows the signal acquired for the accelerometer X-axis placed on the left foot, in which the walking pattern can be perceived. The most significant peaks related to acceleration indicate the swing phase of the gait. The foot is the first point of the body in which the acceleration cancels out with the stance phase.

The step width calculation was done in relation to the relevant peaks of acceleration as seen in the Fig. 2. Velocity and displacement were calculated separately for each step since the integral function is cumulative. However, the foot is stopped during the whole stance phase, that means the speed is annulled in the moment the foot touches the ground.

The average step width, standard deviation, number of steps and total distance travelled were calculated for each of the three samples of the right foot. The results are summarized in Table 1. The average velocity of the walk was 1.6568 m/s for trial 1, 1.822 m/s for trial 2 and 1.837 m/s for the third trial. In this study the average velocity was calculated only measuring total time and distance.

After the step width verification, the patient step height of the patient was calculated. Table 2 summarizes the data for the three samples. This parameter can important when calculated for patients with a higher degree of commitment.
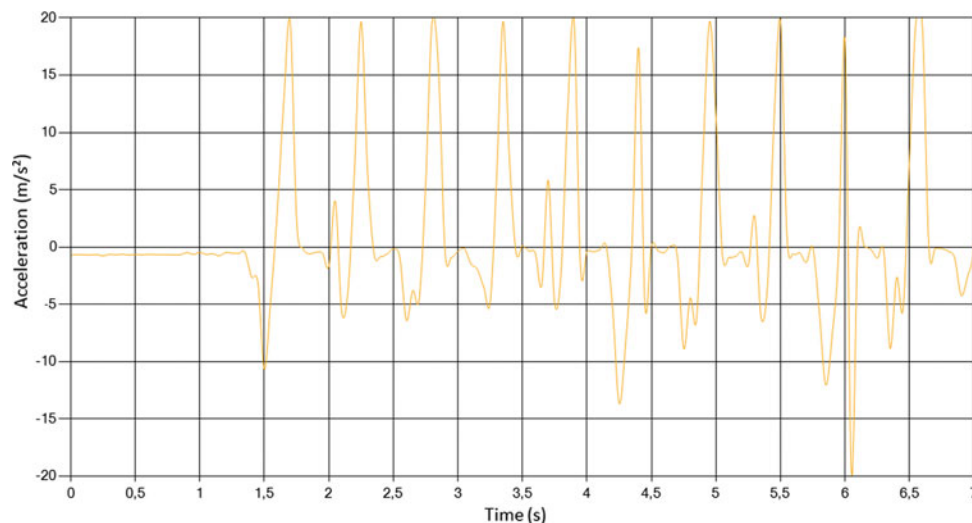
Fig. 3 Accelerometry for the X-axis from the right foot

Table 1 Parameters of the distance the travelled with the left leg

Samples	Traveled distance calculated (m)	Average step width (m)	Standard deviation (m)	Number of steps
Sample 1	9.9408	0.9941	0.3051	10
Sample 2	9.7500	0.8864	0.2342	11
Sample 3	10.3820	1.0382	0.2525	10

Table 2 Data related to the step width

Samples	Height step (mm)	Standard deviation (mm)	Number of steps
Sample 1	27.67	9.11	10
Sample 2	25.84	7.32	11
Sample 3	29.04	8.54	10

A future study with more patients is necessary to evaluate this parameter.

Figure 4 shows the accelerometer Y-axis placed on the left foot. It is possible to notice two abrupt variations, showing that there has been a deviation towards the gait. This graph serves as an indicator for imbalances suffered during the trajectory.

4 Conclusion

The equipment made possible the analysis of gait phases in patients with Parkinson's disease. It was possible to map the stance and swing phases, besides calculating important parameters such as speed and distance travelled. With the support of the video record done simultaneously, the researcher can compare the step width value calculated by the Matlab software with the actual value. The system was also useful in identifying imbalances experienced by the patient through the analysis of the Y-axis.

The system has used components with low cost and purchased in the local market, making feasible for application in studies that requires resolution and have low financial investment. The assembly of the equipment was done in the laboratory by members of the research group in Biomedical Engineering of UFPE. The fact that it was an implementation made by the research group, there is a limitation in relation to the size of the equipment and his layout.

Finally, future implementation of this device and his software in studies on the efficacy of rehabilitation treatment in patients with PD and gait analysis in patients with PD at

Fig. 4 Accelerometer Y-axis of the left foot
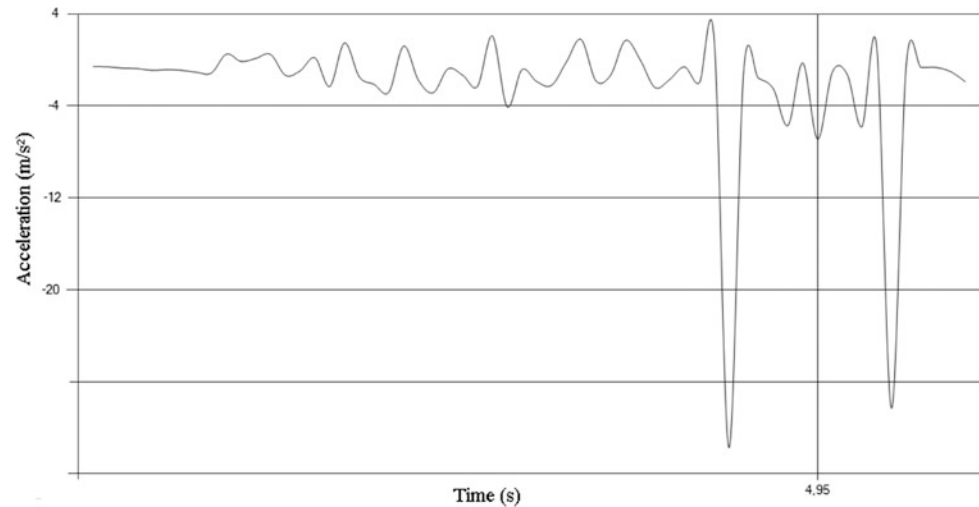
different levels can be performed. Exporting the data in common format archives makes possible his use for offline data processing. As a future challenge, the creation of an application for devices with the Android operating environment would assist in data collection by not using a personal computer or laptop.

References

1. Santos, C.P., Vieira, M.E.M., Sérgio, L., Stevan, J.S.L.: Sensores inerciais aplicados à marcha humana no esporte. In: Seminário de Eletrônica e Automação—SEA 2016. Universidade Tecnológica Federal do Paraná—UTFPR, Curitiba (2016)
2. Sousa, A.S.P.: Análise da Marcha Baseada em Correlação Multifatorial. Master Thesis, Master in Electrical Engineering, Faculdade de Engenharia da Universidade do Porto. Porto (2013)
3. Invensense Homepage. https://store.invensense.com/datasheets/invensense/MPU-6050_DataSheet_V3%204.pdf. Last accessed 01 April 2018
4. Werneck, A.L.S.: Doença de Parkinson: Etiopatogenia, clínica e terapêutica. Revista Hospital Universitário Pedro Ernesto, UERJ. Rio de Janeiro (2010)
5. Mello, M.P.B., Botelho, A.C.G.: Correlação das escalas de avaliação utilizadas na doença de Parkinson com aplicabilidade na fisioterapia. Fisioter. Mov. J. **23**(1), 121–127 (2010)
6. Massano, J.: Doença de Parkinson actualização clínica. Acta Med. Port. **24**(S4), 827–834 (2011)
7. Keus, Sh: Guidelines for physical therapy in patients with Parkinson's disease. Dutch J. Physiother. **114**(3), 1–92 (2004)
8. MBED Homepage. https://os.mbed.com/handbook/mbed-FRDM-KL25Z. Last accessed 03 April 2018
9. Rastegari, E., Marmelat, V., Najjar, L., Bastola, D., Ali, H.H.: Using gait parameters to recognize various stages of Parkinson's disease. In: 2017 IEEE International Conference on Bioinformatics and Biomedicine (BIBM), pp. 1647–1651. Kansas City (2017)
10. Cavalcante, E.L.: Plataforma Dinâmica de Avaliação Fisioterápica. Master Thesis in Electrical Engineering—UFPE. Recife (2015)
11. Haji Ghassemi, N., Hannink, J., Martindale, C.F., et al.: Segmentation of gait sequences in sensor-based movement analysis: a comparison of methods in Parkinson's disease. Sensors (Basel, Switzerland) **18**(1), 145 (2018)
12. Moore, S.T., Yungher, D.A., Morris, T.R., et al.: Autonomous identification of freezing of gait in Parkinson's disease from lower-body segmental accelerometry. J. NeuroEng. Rehabil. 10–19 (2013)
13. Freescale Semiconductor, Inc. Implementing Positioning Algorithms Using Accelerometers. AN3397, 02(0) (2007)

Multivariate Analysis of Determining Factors for Athlete Performances in Judo

F. G. Teixeira, P. T. C. R. Rosa, R. G. T. Mello, and J. Nadal

Abstract

The present study aims at classifying judo athletic levels using multivariate analysis of physical and technical data. A sample of 42 judo athletes from two competitive groups (28 national level and 14 state level) was submitted to the following tests and measurements: (a) skinfold thickness; (b) circumferences; (c) breadths; (d) stabilometric test; (e) Special Judo Fitness test; (f) dynamometry test. Logistic regression (LR) and multilayer perceptron neural network (MLP) were employed to determine variables that best classify the two groups. The classifiers select seven variables and both LR and MLP models presented similar performances with 90.0% and 91.0% accuracy, respectively. These results suggest that a reduced set of biomechanical, anthropometric and physiological variables allow to assess the athletic level of judo players.

Keywords

Logistic regression • Artificial neural network • Judo and physical profile

F. G. Teixeira (✉) · P. T. C. R. Rosa · J. Nadal
Programa de Engenharia Biomédica, COPPE/UFRJ,
Rio de Janeiro, Brazil
e-mail: fegute@peb.ufrj.br

F. G. Teixeira
Laboratório de Biomecânica, Universidade Estácio de Sá,
Rio de Janeiro, Brazil

F. G. Teixeira
Departamento de Lutas, Universidade Castelo Branco,
Rio de Janeiro, Brazil

R. G. T. Mello
Departamento de Educação Física e Esportes (DEFE),
Escola Naval, Rio de Janeiro, Brazil

1 Introduction

The description of the physical profile of athletes is an important tool in the selection of promising athletes. This action is mainly present in the daily life of the coaches who participate in the development of the beginning athletes. To support this process and provide quantitative subsidies for these professionals, some studies have proposed to identify the main biomechanical [1] anthropometric [2] and physiological [3] variables that could directly influence the performance in different sports.

Judo is a combat sport that comprise different athletic profiles, where subjects with different body mass indexes participate in high performance competition into seven weight categories. Regardless of the category, judo athletes aim at achieving the maximum score, Ippon. For this, their success depends directly on the ability to adapt to the high intermittent metabolic demand present in the fight. This physical demand requires the athlete to be able for presenting complex abilities and tactical excellence [4], thus providing greater efficiency in the performance of judo techniques [3, 5], mainly supplied by anaerobic metabolism. However, the aerobic metabolism is essential for a good recovery in the time intervals during and between combat [3].

Two important aspects are related to anaerobic metabolism: (1) the athlete's ability to apply as much force as possible at the right moment, by overturning the opponent, and (2) the ability to maintain the force intensity throughout the combat. One of the main aspects related to this physical quality along the fight is the athlete's ability to apply force when holding the opponent's kimono in order to move and throw. Various authors have investigated the hand grip strength of the judo athlete comparing the dominant and non-dominant hand, and the strength of athletes of different levels [6, 7], as well as analyzing the manual grip strength as a possible predictor of the results in competitions [8]. However, few studies measured the located muscular

resistance in the manual grip for evaluating the maximum strength index [9].

For greater effectiveness in the execution of the techniques, the athlete needs to present postural stability [10]. The ability to maintain and adapt the dynamic balance is paramount for a good performance. In addition, high-level athletes must adapt to the appropriate postures during fight, for improving their ability in maintaining posture and reestablish it after an external or internal disturbance [11, 12].

The performance of the Judo athletes is also associated with their anthropometric profile. Each weight division implies differences between some technical, tactical and physical aspects, which may be directly associated to the athletes' body composition, making it difficult to unify the anthropometric profile for players. However, athletes in each weight category seek to intensify the increase in muscle mass and minimize the fat mass index to gain an advantage over their opponents [13]. In addition, the predominant somatotype among different categories is the mesomorphy, thus suggesting the presence of similarities in the physical pattern [14].

In view of the need to improve athletic performance, the identification of relevant variables among a large set of morphological, physical and technical training characteristics will facilitate the prescription of a more specific training. Franchini et al. [2, 3, 6] have already described the specific physical profile for judo athletes based on anthropometric and physiological assessments of high level fighters, indicating the need of characterizing the main physical qualities and techniques for allocating an athlete at a certain level. However, these studies did not use multivariate methods, which classify and recognize the patterns of these variables, making almost impossible to assess their behavior more accurately. Thus, the present study aims at classifying judo athlete levels using multivariate analysis of physical and technical data.

2 Methods

2.1 Subjects

Participated in this study 42 male judo athletes from two group: Gnational—14 who participate in national level competitions, with age 23 ± 4 years (mean $\pm$ standard deviation), body mass 78.01 ± 15.02 kg and height 1.74 ± 0.07 m; and Gstate—28 of state level, with age 24 ± 4 years (mean $\pm$ standard deviation), body mass 80.41 ± 13.12 kg and height 1.75 ± 0.07 m. All athletes have more than five years of judo practice, with no history of neurological disorders, cardiovascular or orthopedic diseases

in the last seven months. The experimental protocol was approved by the Ethical Human Research Committee of the Federal University of Rio de Janeiro [CAAE—42859115.0.0000.5257], and all subjects were voluntary and signed a free informed consent before inclusion in the study.

2.2 Balance and Anthropometric Assessment

In the first day, the subjects were initially submitted to an anamnesis and the following anthropometric measures were carried out: body mass; height; skinfold thickness (triceps, subscapular, medium axillar, iliac crest, abdominal, front thigh and medial calf); circumferences (thorax, neck, flexed arm, forearm, thigh, waist, hip and leg); bone diameters (biacromial, transverse thorax, iliac crystal, malleolar, greater trochanter, humeral and femoral epicondyle and wrist styloid process); longitudinal dimensions (arm, leg, hand, foot and troncoencephalic). Skinfold thickness corresponded to the average of measures carried out three times on each point. The responsible person for assessment had 10 years' experience in this type of procedure. Fat percentage was estimated based on a Jackson and Pollock [15] protocol.

After anthropometric measurements, the subjects were guided about the objective and test protocol. Each subject was oriented to stay on a calibrated force platform, in the quiet standing position, barefoot and with arms relaxed. The stabilometric test protocol consisted of four randomized conditions: eyes open and feet in a comfortable, open position (EOFO); eyes open and feet in a close position, (EOFC); eyes closed and feet open (ECFO); eyes closed and feet closed (ECFC); and monopodal position with eyes open (EOMP). When the subjects stood in the platform with eyes open they should focus at a fixed point (circle with approximately 5 cm diameter), positioned at 1.5 m. The subjects remained on the platform for a period of 2 min in each condition, interspersed by 2 min resting interval. The first 30 s from each condition was not analyzed to avoid non-stationary transients [16].

2.3 Dynamometry Test

In the second day, the subjects were submitted to three dynamometric tests for the evaluation of static forces and localized muscular resistances. In the scapular test, the athletes positioned themselves according to Fig. 1a and performed horizontal glenohumeral abduction and scapular adduction. In the handgrip test (Fig. 1b), the athletes held the dynamometer with the elbow extended and upper limb along the body. For the lumbar dynamometry test, the athletes positioned themselves according to Fig. 1c and performed

Fig. 1 **a** Scapular dynamometry; **b** handgrip dynamometry; **c** lumbar dynamometry
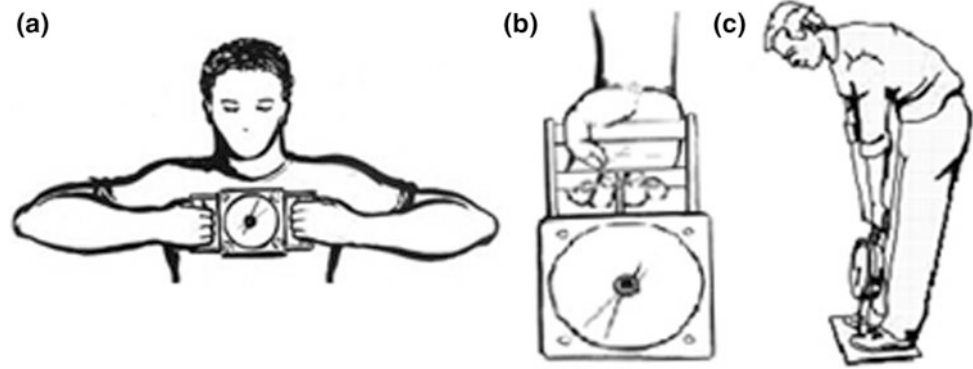
the extension of the trunk. In all tests the athletes produced the maximum static force until exhaustion, for recording the peaks and the decreasing rates of force.

2.4 Special Judo Fitness (SJF) Test

The test was performed in three series of 15, 30 and 30 s separated by 10-s resting intervals. During the test, the athlete must throw two opponents positioned 6 m apart from each other as many times as possible, using the ippon-seoi-nague technique. Heart rate was recorded immediately after the test (HR0) and 1 min later (HR1). The performance index (I) was calculated as:

$$I = \frac{HR0 + HR1}{NT}$$

where NT is the total number of throws in the three series [17]. The smaller the index, the better is the test performance. Heart rate was recorded by using a Polar™ A300 (Polar Electro Oy, Finland).

2.5 Signal Acquisition and Processing

The stabilometric tests were performed on a tailor-made force platform containing four load cells GL-200 (Kratos, Brazil), an amplifier (Kratos, Brazil), and signals were recorded at 50 Hz sampling frequency using a data acquisition board model USB-6211 (National Instruments, USA). Dynamometric signals were obtained from three dynamometers (scapular, lumbar and handgrip, EMG System, Brazil) using a dynamometer digital electromyograph model (EMG System, Brazil) at 2000 samples/s.

Both kind of signals were pre-processed by a 2nd order Butterworth low-pass digital filter with cutoff frequency 5 Hz (stabilometry) and 2 Hz (dynamometry). The filters

were applied in the direct and reverse directions to avoid phase distortions, thus resulting in 4th order filters.

A linear detrend procedure was applied on the center of pressure (COP) displacement signals in the anterior-posterior (COPy) and mediolateral (COPx) directions. Three stabilometric variables were calculated in all conditions: the mean velocity (MV), the elliptical sway area (EA), and the median frequency (Fmedian). MV corresponds to the ratio between the sway path (total length of COP) and the duration of the trial, while EA was calculated by the principal component analysis approach [18]. Finally, Fmedian from COPy and COPx were obtained by the equation:

$$\sum_{i=1}^{\text{Fmedian}} X(i) = \sum_{i=\text{Fmedian}}^{M} X(i)$$

were X(i) is the i-th component of the discrete frequency spectrum and M is the largest harmonic considered (25 Hz).

To evaluate the performance of the athlete in the dynamometric test, two variables were identified: maximum strength (MS) and localized muscular resistance (LMR). MS was identified in the initial 20 s, already the LMR index was calculated from the angular coefficient of the force decrease curve, obtained by linear regression.

2.6 Classifiers Application

The data were organized in a matrix (42×78), in which the lines corresponded to the subjects (42) and the column, the collected variables (78). The Logistic Regression (LR) method and the Multilayer perceptron neural network (MLP) were used to classify the subjects in the Gnational and Gstate groups. Before adjusting RL and MLP, the forward stepwise selection method was used to select the variables with the greatest contribution in the classification model. Only variables that presented significant contribution ($p < 0.05$) to the classification were attained for analysis.

The two models were tested by the leave-one-out cross-validation method. To evaluate their performances, the values of accuracy, sensitivity, specificity and area under receiver operating characteristic curve (AUC) were calculated.

Since the sample distribution by group was unbalanced (national level with 14 athletes and state with 28 athletes) a simulation was applied to ensure that the results of the models would be reliable. For this, the groups were equilibrated, randomly removing 14 subjects from the state level group and repeating the steps to fit the models. This procedure was applied 1000 times. The simulation was performed for the group of variables selected in the forward stepwise selection, using the same original approach for performance assessment.

3 Results

The selection of variables for the classifier application, considering all the combination of them, showed that seven variables had significant contributions: humeral epicondyle diameter ($p = 0.0104$), greater trochanter diameter ($p = 0.0047$), tight skin fold ($p = 0.0001$), total number of throw performed on the SJF test ($p = 1.26 \times 10^{-6}$), COPy Fmedian in EOFO condition ($p = 0.0359$), COPx MV in EOMP condition ($p = 0.0113$), and COPx MV in ECFO condition ($p = 0.0011$). The respective logistics regression coefficient were: -2914.6; 98.2; 29.6; -5.6; 34.4; 205.5; 9.5; and 36.9.

Both LR and MLP models presented similar performances (Table 1), with 90% and 91% accuracy, respectively. With balanced data, both classifiers showed improved performance values, presenting 93% and 96% accuracy for LR and MLP, respectively.

4 Discussion

The application of LR and MLP models to classify state and national level judo athletes using anthropometric, physiological and biomechanical variables presented relevant results in the characterization of these two groups. The

forward stepwise selection identified seven variables capable of classifying the two levels of athletes. With the adjustment of the two classification models, the leave-one-out cross validation method confirmed the good performance of the selected variables, with similar accuracy between LR and MLP, both with unbalanced data (LR 90%, MLP 91%) and balanced data (LR 93%, MLP 96%). The classifiers efficiency in characterizing the physical profile of different athletic levels corroborates the study by Fontana et al. [19], which used the LR method to classify three levels of Rugby athletes using anthropometric variables, as well as the study by Jaksic et al. [20], who classified, using the MLP, the morphological type of physical education students from the university of Novi Sad.

In the group of anthropometric variables, the humeral epicondyle diameter, greater trochanter diameter and thigh skin fold were those selected by forward stepwise selection as the ones that better classified the two levels of athletes. This result corroborates the study of Franchini et al. [2, 3], where the most advanced athletes presented higher humeral epicondyle diameter and greater trochanter diameter. This indicate that those athletes have a better bone adaptation to the judo training, which involves many movements such as carrying and pulling the adversary, or a better bone structure that allows them to withstand the training stress. However, conversely to the present results, these studies [2, 3] found no significant difference between groups when evaluating skinfolds. A possible explanation is the different sample, since these studies evaluated athletes who were part of the first and second main team of the country, presenting little disparity in skin folds.

The SJF test was used to characterize the aerobic and anaerobic power of the Gnational and Gstate groups. The results found in the study corroborate those of Franchini et al. [2], in which the higher level athletes performed more projections during the test. It has been reported that judo athletes with lower fat mass index have higher throwing speed (ippon seoi-nage technique), more power, and increased anaerobic capacity [2, 21], which is characteristic of high level athletes.

The results showed a greater mean velocity for Gnational than Gstate in the mediolateral direction for the EOMP and

Table 1 Performance (accuracy, sensitivity, specificity, and AUC) of the classifiers (LR and MLP) estimated by the leave-one-out cross-validation technique

Classifier	Unbalanced groups		Balanced groups	
	LR	MLP	LR	MLP
Accuracy	0.90	0.91	0.93 ± 0.05	0.96 ± 0.03
Sensitivity	0.86	0.79	0.91 ± 0.07	0.97 ± 0.04
Specificity	0.93	0.97	0.95 ± 0.05	0.97 ± 0.03
AUC	0.91	0.88	0.95 ± 0.04	0.96 ± 0.05

ECFO conditions. Judo athletes need to be particularly able to maintain their dynamic posture and reestablish it after an external or internal disturbance [11, 12]. The interpretation for higher mean velocity postural instability condition for judo athletes may be associated with the exploratory mechanisms attributed to the quiet standing control by Riley et al. [22]. According to Zatsiorsky et al. [23], the center of pressure displacement has two components: the trembling, composed of conventional oscillation around the equilibrium point; and the rambling, which refers to the slow migration of the reference from one instant equilibrium point to another. Whereas the instant equilibrium point does not change, the COP tends to stay in this point and consequently displacement area tends to remain unchanged. Thus, even though *MV* is greater, *EA* does not change ($p > 0.05$).

In conclusion, this study established that LR and MLP can be used to classify biomechanical, anthropometric and physiological variables in judo athletes. Thus, the quantitative description of the athlete physical profile will provide for the coach more tools in the selection of new athletes. Furthermore, it was also noticed the importance of balance, SJF test and anthropometric variables in the identification of high level athletes.

References

1. Barbado, D., Lopez-Valenciano, A., Juan-Recio, C., Montero-Carretero, C.,. Van Dieën, J.H., Vera-Garcia, F.J.: Trunk stability, trunk strength and sport performance level in judo. PLOS One **11**(5) (2016)

2. Franchini, E., Takito, M.Y., Kiss, M.A.P.D.M., Sterkowicz, S.: Physical fitness and anthropometrical differences between elite and non-elite judo players. Biol. Sport **22** (2005)

3. Franchini, E., Vecchio, F.B.D., Matsushigue, K.A.: Physiological profiles of elite judo athletes. Sports Med. **41**, 147–166 (2011)

4. Degoutte, F., Jouanel, P., Filaire, E.: Energy demands during a judo match and recovery. Br. J. Sports Med. **37**, 245–249 (2003)

5. Imamura, R.T., Iteya, M., Hreljac, A., Escamilla, R.F.: A kinematic comparison of the judo throw Harai-goshi during competitive and non-competitive conditions. J. Sports Sci. Med. **2**, 15–22 (2006)

6. Franchini, E., Nunes, A.V., Moraes, J.M., Vecchio, F.B.D.: Physical fitness and anthropometrical profile of the brazilian male judo team. J. Physiol. Anthropol. **26**, 59–67 (2007)

7. Little, N.G.: Physical performance attributes of junior and senior women, juvenile, junior and senior men judokas. J. Sports Med. Phys. Fit. **31**, 510–520 (1991)

8. Sánchez, A.G., Domínguez, A.S., Turpin, J.A.P., Tormo, J.M.C., Llorca, C.S.: Importance of hand-grip strength as an indicator for predicting the results of competitions of young judokas. Arch. Budo **7**, 167–172 (2011)

9. Bonitch-Góngora, J.G., Almeida, F., Padial, P., Bonitch-Domínguez, J.G., Feriche, B.: Maximal isometric hand-grip strength and endurance differences between elite and nonelite young judo athletes. Arch. Budo **9**, 239–248 (2013)

10. Willardson, J.M.: Core stability training applications to sports conditioning programs. J. Strength Cond. Res. **21**(3), 979–985 (2007)

11. Perrot, C., MUR, J.M., Mainard, D., Barrault, D., Perrin, P.: Influence of trauma induced by judo practice on postural control. Scand. J. Med. Sci. Sports **10**, 292–297 (2000)

12. Perrin, P., Deviterne, D., Hugel, F., Perrot, C.: Judo, better than dance, develops sensorimotor adaptabilities involved in balance control. Gait Posture **15**, 187–194 (2002)

13. Brito, C.J., Roas, A.F.C.M., Brito, I.S.S., Marins, J.C.B., Córdova, C., Franchini, E.: Methods of body-mass reduction by combat sport athletes. Int. J. Sport Nutr. Exerc. Metab. **22**, 89–97 (2012)

14. Claessens, A., Beunen, G., Wellens, R.: Somatotype and body structure of world top judoists. J. Sports Med. Phys. Fit. **27**, 105–113 (1987)

15. Jackson, A.S., Pollock, M.L.: Generalized equations for predicting body density of men. Br. J. Nutr. **40**, 497 (1978)

16. da Silva, P.J.G., Cagy, M., Infantosi, A.F.C.: Developing a dynamic virtual stimulation protocol to induce linear egomotion during orthostatic posture control test. Res. Biomed. Eng. **32**, 273–282 (2016)

17. Sterkowicz, S.: Test specjalnej sprawności ruchowej w judo. Antropomotoryka **12**, 29–44 (1995)

18. Oliveira, L.F., Simpson, D.M., Nadal, J.: Calculation of area of stabilometric signals using principal component analysis. Physiol. Meas. **17**, 305–312 (1996)

19. Fontana, F.Y., Colosio, A., De Roia, G.F., Da Lozzo, G., Pogliaghi, S.: Anthropometrics of Italian senior male rugby union players: from elite to second division. Int. J. Sports Physiol. Perform. **10**(6), 674–680 (2015)

20. Jaksic, D., Lilic, L., Popovic, S., Matic, R., Molnar, S.: Application of a more advanced procedure in defining morphological types. Int. J. Morphol. **32**(1), 112–118 (2014)

21. Casals, C., Huertas, J.R., Franchini, E., Sterkowicz-Przybycien, K., Sterkowicz, S., Gutiérrez-García, C., Escobar-Molina, R.: Special judo fitness test level and anthropometric profile of elite spanish judo athletes. J. Strength Cond. Res. **31**(5), 1229–1235 (2017)

22. Riley, M.A., Steven, W., Mitra, S., Turvey, M.T.: Common effects of touch and vision on postural parameters. Exp. Brain Res. **117**, 165–170 (1997)

23. Zatsiorsky, V.M., Duarte, M.: Instant equilibrium point and its migration in standing tasks: rambling and trembling components of the stabilogram. Mot. Control **3**, 28–38 (2000)

Muscle Fatigue and the Importance of Electrical Stimulation Parameters on Functional Electrical Stimulation

Marina Moreira and Antonio Padilha Lanari Bó

Abstract

Different combinations of stimulation parameters can create outcome variations during Functional Electrical Stimulation (FES). This study compared muscle performance and time until fatigue for four different parameter combinations. Standard Protocol used 20 Hz, 200 µs pulse width, and minimum current to evoke movement; Long Pulse Duration (LPD) Protocol utilized 20 Hz frequency, 500 µs pulse width, and minimum current; High Frequency (HF) 100 Hz, 200 µs pulse width, and minimum current; and High Amplitude (HA) used 20 Hz frequency, 200 µs pulse width, and current 25% above the minimum to evoke movement. The results of the present study indicate that higher current amplitudes seemed to slightly positively influence the outcome of the tests but at the cost of greater subject discomfort. Longer pulse durations seemed to produce stronger contractions and further muscle endurance. However the primary outcome of this experiment has to be the finding that the extent and onset of fatigue during ES depends mainly on the frequency of the pulses.

Keywords

Functional electrical stimulation (FES) • Fatigue • Parameters • Frequency • Amplitude • Pulse width

1 Introduction

Electrical Stimulation (ES) is a procedure used for the rehabilitation of persons with upper motor neuron dysfunctions such as cerebral palsy, stroke and Spinal Cord Injury (SCI). Although ES can produce movement in paralyzed or spastic muscles, the contractions have overall diminished efficiency and are prone to neuromuscular fatigue.

Muscle fatigue is a natural phenomenon and also occurs in voluntarily-activated muscles, marked by a loss of force resulting from the metabolic cost of contractions. Using Functional Electrical Stimulation (FES) this regular cause has to be considered alongside the fact that the normal recruitment order of muscle fiber is altered.

It was once believed that the natural order was inverted, with the larger size fibers recruited first [1, 2]. However, recent findings suggest that there is no such pattern, but the fiber is randomly recruited depending on the position of the electrodes [3, 4].

FES parameters have a critical role in the overall outcome of the exercise, but independent effects of altering current amplitude, frequency, and pulse duration are still controversial. Regarding frequency, it was broadly accepted that increasing its value would result in greater fatigue, but that are instances where higher values seem to have an opposite effect [5], or, even not be of importance [6]. There fewer studies on current amplitude with instances where there seems to be of no significance [7] and one instance where greater amplitudes seem to worsen the overall muscle response [8]. Some recent studies have considered the importance of pulse duration [9], finding that low current amplitudes and long pulses generate lower levels of muscle fatigue and pain scores when compared with short pulses and high current.

The main intent of this work was to examine the independent effects of stimulation parameters on muscle fatigue. With that goal, four different protocols were established, with pulse width varying from 200 to 500 µs, frequency ranging from 20 to 100 Hz and current amplitude increased above 25% of the minimum perceived to generate movement.

M. Moreira (✉) · A. P. L. Bó
Automation and Robotics Laboratory, University of Brasilia,
Brasilia, DF, Brazil
e-mail: marinaccmoreira@gmail.com

2 Methods

2.1 Subjects

Five healthy adults (3 females and 2 males) ranging in age between 20 and 30 years old participated in this study. Subjects had no history of upper extremity orthopaedic, neurological or vascular problems, and had previous experience with similar research protocols to address different queries.

All participants restrained from exercise for at least 48 h before stimulation sessions. All procedures were approved on November 2015 by the Research Ethics Committee of University of Brasilia, protocol number 47783815.3.0000.0030 and associated benefits and risks were explained to each subject.

2.2 Apparatus and Setup

The subjects were seated on an adjustable-height chair. Their elbow took rest in a custom-built contraption to keep the forearm elevated and freed to move on the horizontal plane. The mechanical system was completed by a counterweight of 1 kg supported by a pulley and attached to a velcro armband, this way ensuring the arm would return to the resting position, arm and forearm fully extended, with the cease of stimulation.

Electrical stimulation was delivered via two self-adhesive surface electrodes (ValuTrode, 5 cm × 5 cm, Arktus) placed in the subject's non-dominant arm, over the Biceps Brachii.

Using a standard clinical text of motor points [10] as an initial guide for electrode placement, the anode was placed over 70.62% of the distance from Acromion to Fossa Cubitalis and 5.76% arm circumference above medial-perpendicular (to Acromion-Cubitalis) axis (Fig. 1). Cathode was placed at the intersection of the medial point of the Acromion-Cubitalis axis with dorsal portion of the coronal plane.

The investigator performed a test set of stimuli until a visible contraction was attained. The electrode positioning over the muscle was then changed, while the investigator palpated the Biceps Brachii. The electrode placement that produced the greatest elbow flexion without any collateral palpable muscle contractions were accepted as the location of the motor unit, and its position was marked with a hennah in order to maintain electrode placement consistency.

Current was provided by a configurable electrical stimulator (RehaStim, Hasomed). A commercial Inertial Measurement Unit (IMU) (3-Space™ Sensors, Yost Labs) was placed in the inner part of the pulse and used to measure its
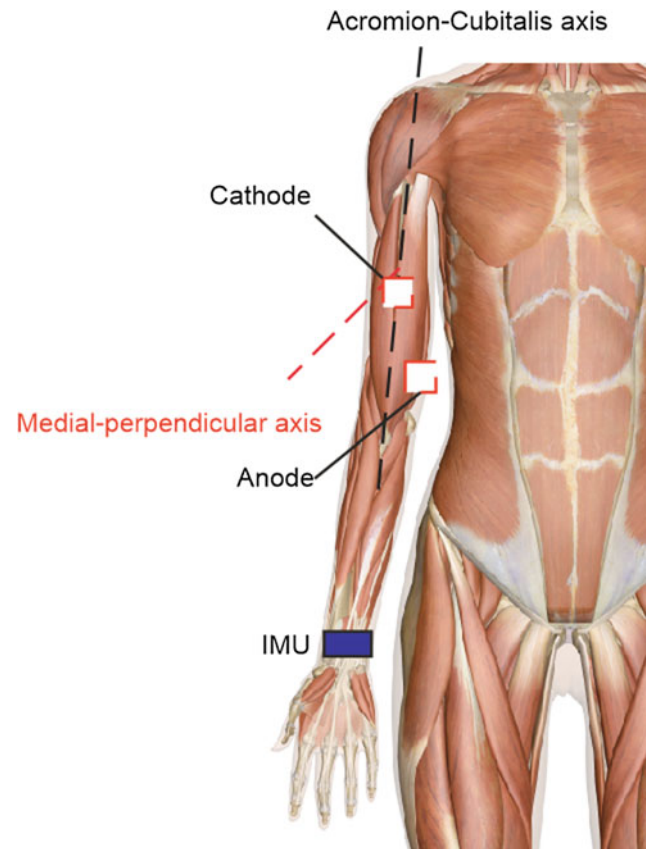
Fig. 1 Representation of the electrode and IMU positioning used for testing

angular displacement as elicited by the contraction of the Biceps Brachii.

2.3 Procedure

Each subject participated in at least four sessions, with a minimum separation of 48 h. At the start of the first session, subjects received an overview of the testing procedures, were ascertained about their health and other significant notes as well as disclosed about possible side effects.

With electrodes in place, current amplitude was adjusted until maximum elbow flexion was obtained and the angle between the wrist position in the relaxed arm and its final point, with a fully contracted Biceps, was recorded. This amplitude was gradually increased in order to ascertain the pain threshold of each volunteer, as to avoid muscle fiber damage in later steps.

FES Delivery. The electrical stimulation procedure consisted of three consecutive sequences of stimulation [11], as follows (Fig. 2).

Fig. 2 The three sets of stimulation were applied until the arm returned to its resting position due to muscle fatigue, when pulses were discontinued for 5 s. Stimulation was then restated four times for 5 s, turned off by 20 s, and finally followed by a 5 min pause
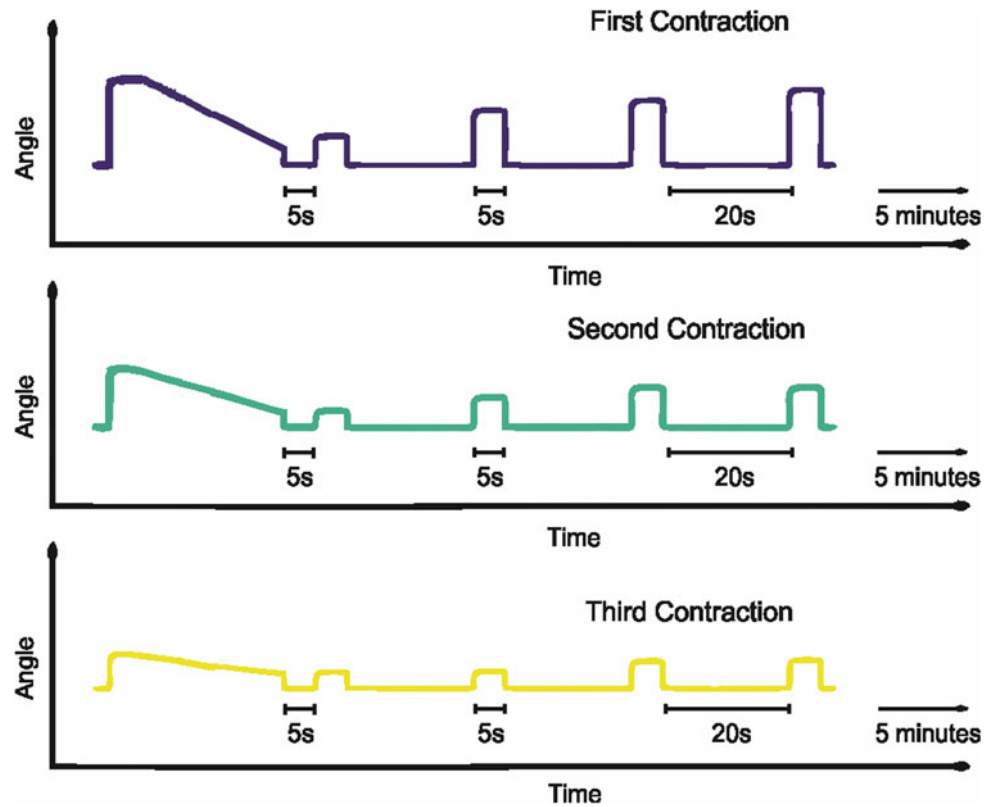
Each sequence was applied until the arm returned to its resting position due to muscle fatigue, then the stimulation was discontinued for 5 s. Next, the stimulation was four times resumed for 5 s, turned off by 20 s, and finally followed by a longer pause of 5 min.

For this section one of four protocols were applied, at this point it is important to note that the subject had no control or knowledge of the parameters received but was given an emergency button in case of acute discomfort. The protocol could be *Standard Protocol* (*STD*) Composed of 20 Hz frequency, 200 µs pulse width, and minimum current to evoke movement. A *Long Pulse Duration Protocol* (*LPD*) with 20 Hz frequency, 500 µs pulse width, and minimum current to evoke movement. *High Frequency Protocol* (*HF*): 100 Hz frequency, 200 µs pulse width, and minimum current to evoke movement. And finally a *High Amplitude Protocol* (*HA*): 20 Hz frequency, 200 µs pulse width, and current 25% above the minimum to evoke movement (Table 1).

Table 1 Summary of protocols and their outcomes

	Contraction set	Amplitude (mA)	Frequency (Hz)	Pulse duration (µs)	Angle (°)	Time until fatigue (s)
STD	1	17.2 + 3.347	20	200	38.424 + 16.705	14.574 + 4.448
	2				32.546 + 14.646	5.9744 + 3.111
	3				21.908 + 3.645	4.9076 + 2.915
LPD	1	12.4 + 2.966	20	500	51.2812 + 24.790	19.292 +10.439
	2				42.388 + 25.396	7.155 + 3.154
	3				24.0488 + 16.143	4.0672 + 2.002
HF	1	15.6 + 4.980	100	200	33.674 + 16.745	8.7682 + 2.601
	2				32.7232 + 15.563	5.9398 + 1.811
	3				30.9634 + 15.626	5.3328 + 1.974
HA	1	23.2 + 5.020	20	200	39.886 + 9.504	11.339 + 3.795
	2				37.035 + 9.886	6.680 + 3.820
	3				25.976 + 6.690	3.9126 + 2.072

2.4 Data Acquisition and Analysis

Muscle fatigue is defined as a decline in the force-generating ability of the muscle [18]. The decline in angle was used as a measure of loss of force-generating ability, given the way in which the arm was positioned the body's natural response was to bring the forearm close to the thorax, as it is stimulated. This way, the 0º of the system is collected by the IMU when both arm and forearm were fully extended as shown in Fig. 3, resting position assured by the presence of the counterweight.

Statistics and general data processing were performed in a custom-written script (MatLab 2015a, MathWorks).

Angular displacement (angle) of the wrist and time until onset of fatigue (TOF) were collected using 3-Space Suite Software (Yost Labs). The main MatLab script was used to calculate the Angle-Time Integral (ATI), here defined as the area under the angle-time curve during the sets of contraction. ATI is presently used as metric of muscle endurance to the fatiguing sets. The nomenclature is just an adaptation of the broadly used Torque-Time Integral (TTI) seen as angular displacement, in this case, is a direct aftereffect of torque.

Differences regarding a decline in angle were used to evaluate the overall muscle recovery process. In that intent second and third iterations were normalized based on the first.

Average and standard deviation of ATI and decline in angle was used in two independent 1-way, repeated measures analysis of variance (ANOVA) in order to examine the effects of each protocol, used here as the independent variable.

3 Results

All five subjects were successfully capable of completing the experiment without any complaints as to excessive pain or discomfort. Table 1 provides detailed information about the mean current amplitudes, frequency, pulse duration, angular displacement (angle) and total time until fatigue, all accompanied by the standard deviation (SD).

3.1 Angle-Time Responses to the Fatiguing Protocols

Expected angle and time responses to the contraction sets are shown in Fig. 4, presenting a smaller angle every time the muscle is electrically stimulated, as well as diminishing time until fatigue.

In some cases there were discrepancies with the pattern above. As presented in Fig. 5, in some occasions the following sequence of stimulation presented a result better than its predecessor, which was a strong indicator of human interference. These results were disregarded and the protocol repeated.

Fig. 3 Representation of resting position on the left, 0º of the system, and final position on the right, maximum angular displacement (angle), as seen from above
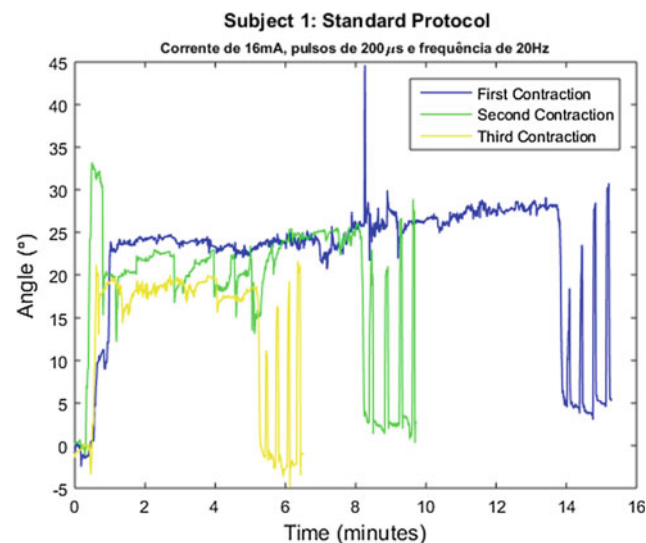
Fig. 4 Outline of the expected electrically evoked angle of all three iterations for the standard protocol. Note the pattern of decreasing time until fatigue and diminishing angle for every reiteration
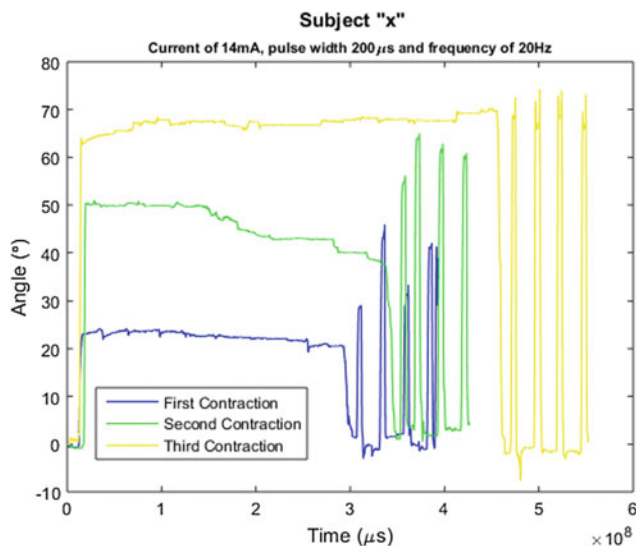
Fig. 5 Outline of the electrically evoked angle for three iterations with an indication of subject interference. Note that the first contraction has a lower angle and smaller time until fatigue than its successor, behavior also noted between second and third sets of contraction

3.2 Angle-Time Integral (ATI)

The Angle-time integral presented in Fig. 6 was calculated by the mean values and SD of the data collected for each subject and divided by protocol. ATI was significantly higher for the first contraction of Long Pulse Duration (6067 ± 660) when compared to other protocols (STD: 4289 ± 1120, HF: 1324 ± 680, HA: 4656 ± 448). The improvement between HA and STD protocols were discrete (STD: 4289 ± 1120 against HA: 4656 ± 448) (Fig. 6).

The more noticeable distinction in the first contraction for the protocols was when HF was compared to its peers.

Regarding the second contraction, it was evident that there were no significant discrepancies between STD (2200 ± 890), LPD (2405 ± 960) and HA (2319 ± 2000), but a sizable drop considering its prior (STD: 4289 ± 1120, LPD: 6067 ± 660, HA: 4656 ± 448), the result also visible for the third iteration (STD: 459 ± 600, LPD: 1547 ± 860 and HA: 548 ± 1200). A reliable indicator of muscle fatigue.

3.3 Angular Displacement (Angle)

Figure 7 portraits the decline in angle for all four protocols. For all the instances there was a significant reduction in ATI from the initial contraction. The more significant drop in value was attributed to the LPD, with fall of ($71\% \pm 9.4\%$) between the first two repetitions, and the overall decline of ($75\% \pm 8\%$) in ATI.

In the case of HF it was noted a more rapid recuperation of the motor units with a drop of only ($3\% \pm 5\%$) when comparing first and second contractions, for first and third
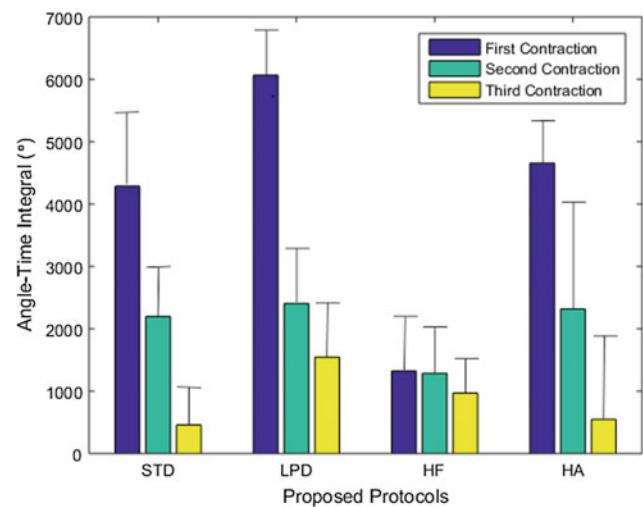
Fig. 6 Angle-time integral (ATI) for each of the four FES protocols. The Angle-Time integral presented in this graph was calculated by the mean values and SD of the data collected for each subject and divided by protocol. Abbreviations: STD, Standard Protocol; LPD, Long Pulse Duration; HF, High Frequency; HA, High Amplitude
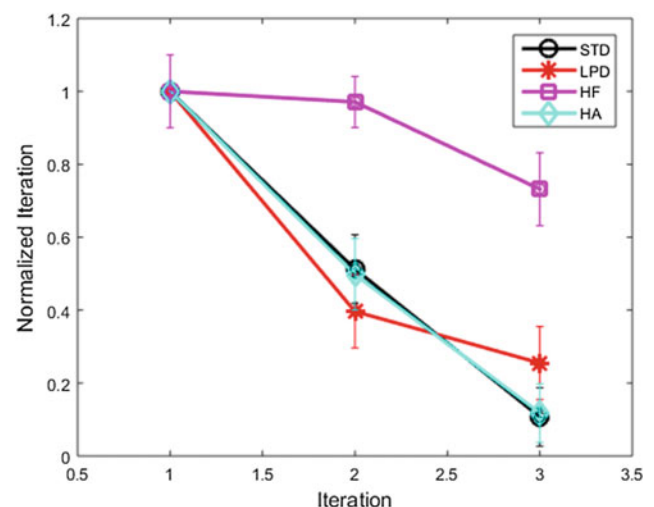
Fig. 7 Angular displacement normalized for the second and third iterations as regards to the first for each protocol

this number rose to ($27\% \pm 11\%$). No discernable differences were noted between the rate of fiber recovery for the STD and HA protocols.

4 Discussion

4.1 Choice of Protocol

A multi-set-stimulation protocol was chosen in order to assess the recuperation from fatigue in small periods, as well as to validate the acquired data. One of the most common

problems of engaging healthy adults in electrical-stimulation is voluntary movements during the proceeding, even when it is not perceived by the patient.

The expected outcome would be for the angle to grow smaller and time until fatigue to lessen as the experimental protocol progresses. This finding suggests that the fiber is increasingly growing weary, which is consistent with the sensation reported by the subjects.

If the results of a given set are better than its priors, there is strong indication of human interference and data is disregarded. This decision can be explained by the knowledge that short rest periods are not enough for the muscle to fully recover.

4.2 Relevance of Each Parameter

Pulse Duration. The time span of a single pulse is referred to as pulse duration or width. In this study increasing this parameter has shown substantial improvement in angular displacement without compromising time until fatigue. This finding may suggest the activation of fast fatigue-resistant motor units, which is substantially more resistant to fatigue than a fast motor unit, and can generate about twice the force of a slow one.

Longer pulse durations have been associated with deeper stimulations, [12] which could explain the superior results of its protocol. In this scenario, large motor units, which are normally located at more profound tissue layers of the muscle, would be recruited, resulting in a rise of torque [13].

An alternate explanation is that the product of the frequency and pulse duration, which has been recently suggested to strongly explain the variance in torque output, could have played a role in maximizing torque output in the LPD protocol [14].

Pulse Frequency. The stimulation frequencies were chosen in the interval of arm muscles firing range. The ones selected represent the steep (20 Hz) and plateau (100 Hz) portions of the force-frequency relationship. The data presently collected shows that higher frequencies of stimulation resulted in more rapid declines of angle, and, therefore, force.

For the initial muscle contraction, there was no notice of significant distinction in angle when compared to the Standard or the High Amplitude Protocols, therefore indicating that the reduced results for Angle Time Integral were due to its reduced time.

In the following iterations there was a significant drop in ATI indicating that the muscle was indeed fatigued and could no longer respond properly to impulse.

The effects of frequency on muscle fatigue have been broadly studied [6, 7] and corroborated that lowering frequencies reduces muscle fatigue.

One must note that there are two kinds of frequency-elicited fatigues. The so-called high-frequency fatigue is characterized by an excessive loss of force at high frequencies but a rapid recovery. Meanwhile, low-frequency fatigue is characterized by greater endurance until diminished force coupled with a slower recovery that may not occur within hours. Indeed, if one considers Fig. 7, it becomes clear that the five-minute interval between stimulations was not sufficient for muscle recovery in STD, LPD and HA protocols, but has a much better healing curve for HF.

This could be explained at a metabolic level [6], where there has been evidence that the 20 Hz contraction has a lower ATP cost when compared with an 80 Hz contraction.

Contrary to these findings, Matsunaga [5] has shown smaller declines in force during stimulation at 100 Hz when compared with 20 Hz. These results are believed to be caused by the duration of the protocol proposed by Matsunaga, which lasted 60 min. In that case, low-frequency fatigue is the most likely culprit, considering that it takes longer to develop, but is also slower to subside. That is, low-frequency fatigue might have reduced muscle responses to the 20 Hz stimulation and therefore resulted in poorer performance when compared to 100 Hz.

Also in disagreement with these results there were instances [15] in which frequency was alleged not to influence in fatigue. In this case trains of 100 and 80 Hz were delivered, and the similarity between these two frequencies is believed to be causing the deceiving results. Both 100 and 80 Hz are described as high frequencies when it comes to ES, and it is possible that 80 Hz is already above the point of saturation for the motor unit.

Higher frequencies were also reported to be more pleasant. That could be explained due to the force response being almost continuous with a general sensation of vibration, whereas lower frequencies elicit a tapping effect where individual pulses can be distinguished.

Current Amplitude. High Amplitude Protocol with current adjusted to 25% over the minimum to move the Biceps Brachii, showed almost no distinction when compared to the STD protocol. Its slight improvement could be explained by the fact that the higher the intensity, the stronger the depolarizing effect in the motor units underneath the electrodes, therefore more forceful contractions [16].

There has been a new discussion about the role of current amplitude, being recently [9] published that low current amplitudes along with long pulses widths generate lower levels of muscle fatigue and pain scores. This result could, however, be more related to pulse duration than current amplitude.

This findings come in disagreement with the belief that more fatigue-resistant muscle fibers would be recruited first [1, 2], resulting in an accelerated loss of force and longer

recovery time. Their findings are based on the knowledge that larger motor units are innervated by larger axons, which would be more electrically accessible [17], but it is now known that there is no such order; instead, motor units are randomly recruited [3, 4].

Intensity will also factor into subject comfort, with higher intensities being less tolerated, therefore this parameter should be dealt with caution.

5   Conclusion

For FES applications, because of the targeted force and duration are determined by the task at hand, it may not be essential to isolate the effects of a single parameter, but to determine the combination of frequency and pulse duration that should achieve the necessary muscle force at the same time as attenuating fatigue. Using stimulus with a frequency closer to 20 Hz and a pulse width of 500 µs may allow longer active exercise sessions, such as, FES cycling where the interval between pedals is very short thus not allowing time for the muscle to fully recover.

If, however, the activity is intermittent with shorter duration, case of FES rowing, it would be more sensible to use 100 Hz and pulse width of 500 µs. Here, the subject would row up to the point of interest and frequently rest, resuming the activity with recuperated motor units.

It is important to note that a limited number of parameter combinations were investigated, therefore future studies should focus on broadening that aspect. Here, it should be noted that these results were obtained for healthy individuals, therefore any adaptation to the Spinal Cord Injured population should be done with prudence.

References

1. Vanderthommen, M., Duchateau, J.: Electrical stimulation as a modality to improve performance of the neuromuscular system. Exer. Sport Sci. Rev. **35**(4), 180–185. Academic Press, United States (2007)
2. Gregory, C.M., Bickel, C.S.: Recruitment patterns in human skeletal muscle during electrical stimulation. Phys. Ther. **85**(4), 358–364. Oxford University Press, United Kingdom (2005)
3. Jubeau, M., Gondin, J., Martin, A., Sartorio, A., Maffiuletti, N.A.: Random motor unit activation by electrostimulation. Int. J. Sports Med. **28**, 901–904. Thieme Medical Publishers, Alemanha (2007)
4. Bickel, C.S., Gregory, C.M., Dean, J.C.: Motor unit recruitment during neuromuscular electrical stimulation: a critical appraisal. J. Appl. Physiol. **111**, 2399–2407. Springer Publishing Company, United States (2011)
5. Matsunaga, T., Shimada, Y., Sato, K.: Muscle fatigue from intermittent stimulation with low and high frequency electrical pulses. Arch. Phys. Med. Rehabil. **80**, 48–53. Elsevier Inc., United States (1999)
6. Russ, D.W., Elliott, M.A., Vandenborne, K., Walter, G.A., Binder-Macleod, S.A.: Metabolic costs of isometric force generation and maintenance of human skeletal muscle. Am. J. Physiol.-Endocrinol. Metab. **282**, 448–457. American Physiological Society, United States (2002)
7. Adams, G.R., Harris, R.T., Woodard, D., Dudley, G.A.: Mapping of electrical muscle stimulation using MRI. J. Appl. Physiol. **74**, 532–537. Springer Publishing Company, United States (1993)
8. Thrasher, T.A., Popovic, M.R.: Functional electrical stimulation of walking: function, exercise and rehabilitation. Ann. Readapt. Med. Phys. **5**, 452–460. Elsevier Masson, France (2008)
9. Jeon, W., Griffin, L.: Effects of pulse duration on muscle fatigue during electrical stimulation inducing moderate-level contraction. Muscle Nerve **57**(4), 642–649. Wiley, United States (2018)
10. Behringer, M., Franz, A., McCourt, M., Mester, J.: Motor point map of upper body muscles. J. Appl. Physiol. **114**, 1605–1617. Springer Publishing Company, United States (2011)
11. Estigoni, E.H., Fornusek, C., Hamzaid, N.A., Hasnan, N., Smith, R.M., Davis, G.M.: Evoked EMG versus torque during fatiguing functional electrical stimulation-evoked muscle contractions and short-term recovery in individuals with spinal cord injury. Sensors **14**(12), 22907–22920. MDPI, Switzerland (2014)
12. Lagerquist, O., Collins, D.F.: Influence of stimulus pulse width on M-waves, H-reflexes, and torque during tetanic low-intensity neuromuscular stimulation. In: Muscle Nerve **42**(6), 886–893. Wiley, United States (2010)
13. Chou, L.W., Binder-Macleod, S.A.: The effects of stimulation frequency and fatigue on the force intensity relationship for human skeletal muscle. Clin. Neurophysiol. **118**, 1387–1396. Elsevier Inc., United States (2007)
14. Gregory, C.M., Dixon, W., Bickel, C.S.: Impact of varying pulse frequency and duration on muscle torque production and fatigue. Muscle Nerve **35**(4), 504–509. Wiley, United States (2007)
15. Russ, D.W., Vandenborne, K., Walter, G.A., Elliott, M., Binder-Macleod, S.A.: Effects of muscle activation on fatigue and metabolism in human skeletal muscle. J. Appl. Physiol. **92**, 1978–1986. Springer Publishing Company, United States (2002)
16. Mesin, L., Merlo, E., Merletti, R., Orizio, C.: Investigation of motor unit recruitment during stimulated contractions of tibialis anterior muscle. J Electromyogr. Kinesiol. **20**(4), 580–589. Elsevier Inc., United States (2010)
17. Purves, D., Augustine, G.J., Fitzpatrick, D., Katz, L.C., LaMantia, A.S., McNamara, J.O., Williams, S.M.: The Motor Unit, 2nd edn. Sinauer Associates, Massachusetts (2001)
18. Edwards, R.H.T.: Human muscle function and fatigue. In: Human muscle fatigue: physiological mechanisms, pp. 1–18. Pitman Medical, London (1981)

Neurorehabilitation Platform Based on EEG, sEMG and Virtual Reality Using Robotic Monocycle

Vivianne F. Cardoso, Alexandre Pomer-Escher, Berthil B. Longo, Flávia A. Loterio, Sara S. G. Nascimento, María Alejandra Romero Laiseca, Denis Delisle-Rodriguez, Anselmo Frizera-Neto, and Teodiano Bastos-Filho

Abstract

A recent study in the literature showed that eight paraplegic patients with chronic spinal cord injury, who underwent 12 months of training in brain-machine interface (BMI), based on neurorehabilitation using a virtual system and a very high cost exoskeleton, experienced neurological enhancements in somatic sensation, as well as motor improvements. A possible low-cost solution is to use a robotic monocycle instead of an exoskeleton, since the exercise of pedaling a monocycle has the potential to provide a high number of flexion and extension repetitions of the lower limb in reasonable therapeutic time periods. The objective of this work is to develop a neurorehabilitation platform based on electroencephalography (EEG), surface electromyography (sEMG) and immersive virtual reality (IVR), and using a robotic monocycle to move the user's legs. The monocycle is instrumented with inertial sensors placed on the pedals, which is used to measure the cadence developed by the user while pedaling, and a customized electronic board to control the monocycle according to the user's motor imagery detected through a Brain-Computer Interface (BCI) using EEG. On the other hand, sEMG signals are collected from the rectus femoris, biceps femoris, tibialis anterior and trochanteric muscles, in order to allow the identification of their onset and offset. In addition, a serious game was designed to be used as part of the rehabilitation platform. As preliminary results, the developed BCI is able recognize motor imagery patterns related to feet movements and resting state with an average accuracy higher than 80%.

Keywords

Lower-limb rehabilitation • Stroke • Motor imagery • Robotic monocycle

1 Introduction

One of the main functions of the spinal cord is to perform electrical communication between different sections of the body and with the brain. Its functions may be altered, temporary or permanently, in the lower parts of the body under certain lesion level. Researches conducted through body information retrieval therapy, stem cell therapy and robotic devices come as a hope of treatment. A recent study showed that eight paraplegics with chronic spinal cord injury experienced neurological improvements in somatic sensation (pain location, fine/gross touch and proprioceptive sensitivity) and motor improvements after a neurorehabilitation training during a period of twelve months. That study used a brain-machine interface (BMI), virtual reality and a high cost exoskeleton [1].

In addition to paraplegics, other kind of patients who can benefit of that neurorehabilitation system are quadriplegic and post-stroke patients. Quadriplegic are those affected with partial or complete paralysis of both the arms and legs especially as a result of spinal cord injury or disease in the region of the neck. On the other hand, Stroke is a neurological syndrome with high prevalence in adults and elderly and one of the main causes of mortality in the world. Stroke is defined as the interruption of the blood supply to the brain, usually because a blood vessel bursts or is blocked by a clot. This cuts off the supply of oxygen and nutrients, causing damage to the brain tissue. Stroke can result in several

V. F. Cardoso · T. Bastos-Filho
Postgraduate Program in Biotechnology, Federal University of Espirito Santo (UFES), Vitoria, Brazil
e-mail: viviannefc@gmail.com

A. Pomer-Escher · B. B. Longo · F. A. Loterio (✉) ·
T. Bastos-Filho
Doctorate RENORBIO, Federal University of Espirito Santo (UFES), Vitoria, Brazil
e-mail: loteriofa.ufes@gmail.com

S. S. G. Nascimento · M. A. R. Laiseca · D. Delisle-Rodriguez ·
A. Frizera-Neto · T. Bastos-Filho
Postgraduate Program in Electrical Engineer, Federal University of Espirito Santo (UFES), Vitoria, Brazil

sequelae, which depends on the type of stroke, the extent of the injury and the site of the brain where the injury occurred [2]. Clinical symptoms and impairments caused by stroke are directly related to the brain area which was injured [3]. Among the neurological impairments are communication disorders, cognitive deficits and visuo-spatial perception disorders and, mainly, losses in the neuromuscular system, affecting the locomotion [4–6].

Neurophysiological data suggest that a considerable amount of repetition of movement is required to induce changes in neuroplasticity and functional recovery of motor deficits [7]. In fact, there are scientific evidences that regeneration of structures and reorganization of neuronal function is directly related to the principles of motor learning, which could induce changes in neuroplasticity and functional recovery of motor deficits [8, 9].

On the other hand, literature shows that pedaling exercises, using cycle ergometer, has the potential to provide a high number of flexion and extension repetitions in the lower limb in reasonable therapeutic time periods. Moreover, this exercise can improve muscle activity, strength, and balance [10].

Therefore, this work has the objective of developing a complete system of neurorehabilitation for people who are quadriplegic, paraplegic or suffer from hemiplegia post-stroke. The system proposed here consists of a Brain-Computer Interface (BCI) based on EEG, in addition to surface electromyography (sEMG), IRV and a robotic monocycle. This whole system is affordable and has low cost. The used robotic monocycle costs around US$150.00 compared with other systems, such as ReWalk (US $70,000.00–85,000.00) and Lokomat (US$200,000.00–300,000.00).

2 Methodology

This research was divided into 6 stages. Stage 1, 2 and 3, which are still in progress, consist respectively of presentation of feedback through biomechanical identification patterns provided by inertial sensors and sEMG; development of virtual reality environments; and recognition of motor logic through electroencephalography (EEG) analysis of the distribution of Event Related Synchronization/Desynchronization (ERD/ERS) patterns on the feet movement brain region. Stage 4 will address the use of motor imagery to trigger an avatar in the immersive virtual reality (IVR) environment. Stage 5 will activate the robotic monocycle according to the motor imagery detected in Stage 3 of the research.

All stages of the research must be synchronized to generate the learning effect needed to achieve an effective rehabilitation. Finally, Stage 6 will evaluate the performance of the developed system, which contemplates its ease of use, comfort and confidence.

The research was previously approved by the Ethical Committee of Federal University of Espirito Santo—UFES/Brazil (Number CAAE: 64797816.7.0000.5542), and all the volunteers signed the Free and Informed Consent Form.

2.1 Stage 1—Identification of Biomechanical Standards

A protocol for the neurorehabilitation system was designed, which has the objective of evaluating four parameters: (1) relationship between the programmed velocity to be executed by the motorized pedal and the actual velocity performed; (2) relationship between the velocity executed by the robotic monocycle and the user's weight and height; (3) pedal's stop position during the full cycle of 360°; (4) muscle onset and offset detection through sEMG on Rectus femoris (RF), Biceps femoris (BF), Tibialis Anterior (TA) and Gastrocnemius lateralis (GM) muscles, during the full cycle of pedaling. Those parameters are used to evaluate the pedal's control in order to synchronize the pedal velocity with the virtual environment, also providing data from the aforementioned muscles to the physiotherapists.

The inclusion criteria for participating in this research were: at least 18 years old; no neurologic diseases or lower-limb impairments; cognitive, language, hearing and visual skills to understand and follow instructions; and to sign the written informed consent. Following these criteria, eight subjects (5 males, mean 27, SD 2.37 years old; 3 females, mean 28, SD 4.24 years) participated of the experiments.

Some of the main features of hemiparesis are limitations in knee flexion and dorsiflexion, usually due to the flexor pattern commonly found in stroke, such as TA and BF weakened and spastic quadriceps and gastrocnemius [11]. Thus, functional recovery of these muscles must be considered on the pedal control system. This way, it is necessary to detect the onset and offset of these muscles during the pedaling cycle whereas the force of the movement is realized.

Four channels of sEMG were used, with the electrodes arranged in the following muscles: RF (responsible for knee extension), BF (responsible for knee flexion), TA (responsible for dorsiflexion), GL (responsible for plantar flexion), in addition to a reference electrode on the ankle. The sEMG recording was made with a sampling frequency of 1 kHz. Figure 1 shows a participant during the experiment.

For the allocation of the electrodes, the correct location of the muscles of interest was first performed, according to Surface ElectroMyoGraphy for the Non-Invasive

Fig. 1 Participant with sEMG electrodes during experiment
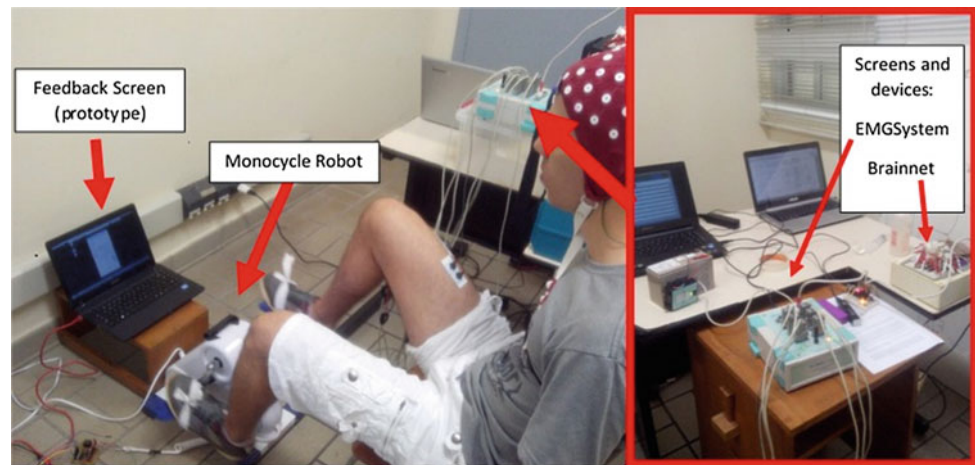
Assessment of Muscles (SENIAM) recommendations [12], followed by trichotomy of the region and further cleansing using alcohol 70%. The placement of the electrodes was aligned with the direction of the muscle fiber and an inter-electrode distance of 20 mm was maintained. The reference electrode was placed on the ankle far from the muscle fibers. After confirmation of the correct allocation of the electrodes, the experiments started. For the experiment, the participant sits comfortably in a chair and starts the movement after a beep. For each participant the seat is suitably positioned, so that the knee flexion angle is between 70° and 80° (referring to knee extension at 0° of the cycle) when the ankle is in the neutral position (i.e., foot and tibia in an angle of 90°).

In this experiment, when the beep is heard, the motor of robotic monocycle is activated, revolving for 2 min at 60 rpm. During this time, the sEMG signals are recorded and stored. The sEMG signals are recorded and stored when a new cycle starts, thus totaling 120 repetitions. The programmed speed of the pedal and the actual velocity performed by it are also recorded and stored, in addition to the stop position. The participants are told about the experiments' goals before starting them, and they have a time period to adapt to the use of the system. The adaptation period may be longer or shorter, according to the participant's needs. Records obtained during the experiments are processed and analyzed using MATLAB.

2.2 Stage 2—Virtual Environment

A Serious Game (SG) was designed to compose the rehabilitation platform. The Virtual Environment (VE) has its structure (wireframes) built using Blender, which is a professional free and open-source 3D computer graphics software. Textures and images used were made in Gimp, a free and open-source raster graphics editor. SG features were developed using Unity 3D Personal Edition.

All these programs run either in Microsoft Windows or in Canonical Ubuntu (and other Linux distributions), except Unity. The latter can only be run on Microsoft Windows, as there is no Linux version yet, but the VE can be exported to run on Linux or Windows independently, as well as other platforms such as iOS and Android, among others.

The SG were built using a computer running Microsoft Windows 10 (64-bit), with an AMD FX-8320E Eight-Core Processor, 8 GB of RAM, and nVidia GeForce GTX 970 graphics card. A screen of the developed environment can be seen in Fig. 2.

2.3 Stage 3—BCI

The BCI used to recognize the motor imagery has a band-pass filter (Butterworth 5th order), from 8 to 30 Hz, and the following methods for feature extraction [13, 14]: Common Spatial Pattern (CSP), Filter-Bank CSP (FBCSP) and Riemannian Kernel (RK). At the first stage, the BCI uses RK and the following classifiers: Linear Discriminant Analysis (LDA) and Regularized Discriminant Analysis (RDA), which recognize two classes: rest state and feet movement. EEG signals are recorded from the following locations: Fz, FC3, FC1, FCz, FC2, FC4, C5, C3, C1, Cz, C2, C4, C6, CP3, CP1, CPz, CP2, CP4, P1, Pz, P2, POz. A total of 72 trials were analyzed for the two classes, and the time interval ranged from 0.5 to 2.5 s after a cue on a screen instructing the user to perform rest state and feet movements. Figure 3 shows a participant during the experiment with the BCI.

Fig. 2 Virtual road designed for the neurorehabilitation process
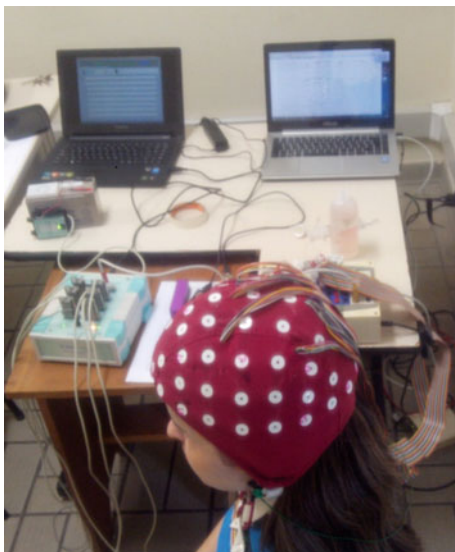
Fig. 3 Participant during experiment with the BCI

3 Results and Discussion

The results presented are referent to the independent stages (1, 2 and 3), and the sub-sequent ones will be developed upon completion of these stages.

3.1 Stage 1—Identification of Biomechanical Standards

After the experiments, it was possible to analyze the relationship between the speed programmed to be executed by the robotic monocycle and the actual velocity executed by it. Although the programmed speed was 60 rpm, the actual mean speed in 120 cycles was 53 rpm (SD $\pm$ 3.09). These results pointed out that the speed control requires dynamic adjustment in order to maintain the programmed speed to provide a cadence feedback that may facilitate a more symmetrical muscular activation learning necessary for the patients [10]. Table 1 shows the results of these experiments. It is worth to comment that the data of participant S02 were excluded from the sample, since it was verified that he applied force during the pedaling.

The relationship between the actual speed in 120 cycles, developed by the robotic monocycle, and the participant's weight and height were analyzed. A comparison using the Pearson coefficients was performed, which indicated that there was no direct correlation between the actual velocity and the participant's weight and height, respectively (P -0.12, p-value 0.39 and P -0.23, p-value 0.31).

To provide rehabilitation, as required by professionals, accurate sEMG data from the RF, BF, TA and GM muscles, and the pedal stop position, are analyzed when the

Table 1 Mean and standard deviation (SD) of the actual velocity executed in 120 cycles for each participant

	S01	S03	S04	S05	S06	S07	S08	Mean
rpm	52.69	58.13	47.36	52.90	51.94	53.08	55.77	53.12
SD	1.59	2.48	3.35	1.92	3.61	8.15	1.45	3.09
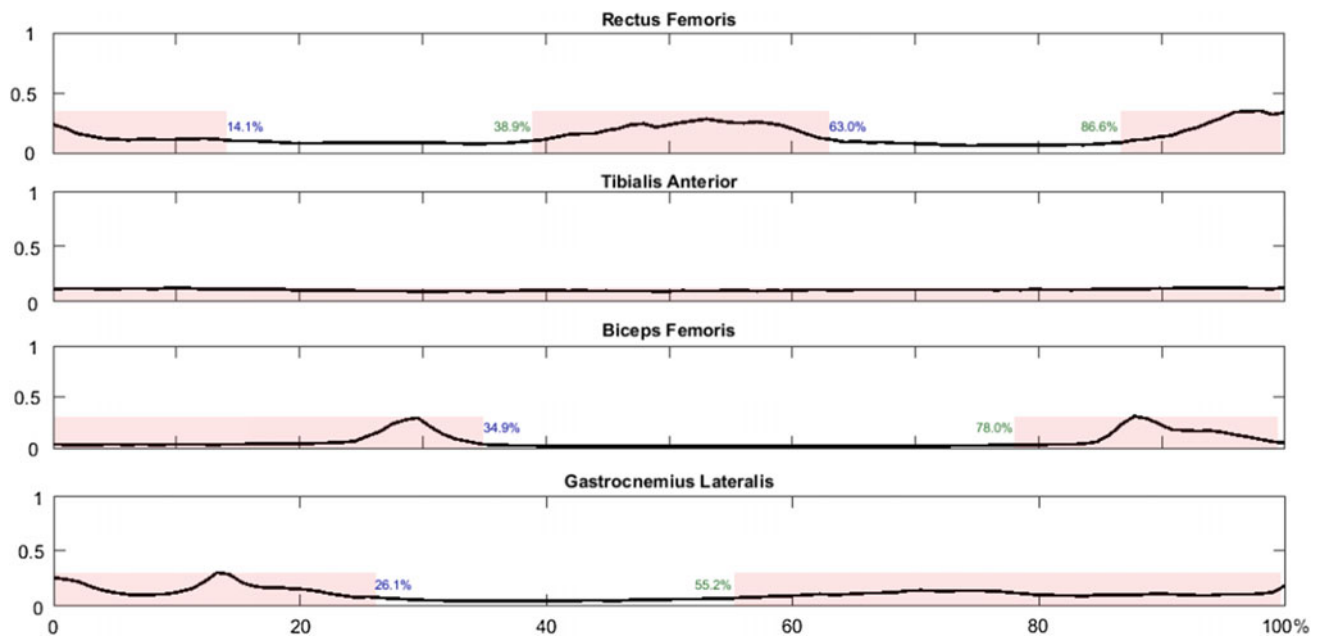
Fig. 4 Mean of the onset and offset of each muscle of participant 3 in 120 cycles

participant performs a full cycle. sEMG signals were collected on the following muscles: Rectus femoris (RF), Biceps femoris (BF), Tibialis Anterior (TA) and Gastrocnemius lateralis (GM) with the objective of identifying the muscle onset and offset when a force is exerted on the robotic monocycle. Figure 4 shows the results for the experiment performed by participant 3, in which it is possible to visualize the mean of the onset and offset of each muscle in 120 cycles.

3.2 Stage 2—Virtual Environment

The model used in the SG is a recumbent tricycle, so the player does not need to worry about its balance. The game genre chosen for this SG is "simulation and action", since they are more suitable for games where the player executes movements. This SG consists of a road where the patient needs to pedal to move forward with his/her bike and cover some distance (Fig. 5). The road is straight, asphaltic and flat, with vegetation on its side. The player (patient) starts in the initial checkpoint, indicated by a metal structure. Flags are placed beside the road to mark the sequential checkpoints. Every time the player passes thought a checkpoint,

time is registered and shown on the screen. The final checkpoint is also a metal structure properly defined, and the session ends when the player crosses it. The distance is set by the health professional, which can be adjusted for every session, making the SG adjustable for the patient's needs. A score tab is shown in the beginning and end of every session to inform the patient his/her achievements, promoting motivation to improve them. This SG uses a Head-Mounted display (HMD) as input/output device to increase immersion and improve user experience.

3.3 Stage 3—BCI

Regarding the BCI's results, Table 2 shows its performance to recognize the rest state and imagination of feet movements in eight subjects. The BCI shows a good performance (accuracy—ACC > 80%) for almost all subjects. Here, the BCI based on linear Support Vector Machine (SVM) improved the recognition for four subjects (A01, A03, A06, and A07). However, the results show that different classifiers may be adopted to enhance the classification. Specifically, the LDA classifier presented ACC values close to SVM, thus, it may be suitable for online implementation, decreasing

Fig. 5 Virtual road designed to the neurorehabilitation process

Table 2 Result of the classifiers

Subjects		A01	A02	A03	A04	A05	A06	A07	A08	A09
Linear discriminant analysis	ACC	89.51	74.83	79.02	93.75	70.63	74.83	90.91	83.92	83.22
	Kappa	78.99	49.53	58.07	87.5	41.21	49.61	81.84	67.78	66.37
	TPR	80.28	57.75	84.51	90.28	64.79	69.01	1.00	73.24	69.01
	FPR	1.39	8.33	26.39	2.78	23.61	19.44	18.06	5.56	2.78
Regularized discriminant analysis	ACC	90.21	65.73	79.72	92.32	66.43	74.83	90.91	86.71	84.62
	Kappa	80.41	31.67	59.47	84.72	32.89	49.8	81.84	73.42	69.21
	TPR	85.92	87.32	85.92	93.06	69.01	95.77	1.00	84.51	78.87
	FPR	5.56	55.56	26.39	8.33	36.11	45.83	18.06	11.11	9.72
Linear support vector machine	ACC	90.21	74.83	80.42	84.03	67.83	80.42	94.41	85.31	83.22
	Kappa	80.24	49.51	60.84	68.06	35.69	60.78	88.82	70.61	66.41
	TPR	81.69	54.93	81.69	80.56	70.42	69.01	1.00	80.28	77.46
	FPR	1.39	5.56	20.83	12.5	34.72	8.33	11.11	9.72	11.11

All values are presented in percent. *ACC* accuracy; *TPR* true positive rate; *FPR* false positive rate

computation cost in both calibration and validation stages. RDA classifier has been little explored on BCIs, thus, it may be another alternative for online applications, due to its low computational cost.

4 Conclusions

This work introduced the proposal of a setup for a neurorehabilitation system. sEMG signals are collected on Rectus femoris, Biceps femoris, Tibialis Anterior and Gastrocnemius lateralis muscles to identify the muscle onset and offset when a force is exerted on the robotic monocycle. A SG using HMD as input/output device was designed to compose the neurorehabilitation platform. The motor imagery recognition system analyzes EEG patterns on the motor region related to feet movements and rest state. The BCI showed a good performance (mean ACC > 80%) with the BCI based on linear SVM, which reached the better result (ACC = 94.41). The stages 1, 2 and 3 are at the final phase of development, and the subsequent stages (4, 5 and 6) will be developed upon completion of the three first stages.

References

1. Donati, A.R.C., et al.: Long-term training with a brain-machine interface-based gait protocol induces partial neurological recovery in paraplegic patients. Sci. Rep. **6**, 30383 (2016)
2. Deb, P., Sharma, S., Hassan, K.M.: Pathophysiologic mechanisms of acute ischemic stroke: an overview with emphasis on therapeutic significance beyond thrombolysis. Pathophysiology **17**, 197–218 (2010)
3. Sommerfeld, D.K., et al.: Spasticity after stroke. Stroke 35–134 (2004)
4. Belda-Lois, J.M., et al.: Rehabilitation of gait after stroke: a review towards a top-down approach. J. NeuroEng. Rehabil. 1–19 (2011)
5. Daly, J.J., Ruff, R.L.: Construction of efficacious gait and upper limb functional interventions based on brain plasticity evidence and model-based measures for stroke patients. Sci. World J. **7**, 2031–2045 (2007)
6. Pang, M.Y.C., et al.: A community-based fitness and mobility exercise program for older adults with chronic stroke: a

randomized, controlled trial. J. Am. Geriatr. Soc. **53**(10), 1667–1674 (2005)

7. Lohse, K.R., Hilderman, C.G.E., Cheung, K.L., Tatla, S., Van der Loos, H.F.M.: Virtual reality therapy for adults post-stroke: a systematic review and meta-analysis exploring virtual environments and commercial games in therapy. PLOS One **9**(3) (2014)

8. Katz-Leurer, M., et al.: The influence of early cycling training on balance in stroke patients at the subacute stage. Results of a preliminary trial. Clin. Rehabil. **20**(5), 398–405 (2006)

9. Lucareli, P.R., Greve, J.M.: Alteration of the load-response mechanism of the knee joint during hemiparetic gait following stroke analyzed by 3-dimensional kinematic. Clinics (São Paulo) **61**(4), 295–300 (2006)

10. Hermens, H.J., et al.: European Recommendations for Surface ElectroMyoGraphy. Roessingh Research and Development, SENIAM (1999)

11. Blankertz, B., et al.: Optimizing spatial filters for robust EEG single-trial analysis. IEEE Signal Process. Mag. **25**, 41–56 (2008)

12. Ang, K.K., et al.: Filter bank common spatial pattern algorithm on BCI competition IV datasets 2a and 2b. Front. Neurosci. **6**, 39 (2012)

13. Barachant, A., et al.: Classification of covariance matrices using a Riemannian-based kernel for BCI applications. Neurocomputing **112**, 172–178 (2013)

14. Sang-I, L., et al.: Biomechanical assessments of the effect of visual feedback on cycling for patients with stroke. J. Electromyogr. Kinesiol. **22**(4), 582–588 (2012)

Numerical Evaluation of Efforts on the Femoral Head in a 3D Model

Rhaíra H. C. Souza and Eduardo L. M. Naves

Abstract

The human body skeletal system provides support and form. Bones make up this system, giving it rigidity and shape. They are like structures capable of being compressed, susceptible to fields of tension and transformation. We can analyze a stress/strain field by means of the analytical, experimental and numerical methods, being as two last techniques the more often used. The finite element method (FEM) is suggested as a numerical method. The objective of this work is to present the finite element method as a biomechanical process evaluation tool, applied to the skeletal system, particularly to a 3D-femur model. The study of the contours and loads of biomechanical structures, such as the femur, is important for understanding the causes of fractures or even complications of ligaments or the hip joint. It helps in the scope of training teams of clinical professionals. The results show that the finite element modeling produces plausible results that meet the real behavior of the biomechanical structure. The technical aspects of the work make possible the understanding of the applied biomass systems over the human femoral head, and other body bone segments are subject to study obeying the requirements of the presented methodology. Therefore, consistent with the objectives of the work that seeks a tool of finite elements as a methodology to support the training of clinical pictures.

Keywords

Femoral head • Finite element method • Stress field • Von Mises stress

1 Introduction

The various conditions of pressure on the bones in the routine of the human being are sources of several factors that can generate bone remodeling in the human skeleton. When the body is exposed to sports and various physical exertion, extreme deformation conditions may occur. The long bones of the lower limbs, such as the femur, have a central cavity containing the spongy bone and an outer portion formed by compact bone.

Bone is a material of anisotropic behavior, whose values and main directions of stiffness change, not only point to point, but also in time, because of the remodeling process. Nevertheless, many models of remodeling consider a distribution of uniform bone mass in all directions, resulting in an isotropic behavior when starting from an isotropic state [1].

Bone has the ability to adapt to certain loads that are imposed on it. The Wolff's Law describes that 'any change in the shape and function of bones or only of their function is followed by certain changes, defined in their internal architecture, and also in their external conformation.'

In this way, the femur can suffer a significant loss of mineral density when subjected to extreme stress situations, such as high-impact sports (such as jumping, running, dancing, etc.). Antonialli [2] emphasizes that the significant loss of mineral density occurs when implanting a prosthesis, remodeling the bone structure, adaptively, being a relevant intervention in the observation of stresses generated in the femur and hip, for example.

A field of stress/strain can be analyzed by means of analytical, experimental and numerical methods, the last two techniques being the most used. For the numerical methods, the most used tool is the finite element method (FEM), which makes it possible to calculate the distribution and concentration of stress and deformation in the components of the system by means of three-dimensional (3D) computerized structure [3].

R. H. C. Souza (✉) · E. L. M. Naves
Federal University of Uberlandia, Uberlandia, MG 38400-902, Brazil
e-mail: rhairahelena@gmail.com

The aim of this study is to evaluate the effect of stresses on the femoral head, using the finite element method, by the hip contact and abductor muscles and tensor fascia latae, mainly in the practice of physical exercises.

2 Methods

FEM can be defined as a method in which a continuous medium is discretized into small elements that maintains the properties of the original element. In other words, it makes a complex problem and subdivides it into several simpler ones and with similar properties, solving them adequately to offer the solution for the whole set [4, 5].

The femur is the longest and strongest bone in the body. In biomechanics, this structure plays a fundamental role and insists complexity in the study of movement, due to its specific angulations. Disorders of the anatomical and mechanical axes of the lower extremities of the human body are important and affect the efficiency of locomotion; can also induce diseases such as hip, knee and ankle osteoarthritis [6]. The presence of stress and deformation fields promote the alteration of the mechanical and anatomical axes, developing pathologies in the movement.

2.1 Mechanical Properties of the Femoral Bone

Queiroz [7] describes the mechanical properties of the femoral bone, which is composed of cortical and spongy tissue; Table 1 shows the mechanical properties.

In the [8] study, the scientific research conducted led them to conclude that the largest loads on the femoral head have approximately constant direction, regardless of the activity performed.

The numerical simulations were conducted in the ANSYS® environment, v. 12, developed by Swanson Analysis Inc., from a 3D human femur model available online [9], which was not developed in this work, is a parametric solid available in the public domain. The model is of a left human femur of 416 mm in length, head of 36 mm in diameter and varum angle of 123°. Such measures are based on morphometric studies of reference in the literature, such as [10].

Force	Acts at point
Hip contact	P_1
Abductor	P_2
Tensor fascia latae	P_2
Vastus lateralis	P_3
Vastus medialis	P_4

Point	x	y	z
P_0	0	0	0
P_1	-44	32	408
P_2	8	31	360
P_3	-8	29	316
P_4	-29	36	316

Direction x: medial ⟶ lateral
Direction y: anterior ⟶ posterior
Direction y: distal ⟶ proximal
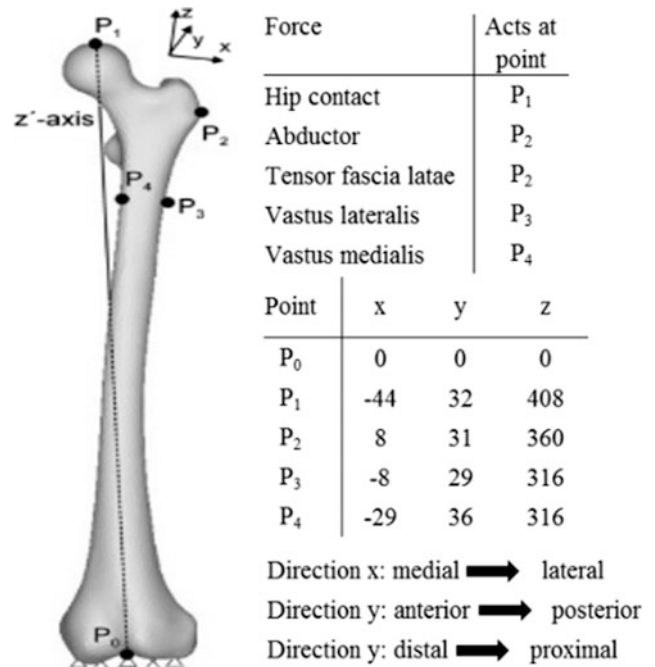
Fig. 1 Boundary conditions (constraints and force acting points) for the intact femur [14]

A simplified analysis with a 3 mm refinement of the mesh was adopted from the edges, which added up to 1004. The solid meshes were generated based on the edges of the 502 faces of the structure representing the human femur. The elements used are parabolic tetrahedral, which exhibit 10 knots, three degrees of freedom at each node, with Jacobian/distortion value at the element level.

From the numerical simulations, it is sought to establish the stress gradient of Von Mises for each situation, since such a stress distribution provides scalars proportional to the elastic deformation energy, calculated from the principal stresses "σ_1", "σ_2" and "σ_3", as shown in the following equation [11], for each Von Mises stress found (σ).

$$\sigma = \sqrt{(((\sigma_1 - \sigma_2)^2 + (\sigma_2 - \sigma_3)^2 + (\sigma_3 - \sigma_1)^2)/2)} \quad (1)$$

The various loads and contour conditions imposed on the healthy femur daily are complex [12, 13], in this work the Von Mises stresses and deformation imposed on the femur are discussed in the action points (see Fig. 1), figure from [14].

Table 1 Mechanical properties of cortical and spongy bone [7]

Material	Young's modulus (GPa)	Stiffness modulus (GPa)	Poisson's ratio
Cortical	$E_x = 11.5$	$G_{xy} = 3.6$	$v_{xz} = 0.31$
	$E_y = 11.5$	$G_{yz} = 3.3$	$v_{yz} = 0.31$
	$E_z = 17.0$	$G_{xz} = 3.3$	$v_{xy} = 0.51$
Spongy	$E = 2.13$		$v = 0.3$
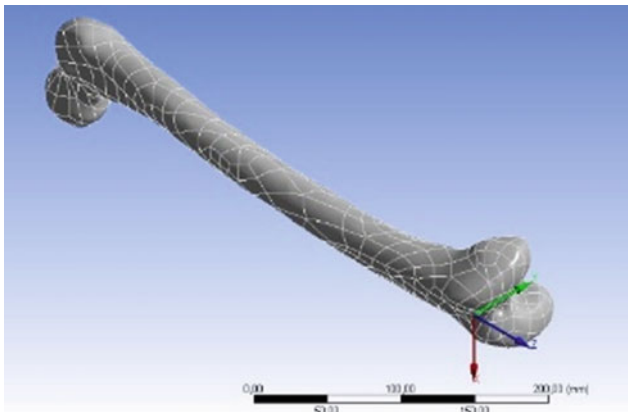
Fig. 2 3D femur adopted for simulations with boundary faces using ANSYS [15]

3 Results

In recent studies, the applications of femoral contour conditions have disregarded less expressive muscle actions in terms of loading.

The representative solid of the human femur can be visualized in Fig. 2, with the distinction of its faces and the origin of the adopted coordinate system.

The forces described in this work are predominantly internal, being those that include the result of muscular activity, unlike external forces, like of ground reaction. A new material was created in the ANSYS® simulations environment to apply the efforts correctly. The physical properties of interest are shown in Table 1.

The project developed in ANSYS® had results in the modal analysis of the human femur, simulating its modes of vibration and their corresponding deformations. Highlighting the maximum and minimum deformations, in the mode 1, frequency 0 Hz, min = 18.23 mm and max = 68.01. In the mode 12, for frequency 1382.1 Hz, min = 2.56 mm and max = 72.85 mm.

For the simulations performed in this section, the distal end set as a boundary condition for the loads application.

In this study, for the distribution of mineral density of the femur, for a healthy and intact bone, the predominance is 1.74 g/cm³, value adopted for the simulations.

The values of Table 2 correspond to the [14] work, for the abductor muscles (gluteus maximus, gluteus maximus and gluteus medius) and also tensor muscle fascia latae, which distribute on the surface of the great trochanter, of the pelvis contact in the femoral head.

The simulations were conducted for the data from Table 2 primarily for isolated pelvic stresses, which are applied to the femoral head. The following data presents the stresses applied for each cycle of the walk for the hip contact loading component. The module, direction and direction of loading is applied just like in Fig. 1, from its components presented in Table 2, for 25% of the cycle of the walk. Figure 2 shows the origin of the coordinate system adopted in the simulations for this study. All the others values are applied on the same circumstances.

Gait cycle 25% performs an 1875.2 N resultant force, by the hip contact. The maximum Von Mises stress observed is 31.297 MPa, at the terminal part of the femur, near the constraint part. Gait cycle 45% performs a 1709.3 N resultant force, by the hip contact. The maximum Von Mises stress observed is 21.281 MPa, at the diaphysis part. Gait cycle 65% performs 856.18 N as resultant force, by the hip contact. The maximum Von Mises stress observed is 26.214 MPa, at the diaphysis part. Gait cycle 85% performs a 273.76 N resultant force, by the hip contact. The maximum Von Mises stress observed is 8.5354 MPa, at the diaphysis part.

For the efforts applied by the hip contact and abductor, at the gait cycle 25%, on the femoral head and greater trochanter, the resultant forces are 1875.2 N and 837.05 N, respectively. The maximum Von Mises stress observed is 35.337 MPa, at the internal diaphysis part. Gait cycle 45% performs 1709.3 and 609.61 N as resultant forces. The maximum Von Mises stress observed is 29.249 MPa, at the internal diaphysis part. Gait cycle 45% performs 1709.3 and 609.61 N as resultant forces. The maximum Von Mises stress observed is 29.249 MPa, at the internal diaphysis part.

Table 2 Gait cycle—contact forces of the pelvis and muscles under the cycle of the walk [14]

Load	25%			45%			65%			85%		
Component	Fx	Fy	Fz	Fx	Fy	Fz	Fx	Fy	Fz	Fx	Fy	Fz
Hip contact	−451.4	−225.7	1806	−393	−41.8	1663	−334.4	−58.5	786	−108	−16.7	251
Abductor	468	0	694	334	−92	501.6	0	0	0	0	0	0
Tensor fascia latae	117	158.8	−75.2	142	158.8	−58.5	0	0	0	8.4	16.7	0

4 Discussion

The modal analysis shows the modes of vibration of the femur, it is interesting to, qualitatively, highlight the regions of greatest deformation and the behavior of the largest bone of the human body when in resonance.

The methodology adopted in this study aims to update the health professional focusing on the internal efforts given by muscles, in the practice of physical activities, under the biggest bone of the human body, how it has undergone modifications throughout of the work development, due to the little (or nonexistent) volume of information found for the topic addressed.

Observing the analyzed work [14], it is possible to perceive that the higher tensions in the femoral head and observed in all extensions of the femur are due to the hip contact, of the force applied in the femoral head. When the forces applied in the greater trochanter are evaluated, it is possible to see that the tensions in the femoral diaphysis increase and change their distribution. In this sense it is important to relate patients' weaknesses, or even their mineral density along the bone, to approve the practice of physical exercise. With the visual/numerical information available, it is possible to observe where the regions that undergo greater tensioning.

5 Conclusion

The study of von Mises stresses in biomechanical structures promotes the knowledge of parts of the bone structure more susceptible to ruptures and weaknesses in the practice of exercises. This work brings quantitatively the application of forces due to muscles under real conditions of an intact bone, in order to perceive how it behaves in the practice of gait.

Conflict of Interest Declaration The authors have no competing interests related to this work.

References

1. Doblaré, M., García, J.M., Gómez, M.J.: Modelling bone tissue fracture and healing: a review. Eng. Fract. Mech. (2004)
2. Antonialli, A.I.S.: Efeito da geometria e da rigidez do projeto da prótese de quadril no estímulo ao remodelamento ósseo. São Carlos: UFSCar, 2014. Tese (Doutorado) – Universidade Federal de São Carlos (2013)
3. Júnior, A.C.F., Rocha, E.P., Assunção, W.G., Santos, P.H.: Bioengenharia aplicada à Odontologia: método dos elementos finitos versus fotoelasticidade. Rev. Implant. **4**(4), 377–382 (2007)
4. Rubo, J.H., Souza, E.A.C.: Métodos computacionais aplicados à Bioengenharia: Solução de problemas de carregamento em próteses sobre implantes. Rev. FOB **9**(¾), 97–103 (2001)
5. Lotti, R.S., Machado, A.W., Mazzieiro, E.T.E., Landre-Júnior, J.: Aplicabilidade científica do método dos elementos finitos. R Dental Press Ortodon Ortop. Facial **11**(2), 35–43 (2006)
6. Moreland, J.R., Bassett, L.W., Hanker, G.J.: Radiographic analysis of the axial alignment of the lower extremity. J. Bone Joint Surg. Am. **69**(5), 745–749 (1987)
7. Queiroz, L.P.: Simulação numérica através do método dos elementos finitos e comparação experimental para obtenção de tensões e deformações específicas em fêmur com prótese total de quadril. Master Thesis Mechanical Engineering. Universidade Estadual Paulista. Guaratinguetá (2014)
8. Souza, A.J.S., Silva, G., Sousa, E.: Estudo comparativo de tensões aplicadas à cabeça do fêmur em uma prótese de quadril através de sistema computacional, considerando os materiais mais utilizados. J. Biomech. **12**(22), 22–28 (2011)
9. D model of a human femur by Enrique. https://grabcad.com/library/femur–1. Last accessed 10 Jan 2017
10. Massin, P., Geais, L., Astoin, E., Simondi, M., Lavaste, F.: The anatomic basis for the concept of lateralized femoral stems: a frontal plane radiographic study of the proximal femur. J. Arthroplast. **15**(1), 93–101 (2000)
11. Beer, F.P., Johnston, J.R., Russell, E.: Resistência dos Materiais, 3rd edn. Pearson, São Paulo (1996)
12. Heller, M.O., Bergmann, G., Kassi, J.P., Claes, L., Haas, N.P., Duda, G.N.: Determination of muscle loading at the hip joint for use in pre-clinical testing. J. Biomech. **38**(5), 1155–1163 (2005)
13. Speirs, A.D., Heller, M.O., Duda, G.N., Taylor, W.R.: Physiologically based boundary conditions in finite element modeling. J. Biomech. **40**(10), 2318–2323 (2007)
14. Behrens, B.A., Nolte, I., Wefstaedt, P., Stukenborg-Colsman, C., Bouguecha, A.: Numerical investigations on the strain-adaptive bone remodeling in the periprosthetic femur: influence of the boundary conditions. BioMed. Eng. Online **8**(7), 1–9 (2009)
15. ANSYS Release 15.0 Documentation. Houston, USA, Ansys Inc. (2013)

On the Use of Inertial Sensors for the Assessment of Step and Stride Time Variability in Individuals with Parkinson's Disease: Preliminary Study

Luiza Luiz, Amanda Rabelo, Gabriel Jablonski, Samila Costa, Luciane Souza, Marcus Fraga Vieira, and Adriano Andrade

Abstract

Parkinson's disease (PD) is a multisystemic pathology compromising, between other signs, the gait performance. The objective of this work is to apply a methodology based on inertial sensors to analyze gait in subjects with PD to detect clinical signs of the disorder. In this study, data were collected from two subjects with PD. The participants walked on a treadmill in a constant velocity of 2 km/h for 1 min. The task was accomplished in two ways: Condition 1—with hand support; and Condition 2—without hand support. The inertial sensors were positioned on the anterior superior iliac spine for detection of step and stride time intervals. The results showed that in Condition 2 the variability of acceleration time series and the variability of step and stride duration increased. Furthermore, these changes are related to the level of patients clinical motor signs.

L. Luiz (✉) · A. Rabelo · G. Jablonski · S. Costa · A. Andrade
Faculty of Electrical Engineering, Centre for Innovation and Technology Assessment in Health, Postgraduate Program in Electrical and Biomedical Engineering, Federal University of Uberlândia, Uberlândia, Brazil
e-mail: luizamaire@gmail.com; luizamaire@hotmail.com

A. Andrade
e-mail: adriano@ufu.br

L. Souza
Federal University of Triângulo Mineiro, Uberaba, Brazil

M. F. Vieira
Bioengineering and Biomechanics Laboratory, Federal University of Goiás, Goiânia, Brazil

1 Introduction

Parkinson's disease (PD) is an idiopathic, multisystemic disorder, that causes intraneuronal lesions in the gray matter, and produces damage to the autonomic, limbic, and somatomotor systems [1]. Previous studies have shown that motor symptoms in PD affect the lower limbs, compromising the performance of several activities [2], including postural control [3], and gait performance [4].

Individuals with PD, due to neurotransmitter decrease have progressive degradation of locomotor responses resulting in gait stereotyped changes with short-stepped, narrow based and shuffling gait [5].

The analysis of gait and other motor signs of PD can be based on the Unified Parkinson's Disease Rating Scale (UPDRS), considered a standard for evaluation in research related to PD. However, the subjectivity of the evaluation makes the results difficult to interpret, and reduces the reproducibility of the tests [6].

The analysis of gait kinematic and kinect patterns in PD is a valuable tool for obtaining quantitative information on motor deficits, and it has been used by several researches using cameras and force platform, being the use of inertial sensors an alternative approach to previous studies [7–10].

In order to investigate the causes and to understand gait disturbances, Hannink et al. [9] analyzed habitual gait in PD patients using inertial sensor on both feet, streaming the signal via Bluetooth to a mobile device.

Moore et al. [10] applied a technique for long-term monitoring of gait in PD, using inertial sensors to analyze the effectiveness of the levodopa therapy, estimating spatial-temporal conditions of gait. Hyung-Soon et al. [11] developed a support treadmill interface designed to provide a safe and controlled walking platform to evaluate gait under various conditions, simulating real life circumstances.

Therefore, the objective of this study is to apply a methodology based on inertial sensors [12] to analyze gait in PD patients as a potential tool to detect clinical signs of the disorder.

2 Materials and Methods

2.1 Participants

In this preliminary study, data were collected from two PD patients. The exclusion criteria were the presence of cognitive deficit and freezing of gait (FOG). After written informed consent has been obtained, the participants were submitted to protocols previously approved by the local Research Ethics Committee (CAAE: 82384418.4.0000.5154).

Each subject had different motor characteristics as consequence of PD. Table 1 reports clinical signs relevant for the analysis, which were characterized through the application of the UPDRS by an experienced professional.

2.2 Description of the Experimental Protocol

The participants walked on a treadmill in a constant velocity of 2 km/h for 1 min. The task was accomplished in two experimental conditions: Condition 1—with hand support; and Condition 2—without hand support. Figure 1 depicts the experimental conditions.

2.3 The Hardware for Data Acquisition

Data were acquired by using a custom-made system called TREMSEN (Precise Tremor Sensing Technology, National Institute of Intellectual Property—Brazil—BR 10 2014 023282 6) [12, 13]. The system employs triaxial inertial measurement units (IMUs) based on MEMS technology consisting of a gyroscope, an accelerometer and a magnetometer (L3G4200D, LSM303DLM). The I2C protocol is used for the communication between the IMU and the microcontroller. The sampling frequency was set to 50 Hz.

The analog to digital conversion used a 12-bit A/D converter. The microcontroller reads the sensor information and transmits the data to the PC via serial communication (USB).

2.4 Detection of Step and Stride Time

There are several alternatives for the detection of step and stride when using inertial sensors [9, 10]. Based on studies reported in the literature the inertial sensors were positioned on the anterior superior iliac spine (ASIS) for the detection of pelvic rotation and translation, aiming to identify the step and stride executed by each of the different lower limbs [12].

To verify the gait cycle we chose the anterior-posterior axis of the accelerometer which is able to capture the swing and support phases through the pelvic movement.

The gait cycle we chose the Z-axis of the accelerometer to measure the variation of the acceleration in the sagittal plane. The signals were filtered by using a zero-phase digital, 20th order bandpass Butterworth filter, with lower cutoff frequency of 0.01 Hz and upper cutoff frequency of 5 Hz. The linear trend of the signal was removed by subtracting it from its mean, and the nonlinear trend was removed by subtracting the signal from a high order polynomial (order = 20) fit. This procedure ensures that the resulting signal oscillates evenly around a given reference. The gait cycle or stride is the time interval or sequence of motions occurring between two consecutive initial contacts of the same foot. The beginning of the first gait cycle or stride (i.e., the heel strike) is the first local minimum of the Z-axis of the accelerometer, and its end is the next local minimum on the same side. Thus, the stride consists of two steps, starting with the step of a limb followed by the step of the other [12].

Briefly, Fig. 2 illustrates typical detections of step and stride time for both limbs. The left and right limbs are represented by the blue line and red lines, respectively. The heel strikes are marked with "o" and "*" on the horizontal axis with their respective colors. The time difference between these markers is the step time interval. The black arrows indicate the stride time intervals.

3 The Results

Table 2 presents the mean and standard deviation for the step and stride time intervals for both subjects in the two experimental conditions. It is possible to verify that the step and stride mean time were smaller for Condition 2 for both subjects independently of the main motor sign present in the subject. The step and stride time interval variability,

Table 1 Clinical signs of the participants of the study

Subject	Main motor dysfunction	UPDRS—Gait
1	Dyskinesia	2—Mild: independent walking but with substantial gait impairment
2	Tremor	1—Slight: independent walking with minor gait impairment

Fig. 1 Experimental protocol. The subject is walking in a treadmill in two experimental conditions

Condition 1: With hand support

Condition 2: Without hand support
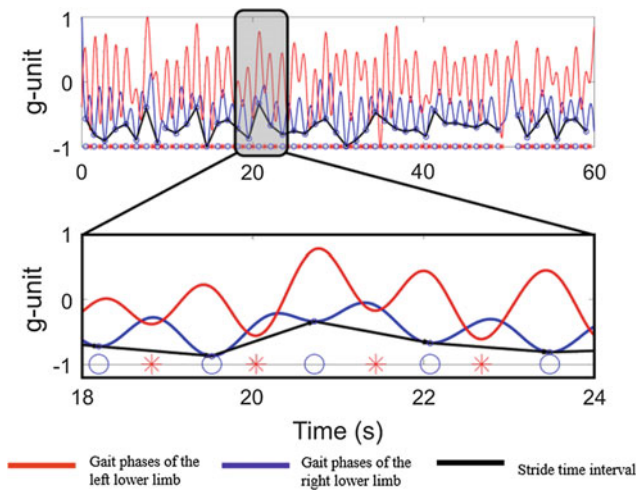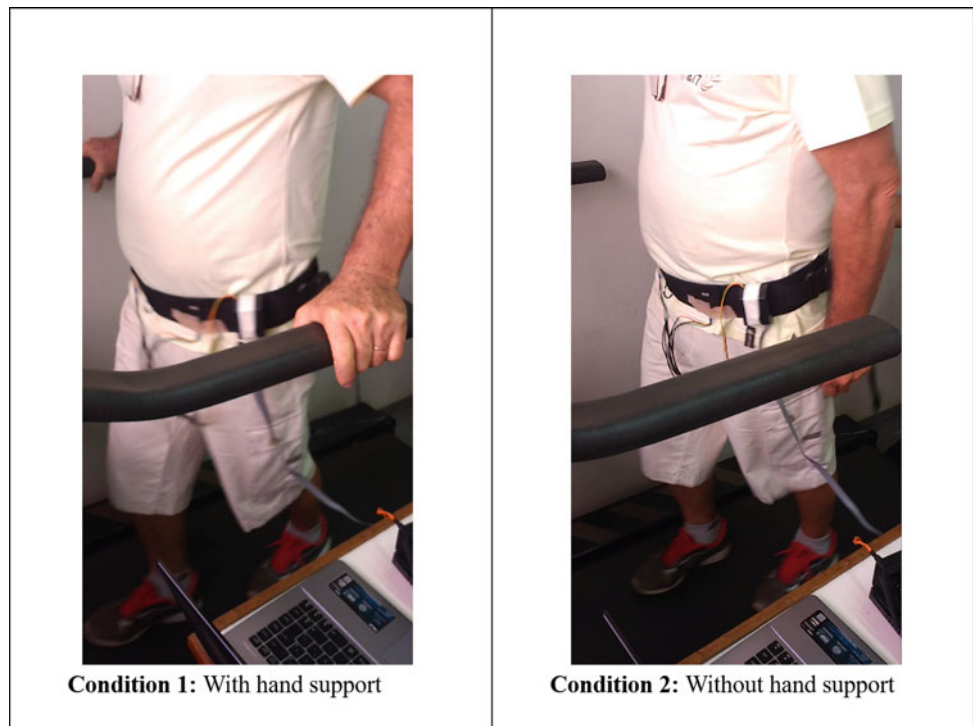
Fig. 2 Filtered signals obtained from *the* Z-axis of the accelerometers. The blue and red lines represent gait phases of the left and right lower limbs, respectively. The left and right heel strikes are indicated with the "o" and "*" markers, respectively. The black solid line which represent the estimated stride time interval (Color figure online)

measured by its corresponding standard deviation, was greater in Condition 2 than in Condition 1. Besides, subject 1 presents greater variability than subject 2, suggesting that step and stride time interval variability can be compromised, beyond a optimum value, by the level of disease.

Figure 3 depicts typical detections of the step and stride time for both lower limbs of subject 1. In addition, in

Condition 2 the amplitude of acceleration is more variable than in Condition 1.

Figure 4 illustrates step and stride time intervals detected from subject 2.

4 Discussion and Conclusion

People with PD may have a progressive degradation of locomotor responses and stereotyped gait with short-stepped, narrow based, shuffling features [5]. From the results of this study it is possible to verify the first of these characteristics.

The results reported in Table 2 show that the variability of step and stride duration for the subject 1 is greater than that for subject 2 in both conditions. This suggest that step and stride time interval variability is compromised by the level of disease. It is known that a variability beyond an optimum value is detrimental for gait balance and stability.

Considering the step and stride time interval, it was observed a decrease and greater variability for Condition 2. This highlight the difficulty of the PD patients to negotiate gait on a treadmill, so that they assume a more conservative gait pattern, with reduction in the estimated stride time interval [5] and gait non-uniform. Such alteration can be view as a strategy to preserve gait balance and stability.

In Figs. 3 and 4, for Condition 2 the step and stride acceleration amplitude shows a pattern less uniform than for Condition 1, indicating reduction in step time interval.

Table 2 Mean and standard deviation for the step and stride time intervals (s) of both subjects

Subject	Condition	Step—Left		Step—Right		Stride—Left		Stride—Right	
		Mean	Std	Mean	Std	Mean	Std	Mean	Std
1	1	0.60	0.10	0.59	0.10	1.20	0.09	1.20	0.11
	2	0.53	0.16	0.38	0.15	1.17	0.39	0.93	0.12
2	1	0.66	0.03	0.68	0.03	1.34	0.03	1.34	0.03
	2	0.63	0.04	0.54	0.03	1.17	0.04	1.17	0.04
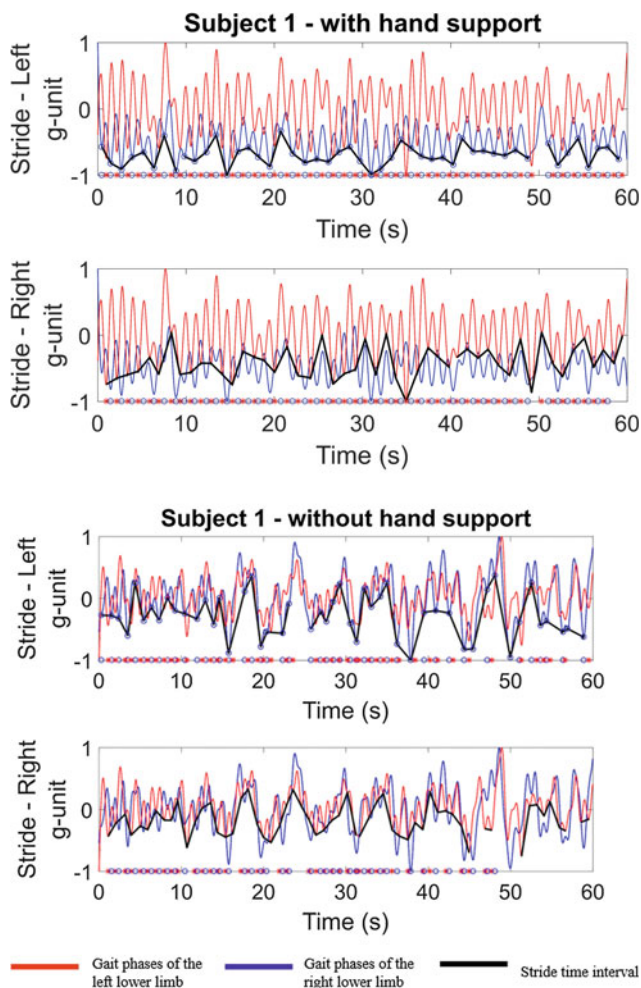
Fig. 3 Illustration of the step and stride for subject 1, for both lower limbs

Fig. 4 Step and stride time for subject 2, for both lower limbs

The step and stride variability can be observed in standard in Table 2, this possible happened because increase in support phase and decrease in balance phase.

There are also considerations to be made about individual characteristics of each subject. Subject 1 (Fig. 3) presents an acceleration pattern less uniform, which can be assumed to have relation to his more compromised motor functions. This highlight that the results from the evaluation based on the method using inertial sensors are compatible with the clinical evaluation based on the UPDRS.

As for subject 2 (Fig. 4), in Condition 1, with hand support, there is a strong similarity to typical results obtained from healthy subjects, as reported in a previous study of our research group [12]. In Condition 2 without hand support, however, the subject shows the stereotyped characteristics of PD, and difficulty to deal with gait on a treadmill, as discussed above. Furthermore, the results to the subjects indicate body side more impaired.

Although the step and stride analyses were effective in detecting changes in the gait patterns of the participants, and the results are consistent with those found in patients with PD, there are limitations to be pointed out in the experimental design.

An important point is that changes in walking speed associated with the use of a treadmill, which controls the walking speed, that decreases the natural gait variability and can increase the fear of fall, leading to the adoption of a more conservative gait patterns for maintaining balance and stability [11].

Hannink et al. [9] highlights the importance of allowing the subject to walk freely. For this, information from the inertial sensors could be transmitted wirelessly to a mobile device.

As for the safety aspect during the execution of the tasks, Hyung-Soon et al. [11] proposed the use of a support to hold the participants. In the present work, we were unable to offer total security for the patients with PD.

Typical gait patterns of PD patients may not be fully identified during brief examinations performed in a clinical scenario, so long-term, unobtrusive monitoring of their activities is essential [8, 10].

From these standpoints, our future research plans involve the evaluation of patients at different times, over an extended period, proposing the analysis of the habitual gait, simulating real life circumstances in free space by using inertial sensors for movement detection.

Conflicts of Interest The authors declare no conflict of interest.

References

1. Braak, H., Ghebremedhin, E., Rüb, U., et al.: Stages in the development of Parkinson's disease-related pathology. Cell Tissue Res. **318**, 121–134 (2004). https://doi.org/10.1007/s00441-004-0956-9

2. Dickson, J.M., Grünewald, R.A.: Somatic symptom progression in idiopathic Parkinson's disease. Park. Relat. Disord. **10**, 487–492 (2004). https://doi.org/10.1016/j.parkreldis.2004.05.005

3. Mancini, M., Carlson-Kuhta, P., Zampieri, C., et al.: Postural sway as a marker of progression in Parkinson's disease: a pilot longitudinal study. Gait Posture **36**, 471–476 (2012). https://doi.org/10.1016/j.gaitpost.2012.04.010

4. Wang, X., Kyrarini, M., Ristić-Durrant, D., et al.: Monitoring of gait performance using dynamic time warping on IMU-sensor data. Med. Meas. Appl. (2016)

5. Morris, M.E., Huxham, F., McGinley, J., et al.: The biomechanics and motor control of gait in Parkinson disease. Clin. Biomech. **16**, 459–470 (2001). https://doi.org/10.1016/S0268-0033(01)00035-3

6. Goetz, C.G., Tilley, B.C., Shaftman, S.R., et al.: Movement disorder society-sponsored revision of the unified Parkinson's disease rating scale (MDS-UPDRS): scale presentation and clinimetric testing results. Mov. Disord. **23**, 2129–2170 (2008). https://doi.org/10.1002/mds.22340

7. Manuscript, A., Magnitude, S.: NIH Public Access. **31**, 1713–1723 (2013). https://doi.org/10.1109/TMI.2012.2196707.separate

8. Yoneyama, M., Kurihara, Y., Watanabe, K., Mitoma, H.: Accelerometry-based gait analysis and its application to Parkinson's disease assessment. Part 2: a new measure for quantifying walking behavior. IEEE Trans. Neural Syst. Rehabil. Eng. **21**, 999–1005 (2013). https://doi.org/10.1109/TNSRE.2013.2268251

9. Hannink, J., Kluge, F., Gassner, H., et al.: Quantifying postural instability in Parkinsonian gait from inertial sensor data during standardised clinical gait tests. In: 2017 IEEE 14th International Conference Wearable Implant Body Sensor Networks BSN'17, pp. 129–132 (2017). https://doi.org/10.1109/bsn.2017.7936024

10. Moore, S.T., MacDougall, H.G., Gracies, J.M., et al.: Long-term monitoring of gait in Parkinson's disease. Gait Posture **26**, 200–207 (2007). https://doi.org/10.1016/j.gaitpost.2006.09.011

11. Hyung-Soon Park, H.-S., Jung Won Yoon, J.W., Jonghyun Kim, J., et al.: Development of a VR-based treadmill control interface for gait assessment of patients with Parkinson's disease. In: 2011 IEEE International Conference on Rehabilitation Robotics, pp. 1–5 (2011). https://doi.org/10.1109/icorr.2011.5975463

12. Andrade, A.O., Ferreira, L.C.V., Rabelo, A.G., et al.: Pelvic movement variability of healthy and unilateral hip joint involvement individuals. Biomed. Signal Process. Control **32**, 10–19 (2017). https://doi.org/10.1016/j.bspc.2016.10.008

13. Rabelo, A.G., Neves, L.P., Paixão, A.P.S., et al.: Objective assessment of Bradykinesia estimated from the wrist extension in older adults and patients with Parkinson's disease. Ann. Biomed. Eng. **45**, 2614–2625 (2017). https://doi.org/10.1007/s10439-017-1908-3

Performance of Contemporary Dancers in Drop Jump Test Assessed by Reactive Strength Index

Ludmila Ferreira dos Anjos, Johelma Galvão, and Marcus Fraga Vieira

Abstract

The aim of this research was to analyze the reactive strength index of contemporary dancers during the execution of a drop jump test. Sixteen contemporary dancers (24.2 ± 3.9 years old, 1.62 ± 0.05 m height, 57.7 ± 6.8 kg mass, 15.6 ± 3.1 time of practice) took part in the study. All volunteers executed the drop jump test from two heights with different positions of the arms (hands placed in the waist and arms free to execute a movement). The jumps were performed on an AMTI force plate and the volunteers were asked to perform tree trials in each condition in a randomized way. The average of the trials in each condition was taken. The reactive strength index (RSI) was computed using a custom Matlab code, and the results were compared using two-way repeated measures Anova (height and arms as factors). No significant differences were found between the different heights of the jump. A significant difference was observed comparing the position of the arms ($p < 0.05$). The jumps with the aiding movement of the arms had a greater RSI, so that the arms influence the performance of the RSI during the DJ. However, contemporary dancers have a poor performance in DJ compared to elite athletes, suggesting the necessity of a specific muscle/power training for improving their performance in dance leaps.

Keywords

Drop jump test • Contemporary dancers • Reactive strength index

L. F. dos Anjos (✉) · J. Galvão · M. F. Vieira
Bioengineering and Biomechanics Laboratory, Federal University of Goiás, Goiânia, Brazil
e-mail: ludmilafa@hotmail.com

1 Introduction

1.1 Contemporary Dancers

The esthetics of a dancer depends of its technical and artistic development, which is the expression of the dimensions, proportions, compositions and shapes of its body that defines a specifically physical profile [1]. Dance requires a high weekly volume of training, so, depending on intensity, this high volume may be a sufficient load to cause physiological adaptations of the muscular strength and muscular power. Vertical jump (VJ) performance is one of the best indicators of lower limbs muscle power [2].

Contemporary dancers often practice specific types of jumps in their classes, but the jumps are not the main objective of their rehearsals. Contemporary dancers tend to have a better balance control in comparison to non-dancers [3], but it's not known if they present better jump performance, which can be assessed in a drop jump test. The reason of the choice of this type of test is because they are good to evaluate the strength performance of dancers in the stretch shortening cycle, since there are kinds of jumps that they execute in classes that are similar to the way this jump is done, the dancers have a short time in contact with the ground. There is a jump called *assemblé* (the dancers have to take one leg of the ground, jump, join both legs in the air and land) that dancers can execute as one single jump or as an impulse to execute a bigger jump as soon as they touch the ground, so they need strength in the short time stretch shortening cycle. Another example is when dancers execute *grand jeté*, they need to get impulse from *gallop* (a step that imitates a horse, the dancer step, then bring his front and back legs together in the air, and when land he/she can do a jump a *pirouette* or other types of exercises) and execute the jump as soon as they touch the floor.

1.2   Drop Jump Test (DJ)

The drop jump (DJ) is a test were the subject comes down of a predetermined height (from a box or similar object) and when he/she lands on the floor he/she has to immediately perform a maximal effort vertical jump [4]. This specific type of jump can be used to improve the vertical jumping achievement of an athlete. This improvement is implicitly assumed as a result of a mechanical output of the muscles [5].

Different techniques are applied to determine parameter values quantifying DJs, such as the jump height or the durations of the phases of downward and upward movements of the center of mass during foot contact with the ground after dropping. The flight-time method estimates the jump height from the time between the instant of leaving the ground and the instant of landing [6]. The DJ test can also give important information to coaches about the stretch-shortening cycle capacity of the athletes [4].

1.3   Reactive Strength Index (RSI)

Reactive strength index (RSI) is a valid tool to analyze the performance of the stretch-shortening cycle. The RSI is described as a measure of a subject to restore and conserve high levels of elastic energy in the stretch-shortening cycle by immediately changing from the landing phase to the jumping phase during a DJ [4, 7].

The RSI is calculated by dividing the height of the jump in a DJ by the ground contact time required to execute the vertical rebound jump [4].

$$RSI = Height\ jumped / Time\ of\ rebound\ jump \qquad (1)$$

The RSI in conjunction with DJ is used in a variety of high-performance tests with athletes, and it can be interpreted as an indicator of the ability of the athletes to withstand the stretch loads during the plyometric component of their conditioning and general preparation [8]. The DJ-RSI is a test used by coaches and sport scientists to monitor reactive-strength and potentially neuromuscular readiness in athletes [9].

2   Aim

The aim of this study was to analyze the RSI of contemporary dancers during the execution of a drop jump test.

3   Methodology

3.1   Subjects

Participated in this study 16 contemporary dancers (6 males and 10 female, 24.2 ± 3.9 years old, 1.62 ± 0.05 m height, 57.7 ± 6.8 kg mass, 15.6 ± 3.1 time of practice). The subjects were all practicing their regular rehearsals during the week and the tests were done in a weekend were the participants weren't doing any physical exercises. The study was approved by the Ethics Commite of Federal University of Goias by the no. 1.003.935. The data were compared with the data of the athletes of the Kobal et al. [7] study whose respective antopometric data are presented in Table 1.

Height and mass of each subject were measured in the day of the test before the execution of the jumps. The volunteers answered a questionnaire about their age, time of practice, how the process of the classes/rehearsals happens and if they already had any injuries. They also signed a consent form before data collection.

3.2   Jumping Protocol

All volunteers had to execute the DJ test from two heights: Drop Jump 3 (DJ3), the jump was executed from the height of tree boxes of 11 cm each with hands positioned in the waist; Drop Jump 3 Free (DJ3F); same height of DJ3, but the participants could use upper limbs freely; Drop Jump 4 (DJ4) the jump was executed from the height of four boxes of 11 cm each with hands positioned in the waist; Drop Jump 4 Free (DJ4F), same height of DJ4 but the participants could use upper limbs freely. The participants were instructed to keep their hands on their waist throughout the drop and the jump in order to restrict arm movement, when the jump was supposed to be performed with no movement of the arms.

Table 1 RSI comparison between athletes from different sports modalities in the study of Kobal et al. [7] and contemporary dancers

	Power	Soccer	Tennis	Endurance
N	19	21	24	15
Body mass (kg)	75.5 ± 6.2	77.6 ± 7	72.4 ± 7.8	59.6 ± 7.1
Height (cm)	179.2 ± 2.6	180.3 ± 6.2	177.4 ± 7	175.4 ± 2.1
Age (years)	23.3 ± 5	21.8 ± 3	24.7 ± 6	24.1 ± 3.3

Each participant performed three maximal DJs in each condition in a randomized order, from 44 cm and the 33 cm of height on a force plate (AMTI OR6-7 model). Participants were instructed to step forward off the box, and on the contact with the force plate to jump "as high as possible and as quickly as possible". The participants had a 30 s of recovery time between each trial.

3.3 Procedures

According to Bosco et al. [10], the displacement of C.G. (center of gravity) during flight (h_0) is calculated using flight time (t_f) as follows:

$$h_0 = 1/8 \, g t_f^2 \qquad (2)$$

where h_0 = jump height (cm), g = acceleration due to gravity (9.81 ms^{-1}) and t_f = flight time of the jump(s) measured as the time during when the ground reaction force remains at zero after the jump.

Next, RSI was calculated according to Eq. 1. The calculations were done using a custom Matlab code.

3.4 Statistics

The average of the trials for each condition was taken.

As the data presented normal distribution (Shapiro-Wilk test, $p > 0.05$), two-way repeated measures ANOVA (height and arm movement as factors) was applied to compare the results in the different conditions. Statistical analysis was performed using SPSS v. 20, and the significance level was set at $p < 0.05$.

4 Results

The graph (Fig. 1) shows the performance of the RSI of the sixteen participants in the different conditions. Significant differences were observed only when the arms were freely used.

The ANOVA did not present any significant effect of box height for the RSI values but presented a significant ($p = 0.005$) arm effect in this variable.

The soccer, tennis and resistance athletes of the study in comparison [7], presented an RSI of 2.31 ± 0.53, 0.84 ± 0.13, 0.76 ± 0.15, 0.91 ± 0.26, respectively.

Contemporary dancers presented the RSI values at least 66% lower than the remaining athletes.

The average flight time of the dancers was 35 ms.
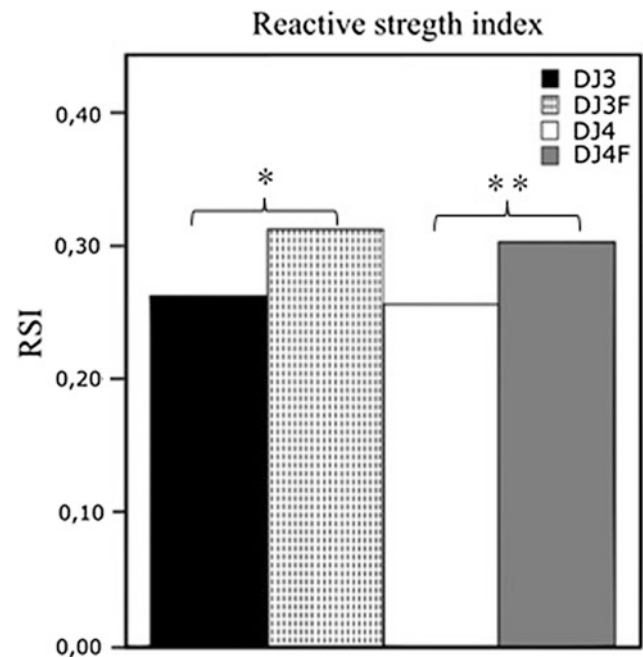
Fig. 1 RSI's mean in DJ for each condition.*$p < 0.05$ when comparing DJ3 and DJ3F regarding the different use of upper limbs. **$p < 0.05$ when comparing DJ4 and DJ4F regarding the different use of upper limbs

5 Discussion

As the results have showed, there was no significant difference between the results regarding the height from which the DJ was made (DJ3 compared with DJ4, and DJ3F compared with DJ4F), so it can be inferred that there is no interference in the RSI of dancers when they perform the DJ in different heights, so there is a detectable strength adaptation to dance practice, when measured by the index.

The results also showed that when comparing the jumps with the aiding movement of the arms (DJ3 compared with DJ3F, and DJ4 compared with DJ4F) the RSI obtained by the dancers was greater than the one without the aid of them. The contact time with the ground was practically the same with few variations. This comparison suggests that the arms influence the performance of the RSI during the DJ. As it has been reported previously, the arms movement helps the subject to perform better, leading the participant to be able to jump higher, therefore, having a higher RSI [11]. Previous studies [12] also contributed to the use of exercises at a moderate level of weight and negative power intensity, which contributed to an average of 10% for the total center of mass.

When the values of the RSI are higher it means that the ability of the subjects to change from an eccentric contraction to a concentric contraction is good [4]. Power athletes

have a greater RSI when compared to soccer players, tennis players and endurance runners, showing that the athletes that don't have jumps as their main training goal don't succeed as well as athletes that do [7]. This also has happened to the dancers, since jumping is not their main objective in practices, they showed lower values of the RSI compared to the values found in other studies (the value of the RSI of power athletes was higher than 1) [7].

Teachers and coaches can use this type of analysis to follow up the efficiency of stretch-shortening cycle training of their dancers to further execute higher and better jumps in their choreographies and routines [7].

Compared with previous studies it was noticed that the contemporary dancers achieved very low RSI performance compared to soccer players, tennis players, power and endurance athletes, even with the aid of the arms. The results suggest that muscle strengthening, and a specific jump training is advisable for contemporary dancers improve their performance in leaps.

References

1. da Silva, A.H., Cattelan Bonorino, K.: IMC e flexibilidade de bailarinas de dança con-temporânea e ballet clássico. Fitness Perform. J. **7**(1) (2008)

2. Pupo, J., Detanico, D., Santos, S.G.: Kinetic parameters as determinants of vertical jump performance. Rev. Bras. Cineantropometria Desempenho Hum. **2** (2010)

3. Sirois-Leclerc, G., Remaud, A., Bilodeau, M.: Dynamic postural control and associated attentional demands in contemporary dancers versus non-dancers. PLoS ONE **12**(3), e0173795 (2017)

4. Healy, R., Kenny, I.C., Harrison, A.J.: Assessing reactive strength measures in jumping and hopping using the optojump™ system. J. Hum. Kinet. **54**(1), 23–32 (2016)

5. Bobbert, M.F., Huijing, P.A., van Ingen Schenau, G.: Drop jumping. I. The influence of jumping technique on the biomechanics of jumping. Med. Sci. Sports Exer. **19**(4), 332–338 (1987)

6. Baca, A.: A comparison of methods for analyzing drop jump performance. Med. Sci. Sports Exer. **31**(3), 437–442 (1999)

7. Kobal, R., Nakamura, F., Kitamura, K., Abad, C.C., Pereira, L., Loturco, I.: Vertical and depth jumping performance in elite athletes from different sports specialties. Sci. Sports (2017)

8. Reilly, T., Cabri, J., Araújo, D.: Science and Football V: The Proceedings of the Fifth World Congress on Sports Science and Football, Routledge (2005)

9. Beattie, K., Flanagan, E.P.: Establishing the reliability & meaningful change of the drop-jump reactive strength index. J. Aust. Strength Cond. **23**(5), 12–18 (2015)

10. Bosco, C., Luhtanen, P., Komi, P.V.: A simple method for measurement of mechanical power in jumping. Eur. J. Appl. Physiol. Occup. Physiol. **275** (1983)

11. Lees, A., Vanrenterghem, J., De Clercq, D.: Understanding how an arm swing enhances performance in the vertical jump. J. Biomech. **40** (2004)

12. Martins, R.: Análise das Variáveis Dinâmicas dos Saltos Verticais. Escola de Educação Física, Fisioterapia e Terapia Ocupacional, Universidade Federal de Minas Gerais **22** (2009)

Polytopic Uncertainties Identification for Electrically Stimulated Lower Limbs

R. G. Teodoro, W. R. B. M. Nunes, M. A. A. Sanches, R. A. de Araujo, M. C. M. Teixeira, and A. A. de Carvalho

Abstract

Functional electrical stimulation (FES) has been used for a wide range of applications in individuals with spinal cord injury. Spinal cord injury rehabilitation modalities based on FES include gait training programs, restoration human-body vital function, and others. The various control methodologies require a system mathematical model, therefore, it is necessary to identify the parameters of this system. It is an extremely complex challenge to control the knee angle or the torque shank-foot complex through the functional electrical stimulation applied to the muscle. The response of the stimulated muscle is nonlinear and time-varying, allowing the fatigue occurrence due to muscle fibers non-physiological recruitment and altered muscle composition caused by FES. Relevant studies show that system developed in closed-loop satisfactorily deals with disturbances and uncertainties of the plant to be controlled. The contribution of this paper is to propose an analysis about polytopic uncertainties identification of the electrically stimulated lower limbs model. Knowing a priori the uncertain parameters of the linearized plant, the performance of a possible controller could be more efficient. In future works, it will be possible to design robust control techniques via linear matrix inequalities. Through this study, it is possible to work a large sample of volunteers with the objective of measuring muscular behavior when using the FES application.

1 Introduction

Functional electrical stimulation (FES) is an important technique to restore movement in people with paralyzed limbs. However, a difficulty in the FES field is to identify the mathematical model parameters and consequently to perform a smooth control for the paralyzed limb movement and with the least muscular fatigue possible.

The system's mathematical model to be controlled is fundamental to controllers design. Particularly in the FES, the dynamic relationship between the voltage or current applied in the muscle and joint position must be well understood. However, this process involves biomechanical interactions and several complex physiological phenomena, which are dynamic, non-linear and uncertains.

Ferrrarin and Pedotti [1] presented experimental results of a second order nonlinear model to represent the dynamics lower limb movement, from electrically stimulated quadriceps. One limitation of this model is not to consider the muscular delay in the relation between active torque and pulse width.

Another important study was by Previdi [2], who used NARX models through polynomial structures and with neural networks to describe the nonlinear relationship between quadriceps stimuli with knee joint movement, both in isometric and isotonic conditions. A practical limitation of this technique was to perform the identification in offline mode (simulation) without experimental results with controllers.

R. G. Teodoro (✉)
IFPR-Federal Institute of Paraná, José Felipe Tequinha St., Paranavaí, PR 1400, Brazil
e-mail: ricardo.teodoro@ifpr.edu.br

W. R. B. M.Nunes
UTFPR-Federal University of Technology – Paraná, Apucarana, PR, Brazil
e-mail: williar@utfpr.edu.br

R. G. Teodoro · W. R. B. M. Nunes · M. A. A. Sanches · R. A. de Araujo · M. C. M.Teixeira · A. A. de Carvalho
Department of Electrical Engineering, UNESP - São Paulo State University, Ilha Solteira, SP, Brazil

Schauer et al. [3] proposed an online approach to identify the parameters. The dynamics of the muscle was represented by a product between nonlinear activation dynamics and a nonlinear static contraction function, described by a neural network. In addition, an extended Kalman filter was implemented to estimate model parameters. By varying the parameter of muscle strength (in simulation mode), the obtained results showed robustness in position control for closed loop response. Although the proposed technique is valid, obviously the implementation of this technique is a challenge for embedded systems.

Teixeira et al. [4] showed that the nonlinear dynamics of the knee joint movement as a result of the electric stimulation applied to the quadriceps can be represented by the Takagi-Sugeno *fuzzy* model. A practical limitation of this approach is to monitor the torque variation in real time.

Most models consider position, velocity, and muscle torque variables as variables. However, obtaining the corresponding torque variation is a difficult process for experimental validation.

To overcome this problem, Sanches [5] proposed a novel model, where position, velocity and angular acceleration are considered as state variables. The state variables proposed in [5] are easily measurable.

We present for the first time in the literature an experimental protocol to obtain the polytopic uncertainties of the dynamic model of lower limbs using the Sanches model. The results obtained in this work contribute significantly to the approach of robust controllers design using the technique of linear matrix inequalities (LMI). The obtained results consider a uncertainty polytope with four vertices for tests in situations of non-fatigue, forced recruitment and fatigue around a desired angle of the knee joint.

2 Modeling of the Lower Limb with Polytopic Uncertainties

In a system that presents parametric uncertainties, these uncertainties can be restricted by a convex linear combination belonging to the set described as polytope.

2.1 State-Space Model

Sanches [5] in his study proposed a state-space model modification to facilitate practical implementation with accelerometers. Using elegant deduction, the torque state variable was replaced by acceleration. Further details of this technique can be found in [5].

Thus, the movement of the knee joint due to electrical stimulation applied in the quadriceps can be represented in state space as follows:

$$\begin{bmatrix} \dot{x}_{1N} \\ \dot{x}_{2N} \\ \dot{x}_{3N} \end{bmatrix} = \begin{bmatrix} 0 & 1 & 0 \\ 0 & 0 & 1 \\ \frac{\tilde{f}_{21}(x_1)}{\tau} & z(x_1) - \frac{B}{\tau J} & -\frac{B}{J} - \frac{1}{\tau} \end{bmatrix} \begin{bmatrix} x_{1N} \\ x_{2N} \\ x_{3N} \end{bmatrix} + \begin{bmatrix} 0 \\ 0 \\ \frac{G}{\tau J} \end{bmatrix} P_N,$$

$$(1)$$

where $x_{1N}(t)$ is the angular position of the knee joint, $x_{2N}(t)$ is the angular velocity, $x_{3N}(t)$ is the angular acceleration, B is the viscous friction coefficient, J is the moment of inertia, G and τ are parameters that express the first-order relation of the torque as a function of the pulse width P_N of the electric stimulus. The function $\tilde{f}_{21}(x_1)$ is a non-linearity of the system which can be described by:

$$\tilde{f}_{21}(x_1) = \frac{1}{Jx_1}\left[-mgl\sin(x_1 + \theta_{v0}) - \lambda e^{-E\left(x_1 + \theta_{v0} + \frac{\pi}{2}\right)}\left(x_1 + \theta_{v0} + \frac{\pi}{2} - \omega\right) + M_{a0}\right],$$

$$(2)$$

where m is the mass of the foot-leg complex; g is the gravitational acceleration; l is the distance between the knee and the center of the mass of the foot-leg complex; θ_{v0} is the angle of the shank, that is, the angulation formed between the shank and the vertical direction in the sagittal plane; λ and E are coefficients of the exponential term; ω the elastic resting angle of the knee; M_{a0} the active torque produced by the electrical stimulation at the desired operating point, given by:

$$M_{a0} = mgl\sin(x_1 + \theta_{v0})\lambda e^{-E\left(\theta_{v0} + \frac{\pi}{2}\right)}\left(x_1 + \theta_{v0} + \frac{\pi}{2} - \omega\right),$$

$$(3)$$

and

$$z(x_1) = \left(\frac{\partial \tilde{f}_{21}(x_1)}{\partial x_1}\right)x_1 + \tilde{f}_{21}(x_1). \qquad (4)$$

The system control input P_N at the equilibrium point is given by:

$$P_N = P - P_0, \qquad (5)$$

where P is the pulse width in μsec, and $P_0 = \frac{M_{a0}}{G}$.

For convenience, we rewrite the expression (1) as follows:

$$\begin{bmatrix} \dot{x}_{1N} \\ \dot{x}_{2N} \\ \dot{x}_{3N} \end{bmatrix} = \begin{bmatrix} 0 & 1 & 0 \\ 0 & 0 & 1 \\ \alpha & \beta & \gamma \end{bmatrix} \begin{bmatrix} x_{1N} \\ x_{2N} \\ x_{3N} \end{bmatrix} + \begin{bmatrix} 0 \\ 0 \\ \Psi \end{bmatrix} P_N, \qquad (6)$$

With the position and pulse width data, the transfer function was estimated for third-order system without delay. With the input and output data, the transfer function of the model was identified. Therefore the linearized system is identified.

$$H(s) = \frac{\Psi}{s^3 - s^2\gamma - s\beta - \alpha}. \tag{7}$$

The parameters were identified from the step-type signal. These parameters correspond to a third order uncertain linear model whose state variables are angular position, angular velocity and acceleration.

In this paper, we adopt the uncertainties in a polytope composed of four vertices. Thus, it is the controllable, linear and time-invariant system described by:

$$\dot{x}(t) = A(\alpha)x(t) + B(\alpha)u(t), \tag{8}$$

being $A(\alpha) \in \mathbb{R}^{n \times n}$ the state matrix, $B(\alpha) \in \mathbb{R}^{n \times m}$ the input matrix, $x \in \mathbb{R}^n$ the state vector, $u(t) \in \mathbb{R}^m$ the input control.

The system (8) can be described as a convex combination of the polytope vertices, with parameters belonging to the unitary simplex :

$$\mathfrak{U} \triangleq \left\{ (A, B)(\alpha) : \sum_{i=1}^{n} \alpha_i(A, B)_i; \sum_{i=1}^{n} \alpha_i = 1; \alpha_i \geq 0; i = 1, 2, \ldots, n \right\}. \tag{9}$$

in which *n* represents the vertices.

It is noticed that the system is described as a convex combination of the vertices, which consists in a convex region that delimits all possible parameters variations within maximum and minimum ranges.

3 Protocol for Parameters Identification

3.1 Subject

The present study was authorized through a research ethics committee involving human beings (CAAE: 79219317.2.1001.5402) in the São Paulo State University (UNESP), Ilha Solteira campus. An able-bodied male subject, 26 years old, participated in the study.

3.2 Test Platform

Experiments were performed on a test platform shown in Fig. 1. Figure 2 shows the identifications made in the volunteer. The platform is composed of a chair instrumented by an electrogoniometer (Lynx®), gyroscope LPR510AL (ST Microelectronics®), two triaxial accelerometers MMA7341 (Freescale®), a NI myRIO controller (National Instruments®), a current-based neuromuscular electrical stimulator (more details can be found in [5]), and an user interface developed in the LabVIEW Student Edition.

Fig. 1 Instrumentated chair for neuromuscular electrical stimulation tests, present at the laboratory of instrumentation and biomedical engineering—UNESP, FEIS

Fig. 2 Identification curves of the non-fatigued (solid line), forced recruitment (dotted line), and fatigued trials (dashed line)
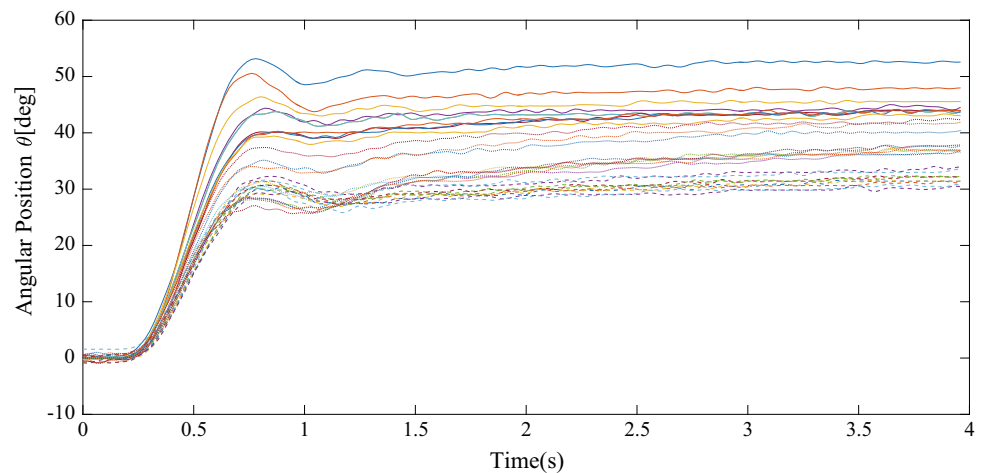
The stimulation intensity is controlled by setting the pulse amplitude to the quadriceps and controlling the pulse width. The stimulus frequency were fixed in 50 Hz. In a preliminary test, pulse amplitude was determined at about 70 mA. The muscular electrostimulator delivers rectangular, biphasic, symmetrical pulse to the individual's muscle, and allows an adjustment of the pulse width in a range of 0–400 μs.

3.3 Experimental Setup

Before applying the stimuli to the quadriceps, a muscle analysis determines the motor point for proper positioning of the surface electrodes. Then, scraping and cleansing procedures are performed at the motor point. The electrodes used are rectangular self-adhesive size 50 × 90 mm.

As a measure of safety and comfort, a stop button deactivates the stimulation pulses. The chair backrest and the knee joint position are adjustable for each volunteer.

After the motor-point identification, open-loop experimental tests are performed. The open-loop test consists of applying a stepping-type signal corresponding to a constant pulse width P_0. The test duration is about four seconds. Thereafter, approximately 2-min time interval is timed for muscle rest. After the rest period, the step-type test is applied again for four seconds.

The pulse width, position, velocity and angular acceleration data are automatically recorded at the end of the step-type signal.

At each test the measured angular position should be the closest to the desired position. It is observed, however, that as the stimulation is applied the error between the measured angular position and the desired angular position becomes greater. After a large number of tests, the error becomes very large. Our hypothesis is that the muscle fibers recruited locally by the surface electrodes are saturated which leads to the fatigue state. The criterion used to determine the saturation condition of the fibers was defined by the evaluation of the error obtained between the desired and measured position. The initials trials have a small error, so we called non-fatigued situation. After ten trials, a 1 kg weight was added to the volunteer's leg to induce fatigue. Consequently, ten step-type tests were performed, which in the so-called forced recruitment. After these tests, we observed a fatigue situation in the muscles. Finally, the weight was removed and muscular behavior was evaluated again for step-type signals. In these trials the obtained results were referred as fatigued situation. Therefore, a total of thirty experimental run were conducted, being ten for each test.

4 Results and Discussion

The data obtained in the thirty tests are shown in Fig. 2, considering results for non-fatigued, forced-recruitment, and fatigued trials.

The position, velocity and acceleration data were obtained from the application of the step-type signal in a period of 4 s. The recording of the data was initially performed 20 ms before the application of the step-type signal.

The model identification was based on output (position) and input data (pulse width) considering a sampling rate of 0.02 s, and the entire procedure was performed in open-loop.

A 10th-order moving average digital filter was applied to attenuate noisy signals of the accelerometer. The identification parameter corresponding to the know uncertainties in the plant were obtained are detailed in Table 1.

The vertices of the polytope are:

Table 1 Uncertain parameters of the model

Parameter	Non-fatigued		Forced recruitment		Fatigued	
	min	max	min	max	min	max
α	−262.6347	−145.2338	−165.6537	−52.2823	−111.4988	−52.2448
β	−85.0702	−66.0235	−63.7912	−37.1104	−58.2557	−42.4420
γ	−9.6953	−7.4066	−7.4829	−5.5056	−5.9278	−4.3872
ψ	0.3631	0.7235	0.0957	0.2909	0.1150	0.2679

$$A_1 = \begin{bmatrix} 0 & 1 & 0 \\ 0 & 0 & 1 \\ \alpha_{min} & \beta_{min} & \gamma_{min} \end{bmatrix}; B_1 = \begin{bmatrix} 0 \\ 0 \\ \Psi_{min} \end{bmatrix}; \quad A_2 = \begin{bmatrix} 0 & 1 & 0 \\ 0 & 0 & 1 \\ \alpha_{min} & \beta_{min} & \gamma_{min} \end{bmatrix}; B_2 = \begin{bmatrix} 0 \\ 0 \\ \Psi_{max} \end{bmatrix};$$

$$A_3 = \begin{bmatrix} 0 & 1 & 0 \\ 0 & 0 & 1 \\ \alpha_{min} & \beta_{min} & \gamma_{max} \end{bmatrix}; B_3 = \begin{bmatrix} 0 \\ 0 \\ \Psi_{min} \end{bmatrix}; \quad A_4 = \begin{bmatrix} 0 & 1 & 0 \\ 0 & 0 & 1 \\ \alpha_{min} & \beta_{min} & \gamma_{max} \end{bmatrix}; B_4 = \begin{bmatrix} 0 \\ 0 \\ \Psi_{max} \end{bmatrix};$$

$$A_5 = \begin{bmatrix} 0 & 1 & 0 \\ 0 & 0 & 1 \\ \alpha_{min} & \beta_{max} & \gamma_{min} \end{bmatrix}; B_5 = \begin{bmatrix} 0 \\ 0 \\ \Psi_{min} \end{bmatrix}; \quad A_6 = \begin{bmatrix} 0 & 1 & 0 \\ 0 & 0 & 1 \\ \alpha_{min} & \beta_{max} & \gamma_{min} \end{bmatrix}; B_6 = \begin{bmatrix} 0 \\ 0 \\ \Psi_{max} \end{bmatrix};$$

$$A_7 = \begin{bmatrix} 0 & 1 & 0 \\ 0 & 0 & 1 \\ \alpha_{min} & \beta_{max} & \gamma_{max} \end{bmatrix}; B_7 = \begin{bmatrix} 0 \\ 0 \\ \Psi_{min} \end{bmatrix}; \quad A_8 = \begin{bmatrix} 0 & 1 & 0 \\ 0 & 0 & 1 \\ \alpha_{min} & \beta_{max} & \gamma_{max} \end{bmatrix}; B_8 = \begin{bmatrix} 0 \\ 0 \\ \Psi_{max} \end{bmatrix};$$

$$A_9 = \begin{bmatrix} 0 & 1 & 0 \\ 0 & 0 & 1 \\ \alpha_{max} & \beta_{min} & \gamma_{min} \end{bmatrix}; B_9 = \begin{bmatrix} 0 \\ 0 \\ \Psi_{min} \end{bmatrix}; \quad A_{10} = \begin{bmatrix} 0 & 1 & 0 \\ 0 & 0 & 1 \\ \alpha_{max} & \beta_{min} & \gamma_{min} \end{bmatrix}; B_{10} = \begin{bmatrix} 0 \\ 0 \\ \Psi_{max} \end{bmatrix};$$

$$A_{11} = \begin{bmatrix} 0 & 1 & 0 \\ 0 & 0 & 1 \\ \alpha_{max} & \beta_{min} & \gamma_{min} \end{bmatrix}; B_{11} = \begin{bmatrix} 0 \\ 0 \\ \Psi_{min} \end{bmatrix}; \quad A_{12} = \begin{bmatrix} 0 & 1 & 0 \\ 0 & 0 & 1 \\ \alpha_{max} & \beta_{min} & \gamma_{max} \end{bmatrix}; B_{12} = \begin{bmatrix} 0 \\ 0 \\ \Psi_{max} \end{bmatrix};$$

$$A_{13} = \begin{bmatrix} 0 & 1 & 0 \\ 0 & 0 & 1 \\ \alpha_{max} & \beta_{max} & \gamma_{min} \end{bmatrix}; B_{13} = \begin{bmatrix} 0 \\ 0 \\ \Psi_{min} \end{bmatrix}; \quad A_{14} = \begin{bmatrix} 0 & 1 & 0 \\ 0 & 0 & 1 \\ \alpha_{max} & \beta_{max} & \gamma_{min} \end{bmatrix}; B_{14} = \begin{bmatrix} 0 \\ 0 \\ \Psi_{max} \end{bmatrix};$$

$$A_{15} = \begin{bmatrix} 0 & 1 & 0 \\ 0 & 0 & 1 \\ \alpha_{max} & \beta_{max} & \gamma_{max} \end{bmatrix}; B_{15} = \begin{bmatrix} 0 \\ 0 \\ \Psi_{min} \end{bmatrix}; \quad A_{16} = \begin{bmatrix} 0 & 1 & 0 \\ 0 & 0 & 1 \\ \alpha_{max} & \beta_{max} & \gamma_{max} \end{bmatrix}; B_{16} = \begin{bmatrix} 0 \\ 0 \\ \Psi_{max} \end{bmatrix};$$

Figure 3 shows the parameters behavior for each situation studied. The median of the parameters α, β, γ tend to increase after the forced recruitment and fatigued test. On the other hand, the parameter ψ presents a decay behavior as the intensity of muscular effort increases. In the non-fatigued trials, a greater dispersion of the data was observed among all tests.

The maximum and minimum parameters obtained by FES application in open-loop delimit the boundary for controller design. In the convex polytope approach, properties present in the vertices extend to all the points contained in the set itself, guaranteeing the controllability and robustness action of the controller designed for that region [6].

The polytopic matrix can be used by exploring its vertex, as an example is the application of the switched controller designed to operate around a desired point of operation.

Another interesting factor is that the non-repeatability in time-domain of the angular position can be mapped to a parametric analysis corresponding to the system model. Thus, the different external situations that the electrically
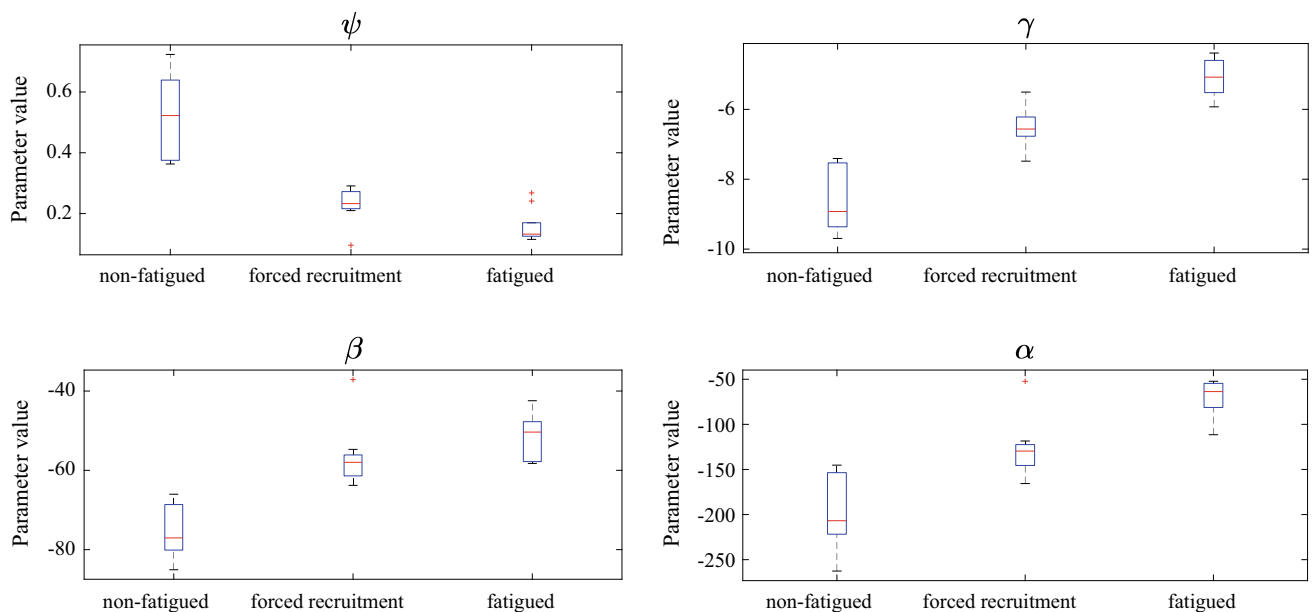
Fig. 3 Comparison between model parameters given in (6) for the cases: non-fatigued, forced recruitment, and fatigued. On each box, the central mark is the median, the edges of the box are the 25th and 75th percentiles, the whiskers extend to the most extreme data points not considered outliers, and outliers are plotted individually

stimulated muscle was subjected externally is characterized by the variation of the α, β, γ, ψ values.

This identification technique that allows to obtain the vertices of the polytope can be used to design controllers for linear and non-linear plants.

Identification techniques such as the one being proposed in this work allows to know in detail the region to be controlled and the uncertainties present in the plant.

One limitation of this identification technique is the impossibility of mathematically identifying muscular stress when electrical stimuli are applied for an indeterminate time.

It is important to note that for each section the plant identification is made. Identification is performed for each volunteer, that is, each identification presents its own uncertainties, justifying the non-linearity in the plant. It is important to note that for each test section, the identification of the plant is carried out.

5 Conclusion

The identification tests carried out in a healthy volunteer demonstrated that the technique used allows a good strategy to perform polytopic uncertainties identification of the electrically stimulated lower limbs model. The bounded convex polytope is considered one of the most general forms

of representation of parametric uncertainties. This identification technique enables robust control design with known plant uncertainties.

This study can be extended with a statistical significance analysis of the parameters for a large number of individuals.

References

1. Ferrarin, M., Pedotti, A.: The relationship between electrical stimulus and joint torque: a dynamic model. IEEE Trans. Rehabil. Eng. **8**, 342–352 (2000)
2. Previdi, F.: Identification of black-box nonlinear models for lower limb movement control using functional electrical stimulation. Control Eng. Pract. **10**, 91–99 (2012)
3. Schauer, T., Negård, N.O., Previdi, F., Hunt, K.J., Fraser, M.H., Ferchland, E., Raisch, J.: Online identification and nonlinear control of the electrically stimulated quadriceps muscle. Control Eng. Pract. **13**, 1207–1219 (2015)
4. Teixeira, M.C., Deaecto, G.S., Gaino, R., Assunção, E., Carvalho, A.A., Farias, U.C.: Design of a fuzzy Takagi-Sugeno controller to vary the joint knee angle of paraplegic patients. In: International Conference on Neural Information Processing, pp. 118–126. Springer (2006)
5. Sanches, M.A.A.: Sistema eletrônico para geração e avaliação de movimentos em paraplégicos. Ph.D. thesis, UNESP—Univ. Estadual Paulista, Ilha Solteira, São Paulo, Brazil, in Portuguese (2013)
6. Barmish, B.R.: Necessary and sufficient conditions for quadratic stabilizability of an uncertain system. J. Optim. Theory Appl. **46**(4), 399–408 (1985)

Quantitative Analysis of Intrinsic Muscle Stiffness in Biceps Brachii of Post-stroke Patients

Silvana Galvão, Denise Xerez, Renato de Lima, Alexandre V. Pino,
Liliam Fernandes de Oliveira, and Luciano L. Menegaldo

Abstract

Introduction. Due to the subjective characteristic of the scales used for evaluation of spasticity, the interest in the tools that can objectively quantify the possible altered components in the spastic muscles have grown. A candidate parameter for muscle stiffness assessment is the shear modulus (μ), quantified using the supersonic shear imaging (SSI). The objective of study is to compare the measure of stiffness estimated by μ in the biceps brachii of the spastic upper limb and of the contralateral side as a control, in patients with chronic stroke. **Methods**. A cross-sectional study was carried out with patients after stroke (n = 10, mean age 51.7 $\pm$ 12.9 years, 6 men). All images were acquired with an Aixplorer® V.9 ultrasound device with the elbow at full extension and the probe over the biceps brachii of both sides. After verifying the normal distribution, the paired t-test parametric test was applied ($p < 0.05$). **Results**. All volunteers but one presented larger μ values in the spastic upper limb compared to control. The paired t-test revealed a significant difference, when the average of the measurements where compared (spastic upper limb = 27.04 kPa; control = 14.81 kPa; p = 0.004). **Conclusions**. Our results, suggest that the μ parameter obtained through SSI elastography is potentially related to muscle stiffness, being a quantitative measure of spasticity.

Keywords

Spasticity • Stiffness • Elastography • Shear wave

S. Galvão (✉) · R. de Lima · A. V. Pino ·
L. F. de Oliveira · L. L. Menegaldo
Biomedical Engineering Program, COPPE/UFRJ,
Rio de Janeiro, Brazil
e-mail: silvanacbgalvao@gmail.com

L. F. de Oliveira
Physical Education and Sports School, EEFD/UFRJ,
Rio de Janeiro, Brazil

D. Xerez
Medicine School, UFRJ, Rio de Janeiro, Brazil

1 Introduction

Stroke is one of the main causes of long-term neurological disability worldwide. Restitution of post-stroke upper extremity motor function is frequently incomplete, with approximately 70% of individuals unable to perform professional duties or activities of daily living by 6 months after illness. Spasticity is one of the most common and potentially disabling complications that affects upper limb post stroke and may significantly contribute to functional loss, reduction of quality of life and results in economic and caregiver burden [1, 2].

It is classically defined as a motor disorder characterized by a speed-dependent increase of the muscle tone, offering an excessive resistance to the passive movement, which is greater at the beginning of the movement. Spasticity is also associated with the exacerbation of deep reflexes and the presence of pathological skin reflexes, such as Babinski's signal. It is estimated that nearly half of stroke patients develop moderate or severe spasticity, especially involving the affected upper limb. The mechanisms involved in the pathophysiology of spasticity are not fully elucidated [2, 3].

To date, spasticity following stroke has been known to have a neurophysiological component (speed-dependent increase in muscle tone and hyperreflexia) and a biomechanical component (soft-tissue stiffness). Regarding this last item, studies suggest that increased muscle stiffness may reflect changes related to tissue properties, such as loss and decrease in sarcomere size and collagen tissue accumulation. Due to the subjective characteristic of the scales used for its evaluation, the interest in tools that can objectively quantify the possible altered components in the spastic muscles have grown [4, 5].

In this context, one of the available parameters for stiffness measurement is the shear modulus (μ), quantified using the supersonic shear imaging (SSI). For isotropic materials, μ represents one-third of the Young's modulus, a property that is

directly proportional to tissue stiffness. Although the 3×1 relationship between the shear modulus and the Young's modulus is valid only for isotropic materials, it has been commonly used in the literature for skeletal muscles, which may be considered as orthotropic material [6]. Thus, the objective of the present study is to compare the measurements of stiffness estimated by μ in the biceps brachii of the spastic and non-spastic upper limb in patients after chronic stroke.

2 Materials and Methods

2.1 Sample

Participants were recruited by screening out-patient clinics at UFRJ's University hospital, in Rio de Janeiro. Patients suffering from hemiparesis were included, with chronic spastic upper limb following ischemic or hemorrhagic hemispheric stroke, diagnosed by a neurologist, who met the following inclusion criteria: (i) stroke onset ≥ 6 months; (ii) muscle tone at the elbow with a modified Ashworth scale (MAS) score $\geq 1+$; (iii) minimum age of 18 years old and maximum age of 80 years; Potential participants were excluded if they (i) use of antispasticity drugs within 6 months before enrollment; (iv) had unstable vital signs; (v) had other neurological diseases.

All patients gave their written informed consent prior to the experiment. The protocol was performed in accordance with the ethical standards and approved by the ethics committee of local Research Ethics Committee (CEP/HUCFF/UFRJ; CAAE: 59885016.7.0000.5257).

2.2 Experimental Design

This study was a cross-sectional to compare the measure of stiffness estimated by μ in the biceps brachii of the spastic and non-spastic upper limb (control) in patients after chronic stroke. The study was conducted at the Federal University of Rio de Janeiro (UFRJ), Rio de Janeiro, Brazil. The enrollment period was from December 2016 to December 2017.

Physical assessments and interviews were carried out with all participants for the collection of clinical and demographic data, which included age, gender, type of stroke, number of stroke events, time since the onset of the stroke. The paretic side and muscle tone at the elbow were evaluated with a MAS scale. The MAS uses a 6-point scale to score the average resistance to passive movement for each joint. Here, the tonus of the elbow flexor muscles was tested [7].

2.3 Acquisition of Images

All images were acquired with a Aixplorer® V.9 ultrasound device (Supersonic Imaging, Aix-en-Provence, France, Fig. 1), with a linear Super Linear TM SL10-2 transducer, 40 mm width, 256 piezoelectric elements, operating in the bands of 2–10 MHz and side resolution of −6 dB: 0.3 mm.

Initially, the equipment was programmed to operate as a conventional B-mode ultrasound. The participant was placed in supine position, with abducted shoulder at 10°, elbow stretched at maximal range of motion, forearm, wrist, and fingers in neutral position and lower limbs in extension. The volunteer was instructed to relax the musculature during image acquisition (two longitudinal images were repeated on each side).

For the acquisition of biceps brachii, the point referring to a one third of the distance between the cubital fossae and the acromion, in the anterior region of the arm, was marked on skin, with a dermographic pen. This point was visualized with the transducer oriented longitudinally and aligned with the muscle fascicles, as seen in the B-mode image. In addition, it was associated with an artifact to generate an acoustic shadow in the image and to facilitate visualization [8].
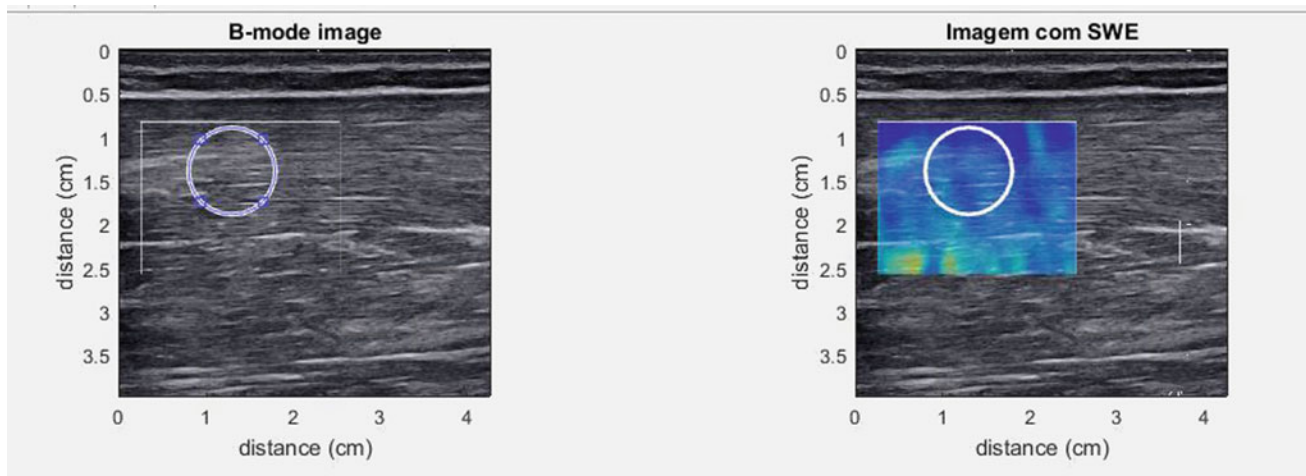
Fig. 1 Results generated by the routine in the analysis of the images of the biceps brachii muscle. The ROI was defined as a circular polygon of 1 cm diameter

During the acquisition of the images, the quantitative analysis is performed in a user-defined region of interest (ROI).

The shear modulus (μ) can be estimated as follows. The density (ρ) is predefined as 1000 kg/m^3 and the shear wave speed (Cs) is obtained by means of the information from the transducer according to Eq. 1 [6]. Considering the biological environment as isotropic and purely elastic, μ is estimated according to Eq. 2.

$$c_s = \frac{\sum_{i=1}^{N} c_s}{N} \tag{1}$$

where N is the number of pixels within the ROI

$$\mu = \rho c_s^2 \tag{2}$$

In all image acquisition, minimal pressure was applied by transducer on the skin and the water-soluble gel was used for the best coupling. The images were exported from the equipment and stored on a personal computer, while maintaining the confidentiality and anonymity of the data.

2.4 Image Processing

All images were exported in DICOM (Digital Imaging and Communications in Medicine) format for later processing in a routine implemented in MATLAB (Mathworks, Massachusetts, USA), developed in the Laboratory of Biomechanics of PEB/COPPE and able to generate estimates with very high correlation ($R^2 = 0.996$) to measurements extracted from the equipment itself. For each volunteer, 4 images were obtained (2 images per side). For a selected image, the velocity data of the shear waves compiled in a file are extracted and processed, being correlated to the respective pixels in the mapping area. Then an interface with the image of the area is presented. In the mapped area it is possible to extract Cs from the user-defined ROI. The ROI was defined as a circular polygon of 1 cm diameter (Fig. 1).

2.5 Statistical Analysis

The descriptive values of the μ measurements were presented with their respective mean ± SD. The data were submitted to an exploratory analysis to verify their normality and dispersion for identification of outliers (Shapiro-Wilk normality test). After verifying the normality of the distribution, the paired t parametric test was performed. The statistical program applied for such analysis was SPSS, version 21 (SPSS IBM, New York, U.S.A), with a significance level of α = 0.05.
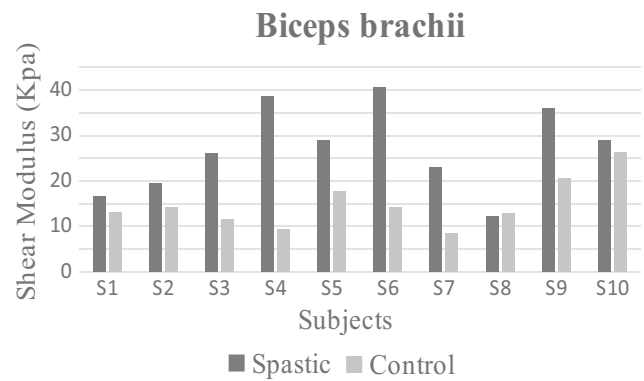
Fig. 2 Shear Modulus in the biceps brachii muscle of the spastic upper limb and control

3 Results

From December 2016 to December 2017, 10 subjects were included (time of stroke 7.4 ± 5.8 years, mean age 51.7 ± 12.9 years, 6 men, 6 right hemiplegia, 9 right handed). The elbow was placed at full extension of 0° for all volunteers except S1 (−10°) and S6 (−74°).

All volunteers except S8 presented systematically larger μ measurements in the biceps brachii muscle of the spastic upper limb when compared to control (μ difference registered: S1 = 21.27%, S2 = 27.44%, S3 = 55.66%, S4 = 75.67%, S5 = 39.24%, S6 = 65.22%, S7 = 63.61%, S8 = −6.08, S9 = 42.71%, S10 = 9.35%). The paired t-test revealed a significant difference when the average of the measurements where compared (spastic upper limb = 27.04 kPa; control = 14.81 kPa; p = 0.004) (Fig. 2).

4 Discussion

Using the Supersonic Shear Imaging elastography technique, the results of the present study demonstrated that the average shear modulus measurements of the spastic biceps brachii is higher when compared to non-spastic (control).

It is known that the stiffness degree of the spastic muscle depends on the changes in the reflex mechanisms, as well as on the passive mechanical properties of the muscle tissues. Currently, clinical exams cannot distinguish these changes, since both of them may cause an abnormal increase in resistance to movement. Thus, researchers have demonstrated an interest in the SSI technique in the analysis of mechanical behavior of soft tissues [9, 10].

The elastography has already been used as a clinical tool to determinate changes in muscle stiffness of subjects with neurological conditions, such as Du-chenne muscular dys-

trophy [11], cerebral palsy [12], stroke, among others. Similar to the present study, other authors found greater muscle stiffness in spastic upper limb when compared to non-spastic upper limb of subjects after stroke, during rest [8].

In 2017, similar results were found in patients with subacute stroke (<6 months), with the Cs measurement performed with the elbow positioned at 90° and 0° [13]. Differently from the study by Wu et al. [13], our study did not exclude subjects with a decrease in maximal range of motion of elbow extension.

This increase in passive stiffness in the spastic limb may be related to changes in intrinsic muscle properties. The mechanisms involved in these changes have not been fully explained yet. Spastic upper limb is usually paralyzed immediately after a stroke, which can lead to reduced longitudinal tension. In studies, an increased extracellular material, stiffer fibers and increased collagen content in spastic muscle, have been observed. Titin, a large protein within the sarcomere that is believed to contribute to passive tension, may also contribute to increased passive stiffness [5, 14].

5   Conclusion

Our results suggest that, potentially, the μ measured through SSI elastography is related to muscle stiffness in patients after stroke and can be used as a parameter to measure spasticity quantitatively.

We observe that μ, as measured using SSI is greater in biceps brachii muscle of the spastic upper limb than in controls of stroke, when the muscle is at rest. To characterize changes in intrinsic muscle properties after stroke and understand their potential causes is important, to determine impairment's fundamental mechanisms, and can also support clinical decisions and guide rehabilitation interventions.

Conflict of Interest We have no conflict of interest to declare.

References

1. Esquenazi, A.: The human and economic burden of post-stroke spasticity and muscle overactivity. J. Sci. Commun. **18**(1), 607–614 (2011)
2. Urban, P.P., et al.: Occurence and clinical predictors of spasticity after ischemic stroke. Stroke J. Cereb. Circ. **41**(9), 2016–2020 (2010)
3. Lance, J.W.: The control of muscle tone, reflexes, and movement: Robert Wartenberg lecture. Neurology **30**(12), 1303–1313 (1980)
4. Dietz, V., Sinkjaer, T.: Spastic movement disorder: impaired reflex function and alteredmuscle mechanics. Lancet Neurol. (2007)
5. Lieber, R.L., Ward, S.R.: Cellular mechanisms of tissue fibrosis. 4. Structural and functional consequences of skeletal muscle fibrosis. Am. J. Physiol. Cell Physiol. **305**(3), C241–C252 (2013)
6. Bercoff, J., Tanter, M., Fink, M.: Supersonic shear imaging: a new technique for soft tissue elasticity mapping. IEEE Trans. Ultrason. Ferroelectr. Freq. Control **51**(4), 396–409 (2004)
7. Ansari, N.N., et al.: Intra-rater reliability of the Modified Ashworth Scale (MAS) in the assessment of upper-limb muscle spasticity. Neuro Rehabil. **31**(2), 215–222 (2012)
8. Lee, S.S.M., Spear S., Rymer, W.Z.: Quantifying changes in material properties of stroke-impaired muscle. Clin. Biomech. (Bristol, Avon) **30**(3), 269–75 (2015)
9. Burke, D., Wissel, J., Donnan, G.A.: Pathophysiology of spasticity in stroke. Neurology **80**(3) Suppl 2, S20–S26 (2013)
10. Lorentzen, J., et al.: Distinguishing active from passive components of ankle plantar flexor stiffness in stroke, spinal cord injury and multiple sclerosis. Clin. Neurophysiol. Official J. Int. Fed. Clin. Neurophysiol. **121**(11), 1939–1951 (2010)
11. Lacourpaille, L., et al.: Non-invasive assessment of muscle stiffness in patients with Duchenne muscular dystrophy. Muscle Nerve **51**(2), 284–286 (2015)
12. Park, G.Y., Kwon, D.R.: Sonoelastographic evaluation of medial gastrocnemius muscles intrinsic stiffness after rehabilitation therapy with botulinum toxin a injection in spastic cerebral palsy. Arch. Phys. Med. Rehabil. **93**(11), 2085–2089 (2012)
13. WU, C.-H., et al.: Evaluation of post-stroke spastic muscle stiffness using shear wave ultrasound elastography. Ultrasound Med. Biol. **43**(6), 1105–1111 (2017)
14. Lieber, R.L., Runesson, E., Einarsson, F., Fridén, J.: Inferior mechanical properties of spastic muscle bundles due to hypertrophic but compromised extracellular matrix material. Muscle Nerve **28**(4), 464–471 (2003)

Rate of Head Tilt in Walk and Trot During Equine Therapy with Actimeter

M. Ranciaro, E. L. Santos, M. F. F. Vara, W. A. D. Strasse, E. F. Manffra,
G. N. Nogueira Neto, and P. Nohama

Abstract

Equine therapy is a multidisciplinary therapeutic tool used to treat different motor disorders whose pre and post-treatment improvements have been demonstrated but not analyzed during the patient treatment sessions on the horse. Many processes, such as Time Up and Go (TUG), gait, pressure centers, among others, were analyzed in a qualitative way, pointing out only an improvement in motor control. The goal of this study was to evaluate quantitatively head, trunk and neck displacement through gyroscopic data acquired with an portable actimeter specially developed to measure kinematic parameters during the practice of equine therapy (walk and trot). The biomedical device (actimeter) was developed for the kinematic analysis of the displacement and the inclination rate of the trunk, neck and head, by means of a gyroscope placed on the volunteer's head, measuring quantitative differences. Three volunteers were evaluated during two (walk and trot) sessions: two patients and one healthy subject. The x, y, and z axes of the sensor were conditioned and processed to obtain mean and RMS values, as well as the mean of inter- and intra-volunteer groups. During the walking laps, the RMS for each axes (X, Y, Z) was 11.802, 20.592, 21.844°/s (non-disabled) and 20.096, 29.785, 28.001°/s (disabled). During the trotting laps, the RMS was 19.910, 57.211, 30.114°/s (non-disabled), 34.087, 51.543, 37.978°/s (disabled). It was possible to observe in RMS a significant difference between disabled and non-disabled individuals, the same differences are present on means, as well as the mean and RMS of inter- and intra-volunteer, who presented numerically greater results in all the comparisons, denoting less stability than the trained individuals and also quantifying these differences between subjects with and without disability.

1 Introduction

Equine therapy is a treatment for reeducation and motor and mental rehabilitation that employs horses. It is an interdisciplinary approach, involving health, education and riding [1]. The movements performed by the horse in different styles of locomotion (walk, trot and gallop) favor the processes of patient postural control in the frontal, sagittal and transverse planes. This is because horse movements are rhythmic, which increase the range of proprioceptive and exteroceptive stimuli to patients undergoing treatment [1–5]. And, since the horse's gait produces repetitive movements, equine therapy allows the patient riders movements similar to human gait [6–8]. In this way, the three-dimensional movement that the horse performs promotes postural adjustments in the patient. As a consequence, it stimulates the trunk, head and neck support muscles [2, 9, 10] and the biomechanical alignment of the spine [2, 7, 8, 11]. Following this approach, equine therapy contributes to achieve improved posture and muscle strength [4], favors the organization of tonus, promotes relaxation, develops body awareness, and improves balance [3, 4, 12, 13]. Therefore, the interaction with the horse, with its continued practice in the physiotherapeutic treatment, can provide greater independence in daily activities and increase self-confidence in patients with compromised nervous system.

M. Ranciaro (✉) · E. L. Santos · M. F. F. Vara · E. F. Manffra ·
G. N. Nogueira Neto · P. Nohama
PPGTS - Pontifícia Universidade Católica do Paraná, Curitiba, Brazil
e-mail: mairaranciaro@gmail.com

G. N. Nogueira Neto
e-mail: nogueira.g@pucpr.br

W. A. D. Strasse · P. Nohama
CPGEI - Universidade Tecnológica Federal do Paraná, Curitiba, Brazil

Nevertheless, during the follow-up of a proposed treatment with equine therapy, the professionals must have mechanisms of evaluation to estimate the effectiveness of the therapeutic program. These evaluations involve direct measurements of patient movement. However, these measures allow evaluating patient improvements by means of measurements such as gait analysis, balance, and pressure points (COP) and/or, without measurements, by visual inspection. However, all are performed pre- and post-treatment [3, 6, 7, 14, 15]. Only one study used electromyography data to investigate muscle contraction simultaneously with treatment [16].

Thus, kinematic measurements, such as angles and displacements, can be used quantitatively during therapy, standing out as the best approach to minimize the subjectivity present in the evaluation process. This is because accelerometers and gyroscopes are small sensors that allow recording movements objectively and their data are more accurate [17–19]. On the other hand, we did not find studies in the consulted literature that address the use of gyroscopes, for an accurate analysis of angular movements during equine therapy for trunk motor control. As a result, this research group is conducting various studies with different horse gaits, in order to establish quantitative differences between the disabled and non-disabled people, initially. Previously only the walk was evaluated by having a larger number of participants [20], but there are participants who perform trot, which has a greater impact on the patient.

In this context, an actimeter was developed, which is a portable biomedical instrument that measures the rotation in the x, y and z axes of the Cartesian coordinate system by means of a triaxial gyroscope [17]. Moreover, with the actimeter, it is possible to obtain data simultaneously with therapy application. This would be an advantage, since it makes the assessment more practical to both therapist and patient. The goal of this study was to evaluate quantitatively head, trunk and neck displacement through gyroscopic data acquired with an portable actimeter specially developed to measure kinematic parameters during the practice of equine therapy.

2 Method

The method involves three items: data collection, electronic instrumentation and data processing.

2.1 Data Collection

The Research Ethics Committee of Pontifícia Universidade Católica do Paraná (PUCPR) authorized the clinical trial by registration number 50724215.8.0000.0020, with the consent of the participants. The investigation was carried out at Mounted Police Regiment of Coronel Dulcídio Center, located in the city of Curitiba-PR (Brazil), in conjunction with the Development and Research Center "Sd. Josué Cipriano Diniz", also headquartered in the Mounted Police Regiment Unit.

Three out of nine volunteers were able to perform both walk and trot, for a quantitative comparison with the actimeter. Three volunteers participated in the study: two patients (P4 and P7) under treatment in the mounted police and one trained and non-disabled subject (control group—CG). Table 1 presents the demographic data.

The protocol consisted of three consecutive laps in the course of 150 m, in sand lane, using the walk and trot of the horse, in two sessions on different days.

The actimeter was positioned in the upper central region of the patient's protective helmet, being fixed by double-sided adhesive tapes and Velcro straps.

The physiotherapist responsible for equine therapy requested that during actimeter placement the patient was already mounted on the horse, with head raised and eyes directed to the horizon. It was also necessary to inform the patient that the actimeter is evaluating the movements performed by the trunk and neck during horse's movements.

2.2 Electronic Instrumentation

A customized individual actimeter (Fig. 1) was developed at PUCPR's Rehabilitation Engineering Laboratory [21]. It has 7.3 cm × 4.0 cm × 5.3 cm dimensions, 9 V battery for power supply, and three internal electronic modules: a microcontroller, an SD card drive and an MPU6050 sensor with accelerometer, gyroscope and I^2C communication. Data were acquired at 30 Hz and recorded in the SD card. The acquired signals were generated by the displacement of the actimeter in three orthogonal directions, as indicated in Fig. 2: x axis—longitudinal displacement; y axis—transverse displacement and axis z—normal displacement.

Table 1 Identification of volunteers

Volunteer identification	Clinical condition	Age (years)	Weight (kg)	Height (m)
CG	Non-disabled	35	80	1.83
P4	Cerebral palsy	24	96	1.69
P7	Hydrocephalus	9	32	1.52
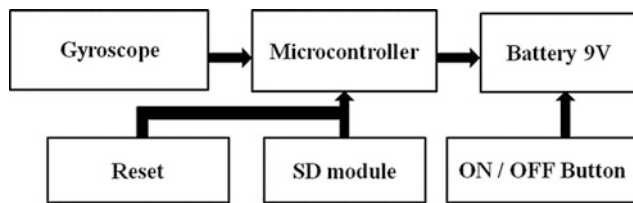
Fig. 1 Actimeter block diagram [20]
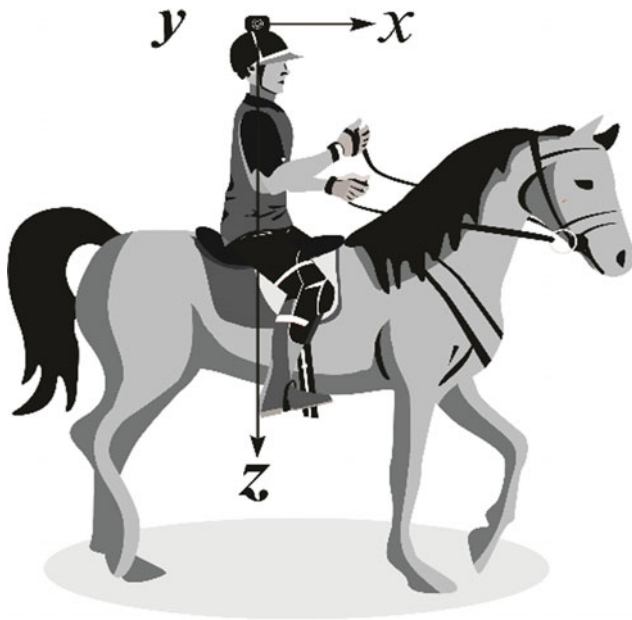
Fig. 2 Actimeter placement on top of volunteer's head. Gyroscope axis displacement: *x*—longitudinal, *y*—transversal, *z*—normal [20]

The sensor was programmed with a full scale of $\pm250°/s$ and a sensitivity of 131 LBS/°/g with a programmable low-pass filter of 256 Hz. The actimeter was triggered by the time of the first movement of the horse, after system auto-calibration.

2.3 Data Processing

Acquired gyroscope signals were converted to angular velocity (in °/s) by dividing all values by sensor sensitivity. Signal mean and root mean square (RMS) were calculated for each axis and volunteer. The mean between the control group (CG) and patient group (PG), and volunteer overall mean was also determined for both sessions.

3 Results

Figure 3 shows a 100 s long sample of a signal acquired by the sensor. These signal excerpts allow visualizing the response of each axis. Gyroscope angular velocity is expressed in degrees per second (°/s), and it indicates how much head, trunk and neck rotation occurred during the sessions.

Tables 2 and 3 present RMS and mean of the sensor values (in °/s), collected at the horse walking indicating (i) the average between sessions and (ii) the average values of

PG compared to CG. Tables 4 and 5 present the same data sequence, but during horse trot.

4 Discussion

The objective of this study was to evaluate quantitatively head, trunk and neck displacement through gyroscopic data acquired with actimeter to measure kinematic parameters during the practice of equine therapy. Evaluation of the different lesions of the patients will be evaluated in the future. In addition to presenting head angular velocity values for sensor axes, the results put into perspective patients with varied dysfunctions and a CG formed by a non-disabled person. Few volunteers were evaluated because of their limitations in performing the trot. Only two of the nine available volunteers were able to perform both marches. Further studies with a larger group of volunteers should be undertaken, but some conclusions may already be considered.

The actimeter was placed on top of the helmet that volunteers used during the sessions to record the equivalent angular velocity and the inclination caused by trunk and neck joints.

One can observe in Tables 2 and 3 that, for RMS value, there was greater variation in the displacement for PG than for CG. This may be due to the fact that rhythmic and three-dimensional movements imposed by the horse's gait would have caused mechanical disturbances in the support base of the individual on the animal, stimulating him/her to perform and practice postural adjustments, which are suggested as mechanisms of action of equine therapy [16, 22].

Therefore, the differences found in the mean between groups are related to the ability of the CG to maintain the most upright posture on the horse during the course.
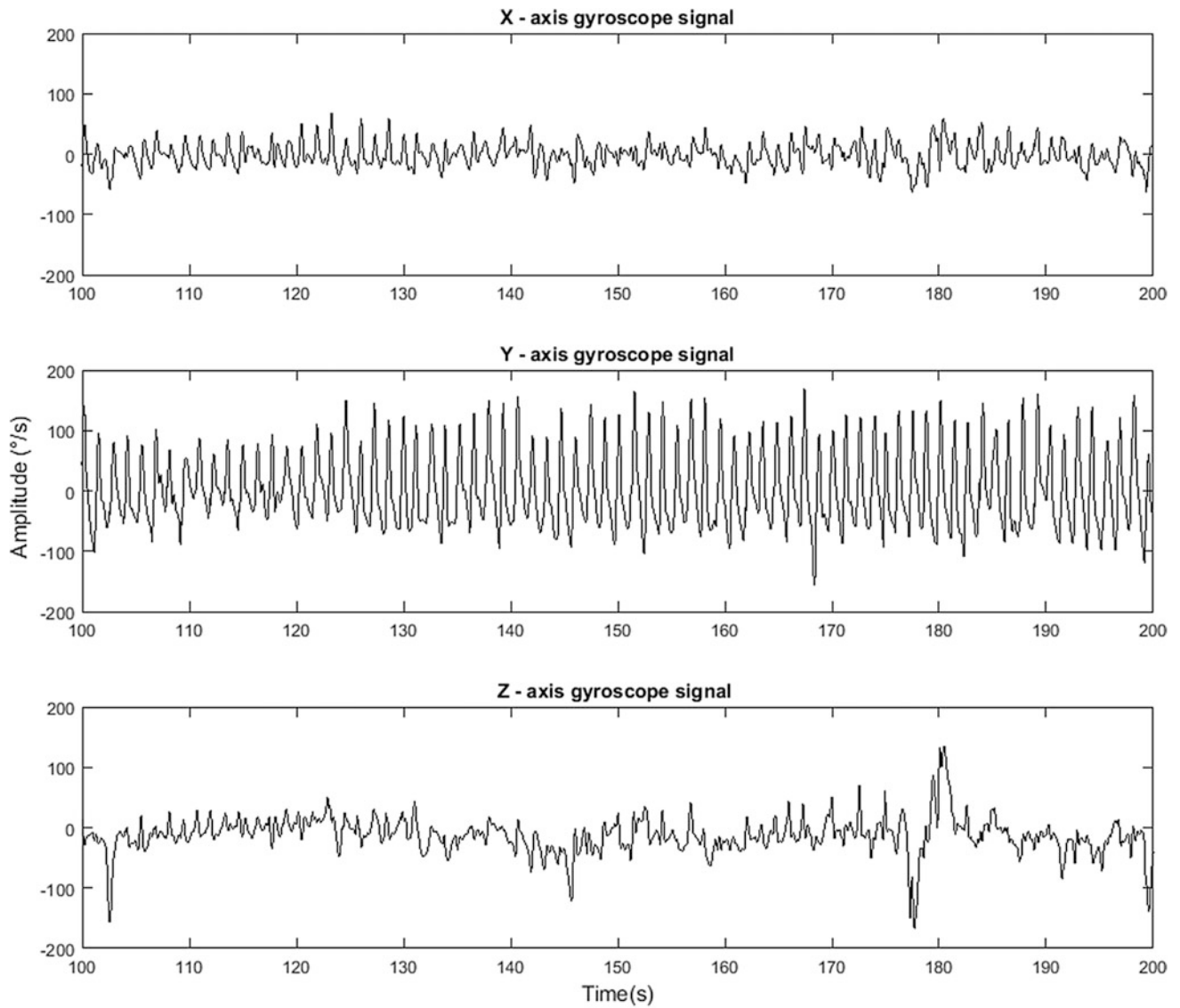
Fig. 3 Triaxial gyroscope signal (°/s) in control group

Table 2 RMS and mean values between sessions and during horse walk

Volunteer identification	RMS (°/s)			Mean (°/s)		
	x	y	z	x	y	z
CG	11.802	20.592	21.844	−0.752	1.481	−5.866
P4	14.068	27.174	18.337	−0.603	0.812	6.467
P7	26.123	32.396	37.664	−0.056	1.271	6.627

Table 3 RMS and mean values between groups of volunteers for horse walk

Volunteer identification	RMS (°/s)			Mean (°/s)		
	x	y	z	x	y	z
CG	11.802	20.592	21.844	−0.752	1.481	−5.866
PG	20.096	29.785	28.001	−0.329	1.042	6.547

Table 4 RMS and mean values between sessions and during horse trot

Volunteer identification	RMS (°/s)			Mean (°/s)		
	x	y	z	x	y	z
CG	19.910	57.211	30.114	−1.314	0.1985	−10.65
P4	34.232	52.159	30.181	−0.212	1.448	10.479
P7	33.941	50.927	45.774	−0.433	1.897	10.517

Table 5 RMS and mean values between volunteer groups and during horse trot

Volunteer identification	RMS (°/s)			Mean (°/s)		
	x	y	z	x	y	z
CG	19.910	57.211	30.114	−1.314	0.1985	−10.65
PG	34.087	51.543	37.978	−0.322	1.672	10.498

Therefore, values are smaller in x and y axes, once he had better body organization through stimuli. In relation to z axis, there were no major changes since the same animal, lane type and course were used. The impact of terrain variation is a matter for future studies, particularly, to z axis and volunteer demography.

Tables 4 and 5 show an increase in angular velocity RMS during trot. RMS values are greater for PG, since patients performed greater head and trunk movements as a mechanism of compensation to the most dynamic movement of the animal.

Table 4 also reveals that, for RMS, there was greater variation between horse trot sessions for PG than for CG, on x and z axes. Table 5 also shows that there was greater tilt variation on PG when compared to CG (a non-disabled person). This result may have been due to the fact that the multidirectional rhythmic movements caused by the horse's gait would have accentuated the imbalance of subjects riding the animal, stimulating the occurrence of postural adjustments, which are pointed out as one of the effects of equine therapy practice [16, 22]. Thus, the differences observed in the results for trunk control, shown in Tables 4 and 5, might be related to a better postural control in people without disabilities (CG) when compared to persons with impairments.

Regarding the x axis and horse trot sessions, both Tables 4 and 5 show that RMS values of PG had greater oscillation in the longitudinal direction. They indicate that people with impairments presented lower angular velocity on the y axis, possibly because of their balance in condition of greater instability. This may be compensation due to non-oscillation in the frontal x axis.

Differences in results regarding head and trunk movement patterns were already expected in the clinical interpretation of physical therapists. However, the quantification of these angular responses in the sagittal and frontal planes may allow more adequate and accurate adjustments in the therapeutic protocols according to patient specific pathologies and trunk movement types during the physical interaction with the horse's movements. Thus, it favors the orientation of custom treatments and proportionates more effective biomechanical parameter responses on trunk stability with fewer treatment sessions.

Using the actimeter was relevant to measure the rotation of the body segments in the triaxial Cartesian coordinate system during the practice of equine therapy, as well as evaluating the different results on the patient in different horse gaits. The results suggest that the actimeter has some advantages because it is small biomedical device and does not require electrode placement and/or cables for signal acquisition. In addition, they corroborate the possibility of using the actimeter for signal processing, to evaluate the acquisition of postural control during on-site training of therapeutic practice [23]. Future perspectives consider the functional classification of patients and its application directly at the site of equine therapy: outdoors.

5 Conclusion

This study showed that the actimeter is an adequate tool for kinematic analysis during equine therapy practice. Also, further studies will investigate the possible changes that occur due to training time, terrain variation, and larger population so that it will be possible to correlate data with patient evolution according to impairment type.

References

1. Holanda, R.L., Lima, F.S.P., Lobo, L.B.C., Nunes, T.T.V.: Equoterapia e cognição em pacientesautistas: um estudo de caso. Revista Expressão Católica **2**(2), 83–96 (2017)

2. Corr, G., Manetta, T., Suter, C., Cerebral, P., Scale, B.B.: A influência da equoterapia no equilíbrio de paciente com paralisia cerebral. Revista Hórus **6**(444), 1–8 (2012)

3. Meneghetti, C.H.Z., da Silva Porto, C.H., Iwabe, C., Poletti, S.: Intervenção da equoterapia no equilíbrio estático de criança com síndrome de Down. Revista Neurociências **17**(4), 392–396 (2009)

4. Bevilacqua Jr, D.E., Lopes, L.L., de Melo., Accioly, M.F., Ribeiro, M.F., Ferreira, A.A., Teixeira, V.P.A., Espindula, A.P.: Avaliação da modulação autonômica em indivíduos com síndrome de Down na equoterapia. ConScientiae Saúde **15**(3), 433–439 (2017)

5. Tabor, G., Williams, J.: Equine rehabilitation: a review of trunk and hind limb muscle activity and exercise selection. J. Equine Vet. Sci. **60**, 97–103.e3 (2018)

6. da Silveira, M.M., Wibelinger, L.M.: Reeducação da postura com a equoterapia. Rev. Neurociencias **19**(3), 519–524 (2011)

7. Pierobon, J.C.M., Galetti, F.C.: Estímulos Sensório-Motores proporcionados ao praticante de equoterapiapelocavalo ao passo durante a montaria. Ensaios e Ciência - Ciências Biológicas, Agrárias e da SaúdeXII(2), 63–79 (2008)

8. Copetti, F., Mota, C.B., Graup, S., Menezes, K.M., Venturini, E.B.: Comportamento angular do andar de crianças com síndrome de Down após intervenção com equoterapia. Revista Brasileira de Fisioterapia **11**(6), 503–507 (2007)

9. Mara, M., Monteiro, L.: Equoterapia como recurso terapêutico na prevenção de quedas em pacientes com Acidente Vascular Cerebral: Revisão de literatura. Revista Portal da Divulgação **IV**(39), 29–40 (2014)

10. Cabiddu, R., Borghi-Silva, A., Trimer, R., Trimer, V., Ricci, P.A., Italiano Monteiro, C., Camargo Magalhães Maniglia, M., Silva Pereira, A.M., Rodrigues das Chagas, G., Carvalho, E.M.: Hippotherapy acute impact on heart rate variability non-linear dynamics in neurological disorders. Physiol. Behav **159**, 88–94 (2016)

11. Lee, C.-W., Kim, S.G., Yong, M.S.: Effects of hippotherapy on recovery of gait and balance ability in patients with stroke. J. Phys. Ther. Sci. **26**(2), 309–311 (2014)

12. Valle, L.M.O., Nishimori, A.Y., Nemr, K.: Atuação fonoaudiológica na equoterapia. Revista CEFAC **16**(1), 511–523 (2014)

13. Lima, M.B.: Terapia assistida porcavalos em crianças com paralisia: uma revisão integrativa. Universidade Federal do rio Grande do Sul, Dept. de Enfermagem (2011)

14. Freire, H.B.G., Andrade, P., Motti, G.S.: Equine-therapy as a therapeutic resource in the treatment of autistic children. Multitemas **32**, 55–66 (2005)

15. Torquato, J.A., Lança, A.F., Pereira, D., Carvalho, F.G., Silva, R.D. da.: A aquisição da motricidade em crianças portadoras de Síndrome de Down que realizamfisioterapia ou praticamequoterapia. Fisioterapia em Movimento **26**(3), 515–525 (2013)

16. Espindula, A.P., Assis, I.S.A. de, Simões, M., Ribeiro, M.F., Ferreira, A.A., Ferraz, P.F., Cunha, I.C., Ferraz, M.L. da F., Souza, L.A.P. S de, Bevilacqua Jr., D.E., Teixeira, V.D.P.A.: Material de montaria para equoterapia em indivíduos com síndrome de Down: estudo eletromiográfico. ConScientiae Saúde **13**(3), 349–356 (2014)

17. Toigo, T., Leal Júnior, E.C., Ávila, S.N.: O uso da equoterapia como recurso terapêutico para melhora do equilíbrio estático em indivíduos da terceiraidade. Revista Brasileira de Geriatria e Gerontologia **8**(1), 391–404 (2006)

18. Varilly, P., Chandler, D.: Actigraphy: analyzing patient movement. Hear. Lung **V**(2), 265–275 (2012)

19. Kavanagh, J.J., Menz, H.B.: Accelerometry: a technique for quantifying movement patterns during walking. Gait Posture **28**(1), 1–15 (2008)

20. Ranciaro, M., Santos, E.L., Vara, M.F.F., Strasse, W.A.D., Franzo, D., Nogueira-Neto, G.N., Manffra, E., Nohama, P.: Kinematic analysis of the evaluation of equine therapy patients with actimeter. In: Global Medical Engineering Physics Exchanges (GMEPE) & Pan American Health Care Exchanges (PAHCE), pp. 1–5. Springer, Porto (2018)

21. Ranciaro, M., Oliveira, M. A.C., Nogueira-Neto, G.N., Nohama, P.: A novel actimeter for postural control analysis: a pilot essay. In: VII Latin American Congress Biomedical Engineering CLAIB 2016, pp. 26–29, Bucaramanga-Colombia (2016)

22. Kwon, J.Y., Chang, H.J., Lee, J.Y., Ha, Y., Lee, P.K., Kim, Y.H.: Effects of hippotherapy on gait parameters in children with bilateral spastic cerebral palsy. Arch. Phys. Med. Rehabil. **92**(5), 774–779 (2011)

23. Ilha, P.M., Silva, R., Petroski, E.L.: Validade do acelerômetro tri-axial tritrac: um estudo de revisão. Rev. Bras. Cineamtropometria & Desempenho Humano **7**(1), 75–81 (2005)

Reliability of Maximal Voluntary Isometric Contraction of Ankle Dorsiflexion in Male Subjects

F. R. Andreis, M. A. Favretto, S. Cossul, P. A. Barbetta, and J. L. B. Marques

Abstract

Maximum voluntary isometric contraction (MVIC) of the ankle dorsiflexion is a common strength measurement used in clinical and research environment. It can be a clinical tool to assess several pathologies, such as amyotrophic lateral sclerosis and diabetic neuropathies. Its practical use depends on many factors, but an important one is the reliability of the technique. Therefore, the purpose of this study was to investigate the reliability of MVIC through a test-retest analysis and with a two-stage nested design. Ten male subjects (age 25.5 ± 1.43 years, mean $\pm$ SD) were investigated in three consecutive days, in each day, the subjects performed the MVIC twice. This procedure allows to investigate test-retest reliability and also to build a two-stage nested design with random factors to estimate the global variances components among the three sources of variation: subjects, days, and trials. The Bland-Altman plots and the paired *t*-test indicated no systematic bias in the data and no significant difference in the within-day analysis for the three days. The intraclass correlation coefficient (ICC) obtained through the two-stage nested design was 86.6%, the variability attributed to days was 8.6% and the variability attributed to trials was 4.6%, therefore presenting excellent reliability according to the typical standard, which consider an ICC higher than 80% to be excellent. This work suggests that the MVIC of the ankle dorsiflexion is a highly reliable measure to study in a young population and consequently may be useful for investigators in training and clinical applications.

1 Introduction

Muscle strength evaluation can be a clinical tool to assess several pathologies, such as amyotrophic lateral sclerosis, diabetic neuropathies, or even the effect of aging and training [1–3]. The maximum voluntary isometric contraction (MVIC) is the most common measurement technique used in the clinical and research environment [3, 4], especially in the ankle strength, given that it is directly related to the ability of an individual to perform daily activities (e.g., climbing stairs, walking, chair rise) [3]. The MVIC is also used as a standard protocol to normalize data from electromyography studies [5, 6]. Typically, the subject performs three MVICs separated by a small interval, generally a rest period of less than five and more than two minutes [7–9]. The maximum value obtained is used to set the submaximal voluntary contractions levels (e.g., 50% of the MVIC) for the subsequent tests.

The application of a measurement technique depends on its reliability. A variable is said to be reliable when it shows acceptable levels of variability over time and, also, the variable proves to be sufficiently sensitive to detect clinically important changes after some intervention. These two concepts are related, as smaller the variability of some variable, the more sensitive it is to detect significant changes [10]. Several studies assessed the reliability of the MVIC [3, 11, 12]. However, they were studied in a test-retest design that means two testing sessions with a few days apart. Also, most of the studies used isokinetic measurements instead of isometric [13, 14] and in a population of older adults [15]. Furthermore, different protocols were used along with different statistical approaches to quantify the errors associated with the experiment.

F. R. Andreis (✉) · M. A. Favretto · S. Cossul · J. L. B. Marques
Department of Electrical and Electronic Engineering, Institute of Biomedical Engineering, Federal University of Santa Catarina, Florianópolis, SC, Brazil
e-mail: felipe.andreis@posgrad.ufsc.br

P. A. Barbetta
Department of Informatics and Statistics, Federal University of Santa Catarina, Florianópolis, SC, Brazil

The purpose of this study was to analyse the reliability of the MVIC of the ankle dorsiflexion in a population of young men with several reliability measurement approaches, not only with test-retest design but also using a two-stage nested design with random factors, which allows to estimate the variance components associated with the sources of error.

2 Materials and Methods

2.1 Subjects

Ten male volunteers participated in the study. The subjects (mean $\pm$ SD) age was 25.5 ± 1.43 years, weight was 85.4 ± 14.0 kg and height was 177.5 ± 5.6 cm. They were all students in the Institute of Biomedical Engineering at Federal University of Santa Catarina, Brazil. None of the subjects showed any signs or symptoms of disease, and none reported any neuromusculoskeletal dysfunction in the tested leg within the past year. Before the start of the study, each participant was informed of the testing procedures, and thereafter gave written consent. The project was approved by the Ethics Research Committee of the Federal University of Santa Catarina (Protocol number: 2.390.994).

2.2 Procedures

The subjects were seated in a chair with the hip, knee, and ankle joints flexed at $90°$. Each subject was investigated for three consecutive days, at approximately the same time of the day. In each day, the dominant leg was tested (defined as the leg that would be used to kick a ball). For each day, subjects were requested to perform two times a MVIC of the ankle dorsiflexion, MVIC was defined as the peak signal. The contractions were 10 s in duration with a 5 min rest interval. Subjects were provided with strong verbal encouragement during the maximal contraction procedure. The experiments were conducted with a portable dynamometer, with an A/D filter with 24 bits of resolution and with a sampling frequency of 80 samples per second. The full scale of the torque sensor is 600 N [16].

2.3 Statistical Data Processing

Several methods were used to assess reliability; the analyses can be divided in two parts:

(i) The first analysis was made to assess independently the within day (trial-to-trial) reliability, for the three days. This step allows to investigate if there are systematic bias (e.g., fatigue or learning effect) in the measuring protocol

within each day. Initially, to check for any significant bias between the trials, a paired *t*-test was performed within each day. The intraclass correlation coefficient (ICC) and its 95% confidence interval was also used, using a (2, 1) formula, that means a two-way random model composed of one measurement [17]. The ICC provides a dimensionless estimate of the reliability of measurement but it does not provide estimates of the precision of measurement. Consequently, we also calculated the standard error of measurement (SEM), that is expressed in the same unit as the original measurement and can be used to form a band around a score [18]. The Bland-Altman plots (individual participant differences plotted against the mean for the day) were created for each day to look for systematic bias, random errors, outliers, and the presence of heteroscedasticity. This plot includes the 95% limits of agreement (LOA): the mean difference between the two trials $\pm$ the random error component ($1.96 \times$ standard deviation of the difference between the 2 trials within a day) [19]. Heteroscedasticity was determined by examining the significance of the correlation between the absolute differences and the mean values [3]. The Pearson's product-moment correlation coefficient (r) was provided as a measure of relative reliability.

(ii) The second analysis involved the use of a balanced two-stage nested design with random factors, in which the linear statistical model is described as:

$$y_{ijk} = \mu + \tau_i + \beta_{j(i)} + \epsilon_{k(ij)}$$

where τ_i represents the effect of the i-th subject ($i = 1, 2, \ldots, 10$). $\beta_{j(i)}$ represents the effect of the j-th day on the subject i ($j = 1, 2, 3$) and $\epsilon_{k(ij)}$ denotes the effect of the k-th trial on day j and subject i. The model has, therefore, three random nested terms with variances denoted by $V(\tau_i) = \sigma_s^2$, $V(\beta_{j(i)}) = \sigma_d^2$ and $\text{V}(\epsilon_{k(ij)}) = \sigma_t^2$. The last one is considered the error term.

The nested design has one null hypothesis for each level, they are $H_0 : \sigma_s^2 = 0$, which is tested by the ratio (F) of the mean squares $MS_{Subject}/MS_{Day(Subject)}$. For this case, if this ratio is significant, according to the magnitude and the associated degrees of freedom, it indicates that the subject variations are significantly larger than the day-to-day variation. The second stage hypothesis is $H_0 : \sigma_d^2 = 0$, that is tested by $MS_{Day(Subject)}/MS_{Error}$ and it enables to check if the day-to-day variability are significantly greater than the experimental noise variability.

One important practical implication of this model is that it allows to estimate the distribution of the global variance among the three sources of variation: subjects (σ_s^2), days

(σ_d^2) and trials (σ_t^2). Therefore, we can use these variances estimates to analyse the repeatability of the parameter. Typically, a variable is said to be repeatable when the variance can be predominantly attributed to subjects, so that day and trial variations can be considered as experimental noise [20]. Finally, the ICC for the whole experiment can be calculated as:

$$ICC = \frac{\sigma_s^s}{\sigma_s^2 + \sigma_d^2 + \sigma_t^2} * 100$$

Usually, "excellent repeatability" is defined for ICC values in the range 80–100%, the range 60–80% appears as "good repeatability" and values below 60% are considered "poor repeatability" [21]. The three variances were obtained using the ANOVA algorithm, using the MVIC as the dependent variable, subject and day within subject as the independent variables.

The statistical analyses were performed with R software [22] with the lme4 package [23]. The model assumptions were checked through normal probability plots and scatter plot of residuals versus fitted values. The level of significance considered for all the analyses was 5%.

3 Results

The results from the analysis for the within day (trial-to-trial) reliability are presented in Table 1. There was no significant difference between the trials, according to the paired t-test ($p > 0.05$), for the three days. Regarding the Pearson's correlation coefficients, all the days showed a strong correlation, the minimum value being 0.92 for day 3.

The ICC values demonstrate near-perfect agreement between measures, even the lowest limit (0.85) of the confidence interval of the ICC, that occurred in day 3, showed excellent repeatability (>80%). Both the highest SEM and LOA were obtained in day three.

The Bland-Altman plots for the three days (Fig. 1) indicates that there is no systematic bias between the trials, as the differences between test days were symmetrically distributed around zero. The middle-dashed line represents the mean difference between the trials and the upper and lower dashed lines indicates the limits of agreement. It was found a significant correlation between the average and difference in

day 2, therefore, displaying a heteroscedastic behaviour. Also, none of the measurements were outside the LOA (extreme dashed lines).

The percentage distribution of total variance between the three sources of variability: subjects (that is the ICC), days and trials for the MVIC, obtained by the balanced two-stage nested design, described previously, is illustrated in Fig. 2. The ICC was 86.8%, in other words, the variability attributed to subjects. The variability attributed to days was 8.6% and the variability attributed to trials was 4.6%.

The results of the ANOVA analysis for the MVIC are reported in Table 2, with the indications of the degrees of freedom (dof) associated to each source of variation and the mean squares (MS) related to each source of variation. Two ratios (F) are indicated: the first is the ratio between MS due to subjects and the MS due to days; the second is the ratio between MS due to days and MS due to trials.
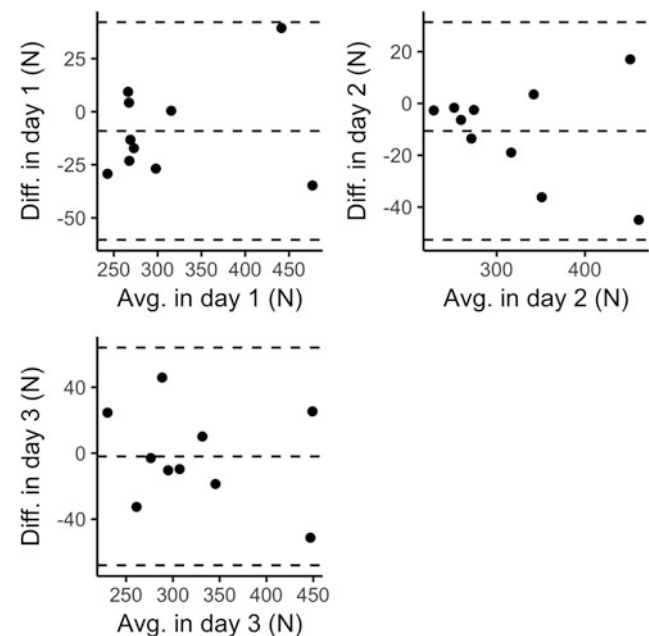
Fig. 1 Bland-Altman plots for the three days. The superior and inferior dashed lines represent the 95% limits of agreement, whereas the middle-dashed line represents the mean difference between the two trials

Table 1 Comparison of the MVIC within days (trial-to-trial)

MVC test	Paired t	r	ICC	CI (ICC)	SEM (N)	LOA (N)
Day 1	0.23	0.96	0.98	0.92−0.99	11.20	−60.3 to 42.1
Day 2	0.10	0.97	0.98	0.93−0.99	11.29	−52.6 to 31.3
Day 3	0.83	0.92	0.96	0.85−0.99	14.60	−67.9 to 64.0

ICC Intraclass correlation coefficient, *CI (ICC)* 95% confidence interval for ICC, *SEM* standard error of measurement in Newtons, *LOA* limits of agreement, *r* Pearson correlation coefficient, paired *t* indicates the resulting *p*-value from the paired *t*-test
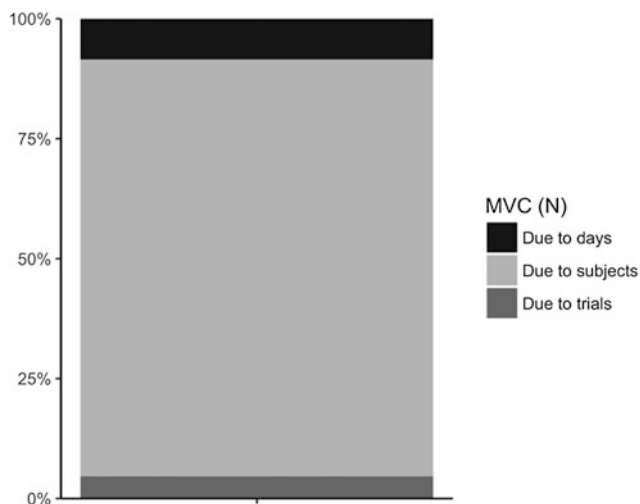
Fig. 2 Repeatability of the maximum voluntary isometric contraction of the ankle dorsiflexion obtained with the ICC method

Table 2 Repeatability of the MVIC with the Fisher method

Sources of variation	dof	MS	F ratio
Between subjects	9	34,140	25*
Between days	20	1358	4.6*
Between trials	30	289	

*$p < 0.01$

4 Discussion

The maximum voluntary isometric contraction of the ankle dorsiflexion is a measure used in several research protocols, such as in electromyography (EMG) research, where the EMG signal obtained in the MVIC is used to normalize the signals [24, 25], and to assess muscle strength, which can be related to aging and to several disorders of the peripheral nervous system, and also to investigate strength training effects [26–28]. As any other variable, the proper application of this measure depends on its reliability, thus, this study was performed to establish the reliability of the MVIC of the ankle dorsiflexion.

The results show excellent reliability in the trial-to-trial evaluation, presented in the three days, with moderate SEM, however, the LOA were high. It was not detected systematic changes between the trials, which enables us to conclude most likely the individuals did not present a learning or fatigue effect during the procedure. Consequently, for a MVIC of the ankle dorsiflexion with duration of 10 s, a 5 min rest interval is sufficient to avoid the effect of fatigue in a young male population.

Also, in day two, there is evidence of heteroscedasticity, due to the significant correlation between the difference between the two trials and the mean value of the two trials. This result is mainly caused by a single individual, therefore we believe it is necessary a larger sample to precisely state the behaviour of the variable, as a recent study also suggested heteroscedasticity in maximum strength [29]. Moreover, this study presents several ways to assess trial-to-trial reliability, given that relying on a single method may be misleading (e.g., when only the Person correlation coefficient is used to answer how well two methods agree but, it truly answers to the question on how well the measures are linearly related).

The ICC method was also evaluated, through a two-stage nested design with random factors. The MVIC showed to have an excellent level of repeatability (86.6%). Although there was a significant difference in the day-to-day measures when compared to the trial-to-trial measures (F test), this was not sufficient to produce a poor reliability value, given that the day-to-day variance represented only 8.6% of the total variability. This significant variability between days may have several explanations, probably related to changes in effort or motivation from the participant, given that we tried to minimize other possible effects, by performing the experiments during three consecutive days at about the same time of the day.

Finally, the ICC is sensitive to the heterogeneity of a sample, because it includes the variance term for individuals, that means a homogeneous sample will result in a lower ICC estimate than if equivalent variability results were obtained in a more heterogeneous sample [30]. In our study, we chose a relatively homogeneous sample, constituted of males in the age range from 23 to 28 years, and even so the ICC showed to be excellent. Consequently, the ICC will get higher as larger and more heterogeneous samples are studied for repeatability.

5 Conclusion

The results of this study demonstrate that the MVIC of the ankle dorsiflexion is a reliable measure to investigate its effects on a young male population. Further research is needed to examine the reliability of other variables associated with the test (e.g., rate of torque development) and also to explore the reliability on different populations (i.e., pathological subjects).

Conflict of Interest The authors declare that there is no conflict of interest.

References

1. Cudkowicz, M., Zhang, H., Qureshi, M., Schoenfeld, D.: Maximum voluntary isometric contraction (MVIC). Amyotroph Lateral Scler Other Mot Neuron Disord. **5**, 84–85 (2004)

2. Allen, M.D., Kimpinski, K., Doherty, T.J., Rice, C.L.: Decreased muscle endurance associated with diabetic neuropathy may be attributed partially to neuromuscular transmission failure. J. Appl. Physiol. **118**, 1014–1022 (2015)

3. Webber, S.C., Porter, M.M.: Reliability of ankle isometric, isotonic, and isokinetic strength and power testing in older women. Phys. Ther. **90**, 1165–1175 (2010)

4. Meldrum, D., Cahalane, E., Conroy, R., Fitzgerald, D., Hardiman, O.: Maximum voluntary isometric contraction: reference values and clinical application. Amyotroph Lateral Scler. **8**, 47–55 (2007)

5. DeLuca, C.J., Adam, A., Woitz, R., Gilmore, L., Nawab, S.: Decomposition of surface EMG signals. J. Neurophysiol. **96**, 1646–1657 (2006)

6. Burden, A.: How should we normalize electromyograms obtained from healthy participants? What we have learned from over 25 years of research. J. Electromyogr. Kinesiol. **20**, 1023–1035 (2010)

7. Kleine, B.U., Schumann, N.P., Stegeman, D.F., Scholle, H.C.: Surface EMG mapping of the human trapezius muscle: The topography of monopolar and bipolar surface EMG amplitude and spectrum parameters at varied forces and in fatigue. Clin. Neurophysiol. **111**, 686–693 (2000)

8. Van Cutsem, M., Duchateau, J.: Preceding muscle activity influences motor unit discharge and rate of torque development during ballistic contractions in humans. J. Physiol. **562**, 635–644 (2005)

9. Watanabe, K., Kouzaki, M., Moritani, T.: Task-dependent spatial distribution of neural activation pattern in human rectus femoris muscle. J. Electromyogr. Kinesiol. **22**, 251–258 (2012)

10. Lexell, J.E., Downham, D.Y.: How to assess the reliability of measurements in rehabilitation. Am. J. Phys. Med. Rehabil. **84**, 719–723 (2005)

11. Bergamin, M., Gobbo, S., Bullo, V., Vendramin, B., Duregon, F., Frizziero, A., Di Blasio, A., Cugusi, L., Zaccaria, M., Ermolao, A.: Reliability of a device for the knee and ankle isometric and isokinetic strength testing in older adults. Muscles Ligaments Tendons J. **7**, 323–330 (2017)

12. Symons, T.B., Vandervoort, A.A., Rice, C.L., Overend, T.J., Marsh, G.D.: Reliability of a single-session isokinetic and isometric strength measurement protocol in older men. J. Gerontol. **60**, 114–119 (2005)

13. Andersen, H.: Reliability of isokinetic measurements of ankle dorsal and plantar flexors in normal subjects and in patients with peripheral neuropathy. Arch. Phys. Med. Rehabil. **77**, 265–268 (1996)

14. Drouin, J.M., Valovich-mcLeod, T.C., Schultz, S.J., Gansneder, B.M., Perrin, D.H.: Reliability and validity of the Biodex system 3 pro isokinetic dynamometer velocity, torque and position measurements. Eur. J. Appl. Physiol. **91**, 22–29 (2004)

15. Ordway, N.R., Hand, N., Briggs, G., Ploutz-Syn, L.L.: Reliability of knee and ankle strength measures in an older adult population. J. Strength Cond. Res. **20**, 82–87 (2006)

16. Favretto, M.A., Cossul, S., Andreis, F.R., Balotin, A.F., Marques, C.M.G., Marques, J.L.B.: Development of a system to evaluate isometric strength of ankle dorsiflexion. In: Brazilian Congress on Electromyography and Kinesiology (2016)

17. Shrout, P.E., Fleiss, J.L.: Intraclass correlations: uses in assessing rater reliability. Psychol. Bull. **86**, 420–428 (1979)

18. Denegar, C.R., Ball, D.W.: Assessing reliability and precision of measurement: an introduction to lntraclass correlation and standard error of measurement. J. Sport Rehabil. **2**, 35–42 (1993)

19. Bland, J.M., Altman, D.G.: Statistical methods for assessing agreement between two methods of clinical measurement. Lancet **327**, 307–310 (1986)

20. Rainoldi, A., Bullock-Saxton, J.E., Cavarretta, F., Hogan, N.: Repeatability of maximal voluntary force and of surface EMG variables during voluntary isometric contraction of quadriceps muscles in healthy subjects. J. Electromyogr. Kinesiol. **11**, 425–438 (2001)

21. Rainoldi, A., Galardi, G., Maderna, L., Comi, G., Lo Conte, L., Merletti, R.: Repeatability of surface EMG variables during voluntary isometric contractions of the biceps brachii muscle. J. Electromyogr. Kinesiol. **9**, 105–119 (1999)

22. R Core Team.: R: A language and environment for statistical computing. R Found Stat. Comput. (2017)

23. Bates, D., Maechler, M., Bolker, B., Walker, S.: Fitting linear mixed-effects models using lme4. J. Stat. Softw. **67**, 1–48 (2015)

24. McKinnon, N.B., Montero-Odasso, M., Doherty, T.J.: Motor unit loss is accompanied by decreased peak muscle power in the lower limb of older adults. Exp. Gerontol. **70**, 111–118 (2015)

25. Bingham, A.: Normalised mutual information of high-density surface electromyography during muscle fatigue. Entropy **19**, 697 (2017)

26. Kent-braun, J.A., Ng, A.V.: Specific strength and voluntary muscle activation in young and elderly women and men. J. Appl. Physiol. **87**, 22–29 (1999)

27. Carolina, N., Section, A.B.: Tibialis anterior architecture, strength, and gait in individuals with cerebral palsy. Muscle Nerve **44**, 509–517 (2011)

28. Holmback, A.M., Porter, M.M., Downham, D., Lexell, J.: Ankle dorsiflexor muscle performance in healthy young men and women: reliability of eccentric peak torque and work measurements. J. Rehabil. Med. **33**, 90–96 (2001)

29. Clark, B.C., Cook, S.B., Ploutz-snyder, L.L.: Reliability of techniques to assess human neuromuscular function in vivo. J. Electromyogr. Kinesiol. **17**, 90–101 (2007)

30. Atkinson, G., Nevill, A.M.: Statistical methods for assessing measurement error (reliability) in variables relevant to sports medicine. Sport Med. **26**, 217–238 (1998)

Serious Games in Neurorehabilitation for People with Intellectual and Cognitive Impairments: A Systematic Study

Felipe Roque Martins⬤, Flávia Gonçalves Fernandes⬤, and Eduardo Lázaro Martins Naves⬤

Abstract

Electronic games are no longer seen as just a form of entertainment and leisure. Current studies have shown their potential as an interesting tool for improving the treatment of patients, ranging from those who are experiencing some serious illness (such as cancer), to those requiring rehabilitation procedures such as physiotherapy. In this line of reasoning, this work presents a systematic review on the use of serious games for rehabilitation of people with some type of intellectual or cognitive impairment, the process called neurorehabilitation. The sources of research were the following undescribed databases: Portal de Periódicos da Coordenação de Aperfeiçoamento de Pessoal de Nível Superior (CAPES), IEEE Xplore, Science Direct and PubMed. It should be noted that the use of systematic mapping in the elaboration of literature review allowed the identification of the main gaps for the development of new researches, aside from directing the main publications related to the study. Finally, the results show that it is an area in constant expansion, with great potential for development and applications, whose benefits extend far beyond the abilities being rehabilitated, bringing improvement in self-esteem, more autonomy, and reinsertion in the social context, among others.

F. R. Martins (✉) · E. L. M. Naves
Universidade Federal de Uberlândia, Uberlândia, MG, Brazil
e-mail: felipe.rmartins@outlook.com

F. G. Fernandes
Universidade Federal de Goiás, Catalão, GO, Brazil

1 Introduction

Frequently, people with some kind of disability, whether physical, mental or cognitive, are victims of prejudice and discrimination. In addition, in some situations they may even suffer differentiation on treatment compared to other healthy individuals and have the freedom of access diminished by the poor conditions of public and private access. The Universal Declaration of Human Rights establishes, however, that all individuals should be treated fraternally, regardless of deficiencies. In the specific case of Brazil, the Federal Constitution defines as a goal the search for the well being of everyone, without any sort of discrimination. In the same line, the Brazilian Penal Code determines as punishable acts the crimes and disrespect caused by discriminatory factors [1].

Intellectual impairment is a deficiency that presents concomitant cognitive deficits to adaptive functioning in at least two of the following areas: communication, personal care, home life, social/interpersonal skills, community resource use, independence, academic skills, work, leisure, health and safety [2].

It is one of the most commonly found deficiencies in children and teenagers, accounting for 1% of the younger population. It is characterized by the reduction in the cognitive development, the Intelligence Quotient (IQ), usually below the expected for the chronological age of the child or adult, often leading to a slower development in speech, neuropsychomotor development and other abilities [3].

Intellectual disability is not considered a disease or a psychiatric disorder, but one or more factors that cause impairment of the cognitive functions that accompany the different development of the brain [4].

As such, the option to use serious games can become an alternative in providing greater motivation in the treatment of rehabilitation through challenges with virtual techniques, working concepts that may aid in cognition, emotional and physical aspects of patients, in the development of lost

abilities, leisure, socialization and coexistence with other people. The promotion of the corporal consciousness of virtual form through serious games aims to simulate real situations. It was also revealed that the use of such tool improves affected cognitive processes and leads the participant to resume activities in the areas of occupational performance [5]. Therefore, it is important to conduct research whose purpose is to make people with intellectual disabilities also have the benefits of using serious games.

In this context, the objective of this study is to verify the panorama of the related research on the use of serious games for the rehabilitation of people with intellectual or cognitive impairment, presenting a systemic study about what has been published for this aspect.

The purpose of this systematic mapping is to analyze the references of the work carried out involving the issue of the application of serious games for people with intellectual disabilities. By doing that, it is also possible to visualize how much the line of research has evolved to this day.

2 Methodology

In order to carry out a review of the literature established by the study, a systematic mapping study was performed according to the methodology proposed by [6, 7], consisting of searching papers registered within a certain database by using specific logical operators for the selection of papers, by choosing the adequate key words or expressions.

The above systematic mapping technique was also used by [8–10].

The databases considered for the present study were Portal de Periódicos da Coordenação de Aperfeiçoamento de Pessoal de Nível Superior—CAPES [11], IEEE Xplore [12], Science Direct [13] and PubMed [14], databases available at the Federal Universities of Uberlândia and Goiás. It should be noted that only peer-reviewed journal articles were analyzed.

The logical expressions used to search the bases were "serious game" AND "rehabilitation". These strings were chosen to search for studies that involved serious games used in rehabilitation processes of individuals. Filters were then applied to narrow the search scope. For example, in terms of language (English and Portuguese), type of publication (peer-reviewed journal article) and year of publication (2008 to March 2018, constituting 10 years of publications). With the filters used in each database, the titles were then read in order to select which ones matched the selected logical expressions. Possible replications between the databases was also observed, and papers that fit the inclusion criteria had any duplicates removed.

Finally, the final selection stage of the papers consisted in directing the search to the rehabilitation of individuals with cognitive or intellectual disabilities. That was done after reading and analyzing the titles and abstracts of each paper, in order to exclude those works that were not directly related to the area of interest, being then the systematic review developed from the results obtained after this step. In this sense, studies that dealt with different themes were discarded, such as those involving the application of serious games to other types of disability (motor disability or hearing impairment, for example).

3 Results and Discussion

After searching the databases, the results were organized in the form of tables as a form of making the data easier to understand. Table 1 shows the total results obtained in the mapping, considering the aforementioned keywords and the deadline of March 2018.

Thus, through a systematic mapping, a secondary database was created with 27 (twenty-seven) references for the combination of "Serious Games" AND "rehabilitation" strings. Those selected works are presented in [15–41].

The evolution of the annual publication of the selected works in the research can be seen in both Figs. 1 and 2, where it is possible to notice that the papers involving the subject addressed in this work were published in recent years, and where the aforementioned researches were conducted. This way, it is observed that the subject of neurorehabilitation is recent and with great possibilities of fields to be explored.

By analyzing the Fig. 1 alone, it is possible to identify that, while countries like Portugal and France have more research on neurorehabilitation ongoing, the field is very spread across the globe, meaning that different countries can bring multiple ideas and different solutions for the same problem, increasing the development rate on the field as a whole.

Table 1 Synthesis of the results obtained in the research

Database	Number of papers	
	Initial	With matching title
Periódicos Capes	232	19
PubMed	95	21
Science Direct	138	11
IEEE Xplore	209	25
Total	674	76
Total number of papers without duplicates between databases	68	
Number of papers selected after reading the title and abstract	27	

Fig. 1 Related papers divided by country of origin

Number of papers by country of origin
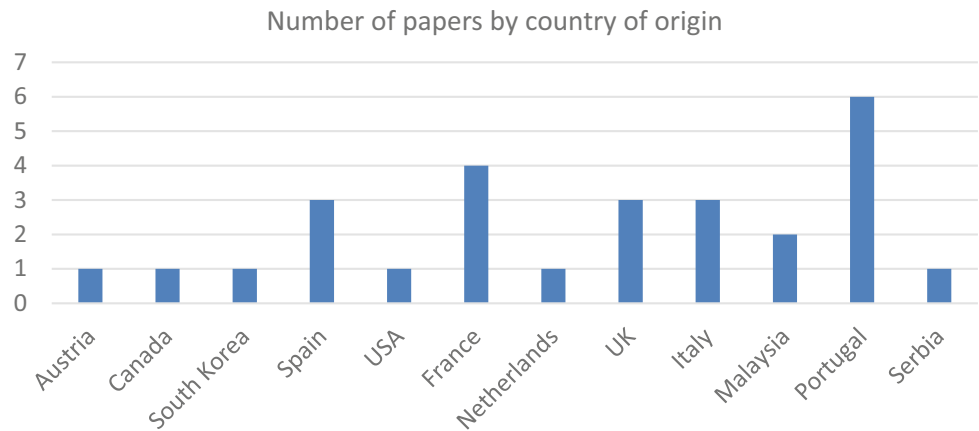
Fig. 2 Researches grouped by year of publication

Number of papers by year of publication
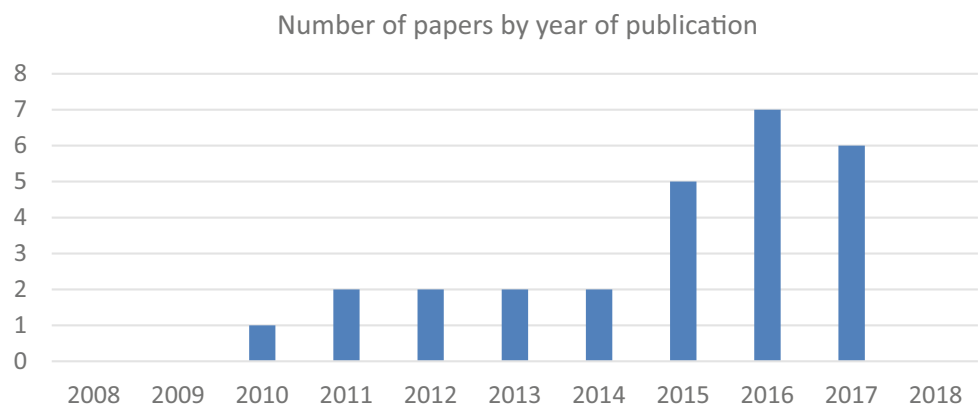
In case of the Fig. 2, it can be perceived an increased interest on the field, starting from 2010. Most of these works have been carried on the last three years, indicating even more the growth being experienced in the field of neurorehabilitation.

It is possible to verify in Fig. 3 that the type of intellectual or cognitive impairment of interest for each work also varies greatly. While some works did not specify what is the impairment that is the focus of the serious game presented, and others worked with more than a single impairment at time, most of them had a very clear goal in mind. This, of course, would change what kind of abilities (math, decision making, memory and concentration, for example) should be exercised and worked upon. This leads to a greater number of options for the different kinds of cognitive and intellectual impairments known currently, which in turn provides a higher chance of finding the ideal one for the process of rehabilitation.

Finally, the selected papers were compiled into a single table presenting the main findings of each article. From the engineering point of view, the works were described according to the type and purpose of serious game used in the work, the equipment that is part of the system, and from the clinical point of view, whether or not patient tests were performed, and whether there was improvement in the case in which the experiments were performed. The results are organized in Table 2.

As it is possible to see, the goal of the selected serious games varies quite a lot, since it depends on what type of intellectual or cognitive impairment is the subject of the study. Goals like attention, memory, planning, decision making and navigation are amongst the most frequent ones. About the possible devices, most of the time only a Personal Computer (PC) is used as the requirement to playing the serious game, with or without internet connection. Out of the 27 selected papers, only six did not perform tests with patients, while two of those performed tests with healthy individuals instead of people with actual disabilities. Moreover, from the 21 that did perform such tests, 14 had a positive improvement of the goal or ability they were trying to assess, while five of them had inconclusive results (needing more testing to make sure of the results) and two had a negative response from the serious game. That shows that, even though the results can vary significantly depending on the objective of the serious game, generally a positive response could be found from using such tool most of the time.

Fig. 3 Intellectual or cognitive impairments focused on the related works
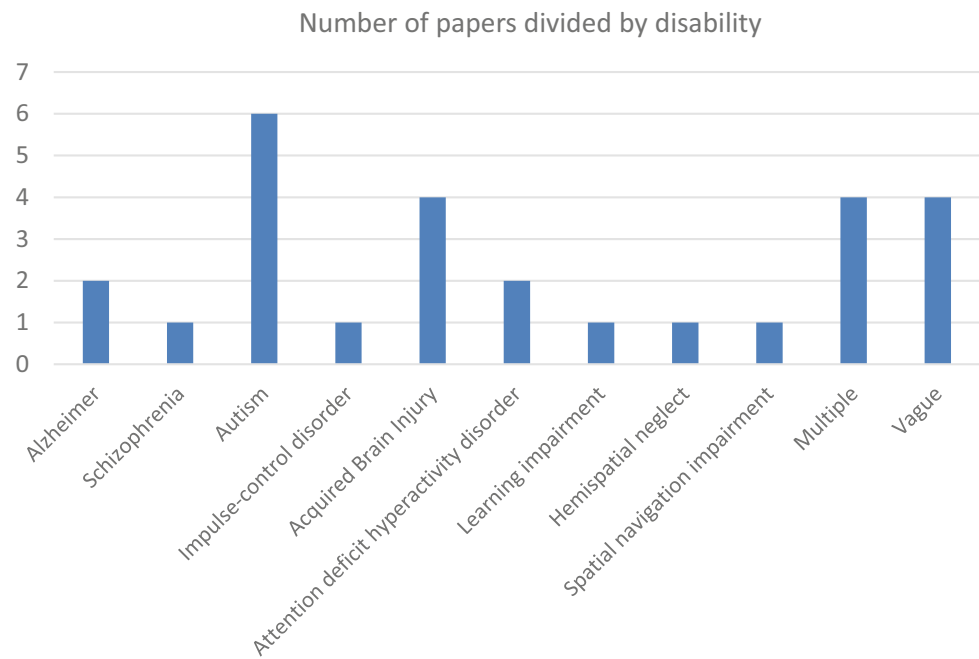
Table 2 Synthesis of the present works found in the research

Paper	Type of game	Devices	Tests with patients	Improved
[15]	Attention, memory, decision making	PC (web)	Yes	Yes
[16]	Decision making	Laptop and joystick	Yes	Yes
[17]	Memory, planning and navigation	Laptop and joystick	Yes	Yes
[18]	Planning and decision making	Tablet	Yes	Yes
[19]	Attention and memory	Laptop	Yes	Yes
[20]	Relaxation and self-control	PC and biosensors	Yes	No
[21]	Planning and interaction	LCD with eye tracker	Yes	Inconc.
[22]	Cognitive rehabilitation	PC	No	–
[23]	Attention, memory and coordination	PC (web)	Yes	Yes
[24]	Manual tasks and skills training	Laptop with mouse	Yes	Yes
[25]	Activities of daily living	PC (web) with HMD	No	–
[26]	Memory	PC, TV and Wiimote®	Yes	Yes
[27]	Cognitive rehabilitation	PC (web)	No	–
[28]	Memory, concentration, planning and problem solving	PC (web)	Healthy	Yes
[29]	Cognitive rehabilitation	PC	No	–
[30]	Planning and decision making	PC	No	–
[31]	Cognitive rehabilitation	PC	Yes	Inconc.
[32]	Navigation	PC, TV and camera	Yes	Yes
[33]	Attention	PC	Yes	Yes
[34]	Organization, perception, math and imitation	PC, Kinect for Xbox 360	Yes	Inconc.
[35]	Cognitive rehabilitation	PC	No	–
[36]	Skill training	PC with HMD	Yes	Inconc.
[37]	Math	PC	Yes	Yes
[38]	Navigation	PC	Healthy	Inconc.
[39]	Imitation and attention	PC or tablet	Yes	Yes
[40]	Skill training	Laptop, board and fruits	Yes	Yes
[41]	Imitation and attention	PC or tablet	Yes	No

4 Conclusion

Through the mapping study, it was possible to verify that there was a growth in the researches on the use of serious games for people with intellectual impairment, since it is a learning option that involves both entertainment and leisure. From what has been presented in this work, it could be observed that there is a growing interest in researching and publishing in this area related to serious games for people with intellectual impairment, seeking to assist in their social inclusion.

In relation to the selected works, it was noticed that there is a great variety in the focus on each serious game, that is, there are several intellectual and cognitive impairments that are worked on within each serious game. In addition, the multiple focus of research in the countries indicates a dispersion of the study area, where the subject is addressed at a global level. This is interesting because of the diversification of the ways in which studies are conducted at each site and country, possibly leading to a more rapid evolution in the research area.

Therefore, there is a need to foster this area of research in order to offer this public with intellectual impairment access to serious games as a form of treatment, knowledge acquisition, motivation, entertainment or even inclusion. In this way, it will be possible to obtain a greater maturity in the obtained results and thus to promote a systematization in the use of the serious games in the aid of the promotion of the well-being of these people.

References

1. Guia de direitos. Discriminação com Deficientes Homepage. http://www.guiadedireitos.org/index.php?option=com_content&view=article&id=1040&Itemid=264. Accessed 18 Mar 2018
2. Tédde, S.: Crianças com deficiência intelectual: a aprendizagem e a inclusão. Dissertação (Mestrado em Educação), Americana: Centro Universitário Salesiano de São Paulo, 99 p (2012)
3. Vasconcelos, M.M. Retardo mental. Jornal de pediatria, Porto Alegre **80**(2), S71–S82. Abr. (2004)
4. Honora, M., Frizanco, M.L.: Esclarecendo as deficiências: Aspectos teóricos e práticos para contribuir com uma sociedade inclusiva. Ciranda Cultural (2008)
5. Grande, A.A.B., Galvão, F.R.O., Gondim, L.C.A.: Reabilitação virtual através do videogame: relato de caso no tratamento de um paciente com lesão alta dos nervos mediano e ulnar. Revista Acta Fisiátrica, Rio Grande do Norte **18**(3), 157–162 (2011)
6. Bailey, J., Budgen, D., Turner, M., Kitchenham, B., Brereton, P., Linkmon, S.: Evidence relating to object-oriented software design: a survey. In: First International Symposium on Empirical Software Engineering and Measurement. Computer Society (2007)
7. Petersen, K., Feldt, R., Mujtaba, S., Mattsson, M.: Systematic mapping studies in software engineering. School of Engineering, Blekinge Institute of Technology. University of Bari, Italy, 26–27 June (2008)
8. Paula, H.M.D., Ilha, M.S.D.O.: Uso da Moringa oleifera no tratamento de águas residuárias de usinas de concreto: mapeamento sistemático. REEC - Revista Eletrônica de Engenharia Civil **11**(1), 50–60 (2016)
9. Bonfim, W.B., Baldin, V., Pereira, R.R., Paula, H.M.: Lama residual de usinas de concreto: características e aplicações na confecção de blocos. REEC - Revista Eletrônica de Engenharia Civil **13**(2), 32–43 (2017)
10. Rodrigues, K.C., Mesquita, H.C., Eduardo, R.C., Paula, H.M.: Mapeamento sistemático de referências do uso do BIM na compatibilização de projetos na construção civil. REEC - Revista Eletrônica de Engenharia Civil **13**(1), 219–239 (2017)
11. CAPES - Portal de Periódicos da Coordenação de Aperfeiçoamento de Pessoal de Nível Superior Homepage. http://www-periodicos-capes-gov-br.ez49.periodicos.capes.gov.br/. Accessed 18 Mar 2018
12. IEEE XPLORE Homepage. http://ieeexplore.ieee.org/Xplore/home.jsp. Accessed 18 Mar 2018
13. SCIENCE Direct Homepage. http://www.sciencedirect.com/. Accessed 18 Mar 2018
14. PUBMED Homepage. https://www.ncbi.nlm.nih.gov/pubmed/. Accessed 18 Mar 2018
15. Cruz, V.T., Pais, J., Bento, V., Mateus, C., Colunas, M., Alves, I., Coutinho, P., Rocha, N.P.: A rehabilitation tool designed for intensive web-based cognitive training: description and usability study. J. Med. Internet Res. (JMIR) Protoc. **2**(2), e59. https://doi.org/10.2196/resprot.2899 (2013)
16. Burdea, G., Polistico, K., Krishnamoorthy, A., House, G., Rethage, D., Hundal, J., Damiani, F., Pollack, S.: Feasibility study of the BrightBrainer™ integrative cognitive rehabilitation system for elderly with dementia. Disabil. Rehabil. Assistive Technol. **10**(5), 421–432 (2015). https://doi.org/10.3109/17483107.2014.900575
17. Amado, I., Brénugat-Herné, L., Orriols, E., Desombre, C., Dos Santos, M., Prost, Z., Krebs, M.O., Piolino, P.A.: Serious game to improve cognitive functions in schizophrenia: a pilot study. Front. Psychiatr. **7**, 64. https://doi.org/10.3389/fpsyt.2016.00064 (2016)
18. Manera, V., Petit, P.D., Derreumaux, A., Orvieto, I., Romagnoli, M., Lyttle, G., David, R., Robert, P.H.: 'Kitchen and cooking,' a serious game for mild cognitive impairment and Alzheimer's disease: a pilot study. Front. Aging Neurosci. **17**(7), 24. https://doi.org/10.3389/fnagi.2015.00024 (2015)
19. Kerns, K.A., Macoun, S., MacSween, J., Pei, J., Hutchison, M.: Attention and working memory training: a feasibility study in children with neurodevelopmental disorders. Appl. Neuropsychol. Child. **6**(2), 120–137. https://doi.org/10.1080/21622965.2015.1109513 (2017)
20. Fernández-Aranda, F., Jiménez-Murcia, S., Santamaría, J.J., Gunnard, K., Soto, A., Kalapanidas, E., Bults, R.G., Davarakis, C., Ganchev, T., Granero, R., Konstantas, D., Kostoulas, T.P., Lam, T., Lucas, M., Masuet-Aumatell, C., Moussa, M.H., Nielsen, J., Penelo, E.: Video games as a complementary therapy tool in mental disorders: PlayMancer, a European multicentre study. J. Ment. Health. **21**(4), 364–374. https://doi.org/10.3109/09638237.2012.664302 (2016)
21. Bernardini, S.; Porayska-Pomsta, K., Smith, T.J.: ECHOES: an intelligent serious game for fostering social communication in children with autism. Inf. Sci. J. **264**, 41–60 (2014)
22. Elaklouk, A.M., Zin, N.A.M., Shapii, A.: Investigating therapists' intention to use serious games for acquired brain injury cognitive rehabilitation. J. King Saud Univ. Comput. Inf. Sci. **27**, 160–169. http://dx.doi.org/10.1016/j.jksuci.2014.03.019 (2015)
23. Rijo, R., Costa, P., Machado, P., Bastos, D., Matos, P., Silva, A., Ferrinho, J., Almeida, N., Oliveira, A., Xavier, S., Santos, S., Oliveira, C., Brites, S., Martins, V., Pereira, A., Fernandes, S.: Mysterious Bones Unearthed: development of an online

therapeutic serious game for children with attention deficit-hyperactivity disorder. J. Comput. Sci. **64**, 1208–1216 (2015). https://doi.org/10.1016/j.procs.2015.08.512

24. Kwon, J., Lee, Y.: Serious games for the job training of persons with developmental disabilities. Comput. Educ. J. **95**, 328–339 (2016). https://doi.org/10.1016/j.compedu.2016.02.001

25. Simões, M., Mouga, S., Pedrosa, F., Carvalho, P., Guiomar, O., Branco, M.C.: Neurohab: a platform for virtual training of daily living skills in autism spectrum disorder. Proc. Technol. J. **16**, 1417–1423 (2014). https://doi.org/10.1016/j.protcy.2014.10.161

26. Benveniste, S., Jouvelot, P., Pin, B., Péquignot, R.: The MINWii project: renarcissization of patients suffering from Alzheimer's disease through video game-based music therapy. Entertain. Comput. J. **3**, 111–120 (2012). https://doi.org/10.1016/j.entcom.2011.12.004

27. Elaklouk, A.M., Zin, N.A.M.: Design and usability evaluation of rehabilitation gaming system for cognitive deficiencies. In: IEEE International Conference on Electrical Engineering and Informatics (ICEEI). 978-1-5386-0475-5/17 (2017)

28. Rocha, R., Reis, L.P., Rego, P.A., Moreira, P.M., Faria, B.M.: New forms of interaction in serious games for cognitive rehabilitation: implementation and usability study. In: IEEE Iberian Conference on Information Systems and Technologies—CISTI (2016)

29. Grau, S., Tost, D., Campeny, R., Moya, S., Ruiz, M.: Design of 3D virtual neuropsychological rehabilitation activities. In: IEEE International Conference on Games and Virtual Worlds for Serious Applications. https://doi.org/10.1109/vs-games.2010.17 (2010)

30. Dores, A.R., et al.: Virtual city: neurocognitive rehabilitation of acquired brain injury. In: IEEE Iberian Conference on Information Systems and Technologies—CISTI (2012)

31. Hussaan, A.M., Sehaba, K.: Adaptive serious game for rehabilitation of persons with cognitive disabilities. In: IEEE International Conference on Advanced Learning Technologies (ICALT). https://doi.org/10.1109/icalt.2013.25 (2013)

32. Borghese, N.A., et al.: A reliable low-cost platform for neglect Virtual Rehabilitation. In: IEEE International Conference on Virtual Rehabilitation (ICVR). 978-1-61284-474-9/11 (2011)

33. Colombo, V., et al.: ANTONYMS: a serious game for enhancing inhibition mechanisms in children with attention deficit/hyperactivity disorder (ADHD). In: IEEE International Conference on Virtual Rehabilitation (ICVR). 978-1-5090-3053-8/17 (2017)

34. Roglić, M., et al.: Serious gaming based on Kinect technology for autistic children in Serbia. In: IEEE Neural Networks and Applications—NEUREL (2016)

35. Standen, P., et al.: MyDailyRoutine—a serious game to support people suffering from a cerebral dysfunction. In: IEEE Serious Games and Applications for Health (SeGAH) (2016)

36. Bernardes, M., et al.: A serious game with virtual reality for travel training with autism spectrum disorder. In: IEEE International Conference on Virtual Rehabilitation—ICVR (2015)

37. Brown, D.J., et al.: Can participating in games based learning improve mathematic skills in students with intellectual disabilities? In: IEEE Serious Games and Applications for Health—SeGAH (2011)

38. Kuil, M.N.A., Ham, I.J.M.: Game technology in cognitive rehabilitation of spatial navigation impairment. In: IEEE International Conference on Virtual Rehabilitation—ICVR (2017)

39. Bono, V., Narzisi, A., Jouen, A., Tilmont, E., Hommel, S., Jamal, W., Xavier, J., Billeci, L., Maharatna, K., Wald, M., Chetouani, M., Cohen, D., Muratori, F.: GOLIAH: a gaming platform for home-based intervention in autism—principles and design. Front. Psychiatr. **7**, 70. Published online 28 Apr 2016. https://doi.org/10.3389/fpsyt.2016.00070 (2016)

40. Durango, I., Carrascosa, A., Gallud, J.A., Penichet, V.M.R.: Interactive fruit panel (IFP): a tangible serious game for children with special needs to learn an alternative communication system. Univers. Access Inf. Soc. **17**(1), 51–65 (2017)

41. Jouen, A.L., Narzisi, A., Xavier, J., Tilmont, E., Bodeau, N., Bono, V., Ketem-Premel, N., Anzalone, S., Maharatna, K., Chetouani, M., Muratori, F., Cohen, D.: GOLIAH (Gaming Open Library for Intervention in Autism at Home): a 6-month single blind matched controlled exploratory study. Child Adolesc. Psychiatr. Ment. Health **11**, 17. Published online 22 Mar 2017. https://doi.org/10.1186/s13034-017-0154-7 (2017)

Superficial Characteristics of Acetone Vapor Treated ABS Printed Parts for Use in Upper Limb Prosthesis

Vivian Thais Leite Costa and Chi Nan Pai

Abstract

Approximately 33% of amputations happen due to external causes, which makes these patients strong candidates for prostheses use. Nevertheless, functional hand prostheses are expensive, costing more than R$ 30,000.00, and are not very accessible, especially in Brazil. Trying to reduce their cost, several groups around the world have been researching the construction of prostheses using additive manufacturing (AM). The most common AM technique is Fused Deposition Modeling (FDM), also known as 3D printing. A heated polymer filament is forced trough a nozzle, and placed in the right position, layer upon layer, until the piece is complete. It is possible to improve surface quality of 3D printed parts by using post processing techniques. Dealing with parts made of Acrylonitrile Butadiene Styrene (ABS), acetone vapor bath is an adequate choice of treatment. Pieces printed in different orientations were treated with acetone vapor for different times, and then submitted to nanoindentation tests and topography and roughness analysis in an Optical Profiler. A reduction in hardness and elastic modulus was observed after treatment. Roughness was also drastically reduced, and staircase effect was eliminated after treatment. It is important to consider the application of printed piece before applying acetone vapor bath, as the process alters external measures and mechanical properties. For future work, it is intended to analyze if the reduction in mechanical superficial properties impacts the use of printed parts in upper limb functional prosthesis.

Keywords

3D printing • Superficial treatment • ABS • Acetone vapor bath

V. T. L. Costa (✉) · C. N. Pai
Universidade de São Paulo - USP, São Paulo, Brazil
e-mail: vivianthais@usp.br

1 Introduction

Amputation is the process that removes, surgically, partially or totally, a limb or part of the body. It is performed to remove extremities that are severely ill, injured or non-functional, when less traumatic treatments are not sufficient to solve the problem [1].

Although it may be considered a reconstructive surgery, amputation brings an enormous physical and psychological loss to the patient [2]. The losses caused due to amputations of the upper limbs are even more severe than those caused by amputations in the lower limbs [3].

According to data from SUS (Sistema Único de Saúde), in 2011 almost 50,000 amputations were performed in Brazil. From that total approximately 33% due to external causes (like trauma, for example), which makes these patients strong candidates for prostheses use [4].

Prosthesis is defined as a device implanted in the body that supplies the lack of a limb, or an organ. Electromechanical prosthesis are the ones that use motors or electric actuators for the movement of parts of the prosthesis, and the myoelectric ones are electromechanical prosthesis that use electromyography signals as command signals [5].

Nevertheless, functional hand prostheses are expensive, costing more than R$ 30,000.00, and are not very accessible, especially in Brazil [6]. Trying to reduce their cost, several groups around the world have been researching the construction of prostheses using Additive Manufacturing (AM) [7].

AM is defined by ASTM as the "process of joining materials to make objects from three-dimensional (3D) model data, usually layer upon layer, as opposed to subtractive manufacturing methodologies" [8].

The most common AM technique is Fused Deposition Modeling (FDM), also known as 3D printing. A heated polymer filament is forced trough a nozzle, and placed in the right position, layer upon layer, until the piece is complete. Extruded filament solidifies quickly, bonding with previous material [9]. When compared to traditional manufacturing

techniques, 3D printing is usually cheaper, faster, capable of producing pieces with more complex design, and more customizable, since it does not require molds.

However, due to the layer by layer construction process, surface roughness is really poor. A staircase effect can be observed in the surface of every piece, caused by the interaction of each individual layer. Printing parameters interfere on surface roughness, especially layer thickness [10, 11].

It is possible to improve surface quality of 3D printed parts using post processing techniques. Dealing with parts made of Acrylonitrile Butadiene Styrene (ABS), acetone vapor bath is an adequate choice of treatment. The acetone vapor "dissolves" the polymeric molecules on the surface, allowing them to rearrange in a more favorable position, when the solvent is withdrawn. This reduces staircase effect and improve surface roughness [10, 11].

The aim of this study is to investigate the effect of acetone vapor bath treatment in roughness and superficial mechanical properties of ABS printed parts, using nanoindentation tests, evaluating hardness and elasticity; and topography studies to determine roughness improvement.

2 Materials and Methods

2.1 Printed Parts

Five parts were printed in each orientation; vertically and horizontally. The chosen design was a rectangular block (10 × 15 × 20 mm) with a holder, as Fig. 1 shows. Pins were used to differentiate treatment time in each part. A 0.20 mm layer thickness was used. Figure 2 shows a comparative of the larger face printed in both orientations.

2.2 Surface Treatment

Surface treatment can be done mechanically or chemically. The mechanical approach uses CNC machines, hence has a limitation to access certain areas due to part geometry, and has an elevated cost. Accessing areas is not a problem in the

Fig. 2 Parts printed vertically (**a**) and horizontally (**b**)

chemical approach, and the costs are lower compared to the mechanical one. The chosen chemical has to be compatible with the polymer used; acetone is a good choice to treat ABS parts [11].

Acetone vapor bath was the chosen method for post processing surface treatment. In this experimental arrangement, a part hangs from a hook in a sealed environment with a little liquid acetone, which is heated, keeping the temperature between 50 and 60 °C. The vapor reaches the part, weakening the bonds between polymer chain, softening the exterior layers, and enabling the molecules to arrange in a better position. After the process, acetone evaporates, leaving the part surface, which rehardens with a smoother, polished surface [10, 11].

Five parts were printed in each orientation, treatment time varied between zero and one hour, in fifteen minutes intervals. First part was not treated, second one spent 15 min in vapor bath, third one spent 30 min, and so on, until last part was treated for one hour.

After vapor bath, parts dried for at least 24 hours, to guarantee that all the acetone evaporated from the ABS part.

2.3 Superficial Properties Analysis

Once dried, the parts were tested in a nanoindenter, to measure hardness and elasticity modulus. Three indentations were used to calculate the mean property. After that, topography and surface roughness of every part were evaluated in a Taylor Hobson CCI MP-HS non-contact optical profiler.

Fig. 1 Printed part design

3 Results and Discussion

3.1 Acetone Vapor Treatment

Even parts which spent less time in vapor bath (were treated for 15 min), had a significant change in their exterior. They became brighter and a little smoother, with more rounded corners. However, it is still possible to see the layers from the printing process, and some parts are not affected yet, leaving some portions of non-treated surface. Results were very similar for parts printed horizontally and vertically. A macro comparison of parts appears in Figs. 3 and 4.

For a 30 min treatment time, it is still possible to see some layer limits, but parts became significantly smoother, brighter and with more rounded edges. Fewer holes in surface can be observed, but they still exist. With a 45 min vapor bath, holes in part surface can no longer be seen, neither does the layers limits; part is more homogeneous, smoother, with more rounded corners and edges, and brighter; the same overall aspect occurs in parts treated for

60 min. Figure 5 shows a comparative between non treated parts, and parts treated for 60 min.

Vapor treatment softens exterior layers, causing a sort of "melting effect" that makes them run down. In some cases, this effect can change part form, as was the case of parts treated for 60 min, were two of the pins merged together after treatment.

Owing to filling characteristics, the parts printed horizontally did not resist so well to longer treatment times. Figure 6 shows that, in some cases, exterior layers have a melted effect and sag, obtaining the format of the filling structure. This phenomenon does not happen with parts printed vertically, due to the position off the filling structure, which is parallel to gravity.

As Fig. 1 shows, every part had a holder, from where they were hanged for vapor treatment. This holder was printed with the part, that way, the holder also is made of ABS, and is affected by acetone. As it supports the entire piece weight, it was very deformed in longer treatment times, losing its initial measurements and forms.
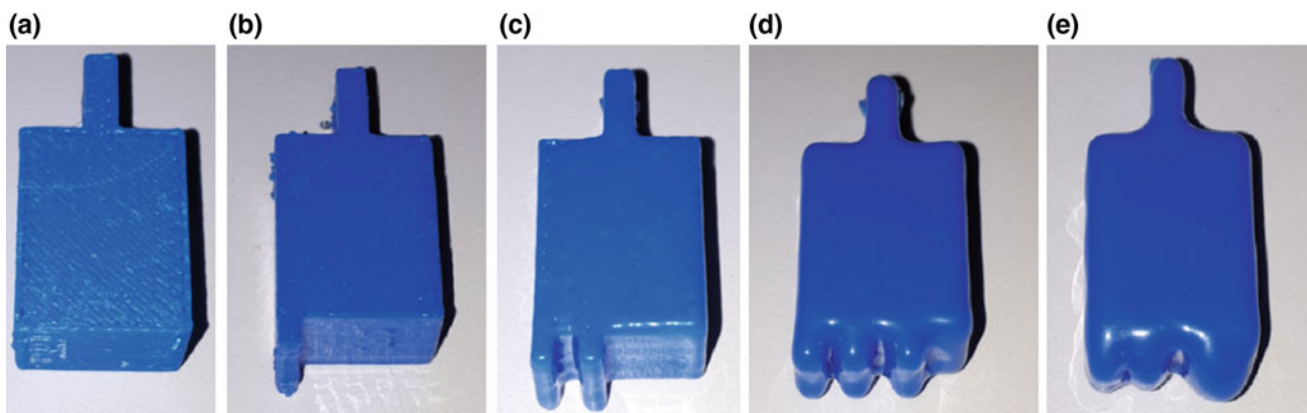
Fig. 3 Parts printed horizontally. **a** Non treated, **b** 15 min treatment, **c** 30 min treatment, **d** 45 min treatment, **e** 60 min treatment
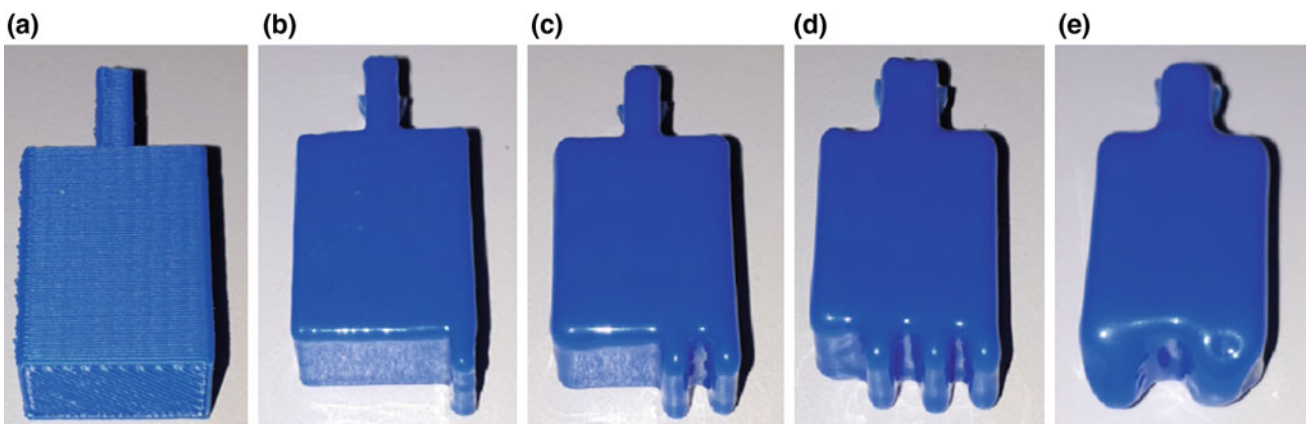
Fig. 4 Parts printed vertically. **a** Non treated, **b** 15 min treatment, **c** 30 min treatment, **d** 45 min treatment, **e** 60 min treatment
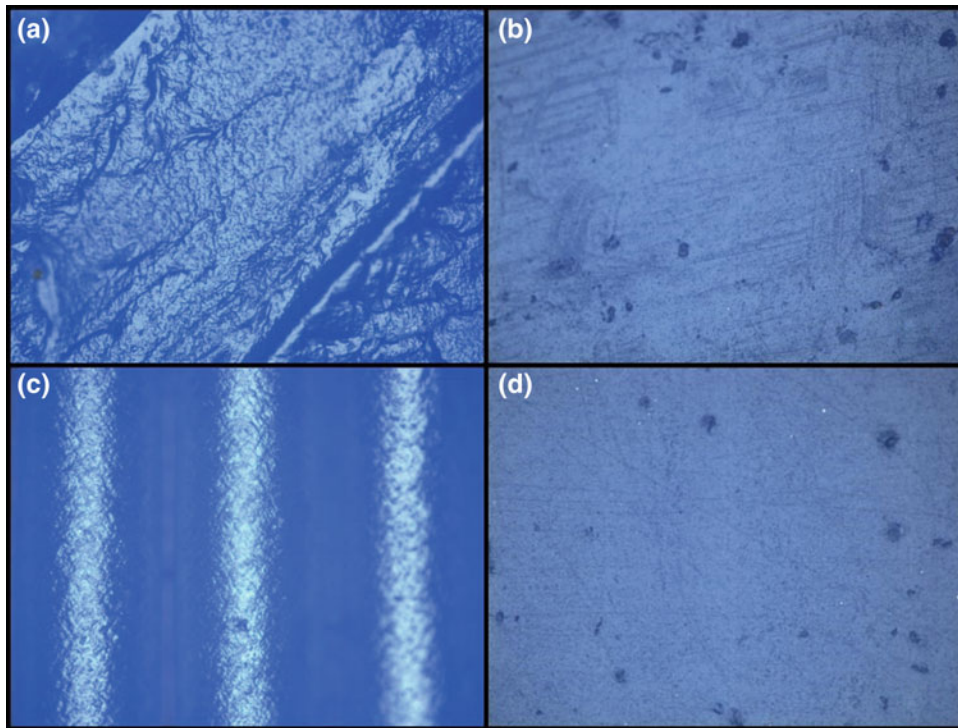
Fig. 5 Non-treated versus treated for 60 min surfaces. 10x lens. **a** Horizontally printed, non-treated; **b** horizontally printed, 60 min treatment; **c** vertically printed, non-treated; **b** vertically printed, 60 min treatment

Fig. 6 Excessively melted surface of horizontally printed part, 60 min treatment

The longer the treatment time, the more evident the alterations in external measurements and shapes, as can be seen by the pins in pieces which were treated for 60 min, and merged together in a bigger pin, due to softening of the material.

3.2 Nanoindentation Tests

Nanoindentation was performed in a Hysitron TI 950 Triboindenter, using a 1 mN load, in a 5 × 2 × 5 loading time (load grows for 5 s, stay stable for 2 s, and unload in 5 s), as shown on Fig. 7. Table 1 shows values of hardness and elastic modulus obtained for every piece.

Due to the fabrication process, printed parts are highly anisotropic, and present a high accumulation of residual stresses. Vapor treatment allows polymeric molecules to reallocate, which reduces anisotropy and relieve residual stress; this causes a reduction in hardness and elastic modulus, as can be seen in Table 1 values.

During the first minutes of treatment, hardness and elastic modulus falls drastically, reducing around 40% and 30%, respectively. After that, properties changes are small. This
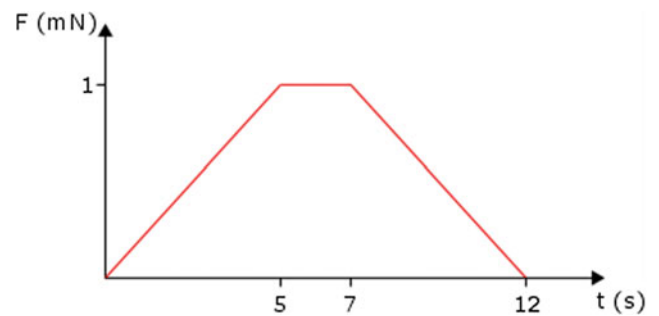
Fig. 7 Nanoindentation loading time

Table 1 Results of nanoidentation

Printing orientation	Treatment time (min)	Contact depth (nm)	E (GPa)	H (GPa)
Vertical	0	404.59 ± 2.18	4.04 ± 0.1438	0.2207 ± 0.0026
	15	533.56 ± 10.53	2.92 ± 0.0599	0.1306 ± 0.0048
	30	500.99 ± 6.41	3.01 ± 0.056	0.1470 ± 0.0037
	45	508.06 ± 2.25	2.98 ± 0.0179	0.1430 ± 0.0011
	60	492.01 ± 8.36	3.03 ± 0.0773	0.1519 ± 0.0046
Horizontal	0	412.94 ± 10.30	3.79 ± 0.0140	0.2122 ± 0.0095
	15	535.15 ± 13.22	2.92 ± 0.0666	0.1299 ± 0.0060
	30	518.06 ± 6.63	2.93 ± 0.0392	0.1381 ± 0.0034
	45	482.77 ± 29.68	3.14 ± 0.1590	0.1588 ± 0.0190
	60	506.20 ± 10.23	2.99 ± 0.1035	0.1443 ± 0.0057

shows that residual stresses are relieved as soon as forces between molecules are reduced.

What changes with treatment time is the profundity of part that is solubilized in acetone, that is why at first layers delimitation are still visible, and after longer treatment times it is no longer possible to identify layers. The decrease in those mechanical properties is significant. Also, Gao showed that acetone treatment also has an effect in macroscopic properties, reducing strength and increasing elongation at failure [10].

3.3 Topography and Roughness

Topography and roughness analysis were performed by a Taylor Hobson CCI MP-HS non-contact optical profiler. For every part, there is a topography map (Figs. 8, 9, 10, 11, 12, 13, 14, 15, 16, 17), a mean profile roughness graph (Figs. 18, 19, 20, 21), and a mean roughness value (Table 2).

From those topography maps, it is possible to observe that even with only 15 min treatment, the Optical Profiler
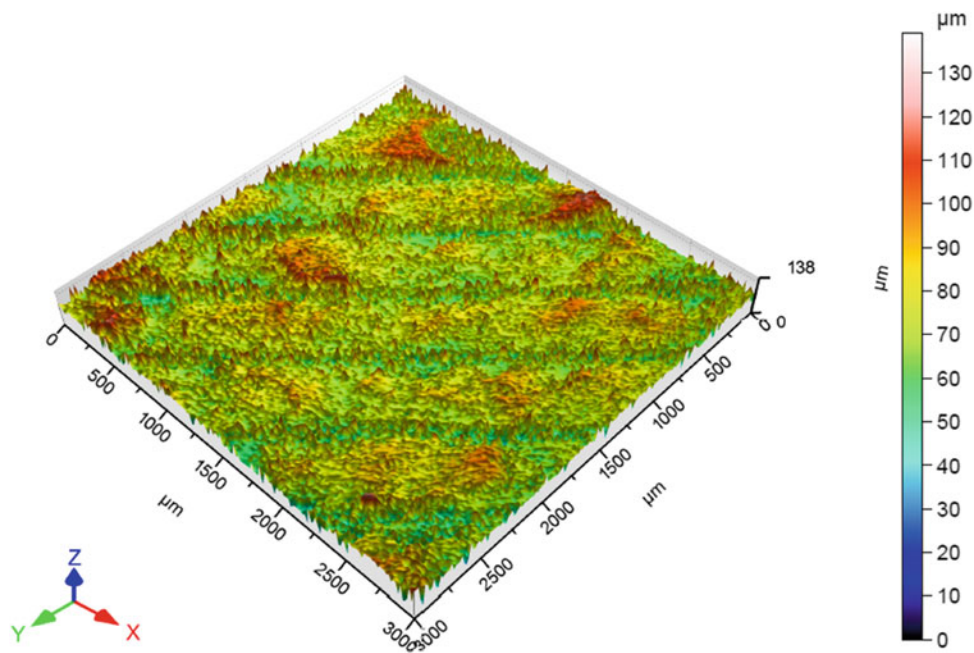
Fig. 8 Topography map. Part printed horizontally, with 0 min. treatment
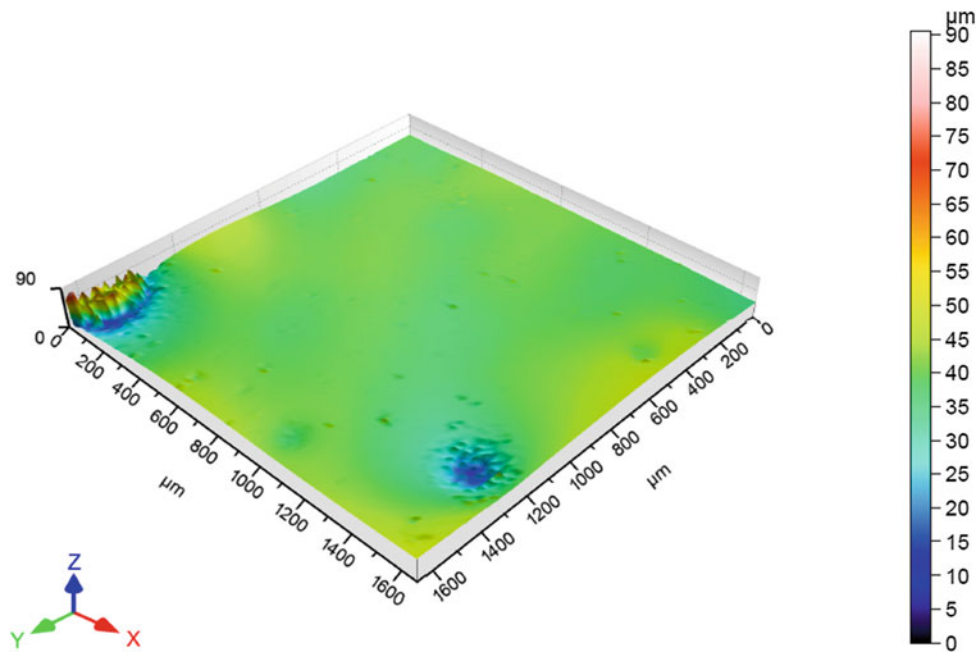
Fig. 9 Topography map. Part printed horizontally, with 15 min. treatment
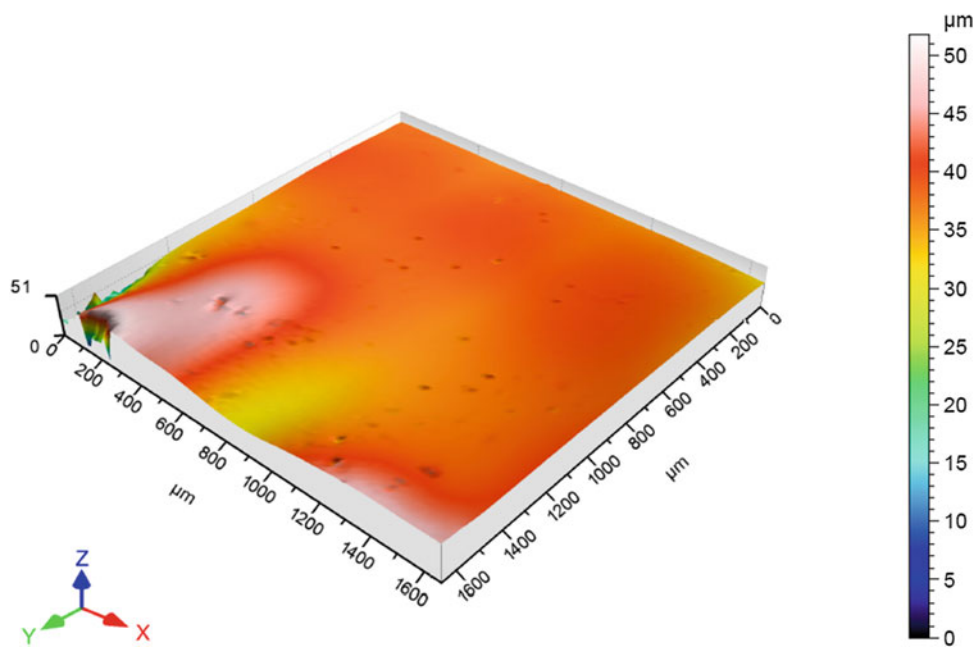
Fig. 10 Topography map. Part printed horizontally, with 30 min. treatment

does not capture the layers and staircase effect anymore. This happens because the more external portions of ABS had already remodeled, showing a smoother surface.

Acetone vapor bath superficial treatment is not fully homogeneous, it leaves some flaws on the surface, like holes in the smooth surface. Despite that, Figs. 8, 9, 10, 11, 12, 13, 14, 15, 16, 17 show that the longer the treatment time, the smaller the difference between peaks and valleys. This can also be observed in Fig. 18, that shows the mean variation of

heights in the surface, which means that those flaws get smaller with longer treatment times.

From Fig. 18 it is also possible to say that material roughness is also reduced, not only the staircase effect is "eliminated", and layers can no longer be seen, but the surface roughness also decreases significantly.

The mean roughness (Ra) reduces drastically with vapor bath treatment. For horizontal printed parts, a decrease of 98.4% in Ra is observed, while for vertical printed parts, this
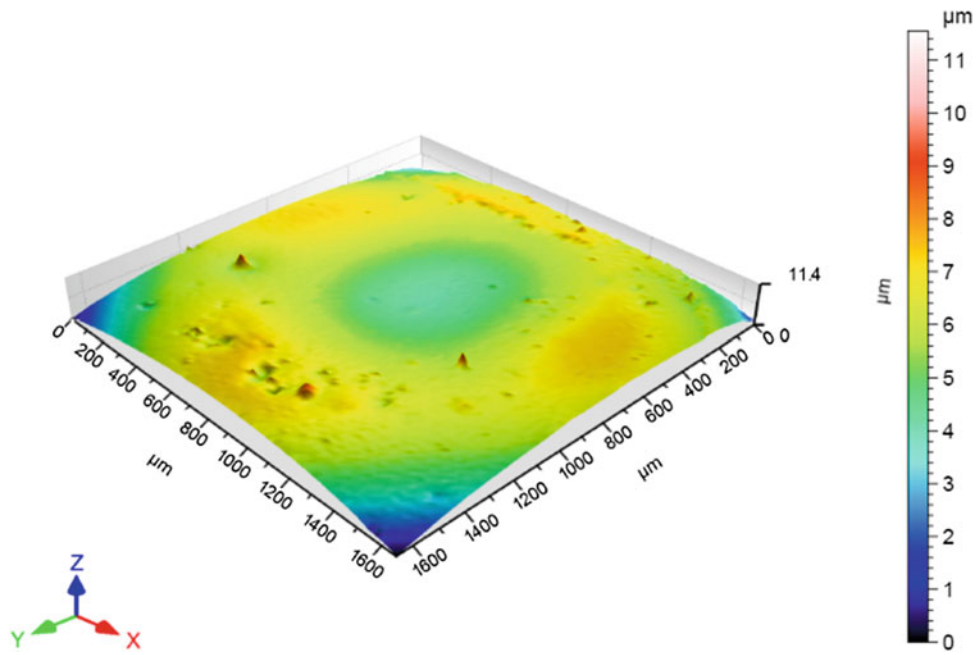
Fig. 11 Topography map. Part printed horizontally, with 45 min. treatment
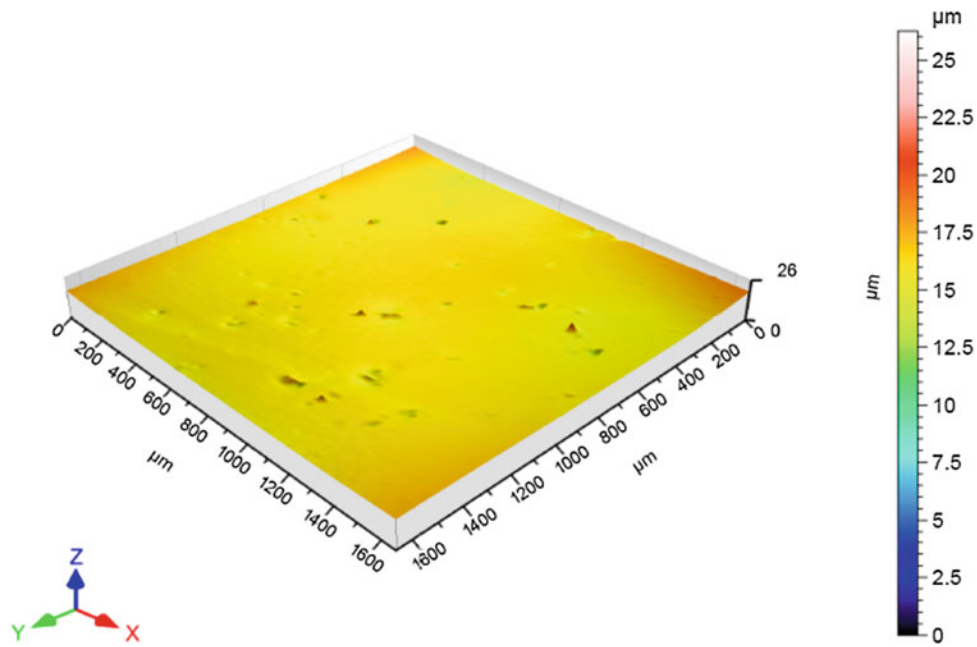
Fig. 12 Topography map. Part printed horizontally, with 60 min. treatment
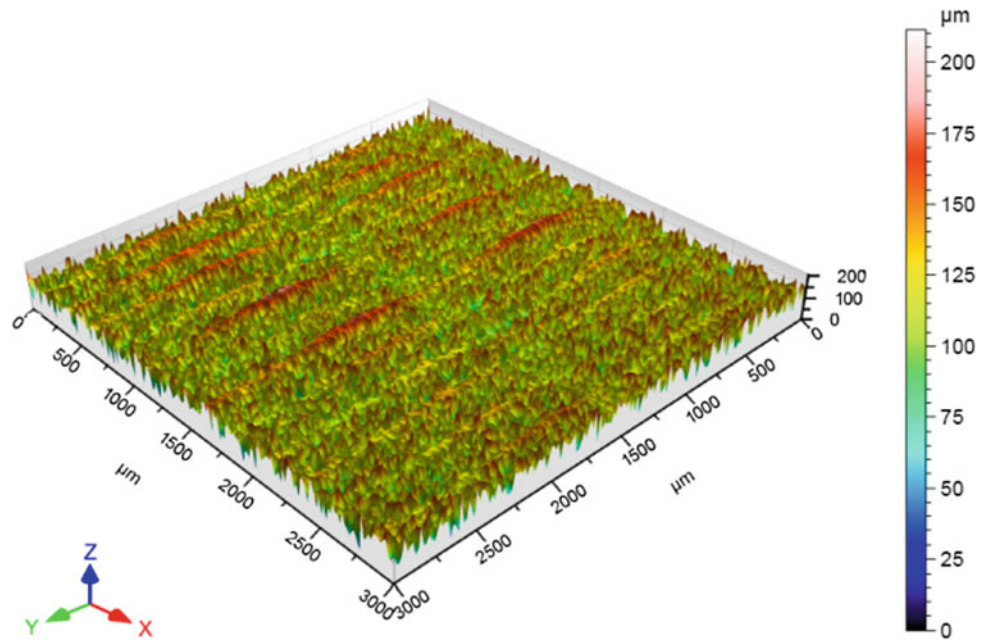
Fig. 13 Topography map. Part printed vertically, with 0 min. treatment
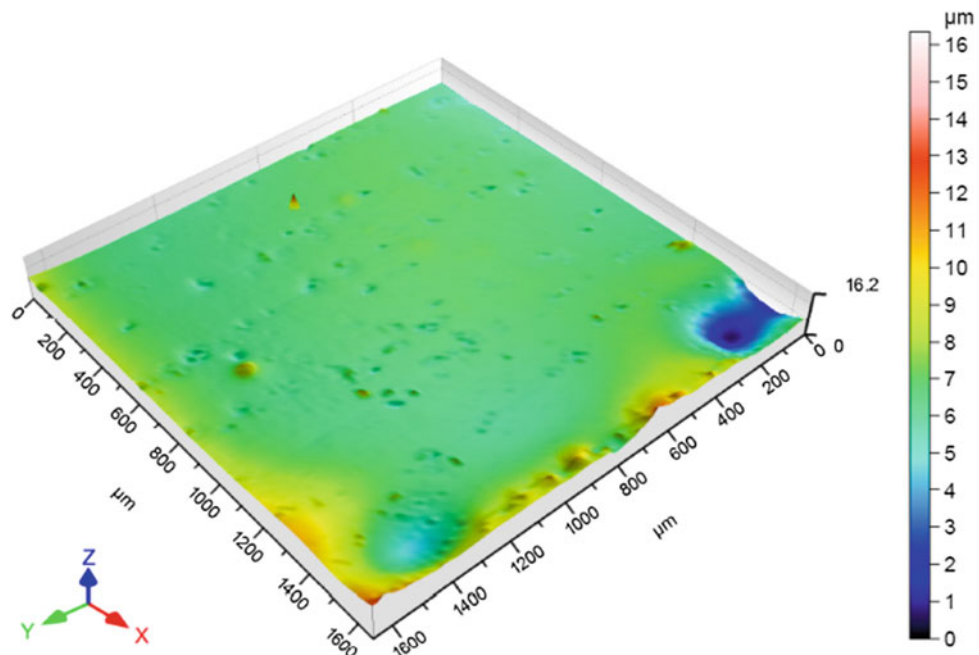
Fig. 14 Topography map. Part printed vertically, with 15 min. treatment
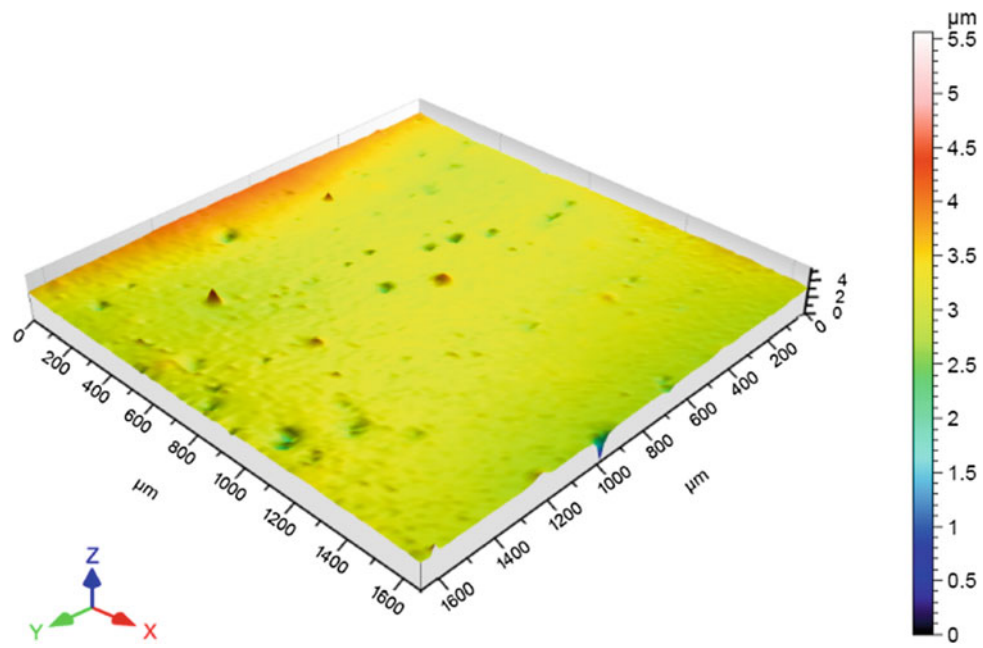
Fig. 15 Topography map. Part printed vertically, with 30 min. treatment
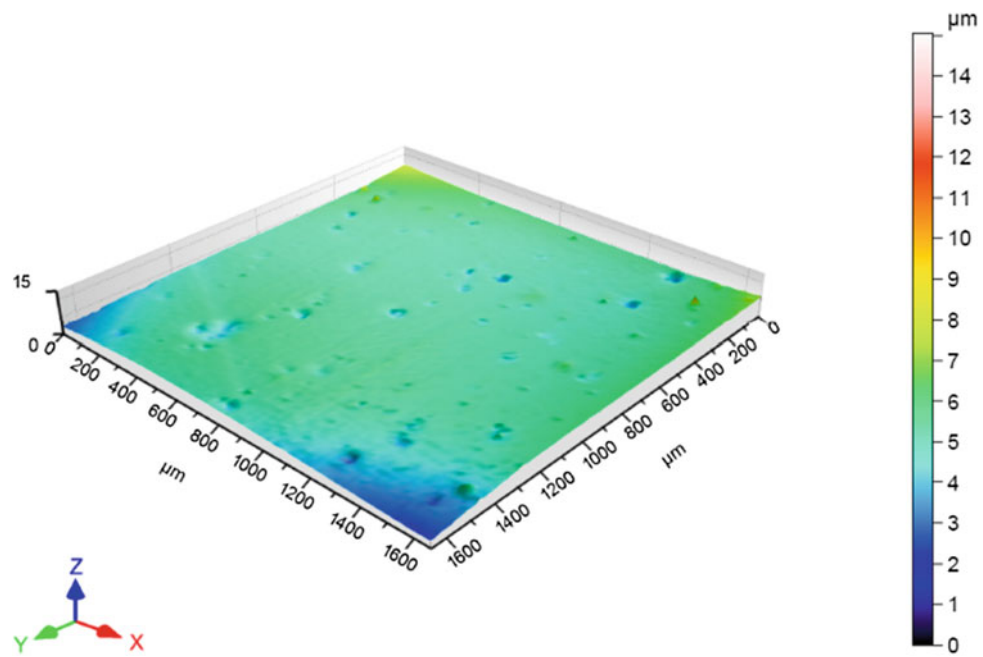
Fig. 16 Topography map. Part printed vertically, with 45 min. treatment
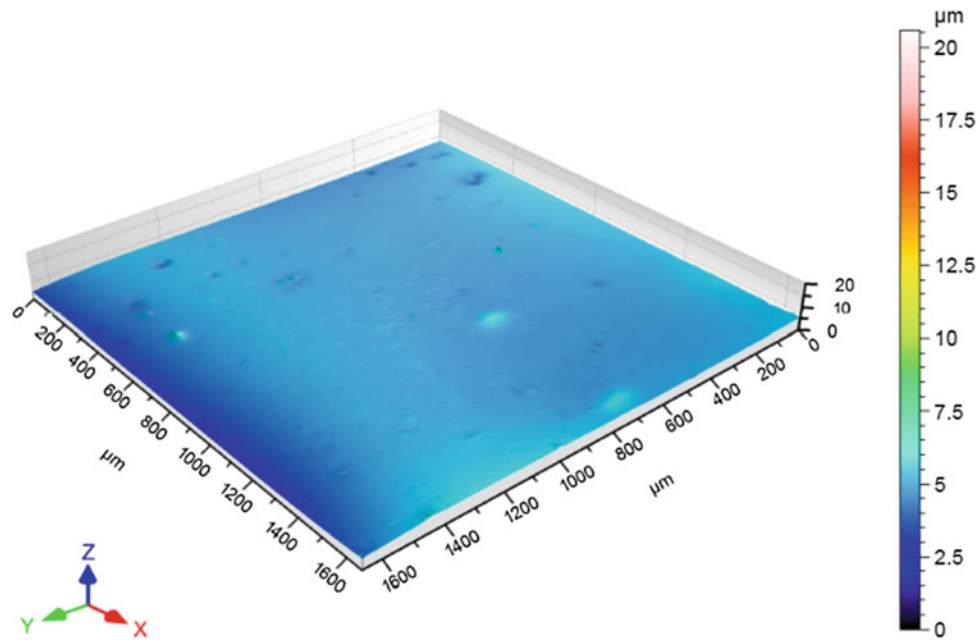
Fig. 17 Topography map. Part printed vertically, with 60 min. treatment
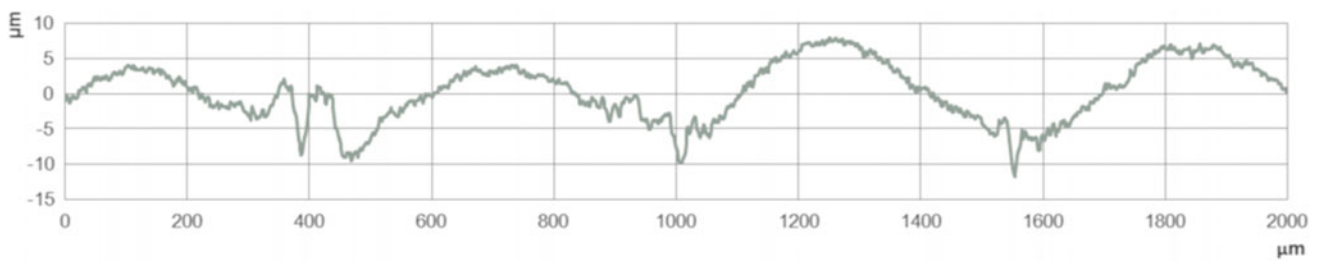
Fig. 18 Mean roughness profile for horizontally printed non treated part
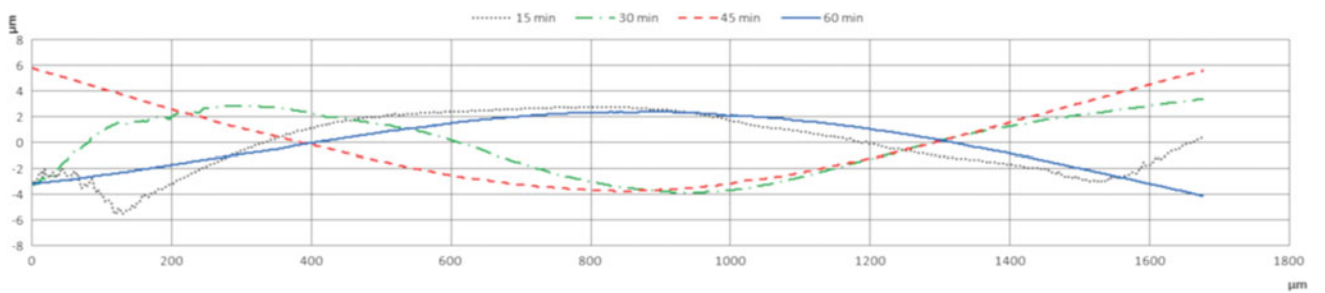
Fig. 19 Mean roughness profile for horizontally printed parts, with different treatment times
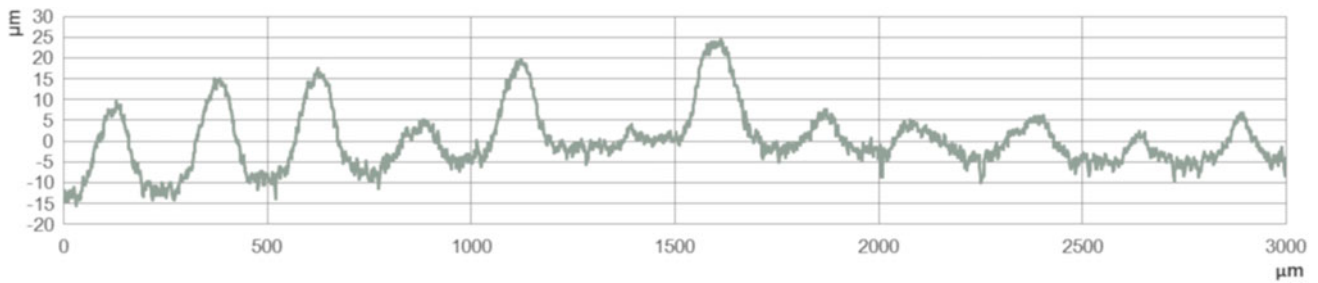
Fig. 20 Mean roughness profile for vertically printed non treated part
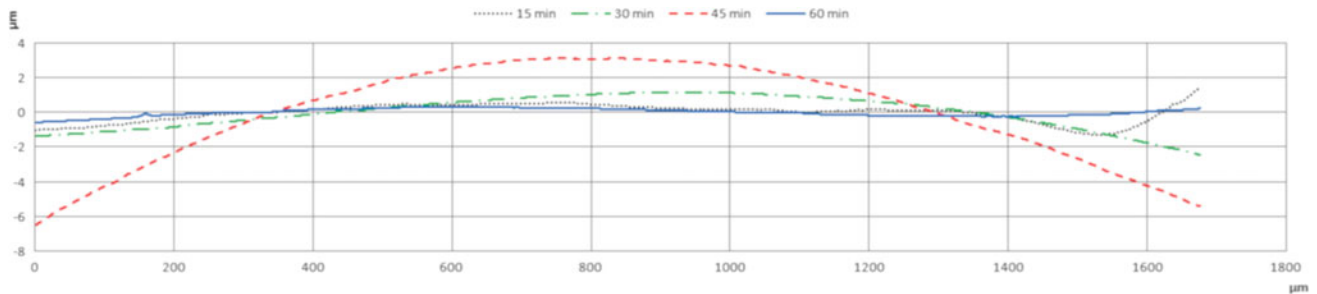
Fig. 21 Mean roughness profile for vertically printed parts, with different treatment times

Table 2 Mean roughness (Ra) for every printed part

Printing orientation	Treatment time (min)	Ra (μm)
Horizontal	0	2.657
	15	0.7138
	30	0.09692
	45	0.05046
	60	0.0420
Vertical	0	6.124
	15	0.04114
	30	0.03955
	45	0.02829
	60	0.02343

number is even higher, reaching 99.6%. As said before, vertically printed parts resist better to vapor bath treatment, due to the position of filling structure, which provides better support; and the layers being perpendicular to gravity, which facilitates polymer's movement.

4 Conclusions and Future Work

Acetone vapor treatment is a proper alternative to improve surface characteristics in ABS printed parts; it can eliminate staircase effect, and reduces roughness significantly. Nevertheless, it can alter part's external measures and corners or edges formats. Use in parts that require precise shapes has to be better studied.

When a printed part intends to be treated, it is important to consider treatment characteristics in part's project, optimizing results and reaching the best surface possible. Choosing the best option of treatment time versus quality of surface and part integrity is also important.

For future work, we intend to explore those superficial mechanical properties, and see if they are adequate for prosthetic material use.

References

1. Smith, D.G., Skinner, H.: Current Diagnosis & Treatment in Orthopedics, 3rd edn. Appleton & Lange, Orange, California (2003)
2. Montiel, A., Vargas, L.: S. M. C. Caracterização de pessoas submetidas à amputação. Enfermagem em Foco 3(4), 169–173 (2012)
3. Gaine, J., Smart, C., Bransby-zachary, M.: Upper limb traumatic amputees. Review of prosthetic use. J. Hand Surg. 22 B(1), 73–76 (1997)
4. Ministério da Saúde.: Diretrizes de Atenção à Pessoa Amputada Diretrizes de Atenção à Pessoa Amputada (2013). Disponível em. http://bvsms.saude.gov.br/bvs/publicacoes/diretrizes_atencao_pessoa_amputada.pdf
5. Cordella, F., Ciancio, A., Sacchetti, R., Davalli, A., Cutti, A., Guglielmelli, E., Zollo, L.: Literature review on needs of upper limb prosthesis users. Front. Neurosci. 10(MAY), 1–14 (2016)
6. Garcia, V.: Próteses no Brasil são para poucos (2009). https://www.deficienteciente.com.br/proteses-no-brasil-sao-para-poucos.html

7. Gretsch, K., Lather, H., Peddada, K., Deeken, C., Wall, L., Goldfarb, C.: Development of novel 3D-printed robotic prosthetic for transradial amputees (2016)

8. Rankouhi, B., Javadpour, S., Delfanian, F., Letcher, T.: Failure analysis and mechanical characterization of 3D printed ABS with respect to layer thickness and orientation. J. Fail. Anal. Prev. **16**(3), 467–481 (2016)

9. Cole, D., Zander, N.: Interfacial mechanical behavior of 3D printed interfacial mechanical behavior of 3D printed ABS. J. Appl. Polym. Sci. (2016)

10. Gao, H., Kaweesa, D., Moore, J., Meisel, N.: Investigating the impact of acetone vapor smoothing on the strength and elongation of printed ABS parts **69**(3), 580–585 (2017)

11. Lalehpour, A., Barari, A.: Post processing for fused deposition modeling parts with acetone vapour bath. IFAC PapersOnLine **49** (31), 42–48 (2016)

Supersonic Shear Imaging 3-D Transducer for Two-Dimensional Evaluation of Patellar Tendon Mechanical Properties

Vinícius Costa Martins, Viviane Bastos de Oliveira,
Maria Clara Albuquerque Brandão,
Wagner Coelho de Albuquerque Pereira,
and Liliam Fernandes de Oliveira

Abstract

Introduction: Tendon is an anisotropic complex structure which transmits muscle force to bone to produce joint motion. Supersonic Shear Imaging (SSI) is an imaging technique capable of measuring Shear Wave Velocity (Cs) of biological tissues, which is proportional to the Elastic Modulus. The aim of this study is to calculate the intra-operator reliability of the Cs values of patellar tendon at 0.5, 1.0 and 1.5 cm from the patella apex and evaluate Cs values at the same sites for both sagittal and transversal planes. **Methods**: Eighteen healthy male volunteers (23.1 ± 4.2 years) were examined with an AIXPLORER V11 (Supersonic Image, Aix-en-Provence, France) with the 3-D transducer (SuperLinear^{TM} SLV, 5–16 MHz) placed longitudinally to the patellar tendon. Three images were acquired for each volunteer and Cs values was measured at 0.5, 1.0 and 1.5 cm from patella apex. The ANOVA OneWay test was used to compare the Cs values at three sites for each plane and the Intraclass Correlation Coefficients (ICC) were used to calculate the intra-operator reliability (CI = 95%). **Results and Discussion**: There were no differences between mean Cs values at three sites for both planes ($p > 0.05$). For both sagittal and transversal planes, the intra-operator reliability was good at 0.5 cm (ICC = 0.856 and 0.817) and at 1.0 cm (ICC = 0.841 and 0.772), but moderate at 1.0 cm (0.705 and 0.647). The 3-D transducer provides a multiplanar view which enables a full visualization of the patellar tendon.

Keywords

Supersonic shear imaging • Patellar tendon • Elastography

V. C. Martins (✉) · V. B. de Oliveira ·
W. C. de Albuquerque Pereira · L. F. de Oliveira
Biomedical Engineering Program, Federal University of Rio de Janeiro, COPPE/UFRJ, Rio de Janeiro RJ, Brazil
e-mail: vcostamartins@gmail.com

V. C. Martins
Physiotherapy School, Federal Institute of Rio de Janeiro, IFRJ, Rio de Janeiro RJ, Brazil

M. C. A. Brandão · L. F. de Oliveira
Physical Education and Sports School, Federal University of Rio de Janeiro, EEFD/UFRJ, Rio de Janeiro RJ, Brazil

1 Introduction

Tendon is a complex structure made up of collagen fibers (type I, II, III, V e IX), cells, proteoglycans and water [1] organized into a hierarchical structure with collagen molecules, fibrils, bundles of fibers and fascicles that are arranged in parallel to the geometric axis allowing the efficient transmission of high loads [2]. Tendons are resistant to mechanical loads [1, 3] and are mechanically responsible for transmitting the force produced by muscles to bones enabling joint movement and locomotion [4, 5]. The insertion tendon-bone is stiffer due to the complex structural and material transition zone which is characterized by less orientation of collagen fibers [6].

Besides the load transmission function, some tendons are also an energy-storing structure, e.g., patellar tendon acts like a spring by storing elastic energy (mechanical buffer) and can reuse it during a vertical jump. A rigid tendon is better for transmitting the force, whereas an elastic tendon can store energy and reuse it to improve work efficiency [3, 7].

The mechanical properties of tendons are related to their components and their organization [2]. Since they are constantly under load/stress, being able to adapt their components and structure to changes in mechanical loads, this can lead to altered mechanical properties [4, 5, 7].

Historically, in vitro studies were performed to evaluate the mechanical properties of the patellar tendon and, more recently, in vivo studies were developed for the same purpose using ultrasonography (US) to calculate the Elastic

Modulus (EM), which is a parameter related to the property of tissue stiffness [2, 3, 7–11].

Ultrasound (US) Elastography is a noninvasive technology to evaluate biological tissues mechanical properties, like breast, liver, tendon and muscles. It consists of a compressive force applied manually or by the emission of acoustic radiation via ultrasound transducer on tissue (stress), causing a displacement in the tissue (strain). Thus, the shear wave speed (m/s) is then measured and the elasticity of a tissue is quantified based on the velocity of the shear wave propagating [12]. Based on this concept, Supersonic Shear Imaging (SSI) technique provides quantitative values of tendon elastic properties estimating the EM, in kilopascal (kPa). Thus, in stiffer tissues, the shear wave propagates faster and the EM value is higher [3, 7, 9, 12].

Soft tissues are viscoelastic, anisotropic and heterogeneous, e.g., muscle and tendon are an anisotropic medium because of the longitudinal arrangement of its fibers [8]. In Medicine, all Ultrasound Elastography are based on the assumption that the material is elastic, homogeneous and isotropic. If tissue density is not equal to 1.0 g/mm^3, the shear speed (Cs) is not exactly correlated with EM [12]. Due to its high anisotropy, tendon imaging depends on ultrasound beam position: parallel (longitudinal) or perpendicular (transversal) to tendon [8, 12]. In addition, the speed of shear wave propagation may change depending on the alignment between the probe and tendon fibers, since the force transmitted to the tendon follows the fiber direction [9].

Three-dimensional (3-D) US transducer is the latest tool in elastography which can evaluate the tissue elasticity in a 3-D map, which linear 2-D transducer is unable to show. Thus, the tissue can be evaluated in three orthogonal planes (sagittal, transversal and coronal) and, in addition, the multi-slice function in each plane provides a full tissue analysis, e.g. breast and liver [13]. However, there are no studies with 3-D transducer for tendon evaluation.

The aim of this study is to calculate the intra-rater reliability of the Shear Wave Velocity (Cs) values of patellar tendon at 0.5, 1.0 and 1.5 cm from the patella apex and to compare the Cs values at these sites for sagittal and transversal planes.

2 Materials and Methods

2.1 Sample

A group of 18 male healthy volunteers (23.1 ± 4.2 years) were recruited from Physical Education School of Federal University of Rio de Janeiro. The exclusion criterion was: painful or damaged patellar tendon, athletes who perform regular vertical jumps or knee pain. One subject was excluded from the study due to a recent knee injury.

The Federal University of Rio de Janeiro Hospital Ethics Committee approved this study (registration numbers 570.945 and 519.230). All participants received instructions about the study procedures and provided informed written consent before testing.

2.2 Experimental Procedure

During the examination, the volunteers were kept lying in supine position and the right patellar tendons were evaluated at 30° of knee flexion. The equipment was an AIXPLORER V11 (Supersonic Imagine, Aix-en-Provence, France) and the 3-D transducer (Super linear^{TM} volumetric SLV 16–5, 5–16 MHz) was placed manually as close as possible to the longitudinal position of the right patellar tendon (Fig. 1). A high amount of a coupling gel was used between the transducer and the skin to provide a suitable medium for ultrasonic wave penetration and, thus, provide a higher image quality. The operator manually adjusted the transducer, without moving it during the image acquisition.

The technique is based on disturbance of the medium by means of an acoustic radiation force caused by a highly focused ultrasonic beam. This force is achieved by the configuration of the piezoelectric elements, which trigger an ultrasonic beam, producing a dipole source of low frequency shear waves. Successive shots occur in depth at a supersonic velocity even faster than the shear wave. The propagation of these waves induces a displacement in the medium, which is captured by an ultrafast ultrasound scanning system
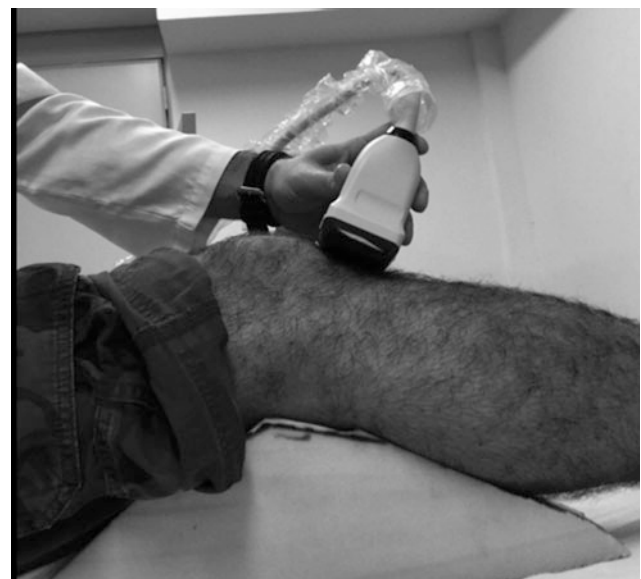
Fig. 1 The 3-D transducer placed longitudinally to the right patellar tendon. The subject is lying in supine (knee at 30° of flexion over a device leg in neutral position)

estimated along the beam. Thus, considering the time and the displacement of the wave, the Cs is estimated [14]. So, the Elastic Modulus can be estimated by Eq. 1 [12]:

$$E = 3\rho Cs^2 \tag{1}$$

where E = Elastic Modulus; ρ = tissue density (1.0 g/mm^3), Cs = shear wave speed.

A total of three images were acquired for each volunteer and were analyzed off-line later. All the image acquisition and the entire experimental procedure were performed by the same examiner on the same day.

2.3 Image Acquisition and Processing

The 3-D transducer gave us images from 3 planes: sagittal, transversal and coronal. Each plane image displays the intersection point for the other two planes which can be adjusted anywhere in the image, i.e., the sagittal plane image displays the intersection point between coronal and transversal planes, and transversal plane image displays the intersection point between both coronal and sagittal planes. In this study, only sagittal and transversal planes images were analyzed.

First, the mapping area was positioned at the proximal portion of the patellar tendon (Fig. 2) and three different regions of interest (ROI) were placed at 0.5, 1.0 and 1.5 cm from the patellar apex. These distances were measured based on the equipment measurement tool available. The three ROI (3.0 mm in diameter) were positioned around at the same intersection points in both sagittal and transversal plane images. The mean Cs values of three acquired images were then measured at 0.5, 1.0 and 1.5 cm for both sagittal and transversal planes, for each volunteer.

In addition, for longitudinal scanning (transducer positioned longitudinally to the tendon), both images of transversal and coronal planes were reconstructed from the sagittal plane image. Similarly, sagittal and coronal planes were reconstructed from the transversal plane during transversal scanning (transducer transversally) [13].

Fig. 2 Ultrasound elastography of patellar tendon for both Sagittal and Transversal Planes. Sagittal Plane: mapping area (Q-Box) and ROI's placed at 0.5, 1.0 and 1.5 cm from the patella apex; transversal plane: ROI placed at the same sagittal three points (according to each intersection point)
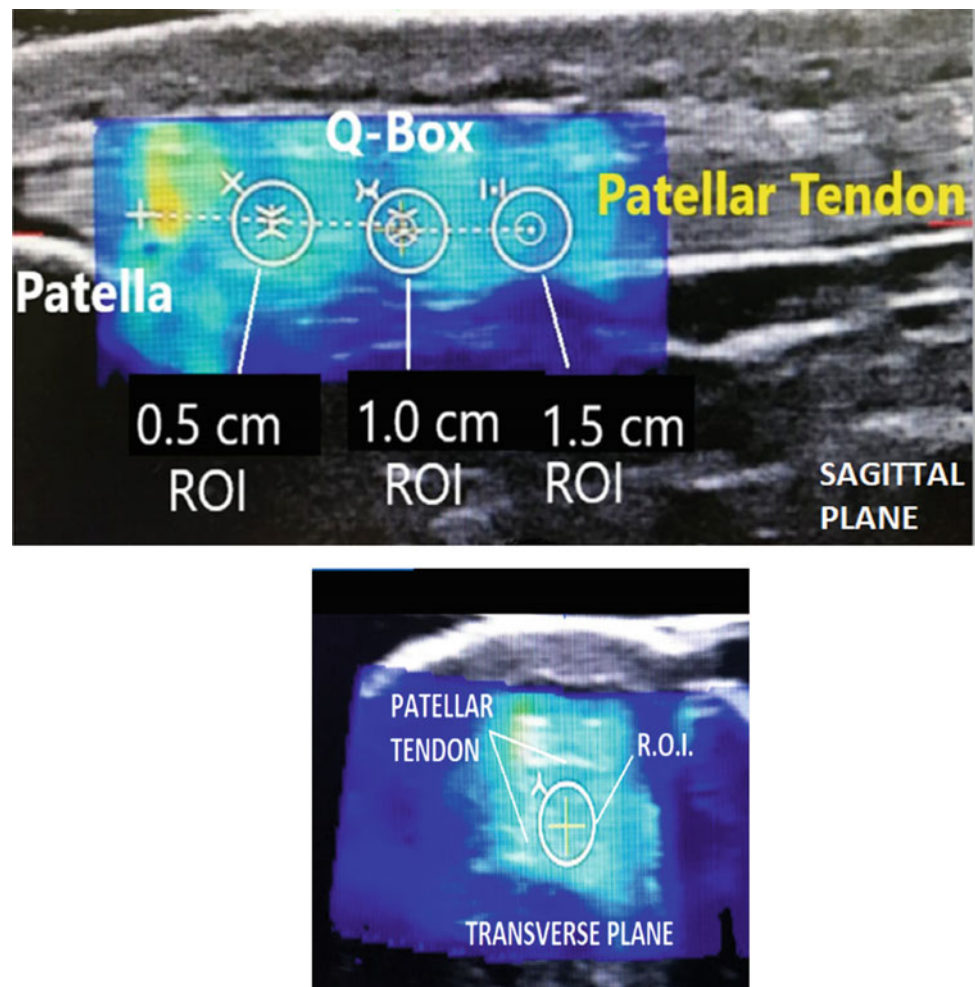
2.4 Statistical Analyses

Pearson's correlation coefficient was used to compare the mean Cs values at 0.5, 1.0 and 1.5 cm for each plane (sagittal and transversal) and the ANOVA Two-way was used to compare total mean C_S values between both planes. To calculate the intra-rater reliability between the three images (1, 2 and 3) at 0.5, 1.0 and 1.5 cm sites, for each volunteer, the Intraclass Correlation Coefficients (ICC) were calculated for both planes sagittal and transversal. Reliability coefficients were classified as follows: <0.499 poor correlation; 0.500–0.7499 moderate correlation, 0.750–0.899 good correlation and 0.900–1.000 excellent correlation [15]. To compare the Cs values between 0.5, 1.0 and 1.5 cm in each tendon, the Post Hoc test was used. The confidence interval (CI) considered was 95%.

3 Results

Table 1 shows the Cs mean values calculated for both sagittal and transversal planes with the ROI's placed at 0.5, 1.0 and 1.5 cm from patellar apex ($p = 0.05$).

The Table 2 shows the ICC between Cs mean values for both sagittal and transversal planes at 0.5, 1.0 and 1.5 cm from patella apex.

4 Discussion

This study aimed at evaluating mechanical properties of different sites of patellar tendon in two planes with longitudinal scanning. There were a very strong correlation between sagittal and transversal values at 0.5 ($p < 0.001$) and 1.0 cm ($p < 0.001$), but a strong correlation at 1.5 cm ($p = 0.034$) for both planes. In addition, comparing the total mean value of each plane, there were no statistically significant differences ($p = 0.968$).

For both sagittal and transversal planes, the intra-operator reliability between the three images was good at 0.5 cm ($p < 0.001$) and at 1.5 cm ($p = 0.001$ and $p < 0.001$, respectively), but moderate at 1.0 cm ($p < 0.001$ and $p = 0.005$, respectively).

Although proximal ROI (0.5 cm from patella apex) showed highest Cs values for both planes (6.3 m/s $\pm$ 0.5), there were no statistical difference between these three ROI ($p > 0.05$). However, these results were in agreement with the current literature, since bone (patella) exerts a tension in the tendon insertion (proximal), making this region more rigid [1, 2, 6].

Comparing these results with the current literature, patellar tendon Cs mean values were in accordance with other studies carried out with 2-D linear transducer at 30º of knee flexion [3, 7, 16, 17]. However, Hsiao et al. [11] performed at 90° of knee flexion, and showed higher values 7.6–9.0 m/s. Dirrichs et al. [18] performed at 0°, and showed SWV values above 4.83 m/s (mean value = 7.48 m/s) in healthy patellar tendon, but the selected ROI was 1.0 mm. Our results are in accordance with Coombes et al. [19] who compared 28 healthy subjects with 22 subjects with patellar tendinopathy. They concluded that pathological patellar tendons showed Cs values above 6.9 m/s and 7.0 m/s in proximal and middle sites, respectively. Therefore, Cs values below theses are related to healthy tendons.

To date, there is no study in the current literature using 3-D transducer to evaluate patellar tendon, but Yin et al. [13] compared 2-D with 3-D Shear Wave Elastography (SWE) of flexor carpi radialis muscle with the transducer placed

Table 1 Shear wave velocity mean values (m/s $\pm$ sd) for both planes (sagittal and transversal) at 0.5, 1.0 and 1.5 cm from patellar apex on patellar tendon

Distance from patellar apex (cm)	Sagittal plane (m/s)	Transversal plane (m/s)	*Pearson's* correlation coefficient	*P value*
0.5	6.3 $\pm$ 0.5	6.3 $\pm$ 0.5	0.969	$p < 0.001$
1.0	6.1 $\pm$ 0.4	6.1 $\pm$ 0.4	0.962	$p < 0.001$
1.5	6.1 $\pm$ 0.5	6.0 $\pm$ 0.5	0.892	$p = 0.034$
Mean values (total)	6.2 $\pm$ 0.1	6.1 $\pm$ 0.2	ANOVA	$p = 0.968$

Table 2 ICC (Intraclass Coefficient Correlation) calculated between the sagittal and transversal planes at three different sites ($p = 0.05$)

Distance (cm)	Sagittal plane			Transversal plane		
	ICC	95% CI	*P value*	ICC	95% CI	*P value*
0.5	0.856	0.684–0.942	<0.001	0.817	0.598–0.928	<0.001
1.0	0.705	0.351–0.881	<0.001	0.647	0.226–0.857	=0.005
1.5	0.841	0.652–0.936	=0.001	0.772	0.499–0.908	<0.001

longitudinally and transversely. They used the Elastic Modulus (EM) parameter and found it similar among sagittal, transversal and coronal planes for 3-D longitudinal scanning, which are in accordance to the results showed in this study, despite the different tissues evaluated (muscle and tendon). In addition, the EM for each plane (sagittal, transversal or coronal) differed significantly between longitudinal and transversal scanning ($p < 0.01$) because of the transducer position (longitudinal or transversal). Thus, the transversal and coronal planes were reconstructed from sagittal plane during longitudinal scanning. Higher Cs values were observed due to shear wave propagation in the same direction of fibers orientation. On the other hand, for transversal scanning which shows lower Cs values, both sagittal and coronal planes were reconstructed from transverse plane. The anisotropy behavior due the fibers orientation should be related to that different in Cs values between these two transducer positions [13]. Longitudinal scanning provides high shear wave propagation velocities for the three planes compared with transversal scanning [12, 13]. In this study, the mean Cs values for sagittal plane (6.2 m/s $\pm$ 0.1) did not differ significantly from transversal (6.1 m/s $\pm$ 0.2) which were reconstructed from the sagittal plane during longitudinal scan. If the 3-D transducer had been positioned transversely, the Cs values would be lower for both planes.

This study had some limitations: first of all, the reduced number of participants (18 volunteers); secondly, the inter-day reliability was not calculated, and finally the transducer was not placed transversally to patellar tendon, which could give different values due to the anisotropic characteristic of tendon, which has already been demonstrated in previous studies.

5   Conclusions

The two-dimensional evaluation of patellar tendon showed no statistically significant difference between Cs values at 0.5, 1.0 and 1.5 cm from patella apex, for both sagittal and transversal planes. The intra-operator reliability was good for both sagittal and transversal planes, except at 1.0 cm.

The results will be useful for future investigations of the diagnose and the rehabilitation progress of patellar tendon injuries, since the 3-D transducer provides a multiplanar view besides being a new method which enables a full visualization of the patellar tendon.

References

1. Galloway, M.T., et al.: The role of mechanical loading in tendon development, maintenance, injury and repair. J. Bone Joint Surg. **95**(17), 1620–1628 (2013)
2. Silver, F.H., et al.: Collagen self-assembly and the development of tendon mechanical properties. J. Biomech. **36**(10), 1529–1553 (2003)
3. Zhang, G.J., et al.: Effects of habitual loading on patellar tendon mechanical and morphological properties in basketball and volleyball players. Europe J. Appl. Physiol. **115**(11), 2263–2269 (2015)
4. Wang, J.H.C.: Mechanobiology of tendon. J. Biomech. **39**(9), 1563–1582 (2006)
5. Wang, J.H.C., et al.: Tendon biomechanics and mechanobiology—a mini-review of basic concepts and recent advancements. J. Hand Ther. **25**(2), 133–141 (2012)
6. Thomopoulos, S., et al.: The development and morphogenesis of the tendon-to-bone insertion—what development can teach us about healing. Musculoskelet. Neuronal Interact. **10**(1), 35–45 (2010)
7. Zhang, Z.J., et al.: Changes in morphological and elastic properties of patellar tendon in athletes with unilateral patellar tendinopathy and their relationships with pain and functional disability. PlosOne **9**(10), e108337 (2014)
8. Yeh, C.H., et al.: Shear-wave measurements for evaluation of tendon diseases. IEEE Trans. Ultrason. Ferroelectr. Freq. Control **11**, 1906–1921 (2016)
9. Lima, K.M.M.E., et al.: Assessment of the mechanical properties of the muscle-tendon unit by supersonic shear wave imaging elastography: a review. Ultrasonography. **37**(1), 3–15 (2018)
10. Özkaya, N., Nordin, M., Goldsheyder, D., et al.: Fundamentals of Biomechanics: Equilibrium, Motion, and Deformation, 3rd edn. Springer, New York, NY (2012)
11. Hsiao, M.Y., et al.: Reduced patellar tendon elasticity with aging: in vivo assessment by shear wave elastography. Ultrasound Med. Biol. **41**(11), 2899–2905 (2015)
12. Ryu, J.A.: Current status of musculoskeletal application of shear wave elastography. Ultrasonography **36**(3), 185–197 (2017)
13. Yin, B.S.L., Ruigang Lu, M.S., et al.: Three-dimensional shear wave elastography of skeletal muscle: preliminary study. J. Ultrasound Med. e14559 (2018)
14. Bercoff, J., et al.: Monitoring thermally-induced lesions with supersonic shear imaging. Ultrason. Imaging **26**(2), 71–84 (2004)
15. Koo, T., et al.: A guideline of selecting and reporting intraclass correlation coefficients for reliability research. J. Chiropr. Med. **15**(2), 155–163 (2016)
16. Mannarino, P., et al.: Analysis of the correlation between knee extension torque and patellar tendon elastic property **38**(3), 378–383 (2017)
17. Tas, S., et al.: Shear wave elastography is a reliable and repeatable method for measuring the elastic modulus of the rectus femoris muscle and patellar tendon. J. Ultrasound Med. **36**(1), 565–570 (2017)
18. Dirrichs, T., et al.: Shear Wave Elastography (SWE) for the evaluation of patients with tendinopathies. Acad. Radiol. **23**(10), 1204–1213 (2016)
19. Coombes, B.K., et al.: Achilles and patellar tendinopathy display opposite changes in elastic properties: A shear wave elastography study. Scand. J. Med. Sci. Sports **8**(3), 1201–1208 (2018)

Switched Controller Applied to Functional Electrical Stimulation of Lower Limbs Under Fatigue Conditions: A Linear Analysis

W. R. B. M. Nunes, R. G. Teodoro, M. A. A. Sanches, Rafael A. de Araujo, M. C. M. Teixeira, and A. A. Carvalho

Abstract

Individuals with spinal cord injury may improve lower limb mobility with neuromuscular electrical stimulation. Several studies propose closed-loop controller simulations, but few of them know the experimental behavior. From experimental results, we observe that the control signal is uncertain for an operating point, because of plant uncertainties. An experimental setup in order to identify the linear model containing polytopic uncertainties is presented in this paper. In addition, a controller $p_{(\sigma,\xi)}(t)$ that compensates uncertain control signal through an adequate switching law was designed. Results obtained from open-loop control $p(t) = p_0$ and switched controllers $p_{(\sigma)}(t)$ and $p_{(\sigma,\xi)}(t)$ are compared. These results indicate that switched controller $p_{(\sigma,\xi)}(t)$ minimizes the uncertain control signal and returns the smallest time derivative value of the Lyapunov function, consequently minimizing the angular position error in electrically stimulated lower limbs under fatigue conditions.

Keywords

Switched control • Linear matrix inequalities (LMIs) • Rehabilitation • Neuromuscular electrical stimulation

W. R. B. M. Nunes (✉)
UTFPR-Federal University of Technology – Paraná, Apucarana, PR, Brazil
e-mail: williar@utfpr.edu.br

R. G. Teodoro
IFPR-Federal Institute of Paraná, José Felipe Tequinha St., 1400 Paranavaí, PR, Brazil
e-mail: ricardo.teodoro@ifpr.edu.br

W. R. B. M. Nunes · R. G. Teodoro · M. A. A. Sanches ·
R. A. de Araujo · M. C. M. Teixeira · A. A. Carvalho
Department of Electrical Engineering, UNESP - São Paulo State University, Ilha Solteira, SP, Brazil

1 Introduction

The number of individuals with spinal cord injury increases annually. Functional electrical stimulation (FES) has been shown to be a suitable technique for motor rehabilitation of such individuals.

However, the challenges in this field are great, among which it is evident to minimize fatigue due to the repetitive number of electrical stimuli applied or by the muscular delay [1, 2].

The musculoskeletal system is a non-linear, complex physiological process and in this study also highlight the effects of uncertain state parameters and the control signal for an operating point of the knee joint.

The state-of-the-art evidences several studies in the FES control area for lower limbs, both for a point of operation [3–5] and for trajectory tracking [6–8]. In this study, we approach the uncertain control around an operating point.

In relation to the studies that controlled around an operating point, in [5] proposed a control methodology based on accelerometers and described by fuzzy TS models. However, shielded cable, processing and filters are required for practical implementation with accelerometers signals.

In the work of [9] a closed-loop control of the angular position through PID controller with robustness checking was performed, observing only the settling time under parametric variation of the model on different days.

In the study of [4] it was indicated a methodology for PID control analysis in a simulation model that revealed the adequate behavior of the data obtained in real experiments.

Through experimental results, it was shown that in fatigue situation the control signal is uncertain to maintain joint position at the desired value. From the previously mentioned studies, none of them performed a control approach by compensating for the uncertain control signal. In this paper, we present the switched controller design that compensates for the uncertain control signal. In addition, this work includes a technique to identify the polytopic uncertainties of

the model. This technique is a differentiated approach that allows practical implementation, overcoming a limitation of the studies that can not measure the dynamics of the state variable relative to the torque.

The article is organized as follows: in Sect. 2, it presents the dynamic model in the state space with polytopic uncertainties; in Sect. 3, it describes the experimental setup for polytopic uncertainties identification; in Sect. 4, it indicates the switched control design of electrically stimulated lower limb considered as a uncertain linear system; and finally it reaches a conclusion about the results and a perspective for future studies.

2 Modeling of the Lower Limb with Polytopic Uncertainties

The dynamic model of the electrically stimulated lower limb is non-linear and uncertain. The linearization approximates the dynamic behavior around an operating point. In this paper, we discuss the robustness of the controller design, where parametric uncertainties are treated in a polytopic region. Robustness is required due to discrepancy between the linearized model and the real plant.

2.1 State-Space Model

In [9] it was proposed a state-space model modification to facilitate practical implementation with accelerometers. Thus, the torque state variable was replaced by acceleration.

This paper considers the linear system with polytopic uncertainties given by:

$$\dot{\mathbf{x}}(t) = \mathbf{A}(\alpha)\mathbf{x}(t) + \boldsymbol{B}(\alpha)u(t) \tag{1}$$

$$\boldsymbol{y}(t) = \mathbf{C}\mathbf{x}(t) \tag{2}$$

being $\mathbf{A}(\alpha) \in \Re^{nxn}$ the state matrix, $\mathbf{B}(\alpha) \in \Re^{nxm}$ the input matrix, $\mathbf{x}(t) \in \Re^n$ the state vector, $u(t) \in \Re^m$ the input control, $\mathbf{y}(t) \in \Re^q$ the output vector, and $\mathbf{C} \in \Re^{qxn}$ the output matrix.

In a system that presents parametric uncertainties, these can be restricted by a convex linear combination belonging to the set described as polytope. The system (1) and (2) can be described as a convex combination of the polytope vertices, with parameters belonging to the unitary simplex $\mathfrak{U}$. For convenience, the following notation is used [10]:

$$\mathfrak{U} \triangleq \left\{ (A, B)(\alpha) \colon \sum_{i=1}^{n} \alpha_i(A_i, B_i); \sum_{i=1}^{n} \alpha_i = 1; \alpha_i \geq 0; i \in \mathbb{Q}_r \right\}, \tag{3}$$

$$\mathbb{Q}_r = \{1, 2, \ldots, r\}, \tag{4}$$

Regarding to knee joint movement due to electrical stimulation applied in the quadriceps, the state-space representation is given by:

$$\dot{\mathbf{x}}(t) = \begin{bmatrix} 0 & 1 & 0 \\ 0 & 0 & 1 \\ \widetilde{\mathcal{L}}(z) & \widetilde{\Im}(z) & \widetilde{\mathfrak{E}}(\tau) \end{bmatrix} \mathbf{x}(t) + \begin{bmatrix} 0 \\ 0 \\ \mathfrak{B}(G, \tau) \end{bmatrix} u(t) \tag{5}$$

$$\mathbf{y}(t) = \begin{bmatrix} 1 & 0 & 0 \\ 0 & 1 & 0 \\ 0 & 0 & 1 \end{bmatrix} \mathbf{x}(t) \tag{6}$$

where the state vector $\mathbf{x}(t) = [\, x_1(t) - \theta_0 \quad x_2(t) \quad x_3(t) \,]^T$, and the control input considered as $u(t) = p_n(t)$, $z = [\, x_1(t) \quad \lambda \quad E \quad \omega \,]^T \in \Re^4$, λ and $E \in \Re$ are coefficients of the exponential term related with movement stiffness; $\omega \in \Re$ the elastic resting angle of the knee; G and $\tau \in \Re$ are parameters that express the first-order relation of the torque and electric stimulus pulse width $p_n(t)$.

In relation to parameters and variables, we define that $x_1(t)$ is the angular position of the knee joint, $x_2(t)$ is the angular velocity, $x_3(t)$ is the angular acceleration, θ_0 is the desired angle.

The system control input $p_n(t)$ at the equilibrium point is given by:

$$p_n(t) = p(t) - p_0 \tag{7}$$

where $p(t)$ is the pulse width in μs, and p_0 is pulse width that produces active torque by the electrical stimulation at the desired operating point.

The vertices number of polytope is given by 2^s, where s is the uncertainties number. In this paper, the model contemplates four uncertainties ($s = 4$).

A linearized model obtained based on the results presented in [11, 12] is presented in (8), such that the model (1) is given by:

$$\begin{bmatrix} \dot{x}_1(t) \\ \dot{x}_2(t) \\ \dot{x}_3(t) \end{bmatrix} = \begin{bmatrix} 0 & 1 & 0 \\ 0 & 0 & 1 \\ l & i & e \end{bmatrix} \begin{bmatrix} x_1(t) \\ x_2(t) \\ x_3(t) \end{bmatrix} + \begin{bmatrix} 0 \\ 0 \\ b \end{bmatrix} p_n(t) \tag{8}$$

where l, i, e, $b \in \Re$ are uncertainties parameters obtained experimentally.

3 Parameters Identification

3.1 Subject

This study was authorized through a research ethics committee involving human beings (CAEE 79219317.2.1001.5402) in São Paulo State University (UNESP), Ilha Solteira

campus. An able-bodied male subject, 26 years old, participated in the study.

3.2 Test Platform

Experiments were performed on a test platform shown in Fig. 1. The platform is composed of a chair instrumented by an electrogoniometer (Lynx®), a gyroscope LPR510AL (ST Microelectronics®), two triaxial accelerometers MMA7341 (Freescale®), a NI myRIO controller (National Instruments®), a current-based neuromuscular electrical stimulator (more details can be found in [12]), and an user interface developed in the LabVIEW Student Edition.

For greater confidence and comfort of the volunteer, the patient can deactivate the stimulation pulses using a stop button. The chair backrest and the knee joint position are adjustable for each volunteer.

The stimulation intensity is controlled by setting the pulse amplitude to the quadriceps and controlling the pulse width. The stimulus frequency were fixed in 50 Hz. In a preliminary test, pulse amplitude was determined at about 70 mA. The muscular electrostimulator delivers rectangular, biphasic, symmetrical pulse to the individual's muscle, and allows an adjustment of the pulse width in a range of 0–500 μs.

3.3 Experimental Setup

Before applying the stimuli to the quadriceps, a muscle analysis determines the motor point for proper positioning of the surface electrodes. Further details on motor point identification are in [13]. Then, scraping and cleansing procedures are performed at the motor point. The electrodes used are rectangular self-adhesive (CARCI 50 × 90 mm).

After the motor-point identification, open-loop experimental tests are performed. The open-loop test consists of applying a step-type signal corresponding to a constant pulse width p_0. The test duration is about four seconds. Thereafter, a two-minutes time interval is timed for to rest. After the rest period, the step-type signal is applied again for four seconds.

The pulse width, position, velocity and angular acceleration data are automatically recorded at the end of the step-type signal.

At each test the measured angular position should be the closest to the desired position. However, after several tests applied sequentially it is noticeable that the measured angular position tends to be more divergent from the desired angular position, Fig. 2. Note that after a considerable number of tests the error becomes very large. Our hypothesis is that the muscle fibers recruited locally by the surface electrodes are saturated which leads to the fatigue state. The criterion used to determine the saturation condition of the

Fig. 1 Instrumented chair for neuromuscular electrical stimulation trials at the Instrumentation and Biomedical Engineering Laboratory—UNESP, FEIS
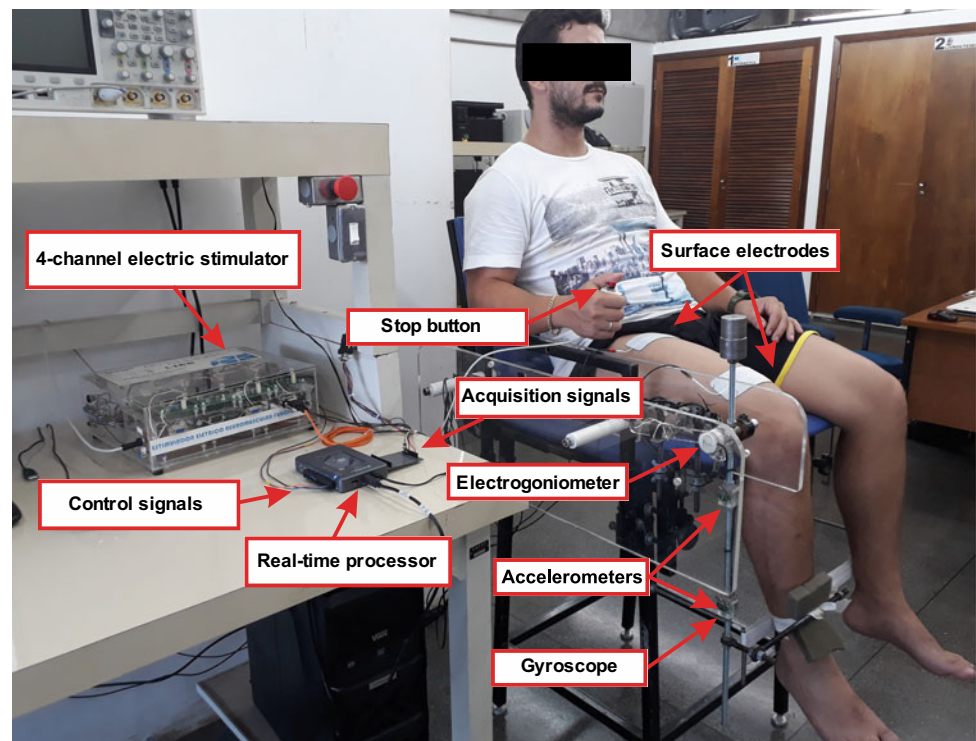
Fig. 2 Parameters identification test, performed by the successive application of step-type signals interspersed 2 min and considering a one-day interval between fatigued and non-fatigued run
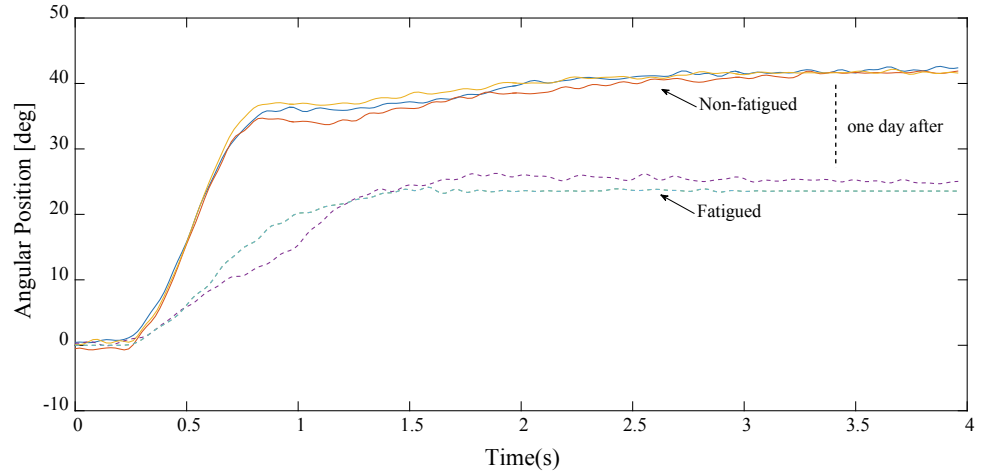
fibers was defined by the evaluation of the error obtained between the desired and measured position. With an relative error greater than 15–20%, the test results are referred to as fatigued situation for identification at an operating point $\mathbf{x}_0$.

After 120 min of tests, we observed an early fatigue in the muscles. Therefore, about 24 hours later, muscular behavior was evaluated again for step-type signals. In these trials the obtained results were referred as fatigued situation, Fig. 2.

3.4 Vertices of Polytope

The experimental data were processed via MATLAB. The parameters values of the identification sets (non-fatigued and fatigued) are shown in the Table 1 and vertices of the polytope (A_i, B_i), are expressed as:

$$A_1 = \begin{bmatrix} 0 & 1 & 0 \\ 0 & 0 & 1 \\ l_{min} & i_{min} & e_{min} \end{bmatrix}; B_1 = \begin{bmatrix} 0 \\ 0 \\ b_{min} \end{bmatrix}; \quad A_2 = \begin{bmatrix} 0 & 1 & 0 \\ 0 & 0 & 1 \\ l_{min} & i_{min} & e_{min} \end{bmatrix}; B_2 = \begin{bmatrix} 0 \\ 0 \\ b_{max} \end{bmatrix};$$

$$A_3 = \begin{bmatrix} 0 & 1 & 0 \\ 0 & 0 & 1 \\ l_{min} & i_{min} & e_{max} \end{bmatrix}; B_3 = \begin{bmatrix} 0 \\ 0 \\ b_{min} \end{bmatrix}; \quad A_4 = \begin{bmatrix} 0 & 1 & 0 \\ 0 & 0 & 1 \\ l_{min} & i_{min} & e_{max} \end{bmatrix}; B_4 = \begin{bmatrix} 0 \\ 0 \\ b_{max} \end{bmatrix};$$

$$A_5 = \begin{bmatrix} 0 & 1 & 0 \\ 0 & 0 & 1 \\ l_{min} & i_{max} & e_{min} \end{bmatrix}; B_5 = \begin{bmatrix} 0 \\ 0 \\ b_{min} \end{bmatrix}; \quad A_6 = \begin{bmatrix} 0 & 1 & 0 \\ 0 & 0 & 1 \\ l_{min} & i_{max} & e_{min} \end{bmatrix}; B_6 = \begin{bmatrix} 0 \\ 0 \\ b_{max} \end{bmatrix};$$

$$A_7 = \begin{bmatrix} 0 & 1 & 0 \\ 0 & 0 & 1 \\ l_{min} & i_{max} & e_{max} \end{bmatrix}; B_7 = \begin{bmatrix} 0 \\ 0 \\ b_{min} \end{bmatrix}; \quad A_8 = \begin{bmatrix} 0 & 1 & 0 \\ 0 & 0 & 1 \\ l_{min} & i_{max} & e_{max} \end{bmatrix}; B_8 = \begin{bmatrix} 0 \\ 0 \\ b_{max} \end{bmatrix};$$

$$A_9 = \begin{bmatrix} 0 & 1 & 0 \\ 0 & 0 & 1 \\ l_{max} & i_{min} & e_{min} \end{bmatrix}; B_9 = \begin{bmatrix} 0 \\ 0 \\ b_{min} \end{bmatrix}; \quad A_{10} = \begin{bmatrix} 0 & 1 & 0 \\ 0 & 0 & 1 \\ l_{max} & i_{min} & e_{min} \end{bmatrix}; B_{10} = \begin{bmatrix} 0 \\ 0 \\ b_{max} \end{bmatrix};$$

$$A_{11} = \begin{bmatrix} 0 & 1 & 0 \\ 0 & 0 & 1 \\ l_{max} & i_{min} & e_{max} \end{bmatrix}; B_{11} = \begin{bmatrix} 0 \\ 0 \\ b_{min} \end{bmatrix}; \quad A_{12} = \begin{bmatrix} 0 & 1 & 0 \\ 0 & 0 & 1 \\ l_{max} & i_{min} & e_{max} \end{bmatrix}; B_{12} = \begin{bmatrix} 0 \\ 0 \\ b_{max} \end{bmatrix};$$

$$A_{13} = \begin{bmatrix} 0 & 1 & 0 \\ 0 & 0 & 1 \\ l_{max} & i_{max} & e_{min} \end{bmatrix}; B_{13} = \begin{bmatrix} 0 \\ 0 \\ b_{min} \end{bmatrix}; \quad A_{14} = \begin{bmatrix} 0 & 1 & 0 \\ 0 & 0 & 1 \\ l_{max} & i_{max} & e_{min} \end{bmatrix}; B_{14} = \begin{bmatrix} 0 \\ 0 \\ b_{max} \end{bmatrix};$$

$$A_{15} = \begin{bmatrix} 0 & 1 & 0 \\ 0 & 0 & 1 \\ l_{max} & i_{max} & e_{max} \end{bmatrix}; B_{15} = \begin{bmatrix} 0 \\ 0 \\ b_{min} \end{bmatrix}; \quad A_{16} = \begin{bmatrix} 0 & 1 & 0 \\ 0 & 0 & 1 \\ l_{max} & i_{max} & e_{max} \end{bmatrix}; B_{16} = \begin{bmatrix} 0 \\ 0 \\ b_{max} \end{bmatrix};$$

4 Switched Control Design

The control technique used in this study is derived from [10]. We assume an analysis of the system around a point of equilibrium $\overline{\mathbf{x}}(t) = \mathbf{x}_0$, so a linearization can be applied to the plant $\dot{\overline{\mathbf{x}}}(t) = f(\overline{\mathbf{x}}(t), \overline{p}(t))$, and control input $\overline{p}(t) = p_0$. Consider that $\mathbf{x}_0$ is known, p_0 is uncertain because it depends on the plant uncertainties, and

$$\mathfrak{D} \triangleq \left\{ p_0 \in \Re_+^* ; p_{0min} \le p_0 \le p_{0max} \right\}, \tag{9}$$

where p_{0min} and p_{0max} are known.

Thus, we considered in this paper the linearized system given by:

$$\dot{\mathbf{x}}(t) = \mathbf{A}(\alpha)\mathbf{x}(t) + \boldsymbol{B}(\alpha)p(t), \tag{10}$$

such that $\mathbf{x}(t) = \overline{\mathbf{x}}(t) - \mathbf{x}_0$, $\overline{\mathbf{x}}(t)$ is the state vector of the plant; $p(t) = \overline{p}(t) - p_0$, $\overline{p}(t)$ is the signal control; $\boldsymbol{B}(\alpha) = \boldsymbol{B}g(\alpha)$, $\boldsymbol{B}$ is a constant matrix, and the bounded function $g(\alpha) \in \Re_+^*$, that depends on uncertain parameters α.

Considering for all α given in (3), so the system linearized (10) can be rewritten as:

$$\dot{\mathbf{x}}(t) = \mathbf{A}(\alpha)\mathbf{x}(t) + \boldsymbol{B}g(\alpha)p(t) \tag{11}$$

where $\boldsymbol{B}$ is a constant, and the $g(\alpha) > 0$.

In this paper, consider the feedback control law with the state vector as

$$\overline{p}(t) = \overline{p}_\alpha(t) = -\sum_{i=1}^{r} \alpha_i \boldsymbol{K_i} \mathbf{x}(t) = -\boldsymbol{K}(\alpha)\mathbf{x}(t) \tag{12}$$

where $\boldsymbol{K_i} \in \Re^{m \times n}$, $i \in \mathbb{K}_r$. Considering (12) and from (3) and (11),

$$\dot{\mathbf{x}}(t) = \mathbf{A}(\alpha)\mathbf{x}(t) + \boldsymbol{B}(\alpha)\boldsymbol{K}(\alpha)\mathbf{x}(t)$$

Table 1 Uncertain parameters of the model

Parameter	Non-fatigued		Fatigued	
	min	max	min	max
l	−104.8630	−45.5413	−53.6807	−18.9582
i	−55.2046	−34.4644	−35.1242	−15.5393
e	−6.3065	−5.0064	−8.6351	−5.6134
b	0.1111	0.2516	0.0279	0.0738

$$\dot{\mathbf{x}}(t) = \sum_{i=1}^{r} \sum_{j=1}^{r} \alpha_i \alpha_j (\mathbf{A}_i + \boldsymbol{B}_i \boldsymbol{K}_j) \mathbf{x}(t) \tag{13}$$

We present below the theorems that include stability, decay rate and input constraint for the control design for linear system with polytopic uncertainties.

4.1 Stability + Decay Rate

Theorem 1 [10]—*The equilibrium point* $\mathbf{x} = 0$ *of the linear system with polytopic uncertainties given in* (13) *is asymptotically stable in the large if there exist a common symmetric positive definite matrix* $\boldsymbol{X}$ *and* $\boldsymbol{M}_i \in \Re^{mxn}$ *such that, for all* $i, j \in \mathbb{Q}_r$, *the following LMIs hold:*

$$\boldsymbol{X}\boldsymbol{A}_i^T + \boldsymbol{A}_i\boldsymbol{X} - \boldsymbol{B}_i\boldsymbol{M}_i - \boldsymbol{M}_i^T\boldsymbol{B}_i^T + 2\beta\boldsymbol{X} < \boldsymbol{0} \tag{14}$$

$$\begin{aligned} (\boldsymbol{A}_i + \boldsymbol{A}_j)\boldsymbol{X} + \boldsymbol{X}(\boldsymbol{A}_i + \boldsymbol{A}_j)^T - \boldsymbol{B}_i\boldsymbol{M}_j - \boldsymbol{B}_j\boldsymbol{M}_i \\ -\boldsymbol{M}_i^T\boldsymbol{B}_j^T - \boldsymbol{M}_j^T\boldsymbol{B}_i^T + 4\beta\boldsymbol{X} \leq \boldsymbol{0}, \ i < j \end{aligned} \tag{15}$$

If (14) *and* (15) *are feasible, the controller gains are given by* $\boldsymbol{K}_i = \boldsymbol{M}_i\boldsymbol{X}^{-1}$, $i \in \mathbb{Q}_r$.

Proof The proof is detailed in [14], considering $\dot{V}(\mathbf{x}) \leq -2\beta V(\mathbf{x})$.

4.2 Input Constraint

Theorem 2 [15]—*Assume that the initial condition* $\mathbf{x}(0)$ *it's known. The restriction* $\|u(t)\|_2 \leq \mu$ *is enforced for all time* $t \geq 0$ *if the following LMIs are feasible:*

$$\begin{bmatrix} \boldsymbol{I} & \mathbf{x}(0)^T \\ \mathbf{x}(0) & \boldsymbol{X} \end{bmatrix} \geq \boldsymbol{0} \tag{16}$$

$$\begin{bmatrix} \boldsymbol{X} & \boldsymbol{M}_i^T \\ \boldsymbol{M}_i & \mu^2\boldsymbol{I} \end{bmatrix} \geq \boldsymbol{0} \tag{17}$$

If (16) *and* (17) *are feasible, the controller gains are given by* $\boldsymbol{K}_i = \boldsymbol{M}_i\boldsymbol{X}^{-1}$, $i \in \mathbb{Q}_r$.

Proof The proof is detailed in [15].

4.3 Switched Law Control for Uncertainty in the Control Signal

Assume that the gains $\boldsymbol{K}_i = \boldsymbol{M}_i\boldsymbol{X}^{-1}$, $i \in \mathbb{Q}_r$ and the matrix $\boldsymbol{P} = \boldsymbol{X}^{-1}$, have been obtained using the vertices of the polytope of the system (10) in the LMIs from Theorem 1. Now, given a constant ξ, define the control law:

$$p_n(\text{t}) = \overline{p}_{n(\sigma,\xi)}(\text{t}) = p_{(\sigma,\xi)}(\text{t}) = \overline{p}_{(\sigma,\xi)}(\text{t}) - p_0 \tag{18}$$

with

$$\overline{p}_{(\sigma,\xi)}(\text{t}) = -\boldsymbol{K}_\sigma\mathbf{x}(\text{t}) + \gamma_\xi(t) \tag{19}$$

where

$$\boldsymbol{K}_\sigma \in \{\boldsymbol{K}_1, \boldsymbol{K}_2, \ldots, \boldsymbol{K}_r\},$$
$$\sigma = arg \min_{i \in \mathbb{K}_r}(-\mathbf{x}^T\boldsymbol{P}\boldsymbol{B}\boldsymbol{K}_i\mathbf{x}),$$

and

$$\gamma_\xi(t) = \begin{cases} p_{0\max}, & \text{if } \mathbf{x}^T\boldsymbol{P}\boldsymbol{B} < -\xi \\ [(p_{0\min} - p_{0\max})\mathbf{x}^T\boldsymbol{P}\boldsymbol{B} + \xi(p_{0\min} + p_{0\max})](2\xi)^{-1}, & \text{if } |\mathbf{x}^T\boldsymbol{P}\boldsymbol{B}| \leq \xi \\ p_{0\min}, & \text{if } \mathbf{x}^T\boldsymbol{P}\boldsymbol{B} > \xi. \end{cases} \tag{20}$$

Consider the index $\Xi(t) \in \mathbb{Z}$, as the signal switching state $\gamma_\xi(t)$:

$$\Xi(t) = \begin{cases} 1 & \text{if } \mathbf{x}^T\boldsymbol{P}\boldsymbol{B}(t) < -\xi \\ 2, & \text{if } |\mathbf{x}^T\boldsymbol{P}\boldsymbol{B}(t)| \leq \xi \\ 3, & \text{if } \mathbf{x}^T\boldsymbol{P}\boldsymbol{B}(t) > \xi. \end{cases} \tag{21}$$

Theorem 3 *Suppose that the conditions from Theorem 1 hold, from the system* (10) *with the control law* (12) *and obtain* $\boldsymbol{K}_i = \boldsymbol{M}_i\boldsymbol{X}^{-1}$, $i \in \mathbb{K}_r$, *and* $\boldsymbol{P} = \boldsymbol{X}^{-1}$. *Then, the switched control law* (18)–(20) *makes the system* (10) *uniform ultimate bounded.*
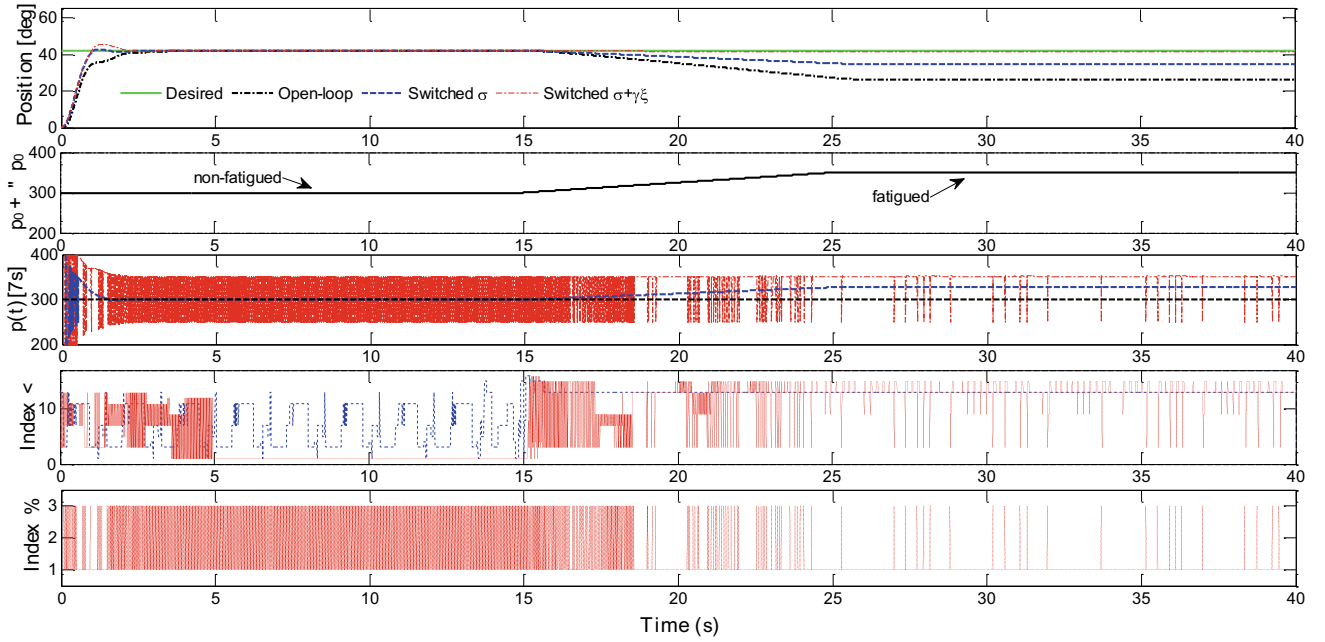
Fig. 3 Dynamic behavior of lower limb electrical stimulation around an operating point (42 [deg]) with uncertain control signal. Considering input constraint $\mu = 183$, decay rate $\beta = 1$, nominal pulsewidth $p_0 = 300\,\mu s$, $\xi = 1\times 10^{-7}$, and variation analysis of the control signal uncertainty around the operating point in $\pm 16\%$

Proof The proof is detailed in [10].

The LMIs were carried out using the modelling language YALMIP [16] with the solver SeDuMi [17]. In this study, we adopted the input constraint $\mu = 183$ and $\beta = 1$. The following symmetric positive matrix P and gains K_i were obtained:

$$P = \begin{bmatrix} 1.8561 & 0.3641 & 0.0354 \\ 0.3641 & 0.1709 & 0.0142 \\ 0.0354 & 0.0142 & 0.0040 \end{bmatrix},$$

$K_1 = [3.8103 \quad 12.0769 \quad 9.3184]$, $K_2 = [2.5066 \quad 11.3130 \quad 8.9398]$,
$K_3 = [-136.0682 \quad -31.8201 \quad 5.0880]$, $K_4 = [-50.4234 \quad -5.3803 \quad 7.9886]$,
$K_5 = [69.5623 \quad 59.7115 \quad 8.5526]$, $K_6 = [65.5889 \quad 54.5087 \quad 8.5939]$,
$K_7 = [-24.2572 \quad 44.5688 \quad 8.0781]$, $K_8 = [21.9736 \quad 43.4125 \quad 9.0712]$,
$K_9 = [174.1688 \quad 31.5380 \quad 8.8588]$, $K_{10} = [159.4661 \quad 30.1603 \quad 8.7490]$,
$K_{11} = [133.2834 \quad 3.7992 \quad 8.1755]$, $K_{12} = [120.4297 \quad 17.0732 \quad 9.1600]$,
$K_{13} = [222.6452 \quad 65.5826 \quad 3.5653]$, $K_{14} = [200.7592 \quad 64.4574 \quad 6.6352]$,
$K_{15} = [201.5643 \quad 66.3596 \quad 7.8898]$, $K_{16} = [179.8473 \quad 60.5283 \quad 8.4729]$.

In relation to the control law (20), the maximum and minimum values of p_0 must be found. However, these values can not be determined analytically. So, we define these values by means of the experimental results obtained in the section parameters identification: $\max\{p_0\} = 350$ μs, $\min\{p_0\} = 250$ μs.

For the numerical simulation, at $t = 0\,s$ it considered the initial condition $\bar{\mathbf{x}}(0) = [0° \quad 0 \quad 0]$, and $p_0 = 300$ μs. In

$t = 2\,s$ from Fig. 3, the system stabilizes in the desired position $\bar{\mathbf{x}}(2) = [42° \quad 0 \quad 0]$. At the time $t = 15\,s$, the p_0 value of the system is purposely altered in order to compare open-loop and control signal $p_\sigma(t)$ and $p_{(\sigma,\xi)}(t)$. During the time interval $t \in [1525]\,s$ the p_0 value increases linearly and remains constant ($p_0 = 350\,\mu s$) until $t = 40\,s$.

Figure 4 shows that control signal $p_{(\sigma,\xi)}(t)$ has a better performance index than $p_\sigma(t)$. In open-loop the position error is $-15.83°$, while that control signal $p_\sigma(t)$ and $p_{(\sigma,\xi)}(t)$ were $-7.10°$ and $-0.38°$, respectively. The control law uses the signal $\mathbf{x}^T PB(t)$ as a decision variable. The control signal uncertainty is evident in $\mathbf{x}^T PB(t)$. By setting a given ξ which minimizes uncertainty, it makes the system uniform ultimate bounded. Thus, it is explicit from the Fig. 2 that the controller with $\gamma_\xi(t)$ law is more efficient than the one commonly used in the literature. It is worth mentioning that if the value ξ tends to zero, it will make the function $\gamma_\xi(t)$ discontinue and consequently the control signal will be discontinuous, causing chattering as shown in Fig. 4.

5 Conclusion

This paper investigated the uncertain control signal problem involving electrical stimulation of lower limbs. The study focused on a linear analysis around an operating point. A comparison between open-loop control and two closed-loop controllers was performed. The switched
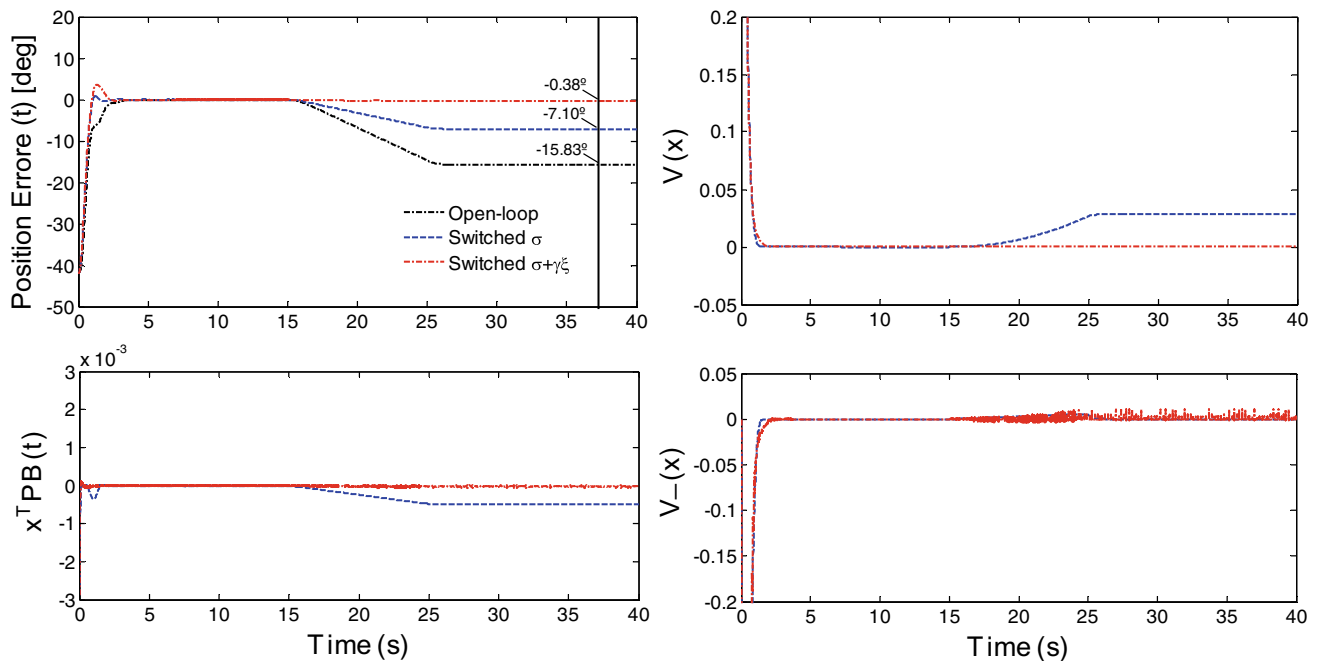
Fig. 4 Position error $e(t)$, dynamic behavior $\mathbf{x}^T PB(t)$ considering uncertain control signal, and $V(\mathbf{x})$ and derivative $\dot{V}(\mathbf{x})$ of Lyapunov function

controller $p_{(\sigma,\xi)}(\text{t})$ returned the smallest time derivative value of the Lyapunov function and compensated the uncertain control signal.

References

1. Sharma, N., Dani, A.: Nonlinear estimation of gait kinematics during functional electrical stimulation and orthosis-based walking. In: Proceedings of American Control Conference, pp. 4778–4783 (2014)
2. Downey, R.J., Merad, M., Gonzalez, E.J., Dixon, W.E.: The time-varying nature electromechanical delay and muscle control effectiveness in response to stimulation-induced fatigue. IEEE Trans. Neural Syst. Rehabil. Eng. **25**(9), 1397–1408 (2017)
3. dos Santos, N.M., et al.: Robust Control of the Knee joint angle of paraplegic patients considering norm-bounded uncertainties. Math. Probl. Eng. **2015**, 1–8 (2015)
4. Sanches, M.A.A., et al.: Digital controller design considering hardware constraints: application in a paraplegic patient. Rev. Bras. Eng. Biomdica **30**(3), 232–241 (2014)
5. Gaino, R., Teixeira, M.C.M.C., de Carvalho, A.A., Assunção, E., Cardim, R., Sanches, M.A.A., Covacic, M.R.: Realimentação derivativa e modelo fuzzy Takagi-Sugeno para controle da articulação do joelho de pacientes paraplégicos com o uso de acelerômetros. Rev. Bras. Eng. Biomed. **27**(2), 67–78 (2011) (in Portuguese)
6. Sharma, N., Gregory, C.M., Johnson, M., Dixon, W.E.: Closed-loop neural network-based NMES control for human limb tracking. IEEE Trans. Control Syst. Technol. **20**(3), 712–725 (2012)
7. Downey, R.J., Cheng, T.-H., Bellman, M.J., Dixon, W.E.: Switched tracking control of the lower limb during asynchronous neuromuscular electrical stimulation: theory and experiments. IEEE Trans. Cybern. **47**(5), 1251–1262 (2017)
8. Gaino, R., et al.: Electrical stimulation tracking control for paraplegic patients using TS fuzzy models. Fuzzy Sets Syst. **314**, 123 (2017)
9. Kozan, R.F., et al.: Controle do Movimento dos Membros Inferiores com Verificação de Robustez. In: XXIV Congresso Brasileiro de Engenharia Biomédica - CBEB, pp. 1022–1025 (2014)
10. De Souza, W.A., Teixeira, M., Santim, M., Cardim, R., Assunção, E.: On switched control design of linear time-invariant systems with polytopic uncertainties. Math. Probl. Eng. **2013** (2013)
11. Ferrarin, M., Pedotti, A.: The relationship between electrical stimulus and joint torque: a dynamic model. IEEE Trans. Rehabil. Eng. **8**(3), 342–352 (2000)
12. Sanches, M.A.A.: Sistema Eletrônico para Geração e Avaliação de Movimentos em Paraplégicos. São Paulo State University (UNESP), Ilha Solteira Campus (2013). (in Portuguese)
13. Gobbo, M., Maffiuletti, N.A., Orizio, C., Minetto, M.A.: Muscle motor point identification is essential for optimizing neuromuscular electrical stimulation use. J. Neuroeng. Rehabil. **11**(1), 17 (2014)

14. Boyd, S., El Ghaoui, L., Feron, E., Balakrishnan, V.: Linear matrix inequalities in system and control theory. SIAM, USA **15** (1994)
15. Tanaka, K., Wang, H.O.: Fuzzy control systems design and analysis: a linear matrix inequality approach. Wiley (2001)
16. Lofberg, J.: YALMIP: a toolbox for modeling and optimization in MATLAB. In: 2004 IEEE International Symposium on Computer Aided Control Systems Design, pp. 284–289 (2004)
17. Sturm, J.F.: Using SeDuMi 1.02, a MATLAB toolbox for optimization over symmetric cones. Optim. Methods Softw. **11** (14), 625–653 (1999)
18. Gear, W.S.: Effect of different levels of localized muscle fatigue on knee position sense. J. Sports Sci. Med. **10**(4), 725–730 (2011)

Towards Indoor Rowing Assisted by Electrical Stimulation for Persons with Paraplegia

L. O. da Fonseca, B. M. Ferreira, M. E. G. Paredes, J. P. Freire, P. Sanches, and A. P. L. Bó

Abstract

Spinal cord injury (SCI) can cause paraplegia, as well as develop health problems resulting from low physical activity. Although there are exercises for persons with paraplegia using only the upper limbs, they are known to deliver low benefits. Functional electrical stimulation (FES) can activate paralyzed muscles, which makes it possible to exercise also lower limb muscles. FES-rowing has been shown to be a good hybrid activity, unifying upper limbs activity with FES-activated lower limbs. In this work we adapted an existing rowing machine to be used by athletes with SCI. It comprises trunk and legs stabilization, real-time FES control by the user and additional safety measures. The result is an accessible platform for individuals with paraplegia to perform high impact exercises.

1 Introduction

Spinal Cord Injury (SCI) is a devastating condition that may cause complete loss of sensory-motor function, producing a vast impact in the life of concerned individuals. Furthermore, SCI is also often associated with the decrease in cardiovascular fitness, the onset of metabolic diseases, the loss of muscle trophism and bone mineral density, among other complications [1].

Physical therapy and exercise have been demonstrated as potential alternatives for reducing the effect of such co-morbidities [2]. Although regular upper body resistance exercise is essential for guaranteeing independence, its limited peak oxygen uptake does not provide a significant contribution to cardiovascular health. An option of aerobic exercise is Arm Crank Ergometry (ACE), in which users with paraplegia or tetraplegia must use their upper limbs to rotate a crankset that features varying load. Nevertheless, this form of exercise also has not demonstrated the capability of generating sufficient exercise intensity to meet recommended levels [3].

An additional alternative for exercise routines on SCI patients is to employ Functional Electrical Stimulation (FES) to contract lower limb muscles, and thus potentially increase the oxygen consumption of muscles during exercise practice. Indeed, a system that applies low-level electrical stimuli to enable lower limb exercise was demonstrated several decades ago [4], when FES-cycling for individuals with SCI was evaluated for the first time. However, regardless of recent efforts from research groups worldwide [5], FES-cycling has also failed to induce a satisfactory level of exercise [6].

In this scenario, the combination of FES-produced lower limb and voluntary upper limb movements may constitute an ideal exercise in terms of prolonged peak oxygen consumption and full body muscle action. Two types of such hybrid exercise have been proposed in the literature: a combination of ACE and FES-cycling, and FES-rowing. Clinical investigations have shown that both exceed the minimum advised metabolic cost for lowering the relative risk of coronary heart disease [6, 7].

To enable the practice of indoor FES-rowing by athletes with paraplegia, adaptations to the regular rowing ergometer are necessary. From the pioneering work of Laskin and colleagues [8] up to recent developments [7, 9], distinct researchers have attempted to improve safety, usability, and user interface of such devices. Nonetheless, despite the proven benefits, the adoption of such technology by individuals with SCI has been limited, to the best of our knowledge, to a few specialized FES Rowing Centers in the USA, UK and Canada, and academic studies.

L. O. da Fonseca · B. M. Ferreira (✉) · M. E. G. Paredes · J. P. Freire · P. Sanches · A. P. L. Bó
Universidade de Brasília, Brasília, Brazil
e-mail: breno@lara.unb.br

In this work, we describe the development of a FES-rowing platform with a novel user-controllable system. We propose a mechanical design presenting minor adaptations with respect to previous works, as well as an innovative control interface, which potentially engages the user to voluntarily and intuitively synchronize upper and lower limbs motion. The integration of all system components and discussion of obtained results are also presented in the paper. Our final goal is to provide an affordable FES-rowing platform for indoor use that will enable independent practice of physical exercise by athletes with SCI.

2 Methods

In order to benefit from an established rowing ergometer system, we adapted one to our needs. These adaptations consisted on mechanical changes and the addition of electronic equipment and a FES stimulator, as well as a control software.

2.1 Mechanical Adaptations

The main needs of a rower with paraplegia are related to trunk and lower limbs stabilization. As for the trunk, we replaced the regular rowing seat with a custom one, similar to a chair, with a broad seat area and a back part to which the user is constrained. The new seat runs free on the regular track, just as the original seat. Differently from other FES rowing machines, the stabilization straps were placed horizontally instead of vertically, reducing the contact and friction in the armpit region, as well as partially enabling trunk movement.

An important safety feature in any device that uses FES for knee extension on SCI users is a way to avoid hyperextension. We installed safety adjustable straps connecting the adapted seat to the feet base. The straps limit the seat range of motion so that the legs are never fully extended.

As the user's lower limbs lack natural stabilization, we built a device that holds the legs, allowing movement only on parasagittal planes. As a result, extension and flexion are permitted, but no adduction or abduction. In addition, the feet are firmly fixed to the platform.

To support lower limbs flexion, the rowing machine is lifted to create a slope of proximately 5°. This and the aforementioned adaptations are illustrated on Fig. 1.

2.2 Control System

The user can control the FES system with a device attached to the handle bar, the interface module, shown on Fig. 1.
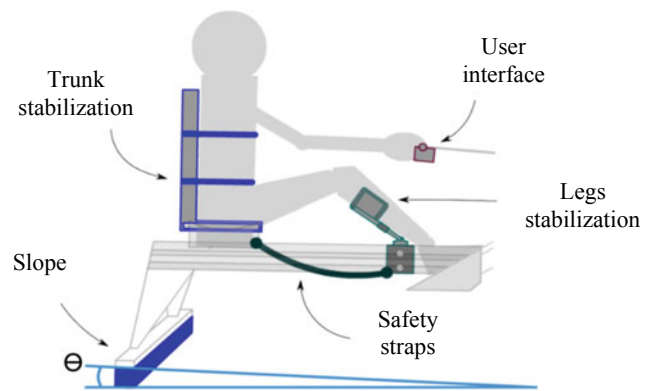
Fig. 1 Detail of the proposed mechanical adaptations to a regular rowing machine

The control device is positioned on the handle bar so it can be operated by the user thumbs while the regular rowing movement is performed. As both legs movements are the same, each button activates the same FES signal for both legs, on the corresponding muscle group.

The three controlling buttons are connected to an Arduino Nano board, which is complemented by a UART Bluetooth module, a display 16 × 02, a 9 V battery and a custom printed circuit board to connect it all. It communicates with the **control module**, consisted by a Raspberry Pi 3, that directly controls the FES stimulator using a USB connection.

2.3 Electrical Stimulator

An 8-channel commercial electrical stimulator (Hasomed Rehastim, Germany) is used to generate the concerned FES signals. It is controlled in real time by the control module. Stimulation is applied through self-adhesive 5 × 10 cm electrodes.

For leg extension, stimulation can be applied to *quadriceps* and *gluteus* muscle groups; and for flexion, to *hamstrings* and *tibialis anterior*, taking advantage of the 8 channels available on the stimulator. Differently from [7, 10, 11], where only *quadriceps* and *hamstrings* were used, here we propose that *gluteus* might be stimulated to stabilize the limb during knee extension, and *tibialis anterior* may aid during leg flexion.

The signal waveform is biphasic square at 30 Hz, although other frequencies may be used. Pulse width and current amplitude shall be set according to each muscle and individual user in order to generate at least force level 4 according to the Manual Muscle Test. Both legs are assumed similar, therefore the parameter set for the two are the same.

When the control system activates the extension phase, all muscle groups involved are activated simultaneously,

Fig. 2 System functioning diagram. When the program starts, it first connects the interface and the control modules, then the user chooses the amount of channels per leg and sets its parameters. After that, during the runtime phase, buttons 1 and 2 controls the stimulation, and button 3 stops it and ends the activity
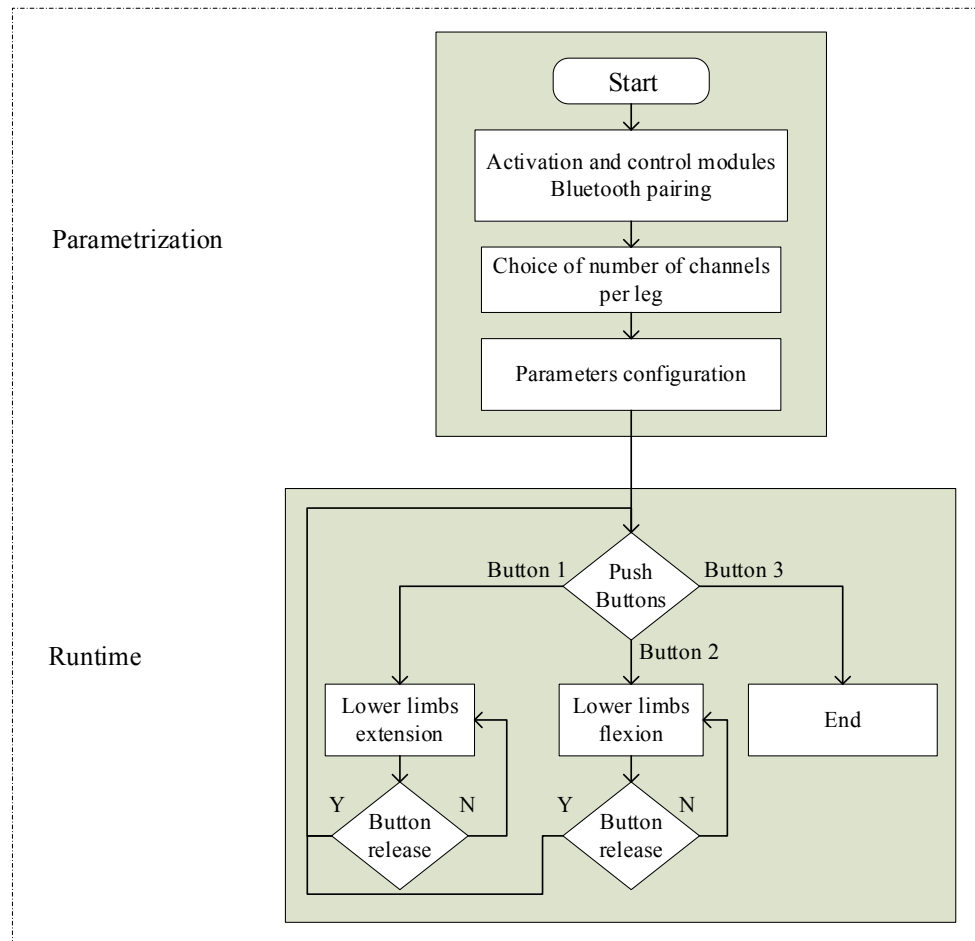
with the appropriate pre-calibrated parameter set. Similarly, during flexion, the other muscles are activated.

2.4 Control Software

We developed a software to both acquire all the required stimulation initial parameters and to control the FES on real time based on user input. The first phase is called parametrization, while the second phase is named runtime. During parametrization, the user is able to set the current, pulse width and frequency. That is done using buttons 1 and 2, and controlling the values shown on the display. Button 3 advances to the next option. As both legs use the same parameters, these are set to all channels of only one leg, and then they are replicated to the other one. The amount of channels on each leg is also expandable for more than the default 2.

During the runtime phase, the button commands are translated to channel activation according to the previously set parameters. The display shows "extension" or "flexion" whenever the corresponding muscles are being activated by the stimulator. Finally, when button 3 is pushed, the activity

finishes and "End" is shown on the screen. This process can be seen on Fig. 2.

3 Results

A comparison between a regular rowing machine and the adapted machine built for this project can be seen on Fig. 3. The new seat, although bigger, slides on the track as easily as the original one. It is also more stable, since its bigger size also increases the whole user-seat mass moment of inertia around sliding track. The safety straps can successfully limit the seat range of motion, however it has an abrupt stop at the end, due the absence of elastic or damping mechanical elements. The legs stabilization device fits well on a regular size adult, with minimal resistance to the rowing movement.

4 Discussion

The device built in this work is a flexible FES rowing platform. The stimulation parameters can be customized and the user can develop a system operation strategy to achieve

Fig. 3 Comparison between the adapted rowing machine and an untouched original one. Note the seat for trunk stabilization, the custom device for legs stabilization, and the safety straps

the best results. We have found in previous studies involving FES-cycling [5] that users may enjoy such manual control better than a more automated strategy. Therefore, it is not incorrect to assume that the same fact can be true for FES-rowing. However, a specific study would be needed to confirm such statement in rowing.

With respect to the user controllability of the FES system in real time during training, it allows the user to change the intensity of the training whenever necessary, providing more independence. That can lead to extended training sessions where the user's fatigue can be delayed by the gradual increase of stimulation intensity. Moreover, other training protocols might be used, such as High Intensity Interval Training (HIIT), protocols that have higher aerobic fitness efficiency when compared to moderate exercise [12].

Although the interface module is attached to the handle bar, the user has to move the thumbs from their original placement to push the buttons. That might be undesirable during the exercise. In order to overcome this, we are planning to build a custom handle bar which will embed the interface module as a single unit. That way the buttons can be much closer to the thumbs natural position. The battery and data access will be made through the handle extremities, facilitating maintenance. In addition, it will be mechanically more robust.

Another potential issue regarding the controllability of the system in real time by the user during is the high cognitive demand that could lead to decrease of efficiency in the exercise. Although previous works have pointed out this could be an important issu [13], we believe an electronic system presenting faster response times and proper training to use the FES-rowing may decrease the cognitive burden, enabling the user to benefit from a more independent operation.

We have assumed that the user's legs have similar muscular strength and endurance between the two, and that the electrodes are positioned the same way contra-laterally. In

fact, that is not always true. Therefore, the same FES parameters should not be applied to both legs. But even if each muscle is individually assessed, the fixed configuration of the feet and the identical movement of legs makes it difficult to observe eventual differences between their performances. That problem has also been identified on FES cycling systems [14]. As proposed by [15], individual force sensors such as the one developed by [16] could help the system adapt the FES parameters automatically during runtime.

The legs stabilizing device holds both legs with protective material, such as foam, and an axis that allows the rowing motion on that plane only. It is important to have a soft contact between the device and a SCI user's legs because, since sensory capabilities are usually weak or nonexistent, pressure points can harm the blood flow and skin. Since the user's distance to the pivot point changes during the activity, there is a telescope mechanism, which shortens the axis when the legs are flexed, and lengthens in when the legs are stretched. The device was initially planned to be installed close to the feet location, but, instead, we chose a further back location on the seat's rail in order to give it a greater range of motion.

The adjustable straps that limit the seat range of motion are not elastic, which can cause an abrupt stop at the end of extension, and even a backlash caused by a rebound motion. Therefore elastic straps or dampers would be more suitable for this situation, reducing the end of course speed while keeping the intended safety.

Even though a second person is required to aid on electrode placement and seat belt adjustments, the transfer from the wheelchair to the rowing machine seat can be performed by the user alone, which is not always true on FES cycling devices.

The applied stimulation is directly controlled by the buttons on the interface module, which are regular push buttons. Therefore, there are no proportional control, and the stimuli only works in a on/off strategy, which delivers enough activation to sustain the rowing motion, but certainly results in excess torque during part of the movement. As a possible solution, a low level high frequency controller must be applied by the control module, ultimately aiming on lower muscle fatigue and smoother motion [10]. That low level control can follow a predetermined activation curve or follow a reference seat speed.

5 Conclusion

We adapted an existing indoor rowing machine to be usable by a SCI user as a FES hybrid exercise system. The stimulation is configurable and controllable in real time, and the mechanical adaptations were planned to provide safety and

comfort. Other than the wires used by the electrical stimulator, the system is completely wireless, adding even more safety to the activity. The adaptations performed on the regular rowing machine are affordable and can be customized to individual needs. Nevertheless, there is opportunity to improve individual leg parametrization and the knee overstretching avoiding method. Also, for future work, we intend to further embed the system with position sensors on the seat and handle, inertial measurement units on the user and force sensors under the feet. With that we will be able to better analyze the rowing kinematics and their effect on SCI rehabilitation.

References

1. Galea, M.P.: Spinal cord injury and physical activity: preservation of the body. Spinal Cord **50**(5), 344–351 (2012)
2. Deley, G., Denuziller, J., Babault, N.: Functional electrical stimulation: cardiorespiratory adaptations and applications for training in paraplegia. Sport. Med. **45**(1), 71–82 (2015)
3. Haisma, J.A., van der Woude, L.H.V., Stam, H.J., Bergen, M.P., Sluis, T.A.R., Bussmann, J.B.J.: Physical capacity in wheelchair-dependent persons with a spinal cord injury: a critical review of the literature. Spinal Cord **44**(11), 642–652 (2006)
4. Petrofsky, J.S., Heaton, H., Phillips, C.A.: Outdoor bicycle for exercise in paraplegics and quadriplegics. J. Biomed. Eng. **5**(4), 292–296 (1983)
5. Bo, A.P.L., et al.: Cycling with spinal cord injury: a novel system for cycling using electrical stimulation for individuals with paraplegia, and preparation for cybathlon 2016. IEEE Robot. Autom. Mag. **24**(4), 58–65 (2017)
6. Hettinga, D.M., Andrews, B.J.: Oxygen consumption during functional electrical stimulation-assisted exercise in persons with spinal cord injury. Sport. Med. **38**(10), 825–838 (2008)
7. Hettinga, D.M., Andrews, B.J.: The feasibility of functional electrical stimulation indoor rowing for high-energy training and sport. Neuromodulation Technol. Neural Interface **10**(3), 291–297 (2007)
8. Laskin, J.J., et al.: Electrical stimulation-assisted rowing exercise in spinal cord injured people. A pilot study. Spinal Cord **31**(8), 534–541 (1993)
9. Wheeler, G.D., et al.: Functional electric stimulation–assisted rowing: increasing cardiovascular fitness through functional electric stimulation rowing training in persons with spinal cord injury. Arch. Phys. Med. Rehabil. **83**(8), 1093–1099 (2002)
10. Davoodi, R.: Rowing with FES. J. Autom. Control **18**(2), 77–84 (2008)
11. Davoodi, R., Andrews, B.J., Wheeler, G.D., Lederer, R.: Development of an indoor rowing machine with manual fes controller for total body exercise in paraplegia. IEEE Trans. Neural Syst. Rehabil. Eng. **10**(3), 197–203 (2002)
12. Kilpatrick, M.W., Jung, M.E., Little, J.P.: High-intensity interval training: a review of physiological and psychological responses. ACSM's Health Fitness J. **18**(5), 11–16 (2014)
13. Halliday, S.E., Zavatsky, A.B., Hase, K.: Can functional electric stimulation-assisted rowing reproduce a race-winning rowing stroke? Arch. Phys. Med. Rehabil. **85**(8), 1265–1272 (2004)
14. da Fonseca, L.O., Bó, A.P.L., Guimarães, J.A., Gutierrez, M.E., Fachin-Martins, E.: Cadence tracking and disturbance rejection in functional electrical stimulation cycling for paraplegic subjects: a case study. Artif. Organs **41**(11), E185–E195 (2017)
15. Reichenfelser, W., Gföhler, M., Angeli, T.: Design of a test and training tricycle for subjects with paraplegia. Technol. Disabil. **17**, 93–101 (2005)
16. Dorado, N., Cristina, M.: Sistema para aquisição e controle de força em ciclismo assistido por estimulação elétrica. In: XXV Congresso Brasileiro de Engenharia Biomédica (CBEB 2016), 2016, Foz do Iguaçu

Upper Limb Muscle Activation: An EMG Analysis Using Myo® Armband

Gabriela Alves Maia de Souza, Marilú Gomes Netto Monte da Silva,
and Alana Elza Fontes da Gama

Abstract

The movements made by the myoelectric prostheses are controlled through the user's muscular electrical activity. This activity can be captured through superficial electrodes. This article aims to study the muscular electrical activity of the upper limb in different movements, in order to investigate the groups that do not have cross-talk influences for use in myoelectric prosthesis. To capture the electromyography signal, it was used an armband containing eight surface electrodes, the Myo®. For this study, two armbands were used, one in the forearm and another in the arm. Volunteers were asked to execute some of the biomechanical movements involving the upper limb muscles, and the RMS curves of the signals captured were analyzed. From the analysis is possibly to notice that there is cross-talk in the forearm, difficulting the biomechanical analysis. On the other hand, the arm results were better to differentiate. Thus, the muscle groups of the arm are more suitable for use in myoelectric prosthesis that perform different movements.

Keywords

Electromyography sign • Myo armband • Upper limb

1 Introduction

Prostheses are accessories that coupled to the body of the amputee try to replace the functions of the lost limb [1]. They can be activated mechanically by body movements or can be powered by external sources of energy. In the latter case, the user controls the movements of the prosthesis using his muscular electrical activity [2]. These are the myoelectric prosthesis, where this signal is captured by internal or surface electrodes positioned at residual limb or near segments [3, 4].

Internal electrodes are thin wires that are connected to a specific muscle through a needle, which is inserted inside the muscle. Thus, it is possible to collect very specific muscle signal, without the interference of other muscles. Although it is needed a surgery to implant the electrodes, this can lead to a bigger variety of movements, since it is easier to differentiate the muscle activity. Such technology is used by the most modern and expansive models from market. On the other side, surface electrodes usually has a conductive gel that glues the electrode on the user's skin, avoiding the discomfort and pain caused by the needles of the internal ones. However, for having a bigger detection volume, these electrodes also detect signals from neighboring muscles, causing cross-talk. Because of the cross-talk it is more difficult to differentiate the movements, resulting in prosthesis with a lower numbers of movements [5].

Some new technologies are being created to optimize the capture of the electromyography (EMG) signal. Between them, there is a recent one called Myo®. Myo® armband is a bracelet that has a gyroscope and eight electrodes, paired and properly spaced around its circumference. These electrodes are capable of detecting the electrical-muscular activity of the region of the arm they are in touch with and, according to the movements done by the arm, generate a response that is able to control computers, drones and even myoelectric prostheses [6–10].

G. Alves Maia de Souza (✉) · M. Gomes Netto Monte da Silva ·
Alana Elza Fontes da Gama
Universidade Federal de Pernambuco, Recife,
50670-901, PE, Brazil
e-mail: gabriela.a.m.souza@gmail.com

M. Gomes Netto Monte da Silva
e-mail: gomes.marilu@gmail.com

Alana ElzaFontes da Gama
e-mail: alanaelza@gmail.com

Once the Myo® has eight surface electrodes and it is capable of differentiate arm movements, this work hypothesizes that using it can be as useful method to capture EMG signal that combines comfort and a bigger differentiation of movements. To better understand these issues and investigate our theory, this article aims is to study and understand the relation muscular activity—electrode—arm muscle in different movements using Myo® armband. And thus determine what would be the best position to place the surface electrodes responsible for generating different movements in a myoelectric prosthesis.

2 Materials and Methods

This is a transversal study aiming to analyze forearm and arm muscles recruitment. For that, two Myo® armbands were used, a myoelectric sensor, to capture the EMG signals during wrist and elbow movements. The capture was done using the software offered in the Myo Market, it is called Myo Data Capture Windows [11]. On Fig. 1 it is possible to observe the steps taken to achieve the final goal; afterwards all the steps will be explained with details.

2.1 Myo® Software

ThalmicLabs™, Myo®'s creator, provides an interface called Myo Data Capture Windows. This software is able to give us some information captured by the bracelet, such as accelerometer, direction, Euler angles orientation and EMG signal captured by all the electrodes [12]. It allows the user to control the exact moment to start and finish acquiring these information, once it generates files containing these data of the exact interval of time that he remained open. This way, we can easily obtain the EMG signal of each channel during the execution of all the desired movements.

This software only provides information of one armband. Therefore, once two Myo® were necessary (one to acquire the arm signal and another for the forearm), it was necessary to use two computers. One of the computers used had a CORE i7 processor with 2.5 GHz and a RAM memory of 8 GB, the other had a CORE i5 with 2.7 GHz and a RAM memory of 8 GB. Furthermore, files generated by this software give us the raw data, so it was necessary to implement a software, described in Sect. 2.3, capable of

reading these files and analyze them in order to give us only the data of our interest.

2.2 Experimental Protocol

To execute the experimental protocol the volunteers should be healthy individuals with intact limbs and who have no apparent motor problems. Besides that, they should not be using any medication that could generate changes in the signal of EMG and they must be over eighteen years old. The recordings were made at the Biomedical Engineering Research Laboratory of the Federal University of Pernambuco in Brazil. All test procedures have been approved by the Ethics and Research Committee on Human Beings according to the resolution N° 466/12 of the National Health Council (CAAE—81837317.0.0000.5208), on 10/04/2018.

The experimental protocol was performed using two armbands to collect myoelectric activities during the performance of wrist and elbow movements. The armbands were located in the distal arm and in the proximal forearm at the dominant side, over the apex of the muscle bulge. In order to reduce artifact influences, both places need to be clean before placing the bracelets.

Once the armband is numerated from 1 to 8 according to a fabric pattern, to guarantee the muscle-electrode correspondence between volunteers, the bracelets were placed in the same position for all volunteers. Both bracelets were

Fig. 1 Research experiment fluxogram followed to analyze upper limb muscle recruitment

Fig. 2 Bracelets position

Table 1 Electrode-muscle correspondence

Electrode number	Muscle correspondence on the forearm	Muscle correspondence on the arm
1	Brachioradialis and extensor carpi radialis longus	Biceps brachii long head laterally
2	Brachioradialis and pronator teres	Biceps brachii short head
3	Pronator teres, flexor carpi radialis and flexor digitorum superficialis and profundus	Biceps brachii long head
4	Flexor carpi ulnaris, palmaris longus, and flexor digitorum superficialis and profundus	Biceps brachii short head laterally
5	Flexor carpi ulnaris	Triceps brachii long head
6	Anconeus and extensor carpi ulnaris	Triceps brachii long head
7	Extensor digitorum and supinator	Triceps brachii lateral head
8	Extensor carpi radialis brevis	Triceps brachii lateral head

positioned with the electrodes 1–4 in the anterior side (Fig. 2). This positioning results in a fixed correspondence between each channel and the muscles that perform the movements, as presented in Table 1.

To capture the muscle activity users were asked to sit in a chair and to perform isometric contraction of wrist and elbow movements with maximum force. This way the volunteer makes the force to execute the movement, but no movement actually happens, what, in biomechanical terms, means that there is muscular contraction, but no joint movement [13]. The isometric contraction was performed by resisting movement with a rigid object, such as a table or wall. For example, for wrist flexion the volunteers position their forearm and hand in the table with volar side facing the table and try to execute the motion. This type of movement seems ideal because when an amputee uses prosthesis, he does contract his muscles, but he has no joints to move.

With the objective to do a complete study of the upper limb muscle activation, it was chosen to each volunteer execute all the movements involving those muscles. These movements are: elbow flexion and extension, wrist flexion and extension, radial and ulnar deviation, hand flexion and extension, pronation and supination of the forearm.

In order to better organize and interpret the data, the following pattern was determined for the moment of signal capture. After two seconds of basal (when the volunteer stays motionless), the person in charge should give a verbal command to the volunteer start doing the movement, after three seconds another command should be given to the volunteer stop doing the movement, finally, two more seconds of basal (Fig. 3). This should be repeated three times per movement to reduce the chance of error and guarantee the coherence of the data.

The basal phase is very important for the synchronization between the bracelets, upon initiation of the movements a response is obtained on all electrodes of both bracelets.

2.3 Signal Processing

According to Kamen and Gabriel [14] there are two EMG descriptors on the time domain that are rapidly processed, they are the average rectified value and the root-mean-square (RMS). However the RMS is better due to the fact that it is not affected by the amplitude cancellation that happens with the superimposition of positive and negative phases of the EMG signal [14]. The RMS calculation can be done using the Eq. 1:

$$RMS = \sqrt{\frac{1}{N}\sum_{i=1}^{N} x_i^2} \qquad (1)$$

where x is the EMG sign and N is the total of points in the sample.

In order to analyze the captured data, an algorithm was developed in MATLAB©. The EMG signals were divided by
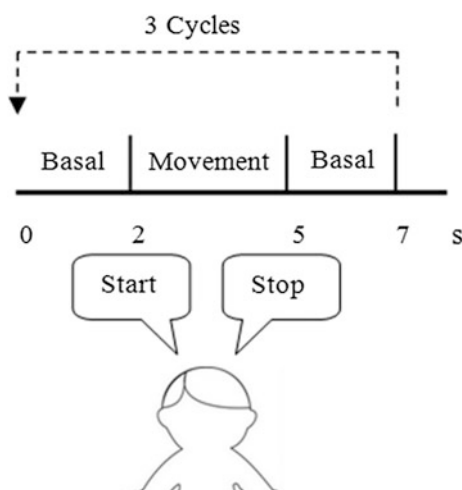
Fig. 3 Illustration of the protocol executed

movement and the software created is responsible to analyze all the data for each movement. The software calculate the RMS curve of each EMG signal, using all the points given, and generate a file containing the values of the peak of each curve, allowing to analyze the muscular groups that generate greater amplitude during its activation in each movement.

2.4 Data Analyzes

Since the muscle-channel relationship is known, it is possible to analyze the data obtained and to estimate how much each muscle contracts in each movement. For this estimation, the mean of all RMS peak curves was analyzed. For each movement, the channels which had the highest average values of the RMS peak represents the most active muscles, and the ones with the lowest average values, the least active.

3 Results and Discussion

To analyze the muscular recruitment, the myoelectric signal was collected through two armbands Myo® positioned on the arm and on the forearm of 8 volunteers, with average age

of 20.71 years, being 6 females. Due to the limited size of the bracelet (19–34 cm), it was not possible to recruit volunteers with large arm circumference [15]. Furthermore, when collecting surface EMG data, it is important to avoid the innervation zone (IZ) [16]. However, since there is a variation in the location of this zone and the Myo has predetermined disposition of the electrodes, the IZ was not considered in this study [16].

To verify the quality of the signal captured by Myo®, after following the experimental protocol, MATLAB© was used to plot the signals obtained. At Fig. 4 there is an example of the signal captured by each channel of the forearm bracelet during one execution of radial deviation. As it is possible to observe, we can see clearly what channels were more activated and when this happened. In addition, the signal is provided by the armband is free of high frequency artifacts. This can be explained by the fact that this armband was created only to identify gestures using the muscle activation, without the need of the details about the EMG.

Also using MATLAB© the RMS curves were plotted in the same figure as the EMG signal to verify its fidelity to the original signal. As it is possible to see in Fig. 5, the curves are consistent with the signal, once they follow the signal rise and its nuances.

Fig. 4 Signal captured from the forearm during radial deviation
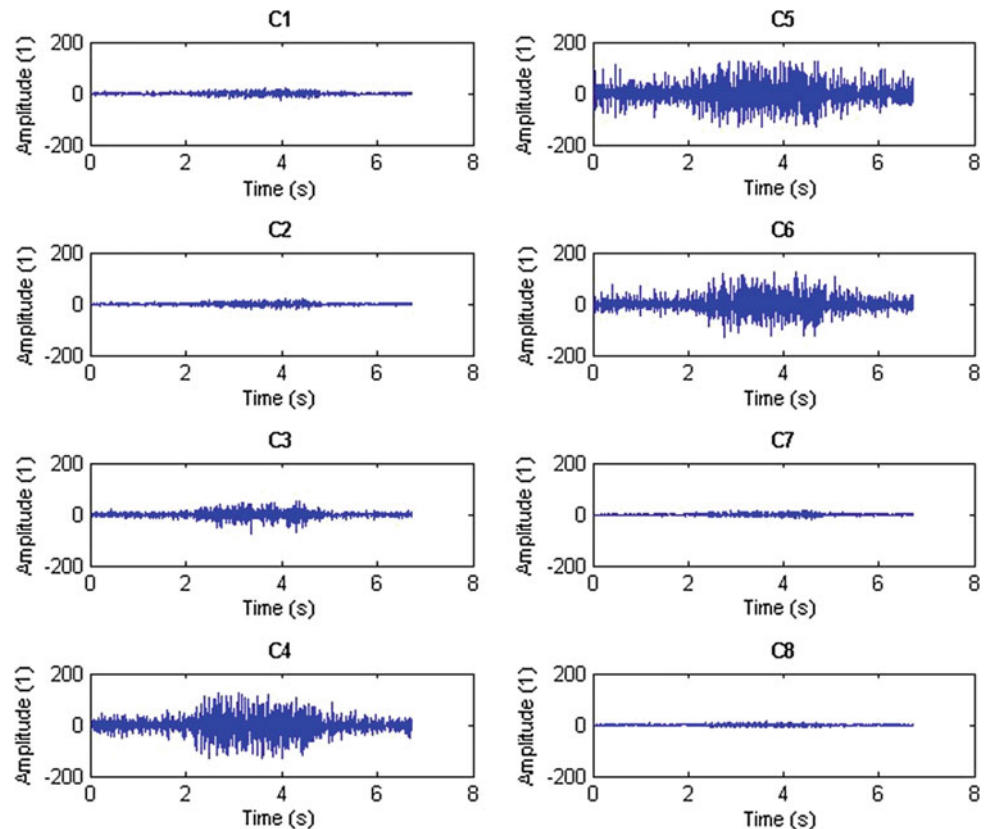
Fig. 5 RMS test with a signal captured from the arm during the elbow extension
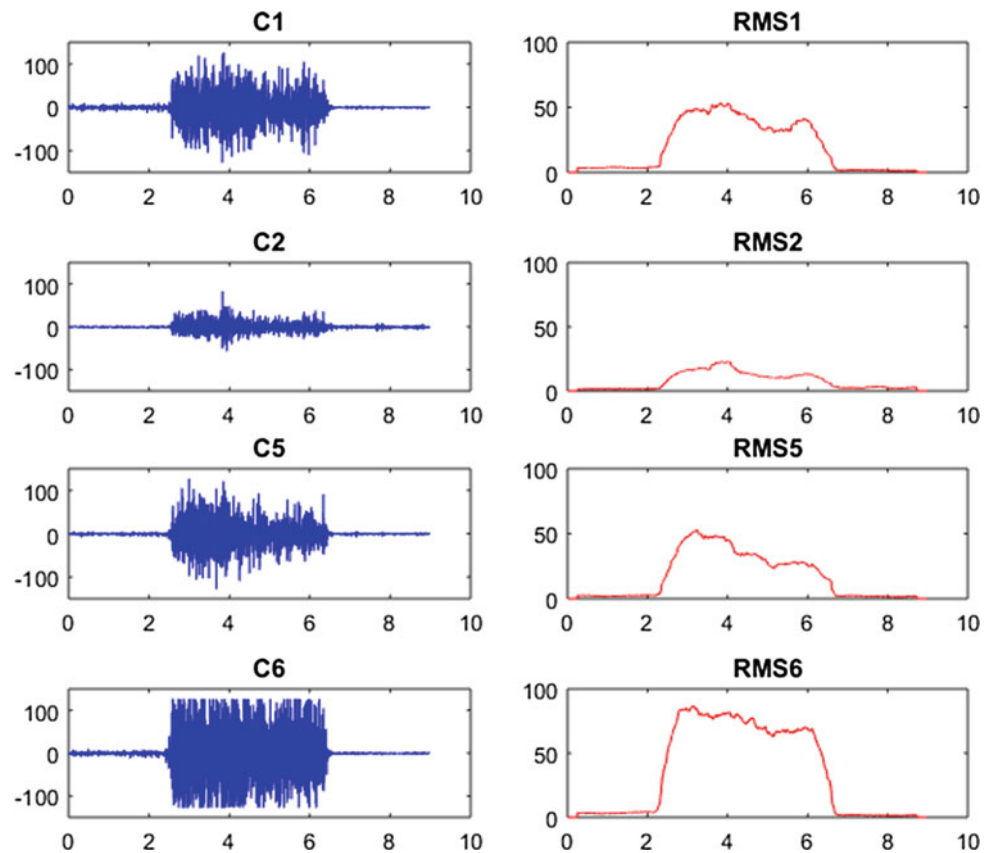
Once the signal is well represented by the RMS curve, the peak value of this curve can be used as reference for analysis. Due that, to represent each movement, an average of the RMS curves peak from all users was computed and graphically presented at Figs. 6 and 7. As it is possible to notice, in some cases, the standard deviation is very large. This happens because some volunteers are stronger than others, resulting in very distinct envelope peaks.

Comparing the results with what has in the literature about the muscle activation for each movement [17], it was possible to notice that in the arm results the movements can be identified easier. On this case the electrodes are in specific muscles, reducing the cross-talk. Thus, the interpretation of the data is facilitated.

Differently, in the forearm there are different layers of muscles, and some of them have almost no surface area where their signal can be captured [18]. This study results corroborate showing the cross-talk influences, causing difficulty to verify the individual muscles activation. This result was already expected since the electrodes, even being small ones, catch de EMG signal from more than one muscle, as could be seen at Table 1. Furthermore, the

electrodes are very close from their neighbor's ones, therefore, the same muscle can activate more than one channel (Fig. 7).

Although seems easier to differentiate movements using the arm muscles, nowadays, big part of transradial myoelectric prostheses with surface electrodes uses the EMG signals from the forearm muscles to control the movements available [19]. This choice is made because it is easier to put the electrodes in the socket of the prosthesis and it is more aesthetical, once they are hidden in the socket. However these prosthesis usually has only two movements available at a time, and if you want to change them, you have switch to different modes [19].

One algorithm that can help to classify the results is an artificial neural networking. This approach uses statistics and predictive treatments to get a better classification of the signals entered [20]. The use of this approach could help to differentiate the activation of the muscles during different movements, especially for the forearm ones. The results obtained using artificial intelligence are in fact used in modern prosthesis to differentiate complex movements automatically [21, 22].
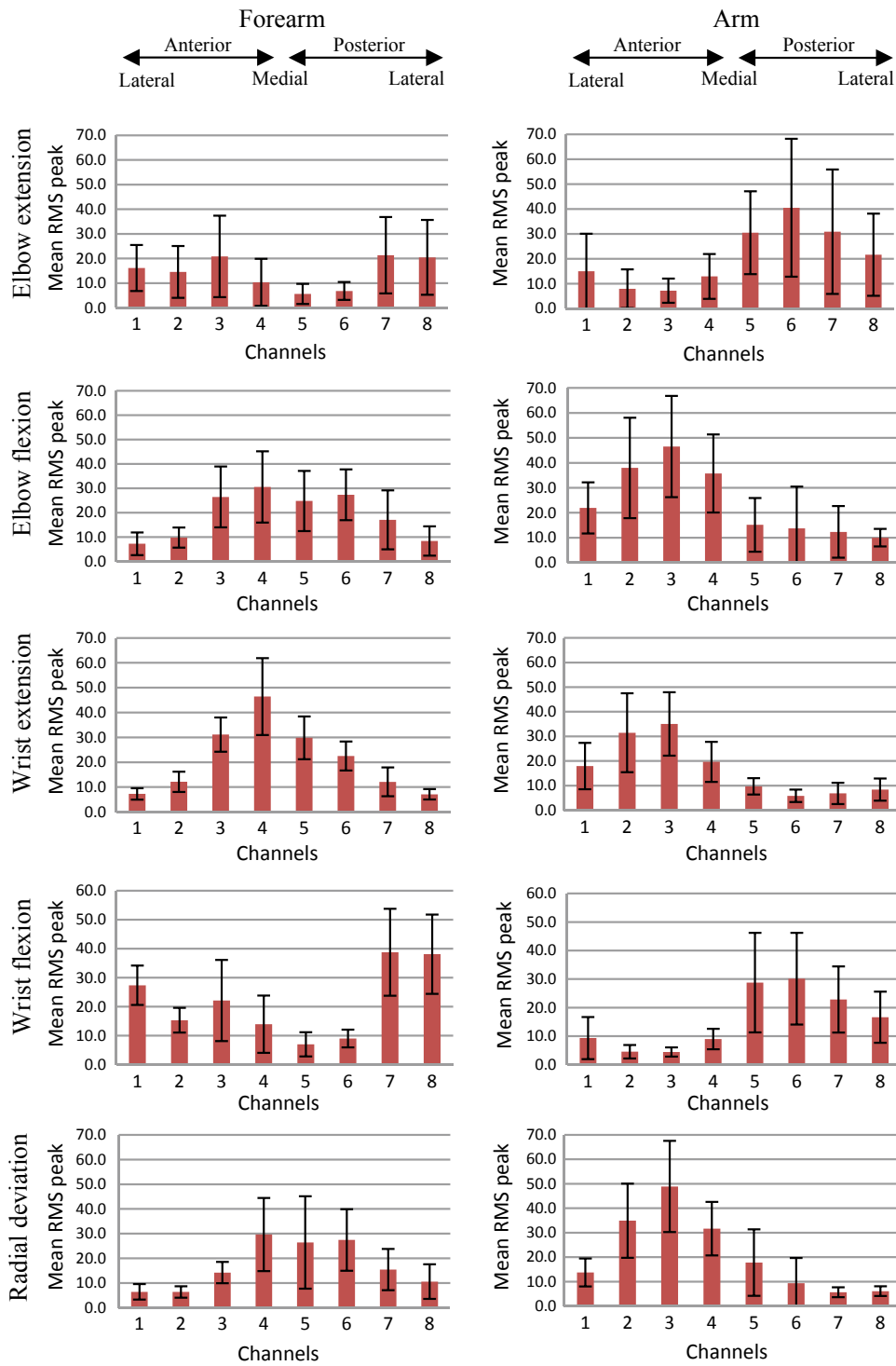
Fig. 6 Mean value of the RMS peak for each channel
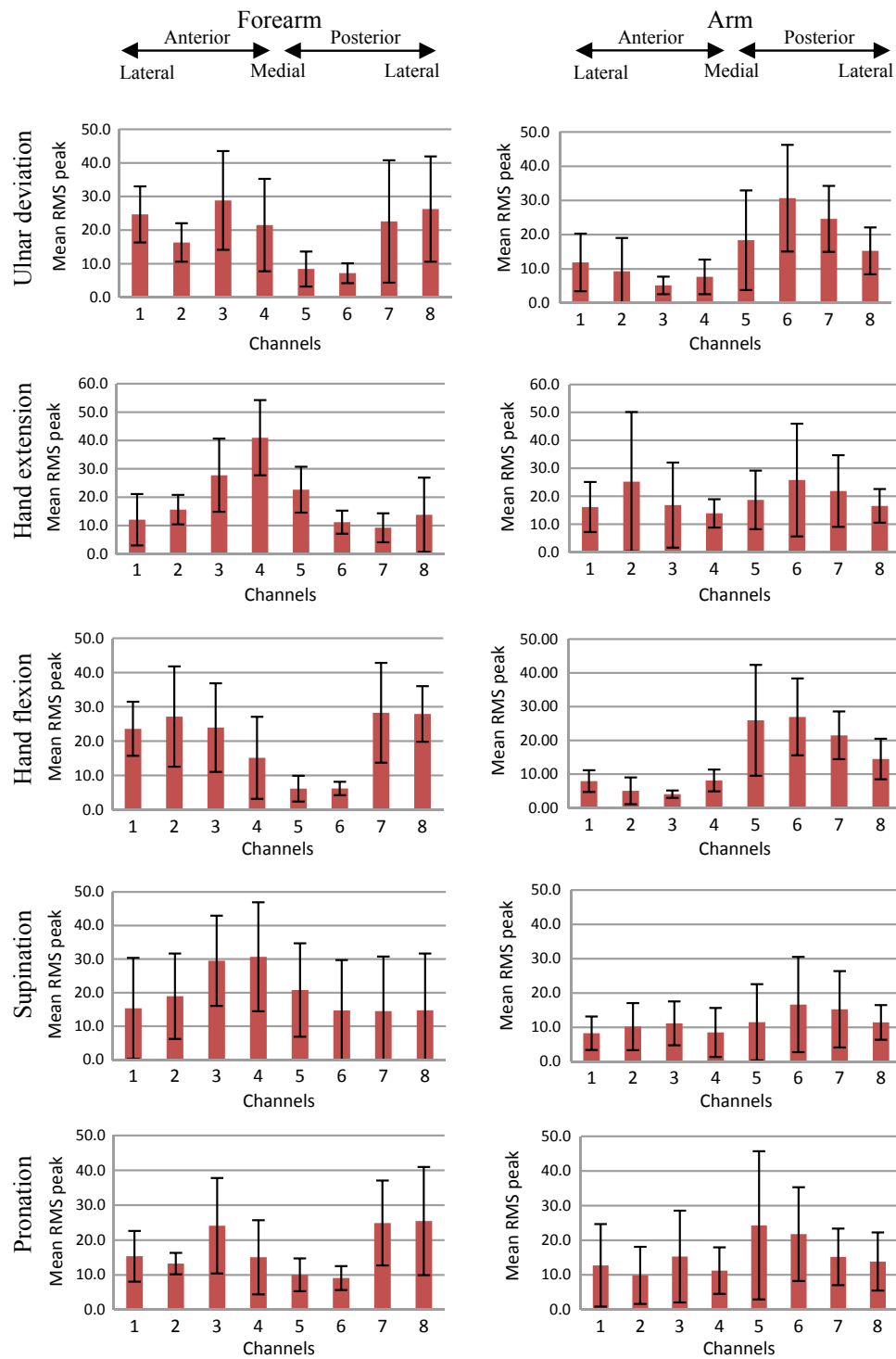
Fig. 7 Mean value of the RMS peak for each channel

4 Conclusion

The idea of using Myo® to study muscle activation emerged, mainly, from the fact of the bracelet having 8 electrodes spatially distributed. This distribution was useful in the arm, where each electrode represented one muscle, facilitating the identification of the movements. However, in the forearm, some electrodes captured signals from more than one muscle, causing cross-talk. This way, the use of muscle groups of the arm is more appropriate for use in myoelectric prosthesis that performs different movements.

For future studies the volunteers will be amputees with transradial amputation and the data will pass through an artificial neural network to be classified between the desired movements.

References

1. Both, J.E., et al.: Acompanhamento de paciente com amputação de membro superior: um estudo de caso. Revista Contexto & Saúde **11**(20), 611–616 (2013)
2. Barros de, K.R., et al.: Metodologia para classificação de sinais EMG para controle de próteses com baixo esforço computacional, Uberlândia (2005)
3. May, B.J., Lockard, M.A.: Prosthetics & orthotics in clinical practice: a case study approach. FA Davis (2011)
4. Carvalho de, G.L.: Proposta de um método de projeto de próteses de membros superiores com a utilização da engenharia e análise do valor. Ph.D. thesis. Universidade de São Paulo, São Paulo (2004)
5. Godoi, Tomás da Silva Martins de; DUQUE, Luciano Henrique; DÍAZ, Francisco Javier de Obaldía. Prótese mioelétrica controlada por redes neurais, Brasília (2014)
6. Bernhardt, P.: #MyoCraft: EMG in the Bluetooth Protocol. 2015. Myo BLOG Homepage. http://developerblog.myo.com/myocraft-emg-in-the-bluetooth-protocol/. Accessed 22 July 2017
7. Abraham, Z., et al.: Control of an affordable hand and wrist prosthesis. In: 15th Research Symposium, Rutgers School of Engineering, pp. 1–13, New Jersey (2015)
8. Thalmic Lab. Deliver Presentations with the Myo Armband. Thalmic Lab Homepage. https://www.myo.com/present. Accessed 22 July 2017
9. Bernhardt, P.: #MyoCraft Fly your Parrot AR. Drone 2.0 with AutoFlight 2015. Myo BLOG Homepage. http://developerblog.myo.com/myocraft-fly-your-parrot-ardrone-2-0-with-autoflight/. Accessed 22 July 2017
10. Fernandes, F.G., Cardoso, A., Lamounier, E.A.: Arm rehabilitation: serious game para apoio à reabilitação utilizando interfaces naturais, Uberlândia (2016)
11. Myo Market Homepage. https://market.myo.com/. Accessed 22 July 2017
12. Bernhardt, P.: #MyoCraft: Logging IMU and Raw EMG Data 2015. Myo BLOG Homepage. http://developerblog.myo.com/myocraft-logging-imu-and-raw-emg-data/. Accessed 22 July 2017
13. The Adventure, Jim Lien. http://colebradburn.com/2013/02/06/biomechanical-work/. Accessed 19 Apr 2018
14. Kamen, G., Gabriel, D.: Essentials of electromyography. Human kinetics, United States of America (2010)
15. Myo Tech Specs Homepage. https://www.myo.com/techspecs. Accessed 08 June 2018
16. Defreitas, J.M., et al.: Innervation zone location of the biceps brachii, a comparison between genders and correlation with anthropometric measurements. J. Electromyogr. Kinesiol. **20**(1), 76–80 (2010)
17. Houglum, P.A.: Bertoti, D.B.: Brunnstrom's clinical kinesiology. FA Davis (2011)
18. Mogk, J.P.M., Keir, P.J.: Crosstalk in surface electromyography of the proximal forearm during gripping tasks. J. Electromyogr. Kinesiol. **13**(1), 63–71 (2003)
19. Li, G., Schultz, A.E., Kuiken, T.A.: Quantifying pattern recognition—based myoelectric control of multifunctional transradial prostheses. IEEE Trans. Neural Syst. Rehabil. Eng. **18**(2), 185–192 (2010)
20. Barros de, K.R., et al.: Metodologia para classificação de sinais EMG para controle de próteses com baixo esforço computacional, Uberlândia (2005)
21. Favieiro, G.W.: Controle de uma prótese experimental do segmento mão-braço por sinais mioelétricos e redes neurais artificiais, Rio Grande do Sul (2009)
22. Mattioli, F., et al.: Utilização de redes neurais para a classificação de sinais emg aplicados no controle de próteses virtuais de mão. Proceedings of the WRVA, pp. 230–235, Uberlândia (2010)

3D-Endoluminal Ultrasound Biomicroscopy of Mouse Colon Tumor and Mimicking Phantom

Rodrigo Pereira de Oliveira, Rossana Colla Solleti, and João Carlos Machado

Abstract

Colon cancer is the third most common cancer in Brazil and in the world. Despite the high incidence and high mortality rate, most of the cases could be prevented by using accurate techniques for early cancer detection. In this sense, it is important to conduct preclinical studies using animal models of colon diseases, which requires the implementation of appropriate instrumentation. Therefore, a technique to generate three dimensional endoluminal ultrasound biomicroscopic images (eUBM-3D) of the mouse colon was developed using an ultrasound system operating at 40 MHz. The eUBM-2D (bi-dimensional) images were acquired and used to construct the eUBM-3D images. The technique was initially tested in a phantom mimicking the colon of small animals and subsequently in control- or tumor-bearing mouse colon, in vivo, with some of the eUBM-2D images segmented to highlight the region of interest. The eUBM-3D system allowed the identification of colon layers and lesions, or tumor, in both phantom and mouse colon.

Keywords

Phantom • 3D ultrasound biomicroscopy • Colon cancer • Mouse

1 Introduction

Colorectal cancer is among the third and fourth most common type of cancer diagnosed worldwide [1]. The United States National Cancer Institute estimated 140,250 new cases of cancer in 2018 and 50,630 deaths as a result of the disease [1]. The Brazilian National Cancer Institute (INCA) estimates the detection of 36,390 new cases, per year, of colorectal cancer in Brazil to biennium 2018–2019 [2], with colorectal cancer being the third most frequent cancer in men and the second among women. Despite the high incidence and high mortality rate, most cases of colon cancer could be prevented by improving diagnostic techniques for early detection and follow-up [3, 4].

In vitro studies using materials that reproduce ultrasonic wave propagation in each biological tissue are of vital importance in developing diagnostic equipments and techniques. In this context, phantoms that mimic different biological tissues are used as an in vitro low cost tool during scientific investigations [5, 6]. Regarding the in vivo situation, then animal models of human diseases are also vitally important in preclinical studies to develop new diagnostic instrumentations and treatment strategies. In this sense, several advances have been made including insulin discovery, vaccine development, the establishment of therapeutic use of antibiotics and the development of techniques for organ transplants [7]. Animal models are advantageous once they provide information about the physiology of the organism. However, the inability or exhaustion of other methods of study such as in vitro approaches should be firstly observed. Mice are the most common animals used for preclinical studies, given the following advantages: reduced size, short gestation period, and easy breeding and maintenance [7].

The standard procedure for the diagnosis of lesions and tumors in the intestinal mucosa is colonoscopy. However, endoscopic examinations are not always able to identify small lesions, especially non-polypoids and other lesions

R. P. de Oliveira (✉) · J. C. Machado
Biomedical Engineering Program - COPPE/UFRJ, Rio de Janeiro, Brazil
e-mail: rpo@peb.ufrj.br

R. C. Solleti
Pharmacy Unit, Universidade Estadual da Zona Oeste, Rio de Janeiro, Brazil

J. C. Machado
Post-Graduation Program on Surgical Sciences - FM/UFRJ, Rio de Janeiro, Brazil
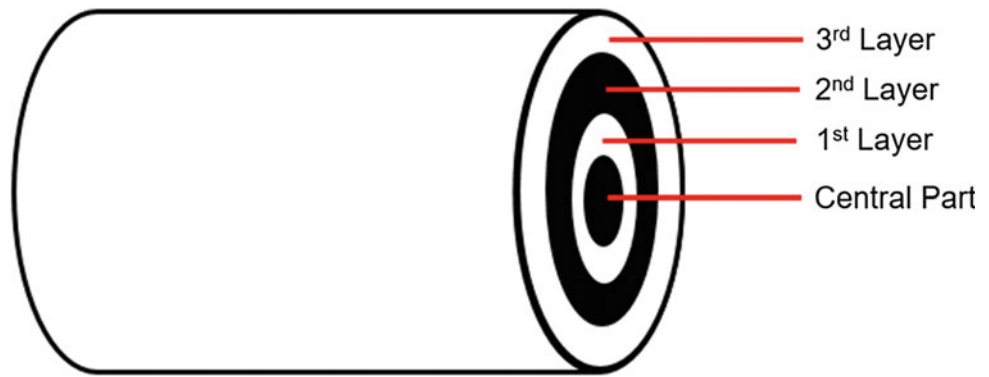
located inside the colon wall, since inspection is only of the surface. Thus, some studies have proposed the use of endoscopic ultrasound in the evaluation of colon lesions in humans [4, 8, 9]. However, conventional ultrasound and colonoscopy are operator-dependent technologies and despite of that, colonoscopy is still used for almost all colonic cancer diagnosis [1]. Therefore, new imaging technologies are needed to increase the detection rate of tumors that are difficult or impossible to detect by current techniques, thus providing real time histological analysis or lesion detection [4, 8, 9], and to circumvent the operator dependency.

The current work focus on the generation of three dimensional (3D) ultrasonic images as a mean to implement an ultrasonic imaging technique that provides dynamic information of the whole organ segment and thus precludes the condition of operator-dependent static images, attributed by specialists, of the commonly used two dimensional (2D) ultrasound images for diagnosis. In this sense, 3D endoluminal ultrasonic biomicroscopy (eUBM-3D) images of colon tumors in a mouse were obtained.

2 Materials and Methods

2.1 Phantoms

Two phantoms were made: one multilayered phantom, named Ph1, to mimic the healthy colon walls of small animals and one multilayered phantom, named Ph2, to mimic a colon wall with a lesion of known dimensions. The phantom wall was made of porcine gelatin powder (G2500; Sigma Chemical, St. Louis, MO, USA), dissolved in water and mixed with silica powder (S-5631; Sigma Chemical, St. Louis, MO, USA) to act as a scatterer and cause the speckle in the ultrasound image. The layers are classified as hyperechoic (high brightness), or hypoechoic (low brightness). The hyperechoic layer consists of gelatin, dissolved in deionized water in a proportion of 15% of the mass of water, and silica powder (scattering agent), at the concentration of

5% of the water mass. The hypoechoic layer consists of only gelatin dissolved in water in a proportion of 15% of the mass of water.

In both phantoms, the inner (first) and outer (third) layers mimicking the *mucosa* + *submucosa* and *serosa* layers, respectively, were composed of the same material and were hyperechoic. The intermediate (second) layer, mimicking the *muscularis externa* layer, was hypoechoic (Fig. 1). The phantom central part, which mimics colon lumen, was filled with saline solution before image acquisition.

For phantom manufacturing, a melted mixture of gelatin and silica powder (to form the inner layer) was initially deposited over a plastic rod mold (4.2 mm diameter). After its solidification, melted gelatin was deposited to form the intermediate layer. Following this second layer solidification, then the melted mixture of gelatin and silica powder was deposited over the intermediate layer. The uniformity of layers was achieved rolling the rod over its axis as the gelatin mixture solidified. The mimicking lesion in phantom Ph2 was made using a rod mold containing a circular hole (3 mm diameter). Therefore, the phantom Ph2 had an elevation on the inner layer.

2.2 Animal

A male C57BL/6J lineage and 15-weeks old mouse was used All the procedures were approved by the Ethics Committee for Animal Research in Laboratory of the Federal University of Rio de Janeiro (DAHEICB042). The animal was maintained at room temperature with appropriate circadian cycle and diet.

2.3 Tumor Induction

Azoxymethane (AOM) and Dextran Sulfate Sodium (DSS) were used to induce colon tumors in the mouse [10]. AOM, a colon-specific carcinogen, associated with DSS, a mucosal-irritant agent, mimics an inflammation-associated

colon carcinogenesis [10]. The animal was subjected to a single intraperitoneal injection of AOM (A5486; Sigma Aldrich, St Louis, MO) at a concentration of 12.5 mg/kg. One week following AOM administration, the animal was fed with water containing 3% DSS salt, 36,000–50,000 Da (02160110; Sigma Aldrich), during 1 week. The animal received solid food and water ad libitum, with regular water given after DSS intake.

2.4 Animal and Phantom Positioning System

The basis to generate a eUBM-3D image consists in acquiring several equally spaced eUBM-2D images. Therefore, a positioning system was developed and mounted to promote alignment and relative positioning adjustment between animal and endoscopic instrumentation as well as to promote the automatic acquisition of a set of equally spaced eUBM-2D images. The system, depicted in Fig. 2, contains a linear stage (MFA-CC, Newport, Irvine, California, USA), activated by a DC motor, with a travel range of 25 mm and precision of 0.125 µm between each step, controlled by a motor driver (ESP 300 Newport, Irvine, California, USA). Over the linear stage is fixed the colonoscope (Hopkins II 64301 AA; Karl Storz, Tuttlingen, Germany), with 1.9 mm outer diameter and 10 cm length, passing through a trocar (27021 CO; Karl Storz) having 2.5 mm outer diameter and 1.1 mm working channel diameter. The colonoscope has a camera (H3-Z; Karl Storz, Tuttlingen, Germany) attached toits ocular lens and the trocar working channel was used to guide the eUBM mini-probe.

2.5 eUBM Image Acquisition System

An eUBM system, that generates radial-scanned conventional grayscale B-mode ultrasonic images [6], was used for the acquisition of eUBM-2D images. This system uses a commercially available 3.6-F mini-probe ultrasound catheter (Atlantis SR Pro Coronary Imaging Catheter; Boston Scientific Corporation, Natick, MA, USA), operating at 40 MHz, to transmit pulses of ultrasound and receive the echo signals. The sequence of equally spaced eUBM-2D images was obtained with an automated pullback of the whole set comprising the trocar, endoscope, camera and mini-probe catheter inserted into the trocar's working channel. In this sense, eUBM-2D images, spaced by 50 µm, were acquired in sequence under the action of the motorized linear stage. The entire eUBM-2D and colonoscopy imaging system is presented in Fig. 3.

During eUBM imaging acquisition, the phantom was immersed in a water bath placed over the animal platform depicted in Fig. 2. The trocar (with colonoscope and mini-probe inside) was passed through a hole on the wall of the water bath container and was inserted directly into the phantom lumen. The hole on the wall of the water bath container had a seal valve to prevent water escaping out of the container.

During eUBM image acquisition of the mouse colon, the animal was kept under inhalatory anesthesia with isoflurane (Cristália, São Paulo, Brasil), at 5% for induction and 1.5% for maintenance, in 1.5 L/min of oxygen, using the Laboratory Anesthesia System (EZ-7000; Euthanex, Palmer, PA, USA). While anesthetized, the animal was placed in dorsal

Fig. 2 Alignment system with the linear stage, the trocar-colonoscope unit, the camera, and the ultrasound mini-probe inserted into the trocar's working channel

Fig. 3 eUBM and colonoscopy imaging system containing the anesthesia system, the positioning system, the motordrive, the linear stage driver to control the linear stage motion (used to pull-back the mini-probe), the colonoscopy video processing unit, the eUBM power supply and the xenon light source (which was coupled to the colonoscope for lumen lighting
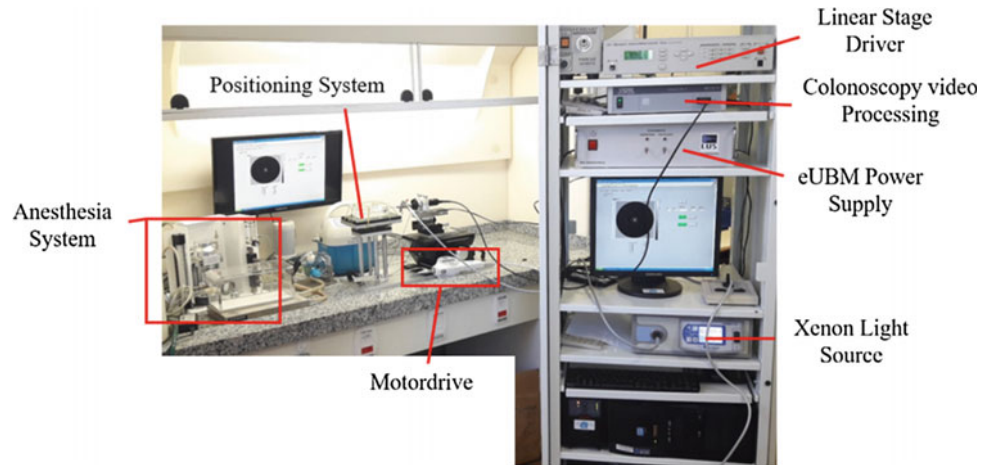
decubitus over the heated animal platform (@ 37 °C). The eUBM-2D images were acquired in vivo.

2.6 eUBM-3D Image Reconstruction

The set of equally spaced eUBM-2D images was processed with the public domain Java image processing program ImageJ (version 1.47v; NIH Image, Bethesda, MD, USA). Prior to the generation of the eUBM-3D image, segmentation of the tumor sites was comprised semi-automatically using the LiveWire2D tool to contour the site at each eUBM-2D image. The segmentation of the simulating lesion was performed contouring it using the oval selection tool in ImageJ. Thereafter, the segmented sites were colored in red in order to become distinguishable inside the eUBM-3D grayscale image. Finally, the eUBM-3D image was generated executing the 3D plugin of ImageJ.

3 Results

3.1 Phantoms

Figure 4 depicts details of phantom Ph1, including an external view (4a), a cross-section view (4b), an eUBM-2D cross-sectional image (4c), the eUBM-3D images corresponding to a phantom segment of 2.2 mm (4d–e) and an endoscopic image (4f) acquired simultaneously with the eUBM-2D image. The central part (lumen) and the three

layers are clearly observed in the eUBM-2D image, with the inner and outer layers as hyperechoic, due to the presence of silica powder used as scatterer, and the middle layer as hypoechoic. eUBM-3D images shows cross-sectional (4d) and lateral (4e) views of the phantom. Figure 4f shows a colonoscopic image, which was acquired simultaneously with the eUBM-2D imaging. The phantom wall layers are also clearly observed in the eUBM-3D images that also contain the interior of the phantom, the ultrasound mini-probe and some air bubbles that were impregnated in the phantom inner wall.

Figure 5 presents the results for phantom Ph2, including the eUBM-2D image (5a), the eUBM-2D image containing the lesion mimicking site colored in red (5b) and the eUBM-3D images of the 4.0 mm phantom segment (5c–d). The eUBM-3D image of the mimicking lesion site corresponds to a set of 57 images spaced by 50 mm each, which corresponds to a lesion-mimicking site with 2.75 mm in the phantom axial direction.

3.2 Animal

The results for the mouse colon are presented in Fig. 6, including an eUBM-2D image of the colon site without a lesion (Fig. 6a). The corresponding colonoscopy image (Fig. 6b), an eUBM-2D image of the colon site with the tumor segmented and colored in red (Fig. 6c) and the eUBM-3D image for a colon segment of 3.2 mm containing the lesion extended along the axial direction of the colon.

Fig. 4 Details of phantom Ph1, including: **a** an external view of phantom. **b** A phantom cross-sectional view, with all three layers visible. **c** The phantom eUBM-2D cross-sectional image. **d** eUBM-3D front-view image. **e** eUBM-3D side-view image. **f** Endoscopic image of the phantom, showing the mini-probe and the presence of air bubbles
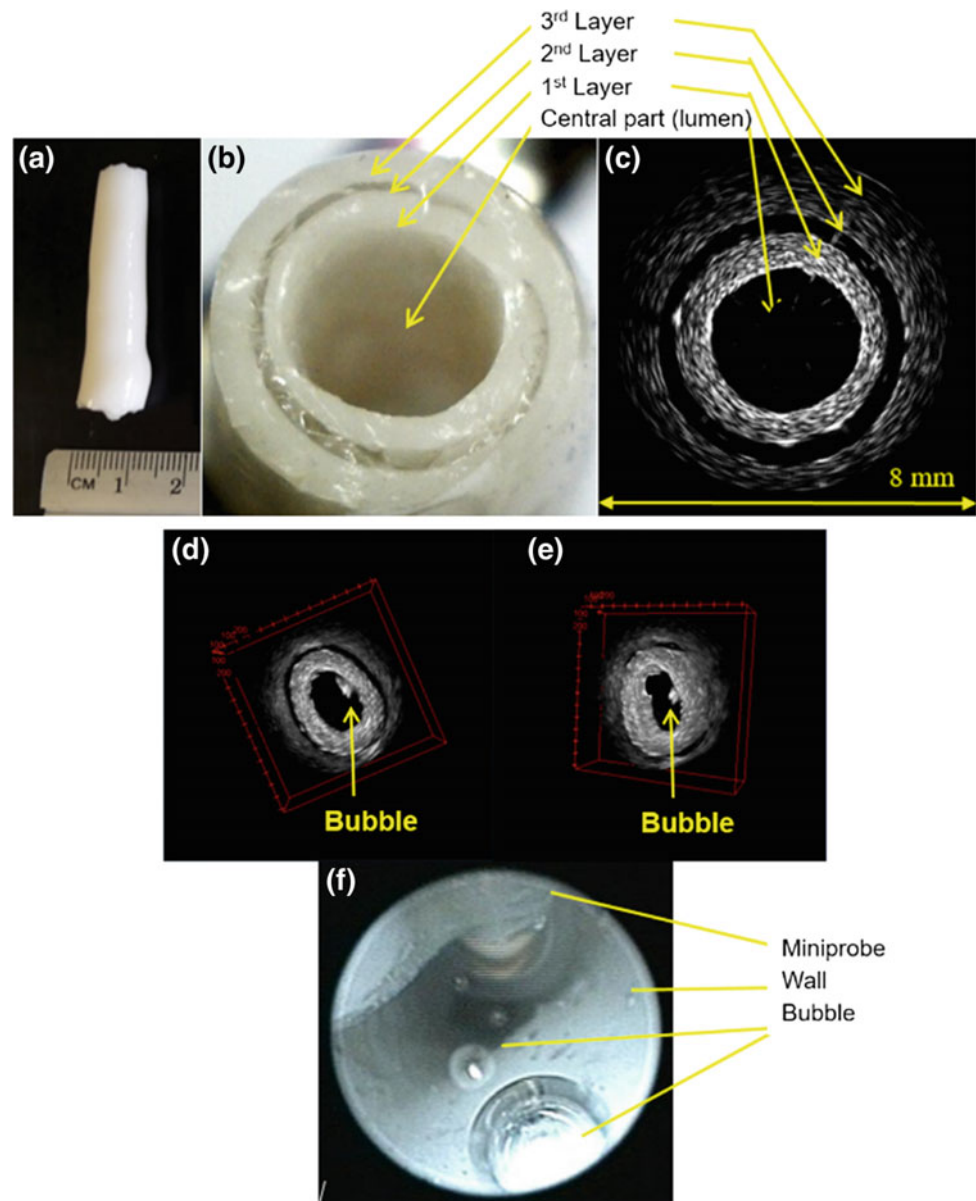
It is possible to observe the different colonic layers: *mucosa + submucosa* (hyperechoic) and *muscularis externa* (hypoechoic)

A coronal view of the colon eUBM-3D image containing the lesion, presented in Fig. 7a, was generated after clearing the part of the image outside the region of interest (ROI) indicated with an yellow rectangle (Fig. 7b), for all eUBM-2D images. The elevations and depressions related to the lesion are noticed in the eUBM-3D image of the colon segment (Fig. 7a).

4 Discussion

Currently, the gold standard tool for colon examination is optical colonoscopy, which allows analysis of the mucosal surface and observation of possible lesions. As seen in the results section, the eUBM-2D image allows the visualization of other colonic layers beneath the mucosa, conferring an advantage in detecting changes not noticeable by colonoscopy. However, ultrasound 2D images are operator-dependent.

Fig. 5 Images of phantom Ph2.
a The eUBM-2D image. **b** The
eUBM-2D image with the lesion
colored in red. **c–d** eUBM-3D
front and side-view images for a
phantom segment of 4.0 mm,
including the mimicking lesion in
red
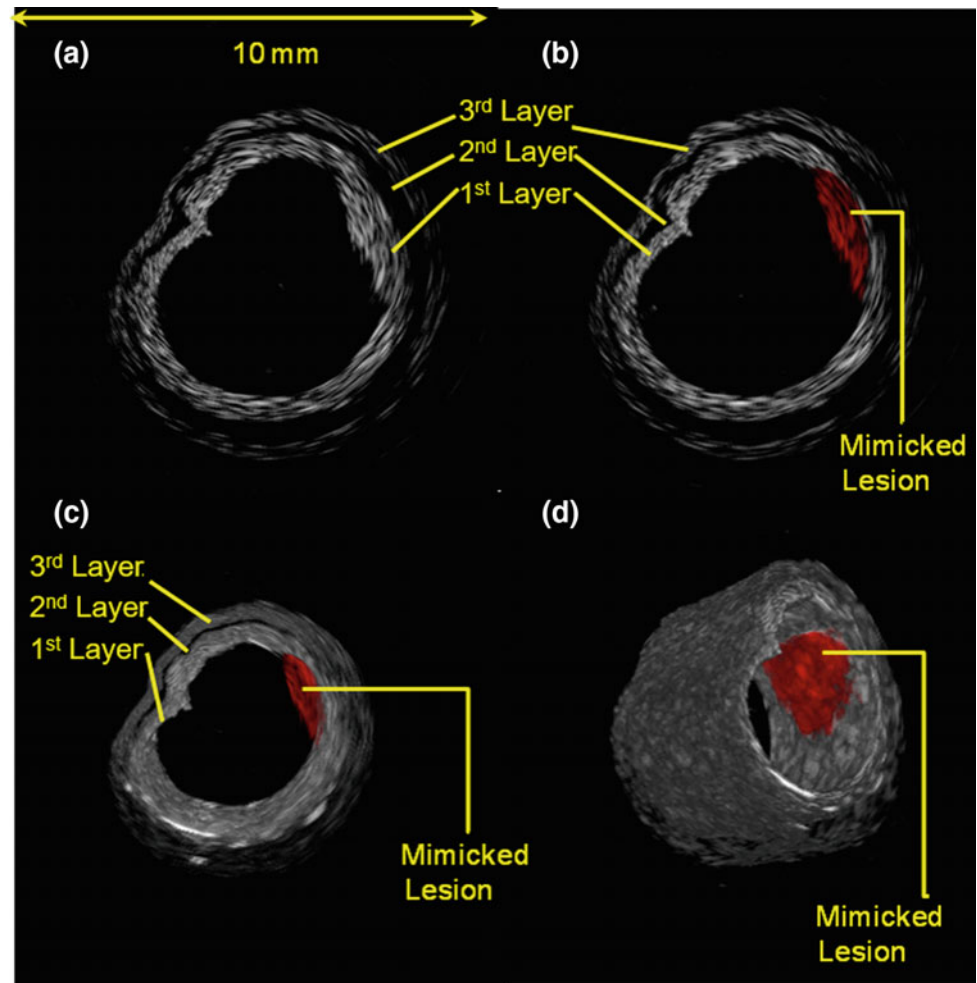
On the other hand, 3D imaging allows the possibility of determining lesion or tumor volumes, thus decreasing the operator-dependent characteristic of 2D US images. Segmentation allows differentiation of the tumoral area from healthy regions. These parameters have direct implications on tumor classification, treatment directions and follow-up.

The mini-probe displacement for image acquisition and 3D reconstruction was performed mechanically with controlled and predetermined step, which allows an exact knowledge of the rendered length. Images with displacements of 50 µm (of the animal colon), 10 µm (phantom Ph1) and 50 µm (phantom Ph2) were obtained, with the equip-ment displacement accuracy of 0.175 µm. Thus, a margin below the capacity of the equipment was used, to move the mini-probe in the acquisition of images.

The segmentation of medical images is used to analyze a region of interest and the main challenge in the segmentation of ultrasonic image is the characterization of the texture and geometry of a lesion compared to the surrounding tissue. Unfortunately, this image processing is strongly influenced by the quality of the data, which is compromised by wave attenuation, speckle and shadows. In addition, operator training may also be required to improve precision of anchoring the segmentation border.

Fig. 6 **a** eUBM-2D image of mouse colon, showing colonic walls. **b** Colonoscopy image. **c** eUBM-2D image of mouse colon with lesion site highlighted in red. **d** eUBM-3D image of mouse colon with lesion site highlighted in red
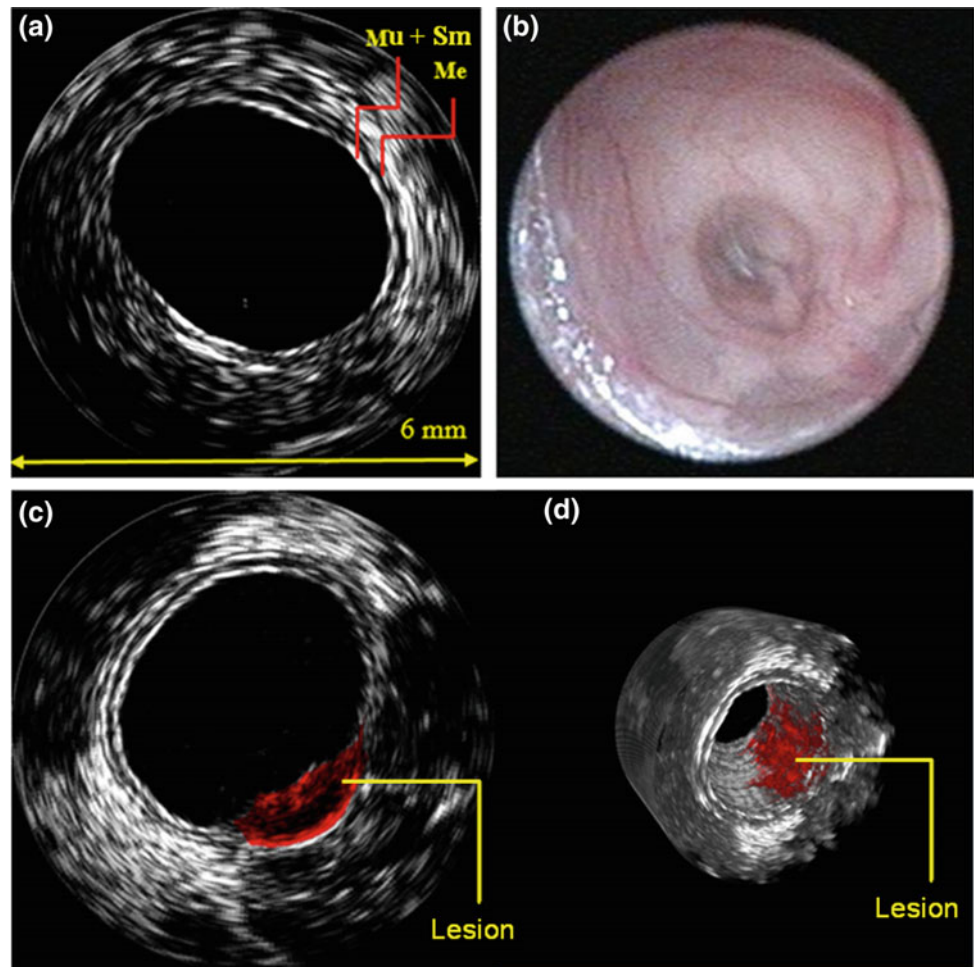
Fig. 7 **a** eUBM-3D images of mouse colon segment containing the lesion; **b** eUBM-2D image of mouse colon with lesion site inside the region of interest (ROI) marked by an yellow square
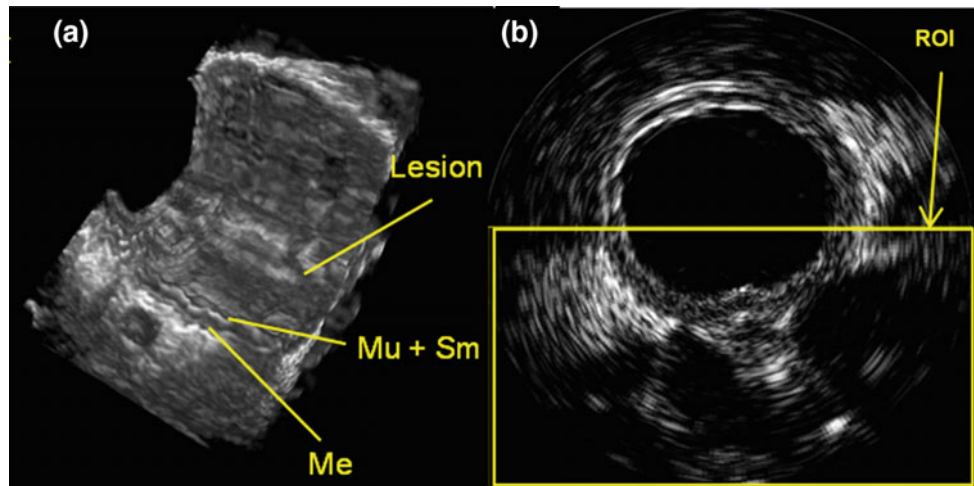
5   Conclusion

eUBM images of the multilayer phantoms prepared to mimic mouse colonic walls and lesions were acquired. These images presented an anatomic shape as well as scattering characteristic of the layers similar to those of the animal colon and lesions. Thus, it was possible to mimic colonic tissue, the lesion and to test eUBM instrumentation.

The eUBM-3D generated images also allowed the analysis of the phantom, lesion and colon layers of animal. It was possible to identify layers in the phantom and in the animal as: the *mucosa + submucosa* and the *muscularis externa*, as well as to identify lesions.

Thus the eUBM-3D system was able to render 3D images of structures with millimetric dimensions, characterizing different layers of the animal colon.

The possibility of rendering the eUBM-3D system allows any operator to change the viewing angle, allowing a new interactive evaluation of the volume even after the examination, for evaluation of tumor penetration and volume estimation.

Conflict of Interest The authors certify that they have no conflict of interests in the subject matter or materials discussed in this manuscript.

References

1. Nacional Cancer Institute: Homepage. http://seer.cancer.gov/statfacts/html/colorect.html. Accessed 16 Apr 2018
2. Instituto Nacional de Câncer: Homepage. http://www.inca.gov.br/estimativa/2018/sintese-de-resultados-comentarios.asp. Accessed 16 Apr 2018
3. American Cancer Society: Colorectal cancer facts & figures 2011–2013. American Cancer Society, Atlanta, p. 4 (2011)
4. Soletti, R.C., Alves de, K.Z., Britto de M.A.P., Matos de D.G., Soldan, M., Borges, H.L., Machado, J.C.: Simultaneous follow-up of mouse colon lesions by colonoscopy and endoluminal ultrasound biomicroscopy. World J. Gastroenterol. https://doi.org/10.3748/wjg.v19.i44.8056 (2013)
5. Ryan, L.K., Foster, F.S.: Tissue equivalent vessel phantom for intravascular ultrasound. Ultrasound Med. Biol. **23**(2), 261–273 (1997)
6. Oliveira, R.P., Geremia, J., Soletti, R.C., Machado, J.C.: Geração de imagens 3D de Biomicroscopia Ultrassônica endoluminal do cólon de camundongo XXV Congresso Brasileiro de Engenharia Biomédica (2016)
7. Chorilli, M., Michelin, D.C., Salgado, H.R.N.: Animais de Laboratório: o camundongo. Revista de Ciências Farmacêuticas Básica e Aplicada **28**(1), 11–23 (2007)
8. Alves, K.Z., Soletti, R.C., Britto de, M.A.P., Matos de, D.G., Soldan, M., Borges, H.L., Machado, J.C.: In vivo endoluminal ultrasound biomicroscopic imaging in a mouse modelo of colorectal cancer. Acad. Radiol. **20**(1) (2013)
9. Soletti, R.C., Britto de, M.A.P., Borges, H.L., Machado, J.C.: Analysis of tumor morphology and vasculature in an animal model of colorectal cancer using in vivo contrast-enhanced endoluminal ultrasound biomicroscopy. In: Ultrasonics Symposium (IUS), 2012 IEEE International (2012)
10. Tanaka, T.: Colorectal carcinogenesis: review of human and experimental animal studies. J. Carcinog **8**, 1–19 (2009)

Attentional Bias for Faces in Relation to Severity of Depressive Symptoms: An Eye-Tracking Study

Germano R. Figueiredo, Daniel Campos, Wagner L. Ripka, and Leandra Ulbricht

Abstract

Depressive symptoms are associated with attentional bias for negative stimuli. A large body of research of attentional bias in subjects with affective disorders relies heavily on manual reaction time measures that cannot delineate the time course and components of attentional bias precisely. This study proposes to use the eye tracker technology to detect attentional bias for faces in individuals with different severity of depressive symptoms. All participants completed the Beck Depression Inventory-II (BDI-II). The eye tracker test included 4 types of facial expressions: neutral, sad, angry and happy. For the attention indexes, it was analyzed: total time for eye events, total fixation duration, ratio of total fixation and eye events, and fixation duration on each face. The free-viewing task was composed of 72 trials. The total test duration was 6 min and 36 s. In total, 31 individuals took part in this study (15 were patients with minimal severity, 5 with mild severity, 6 with moderate and 5 with severe diagnose). The results showed that severe BDI-II participants' score are significative ($p = 0.001$) and related to lower faces fixation and total fixation duration on each face ($p = 0.001$). In additional, a large difference was verified for null events (without fixation at the area of interest) with the severe group (75%). Analysis of data demonstrates the possibility to use this technology in detecting patterns of eye movements related to psychopathology. With that, it is an opportunity to improve diagnosis technics in mental health research and clinical assessment.

Keywords

Eye tracking • Attentional bias • Depression

1 Introduction

Depressive symptoms are related to increased attention towards negative stimuli and the loss of positive information in the social and emotional interaction between the individual and the environment [1]. According to behavioral and cognitive models, these attentional bias are crucial to the onset and maintenance of affective disorders [2, 3].

Studies of attentional bias in individuals with affective disorders have primarily used reaction time (RT) as a measure of attention [4]. With "dot-probe task" and "stroop-color name", for example, some evidence has demonstrated that depressed children have a tendency to respond differently to negative stimuli compared to neutral or positive stimuli [5, 6]. In these experiments, a probe task appeared with two or more types of stimuli. Participant was asked to press a button. Then RTs (key press) were measured to assess participant's attentional bias.

The application of RT experiments contributed to innovation and improvement of findings in cognitive and behavioral science. However, when using the RT paradigm, important information about the time course and the components of attentional bias are missed [7]. The distal relation between a key press and attention and the use of RT measurement only, cannot fully delineate the time course and components of attentional bias precisely [8]. Also the asses to attentional bias is indirect and implicit [9].

With the advances in this area, researchers have used eye tracking technology. Eye tracker devices provide gaze analysis of the sequential eye movements, saccades, fixation, pupil dilatation and blinks in real-time and continuous measure of eye positions [7, 10].

Recent studies investigated the attentional bias in individuals suffering from depression and anxiety and used eye tracking. For depression, the severity of depressive symptoms is found to be associated with longer fixation duration on "negative" images compared to positive ones. For anxiety, the severity has been found to be related to attention on

G. R. Figueiredo (✉) · D. Campos · W. L. Ripka · L. Ulbricht
Federal University of Technology – Paraná, Curitiba, Brazil
e-mail: germanorosafigueiredo@gmail.com

threat-related information while avoiding negative visual information [11, 12]. These studies suggest that affective disorders are correlated to attentional gaze fixations durations and eye movement patterns with regard to positive and negative information.

Even though, some of the results remain unclear regarding the type of attentional bias to negative information and the "modulation" of attention in depressed individuals [12, 13]. Besides that, the extensive literature on mental health examination in the clinical context has shown that the diagnosis of depression and other disorders are usually made by using psychological questionnaires, interviews and observation [14]. The importance of having an objective method like eye tracking seems promising for more precise data and consequently a better understanding of psychopathologies.

To overcome RT limitations and suggest improvement in psychodiagnosis, the present study uses the eye tracking technology to evaluate attentional bias for faces in individuals with different severity of depressive symptoms. This study used an eye tracker device that allowed for recording at frequency of 500 Hz. The Brazilian faces' data base was used to select faces with emotional expressions. Emotional facial expressions (angry, sadness, happy and neutral) are used as stimuli because they contain more interpersonal information, and simulates social context appropriately [9].

2 Methods

2.1 Participants

The present study included outpatients and undergraduate students from a city localized in the south of Brazil. The outpatients consisted of patients with depression and affective disorders. All the participants signed written informed consent. This study was approved by the ethics and research committee through *Plataforma Brasil* under the protocol no. 62432616.3.0000.5547.

2.2 Eye Tracking Device

Participant's eye movements were recorded using a RED 500 infrared eye tracking system (SMI) that allowed for recording at frequency of 500 Hz. The direction of gaze was measured with x and y coordinates. Areas of Interest (AOIs) were also identified. The system was composed of a DELL Notebook Precision M4800 and a DELL 22″ monitor. The eye tracker was equipped by tree software: BeGaze, iViewX and Experiment Center, that allow for calculating gazes based on the corneal reflex and the pupil position. The

device has an accuracy of 0.4º of visual angle and a short latency <4 ms.

The head of the participants was kept stable and at a distance of 60 cm from the monitor and the eye tracker device.

2.3 Self-report Measure of Depressive Symptoms

All participants completed the Beck Depression Inventory-II (BDI-II) [15], a clinical assessment tool that contains 21 items. The items correspond to subgroups of depressive symptoms. Each item is rated on a 4-point Likert scale ranging from 0 to 3. The total BDI-II score ranges from 0 to 63; The classification of severity is as follows: 0–13 (minimal); 14–19 (mild); 20–28 (moderate); 29–63 (severe).

2.4 Procedure and Stimuli

Procedures were based on previous studies [11, 16]. After signing informed consent, BDI-II was administered. Subsequently, the participant was sat centrally in front of the monitor in the laboratory to view the stimuli freely while their eye-movements were recorded.

The stimuli consisted of pairs of images (Fig. 1) of emotional (angry, sad, happy) and neutral facial expression made by the same actor. The set of 6 male and 6 female faces used in the present study was selected from the Brazilian Facial Expressions Database [17]. A free-viewing task of the images was used to increase external validity.

The free-viewing task was composed of 72 trials (Fig. 2). Emotional and neutral expressions were presented equally on both left and right side of the screen. Each trial began with a black screen for 500 ms, followed by the presentation of a white fixation cross centered on the screen for 500 ms. The cross is replaced by a random one-digit number (1–9) that remains for 1000 ms on the screen. Participants were instructed to verbalize this number. After the offset of the random one-digit number, a pair of faces was then displayed on the screen for 3500 ms. Participants were instructed to freely observe the images.

2.5 Attentional Indexes

The following variable was extracted and analyzed, based on previous research [11, 16]: total fixation duration on each type of facial expression in each trial.

Fixations are defined as periods above 100 ms where the eyes have a focal point concentration and standard deviation of less than 0.5° of visual angle [18].

Fig. 1 Example of a pair of faces shown to the participants while eye-movements were recorded. The AOIs were the left and the right face separately
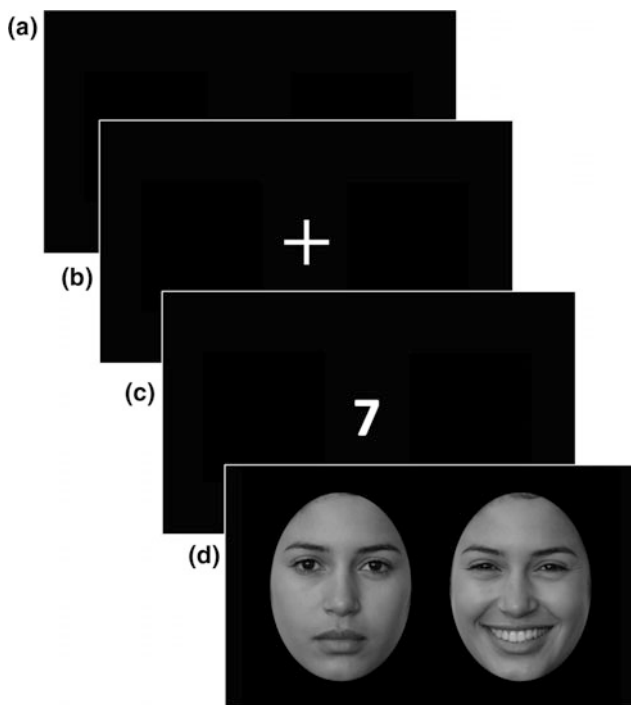
Fig. 2 Trial sequence. Black screen **a** for 500 ms, white cross **b** for 500 ms, a one-digit number **C** for 1000 ms and a pair of faces **D** for 3500 ms

Firstly, the fixation durations on each face (neutral vs. emotional) was summed up and considered as the total fixation duration. These values were converted to a previously used bias measure; values above 50% correspond to a bias for the emotional face; values lower than 50% corresponded to a bias for the neutral face. Scores indexes based in differences have been employed in previous research [19].

2.6 Data Analysis

For statistical analysis, the sample was characterized using position (median) and dispersion (interquartile range) measurements. The normality of data was testing by Shapiro-Wilk test. In order to verify differences between groups, the Kruskal-Wallis non-parametric test was applied. The Statistical Package for the Social Sciences (SPSS), version 17.0 (SPSS Inc. Chicago, IL) was used in all procedures. The value of $p < 0.05$ was adopted as statistical significance.

3 Results

In total, 31 individuals took part in this study. According to BDI-II, 15 were patients with minimal severity of depressive symptoms, 5 with mild severity, 6 with moderate and 5 with severe.

Table 1 presents descriptive analysis of total fixation events to the pair of faces images, and the ratio between fixation duration for faces and total fixation duration for all the trial sequence.

In the Table 2 it was presented the relation of fixation duration and total fixation duration on each face (neutral vs.

Table 1 Fixation events for all trial sequence according to BDI-II score

BDI-II score	n	Age (years)	Total fixation events (s)	Fixation faces events (s)	Fixation faces/total fixation events
Minimal	15	21.0 ± 9.5	235.6 ± 20.6	168.6 ± 54.5*	0.74 ± 0.2*
Mild	5	32.0 ± 22.5	244.9 ± 10.1*	197.8 ± 29.3	0.81 ± 0.1
Moderate	6	25.0 ± 10.5	241.7 ± 37.0	195.6 ± 61.7*	0.81 ± 0.2*
Severe	5	33.0 ± 20.5	212.7 ± 62.2	42.1 ± 141.3	0.25 ± 0.6

*$p < 0.05$ with Severe group

Table 2 Relation between neutral fixation, emotional fixation, and Null events according to BDI-II

BDI-II score	n	Neutral fixation	Emotional fixation	Null
Minimal	15	0.37 ± 0.1	0.48 ± 0.1	0.11 ± 0.1
Mild	5	0.45 ± 0.1	0.47 ± 0.1	0.11 ± 0.1
Moderate	6	0.43 ± 0.1	0.40 ± 0.2	0.15 ± 0.2
Severe	5	0.08 ± 0.1*	0.15 ± 0.8*	0.75 ± 0.8*

* Significative difference between severe diagnoses and all different groups
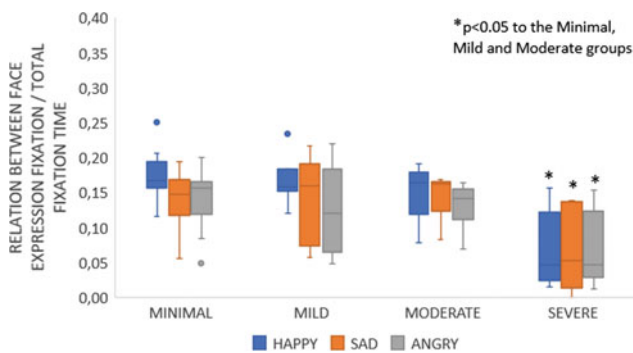
Fig. 3 Relation between face expression fixation and total duration fixation in each emotional face

emotional) and null events. The group with severe depressive symptoms has showed lowest values when compared to minimal, mild and moderate group. A large difference was verified for null events (without fixation at the AOI area—faces) for the severe group.

The emotional faces (Happy, Sad and Angry) were analyzed separately (Fig. 3). The severe group presented the lowest medians values of fixation compared to other groups.

4 Discussion

Our study supports the idea that eye tracking is superior to RT measures, because it collects data objectively and in real-time. Other advantages of eye tracking in this kind of research are that it is a non-invasive method capable of calculate gaze positions and serving as a measure of attention with higher precision [20].

Results of the present study show that participants with severe depressive symptoms tend to have lower fixation duration for faces compared to other groups. Most related works indicates that depressive individuals show attentional bias toward negative information. But in affective disorders, the disengagement from threat-related stimuli should be expected [21]. This study observed the relation between severity of depressive symptoms and attentional bias, not only in individuals with Major Depressive Disorder (MDD). Depressive symptoms are present in most of mental disorders and are predictive from MDD. For future studies, in order to identify attentional bias components in relation to severity of depressive symptoms, it is important to include more attentional indexes and measures of anxiety. This study used the total fixation duration on each type of facial expression in each trial as an attentional index.

Data from gaze positions and the total duration of fixation in each face provide a good measurement of attentional bias [19]. Analyzing relationships between eye-movement behavior and severity of depressive symptoms according to BDI-II or other assessment tools might help to understand the underlying processes in affective disorders. This type of analysis improve the understanding of the role of attentional bias in the onset and the maintenance of these disorders.

Our study used emotional Brazilian faces of the Brazilian Facial Expressions database [17]. The choice for faces was due to a greater propensity to elicit real emotional responses in participants [9]. Other works that used faces to show attentional bias, found that specific regions of the face are particularly relevant for "decoding" of emotional expressions and could enhance emotional responses in individuals [22]. Congruent with these findings are the results of Sagliano et al. [23], showing that the affective state in the moment of the experiment could enhance stimuli salience and modulate attention allocation for mood-congruent information.

This idea is linked to the findings that depressed individuals attend differently to emotional stimuli. But, compared to other studies [7, 13] which observed that depression is related to attend more to negative stimuli, this study provides the idea that depression is related to lower fixation for faces.

There are some limitations to our study. It is important to have a bigger sample size for the different groups of BDI-II score. In addition, is necessary a deeper understanding of frames in collecting data, that the eye tracker does not point to eye events.

The current findings demonstrate that it is important to analyze additional eye data, like the count of blinks and blinks duration, saccades, pupil dilatation and times of fixations on each face. Sanchez and Vazquez [16] and Duque and Vazquez [11], for example, have used gaze data of the first fixation time latency and the direction of the initial gaze. Additionally, the study of Kret et al. [24] recorded the pupil-size during a face-body-scene combination experiment and found that angry faces presented together with an aggressive context in aggressive social scenes elicited greatest pupil size compared to other conditions. Pupil-size dilatation for faces might be worth considering as an additional variable when investigating eye movement patterns of subjects with affective disorders.

The eye tracker used in this experiment provides a valuable opportunity to record a detailed eye movement. Analysis of data demonstrates the possibility to use this technology in detecting patterns of eye movements related to psychopathology. With that, it is a significant opportunity to improve diagnosis technics in mental health research and clinical assessment.

References

1. Lichtenstein-Vidne, L., Okon-Singer, H., Cohen, N., Todder, D., Aue, T., Nemets, B., Henik, A.: Attentional bias in clinical depression and anxiety: the impact of emotional and non-emotional distracting information. Biol. Psychol. 122, 4–12 (2017)
2. Beck, A.T., Bredemeier, K.: A unified model of depression: Integrating clinical, cognitive, biological, and evolutionary perspectives. Clin. Psychol. Sci. 4, 596–619 (2016)
3. Rehm, L.P.: Cognitive and behavioral theories of depression. Depress Discord 1–54 (1990)
4. Posner, M.I.: Orienting of attention: then and now. Q. J. Exp. Psychol. 69, 1864–1875 (2016)
5. Günther, V., Dannlowski, U., Kersting, A., Suslow, T.: Associations between childhood maltreatment and emotion processing biases in major depression: results from a dot-probe task. BMC Psychiatry 15, 1–9 (2015)
6. Pool, E., Brosch, T., Delplanque, S., Sander, D.: Attentional bias for positive emotional stimuli: a meta-analytic investigation attentional bias for positive emotional stimuli: a meta-analytic investigation. Psychol. Bull. 142, 79–106 (2015)
7. Armstrong, T., Olatunji, B.O.: Eye tracking of attention in the affective disorders: a meta-analytic review and synthesis. Clin. Psychol. Rev. 32, 704–723 (2012)
8. Figueiredo, G.R., Ulbricht, L., Borba, G.B: Estudo da atenção visual encoberta utilizando um equipamento de rastreamento ocular. V Congr Bras Eletromiografia e Cinesiologia| X Simpósio Eng. Biomédica. Estud. 0–3 (2017)
9. Li, M., Lu, S., Feng, L., Fu, B., Wang, G., Zhon, N., Hu, B.: Attentional bias in remitted depressed patients : evidence from an eye. Track. Study 19 (2016)
10. Mele, M.L., Federici, S.: Gaze and eye-tracking solutions for psychological research. Cogn. Process. (2012)
11. Duque, A., Vázquez, C.: Double attention bias for positive and negative emotional faces in clinical depression: Evidence from an eye-tracking study. J. Behav. Ther. Exp. Psychiatry 46, 107–114 (2015)
12. Gindt, M., Nachon, O., Chanquoy, L., Nachon, O., Chanquoy, L., Faure, S., Garcia, R.: Attentional bias in post-traumatic stress symptoms or anxiety. Eur. J. Trauma Dissociation 1, 159–164 (2017)
13. Fernandes, C., Silva, S., Pires, J., Reis, A., Ros, A.J., Janeiro, L., Faísca, L., Martins, A.T.: Eye-tracking evidence of a maintenance bias in social anxiety. Behav. Cogn. Psychother 46, 66–83 (2018)
14. Lucas, G.M., Gratch, J., Scherer, S., Boberg, J., Stratou, G.: Towards an affective interface for assessment of psychological distress. 2015 International Conference on Affect Computing and Intelligent Interact ACII 2015, pp. 539–545 (2015)
15. Beck, A.T., Steer, R.A., Brown, G.K.: Beck depression inventory second edition (BDI-II) manual. Psychol. Corp. Bower (1996)
16. Sanchez, A., Vazquez, C.: Looking at the eyes of happiness: positive emotions mediate the influence of life satisfaction on attention to happy faces. J. Posit. Psychol. 9, 435–448 (2014)
17. Rodrigues, M.R.: Composição de um banco de expressões facial brasileiro: um estudo de validação e comparação transcultural. Universidade Federal da Paraíba (2015)
18. Marks, K.R., Roberts, W., Stoops, W.W., Pike, E., Fillmore, M.T., Rush, C.R.: Fixation time is a sensitive measure of cocaine cue attentional bias. Addiction 109, 1501–1508 (2014)
19. Lu, S., Xu, J., Li M, Xue, J., Lu, X., Feng, L., Fu, B., Wang, G., Zhong, N., Hu, B.: Attentional bias scores in patients with depression and effects of age: a controlled, eye-tracking study. J. Int. Med. Res. 45, 1518–1527 (2017)
20. Horsley, M., Eliot, M., Knight, B.A., Reilly, R.: Current Trends in Eye Tracking Research (2014)
21. Fox, E., Russo, R.: Attentional bias for threat: evidence for delayed disengagement from emotional faces. Apr 2014, 37–41 (2010)
22. Eisenbarth, H., Alpers, G.W.: Happy mouth and sad eyes: scanning emotional facial expressions. Emotion 11, 860–865 (2011)
23. Sagliano, L., Trojano, L., Di Mauro, V., Carnevale, P., Di Domenico, M., Cozzolino, C. D'Olímpio, F.: Attentional biases for threat after fear-related autobiographical recall. Anxiety Stress Coping 5806, 1–10 (2017)
24. Kret, M.E., Roelofs, K., Stekelenburg, J.J., de Gelder B.: Emotional signals from faces, bodies and scenes influence observers' face expressions, fixations and pupil-size. Front. Hum. Neurosci. 7 (2013)

Behavior of Electrical Reactance in Gastrocnemius Muscle of Rats During Contractions of Different Intensities

A. B. B. Coutinho, J. P. Wereneck-de-Castro, A. V. Pino, and M. N. Souza

Abstract

Electrical Impedance Myography is an experimental myography technique that assesses two passive electrical components of muscle, the resistance and the reactance. Few studies in the literature have addressed and discussed the behavior of the reactance during muscle contractions. Moreover, the rare results are contradictory about these changes, i.e. during the muscular contraction the reactance sometimes increases, decreases or does not change. The present work used an electrical stimulation protocol able to provide different intensities of muscle contraction in the gatrocnemius muscle of Wistar rats (in vivo experiments) in order to assess in real-time the reactance behavior during these contractions. The results have showed a significant positive correlation ($r = 0.57$) between the reactance magnitude and muscle strength. We conclude that the suitable experimental protocol for electrical stimulation and the electrical impedance measures performed invasively in gastrocnemius muscle had improved the sensitivity in obtaining the reactance findings. However, further studies are required to better understand biochemically, physiologically and morphologically, the reactance behaviors found at the present work.

Keywords

Muscle contraction • Reactance • Muscle impedance • EIM

1 Introduction

Electrical impedance myography (EIM) is composed by two components, the resistance or real part, and reactance or imaginary part [1]. Resistance is often associated to muscle morphological and biochemical changes and is the impedance component more explored and discussed in the literature [2]. Reactance concerned to muscle cell membrane features and other dielectric tissues (e.g. fat, connective) that are present around or among muscular tissue [1, 2].

An important application of EIM is the one related to the muscle contractions, which can be called as dynamic EIM, because it can be applied to study healthy muscles or non-healthy ones [2, 3]. As above-mentioned, results related to electrical resistance are better known and interpreted then reactance ones, including in dynamic EIM papers.

According the literature, the few reactance data in EIM papers shows contradictory results. Some works present an increase [2, 3], while some others a decrease [4], or even non changes [5] of reactance related to muscle strength. This fact is also due the heterogeneity of studies, which present different subjects (human or animal models) and instrumentation technique. However, dynamic EIM studies appoint a less sensitivity of reactance comparing with resistance. And it can also be one of the causes for the different pattern found in literature. Then, this situation indicates that an improvement of reactance behavior knowledge during muscle activity is required.

Our study aims to investigate the behavior of reactance data with different muscle contraction intensities, in order to assess if this impedance component influences the dynamic EIM changes.

A. B. B. Coutinho (✉) · A. V. Pino · M. N. Souza
Biomedical Engineering Program, Universidade Federal do Rio de Janeiro, COPPE, Rio de Janeiro, Brazil
e-mail: brand@peb.ufrj.br

J. P. Wereneck-de-Castro
Exercise Biology Laboratory, Universidade Federal do Rio de Janeiro, Rio de Janeiro, Brazil

2 Methods

2.1 Sample

The experiments were realized in nineteen male wistar rats, weighting between 250 and 400 g, and aging between 2 and 4 months. The animals were exposed to a 12 h light-dark cycle and were feed ad libitum. Because it is an in vivo experiment, the rats were kept anesthetized with 3% iso-flurane throughout the experimental procedure and the surgical procedure, which consisted on gastrocnemius expose. The experimental protocol was submitted and approved by the Institutional Ethics Committee for Research with Animals under the number 019/15.

2.2 Instrumentation

Electrode Placement. To measure bioimpedance signal four needles electrodes were placed in the rat gastrocnemius belly transversally to the muscle shortening direction. The stainless-steel needles, 5 mm length and 0.2 mm diameter, were equally and fixed spaced with 0.8 cm distance between the first and the forth needle and fixed on an insulated material. Because the electrodes are too small their impedances are high. Then, tetrapolar measurement technique as used, to avoid the influence of electrodes' impedances on the bioimpedance signal. Two others stainless steel needles were fixed in muscle ends (proximal and distal) and used for electrical stimulation. Figure 1 illustrates schematically the electrodes placements on rat gastrocnemius (top and side view).

Devices. For force (F) data acquisition we used a calibrated load cell (MLB 50, HMB, USA) and a signal conditioning system specially developed for this purpose with a sensitivity of 379 mV/N. This system provides a DC signal
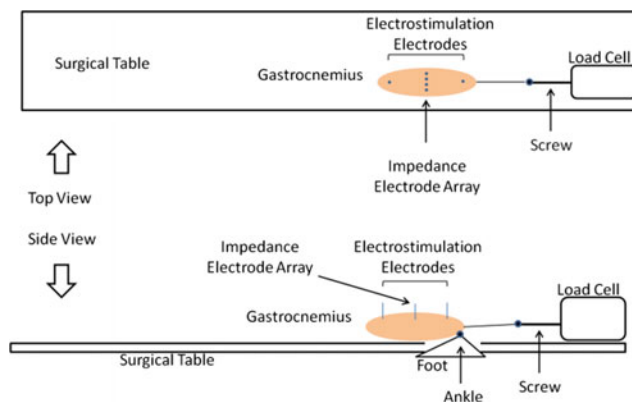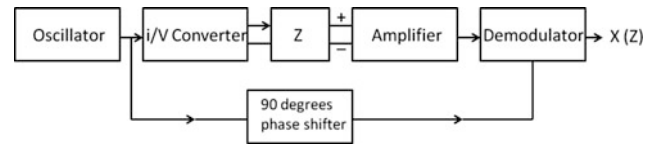
Fig. 2 Block diagram of impedance measurement system

proportional to the force applied to the load cell, which was attached to the gastrocnemius tendon of the animal by an inextensible fine cord. To perform the electrical stimulation, we used a buffer amplifier connected to one of the D/A outputs of a NI6252 board (National Instruments, USA) updated at a rate of 2.86 Ms/s and controlled by a LABView software specially developed for this purpose. The system is capable to generate a −2.5 to 2.5 V biphasic voltage square waveform, with a minimum pulse-width of 500 μs and a longest duty cycle of 2 s. These characteristics are enough to provide the electrical stimulus needed in this work. For impedance measurements a prototype system developed on our laboratory was used to measure reactance in real time. This prototype is basically a single frequency system (50 kHz) with a 1 mA amplitude current sinusoidal excitation and that detects the voltage signal 90° out-of-phase, i.e. a voltage signal proportional to the reactance. Figure 2 shows a block diagram of such system where one can see that the reactance signal is obtained at the output of a quadrature demodulator that receives as a reference signal a square wave 90° out-of-phase with current excitation signal, resulting in a DC signal proportional to reactance, which was calibrated for the range of reactance between 0 and 100 Ω.

The reactance signal (X), the electrical stimulation pulses, and the load cell signal were sampled and digitalized at a rate of 4 kS/s by NI 6009 data acquisition board (National Instruments, USA). The communication between the data acquisition board and computer was set via USB interface. A LabVIEW (National Instruments, USA) program was designed to data acquisition and data visualization in real-time.

2.3 Experimental Protocol

Frequency x Force ($f \times F$) curve for each rat was provide through neuromuscular electrical stimulation based on a previous study [6]. The electrical stimulation parameters can be seen at Table 1. Briefly, ten pulse trains were applied on gastrocnemius muscle during 1 s with 40-s rest between each stimulus. The frequency of each pulse train was randomized (see frequencies on Table 1). The reactance (X) and force (F) signals were acquired and recorded during all experiment.

Fig. 1 Simplified schematic of sensors placement on rat's gastrocnemius muscle

Table 1 Electrical stimulation parameters used on experimental protocol

Pulse duration	Frequencies	Pulse train duration	Rest duration
500 μs	2, 10, 20, 30, 40, 50, 60, 75, 100, 150	1 s	40 s

2.4 Analysis and Data Processing

X signal passed through a low-pass filter (Butterworth, second order) with 30 Hz cutoff frequency to remove high frequency interferences. Considering the impedance baseline normally varies along the experiment, a high-pass filter (Butterworth, second order) with 0.01 Hz cutoff frequency was also applied to the reactance data. Peak of X and F signals were determined, during pulse train stimulation, and the changes on X and F signals were considered as a difference between the peaks and baseline (Eq. 1).

$$\Delta S = S_p - S_b \qquad (1)$$

where ΔS is the change of the signal in respect to its baseline, S_p is the signal peak and S_b is signal baseline. For instance, S can be F or X.

As each animal has its own range of force and reactance, the processed data were normalized by the highest modulus of the change ($|\Delta S_{max}|$) and also multiplied per 100%. Then, all the results are values relative to $|\Delta S_{max}|$ ranging between 0 and 100%. See Eq. 2.

$$\Delta S_{rel} = \frac{\Delta S}{|\Delta S_{max}|} \times 100\% \qquad (2)$$

where ΔS_{rel} is the relative change of signal, ΔS is the change of the signal in respect to its baseline, and $|\Delta S_{max}|$ is the highest modulus of such change.

Box plots were used to describe the behavior of $\mathbf{\Delta S}$ and ΔS_{rel} as a function of the electrical stimulation frequencies; and a scatter plot was used to analysis the behavior of ΔF_{rel} and ΔX_{rel}. Pearson correlation coefficient (r) and a linear regression were calculated to assess the relation between ΔF_{rel} and ΔX_{rel}. The signals processing were made in MATLAB R2017a (Mathworks, USA) and statistical analysis through R 2.13.

3 Results

Results show an increase in the muscle strength as the electrical stimulation frequencies increased (Fig. 3, left), showing that different intensities of muscular contraction were evoked by electrical stimulation. The peaks of the X signal presented a similar behavior, i.e. an increase as the electrical stimulation frequencies increases (Fig. 3, right). However X increase was in a narrow range, less than 5 Ω for non-outliers. After normalization the ΔX_{rel} data was at the same range for every animal and seemed to increase the sensitivity of the results comparing with ΔX (Fig. 4, left).

Fig. 3 Boxplot of force changes (left) and reactance changes (right) as function of electrical stimulation frequencies
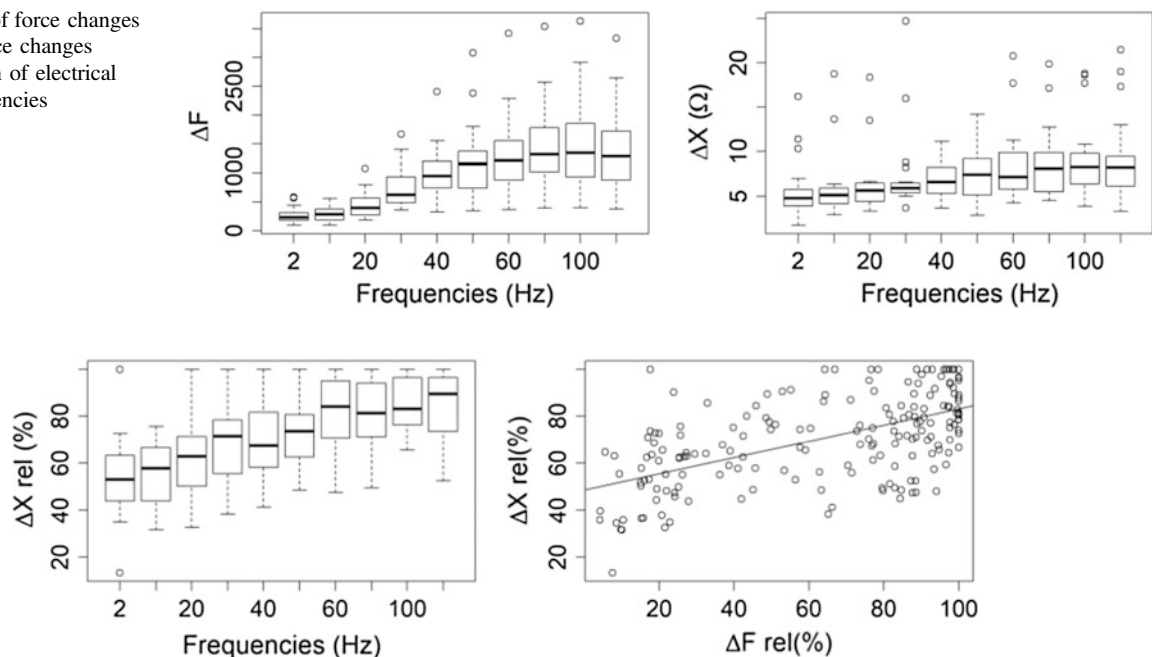
Fig. 4 Boxplot of percentile changes of reactance as function of electrical stimulation frequencies (left) and scatter plot between percentile changes of reactance and percentile changes of force (right)

The scatter plot of ΔX_{rel} versus ΔF_{rel} (Fig. 4, right) shows the tendency between variables and with a Pearson coefficient $r = -0.57$.

4   Discussion

The reactance changes corroborate with previous works [3, 7] with murine model, where X data also increased due muscle contraction. But as previously mentioned some works have presented opposite behavior (reactance decrease) or a non-correlation.

Our experimental protocol used an invasive measurement that avoids some capacitance influences as skin and fat layers. Also, the electrodes were placed equally, transversally to muscle contraction direction, at all rats in order measure a higher number of muscle fibers and to avoid anisotropy influences. Moreover, tetrapolar measurement neglects electrode impedance [8]. Then, the used approach may have improved the reactance sensitivity, allowing stablishing a relationship between reactance and muscle strength.

The electrical stimulation muscle contraction at different intensities (Fig. 3, left) showed that frequencies from 75 Hz were associated to the maximum tetanic force. Results also showed an increase of muscle reactance as the developed force increased. However, for stimulation frequencies higher than 75 Hz the force achieved a kind of a plateau, at least until 150 Hz. Reactance data presented a similar behavior but starting early, at 60 Hz (Fig. 4, left). Then, we can assume that reactance changes can be related to force changes, but has a limited relationship. Beyond of the same reactance changes at from 60 to 150 Hz stimulus, the correlation between ΔX_{rel} and ΔF_{rel} was 0.57, it is statistically significant ($p < 0.05$) but indicates that other factors might be influencing the reactance changes. Muscle anisotropy

further experiments are required to better associate the biochemical, physiological and morphological muscle changes with the reactance increase found at present work.

Conflict of Interests   The authors declare that they have no conflict of interest.

References

1. Grimnes, S., Martinsen, Ø.G.: Bioimpedance and Bioelectricity Basics. Academic, London (2008)
2. Shiffman, C.A., Aaron, R., Rutkove, S.B.: Electrical impedance of muscle during isometric contraction. Physiol. Meas. **24**(1), 213–234 (2003)
3. Sanchez, B., Li, J., Geisbush, T., Bragos, R., Rutkove, S.: Impedance alterations in healthy and diseased mice during electrically-induced muscle contraction. IEEE Trans. Biomed. Eng. (2014)
4. Rutkove, S.B.: Electrical impedance myography: background, current state, and future directions. Muscle Nerve **40**(6), 936–946 (2009)
5. Li, L., Shin, H., Li, X., Li, S., Zhou, P.: Localized electrical impedance myography of the biceps brachii muscle during different levels of isometric contraction and fatigue. Sensors (Basel) **16**(4) (2016)
6. Mrówczyński, W., Celichowski, J., Krutki, P., Cabaj, A., Slawińska, U., Majczyński, H.: Changes of the force-frequency relationship in the rat medial gastrocnemius muscle after total transection and hemisection of the spinal cord. J. Neurophysiol. **105**(6), 2943–2950 (2011)
7. Sanchez, B., Li, J., Geisbush, T., Bragos, R., Rutkove, SB.: A pilot spectroscopy study on time-varying bioimpedance during electrically-induced muscle contraction. In: Conference on Proceedings of the IEEE Engineering in Medicine and Biology Society 2014, pp. 3739–42 (2014)
8. Grimnes, S., Martinsen, Ø.G.: Sources of error in tetrapolar impedance measurements on biomaterials and other ionic conductors. J. Phys. D Appl. Phys. **40**(1), 9 (2007)

5   Conclusion

Our findings showed that there is a significant positive correlation between the measured electrical reactance and the muscle contraction intensities. The experimental protocol with invasive measurements could be essential to improve the reactance measurement sensitivity. Despite such results,

Design of an EEG Acquisition System Based on Front-End ADS1292

L. M. Luza, F. R. Andreis, and A. F. Balotin

Abstract

The signals obtained through electroencephalography are used to the identification of several pathologies, neurological and psychiatric disturbs. The present work describes the hardware, firmware and software of an EEG acquisition module based on the analog front-end ADS1292, with two channels and ADC conversion with a resolution of 268 nV. The system has a composition of filters and amplifiers capable of extracting signals in the amplitude and frequency range for EEG signals and the acquired data is recorded and presented online with a software developed in the LabVIEW 2016 environment and post-processed with software Matlab. The system showed to be adequate to acquire EEG signals and present the results in an online software, along with the possibility of storing the data for offline analysis. To conclude, this EEG system acquisition can be a useful tool for engineering students to develop their abilities and build a practical device in which several fields of knowledge are related, therefore presenting a possibility to develop a complete project with real applications.

Keywords

Multichannel acquisition • ADS1292 front-end • Biopotentials

1 Introduction

The electroencephalogram signal (EEG) is defined as the recording of electrical potentials produced from the synaptic excitation process of the dendrites of many pyramidal neurons in the cerebral cortex [1, 2]. These potentials are recorded by surface electrodes in a range of amplitude between 10 and 150 µV. Clinically, the frequency of interest of this signal ranges from 0.5 to 50 Hz [3].

Recent studies have shown the importance of identifying the synchronized activities of different areas of the brain to evaluate signal patterns. Thus, the use of EEG plays a fundamental role in the assessment of neurological and psychiatric disorders, such as Alzheimer's disease, epilepsy and seizures, autism, schizophrenia, attention deficit disorder and hyperactivity [4]. Thus, this work aims to develop a system for the acquisition of biopotentials, with a focus on EEG signals, characterizing an alternative to commercial systems that, generally, have a high cost and size.

The system uses a preamplifier with high CMRR and gain, which is capable of low amplitude acquisition and a set of filters that limits the signal only the frequency range of interest to the EEG. After this initial processing stage, a 24-bit sigma-delta analog-to-digital converter (ADC) is used to convert the signals into digital data. The converted data is sent to a computer which, through a user-friendly software, displays the signals in real time and stores the data for later analysis.

Therefore, this article presents the hardware and the software developed; along with the results obtained through tests to evaluate the system performance.

2 Materials and Methods

The prototype of a module to acquire EEG signals of two channels can be divided into three main parts: hardware; firmware; and software.

L. M. Luza (✉) · A. F. Balotin
Department of Electrical Engineering, University of Passo Fundo, Passo Fundo, Brazil
e-mail: lucas.luza@posgrad.ufsc.br

F. R. Andreis · A. F. Balotin
Department of Electrical and Electronic Engineering, Federal University of Santa Catarina, Florianópolis, Brazil

2.1 Hardware

The hardware is based on the analog front-end (AFE) ADS1292, that is a low power integrated circuit (335 μW/channel), which have two ADCs with 24 bits of resolution with a second order delta-sigma approximation and an internal oscillator of 512 kHz. The sampling rate can be up to 8.000 samples per second (SPS) simultaneously in each channel, in addition, it has integrated programmable gain amplifiers (PGAs) with the specific values of 1, 2, 3, 4, 6, 8, and 12 for each one of the channels. This AFE was chosen due to the specific characteristics for biopotential signal acquisitions, like high common mode rejection ratio (CMRR) of −105 dB and low input-referred noise (8 μVpp), besides, it has reduced size and low power consumptions, which allows the construction of small dimension devices.

The AFE ADS1292 was powered symmetrically (±2.42 V). Therefore, using a gain of 8, it is necessary that its inputs have voltage levels in the range of ±300 mV to use all the possible ADC range. As the EEG signals have an amplitude of up to 150 μV it is necessary to have a pre-amplification of 5.800 times. Henceforth, it is necessary a pre-amplification stage, this was performed with the low-power instrumentation amplifier INA128 (Texas Instruments INC., US) which has a minimum CMRR of 120 dB and a maximum gain of 10 k, thus, fulfilling the needs of the project.

The frequency of interest of the signal is in the range of 0.5–50 Hz, for this reason, active filters were developed to analyze only the signal of interest. To achieve this task, the operational amplifier LM358 (Texas Instruments Inc., US) was used, mainly because it allows the same supply voltage from the AFE ADS1292 (±2.4 V). The high-pass filter was developed as a second order Butterworth filter, with a Sallen-Key topology, since it generates a flat frequency response in the pass-band [5]. The same Sallen-Key topology was used for the low-pass filter, but in this case, it was used an eighth order Butterworth filter [5]. Also, as the highest interference in the signal acquisition comes from the power-line (60 Hz), and to attenuate this signal, it was used a Fliege notch topology. The Fliege notch filter allows to adjust the Q of the filter independently from the center frequency, also, the center frequency of the filter can be adjusted over a narrow range without seriously eroding the depth of the notch [6].

After the analog-to-digital conversion and amplification, the data was transferred to a computer. As the AFE ADS1292 uses the SPI communication and, in this case, can be considered a slave device, it is necessary an additional master component to set the AFE parameters (e.g., read and write registers, configure gain). Henceforth, it was used a

microcontroller (μC) PIC18F4550 (Microchip Technology Inc., US) to adjust and monitor the AFE settings. Furthermore, the μC is also responsible for the communication with USB-serial converter PL-2303HX (Prolific Technology Inc., TW), which performs the interface between the computer USB and the RS-232 protocol implemented by the μC.

To ensure electrical isolation from the subject to the electrical grid, the communication buses between the AFE ADS1292 and the μC must have electrical isolation. For that, the authors chose the Dual-Channel Digital Isolator ADuM1200 (Analog Devices Inc., US), which can achieve transference rates of up to 25 Mbit/s, as well as having a relatively easy application, requiring only voltage supply and two capacitors to function properly. Due to the necessity for the μC to send a reset signal to the AFE in the initialization of the system, it is also necessary to isolate this signal. Therefore, the component 4N25 (Vishay Intertechnology Inc., US) was chosen since it is a single channel phototransistor coupler with isolation test voltage of 5.000 V_{rms}.

The power supply for the whole circuit comes through the USB bus available in most of today's computer, providing a voltage of +5 V and a current capacity of up to 500 mA. The source was designed to provide different voltage levels, thus meeting the need for each component (e.g., microcontroller, isolators) of the system. Figure 1 shows the diagram that define the system power source.

The DC/DC converter DCP020505 (Texas Instruments Inc., US) was used to isolate the subject from the electrical grid. This component presents an operational isolation of 1 kV and a power capacity of 2 W. The input and output voltage are in the range of 4.5–5.5 V, therefore allowing to use the USB output as power supply for the DCP020505.

The AFE ADS1292 was supplied symmetrically with ±2.4 V. This voltage level was obtained through the LM317 voltage regulator (Texas Instruments Inc., US) that has a thermal overload protection and maximum output current of 1.5 A. To obtain the negative voltage (−2.4 V), it was used the voltage converter ICL7660 (Intersil Inc., US) that performs voltage conversion from positive to negative for an input range of +1.5 to +10 V, resulting in complementary output voltages from −1.5 to −10 V. The digital part of the AFE 1292 works with a voltage level of +3.3 V, hence, to perform the conversion from +5 to +3.3 V, the LM3940 was used. This is a low dropout regulator designed to provide +3.3 V from a +5 V supply. The bus isolator is also supplied by +3.3 V, consequently, the same regulator was used.

Figure 2 shows the block diagram of the system, presenting the isolated and non-isolated power supply and the flowchart of the signals, from its acquisition to the final paths.

Fig. 1 Block diagram of the source power
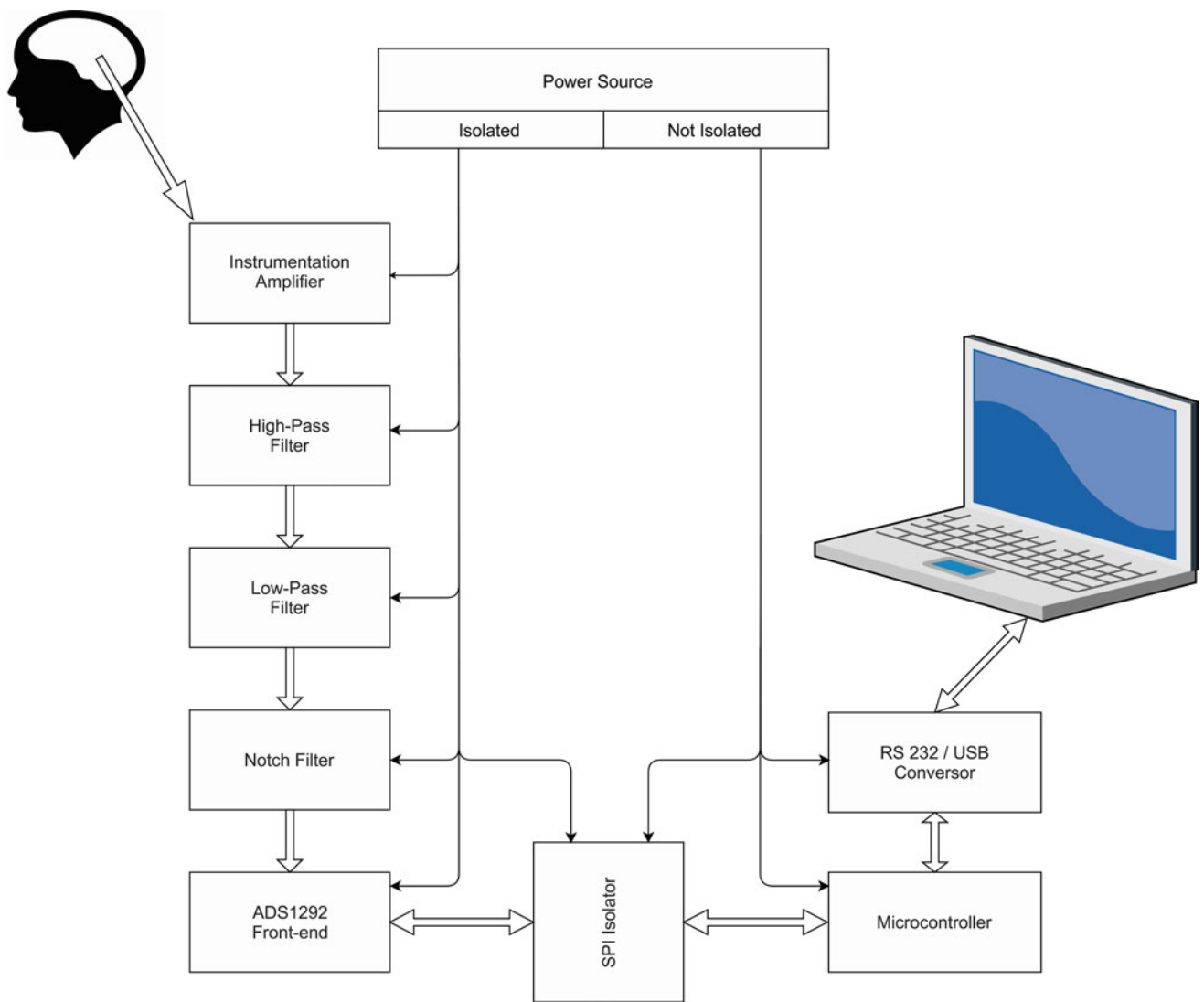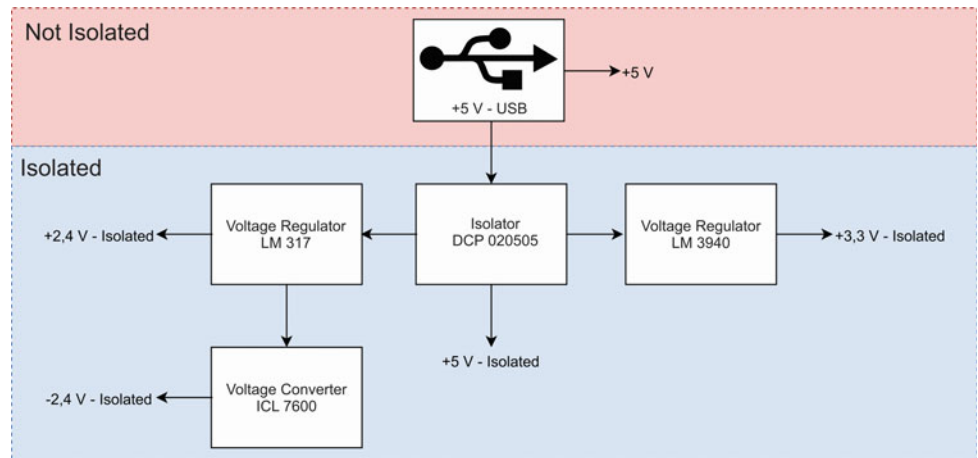
Fig. 2 Block diagram of the system

2.2 Firmware

The firmware is implemented by the μC to control the SPI and RS232 communication protocol, with the AFE ADS1292 and the PL-2303HX, respectively. This implementation follows the flowchart presented in Fig. 3.

2.3 Software

The software was developed in LabVIEW (National Instruments Inc., US), which allows an online visualization and characterization of some signal parameters (e.g., signal amplitude and duration). The software also can generate an executable file, which can be an important tool for users who do not have the LabVIEW installed.

The software receives the data from the serial interface through the RS232 protocol, with a baud-rate of 128.000. The data is received in string format and are composed of the two inputs acquired by the ADC, after the signal treatment. Finally, the software produces a file of the signals in the text format and stores in the hard disk of the computer, allowing the user to perform a more complete offline analysis in any other signal processing software the user chooses to.
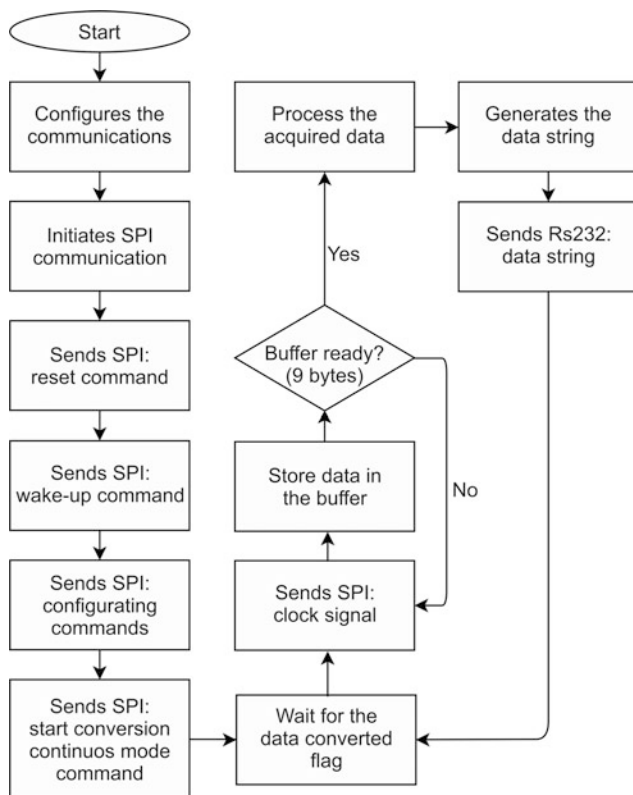
Fig. 3 Firmware diagram

3 Results

3.1 Data Communication

The AFE ADS1292 has a high-resolution ADC and its data can be transferred at rates up to 8 kSPS through the SPI communication with the 1.25 MHz clock. However, this feature was limited by the maximum baud rate permitted by the RS232 serial communication, which is 128 kbits/s. Under those circumstances, the highest sampling rate used in the ADS1292 was of 500 SPS.

3.2 System Frequency Response

The frequency response of the acquisition system was tested with a waveform generator (AFG2021-BR, Tektronix Inc., US) which applied, in the input of filter composition, sinusoidal signals of 200 mVpp of amplitude in a frequency range from 0 to 150 Hz with steps of 1 Hz. The frequency response of the system can be seen in Fig. 4.

The cut-off frequency is defined as the point where the frequency response has a—3 dB of attenuation. Considering that the system has a gain of approximately 17 dB, the cut-off frequency was defined where the results is a gain of 14 dB. This gave in an inferior cut-off frequency of 0.7 Hz and a superior cut-off frequency of 45 Hz. Also, the attenuation in the 60 Hz frequency was—46 dB.

3.3 Sinusoidal Signal Test

To verify if the system was able to amplify such small signals, a 40 mVpp signal was generated (this is the minimum amplitude provided by the equipment), in a frequency of 20 Hz, then reduced to 400 μVpp and applied in the two inputs of the system. The result can be seen in Fig. 5.

From Fig. 5 it is possible to see the output signal, which has a duration of 1-second and a peak-to-peak amplitude of about 2.3 V, meaning a gain of 5.800 times, as expected. Figure 6 also presents the graphical interface developed in LabVIEW, showing simultaneously the two output channels of the system. Furthermore, this data was saved as a text file and evaluated through a more complete analysis in Matlab (Mathworks, US) to verify if there was any significant effect from other frequencies.

The result of the frequency spectrum for both output channels is shown in Figs. 6 and 7.

From Figs. 6 and 7, it is possible to see that there is no interference from any other frequency range other than the 20 Hz applied in the input.

Fig. 4 System response
frequency
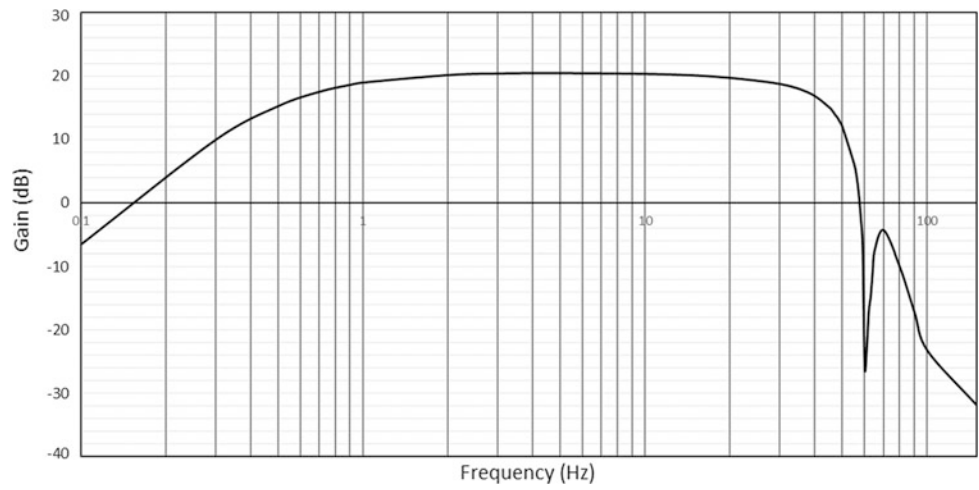
Fig. 5 Sinusoidal signal
acquired shown in the graphical
interface
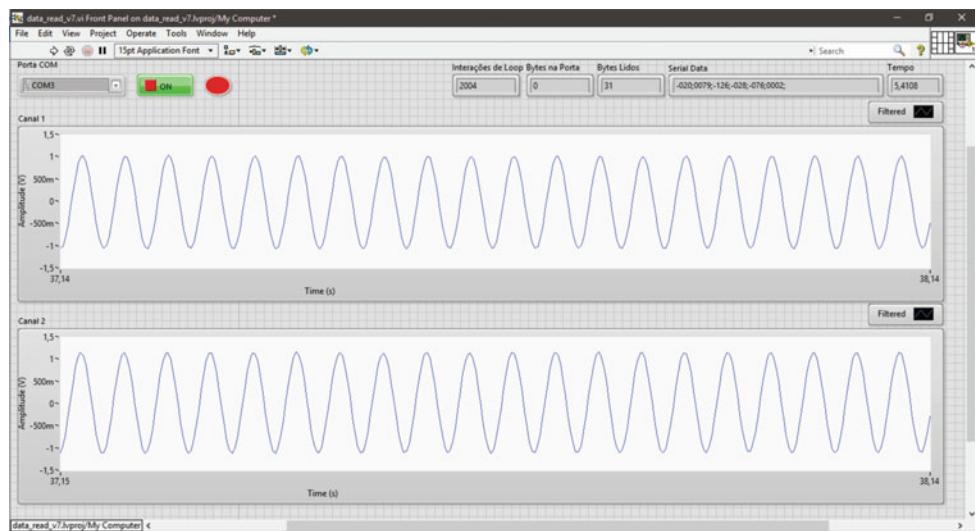
Fig. 6 Frequency spectrum of
the sinusoidal signal in channel 1
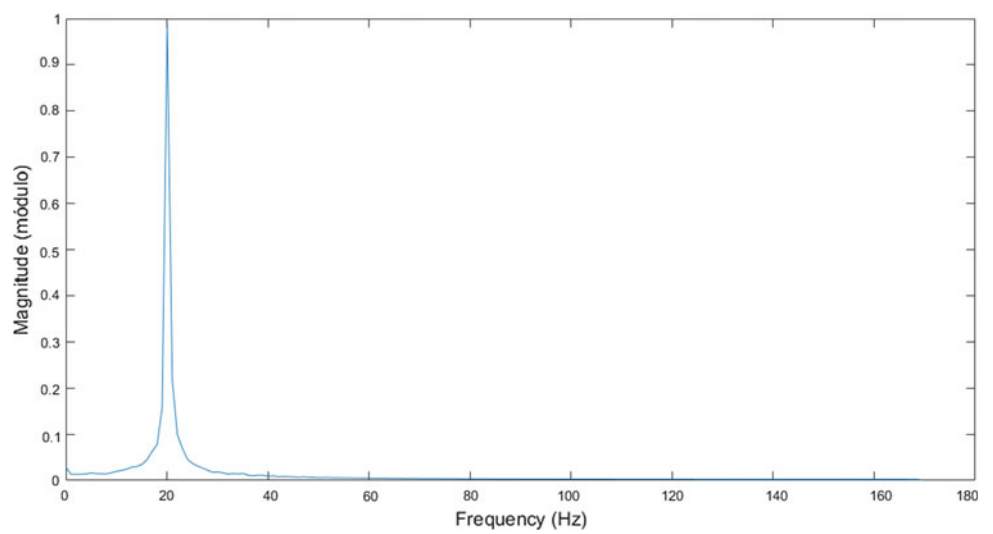
Fig. 7 Frequency spectrum of the sinusoidal signal in channel 2
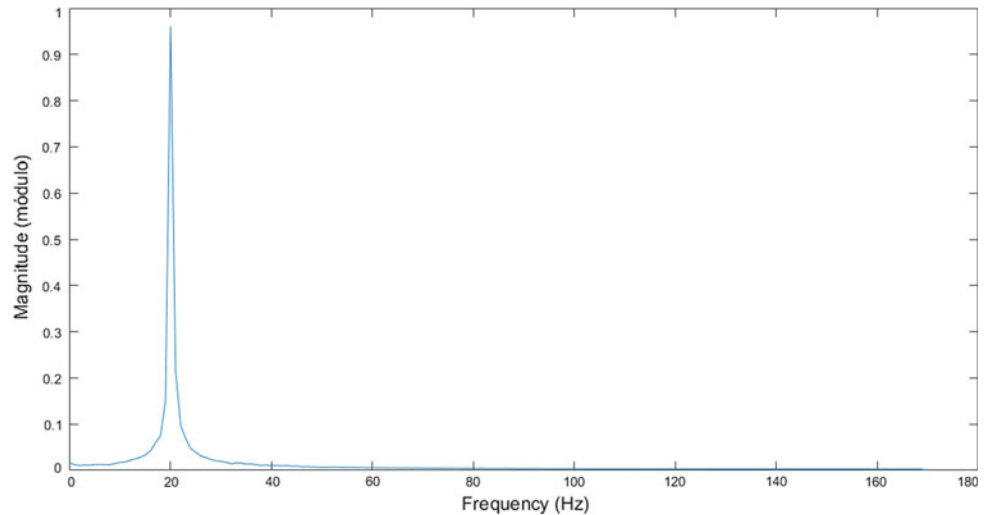
4   Discussion

The results achieved through this work shows that the system can be a simple and useful tool for the study of EEG signals. The main advantage when compared to commercial systems is the high-resolution ADC (24 bits) where most of the solutions available have resolutions of 16 bits. Moreover, by adjusting easily programmable parameters such as sampling frequency and gain, it is possible to work with other biological signals (e.g., electrocardiographic and electromyographic signals), the user just needs to build adequate filters for the frequency of interest. The system has also the advantage of being portable and with reduced size, which allows the signal acquisition even in remote places.

The development of the software based in the LabVIEW tool showed up an interesting alternative when compared with textual languages of programing (e.g., Visual Basic, C/C++, Java), once this tool allows to build up a model based in dataflow with a graphical language that permits, besides the processing of the data, to create a graphical interface and easily handle the information acquired.

Furthermore, as the system have only two channels, it is relatively easy to expand it to more channels. This task can be completed using an ADS1292 in multiple device configuration or using another AFE like ADS1298 that has 8 channels and has very similar configurations to the AFE used in this work.

5   Conclusion

From the above, it is possible to conclude that the equipment has the necessary characteristics to acquire EEG signals, once it presents a high-resolution ADC (286 nV) and a frequency response that eliminates signals outside the range of interest.

This work had the focus to present a hardware designed with accessible devices and that can be developed by undergraduate students to apply their knowledge to a real problem in a complete project, from the acquisition of a signal to an online analysis, as well as bring up an initial contact with the field of biomedical engineering. Moreover, this system can be easily modified to investigate other bio signals (e.g., electrocardiogram and electromyogram).

Conflict of Interest The authors declare that they have no conflict of interest.

References

1. Bear, M.F., Connors, B.W., Paradiso, M.A.: Neuroscience: Exploring the Brain, 3rd edn. Lippincott Williams & Wilkins, US (2007)
2. Bronzino, J.D., Peterson, D.R.: The Biomedical Engineering Handbook, 4th edn. CRC Press, US (2015)
3. Webster, J.G.: Encyclopedia of Medical Devices and Instrumentation. Wiley, US (2006)
4. Ahmadlou, M., Adeli, H.: Functional community analysis of brain: a new approach for EEG-based investigation of the brain pathology. Neuroimage **58**, 401–408 (2011)
5. Bianchi, G., Sorrentino, R.: Electronic Filter Simulation & Design. McGraw-Hill, US (2007)
6. Carter, B.: High-speed notch filters. Analog Appl. J. 19–25(2006)

Development and Testing of a High Intensity Electrical Stimulator for Isolated Rat Heart Defibrillation

Priscila Correia Antoneli and Pedro Xavier de Oliveira

Abstract

Researches with animal models have been carried out aim to study and optimize defibrillatory procedures. Isolated rat hearts stimulation by electric fields is one of the techniques used. Defibrillate the hearts in this type of preparation requires a high intensity stimulator able to provides pulses with high voltage levels and well defined durations. This work presents the development of a high intensity stimulator (HIS) that provides voltage pulses of 1 V to 1 kV and duration of 0.2–10 ms. The HIS consists mainly of a Flyback converter, high voltage capacitors and a firing circuit containing an Insulated Gate Bipolar Transistor (IGBT) controlled by a microcontroller. The energy stored in the capacitor was applied to a chamber containing isolated rat hearts in a Langendorff adapted preparation, which made possible to test the equipment. After applying the electric pulses, the residual capacitor voltage is dissipated in a power resistor. The stimulator presented satisfactory results since it was possible to defibrillate the hearts with quality and safety.

1 Introduction

Despite defibrillation being the only treatment capable to terminate ventricular fibrillation (VF), it can submit some points of cardiac tissue to high electric fields capable to cause cell death (around 100 V/cm or more) due to irreversible electroporation [1–3], which may result in blockage of electrical conduction and VF re-induction or contractile function depression [4, 5]. Therefore, several studies are performed aim to optimize defibrillatory parameters in order to increase defibrillation efficiency [6–9]. In this way, animal models may be used, in which hearts in ex vivo preparations are stimulated in order to induce VF and defibrillation [10, 11]. Among the stimulation techniques of excitable tissues, the stimulation by electric field is highlighted, because the physical contact between the sample and the electrode is not necessary. In this type of experimental setup the excitatory electric field is given by the current flowing through the conductive volume that surrounds the hearts [11]. In order to perform these experiments, a stimulator is required to provide high intensity electric pulses due to the demand for high currents and voltages to generate the adequate electric field. Several hardware designs can be used to construct a high intensity stimulator (HIS), however a simple and affordable option is to use a Flyback converter (FC). FC topology is attractive and widely used in defibrillators because of its relative simplicity and reduced size when compared to other topologies, its high output voltages and high efficiency, and security since it eliminate any direct electrical connection between the input and the output of the converter power stage. Besides that in this topology the output voltages can be either positive or negative [12, 13].

This work describes the development of a HIS based on a FC and presents the test of its operation in the isolated rat hearts defibrillation to several pulse durations.

2 Materials and Methods

2.1 Development of a High Intensity Electrical Stimulator

The HIS developed in this work has the characteristics necessary to defibrillate isolated rat hearts by electric field,

P. C. Antoneli · P. X. de Oliveira (✉)
Biomedical Engineering Department, FEEC/UNICAMP, Campinas, Brazil
e-mail: pedrox@ceb.unicamp.br

P. X. de Oliveira
Biomedical Engineering Center, CEB/UNICAMP, Campinas, Brazil

Fig. 1 Block diagram of the high intensity electrical stimulator developed
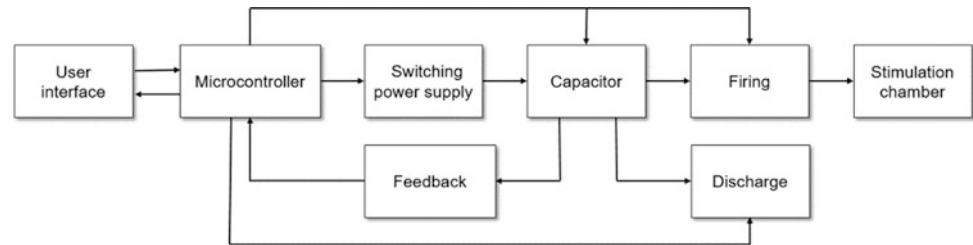
that means, it generate monopolar pulses of 1 V to 1 kV, with duration of 0.2–10 ms. The HIS block diagram is shown in Fig. 1. The user chooses the voltage and duration of the electric pulse in the user interface. After pressing the confirmation button, the microcontroller evaluates which high voltage capacitor will be charged and sends pulses to the switching power supply in order to charge the selected capacitor. When the voltage of the feedback circuit corresponds to the voltage selected by the user, the microcontroller stops the capacitor charging and it waits the user pushes the firing button to send the firing pulse, with the duration previously selected by the user, to the firing circuit. Finally, after the firing, the microcontroller sends an electrical signal to the discharge circuit that carries out the internal discharge of the remaining charge on the capacitor.

User interface

User interface consists of buttons and a 16 × 2 LCD display. Buttons are used to select voltage and time pulse, confirmation of actions and screen changes, and fire the electric pulse. In the LCD display messages are displayed for guidance and user safety.

Microcontroller

Microcontroller used to control the HIS is PIC 18F4550 (Microchip Technology Inc., Chandler, AZ, USA). The software was developed in C language on the MPLAB IDE® platform (Microchip Technolgy Inc., Chandler, AZ, USA). After the user chooses the voltage and duration pulse and press the confirmation button, the microcontroller selects which capacitor will be charged (activating or not the relays RL1 and RL2 in Fig. 2). It occurs because we used different pulse durations and it is not desirable that voltage drop more than 10%, until the pulse end, which can compromise the results. To solve this issue the stimulator was developed with two high power electrolytic capacitors. One with 5 mF (720 V), to be used in pulses with longer durations, which, as we know from the strength-duration curve for excitable tissues [14–16], require lower voltages to defibrillate the hearts, and another with 195 μF (2200 V) for pulses with shorter duration and higher voltages. If the chosen voltage is less than or equal to 100 V, the microcontroller connects the 5.5 mF capacitor (two 11 mF, 360 V capacitors in series) to the FC and firing circuit. If the voltage chosen is greater than

Fig. 2 High voltage capacitors, discharge circuit and feedback circuit. The outputs FIRE1 and FIRE2 are linked with the fire circuit
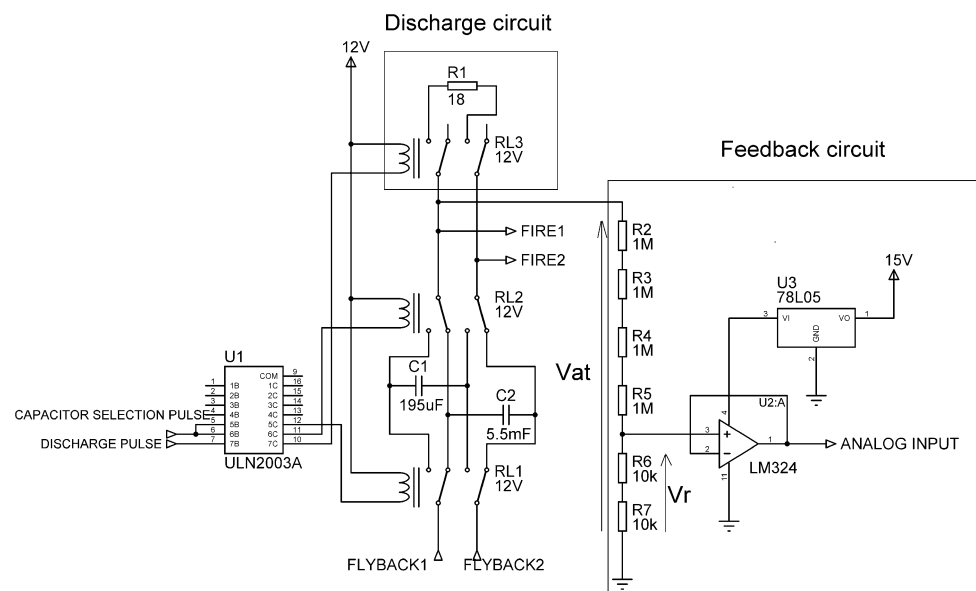
Fig. 3 Switching power supply. The microcontroller provides the switching signal. The overcurrent circuit ensures the integrity of the Flyback converter, which charges the high voltage capacitor
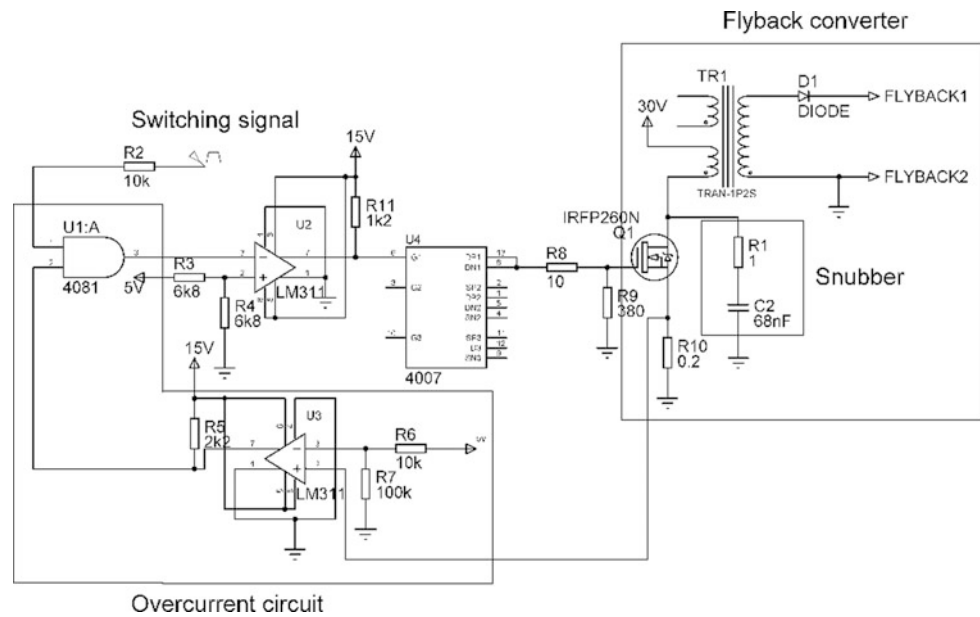
100 V the microcontroller connects the 195 μF capacitor to the FC and the firing circuit. After selecting the capacitor, the microcontroller starts generating the pulses for the switching power supply, with a 47.8 kHz (FC operating frequency), 5 V and 10% duty cycle, until the voltage is reached in the capacitor, which is detected by the analog input of the microcontroller connected to the feedback circuit. After full charging of the capacitor, the microcontroller waits for the user press the firing button to generate the firing pulse, sent to the firing circuit with a 5 V and duration equal to the one previously selected by the user. Then a pulse of approximately 3.5 s is sent to the discharge circuit, so that the voltage remaining in the capacitor is discharged. Finally the microcontroller waits until the confirmation button is pressed to restart the program.

Switching power supply and high voltage capacitors
Switching signal from the microcontroller is conducted through an overcurrent circuit, to protect the FC of high currents, and increase by the LM311 to 15 V as it is shown in Fig. 3. In sequence the integrated circuit cd4007, composed of a push pull circuit, is used to guarantee the Metal Oxide Semiconductor Field Effect Transistor (MOSFET) switching in a shorter time (Q1 element in Fig. 3), that operates in the cut and triode regions as a switch, in the open (cut) or closed (triode) state. When the MOSFET is conducting, a current flows through the primary FC winding, however, a current is not induced in the secondary winding, by the magnetic coupling between the coils, because the diode (D1) is reverse polarized. In this way the energy is stored in the inductance of the primary winding as magnetic field. When the MOSFET is not conducting, the current has its flow interrupted in the primary winding and there is a

voltage surge that rises in the secondary coil, it forces the appearance of a path to the current that allows continuity of the flow [17]. In doing so, the energy stored in the magnetic field is sent to the capacitor connected to the FC, charging it. The charging speed and voltage depend on the operating frequency of the switch and the time it is switched on [18]. The number of turns in the TR1 windings is 10 on the primary and 224 in the secondary.

The R2 resistor and C2 capacitor forms the snubber in Fig. 3. They purpose is to dampen the high voltage transients that occur in the switching of a load [19].

Feedback circuit
Feedback circuit is used to interrupt the generation of the switching pulses by the microcontroller when the desired voltage value (voltage selected by the user) is reached in the high voltage capacitor. This voltage is measured indirectly (Eq. 1) by means of a resistive divider, consisting of 6 resistors (R2–R7 Fig. 2), connected in series with each other and in parallel with the high voltage capacitor. The voltage over R6 and R7 resistors (Fig. 2) passes through a current driver (LM324) connected to a microcontroller terminal configured as an analog input. The microcontroller monitors the analog signal and as soon as the desired value is reached in the capacitor loading is terminated.

$$V_r = \frac{V_{at} * 5}{1000} \tag{1}$$

where V_r is the feedback voltage and V_{at} is the voltage in the high voltage capacitor (Fig. 2).

HIS output was calibrated to present a voltage similar to the chosen voltage by the user, ensuring the safety and reliability of the equipment. In order to evaluate the
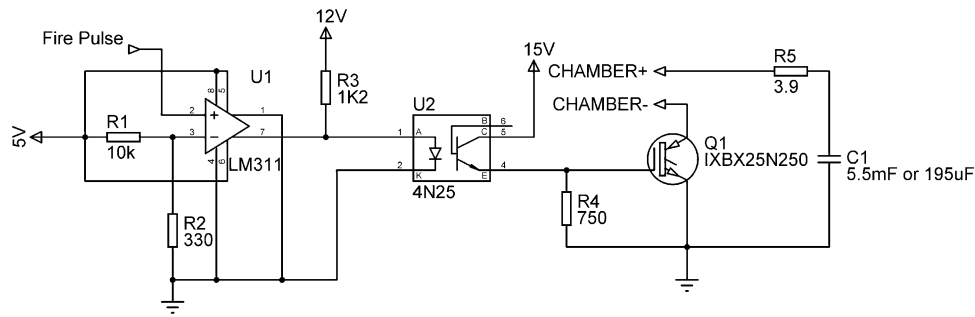
Fig. 4 Firing circuit: The LM311 increases the fire pulse, which actives the optocoupler 4N25 and triggers the IXBX25N250. Then the voltage stored in the capacitor C1 is applied in the stimulation chamber

calibration, 5 tests were performed for each voltage, where the desired voltage was chosen in the display and the equipment output voltage was measured.

Firing circuit

Firing is performed when the fire pulse, sent by microcontroller, is increased by LM311 and activates the 4N25 optocoupler, used to isolate electrically the control circuit to the fire circuit. Following the IXBX25N250 Insulated Gate Bipolar Transistor (IXYS, Milpitas, CA, USA) is triggered, which does the voltage stored in the high voltage capacitor be applied in a resistance selected by the user (stimulation chamber, Fig. 4).

Discharge circuit

This circuit consists of a relay which terminals are connected to the high voltage capacitor and a power resistor (RL3 and R1 in Fig. 2). The microcontroller sends to the discharge circuit a pulse of about 3.5 s shortly after the firing pulse occurs. Then the relay is switched on and the high voltage capacitor is fully discharged on the resistor.

2.2 Testing of a High Intensity Electrical Stimulator

To test the HIS developed in this work we defibrillated isolated Wistar rat hearts in a Langendorff adapted preparation. The electrical pulses were applied to rectangular plate electrodes positioned on the sides of a stimulation chamber, filled with Krebs Henseleit solution (152 ml, pH 7.4 at 37 °C), its resistance is about 45.06 Ω.

Before defibrillate the hearts, we applied an electric sine pulse, with 60 Hz, 1–3 V/cm and 0.5–2 s duration to induce sustained VF. After the fibrillation induction we started the defibrillation protocol. The HIS was coupled to the stimulation electrodes. Then the heart electrophysiological signals were analyzed and if the heart remained in the same state, the pulse amplitude was increased and the defibrillatory shock was reapplied. This procedure was repeated until defibrillation was confirmed. Defibrillation confirmation was made when, after the application of defibrillatory shock, the electrophysiological signals was reestablished. We waited about 5 min until the heart's spontaneous heart rate was

Fig. 5 Waveforms taken from the HIS. **a** The confirm button is pressed; **b** microcontroller sends switching pulses to the switching power supply; **c** the high voltage capacitor is charged and discharged; **d** voltage in the feedback circuit follows the capacitor voltage; **e** microcontroller sends a firing pulse to the firing circuit; **f** microcontroller sends discharge pulse to the discharge circuit
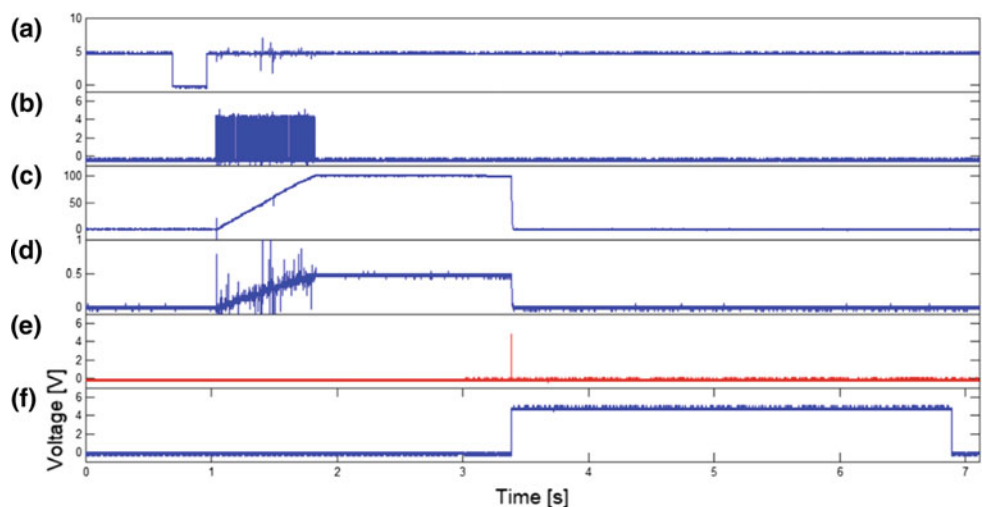
restored, we configured the HIS to apply a pulse with a new duration and we started the fibrillation-defibrillation protocol again for the durations 0.2, 0.5, 1, 3, 5, 8 and 10 ms.

This protocol was approved by the institutional Committee for Ethics in Animal Research (IB/UNICAMP, No. 4355-1) in 5th September 2016.

3   Results

Waveforms taken from the HIS circuits are shown in Fig. 5. When the user presses the confirmation button (Fig. 5a) the microcontroller selects the capacitor to be charged and it starts the generation of the switching pulses (Fig. 5b), which are sent to the switching power supply. The activation of the switching power supply charges the high voltage capacitor (Fig. 5c). The voltage in the capacitor generates a linear voltage increase in the feedback circuit (Fig. 5d), accompanied by the microcontroller. When the feedback voltage corresponds to the desired voltage on the high voltage capacitor, the pulses are interrupted, so the capacitor charging is terminated. After charging the capacitor the microcontroller sends a pulse, with the duration initially chosen by the user, to the firing circuit, as can be seen in Fig. 5e (10 ms pulse was used as an example). Finally, the microcontroller triggers the discharge circuit (Fig. 5f), completely discharging the capacitor and consequently eliminating the voltage present in the feedback circuit (Fig. 5c, d, in 3.4 s).

Charging waveform of the 5.5 mF high voltage capacitor, up to about 100 V, is shown in item (a) of Fig. 6. As we can see, the switching power supply takes about 32 s to charge the capacitor with mentioned voltage. Figure 6b shows the load curve of the 195 µF high voltage capacitor. The voltage in the capacitor takes about 5 s to reach about of 300 V.
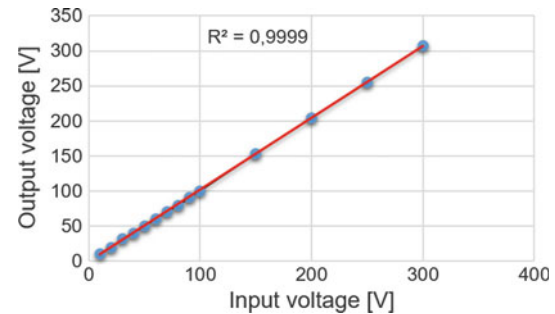
Fig. 8 Relation between the input and output voltages of the high intensity stimulator, where the input voltage was selected by the user and output voltage was measured at the stimulator output

Fig. 6 Capacitors charging waveforms. **a** 100 V in the 5.5 mF capacitor. **B** 300 V in the 195 µF capacitor
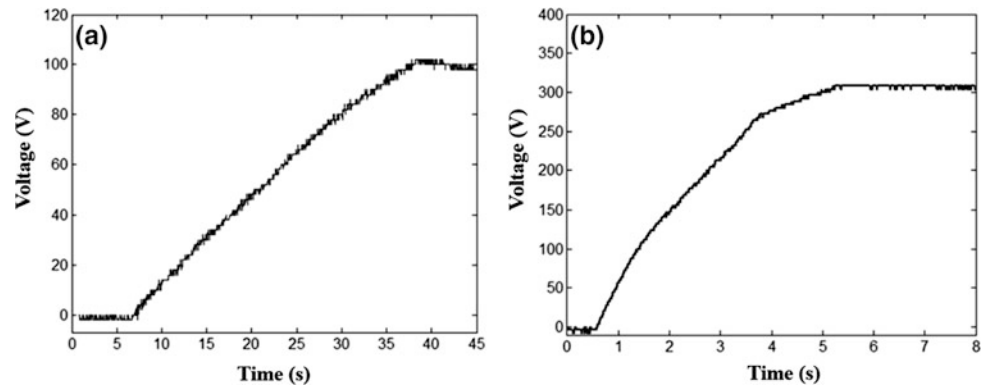
Fig. 7 Voltage pulses waveforms applied in the stimulation chamber. **a** Duration: 0.5 ms and Intensity: 130 V, using 195 µF capacitor. **b** Duration: 10 ms and intensity: 50 V, using 5.5 mF capacitor
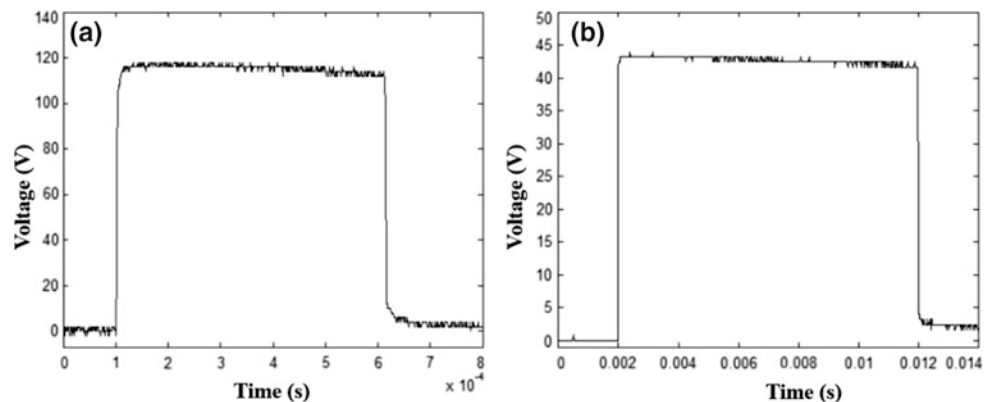
Table 1 Voltage values that defibrillated the hearts for each duration

Animal	Duration (ms)	0.2	0.5	1	3	5	8	10
1	Peak voltage (V)	253	104	57	33	27	32	20
2		330	174	72	48	50	24	56
3		176	120	110	57	36	43	16
4		318	126	79	74	59	55	85
5		251	170	81	60	46	63	15
6		201	68	139	56	46	63	37
7		387	135	113	44	59	44	38
8		356	133	145	48	46	53	39
9		312	132	128	38	46	29	51
10		285	134	118	66	54	59	48

Tests have been performed up to 1000 V. The waveform to charge 1000 V in the 195 µF capacitor is similar to the item (b) in Fig. 6, but it takes more time to charge.

Voltage pulses applied in the stimulation chamber are shown in Fig. 7 for 0.5 ms and 130 V, using the 195 µF capacitor in (a), and 10 ms and 50 V for the 5.5 mF capacitor in (b).

The graph shows in Fig. 8 the voltage selected in the user interface, and the voltages present at the stimulator output. The relationship was linear (Output voltage = 1.025 * Input voltage = 1.027 and R^2 = 0.99) and the points are larger than the error bars (n = 5).

Table 1 shows the experimental results. Voltage values that defibrillated the hearts for each duration. We can see that, as expected, for the shorter durations higher voltage values were required to perform the defibrillation and for longer duration values, less voltage [14–16].

4 Discussion

With the HIS developed in this work we succeed to defibrillate isolated rat hearts applying pulses with a specified duration and intensity, with a maximum error of 13.8 V for a desired voltage of 373.2 V. There were no accidents or intercurrences related to the manipulation of the equipment, despite the risks associated with working with such voltage levels.

We considered that about 32 s to charge up to 100 V on the 5.5 mF capacitor was acceptable for the experiments, since the hearts even being in fibrillation, was being perfused properly and the damages would be minimal because it was maintained condition during charging of the capacitor. In addition, an average of 5 defibrillatory pulses were applied for each duration, totaling 35 pulses applied in each heart, which resulted in an experiment average time of 2 h. Moreover, the 195 µF capacitor was also used for stimulus voltages greater than 100 V, this greatly reduced the waiting time

for pulse application, as can be seen in item (b) of Fig. 6, a voltage of 300 V was rapidly (5 s) stored in this capacitor.

We can see that our solution, to switch the charge of two high voltage capacitors to improve the system time constant (RC), since the resistance of the chamber is fixed, was satisfactory, since the voltage drop during the application of the firing was less than 10% (Fig. 7).

Due to the modular structure in which the circuits were implemented it is possible to carry out improvements and maintenance of the equipment without major changes. A possible improvement would be the generation of bipolar pulses, by means of the exchange the firing circuit by a bridge H.

The use of a resistive divider in parallel with the high voltage capacitor, associated to the signal acquisition by the microcontroller, ensured stability and accuracy of the equipment response (Fig. 8), since it was possible to find a linear relation between the voltage in the feedback circuit and the high voltage capacitor (Eq. 1). In addition, the use of the IGBT as a switch in the firing circuit enabled the firing time to be controlled.

Despite the switching noise in the feedback signal (Fig. 4d), the capacitor charging control was not impaired as can be seen in calibration curve of Fig. 8.

Among the switching power supply topologies, the FC has the lowest cost for power up to 300 W, and it is isolated. Its control is simplest because it has a single transistor on the low side; other topologies would need at least two semiconductors on the low side, which would require much more complex switching control. Compared to linear transformers FC is much lighter and much more efficient [17].

There are other circuits developed to the isolated hearts stimulation that use Variac and diode bridge for capacitor loading and relays for firing [11]. However, in spite of the simplicity of the circuit, its size and weight are high compared to our solution and less precise, since a relay delays hundreds of µs to be activated [7].

5 Conclusion

Using the HIS developed in this work, we were able to defibrillate isolated rat hearts. Its logic operation is simple and the circuits modular construction facilitate design changes. The bigger challenge was to provide a pulse with small voltage decay to the many required pulse durations. The solution found was to use two capacitors with which we were able to maintain the desired characteristics of the defibrillatory pulses. Microcontrolled processes were fundamental in ensuring the fast and reliable operation of the equipment. The nearness between the voltage selected by the user and the stimulator output ensured the reliability of the equipment.

References

1. Prado, L.N., Goulart, J.T., Zoccoler, M., Oliveira, P.X.: Ventricular myocyte injury by high-intensity electric field: effect of pulse duration. Gen. Physiol. Biophys. **35**(2), 121–130 (2016)
2. Goulart, J.T., Oliveira, P.X.D., Bassani, J.W.M., Bassani, R.A.: The influence of cell dimensions on the vulnerability of ventricular myocytes to lethal injury by high-intensity electrical fields. Res. Biomed. Eng. **28**(4), 337–345 (2012)
3. de Oliveira, P.X., Bassani, R.A., Bassani, J.W.M.: Lethal effect of electric fields on isolated ventricular myocytes. IEEE Trans. Biomed. Eng. **55**(11), 2635–2642 (2008)
4. Waldmann, V., Narayanan, K., Combes, N., Jost, D., Jouven, X., Marijon, E.: Electrical cardiac injuries: current concepts and management. Eur. Heart J. (2017). https://doi.org/10.1093/eurheartj/ehx142
5. Yamaguchi, H., Weil, M.H., Tang, W., Kamohara, T., Jin, X., Bisera, J.: Myocardial dysfunction after electrical defibrillation. Resuscitation **54**(3), 289–296 (2002)
6. White, R.D.: New concepts in transthoracic defibrillation. Emerg. Med. Clin. **20**(4), 785–807 (2002)
7. Viana, M.A., Bassani, R.A., Petrucci, O., Marques, D.A., Bassani, J.W.M.: System for open-chest, multidirectional electrical defibrillation. Res. Biomed. Eng. **32**(1), 74–84 (2016)
8. Bruegmann, T., Boyle, P.M., Vogt, C.C., Karathanos, T.V., Arevalo, H.J., Fleischmann, B.K., Sasse, P.: Optogenetic defibrillation terminates ventricular arrhythmia in mouse hearts and human simulations. J. Clin. Investig. **126**(10), 3894–3904 (2016)
9. Crocini, C., Ferrantini, C., Coppini, R., Scardigli, M., Yan, P., Loew, L.M., Sacconi, L.: Optogenetics design of mechanistically-based stimulation patterns for cardiac defibrillation. Biophys. J. **112**(3), 424a (2017)
10. Gazmuri, R.J., Berkowitz, M., Cajigas, H.: Myocardial effects of ventricular fibrillation in the isolated rat heart. Crit. Care Med. **27**(8), 1542–1550 (1999)
11. Sabo, M.Z., Godoy, C.M.G.D., Gomes, P.A.P.: Desenvolvimento e testes de um estimulador elétrico de alta potência para estimulação por campo elétrico em coração isolado de rato. Res. Biomed. Eng. **17**(1), 13–17 (2001)
12. Sokal, N.O., Redl, R.: Control algorithms and circuit designs for optimal flyback-charging of an energy-storage capacitor (e.g., for flash lamp or defibrillator). IEEE Trans. Power Electron. **12**(5), 885–894 (1997)
13. Watson, R., Lee, F.C., Hua, G.C.: Utilization of an active-clamp circuit to achieve soft switching in flyback converters. IEEE Trans. Power Electron. **11**(1), 162–169 (1996)
14. Shorofsky, S.R., Kavesh, N.G., Gold, M.R.: Strength-duration relation for human transvenous defibrillation. Circulation **94**(8), 769–769 (1996)
15. Lapicque, L.: Definition experimentale de l'excitabilite. Soc. Biol. **77**, 280–283 (1909)
16. Weiss, G.: Sur la possibilite de rendre comparables entre eux les appareils servant a l'excitation electrique. Arch. Ital. Biol. **35**(1), 413–445 (1990)
17. Coruh, N., Urgun, S., Erfidan, T.: Design and implementation of flyback converters. In: 5th IEEE Conference on Industrial Electronics and Applications (ICIEA), pp. 1189–1193. IEEE (2010)
18. Pomilio, J.A.: Web Page. http://www.dsce.fee.unicamp.br/~antenor/fontchav.html. Las accessed 19 April 2018
19. Harada, K., Sakamoto, H.: Switched snubber for high frequency switching. In: 21st Annual IEEE 1990 Power Electronics Specialists Conference, PESC'90 Record, pp. 181–188. IEEE (1990)

Development of Equipment for Automatic Diagnosis of the Neuromuscular Condition

Jonathan Bispo, Paulo Eugênio, Joao Durigan,
and Henrique Martins

Abstract

Electrically evoked muscle contraction has become a relevant therapeutic strategy in the rehabilitation practice and in the research field. In Intensive Care Unit (ICU), for instance, critical ill patients can present significant muscle weakness and neuromuscular electrophysiological disorders due to long periods of immobility. Neuromuscular Electrical Stimulation (NMES) has been shown an important tool to avoid such problems. However, in crically-ill patients with neuromuscular electrophysiological disorders the assessment of neuromuscular excitability is essential for improving NMES efficacy. Neuromuscular excitability has been assessed by Stimulus Electrodiagnosis Test (SET) which measures: rheobase, chronaxie and accommodation. However, SET is a time demanding procedure and depends on the subjective visual detection of each examiner. The objective of this work was to develop an equipment capable to automating SET, making it feasible accurate and reliable. Such equipment is capable of generating the electrical stimuli with the parameters necessary for SET, modify these parameters in real time and stop the stimulation when the contraction is detected. This detection is possible through a biofeedback system implemented using an accelerometer placed on the muscle in which contraction will occur due to electrostimulation. Through the workbench tests it was possible to generate biphasic electric stimuli up to 225 mA with load of 1 kΩ and monophasic up to 104 mA with load of 1 kΩ too. It was possible to vary the pulse width of the stimuli from 20 μs to 50 ms with steps of 20 μs. Tests performed on biofeedback algorithm showed it was capable to detect automatically voluntary muscle contractions.

J. Bispo (✉)
Graduate Program in Electrical Engineering, Federal University of Minas Gerais, Belo Horizonte, MG, Brazil
e-mail: jfb0101@gmail.com

P. Eugênio
Health Sciences and Technologies Ph.D. Program, University of Brasilia, Federal District, Brazil

J. Durigan
School of Physical Therapy at the University of Brasilia, Brasilia, Federal District, Brazil

H. Martins
Engineering School at the Federal University of Minas Gerais, Belo Horizonte, MG, Brazil

1 Introduction

The number of patients in recovering ICU has increased in recent years [1]. While this is extremely positive, some problems can occur as a result of long periods of time of immobility, such as ICU-acquired weakness (ICUAW) [2]. The main causes of ICUAW are critical polyneuropathy and myopathy, identified by weakness, loss of muscle mass and decreased neuromuscular excitability [3]. One strategy to prevent such problems would be the realization of artificial muscle activation through of the NMES, which can be used for the prevention or rehabilitation of partially or fully immobilized patients [1].

The efficiency of NMES can be evaluated by the strength of the evoked muscular contraction, that is, by the torque caused due to the artificial stimulus [4]. Such torque is directly related to the pulse width of the stimulus [5]. In patients with electrophysiological neuromuscular disorders, the pulse width should be increased to improve the results of NMES [2].

Beyond the pulse width, the amplitude of stimulus is important to the efficiency of NMES [6]. As there is no consensus on these values, they can be determined by reference to the rheobase and chronaxie tests of the electrodiagnostic of the patient's neuromuscular condition [2, 6, 7].

However, because it is operator-dependent, that is, it needs the visual perception of the evaluator, it can generate false positives or false negatives of muscular contraction, conferring a lot of variability to the values of the tests. The lack of specific equipment to this type of exam also makes difficult its application. The test needs to be done with standard commercial electrostimulators, where the parameters are changed manually by the operator, which takes a lot of time.

The objective of this work was to develop a neuromuscular electrostimulator to perform SET automatically through of a biofeedback system capable of detecting minimal muscle contraction. In this way, it is expected to increase the reliability and reproducibility of the test, being able to be executed by professionals of the health, independently of its clinical experience for that.

2 Materials and Methods

The development of the equipment adopted the architecture presented in Fig. 1.

The system is subdivided into four main parts: Control Unit, Power Unit, Biofeedback and Graphical Interface. The control unit consists of a Bluetooth module HC-05 and a STM32F446RET microcontroller from ST Electronics whose firmware calculates and generates, in real time, the waveforms through the DACs of the microcontroller itself. The Power Unit is composed of a high voltage DC–DC converter (± 150 V DC) that allows the generation of stimuli of sufficient intensity to overcome skin resistance, a medical source of ± 5 V DC and 30 W for to feed all system and current sources controlled by the voltages generated by the control unit (DAC), with topology based on Wilson Current

Mirror [8]. The biofeedback circuit is composed of two tri-axial accelerometers, one for each channel, connected to the microcontroller through Inter Integrated Circuit (I2C), used to detect muscle contractions. In the present work only one accelerometer was used, the LSM9DS1 in the STEVAL-MKI59v1 encapsulation of ST Eletronics, because only one muscle group was evaluated.

For the graphical interface an Android app was developed able to send and receive messages of the equipment. Through this app it is possible to select the parameters of stimulation and to carry out any of the two tests, rheobase or chronaxie. It is also possible to record in the app the individual's data and which muscle will be stimulated during the exam. The equipment firmware starts the requested test and progressively increments the values of the pacing parameters until the contraction is detected. At the end of each test the amplitude value or pulse width is sent to the software.

Firmware can also cease electrostimulation automatically when muscle contraction is detected. Figure 2 details this process.

The biofeedback algorithm receives acceleration values from the Z axis from accelerometer and stores 500 ms of data before de stimuli is applied and 500 ms after that. If the standard deviation read in 500 ms after the stimuli is 1.2 times grater than the one read in first 500 ms, a contraction was detected. The value of 1.2 was obtained empirically during the study. The accelerometer's Z axis is positioned in the muscle, as close as possible the gravity orientation.

Workbench tests were performed using a 1 kΩ resistor as the load. In order to obtain the waveforms generated, as well as to evaluate the maximum limits reached for both intensity and pulse width, an Agilent Technologies oscilloscope model DSO-X 2012A was used.

Fig. 1 Hardware block diagram
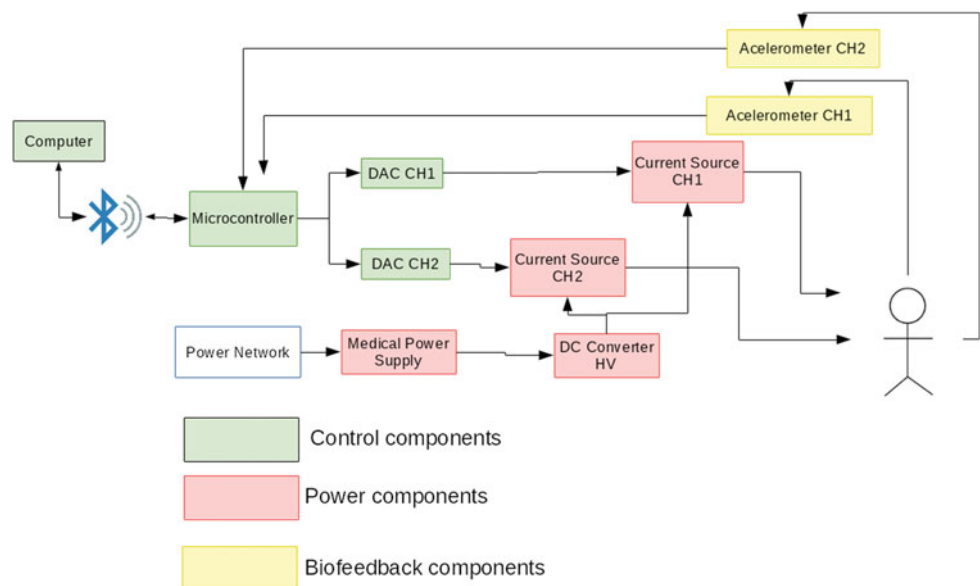
Fig. 2 Firmware algorithm flowchart
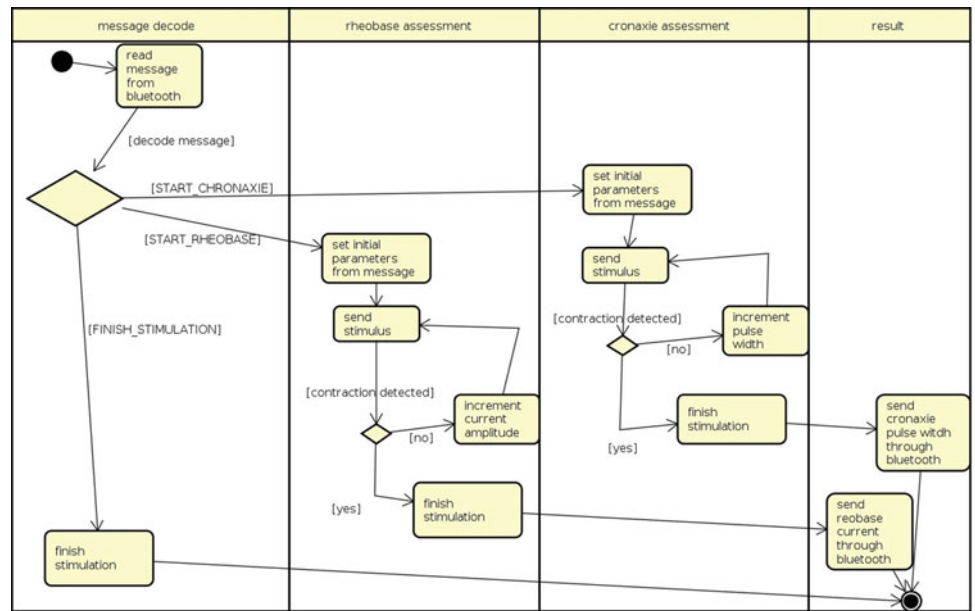
Fig. 3 3D picture of developed PCB
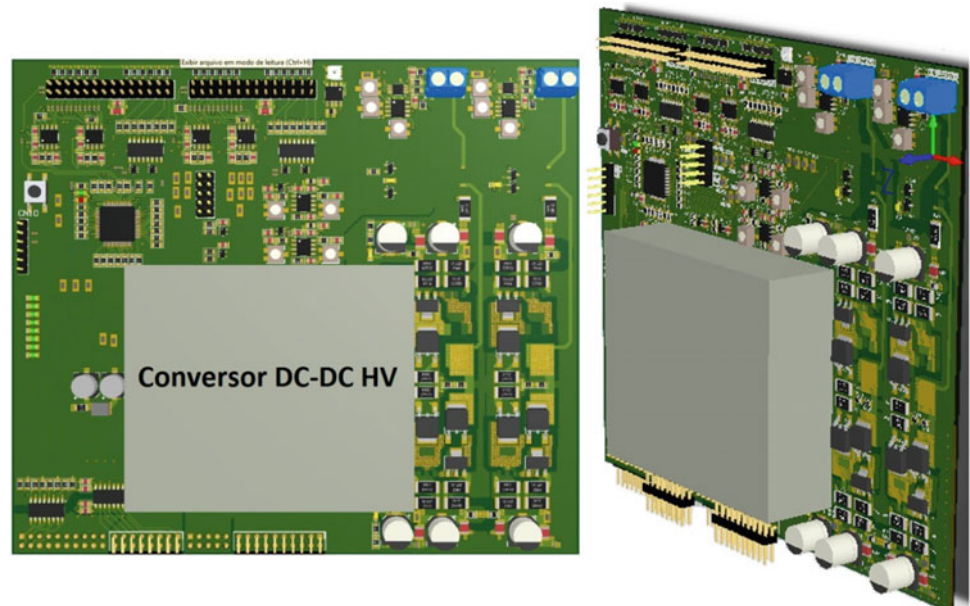
To assess the developed algorithm capacity in order to detect automatically muscle contractions, the accelerometer was positioned on the tibial muscle of the author, that realized 10 voluntary contractions with differents intensities.

3   Results

In this work a complete system of NMES was developed to perform rheobase and chronaxie tests automatically.

The 3D picture of the equipment is shown in Fig. 3.

The developed PCB can be seen in the Fig. 4.
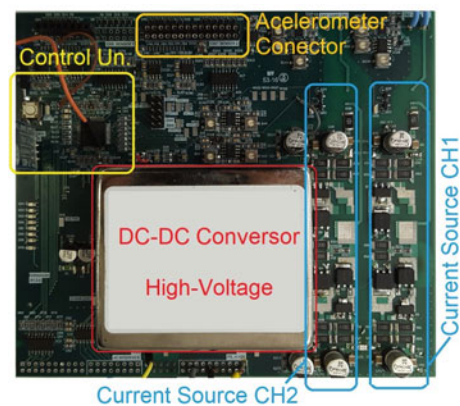
Fig. 4 PCB mounted with main parts highlighted

Fig. 5 Developed equipment
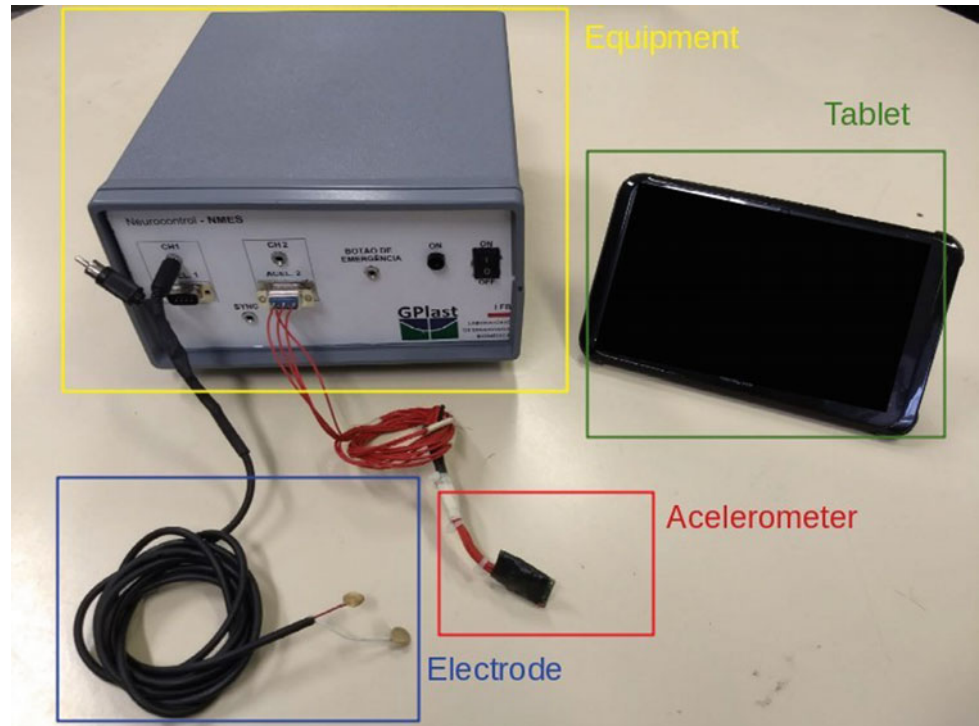
Fig. 6 Generated biphasic
stimuli in workbench tests
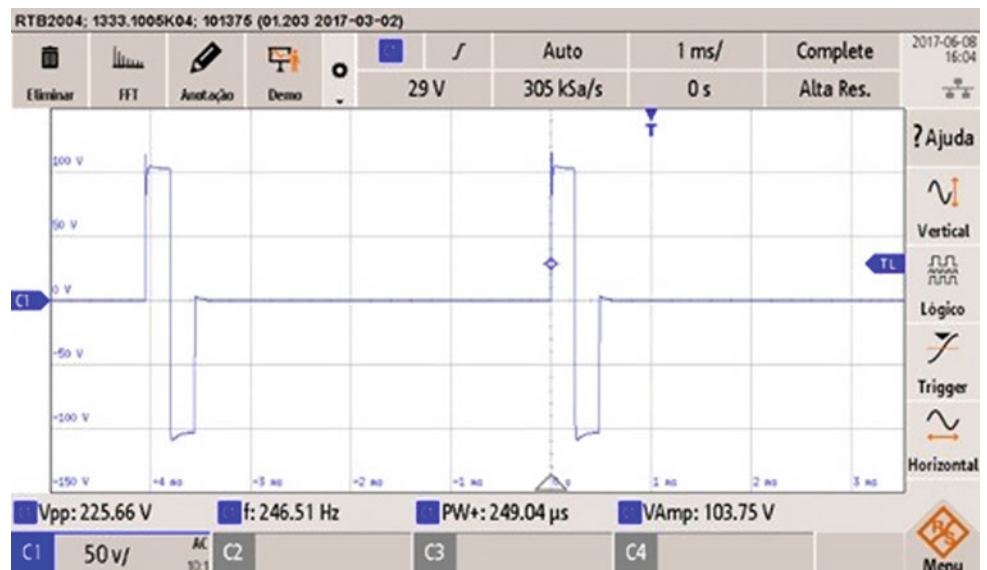
The full equipment with its parts highlighted is shown in Fig. 5. It is composed by the equipment itself, the tablet where the Android app is executed, the electrodes for stimulation and the accelerometer for biofeedback circuit.

The stimuli generated in workbench tests by the equipment with maximum amplitude of 104 mA and a load of 1 KΩ are shown in Fig. 6.

The app print are shown in Fig. 7.

The biofeedback tests performed by the author obtained a hit rate of 100% for Z axis values. For X and Y axis, hit rates was below to 10%.

The system was able to generate biphasic symmetrical electrical stimuli with a maximum intensity of 225 mA in a load of 1 kΩ and monophasic stimulus up to 104 mA in a load of 1 kΩ too. It was possible to generate stimuli between 20 µs and 50 ms wide without changing the thermal pattern of the system. Communication via Bluetooth with the

Fig. 7 Develped Android app
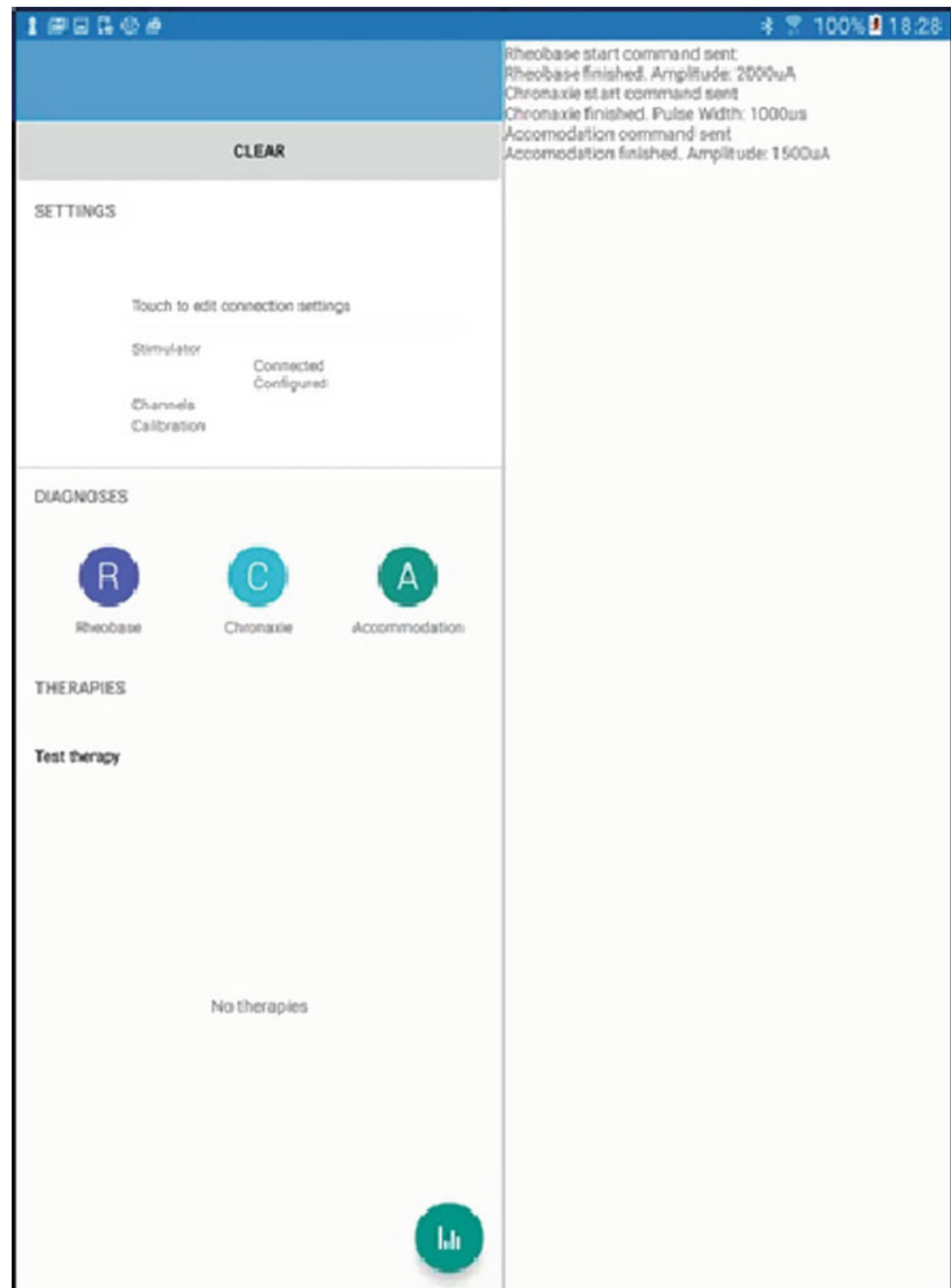
software running on the computer did not show packet losses in communications with speeds up to 115.200 bps. No higher speeds were tested as the throughput required for system operation is below this value.

4 Discussion and Conclusion

The developed system proved to be stable and efficient, with no loss of packets in the communication and the generated waveforms were as expected. The system hardware was assembled through of an 8-layer 15.5 × 13.5 cm printed circuit board, one was for ground and other for VCC. This avoided the creation of loops and allowed the generation of stimuli with low incidence of noise. Workbench tests has shown that the system is capable of generating electrical stimuli that meet the demands of NMES [9]. It has also been shown to be promising for use in ICU because it allows a faster and more efficient execution of neuromuscular examination. The electrostimulation device was designed in compliance with the NBR IEC 60601-1 standard, which evaluates the electrical safety of the equipment. However,

for its use in ICU environments, it will still be necessary to submit the equipment to the normative tests recommended by NBR IEC 60.601-1-2 standard that evaluate the electromagnetic compatibility of the system, i.e., verify both the immunity of the system for conducted interference and irradiated, as to whether the level of interference radiated by the equipment is within the desired values. This ensures that the system will not interfere with the operation of other ICU equipment.

The graphical interface developed proved to be efficient for operation and obtaining results in real time.

The biofeedback system and the high sensitivity of the accelerometers allowed muscle contraction to be detected as soon as it occurred.

When the muscle contraction happens, actin and myosin filaments overlap each other, causing a movement of the muscle in the X and Y accelerometer axis direction, and an increase in the muscle volume in the Z accelerometer axis direction [10]. The movement in X and Y axis is not strong enough to move the accelerometer, but the increase in the volume causes a variation in the position of the Z axis, which should explains the high hit rate obtained in this axis compared to another axis.

These results show that the system developed in this work can be a valid tool to increase the use of SET with accelerometer and, consequently, to improve therapies with NMES within ICU settings. Also, the human machine interface can be used to control the stimulator and adjust its parameters in an easy and agile manner. It is also possible to follow up the diagnosis or therapy progress in real time.

Future studies will be conducted with healthy subjects and compare reliability of the automatic method with the manual currently performed with commercial equipments.

References

1. Kress, J.P., Hall, J.B.: Icu-acquired weakness and recovery from critical illness. N. Engl. J. Med. **370**(17), 1626–1635 (2014)
2. Silva, P.E., et al.: Safety and feasibility of a neuromuscular electrical stimulation chronaxie-based protocol in critical ill patients: a prospective observational study. J. Crit. Care **37**, 141–148 (2016)
3. Lacomis, D.: Electrophysiology of neuromuscular disorders in critical illness. Muscle Nerve **47**(3), 452–463 (2013)
4. Gondin, J., Cozzone, P.J., Bendahan, D.: Is high-frequency neuromuscular electrical stimulation a suitable tool for muscle performance improvement in both healthy humans and athletes? Eur. J. Appl. Physiol. **111**(10), 2473–2487 (2011)
5. Gregory, C.M., Dixon, W., Bickel, C.S.: Impact of varying pulse frequency and duration on muscle torque production and fatigue. Muscle Nerve **35**(4), 504–509 (2007)
6. Paternostro-Sulga, T., Schuhfried, O., Vacariu, G., Lang, T., Fialka-Moser, V.: Chronaxie and accommodation index in the diagnosis of muscle denervation. Am. J. Phys. Med. Rehabil. **81** (April) 253–260 (2002)
7. J. Kimura. Electrodiagnosis in Diseases of Nerve and Muscle, 4th ed. Oxford (2013)
8. Sedra, A.S., Smith, K.C.: Microelectronic Circuits, 6th ed., pp. 539–541. Oxford University Press (2010)
9. Maffiuletti, N.A., Minetto, M.A., Farina, D., Bottinelli, R.: Electrical stimulation for neuromuscular testing and training: state-of-the art and unresolved issues. Eur. J. Appl. Physiol. **111** (10), 2391–2397 (2011)
10. Cooper, G.M.: The Cell: A Molecular Approach. Sinauer Associates (2000)

Device for Evaluating the Bite Force of Night Bruxism

Renato de Brito Sanchez, Chrystianne de Melo Setter,
Jean Corrêa Rodrigues, Jefferson Valladão Oliveira de Mello,
José Arnaldo dos Santos Junior, Silvia Cristina Martini Rodrigues,
Silvia Regina Matos da Silva Boschi, Terigi Augusto Scardovelli,
and Alessandro Pereira da Silva

Abstract

Bruxism is a movement disorder that occurs during sleep, characterized by the involuntary movement of tightening and moving the mandible in different directions, producing muscular pain and tooth wear. In addition, bruxism can lead to changes in sleep and headaches. The aim of this study was the development of a device to evaluate the bite force of bruxism in a domestic environment. The methodology was the creation of an intraoral device, added to the inclusion of resistive sensors, which measure mechanical deformation. An electronic circuit has been developed capable of capturing the frequency of these deformations that are captured during sleep. This information is stored and generates data capable of correlating with sleep periods, evaluating the amount and frequency of dental occlusions. The results are in accordance with the literature, demonstrating that the period of greatest "clenching" of the teeth is precisely in stages 1, 2 and 3 of NREM sleep.

Keywords

Bruxism • Evaluation of bite force • Biomedical equipment

1 Introduction

The term bruxism was introduced in the dental literature as of 1907 by Marie and Pietkiewicz. Since then the term has been used persistently in the literature to indicate "an unconscious and sometimes conscious grinding habit, pinch and slide the teeth with no apparent functional goals." [1].

Bruxism is described as a movement orofacial called parafunction, whose etiology is complex and multifactorial [2]. The activities of the masticatory muscles can be divided into two basic types: Functional including chewing, swallowing and speaking and parafunctional (non-functional) that includes teeth clenching or grinding (bruxism) and various other oral habits [3].

Various settings are found in the literature, but according to Lobbezzo et al. the international consensus 2013; define bruxism as Bruxism has two distinct circadian expressions "a repetitive muscle activity characterized jaw by clenching or grinding of the teeth or hold and push the jaw.": it can occur during sleep (indicated as bruxism sleep) or during wakefulness (indicated as agreed bruxism) [4].

The term is used especially when bruxism the duration and intensity of pressing or griding influences has an influence on wear and dental problems lead to the development of the temporomandibular joint (TMJ). However, it is important to note that all people subconsciously clench their teeth at some point, even healthy population due to dental changes, bodily pain and social conflicts, and this can also be considered bruxism activity [5].

Individuals with sleep bruxism (SB) symptoms reported primarily on waking such as headache in the temporal region of the rigid jaw muscles, locking difficulties or mouth opening and tooth hypersensitivity. Clinically it may be noted, in these patients, an incompatible tooth wear with age and function, muscle hypertrophy in masseter region, restorations of fractures. Also, there are reports of dental noises during sleep that are mostly noticed by relatives [6].

R. de Brito Sanchez (✉) · C. de Melo Setter · J. C. Rodrigues ·
J. V. O. de Mello · J. A. dos Santos Junior · S. C. M. Rodrigues ·
S. R. M. da Silva Boschi · T. A. Scardovelli · A. P. da Silva
Universidade de Mogi das Cruzes, Av. Dr. Cândido Xavier de
Almeida e Souza, 200 Mogi das Cruzes, SP, Brazil
e-mail: renatobritosanchez@gmail.com

R. de Brito Sanchez
Centro Universidade ENIAC, Rua Força Pública, 89, Guarulhos,
SP, Brazil

Despite the limitations to complete the diagnosis, studies show that bruxism during sleep occurs around 12, 8% of adults and 35.3% of children [7].

The etiology of bruxism is still unclear and there are several factors that may be related to your trigger. Some studies report that certain medications can increase bruxism events, although the evidence is still weak, others suggest that there may be a genetic predisposition [3].

The American Academy of Sleep Medicine classifies sleep bruxism (BS) as a movement disorder and defines an oral activity characterized by grinding or clenching the teeth during sleep, usually associated with arousals (American Academy of Sleep Medicine. International Classification of Sleep disorders: Diagnostic and coding manual 2nd ed Westchester, Illinois: American Academy of Sleep Medicine; 2005) [8].

The classification of bruxism according to the International Classification of Sleep Disorders—2005, describes bruxism as a movement disorder related to sleep which can be divided into:

1. *Centric*—the act of clenching.
2. *Eccentric*—the act of clenching and laterally move the lower jaw (teeth grated).
3. *Primary*—when it occurs alone, without connection to any other medical condition.
4. *Secondary*—when connected to another medical condition.
5. *Vigil*.
6. *During sleep*.

The symptoms are: a headache in the temporal region, rigid jaw or fatigued muscles, or difficulty catching mouth opening and tooth hypersensitivity. Clinically it may be noted, in these patients, an incompatible tooth wear with age and function, muscle hypertrophy in masseter region, restoration of fractures or teeth, recessions. Also, dental noises reports during sleep mainly noticed by relatives [6].

Sleep is a state marked by decreased consciousness, reduced skeletal muscle movements and slowing metabolism, has the essential restorative function and role in memory consolidation [9]. It is divided into known phases NREM (divided into 4 phases) and REM sleep (rapid eye movement). During phase 1, which is superficial and fleeting, many people experience sudden muscle contractions, known as 'hypnotic myoclonus', often preceded by a falling sensation. It is at this stage that nocturnal bruxism occurs.

To date, the best tools for the diagnosis of bruxism and TMD research are respectively polysomnography (PSG) and the Diagnostic Criteria Research index (RDC/TMD). As the clinical diagnosis of bruxism through history has limitations, the ideal would be that all probable bruxists were submitted to the test of PSG [10].

On examination PSG the patient sleeps with electrodes attached to the body, which allows simultaneous recording of electrophysiological variables such as brain electrical activity, eye movement, muscle activity, heart rate, flow and respiratory effort, blood oxygenation, snoring and body position [10].

The exam is important to confirm the diagnosis, ruling out other orofacial movements made during sleep, such as swallowing, coughing, grunting or switch opening and closing the mouth, which can be confused with bruxism. But unfortunately, the PSG is still costly because it depends on structured sleep laboratory, skilled technical and displacement of the patient [3].

Despite Polysomnography be considered "gold standard" in the diagnosis, when examining patients often have difficulty initiating and maintaining sleep the first night that perform PSG (the first night effect); Also, insomnia varies from night to night, so that one may be insufficient to detect physiological changes related to it. Patients with poor perception of sleep cannot reveal any specific change in PSG, and even normal adults may have changes in the perception of sleep when their time cues are changed. For these reasons, the specificity of a single night PSG is very limited in the diagnosis of insomnia, and consequently bruxism [11]. Measurements of intraoral bite force are of great importance, especially when related to the study of bruxism, especially as a complement to the polysomnographic diagnosis, which is still the most suitable process to monitor the progress of patients and comparing different possible treatments [5].

The study of Nishigawa results on the bite force produced during bruxism events suggests high values as 1100 N. The pressure on tooth surfaces may reach 40 MPa alarming levels sufficient to cause wear and even breakage of the tooth. Regarding the duration of bruxism events, an average of about 7 s was reported [5].

The objective this study was to create a device for evaluating the bite force of nocturnal bruxism in the home.

2 Methodology

The methodology applied in this study consisted of two distinct procedures. First the dental molds were made, and then the installation of the sensors and other electronic components.

The measurements of the contacts between the teeth are of great importance for the diagnosis and establishment of the level of bruxism. It was developed for diagnosis, an intra-buccal device respecting the characteristics of

stabilizing myorelaxant plaques, used in the treatment of the parafunctional habit. Mechanical deformation sensors of the strain gauge type were installed in the device, besides a mini Arduino device, that was connected with an SD card module.

The objective of the device is to account for the number of occlusal contacts generated during the patient's sleep, revealing if it has characteristics to be diagnosed with bruxism, in addition to establishing a level for the pathology.

2.1 Intraoral Support/Muscle Relaxants Plates

An intra-buccal support was developed for placement of the mechanical deformation sensors, respecting the characteristics of stabilizing muscle relaxants plates: thickness up to 3 mm, occluded contacts distributed and a smooth and rigid surface. The material used for confection was silicone and acetate, thermoformed through gypsum models of the dental arches of the patient. The mechanical deformation sensors and accessories wires were placed between the plates, generating a total comfort for their use (Fig. 1).

2.2 Sensors

To perform the measurement of bite force used two strain gauge sensors BF350-3AA. These transducers are resistive sensors, or to undergo axial deformation or bending deformation, their ohmic resistance varies, thus allowing to realize a correlation between the applied force and bite an electrical signal. Additionally, they feature a compact size facilitating the positioning of intraoral sensors in the apparatus. The strain gauge bridge room require completion resistors to complete the Wheatstone bridge, wherein R1 is an active strain gauge that measures the deformation.

2.3 Electronic Device

Through prototyping board Arduino Pro Mini ATmega328P using the microcontroller, the sensor data are processed. The values provided by Strain Gauge are analog data, it used its own A/D converter of the microcontroller to turn into digital signals. In addition, we use a RTC (Real Time Clock) and a semiconductor temperature sensor, which are provided on the date, time and temperature, such that allows us to get the exact record of events and thus facilitate data interpretation.

In the idealized device was inserted a module for Micro SD card, so the data provided by Strain Gauge sensors, the RTC and the temperature sensor are stored in a file with format "txt", then the equipment results in a datalogger offline that operates locally in the application.

To ensure that data continued to be measured and recorded the RTC has a unique CR3032 3 V × 500 mAh to keep your active internal clock even without the main source, which is arranged by a 9 V battery that powers all components through a 5 V voltage regulator (Fig. 2).

2.4 Electronic Circuit

The use of compact components and SMD technology facilitated the assembly and placement of components inside the mask to sleep. Figure 3 shows the electronic circuit with the connections between the microcontroller and other components.

2.5 Operation Mode

In the operation mode as initially energizing device in the set all the constants and microcontroller pins followed by the ISP serial bus initialization may be initialized to the Micro SD card and the RTC. The program runs in "Loop"

Fig. 1 Scheme showing the position of the sensors within the support plate
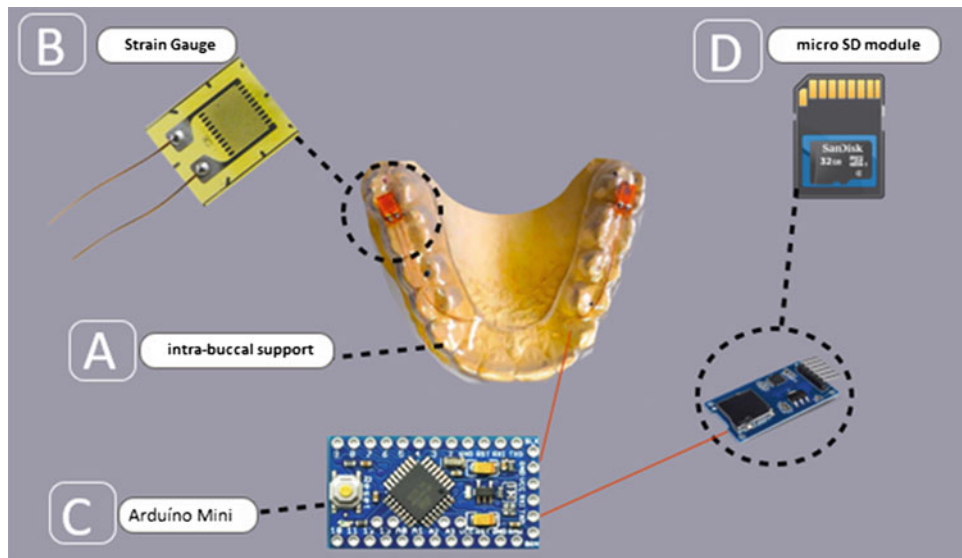
Fig. 2 Details of device components
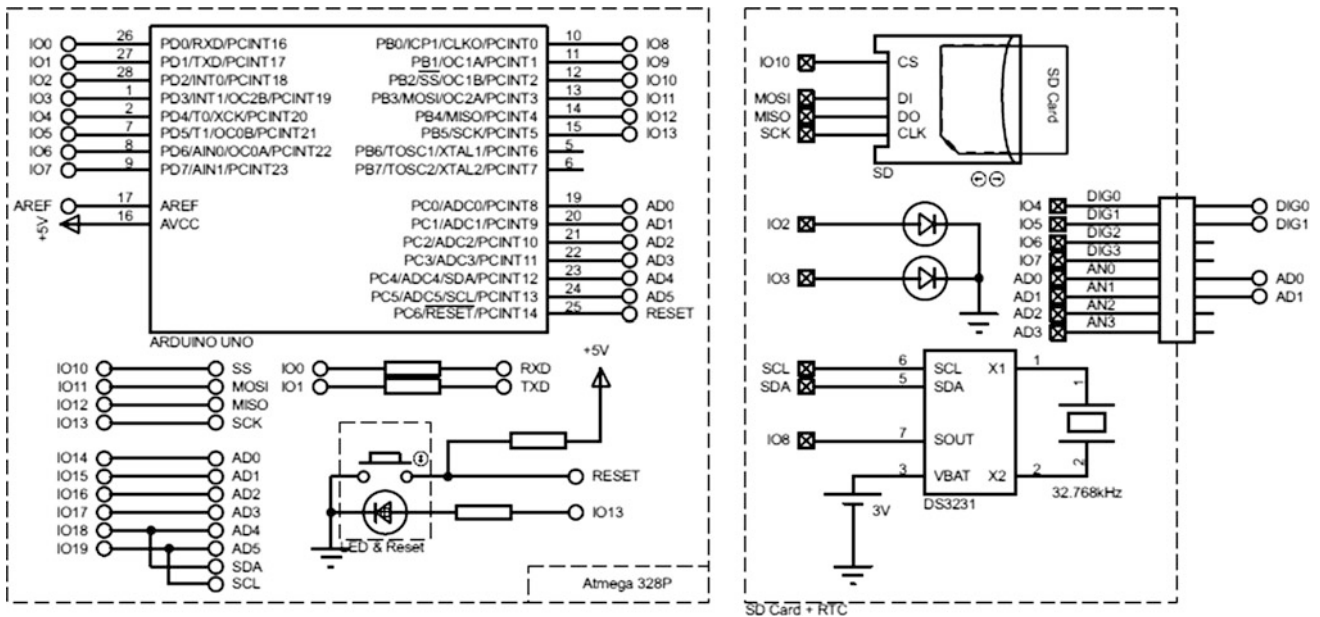
Fig. 3 Details of electronic circuit and components

until there is infinite power down, so the library "Time" synchronize every 5 min to the RTC to ensure the subroutines time and the correct sampling of the measurements. As the bus checks were manually updating RTC and proceeds, if new data entered, with the new schedule in the RTC. This process may be visualized in the flowchart of Fig. 4.

After initialization of the main routine program operates based on two constants, with 1 being the TempEmerg that defines the time of reading and writing of the analog inputs in the Micro SD after the set-point event. The other is the timing of the second RTC with the sub-data recording.

Thus the device operates constantly reading both analog inputs, which have a correction value for adjustment to the N range (Newton), but the data are written in Micro SD only when the latter reach 00, the result of the overtaking 1 min, so this event is sampled every minute, but there are 2 loops while monitoring if the read values do not exceed the set-point, in this case defined 350 N which results in approximately 35.7 kgf on a scale of 0 initial the 1000 N. If any of the sensors exceed 350 N its while loop writes the variable measured every 100 ms, this time can be adjusted minimally in 10 ms.

Fig. 4 Functional Flowchart
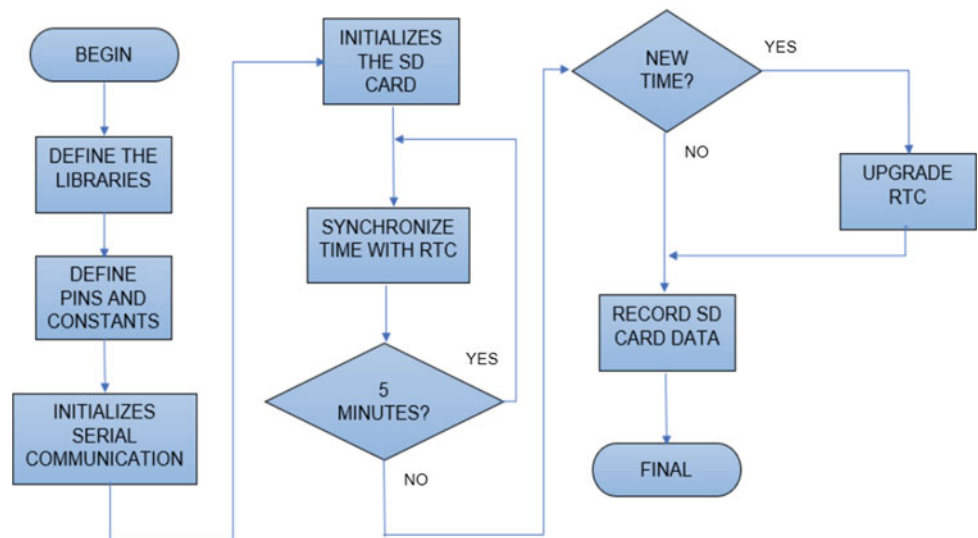
Thus, the program ensures measures the lower 350 N do not fire readings and maintain per minute, so if there is no overrun will have a period 1 h a total of 60 measurements, which results in a night's sleep 8 h 480 measurements.

Managed in this way could easily separate the data between measurements below the set point and the relevant measurements for the analysis of expressive work and have to occur when a higher power than that imposed by the simple touch of the teeth.

2.6 Validation of the Device with a Standard

To validate the device was used to measure the standard mass and calibration of an analytical balance, and a calibrated digital multimeter, and a source of stabilized voltage.

Masses were used 1, 2, 3, 4, 5 and 10 kg, which were positioned for 30 s to ensure stabilization and sampling of the sensors installed on board initially being in the element positioned to the left, then the right and concluding with both sensors subjected to the same load.

The values obtained are shown in the Table 1.

3 Discussion and Results

The data measured by the two analog inputs comprise a sampling of 320 values, which have values equal to 0 for long periods during sleep and values that identify the situations of teeth tipping and the values in which the max is identified and its intensity. These values are recorded as described in the development of the item of this work, '.txt' format file on the Micro SD card called the data logger (Table 2).

3.1 Graphical Representation of Data

See Figs. 5, 6 and 7

3.2 Discussion

According to Pallikarakis Biomedical Engineering is a dynamic field that is undergoing a rapid evolution in the last

Table 1 Test and validation of the sensors

Measured values	Mass (kg)	Individual measurement (N)		Simultaneous measurement (N)	
		Sensor 1	Sensor 2	Sensor 1	Sensor 2
1	1	95.998	96.002	95.998	96.002
2	2	191.997	191.803	191.997	191.803
3	3	287.996	287.900	287.996	287.900
4	4	383.994	384.050	383.994	384.050
5	5	479.993	479.998	479.993	479.998
6	10	959.985	959.900	959.985	959.900

Table 2 Data measured of sensors 1 and 2

Values	Sensor 1 (N)	Sensor 2 (N)
Average	23.698	25.460
Minimum	0	0
Maximum	450.800	463.300
Average non-zero	280.874	271.576

Fig. 5 Plot of the non-zero values of sensor 1
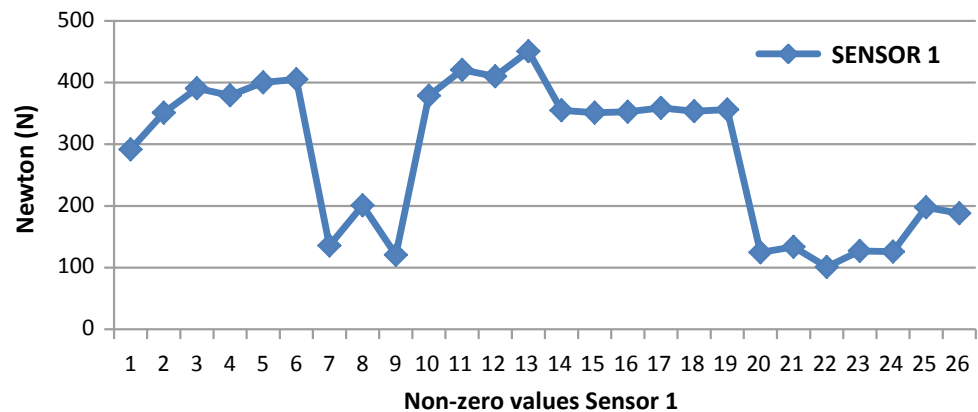
Fig. 6 Plot of the non-zero values of sensor 2
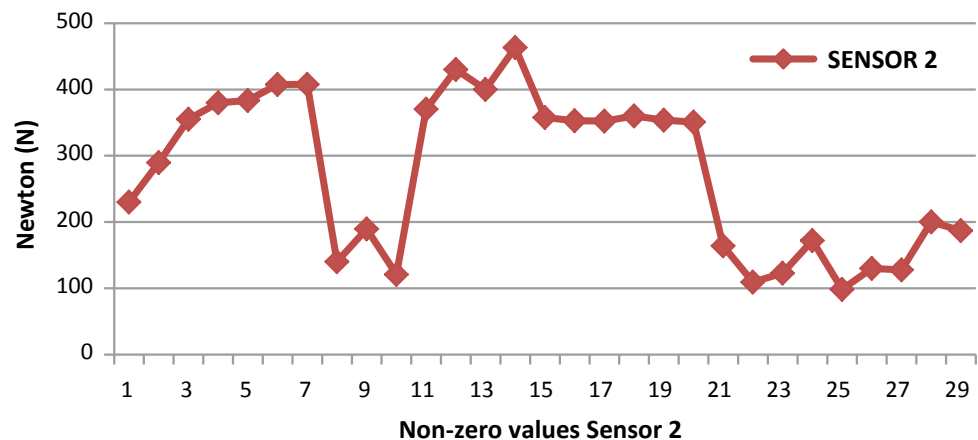
decades and these advances are closely related contributions of basic sciences and engineering that need the knowledge of the interdisciplinary team [12]. In this study, this participation of the team was fundamental to the creation and accomplishment of the device. Recalling that this was created from a challenge launched during the semester of the discipline of transduction of biomedical magnitudes, taught by Prof. Dr. Alessandro P.S.

According to Manfredini (2015) bruxism is a repetitive activity of the muscles of the mandible characterized by tightening or grinding the teeth and push the mandible, which presents distinct circadian manifestations and that has negative effects on the temporomandibular joint [13]. The force exerted by the masticatory muscles determines the amount of load destined to break the food and this, can be

measured through the use of specific equipment. Among these devices we can highlight the gnatodynamometer, the unilateral force transducers and the bilateral ones. The use of these instruments is of great relevance for several health professionals such as dentists, physiotherapists and especially for speech therapists, since FM measurement has clinical value, since it can be used in understanding the masticatory function of healthy individuals and patients with SE dysfunctions and other related pathologies [14].

The device developed here proved to be effective, since besides helping in the diagnosis of bruxism, it has characteristics of stabilizing miorrelaxants plaques, thus cooperating for the treatment of the disorder.

McAuliffe et al. in 2015 also created a device to record events of nighttime bruxism at home, where pressure sensors

Fig. 7 Graph of the representation of all values of sensors 1 and 2
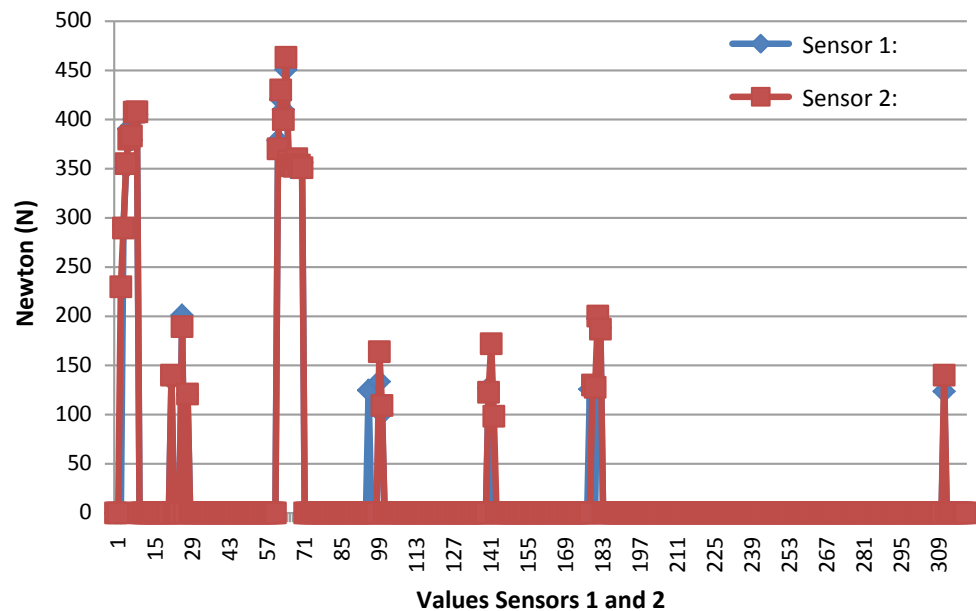
were developed beneath the surface of an occlusal plate, and a circuit was designed to facilitate recording and wireless transmission of the pressure sensor, although with an internal battery, which seemed inconvenient to the patient [15].

Therefore in our device was created a specific adaptation and in addition, the device showed little increase in the vertical dimension of occlusion (DVO), facilitating its use. It also presented a contact establishment that was uniform and without occlusal interference.

4 Conclusion

The intra-oral device developed was effective for the diagnosis of parafunctional habit. Unlike polysomnography, the device was made with low cost, easy implementation, being able to be used in the domestic sphere.

References

1. Molina, O.F., Jay, D.C., Cury, M.D.N., Cury, S.E., Gimenez, S.R.M., Solomon, E.C., Pinesci, E.: A critical analysis of the classification systems for bruxism: implications for diagnosis, severity and treatment of TMJ signs and symptoms associated with the habit. JBA Curitiba **2**(5), 39–61 (2002)
2. Kato, T., Yamaguchi, T., Okura, K., Abe, S., Lavigne, G.J.: Sleep less and more bite: sleep disorders associated with occlusal loads during sleep. J. Prosthodont. Res. **57**, 69–81 (2013)
3. Morais, D.C., Oliveira, A.T., Monteiro, A.A., Alencar, M.J.S.: Bruxism and its relationship to the central nervous system: literature review. Rev. Bras. Odontol. (Rio de Janeiro) **72**(1/2), 62–65 (2015)
4. Lobbezoo, F., Ahlberg, J., Glaros, A.G., Kato, T., Koyano, K., Lavigneg, J., Leeuw, R., Manfredini, D., Svensson, P., Winocur, E.: Bruxism fined and graded: an international consensus. J. Oral Rehabil. **40**, 2–4 (2013)
5. Lantada, A.D., Bris, C.G., Morgado, P.L., Maudes, J.S.: Novel system for bite-force sensing and monitoring based on magnetic near field communication. Sensors **12**, 11544–11558 (2012). Department of Mechanical Engineering of the Polytechnic University of Madrid. https://doi.org/10.3390/s120911544
6. Dias, I.M., Mello, M.R.L., Maia, I.D., Reis, L.O., Milk, I.C.G., Leite, F.P.P.: Evaluation of risk factors for sleep bruxism. Arq. Odontol. (Belo Horizonte) **50**(3), 113–120 (2014)
7. Araujo, S.C.C.S., Vieira, M.M., Gasparoto, C.A., Bomarrito, S.: Bite force analysis in different types of Angle malocclusions. Rev. CEFAC **16**(5), 1567–1578 (2014)
8. Thorpy, M.J.: Classification of sleep disorders. Neurotherapeutics **9**, 687–701 (2012)
9. Magalhães, F., Mataruna, J.: Sleep. In: Jansen, J.M., et al. (eds.) Medicine of the Night: The Chronobiology to Clinical Practice. Rio de Janeiro, Editora FIOCRUZ, 2007, pp. 103–120. ISBN: 978-85-7541-336-4. Available from SciELO Books. http://books.scielo.org
10. https://www.unicamp.br/unicamp/ju/noticias/2017/05/19/estudo-aprimora-diagnostico-do-bruxismo-do-sono
11. http://www.absono.com.br/abms/artigos/informacoes-sobre-o-sono
12. Pallikarakis, N.: A view on the biomedical engineering education in Europe. In: Anais do XXV Congresso Brasileiro de Engenharia Biomédica—CBEB (2016)
13. Manfredini, D., Ahlberg, J., Winocur, E., Lobbezo, F.: Management of sleep bruxism in adults: a systematic qualitative literature review. J. Oral Rehabil. **42**, 862–874 (2015)
14. Birth, G.K.B.O.N., Lima, L.M.L., Rodrigues, C.B.S., Wedge, R.A., Cunha, D., Silva, H.J.: Verification of bite force and electrical activity of the masseter muscles during chewing in total laryngectomy, Rev. Bras. Odontol. (Rio de Janeiro) **68**(2), 175–179 (2011)
15. McAuliffe, P., Kim, J.H., Diamond, D., Lau, K.T., O'connell, B.C.: The sleep bruxism detection system based on sensors in a splint —pilot clinical data. J. Oral Rehabil. (2015) Center for Sensor Web Technologies, University, Dublin, Irland

Diagnosis of Respiratory Abnormalities Using Tracheal Sounds Analysis: Instrumentation and Evaluation in Simulated and In Vivo Tests

N. A. Lima Junior, I. M. Queiroz, N. V. Oliveira, A. J. Lopes, and P. L. Melo

Abstract

Several respiratory diseases introduce increases in upper airway obstruction. This work describes the design and application of a system based on Tracheal Sounds Analysis (TSA) able to evaluate this obstruction. A miniature microphone was used, providing analog signals to a virtual instrument developed in LabVIEW^{TM} environment. The design of the instrument is described, as well as in vitro and in vivo results obtained with orifice plates and patients with acromegaly, respectively. It was observed that the mean power (Pm) using orifice plates increased in comparison to that observed for free airflow, which is in agreement with the presence of turbulent airflow, associated with increased resistance. The comparative analysis of the Pm in controls and patients during spontaneous ventilation showed increased values in Pm ($p < 0.009$) and reduced values of the slope of the regression lines in the spectra ($p < 0.006$) in patients. These results are in agreement of the physiopathology of the studied disease, and provide clear evidence that TSA is able to detect the increased upper airway obstruction associated with acromegaly. Considering that TSA is performed during spontaneous breathing, requiring minimal patient effort, we concluded that the developed system could be a useful tool for the evaluation of changes in the airway obstruction introduced by acromegaly.

1 Introduction

Recent studies showed that lung diseases are a major burden of disease globally [1]. This burden can be anticipated to grow with climate change because global warming is closely coupled with rising concentrations of air pollutants [2]. This resulted in increased interest in the improvement of the methods used in research and diagnosis of respiratory abnormalities.

Tracheal sounds analysis (TSA) is performed during spontaneous breathing, requiring minimal patient effort and potentially providing sensitive functional parameters [3]. Recently, it has attracted considerable attention for acoustical flow estimation and investigation of obstruction in the upper airways [4].

Acromegaly is a syndrome characterized by excess of growth hormone secretion [5] which stimulate abnormal growth of the soft tissues of the pharynx and larynx. This introduces morphological alterations such as tracheal sinuosity, tracheomegaly and tracheal stenosis, which are present in approximately 25% of the patients [6].

Although TSA may provide a significant contribution to the functional evaluation of these patients, to the best of our knowledge, these analysis have never been used previously in acromegaly.

In the present study, our first objective was to describe the design of an instrument capable of evaluating respiratory parameters through TSA, and to evaluate the performance of this system in a model analysis. We also evaluated the

N. A. Lima Junior · I. M. Queiroz · N. V. Oliveira · P. L. Melo (✉)
Biomedical Instrumentation Laboratory, State University of Rio de Janeiro, Institute of Biology and Faculty of Engineering, Rio de Janeiro, Brazil
e-mail: plopes@uerj.br

A. J. Lopes
State University of Rio de Janeiro, Pedro Ernesto University Hospital, Rio de Janeiro, Brazil

A. J. Lopes
Augusto Motta University Center, Rio de Janeiro, Brazil

P. L. Melo
Laboratory of Clinical and Experimental Research in Vascular Biology, State University of Rio de Janeiro, Rio de Janeiro, Brazil

contribution of TSA in the diagnostic of airway abnormalities in acromegaly.

2 Materials and Methods

After approval of the study by the Ethics Committee of the University Center Augusto Motta (UNISUAM, protocol number 275.511), all volunteers signed an Informed Consent Term. Forced expiratory volume in the first second (FEV_1) and as a percentage of the predicted value (%pred) forced vital capacity (FVC), FEV_1/FVC ratio, peak expiratory flow (PEF), forced expiratory flow (FEF) between 25 and 75% of the FVC, and the FEF25-75/FVC ratio were obtained according to the Brazilian Spirometry Consensus [7] for all study volunteers, as well as anthropometric measurements.

2.1 Instrumentation

A simplified block diagram of the instrument is described in Fig. 1. Tracheal sounds were measured using a miniature omni-directional microphone (Sony, ECM-77B) that was positioned in the anterior face of the neck at the level below of the thyroid cartilage. The balanced outputs are initially processed using an Instrumentation Amplifier (INA118, Texas Instruments Incorporated, Texas, USA) and then analogically high-pass filtered (0.05 Hz, first order) to remove off-set and low-pass filtered (Butterworth, 8th order, 5000 Hz) to reduce external noise.

The resulting signal was measured at a sampling rate (fs) of 40 kHz [8] by a data acquisition module (NI 6003, National Instruments, Austin, Texas, USA), which presents a resolution of 16 bits, eight channels and fs maximum of 100 kHz. To simplify the practical use of the system, the hardware platform used was a touch screen notebook (Dell Inspiron series 137000, Intel, Core i5, 4G of RAM, hard disk of 456 GB). The airflow measurement system is composed by a fleisch pneumotachometer (PNT) coupled to a differential pressure transducer (176PC, Honeywell Inc. USA), whose signal is amplified by an instrumentation amplifier (INA118, Texas Instruments Incorporated, Texas, USA) and subsequently processed by a low-pass filter (Butterworth, 4th order, 10 Hz) and adapted to the data acquisition system.

The software is composed by two main modules, and was developed in LabVIEW 2012 environment (National Instruments, Austin, TX). The first module contains the data acquisition subroutines through the USB port, allowing the visualization of PNT and tracheal sounds signals and a visual quality control analysis. At the end of each exam the system allows researchers to save the data in an ASCII file.

The tracheal sounds signal processing is performed by the second module, which initiates down-sampling the signals to 5 kHz. The airflow is then high-pass filtered (Butterworth, zero-phase, first order, 0.1 Hz), while a bandpass filter (Butterworth, zero-phase, fourth order, 100 Hz–2.5 kHz) is used in tracheal sounds to minimize cardiac effects and to remove noise from the external environment. Respiratory sound signals were automatically segmented by extracting respiratory phases from the airflow signal. Then, a short-time Fourier transform of the tracheal sounds (spectrogram, or sonogram) was computed on segments of 500 points (or 100 ms), with an overlapping factor of 10% between adjacent segments and a Hanning window.

2.2 Simulated Studies

The aim of this first analysis was to evaluate the sensitivity of the developed TSA system to varying degrees of constriction simulated by external orifices. To this end, orifice plates of 12 and 6 mm were introduced between the subject and the bacterial filter (Fig. 1). We compared the results obtained in 5 normal subjects (age: 27.0 ± 9.3 years; body mass: 86.2 ± 16.1 kg; height: 176.0 ± 2.9 cm; 4 male; $FEV_1\% = 89.9 \pm 9.1$) during the use of these external orifices with that obtained in the absence of any external orifice.
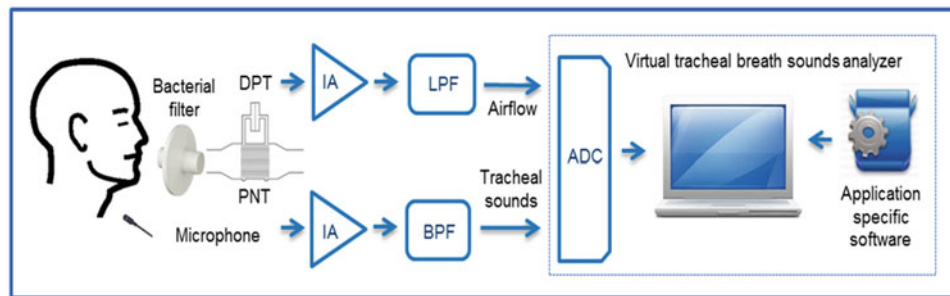
Fig. 1 Simplified block diagram of the instrument. BF: biological filter, DPT: differential pressure transducer, PNT: pneumothacometer, IA: instrumentation amplifier, LPF: low pass filter, BPF: band-pass filter, ADC: analog-to-digital converter

Fig. 2 Typical spectra of tracheal sounds for free airflow (**a**) and an orifice plate of 6 mm (**b**)
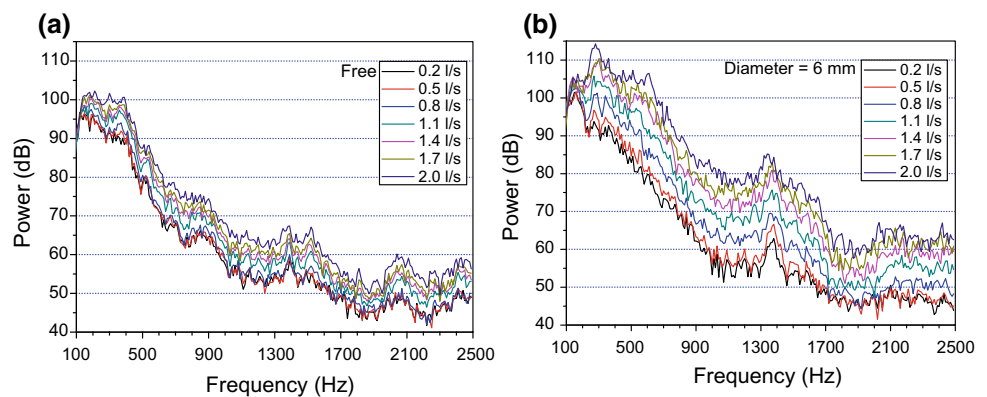
These evaluations were performed under conditions of maximal ventilator maneuver, including at least 6 respiratory cycles for each subject. A gating algorithm was applied to extract only tracheal sounds at specified flows (0.2, 0.5, 0.8, 1.1, 1.4, 1.7 and 2.0 l/s $\pm$ 1% tolerance). The power spectra were interpreted using the mean power in the frequency range studied normalized to the mean power observed at 0.2 l/s ($P_m$norm). We then verified whether the behavior of the TSA predicted by external orifices is applicable to patients with acromegaly for whom airflow obstruction is generated internally.

2.3 In Vivo Studies in Normal and Patients with Acromegaly

These studies were conducted using flow gates of 0.0, 0.1, 0.2, 0.3, 0.4, and 0.5 l/s $\pm$ 1% tolerance in the inspiratory and expiratory phases. In this case, $P_m$norm was obtained using normalization to the value observed in 0 l/s. The power spectra was also interpreted using the slope of the regression lines in the spectra (S), which was obtained using the Least Square fitting method. The mean power in the frequency range of 130–250 Hz (Pm1) was useful in the evaluation of patients with sleep apnea [9] and was also investigated. Twelve subjects were analyzed. The control group was composed of 6 subjects with a normal spirometric exam who did not have a history of smoking or pulmonary disease (age: 35.8 $\pm$ 13.7 years; body mass: 81.0 $\pm$ 10.4 kg; height: 176.0 $\pm$ 4.6 cm; 6 male; $FEV_1\% = 94.3 \pm 7.0$). Six never-smoking patients with acromegaly were also studied (age: 56.8 $\pm$ 9.2 years; body mass: 88.0 $\pm$ 7.2 kg; height: 170.6 $\pm$ 5.5 cm; 2 male; $FEV_1 \% = 91.3 \pm 18.1$). A nonparametric test (Mann-Whitney) was used in the comparison between these two groups, and differences with $p < 0.05$ were considered statistically significant.

3 Results

3.1 Simulated Studies

Representative spectra of tracheal sounds at free airflow and an orifice plate of 6 mm are described in Fig. 2.

Figure 3 shows the mean power observed in the two external orifices studied, as well as for free airflow.

3.2 In Vivo Studies in Normal and Patients with Acromegaly

Figure 4 presents typical spectrograms obtained during spontaneous ventilation in normals (A) and patients with acromegaly (B).
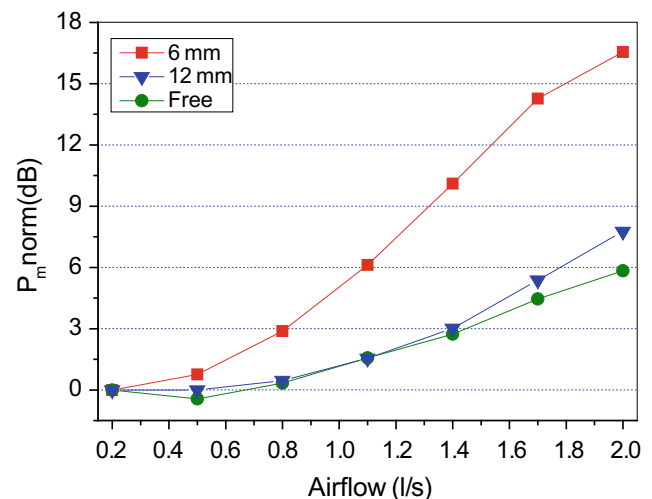
Fig. 3 Normalized mean power of tracheal sounds for the two external orifice and free airflow in the airflow range from 0.2 to 2.0 l/s
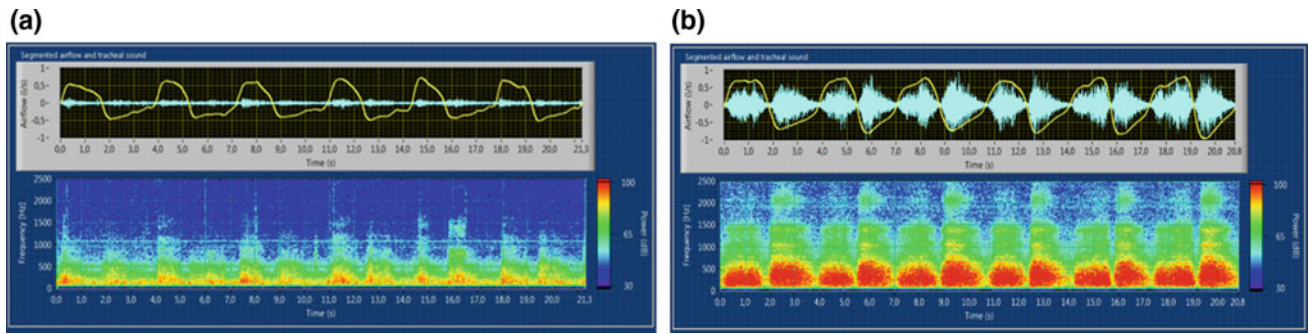
Fig. 4 Tracheal sound signal (top graph, blue) and the corresponding typical flow (top graph, yellow) along with tracheal sound signal spectrogram (low graph) observed during spontaneous ventilation in a typical normal (**a**) and acromegaly (**b**) subjects (Color figure online)
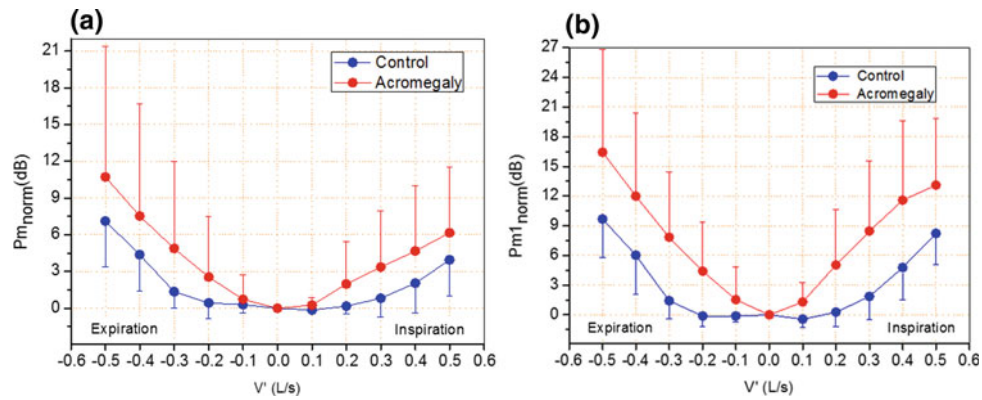
Fig. 5 Mean values of normalized tracheal sound signal power in the hole frequency range studied (100–2.5 kHz, **a**) and the corresponding power at the frequency range of 130–250 Hz (**b**) as a function of airflow (V') observed in controls and patients during spontaneous ventilation. The vertical bars describes standard deviation

Figure 5 describes the mean values tracheal sound signal power observed during measurements in controls and patients during spontaneous ventilation.

Pm_{norm} was not significantly different in −0.3 l/s. The comparative analysis revealed a significant increase of the Pm1Norm in the same airflow level (Fig. 6a), accompanied by a significant reduction in the slope of the power spectra in patients with acromegaly (Fig. 6b).

4 Discussion

Spirometry is a traditional pulmonary function test that is usually applied to study intra and extra-thoracic airway obstruction. However this method requires understanding, collaboration and maximum effort. In order to develop a methodology that allows a simpler examination and offers
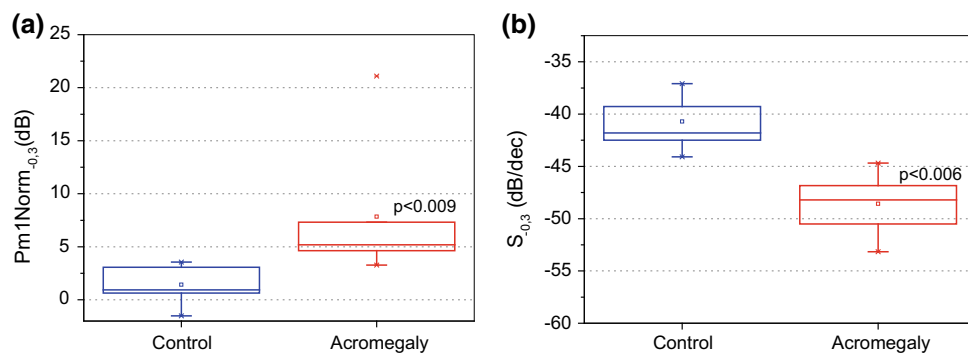
Fig. 6 Comparative analysis of the power in the frequency range of 130–250 Hz at an expiratory airflow of −0.3 l/s (**a**) and the slope of the regression lines in the spectra (**b**) observed in controls and patients during spontaneous ventilation. The top and the bottom of the box plot represent the 25th- to 75th-percentile values, while the circle represents the mean value, and the bar across the box represents the 50th-percentile value. The whiskers outside the box represent the 10th- to 90th-percentile values

new information about extra-thoracic obstruction, our group has been working on a system based on TSA for the identification of airflow obstruction (Fig. 1). The system is based on the production of increased noises due to the presence of turbulent flow, which is associated with the passage of air into obstructed points in the trachea. Advantages of this method are considerable in relation to spirometry: to be carried out in spontaneous ventilation, depends on little understanding, and is fast and inexpensive.

Several studies have reported a connection between the sound spectrum measured on the neck over the extra thoracic trachea and the underlying airway geometry and flow [10]. Based on this principle, Yonemaru et al. [11] developed a new method for the detection of tracheal stenosis by the use of frequency analysis of tracheal sounds, while Shirazi et al. [12] used this principle to detect swallows with silent aspiration.

Considering the simulated study (Fig. 2), it was observed that the power was concentrated at low frequencies (near 100–500 Hz) for both the group with free airflow (Fig. 1a) and the group that simulated obstruction using the 6 mm plate (Fig. 2b) for all studied flows. In higher frequencies, there was a reduction in the power, with a power peak in approximately 1.4 kHz for both groups. In agreement with these simulations, Yonemaru and coworkers [11] also observed increased power at low frequencies with a further fall in higher frequencies and a power peak near 1 kHz in subjects with tracheal stenosis. This study also showed that in normal subjects when the frequency exceeded approximately 500 Hz, there was a decrease of the power, with small power peak in 1 kHz. These results are also consistent with that described by Beck et al. [13], in which spectral power peaks near 1280 Hz were observed.

Figure 3 shows that $P_m$norm increased with flow in conditions of free airflow, and that the introduction of orifice plates increased the $P_m$norm. This increase was clearer in higher flows. The spectra described in Fig. 2 shows a slight increase in the mean power in conditions of free airflow (Fig. 2a), while in the presence of the 6 mm orifice the increase in the mean power was more clearly evident. These results are in line with that presented by Yonemaru et al. [11] describing a correlation between the smallest tracheal cross-sectional area with increased tracheal sounds power. These authors reported increased power when the area was smaller than 0.75 cm^2, which is equivalent to a diameter of 10 mm. In agreement with this proposition, Fig. 3 shows a small change in power in the presence of an orifice plate of 12 mm, and a more significant increase in the presence of the 6 mm orifice plate. This indicates that the proposed system was able to detect the presence of greater turbulence (higher Reynolds numbers) associated with the simulated obstruction.

It is interesting to note that the orifice plates simulates an intrathoracic obstruction through an artificial extracorporeal obstruction. This procedure produced increased power even with the microphone positioned far from the simulated obstruction point. This is a very disadvantageous condition from the measurement point of view, since we can expect a great attenuation of the turbulence from the simulated obstruction point to the measuring point in the trachea. Considering that in actual clinical application the obstruction will be produced much closer to the measurement point, it can be expected a signal of greater amplitude so that the system performance may be better than that observed in the simulated studies described in Figs. 2 and 3.

The comparative analysis between controls and patients showed increases values of power in patients (Figs. 4 and 5). This increase was observed in the whole frequency range studied (Fig. 5a), and was more clear in the frequency range of 130–250 Hz (Fig. 5b). The lower frequency analysis allowed us to discriminate the two populations even in conditions of low flow (± 0.1 and ± 0.2 l/s) in which the controls showed near zero values, indicating the absence of turbulence, while patients showed increased values indicating the presence of turbulence associated with increased obstruction. These results are in line with the simulations described in Figs. 2 and 3.

Considering the good discrimination observed in the simulated studies (Figs. 2 and 3) and the results in patients (Fig. 5) in the airflow of −0.3 ml/s, and that this airflow may be easily obtained in practical exams, we used this airflow value to compare the power obtained in controls and patients (Fig. 6a). It was observed a significant increase in patients ($p < 0.009$). This is in agreement with the presence of increases airflow turbulence, associated with increased airway obstruction, which is in close agreement with the pathophysiology of the disease [6]. The comparative analysis of S showed significantly ($p < 0.006$) more negative mean values in patients (Fig. 5b). This is associated with the presence of increased power in the tracheal sound signal of patients, mainly in the lower frequency range.

Noninvasive methods of the evaluation of the sounds generated during the respiratory cycle have over the years been shown to be promising for the detection of pulmonary and extrapulmonary abnormal changes. Sovijarvi et al. [14] reported that improved standardization of recording methods and analysis of respiratory sounds that occur in pulmonary disorders occurred due to advanced computer techniques, the use of flow-standardized spectra and respirosonograms. The authors measured respiratory sounds simultaneously in the trachea and both lungs, observing that the variation in all parameters for sounds measured in the trachea was greater than when captured in the lungs. Mussell et al. [15] reported that assessment of respiratory sounds through analysis of the principal components analysis could become a new diagnostic method. The authors also observed that the spectral amplitudes were significantly higher in people with respiratory diseases (asthma, sarcoidosis, pulmonary fibrosis and

chronic bronchitis) than in the control group, which was also observed in our study. Fiz et al. [16] used a microphone attached to the back of the patient to assess the pulmonary sound intensity in flows from 1.2 to 2.4 l/s in patients with phrenic injury. The authors observed that lung sound intensity was significantly higher on the normal side ($p = 0.0002$) in all patients, increasing with airflow. The latter result is in agreement with our study, where the increase in flow was related to the increase in the power of the tracheal sound signal (Figs. 2, 3, 4 and 5).

5 Conclusions

In the present study, a novel system for the acquisition and processing of tracheal sounds signals was initially described. The ability of the system to evaluate airflow turbulence associated with respiratory obstruction was first evaluated in a simulated study. Based on the results of these simulations, a study comparing normal subjects and patients with acromegaly showed an adequate discrimination and results in close agreement with the involved pathophysiological changes. The proposed system may be useful in a wide spectrum of clinical and research studies of subjects with respiratory diseases, enabling simple and noninvasive exams and improving the assistance offered to these patients.

References

1. FIRS: Respiratory diseases in the world. Realities of today—opportunities for tomorrow. In: Forum of International Respiratory Societies—FIRS, 15 Jan 2018
2. Zar, H.J., Billo, N., Ferkol, T., Vestbo, J.: Decade of the lung–a call for action to promote lung health globally. Lancet Respir. Med. **4**, e3–e4 (2016)
3. Moussavi, Z.: Fundamentals of Respiratory Sounds and Analysis. Morgan & Claypool Publishers, USA (2006)
4. Yadollahi, A., Moussavi, Z.: Detailed analysis of the relationship between tracheal breath sounds and airflow in relation to OSA during wake and sleep. In: Conference of the IEEE Engineering in Medicine and Biology Society, vol. 2011, pp. 6797–800 (2011)
5. Melmed, S.: Medical progress: acromegaly. N. Engl. J. Med. **355**, 2558–2573 (2006)
6. Camilo, G.B., Carvalho, A.R., Guimaraes, A.R., Kasuki, L., Gadelha, M.R., Mogami, R. et al.: Computed tomography airway lumen volumetry in patients with acromegaly: association with growth hormone levels and lung function. J. Med. Imaging Radiat. Oncol. (2017)
7. Pereira, C.A.: Espirometria. Jornal de Pneumologia 28 (2002)
8. Huq, S., Moussavi, Z.: Acoustic breath-phase detection using tracheal breath sounds. Med. Biol. Eng. Comput. **50**, 297–308 (2012)
9. Elwali, A., Moussavi, Z.: Obstructive sleep apnea screening and airway structure characterization during wakefulness using tracheal breathing sounds. Ann. Biomed. Eng. **45**, 839–850 (2017)
10. Harper, V.P., Pasterkamp, H., Kiyokawa, H., Wodicka, G.R.: Modeling and measurement of flow effects on tracheal sounds. IEEE Trans. Biomed. Eng. **50**, 1–10 (2003)
11. Yonemaru, M., Kikuchi, K., Mori, M., Kawai, A., Abe, T., Kawashiro, T., et al.: Detection of tracheal stenosis by frequency analysis of tracheal sounds. J. Appl. Physiol. **1985**(75), 605–612 (1993)
12. Sarraf Shirazi, S., Moussavi, Z.: Silent aspiration detection by breath and swallowing sound analysis. In: International Conference of the IEEE Engineering in Medicine and Biology Society, vol. 2012, pp. 2599–602 (2012)
13. Beck, R., Rosenhouse, G., Mahagnah, M., Chow, R.M., Cugell, D.W., Gavriely, N.: Measurements and theory of normal tracheal breath sounds. Ann. Biomed. Eng. **33**, 1344–1351 (2005)
14. Sovijarvi, A.R., Malmberg, L.P., Paajanen, E., Piirila, P., Kallio, K., Katila, T.: Averaged and time-gated spectral analysis of respiratory sounds. Repeatability of spectral parameters in healthy men and in patients with fibrosing alveolitis. Chest **109**, 1283–1290 (1996)
15. Mussell, M.J., Nakazono, Y., Miyamoto, Y., Okabe, S., Takishima, T.: Distinguishing normal and abnormal tracheal breathing sounds by principal component analysis. Jpn. J. Physiol. **40**, 713–721 (1990)
16. Fiz, J.A., Jane, R., Lozano, M., Gomez, R., Ruiz, J.: Detecting unilateral phrenic paralysis by acoustic respiratory analysis. PLoS One **9**, e93595 (2014)

Dual Channel Wireless Electronic Stethoscope for Lung Sound Acquisition

Willian Mattos, Carlos G. Speranza, Leandro Schwarz, and Raimes Moraes

Abstract

Crackles are heard on the thorax of patients with lung diseases, being widely employed by examiners to assist diagnosis. The path between the lungs and microphone of electronic stethoscopes attenuates the crackles waveforms, hampering the investigation of quantitative indices for their characterization. This work describes a wireless device that samples different crackles bandwidths with different gains, aiming to reduce the effects of thorax attenuation on the crackles waveforms. The assessment of the proposed system was carried out by applying simulated crackles to a volunteer's mouth that were compared to the ones recorded on the chest. Discrete-time signal processing techniques were employed to recover, from the two channels, a waveform similar to that applied. The results show that the developed system may be useful to recover a crackle waveform more similar to the original one. The developed system will be used to acquire crackles from patients in order to assess its potential to assist the diagnosis of different lung diseases.

Keywords

Wireless stethoscope • Blind equalization • CORSA

1 Introduction

Adventitious respiratory sounds (ARS) are heard on the thorax of patients with lung diseases. Chest auscultation is widely used during clinical assessment of the respiratory system, since ARS may be related to different pulmonary diseases, such as cystic fibrosis, congestive heart failure, and chronic obstructive pulmonary disease (COPD) [1]. Crackles are among the most relevant ARS used by medical staff to diagnose respiratory diseases. The crackles are described as discontinuous, short, explosive, and transient sounds. Its waveform shows an initial fast pressure deflection followed by a short oscillatory segment, being associated to pressure equalization in collapsed airways [2].

Auscultation by means of a stethoscope is a non-invasive low-cost exam that has a fast response time [3]. Nevertheless, it has limitations. The analysis of the different sounds depends on the examiner's experience, as well as his/her auditory acuity. The absence of quantitative indices measured from ARS hampers the clinical follow up and the exchange of information among experts. To circumvent such limitations, electronic stethoscopes have been employed to investigate quantitative indices. However, researchers were using systems with different technical specifications, preventing a better characterization of ARS generated by different respiratory disorders. A task force of the European Respiratory Society proposed guidelines for the research and clinical practice in the field of computerized respiratory sound analysis (CORSA) [4]. Even though, there are no reliable indices to assist the diagnosis based on ARS.

We hypothesize that such difficulty to obtain consistent quantitative indices from crackles is partially related to the large inter-individual variability of sound attenuation by the path between the lungs and the recording system microphone. The thorax acts as a low-pass filter, attenuating the higher-frequency components of crackles [5]. The attenuation depends on the weight, height, body structures, organ arrangement, affected lung, and disease. Therefore, crackles acquired from different patients with a same disease may have different frequency content due to the thorax attenuation. Thus, techniques to compensate the thorax attenuation may provide crackle sounds with more diagnostic information.

Electronic stethoscopes built according to the CORSA guidelines acquire sounds with a bandwidth ranging from

W. Mattos (✉) · R. Moraes
Universidade Federal de Santa Catarina, Florianópolis, SC 88040-900, Brazil
e-mail: willian.mattos@outlook.com

C. G. Speranza · L. Schwarz
Instituto Federal de Santa Catarina, Florianópolis, SC 88020-300, Brazil

60 to 2000 Hz. Since the thorax highly attenuates frequencies above 300 Hz, the stethoscope gain may not be suitable to avoid saturation of the lower frequencies components (below to 300 Hz) while providing good amplification for the higher frequency components (above 300 Hz), mainly for patients with large body mass index (BMI).

This work describes a wireless electronic stethoscope designed to acquire crackles by means of two channels that have different gains and bandwidths. Such approach allows selecting a higher gain for the frequencies more attenuated by the thorax. The aim is to recover more diagnostic information from crackles. The sampled signals are processed off-line to obtain a sound waveform more similar to that generated within the lungs. Result of experiment to validate the proposed approach is reported.

2 Methods

A block diagram of the developed system is shown in Fig. 1; its main components are: sound acquisition front-end, radio frequency (RF) transmitter, RF receiver, and application software for Windows® operating system (OS).

The respiratory sounds are acquired by an electret microphone (EM172—Primo Co.) with a flat frequency response (60–2000 Hz) and high sensitivity (−28 dB ± 3 dB at 1 kHz). The microphone, housed into an aluminum acoustic coupler with the dimensions recommended by CORSA [6], is connected to a preamplifier (MAX4465EXK —Maxim Integrated Products) with a typical common-mode rejection ratio of 126 dB. The preamplifier output is applied to two different channels containing second-order band-pass

Fig. 1 Block diagram of the developed stethoscope
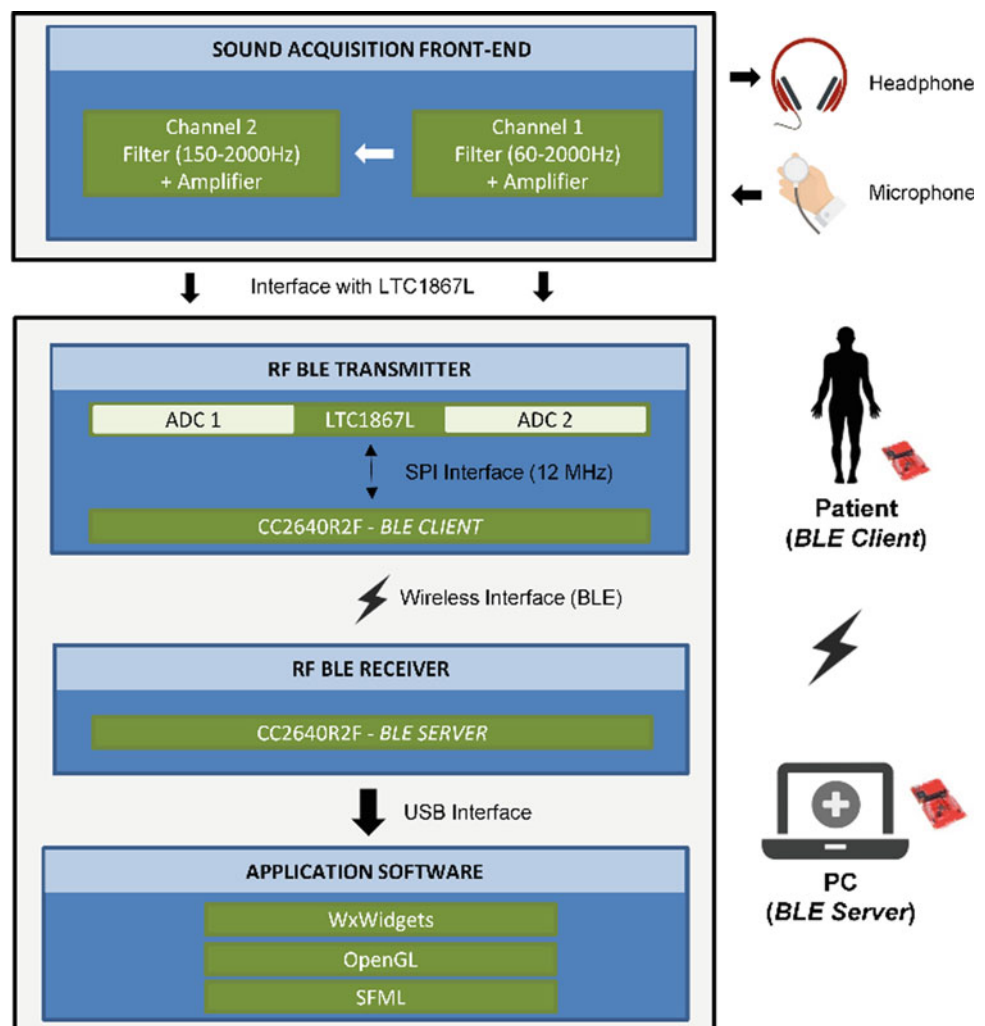
Table 1 Gains and cut-off frequencies of the second-order HPF and LPF of the two channels

Channel	Gain	HPF (Hz)	LPF (Hz)
1	30	60	2000
2	210	150	2000

Bessel filters with different gains. These filters were built by cascading second-order high-pass filter (HPF) and second-order low pass filter (LPF) using the operational amplifier MCP6004 (Microchip Technology Inc.). Table 1 shows the gains and cut-off frequencies of the filters of each channel. The channel 1 has the bandwidth recommended by the CORSA (60–2000 Hz) [6]. The HPF cut-off frequency of the channel 2 is 150 Hz; this specification has two purposes. The first one is the attenuation of the lower frequency components of the respiratory sounds in order to provide a higher gain for the higher frequency components of crackles. The second one is related to the non-linear phase of HPFs (including the Bessel topology [7]); to minimize such effect, a linear phase digital filter with higher cut-off frequency (300 Hz) will be used to remove the bandwidth affected by the phase distortion. Based on computational simulations, the 150 Hz cut-off frequency provides a good trade-off between higher gain and lower phase distortion for the crackles waveforms.

The gains were estimated based on an average sound attenuation curve of the thorax [5]. As the bandwidth of the channel 2 is narrower than that of the channel 1 (Table 1), the channel 1 output is used as input of the channel 2; by doing so, the stop band attenuation for frequencies below 60 Hz corresponds to that of a fourth order filter. Therefore, it is possible to further increase the gain of the channel 2 (without signal saturation) to improve the sampling (SNR) of the higher frequency components. Outputs of the two channels are applied to a stereo audio amplifier (TPA6100A2—Texas Instruments) which drives a headphone used by an examiner to interrogate a suitable auscultation position.

Each channel output is sampled at the rate of 5 kSPS using a 16-bit analog to digital converter (ADC) that may be multiplexed among up to eight inputs (LTC1867L—Linear Technology). The samples are read by a SPI interface of the RF transmitter which is based on the CC2640R2F launchpad kit (Texas Instruments). The CC2640R2F device is a wireless microcontroller (MCU) that has a 32-bit ARM® Cortex®-M3 core (48 MHz) and Bluetooth 5 protocol stack for single-mode Bluetooth low energy (BLE) applications. The

firmware was developed in the Code Composer Studio™ 7 (CCS), an integrated development environment (IDE). After acquiring 100 samples, the data are transmitted in packets of 202 bytes. The first word of each packet contains a sequential number [0–65535] used to identify data losses in the receiver.

The front-end parts and the transmitter were chosen to minimize the power consumption since they are assembled as a portable battery-powered device (9 V); the current supplied to the device (front-end and transmitter) is around 27 mA.

Another CC2640R2F launchpad kit connected to a notebook via USB receives the transmitted data since a compact module (USB Dongle) compatible with BLE 5.0 technology is not currently available. The received data are sent to the notebook by means of a serial port profile developed by Texas Instruments.

Application software was written in C++ (GCC) for Windows® OS using the open source Code::Blocks IDE. A graphical interface developed with wxWidgets controls the acquisition, presentation, storage, and playback of patient's breath sounds. The sampled signals are shown on the screen using OpenGL library. The audio signals are stored into WAV format files; for that and for playback, the Simple and Fast Multimedia Library (SFML) is used. The WAV format was chosen due to its large compatibility to several audio player applications.

2.1 Experimental Setup

The volunteers who took part of the experiments were informed about the aims and procedures of the investigation; they provided written informed consent. The protocol was approved by the Ethics Committee on Human Research of Federal University of Santa Catarina, Florianopolis, Brazil (CAAE no: 53092416.9.0000.0121-02/29/16).

The performance of the developed system was assessed by applying simulated crackles to mouths of healthy volunteers. The simulated crackles were generated as proposed elsewhere and saved as audio files [8]. A notebook reproduced the simulated crackles by means of an audio player application; its audio output was connected to an amplified loudspeaker (MDR-ZX100—Sony) with the following characteristics: 3 cm diameter, flat response (12–22 kHz), and sensitivity of 100 dB/mW. The loudspeaker was placed into an acoustic insulation box to allow sound propagation only by means of a hollow plastic duct (3.5 × 40 cm) that conveyed the simulated crackles to the mouths of volunteers. At the end of this duct, an electret microphone (MD9745APA-1—Knowles Acoustics) acquired the applied sounds. A force sensitive
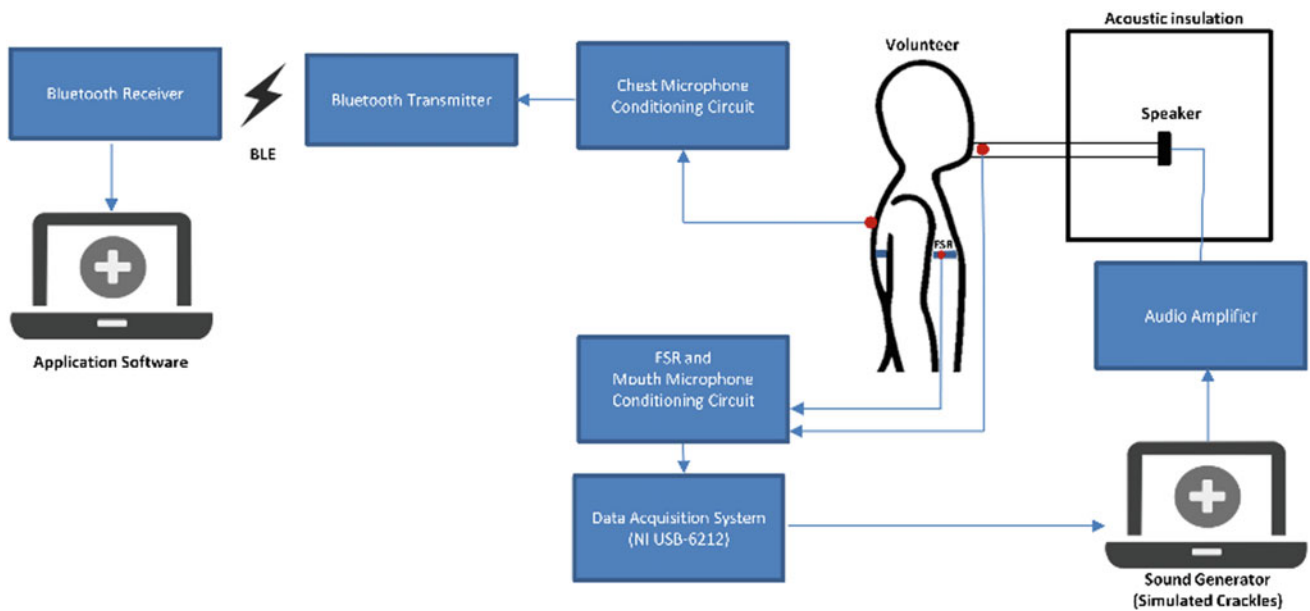
Fig. 2 Experimental setup to assess the developed stethoscope

resistor (FSR) placed on the chest registered the thorax wall displacements (TWD) to identify the inspiratory phase. A commercial data acquisition system (NI USB-6212—National Instruments) sampled the applied sounds and TWD at the rate of 20 kSPS with a 16-bit resolution. Figure 2 depicts the experimental setup.

The sounds acquired on the chest by the developed system were compared to those applied to the mouth. During the measurements, the subject was seated. The acoustic coupler was fixed with double-sided tape on the chest wall. The sounds were recorded during the inspiratory phase when the glottis is opened. The opened glottis allows the sound propagation through the respiratory tract such that it reaches the thorax surface with higher intensity.

To recover a sound closer to the one applied to the mouth, the two signals sampled on the chest were first interpolated to achieve a sampling rate of 20 kSPS. They were then filtered by a digital filter bank (DFB) with approximately flat magnitude and linear phase [9]. The DFB avoids the superposition of the two channels bandwidths; channel 1 and channel 2 are limited to the bandwidths of 60–300 Hz and 300–2000 Hz, respectively. Aiming the compensation of thorax attenuation, the filtered signals are summed; the resulting signal is blind equalized by a technique named eigenvector approach (EVA). A more detailed description and preliminary results of such approach were reported elsewhere [10]. The purpose of this work is to show the suitability of the developed system to record ARS from subjects with large BMI (above 25 kg/m^2). A single result obtained from one volunteer (BMI = 25.7 kg/m^2) is presented to illustrate the feasibility of the approach.

3 Results

Figure 3 shows the waveforms of a simulated crackle applied to the mouth and that acquired by the channel 1 (60–2000 kHz) after equalization by EVA with 30 coefficients. These waveforms acquired from one volunteer (BMI = 25.7 kg/m^2) illustrate typical obtained results.

Figure 4 shows the waveforms of the crackle applied to the mouth and that obtained after processing the signals sampled by the two channels (that is, interpolation, filtering
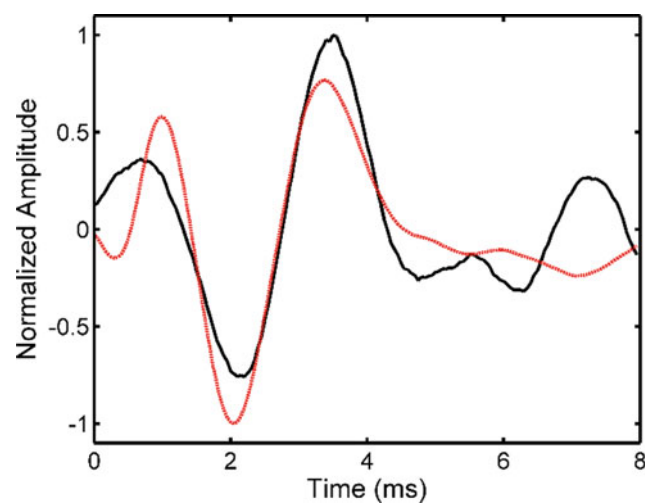
Fig. 3 Crackle waveform applied to the mouth (red line) and that acquired by the channel 1 of the developed system (black line) after equalization by EVA (30 taps) (Color figure online)
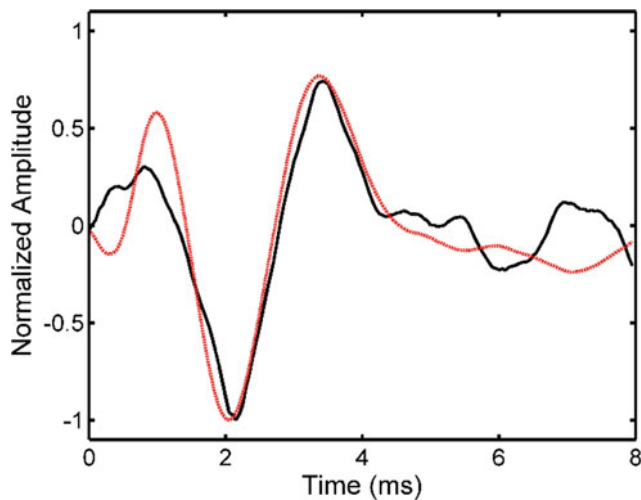
Fig. 4 Crackle waveform applied to the mouth (red line) and that acquired by the two channels of the developed system (black line) after discrete-time signal processing (details in the text) (Color figure online)

by the DFB, summing, and equalization by EVA with 70 coefficients). The waveforms presented in the figures were normalized by their respective maximum amplitude. In both cases, the use of an equalizer with a larger number of taps did not improve the results.

The root-mean-square error (RMSE) was obtained for each pair of waveforms according to Eq. 1:

$$RMSE = \sqrt{\sum_{i=0}^{N-1} \frac{(y_i - x_i)^2}{N}} \qquad (1)$$

where y_i is a normalized sample of the measured waveform, and x_i is a normalized sample of the applied waveform; the RMSE corresponds to the standard deviation of the differences between the applied crackle (mouth) and the measured one (thorax).

A RMSE of 0.3114 was obtained from the signals of Fig. 3; for the signals of Fig. 4, the RMSE was 0.17. Table 2 shows two indices (two cycle duration—2CD—and maximum frequency) measured from the applied crackle and from that acquired on the thorax after the described

Table 2 Comparative table between applied and measured crackle (after equalization)

Waveform	2CD (ms)	Maximum frequency (Hz)
Applied crackle (mouth)	5.32	547
Acquired crackle (channel 1)	5.94	537
Acquired crackle (both channels)	5.30	547

processing (Figs. 3 and 4). These two indices are largely used to characterize crackles generated by different illnesses [11].

Based on these results, it is possible to verify that the proposed approach recovered a waveform more similar to the applied one.

4 Discussion and Conclusions

The development of consistent quantitative indices based on ARS to assist respiratory diseases diagnosis would reduce the number of more harmful and expensive exams (X-rays and others). Nevertheless, there are technical challenges to achieve that.

CORSA states that crackles have a frequency content ranging from 100 to 2000 Hz [2]. However, the maximum frequency reported for crackles acquired on the chest is usually much lower than that [11]. Such discrepancy of figures may be related to the high thorax attenuation for frequencies above 300 Hz. Electronic stethoscopes usually have one channel to acquire sounds with a bandwidth ranging from 60 to 2000 Hz. Therefore, stethoscopes gain cannot be very large to avoid the saturation of the lower frequencies components (below 300 Hz); on the other hand, the higher frequency components (above 300 Hz) have poor SNR due to the high attenuation (poor ADC resolution). Researchers report a large variability of quantitative indices proposed to characterize crackles generated by different diseases. Such variability may be related to the physical characteristics of patients. Preliminary results of this laboratory support that the BMI has a large impact on the quantitative indices [10].

This work describes a dual channel wireless electronic stethoscope developed to acquire crackles from patients in order to recover their higher frequency components. Our preliminary observations based on the application of simulated crackles (as reported here) suggest that two channels are enough to acquire the higher frequency components of crackles with good SNR. The developed system can be promptly modified to include additional channels (larger HPF cutoff frequency and higher gain) if the field results show otherwise.

The presented results show the performance of the developed device in recovering the higher frequency components of the original waveform that were attenuated by the thorax. These and previously reported results [10] provide evidence that the proposed approach may have impact on the estimation of quantitative indices; thus, they can be more useful to characterize illnesses. Future research involves the acquisition of data from patients with different diseases; it is

expected to better characterize the crackles acquired with the described device to assist diagnosis.

References

1. Bohadana, A., Izbicki, G., Kraman, S.S.: Fundamentals of lung auscultation. N. Engl. J. Med. **370**, 744–751 (2014)
2. Sovijärvi, A.R.A., Malmberg, L.P., Charboneau, G., Vanderschoot, J., Dalmasso, F., Sacco, C., Rossi, M., Earis, J.E.: Characteristics of breath sounds and adventitious respiratory sounds. Eur. Respir. Rev. **10**(77), 591–596 (2000)
3. Postiaux, G.: Fisioterapia respiratória pediátrica: o tratamento guiado por ausculta pulmonar, 2ª edn. ArtMed, Porto Alegre RS (2004)
4. Sovijärvi, A.R.A., Vanderschoot, J., Earis, J.E.: Standardization of computerized respiratory sound analysis—CORSA. Eur. Respir. Rev. **10**(77), 585 (2000)
5. Ponte, D.F., Rocha, A.C.F., Hizume, D.C., Moraes, R.: Equalization of crackle sounds to compensate thorax attenuation. IEEE Trans. Inst. Meas. **63**(8), 1983–1990 (2014)
6. Vannuccini, L., Earis, J.E., Helisto, P., Cheetham, B.M.G., Rossi, M., Sovijärvi, A.R.A., Vanderschoot, J.: Capturing and preprocessing of respiratory sounds. Eur. Respir. Rev. **10**(77), 616–620 (2000)
7. Gomez-Clapers, J., Serra-Rocamora, A., Casanella, R., Pallas-Areny, R.: Towards the standardization of ballistocardiography systems for J-peak timing measurement. Measurement **58**, 310–316 (2014)
8. Kiyokawa, H., Greenberg, M., Shirota, K., Pasterkamp, H.: Auditory detection of simulated crackles in breath sounds. Chest **119**, 1886–1892 (2001)
9. Schafer, R.W., Rabiner, L.R.: Design of digital filter banks for speech analysis. Bell Syst. Tech. J. **50**(10), 3097–3115 (1971)
10. Speranza, C.G., Alves D.D., Rocha, C.A.F., Moraes, R.: Aquisição de estertores pulmonares com banco de filtros para reduzir atenuação do tórax. In: XXV Congresso Brasileiro de Engenharia Biomédica, pp. 1658–1661. SBEB, Foz do Iguaçu PR (2016)
11. Ponte, D.F., Moraes, R., Hizume, D.C., Alencar, A.M.: Characterization of crackles from patients with fibrosis, heart failure and pneumonia. Med. Eng. Phys. **35**(4), 448–456 (2013)

Electric Field Distribution and Electroporation in Discontinuous Regions Using Vegetal Model: In Vitro and In Silico Study

A. B. Heyse, G. B. Pintarelli, and D. O. H. Suzuki

Abstract

Electrochemotherapy (ECT) is a recognized electroporation-based technique for treatment of cutaneous and subcutaneous tumors. The treatment is based on cell membrane permeability increase, or electroporation phenomenon, which facilitates the entrance of anti-cancer drugs on cells. Electroporation occurs as function of local electrical field amplitude. Inappropriate electric field distribution can produce tumor recurrence and ECT will fail. This explains the importance of pre-treatment analysis of electrical field distribution and determination of electrical field coverage for electroporation occurrence. The irregularities (e.g., holes and protuberances) may reduce ECT effectiveness as provoke unsuitable electric field. The potato tuber is recognized as an in vitro model of electroporation and provides direct visualization of the affected region. In this study, the impact of protuberance was evaluated using in vitro vegetal model and in silico model. Both analysis demonstrate occurrence of insufficient field for ECT in the protuberance neighborhood.

1 Introduction

Electroporation is a permeabilization increase process which occurs on bilayers membranes after application of intense electric fields. The phenomenon is explained by the phospholipids rearrangement and creation of pores in the cell membrane. These pores allow the passage of ions and molecules into the cell [1].

Electroporation can be categorized in two levels, depending on the energy applied and cell response. It is called reversible electroporation if after applied fields the pores eventually close. Irreversible electroporation if the applied field is sufficiently intense, which prevents membrane restoration to the original state and cell death results due apoptosis [1].

There are two electroporation-based technologies for cancer treatment. Electrochemotherapy (ECT) introduces chemotherapy drugs (bleomycin) into tumor cells [2]. The cells die in consequence of the drugs action (reversible electroporation). Secondly, irreversible electroporation (IRE) induces cell membrane destruction. This technique exceeds membrane perturbation in a way the pores created cannot reseal, without the need of additional drugs [1]. Both techniques have advantages and disadvantages and they are used successfully in the clinical area [3, 4].

The electroporation protocol used for ECT is eight pulses with 100 μs duration, 1 Hz repetition rate (i.e. one 100 μs pulse per second) and amplitude of 100–130 kV/m [5, 6]. This protocol is recommended by European Standard Operating Procedures of Electroporation (ESOPE) created in 2006 [7]. Currently, ECT is used for removal of cutaneous and subcutaneous tumors in European clinics [2, 8] and oral cavities, cutaneous and subcutaneous in Brazilian veterinary clinics [3, 9, 10]. ECT benefits from higher selectivity when compared to other treatment (i.e. surgical removal). Treatment selectivity means the destruction of tumor tissue without destruction of healthy tissue which is important to treat critical and sensitive parts of the body, such as head and neck.

Tumor's disordered growth can reach irregular shapes state. Diffraction of electric field will occur in irregular shapes and electric field distribution may not be simple to predict. For instance, conductivity in boundaries between tumor and air. Regions with insufficient field for electroporation are named blind spots. Blind spots are harmful for ECT, as may produce tumor recurrence. Pretreatment can simulate electrical field distribution to instruct the best procedure for ECT (electrode arrangement and type).

A. B. Heyse · G. B. Pintarelli · D. O. H. Suzuki (✉)
Instituto de Engenharia Biomédica, Universidade Federal de Santa Catarina, Florianópolis, Brazil
e-mail: suzuki@eel.ufsc.br

Vegetal models, such as potatoes, could be used to validate the effectiveness of new electrodes sizes and configurations and to assess the impact of pulse parameters (e.g. frequency and number of pulses) [8, 11]. The potato is an electroporation model that allows studying the distribution and intensity of electric fields on tissues in a simplified way. Similar approaches are found in literature [1, 8, 12, 13]. Vegetable models offers advantage as being easily acquired, handled, and reduces animal use in experiments. Besides that, it also has a fast feedback appeal, which are very important for tests involving new configuration for electrodes, non-homogeneous tissues and demonstrations for electroporation devices' users and engineers. On the other hand, in vivo tissue affirmation of ECT occurrence may take weeks, by looking at the tumor reduction and death.

Our aim is to improve the method of potato tuber preparation and emphasize the importance of the vegetal model to show potential risk areas when using ECT. A case of study with cylindrical protuberance was used. The work was conducted in parallel with in vitro and in silico experiments and then compared.

2 Materials and Methods

2.1 In Vitro Study

All the potatoes (*Solanum tuberosum*) were washed and cut until they reached the right shape. The potatoes were acquired at the groceries store the day before the experiment.

The shaping and cutting procedures were made using a tool designed for this experiment, as seen in Fig. 1. This instrument acts as a scissors that does not remove the cylindrical center. The cylindrical shape is made manually using a knife and caliper.

An electroporation device designed on lab for electroporation treatment was used on this study [14]. Eight pulses with duration of 100 μs, repetition rate of 1 Hz (1 s interval) and amplitude of 100 kV/m was applied on each sample, following ESOPE standard [7] (Fig. 2). The stainless-steel needle electrodes present dimensions of height 150 mm (maximum depth on the tissue), diameter of 0.5 and 3 mm separation. The perforation was performed at the edge of the sample protuberance. Consequently, one of them is fully inside the protuberance and the other is parallel but outside of the protuberance.

A sample control group was also tested along with the group that followed the electroporation procedures. The control group went through the same procedure, including the placement of the electrodes, but without any voltage being applied. The test was run five times (N = 5).
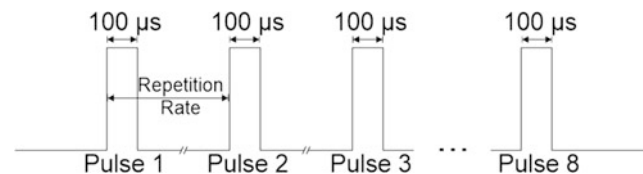
Fig. 2 Pulses applied in the sample

Fig. 1 Tool designed and used to shape the potato samples used in the experiment
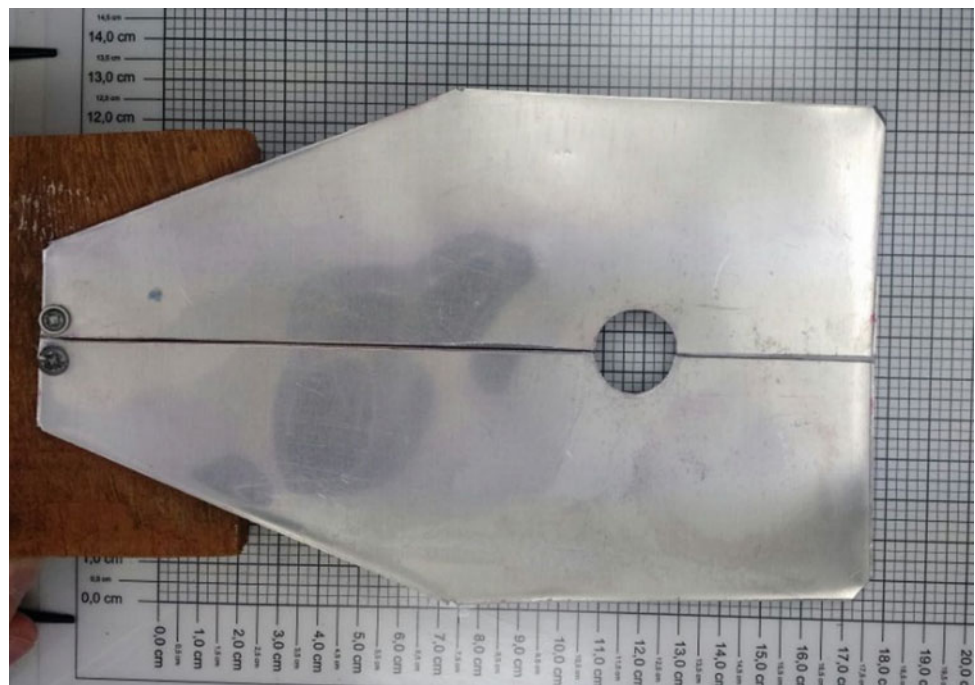
The samples were stored in a sealed place with room temperature of 25 °C and in an acid environment (sealed environment with wet paper towel with 2.5 ml of citric acid 4% diluted in deionized water) for a period of 8 h. Acid environment preserves the vegetable tissues (i.e. no natural oxidation).

Electroporation technique overly extracts polyphenol oxidase enzyme which reacts with the oxygen, this reaction leads to a darkening of the vegetable tissue. The marking can be perceived with unassisted vision after 8-h interval. This same mechanism acts when potatoes are cut. Natural oxidation can be reduced if placed on an acid environment [1]. The area affected by electroporation (the darkened areas) where measured with ImageJ.

2.2 In Silico Study

The in vitro geometry according to the in vitro experiment was simulated with three dimensional models using the software COMSOL Multiphysics (COMSOL AB, Sweden). Potato slices were built as geometry of Fig. 3. The two
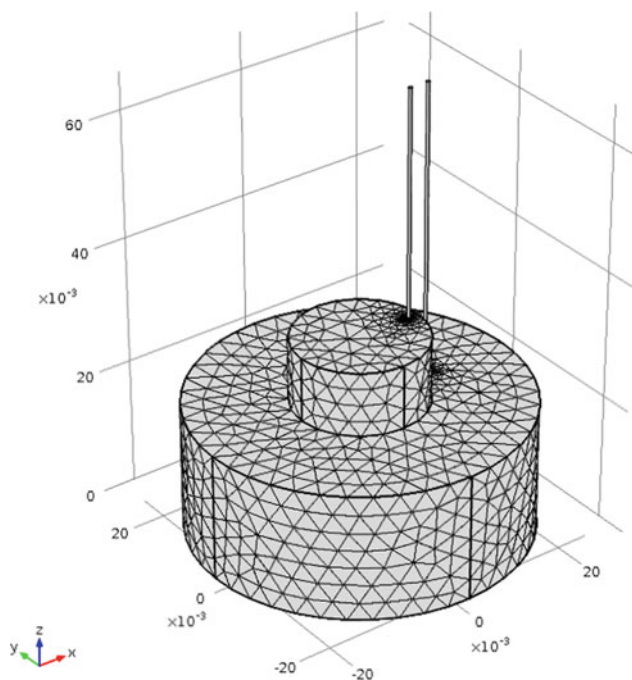
Fig. 3 Geometric model and mesh built in simulation software

needles had 5 cm of height, 150 mm perforation, 0.5 mm as diameter and 3 mm apart. Modeled geometry is presented in Fig. 3. The height of the protuberance is 1 cm, the same as the in vitro experiment. The fine-grained mesh was automatically generated by the software, resulting 41,736 tetrahedral elements in total.

It was considered steady-state regime, and the applied EFs was 130 V/m as ESOPE [5]. The Dirichlet boundary condition (contact between electrodes and tissue), and Neumann (insulating external surfaces) were applied. The tissue was considered homogeneous, and the Laplace Eq. (1) was solved by the finite element method.

$$\nabla \cdot (\sigma \cdot \nabla V) = 0 \tag{1}$$

The parameters of materials needed to compute the simulation are as shown in Table 1.

3 Results

3.1 Lapidate Potato with Protuberance

Processed samples are according to Fig. 4. The cylindrical protuberance represents irregular a tumor.

3.2 In Vitro Results

The in vitro experiment result is shown on Fig. 5. The samples were cut at between needles where the field was applied (side cut). It can be seen on the pictures that the darker area (area that was visibly affected by the electroporation) is concentrated at the area bellow the protuberance. The darker area average was calculated as 0.33 cm^2 with standard deviation of ± 0.03 cm^2. In Fig. 5 regions without enough electrical field to electroporation were circled in red circled in situations. This type of situation is known as blind electrical field spot.

3.3 In Silico Results

The in silico results are shown on Fig. 6. The cut plane performed in silico is in the same way as in vitro.

Table 1 Parameters used for simulation

Material	Property	Value
Electrodes (Stainless Steel 405)	Electrical conductivity	1.74×10^9 S/m
Electrodes (Stainless Steel 405)	Relative permittivity	1
Potato tissue	Electrical conductivity	0.03 S/m [1]
Potato tissue	Relative permittivity	1 [1]
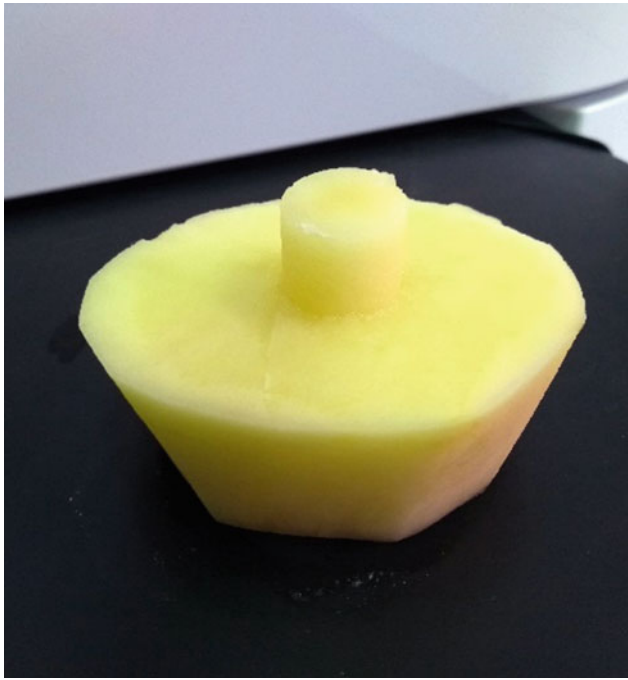
Fig. 4 Samples cut and shaped

The applied electric field was 100 kV/m. The black area occurs when local electric field was higher than 80 kV/m, thus it resulted in irreversible electroporation. On the dark gray area, the electric field was between 20 and 80 kV/m, producing reversible electroporation, which cannot be seen on the in vitro experiment samples. The light gray area is where the electric field was below 20 kV/m and it has no significant effects. The software ImageJ was used to measure the area where the electric field was higher than 20 kV/m and the region where the field was higher than 80 kV/m, results were 0.54 cm^2 and 0.19 cm^2, respectively. Similar to in vitro (Fig. 5), blind spots are observed in in silico.

4 Discussion

The ECT pre-treatment is significant in analysis of electroporation region. The protuberance was analyzed, and a possible treatment failure region was indicated (blind area in Fig. 4 agrees with Fig. 5). The potato model, as exposed in the literature [1, 8, 11–14], has been shown to be an alternative electroporation model to be used in the place of living beings and can provide visual evidence of field distribution.

Both in vitro and in silico results shown blind spots in the protuberance neighborhood The electric tissue discontinuous region (protuberance) produces non-uniform electric field distribution. This type of situation is harmful for ECT, as may produce tumor recurrence. The average area found in the in vitro results is 40% smaller than the area representing the region where the electric field was higher than 20 kV/m and 73% bigger than the area representing a field higher than 80 kV/m. The difference between measured areas can be explained by the lack of detailed borders in the potato samples, and the regions where the field is weaker and may cause electroporation without noticeable darkening area [15].

Potato models are evaluators of new pulse parameter settings [11]. Based on our studies, it is possible the evaluation of geometric forms with potato model. A case of study with cylindrical protuberance was used. With this type of protuberance, it was possible to show tumor irregular

Fig. 5 Results showing the lump area using potato model eight hours after the electric field application. In all six images is observed that there is a region of non-electroporation (blind area) shown in red (Color figure online)
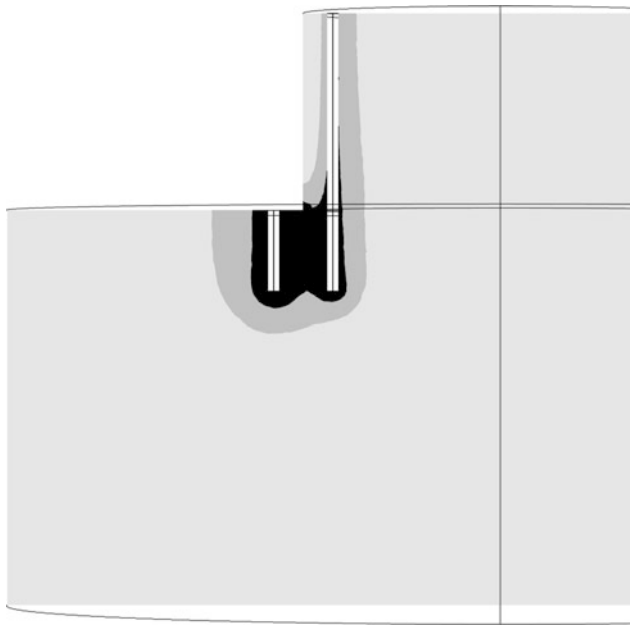
Fig. 6 Result of the in silico study. The black area represents the electric field higher than 80 kV/m. In the dark gray area, the electric field was between 20 and 80 kV/m. The light gray area is where the field was below 20 kV/m

geometry and possible positioning of the electrodes. Future studies can analyze different geometric shapes.

It should be noted that simulations may provide detail and ease of execution of complex geometries, as well as the electroporation conductivity model. However, it is known that the visual appeal of the potato is a fast and inexpensive evidence of success or not of electroporation. In addition, the potato model is interesting in the design of new electrodes, case studies of irregular geometries and feedback for clinicians and engineers. Nevertheless, it is known that the electrical characteristics of the plant tissue are different from an animal tissue [14].

The fine-grained mesh was automatically generated by COMSOL and the experiment converged without apparent noises or discrepancies. The in silico three-dimensional study makes possible the analysis of different types of plane cuts in future works.

5 Conclusion

The in vivo model of potato and in silico studies demonstrated that regions of irregular geometry can impair electric field distribution and cause failure in the ECT treatment. There are indications that the in vitro study can be used as a quick and low cost way of analyzing the effectiveness of ECT and integrity of equipment.

References

1. Ivorra, A., Mir, L.M., Rubinsky, B.: Electric field redistribution due to conductivity changes during tissue electroporation: experiments with a simple vegetal model. IFMBE Proc. **25**, 59–62 (2009)
2. Pucihar, G., Mir, L., Miklavčič, D.: The effect of pulse repetition frequency on the uptake into electropermeabilized cells in vitro with possible applications in electrochemotherapy. Bioelectrochemistry **57**, 167–172 (2002)
3. Suzuki, D.O.H., Berkenbrock, J.A., de Oliveira, K.D., et al.: Novel application for electrochemotherapy: immersion of nasal cavity in dog. Artif. Organs **41**, 767–773 (2017)
4. Suzuki, D.O.H., Berkenbrock, J.A., Frederico, M.J.S., et al.: Oral mucosa model for electrochemotherapy treatment of dog mouth cancer: ex vivo, in silico, and in vivo experiments. Artif. Organs **42**, 297–304 (2018)
5. Marty, M., Sersa, G., Garbay, J.R., et al.: Electrochemotherapy—an easy, highly effective and safe treatment of cutaneous and subcutaneous metastases: results of ESOPE (European Standard Operating Procedures of Electrochemotherapy) study. Eur. J. Cancer Suppl. **4**, 3–13 (2006)
6. Silve, A., Guimerà Brunet, A., Al-Sakere, B., et al.: Comparison of the effects of the repetition rate between microsecond and nanosecond pulses: electropermeabilization-induced electro-desensitization? Biochim. Biophys. Acta Gen. Subj. **1840**, 2139–2151 (2014)
7. Mir, L.M., Gehl, J., Sersa, G., et al.: Standard operating procedures of the electrochemotherapy: instructions for the use of bleomycin or cisplatin administered either systemically or locally and electric pulses delivered by the Cliniporator™ by means of invasive or non-invasive electrodes. Eur. J. Cancer Suppl. **4**, 14–25 (2006)
8. Suárez, C., Soba, A., Maglietti, F., et al.: The role of additional pulses in electropermeabilization protocols. PLoS One **9**, e113413 (2014)
9. Calvet, C.Y., Famin, D., André, F.M., Mir, L.M.: Electrochemotherapy with bleomycin induces hallmarks of immunogenic cell death in murine colon cancer cells. Oncoimmunology **3**, e28131 (2014)
10. Suzuki, D.O.H., Marques, C.M.G., Rangel, M.M.M.: Conductive gel increases the small tumor treatment with electrochemotherapy using needle electrodes. Artif. Organs **40**, 705–711 (2016)
11. Bhonsle, S.P., Arena, C.B., Sweeney, D.C., Davalos, R.V.: Mitigation of impedance changes due to electroporation therapy using bursts of high-frequency bipolar pulses. Biomed. Eng. Online **14**, S3 (2015)
12. Castellví, Q., Banús, J., Ivorra, A.: 3D assessment of irreversible electroporation treatments in vegetal models. In: IFMBE Proceedings, pp. 294–297 (2016)
13. Hjouj, M., Rubinsky, B.: Magnetic resonance imaging characteristics of nonthermal irreversible electroporation in vegetable tissue. J. Membr. Biol. **236**, 137–146 (2010)
14. Berkenbrock, J., Pintarelli, G., Antônio, A., Suzuki, D.: In Vitro simulation of electroporation using potato model. In: CMBES Proceedings (2018)
15. Winnipeg, C., May, M.B.: Electrochemotherapy I, Electroporation I 2017 CMBEC40 Conference, Winnipeg MB, 23–26 May 2017

Electromyographic Monitoring System for Masticatory Muscles

R. J. R. S. Lucena, A. M. X. Silva, É. L. Cavalcante, A. V. M. Inocêncio, T. V. A. Silva, C. C. S. A. Lins, and M. A. B. Rodrigues

Abstract

Mastication is one of the processes responsible for reducing the size of food, facilitating its absorption. For mastication to occur efficiently, mandibular movements must be performed properly. Due to this important fact, it is necessary to develop procedures to evaluate, among other aspects, the potential of the masticatory muscles, in order to point out and analyze possible functional asymmetries between the muscular pairs. The electrical potentials generated by the chewing muscles are generally smaller than those produced by other muscles in the human body. Thus, it is necessary to apply amplification and filtering circuits to improve the signal-to-noise ratio. This work proposes the development of a portable system for acquiring, in real time, electrical signals from the masseter and temporal muscles for graphic registration in computers through wireless communication. The system described in this work was based on a platform already developed for another purpose, which allowed the project a faster prototyping. The data obtained through simulation led the work to the desired parameters. At the end a real acquisition was made using the developed system and a commercial acquisition system only to check the operation. From the theoretical and simulated results, it is possible to affirm that the system was successful both in relation to hardware and software, that executed the proposed objective in an expected way. With a promising future in the evaluation of bite force in people with neurogenic orofacial dysfunctions, needing to increase the number of channels.

Keywords

Electromyography • Portable system • Masticatory muscles

R. J. R. S. Lucena (✉) · A. M. X. Silva · É. L. Cavalcante · A. V. M. Inocêncio · T. V. A. Silva · C. C. S. A.Lins · M. A. B. Rodrigues
Federal University of Pernambuco (UFPE), Recife, PE, Brazil
e-mail: rafael.jrslucena@gmail.com

1 Introduction

Mastication is a complex neuromuscular function that involves masticatory cycles necessary to reduce the food to an adequate size, in order to facilitate absorption by the gastrointestinal tract [1]. However, for chewing occurs efficiently, it is necessary teeth good health and proper mandible movements, which occur in the temporomandibular joints and are controlled by the neuromuscular system [2].

The mastication muscles present an anatomical variability throughout life due to the constant remodelling of the masticatory act, as a consequence of human aging. Therefore, it is important to evaluate the aspects involved in this action, such as the bite force potential and the electric potential of the masticatory muscles [3].

In this context, the surface electromyography (EMG) signal appears as a relevant alternative capable of recording the bioelectrical activity of the muscular fibers related to the mandibular kinematics [4, 5]. An electromyographic analysis during mastication can indicate possible functional asymmetries between analyzed muscle pairs. It allows describing numerically the amplitude and velocity of the movements performed by the masticatory musculature during the stomatognathic functions involved. In this way, it is possible to check the kinematics by means of graphs [6].

However, although there is still insufficient standardization in relation to the evaluation procedures of the muscles involved in orofacial functions, the EMG provides a broad horizon of application related to the therapeutic efficacy demonstration of exercises, improvement of speech therapy and in myofunctional orofacial disorders [7].

The muscles related to mastication are: temporal, masseter, pterygoid late-ral, medial pterygoid and anterior digastric belly. Due to the format and importance the related studies prioritize the masseter and temporal muscles, and show that the maximum amplitude of the myoelectric signal is generally less than 400 μV [8, 9]. This amplitude occurs mainly because of the reduced size of the analyzed muscles

compared to others in the human body that are normally used to acquire EMG.

Due to the facts presented, this research sought to develop a portable electromyographic monitoring system focused on the masticatory muscles. Given the characteristics of the myoelectric signal of these chewing muscles, the acquisition system needs to present circuits of amplification, filtering and signal normalization specific to these muscle groups. From these data, it is possible to perform the digital signal processing and to identify possible inadequacies of the masticatory movement.

2 Materials and Methods

The system for acquisition of EMG signals developed was based on the work of Souza [10]. From an already developed equipment that has only two acquisition channels, it was possible to employ a new application changing some parameters. With this, it was not necessary to start the equipment development from the beginning, starting from the calculations of the filters and amplification. As a system limitation is available only two channels, which are used in order to perform the unilateral acquisition in muscles of mastication. A program was also developed to make the signal acquisition, generating a real-time graphic record.

The project aimed to implement a low-power, portable, two-channel EMG system for acquiring activation signals from the masseter and temporalis unilateral muscles, using wireless communication through the Bluetooth protocol and recording graphics in real-time. In order to make the system portable and compatible with current cell phones and computers, the Bluetooth 2.0 protocol was chosen, primarily for his wide application in these types of equipment [10, 11], in addition, components with low energy consumption were chosen. The choice of the masseter and temporal muscles for monitoring was based on the importance of these muscles to the masticatory function [3, 5, 12].

The following sections are intended to provide a system strategy for the acquisition of bioelectric signals. From this instrument it is possible to develop innumerable researches, such as: in the evaluation of the masticatory muscles asymmetry [12]; in the treatment of neurogenic orofacial dysfunctions [7]; in bite analysis in candidates for gastroplasty [13]; etc.

2.1 Amplification System

The acquired myoelectric signals have an amplitude lower than 400 μV and must be amplified so that the resulting signal occupies the entire input range of the Analog to Digital Converter (ADC), improving the resolution of the

signals when in the digital domain. For this purpose, the INA129 instrumentation amplifier was used, which among its main characteristics, it is possible to emphasize: differential input; operates with voltages between ±2.25 V (symmetric); common mode rejection ratio up to 130 dB; low resting current (700 μA) and configurable gain through the resistor (RG) according to Eq. 1 [14]. Because of these characteristics, common mode noise is mitigated by the INA129.

$$G = 1 + \frac{49.4\,[\text{k}]}{RG} \tag{1}$$

According to the datasheet the cutoff frequency value of the instrumentation amplifier's passband decreases as the gain increases. Since the cutoff frequency of the passband for a 1000-fold gain is 20 kHz, then it is possible to state based on the datasheet information that for a gain of 495 times the passband will be greater than a limited signal at 700 Hz.

The cables used in the two channels are 3-way with shielding and the electrodes are type 2223BRQ, from 3 M®.

2.2 Filter System

The choice of passive filters is based on the work of de Souza [10], who requires few components and consequently a lower power consumption. Should an active filter were used the need for an operational amplifier would lead the system to consume at least a base power to power the amplifiers. The initial values of the filters were elaborated after tests and simulations. The designed frequency range is approximately 100–500 Hz, in which the system has shown to be stable.

The average frequency system having a passband set between 100 Hz and 500 is approximately 224 Hz. This is close to the value shown in Fig. 1, which shows the mean and median of the EMG signal from the muscles of mastication frequencies.

Although the filter was passive and cascaded, the passband attenuation was only 5.7 dB. To compensate this attenuation and to increase the total gain, keeping the system stable, we chose to apply a gain of 28 times after filtration. Based on this study, it is possible to readjust for the next applications the bandwidth for a band more restricted and, consequently, with a higher signal-to-noise ratio.

2.3 Analog Signal Acquisition System

In order to build a portable system, in the phase of development, the board was rendered by software (Fig. 2). In this

Fig. 1 Mean and median frequencies of the EMG signal
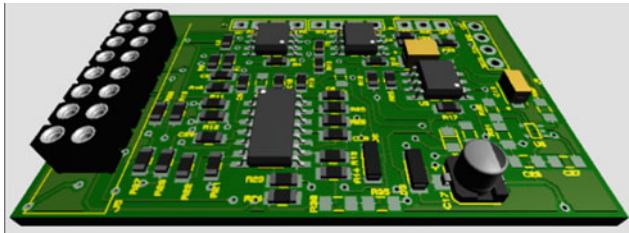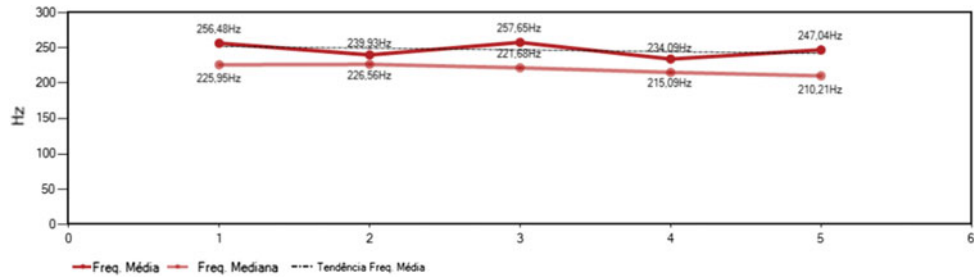
Fig. 2 Front view of the signal acquisition board to EMG
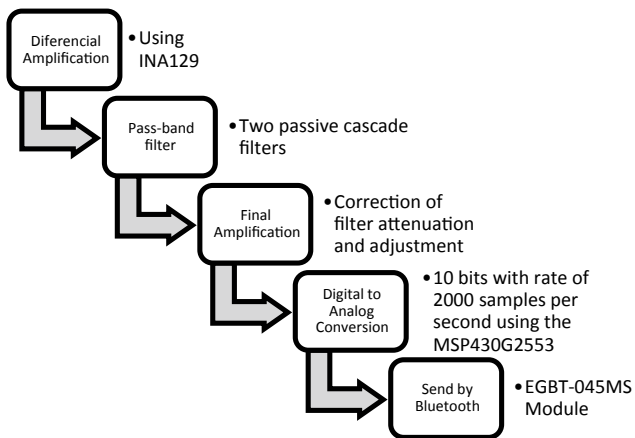
Fig. 3 Block diagram of the physical system used in the prototype

Fig. 4 Analog to digital conversion circuit and signal processing using MSP430G2553

has several features including: low power operating modes (Ultra Low-Power technology), operating voltage in the range of 1.8–3.3 V; 10-bit ADC; and serial interface [10, 15]. The schematic of the connections and ports used in the microcontroller is shown in Fig. 4.

The firmware was developed in the Code Composer Studio environment. Which enables the ADC, for each channel, at a rate of 2000 samples per second. This sample rate respects Nyquist–Shannon sampling theorem for reconstruction of the proposed signal. During the acquisition, a moving average filter was implemented to send wireless only the envelope of the signals. The communication is performed by EGBT-045MS module with Bluetooth 2.0 protocol [16]. With a baud rate of 115,200 bits per second. This value is enough to transmit all necessary data and conform to the receiving software.

model, it is possible to visualize the acquisition system. At the end of the project, the acquisition board was 50 mm (wide) per 30 mm (long). Figure 3 shows the block diagram with the workflow of the signal through the developed hardware, indicating the components used. Starting with the differential amplification block and ending with the bluetooth sending step.

2.4 Conversion System and Signal Processing

The MSP430G2553 was the microcontroller chosen to perform the conversion of the analog signal to digital and the processing of the signal for transmission. This microcontroller

2.5 Electromyographic Registration Software

The reliability software is used to interface the system with the user [17]. This was developed in Visual Studio
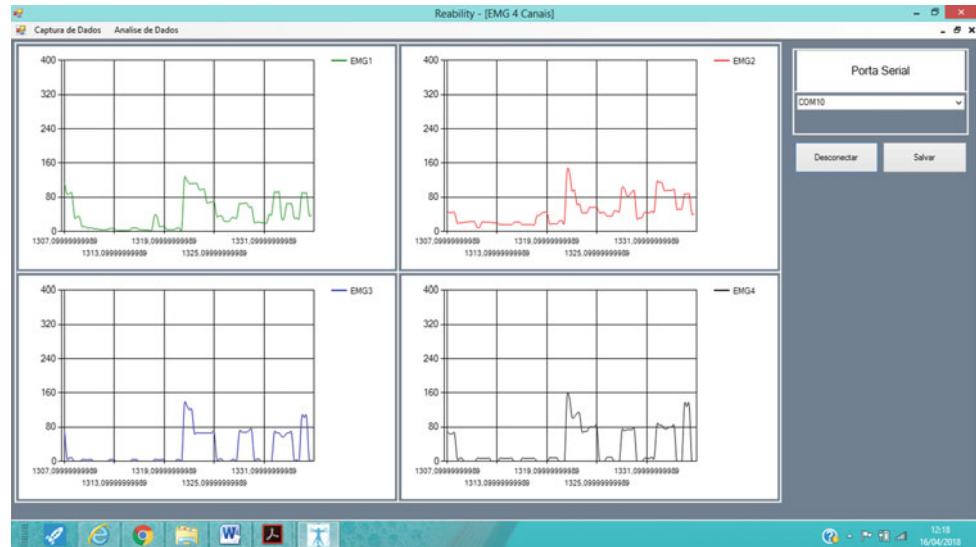
environment, using C# language and Windows Presentation Foundation (WPF) interface. The software is responsible for receiving, storing and recording data in real time.

2.6 EMG Signal Acquisition Methodology

After developing the system, its response was analyzed through simulations by the Proteus® software in the demo version. At this stage the goal is to analyze the signal behavior of the bandpass.

After confirmation of the simulation values in relation to the theorists, an acquisition of the EMG signal with the complete system was performed in the researcher-pain. According to the protocol approved by the Ethics Committee in Research with Human Beings of this University (CAAE: 80738617.3.0000.5208). For this, it was necessary 6 surface electrodes. A pair of electrodes was placed on the masseter muscle, the second pair on the temporal muscle and the other two electrodes used as reference were placed on the clavicle.

To acquire the data, is needed the Bluetooth pair with the computer. Figure 5. In the area of post-acquisition analysis, it is possible to verify the amplitude (vertical axis) and the time (horizontal axis) of the muscular activations using a cursor, Fig. 6.

3 Results

During the analysis phase, the EMG channels were simulated to confirm the gains obtained. The signal amplitude, according to the literature, is generally less than 400 µV.

A gain was chosen to provide 2.3 V at the ADC input when the signal was 320 µV (20% less than the maximum value). Equation 2 shows the calculation to obtain the total theoretical gain:

$$G < \frac{2.3\,[\text{V}]}{320 \times 10^{-6}\,[\text{V}]} = 7186 \qquad (2)$$

The following results were obtained in the simulations: the instrumentation amplifier the gain was 53.9 dB (495 times), according to the presented by INA129 datasheet [14]; the bandpass filter has an attenuation of 5.7 dB (-1.93 times), and the operational amplifier simulated gain was 28.9 dB (28 times), in agreement with the calculated gain. Thus, the total simulated amplification of the system is 77.1 dB (7181 times). The variation between the simulated and theoretical value is less than 0.07%.

The bandwidth was adjusted after numerous tests and signal analysis, for the following values: lower cutoff frequency of 100 Hz and cutoff frequency higher of 500 Hz.

The theoretical current consumption of the complete system was around 111.5 mA, using the values provided by datasheets [14–16, 18]. Which consider the maximum consumption of standby components without considering the dissipation of the passive components.

In the firmware, data rate and sample rate were analyzed, respecting the theorem of Nyquist. The developed software was able to graphically record the data envelope in real time, using a window of 250 points.

To assess the functionality of the system, the first test were performed electromyography in a calm and quiet environment. Initially using a consolidated device in the

Fig. 6 Graphics analysis screen of the reability program

Fig. 7 CVM registry for the masseter and left anterior temporal muscles during the protocol, using miotool face
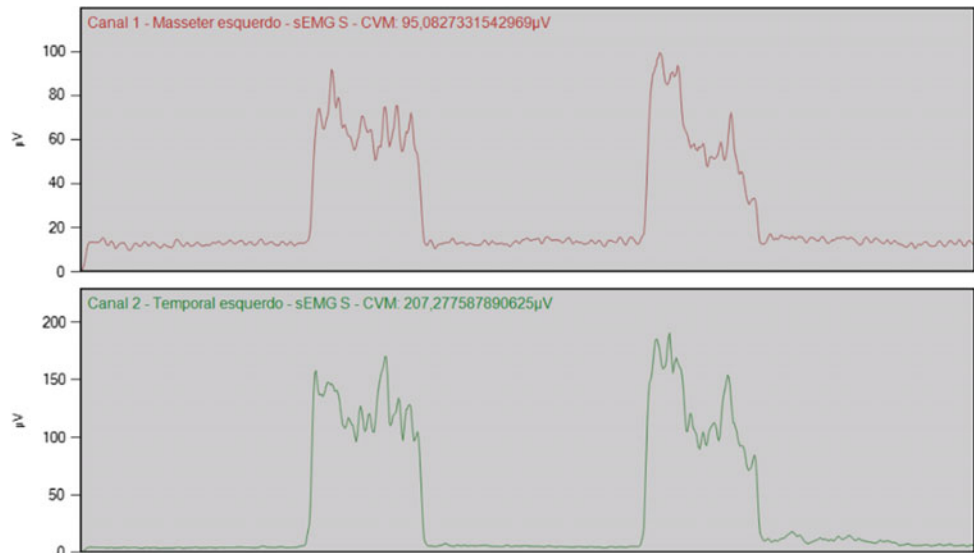
market (Miotec®, model Miotool Face 200/400), then using the developed system.

To obtain the Maximum Voluntary Contraction (CVM) in the EMG, cotton rollers were placed between the dental arches in the molar region. Then, the following protocol was performed: remaining for 10 s with the mouth muscles relaxed, slightly open, followed by dental occlusion, which consisted of maximal habitual intercuspation (MIH) for 5 s, repeated twice, with 10-s intervals between actions [19].

The CVM values of the masseter and anterior temporal muscles on the left side are represented in Fig. 7, using Miotool Face and Fig. 8, using the developed system.

4 Discussion

As the scope of this work is to present an electromyographic acquisition device of the main masticatory muscles. An emphasis was placed on the equipment description and the analogue treatment of the obtained signal. At the end, it was possible to perform the first acquisition of the equipment in an experimental manner compared to a commercial equipment.

The values used in the components of this project were successful close of the idealized gain after several simulations and tests. The gain value of 7186 theoretical times,

Fig. 8 CVM registry for the masseter and left anterior temporal muscles during the protocol, using the developed system
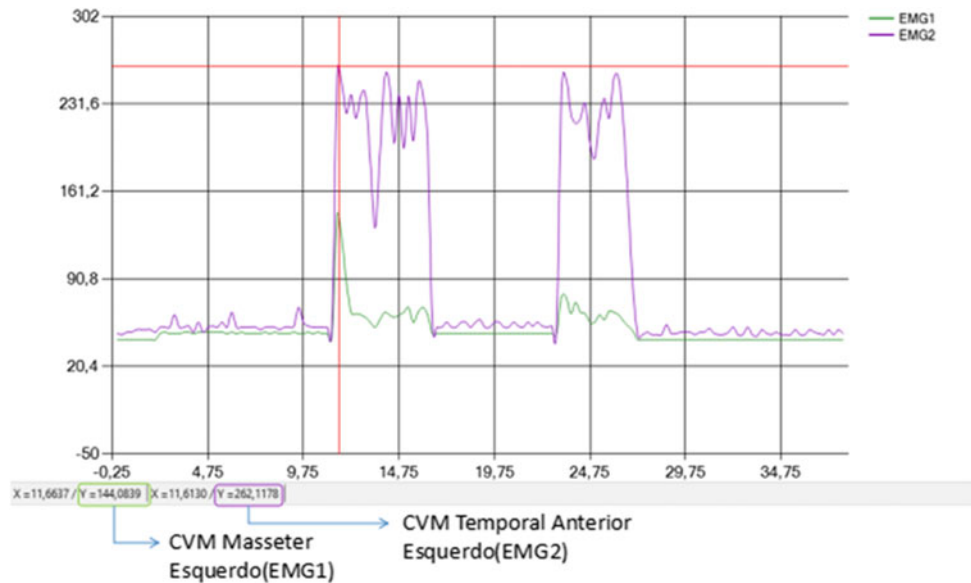
compared to the gain of 7181 times simulated presents a variation smaller than 0.07%. Which implies, in the worst case, a variation smaller than the resolution of the ADC, and can thus be neglected.

In spite of filters used are passive, it was possible to disregard the negative effects of noise outside the band of interest. The bandwidth had flat response throughout its range with attenuation of only 5.7 dB. To balance the filter set to keep the bandwidth flat and attenuation less than 6 dB, it was necessary to manipulate: the lower and upper cut-off frequencies and the commercial values of the capacitors and resistors.

The developed system performed well on its first test. The posterior analysis with clinical validation, present in the protocol of the Research Ethics Committee, will be performed at a later time.

5 Conclusion

Among the various challenges encountered in this project can be highlighted in terms of hardware: amplify a signal smaller than 400 μV, balance a passband filter composed of passive filters cascaded and make the portable system behave in a stable way during the acquisition of the signal.

Despite the simplicity of the system, relative to other EMG systems, it was possible to obtain satisfactory and promising results so far, the simulations using software and theoretical calculations.

Communication between the hardware and the software performed well receiving and illustrated the real-time data, enabling a prior and detailed analysis.

The purpose of verifying the suitability of a new application of the existing equipment has been successfully completed. Given the initial validation, the analysis of the mastication symmetry will be done by a professional through the data of the complete equipment with more acquisition channels. Adequate parameters to evaluate the bite force in people with neurogenic orofacial dysfunctions. Which is part of a bigger project.

References

1. Tagliaro, M.L., Calvi, C.D.L., de Chiappetta, A.L.M.L.: A fase de incisão no processo da mastigação: Enfoque clínico. Rev. CEFAC **6**(1), 24–28 (2004)
2. Nascimento, G.K.B.O., de Lima, L.M., da Rodrigues, C.B.S., Cunha, R.A., Cunha, D.A., Silva, H.J.: Verificação da força de mordida e da atividade elétrica dos músculos masseteres durante a mastigação em laringectomizados totais. Rev. Bras. Odontol. **68**(2), 175–179 (2011)
3. de Silva, T.V.A., do Sobral, A.V., Fraga, A.S., Coriolano, M. das G.W. de S., dos Lins, C.C.S.A.: Contração Voluntária Máxima de Masseter e Temporal em pessoas com doença de Parkinson: um estudo eletromiográfico. In: V Congresso Internacional de Envelhecimento Humano, vol. 1, pp. 494–506 (2017)
4. Park, S., Shin, W.-S.: Differences in eating behaviors and masticatory performances by gender and obesity status. Physiol. Behav. **138**, 69–74 (2015)
5. Berlese, D.B., Copetti, F., Weimmann, A.R.M., Fontana, P.F., Haefffner, L.S.B.: Atividade dos músculos masseter e temporal em relação às características miofuncionais das funções de mastigação e deglutição em obesos. Rev. Distúrbios da Comun. **24**(2), 215–221 (2012)
6. Oncins, M.C., de Freire, R.M.A.C., Marchesan, I.Q.: Mastigação: análise pela eletromiografia e eletrognatografia. Seu uso na clínica fonoaudiológica. Rev. Distúrbios da Comun. **18**(2), 155–165 (2006)

7. de Freitas, G.S., Mituuti, C.T., Furkim, A.M., Busanello-Stella, A. R., Stefani, F.M., da Arone, M.M.A.S., Berretin-Felix, G.: Biofeedback eletromiográfico no tratamento das disfunções orofaciais neurogênicas: revisão sistemática de literatura. Audiol. Commun. Res. **21**, 1–10 (2016)

8. Boton, L.D.M., da Silva, A.M.T., Bolzan, G.D.P., Corrêa, E.C.R., Busanello, A.R.: Estudo eletromiográfico dos músculos faciais de respiradores nasais, respiradores orais viciosos e obstrutivos. Rev. CEFAC **13**(1), 27–34 (2011)

9. Niijima, A., Ogawa, T.: A proposal of virtual food texture by electric muscle stimulation. In: 2016 IEEE International Conference on Multimedia & Expo Workshops (ICMEW), pp. 1–6 (2016)

10. de Souza, P.V.E.: Sistema de aquisição de sinais de EMG e ECG para plataforma Android. Dissertação (Mestrado em Engenharia Elétrica). Universidade Federal de Pernambuco (2015)

11. Cosmanescu, A., Miller, B., Magno, T., Ahmed, A., Kremenic, I.: Design and implementation of a wireless (Bluetooth®) four channel bio-instrumentation amplifier and digital data acquisition device with user-selectable gain, frequency, and driven reference. In: 2006 International Conference of the IEEE Engineering in Medicine and Biology Society, pp. 2053–2056 (2006)

12. Botelho, A.L., Bronchini, A.P.Z., Martins, M.M., Melchior, M.O., da Silva, A.M.B.R., da Silva, M.A.M.R.: Avaliação eletromiográfica de assimetria dos músculos mastigatórios em sujeitos com oclusão normal. Rev. da Fac. Odontol. RFO **13**(3), 7–12 (2008)

13. dos Santos, A.C., da Silva, C.A.B.: Surface electromyography of masseter and temporal muscles with use percentage while chewing on candidates for gastroplasty. ABCD. Arq. Bras. Cir. Dig. (São Paulo) **29**(suppl 1), 48–52 (2016)

14. Instruments, T.: INA12x precision, low-power instrumentation amplifiers. SBOS051D, Datasheet, p. 29 (2018)

15. Instruments, T.: MSP430G2x53 MSP430G2x13. SLAS735 J, Datasheet, p. 76 (2013)

16. Wavesen: HC serial Bluetooth Module. HC-05, Datasheet, p. 16 (2011)

17. Cavalcante, É.L.: Plataforma Dinâmica de Avaliação Fisioterápica. Dissertação (Mestrado em Engenharia Elétrica). Universidade Federal de Pernambuco (2015)

18. Instruments, T.: OPAx172 36-V, Single-supply, 10-MHz, rail-to-rail output operational amplifiers. SBOS618H, Datasheet, p. 52 (2015)

19. Nascimento, G.K.B.O., da Cunha, D.A., de Lima, L.M., de Moraes, K.J.R., de Pernambuco, L.A., Régis, R.M.F.L., da Silva, H.J.: Eletromiografia de superfície do músculo masseter durante a mastigação: uma revisão sistemática. Rev. CEFAC **14**(4), 725–731 (2012)

Evaluation of Cytotoxicity of Nickel-Titanium Electrode for Hepatic Ablation Equipment with Carcinosarcoma Walker 256 Tumor Model

M. S. Monteiro, J. S. S. Casado, R. D. Fonseca,
M. L. B. Carneiro, and S. S. R. F. Rosa

Abstract

The worldwide epidemiology of hepatocellular carcinoma (CHC) positions it as the fifth most common malignancy globally and the third cause of cancer-related death and high morbidity and mortality in Brazil sufficient to seriously burden the Unified Health System (SUS). The use of radiofrequency ablation is already consolidated as the best therapeutic option in the stages 0 and A of BCLC (Barcelona Clinic Liver Cancer), in unresectable cases and to reduce the staging or increase of survival to wait for transplantation. Due to its high cost, the Ministry of Health and the LaB-Laboratory of Biomedical Engineering of the University of Brasilia have innovated with the production of a low cost national radiofrequency ablation equipment called SOFIA (Software of intensive ablation). This study proposes the validation of the SOFIA equipment in its preclinical phase investigating the biological effects produced by the use of the umbrella electrode of NiTi, device coupled to the equipment. A tumor model, carcinosarcoma (*Walker* 256 tumor) was used for analysis of in vitro cytotoxicity by colorimetric cell viability spectrophotometry with the NiTi (Níquel-titânio) MARINA 5H electrode. The nickel-titanium (NiTi) alloy of the MARINA 5H electrode was considered to be non-cytotoxic and no harmful residues were formed at the cellular levels, biocompatible for use in clinical phase I tests.

M. S. Monteiro (✉) · R. D. Fonseca · M. L. B. Carneiro ·
S. S. R. F. Rosa
University of Brasilia, Brasilia, Brazil
e-mail: melcomenator@gmail.com

J. S. S. Casado
Federal University of Alagoas, Maceió, Brazil

1 Introduction

The worldwide epidemiology of hepatocellular carcinoma (CHC) positions it as the fifth most common malignancy globally and the third leading cause of cancer-related death [1]. In the specific case of Brazil, Portaria nº 602 of 2012 [2] indicates that 98% of HCC cases are related to hepatic cirrhosis and may be associated with chronic hepatitis secondary by hepatitis C virus infection (54%) or hepatitis B (16%) and alcohol consumption (14%), risk factors per regional differences are relevant to epidemiology.

The Ministry of Health proposes that actions for prevention and control of HCC should be on the agenda of local public health management, including clinical research for new equipment that provide safe therapy options favoring new perspectives for reducing these statistics.

After the positive diagnosis of CHC is the staging of the patient that will allow the choice of treatment and will involve analysis of the patient's clinical conditions, liver function and tumor extension for the decision. Preferably, surgical resection is considered the best survival option—between 40 and 50%—but only 10–15% of the patients are compatible with this possibility [3]. Also, the advantages for the patient on the waiting list for the transplant are crucial. The accessory (non-invasive) procedures are the ideal option to guarantee their survival, as well as reducing staging for tumors up to 3 cm [4].

Among these accessory procedures is radiofrequency ablation (RFA), which consists of a therapeutic resource designed to cause tissue damage by local heating [5]. Through the application of radiofrequency waves, tissue heating has become a therapeutic alternative using tissue necrosis of the tumor volume with minimal damage to the normal peripheral tissue [6].

A project financed by the Ministry of Health in partnership with the University of Brasilia is one of the research fronts of LaB—Laboratory of Biomedical Engineering, linked to the LEI (Laboratory of Engineering and

Innovation) of FGA (Faculty of Gama), proposed the development of a radiofrequency ablation equipment consisting of a radiofrequency generator, active monopolar electrode and control *software*.

The prototype that will be used in Phase I of the clinical essay was finalized and this study involved a stage of validation in animals and involved an analyses in vitro cytotoxicity of the electrode configuring as a stage of the preclinical phase.

2 Materials and Methods

The present study was carried out in the Laboratory of Electron Microscopy of the Institute of Biology of the University of Brasilia (UnB), in Brasilia, both cell culture and in vitro toxicity analysis.

2.1 In Vitro Toxicity Analysis by Cellular Viability Assessment

Cell viability could be analyzed by the reduction of the MTT reagent (3- (4,5-dimethylthiazol-2-yl) -2,5-diphenyl-tetrazolium bromide). This is a colorimetric technique based on the absorbance of the concentration of the purplish, insoluble formazan product obtained after reduction of the MTT reagent (3- (4,5-dimethylthiazol-2-yl) -2,5-diphenyl bromide-tetrazolium)—yellow coloration salt soluble in water, by action of mitochondrial dehydrogenases, indicating the activity of these organelles. Thus, the reduction of MTT to formazan will be directly proportional to mitochondrial activity and cell viability.

2.2 Procedure

For the MTT positive control group, a culture of fibroblast primary cells obtained from human tooth pulp was used and transferred to culture bottles for maintenance and expansion using DMEM medium (Dulbecco's modified Eagle's medium, medium synthetic complex). A 250 mL bottle was used for the cell viability test.

Two groups were analyzed: a group of normal fibroblast cells and an experimental group of an aliquot of the in vitro cell culture *Walker* 256. Cultures were produced in 24-well plates of each group for 24 h after counting the cells in the Neubauer chamber. For each well, 1×10^5 cells were placed from each lineage cells.

The wells were organized in triplicates as described below: 3 (three) wells with fibroblasts and DMEM medium (Dulbecco's modified Eagle's medium, complex synthetic medium) without electrode and another 3 (three) with the same components, but with one electrode rod added positioned at the bottom of the well; 3 (three) wells with Walker 256 cells and RPMI medium, (Roswell Park Memorial Institute medium, complex synthetic medium) without electrode and another 3 (three) with the same components, but with an electrode rod positioned at the bottom of the well. Figure 1 shows the nickel-titanium electrode and its stems used in the experimental procedure The stems were previously sterilized using ultraviolet light for 20 min.

After 72 h, 350 μL of the MTT reagent was added to each well (in laminar flow with cold light off) and after 4 h, the plate was packed in foil. After this each well was resuspended with 500 μL of DMSO (dimethylsulfoxide) for later reading at the spectrophotometer at the wavelength of 595 nm. The use of this protocol for toxicity evaluation was proposed by Mossman [7].
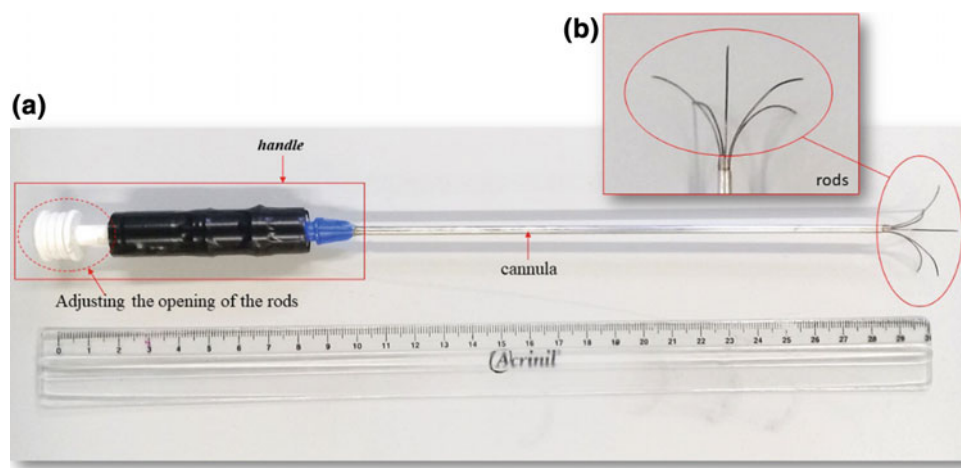
Fig. 1 a Photo of the prototype of the electrode MARINA 5H produced in the Laboratory of Biomedical Engineering (LAB/UnB). In the red contours are the electrode parts: the manual manipulator—the handle–the cannula, which allows the insertion and exit of the rods and the nickel-titanium (NiTi) rods. **b** Detail of nickel-titanium rods used at the viability test (Personal file) (Color figure online)

2.3 Statistical Analysis

To analyze the cell viability estimated by the MTT technique of the experimental groups the unpaired Student t test was performed to evaluate the reduction of the percentage of viable cells due to electrode cytotoxicity. Statistical analysis considered the initial population of cells in each group as 100%. In all cases differences were considered significant when $p < 0.05$.

3 Results

It was considered not to cause cytotoxicity the presence of whole stems of the MARINA 5H electrode on 72 h time. Considering a statistical significance of 5%, the data collected did not lead to rejection of the null hypothesis that the means of the control and tumor groups are statistically equal.

The non-paired t-student statistical method was used to perform a comparison of the groups in Graph Pad 5.0, there was no statistical difference when comparing the control and electrode triplicate for each lineage. The mean of the fibroblast lineage for both groups was 105.8 ± 5.76 and for the Walker lineage it was 100 ± 11.15 and the graphic representation used was boxplot for better visualization of the values obtained for the percentage of viable cells (Fig. 2).

This result corroborates with the already consolidated expectation of the use of nickel titanium (NiTi) as a biocompatible material and that the presence of nickel with the heavy metal in its constitution does not generate the production of residues that can be released to the metabolism of an organism.

4 Discussion

Nickel is a heavy metal present in our daily life due to its property of forming alloys with high resistance to heating and corrosion and therefore very used in implants and medical equipment but also in food processing [8]. Therefore, our digestive tract is exposed to contact with this alloy in some way in daily life.

However, even considering this perspective and considering the local temperature increase caused by ARF in the electrode for the duration of the procedure, the in vitro analysis guarantees that the cellular behavior of the burning area is free of contamination.

From the data of the MTT techniques for cell viability, the electrode can be validated as non-toxic and without alteration of the biological tissue metabolism, and from this data, it is possible to infer a biological indicator that will influence the two main areas of ablation—lethal and sublethal. It is noticed that the parameter of the metabolism of the biological tissue that results from the cellular metabolism arising from the agitation of the intra and extracellular ions will influence the Pennes bioheat transfer equation used to model a physical phenomenon of thermal electric heating in a biological system.

Fig. 2 Boxplot graph for cell viability. This graph indicates the dispersion of the two cell lines and their corresponding control groups. The data dispersion indicates a slight decrease in the mean for the nickel titanium—NiTi—Walker group. Such a decrease is due to cell death in one of the triplicates due to overpopulation, but still the confidence interval of the data is equivalent (Color figure online)
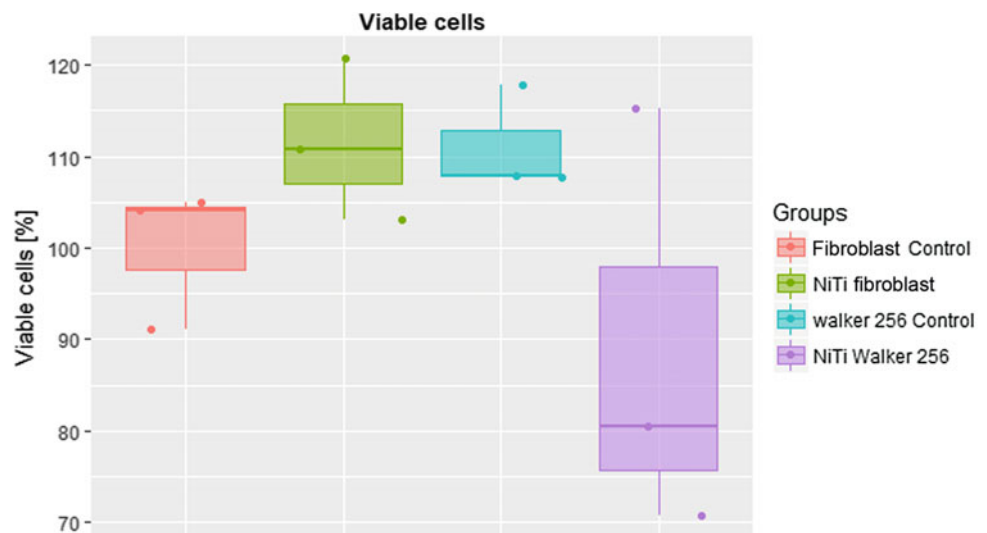
As a proposal of future work, a simulation in the COMSOL where a distribution of the temperature curve would be carried out with the parameters pertinent to this model of this study and another for comparison is suggested.

5 Conclusion

It is clear from the in vitro toxicity test that the nickel-titanium alloy (NiTi) is not cytotoxic to the enzymes involved in the cell-viability test in vitro and has a degree of biocompatibility with no harmful residues formation at the cellular level.

This parameter allows to indicate that the nickel titanium electrode also does not have cytotoxicity for the tumor cells in the enzymatic route involved at the test, but it is still possible to extrapolate and affirm that there will be no transfer between cells post procedure, which would risky in cases of sublethal area.

It is concluded that It is also not cytotoxic to the safety margin of 1 cm commonly included by clinicians to ensure that there is no recurrence. This safety margin it is constituted of normal cells that have different characteristics of a neoplastic cell, there could be cellular metabolic alterations and transfer this cytotoxicity to the remaining tissue.

Therefore, the nickel titanium electrode is considered ready for the next steps with other in vitro tests and new animal tests that will provide in vivo results that will ensure safety in the use of the SOFIA equipment for the clinical phase with the electrode MARINA 5H produced by Biomedical Engineering Laboratory—LaB.

References

1. Magistri, P., et al.: The evolving role of local treatments for HCC in the third millennium. Anticancer Res. **37**(2), 389–401 (2017). International Institute of Anticancer Research
2. Portaria, nº. 602, de 26 de junho de 2012. Diretrizes Diagnósticas e Terapêuticas do Câncer de Fígado no Adulto (2012)
3. Paranaguá-vezozzo, D.C., et al.: Epidemiology of HCC in Brazil: incidence and risk factors in a ten-year cohort. Ann. Hepatol. Off. J. Mex. Assoc. Hepatol. **13**(4) (2014)
4. Carrilho, F.J., et al.: Brazilian society of hepatology recommendations for the diagnosis and treatment of hepatocellular carcinoma. Arquiv. Bras. de Gastroenterol. **52**, 2–14 (2015)
5. Majumdar, A., et al.: Management of people with early-or very early-stage hepatocellular carcinoma. Cochrane Libr. Wiley Online Library (2017)
6. Balogh, J., et al.: Hepatocellular carcinoma: a review. J. Hepatocell. Carcinoma **3**, 41 (2016). Dove Press
7. Mossman, T.: Rapid colorimetric assay for cellular growth and survival: application to proliferation and cytotoxicity assays. J. Immunol. Methods **65**(1–2), 55–63 (1983). Elsevier
8. de Campos Júnior, F.F.: Avaliação da citotoxicidade in vitro da liga níquel-berílio às células bacterianas e à linhagem celular NCTC clone 929. Tese de Doutorado. Universidade de São Paulo

Insulated System for Capacitive ECG Measurement

G. V. Resende and M. N. Souza

Abstract

Conventional systems for electrophysiological measurement use wet electrodes that require contact with skin. Those systems may not be feasible for a long term monitoring due to skin irritation and allergic reactions, caused by the conductive gel present on the electrode. To avoid these issues, different approaches have been proposed, including dry contact and insulating electrodes. Recently, several researchers have explored insulating electrodes, also known as capacitive electrodes, achieving good signal results. This work presents a fully insulated system to acquire electrocardiogram (ECG) with capacitive coupling, bootstrap technique, and also a capacitive driven right leg circuit (DRL). The development and some results of examples of the acquired signal are presented. From results we conclude that the proposed system of capacitive electrode system for acquiring ECG signals worked properly supling results similar to the ones acquired by using conventional wet Ag/AgCl electrodes.

1 Introduction

The heart electrical activity is widely employed in clinical practice to diagnose and follow up cardiovascular diseases. The traditional method of acquiring electrocardiogram (ECG), using wet electrodes (i.e., Ag/AgCl electrodes), can provide high quality signals but the gel can cause skin irritation and requires skin preparation, like shaving and cleaning with alcohol [1].

To overcome these issues, capacitive electrode gives an alternative way for acquiring ECG signals. The basic principles behind have been subject of studies for decades [2–5], despite that the standard wet Ag/AgCl electrode is almost universally used for clinical and research applications.

The main issue when acquiring biopotentials through clothing is the coupling capacitance of only tens of pF, requiring extremely high input impedances to reach a cutoff frequency of hundredth of Hertz. The high impedance makes this technique highly vulnerable to electromagnetic interference, requiring a carefully shielding. In addition, the technique implemented to obtain such high impedance increases the electrode noise. This works aims to develop a capacitive electrode system for acquiring ECG signals using a bootstrap technique.

2 Materials and Methods

Three electrodes, a differential pair and a feedback electrode providing the driven right leg (DRL), compose the system. The differential pair is connected to an instrumentation amplifier through a small shielded cable. The operational amplifiers used are OPA2350, which provides low noise, high input impedance and low input bias current (Fig. 1).

The system has also a baseline correction circuit connected to the reference pin of the instrumentation amplifier; the circuit consists of a low pass filter (1 Hz) with a small

G. V. Resende (✉) · M. N. Souza
Polytechnical School, Electronic and Computer Engineering Department, Universidade Federal do Rio de Janeiro, Rio de Janeiro, Brazil
e-mail: gabrielresende@poli.ufrj.br

M. N. Souza
Biomedical Engineering Program, Universidade Federal do Rio de Janeiro, COPPE, Rio de Janeiro, Brazil

Fig. 1 Block diagram of the
measurement system
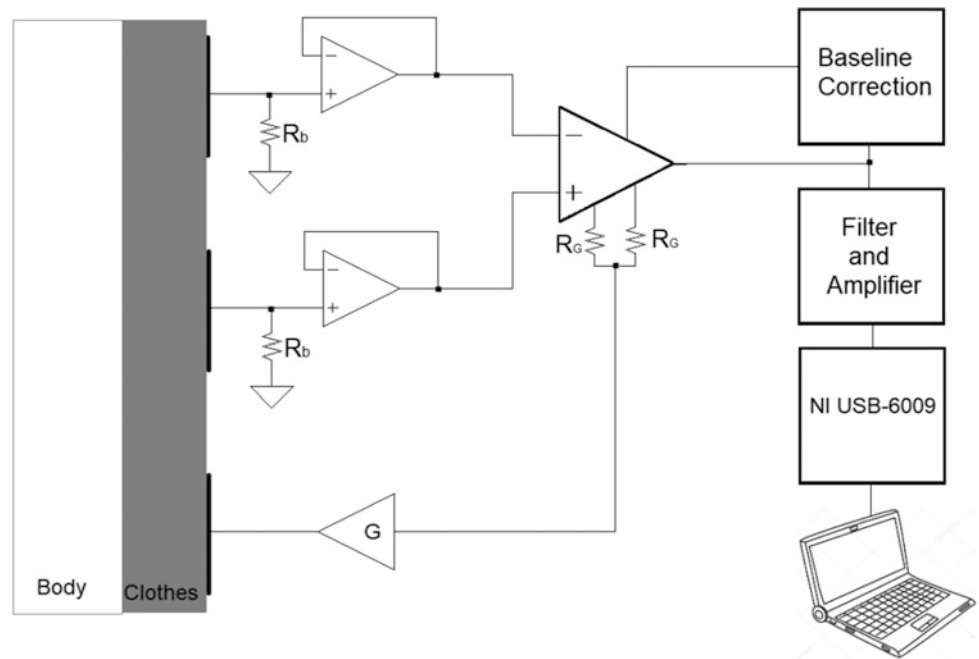
negative gain (−2.5). That way, the DC level is subtracted
from the signal, avoiding the output saturation.

The ECG signal acquire is filtered by a low pass with
cutoff frequency of 100 Hz (fist order), because most of the
power of such signal are in within this band [6]. After that,
the signal is sampled at the rate of 1 kHz by the National
Instruments USB-6009 acquisition board (14 bits differential
analog inputs). A program developed in LabVIEW con-
trolled the acquisition board and exhibited the acquired
signal.

2.1 Electrode

Previous studies have shown that the sensing part could be
the limitation factor in the entire system design as it directly

determines the skin electrode interface [7]. Different tech-
niques have been used in an attempt to create an electronic
analog front end (AFE) such as charge amplifier, transcon-
ductance amplifier, instrumentation amplifier and voltage
follower [8]. In order to preserve the signal integrity and
reduce the interference coupled into leads, the AFE topology
chosen was the voltage follower.

The AFE was mounted in a printed circuit board, with an
active shielding to diminish stray capacitance and avoid
leakage current. That way, we buffered the output to drive a
shielded cable, reducing the sensibility to the power line
interference (Fig. 2).

In the coupling impedance composition, the coupling
capacitance is much smaller than the stray resistance; for this
analysis C_s is used to represent the skin-electrode interface
(including clothing), as it is the dominant layer. The model

Fig. 2 Equivalent circuit model
for capacitive interface
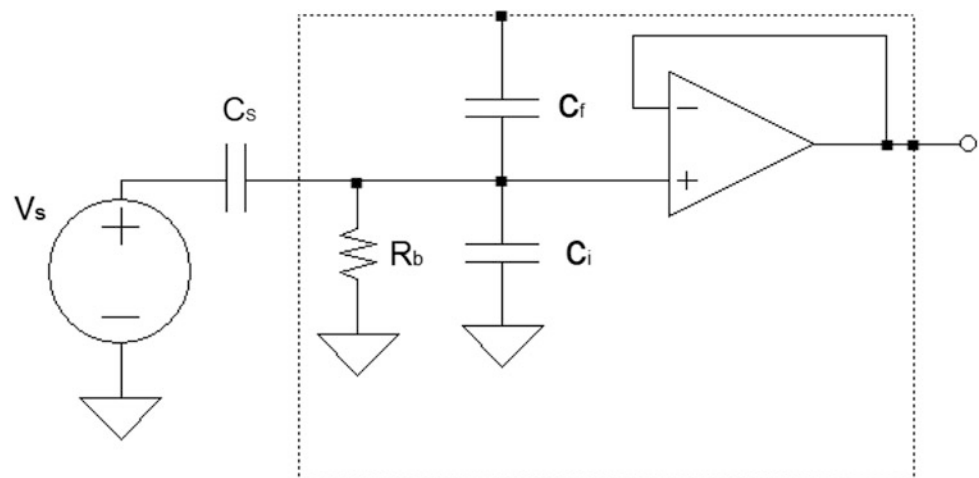
illustrate a high pass response of the passive components and the actual input voltage for the voltage follower is (1). C_x models the parasitic capacitances such as the one due to the shielding and C_i represents the operational amplifier input capacitance.

$$V_{in} = \frac{j\omega R_b C_s}{1 + j\omega R_b(C_i + C_s + C_x)} V_s \qquad (1)$$

Which gives a low cut of frequency (2)

$$f_c = \frac{1}{2\pi(C_i + C_s + C_x)R_b} \qquad (2)$$

For ECG signal such frequency is normally set as low as 0.05 Hz. The bias resistance is not necessarily very precise but it has a limit value, given by $R_{b\,MAX} < V_{cc}/i_{bias}$ [9]. Because of the bias resistor, the electrode output can has an offset voltage. We used a high pass filter with 0.03 Hz cutoff frequency between the electrode and the instrumentation amplifier, preventing the offset voltage of being amplified.

The bias resistance was implemented using a bootstrap technique (Fig. 3) [10]. This technique uses a small positive feedback to multiply resistor R_1. Equation (3) gives the resulting impedance.

$$R_b = R_1 R_2 / R_3 \qquad (3)$$
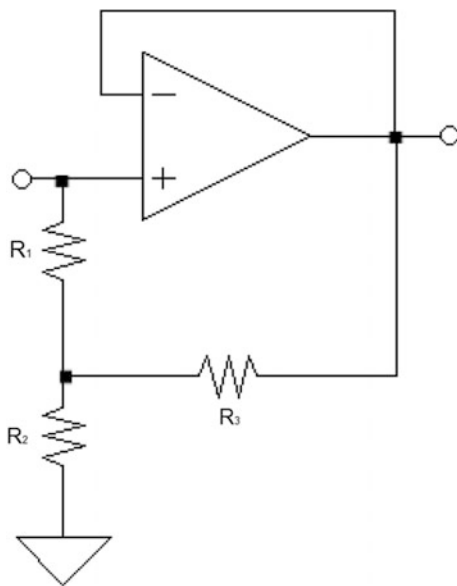
Fig. 3 Bootstrap topology

In our design, the electrode has a round format with 25 mm diameter. The capacitive coupling can be estimated as

$$C_S = \epsilon_0 \epsilon_r \frac{A}{d} = 14.5\,\text{pF}$$

Considering $d = 0.3\,\text{mm}$, $\epsilon_r = 1$, $\epsilon_0 = 8.85 \times 10^{-12}\,\frac{\text{F}}{\text{m}}$.

The bias resistor was calculated using this value for the coupling capacitance and the low cutoff frequency of 0.05 Hz

$$R_b = \frac{1}{2\pi C_s f_1} = 219\,\text{G}\Omega$$

However, considering the available resistors values and that the relative permittivity of a cotton shirt may be bigger than 1, the chosen value for the bias resistor was 183 GΩ. Giving the resistors $R_1 = 10\,\text{M}\Omega$, $R_2 = 2.2\,\text{M}\Omega$, $R_3 = 120\,\Omega$.

2.2 Driven Right Leg Circuit

The driven right leg (DRL) circuit is commonly used for noise reduction on ECG measurements. For a completely insulated system, its implementation is quite a challenge due to the high pass filter formed on the coupling. Many researches had implemented with a large coupling area, such as on chair [11] and automotive applications [12]. In our case, a smaller plate was proposed, with a rectangular shape $(8\,\text{cm} \times 4.5\,\text{cm})$.

The DRL provides a negative feedback of the common mode noise. It is very effective for reduce power line interference. In our system, the common mode is obtained through a characteristic of the instrumentation amplifier. The INA128 has a symmetric topology that allows, by splitting the gain resistor in two, to take a good estimative of the common mode signal (Fig. 4).

The buffers are necessary to preserve the signal quality between stages. The high pass filter formed by C_H and R_H was necessary for preventing that any offset voltage from the instrumentation amplifier saturates the DRL output. The low pass in the gain stage was also needed to prevent output saturation, but in this case is due to high frequencies interferences. The gain was experimentally (Av = −392) adjusted until the power line interference got imperceptible. We also tried increasing the gain, but it leads to system instability.

Fig. 4 Driven right leg circuit
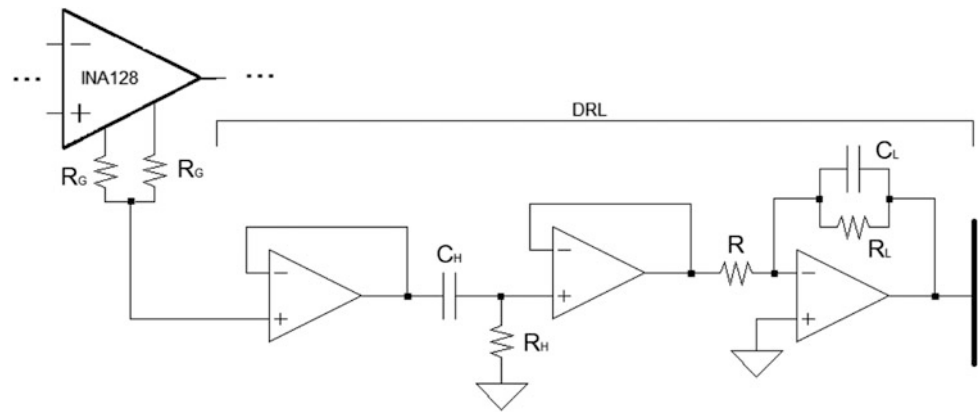
Fig. 5 Example of an ECG signal acquired on the developer
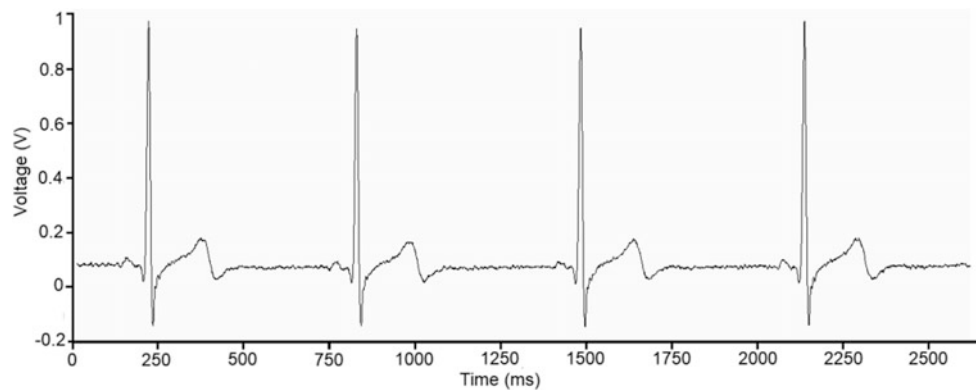
3 Results and Conclusion

An elastic band helped to fix the electrodes in the body (over the clothing). As above-mentioned, a program developed in LabVIEW environment records the signal. Figure 5 shown an ECG obtained with our measurement system, where one can observe that the P, Q, R, S and T waves are all present in the recorded signal.

Using a simplest topology, this work presents similar results when compared to previous studies [13, 14]. Anyway, a more complex design may be needed for a better control of the electrode parameters [13].

No gel electrodes were used during the signal acquisition. Some previous works have acquired [15, 16] their data using a conventional wet Ag/AgCl electrode system in parallel with the capacitive system. By doing so, the capability of evaluate the DRL functionality is annulled, because the traditional system provides a better common mode canceling due to the electrode galvanic conduction.

From the results we conclude that the proposed system of capacitive electrode system for acquiring ECG signals using a bootstrap technique worked properly suppling results similar to the ones acquired by using conventional wet Ag/AgCl electrodes. However, further efforts must be made to integrate the all circuit into a smaller area in order to be better arranged in ordinary clothes. Also, more acquisitions must be made to a better comparison with conventional wet electrodes.

References

1. Meziane, N., Webster, J.G., Attari, M., Nimunkar, A.J.: Dry electrodes for electrocardiography. Physiol. Meas. **34**(9), R47–R69 (2013)
2. Bourland, J., Geddes, L., Sewell, G., Baker, R., Kruer, J.: Active cables for use with dry electrodes for electrocardiography. J. Electrocardiol. **11**(1), 71–74 (1978)
3. Lopez, A., Richardson, P.C.: Capacitive electrocardiographic and bioelectric electrodes. IEEE Trans. Biomed. Eng. **16**(1), 99–99 (1969)
4. Taheri, B.A., Knight, R.T., Smith, R.L.: A dry electrode for EEG recording. Electroencephalogr. Clin. Neurophysiol. **90**(5), 376–383 (1994)
5. Matsuo, T., Iinuma, K., Esashi, M.: A barium-titanate-ceramics capacitive-type EEG electrode. IEEE Trans. Biomed. Eng. **20**(4), 299–300 (1973)
6. Webster, J.G., Clark, J.W.: Medical Instrumentation: Application and Design, 4th edn. Wiley, New York (1998)
7. Gandhi, N., Khe, C., Chung, D., Chi, Y.M., Cauwenberghs, G.: Properties of dry and non-contact electrodes for wearable physiological sensors. In: 2011 International Conference on Body Sensor Networks (BSN), pp. 107–112. IEEE, Texas (2011)

8. Sun, Y., Yu, X.B.: Capacitive biopotential measurement for electrophysiological signal acquisition: a review. IEEE Sens. J. **16**(9), 2832–2853 (2016)

9. Spinelli, E., Haberman, M.: Insulating electrodes: a review on biopotential front ends for dielectric skin-electrode interfaces. Physiol. Meas. **31**(10), S183–S198 (2010)

10. Spinelli, E.M., Haberman, M., García, P.A., Guerrero, F.N.: Electrodos capacitivos. In: II Jornadas de Investigación y Transferencia de la Facultad de Ingeniería, pp. 405–410, La Plata (2013)

11. Aleksandrowicz, A., Leonhardt, S.: Wireless and non-contact ECG measurement system—the 'Aachen SmartChair'. Acta Polytech. **47**(4–5), 68–71 (2007)

12. Leonhardt, S., Aleksandrowicz, A.: Non-contact ECG monitoring for automotive application. In: 5th International Summer School and Symposium on Medical Devices and Biosensors, pp. 183–185. IEEE, Hong Kong (2008)

13. Chi, Y.M., Cauwenberghs, G.: Wireless non-contact EEG/ECG electrodes for body sensor networks. In: 2010 International Conference on Body Sensor Networks (BSN), pp. 297–301. IEEE, Singapore (2010)

14. Chi, Y.M., Mayer, C., Cauwenberghs, G..: Ultra-high input impedance, low noise integrated amplifier for noncontact biopotential sensing. IEEE J. Emerg. Sel. Top. Circuits Syst. **1**(4), 526–535 (2011)

15. Wu, K., Zhang, Y.: Contactless and continuous monitoring of heart electric activities through clothes on a sleeping bed. In: 2008 International Conference on Information Technology and Applications in Biomedicine, pp. 282–285. IEEE, Shenzhen (2008)

16. Ueno, A., Akabane, Y., Kato, T., Hoshino, H., Kataoka, S., Ishiyama, Y.: Capacitive sensing of electrocardiographic potential through cloth from the dorsal surface of the body in a supine position: a preliminary study. IEEE Trans. Biomed. Eng. **54**(4), 759–766 (2007)

Integrated Optical Guide

Lívia Batista, Saulo Moreira, Marcelo Okamura, Marcelo Santoni,
Filipe Bueno, and Rani Alves

Abstract

Endotracheal intubation is a procedure performed over many years but it can still cause damages to the patient. In order to enhance the results obtained by this technique, it was developed an optical guide which is composed by a camera and a 3D-printed plastic structure to replace the conventional guide used conventionally. The prototype developed proved to be functional in tests performed on mannequins, which results indicate to benefits within the intubation process.

Keywords

Laryngoscopy • Guide • Airways • Video

1 Introduction

Endotracheal intubation is a medical procedure that uses a laryngoscope, an endotracheal tube and a guide to perform mechanical ventilation for the patient, when he is not able to perform it by himself. It is commonly used in cases of accident, respiratory and cardiac arrest, severe respiratory insufficiency, obstructions of the airways, presence of abundant secretions in the lung or when the patient undergoes a surgery that needs general anesthesia [1–4].

For performing the direct laryngoscopy, the patient should be positioned with chest upwards and inclined chin and then the qualified professional holding the cable of the laryngoscope inserts the blade into the sedated patient's mouth aiming the airway visualization. Thus, an endotracheal tube is introduced into the trachea. After the intubation procedure, an external source carries oxygen to the patient's trachea, ensuring the ventilation control [1–8].

The visibility of glottis is important to the laryngoscopy procedure. It may change according to the patient's physical type. Therefore, a scale was created to classify the visibility of airways, known as the Cormack Lehane scale. This scale was developed in 1984 by the physicians R. S. Cormack and J. Lehane to rank the difficulty of visualizing the patient's glottis (Fig. 1). The first level (level 1) represents a complete and clean glottis' view, as well as it is considered an ideal condition for intubation. In level 2, only the top is visualized. In level 3 only the epiglottis can be seen. Furthermore, level 4 represents no vision of glottis and it is known as a difficult scenario for intubation [1–3, 9].

Some problems may happen during the procedure of endotracheal intubation, as mistaken esophagus intubation, breaking teeth and injuring the patient's airway, for example trachea and larynx, especially in people with difficult airways. Visualization is further hampered in emergency situations due to possible injuries to the patient's airway or if the patient is in an inadequate position to perform intubation [8, 9].

Some products can be found to decrease intubation time and turn the intubation easier [10–14]. The Glidescope, KingVision and McGrath are examples of these devices. However, they do not offer reasonable results in terms of usability and portability. These products have the same function of performing endotracheal intubation by replacing the common laryngoscope for an indirect intubation, with a coupled camera that uses an optical device to show the image to the user. With the objective of creating a product more accessible, it was developed a portable device which replace the guide used by physician that aims to facilitate the visualization of the path through which the endotracheal tube performs, ensuring success of the procedure, proving that the intubation was performed correctly.

L. Batista · S. Moreira · F. Bueno · R. Alves (✉)
Instituto Nacional de Telecomunicações (Inatel),
Santa Rita do Sapucaí, Brazil
e-mail: cdtta@inatel.br

M. Okamura · M. Santoni
SAMU Municipal de Jundiaí, Jundiaí, Brazil
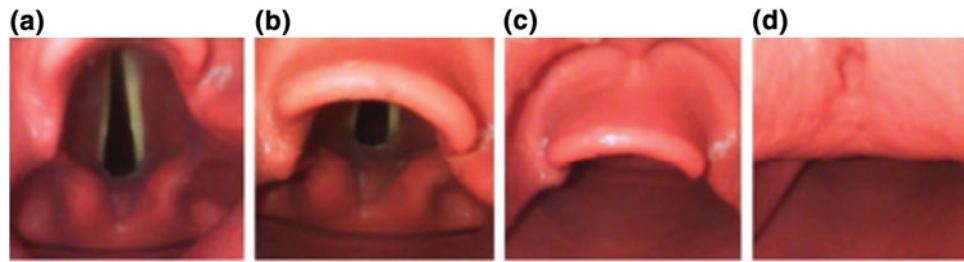
Fig. 1 Visibility of the airways according to the Cormark Lehane scale. **a** Level 1, the glottis is completely visible. **b** Level 2, only the top of glottis is visible. **c** Level 3, only the epiglottis is visible. **d** Level 4, no glottis structures are visible [1]

2 Materials and Methods

In the first moment, it was obtained more data on the matter and a review of the applicable technologies for endotracheal intubation, focusing on the equipment, medical restrictions and the most used blades. The blade Macintosh is curved and more used in adults. Moreover, it may vary the size and gives more space for the pass of the tube. The blade Miller is straight, also may vary the size, and it is more used in children due to anatomy [2]. Also, it was studied the main problems find out by the physicians to realize the procedure and the main risk that could happen. Were collected studies information about the time of intubation, error rate and the relation with professional experience.

Looking for facilitate the proceeding comparing to the conventional version, it was proposed the development of a guide for intubation with optical resource in its extremity, that is easily coupled to a mobile device. This device allows the user to quickly see and easily manipulate the images.

The first step in the development of the project was the acquisition of an Android Camera that has 7.0 mm in diameter, 1.5 m in length, focal distance until 4.0 cm and 6 LEDs that aid in lighting. This camera can be connected and installed with an app on both smartphones and tablets as well as on a computer. It was verified that the camera passes easily through tubes with 8.0 mm of diameter or higher. However, in tubes with smaller diameter it has more difficulty, making it unfeasible for intubation in children or in situations that requires a tube with smaller diameter.

To solve the problem mentioned above, a 5.0 mm diameter camera with the same characteristics was acquired, solving the difficulty of insertion in tubes with diameters smaller than 8.0 mm.

The camera with the smallest diameter was coupled with a rigid wire and a thermo retractable tube, maintaining the malleability and stiffness memory of the guide. In this way, it was possible to shape the endotracheal tube in the best way to perform the procedure, replacing the guide that is commonly used by doctors.

Tests with this first prototype were performed at the Universidade Federal de Itajubá - Unifei, in the Laboratório de Usabilidade e Fatores Humanos (Fig. 2). The procedure of laryngoscopy using the rigid camera was done in Laerdal and model SimMom manikins, which simulate the human anatomy, including its airways. Along the equipment to perform the intubation was used a mobile phone with Android system that belongs to one of the team members. To lubricate and moisten, it was used a water-based jelly that simulates human saliva.

One of the problems found during the tests was the camera lens fog, which could happen to the humidity found within the patient's airway. To solve this problem, tests were performed with a Speedo antifog, which is used by swimmers to not fog the lens of their glasses. To assess the results, it was used 100 ml of saline solution, a Erlenmeyer flask, an endotracheal tube, a 5.0 mm diameter camera, Bunsen burner to create fire to heat the flask and a coin to
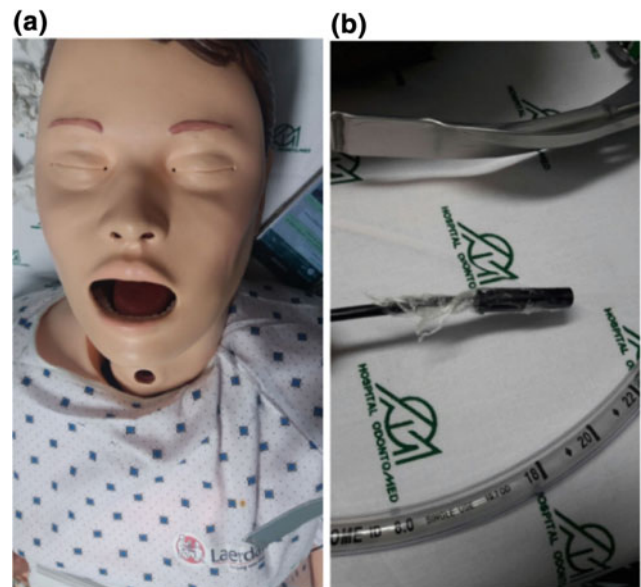
Fig. 2 a Manikin that simulate the human anatomy. **b** Laryngoscope, prototype and tube endotracheal used on tests

Fig. 3 Test made without and with antifog on lens
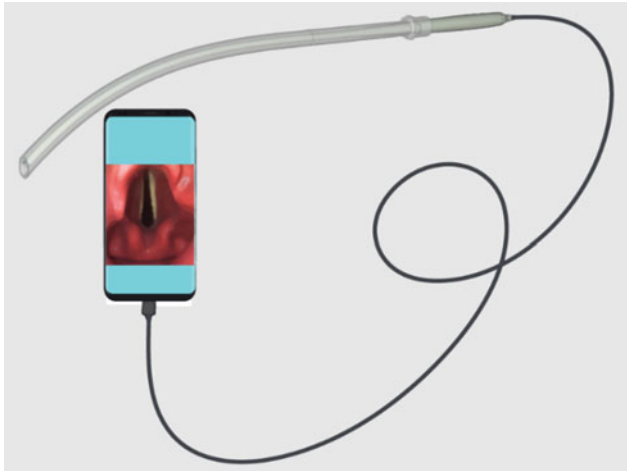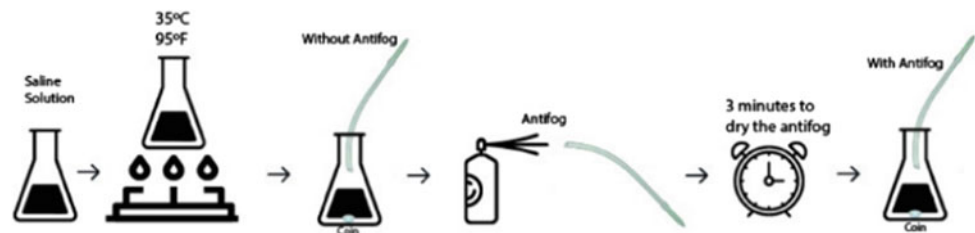
Fig. 4 Design of the prototype. Shows an easy airway (level 1 of Cormark Lehane scale)

serve as the image standard which were placed in the flask bottom.

In the first step, the saline solution was heated until it steams to simulate the humidity of a person. Then the camera was placed inside the endotracheal tube, which was placed in contact with the humidity without the antifog protector. The next step was to apply the antifog on the camera lens, waiting about 3–4 min and repeating the process (Fig. 3). After the contact of the camera with the humidity (with and without the antifog), it was taken a picture of the coin.

After that, it was done adjustments to the prototype so that it can be used in research and tests to validate its practicality and usability. The mechanical design has been made keeping in one end the camera with the LEDs for illumination, but, the body of the prototype has been developed so that the camera is adjusted at the right height according the size of the tube. Furthermore, the other tip has an USB cable which can be plugged with the user's mobile phone. This prototype has at its tips a rigid part that ensures the protection of the camera and the wires. Its central region is made of a soft polymer (PLA), durable, which has position memory and at the other tip there is a limiter that does not allow the camera to pass out of the tube (Fig. 4).

The prototype also includes an Android app to view the camera.

The app is being developed for Android, which has connection with a clouding database and each camera that will be developed can only be used in an account. So, the Integrated Optical Guide will be used by a doctor or a hospital.

3 Results and Discussion

From the tests realized at Unifei, it was possible to see all the route of the tube, ensuring that it passed through the airways, confirming the efficiency of the equipment. The malleability was essential for the device to mold the tube of the most suitable to perform the procedure.

The antifog tests were concluded by two ways. First, the camera was placed in contact with vapor without protection (Fig. 5a) and it was possible to confirm that the picture was fogged. Second step was applied the antifog protection and a test was made by the same way (Fig. 5b) and the lenses were not fogged. Figure 5 quality may not be clear due to camera focus, which is limited by up to 4.0 cm.

According to the tests performed with the antifog, it was possible to see that without it the camera has accumulated fog, which complicates the visualization of the camera lens. After applying to the lens, you can see the difference as the lens become clearer during the same test. It is possible to state that the application of the antifog on the camera lens works as expected. It was possible to conclude that the antifog is functional and that can be used to protect the camera lens from fog during the procedure.

The mechanical design was developed and features a door rolled at the tip of an endotracheal guide at one tip (Fig. 6a) and a USB connection at the other tip (Fig. 6b). It was made using a 3D print with soft material in its central region and a rigid material at the tip.

In the market there are some other types of optical guides, such as the Stylet Scope, that is a semi-rigid optical metal guide that has only the tip flexible, and the Clarus Video System that has a display attached to the guide. According to the studies done comparing the performance of these devices with the use of a conventional intubation

Fig. 5 a Lens without protection. **b** Lens with protection antifog
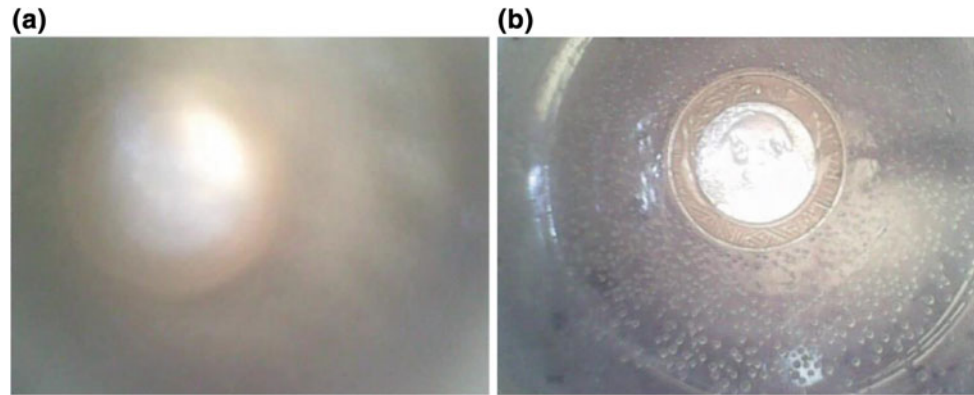
Fig. 6 a A camera at one tip. **b** A USB plug at the other tip
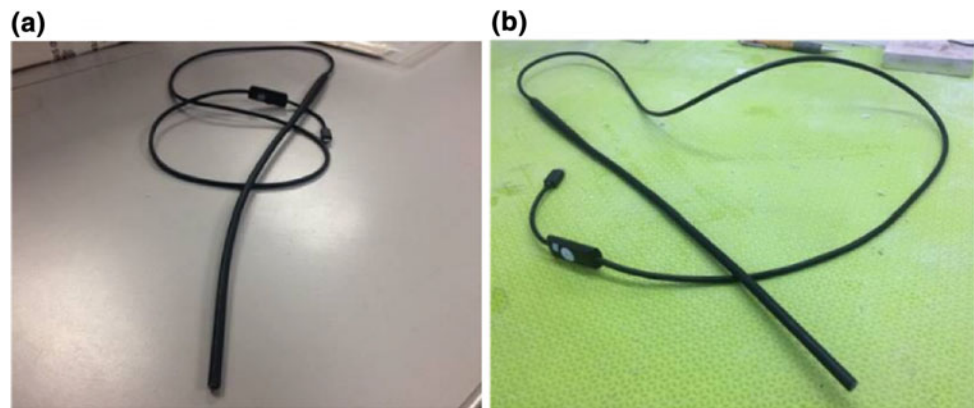
guide, positive results were observed. In easy airway situations (grade 1 and 2 of the Cormack Lehane scale) the success of intubation was much greater using these devices. For grade 3 and 4 cases of the scale, the number of errors was much lower [3, 10–14].

In this way, the efficiency of using optical guides relative to conventional guides is proven [10–14]. The developed design, in addition to having the whole body malleable, being able to shape the tube of the format that is easier for performing the procedure, is coupled to a mobile device, with its own application, that is able to save the images of the procedure.

4 Conclusion

Based on the studies performed, on the development of the prototype and on the results obtained, it was possible to validate the design and could be considered suitable for its use in patient applications, reaching the goal of becoming practical and easy to use for endotracheal intubation. Besides that, the prototype can have a larger area of view of the patient's airway because the camera is located at the tip of the guide, not the laryngoscope, which is of primary importance for intubation analysis.

References

1. Collins, S.R.: Direct and indirect laryngoscopy: equipment and techniques. Respir. Care **59**(6), 850–864 (2014)
2. Manica, J.: Anestesiologia: princípios e técnicas. v. 3, pp. 492–494 (2004)
3. Martin, L.D. et al.: 3,423 emergency tracheal intubations at a university hospital: airway outcomes and complications. Anesthesiol. J. Am. Soc. Anesthesiol. http://anesthesiology.pubs.asahq.org/article.aspx?articleid=1924886&resultClick=1. Accessed 01 Feb 2018
4. Amantéa, L.S., et al.: Acesso rápido à via aérea. Jornal de Pediatria **79**, 127–138 (2003)
5. Martin. L.D., et al.: 3,423 emergency tracheal intubations at a university hospital: airway outcomes and complications. Anesthesiology, v. 114, pp. 42–48 (2011)
6. Gaudry, P.: Securing the airway, ventilation and procedural sedation. https://aneskey.com/securing-the-airway-ventilation-and-procedural-sedation/. Accessed 28 Feb 2018
7. Matsumoto, T., de Carvalho, W.B.: Intubação traqueal. Ed. Porto Alegre, Jornal de Pediatria (2007)
8. Martins, R., et al.: Airway complications associated with endotracheal intubation, v. 70, pp. 7–12. São Paulo (2004). http://www.scielo.br/scielo.php?script=sci_arttext&pid=S0034-729920040005 00015

9. Mota, L.A.A., Carvalho, G.B., Brito, V.A.: Complicações laringeas por intubação orotraqueal: revisão da literatura. Int. Arch. Otorhinolaryngol. **16**, 12–15. São Paulo (2012). http://www.scielo.br/scielo.php?script=sci_arttext&pid=S1809-486420120002 00014

10. Mosier, J.M., et al.: Video laryngoscopy improves intubation success and reduces esophageal intubations compared to direct laryngoscopy in the medical intensive care unit. https://ccforum. biomedcentral.com/articles/10.1186/cc13061. Accessed 20 Dec 2017

11. Griesdale, D.E.G., Liu, D., McKinney, J., Choi, P.T.: Glidescope® video-laryngoscopy versus direct laryngoscopy for endotracheal intubation: a systematic reiew and meta-analysis. Can. J. Anaesth. **59**(1), 41–52 (2012). https://www.ncbi.nlm.nih.gov/pmc/articles/ PMC3246588/. Accessed 23 Feb 2018

12. Cooney, D., et al.: Endotracheal intubation with a video-assisted semi-rigid fiberoptic stylet by prehospital providers. Int. J. Emerg. Med. **7**(1), 45 (2014)

13. Can, J., et al.: Anaesth. Fibreoptic and stylet aided orotracheal intubation: a different approach for the difficult intubation, p. 401 (2004)

14. Kihara, S., et al.: The StyletScope™ is a better intubation tool than a conventional stylet during simulated cervical spine immobilization. Can. J. Anesthesia 105–109 (2005)

Low-Cost Functional Near Infrared Spectroscopy (fNIRS) Applied on Brain-Computer Interfaces (BCIs)

E. A. B. Santos, R. J. R. S. Lucena, E. G. Lima, Lucas T. Lins, and M. A. B. Rodrigues

Abstract

Functional Near-Infrared Spectroscopy (fNIRS) is an instrumentation method that performs both the cerebral hemodynamic, by using near-infrared light, and continuous non-invasive analysis of the oxygen level inside the tissue. Furthermore, this approach provides additional physiological parameters that can be correlated with cerebral activities by measuring the levels of oxygenation. In comparison to other techniques, fNIRS is well known for being low-cost, compact and presenting satisfactory spatial and temporal resolutions. Currently, hot topics in neuroscience are related to the studies of visual area, somatosensory, auditory, motor, language, cognitive and psychiatric. Such studies, generally, focus on cerebral physiology and biochemistry during certain stimulus or conditions imposed on the patient, in addition to their impact on cerebral hemodynamics. This work proposes a multichannel fNIRS system that implements the acquisition, control and digital signal processing in a portable platform. Such implementation of this system aims to jointly work with a Brain Computer Interface (BCI), where research about cerebral cortex are intended of being conducted.

E. A. B. Santos (✉)
Polytechnic School of Pernambuco (POLI-UPE), Recife, PE, Brazil
e-mail: emmanuel.andrade@poli.br

R. J. R. S. Lucena · E. G. Lima · L. T. Lins · M. A. B. Rodrigues
Federal University of Pernambuco (UFPE), Recife, PE, Brazil

1 Introduction

1.1 The fNIRS Background

Nowadays, several functional techniques to measure cerebral activities can be found in literature, and they can be classified as invasives or non-invasives. Many of those techniques are both used in clinical and psychiatric fields [1]. One of the first developed approaches for this purpose was the Electroencephalography (EEG). Examples of other methods that emerged after EEG are: Magnetoencephalography (MEG), Functional Magnetic Resonance Imaging (fMRI), etc. [1]. In addition, Functional Near-Infrared Spectroscopy (fNIRS) is an instrumentation method that performs both the cerebral hemodynamic, by using near-infrared light, and continuous, non-invasive analysis of the oxygen level inside tissues (specifically, inside the cerebral tissue).

The pioneer in the use of the near-infrared technology for monitoring cerebral oxygenation was Jöbsis [2], in 1977. His work showed that it is possible to detect the changes in the level of cerebral oxygenation and other cellular markers by using a light spectrum capable of penetrating the cranial cavity through direct lighting. For example, in the mid-1980s and 1990s, Delpy et al. [3] developed a mathematical method that relates NIRS signals acquisition to cerebral oxygenation, by considering the scattering of light as it penetrates the cerebral cortex. Such model is well known as the Modified Beer-Lambert Law (MBLL) [4].

Considering its great spatial and temporal resolutions [6], fNIRS, in comparison with other techniques, is well known for being low-cost, compact and also non-invasive. Due to the advances of electronics, fNIRS has been evolving to a portable platform in which allows it to be handled near the user (generally by fixing it to the scalp). Such portable platforms come along with wireless data transmission, and fewer restrictions in terms of patient's movement. fNIRS also can be used to provide additional parameters (or as an alternative forms of acquisitions) to obtain information on
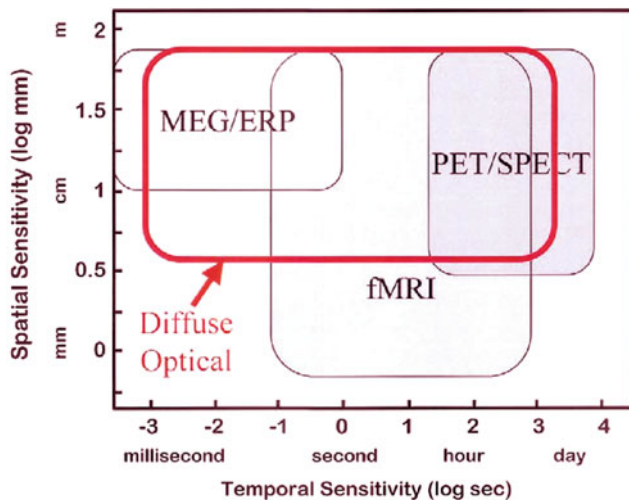
Fig. 1 Comparison between spatial and time sensitivities of non-invasive or minimally invasive techniques in neuroimaging [6]

physiological parameters that other techniques do not provide, such as the level of oxygenation in particular areas of the brain [5].

Figure 1 presents a comparison between different techniques of brain activities acquisition relating its spatial and temporal sensitivities.

The fact that fNIRS became a hot topic in the research community led it to the development of technological solutions that are strongly invested and studied by plenty of research groups and medical equipment companies [7]. However, most of the instruments on the market do not have the capability of being easily handled and transported. Many of them are non-portable and depend on the use of a personal computer [7]. The older versions of the same type of equipment use lasers, high voltage photo-amplifiers and optical fibers for signal transmission and reading. Such features contribute to the difficulty of transportation and maintenance performance, thus increasing the price of the equipment and preventing its accessibility to the public. In summary, there are several barriers to overcome in order for the system to become portable, reliable and comfortable to perform its instrumentation. Some challenges related to fNIRS are: fixation and arrangement of the emitters and receivers in the patients head, in order to ensure a stable optical contact with the scalp; deliver comfortability to users by not restricting the their movement when fixing the system for signal acquisition; defining and embedding the hardware responsible controlling and processing the system.

1.2 The Principles of fNIRS

In general, fNIRS aims on measuring the rate of oxygenation variation in a particular area of interest, stimulated in the cerebral cortex. In such cases, there is an hemodynamic activity in the region, related to the concentrations of oxygenated hemoglobin (oxy-Hb or HbO2) and deoxygenated hemoglobin (deoxy-Hb or Hb). Such proteins have characterized optical properties in the visible and near-infrared spectrum. The changes in the concentration of those proteins during brain activities can be measured by using optical approaches [8]. The simplest possible approach can be implemented by measuring the proportion of oxyhemoglobin per volume of blood using the near-infrared spectrum [6].

For measuring the variation of oxyhemoglobin and deoxyhemoglobin a light-emitting device is applied, in a specific position, in contact with the skin onto the skull. The light that passes through the skull undergoes a process of scattering and absorption. In addition to that, the signal is attenuated when it passes through all the layers of tissues. A fraction of the emitted light signal is propagated through the cortex, taking its path back to a curved surface (optical path) [1], where it can be detected by specific photodetector. This process is shown in Fig. 2.

Most biological tissues are relatively transparent to near-infrared light (range of 700–900 nm) because the water, an important component of most tissues, absorbs a small amount of energy at such wavelengths. However, oxy-Hb and deoxy-Hb chromophores absorb a great amount of energy in this range. This spectral band, presented in Fig. 3, is often called the Optical Window for noninvasive evaluation of cerebral activities [6]. The absorption peak for
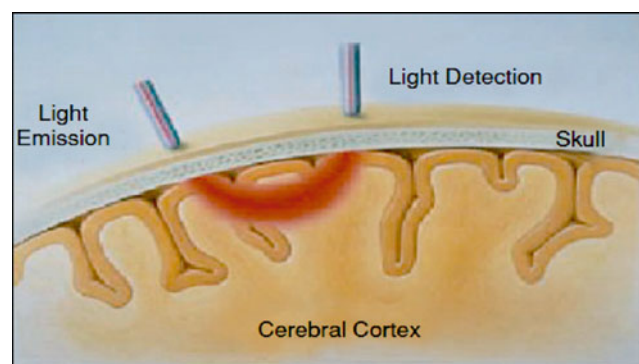
Fig. 2 Light behavior inside the cortex region [9]
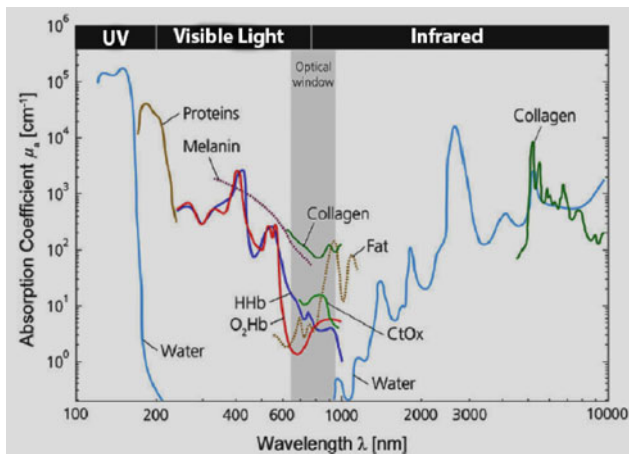
Fig. 3 Optical window close to the near-infrared band. In the highlighted region, a small amount of light absorption occurs, due to the water contained in the tissues [6]

oxy-Hb occurs at approximately 850 nm, whereas for deoxy-Hb it is around 750 nm.

2 Materials and Methods

2.1 Data Acquisition System

The implemented system was based on the work of Von Lühman [7]. It is based on CW NIRS (Continuous Wave NIRS). Furthermore, it is a simplified system (Fig. 4), carrying less electronic resources, aiming, mostly, to analyze the variation of cerebral oxygenation through the amplitude

of the signal detected by the sensor, in which is triggered by some cerebral activity.

Regarding the emitter-receiver assembly, bicolor LEDs (containing two types of wavelengths operating in the Optical Window) and photoreceptors type silicon photodiode (SPD) were used. The LED driver system provides stable current through a voltage-current converter for the LED0 in order to ensure a steady illumination at the moment of the measurement, making the LED switch at a frequency of 524 Hz. This is the minimum frequency at which the ATMega328 microcontroller is able to generate.

The microcontroller has the functions of controlling the LED driver through the modulation signal and configuring the Programmable Gain Amplifier (PGA) located on the circuit board of the Electronic System. Furthermore, the system contains both filters and demultiplexers that are used to set a suitable wavelength for the LED.

For communication purposes, the National Instrument's DAQ (Data Acquisition) NI-USB 6009 serves as an interface system, since it has both analog and digital inputs. For this reason, it is possible to communicate with some BCI via USB cable or Bluetooth communication.

All sensors and LEDs were placed in a handcrafted adapted strip that is composed of non-translucent materials, in order to prevent the ambient light interference in the instrumentation. Figure 5 shows the arrangement of the components in terms of their signal pickup range, therefore the respective distances between each of them must respect such criteria.

The measuring system is composed of four channels, one LED that can emit two wavelengths and two sensors.

Fig. 4 Block diagram representation of the proposed system
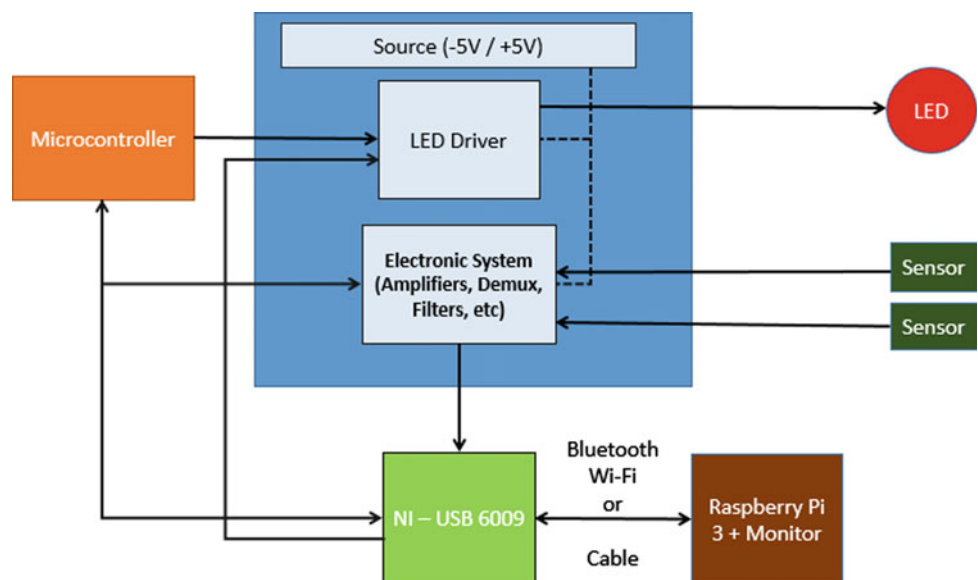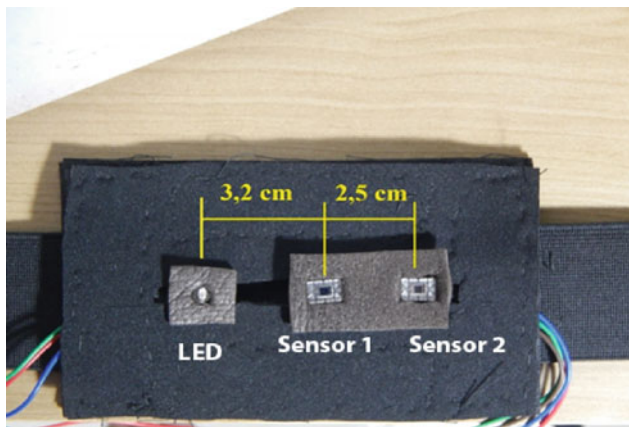
Fig. 5 Acquisition prototype each sensor and the LED

Fig. 6 Anatomical views of the prefrontal cortex [11]

Channels 0 and 1 use the photodetector number 1, while channels 2 and 3 use photodetector number 2. All channels detect light emitted by the two wavelength LED (750 and 850 nm). The position of the LED is adjustable and can be placed close or further the group of sensors.

The Analog to Digital Converter (ADC) used by the DAQ consists on a Successive Approximations topology, composed by a 10-bits resolution. The minimum sampling rate that could be used by such converter is 1.2 kS/s, being suitable for the application, by respecting the Nyquist-Shannon Theory and avoiding aliasing for the frequencies at which the signal, sent to the LED, was modulated. All data was sent either via an USB cable or a Bluetooth 4.0 interface.

2.2 Testing Protocol and Stimuli

Before determining the testing protocol, defining the desirable area to measure the cerebral activity was fundamental, since the protocol is directly related to the area of stimulation. Regarding the preliminary study, the prefrontal cortex (PFC) was adopted due to its easy access, in terms of sensor fixation, as well as the absence of hair in the region.

The frontal cortex region, which is shown in Fig. 6, makes up the frontal part of the frontal lobe of the brain. According to some authors [9–11], this is an area that is responsible for several functions, such as: abstract and creative thoughts; fluency of thoughts related to language; personality expressions; determination of actions, selective attention, decision-making strategies, results based on internal goals, among others.

The defined protocol was based on the "Stroop Effect" [10], due to its simplicity and objectivity of implementation aiming an initial analysis. Developed by John Ridley Stroop, for studies in the field of psychology, the effect demonstrates
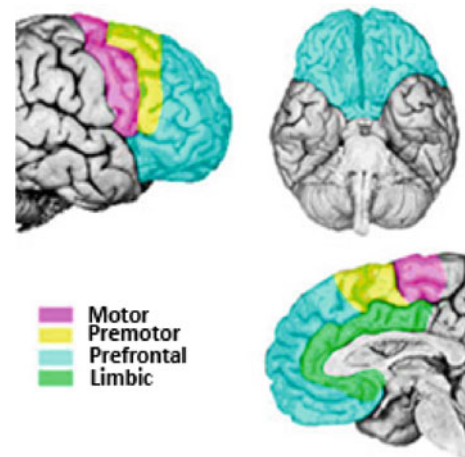
an interference at the reaction time of a task during the moment that the individual is submitted to a certain visual inconsistencies (incongruousness). The test usually involves color detection and the individual is instructed to take certain actions when the colors are congruent or not with the names that describe them.

Some works in fNIRS [11] have already used the "Stroop Effect" to analyze the PFC region. On the other hand, in this specific work, the protocol was adapted to perform different types of analysis. The main goal of the developed protocol in this work is to measure the levels of oxygenation of the PFC region for cases of consistency (congruency) or non consistency, related to each color recognition.

In addition to the employed stimuli, a control group was added to the test in this preliminary study. Three corresponding colors, three non-corresponding colors and three control stimuli were applied. This process is shown in Table 1.

The platform that runs the Brain-Computer Interface (BCI) was developed by using a Raspberry Pi 3 board, in which supports USB, Wi-Fi, and Bluetooth communications. The programming language used for developing the BCI was Python 3.0.

The program that performs the Stroop Effect test starts with a white screen for 20 s. Each stimulus, randomly chosen in between all 9 options, is displayed on a monitor for 3 s. During the interval between one stimulus and another, a white screen is shown for 15 s. Therefore, the total duration of the test is approximately 182 s.

Before starting the test, the individual is instructed to press the "d" key if the color is matching with the name, and "k" if it is not. If a control stimulus appears, the individual should not take any action. The program stores the results to verify if there was a hit or an error in cases of matching or not.

Table 1 Stimuli types

Congruent Group	Incongruent Group	Control Group
GREEN	RED	■
RED	GREEN	
BLUE	BLUE	■
	RED	
	BLUE	■
	GREEN	

3 Results

All data obtained during the tests were processed using the software Origin Pro 8. The analysis process for each signal followed the subsequent steps:

- Frequency spectrum analysis using the Fast Fourier Transform (FFT) algorithm, altogether with rectangular windowing, in order to identify the modulation frequencies and the presence of noise;
- Utilization of a Finite Impulse Response (FIR) filter;
- Normalization of the amplitude (range of 0 to 1);
- Employment of a moving average of 1200 points.

Figure 7 shows the signals of channels 0 and 1 after applying the moving average filter. Both channels 2 and 3 did not show any significant signal to be recorded during the trial. Regarding channels 0 and 1, 1200 points were used, since the sampling rate is 1200 samples per second, Therefore, the behavior of the signal was evaluated every second.

The stimulus sequence used in the adopted test protocol is presented in Table 2.

4 Discussion

By analyzing Fig. 7 and Table 2, it is possible to perceive that in some cases an inconsistent stimulus occurs and the absorption of the LED spectrum, by the user, is highlighted. In contrast to that, during control or consistent stimuli, the demand for oxygen remains constant or shows a small amount of variation. The oxygenation change was detected, on average, after 6.5 s following the stimulus.

However there are some occasions when the oxygen demand occurs outside the stimulus intervals, or it simply can not be identified, even though the individual is making the decision related to the color congruence. Currently, the project is involved with an ethics committee and a newly developed version of the system will be tested by other individuals. Therefore, future results will be presented in upcoming publications.

Fig. 7 Processed signals versus stimuli instants

Table 2 Sequence of stimuli used in the test

Stimulus	Type
1°	Congruency
2°	Incongruity
3°	Incongruity
4°	Control
5°	Incongruity
6°	Control
7°	Congruency
8°	Control
9°	Congruency

There is also a need for improving two main aspects of the project: the testing protocol and the technique for imaging the region of interest. Regarding the former, random, but mandatory, resting intervals in between groups of stimuli must be generated, so the individual will not track any kind of pattern or periodic stimuli. Otherwise, this may end up conditioning the volunteer's brain activity and influencing the results. Concerning the latter, the optodes should be spatially distributed in a way that will measure in 2D (or even 3D), forming an image by using algorithms and models that can be found in the literature.

5   Conclusion

Near Infrared Functional Spectroscopy is a very promising technique with great potential for the development of passive or active Brain-Computer Interfaces, as well as Brain-Machine Interfaces. Although the response, in the cerebral hemodynamics, endures a relatively long time after the stimulus, due to its temporal sensitivity, it is possible to integrate techniques of digital signal processing and Artificial Intelligence to reduce the period of detection and extraction of parameters.

As an initial study in the field of fNIRS, it is possible to infer that this system showed satisfactory results regarding the brain activity measurement. It was possible to perform the instrumentation by using a relatively simple electronic system, prototyped with low-cost peripherals.

It is well known that the faithfulness of the digital system to its analog representation is directly proportional to the number of samples per signal. On the other hand, the amount of data samples carried by the processor can compromise its own processing speed and memory storage. This massive amount of data extracted from each test is due to the sampling rate of 1.2 kS/s. Since the protocol commonly lasts more than 180 s, the amount of samples to be processed has become difficult to manage. Furthermore, there is a high computational cost for the system to perform all necessary analysis. Therefore, there is a need of improving the interaction technique with the cerebral cortex by acting on the reduction of the switching rate of the LED or sensors, in order to reduce the global sampling rate of the system without compromising the quality of the results.

References

1. Stragman, G., Sutton, J.: Non-invasive neuroimaging using near-infrared light. Biol. Psychiat. **52**(7), 679–693 (2002)
2. Jöbsis, F.: Noninvasive. Infrared monitoring of cerebral myocardial oxygen sufficiency and circulatory parameters. Science **198** (4223), 1264–1267 (1977)
3. Delpy, D., Cope, M., Van der Zee, P., Arridge, S., Wray, S., Wyatt, J.: Estimation of optical pathlength through tissue from direct time of flight measurement. Phys. Med. Biol. **33**(12), 1433 (1988)
4. Yazici, B., Son, I.Y.: Near infrared imaging and spectroscopy for brain activity monitoring. NATO Security through Science Series-A: Chemistry and Biology. Springer, pp. 341–372 (2006)
5. Delpy, D., Cope, M.: System for long-term measurement of cerebral blood and tissue oxygenation on newborn infants near infra-red transillumination. Med. Biol. Eng. Comput. **26**(3), 289–294 (1988)
6. Scholkman, F., Kleiser, S., Metz, A.J., Zimmermann, R., Pavia, J.M., Wolf, U., Wolf, M.: A review on continuous wave functional near-infrared spectroscopy and imaging instrumentation and methodology. NeuroImage (2013)
7. Von Lühmann, A., Herff, C., Heger, D., Schultz, T.: Toward a wireless open source instrument: functional near-infrared spectroscopy in mobile neuroergonomics and BCI applications. Front. Hum. Resour. **9**(617), 1–14 (2015)
8. Hemmati, N., Setarehdan, S., Noubari, H.: Multi-channel near-infrared spectroscopy (NIRS) system for noninvasive monitoring of brain activity. In: Proceedings of 2012 IEEE-EMBS International Conference on Biomedical and Health Informatics, pp. 212–215, Hong Kong (2012)
9. Bunce, S., Izzetoglu, M., Izzetoglu, K., Onaral, B., Pourrezaei, K.: Functional near-infrared spectroscopy. IEEE Eng. Med. Biol. Mag. **25**(4), 54–62 (2006)
10. Stroop, J.R.: Studies of interference in serial verbal reactions. J. Exp. Psychol. **18**, 643–662 (1935)
11. Zhang, L., Sun, J., Sun, B., Luo, Q.: Studying hemispheric lateralization during a Stroop task through near-infrared spectroscopy-based connectivity. J. Biomed. Opt. **19**(5), 57012 (2014)

Modeling of a Simple and Efficient Cascaded FPGA-Based Digital Band-Pass FIR Filter for Raw Ultrasound Data

Amauri Amorin Assef, Jonathan de Oliveira, Lucas Scherbaty,
Joaquim Miguel Maia, Acácio Zimbico, Breno Mendes Ferreira,
and Eduardo Tavares Costa

Abstract

In this paper, we present the modeling and implementation of a FPGA-based Digital Band-Pass FIR (DBPF) filter to reduce the undesired noise levels in raw ultrasound data. The cascaded tapped delay line FIR filter was built within the Simulink environment combined with the DSP Builder toolbox, allowing easy and automatic generation of synthesizable VHDL code. In order to demonstrate the feasibility and flexibility of our design, we employed eight symmetrical 8-tap cascaded FIR filter structures to implement a 64-tap DBPF filter. The fractional coefficient values were obtained by the equiripple design method assuming a pass-band frequency between 1.4 and 5 MHz, stop-band of -50 dB and sampling frequency of 40 MHz. The experimental implementation was done on an Intel Stratix IV FPGA by using a linear chirp signal and real raw data added with DC and low- and high-noise frequency components. The accuracy of the model was analyzed by using the normalized root mean square error (NRMSE) cost function for comparison with a reference filter structure designed with FDATool and exported to Simulink. An excellent agreement was achieved between the simulation and experimental results. The overall FPGA utilization was less than 5% and the calculated NRMSE was 0.013%, corroborating the effectiveness of the proposed hardware architecture.

Keywords

Ultrasound • Filtering • Raw data • FPGA

1 Introduction

Digital band-pass filters are extensively used in ultrasound (US) imaging systems to remove the undesired noise components during the radio-frequency (RF) echo signal acquisition prior to further image processing operations. Such noise components, usually generated from switching circuitry and by inter-channel cross-talk, degrade the performance of noise sensitive elements, including, for instance, low noise amplifiers (LNAs) and programmable gain amplifiers (PGAs) [1].

In an attempt to remove the noise interference in US signals, several hardware-based signal processing algorithms have been proposed by the scientific community [2, 3]. However, these studies also reported significant arithmetic requirements and complexity, which can be a problem in terms of power consumption, latency and chip area occupation. On the other hand, simpler and more easily applied strategies are expected, especially from academia, in order to accelerate the investigation of new digital signal processing (DSP) methods and shorten the development cycle considerably.

This paper presents the modeling, implementation and evaluation of a simple and efficient FPGA-based Digital Band-Pass FIR (DBPF) filter for raw US data. The DBPF was built as a tapped cascaded interconnection of identical subfilters within the Simulink environment combined with the DSP Builder toolbox, allowing easy and automatic generation of synthesizable VHDL code.

A. A. Assef (✉) · J. de Oliveira · L. Scherbaty · J. M. Maia · A. Zimbico
Federal University of Technology - Parana (UTFPR), DAELT/PPGSE, 3165, Curitiba, Brazil
e-mail: amauriassef@utfpr.edu.br

B. M. Ferreira
University of Brasilia (UnB), ENE/FT/PGEA, Brasilia, 70910-900, Brazil

E. T. Costa
State University of Campinas (UNICAMP), DEB/FEEC/CEB, 266, Campinas, Brazil

2 Methods

Each value of the output sequence of a conventional discrete time FIR filter of order N can be expressed by the following discrete convolution sum form [4]:

$$y(n) = b_0 x(n) + b_1 x(n-1) + \cdots + b_N x(n-N)$$
$$= \sum_{i=0}^{N} b_i x(n-i) \tag{1}$$

where n is the sample index ($n = 0, 1, 2, \ldots, N$), $x(n)$ is the input signal, $y(n)$ is the output signal and b_i is the i-th filter coefficient. By taking advantage of the symmetry impulse response (i.e., $b_0 = b_N$, $b_1 = b_{N-1}$, ...) and assuming an odd N-order, we obtain (2), which is used in this work to reduce the hardware cost and complexity by about half.

$$y(n) = \sum_{i=0}^{\frac{N-1}{2}} b_i [x(n-i) + x(i)] \tag{2}$$

The fractional coefficients for a 63th-order FIR filter were calculated by Matlab FDATool using the equiripple design method [5]. The band-pass filter was set to a pass-band frequency between 1.4 and 5 MHz, stop-band attenuation of −50 dB and sampling frequency of 40 MHz. These values were obtained taking into account that the echo signals to be evaluated here have a Gaussian spectrum with a center frequency of 3.2 MHz. Its impulse and magnitude responses with 1 dB equiripple in the pass-band are shown in Fig. 1a and b, respectively.

Eight symmetrical 8-tap cascaded FIR filter structures were used to implement the 64-tap DBPF. The symmetry properties of the impulse response were exploited to reduce the hardware complexity. The FPGA-based DBPF was modeled in Simulink by using the integrated Intel DSP Builder toolbox. Figure 2 shows the top-level design of the

proposed model and Fig. 3 shows the subfilter block implemented to modularize and simplify the design.

Initially, the input *RF_signal* block casts double precision raw RF data loaded from the Matlab workspace into 16-bit signed fixed-point representation for hardware efficiency. Based on (2), the convolution sum is obtained by the interconnection of eight identical tapped FIR subfilters. These blocks consist of eight shared Multiplier blocks based on predefined signed fractional coefficients, 4 "Parallel Adder" used to reduce the number of multipliers to N/2, and 8 "Delay" blocks. Each block has two input signals and three output signals. Signals *In_From_1* and *Out_Goto_1* are the input of the incoming samples and the output signal delayed by an amount of 4 cycles, respectively. To simplify the design, each subfilter has a Parallel Adder block to sum the multipliers result, which is available from the *Out1* signal. The signals *In_From_2* and *Out_Goto_2* have the same function of the previous signals, however, used for the incoming samples of the second half of the filter. A Parallel Adder block with eight inputs is used to sum the convolution result of each subfilter.

In order to evaluate the FPGA implementation, we used as input data two vectors composed of 2000 samples (12-bit) each acquired at 40 MSPS. Firstly, a linear chirp signal from 400 kHz to 6.5 MHz was applied to the DBPF. Then, we employed real raw US data obtained from a tissue-mimicking phantom (84-317, Nuclear Associates). The RF signal was acquired by a US system, developed by our group [6], connected to a convex transducer (AT3C52B —Broadsound Corp., Taiwan). A superimposed DC offset and two sinusoids, 400 kHz and 8 MHz, with amplitudes of 2.5%, 10%, and 10%, respectively, of the maximum value of the RF signal were added to the original signal. The experimental implementation was done on a Terasic DE4-230 board, which uses an Intel Stratix IV EP4SGX230 FPGA. The accuracy of the model was analyzed by using the
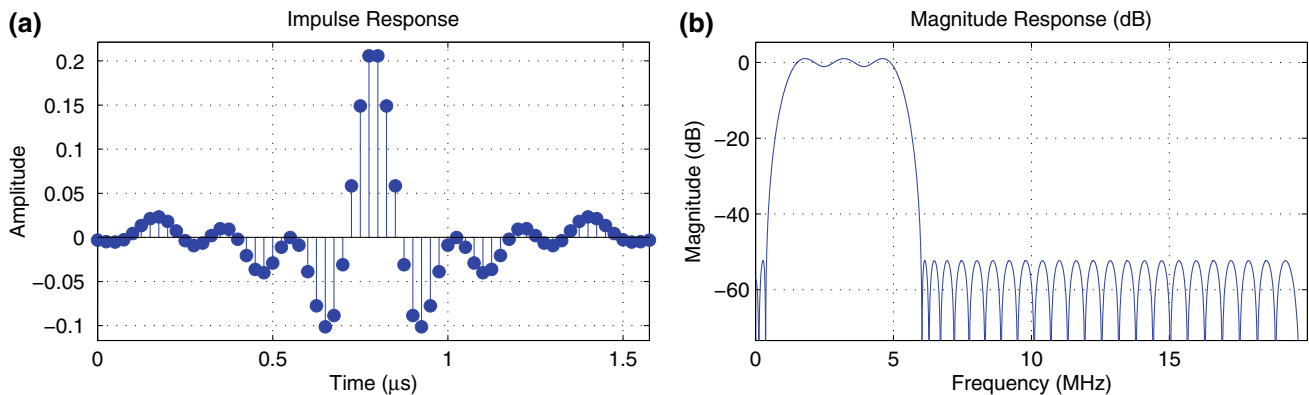
Fig. 1 Band-pass equiripple FIR filter responses calculated by FDATool in Matlab. **a** Impulse response and **b** magnitude response of the 64-tap FIR filter
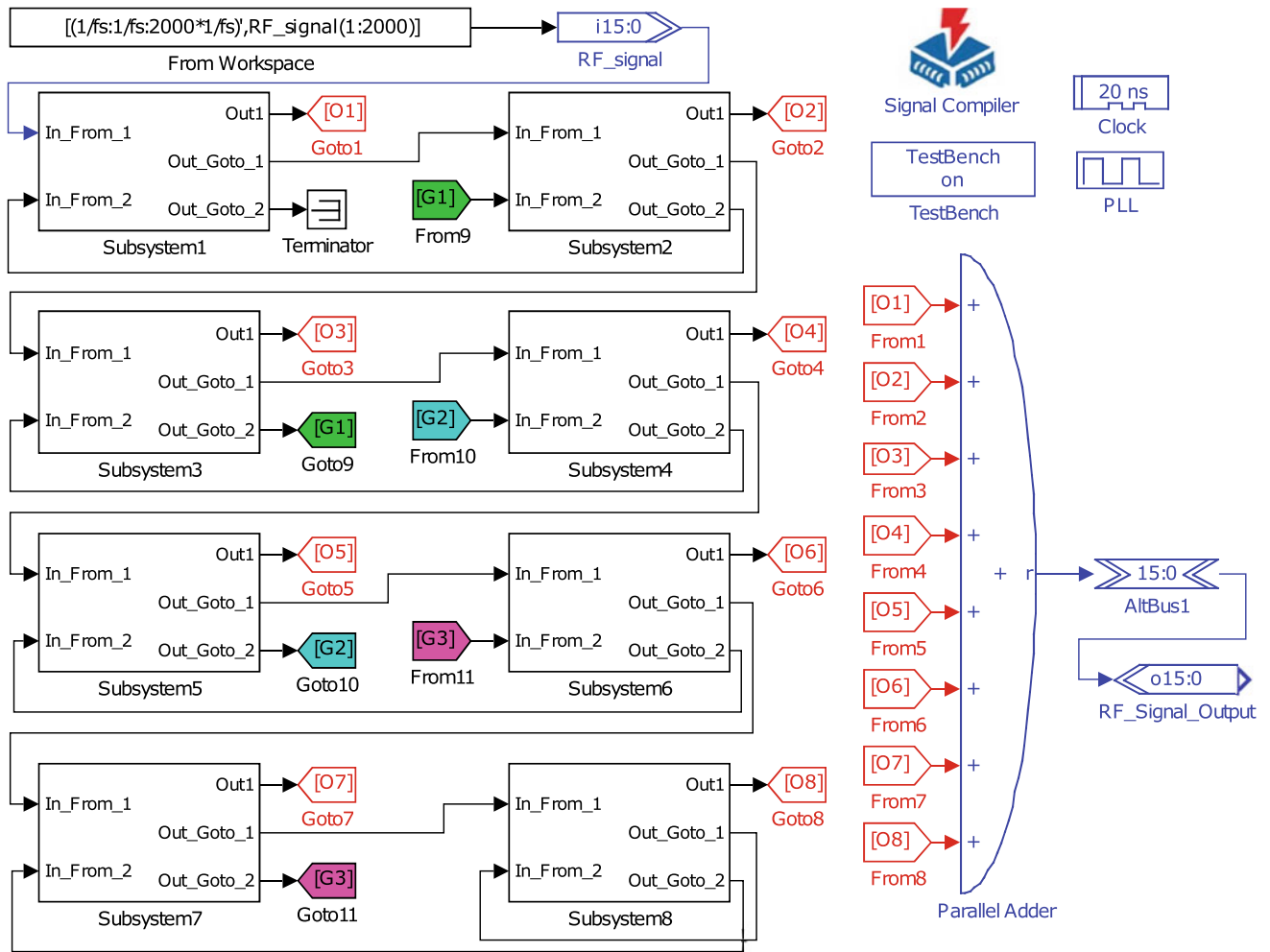
Fig. 2 Top-level of the FPGA-based DBPF filter using the DSP builder blockset
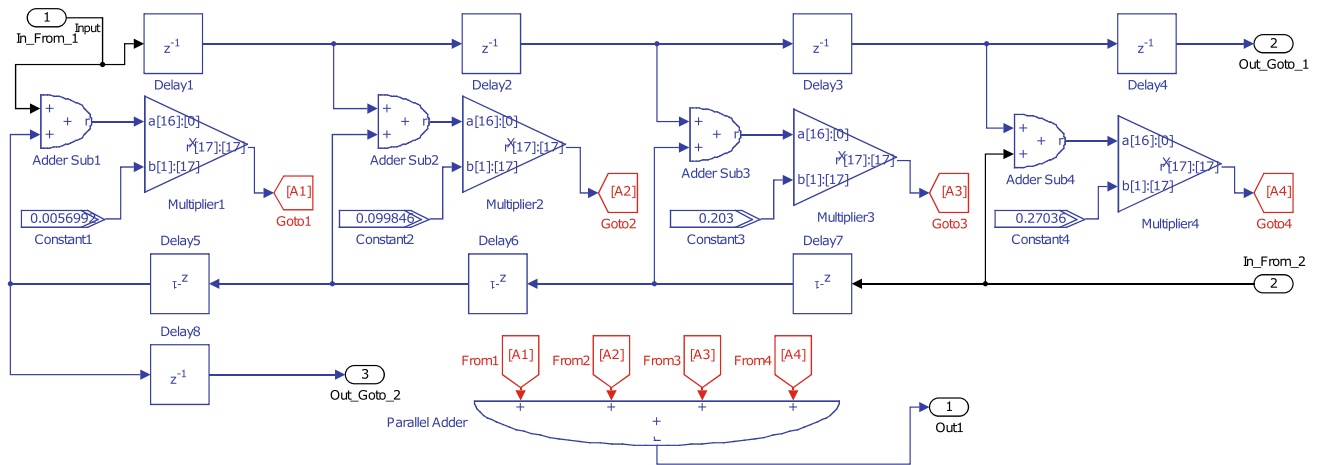
Fig. 3 Subfilter implementation (Subsystem8 in Fig. 2)

normalized root mean square error (NRMSE) [7] cost function for comparison with a direct form double-precision floating-point reference filter structure designed with FDA-Tool and exported to Simulink.
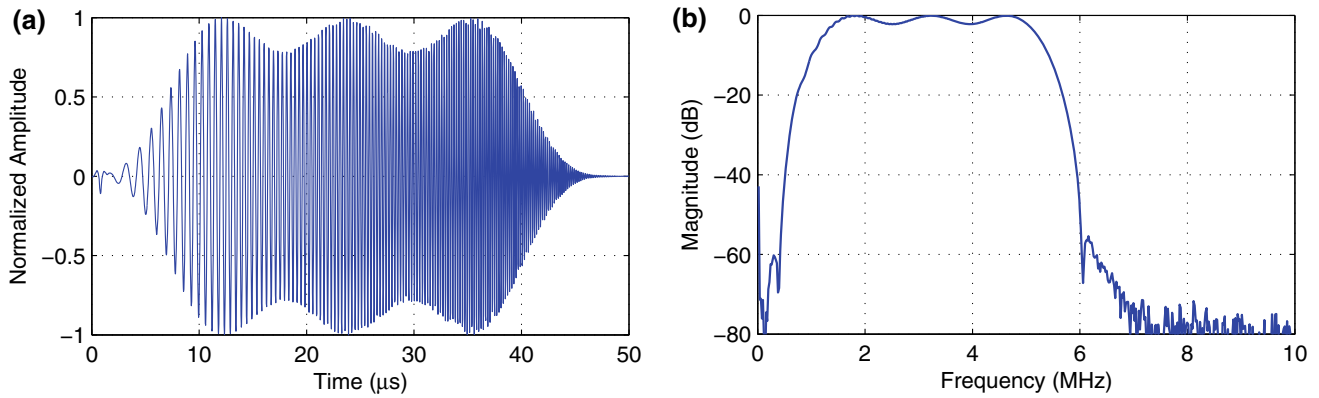
Fig. 4 Results of the DBPF computation using the chirp signal to vary the frequency of the input signal. **a** Output signal by the DBPF and **b** its FFT spectrum

3 Results

Figure 4a shows the experimental result using the chirp signal as input. A characteristic ripple pattern response in the pass-band is noted due to the equiripple property of filters designed by the Parks-McClellan method [5]. An excellent agreement was achieved between the reference model and our method with a NRMSE of 0.013%. The respective calculated spectrum is shown in Fig. 4b. The maximum pass-band ripple was 1.11 dB and a stop-band attenuation larger than 49 dB was achieved.

By similar testing, Fig. 5 shows the graphical comparison between the noisy raw input data and the experimental output signal. Figure 5a shows the reference input signal added to the noise components, which can easily be seen in
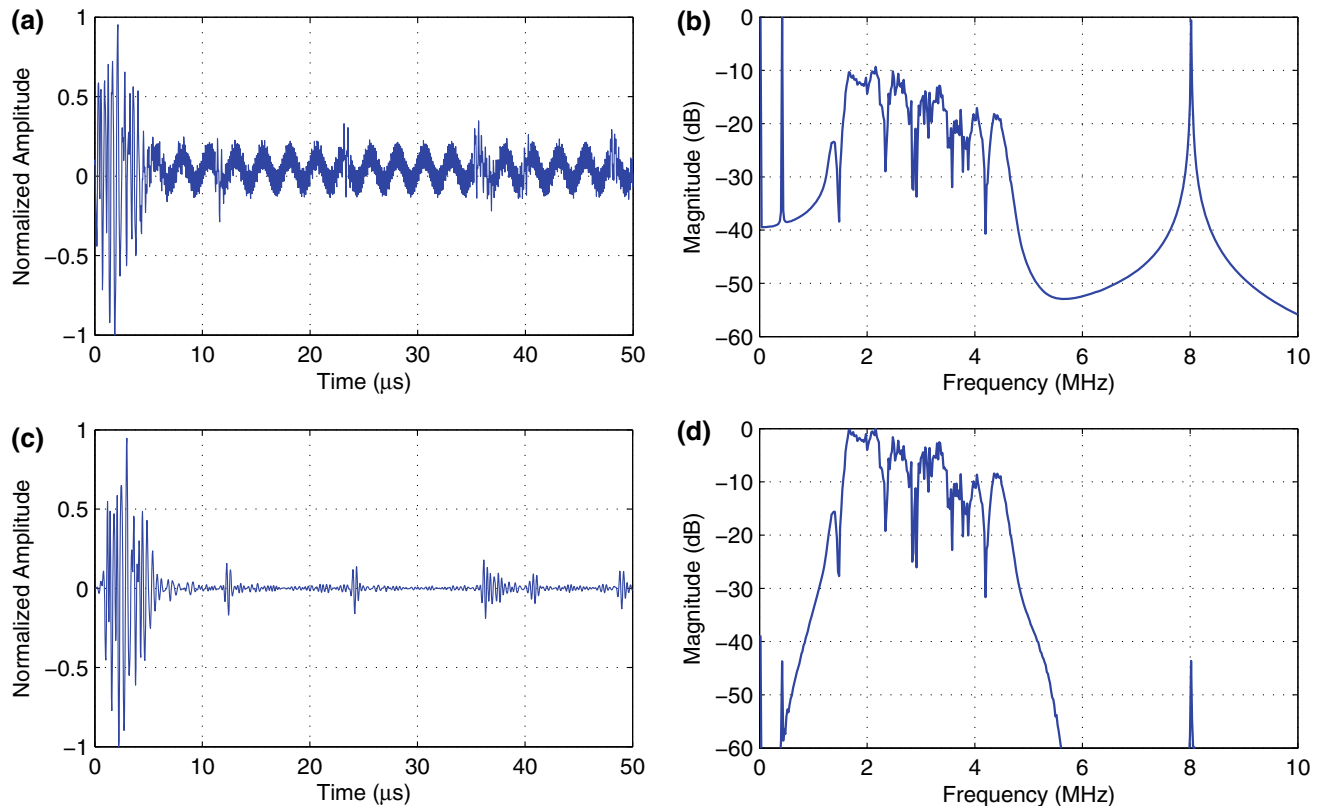
Fig. 5 Graphical comparison between the input and the experimental output signal. **a** Reference input signal added to the DC, 400 kHz and 8 MHz noise components and **b** its spectrum. **c** Experimental output filter response and **d** its spectrum

its spectrum in Fig. 5b. Figure 5c presents the processed signal by the DBPF computation, where it is possible to estimate the depth of some targets, considering a known speed of sound. The NRMSE was also 0.013%. As it can be seen in Fig. 5d, the DC signal and both the 400 kHz and 8 MHz noise levels were attenuated in 38.8 dB, 43.7 dB and 43.6 dB, respectively.

The FPGA logic utilization was approximately less than 1%. The resulting design used 64 18-bit elements DSP blocks (5%) and one PLL block (13%). In terms of FPGA clock cycles, our hardware design is capable to generate filtered data at every clock cycle after 33 clock cycle latency (825 ns) with a maximum operating frequency of 152 MHz. Compared to the reference simulation the FPGA implementation presented a pipeline delay of only one clock cycle 25 ns.

4   Conclusion

The presented results demonstrate the potential of our approach for noise reduction in real-time biomedical US imaging, allowing, for instance, further studies based on 2D and multi-channel filtering approaches. The fully hardware-based DBPF model presented here offers an excellent alternative that can be used for students and researchers to accelerate the investigation of new DSP algorithms.

References

1. Yoon, J. et al.: Low-noise amplifier path for ultrasound system applications. In: 2010 IEEE Asia Pacific Conference on IEEE Circuits and Systems (APCCAS), pp. 244–247. IEEE, Kuala Lumpur (2010)
2. Schneider, F.K., et al.: A fully programmable computing architecture for medical ultrasound machines. IEEE Trans. Inf Technol. Biomed. **14**(2), 538–540 (2010)
3. Kim, G.D., et al.: A single FPGA-based portable ultrasound imaging system for point-of-care applications. IEEE Trans. Ultrason. Ferroelectr. Freq. Control **59**(7), 1386–1394 (2012)
4. Cetin, A.E., Gerek, O.N., Yardimci, Y.: Equiripple FIR filter design by the FFT algorithm. IEEE Signal Process. Mag. **14**(2), 60–64 (1997)
5. Elliott, D.F.: Handbook of Digital Signal Processing: Engineering Applications. Elsevier, United Kingdom (2013)
6. Assef, A.A., et al.: Initial experiments of a 128-channel FPGA and PC-based ultrasound im-aging system for teaching and research activities. In: 2016 IEEE 38th Annual International Conference of the Engineering in Medicine and Biology Society (EMBC), pp. 5172–5175. IEEE, Orlando (2016)
7. Montgomery, D.C., Runger, G.C.: Applied Statistics and Probability for Engineers, 6th edn. Wiley, USA (2010)

Multichannel System for Measuring the Magnetic Flux Density Generated by TMS Devices

Carlos Vinicius Nascimento Barbosa, Elisabeth Costa Monteiro,
Carlos Roberto Hall Barbosa, and Daniel Ramos Louzada

Abstract

Transcranial magnetic stimulation (TMS) is a noninvasive technique that promotes the neuromodulation effect aiming at treating diseases of neuro-psychiatric origin. TMS electromagnetic coils provide an alternating magnetic field that induces bioelectric currents in a targeted region of the brain tissue. The guarantee of treatment effectiveness and safety of both patients and device operators depends on the distribution of the magnetic flux density emitted in the vicinity of the TMS equipment, according to the design of the induction coil employed. This work presents the development of a multichannel measuring system to evaluate the configuration of magnetic flux density generated in the proximities of TMS devices. By using the developed measuring system, it is performed the magnetic mapping along a plane under the figure-of-eight TMS coils, including the study of its response to different intensities and distances from the device. The results allow characterizing the decay of field magnitude towards the region closer to the operator's hand position and its spatial distribution in areas intended to receive the therapeutic effect.

Keywords

Transcranial magnetic stimulation • Measurement system • Metrological reliability

1 Introduction

Transcranial magnetic stimulation (TMS) devices provide noninvasive therapeutic neuromodulation with applications in a range of neurological and psychiatric disorders. This technique has been recently used when patients are unresponsive to drug therapy [1, 2], being considered a therapeutic alternative with a low recurrence of side effects [1].

TMS electromagnetic coils are positioned in the proximity to the patient's scalp, where it delivers an alternating magnetic field that induces bioelectric currents in a targeted region of the brain tissue. The protocol of stimulation defines the pulse duration, intensity, and frequency of repetition according to the specified application or neurophysiological effect desired.

Several coil configurations can be used in TMS devices: circular, figure-of-eight, double cone, etc. The geometric parameters of each coil shape (inner and outer radius of the spiral coil, number of turns, distance between the coil centers, angle between two adjacent circular windings, among others) determine the distribution of the emitted magnetic flux density (B-field) [3]. As a consequence, the TMS coil designs are responsible for the distinct electric field patterns produced in the brain tissue, which, in turn, are associated with the neurobiological effects [2, 4].

The inherent risks of adverse events associated with possible inadequacies of intensity and distribution of magnetic flux densities provided by the distinct TMS coil types point toward the need of measuring this density generated by different coil designs [5]. In the literature, most of the publications present the results of simulated studies [2, 3, 6–8], and only a few experimental studies have been performed in this field [7–10]. Although being in clinical use for decades, there is no international technical standard available that contains specific requirements for the TMS devices' evaluation [5, 11, 12]. The adequacy of electrical activity induced in the targeted brain cortex depends upon the appropriateness of intensity and space distribution of B-field delivery from TMS [2, 6, 8]. Additionally, it is essential to evaluate the safe distance from TMS coils to assure acceptable levels of staff exposure to magnetic flux densities, according to occupational safe limits for operators published in the guidelines of the International Commission on Non-Ionizing Radiation Protection (ICNIRP) [13]. Therefore, magnetic

C. V. N. Barbosa (✉) · E. Costa Monteiro · C. R. H. Barbosa · D. R. Louzada
Pontifícia Universidade Católica do Rio de Janeiro (PUC-Rio), Rua Marquês de São Vicente, 225, Gávea, Rio de Janeiro, Brazil
e-mail: eng.carlosvinicius@outlook.com

E. Costa Monteiro
e-mail: beth@puc-rio.br

flux density measurements in the vicinity of TMS equipment could allow the assessment of its performance and the guarantee not only of the treatment effectiveness but also the safety of both patients and staff [5, 8, 12].

This work aims at developing a multichannel magnetic measuring system to map the magnitude and spatial distribution of the magnetic flux density generated in the proximities of TMS device coils. By using the developed system, the study performs preliminary 3D measurements of the B-field generated by an angulated figure-of-eight TMS AFEC-02-100-C (Neurosoft) and evaluates the adequacy of the field levels in positions closer to the TMS holder used by the operator, to the established limits for staff exposure, according to ICNIRP recommendations.

2 Materials and Methods

The proposed multi-channel measurement system (MMS) consists of a device for measuring the magnetic flux density emitted by transcranial magnetic stimulation equipment, which typically emits pulses of a few hundreds of microseconds duration, with up to three teslas of peak intensities when 100% of TMS output is selected among the device stimulation parameters. This system is an evolution of the sensor idealized in the Biometrology Laboratory of the PUC-Rio [7, 10]. Figure 1 shows the MMS comprising 15 sensing coils, evenly distributed along an axis, and printed in a circuit board (PCB). These coils have a circular shape, with 4.5 mm and 5.5 mm of inner and outer radius, respectively, and are 1.2 cm apart from each other. In the current version of the MMS the flat cables have been replaced by a set of USB cables (one pair for each channel). In addition, excess copper was extracted from the PCB as well as the elimination of islands and connectors from the data cables. Considering the existing large amount of copper to be withdrawn, the present MMS version was made using a photographic technique in contrast to the prototyping technique of LPKF Laser & Electronics [10]. The system of

Fig. 2 Experimental setup developed for measuring B-field generated by TMS devices, constituted by an acrylic structure for displacement of the MMS channels along the XY plane of a fixed grid plate and positioning of the TMS coil in a moving plate adjustable for different possible distances, in the Z-axis, from the measuring system

transducers is connected to a National Instruments USB-6229 acquisition board, and measurements were performed at 250 kHz sampling rate.

The MMS was designed to be able to measure the magnetic flux density from 15 different positions (along one axis) simultaneously. The experimental setup for measuring the space distribution B-field generated by TMS coils consisted of an acrylic structure (Fig. 2), with three parallel square plates, fixed by four cylinders, one in each vertex of the plates. The bottom plate is fixed and presents a two-dimensional grid of 5 mm (XY plane). Between two fixed plates, a third one is coupled, by the cylinders, allowing its movement along the Z-axis, perpendicular to the XY plane of the base (Fig. 2).

The MMS is positioned on the fixed grid plate, under the moving plate, where the TMS coil is fixed (Fig. 2). By moving the MMS line of sensors along the grid plate, the 2D map of B-field emitted by the TMS device is performed along a plane, at each distance from the device coil, according to the selected position of the moving plate along the Z-axis (Fig. 2).

Experimental measurements of the B-field generated by a TMS model MS/D with a cooling module and

Fig. 1 Multi-channel measuring system with 15 sensor coils, 5 mm median radius, and 1.2 cm distance between centers of sensor coils
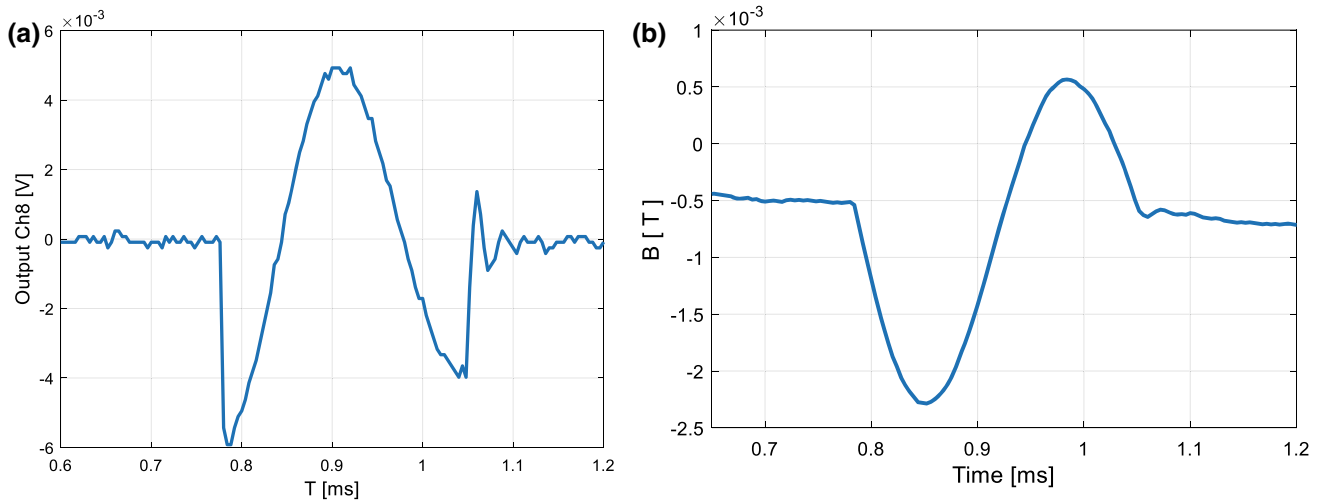
Fig. 3 Pulse voltage recording (**a**), measured by the channel 8, and the corresponding variation of magnetic flux density (**b**), in tesla

figure-of-eight type induction coil, model AFEC 02-100-C, (Neurosoft LTD) were performed, with a frequency of magnetic field pulsing of 5 Hz. The stimulating coil was fixed on the moving plate with its center coinciding with the projection of the center marked on the upper fixed plate of the acrylic structure (Fig. 2). The row of 15-channel sensor coils of the measuring system was positioned parallel to the X-axis. Measurements along a plane were performed by moving the sensing system along the Y-axis. The distance Z between the MMS and the TMS device was determined from the central channel (eighth sensor) to the center of the figure-of-eight coil, being both references aligned with the center of the acrylic structure. Measurements were performed for Z values of 1.46, 3.34 and 5.22 cm.

Aiming at analyzing the response decay of B-field as a function of the selected percentage of the maximum output intensity, a treatment parameter also available, measurements for 10, 20 and 40% of the maximum absolute amplitude value were obtained.

The magnetic signal measured by the MMS was digitized by an NI USB 6229 A/D acquisition card with a 250 kHz sample frequency. Through a program in LabVIEW® the system detects values of the magnetic flux density above a predetermined level, which takes into account the intensity of the ambient noise. The acquired signal is stored, in voltage values, in Excel format file.

To convert the volt signal (V) to tesla (T), the Faraday-Lenz law was used (Eq. 1). This processing step is entirely relevant, since the reference values of the TMS, according to its manual, are expressed in units of magnetic flux density.

$$B = \frac{\phi}{A} = \frac{-1}{A} \int_0^t V dt \qquad (1)$$

In Eq. 1, A is the representation of the sensor coil area; V is the measured electrical voltage; ϕ the magnetic flux; and B the magnetic flux density.

3 Results

The developed multichannel system, comprising 15 sensor coils aligned along an axis, was positioned in the measurement setup to evaluate the configuration of magnetic flux density in the proximities of an angulated figure-of-eight TMS AFEC-02-100-C (Neurosoft) at 5 Hz stimulation frequency. The voltage across the terminals of each of the 15 sensing coils was recorded for different positions, stimulus intensities, and distances relative to the emitting TMS device. Figure 3a shows the output voltage of the channel 8, the central sensor of the system, for the position 1 of the line of sensors, with a distance from the TMS coil equal to 3.34 cm (Z-axis) and magnitude of 10% of the maximum output intensity. The output voltage signal is processed using a MatLab programming code, and converted to magnetic flux density, in tesla (Fig. 3b).

Figure 4 shows the peak-to-peak amplitude of the magnetic flux density (B) obtained for each of the 15 measurement channels, with the system positioned so that its central sensor (channel 8) was aligned with the center of the TMS coil. These measurements were performed at a distance Z = 3.34 cm between the MMS and the TMS coil surface, for three different magnitudes of the emitted field (10, 20 and 40% of the maximum output intensity).

The curves of the peak-to-peak amplitude of magnetic flux density along a line of measurements, shown in Fig. 4, present a similar behavior for the three different intensities provided. A numerical analysis of the curves indicates

Fig. 4 Comparison of the peak-to-peak amplitude of magnetic flux density measured with the multichannel at the position 1 of the XY plane, at a distance Z of 3.34 cm relative to the TMS coil surface, for 10, 20 and 40% of the maximum output intensity
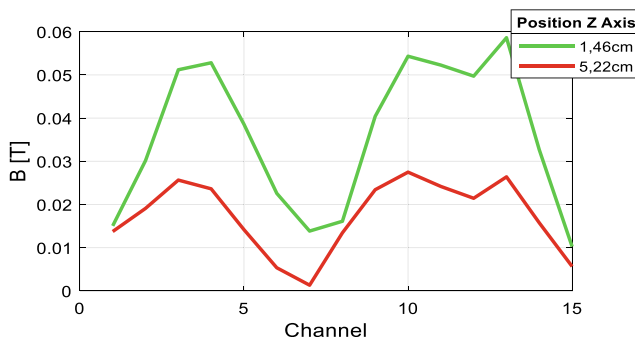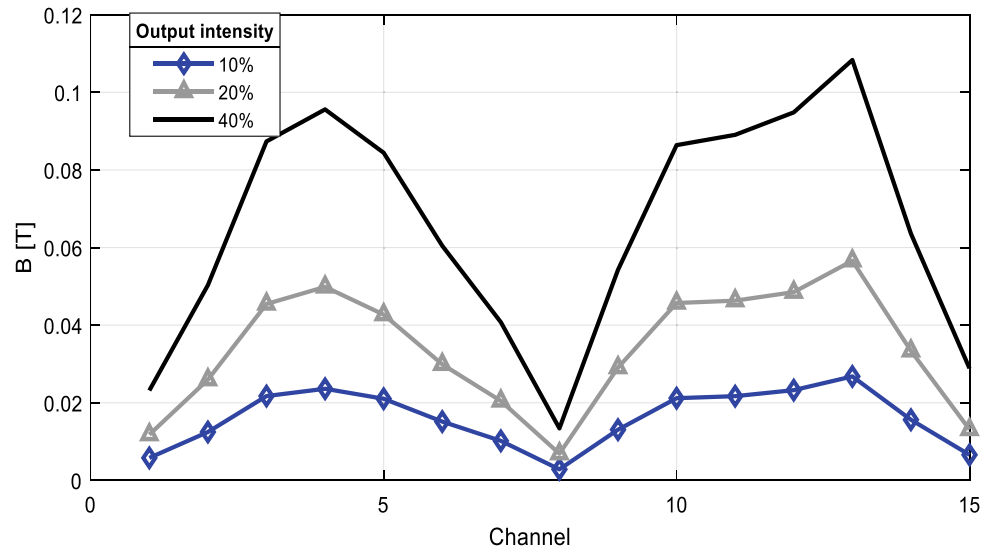
Fig. 5 Comparison of the peak-to-peak B-field amplitude, measured at a position shifted one cm along the Y-axis relative to Fig. 4, with 20% of maximum output intensity, at two distances Z from the of TMS coil surface: 1.46 and 5.22 cm
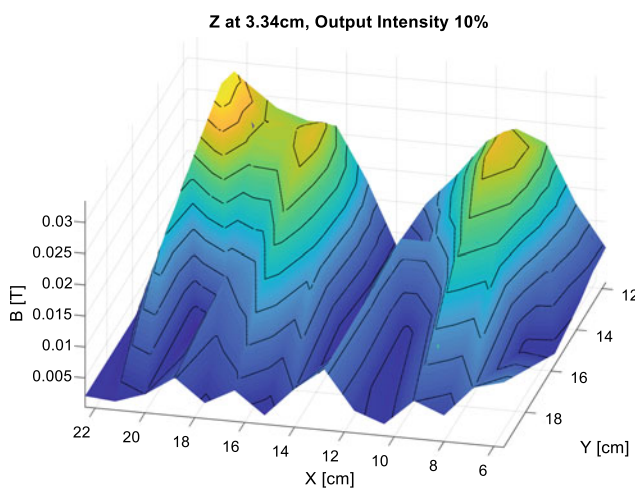
Fig. 6 Magnetic flux density map in a plane at a distance Z of 3.34 cm, for an intensity of 10% of the maximum TMS output

adequacy of proportion factors according to the percentage variation.

Figure 5 shows a comparison of the measured B-field values (tesla), at a Y-axis row positioned one cm from the TMS coil center, as presented in Fig. 4. These measurements were performed for two different distances between the measurement system and the TMS coils surface: 1.46 and 5.22 cm; with the TMS output fixed on 20% of the maximum intensity.

In Fig. 5, despite the similar behavior of the curves at different Z distances, considering the complex dependence of the magnetic flux density distribution with the distance from the coils and their geometry, as expected, a nonuniformity of proportionality factors of B-field decay is observed between the measuring channels. The possibility of evaluating how deep the magnetic stimulation is achieved should be considered, in future studies, for characterizing the B-field emitted by each TMS coil configuration and correlate them with the resulting cortical effects.

Figure 6 shows the configuration of magnetic flux density along a plane of measurements performed at a distance Z of 3.34 cm, for an intensity of 10% of the maximum TMS output. The map was obtained by interpolating the measurement results obtained in the XY plane, from the Y-axis position corresponding to the measurement results presented in Fig. 4, centered under the figure-of-eight stimulating coil to a y-axis position 8 cm shifted toward the TMS holder. Higher levels of the emitted field are observed closer to the center of the coils, in the region expected to induce the desired effect in the cortical tissue. The B-field decay toward the coil holder was measured, allowing the evaluation of staff exposure. The results, obtained for an intensity of 10% of the maximum output, indicate levels of 0.5 mT in this region, which corresponds to 50 mT at 100% of the device

amplitude. This value is fifty times greater than the recommended levels of exposure (0.1 mT), estimated for the short duration pulses of around 3 kHz emitted by the AFEC-02-100C coil, according to the guidelines of the International Commission on Non-Ionizing Radiation Protection (ICNIRP) [13].

4 Conclusion

The developed multichannel magnetic transducer comprising 15 aligned sensor coils printed onto a circuit board was assembled in an experimental setup intended for 3D mapping the magnetic flux density generated by TMS devices. Preliminary experimental measurements with the developed system were performed with an angulated figure-of-eight TMS AFEC-02-100-C (Neurosoft).

Variations of intensities emitted by providing different percentages of the device's maximum output resulted in the expected adequacy of proportion factors between B-field values.

The behavior of B-field distribution as a function of the distance Z between sensors and the stimulation coil surface presented an also expected nonuniformity of proportionality factors of B-field decay. Future detailed experimental studies of the 3D behavior B-field performed for each of the several TMS coil shapes available may contribute for providing information regarding the penetration depth of the field to stimulate deeper regions of the brain as well as the level of bioelectric activation focality [2].

The possibility of performing the 3D mapping of magnetic flux density emitted by TMS coils allows further investigations regarding the appropriateness of space distribution of B-field intensities for stimulating the targeted brain regions, where the desired effect is intended to be produced. Concerning the adequacy of the B-field levels to staff exposure safety limits, the present results indicated higher values than those recommended by ICNIRP, in positions closer to the holder of the figure-of-eight coil model evaluated. The current experimental results corroborate with simulated studies [7, 8], and with experimental research performed along one measurement axis [9]. These studies, also analyzing angulated figure-of-eight coils, indicate that an operator reaches a safe position at a distance of, at least, several tens of centimeters from the magnetic stimulation equipment [7–9].

Considering the growing variety of coil designs available for TMS devices, the study of the 3D behavior of B-field

emitted is essential to guarantee the adequacy of stimulation intensity to the target brain regions where the effect is desired, as well as the safe exposure limits for patients and staff.

References

1. Rossi, S., Hallet, M., Rossini, P.M., Pascual-Leone, A.: The safety of TMS consensus group, safety, ethical considerations, and application guidelines for the use of transcranial magnetic stimulation in clinical practice and research. Clin. Neurophisiol. **120**(12), 2008–2039 (2009)
2. Lu, M., Ueno, S.: Comparison of the induced fields using different coil configurations during deep transcranial magnetic stimulation. PLoS One **12**(6), e0178422 (2017). https://doi.org/10.1371/journal.pone.0178422
3. Nadeem, M., Thorlin, T., Gandhi, O., Persson, M.: Computation of electric and magnetic stimulation in human head using the 3-D impedance method. IEEE Trans. Biomed. Eng. **50**(7), 900–907 (2003)
4. Peterchev, A.V., Wagner, T.A., Miranda, P.C., Nitsche, M.A., Paulus, W., Lisanby, S.H., Pascual-Leone, A., Bikson, M.: Fundamentals of transcranial electric and magnetic stimulation dose: definition, selection, and reporting practices. Brain Stimul. **5**(4), 435–453 (2012)
5. Costa Monteiro, E., Leon, L.F.: 2015 metrological reliability of medical devices. J. Phys. Conf. Ser. **588** (2015)
6. Lu, M., Ueno, S.: Dosimetry of typical transcranial magnetic stimulation devices, J. Appl. Phys. **107** (2010)
7. Sousa, I.P.: Metrological reliability of transcranial magnetic stimulation. Dissertação de Mestrado PUC-Rio (2016)
8. Palatnik-de-Sousa, I.P., Barbosa, C.R.H., Costa Monteiro, E.: Safe exposure distances for transcranial magnetic stimulation based on computer simulations. PeerJ **6**, e5034. San Diego (2018)
9. Karlström, E.F., Lundström, R., Stensson, O., Mild, K.H.: Therapeutic staff exposure to magnetic field pulses during TMS/rTMS Treatments. Bioelectromagnetics (2006)
10. Barbosa, C.V.N., Costa Monteiro, E.C., Barbosa, C.R.H., Louzada, D.R.: Sistema para medição da densidade de fluxo magnético emitida por equipamentos de estimulação magnética transcraniana. Congresso Brasileiro de Metrologia 1–4 (2017)
11. Sousa, I.P., Costa Monteiro, E.: Transcranial magnetic stimulation: terminology and safety aspects concerning therapeutic protocol and device reliability. In: XXIV Brazilian Congress Biomedical Engineering, pp. 1–4 (2014)
12. Souza, I.P., Costa Monteiro, E.: Transcranial magnetic stimulation conformity assessment. In: XXI IMEKO World Congress "Measurement in Research and Industry", Prague, Czech Republic, pp. 1–6 (2015)
13. The International Commission on Non-Ionizing Radiation Protection: Guidelines for limiting exposure to time varying electric and magnetic fields (1 Hz–100 kHz). Health Phys. **99**(6), 818–836 (2010)

Parameter Estimate from Accelerometer and Gyroscope for Characterization of Wrist Tremor in Individuals with Parkinson's Disease

Ana Paula Sousa Paixão, Luciano Brinck Peres, and Adriano O Andrade

Abstract

Researchers have been working on the quantification of tremor to assess the severity of neurodegenerative diseases that present it as a pathological symptom. Usually, clinical rating scales are employed for the qualitative assessment of tremor. This research presents quantitative results, estimated by the root mean square (RMS) of signals estimated from accelerometers and gyroscopes, to quantify the degree of severity of tremor in individuals with Parkinson's disease (PD). In total, 27 individuals participated in the study, being 15 with PD (GI) and 12 healthy (GII). Two set of inertial sensors capable of jointly measuring acceleration and angular speed were positioned respectively on the back of the hand and forearm of the participants. The detected signals were digitized and annotated for the identification of the beginning and end of the region of interest. Signals were acquired while the wrist was maintained at rest for 15 s, without and with a load of 92 g on the back of the hand. Three data collections were performed with 60-s intervals. From the RMS it was defined an index (In) that showed to be sensitive to the variation of the amplitude of tremor. The index In showed that PD tremor is larger than that for the healthy participants, and that the addition of load significantly reduces the tremor in PD. This research is relevant because it quantifies the tremor by means of an index that takes into account both patterns of normality and severity of tremor.

1 Introduction

Human tremor may be defined as an involuntary movement having oscillatory and rhythmic characteristics in any part of the body [1]. Tremor may be a physiological human motor function present in all human beings or pathological in sequels of neurological disorders [2]. Studies show that the senile population is most affected by tremor. This manifestation can cause considerable functional disability and leads the individual to social withdrawal [3]. The present study evaluated tremor in Parkinson's disease (PD), which is a progressive and neurodegenerative disorder of the central nervous system (CNS). The diagnosis of PD is still clinical, and the evaluator's experience is an important factor for the correct diagnosis. The severity of PD is usually assessed using a qualitative scale called Unified Parkinson's Disease Rating Scale (UPDRS), which is widely used even with advances in health-related technologies. As the symptoms of patients vary throughout the day, the time at which the diagnosis is given may not represent the degree of severity of the tremor. Studies comparing different methods of PD treatment also use the UPDRS scale to evaluate treatment outcomes [4], and several ways of treatment are indicated for PD, which include: (i) pharmacological, (ii) surgical and (iii) physiotherapeutic [5]. Currently, for the evaluation of tremor, studies have suggested objective methods to quantitatively characterize the dysfunction derived from PD. The literature [6] suggests the use of wearable devices (gloves) with built-in inertial sensors, in which they use data extracted from the accelerometer, gyroscope and magnetometer to determine the severity of the tremor. A major limitation of several studies is the lack of comparative results showing the performance of healthy people compared to that of individuals with PD, in the experimental conditions as proposed in this study. The present study proposes the estimate of an index that compares the tremor of individuals with PD with the tremor of healthy individuals. There are studies that demonstrate how the presence of a weight on the

A. P. S. Paixão (✉) · L. B. Peres · A. O. Andrade
Centre of Innovation and Technology Assessment in Health,
Federal University of Uberlândia, Uberlândia, Brazil
e-mail: anapaulasouzap@yahoo.com

hand of the patient with PD can attenuate tremor [7]. However, there is no consensus in these results, for instance in [8], the authors verified that the presence of a load decreases tremor amplitude of patients with cerebellar tremor, but the same benefit was not observed by patients with PD. However, some authors [9–11] agree that the variation in tremor in both amplitude and frequency is proportional to the weight placed on the individual's hand. Related studies [6, 10, 11] suggest the use of loads varying from 10 to 960 g. This range of mass can be explained by the difference in the methodology used for data collection. Although the lowest weight used in patients with PD was 10 g, a clinical analysis done exclusively in individuals with PD showed that the weight of 240 g is sufficient for this population, who reported difficulty in performing movements when supporting this load. In the present study, for the quantification of the tremor, we used a load of 92 g, since it is believed that the results found in [11] show an overload for individuals with PD when using loads above 92 g. Therefore, this study proposes the evaluation of the characterization of PD tremor with and without a load of 92 g on the back of the hand of individuals. The main contribution of this study is the proposal of a relatively simple index to characterize the severity of tremor, which is sensitive to the presence of a load.

2   Methods

This study was observational cross-sectional and approved by the Ethics Committee on Research in Human Beings (CEP—nº 270.782) of the Federal University of Uberlândia, with approval on May 13, 2013, and the National Commission of Ethics in Research (CONEP—nº 361.526), with approval on November 27, 2013.

In all, 27 people from both sexes were recruited, aged 50 or over, of these 12 healthy individuals and 15 with wrist tremor due to PD, diagnosed by a specialized physician and evaluated through the UPDRS scale. Two study groups were created: group I—GI (15 individuals diagnosed with PD, without use of load and with use of load); group II—GII (12 healthy subjects, without use of load and with use of load). For the data collection, all participants signed the informed consent form. All groups underwent the same experimental

protocol of activity performed in one day, with an average duration of 10 min. For the accomplishment of the activity they supported the forearm in a specific support and left the hand pendent (palm of the hand down), without load and later with load. The activity was performed with the wrist held at rest for 15 s, without and with a load of 92 g, on the back of the hand. In the GI, the limb most affected by the tremor was submitted to activity. In the GII, the evaluated limb was the dominant one, and the activity consisted of 3 valid repetitions, with a 60 s interval between the repetitions. All collected data were analyzed offline. Data collection was performed using the TREMSEN device (Precise Tremor Sensing Technology, INPI: BR 10 2014 023282 6) developed by researchers from the Center for Innovation and Technological Health Assessment (NIATS) of the Federal University of Uberlândia. The device provides two sets of inertial sensors (L3GD20H and LSM303D, STMicroelectronics, Switzerland), which were positioned, on the back of the participant's hand (sensor 1—approximately in the carpometacarpal joints II, II and IV) and on the forearm (sensor 2—approximately 3 cm from the wrist joint). Only the sensor 1 was used to collect the tremor. Each inertial sensor is composed of triaxial accelerometers and gyroscopes. Sensitivity for each sensor was set respectively to ± 2 g and $\pm 245°$/s. The signals were digitized at a frequency of 50 Hz using a microcontroller (Atmel SAM3X8E ARM Cortex-M3) of 12-bit resolution. The data were sent to a computer via serial communication. Visualization of the collected data was done in real time through TREMSEN data collection and visualization software, developed in C # (Microsoft). The data were saved in plain text for analysis and processed in Matlab (MathWorks, USA). The steps of data analysis are shown in the block diagram (Fig. 1).

The resulting component was calculated by using (1).

$$R = \sqrt{X^2 + Y^2 + Z^2} \tag{1}$$

The resultant component was filtered through a Butterworth filter of order 4, with high pass frequencies of 1 Hz and low pass of 50 Hz. The beginning and end of each activity were visually detected, and then the root mean square (RMS) of a 5-s signal window was estimated. Many researchers have

Fig. 1 Flow diagram of information processing, showing all steps of data analysis
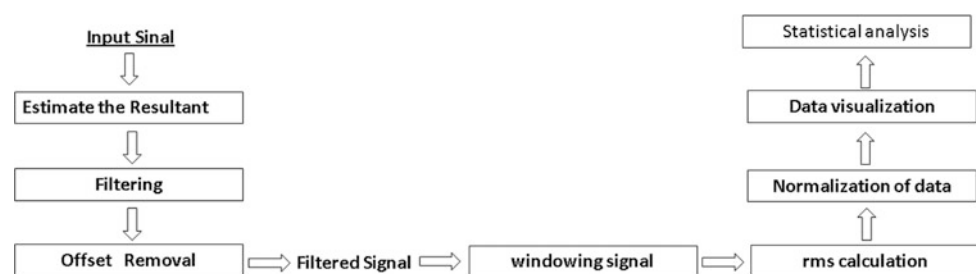
adopted the RMS calculation as a way to measure signal amplitude [12, 13]. The RMS of the signal was calculated using (2).

$$rms = \sqrt{\frac{1}{n}\sum_{i=1}^{n} x_i^2} \qquad (2)$$

Following the RMS calculation, the data were normalized using the mean and standard deviation, calculated by the Bootstrap [14] technique, for the healthy individuals. The normalization process was executed separately for the conditions with and without load.

By normalizing data from GI and GII, it was possible to verify how much the tremor of each individual with PD is higher than the mean of the healthy population. This stage was developed to quantify the tremor coming from PD, and to detect how much the PD tremor is larger than the healthy population, and for this detection an index was created. The calculation of the tremor index is the result of the normalization process quoted above and it is given by Eq. 3:

$$In_j = \frac{rms_j - MPS}{STDPS} \qquad (3)$$

where: In_j is the normalized tremor index of individual j; rms_j is the RMS calculated using (2) of individual j; MPS is the mean of the RMS value calculated only from the population of healthy individuals; STDPS is the standard deviation calculated only from the population of healthy individuals.

The index In of individuals in the GII ranges from 0 to 1. If an individual with PD has = 20, it means that the tremor amplitude of this individual is 20 times greater than the tremor of the healthy population. This shows us how severe the tremor of that individual is. The data visualization was done through a graph that presents the values of the indices In_j in a cartesian plane, where the abscissa axis represents the individual j and the axis of the coordinates represents the index. This step can be visualized in Figs. 3 and 4.

In order to verify if there were significant differences between the groups, statistical tests were applied. The verification for normality was carried out by applying the Shapiro test, where p-values for GI and GII were respectively: $p_{GI} = 0.4879$ and $p_{GII} = 4.32^{e-6}$. The GI and GII groups did not present a normal distribution, so the statistical test to determine if there were statistical differences between the groups was Wilcoxon's. Paired Wilcoxon was used to detect differences between the unloaded and loaded conditions for both groups. The unpaired test was performed to detect if there were differences between the GI and GII groups without load and between the GI and GII groups with load, using a significance level of 95% for the tests.

3 Results

The In_j estimated from (3) is shown in Figs. 2 and 3. Figure 2 shows the In_j of the unloaded GI and unloaded GII groups while Fig. 3 shows the In_j of the groups GI with load and GII with load, observed by means of information estimated from accelerometers.
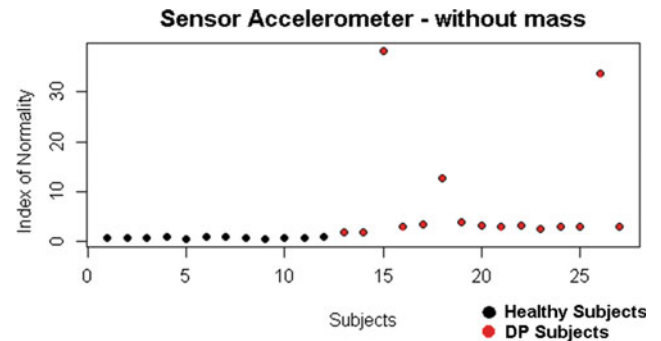
Fig. 2 Visual representation of the calculated normality index using (3) with the population of the GI and GII groups without load, through the accelerometer sensors
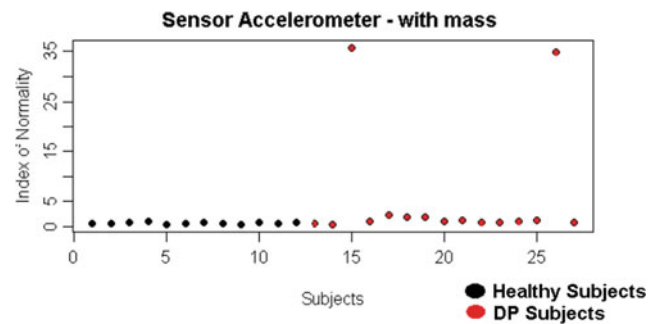
Fig. 3 Visual representation of the calculated normality index using (3) with the population of the GI and GII groups with load, through the accelerometer sensors

Likewise, In_j estimated from (3) is also shown in Figs. 4 and 5 for data collected from the gyroscope. Figure 4 shows the In_j for groups GI and GII for the condition without load, and Fig. 5 shows the In_j for both groups for the condition with load.

The Wilcoxon test showed that there were significant differences in the In between GI groups without load and GII without load, and between GI without load and GI with load. Differences between unloaded GII and loaded GII groups did not show statistically significant differences. Tables 1 and 2 present the results for each type of sensor, i.e., accelerometer and gyroscope.
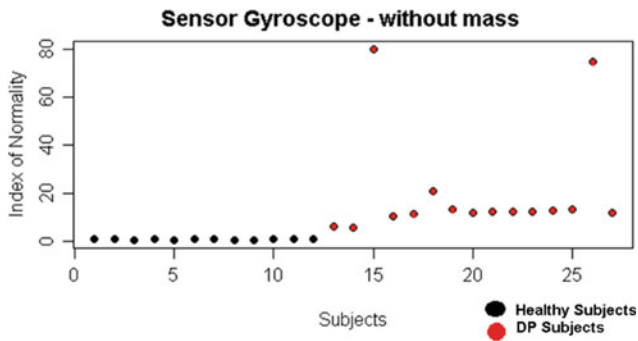
Fig. 4 Visual representation of the calculated normality index used (3) for the unloaded protocol in the GI and GII, through the gyroscope sensors, without load
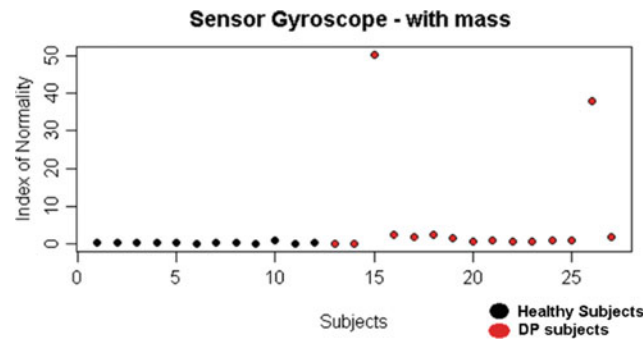
Fig. 5 Visual representation of the calculated normality index used (3) for the protocol with load in the GI and GII, through the gyroscope sensors, with load

In values were estimated using the RMS characteristic of the signal amplitude, in relation to the groups with Parkinson and healthy in the absence and presence of load. These comparisons showed the *In* of the study participants, observed, in each group. The values of p for load and without load are respectively:

$$p_{GI,GII} = 0.0000002 \text{ e } p_{GI,GII} = 0.0000017$$

4 Discussion

The present research proposes a way of quantifying Parkinson's tremor by estimating an index that takes into account the severity of the tremor as well as the relative comparison to healthy individuals and PD. Traditionally, Parkinson's tremor is measured using a purely qualitative scale (UPDRS). This work is innovative because it presents an alternative to the qualitative method already in use. The quantitative method gives the investigator the possibility of observing the severity of an individual's tremor in a way that does not depend on the personal experience of the person doing the analysis, as in the evaluation using the UPDRS scale, being an important diagnostic tool and thus may be validated in the future. From the RMS value of the amplitude of the tremor signal, the normality index (*In*) of the tremor for the accelerometer and gyroscope used in each evaluated group can be calculated, with reference to the

Table 1 Measurements per group, p-value and test applied for comparison of two groups for the accelerometer sensor

Statistic					
Feature	Groups	Average	Standard deviation	P-value	Test
RMS accelerometer	Parkinson without mass	8	11.6538047	1.15e−07	Wilcoxon-Mann-Whitney
	Healthy without mass	1	0.28867513		
	Parkinson with mass	7	12.0399236	0.0007516	Wilcoxon-Mann-Whitney
	Healthy with mass	1	0		
	Parkinson without mass	8	11.6538047	0.0001221	Wilcoxon
	Parkinson with mass	7	12.0399236		
	Healthy without mass	1	0.28867513	0.021	Wilcoxon
	Healthy with mass	1	0		

Table 2 Measurements by group, p-value and test applied to compare two groups for the gyroscope sensor

Statistic					
Feature	Groups	Average	Standard deviation	P-value	Test
RMS gyroscope	Parkinson without mass	21	23	1.15e−07	Wilcoxon-Mann-Whitney
	Healthy without mass	1	0		
	Parkinson with mass	9	15	0.001421	Wilcoxon-Mann-Whitney
	Healthy with mass	1	0.288675		
	Parkinson without mass	21	23	6.104e−05	Wilcoxon
	Parkinson with mass	1	0.288675		
	Healthy without mass	1	0	0.06396	Wilcoxon
	Healthy with mass	1	0		

groups healthy, GII. *In* shows that the tremor of a healthy individual will have values ranging from 0 to 1. In this way, a person with a very intense Parkinson's tremor will have In values greater than 1. When looking at Fig. 2 of the accelerometer and 3 of the gyroscope, it can be seen that the *In* of subject 15 and 26 have values above 35 and 25 respectively. This value indicates that the subject's tremor 15 is 35 times greater than the tremor of a healthy person, just as in individual 26 it is 25 times greater. The *In* is extremely relevant because it not only gives a quantitative measure for an individual's parkinson's tremor, but also a reference to how this tremor is above the normal tremor.

The added burden on individuals is relevant with respect to the magnitude of the tremor. It can be verified by means of Figs. 3 and 5 that the In of the healthy individuals is still between 0 and 1, as this is the index considered normal. In contrast, individuals with Parkinson's decreased. When evaluating individuals 15 and 26, it is remarkable how much the addition of the load decreases the amplitude of the tremor. This result is in agreement with the result found in [6, 10]. The fact that some individuals with Parkinson's loaded had a major tremor in Figs. 3 and 5 is probably related to Parkinson's tremors throughout the day because, at the time of data collection without the load, these individuals had a tremor lower than at the time of collection with the load. As data collection without the load was done before data collection with the load, it is possible that Figs. 3 and 5 reflect the muscular exhaustion of the individuals, which led to the increase of the tremor, thus, the increase of *In* these individuals in Figs. 3 and 5, is not related to the burden but to the symptoms of the disease itself.

The study is relevant in different areas. In health, the measurement of Parkinson's tremor is a strong ally in the characterization of disease severity. In biomedical engineering, the techniques used in this work may be of great value in the measurement of different tremors in different diseases, as observed in a study shown [11] to verify quantitatively how is the tremor progression of these individuals. The greatest limitation of this study is related to the number of participants in the research. A study with a larger sample can solve it.

5 Conclusion

It is concluded that the index estimated from the RMS value of the accelerometer and gyroscope, allowed us to objectively characterize the wrist tremor. The group with Parkinson's disease showed a higher RMS value in relation to the healthy group. The 92 g load presented a significant decrease in tremor in individuals with PD. The objective evaluation index proposed in this research was sensitive to these tremor amplitude variables.

References

1. Vieira, S.: Tremores. Rev. Port. Clin. Geral **21**, 61–67 (2005)
2. Chan, P.Y., Ripin, Z.M.: Development of wearable inertial sensors for measurement of hand arm tremors. In: IEEE International Conference on Smart Instrumentation, Measurement and Applications (ICSIMA) (2013)
3. Dror, B., Yanai, E., Frid, A., Peleg, N., Goldenthal, N., Schlesinger, I., Hel-Or, H., Raz, S.: Automatic assessment of Parkinson's disease from natural hands movements using 3D depth sensor. In: IEEE 28-th Convention of Electrical and Electronics Engineers in Israel (2014)
4. Fisher, J.M., Hammerla, N.Y., Ploetz, T., Andras, P., Rochester, L., Walker, R.W.: Unsupervised home monitoring of Parkinson's disease motor symptom s using body-worn accelerometers. Park. Relat. Disord. **33**, 44–50 (2016)
5. Saito, T.C.: A Doença de Parkinson e Seus Tratamentos: uma revisão bibliográfica. Centro Universitário Filadélfia – UniFil/Londrina (2011)
6. St George, R.J., Nutt, J.G., Burchiel, K.J., Horak, F.B.: A meta-regression of the long-term effects of deep brain stimulation on balance and gait in PD. Neurology **75**(14), 1292–1299 (2010)
7. Patel, S.P., Lorincs, K., Hughes, R., Huggins, N., Growdon, J., Standaert, D., Akay, M.: Monitoring motor fluctuations in patients with Parkinson's disease using wearable sensors. IEEE Trans. Inf. Technol. Biomed. **3**(16) (2009)
8. Ma, H.-I., et al.: The effect of eating utensil weight on functional arm movement in people with Parkinson's disease: a controlled clinical trial. Clin. Rehabil. **23**, 1086–1092 (2009)
9. Koller, W.C.: Diagnosis and treatment of tremors. Neurol. Clin. **2**, 499–514 (1984)
10. Meshack, R.P., Norman, K.E.: A randomized controlled trial of the effects of weights on amplitude and frequency of postural hand tremor in people with Parkinson's disease. Clin. Rehabil. **16**, 481–492 (2002)
11. Homberg, V., Hefter, H., Reiners, K., Freund, H.-J.: Differential effects of changes in mechanical limb properties on physiological and pathological tremor. J. Neurol. Neurosurg. Psychiatry **50**, 568–579 (1987)

Passive Acoustic Localization Based on Time of Arrival Trilateration

Karin Cristine Grande, Nicole Becker Schneider,
Gilson Yukio Sato, and Bertoldo Schneider Jr.

Abstract

In Biology is very common the field researcher need to locate or to count subjects of determined specie. Sometimes, the animal cannot be seen but it can be listening, like is the case of the frogs and some birds. Localization and counting of individuals demand a lot of training, people, time and money. An automated device capable to count and locate sound sources, without seen them, is a very useful thing for biologists, police officers, tragedies attendants, military people, and engineers. Different of echo localization, like radar or sonar, in acoustic localization it is not possible to know the distance from the sound soured, a priori, because there is no synchronization. In the world wars there were some purely mechanical military devices using the sound emitted by the source, emulating big ears, trying to locate bombers at great distances. It was not found any work using multilateration of a real sonic source applied to biology. The passive acoustic localization based on time of arrival try to locate a sound emitter by processing the times that the sound takes to arrive from the source to the sensors, generally in number of three. Normal methods use heavy math to deal this. Here is presented a simple method using simple math to solve the problem of localization of a sound emitter. The results demonstrate successfully the concept, showing the problems, the errors and how to minimize them. The device will be used in field by biologists to counting an locating frogs and birds.

Keywords

Animal tracking • Biotelemetry • Acoustic • Localization

1 Introduction

One of the most important subjects in Biology is the biodiversity study and its relation with the rest of the planet. To study this biodiversity the scientists need customized devices to help them collect the necessary data. The localization and counting of subjects of one or more species is fundamental for this work, and devices and machines that help this work are very desired by biologists. The biomedical engineer is the right professional to create these devices and machines. Know the space-time distribution of animals is essential to understand their relation to the environment and humans [1].

In Biology, according to International Union for Conservation of Nature, when a population of any specie has less than 4,700 individuals, this specie is considered in extinction. To know that biologists make senses identifying, locating and counting the individual. Generally this work is made by visual and acoustic observation, and even local inhabitants interviews, without instrumentation. These methods are imprecise and need training and large teams. Some species, like the frogs (Anura order), are indicators of quality of the environment [1–5]. Study them turn possible to deal with areas of great biological and/or economic values. Exploration and preservation of these areas are very important for any nation. Some species dies so fast that are not registered, and they are not registered [2] because the methods takes a long time to do what could be faster with appropriated devices.

This aim of this work is to create a device to automate the localization and counting of species capable of vocalization.

K. C. Grande (✉) · G. Y. Sato · B. Schneider Jr.
Federal University of Technology - Paraná, Av. 7 de setembro, 3165, Curitiba, PR, Brazil
e-mail: karincristine13@gmail.com

N. B. Schneider
Federal Institute of Parana, R. João Negrão, 1285, Curitiba, PR, Brazil

2   Materials and Methods

It is known that three points in the space suffice to determinate the position of an object. This is true if the three point of view directions are completely known. Imagine the problem of locate a little animal capable of vocalization, a frog for instance. When the sound arrives in our ears it is almost impossible to know the distance of the source, and almost always the direction is imprecise too. Or someone shooting in the crowd or even to locate a IoT transmitter device [6] (example in the electromagnetic field). In the first and second world wars there were a lot of mechanical systems to listening the bomber aircrafts trying to locate them, almost all were great replication of human ears, like giant gramophone pairs. The problem is that there is no synchronism in these cases. Generally, triangulation methods are used to estimate angles and trilateration are used to estimate distances. Trilateration is the use of three sensors to determinate distances and multilateration the use of more than three sensors for the same objective. There are many approaches used to localization of sound (and electromagnetic) sources, like intersection of spheres or goniometry, and no one is immune to errors [6]. In this work a different and simple approach is studied to solve these kind of problems.

2.1   Time of Arrival

In Time of Arrival (TOA) propagation an object or subject emits a sound pulse and some receiver try to infer information from the sound. The information can be distance, position, or direction if we consider only the static sound sources. Something analog happens with localization of wireless devices using electromagnetic waves in the place of the sound [7–12], where "Time of arrival" [13] and some variations like "time difference of arrival", the "received signal strength" [14], "angle of arrival" and "direction of arrival" [15]. Theoretically, it is possible to estimate the position of the source of a sound by processing the difference of arrival times, or the strength of the signal, or the angle of arrival sound and it is necessary two or more sensors to take multiple points of views for the necessary processing. Typically, it is necessary at least two sound sensors (microphones) to turn possible estimate the position of the sound source. It is a more difficult problem than the echolocation like in the sonar or radar systems. In echolocation, both emitted and received times are known, because a generated energy travels to the object and is reflected by it, returning to the sensor. In TOA problems, the emitted time of the sound is unknown. So, the algorithms cited in this paragraphs are used.

In the 50's an extensive study was made in binaural and stereophonic listening [16]. The brain knows the position of a sound source by processing the inter-aural time arrival difference. Our natural earing system can deal with differences about 0.5 ms, time when sound travels something like 30 cm in air. That is why humans and other animals shake the head to enhance the precision of the localization estimation [16].

In this project it was chosen a confined space with length L and width W, like a room of the Fig. 1. The left inferior corner is the zero reference for x and y. x and y are the Cartesians coordinates of point P. P is the place where a sound was generated, t_1 is the time required to the sound waves travel the distance d_1 from P to point A, t_2 is the time required to travel the distance d_2 from P to point B, and t_3 is the time required to travel the distance d_3 from P to point C.

From the velocity equation, the following time distance relations can be written, using the Fig. 1 like reference and c is the sound velocity in the air:

$$d_1 = c \cdot t_1 \tag{1}$$

$$d_2 = c \cdot t_2 \tag{2}$$

$$d_3 = c \cdot t_3 \tag{3}$$

Using basic triangle relations in diagram in Fig. 1 is possible to write the following equations:

$$y = \frac{L^2 + d_2^2 - d_1^2}{2W} \tag{4}$$

$$x = \frac{C^2 + d_2^2 - d_3^2}{2L} \tag{5}$$

Supposing that in an instant t_0 something in point P emits a sonic pulse, the front of the wave of this pulse expands in all directions with a velocity c, forming a circumference in
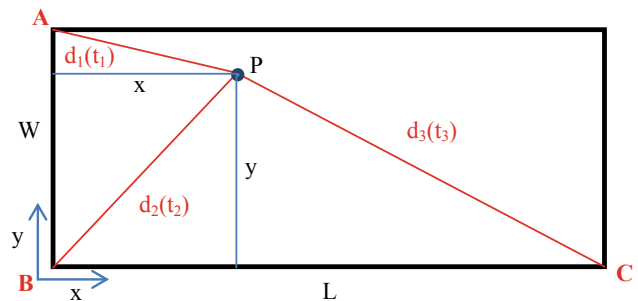
Fig. 1 Area used to study the proposed time of arrival trilateration where A, B and C are the places where three microphones record the ambient sounds. The distances are represented by dn, with n = {1, 2, 3} and tn are the times need to the sound emitted in point P arrive in points A, B and C. L is the length and W is the width. The coordinates of the point P are (x, y)

the plane xy arriving at the points A, B, and C in t_1, t_2, and t_3 s, respectively. If three microphones are placed in A, B and C points three arrival times t_1', t_2', and t_3' can be recorded. At this time t_0 is not known. The first sound (that one with the lower time index) defines t_1'. The second defines t_2', and the last one t_3'. So the lower value is deduced of all the times values: $\Delta t_1 = t_1' - t_1'$, $\Delta t_2 = t_2' - t_1'$, $\Delta t_3 = t_3' - t_1'$. At this point, if t_0 is known, the determination of the distances and coordinates x and y is easy, but it is not. It is necessary to know it.

$$d_1 = c \cdot (\Delta t_1 + t_0) \tag{6}$$

$$d_2 = c \cdot (\Delta t_2 + t_0) \tag{7}$$

$$d_3 = c \cdot (\Delta t_3 + t_0) \tag{8}$$

So, an algorithm where t_0 can be determined increments t_0 till a value where the three radii d1, d2, and d3 touch themselves in a region close to P, satisfying the following condition: The area A1 of the triangle BCP must be equal to the area A2 of the same BCP triangle determined by ancient Heron formula. Meaning that the areas determined by using the distances must be equal that one determined by the coordinates. Like will be demonstrated, for computation this criterion must be a little modified. The area A1 is given by:

$$A1 = \frac{L \cdot y}{2} \tag{9}$$

And the Heron formula for the BCP triangle is:

$$A_{Heron} = A2 = (p \cdot (p - d_2) \cdot (p - d_3) \cdot (p - L))^{0.5} \tag{10}$$

where:

$$p = \frac{(d_2 + d_3 + L)}{2} \tag{11}$$

For t_0 lower than true t_0, the radicand of Eq. (10) is negative. This can be used to accelerate the loop process.

The algorithm derived from this approach was tested in a virtual room of 10×10 m (L = W = 10.0 m) for increments of dt = 100 μs, and was fed with computed t_1, t_2 and t_3 related to times of arrival of the sound sources locations (sound velocity considered here was c = 340 m · s^{-1}) of the matrix of points (hollow circles) in Fig. 2. Times t_n, with n = {1, 2, 3}, fed a program embodied in an Arduino UNO platform. This program was written in wiring language, and implemented the algorithm described below.

The microcontroller time is the time the most of microcontroller can generate. In the ATMega328P is very easy to have it in ms, just for compute the time of execution of a procedure. The index time used here is something like an absolute time like year-month-day-hour-min-sec where seconds can be in mille or μs.
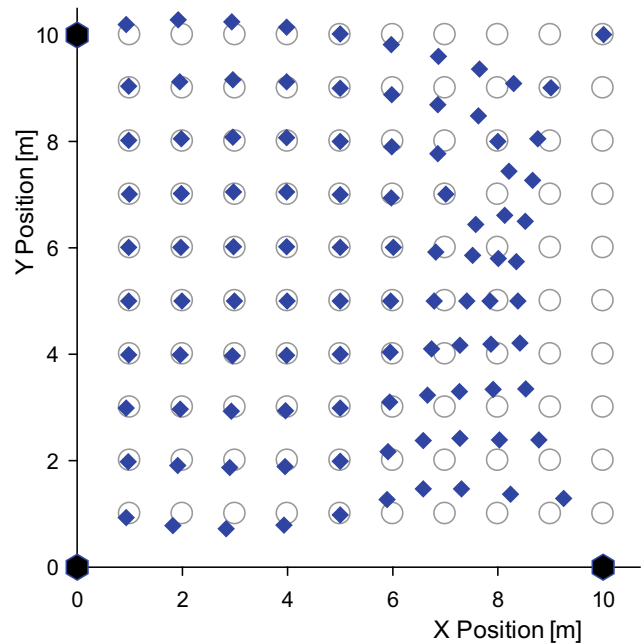
Fig. 2 Matrix of sound emitters represented by the hollow circles. The points are the determined positions using criterion 1. The difference between the points and the centers of the circles are errors

In a complete system, here studied, three microphones are placed in coordinates (0.0, 0.0), (0.0, 10.0) and (10.0, 0.0), shown by the hexagons in Fig. 2, and the points A, B, and C in Fig. 1. The basic idea is to detect where in (x, y) coordinates the three distances d_1, d_2, and d_3 touch themselves. Like it is not possible to know the value of the distance a priori, here we begin with one of them with modulus zero (see first step in algorithm below) and those distances, or radii of the three circumferences, are incremented till some convergence criterion is achieved (in this case are presented three criteria).

The basic algorithm is:

- Given the times t_1, t_2 and t_3, which are the time index or the instant in the time that the microphones A, B and C kept the sound information, a procedure choice the minor index of time attributes this value to variable ti;
- tnx (n = {1, 2, 3}) receive the value tnx-ti, and the lower index time is related with the length zero of one of the distances d_1, d_2 and d_3, trough dn = c * tnx;
- p = Eq. 11;
- radicand = radicand of Eq. 10
- A_{Heron} = value of the Eq. 10 (if radicant greater than zero. If not,)
- Determine x and y by Eqs. 4 and 5;
- A1 receives the value of the Eq. 9;
- If criteria are satisfied, the result (x; y) is valid

- if not, increment d_1, d_2 and d_3 by approximately 34 cm (dt = 100 μs and the sound travels 34 cm in this time), and return to the second step.

The criteria used here to test the algorithm were: (1) x and y are considered valid when $A_{Heron} > A1$; (2) x and y are considered valid when $(A_{Heron} > A1)$ AND the area of the triangle APB (in Fig. 1) determined by Heron equation is greater than the area determined by Eq. 9 adapted to (W · x/2); and (3a) x and y are considered valid when $(A_{Heron} > A1)$ AND the area of the triangle APB (in Fig. 1) determined by Heron equation is *greater* than the area determined by Eq. 9 adapted to (W · x/2), when the point is *below* the diagonal AC, and (3b) x and y are considered valid when $(A_{Heron} > A1)$ AND the area of the triangle APB (in Fig. 1) determined by Heron equation is *smaller* than the area determined by equation (W · x/2) when the point is *above* the diagonal AC. This means that an additional logical effort must be made (because a priori we do not know where the point is), so when the (x, y) coordinate is not valid until d2 have the length of half of the diagonal, the criterion change from 3a to 3b.

The simulated time of arrival times fed the system and the results are presented in the next section.

3 Results

Using the criterion 1 (x and y are valid when $A_{Heron} > A1$) for a matrix of sound sources shown in the hollow circles in Fig. 2, the result of the position determination were the points in Fig. 2. It is easy to note the great error caused by the algorithm used with criterion 1, especially at the right sector of the square area. In this case, if the algorithm continues the increment for more a couple of steps, the right place is achieved. This means that the geometry of intersection of the three circumferences are complicated and much more logic is necessary to create an useful criterion.

Using the criterion 2 (x and y are considered valid when $(A_{Heron} > A1)$ AND the area of the triangle APB (in Fig. 1) determined by Heron equation is greater than the area determined by Eq. 9 adapted to (W · x/2) for a matrix of sound sources shown in the hollow circles in Fig. 3, the result of the position determination was the point in Fig. 2. Two things are immediately noted. First, the precision of estimation for the coordinates are very good for the right points. Second, for the wrong points the precision were very bad. In fact, criterion 2 works very well for the part below the diagonal AB (referring Fig. 1), what lead to the criterion 3. In the criterion 3, the logic was divided for below (criterion 3a) and above (criterion 3b) the AB diagonal. What differentiate one for another is the length of the d2. Form d2 greater than half AB distance, criterion is 3b. The geometry
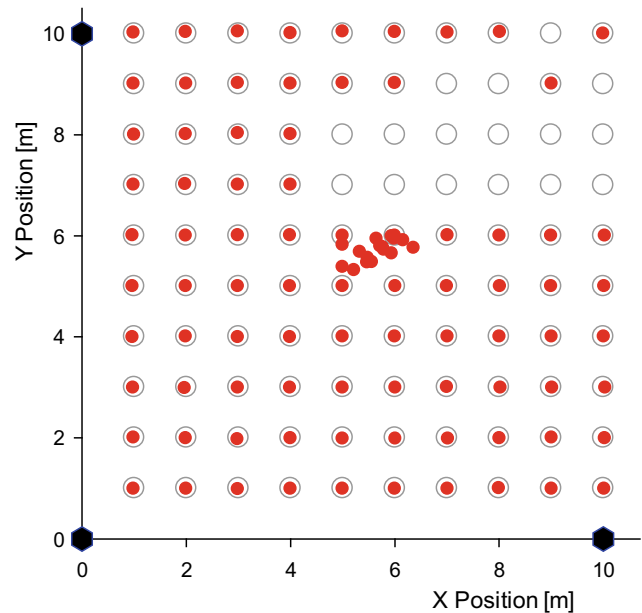
Fig. 3 Matrix of sound emitters represented by the hollow circles. The points are the determined positions using criterion 2. The difference between the points and the centers of the circles are errors

of intersection of the three circumferences are decisive for this approach. In the case of the criterion 3a the (x, y) coordinate is inner to the three circumferences and for the 3b criterion the coordinate is inner to circumferences 1 and 3 (caused by d_1 and d_3 radii), but out of the circumference 2 (caused by d_2 radium). Using the criterion 3 all the points fit very well in the hollow circles, like shown in Fig. 4.
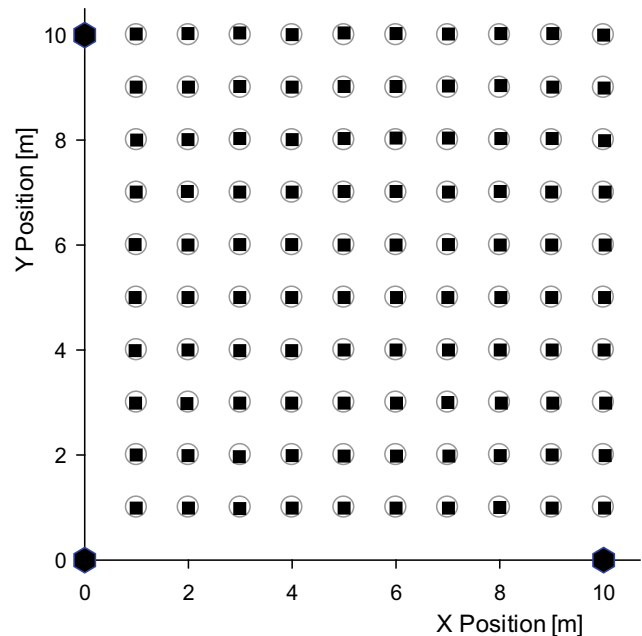
Fig. 4 Matrix of sound emitters represented by the hollow circles. The points are the determined positions using criterion 3a and 3b. The difference between the points and the centers of the circles are errors

4 Conclusion and Discussion

This concept of a simple trilateration system was successfully demonstrated. It can be used for localization of frogs and birds in a 2D space, as well for another uses like localization of a shooter in the middle of a crowd or an elder or patient that had triggered a help sound through your bracelet sound generator. A fourth microphone could resolve the errors too, enhancing the precision of the localization. The simplicity of the method is great when compared with literature [7–22] and can be implemented easily with cheap microcontrollers. The device concept is useful to deal with two dimension counting and localization. Some enhance is necessary to transform this device in a system capable to locate and count in 3D using spherical geometry [23], and using four or five microphones. It also will be tested by biologists for counting and locating a special specie of frogs in Mehl island, Paraná.

The great advantage of this method is that there is no introduction of any kind of energy or device in the habitat or animal under study, causing no animal stress. The proposed system will be able to work with the sound emitted by the animal under study, without any other intervention in it or in its habitat, except for the microphones placed around the area under investigation. Other methods, also called acoustic telemetric systems, use some kind of active sonic tags [24] where fishes are tagged with sound generators devices, or lake trouts marked with acoustic tags [25]. The same occurs with pelagic species [26] in a system called 'passive acoustic telemetry', where the fishes were equipped with acoustic transmitters. A lot of another works use sonic transmitters, what is considered a habitat interference by the biologists. It was no found any work containing a system capable to locate an animal by its natural sound. Authors believe that, when completely developed, it will be a great new tool for field biologists, naturalists, security and other services related with telemetry or biotelemetry.

References

1. Ferreira, R.B., Dantas, R.B., Tonini, J.F.R.: Distribuição espacial e sazonal de anfíbios em quatro poças na região serrana do Espírito Santo, sudeste do Brasil: influência de corredores florestais. Iheringia, Série Zoologia. Porto Alegre **102**(2), 163–169 (2012)
2. Mônico, A.T., Carvalho, R.B.G.C., Lopes, S.R., Peloso, P.L.V.: Anfíbios anuros de brejos e lagoas de São Roque do Canaã, Espírito Santo, Sudeste do Brasil. Papéis avulsos de zoologia **57**(16), 197–206 (2017)
3. Prado, G.M., Pombal, J.P.: Distribuição espacial e temporal dos anuros em um brejo da Reserva Biológica de Duas Bocas, sudeste do Brasil. Arquivos do Museu Nacional **63**, 685–705 (2005)
4. Grande, K.C., Schneider, B., Oliveira, R.L.. Monitoramento da scinax imbegue através de registros fotográficos e sonoros, para o desenvolvimento de banco de dados e material didático. Anais do XXIV Congresso Brasileiro de Engenharia Biomédica. Uberlândia: UFU, pp. 1789–1791 (2014)
5. Grande, K.C., Schneider, B.: Uso de tecnologias globais para a determinação de habitats de espécies bioindicadoras e transformações de territórios. Anais do XXV Congresso Brasileiro de Engenharia Biomédica (XXV CBEB). Curitiba: UTFPR, v. 1, pp. 2161–2164 (2016)
6. Ravindra, S., Jagadeesha, S.N.: Time of arrival based localization in wireless sensor networks: a linear approach. Signal Image Process. Int. J. (SIPIJ) **4**(4), 13–30 (2013)
7. Patwari, N., Ash, J.N., Kyperountas, S., Hero, A.O., Moses, R.L., Correal, N.S.: Locating the nodes: cooperative localization in wireless sensor networks. IEEE Signal Process. Mag. **22**(4), 54–69 (2005)
8. Wymeersch, H., Lien, J., Win, M.Z.: Cooperative localization in wireless networks. IEEE Signal Process. Mag. **97**, 427–450 (2009)
9. Zekavat, R., Buehrer, R.M.: Handbook of Position Location: Theory, Practice and Advances. Wiley, Hoboken, NJ (2011)
10. Sayed, A.H., Tarighat, A., Khajehnouri, N.: Network-based wireless location: challenges faced in developing techniques for accurate wireless location information. IEEE Signal Process. Mag. **22**(4), 24–40 (2005)
11. Patwari, N., Hero, A.O., Perkins, M., Correal, N.S., O'dea, R.J.: Relative location estimation in wireless sensor networks. IEEE Trans. Signal Process. **51**(8), 2137–2148 (2003)
12. Yerriswamy, T., Jagadeesha, S.N.: IFKSA-ESPRIT-estimating the direction of arrival under the element failures in a uniform linear antenna array. ACEEE Int. J. Signal Image Process. **3**, 42–46 (2012)
13. Jagoe, A.: Mobile Location Service: The Definitive Guide. Prentice-Hall, Upper Saddle River (2003)
14. Liberti, J.C., Rappaport, T.S.: Smart Antennas for Wireless Communications: IS-95 and Third Generation CDMA Applications. Prentice Hall PTR (1999)
15. Yerriswamy, T., Jagadeesha, S.N.: Joint azimuth and elevation angle estimation using incomplete data generated by faulty antenna array. Signal Image Process. Int. J. **3**(6), 99–114 (2012)
16. Brittain, F.H.: Sound location in live and stereophonic systems. Proc. IEE Part B Electron. Commun. Eng. **106**(14), 209–210 (1959)
17. Bancroft, S.: An algebraic solution of the GPS equations. IEEE Trans. Aerosp. Electron. Syst. **21**(1), 56–59 (1985)
18. Carter, G.C.: Variance bounds for passively locating an acoustic source with a symmetric line array. J. Acoust. Soc. Am. **62**, 922–926 (1977)
19. Chan, Y.T., Ho, K.C.: A simple and efficient estimator for hyperbolic location. IEEE Trans. Signal Process. **42**(8), 1905–1915 (1994)
20. Collier, T.C., Kirschel, N.G., Taylor, C.E.: Acoustic localization of antbirds in a Mexican rainforest using a wireless sensor network. J. Acoust. Soc. Am. **128**(1), 182–189 (2010)
21. Friedlander, B.: A passive localization algorithm and is accuracy analysis. IEEE J. Ocean. Eng. **12**, 234–245 (1987)
22. Schau, H.C., Robinson, A.Z.: Passive source localization employing intersecting spherical surfaces from time of arrival differences. IEEE Trans. Acoust. Speech Signal Process. **35**(8), 1223–1225 (1987)
23. Abel, J.S., Smith, J.O.: The spherical interpolation method for closed-form passive source localization using range difference measurements. In: IEEE International Conference on Acoustics, Speech and Signal Processing, vol. 12, pp. 471–474 (1987)
24. Behrens, J.W., Svendsen, J.C., Deurs, M., Sokolova, M., Christofersen, M.: Effects of acoustic telemetry transmitters on gill ventilation rate and haematocrit levels of round goby Neogobius melanostomus. Fish. Manag. Ecol. **24**(5), 416–419 (2017)

25. Binder, T.R., Farha, S.A., Thompson, H.T., Holbrook, C.M., Bergstedt, R.A., Riley, S.C., Bronte, C.R., He, J., Krueger, C.C.: Fine-scale acoustic telemetry reveals unexpected lake trout, Salvelinus namaycush, spawning habitats in northern Lake Huron, North America. Ecol. Freshw. Fish. **27**(2), 594–605 (2018)

26. Capello, M., Robert, M., Soria, M., Potin, G., Itano, D., Holland, K., Deneubourg, J., Dagorn, L.: A methodological framework to estimate the site fidelity of tagged animals using passive acoustic telemetry. PloS One **10**(8), e0134002 (2015)

Platform for Automated Acquisition of Ultrasonic Signals in Acoustic Tank for Tissue Characterization

Felipe Araujo Hollanda, Rodrigo Pereira de Oliveira,
Flavia Fernandes Ferreira da Silva, Marco Antonio von Krüger,
and Wagner Coelho de Albuquerque Pereira

Abstract

Quantitative ultrasound for diagnostic and analysis of bone diseases has been studied and development in ultrasonic characterization by several authors. The present study, with support of free software, presents a collection of tools written in python language. This enables the automation of a XYZ positioning system of an acoustic tank to scan samples of biological tissue with ultrasound. A platform with the embedded devices interfaces and a web application was developed in a single-board computer—Rapberry Pi (RPi). Webpages designed for human-computer interaction enable the operation of this plataform. The RPi was used to support the system that controlled the mechanism.

1 Introduction

Ultrasound (US) imaging is widely used in a range of medical applications. It has a series of advantages: Is non-ionizing, relatively inexpensive method, capable of imaging in real time. In addition, US examination is painless and provides real-time data about morphology, texture, size and shape of living tissues [1].

US imaging uses the pulse-echo technique: A function generator excites a piezoelectric transducer that generates ultrasonic pulses that travel through the medium under investigation interacting with its scatterers and surfaces. The reflected and back-scattered pulses return to the transducer carrying information of tissue parameters like propagation velocity and attenuation. In biological tissues such parameters may vary as a function morphology, composition and pathology [2, 3]. In ultrasonic manual operation techniques, the clinician can guide a conventional ultrasound probe over the anatomy to gather several scans. If the geometric orientation of each scan is precisely known, a map of any tissue surface at a desired dept can be constructed [4]. To evaluate small variations on surfaces of interest, precisely positioning the transducer is crucial.

Computerized systems that assist laboratory studies and practices are always required [5]. Automation of equipment used in this purpose may reduce acquisition time and improve the consistency of resulting images leading to better quality results [6]. The present work describes the development of an experimental platform for automation presenting a collection of open code software solutions with user-friendly input devices. It is applied in an acoustic tank for tissue characterization by quantitative ultrasonography in the Laboratory of Ultrasound (LUS) of the Federal University of Rio de Janeiro (UFRJ).

2 Materials and Methods

The platform developed in this work, used in the acquisition of data from an acoustic tank, consists of an automated device with a system responsible for mapping biological tissues using ultrasonic transducers. The system contains: a command interface for the stepper motors responsible for positioning the transducers; an interface to collect electrical signal coming from the transducer as digital data after performing a scan task, consecutive captures of ultrasonic waves, and, an interface control which deliveries the obtained data to the user by a synchronous logic mechanism after the scan task.

F. A. Hollanda (✉) · R. P. de Oliveira
Instituto Infnet, Rio de Janeiro, Brazil
e-mail: fhollanda@live.com

R. P. de Oliveira · F. F. F. da Silva · M. A. von Krüger ·
W. C. de Albuquerque Pereira
Programa de Engenharia Biomédica – COPPE, Universidade
Federal do Rio de Janeiro – UFRJ, Rio de Janeiro, Brazil

2.1 Stepper Motor Interface

In computational science, the term interface can be used, for example, to represent the form in which a software shows its functionalities to other softwares that do not require direct implementation, only their functionalities [7]. Taking advantage of this concept, the platform development began with the stepper motor interface.

The Stepper Motor Interface (SMI) was logically divided in services depending on the microservice architecture. With this architectural style, rather than thinking of software as an autonomous unit, the application is separated into several services, each with specific functionalities. Once the platform integrates different devices, this logical division allows the usage of the equipment interfaces for other purposes in the laboratory.

The main functionality of the SMI is to supply an abstraction for the communication with the Arrick Robotics C4 controller, which receives text instructions in ASCII in a specific format described in the manual. The SMI also communicates with the signal acquisition module that acts as an interface of the measurement instrument.

With the platform, the user does not have to write commands texts and send them to the serial port, not even know how the instructions are produced. It is only necessary to insert the parameters on the form screen and begin the scan task. It is enough to promote the movement of the motors and obtain a matrix of values during the acquisitions.

Based on the idea that a service has only one task, the structure was built in a way that one API acted as an orchestrator and the others could be independent. Figure 1 shows the block diagram of the system, and its relation between the user, SMI, Arrick stepper motor and Signal

Acquisition Module. The SMI and Signal Acquisition Module ran embedded at the RPi and were written in Python language.

The main blocks of Fig. 1 are described as follows:

Motor. Backend service that acts as an interface to the C4 controller, translating the data obtained in JavaScript Object Notation (JSON) to the language of the controller, indirectly driving the proper function of the motors.

Adapter. Responsible for interpreting the commands abstraction from the web application. Acts as a manager once orchestrate the motor service or signal acquisition module activation. After obtaining digital data from the signal acquisition module, the adapter saves them in a structure that allows the user to download data any time.

Web-App. As the name suggests, it contains all screens to users. It is the system input port, so it must be friendly-designed so all functionalities should be easily found.

2.2 Communication Between Interfaces

The user accesses web application screens and, through them, provides the system with the required information so the adapter may activate the interface of the equipment. When required, the motor translate data received by the adapter and send them to the C4 controller. Once the scan is finished, the user receives a confirmation on the screen that the capture is available. The user is also informed when errors occur.

Fig. 1 Block diagram of the system
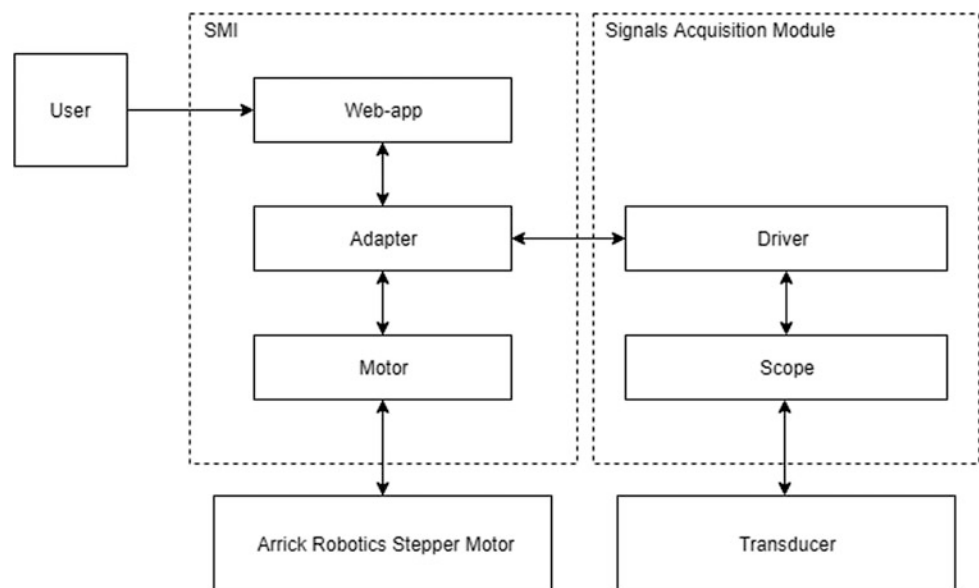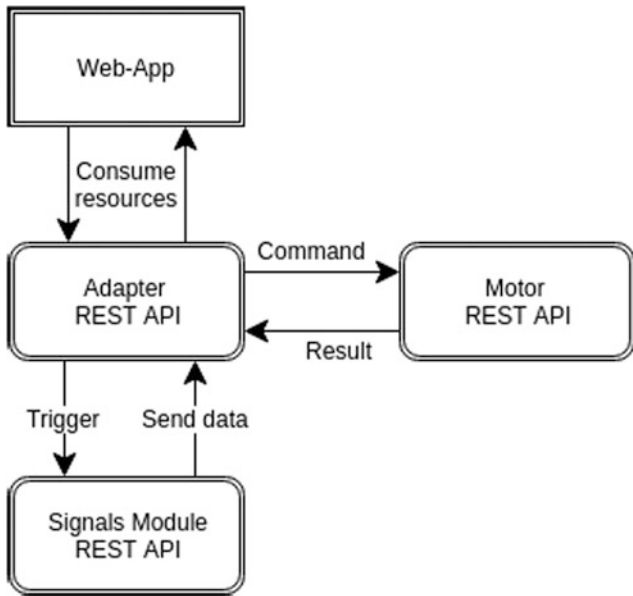
Fig. 2 Block diagram of the communication between the interfaces of the platform

A standardization of data exchange is needed. For the communication between interfaces may happen, JSON has been used for this purposed once it is a lightweight data-interchange format. It is easy for humans to read and write and is completely language independent [8]. These exchanged data use the Hypertext Transfer Protocol, also known as HTTP. This protocol was selected because it is widely used in several computational applications. Figure 2 shows the communication between the interfaces of the platform.

2.3 Implementation of the Pulse-Echo Mode in an Acoustic Tank

Figure 3 shows the diagram of the pulse-echo mode used in this work. The transducer acts as both transmitter (TX) and receiver (RX) of ultrasonic waves. An electric pulse is applied to the transducer, which generates an ultrasonic wave [9]. This wave propagate trough the water in the acoustic tank and through the submersed sample (at a known distance from the transducer), interacts with the different tissues and is partially reflected back to the transducer at every interface. By the differences between the emitted and received pulses, it is possible to describe the interaction of the wave with the sample and use this information on developing new diagnosis techniques.

This pulse-echo method may be implemented by using a function generator to produce sine waves bursts in conjunction with the input of one of the channels of the oscilloscope, which is also connected to the transducer. The function generator will emit the electrical signal to the transducer and the oscilloscope will capture the reflected ultrasonic wave. To synchronize the equipment, it is necessary to connect the output trigger of the function generator with the input trigger of the oscilloscope. In the setup, it is possible to visualize and capture both emitted and reflected signals.

2.4 Signal Acquisition Module

The function of the Signal Acquisition Module is to obtain analog signals coming from the ultrasonic transducer,

Fig. 3 Diagram of the ultrasonic pulse-echo mode

digitize them with a digital oscilloscope and send this data in a simple structure to the RPi. This means that when activated by the Adapter service, a "data-request" is sent in the expected format to the serial port to the oscilloscope. In the same way, the acquisition module receives back the values of the digital signals; converts this data to JSON, and save them in file format and return them back to the Adapter. Figure 4 shows the block diagram of the communication between the service interface with the control module, which acts as a driver, and the oscilloscope.

An ultrasonic Signals Acquisition Module was implemented using the oscilloscope used in the Laboratory. The driver available as a free software supported the translation of the commands to this device. An API REST was created so the control could be executed independently from the web application.

The captured data may be downloaded in JSON or Matlab® formats. The user may choose which tool is more convenient for posterior reconstruction and processing of the ultrasonic spectra and visualization of the characterized
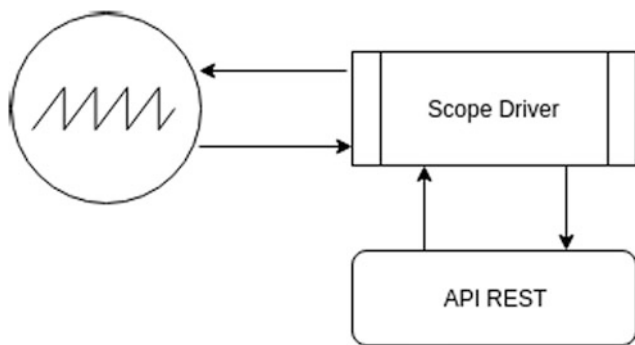
sample in grey scale. Further studies will computerize the map construction from the collection of scans.

2.5 Complete Platform Hardware

The platform contains hardware, such as Olympus Panametrics V303-SU 1 MHz ultrasonic transducers, Tektronix TDS2024B oscilloscope, Tektronix AFG3021B arbitrary functions generator, an Arrick Robotics XYZ positioning system and, for controlling these equipment, a Raspberry Pi computer. Figure 5 shows the complete platform using RPi, placed in front of the oscilloscope.

The developed system was used to acquire US signals. Figure 6 shows an acquisition made with the plataform. There on can see the excitation signal (1) and reflected signal (2).

3 Discussion

As much as Fowler [10] stated that the construction of a monolithic application is easier and the right way to work for productivity purposes, building the system into a structure of services helped the better visualization of boundaries of each part of the system, so, they could be reused in different experiment setups in the laboratory.

The initial motivations to use the architecture of microservices were based on the requirements, which included not knowing how much the RPi would be loaded and or if it would be necessary to use more than one board, the easiness of changing and/or implementing new graphical interfaces and the possible change in requirements during the project. A suite of smaller services is easier to maintain, to evolve and to be replaced than a monolithic architecture.

Fig. 4 Block diagram of the communication between the service interface with the control module and the oscilloscope

Fig. 5 Photograph of the complete experimental setup for acoustic characterization of samples
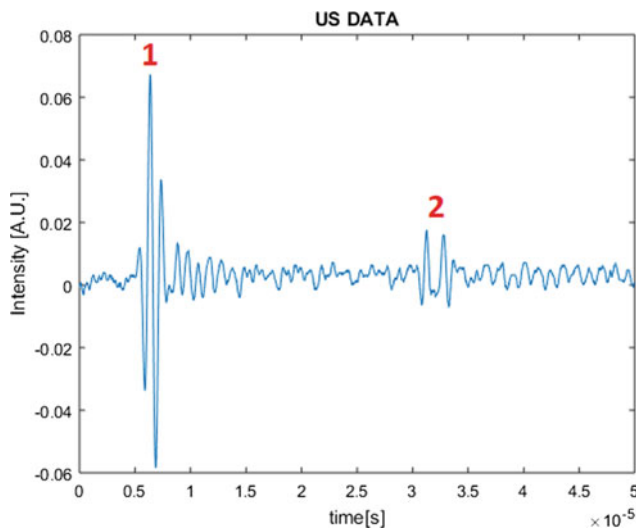
Fig. 6 Signal acquisition made with the platform: (1) excitation signal and (2) reflected signal

The development trough interfaces with architecture based on smaller and replaceable services may be an option for lowering the impact of requirement changes during the elaboration of bigger projects.

4 Conclusion

This work develops a platform to automate the acoustic characterization of living tissues that is available under the GNU GPL (GNU General Public License), in the repository of version control Github (https://github.com/fhollanda/Stepper-Motor-Interface). By this way, this platform may be used and modified for everyone who has interest in the matter, without explicit approval of the authors, as its license is open. The microservices architecture choice favors the reuse, which contributes to the project to remain in

replaceable smaller modules and independent of new technologies.

A complete interface was developed for the intelligent movement controller, Arrick Robotics C4 device using REST architecture style, in such manner that its API could control the motor operation. This interface may be used in future experiments of different research institutions.

Conflict of Interest The authors certify that they have NO conflict of interest in the subject matter or materials discussed in this manuscript.

References

1. Kiessling, F., et al.: Recent advances in molecular, multimodal and theranostic ultrasound imaging. Adv. Drug Deliv. Rev. **72**, 15–27 (2014)
2. Jaeger, M., et al.: Computed ultrasound tomography in echo mode for imaging speed of sound using pulse-echo sonography: proof of principle. Ultrasound Med. Biol. **41**(1), 235–250 (2015)
3. Caschera, L., et al.: Contrast agents in diagnostic imaging: present and future. Pharmacol. Res. **110**, 65–75 (2016)
4. Chen, T.K., et al.: Importance of transducer position tracking for automated breast ultrasound: initial assessments. In: 2012 IEEE International Ultrasonics Symposium (IUS), pp. 2623–2626, Dresden, Germany (2012)
5. Shortliffe, E.H., Cimino, J.J.: Biomed. Inform. Springer Science +Business Media, LLC (2006)
6. Brandli, L.: Benefits of protocol-driven ultrasound exams. Radiol. Manag. (4), 56–59 (2007)
7. IEEE 100: The Authoritative Dictionary of IEEE Standards Terms, pp. 574–575 (2000)
8. JSON.org: https://www.json.org. Accessed 20 Mar 2018
9. Assef, A.A., et al.: Sistema para geração, aquisição e processamento de sinais de ultra-som (2009)
10. Fowler, M.: Microservice premium: the microservices architectural style (2015). https://martinfowler.com/bliki/MicroservicePremium.html. Accessed 20 Mar 2018

Pulse Transit Time Measurement Using Bioimpedance

Andrei L. A. Pires and Marcio N. Souza

Abstract

Cardiovascular disease is a factor that leads to mortality in the populations of industrialized countries, being the large arteries pathology the main cause of morbidity and death from such disease. A functional characteristic of arteries that is changed under pathological conditions is their wall stiffness. Early diagnosis of such arterial alterations may identify individual risks to clinical complications, allowing retardation of the pathological process. Some examples of non-invasive methods of arterial stiffness assessment are the pulse wave velocity (PWV) and the pulse transit time (PTT). The present work proposes a PTT measurement system that estimates the time interval between the R wave of the QRS complex and the arrival of the pressure pulse wave at radial artery by using the bioimpedance technique to detect such arrival, instead of pressure transducers. Preliminary tests were made, taking two different points of the bioimpedance signal, and discounting or not the pre-ejection period. The PTT results, obtained from six volunteers, were on average close to the ones obtained by some other works using different techniques and measure points: 240 ms against 250 ms (literature) and 112 ms against 110 ms (literature). These values were collected by taking the interval between ECG peak and bioimpedance peak or bioimpedance maximum slope, respectively. Despite the need for more tests, the findings indicate that the system designed in this work may be used for arterial stiffness evaluation.

1 Introduction

Cardiovascular disease is a factor that leads to mortality in the populations of industrialized countries, being the large arteries pathology the main cause of morbidity and death from such disease [1]. A functional characteristic of arteries that is changed under pathological conditions is their wall stiffness, which is linked to several cardiovascular risk factors, such as age, male gender, abnormalities in lipoproteins and diabetes. It has been proposed that an increase in arterial stiffness is associated to the beginning and/or progression of atherosclerosis and arterial hypertension [2].

Given the insidious nature of those diseases, early diagnosis of such arterial alterations may identify individual risks to clinical complications, allowing retardation of the pathological process. Even though many ways to detect arterial stiffness are employed nowadays (e.g. pressure pulse [3]), some are invasive and/or use a measurement method that interferes on the measured value.

Some examples of non-invasive methods of arterial stiffness evaluation are the pulse wave velocity (PWV) [4], defined as the velocity of the blood pressure pulse wave within a vessel, and the pulse transit time (PTT) [5], defined as the time interval between the electrical activity of the left ventricle and the peripheral pulse wave. Both methods normally use pressure transducers placed on superficial arteries (e.g. brachial and radial arteries), but because the transducers are fixed to the monitored limb with elastic strips they can provoke a counter pressure that may influence the measurement. Thus, a measurement technique that could estimate the arterial pulse passing through the desired superficial arterial measurement site without influence on the pressure mechanical wave could be used to substitute the

A. L. A. Pires (✉)
Polytechnical School, Electronic and Computer Engineering Department, Universidade Federal do Rio de Janeiro, Rio de Janeiro, Brazil
e-mail: andreilenine@poli.ufrj.br

M. N. Souza
Biomedical Engineering Program, Universidade Federal do Rio de Janeiro, COPPE, Rio de Janeiro, Brazil
e-mail: souza@peb.ufrj.br

pressure transducers and provide better estimations of PWV and PTT.

The present work proposes a PTT measurement system that estimates the time interval between the R wave of the QRS complex and the arrival of the pressure pulse wave at radial artery by using the bioimpedance technique to detect such arrival, instead of pressure transducers.

2 Materials and Methods

As aforementioned, PTT reflects the delay between ventricular contraction and the mechanical blood pulse wave arrival at a determined part of the body, the radial artery in present case. ECG R wave occurs at the beginning of heart systole, when blood is injected in aorta artery and creates the pulse pressure wave, which travels to body periphery. So, the R wave is a good reference as the start of the pumping cycle, being easy to detect via an ECG acquisition system.

A vessel elasticity is one of the factors related to how fast a pressure pulse travels within such vessel, as proposed in 1878 by Moens and Korteweg [6] (Eq. 1). Hence, each left ventricle contraction ejects a blood pressure wave from the heart to the arterial system, whose speed depends mostly on the bigger caliber elastic arteries.

$$PWV = \frac{D}{PTT} = \sqrt{\frac{tE}{\rho d}} \qquad (1)$$

where D is the length of the vessel, t is the thickness of its wall, d is its diameter, ρ is blood density and E refers to Young's modulus of arterial wall elasticity.

By Eq. (1) one can see that small PTT values are associated with reduction of arteries' calibers and/or their elasticity; considering equally large arterial segments and with small blood density variability.

2.1 Instrumentation

In order to detect the ventricular contraction, a basic ECG acquisition system was implemented with an instrumentation amplifier (voltage gain = 139), right leg driver (DRL), a high-pass filter (cutoff frequency of 0.87 Hz) for baseline removal and a low-pass amplifier (cutoff frequency of 50 Hz) to remove high frequency interferences (Fig. 1). This system was used in CC5 setting (left and right fifth intercostal spaces, with reference electrode above belly button scar) to minimize the influence from the bioimpedance detection system on the ECG acquisition system.

The bioimpedance system used to evaluate the arrival of the blood pressure pulse at the radial artery was composed by many modules. The first one may be described as a classical bioimpedance tetrapolar measurement system, constituted of two current-excitation electrodes and two voltage-measure electrodes. Excitation electrodes were placed on the medial part of the forearm and on the back of the ipsilateral hand (reference electrode). Electrodes for the measurement of the resulting voltage on the bioimpedance were placed on the medial epicondyle of the arm and on the radial artery site (Fig. 1).

The chosen frequency for the current excitation of the bioimpedance system was 50 kHz, as it is the most used in single frequency bioimpedance measurements [7].

Fig. 1 Diagram showing the main system blocks and the electrodes placement for ECG and bioimpedance associated with blood pressure pulse
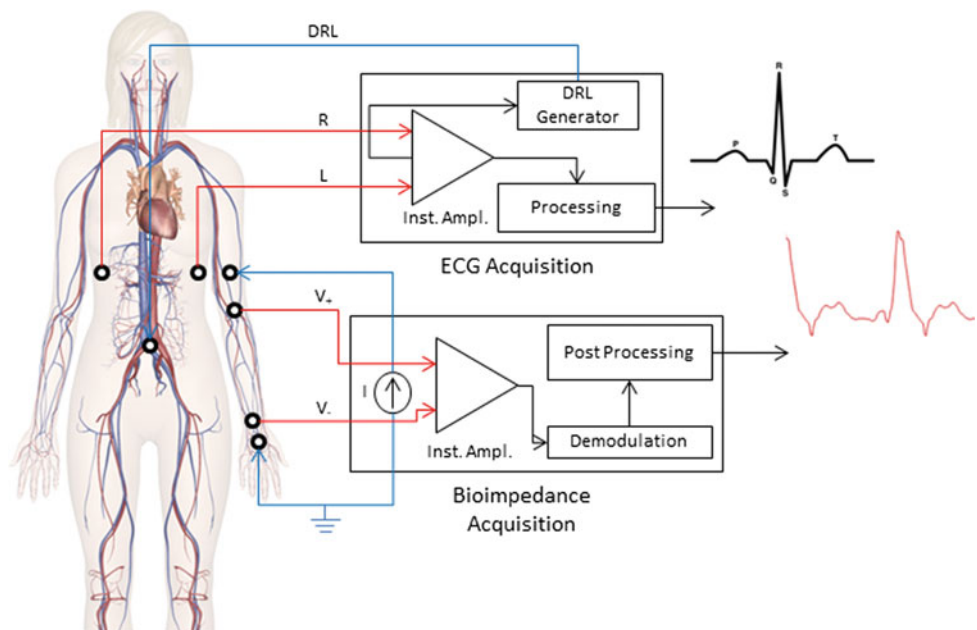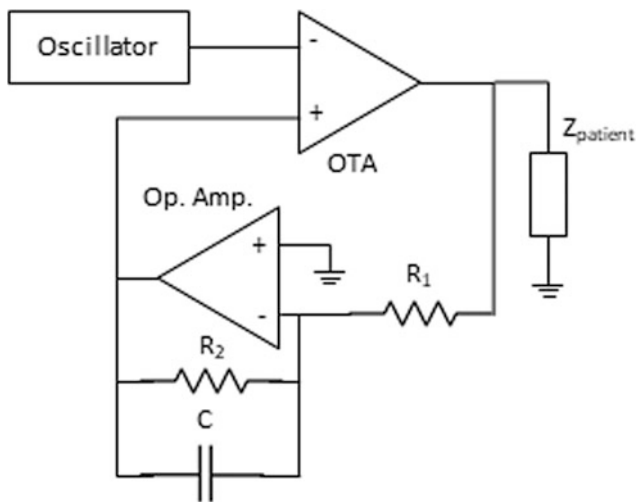
Fig. 2 Diagram illustrating schematically the generation of the electrical current excitation

The sinusoidal excitation current signal was generated using a classic Wien bridge oscillator, later converted from voltage to current by an operational transconductance amplifier (OTA). The output current peak was adjusted to 1 mA. A circuit for DC level correction was employed to stabilize the offset in the output current (Fig. 2). It must be mentioned that the ground symbol refers to the circuit potential reference and not the power outlet ground. Moreover, the circuit uses an isolate DC power supply.

Bioimpedance-related voltage measurement starts in an instrumentation amplifier (voltage gain = 6) followed by a synchronous demodulator with cutoff frequency of 30 Hz, that supplies a signal proportional to the magnitude of the evaluated segment bioimpedance (Fig. 3).

Because the aimed signal is related to the arrival of the arterial pulse and that such arrival will cause a change on the basal bioimpedance under the radial artery, the post-processing circuit for the bioimpedance signal from the demodulator was constituted of a high-pass filter (1st order) with cutoff frequency of 0.87 Hz, intended to reduce breathing artifacts; followed by two amplifying stages with 150 gain each and cutoff frequency of 15 Hz (1st order low-pass), intended to reduce high-frequency interferences.
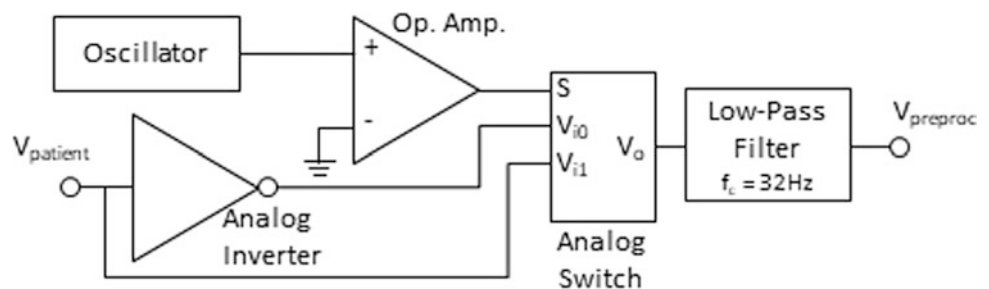
From the block diagram of Fig. 1 and the description of the main block, one can realize the ECG and the output of impedance circuit are continuous signals. In this first version of the proposed method such signals were visualized and captured using a digital oscilloscope (*Tektronix* model TDS 210) for post processing the PTT values.

To compensate the greater quantity of low-pass circuits in bioimpedance acquisition system, when compared with the ECG system, the biggest possible group delay was estimated, taking the ECG as reference. From the analytic expressions and simulations of the low-pass filters, the biggest possible group delay was estimated around 23 ms.

2.2 Measurement Protocol

The evaluation of the PTT by using bioimpedance was made by measurements in six volunteers (procedure approved at the Ethics Committee in Research of the University Hospital Clementino Fraga Filho under number 1.343.260). Two PTT measures were taken from each volunteer, from which an average was obtained.

PTT measures were taken with the volunteer seated, after a resting period of 5 min, following the reading and signature of the Free and Informed Consent Form. Before the electrodes placement the stratum corneum was removed by abrasion with alcohol-soaked gauze. The electrodes used for ECG and bioimpedance were *Meditrace* (model 200—Adult). Due to the system high sensibility, it was recommended that the volunteer stayed in apnea for the PTT measurement.

2.3 Evaluation

PTT measurement is not exactly standardized in what concerns how to obtain the measured value ([5, 6, 8–11]), so for the evaluation of the proposed measurement system three methods already cited in the literature were tested. The first method considers the peak of ECG R wave and also the peak of the bioimpedance signal, without discounting the time between electrical depolarization of the left ventricle and

Fig. 3 Diagram illustrating schematically the demodulation system

aortic valve opening (Pre Ejection Period—PEP, which is estimated as 7% of ECG R-R interval [6]). The second method considers the same time instants in the mentioned signals, but does discount PEP. The third method uses the same reference in ECG signal and considers the greatest slope point (that is close to, but not the peak) in the bioimpedance signal.

PTT average values considering the three mentioned methods of calculation were compared to values reported in literature, regarding the age range and physiological state of the volunteers.

3　Results

During some bioimpedance measurements, power line interference was noticed. Nevertheless, it was not comparable in amplitude to the peak associated with the highest pressure variation. Then, there was no direct interference on the result.

Table 1 shows raw PTT average values (just subtracting the biggest group delay) for the six volunteers organized in ascending order of age. Table 2 depicts the values before and after correction by the two above-mentioned methods of calculation. In both tables one can see the PTT values decrease with the age, which can be an ordinary consequence of the increase of the arterial stiffness.

4　Discussion

PTT values obtained from method 1 were on average smaller than some ones previously mentioned [8, 9] (250 ms); these works considered PTT obtained mainly from the peak of R wave to 25% of the pressure peak height on the patient's finger, with no discount of PEP. Results obtained using method 2 were also consistent, at least if the patient has a heart rate close to 75 bpm. Calculation by method 3 produced results close to those obtained in [5] (about 112 ms); this work measured PTT using the peaks in the signal of the pressure pulse in radial artery, the same studied in the present work. Moreover, method 3 better exposed the inverse relationship between age and PTT, as expected.

5　Conclusion

According to our findings, the proposed PTT measurement system is capable of evaluating correctly the pressure pulse progression time through large arteries. However, further tests, in a greater quantity of volunteers, must be made to really evaluate the system. Furthermore, improvements in the circuit assembly and the implementation of a digital data acquisition system to obtain automatic measurement of PTT will be performed, in order to make the system more reliable and useful for determining the increase in arterial stiffness.

Table 1 PTT values of the volunteers (deducted the group delay from the measurement circuit)

Volunteer	Sex	Hypertension	Age (years)	PTT (ms)
1	M	No	18	317
2	F	No	20	217
3	M	No	23	241
4	M	No	49	241
5	F	No	50	209
6	M	Yes, controlled	59	222

Table 2 PTT values of the volunteers before and after proposed corrections (see the text for more details)

Volunteer	Sex	Hypertension	Age (years)	Method 1 (ms)	Method 2 (ms)	Method 3 (ms)
1	M	No	18	317	258	144
2	F	No	20	217	180	145
3	M	No	23	241	185	136
4	M	No	49	231	179	97
5	F	No	50	209	150	75
6	M	Yes, controlled	59	222	173	73
General average			37	240	187	112
General std. deviation			17	36	33	31

In future further studies can consider the comparison of the proposed method with the ones that use pressure transducers placed on superficial arteries.

References

1. Gunjača, G., Budimir, D., Boban, M.: Increased arterial stiffness and central systolic blood pressure as indicators of impaired vascular function in hypercholesterolemic subjects. In: 6th Croatian Congress of Pharmacology with International Participation (2010)
2. Sá Ferreira, A.: Plasma homocysteine and arterial stiffness: risk factors or risk markers for cardiovascular diseases? J. Clin. Hypertens. 17(8), 601–602 (2015)
3. Mackenzie, I.S.: Assessment of arterial stiffness in clinical practice. QJM 95(2), 67–74 (2002)
4. Ferreira, A.S., et al.: Determination of radial artery compliance can increase the diagnostic power of pulse wave velocity measurement. Physiol. Meas. 25, 37 (2004)
5. Zhang, Y.-L.: Radial pulse transit time is an index of arterial stiffness. Nat. Hypertens. Res. 34, 884–887 (2011)
6. Sharma, M., Barbosa, K., Ho, V., Griggs, D., Ghirmai, T., Krishnan, S.K., Hsiai, T.K., Chiao, J.-C., Cao, H.: Cuff-less and continuous blood pressure monitoring: a methodological review. Technologies 5, 21 (2017)
7. Martinsen, O.G., Grimnes, S.: Bioimpedance and Bioelectricity Basics. Academic Press (2011)
8. Pitson, D.J.: Value of beat-to-beat blood pressure changes, detected by pulse transit time, in the management of the obstructive sleep apnoea/hypopnoea syndrome. Eur. Respir. J. 12(3), 685–692 (1998)
9. Pitson, D., et al.: Changes in pulse transit time and pulse rate as markers of arousal from sleep in normal subjects. Clin. Sci. 87(2), 269–273 (1994)
10. Wong, M.YM., Poon, C.C.Y., Zhang, Y.T.: An evaluation of the cuffless blood pressure estimation based on pulse transit time technique: a half year study on normotensive subjects. Cardiovasc. Eng. 9, 32 (2009)
11. Buxi, D., Redouté, J.-M., Yuce, M.R.: A survey on signals and systems in ambulatory blood pressure monitoring using pulse transit time. 2015 Institute of Physics and Engineering in Medicine, IOP Science

Quantification of the Finger Tapping Test Based on the Flex Sensor—A Single Case Study

Gabriel Jablonski, Luiza Maire David Luiz,
Amanda Gomes Rabelo, and Adriano O. Andrade

Abstract

Bradykinesia is one of the main motor symptoms caused by Parkinson's disease (PD). Together with other impairments, PD can severely impact activities of daily living. A proper diagnosis and continuous monitoring of PD can lead to motor rehabilitation and the use of medication that can ease the burden of the symptoms. One of the tests used to assess the severity of the PD is the Finger Tapping Test (FTT), which is already extensively used along with several methods to quantify hand movements and verify the presence of slowness of movement and/or its increase over time, however these methods can be rather expensive and hard to implement in a clinical scenario. In this research, we present a relatively cheap and easy-to-use device, capable of measuring certain hand movements made during the FTT, namely pinch movements, using an ink-based flexion sensor (Flex Sensor). Comparing readings made with this sensor against data acquired through inertial sensors, it was possible to confirm the reliability of this alternative method for quantifying the FTT.

Keywords

Parkinson's disease • Bradykinesia • Finger tapping test

1 Introduction

Parkinson's Disease (PD) is a neurodegenerative disorder which causes significant motor disabilities. One of its main signs of incapacitation is bradykinesia, defined as the progressive reduction of the velocity and amplitude of motion associated with general motor actions. The slowness of movements causes difficulties in carrying out activities of daily living [1].

The Movement Disorder Society—Unified Parkinson's Disease Rating Scale (MDS-UPDRS) is considered the gold standard for the clinical evaluation of PD [2, 3]. In Part III of the scale, which is related to motor examination, the item 3.4 proposes the Finger Tapping Test (FTT) for the evaluation of the severity of PD. An inadequate performance on the FTT can be associated with the loss of neurons in the substantia nigra [4, 5]. However, the subjectivity of the MDS-UPDRS can lead to results that are hard to reproduce, causing difficulty in its interpretation [6], hence the need for quantitative methods which are simple and easy to apply.

Some studies present the possibility of measuring the finger tap movements using inertial sensors [6], special cameras [7], and other types of sensors [8]. In clinical practice, it is desirable to use devices that are inexpensive and simple to operate, characteristics generally not associated with the instruments aforementioned, as high-quality cameras can cost thousands of US dollars (e.g. OptiTrack, USA), and inertial sensors have complex features [9] that can be unnecessary for this type of analysis.

Considering the need of an easy-to-operate device dedicated to the evaluation of bradykinesia in the clinical practice, this study presents a solution capable of acquiring and analyzing parameters involved in the application of the FTT. The system employs an ink-based flexion sensor, called Flex Sensor. A preliminary description and results of the system were reported in [10].

In the present work, the main features of the developed hardware and software are presented. Ergonomic advancements of the system are discussed, although the focus is on the validation of the Flex Sensor for the measurement of the speed of pinch. The results, which are based on a single case study, are compared with those obtained from inertial sensors available in the well-established TREMSEN (Precise Tremor Sensing Technology, the National Institute of Industrial Property, Patent number BR 102014023282-6

G. Jablonski (✉) · L. M. D. Luiz · A. G. Rabelo · A. O. Andrade
Centre for Innovation and Technology Assessment in Health,
Federal University of Uberlândia, Uberlândia, Brazil
e-mail: gabriel.jablonski.ufu@gmail.com

A. O. Andrade
e-mail: adriano@ufu.br

A2), which was developed by our research group and has been applied in several studies [11–13].

2 General Description of the Device

2.1 Sensor and Hardware

Figure 1 shows the main sensor of the device, which is a resistive ink-based flexion sensor, the Flex Sensor, produced by Spectra Symbol (USA). Its relevant characteristics, as claimed by the manufacturer, are high durability (it can withstand over 1 million flexions), compact size, and versatility, as it is extremely straightforward to use, functioning as if it were a simple resistor with a variable resistance.

The sensor has a flat resistance value, which increases depending on how much it is being bent, up to at least two times the flat resistance at an angle of 180°. With the intention of capturing this change in resistance, the sensor was connected to a voltage divider, alongside a resistor, properly dimensioned as to provide a significant range in the output voltage, taking into consideration the minimum and maximum values of resistance of the sensor and the desired input and expected output of the voltage divider. As suggested by the manufacturer, an operational amplifier (namely the LM324) was employed between the voltage divider and the final output, to reduce possible unwanted fluctuations in the readings due to the source impedance of the Flex Sensor when used with a voltage divider.

The input and output voltage of the voltage divider, as well as the control of all other features in the hardware, are handled by the microcontroller board Arduino Uno, an entry level board from the prototyping platform Arduino, widely used by both novices and professionals for projects in the field of electronics. Some of the output ports of the board (5 V) were used to supply the voltage divider, two LEDs, and other secondary features, which will be mentioned ahead. The output of the voltage divider is read by an analog port and then converted by the board's 10-bit resolution analog-to-digital converter, that produces 1024 discrete values, or levels, available from the conversion. The pins have an operating voltage of 5 V, meaning the resolution of the converter is of approximately 4.88 mV.

Following the results reported on the initial assessment of the device [10], some aspects were changed, accompanying some new features, shown in Fig. 2 and followed by the description.

Fig. 1 The flex sensor

1 - Test state LED
2 - Device state LED (RGB)
3 - Arduino USB port
4 - Flex Sensor connector
5 - Trigger connector
6 - Signal input connector
7 - Signal output connector
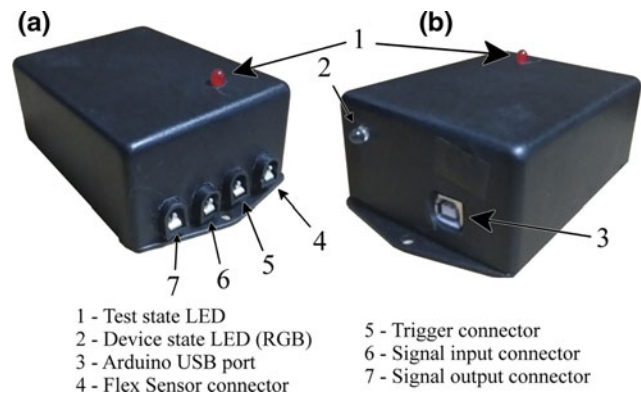
Fig. 2 Identification of the main features of the device. **a** Front view. **b** Rear view

Two LEDs are available, one indicating that the device is operating (feature 2), and the other one that a test protocol is running (feature 1). The latter can be used to provide visual feedback for a subject while performing a task.

The system has 5 inputs, all indicated in Fig. 2. The trigger is used for data annotation purposes. A pushbutton is connected to the trigger input (feature 5) so that the user can generate annotations whenever necessary. An auxiliary signal can be connected to one of the inputs (feature 6) and it will be reproduced in the output (feature 7).

2.2 Software

The source code for the Arduino board, written in the Arduino Language, based on the well-known and widely used programming language C++, is responsible for controlling the LEDs and the other features, as well as for setting the sampling rate for the data acquisition, which was 200 Hz in our tests. The signal is sent to the serial port of the PC via an USB cable.

The online plotting and general handling of the signal is made with the high-level, general-purpose programming language Python, where ready-to-use code is available in countless libraries, or modules, mostly made by the community, covering a broad range of subjects. The main modules utilized in this project are: PyQt5, dedicated to building complete, fully-operational graphical user interfaces (GUIs); Matplotlib [14], also dedicated to GUIs, focusing on publication-quality image generation; and the scientific computing tools package SciPy [15], used to efficiently deal with constant flow of data, and for statistical analysis.

2.3 Sensor Positioning and Ergonomics

Another point to be taken into consideration is the positioning of the sensor on a subject's hand. Originally, the Flex
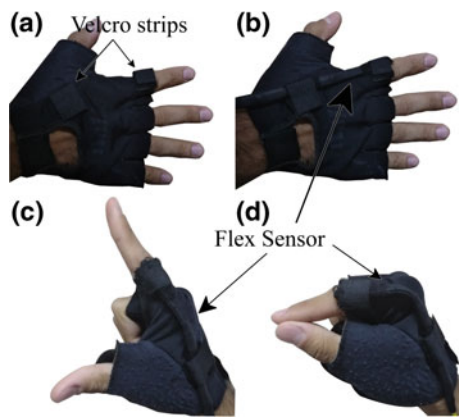
Fig. 3 **a** The glove with the added Velcro strips. **b** The sensor positioning. **c** The beginning of the pinch movement. **d** The end of the pinch movement

Sensor was positioned directly between the thumb and index finger [10], but it turned out to be not ideal.

Currently, the positioning that seems to work best is in the region that comprehends the metacarpus and the proximal phalanx of the index finger. In this way, the hand movement is unobstructed, and the impact of the fingers during the FTT does not interfere on the detected signal. To avoid the need for tape or any other kind of tool for fixating the sensor to the hand, a fingerless glove was employed. Velcro strips were added to the points in the glove correspondent to the areas described above. Figure 3 depicts the glove, the position chosen for the sensor and the finger positioning in beginning and end of the FTT.

3 Methods for Data Analysis

To ensure the data acquired with the Flex Sensor is consistent with the hand movements, at least to the point where it can be used to determine the period between pinches, the TREMSEN system was used simultaneously during data acquisition. It is safe to assume that the inertial sensors available with the TREMSEN, each one equipped with an accelerometer, a gyroscope, and a magnetometer, if properly utilized, can precisely describe the type of movement being analyzed.

3.1 Data Acquisition

This study was approved by the Ethics Committee on Human Research (CAAE: 65165416.4 0000.5152) of the Federal University of Uberlândia. Prior to participation in the study, the participant received a detailed explanation, who then voluntarily signed a consent form.

A single healthy subject, aged 20 years old, was instructed to perform the fine pinch movement repeatedly, in four different test blocks. In the first three, the subject was prompted to try and follow the rhythm provided by a digital metronome, set to different frequencies (3.33 Hz, 1 Hz and 2 Hz, respectively). In the last task, the movement was performed without the audio stimulus, but with the instruction to try and keep a uniform rhythm. In each block, the subject executed at least 40 pinches.

Figure 4 shows the placement of the inertial sensors, with their respective axis orientations, as well as for the glove with the Flex Sensor.

3.2 Signal Pre-processing

As the validation is based on the detection of central points in the signals, and they generally present a substantial amount of noise, applying a filter is essential to improve the performance of the algorithm responsible for detecting these points. A second order low-pass digital Butterworth filter, with a 15 Hz cutoff frequency, was applied to the signal from both sensors. Although the amplitude may be attenuated by the filter, the signal does not get displaced in time, guaranteeing that this analysis will still generate consistent results.

Since each sensor has its own unique measurement unit (volts for the Flex Sensor, Gauss for the magnetometer, degrees per second for the gyroscope, and g-units for the accelerometer), to facilitate operating with data from

Fig. 4 **a** Top view of the hand with all sensors positioned. **b** Orientation of the axes for the inertial sensors during the pinch movement
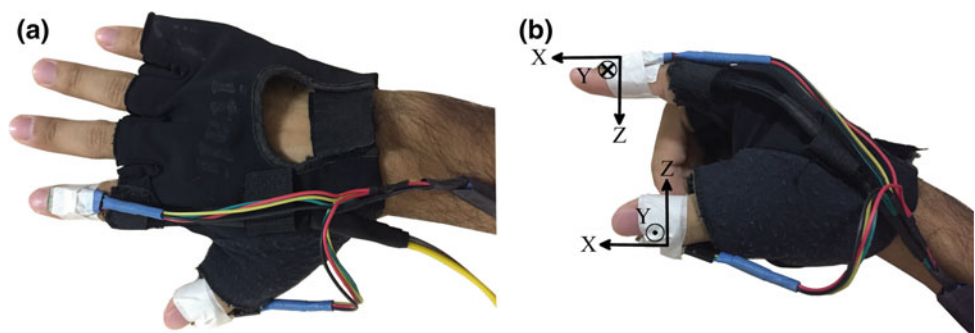
Fig. 5 Visual depiction of the center point detection algorithm
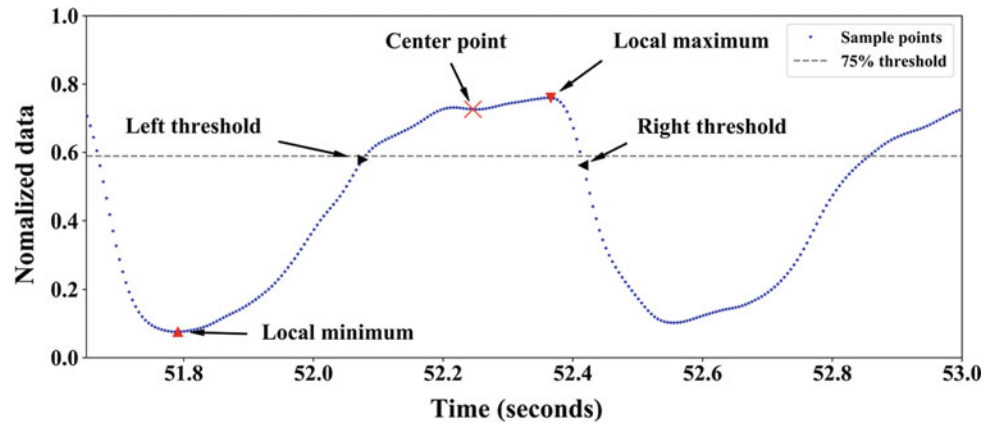
different sensors simultaneously, all signals were normalized between 0 and 1, using Eq. 1,

$$x_i' = \frac{x_i - \min(x)}{\max(x) - \min(x)} \tag{1}$$

where x is the input signal, x_i is the sample to be normalized, $\min(x)$ and $\max(x)$ are the minimum and maximum values of x, and x_i' is i-th normalized sample.

The z axis of the accelerometer placed on the index finger (A_z) was chosen as the reference for comparison with the data acquired with the Flex Sensor.

3.3 Central Point Detection Algorithm

In the present work, the "central point" was defined as the center point of a pinch movement. Figure 5 depicts the main elements necessary for the definition of a central point. For its detection, firstly, the local maxima (peaks), and local minima (valleys), are detected. Based on each one of the peaks and their respective closest valley, a threshold value is set to 75% of the difference in amplitude between the two

points. The first points to transpose the threshold are then marked, one to the left and one to the right. Based on these landmarks, the center point is determined as the half way point between them.

Figure 6 shows a sample from each one of the signals being analyzed, already filtered and normalized, along with the output from the center point detection algorithm.

3.4 Analysis of the Time Between Central Points

The final step in data processing was to estimate the period (Δt) for each pinch movement performed by the subject, to be used as the comparison parameter. This period is defined as the time elapsed between each central point and the following one. For each block, 31 points, or 30 periods, were considered.

Statistical Analysis. The Tukey Mean-Difference plot, a statistical method to assess agreement between two measurement techniques [16], was popularized in the field of medical statistics by Bland and Altman [17], thus being referred to as the Bland-Altman plot. This analysis became

Fig. 6 Signals from the accelerometer's z axis and the flex sensor, filtered and normalized, with the center points marked
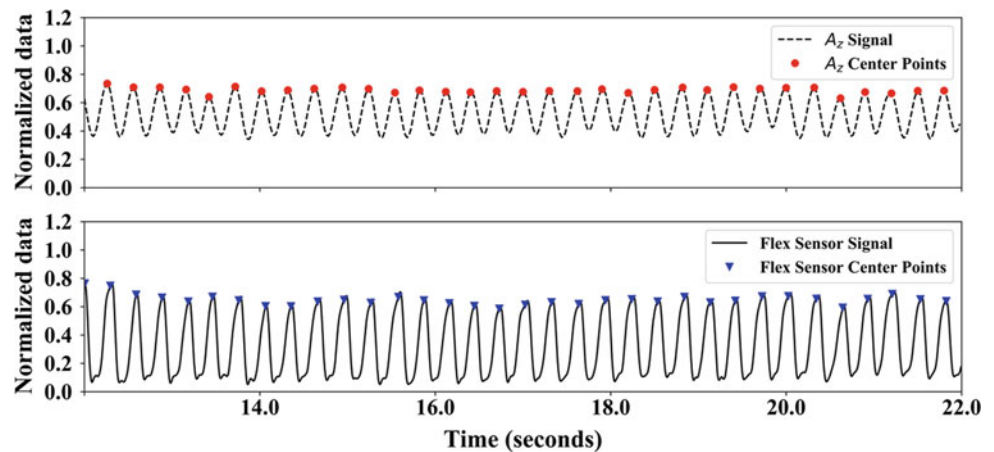
Fig. 7 Bland-Altman plot for each task performed by the subject. Task 1: 3.33 Hz audio stimulus. Task 2: 1 Hz audio stimulus. Task 3: 2 Hz audio stimulus. Task 4: no stimulus
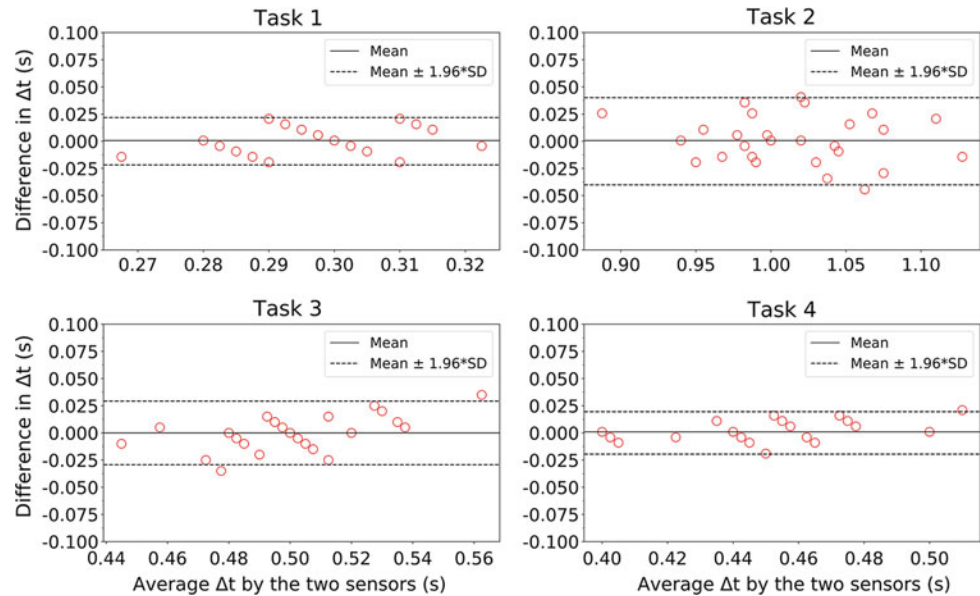
increasingly adopted over the last two decades [18], as it is extremely easy to apply and to interpret, and the results are highly reliable.

The analysis is based on what are called "limits of agreement", defined as the $\bar{x} \pm 1.96\,s$ interval, where $\bar{x}$ is the mean difference in measurements, and s is the standard deviation (SD) for the differences. If the differences are normally distributed, 95% of them will fall within these limits.

up to 0.0395 s below or 0.0407 s above the same measurement made with the TREMSEN.

To determine whether these differences are clinically significant or not, we can evaluate how considerable they are in relation to our reference, in this case, the TREMSEN. Using the maximum differences (see Table 1), and each respective Δt measured with the TREMSEN, we observe the following disparities: 6.67% for Task 1, 3.85% for Task 2, 6.03% for Task 3, and 3.85% for Task 4.

4 Results

Since there is no significant evidence in any of the 4 tasks that the differences between measurements made by the TREMSEN and the Flex Sensor are not normally distributed (Shapiro-Wilk test, p-value > 0.05), we can expect most of the differences to lie within the limits of agreement. Figure 7 shows the Bland-Altman plot for each task.

Table 1 presents relevant data from Fig. 7.

With these values, we can say with a high degree of certainty that, at least for pinch movements being executed at frequencies between 1 and 3.33 Hz, based on our worst case (task 2, pinches at a lower frequency), most of the measurements made with the Flex Sensor are expected to be

5 Discussion and Conclusion

This research proposed a different approach for quantifying the Finger Tapping Test, an already established test for assessing severity of the Parkinson's Disease, using an ink-based resistive sensor, the Flex Sensor. The results display a satisfactory performance, showing that the Flex Sensor is reasonably adequate to acquire, at least, the speed of pinches (period of movement) from the FTT.

The worst difference (0.040 s, or 40 ms, for Task 2) and the largest relative error in measurement (6.67% for Task 1), supported by the Bland-Altman analysis, suggest that the Flex Sensor will likely not deviate more than 40 ms in a pinch

Table 1 Information from the data plotted in Fig. 7

Tasks	Mean ± 1.96 * SD (s)	Maximum difference (s)
Task 1 (3.33 Hz)	0.0006 ± 0.0218	0.0200
Task 2 (1 Hz)	0.0006 ± 0.0401	0.0400
Task 3 (2 Hz)	0.0000 ± 0.0292	0.0350
Task 4 (No stimulus)	0.0010 ± 0.0195	0.0200

period measurement, and that this deviation may not exceed 6.67% of the approximate actual period of the movement.

Given the disparity between the expected FTT response from a healthy subject, compared to one with PD, as well as the disparity between subjects with different degrees of severity of the PD, it can be said that this deviation of the Flex Sensor from the real measurement is negligible, and the possibility of a misclassification is quite remote, thus deeming the Flex Sensor fairly reliable for this application.

For the future of this project, a proper glove must be devised so that it will not interfere on the hand movements. We then expect to be able to use this device on a longitudinal study with patients with PD.

Conflicts of Interest The authors declare no conflict of interest.

References

1. Graça, R., Sarmento e Castro, R., Cevada, J.: ParkDetect: early diagnosing Parkinson's disease. In: 2014 IEEE International Symposium on Medical Measurements and Applications (MeMeA). IEEE, pp. 1–6 (2014)
2. Okuno, R., Yokoe, M., Fukawa, K., et al.: Measurement system of finger-tapping contact force for quantitative diagnosis of Parkinson's disease. In: 2007 29th Annual International Conference of the IEEE Engineering in Medicine and Biology Society. IEEE, pp. 1354–1357 (2007)
3. Goetz, C.G., Tilley, B.C., Shaftman, S.R., et al.: Movement disorder society-sponsored revision of the unified Parkinson's disease rating scale (MDS-UPDRS): scale presentation and clinimetric testing results. Mov. Disord. 23, 2129–2170 (2008). https://doi.org/10.1002/mds.22340
4. Baston, C., Ursino, M.: A neurocomputational model of dopamine dependent finger tapping task. In: 2016 IEEE 2nd International Forum on Research and Technologies for Society and Industry Leveraging a better tomorrow (RTSI). IEEE, pp. 1–4 (2016)
5. Bustamante, P., Grandez, K., Solas, G., Arrizabalaga, S.: A low-cost platform for testing activities in parkinson and ALS patients. In: The 12th IEEE International Conference on e-Health Networking, Applications and Services. IEEE, pp. 302–307 (2010)
6. van den Noort, J., Van Dijk, K., Kortier, H., et al.: Applications of the powerglove for measurement of finger kinematics. In: 2014 11th International Conference on Wearable and Implantable Body Sensor Networks Workshops. IEEE, pp. 6–10
7. Krupicka, R., Viteckova, S., Cejka, V., et al.: BradykAn: a motion capture system for objectification of hand motor tests in Parkinson disease. In: 2017 E-Health and Bioengineering Conference (EHB). IEEE, pp. 446–449 (2017)
8. Kupryjanow, A., Kunka, B., Kostek, B.: UPDRS tests for diagnosis of Parkinson's disease employing virtual-touchpad. In: 2010 Workshops on Database and Expert Systems Applications. IEEE, pp. 132–136 (2010)
9. Shaeffer, D.K.: MEMS inertial sensors: a tutorial overview. IEEE Commun. Mag. 51, 100–109 (2013). https://doi.org/10.1109/MCOM.2013.6495768
10. Jablonski, G., Costa, S.C., Zaruz, T.F., Andrade, A.O.: Avaliação Inical Do Uso De Um Sensor Resistivo Para Quantificação Do Movimento De Pinça Polpa-A-Polpa Nos Distúrbios Motores Da Doença De Parkinson. In: Anais do V Congresso Brasileiro de Eletromiografia e Cinesiologia e X Simpósio de Engenharia Biomédica. Even3, Uberlândia, Minas Geraisc (2018)
11. Rabelo, A.G., Neves, L.P., Paixão, A.P.S., et al.: Objective assessment of bradykinesia estimated from the wrist extension in older adults and patients with Parkinson's disease. Ann. Biomed. Eng. 45, 2614–2625 (2017). https://doi.org/10.1007/s10439-017-1908-3
12. Andrade, A.O., Ferreira, L.C.V., Rabelo, A.G., et al.: Pelvic movement variability of healthy and unilateral hip joint involvement individuals. Biomed. Signal Process. Control 32, 10–19 (2017). https://doi.org/10.1016/j.bspc.2016.10.008
13. Machado, A.R.P., Zaidan, H.C., Paixão, A.P.S., et al.: Feature visualization and classification for the discrimination between individuals with Parkinson's disease under levodopa and DBS treatments. Biomed. Eng. Online 15, 169 (2016). https://doi.org/10.1186/s12938-016-0290-y
14. Droettboom, M., Caswell, T.A., Hunter, J., et al.: Matplotlib (2018). https://doi.org/10.5281/zenodo.1202077
15. Oliphant, T.E.: Python for scientific computing. Comput. Sci. Eng. 9, 10–20 (2007). https://doi.org/10.1109/MCSE.2007.58
16. Kozak, M., Wnuk, A.: Including the tukey mean-difference (Bland-Altman) plot in a statistics course. Teach. Stat. 36, 83–87 (2014). https://doi.org/10.1111/test.12032
17. Martin Bland, J., Altman, D.: Statistical methods for assessing agreement between two methods of clinical measurement. Lancet 327, 307–310 (1986). https://doi.org/10.1016/S0140-6736(86)90837-8
18. Martin Bland, J.: Citation history of Bland and Altman (1986). https://www-users.york.ac.uk/~mb55/meas/history.htm. Accessed 20 Mar 2018

Safety Device Against Overcurrent and Overheating in Radiofrequency Hepatic Ablation Equipment

Lívia Sant' Anna Alves, Gilvandson Costa Cavalcante,
Suélia Rodrigues Siqueira Fleury Rosa, and Gabriel Augusto Silva

Abstract

The E-Medical Equipment industry has been gaining momentum since the 1950s and 1960s. With this advancement, the use of innovative technologies has been on a large scale. This fact has brought with it numerous concerns about the safety of these innovations in the health sector. Taking this into consideration, this paper provides an analysis over the main problems that this type of equipment may pre-sent during its operation, and how much these damages may imply and harm the health of professionals and patients who are in contact with these devices. This analysis extends to the case of the hepatic ablation equipment SOFIA, developed by the Laboratory of Biomedical Engineering—LaB, at the University of Brasília—UnB, with the economic incentive of the Ministry of Health. This equipment doesn't have yet an internal electrical safety module, therefore, a system was developed, which identifies overcurrent and overheating of components by means of specific sensors and the microcontroller PIC16F628A, and so ensure patient safety. The techniques used to develop this project not only impact on the applications for the EEM industry, which has been developing in the country, but can also be applied in several sectors of the electronics industry, as is the case of initiatives that involve the monitoring of critical systems, extreme environmental conditions and control of the drive of various circuits.

Keywords

Security system • Overcurrent • Overheating

1 Introduction

Medical-Assistance Devices (MAD) are used for diagnostics, treatments, monitoring and aesthetics within the medical, dental, laboratory and physical therapy areas, being the main objective to assist the professionals of these areas in the identification of dis-ease and possible treatments of patient care [1].

Taking into consideration the development of MAD in Brazil, the LaB—Biomedical Engineering Laboratory located at UnB—University of Brasilia, both linked to the BioEngLab—Laboratory of Engineering and Biomaterial of FGA—Faculty of Gama, with the support and financing of the Ministry of Health since January 2015, develops a project named SOFIA (Software of Intense Radiofrequency Ablation), which proposed the construction of a radio frequency liver ablation equipment [2].

In relation to the equipment developed through the project SOFIA, among others equipments that perform radio frequency ablation, the goal is to induce thermal damage to the cancerous tissue by means of electromagnetic energy. In this way, the quality of the ablation procedure depends on the efficient control of current delivered to the patient [2].

In SOFIA, the current delivered to the patient is controlled by the power control board [3]. In case of malfunction of the board due to excessive heating or defects in the power transistors, during the time of use of the equipment, the current can exceed the threshold defined for performing the ablation, and offer risks to the patient [4].

Therefore, in view of the possible electronic defects in the power stage induced by operating faults that offer health risks of patients and health professionals [5], this article aims at the presentation of a safety system against overcurrent and

L. S. A. Alves (✉)
Department of Electronic Engineering, Federal University of Brasília, Brasília, Brazil
e-mail: livia_sant@live.com

G. C. Cavalcante
Department of Mechanical Engineering, Federal University of Brasília, Brasília, Brazil

S. R. S. F. Rosa
Department of Aerospace Engineering, Federal University of Brasília, Brasília, Brazil

G. A. Silva
Federal University of Brasília, Brasília, Brazil

overheating of the SOFIA circuits, in order to avoid health risks of the members involved in the ablation procedure.

2 Materials e Methods

The topology of the safety system (see Fig. 1), which was set in the project, will be detailed along with the characterization of the sensors and devices for acquisition current and temperature measurements.

The circuit works as follows: the outputs of the overcurrent and overheating detection modules are selected by the multiplexer HEF4052 [6] through the microcontroller PIC16F628A. The output of the multiplexer is connected to pin 17 of this microcontroller which rep-resents the input of an A/D converter with 4 bits.

Thus, based on the information received and processed, the PIC16F628A enables two outputs, pins 6 and 7, which are meant to drive the coolers and the relay responsible for the current flow from the control board to the RF generator board, respectively; and the other output, pin 8, is reserved for data transmission, through the serial communication.

The LEDs in the region outlined by the green color are used only for the visualization of the operation of the internal analog-to-digital converter. In this way, the final circuit does not need them.

2.1 Overcurrent Detector

In the process of ablation of the liver tumor region, the RF generation board of SOFIA equipment, is controlled by the voltage variation in the center tap of its transformer, which is provided by the control circuit [7].

The electrical current measures supplied by the power control circuit to the radiofrequency generation board, is done by the ACS712 current sensor that detects levels of current of ±30 A, with sensibility of 66 mV/A. The principle of functioning of this sensor is by Hall effect.

The circuit of Fig. 2 was projected in a way that a variation of current of 0–6 A in the entry of the sensor would result in a excursion of the exit voltage level of 0–2.5 V.

As the current increases during the ablation procedure, the drive circuit (Fig. 2) sends the corresponding voltage value to the PIC16F628A, which verifies if the identified value has not exceeded the maximum operating threshold of 6 A, which in turn, represents the maximum power reached by the equipment in the ablation process [3], according to measurements taken at the output of the power control board.

The curve of behavior of the comparator circuit (Fig. 5) was obtained inserting current in the input of the circuit from Fig. 2, using a bench current source, having as output voltage values that were collected by means of a digital

Fig. 1 Schematic diagram of the safety circuit of the hepatic ablation equipment developed in the SOFIA project. The area delimited by the red dashed line corresponds to the current sensor module; the area in blue, in the module of temperature sensors; in yellow, is the multiplexer; in green, is the display module of the analog-to-digital converter; in orange, the relay drive module; and finally, in violet, is the drive module of the coolers. Lastly, in black, there's the microcontroller PIC16F628A, responsible for the digital processing of the circuit (color figure online)
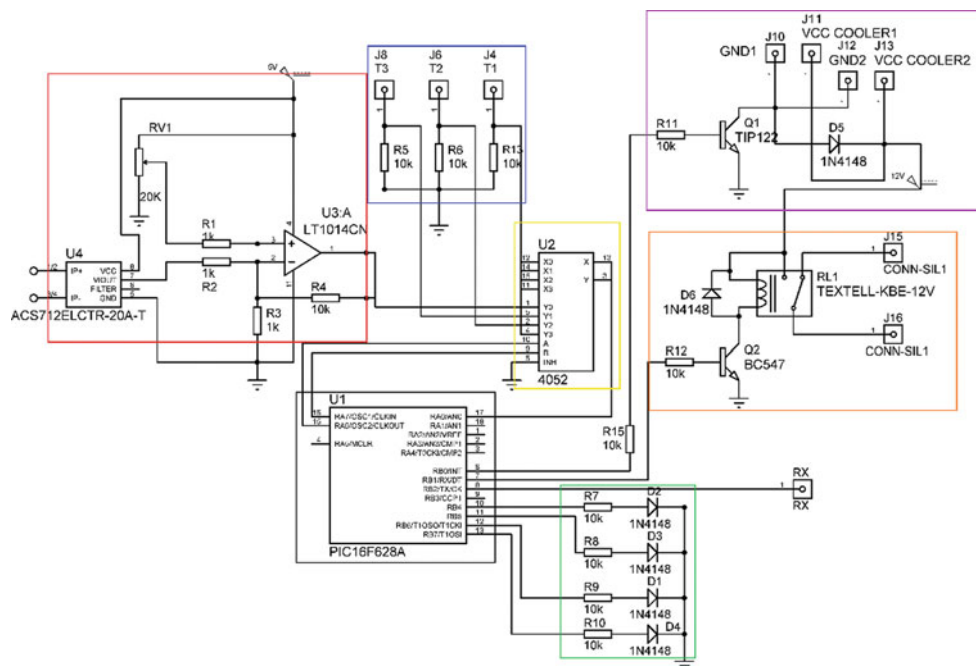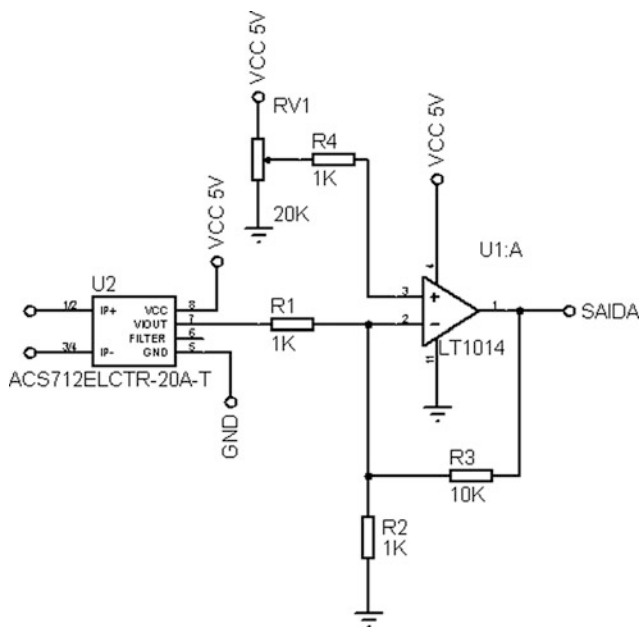
Fig. 2 Schematic of the comparator circuit, where IP+ and IP− are the current inputs on the ACS712 sensor; V1OUT is the sensor output voltage; RV1 is a potentiometer; pin 2, identified with the negative sign, refers to inverter input of the LT1014 operational amplifier; and pin 3, identified with the positive sign, refers to the non-inverting input

multimeter of the brand Multitoc, model DT830L, and with resolution of 1 mV then it's stored in a spreadsheet.

2.2 Overheating Detector

The electronic components, in which the temperature monitoring was performed, were: power transistors, present on the control board; and power transformer, located on the RF generation board. These devices are more susceptible to damage from high temperature.

The thermistors of the type NTC 3950 of 100 kΩ are used, that assist in the identification of the current temperature through the variations of resistance in its exit, which in turn are converted into measures of voltage, by the circuit from Fig. 2.

The information in J2 (see Fig. 2) will be sent to the PIC16F628A.

In the circuit of Fig. 3, bench tests were performed using heated water inside a vessel. The temperature reading was performed simultaneously by means of a thermocouple associated with a multimeter for comparison.
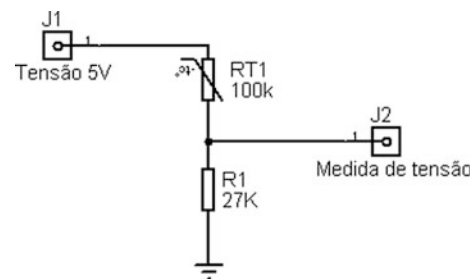
Fig. 3 The voltage divider used to acquire the voltage measurements according to resistance variations. Through connector J1, the sensor is powered with 5 V and voltage measurements are located via connector J2. The 27 kΩ resistor has been chosen so that the output of the voltage divider does not exceed 3.7 V

In this analysis, with the increase of the temperature of 35–84 °C, there was a excursion of 2.28–3.7 V, therefore, the microcontroller supports this voltage range.

To guarantee the security of the power transistors during the ablation procedure, the maximum threshold of temperature is 60 °C.

2.3 Control Performed by PIC16F628A

Initially, for analog voltage information to be processed by the PIC, it was necessary to convert it to digital data. For that, using successive approximation techniques [8], an analog-digital converter was implemented through the microcontroller hardware re-sources using assembly language.

After the converter was implemented, the following test was performed: using a power supply, a variation of 0–3.02 V was performed, and with each change, observed by means of the LEDs indicated in Fig. 1, the voltage value was acquired by means of a multimeter and registered in order to obtain information about the behavior of the converter.

Through the Assembly code, routines were developed to start protection relay and coolers. The operation of the two routines takes place as follows: current and temperature limits are defined. Thereafter, the limit is subtracted from the value acquired by the analog-to-digital converter. If the result is positive, the current or maximum temperature value is below the threshold established. Otherwise, respectively the interruption of the current supply leaving the control board to the RF generator board and/or triggering of the coolers occurs, if identified overcurrent and overheating, respectively.

2.4 Transmission of Data via Serial Communication

For the development of serial communication, the RS232 protocol and the CP2102 converter [9], used for communication between the computer and devices such as micro-controllers, modules and other equipment with USB interface.

The PIC has a USART module—Universal Synchronous Asynchronous Receiver Transmitter, with data transmission and reception routines. For this application, only the transmission was enabled, which can be configured through the information presented by the manufacturer's datasheet [10].

3 Results and Discussions

In this section, the curves that reflect the behavior of the analog-digital signal conversion modules and the current and temperature sensors are showed, as well as the results obtained through the microcontroller routines, which perform the control using the Assembly language.

3.1 Analog-Digital Conversion

The main routine developed has the objective of performing the analog-digital conversion. The behavior of this routine can be visualized through the operation of the LEDs (see Fig. 1). The order of activation of the LEDs has the function of representing the digital outputs referring to the analogue value of the sensors.

After the implementation of this routine was carried out the survey of the curve that represents the behavior of the 4-bit analog-digital converter. The data obtained can be verified by means of Fig. 4.

The resolution (R) of this analog-to-digital converter is satisfactory and sufficient for reading in the determined voltage range from 0 to 3.02 V, i.e. the smallest amount of data that can be converted within the dynamic range of the input signal. This is specified by the number of bits (N) of the converter, and was calculated by Eq. 1, where V corresponds to the maximum voltage of 3.02 V.

$$R = \frac{V}{2^N} \qquad (1)$$

Non-uniform steps (see Fig. 4) did not impact the proper functioning of the safety system. These changes are consequences of the quantization error, which is a random variable of values confined within the half-step range and caused by the truncation and rounding of the analog signal.

3.2 Relay Activation

For the safety system to be effective, when current values greater than 6 A are detected, the relay located between the output of the power control board and the RF generation board input is triggered. In this way, the power delivered to the patient is interrupted.

The curve of Fig. 5 was drawn to verify exactly which level of voltage that refers to the current considered as limit.

This analysis was necessary to verify the behavior of the output signal of the over-current detector. Although the

Fig. 4 Characteristic curve of the analog-to-digital converter implemented in the PIC16F628A. During the experiments, it was noticed that the voltage excursion in which there were changes in the state of the inverter occurred between 0 V and 3.02 V, with digital representation of 0000 to 1111, respectively

Tensão x Corrente
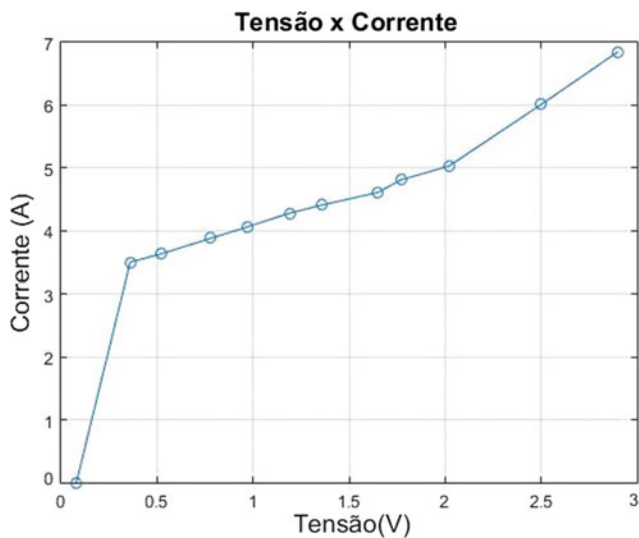
Fig. 5 A characteristic curve of the current sensor that relates the input current to the output of the current sensing module. It is noticed that the voltage increases as the current also increases

behavior was not linear, the trend was always increasing, without peaks of decision, if there was, it would not be possible to guarantee the chain-up in a safe way.

3.3 Coolers Drive

For the cooling of the control board transistors and of the transformer of the SOFIA RF generation board in case of overheating, a coolant drive routine was implemented, which is very similar to the routine implemented for the drive of the relay.

Tensão x Temperatura
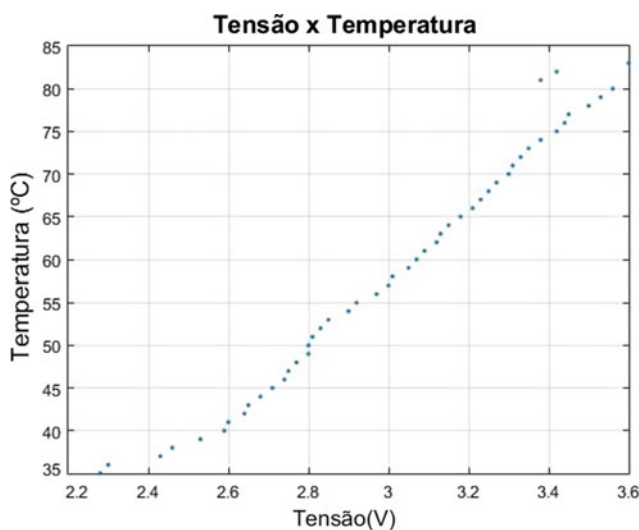
Fig. 6 Characteristic curve of the temperature sensor. The tests were performed at temperatures between 35 and 84 °C. This curve indicates that the identified voltage increases proportionally to the temperature

The cooler drive routine is very similar to the routine implemented for relay activation. It was also performed a survey of the temperature and voltage-related curve of temperature sensors NTC 3950 (see Fig. 6), in the configuration indicated by Fig. 3.

The curve relating temperature and resistance of an NTC sensor has a negative co-efficient. However, because voltage and resistance are inversely proportional, the curve of Fig. 4 shows a positive coefficient, i.e., the voltage increases with increasing temperature.

In the curve shown in Fig. 6, the anomalous behavior identified between 80 and 85 °C may have occurred due to external interferences that couldn't be detected at the moment of the experiment. This fact didn't cause problems in the operation of the circuit.

4 Conclusion

Therefore, a security system has been developed that acts in the interruption of the radiofrequency ablation, after the detection of sudden change of electric current provided by the power control circuit to the radiofrequency generation plate.

Additionally, the system triggers coolers responsible for the cooling of the power transistors of the control board, when detecting elevation of temperature superior to the threshold specified in the project. The preservation of the internal circuits of electrical and electronic equipment is of fundamental importance for the protection of the professionals who handle them and patients undergoing medicals procedures.

Considering the researches carried out in the literature and the analyzes developed after the elaboration of the security system for the medical equipment of hepatic ablation, SOFIA, it can be affirmed that the project developed by means of this work met the minimum requirements for the preservation of the safety of the professionals and patients.

Regarding the cooling system constituted by the coolers, the fact that they are activated only when there is excessive temperature detection, guarantees economy of electric energy, especially if the use of SOFIA in the long term is considered.

Regarding the use of a microcontroller, in conjunction with the analyzes and characterizations of the sensors, the accuracy and precision of the data obtained in the acquisition process that are important in the decision making for quick interruption of the procedure and activation of the coolers was guaranteed.

The microcontroller replaces a lot of components that would be needed for construction of this system. This fact made it possible to obtain a module from the system more compact.

Finally, the serial communication is of great interest in identifying events that interrupt the normal operation of SOFIA, as well as facilitating the technical maintenance of the equipment, since it is possible to identify the problem immediately.

Lísta de Siglas

BioEngLab	Laboratório de Engenharia e Biomateriais
EMA	Equimentos Médicos Assistenciais
FGA	Gama College
LaB	Laboratório de Engenharia Biomédica
SAR	Successor Approach Recorder
SOFIA	Software of Intense Ablation
UnB	Universidade de Brasília
USART	Universal Synchronous Asynchronous Receiver Transmitter

References

1. Pidone, L.A.: Utilização das diretivas rohs e weee para equipamentos eletromédicos fabricados no brasil. São Paulo, SP, Brasil, p. 14 (2011)

2. Marques, M.P.: Desenvolvimento de um eletrodo expansível de níquel-titânio para ablação hepática por radiofrequência. Brasília, DF, Brasil, p. 26 (2016)

3. Cavalcante, G.C.: Desenvolvimento e Avaliação de um Equipamento Médico Assistencial: Ablador Hepático por Radiofrequência – Sofia. Departamento de Engenharia Mecânica, Universidade de Brasília. Brasília, DF, p. 46 (2018)

4. Barbosa, A.T.R., Iaione, F., Wendling, R.F.: Um sistema de segurança elétrico hospitalar interligado por rede sem fio. XXVII Simpósio Brasileiro de Telecomunicações (2009)

5. Silva, D.R.C.: Engenharia clínica: manutenção de equipamentos de eletromedicina. Tese (Doutorado) (2015)

6. Schneider Jr., B.: Estudo teórico-prático de parâmetros técnicos e fisiológicos utilizados em eletrocirurgia, visando a otimização do desenvolvimento e performance de um bisturi eletrônico. Curitiba: Programa de Pós-graduação em Engenharia Elétrica e Informática. Industrial, Centro Federal de Educação Tecnológica do Paraná (2004)

7. Philips: HEF4052B MSI dual 4-channel analogue multiplexer/demultiplexer. http://pdf.datasheetcatalog.com/datasheet/philips/HEF4052BN.pdf. Accessed 19 Apr 2018

8. do Amaral, F.G.d.S., Alberto, J.G.C., et al.: O método de Newton-Raphson no cálculo do Tir. UNOPAR Científica Ciências Exatas e Tecnológicas, v. 11, n. 1 (2015)

9. Silicon Labs: Single-chip USB-to-UART bridge. https://www.silabs.com/documents/public/data-sheets/CP2102-9.pdf. Accessed 20 Apr 2018

10. Microchip: PIC16F627A/628A/648A EEPROM memory programming specification. http://ww1.microchip.com/downloads/en/DeviceDoc/41196g.pdf. Accessed 19 Apr 2018

Simultaneous Myoelectric Pattern Recognition Using BioPatRec Platform for Hand Prosthesis

Luiz José Lucas Barbosa, Paulo Roberto Fernandes de Oliveira,
Philippe Dias Araujo, Adson Ferreira da Rocha,
Denis Delisle-Rodriguez, John Jairo Villarejo Mayor,
Suélia Rodriguez Fleury Rosa, and Alberto López-Delis

Abstract

Currently, commercial hand prosthesis use a sequential control mesh, which makes the movement of the prosthesis counter-intuitive and clunky, often dependent on external sensors for movement execution. Pattern recognition is a method that has been developed to address these limitations. Unlike traditional strategies, pattern recognition is based on the idea that learning is done by a classification software. For that, the subject can use the natural contractions of the movement that one wishes to control. The software identifies the muscle pattern and classifies it as a target movement. Then, it will recognize the pattern the next time it is generated and create the intended prosthetic movement. In this work were proposed the combination of several methods for feature extraction together with feature selection, applying multilayer perceptron network (MLP) to recognize the motor pattern, using the BioPatRec platform (Ortiz-Catalan et al. in Source Code Biol Med, 2013, [1]). BioPatRec is an open source platform, that allows the implementation and test of several algorithms in the fields of signal processing, feature extraction and selection, pattern recognition and real-time control. The experimental results showed that the proposed features could achieve an average classification accuracy of 97.88%, which was 4.54% higher than the analysis without the features proposed in this work. The results suggest that the new features and the addition of featuring selection have the potential for the use with a myoelectric prosthesis with simultaneous control.

1 Introduction

Pattern recognition for myoelectric signal processing plays an important role on research for prosthetics [1]. In addition, the application of machine learning techniques has become widespread in the area of surface electromyography (sEMG) signals analysis, to enhance the feature extraction and selection as well the classification of the myoelectric pattern [2–5]. Furthermore, the use of pattern recognition brings an improvement in the degrees of freedom and movement of the prosthesis beyond the capacity of its sequential control [6].

In this study, the open source BioPatRec platform was used [1, 6, 7]. With a modular and customizable concept, researchers can compare their algorithms easily and efficiently, applying them to control a prosthesis. As advantages, users, by means of this platform, can access the sEMG signals database for both sequential and simultaneous analysis, including quantitative metrics to evaluate the performance of sequential and simultaneous control in a standardized way, as well as to apply methods that the platform provides for feature extraction, feature selection, feature reduction and myoelectric pattern classification.

The objective of this work is to analyze new algorithms for feature extraction and selection methods not provided by BioPatRec platform, four additional feature extraction methods were used: the Levinson-Durbin Recursion, the Absolute value of the Summation of the Exp[th] Root Mean, the Mean value of the Square Root and the Absolute value of the Summation of Square Root [8]. Additionally, an unsupervised method for feature selection (UFS) was used [9].

These additions were made for the improvement of the classification of the myoelectrical signal to provide a better

L. J. L. Barbosa (✉) · P. R. F. de Oliveira · P. D. Araujo ·
A. F. da Rocha · D. Delisle-Rodriguez · J. J. V. Mayor ·
S. R. F. Rosa · A. López-Delis
Electrical Engineering Department, Universidade de Brasília,
Brasília DF, 70910-900, Brazil
e-mail: contato@luizbarbosa.net

performance for the simultaneous movement of an upper-limb prosthesis, aiming at increasing the user comfort and giving easing for the movement.

2 Methodology

For this study, the "6mov8chUFS" (Untargeted Forearm Simultaneous) [7] database was used, which is freely available on the BioPatRec platform [1]. The sEMG signal is analyzed, and the features are extracted, following the main features are selected and finally the neural network classifies the movement (Fig. 1).

2.1 BioPatRec Platform

As previously mentioned, the biomedical signal analysis platform, BioPatRec, was used, using the Multilayer Perceptron Network with backpropagation, already configured on the platform for pattern classification.

2.2 Features Extraction

In this study were added four time-domain features described below:

(a) The Absolute value of the Summation of the Square root (ASS) [8]: This is the first time-domain feature. For calculation of the ASS, the first step is to first execute a full-wave rectification on the sEMG data, this help in retaining the entire energy content of the signal. Next, the integral of the rectified EMG signal is calculated with respect to the current analysis window, as expressed mathematically in Eq. (1)

$$ASS = \left| \sum_{n=1}^{k} (x_n)^{\frac{1}{2}} \right| \tag{1}$$

where k represents the analysis window, x_n denote the data within the corresponding analysis window.

(b) The Mean value of the Square Root (MSR) [8]: This is the second time-domain feature. It provides an estimated measure of the total amount of activity in the analysis window.

$$MSR = \frac{1}{k} \sum_{n=1}^{k} (x_n)^{\frac{1}{2}} \tag{2}$$

where k represents the analysis window, x_n denote the data within the corresponding analysis window.

c) The Absolute value of the Summation of the exp^{th} root (ASM) [8] of the data is the third time-domain feature, as shown in Eq. (3). The ASM feature provides a comprehensive insight into the amplitude of the EMG signal since it gives an approximate measure of the power of the signal which also produces a waveform that is easily analyzable. This feature contains information from which the amplitude of the rectified EMG signal could be obtained.

$$ASM = \left| \frac{\sum_{n=1}^{k} (x_n)^{exp}}{k} \right|$$

$$ex' = \begin{cases} 0.50, & if \ (n \geq 0.25 * k \ n \leq 0.75) \\ 0.75, & otherwise \end{cases} \tag{3}$$

The exp. variable can assume one of two possible values (0.50 or 0.75) based on the characteristic of the EMG signal segment under analysis. The ASM is therefore determined in

Fig. 1 Block diagram of the proposals myoelectric algorithm with the use of BioPatRec platform
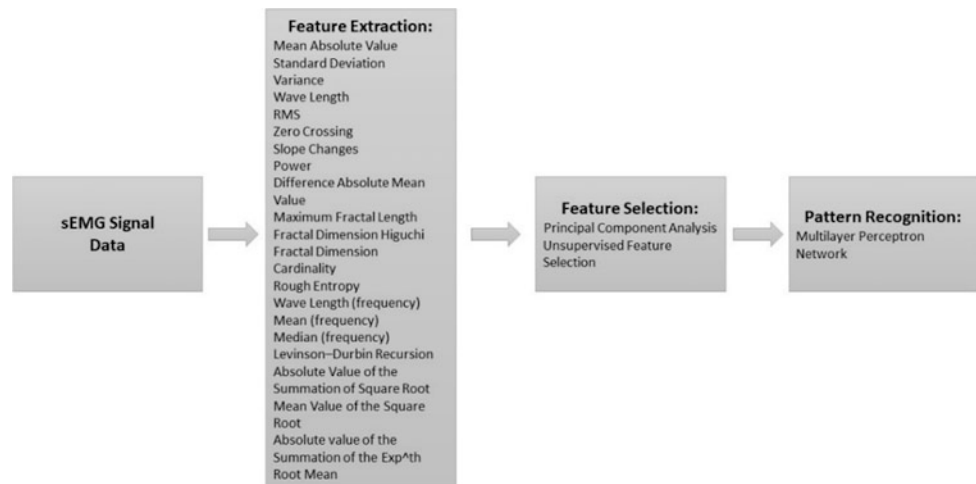
the following three steps: first the summation of the $\exp^{th}$ root of all values in a given analysis window is computed; followed by the mean of the resultant values; and lastly, the absolute value of the resultant mean is evaluated.

(d) The last feature added was the Levinson–Durbin Recursion [10], it is a recursive order-update method to the calculation of linear predictor coefficients, it has applications in filter design, coding, and spectral estimation. This method was used to estimate parameters of the sEMG signal.

2.3 Features Selection

A method based on the Maximal Information Compression Index (MICI), and the Entropy Representation (ER) was applied for unsupervised feature selection, in order to obtain the best feature sets for the classification [9]. Analyzing through the MICI to obtain combinations of characteristics with lower value or high redundancy. Those redundant features come together with the rejected features, in order to obtain an updated set formed by the features that provide the highest ER value during the combination with non-redundant features.

On the other hand, principal component analysis (PCA), an orthogonal linear transformation, that rearrange the components in the inverse order of variance It is used for dimensionality reduction in the BioPatRec platform as default., as it is a widely used technique.

In that study, PCA reduced the 160 features (20 for each channel) to the 64 best features for classification.

2.4 Neural Network Classifiers

Despite the existence of a wide variety of different pattern recognition algorithms, the Multi-Layer Perceptron (MLP) as a supervised Artificial Neural Network was chosen because of its inherent capacity of simultaneous classification [1, 6, 11].

An MLP can be used as a logistic regression classifier, where the input is first transformed nonlinearly by a learned transformation. This transformation projects the input data into a space in which it becomes linearly separable. This middle layer is called the hidden layer. A single hidden layer is sufficient to make MLPs a universal approximator. For this study an MLP with 3 hidden layers with eleven neurons was used, the transference function was the softmax function.

2.5 sEMG Database

As mentioned before, the 6mov8chUFS database was used, and it is available on the BioPatRec platform. This database is formed by 17 subjects, six classes of individual movements were selected, such as hand opening and closing, flexion and extension of the wrist, and prono-supination of the hand, forming 27 possible movements. The signal was measured as follows: 3 s contraction time with 3 s for relaxation between each repetition, repetitions of each motion. 8 bipolar electrodes (Disposable Ag/AgCl), 1 cm electrode diameter, 2 cm inter-electrode distance for the bipole. Electrodes were equally spaced around the most proximal third of the forearm.

The signal was extracted using overlapped time windows of 0.2 s and time increments of 0.05 s.

2.6 Statistical Evaluation

The tests were performed on seventeen subjects of the original base "6mov8chUFS". First, the BioPatRec feature selection methods were used with and without PCA. Finally, the feature selection algorithm unsupervised (UFS) was used for reducing features in place of the PCA. Thus the tests were completed they were repeated by adding the new characteristic vectors proposed in this study.

The evaluation of the classifier used a cross-validation of 48 trainings with randomized datasets were per subject and for each algorithm, 24 validation sets, and 49 test sets. For this study was used unitary range normalization.

The BioPatRec provides statistical tools to evaluate the proposed algorithms on the platform, thus, it has a wide variety of metrics [6] that were used to analyze the results, such as Accuracy (Class Specific), Sensitivity (Recall), PPV (Precision), F1, Specificity (Negative Condition), NPV (Negative Outcome) and Accuracy (Global).

(a) Accuracy—Class Specific

$$AccCS = \frac{absolute\ correct\ predictions}{total\ absolute\ predictions} \qquad (4)$$

(b) Sensitivity

$$Sensitivity = \frac{TPs}{TPs + FNs} \qquad (5)$$

(c) PPV

$$PPV = \frac{TPs}{TPs + FPs} \qquad (6)$$

(d) F1

$$F1 = 2 * \frac{precision * sensitivity}{precision + sensitivity} \qquad (7)$$

(e) Specificity

$$Specificity = \frac{TNs}{TNs + FPs} \qquad (8)$$

(f) NPV

$$NPV = \frac{TNs}{TNs + FNs} \qquad (9)$$

(g) Accuracy—Global

$$AccG = \frac{TPs + TNs}{TPs + TNs + FN + FPs} \qquad (10)$$

where TP means true positive, the correct activation; TN is true negative, the correct inactivation; FP is false positive, the incorrect activation; and FN is false negative, incorrect inactivation.

3 Results and Discussion

It has been shown that the individual movements can be successfully predicted offline using pattern recognition algorithms [1, 3, 12, 13] and in this study was demonstrated an increase in terms of classification accuracy was achieved when the new features were used in conjunction with a feature reduction algorithm. Table 1 shows the results obtained using the characteristics present in BioPatRec and the use of PCA or UFS to reduce characteristics.

Table 2 shows the results obtained using the characteristics present in BioPatRec and those added by this study, in addition to the use of PCA or UFS to reduce the characteristics. As more characteristics are sorted, the MLP begins to diverge, but when selecting the most divergent characteristics, through the methods of selecting characteristics, rating the signal becomes easier. The performance of the proposed and the conventional methods present in the BioPatRec is shown by the gain in the accuracy and deviation shown in Tables 1 and 2.

The below figure shows the distribution curves of the experiment, while the blue curve represents the old features the red one represent the experiment with the added features. The difference between two means divided by a standard deviation for the data is represented with the "d" letter in the graphic (Fig. 2).

According to Cohen and Sawilowsky:

- d = 0.01 => very small effect size;
- d = 0.20 => small effect size;
- d = 0.50 => medium effect size;
- d = 0.80 => large effect size;
- d = 1.20 => very large effect size;
- d = 2.00 => huge effect size.

The experiment was offline, and the mean training and validation time was of 34 s and the mean testing time was of 0.004 s.

The use of BioPatRec allows a fast and accurate simulation of the pattern recognition algorithms, which streamlines the process of development and testing of theories that will be applied in the control of a myoelectric prosthesis. This platform is being used in this study and it is hoped that it can assist in the development of an adaptive learning pattern recognition system for the control of an upper limb

Table 1 Quantitative indicators obtained with the comparison between old features with feature reduction algorithms

Features selection	Accuracy class	Sensitivity	PPV	F1	Specificity	NPV	Accuracy global
None	83.10	85.11	92.30	0.89	99.73	99.43	99.19
PCA	92.74	94.78	94.78	0.95	99.80	99.80	99.61
UFS	90.63	92.29	95.02	0.94	99.81	99.70	99.54

Table 2 Quantitative indicators obtained with the comparison between the new features added to the old features sets with feature reduction algorithms

Features selection	Accuracy class	Sensitivity	PPV	F1	Specificity	NPV	Accuracy global
None	82.39	83.60	95.76	0.89	99.86	99.37	99.26
PCA	94.63	96.22	96.95	0.97	99.88	99.85	99.75
UFS	93.50	94.71	96.68	0.96	99.87	99.80	99.68
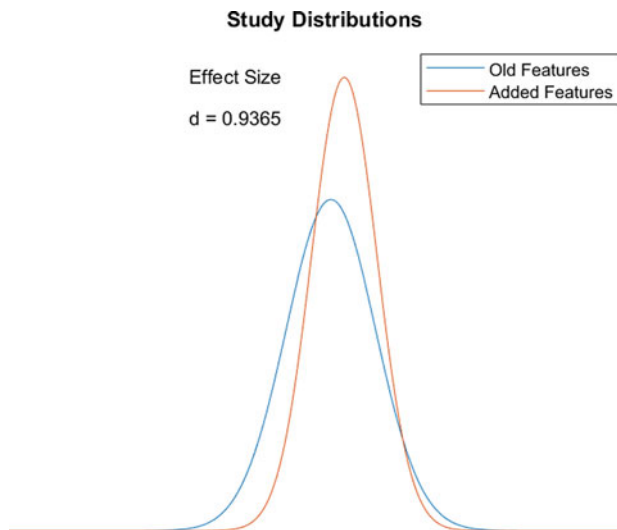
Fig. 2 Distribution of the experiment with the old features and the added features

electrical prosthesis. In addition, the fact that the BioPatRec platform is modular allows the study to be better divided into stages, such as signal processing, extraction of characteristics, classification and the decision-making system of the prosthesis, making the process agiler.

4   Conclusion

The addition of the new features in conjunction with the selection algorithms improved the characterization of the myoelectric signal, which will facilitate the decision process for the control of the myoelectric prosthesis. The help of the BioPatRec platform made the work agiler and the statistical metrics helped to evaluate the effectiveness of the algorithms applied in this study. Furthermore, this study showed that simultaneous control can be considered since it improves user comfort. In addition, simultaneous control is required for more natural control of artificial limbs, and pattern recognition has proved to be an excellent means of working with the complexity generated by simultaneous movement.

References

1. Ortiz-Catalan, M., Brånemark, R., Håkansson, B.: BioPatRec: a modular research platform for the control of artificial limbs based on pattern recognition algorithms. Source Code Biol. Med. (2013)
2. Huang, Y., Englehart, K.B., Hudgins, B., Chan, A.D.C.: A Gaussian mixture model-based classification scheme for myoelectric control of powered upper limb prostheses. IEEE Trans. Biomed. Eng. (2005)
3. Khezri, M., Jahed, M.: A neuro-fuzzy inference system for sEMG-based identification of hand motion commands. IEEE Trans. Ind. Electron. (2011)
4. Duan, F., Dai, L., Chang, W., Chen, Z., Zhu, C., Li, W.: SEMG-based identification of hand motion commands using wavelet neural network combined with discrete wavelet transform. IEEE Trans. Ind. Electron. (2016)
5. Luh, G.-C., Ma, Y.-H., Yen, C.-J., Lin, H.-A.: Muscle-gesture robot hand control based on sMEG signals with wavelet transform features and neural network classifier (2016)
6. Ortiz-Catalan, M., Rouhani, F., Branemark, R., Hakansson, B.: Offline accuracy: a potentially misleading metric in myoelectric pattern recognition for prosthetic control. In: Proceedings of Annual International Conference of the IEEE Engineering in Medicine and Biology Society EMBS, vol. 2015, pp. 1140–1143 (2015)
7. Ortiz-Catalan, M., Håkansson, B., Brånemark, R.: Real-time and simultaneous control of artificial limbs based on pattern recognition algorithms. **22**(4), 756–764 (2014)
8. Samuel, O.W., et al.: Pattern recognition of electromyography signals based on novel time-domain features for amputees' limb motion classification. Comput. Electr. Eng. (2017)
9. Delisle-Rodriguez, D., et al.: Adaptive spatial filter based on similarity indices to preserve the neural information on EEG signals during on-line processing. Sensors **17**(12), 2725 (2017)
10. Zeinali, M., Shafiee, M.: A new Levinson-Durbin based 2-D AR model parameter estimation method. Multidimens. Syst. Signal Process. **20**(1), 35–47 (2014)
11. Asghari Oskoei, M., Hu, H.: Myoelectric control systems-a survey. Biomed. Signal Process. Control (2007)
12. Sensinger, J.W., Lock, B.A., Kuiken, T.A.: Adaptive pattern recognition of myoelectric signals: exploration of conceptual framework and practical algorithms. IEEE Trans. Neural Syst. Rehabil. Eng. **17**(3), 270–278 (2009)
13. Geethanjali, P.: Myoelectric control of prosthetic hands: state-of-the-art review. Med. Dev. Evid. Res. (2016)

Stimulation of Carotid Baroreceptors in Humans: A Technique for the Evaluation of Reflex Control of Blood Pressure

Alessandro Pinheiro, Lauro C. Vianna, Sandoval Menezes, and Jake do Carmo

Abstract

Hypertension is a disease that can cause serious health issues such as acute myocardial infarction and stroke (cerebral vascular accident) and constitutes a matter of public health. Blood pressure is controlled by the cardiovascular system through various mechanisms, and the baroreceptors play a key role in this regulation. It is possible to verify the responses relevant to the control of blood pressure by stimulating these pressure sensors. It is important to understand how the baroreceptors work given the difficulty in diagnosing problems in accordance to these mechanisms. To the best of the authors's knowledge, there has been no prior study in Brazil that has statistically evaluated within the population the prevalence of problems attributed to the baroreflex system. Normalized data for different population groups are also absent. Therefore, given the difficulty in identifying the exact origin of the elevation of blood pressure and the lack of information on baroreflex within the population, we developed an equipment that is capable to determine these factors. Baroreceptors can be stimulated by applying external negative pressure through a collar positioned around the neck, in synchrony with an electrocardiogram. A decrease in the heart rate and a reduction in blood pressure are expected during the stimulation.

A. Pinheiro (✉) · S. Menezes
School of Technology, University of Brasília, Brasília-DF, Brazil
e-mail: alessandro@ieee.org

L. C. Vianna · J. do Carmo
School of Physical Education, University de Brasília, Brasília-DF, Brazil

1 Introduction

Systemic arterial hypertension (SAH) is currently one of the most prevalent condition and contributes significantly to cardiovascular morbidity in Brazil and elsewhere in the world. In 2008, the estimated number of patients with SAH was 1 billion. According to the World Health Organization, 40% of adults aged 25 or over were diagnosed with hypertension [1]. Similarly, the Ministry of Health has provided alarming data indicating that approximately 24.8% of the Brazilian adult population has been the diagnosed with hypertension [2]. Hypertension is characterized by a systolic pressure greater than 140 mmHg and a distal pressure greater than 90 mmHg.

It is important to remember that the mechanisms responsible for the development and maintenance of SAH are not fully known and involve a combination of vascular, neurohormonal and other emerging factors [3]. Therefore, careful consideration is recommended before diagnosing hypertension, since false positive detections are possible [4]. In this context, determining the mechanism by which blood pressure increases may reveal important strategies to allow extension of the benefits of pharmacological and nonpharmacological treatments.

A potential mechanism for controlling blood pressure is the arterial baroreflex control. Blood pressure is determined at each cardiac cycle by the cardiac output and peripheral vascular resistance. Thus, any change in one of these components, or even both, directly affects blood pressure levels. Arterial baroreceptors are involved in the most important mechanism of blood pressure reflex regulation exerting beat-to-beat control. However, hypertensive patients have a reduced baroreceptor sensitivity that causes a deficient blood pressure reflex regulation.

The baroreceptors, located in the carotid sinus, can be stimulated externally with negative pressure by means of a collar positioned around the neck. This collar is synchronized with the an electrocardiogram [5–7].

Evaluation of the carotid baroreceptor is accessible only at research centers and the elicited results are not extensively disseminated among practitioners who prescribe it. Owing to the difficulty in finding the exact origin of the elevated blood pressure in certain patients and to the lack of information on baroreflex sensitivity within the population, the development of dedicated equipment that contributes to the diagnosis of SAH is proposed.

2 Methodology

A vacuum pump, a collar used for stimulation, solenoid valves, and a 20 L tank, were used to develop the equipment used for the stimulation of baroreceptors. The system is controlled via an ATmega328P microcontroller connected to a computer's USB port and an electrocardiograph, Cardiomatic model MSC 6111 (ECG). A summary of the operation system is summarized (see Fig. 1a, b).

The vacuum pump is responsible for creating a negative pressure that is stored in a 20 L steel tank. The set of analog ports in the microcontroller read the pressure of the collar and tank. Digital ports trigger the pump and release air into the collar.

A software program that changes the logical level of the digital port at the exact time point of the occurrence of the R-wave peak. The peak is easily detected since it is the point where rapid ECG changes occur.

The release valve was activated using an AND logic gate, whereby one of its terminals receives set to the logic level 1 each time the R-wave is detected. The other terminal is connected to the trigger button that releases the logic level 1 when pressed. Through this combination, a precise activation is possible (see Fig. 2).

A pressure sensor that was installed inside the stimulation collar measures the pressure applied between the collar and the neck's skin. A pressure sensor from Sensor Technics (model SZ75120E) was connected to the analog input of the microcontroller. The collar was made of silicone (see Fig. 3).
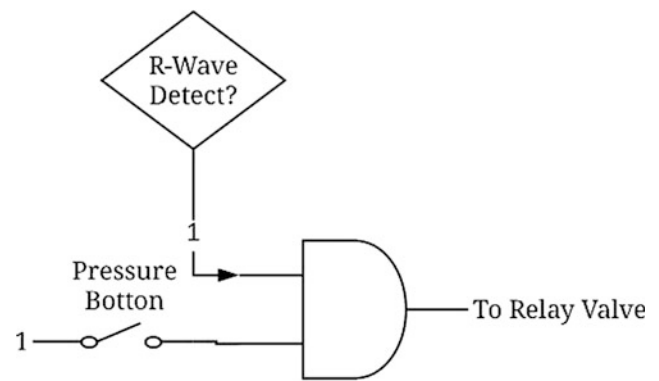
Fig. 2 Schematic of the logic system used for the activation of vacuum synchronized with the R wave

Fig. 3 Collar positioned in the neck area to stimulate baroreceptors located in the carotid
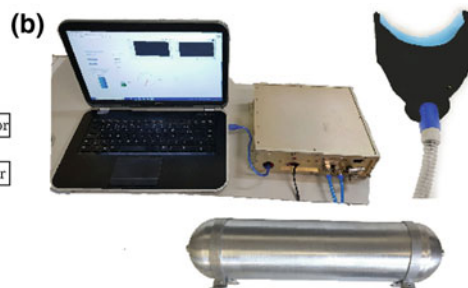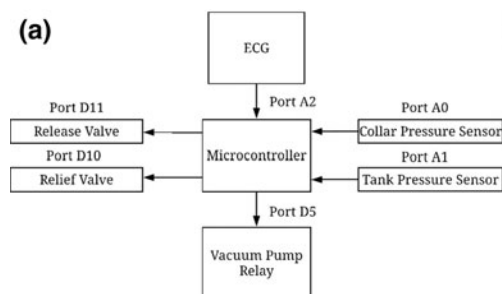
Fig. 1 **a** Schematic of the proposed equipment in block form. The ATmega328P microcontroller is responsible for reading the sensors and activation of the valves. **b** Show the equipment

3 Results

A calibration curve of the detected voltage as a function of the measured pressure ratio was generated using an external pressure monitor (Rise HT-1890) that was able to read up to −200 mmHg. A system modification was implemented and installed to record the pressure measurement obtained by the external monitor. Pressures of −20, −40, −60 and −80 mmHg were manually applied (see Fig. 4).

The PowerLab signal integrator of AD Instruments was used. The signal was acquired and stored through the analog inputs. The data was subsequently analyzed using the LabChart Pro software from AD Instruments.

An acquisition with pressure set at −60 mmHg for 5 s. The data were acquired and stored. The ECG wave is observed on the top, the heart rate is shown in the middle, and the bottom trace is the pressure applied inside the stimulation collar (see Fig. 5). It is noteworthy that the recorded pressure values (in mmHg) are negative, since the value obtained by the analog port was converted.

The tank plays a crucial role in stabilizing the vacuum formed in the collar, because it is important that the collar presents a known and stable pressure during the stimulation for the appropriate stabilization of the system.

The RR interval was stable until the moment of pressure on the collar, corresponding to the third RR (see Figs. 5 and 6).

The graph of the RR differences show that they were stable, with values of 1.15 s. At the time of the pressure on the collar, there was a peak for 1.4 s. It is important to remember that the higher the RR interval have the lower the heart rate.

4 Discussion

The ECG wave and Heart Rate curve (see Fig. 5a, b) show decrease approximately 10 BPM in the heart rate. The vacuum tank had a significant effect on the vacuum stabilization
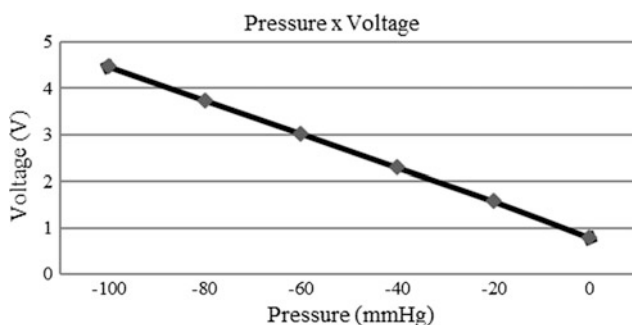
Fig. 4 Calibration graph of detected voltage and applied pressure at the sensor's output terminal
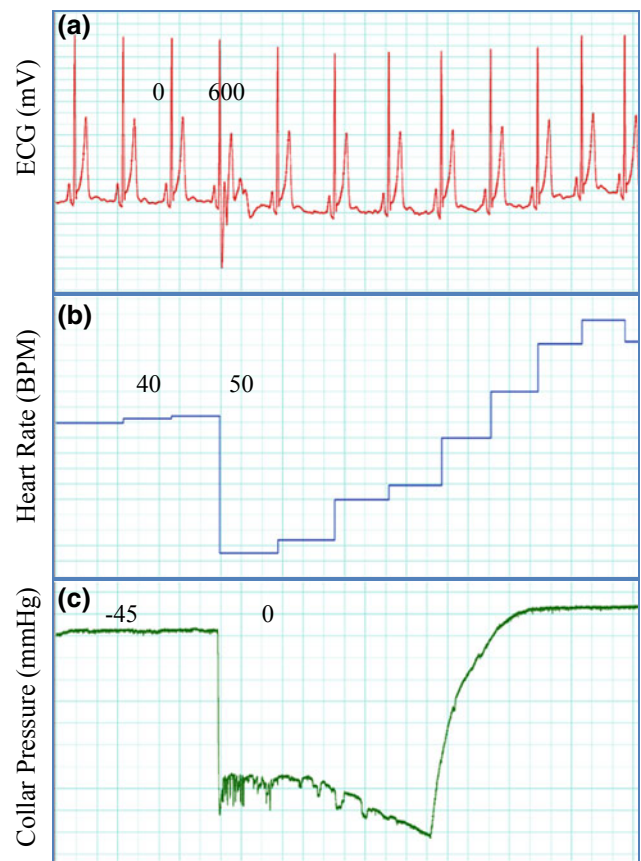
Fig. 5 LabChart pro software screen capture during acquisition. **a** ECG signal, **b** heart rate, **c** internal pressure applied at the stimulation collar
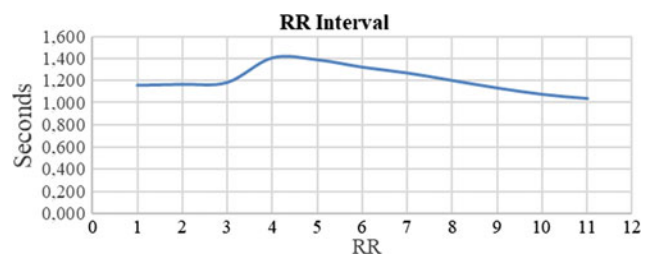
Fig. 6 Interval RR. The pressure was applied in third RR. After pressure, there is an increase in the RR interval, consequently a decrease in heart rate

release. It was observed that collar pressure occurred instantly. Small oscillations occurred on the negative plateau but did not impact the result. These oscillations are due to small air leaks caused the contact between the collar and the neck.

The synchronism was satisfactory. It is possible to observe that the peak of the R wave coincides exactly with the beginning of the pressurizing of the collar. The manufacture of the collar is labored because it is difficult to use the same collar for different patients, since everyone has different anatomical parts of neck.

However, in the final part of the stimulus, the return to zero pressure was not instantiated. This is due to the small dimension of the equalizing valve, because airflow has been restricted. The performance of the system was not impacted.

Calibration of pressure transducers (see Fig. 4) plays an important role in the safety of the test participant. Increased pressure can cause neck damage. Therefore, before any test, a 6-point calibration with a calibrated pressure monitor is always performed. The calibration procedure is performed on both pressure sensors.

It is important to show that depending on the SAH treatment strategy, the therapy may be less effective. If the problem is related to the baroreceptors, the cause will not be treated properly, but only the symptom. Therefore, the dissemination of the existence and functionality of the proposed equipment to major health centers will improve the diagnosis and provide important treatment and therapeutic advancements.

SAH is a condition that does not present clear symptoms. In most cases, the patient goes to the hospital only when there is a serious complication. To-this-date, there no other study has been conducted in Brazil that statistically indicates the prevalence of baroreflex system problems within the entire population.

The equipment can provide more information for healthcare staff because what is used today, in some cases, may not be enough. Nowadays, some tools, such as the ambulatory blood pressure monitor (ABPM), are currently used by health professionals to diagnose hypertension. It is possible to verify the prevalent blood pressure behaviors in studied patients by analyzing the recorded data.

5 Conclusions

The availability of parts and discrete components currently available in the local market allowed the development of the equipment. The greatest difficulty was the assembly of the collar, because any air intake would affect the stability of the vacuum, thus preventing the achievement of a perfect pressure plateau. The collar that makes contact with the neck has an function in the functioning of the system, as it is responsible for contact on the skin of the neck.

Behavioral data of blood pressure in response to forced stimulation of baroreceptors with this equipment is not yet available, but their collection will be done as soon as the study proposal is was approved by the ethics committee.

It has been shown that the development of the equipment is technically feasible. In this way, the device will make an important contribution to the health of the population.

Conflict of Interest Statement The authors declare that there are no conflicts of interest in the preparation of this article.

References

1. World Health Organization: World Health Day 2013. Global Brief Hypertension, p. 9 (2013)
2. Secretaria de Atenção à Saúde, Ministério da Saúde, Brasil: Departamento de Atenção Básica, Estratégias para o cuidado da pessoa com doença crônica: hipertensão arterial sistêmica. Brasília, Ministério da Saúde (2013)
3. Guyton, A.C., Hall, J.E.: Tratado de Fisiologia Médica, 12th edn. Elsevier, Rio de Janeiro (2011)
4. de Fontes, W.D., Barboza, T.M., Leite, M.C., Fonseca, R.L.S., dos Santos, L.C.F., de Nery, L.T.C.: Hipertensão arterial sistêmica para o Sistema Único de Saúde, 1st edn. Brasília (2006)
5. Cooper, V.L., Hainsworth, R.: Carotid baroreflex testing using the neck collar device. Clin. Auton. Res. **19**(2), 102–112 (2009)
6. Hosokawa, K., Sunagawa, K.: Closed-loop neuromodulation technology for baroreflex blood pressure control. Proc. IEEE **104**(2), 432–443 (2016)
7. Eckberg, D.L., Sleight, P.: Human Baroreflexes in Health and Disease, 1st edn. Oxford, New York (1992)
8. Tsekouras, N.S., et al.: Alterations of baroreflex sensitivity after carotid endarterectomy according to the preoperative carotid plaque echogenicity. J. Vasc. Surg. **56**(6), 1591–1597 (2012)

The Interrelationship Between Industry/Medical/Patient in the Analysis of Failures in Orthopaedic Implants

Bruna Luciana Silverio and Christiane Ribeiro

Abstract

The interdisciplinary involving Biomedical Engineering, especially in orthopaedic devices requires better communication between the related areas. This is an action that is essential for the identification, tracking and improved information management, relating to failures that can affect these devices. This study searched to understand the relationship of the main details in the related axis in this market: industry—medical/health institution—patient, to obtain data capable of guiding the country's situation regarding the development of orthopaedic implants and their surgical practice. Post-installation monitoring was also analyzed to predict the device's performance and impact on patients' quality of life. There was a disagreement of judgment on the nature of failures, and many surgeons said the devices fail because of problems inherent to the patient. Other said that failures occur mainly because of wear. Most patients have argued that the problems are more related to unsuitable surgical procedure. The companies associated the failures with improper surgical procedures, as well as the physician`s lack of instruction to the patient about the limitations imposed by the device. The absence of a cooperative relationship between the related axis make it difficult to understand casuistry of failures, as well as obtaining data regarding these occurrences. This fact can reverse both the research advances in Biomedical Engineering and the search for better preventive practices in the development of high performance biomaterials for implants and prosthetic devices.

1 Introduction

The increasing pressure regarding the quality and costs of products for the health area has been motivating the introduction of technological innovations with a better cost-benefit in Biomedical Engineering, mainly in the sector of prosthetic devices and implants. In this context, the Brazilian medical equipment industry has evolved and stood out in the recent years, with a very significant market share in the home economy [1, 2].

The research process involved in the development of implantable materials, among the orthopaedic devices (OD), is more complex than most products in the medical equipment industry. This complexity is due to the different characteristics of the materials explored, the type of contact and the interaction time with the biological system. In addition, the need for different types of physical-chemical analysis, as well as mechanical analysis, to evaluate the same responses, and may suggest a different behavior due to the used technique for characterization, besides having biocompatibility and bifunctionality proven. All these characteristics must ensure the health and clinical safety of these devices [3, 4].

To adequately meet this diversity of requirements, professionals from the related areas are involved in the research and development OD, from raw material selection to failure prevention mechanisms during their lifespan, a task usually performed by the clinician involved [2].

Therefore, there are three important related axes in the market for orthopaedic devices that must act cooperatively: the industries, responsible for research and development; physicians and health institutions, responsible for setting up

B. L. Silverio (✉) · C. Ribeiro
Biomedical Engineering – Center of Engineering, Modeling and Applied Social Sciences, Federal University of ABC (UFABC), Alameda Universitária S/N, 09606-045 São Bernardo do Campo, SP, Brazil
e-mail: bruna.silverio@ufabc.edu.br

and monitoring the performance of a device; and patients, users of these devices.

The interdisciplinarity of the segment highlights a better communication between the links involved in the market for OD, fundamental action for the tracking, identification and better management of information regarding the failures. This connected relationship can have a positive impact in both, research and development, and in the social aspect, reducing the associated risks for users

From this perspective, this research aimed to obtain information that may be useful in monitoring the behavior of orthopaedic devices during their lifespan, understanding the causes of failures, their corrective and preventive actions. It was considered the current legislation applied to the development and market of these devices, considering the industry-medical-patient relationship.

2 Methodology

This study was submitted and approved by the Ethics Committee on Human Research of the Federal University of ABC, properly registered in Brazil Platform (Certified Ethical Consideration—58609616.9.0000.5594). All participants signed a free and informed consent, in accordance with the principles of the Declaration of Helsinki.

A mapping of the main companies developing and marketing OD and health institutions (HI) that perform surgery for installing these devices. The selection considered the following inclusion criterion: (i) only companies, hospitals and patients that signed a free and informed consent; (ii) medical expert in orthopaedic surgery proficient in the installation of implants and prosthetic devices; (iii) representatives of the main prosthesis industries of development and distribution in Brazil; (iv) patients undergoing orthopaedic surgeries with installation of prosthesis or due to revision surgery in the last 15 years.

According to the inclusion criteria, it's been selected 70 orthopaedic surgeons working for over 10 years and responses were obtained from 57 of them. Also answered 6 of the top 7 companies in this segment of the market that serve the public and private sector, according to data obtained of the Brazilian Association of Medical and Dental Equipment Industry (ABIMO-2016) [5] and Interinstitutional Working Group on prostheses and special materials (OPME GTI-2015) [6]. This research interviewed 109 patients out of a population of 150 using an OD were interviewed.

Failures searches were also carried out in public databases, such as the Department of the Unified Health System (DATASUS), Ministry of Health, and Technical surveillance system—ANVISA.

The sample size of this research was obtained from the calculation, considering the description of qualitative variables of a finite population. The obtained proportion of favorable results was 0.035 (for companies), 0.012 (for doctors) and 0.010 (patients)—as Eq. (1) described by Miot 2011. The values obtained were representative and had a high reliability when compared to other similar studies.

$$n = \frac{N \cdot p \cdot q \cdot \left(\frac{Z\alpha}{2}\right)^2}{(N-1) \cdot (E^2) + p \cdot q \cdot \left(\frac{Z\alpha}{2}\right)^2} \quad (1)$$

At where:

n it is the sample size.
N is the population size.
$Z\alpha$ is the critical value for the degree of confidence (usually 1.96).
E is the standard error.
p is the proportion of positive results in the population.
q is the proportion of unfavorable results in the population (usually 0.05).

3 Results and Discussion

Orthopaedic devices may fail for different reasons during their development or lifetime, considering the various steps in their processing, the surgeon's inexperience and lack orientation to patients regarding the limitations imposed by the device [1].

There are no official numbers on the incidence of failures in the recent years in Brazil and they may be related, among other factors, to the irregularities found in this sector. ABIMO estimates that 30% of prosthetic components are irregular due to illegal companies operating in the sector. Adulteration can encourage illegality, putting the health of the population at risk, and even promote unfair competition from the market point of view, suggesting a worrying scenario from a legal sanitary point of view [1, 5].

The market for OD has a diversity of products available, which, combined with the lack of a universal nomenclature for such devices, results in the difficulty or impossibility of comparing them. In this context, besides this difficulty, several questions can influence the decision of the surgeon in the choice of the best device. However, the ideal method of selection would be a joint decision, whereas the patient's opinion and history, along with the experience of his surgeon [1, 2].

The data obtained in this study showed that 62% of physicians stated that there is a limited possibility of choice in the type of recommended device. The surgeon can only

opt for the devices that HI and/or insurance offer coverage, even knowing that other materials would be better intended for the specific purpose. Already 23% exposed the critical situation when the patient suffers some trauma and need an immediate surgery, in this case, the surgeon makes the choice over the devices already available at the clinic/health institution via Public Unified Health System—SUS or private plan. And 15% were precise when affirming that the choice is limited to different classes of materials (metal, ceramics and polymer), being the metal the material chosen primarily. This class of material is the most commonly used and exploited by the industries due to their structural characteristic and lower costs (Fig. 1).

These factors justify and reinforce the use of metals by the Public Unified Health System in the recent years [7]. One of the most recommended in Brazil is the stainless steel-316-L, material already in disuse in Europe and the USA, due to the loss of its properties, due to in vivo corrosion process. Reinforcing this information, the companies participating in the research stated that 83% of the orthopaedic devices are made from metallic biomaterials, with emphasis on titanium and its alloys, which has been taking the place of steel and Co–Cr alloys, following the worldwide trend observed in other countries. The other companies stated that an orthopaedic device is currently made of more than one type of biomaterial, that is, a composite. It is also important to note that it is difficult for the surgeon to follow technological advances in the biomaterial development for orthopaedic use, trusting entirely on the information of its manufacture.

Data from the literature indicates there are still difficulties in incorporating technology into health plans and the SUS, a theme currently placed as one of the top priorities of the Brazilian health systems [9]. The incorporation of new technologies in the health system is an important tool for the inclusion of more sophisticated and better performing prostheses. The data obtained in this research confirm this information, 87% of physicians/HI affirmed that health systems do not offer accessibility to existing technologies, while 13% stated that they have access to new technologies, given the medical freedom to suggest to the patient (if possible) the acquisition of a given device. The difficulty of this type of access can be related to the occurrence of failures, since each device can now be developed in a personalized way, according to the necessities of each patient, considering their age and lifestyle [2].

Failures are known to occur for various reasons, but there are currently no official data on its casuistry [1]. The complexity of the surgical technique, such as the correct positioning of the patient's limb in a manner compatible with the installation, together with the surface characteristics and the perfect geometry of the device, can justify these very expressive numbers. Factors such as: unsuitable surgical procedure; corrosive action of body fluids; early loading request due to patient movement and overload due to bone repair problems; implant design; surface defects and metallurgical, also have strong relation with failures [2, 10]. In this study, the data showed that 71% of health professionals stated that the orthopaedic devices that presented the most incidents in the last years are those destined to arthroplasty.

Fifteen percent of the physicians stated that they are the most problematic osteosynthesis devices, and the other 14% said that the highest incidence of intercurrences is in grafting materials normally used for filling. It is emphasized that the surgical technique is essential for successful installation of the OD, so the surgeon must have extensive experience in its installation, as well as much technical knowledge, obtained only with an infinity of practices. The data showed that 27% of doctors said that the nature of the failures happens due to problems inherent to the patient, such as immune reaction,

Fig. 1 Representative graph of choice of device and biomaterial by surgeons
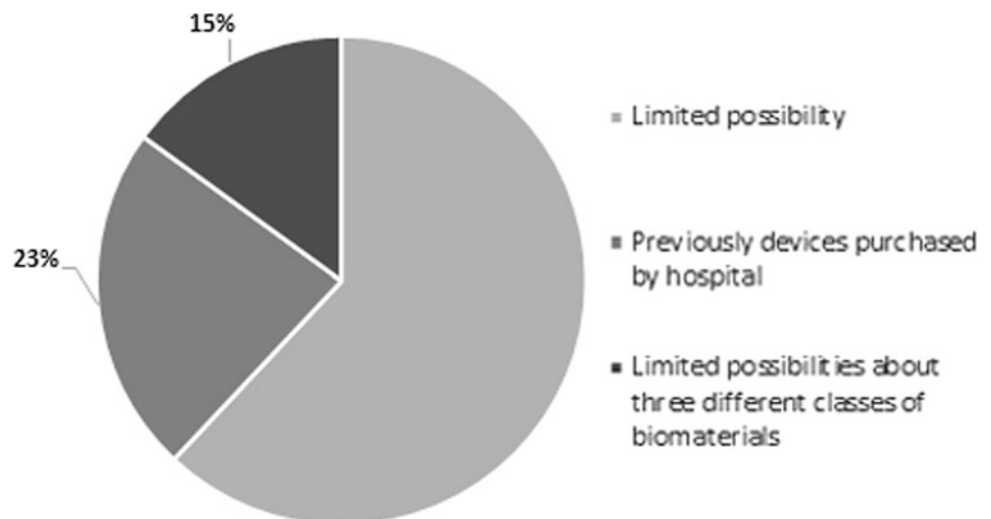
Fig. 2 Representative graph of the casuistry of the failures according to the physicians and patients
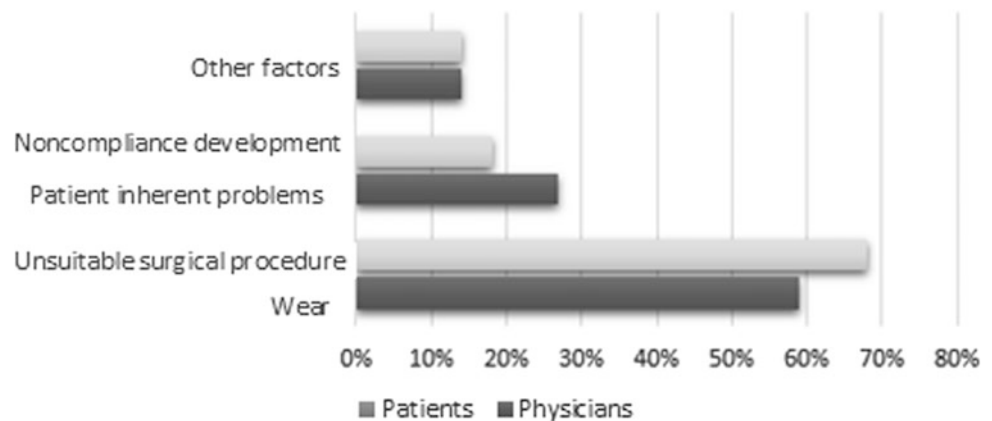
Fig. 3 Representative graphic of the estimate of failures in DO pre-commercialization and post installation
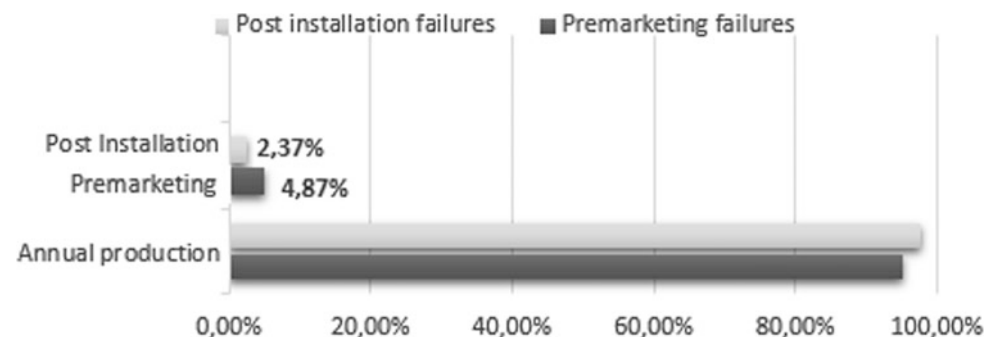
weakness, allergies, among others. While 59% claimed that failures occur due to wear or poor fixation, and others stated that failures are associated with production problems. For patients, the casuistry it is a result of other reasons, 68% of them agree that the failures come from unsuitable surgical management, and 14% that these occurrences are due to the development non-compliant device. Others believe that the failures occur from a combination of factors, including those already mentioned, and the lack of information to the patients about the limitations imposed by the device in use (Fig. 2).

In this study, the data showed that 60% of the patients needed revision surgery until their 51 years of age. With aging, the endocrine system undergoes a series of changes that influence the reduction of hormones and proteins essential for bone remodeling. In this way, the bones present greater fragility, being more susceptible to fractures. These factors may influence the number of revision surgeries observed in this age range. This study showed that 79% of the patients submitted revision surgery between 10 and 15 years after the first orthopaedic surgical procedure, the others needed revision surgery between 4 and 8 years after the first surgical procedure [11].

When an adverse event is detected in products already on the market, it is possible to trigger a recall, a procedure whereby the supplier informs the public of defects found in the products. In this research, 67% of the companies interviewed never had to trigger recall and the others have

already triggered for some type of products. Companies that used such a resource fit both in production, distribution or resale, while the others had only distribution/resale function. The incidence of failures detected by the companies in the device before being released to the market for clinical use, according to the companies interviewed, is less than 5% and after release is less than 2.5% according to the results obtained (Fig. 3).

According to the previous data, the results showed that the number of devices that failed in the years of 2015 and 2017 is negligible. Of the 109 physicians who participated in the survey, most stated that the intercurrent estimate is up to 1% of devices implanted annually. The minority stated that cases of noncompliance amount to between 2 and 10% of devices implanted annually (Fig. 4).

The numbers obtained for the period of 2015 and 2017 in Brazil show that the incidence is very high when compared to the 1970s in the USA, where the failures was less than 0.01% in annual orthopaedic procedures. The hypothesis for this fact to occur, in a period where the technology surpasses that of the previous period, may be due to the high number of needless surgeries, that are performed with unreliable materials and even by professionals who take advantage of a fragile system for illicit practices.

The information obtained may diverge between the different axis investigated in this study, which is according with the information available in the literature. The data confirmed that there is still unsuitable communication
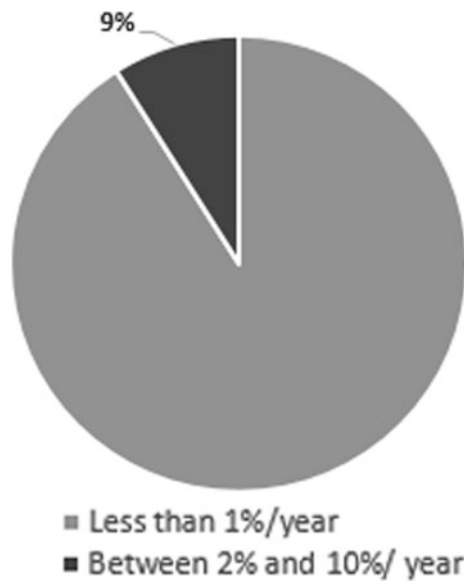
Fig. 4 Representative graph of the estimative of failures in orthopaedic devices according to medical opinion

among the related axes, and that there is still a need for better monitoring, both in production of OD, as well as in the performance of the professionals who install these devices, in addition to the proper guidelines to these devices users.

4 Conclusions

According to the results obtained, it was concluded that:

- It was noticed a great difficulty in obtaining data on the occurrence of faults, either through access to public data, or through direct and indirect contact with companies and health institutions.
- The evaluation of the causes of failure in OD can't be performed only based on the interest of each segment, as there are more technical interpretations and others who consider legal aspects, while others address a socioeconomic context. As a multidisciplinary market hardly, all respondents will be experts or lay people in all observed criteria.

- Surgeon and patient users of the orthopaedic devices need an effective method of communication. The integrated partnership of these groups is a valuable source of information on actual clinical needs, possible adaptations in the design of the device and above all, the prevention failure. Therefore, it is reinforced the need of tools that can ensure the relationship between industry/physicians/patient in the analysis of failures in OD.

References

1. Azevedo, C., de Farias, R., Hippert Junior, Eduardo. Análise de falhas de implantes cirúrgicos no Brasil: a necessidade de uma regulamentação adequada. Cadernos de Saúde Pública **18**(5), 1347–1358 (2002)
2. Belloti, J.C.: Cenário atual do uso de próteses ortopédicas—Discussão sobre próteses nacionais versus importadas. Diagn e Tratamento **14**, 9–11 (2012)
3. Fonseca, F., et al.: Fundamentos da Biomecânica: Músculo-Esquelético e Ortopédico. Publindústria. Edições Técnicas, Portugal (2011)
4. Hench, L.L., Best SM.: Em Biomaterials Science: An introduction to Materials in Medicine. Academic Press: Oxford. I.2.4 (2014)
5. ABIMO. Dados de Comércio Exterior. Edições técnicas, Brasil 2016
6. PEREIRA, SS. da S., GRIJÓ, G.C., RAMALHO, P.I.S.: Grupo de Trabalho Interinstitucional sobre órteses, próteses e materiais especiais (GTI-OPME). Relatório Final. Brasília (2015)
7. Pereira, S.S.S., Grijó, G.C., Ramalho, P.I.S. (Coord). Grupo de Trabalho Interinstitucional sobre órteses, próteses e materiais especiais (GTI-OPME). Relatório Final. Brasília, julho de (2015)
8. Guimarães, R.: Technological incorporation in the Unified Health System (SUS): the problem and ensuing challenges. Ciência Saúde Coletiva **19**(12), 4899–4908 (2014)
9. Landim, André et al. Equipamentos e tecnologias para saúde: oportunidades para uma inserção competitiva da indústria brasileira. BNDS 37, 173–226 (2015)
10. Melchior, S.C., et al.: Pré-qualificação de artigos medico-hospitalares: uma estratégia de vigilância sanitária de prevenção. Núcleo de vigilância em Eventos Adversos e Queixas Técnicas (NUVIG). Brasília, junho de (2008)
11. Parfitt, A.M. et al.: Relationships between surface, volume, and thickness of iliac trabecular bone in aging and in osteoporosis. Implications for the microanatomic and cellular mechanisms of bone loss. J. Clinic. Investig. **72**(4), 1396–1409 (1993)

Ultrasound Transducer for Deep Quantitative Elastography

José Hilton Nascimento, Julio Cesar Adamowski, and Chi-Nan Pai

Abstract

Ultrasound elastography is a new technique capable of estimating the elasticity of soft tissue. In the present work, the elastography technique studied is the imaging by acoustic radiation force impulse (ARFI). It uses a transducer to vibrate a tissue remotely using a focused acoustic beam, and focused tracking beams are used to monitor tissue displacement. This method is interesting because it allows a quantitative analysis of the mechanical properties of soft tissues. However, ARFI is limited to depths lower than 80 mm, which prevents its use in obese patients due to the inability of the transducers to concentrate the required energy at higher depths without compromising the patient's health. In this work, a 32-element linear matrix transducer was developed to concentrate energies at high depths. First, it was tested in pulse-echo mode. The next step will be to apply the ultrasound wave-focus technique to a 120 mm point that will be monitored using a hydrophone.

Keywords

Elastography • ARFI • Linear array

1 Introduction

One of the only methods for diagnosing the degree of liver fibrosis was biopsy. This remains as the golden standard method, not only to identify the stage of fibrosis (F0 = normal liver, F1 = minimal fibrosis, F2 = significant fibrosis, F3 = severe fibrosis and F4 = cirrhosis), but also for identifying steatosis, necrosis, and inflammatory activity [1]. However, biopsy is an invasive procedure that causes temporary pain in 20% of patients [2], and in 1.1% of patients it generates complications such as pneumothorax, hemobilia (hemorrhage in bile), and hematoma [3]. For this reason, non-invasive methods have been widely studied.

One such method is ultrasound elastography. Ultrasound imaging technique where local tissue displacements are estimated by quasi-static tissue deformation or by shear mechanical waves via analysis of tissue stiffness. If the behavior of one part of the fabric presents a modulus of elasticity different from the others, it will deform less or more than the material that surrounds it [4].

Among the techniques under development is the impulse of acoustic radiation force (ARFI). This is characterized by the emission of a bundle of short-duration high amplitude mechanical waves (less than 1 ms duration) focused on the target tissue to vibrate it remotely [5]. The vibration will generate shear waves in the tissue, which speed is related quantitatively to the tissue stiffness. The shear wave speed can be estimated by using imaging techniques, and the images can be obtained by using the transducer that generated the ARFI, or by using other exclusive imaging transducer [6]. This is justified, therefore, in an ideal situation where the tissue is isotropic and incompressible; the speed of the shear wave is proportional to the square root of the elastic stiffness of the tissue [7].

The ARFI elastography is a technique that presents a high success rate (90–99%) when referring to patients with a body mass index (BMI) below 25 kg/m^2 [8]. However, in the case of patients with BMI $\geq$ 30 kg/m^2, this success rate drops to 82.4% [9]. Furthermore, over one-third of the adult population has a body mass index (BMI) of 25 kg/m^2 or greater [9]. The currently available ARFI transducers can only generate vibration in tissue up to depth of 8 cm, which is insufficient to reach all regions of the liver in patients with high abdominal circumference [10].

Thus, the development of a transducer that achieves greater depth to increase the reliability of ARFI in obese patients is necessary.

In the literature, there is a development of an XL mono-element transducer with 2.5 MHz frequency for obese

J. H. Nascimento (✉) · J. C. Adamowski · C.-N. Pai
University of Sao Paulo, Sao Paulo, Brazil
e-mail: jhnn@usp.br
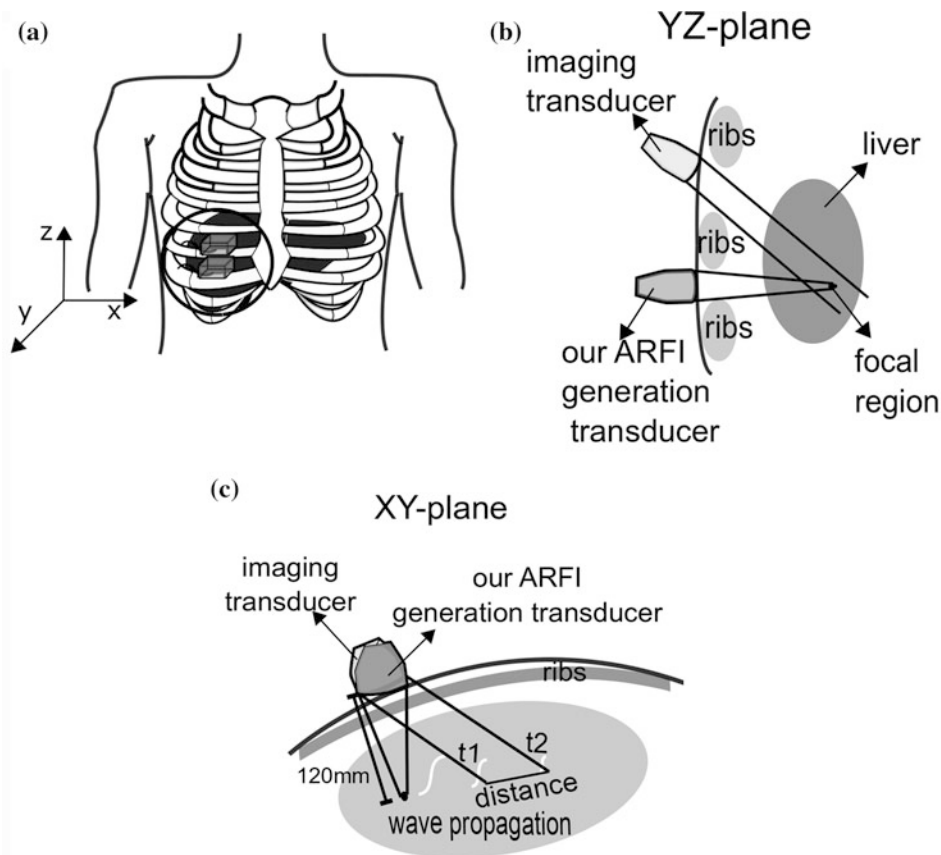
Fig. 1 **a** Transducers positioned in the body; **b** transducers positioned between the ribs; **c** tracking of shear velocity

patients, but the focal point is 80 mm [11]. And in biomedical engineering laboratory, a transducer capable of reaching tissue at 120 mm depth is being developed, but this study does not take into account the thoracic cavity present between the target (liver) and the transducer [12].

Therefore, the study proposed in this article aims to present the fabrication of a multi-element ARFI transducer to remotely generate the vibration of a biological tissue at 120 mm depth. The manufactured ARF transducer (our ARFI generation transducer) will generate vibration, while an image transducer (see Fig. 1) will track the propagation of the shear waves. For this purpose, it was assumed that the transducer is placed between the inter-costal spaces so that the bundle of acoustic waves is not blocked by bone tissue. As the intercostal space has an average width of 14.5 to 19.7 mm [13], a linear transducer with a ceramic height of at most 10 mm was chosen. When combined with the encapsulation, it reaches a maximum height of 14 mm, see Fig. 1.

This article also presents an analysis of the acoustic waves of the transducer operation in pulse-echo mode that was performed to characterize its operation.

2 Materials and Methods

As the ultrasonic waves propagate in a medium, they undergo a process of reducing the amplitude of the acoustic wave. In the case studied, the loss of energy is more significant because of the high depths. One way of increasing the energy at a specific point of the cellular tissue is to divide the piezoelectric elements used, since doing that it is possible to focus the acoustic waves through emission delays, which also increases the concentration of mechanical energy.

For this purpose, a 32-element linear array ultrasonic transducer was built with a 2.25 MHz piezoelectric ceramic (pz37, Ferroperm Piezoceramis A/S, Denmark).

2.1 Construction

The multi-element linear array transducer constructed for this study is represented by the Fig. 2.

As already mentioned, the transducer is composed of a piezoelectric ceramic of 2.25 MHz frequency (pz37, Fer-roperm, Denmark) and was segmented into 32 elements in a disk-cutting machine (DAD322, Disco Corp, Japan). Each element is 1.2 mm wide and 10 mm high.
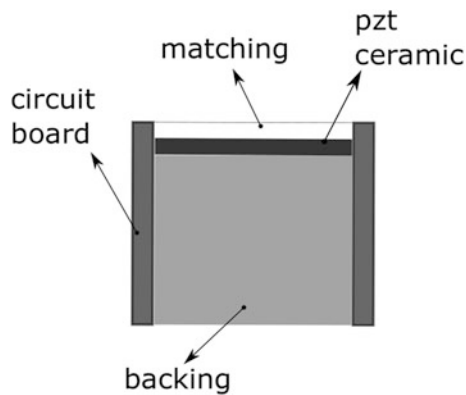
Fig. 2 Transducer structure

For the transducer, assembly printed circuit boards (each with 64 connectors) were glued to the ceramic by using conductive epoxy (Circuit-Works Conductive Epoxy, Chemtronics, USA). These circuit boards were used to facilitate the connection of wires to the ceramic.

In the developed transducer, the backing composition was 30% by mass of tungsten [14]. This mass percentage produced the best attenuation result for the studied cases.

The matching layer (the layer between the piezoelectric ceramic and the medium where the wave propagates) is capable of maximizing the transmission of the acoustic wave. In order to achieve this acoustic compatibility, the matching's acoustic impedance (Z_m) is calculated by the formula $Zm = \sqrt{Z_{cer} \cdot Z_{medium}}$, where Z_{cer} is the acoustic impedance of the ceramic and Z_{medium} is the impedance of the medium [15]. In the case under study, the matching's acoustic impedance is 5.1 MRayls, because Z_{cer} is 18 MRayls and Z_{medium} 1.5 MRayls.

The encapsulation was added last. It has been mounted to allocate the connecting wires and the ground wire and, for this reason, it must be well sealed. The characteristics of the transducer are shown in Table 1.

2.2 Experimental Setup

One of the experiments performed with the linear array transducer was the pulse-echo technique. Through its application, it is possible to obtain the frequency spectrum or frequency response, as well as the measurements of the amplitudes of the pulse-echo responses as a function of the frequencies. This spectrum is then used to establish the operating parameters of the transducer such as the central frequency, peak frequency and bandwidth. Furthermore, it is possible to obtain the emitted pulse-echo sensitivity, by comparing the amplitude of the applied voltage with that of the acoustic wave return voltage [16].

Table 1 Properties of our ARFI generation transducer

Property	Value
Center frequency	2.25 MHz
Thickness of ceramics	0.6 mm
Number of elements	32
Element height	10 mm
Element width	1.1 mm
Space between elements	0.1 mm
Pitch	1.2 mm

For this experiment, a tank was filled with sufficient water to completely submerge the transducer created, a structure was designed to keep the transducer parallel to the bottom of the tank and a flat reflector was placed at a distance of 50 mm of the transducer. In addition to the pulser/receiver system (5077PR, Panametrics-NDT), an oscilloscope (MSO8064A Infiniium, Agilent Technologies) was used for visualizing the propagation of the acoustic wave as a function of time (see Fig. 3).

The acoustic wave data obtained from the oscilloscope were saved. Using this information it was possible to rebuild the acoustic wave in MATLAB, and thus compare the waves through a pulse-echo simulation performed in Field II. Moreover, through processing of this data and using the Fast Fourier Transform function (FFT) in MATLAB, it is possible to describe the frequency spectrum.

Another information acquired was the electrical impedance of piezoelectric ceramics (the measurement of the resistance of a material to the electric current in given a frequency band and phase). With the impedance analyzer (HP4194A), it was possible to obtain the impedances of the piezoelectric ceramic in their original state, of the elements that make up the transducer (individually), of the elements of
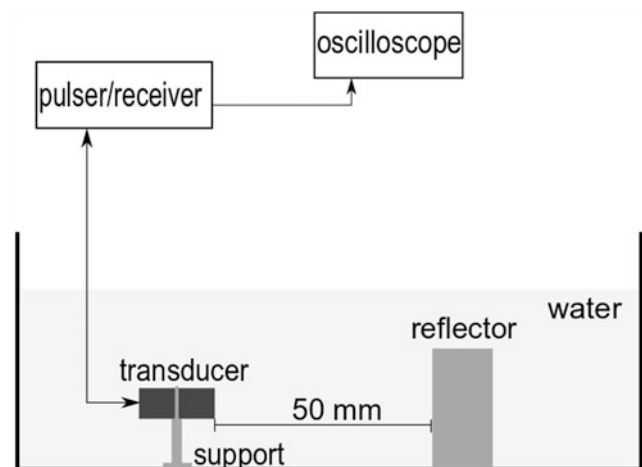
Fig. 3 Pulse-echo measurement

the transducer under construction (with the backing layer only) and of the elements of the fully assembled transducer.

3 Results

The electrical impedances of the ceramic were measured after each step of the construction of the transducer. Figures 4 and 5 show the electrical impedance and phase curves of the ceramic pz37 in the dimensions and conditions acquired from the manufacturer, of the ceramic after cutting the element, of the element with the backing layer and of the element in the fully assembled transducer.

The acoustic impedance of pz37 in its original state has the resonance and anti-resonance frequencies with values close to 2.2 MHz and 2.58 MHz, respectively.

After the cut, the element has two resonance and anti-resonance points close to the original configuration, although there was a slight drop in frequency values. On the other hand, the electrical impedance of the elements with the backing layer and the fully assembled transducer were not evident in the graph.

When analyzing the phases, a similar behavior to the impedance can be observed. The element made of ceramic presents two phase peaks close to each other, while the elements with the presence of the backing have a low phase amplitude.

The pulse-echo experiment was performed in each one of the elements individually. Figure 6, captured on the oscilloscope, shows the wave propagated and received by the element 3, which was similar to those emitted by the other elements. To improve the image representation, a gain of 20 decibels (dB) was assigned to the pulser/receiver and an

Fig. 5 Phase as a function of frequency

average acquisition of 16 frames per image was performed on the oscilloscope.

In Fig. 7, the acoustic wave emitted by element 3 is shown with its normalized values, and compared to a pulse-echo wave simulated in MATLAB, also normalized. It is possible to see that the waves' shapes are very close, meaning the waves emitted by the elements presented a response very similar to the simulation regarding to the shape of the acoustic wave.

The gain of 20 dB of the acoustic waves was removed from the data processing performed in MATLAB, this gain in the voltage would represent a 10 times increase of the real value. Thus, the values of maximum and minimum pressure of the acoustic waves of the echo pulse captured by the elements were determined. The maximum pressures of each element are around 0.25 V while the minimum is around

Fig. 4 Electromechanical impedance as a function of frequency
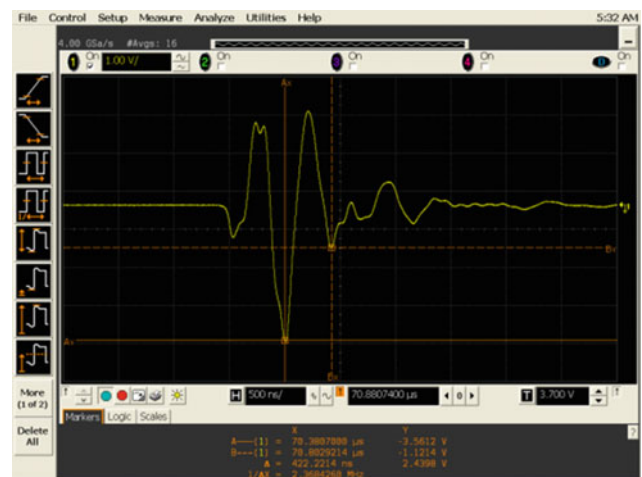
Fig. 6 Pulse-echo measurement on the oscilloscope

Simulated wave and wave of element 3
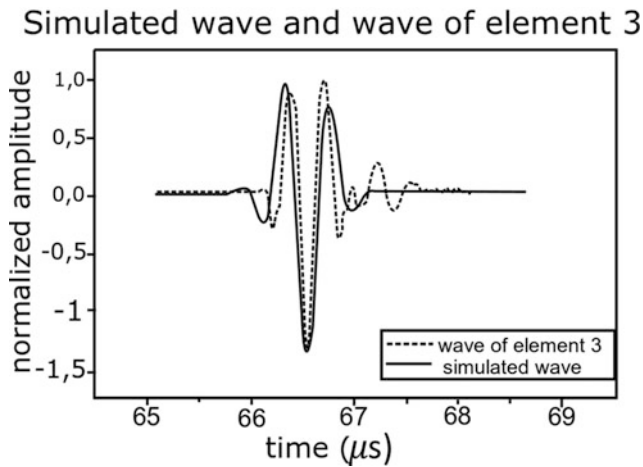
Fig. 7 Comparison of the simulated and measured echo pulse in the oscilloscope

Frequency spectrum
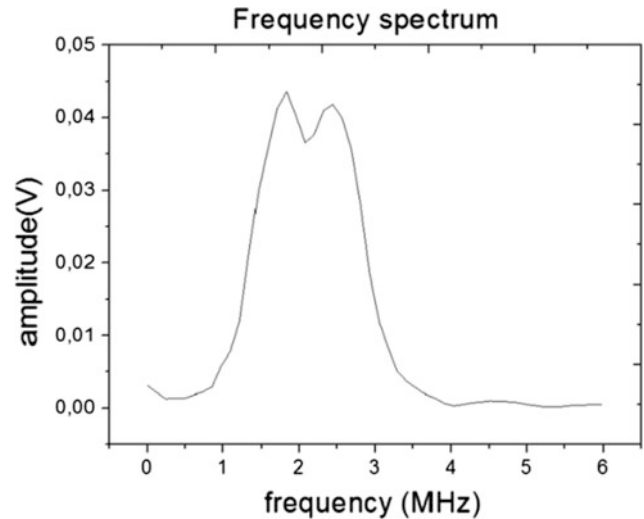
Fig. 9 Frequency spectrum
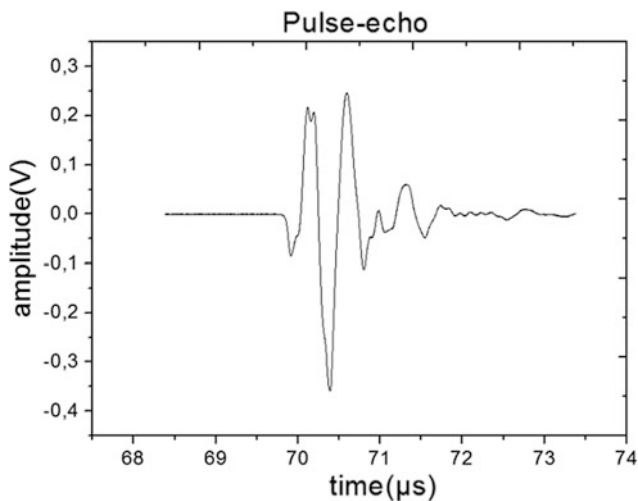
Pulse-echo

Fig. 8 Reproduction of the echo pulse waveform of element 3 in MATLAB

0.3 V, and the potential differential supplied by the pulser was 100 V, as the Fig. 8 shows:

Another important aspect that is obtained from the acoustic wave is the frequency response (also called frequency spectrum), see Fig. 9. This information is obtained through the Fourier transform of the acoustic wave in time.

With the frequency spectrum, the center frequency (fc) is obtained, which is calculated as the average of the low frequency (fb) and the high frequency (fa) that can be found at the point where the amplitude reaches 6 dB [17], see Fig. 10. The peak frequency (fp) is the point of maximum amplitude of the wave. The bandwidth is the difference between the high frequency and the low frequency.

The Fig. 10 shows the frequency spectrum from the FFT (made in MATLAB) of the acoustic wave of Fig. 8. For a better identification of the mentioned parameters, we plotted the spectrum in decibels on the vertical axis Fig. 10.

Like the frequency response of element 3, all the curves of the frequency spectra of the other elements presented an asymmetrical shape, that is, in no case the center frequency was the same as the peak frequency. On the other hand, the bandwidth varied between 60 and 76%, a value that positively influences the axial resolution of the signal.

The bandwidth of the frequency spectrum of the acoustic waves emitted and received from the elements fluctuated from 60 to 75%, a value that allows a good axial resolution of the signal [12] The center frequencies remained around

Spectrum frequency in decibels
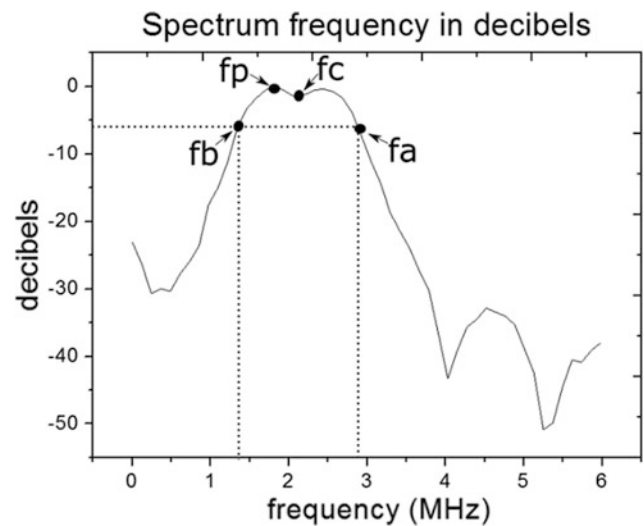
Fig. 10 Spectrum frequency in decibel
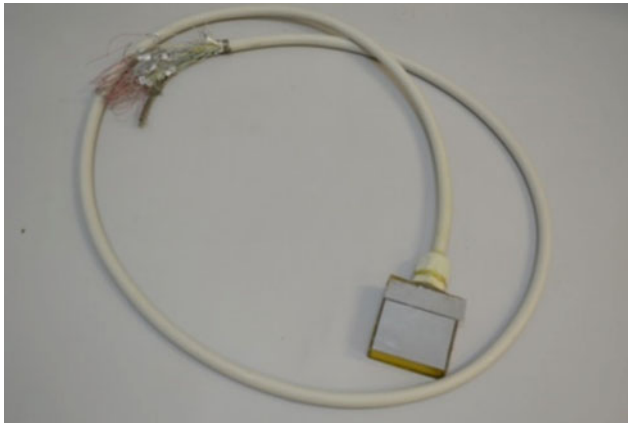
Fig. 11 Photo of transducer built

1.8 MHz and the peak frequencies around 2 MHz, that is, the frequency response presented an asymmetric form.

A photograph of the completed ultrasound transducer linear array is shown in Fig. 11.

4 Conclusion

The development of an ultrasound transducer is a complex procedure because it has many manual steps, which causes some errors in the dimensions and characteristics of the designed and assembled transducer. Even so, the transducer presented results within the expected values for the electrical impedance curve and the phase. As for the operation in pulse-echo mode the acoustic waves behaved almost as the simulated waveform and presented a good bandwidth.

In future works, the aim is to focus all the acoustic waves emitted by the elements of the transducer in a focal point located 120 mm deep and to calculate the resultant pressure at this point.

References

1. Sigrist, R.M.S., Liau, J., El Kaffas, A., Chammas, M.C., Willmann, J.K.: Ultrasound elastography: review of techniques and clinical applications. Theranostics **7**(5), 1303–1329 (2017)
2. Barr, R.G.: Elastography assessment of liver fibrosis: society of radiologists in ultrasound consensus conference statement. Ultrasound Q **32**(2), 94–107 (2016)
3. Kose, S., Ersan, G., Tatar, B., Adar, P., Erturk, Sengel B.: Evaluation of percutaneous liver biopsy complications in patients with chronic viral hepatiti. Eurasian J. Med **47**(3), 161–164 (2015)
4. Ophir, J., Miller, R.K., Ponnekanti, H., Cespedes, I., Whittake, A. D.: Elastography of beef muscle. Meat Sci. **36**, 239–250 (1994)
5. D'Onofrio, M., et al.: Acoustic radiation force impulse of the liver. World J. Gastroenterol. **19**(30), 4841–4849 (2013)
6. Nightingale, K.: Acoustic radiation force impulse (ARFI) imaging: a review. Curr. Med. Imag. Rev. **7**(4), 328–339 (2012)
7. Faruk, T., Islam, M.K., Arefin, S., Haq, M.Z.: The journey of elastography: background, current status, and future possibilities in breast cancer diagnosis. Clin. Breast Cancer **15**(5), 313–324 (2015)
8. Yin, M., Venkatesh, S.K.: Ultrasound or MR elastography of liver: which one shall I use? Abdom. Radiol. 1–6 (2017)
9. Bota, S., et al.: Factors associated with the impossibility to obtain reliable liver stiffness measurements by means of Acoustic Radiation Force Impulse (ARFI) elastography—analysis af a cohort of 1031 subjects. Eur. J. Radiol. **83**(2), 268–272 (2014)
10. Mcmurray, A.: Acoustic radiation force impulse and shear wave detection imaging in the liver and shear wave detection imaging. Global Siemens Headquart. (2014)
11. Myers, R.P., et al.: Feasibility and diagnostic performance of the FibroScan XL probe for liver stiffness measurement in overweight and obese patients. Hepatology **55**(1), 199–208 (2012)
12. Santos, D.S., Cardoso, F.M., Furuie, S.S.: Two-dimensional ultrasound transducer array for acoustic radiation force impulse imaging. ABCM International Congress of Mechanical Engineering, COBEM 2017, Curitiba (2017)
13. Kim, Y.S., Park, M.J., Rhim, H., Lee, M.W., Lim, H.K.: Sonographic analysis of the intercostal spaces for the application of high-intensity focused ultrasound therapy to the liver. Am. J. Roentgenol. **203**(1), 201–208 (2014)
14. Coelho, B.S., Pai, C.N.: Manufacturing of multi-element piezoelectric transducer for use in ultrasound elastography. ABCM International Congress of Mechanical Engineering, COBEM 2017, Curitiba (2017)
15. Shung, K.K., Zipparo, M.J.: Ultrasonic transducers and arrays. IEEE Eng. Med. Biol. Mag. **15**(6), 20–30 (1996)
16. ASTM E1065/E1065 M—14. Standard Guide for Evaluating Characteristics of Ultrasonic Search Units. ASTM International (2016)
17. Trots, I., Nowicki, A.: Influence of the transducer bandwidth on compressed ultrasonic echoes. Arch. Acoust. **32**(4), 903–915 (2007)

Virtual Reality Game Development Using Accelerometers for Post-stroke Rehabilitation

Gustavo R. P. Esteves, Bruno A. M. Miranda, André F. P. Aleixo, Malki-çedheq B. C. Silva, and Marco A. B. Rodrigues

Abstract

stroke can generate several types of sequelae, including motor difficulties in both upper and lower limbs. One way to eliminate or reduce these difficulties is through physical therapy, but this type of treatment can often become tiresome and monotonous, decreasing the patient's interest. Thus, aiming to assist in the rehabilitation of patients, this work seeks to use immersive virtual reality games with the purpose of interacting with physiotherapy exercises. In this type of game the individual must use special equipment (glasses) to feel in an environment where they can interact in different ways with the scenery. Among the possible equipment used for immersive virtual reality was chosen to use a smartphone in conjunction with a virtual reality glasses. In this way an environment was developed that allows the individual to move through the scenario by the control of the upper virtual members by accelerometry sensors, which will be positioned properly to identify the actual movement of the limbs. Thus, an equipment was developed capable of reading the movements and sending this information to a smartphone that executes the developed game.

1 Introduction

A stroke (cerebrovascular accident) occurs when the bloodstream in the brain suffers from a problem such as rupturing or obstructing vessels. Stroke is one of the leading causes of death around the world, its incidence increases with age, and half of individuals who survive have some kind of limitation in their daily lives [1]. Motor problems are examples of these limitations, be they upper or lower limbs.

One of the ways to recover limited movements due to a stroke is through physical therapy exercises [2]. Such exercises often require repetitive movements to be performed by the affected limb, so treatment can become tedious, increasing patient evasion [3]. To minimize this problem it is possible to use electronic games, seeking to motivate patients in a pla`yful way.

Games that have a purpose beyond entertainment such as educating or training the player are called serious games. Its applications can cover several areas such as school teaching in an interactive way, military training, simulations of the most diverse types such as surgeries, constructions, etc. For physiotherapy, they are becoming increasingly common [4], and their use should mainly focus on the correct execution of exercises, fun and simplicity.

Aiming for greater interaction, many of the games seeks to use the concepts of augmented reality and virtual reality. In the first one, virtual elements are inserted in a real environment, so it is necessary to film the environment, process the image, and show the result in some video device, such as a television. In the second case, everything that is shown is virtual, both the scene and the objects, so there is no need for a camera device and the result can also be shown on a television [5].

Among virtual reality games there are those where the player feels external to the environment, being known as non-immersive games, and those where the player feels inside the environment, these are known as immersive games, each type has its different forms interaction with the environment. In non-immersive games the interaction can be made in a less natural way like the use of joystick, mouse or keyboard. In immersive games, a form of interaction that is closer to the natural is usually sought, commonly some kind of virtual reality glasses are needed to show the scene according to the movement of the player's head or gloves that recognize the fingers movements [5].

G. R. P. Esteves (✉) · B. A. M. Miranda · A. F. P. Aleixo · Malki-çedheq B. C. Silva · M. A. B. Rodrigues
Federal University of Pernambuco (UFPE), Recife, PE, Brazil
e-mail: gustavorpe@gmail.com

The virtual reality glasses is an equipment that has been very prominent in recent years [6]. It is able to recognize the movement of the head and generate the corresponding image of the region being visualized for the user, so that it has adequate sensors for this purpose as gyroscopes and enough image processing capacity to generate an image for each eye in real time. Some of the current virtual reality glasses are used in conjunction with some computer, the computer is responsible for processing the images and the glasses being responsible for showing these images and identifying where the individual is looking. Other models use smartphones that already have built-in sensors and have enough processing power to generate three-dimensional images.

With the use of interaction devices, focused on immersive virtual reality, it is possible to seek a direct connection with the concept of biofeedback. In biofeedback the biological signals are captured through specific sensors and then presented to the individual in order to understand and improve the measured signal, such as heart rate, muscle activity, body temperature, etc. For use in physiotherapeutic exercises, sensors should be able to recognize limbs movements and may be best suited to create an interaction in a game that represents their movement [7].

With the use of virtual reality and sensors it is possible, for example, to capture the movements of a member and to show the same being moved in a larger amplitude in the virtual world, in this way the neurons mirror can be activated helping in the recovery of the patient [8]. It is also possible to recognize the movements and interact in the virtual environment to recognize objects, training their near and distant vision in patients who had this type of sequel [9]. Another way is to use virtual reality glasses in conjunction with a treadmill to motivate patients to hike [10]. Thus, there are several possibilities of applications for immersive virtual reality in the recovery of post-stroke patients.

This work proposes the use of immersive virtual reality, with recognition of movements using a portable system aiming to make the treatment more pleasant. The system consists of motion sensors, microcontroller, Bluetooth transmitter, virtual reality glasses and a smartphone that will perform the game specifically developed for this purpose.

2 Materials and Methods

The development of the project was based on using consolidated concepts of physiotherapeutic treatments with the application of immersive virtual reality technologies. Therefore, the designed system serves to give more stimulus to the patient in rehabilitation so that it has greater adherence to the treatment. Among the requirements, we sought an equipment that was portable, easy to use and able to motivate the execution of the exercises. In this way, a

smartphone was chosen together with a virtual reality glasses and an equipment capable of detecting the movements performed and transmitting this information to the smartphone.

Among the smartphones on the market, it is necessary for the device to have the necessary sensors to track the position of the head and with enough processing power to render the virtual environment, that is, compatible with virtual reality. We also opted for devices that had an Android operating system because it is widely used nowadays for portable devices and with vast material on it [11].

Another advantage of using the Android operating system is that Google, the company responsible for creating the same, provides software packages aimed at the development of immersive virtual reality games. These packages have routines needed to capture the information read by the smartphone's sensors and use that information to generate the images that will be displayed for each eye.

To create the virtual environment was used the game engine Unity, this tool has several features that facilitate the development of various types of games. For virtual reality on smartphones with Android operating system can use the packages made available by Google, so you can integrate the environment molded in Unity with the sensors and the screen of the smartphone.

In addition to using sensors embedded in the smartphone, to monitor the movements of the upper or lower limbs requires the use of more equipment. This was developed from the use of accelerometry sensors that are capable of both detecting acceleration of limbs and detecting gravitational acceleration, so it is possible to use gravity as a reference to limb movements. The information readed by the accelerometer is sent to a microcontroller that is responsible for converting this information and sending it to the smartphone from a Bluetooth transceiver, as shown in the diagram in Fig. 1.

To measure the accelerometry of the members was chosen the MPU6050 module, which has sensors in three axes and also three-axis gyro, as well as temperature sensor. This module communicates from the I2C protocol, and allows its sensitivity level to be configured. The MPU6050 is small in size, allowing it to be placed on both upper limbs and lower limbs without causing discomfort.

The data measured by the MPU6050 through the I2C are sent to the Freedom FRDM-KL25Z NXP development board which has as its main component the microcontroller MKL25Z128VLK4. This microcontroller has an internally implemented I2C module that can communicate easily with the MPU6050. In this way the device has been programmed to receive information from the MPU6050 and convert this information into data packets in order to simplify its sending to the smartphone through the Bluetooth module.

The Bluetooth module used was the HC-05, it uses UART communication and can be interfaced directly with

Fig. 1 Block diagram of the
developed system
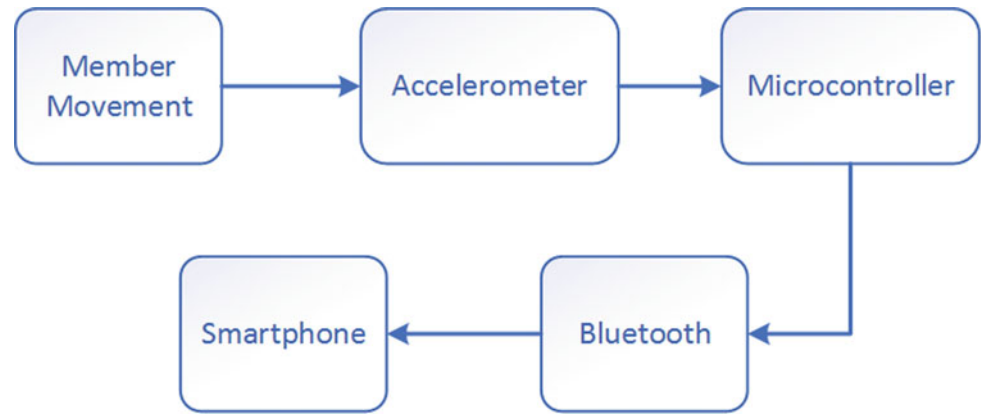
the microcontroller. Already the data that is sent or received to the smartphone follows the Bluetooth protocol version 2.0. Therefore, most devices that have Bluetooth communication can communicate with this module.

All the equipment developed is powered by a lithium battery, so it is possible to use the equipment for approximately one hour, which is sufficient for a conventional physiotherapy session. To recharge the system also developed a specific charger for this type of battery and with connector that avoids risks due to an incorrect connection.

The equipment allows the use of four accelerometers simultaneously, each of them was placed in a plastic casing in order to protect from impacts and oxidation, the same was connected by wires to the development board. The other components were also protected in a plastic housing that besides holes for the output of the wires of the accelerometers, having an indicative light of connection, switch of drive and connector for charger according to Fig. 2.

Fig. 3 Positioning the accelerometer on the left arm

Fig. 2 Motion detection, processing and sending via Bluetooth

Each accelerometer can be placed on both the upper limbs and the lower limbs, not needing to use all simultaneously. Its fixation on the chosen limb can be seen in Fig. 3. In this way, when the forearm is tilted, the values of accelerometry read by the sensor will change and with this it is possible to know the new position of this member.

Fig. 4 Virtual reality glasses that works together with smartphone

Fig. 5 Environment developed with trees and mountains

The final system used an Android smartphone with 5-inch screen, which has the sensors needed to run the application made for immersive virtual reality and Bluetooth communication. It was inserted into the virtual reality glasses in the Google Cardboard standard to be able to be used on the head according to Fig. 4.

3 Results

The scenario of the game, created in Unity, should be pleasant, for it was chosen a sunny day in an open space containing trees and mountains as indicated in Fig. 5. However the same could not be very large and detailed because many graphic resources may cause your smartphone

to fail to render it properly. To move around the scene it is enough that the user uses the sensors in the legs and moves them. It is also possible to control virtual upper limbs by simply placing the sensors on the arms and moving them.

As the application is executed on a smartphone, and in order to obtain a satisfactory sensation of immersion it is necessary that the screen of the same manages two distinct images, one for each eye, as Fig. 6. Such images should show the scene around the individual as he moves his head as well as moving forward according to the movements of the lower limbs, if they are being used.

Because it is a game some goals must be imposed in order to stimulate the patient to reach them. For the upper limbs it is proposed to make consecutive surveys, for the upper limbs it is proposed to make consecutive withdrawals, these exercises being frontal shoulder lift, with each lifting the virtual limbs will also move in the same movement. A counter will indicate how many repetitions have been made, the total number of repetitions to be reached should be

Fig. 6 Screenshot of the game generated on the smartphone screen
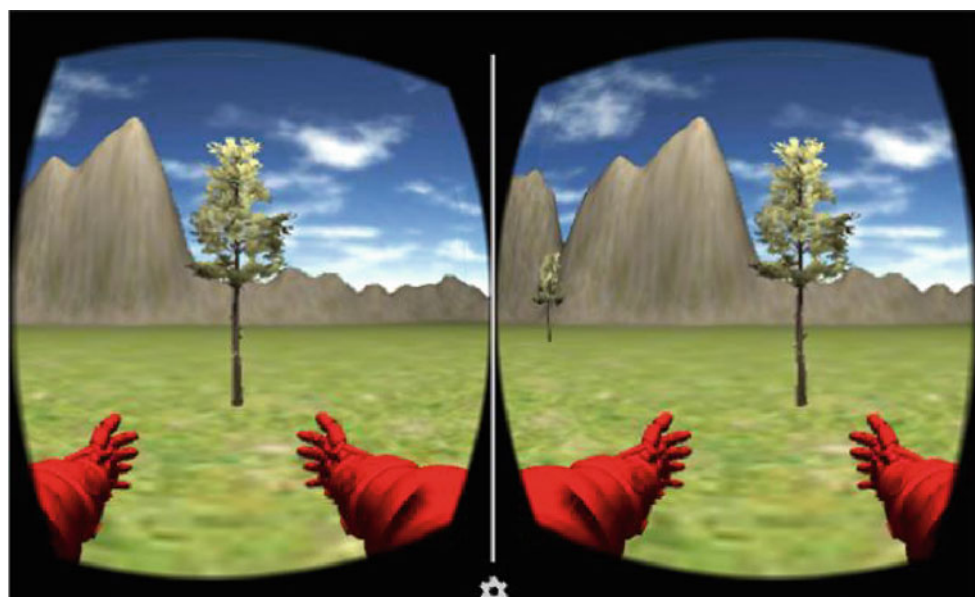
recommended by the physiotherapist. For the lower limbs it is proposed to perform the leg extension movement resulting in the displacement equivalent to a step in the virtual environment, a counter will indicate the number of movements performed. Ideally the patient should, overtime, be able to increase the number of withdrawals or steps and in less time.

The equipment developed was tested in the laboratory in order to evaluate its operation, and then to be tested in patients. The movements were duly captured by the accelerometry sensor, processed by the controller and control data was sent to the smartphone through the bluetooth module in a satisfactory way.

4 Conclusion

With the increased processing power of smartphones and the sensors that some models use, the use of immersive virtual reality becomes more accessible and portable. The developed system allows the patient with motor sequelae due to a stroke to have a more attractive way to perform physiotherapy exercises. The use of accelerometers allows you to recognize the movements of the upper and lower limbs and from them control virtual arms or move around the scene respectively. Thus, the stimuli provided by a pleasant environment and a punctuation system for performing the exercises seek to increase patients' adherence to the physiotherapeutic treatment. Patient testing is expected to indicate acceptance of the system and its efficacy as adjunctive therapy.

References

1. Monteiro, A.: Qualidade de vida (QV) em Indivíduos com Sequelas de Acidente Vascular Cerebral (AVC). Vila Nova de Gaia: Escola Superior de Tecnologias da Saúde do Porto. Vila Nova de Gaia (2011)
2. Lennon, S., Hastings, M.: Key physiotherapy indicators for quality of stroke care. Physiotherapy **82**(12):655–664 (1996)
3. Deutsch, J.E., Mirelman, A.: Virtual Reality-based approaches to enable walking for people poststroke. Topics Stroke Rehabil. **14**(6):45–53 (2007)
4. Dores, A.R., et al.: Realidade Virtual na Reabilitação: Por Que Sim e Por Que Não? Uma Revisão Sistemática. Acta Médica Portuguesa, v. **25**(6) (2012)
5. Tori, R., Kirner, C., Siscoutto, R.A.: Fundamentos e tecnologia de realidade virtual e aumentada. Editora SBC (2006)
6. Pompeu, J.E., Alonso, T.H., Masson, I.B., et al.: Os efeitos da realidade virtual na reabilitação do acidente vascular encefálico: Uma revisão sistemática. Motricidade **10**(4) (2014)
7. Sha, M.A., et al.: EMG biofeedback based VR system for hand rotation and grasping rehabilitation. In: 14th International Conference on Information Visualisation (IV). IEEE, pp. 479–484 (2010)
8. Kang, Y., Park, H., Kim, H. et al.: Upper extremity rehabilitation of stroke: facilitation of corticospinal excitability using virtual mirror paradigm. J. NeuroEng. Rehabil. **9**(1):71 (2012)
9. Yasuda, K., Muroi, D., Ohira, M., et al.: Validation of an immersive virtual reality system for training near and far space neglect in individuals with stroke: a pilot study. Topics Stroke Rehabil. **24**(7):533–538 (2017)
10. Kang, H.K., Kim, Y., Chung, Y., Hwang, S.: Effects of treadmill training with optic flow on balance and gait in individuals following stroke: randomized controlled trials. Clinic. Rehabil. **26**(3):246–255 (2012)
11. Brahler, S.: Analysis of the Android Archtecture. Karlsruher Institut fur Technologie. [S.l.], p. 43 (2010)

Wearable Device for Acquisition of SpO₂ and Heart Rate

André F. P. Aleixo⊙, Euller G. Lima⊙, Érico C. Leite⊙,
Ana V. M. Inocêncio⊙, Lucas T. Lins⊙, and Marco A. B. Rodrigues⊙

Abstract

By being a practical and non-invasive method, the use of oximetry has become increasingly common in both hospital and residential environments. In 2004, the Committee on Quality and Safe Practices of Anesthesiology spearheaded this process when it prioritized the provision of oximeters for patients undergoing anesthesia, promoting progress in reducing the mortality of patients covered by this resolution. The great majority of oximeter devices are non-portable, however, one of the tremendous advantages of wearable technologies is the realization of real-time instrumentation for vital signals. Also, pre-programmed decision-making features allow a third-party device to define some kind action when any irregularity, related to any sort of monitored variable, is detected. However, besides the accessibility in terms of its measurement and data transmission, it is necessary to have some sort of integrity of results so that the system can be considered reliable. In such scenario, this work presents the implementation of a prototyped system that uses Near Field Communication's (NFC) transmission, and both low power consumption and connectivity. Furthermore, an application implemented in Android platform, with an intuitive interface, was designed.

Keywords

NFC • Oximetry • Wearable devices

1 Introduction

Oximetry is a non-invasive method capable of indicating the percentage saturated hemoglobin (Hb) with oxygen in the blood [1]. The instrumentation can be performed in areas such as fingers, wrist, forehead, ear lobes or feet (for premature newborns).

Also in 2004, the Committee defined as priority the provision of oximeters for patients undergoing anesthesia [2]. After this resolution, the World Health Organization reported a 36% reduction in mortality, due to surgeries performed after the checklist for different safety equipment, including the oximeter [3].

Currently, the capture of oximetry data can be performed through two different types of methods: by reflection or by transmission. For pulse oximetry, by utilizing a transmission sensor, light is detected after being scattered through some sort of organ. This approach is limited to fingers and lobes of the ear. On the other hand, in reflection oximetry, the light source and the photosensor are located on the same surface, as presented in Fig. 1. Thus, this type of oximetry presents, as main advantage, the capture of the SpO₂ percentage value in only one surface [4].

The relationship between the light source and the photosensor is also known as the R ratio. Such variable directly depends on the type of blood tonality. However, it has a low sensibility related to skin color, epidermal layer thickness and blood volume during the process of measurement.

It can be defined as wearable technologies, the ones used as daily items by users. Watches, bracelets, shoes, glasses and shirts are the prime examples of how this technology can be inserted into different accessories, serving primarily as a source of information for the user and monitoring systems.

Near Field Communication (NFC) is a technology that enables wireless data exchange between compatible devices that are very close to one another. NFC is commonly misunderstood as a type of passive RFID because it uses the same communication, 13.56 MHz, and the same standard of communication RFID system HF (High Frequency). In order words, NFC can be seen as a subtype of RFID, in which the protocol of communication defers from the passive RFID standards. In general passive RFID systems mostly communicate with each other by using a one direction topology,

A. F. P. Aleixo (✉) · E. G. Lima · É. C. Leite ·
A. V. M. Inocêncio · L. T. Lins · M. A. B. Rodrigues
Federal University of Pernambuco, Recife, Brazil
e-mail: andrealeixo32@gmail.com
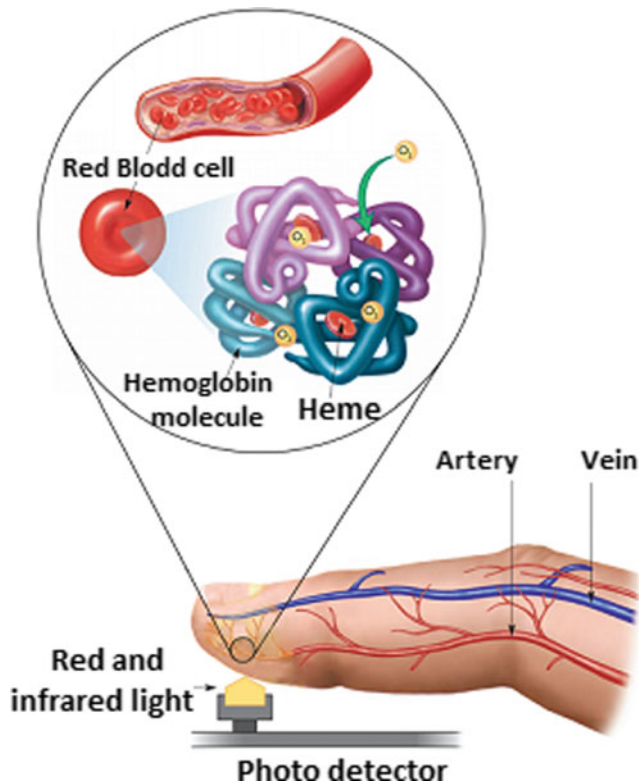
Fig. 1 Representation of the oximetry by reflexion topology. Image adapted from The American Journal of Nursing [5]

while NFC systems are able to impose a bidirectional data flow protocol of communication [6].

This work aims to develop a prototype of wearable equipment capable of capturing data related to the level of blood oxygenation, heart rate and temperature, and to emit, in real time, this data via NFC. Along with the prototype, the BLOO$_2$D application for Android platform was developed. This application receives the data from the wearable equipment, storing and presenting the data.

2 Materials and Methods

The prototype presented in this article was developed in two stages. In the first one, the acquisition and treatment of data on heart rate, blood saturation and temperature were performed. The second one consisted of sending the data acquired through the NFC communication, as well as the development of the application for the Android operating system in order to show the captured data. This way, this session is divided in three topics: hardware, software and final system.
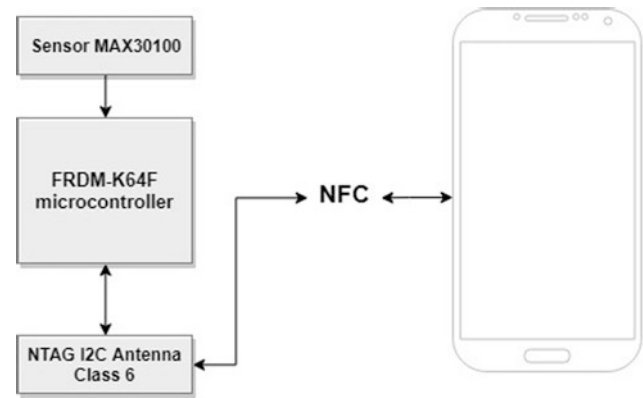
Fig. 2 System's block diagram

2.1 Hardware

The development board used to make the connection between data acquisition and the communication system was the Freedom Board K64F, which contains the microcontroller MK64FN1M0VLL12, the ARM Cortex M4 line, which combines robustness in relation to high processing speed (up to 120 MHz) and low power consumption (250 µA/MHz) [7]. Other development boards were also discussed to carry out the project, however it was chosen because of its characteristics and availability.

For the acquisition of data was used the integrated circuit (IC) MAX30100 that has I^{2}C communication. This communication uses two control pins, the SCL pin being responsible for the bus clock and the SDA pin responsible for transmitting the data. For IC MAX30100, once the initialization and data acquisition values have been set in the registers, it is possible to obtain parameters of oximetry and body temperature.

The heart rate and blood oxygenation are both obtained through the digital processing of the oximetry signal provided by the MAX30100 IC. Such device proved to be the most viable alternative due to its I^{2}C communication protocol standard and its dimensions, in which are given as 5.6 mm × 2.8 mm × 1.2 mm (in millimeters). We also analyzed the ICs MAX30101 and MAX30102, which have additional circuits and functionalities when compared to the ones used in the project, however, the increase in cost, consumption and unnecessary functions to the development of the prototype were sufficient criteria to exclude these ICs.

Figure 2 represents the system's block diagram. It is important to note that the MAX30100 sensor is connected to the microcontroller using the I^{2}C communication and, using the same communication protocol, the NTAG I^{2}C Antenna that communicates with the microcontroller according to the smartphone data.

Table 1 Partial and total expected consumption

Name	Maximum or typical value	Unity
Expected consumption for the NTAG I^{2}C antenna [8]		
Supply voltage	3.6	V—volts
Supply current	155	μA—microamperes
Power consumed	558	μW—microwatts
Expected consumption for the MAX30100 [9]		
Supply voltage	2	V—volts
Supply current	1.2	mA—milliamperes
Power consumed	2.4	mW—milliwatts
Expected consumption for the K64F [7]		
Supply voltage	3	V—volts
Supply current	1.7	mA—milliamperes
Power consumed	5.1	mW—milliwatts
Expected consumption for the entire prototype		
Power consumed	8.06	mW—milliwatts

One of the purposes of the project is to create a low energy consumption device and make a wearable accessible to any patient. Therefore, a study of all consumption expected for the system was carried out, containing analysis of acquisition, communication and processing. Table 1 gives the partial and total consumption of what is expected for the project.

The data entered was taken from the datasheet of the components, it is noted that the power consumption is mainly due to the microcontroller. The expressed data is related to the consumption in very-low-power run mode current, because system will spend most of the time in this mode.

2.2 Software

One of the project objectives is to use NFC communication to obtain the data from the acquisition system. Based on an NXP demo code and the NFC Professional Application Development for Android book [10], an application was developed to perform communication, security protocol, and finally acquisition of all data.

The application was developed on the Android Studio platform and uses only one screen to perform its functions.

Fig. 3 Screenshot sample of the main menu for the BLOO$_2$D application, developed for Android devices

Figure 3 illustrates the application after initialization. In the Testes e Habilitações (from Portuguese, means 'Tests and Configurations') tab, the system provides a synchronization option with the connected device and, below it, provides an option that enables the reception of data. When you approach in on the device, the Leituras de Comunicação (from Portuguese, means 'Communication Readouts') tab shows the communication status and all data coming from the acquisition. In its specifications, the application requires 4.06 Mb of storage to be installed. The power consumption corresponding to RAM can be considered null when out of NFC operation.

Fig. 4 CAD design and 3D printed sample of the BLOO$_2$D bracelet
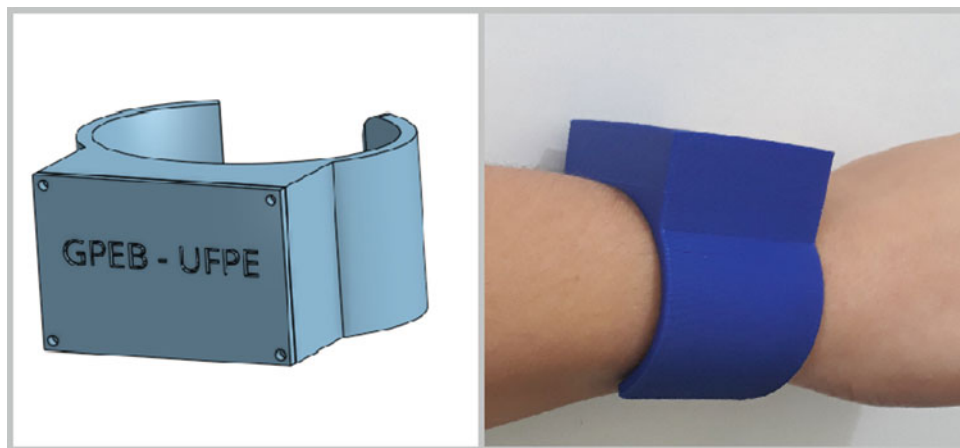
2.3 Final System

The format of the device was developed from the dimensions of the acquisition system. The bracelet was constructed in CAD environment and printed in ABS plastic. This material has high strength and hardness; in addition to its water resistance make it possible to use it in different environments. The assembly is shown in Fig. 4. The bracelet will be active when there is proximity to the smartphone, as it will send security information with an initializer. Then, with the application running, the data will be displayed on the screen.

Regarding the bracelet design, its architecture was developed to avoid noise disturbance when the data is transmitted by a certain amount of distance from the smartphone. Such design is planned to be improved in other versions of the equipment by contemplating an adjustable clip to fix it on the wrist. Even materials with different nanostructures can be tested, which would allow variations in the rigidity, comfort and feasibility of low cost materials to make the bracelet potentially disposable, and reusable in terms of its electronic parts for acquisition.

3 Results and Discussion

The results were obtained with the development board. In this first moment, the custom design plate, with smaller dimensions, is in the manufacturing stage.

First, it was using the MAX30100 to get a response from the signals from the infrared receiver. Figure 5 indicates the SpO$_2$ levels as a function of the number of samples collected. By analyzing the graph, it is possible to notice a high frequency interference generated at the acquisition system.

In order to obtain an instrumentation without the high frequency components acquired from the SpO$_2$ level, both an adjustable parameter for its adaptations and an implementation of a fifth order FIR low-pass filter with a cutoff frequency of 6 Hz were performed. After the modifications, the result obtained was more reliable to be analyzed and, with this, to obtain the values of heart rate and oxygenation of the blood. Figure 6 illustrates the signal that has been worked on.

After stabilizing the acquisition of oximetry, data was collected from the MAX30100 sensor at every second. In
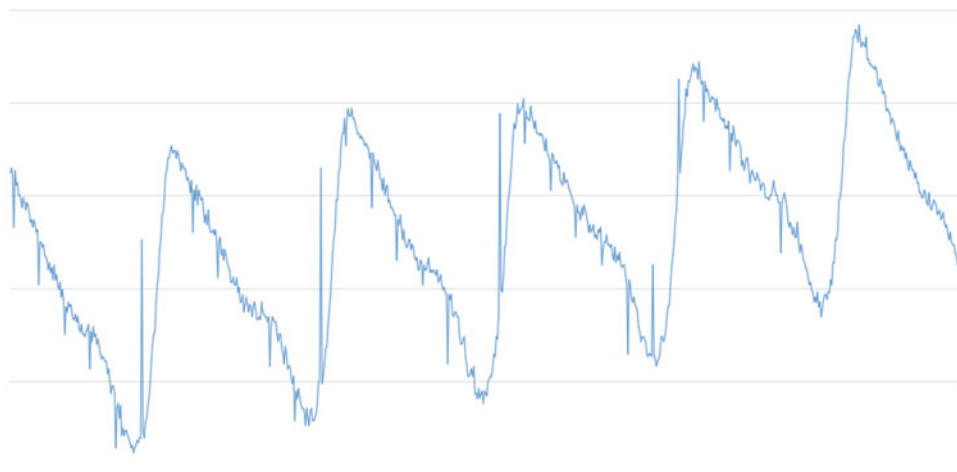
Fig. 5 Obtained oximetry signal of sensor MAX30100

Fig. 6 Obtained oximetry signal after fifth order filtering
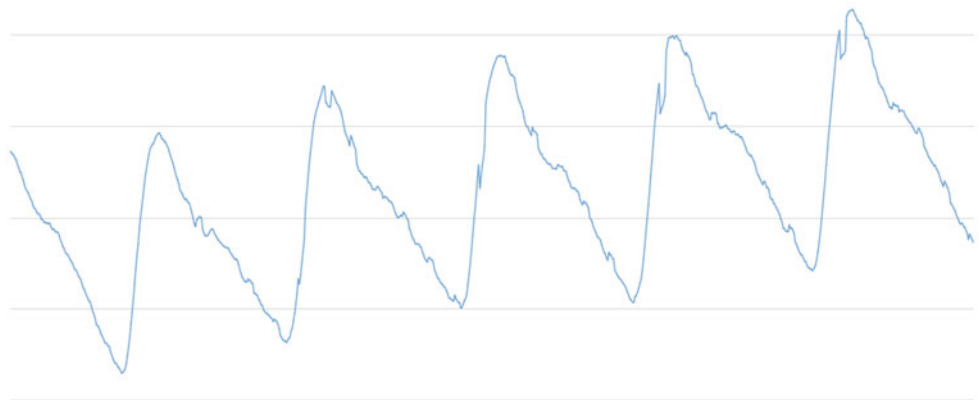
Fig. 7 Terminal with heart rate and SpO$_2$ values

order to preview the results, a PC with UART communication was used. This result is shown in Fig. 7 which shows the heart rate and SpO$_2$ values at 1 s intervals.

Figure 8 again illustrates the application with the smartphone near the antenna. On the Testes e Habilitações tab, the Habilitar recebimento de dados (from Portuguese, means 'Enable Receive Data') text box must be selected to receive the information. In this configuration, the Leituras de comunicação (from Portuguese, means 'Communication Readouts') tab provides the user with information on heart rate and blood oxygenation rate.

The validation of the prototype was performed by comparing the heart rate and SpO$_2$ levels recorded with commercial equipment, model CMS50DL, brand Contec Medical Systems. The comparison of the signals acquired by the prototype was performed with a pulse oximeter, in which acceptable results were obtained. Tables 2 and 3 illustrate the responses obtained by the pulse oximeter and the MAX30100 simultaneously.

Taking into consideration that the data was collected at the same time, the maximum difference of 6.1% for the heart rate is considered quite acceptable, mainly because the oximetry equipment serves as monitoring aid and not as an outlet equipment decision [11]. In relation to SpO$_2$ the maximum difference was 3%, which makes valid the data presented by the prototype. In the work of Webb [12], he presented measurements related to the precision of a total of

Fig. 8 Screenshot sample of the application BLOO$_2$D showing its functioning and enabling for data transmission

Table 2 Heart rate data of the CMS50DL and MAX30100

Heart rate (bpm)		
MAX30100 (bpm)	CMS50DL (bpm)	Percent difference (%)
71.3	76	6.1
74.6	73	2.2
71.4	68	5
71.3	68	4.8
71.1	72	1.25
69.8	71	1.69
72.8	70	4
72.0	70	2.8

Table 3 SpO$_2$ data from CMS50DL and MAX30100

SpO$_2$		
MAX30100 (%)	CMS50DL (%)	Percent difference (%)
96	99	3
96	99	3
96	97	1
96	98	2
97	99	2
97	99	2
97	99	2
97	99	2
96	98	2
96	98	2

244 oximeters. He could conclude that 2/3 of such devices had an average reading difference of 2%, while the rest showed to be less then 3%. Therefore, since the results showed to provide a measurement error of less then 3%, such implemented device is according to the standards and can be accurately used in any kind of environment.

4 Conclusion

The relevance of oximetry systems and the possibility of simultaneous acquisition of the heart rate parameters and SpO$_2$ level transmitted to smartphones via NFC developed in this prototype, facilitates the continuous monitoring of the patient by health professionals in the most varied environments.

From the comparison with the commercial model, it was verified that the prototype guaranteed not only secure transmission of data, but also accuracy similar to consolidated brands in the development of medical equipment.

Unlike the commercial models that generally use the Bluetooth technology, the BLOO$_2$D counts with the power of communication provided by the NFC technology, that not only brings the system to provide a high information integrity, but allows it to be commercialized at a low price with an optimal energy consumption [13].

The use of the Android platform has enabled integration with the vast majority of smartphones used worldwide, illustrating an interactive and enjoyable interface to handle.

References

1. Andrade, L.A.K.D.: Sistema de medição para oximetria de pulso. Master's thesis, Universidade Tecnológica Federal do Paraná (2009)
2. Merry, A.F., Eichhorn, J.H., Wilson, I.H.: Anaesthesia. J. Assoc. Great Br. Irel. (2009)
3. Haynes, A.B., Weiser, T.G., Berry, W.R., Lipsitz, S.R., et al.: A surgical safety checklist to reduce morbidity and mortality in a global population. New Engl. J. Med. (2009)
4. Moyle, J.T.B.: Pulse Oximetry, 2nd ed. BMJ, London (2002)
5. Valdez-Lowe, C., Ghareeb, S.A., Artinian, N.T.: Pulse oximetry in adults. AJN, Am. J. Nurs. (2009)
6. Coskun, V., Ok, K., Ozdenizci, B.: Near Field Communication: From Theory to Practice. Wiley (2012)
7. NXP Semiconductors Kinetics K64F Sub-Family Data Sheet. https://www.nxp.com/docs/en/data-sheet/K64P144M120SF5.pdf. Last accessed 21 Feb 2018
8. NXP Semiconductors NTAG I2C Data Sheet NT3H1101/NT3H1201. https://www.nxp.com/docs/en/data-sheet/NT3H1101_1201.pdf. Last accessed 21 Feb 2018
9. Maxim Integrated MAX30100 Pulse Oximeter and Heart-Rate Sensor IC Data Sheet. https://datasheets.maximintegrated.com/en/ds/MAX30100.pdf. Last accessed 21 Feb 2018
10. Coskun, V., Ok, K., Ozdenizci, B.: Professional NFC Development for Android. Wrox (2013)
11. Alexander, C.M., Teller, L.E., Gross, J.B.: Principles of pulse oximetry: theoretical and practical considerations. Anesth. Analg. (1989)
12. Webb, R.K., Ralston, A.C., Runciman, W.B.: Potential errors in pulse oximetry. Anaesthesia (1991)
13. Strommer, E., Kaartinen, J., Parkka, J., Ylisaukko-oja, A., Korhonen, I.: Application of near field communication for health monitoring in daily life. In: International Conference of the IEEE Engineering in Medicine and Biology Society, New York, NY (2006)

A Multi-Kinect System for Serious Game Development Using ROS and Unity

Mariana Lyra Silveira, Thiago Loureiro Carvalho, Anselmo Frizera Neto, and Teodiano Bastos Filho

Abstract

Game-based rehabilitation systems are often proposed as an appropriate technology for improving patients' motivation during the therapy. They have potential to increase the intensity and frequency of physical activity of stroke patients. In this work we present a Unity integrated ROS-based multi-Kinect system for serious game development. A multi-camera setup offers the advantages of enabling the player (patient) to walk along a wider area and minimizes the risk of occlusion due to people moving along the camera's detection area or even to the patient's own body. The proposed system merges the user joint position provided by multiple Kinect V2 sensors and delivers the results to Unity. A linking mechanism was used so that Unity can listen to and inject messages into ROS environment. We present data from a preliminary technical validation, which consists of an interface controlled by hand movements. The results show that 98.8% of the data obtained by the system were consistent with the user's actions.

Keywords

Stroke rehabilitation • Serious game • RGBd sensor

M. L. Silveira (✉) · T. L. Carvalho · A. F. Neto · T. B. Filho
Federal University of Espírito Santo, Vitória, 29075-91, Brazil
e-mail: mariana.silveira@aluno.ufes.br

T. L. Carvalho
e-mail: thiago.l.carvalho@aluno.ufes.br

A. F. Neto
e-mail: frizera@ieee.org

T. B. Filho
e-mail: teodiano.bastos@ufes.br

1 Introduction

According to the World Health Organization, 15 million people worldwide suffer a stroke annually [1]. Among the survivors, approximately 50% present a permanent disability characterized by one or more of the following deficits: motor, cognitive, sensory and perceptual [2]. Some studies performed with post-stroke patients have shown that motor functions are directly associated with patients' self-care ability and their independence level in daily living activities [3, 4]. Therefore, one of the main focus of stroke rehabilitation is to recover affected neuromuscular functions [5].

In this context, several alternative therapy techniques have been explored to assist motor rehabilitation (e.g. Function Electrical Stimulation, Robotic Systems, Serious Game) [6]. These techniques aim to provide more benefits or enjoyment for patients in comparison to traditional therapy [7]. Gaming platforms are a promising approach to motivate stroke patients with motor injury to perform intensive and frequent physical activity [8]. They provide feedback information about "winning" or "losing" and consequently enhances the patient participation, especially when it comes to motor activities based on repetitive tasks [9].

Capturing human motion can provide useful information for gaming therapy [10]. For instance, human activity recognition based on skeleton tracking might be a fundamental component for human-computer interaction, especially when it comes to serious games. Conversely, markerless motion capture is challenging in the absence of accurate depth information. In this way, the introduction of the Microsoft Kinect sensor had a significant impact in full-body pose tracking. It features a RGB camera and a depth sensor (infrared laser), proving fast and high-quality dense depth images [10].

This paper presents a multi-Kinect system for game development using Unity, which is a well established game development platform. This work aims to enable a game

designer to develop serious games for stroke rehabilitation using a multi-camera skeleton tracker system.

The rest of the paper is organized as follows: Sect. 2 contains an overview of rehabilitation systems focused on serious games. A system description is presented in Sect. 3. Section 4 presents the preliminary results, being followed by the conclusion and future work, found on Sect. 5.

2 Related Works

Rehabilitation systems have become an important research focus in recent years. However they require a specialized hardware designed to solve interaction problems, since its users possess some limitation due to a disability. Compared to wearable sensors, such as accelerometers and gyroscopes, camera-based systems have the advantage of dismissing qualified personnel, which may be needed to correctly put the sensors in place [11].

However, according to Bunger [12], image processing algorithms are subject to some limitations. Occlusion may occur due to objects or people moving along the camera detection area or even by the user's own body, which may overlaps other body parts. In addition, the detection area may be short depending on the desired application. In order to solve or minimize these problems, Bunger proposes the use of multiple cameras.

In this context, Oliver et al. [11] analyzed the precision of a system based on multiples Kinect sensors for the purpose of investigating its feasibility as a rehabilitation assistance platform. They showed the better arrangement of the devices in order to avoid interference from infrared sensors and concluded that the system presented satisfactory results as a rehabilitation tool.

Carvalho et al. [13] also explored the advantages provided by a multiple cameras setup, using the Robot Operating System (ROS) to develop a multi-Kinect based platform. The system was able to track the center of mass of a moving user with a small average error compared to the whole workspace area. They concluded that the platform had satisfactory performance and could be applied to assistive applications such as virtual reality environments.

With the purpose of improving patients' motivation and compliance before therapy, many rehabilitation systems are composed of interactive games. Wittmann et al. [7] developed a serious game in which the player uses arm movements to destroy targets displayed in different locations of a virtual scene. The main goal was to improve the arm reaching workspace. The player motion was detected through the ArmeoSenso system, which consists of three inertial measurement units (IMUs) fixed to the impaired lower and upper arm as well as the trunk.

Dehem et al. [14] opted for the use of a rehabilitation robot to enable the user interaction with a serious game, aiming to improve motor and cognitive deficits simultaneously. The proposed game was based on the target-pointing principle. Therefore, the participant had to reach a specific target with the handle of the robot and bring it to a starting point, repeating this task in a particular order.

It is common for post-stroke patients to present spasticity in elbow muscles, which limits flexion and extension and impairs the whole arm reaching workspace. Given this background, Valencia et al. [15] developed a serious game in order to improve the elbow joint range of motion, in which the user movement was detected through a Kinect V2 device. A surface Electromyography sensor (EMG) was also used with the purpose of investigating the patient's muscle activity, making possible to predict signals of fatigue and evaluate the muscles involved in a specific motor task.

In order to explore the advantages provided by a multi-camera setup, we propose a multi-Kinect based system for gaming rehabilitation. This approach enables the player (patient) to walk along a wider area, allowing the development of complex applications for lower limbs rehabilitation. In addition, the player may perform a greater number of poses without occluding its own body parts. Also, therapists can move along the cameras detection area and assist the patient during gaming with a minimized risk of occlusion.

This work presents a ROS/Unity integrated multi-Kinect system for game development. The cameras data are merged and the result is delivered to Unity, allowing a game designer to create a serious game based on a desired principle, such as mirror therapy [16] or target-pointing [14].

3 Methods

3.1 Multi-Kinect System

The system is composed of a group of RGBd cameras (Microsoft Kinect V2) connected to a heterogeneous computer network. It was designed to support n devices as long as they are connected to different CPUs and video cards. The largest configuration tested, however, connected tree cameras, thus more tests are needed to confirm this feature. The system's overall topology is shown in Fig. 1.

Each Kinect is connected to a client computer, which estimates the user skeleton joint tracking through NiTE2.2 API, released by PrimeSense. NiTE 2.2 algorithms perform functions such as scene analyzer (separation of users from background), accurate user joint tracking and gestures recognition [17]. Many works of literature utilize the Microsoft Kinect Software Development Kit (SDK) alternatively to NiTE. However, as Microsoft SDK was designed

Fig. 1 An overview of the
proposed system
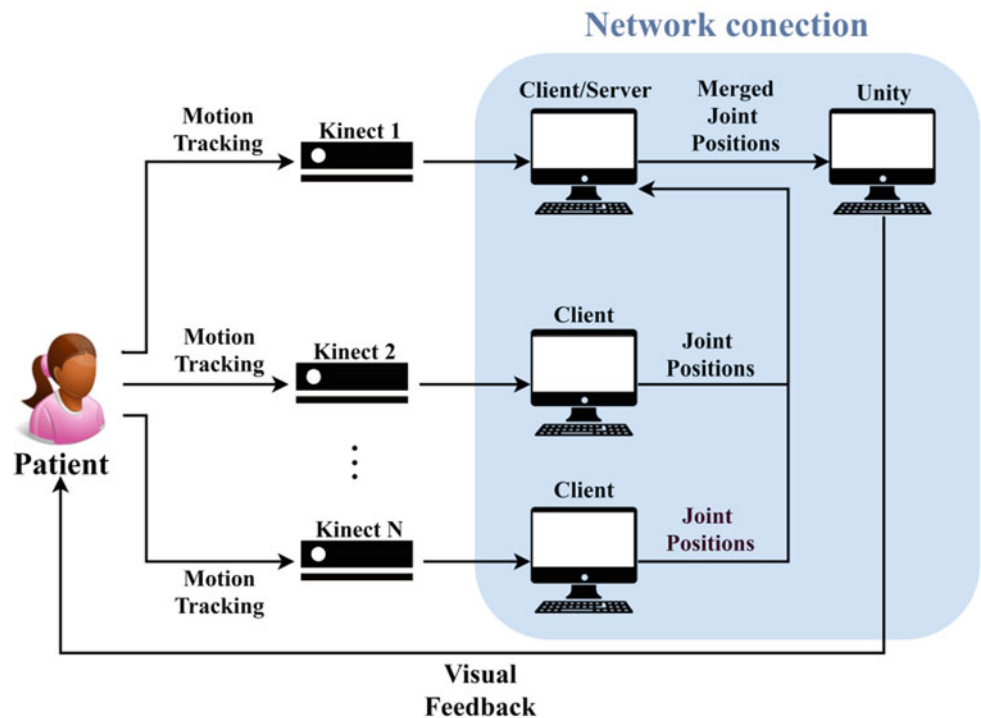
for Windows platforms, we used a Linux supported API, since clients computers run Linux due to the Robot Operating System[1] (ROS). Although it is possible to install and use ROS on Windows, there are some limitations in comparison to its performance on Linux [18].

The network protocols management is performed by ROS, therefore it is necessary that client and server be connected to a same router or switch. Although ROS is designed for robotic applications, we chose to use this framework due to its advantage of providing a software middleware for the development of autonomous systems [19].

The Network Time Protocol (NTP) is used to synchronize the server and client time, enabling the network calibration and the fusion algorithm execution.

Furthermore, the proposed system has a computer running Windows with the purpose of supporting Unity. The communication between the game development platform and server occurs through a linking mechanism described in Sect. 3.4.

3.2 Kalman Filter

The joint positions provided by the clients are merged through a fusion algorithm (Kalman Filter [20]) performed by the system server. Data fusion with Kalman filtering has been studied by several researchers focused on using a multi-Kinect setup [10]. This filter addresses the general problem of trying to estimate the estate x of a discrete-time controlled process that is governed by the following time-space model [21]:

$$x_k = Ax_{k-1} + Bu_{k-1} + w_{k-1} \qquad (1)$$

$$z_k = Hx_k + v_k \qquad (2)$$

where k represents the discrete-time index and x, z, u, A, B and H are the state vector, measurement vector, input control vector, state transition matrix, input transition matrix and measurement transition matrix, respectively. It is assumed that w is the process noise vector, which has zero mean with a covariance matrix Q, and v is the measurement noise vector, which also has zero mean with a covariance matrix R.

A state-space representation of position and velocity can be used to estimate the final state of each joint [10], replacing matrices A and B of Eq. 1. The covariance matrices Q and R were empirically estimated.

3.3 Cameras Calibration

In order to consistently apply the fusion algorithm, the joint positions provided by each client must be estimated from a

common coordinate system. Therefore, it is necessary to calibrate all the cameras connected to the system.

The cameras calibration was made using the OpenCV[2] package. A checkerboard pattern with known dimensions is shown so that at least two cameras can identify it at the same time. The position and orientation of a real object is estimated by relating its 3D coordinates with its projection onto the image. Then, the pattern is placed on the floor, where the global coordinate system is identified. It will be used as basis for 3D representation of the scenes captured by the cameras.

3.4 Linking ROS and Unity

Here we describe the linking mechanism used to integrate a Unity-based game interface with a ROS-based multi-camera system. As we intend to develop a game, it is more feasible to use an existing game development software instead of ROS native visualization tools. In comparison to other game engine systems, Unity offers a number of advantages, as it provides different scripting options, supports a wide range of platforms and provides well supported libraries for access Virtual Reality hardware [22].

Codd-Downey et al. [19] linked ROS and Unity using the rosbridge framework. Rosbridge enables an external agent to listen to and to inject messages into ROS environment. It communicates through yaml-encoded messages.

This process utilizes the WebSocket protocol as a communication layer. For that reason, Unity can communicate with ROS environment through massage passing, since its scripting environment contains many libraries that support the WebSocket protocol. It is more convenient to use the JavaScript Object Notation[3] (JSON), which consists of a file format for data exchange, to map the yaml strings to instances of objects within the Unity scripting environment [19].

The described linking mechanism consists of transmitting yaml-encoded messages through web-sockets, in order to allow ROS and Unity to operate on a completely separate hardware, requiring only a reliable network connection.

3.5 Preliminary Technical Validation

In order to analyze the Nite 2.2 performance and to verify the workspace in which it is capable of correctly identifying the user skeleton, an experimental protocol was proposed. To facilitate data analysis, we chose to evaluate the right
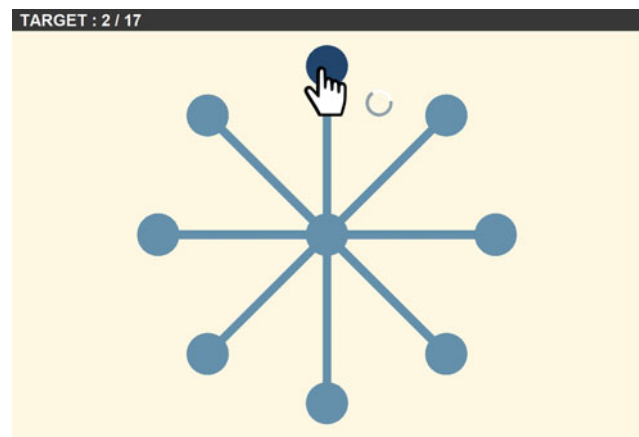
Fig. 2 Developed interface using Unity
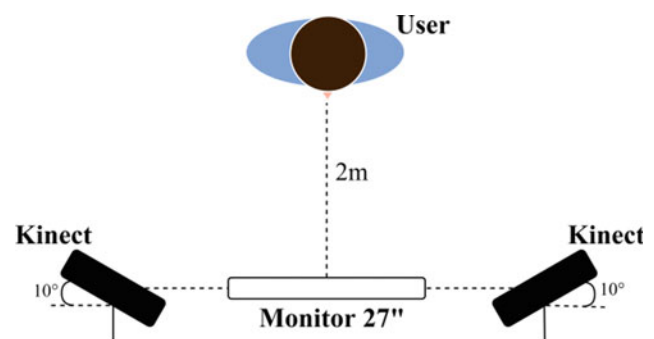
Fig. 3 Kinects arrangement of the experimental protocol

hand joint behavior. Therefore, a 2D Unity interface was developed, with which the user interacts by hand motion.

As shown in Fig. 2, the interface displays nine targets: a central one and eight equally spaced around a circle. A hand shaped cursor informs the user about his/her current hand position.

The protocol consists of moving the cursor from the center to each target and back, starting from "north" and proceeding clockwise. Once the cursor stays above the correct target edge, the next target is highlighted after 10 s. From now on, we will call this event as target selection. The right hand joint position estimated by the fusion algorithm was saved in a text file with JSON format, such as the Unity interface cursor position. This information was subsequently processed using Matlab software.

The described experiment was applied to a healthy subject, since we focused only on technical validation. Two Kinects were positioned one meter away from each other. They were slightly rotated, as shown in Fig. 3, in order to point to the user, which was two meters away from an imaginary line that attached the sensors centers. A 27 inches monitor was used to display the designed interface.

---

[2]http://docs.opencv.org/2.4/.

[3]https://www.json.org/.

Fig. 4 User skeleton reconstruction. **a** Merged joint positions obtained within the ROS environment. **b** Corresponding data received by Unity

(a) User skeleton displayed by RVIZ

(b) Skeleton displayed by Unity
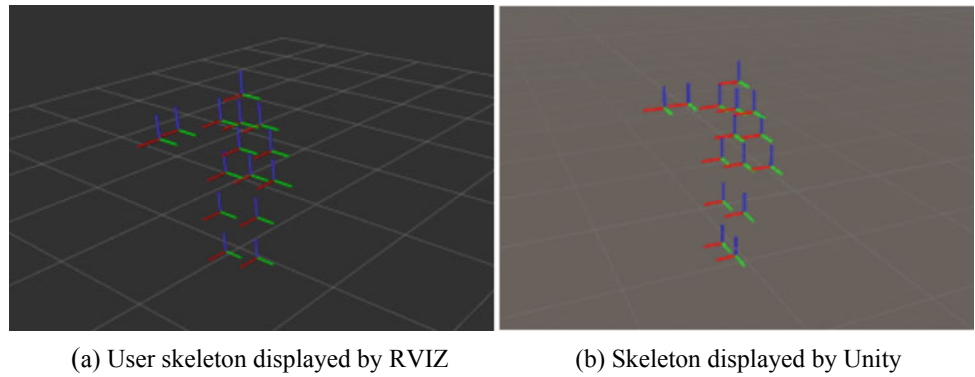
The experiment was started only after the user become accustomed to the cursor controller.

4 Results and Discussion

The system presents a 30 fps frame rate and identifies at most one person. NiTE 2.2 API provides the position of fifteen joints. Figure 4a shows a user skeleton displayed by RVIZ, which is a ROS visualization tool. The skeleton was obtained within the ROS environment as an output of the fusion algorithm. In this case, two Kinects were arranged as shown in Fig. 3. Figure 4b shows the corresponding data received by Unity.

Figure 5 shows the user right hand joint behavior during the entire experiment. The red squares represent the moments when the system could not correctly identify the hand position, although there was no occlusion or obstructions. When it occurred, the system placed the joint data in a default zone (yellow circle) that represents the position in

Fig. 6 Cursor position over the screen along the experiment

which the user remains with the arms lowered and close to the body.

Figure 6 shows the cursor tracking position during the experiment. The cursor was represented in the interface by a hand image. For a target to be selected, it was necessary that any part within the cursor image edge touched it. Therefore, there were times when the cursor center did not touch the target, although other parts did it. For this reason, Fig. 6 does not always show the cursor central position touching the target edges.

As can be seen, the cursor presented an anomalous behavior when the system could not correctly identify the user's hand. However, it did not disturb the experiment progress, since the target had already been selected in both cases.

Approximately 98% of the data obtained by the system were consistent with the user actions. The user performed the entire experiment in a continuous manner, without having to repeat a target selection. In the case of the experiment, the failure detection was not relevant, since it

Fig. 5 User right hand joint position along the experiment

happened for a brief moment (approximately during one second in both cases).

5   Conclusion and Future Work

This paper describes a ROS-based multi-Kinect system for serious game development using Unity. The system was designed to support n devices connected to different CPUs and video cards, presenting the benefits of using a multi camera setup for gaming rehabilitation. The user skeleton is estimated by PrimeSense NiTE 2.2 API and merged through Kalman Filter. A linking mechanism was needed so that Unity could listen to and inject ROS messages into ROS environment. For this purpose, the rosbridge framework and the websocket protocol were used.

In order to analyze the system operation and study its limitations, we developed an interface, which is based on hand motion to interact with the user. In the proposed experimental protocol the user had to perform target-pointing movements in order to select a specific target. The results show that the system properly tracked the user's hand most of the experiment, enabling him/her to select all the targets. Despite that fact, in 2% of time the hand position was not correctly identified, although there was no occlusion or obstructions.

The experimental protocol tracked one body joint (right hand), presenting some failures regarding the tracking algorithm. Therefore, more effort is warranted in order to decrease the number of failure in joint detection, for instance by using a different skeleton tracker API and/or filtering the time series. Hence, the immediate continuation of this work will be the search of skeleton tracker APIs and online filtering algorithms to obtain a more robust tracking system.

In addition, to enable the therapist to assist the patient while he/she interacts with the game, it is necessary for the system to identify a greater number of users at the same time.

References

1. Mackay, J., Mensah, G.: The Atlas of Heart Disease and Stroke. World Health Organization, Geneva (2004)
2. Mercier, L., Audet, T., Hébert, R., Rochette, A., Dubois, M.F.: Impact of motor, cognitive, and perceptual disorders on ability to perform activities of daily living after stroke. Stroke **32**(11), 2602–2609 (2011)
3. Bernspang, B., Asplund, K., Eriksson, S., Fugl-Meyer, A.R.: Motor and perceptual impairments in acutes stroke patients: effects on self-care ability. Stroke **18**(6), 1081–1086 (1987)
4. Lincoln, N.B., Blackburn, M., Ellis, S., Edmans, J.A., Nouri, F.M., Walrer, M.F., Haworth, H.: An investigation of factors affecting progress of patients on a stroke unit. J. Neurol. Neurosurg. Psychiatry **52**(4), 493–496 (1989)
5. Resquín, F., Gómez, A., Gonzalez-Vargas, J., Brunetti, F., Torricelli, D., Molina Rueda, F., Cano de la Cuerda, R., Miangolarra, J.C., Pons, J.L.: Hybrid robotic systems for upper limb rehabilitation after stroke: a review. Med. Eng. Phys. **38**(11), 1279–1288 (2016)
6. Saposnik, G., Cohen, L., Muhammad, M., et al.: Efficacy and Safety of non-immersive virtual reality exercising in stroke rehabilitation (EVREST): a randomized, multicentre, single-blind, controlled trial. Lancet Neurol. **15**(10), 1019–1027 (2016)
7. Wittmann, F., Lamercy, O., Gonzenbach, R., et al.: Assessment-driven arm therapy at home using an IMU-based virtual reality system. In: IEEE International Conference on Rehabilitation Robotics, pp. 707–712. IEEE, Singapore (2015)
8. Park, D.S., Lee, D.G., Lee, K., Lee, G.: Effects of virtual reality training using Xbox Kinect on motor function in stroke survivors: a preliminary study
9. Thornton, M., Marshall, S., McComas, J., Finestone, H., McCormick, A., Sveistrup, H.: Benefits of activity and virtual reality based balance exercise programmes for adults with traumatic brain injury: perceptions of participants and their caregivers. Brain Inj. **19**(12), 989–1000 (2005)
10. Moon, S., Park, Y., Wook, D., Suh, H.: Multiple Kinect sensor fusion for human skeleton tracking using Kalman filtering. Int. J. Adv. Robot. Syst. **13**(65) (2016)
11. Oliver, M., Montero, F., Moline, J.P., González, P., Fernández-Caballero, A.: Multi-camera system for rehabilitation therapies: a study of the precision of Microsoft Kinect sensors. Front. Inf. Technol. Electron. Eng. **17**(4), 348–364 (2016)
12. Bunger, M.: Evaluation of skeleton trackers and gesture recognition for interaction. Ph.D. Thesis, Aaborg University (2013)
13. Carvalho, T., Ramirez, A., Frizera, A., Bastos, T.: Estudo de precisão de uma plataforma multi câmeras RGBd para sistemas de reabilitação. In: V Congresso Brasileiro de Eletromiografia e Cenesiologia e X Simpósio de Engenharia Biomédica. Uberlândia, Brasil (2017)
14. Dehem, S., Montedoro, V., Heins, S., Rocca, F.: Robotic-assisted serious game for motor and cognitive post-stroke rehabilitation. In: Serious Games and Applications for Health. IEEE, Perth (2017)
15. Valencia, N., Cardoso, V., Lyra, J., Longo, B., Glasgio, G., Frizera, A., Bastos, T.: Jogos sérios para reabilitação motora de pacientes pós-AVE. In: XXV Congresso Brasileiro de Engenharia Biomédica. Paraná, Brasil (2016)
16. Stevens, J., Stoykov, M.E.: Using motor imagery in the rehabilitation of hemiparesis. Arch. Phys. Med. Rehabil. 1090–1902 (2003)
17. OpenNI Homepage. http://openni.ru/files/nite/index.html. Last accessed 02 June 2018
18. ROS Homepage. http://wiki.ros.org/Installation/Windows. Last accessed 02 June 2018
19. Codd-Downey, P., Forooshani, P., Speers, A., Wang, A., Jenkin, M.: From ROS to Unity: leveraging robot and virtual environment middleware for immersive teleoperation. In: International Conference on Information and Automation. IEEE, China (2014)

20. Kalman, R.E.: A new approach to linear filtering and prediction problems. J. Basic Eng. **82**(1), 35–45 (1960)
21. Welch, G., Bishop, G.: An Introduction to the Kalman Filter. Department of Computer Science, University of North Carolina, Chapel Hill (2001)
22. Coognan, C., He, B.: Brain-computer interface control in a virtual reality environment and applications for the internet of things. IEEE Acess **6**, 10840–10849 (2018)

A Novel Digital Speller Based on a Hybrid Brain Computer Interface (hBCI) SSVEP with Eye Tracking

Raphael Rebello Haddad, Teodiano F. Bastos-Filho, and Richard J. M. G. Tello

Abstract

Many individuals with severe muscle atrophy caused by advanced Amyotrophic Lateral Sclerosis (ALS), brain stroke or spinal cord injury have a loss of their communication abilities. For those, who have problems or absence of speech capabilities, a speller system represents more than a tool as sometimes it is the only window that allows interaction with others and with the world. The objective of this work is to evaluate the performance of a speller in Brazilian Portuguese, based on a Novel hybrid Brain Computer Interface (hBCI), which uses Steady State Visual Evoked Potentials (SSVEP) from Electroencephalography (EEG) signals in addition to eye tracking acquired by a camera system with near field infrared light (NIR). The system uses a combination of both informations to ensure that a word is not misspelled. This way, it's expected a reduction on the time to spell a word and on the user's frustration, for having to correct mistyped letters. The interface also allows individuals with severe muscle palsy to communicate using only the eyes. This speller is particularly special because until the writing of this article there was no parallel in the Brazilian language. The tests were conducted with three volunteers who were asked to spell four words of everyday use on three trials. The experiment used en Emotiv EPOC + wireless device to obtain EEG signals and a Tobii Eyetracker 4C to obtain eye movements. The results obtained with the system are promising; the participants were able to perform the spelling tasks with an average typing speed of 4.2 characters per second and an accuracy of 80%.

1 Introduction

1.1 Why a Speller hBCI?

It is estimated that in the world the number of people afflicted by ALS will reach approximately 376,674 in 2040, which would represent a 69% increase in the population of individuals with severe motor restrictions [2].

People diagnosed with ALS have their motor neurons affected, and their muscles gradually lose strength and the ability to move. In very advanced cases, the individual is unable even to speak [3]. The growing scientific advance in the acquisition of EEG signals in the last 20 years contributes to the development of research related to human-machine interaction [13]. Through information and commands collected directly from the brain, scientists around the world are developing systems that allow people with severe paralysis to interact with the world around them. A Brain-Computer Interface (BCI) can be defined as a communication system that does not rely on peripheral nerves or muscles. A BCI describes a group of devices and technologies that allow the user to control or command a computer with only its brainwaves [6]. These interfaces have several approaches in the acquisition of brain data, which can be: invasively, with electrodes inserted into the brain trough the skull, as is the case of ECoG, or non-invasive, such as EEG, with dry electrodes or not, positioned on the scalp with the use of a helmet [14]. Steady State Visual Evoked Potentials (SSVEP), in turn, is a technique of brain signal analysis in which modulated attention by using

R. R. Haddad (✉) · R. J. M. G. Tello
Postgraduate Program in Control Engineering and Automation, Federal Institute of Espirito Santo, Serra, 29173-087, Brazil
e-mail: haddadrr@gmail.com

R. J. M. G. Tello
e-mail: richard@ifes.edu.br

T. F. Bastos-Filho
Postgraduate Program in Electrical Engineering Department, Federal University of Espirito Santo, Vitoria, 29075-073, Brazil
e-mail: teodiano.bastos@ufes.br

Fig. 1 hBCI examples with sequential processing (**a**, **d**, **e**, **f** and **g**) and parallel (**b**, **c**). Adapted from Pfurtscheller et al. [9]
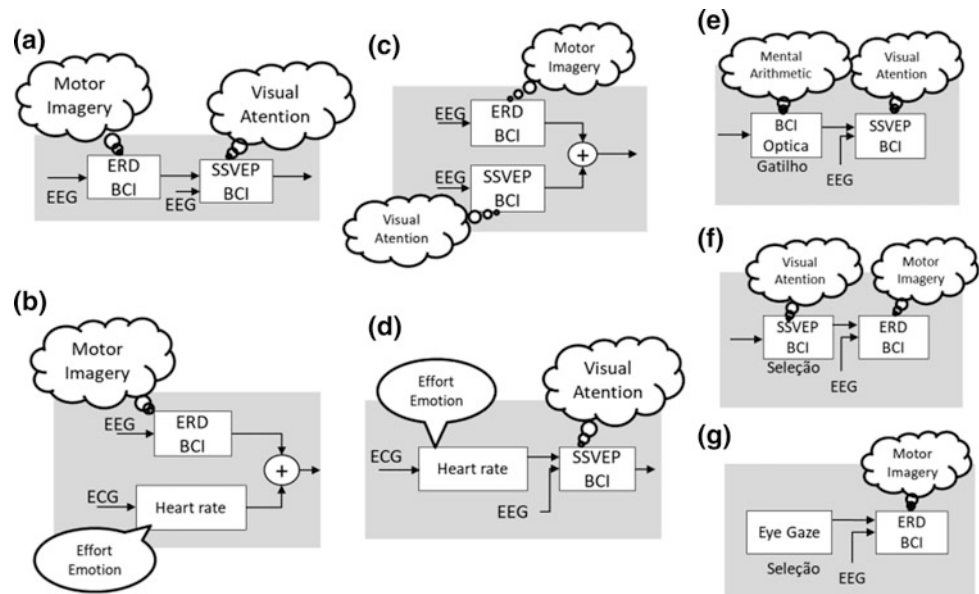
flashing lights at a known frequency allows the capture of these stimuli in the brain through EEG devices [14, 15, 17, 20, 21].

In many works, more than one type of interface have been used to improve the results and the reliability of the system; these are the hybrid Brain Computer Interfaces (hBCI) (see Fig. 1).

A spelling system is usually an interface with graphical representation of letters, numbers and symbols that uses different ways of interacting in typing. Many spell systems have been developed over the last decade, at least 400 publications since 2010 address the development of BCI spellers [10]. From Tables 1 and 2 is noticeable that their performance varies from one study to another, which is due the use of different resources. Different researchers utilize different hardware for these spellers, and build their software which are suitable for them or make use of available tools on the market. In fact there are several available bio amplifiers

on the market as well as a variety of EEG caps and electrodes, who specifications affect their performance greatly.

It is also noticeable from the tables that there are variations between the systems, whose main reason is that their Information Transfer Rate (ITR) and accuracy are calculated differently for different interfaces, which means that it is almost impossible to carry out an objective evaluation or comparison between the systems [10]. In some cases, the improvement in the spelling speed affects the accuracy negatively or vice versa.

Such as suggested by Stawicki et al. [11], the hBCI of this work aims to mitigate two common problems of spellers formed by only one of the interfaces: for spellers based only on the eye tracking there is a problem known as Midas touch, because for the activation of the system the user needs to keep focus on the position of interest for some time, however, the system is not able to distinguish whether the action was intentional or not, so that false positives may

Table 1 Spellers based on P300 BCI (adapted from Rezeika et al. [10])

Name/Topic	Author/Year	Test subjects	ITR/digit speed	Accuracy
Matrix speller	Farwell and Donchin 1988	4	12 bits/min	95.0%
Stimuli variations	Jin et al. 2010	8	14.8 bits/min	92.9%
Matrix speller with prediction	Ryan et al. 2011	24	17.71 bits/min	84.88%
Hex-O-spell with ERP	Schmidt et al. 2012	11	2.75 char/min	89.1%
Chroma speller	Acqualagna et al. 2013	9	1.4 char/min	88.4%
3D blocks matrix speller	Noorzadeh et al. 2014	16	N/A	∼90%
T9	Akram et al. 2015	10	26.125 s/char	N/A
Geospell	Zhou et al. 2016	10	N/A	N/A
Rapid serial visual presentation	Sato and Washizawa 2016	11	0.85 bits/s	70.3%

Table 2 Spellers based on SSVEP, Motor Imagery and Hybrids BCIs (adapted from Rezeika et al. [10])

Name/Topic	Author/Year	Test subjects	ITR/digit speed	Accuracy (%)
Multi-phase spellers	Cao et al. 2011	4	61.64 bits/min	98.78
Multi-target one-phase spellers	Spüler et al. 2012	9	143.95 bits/min	96.18
RC SSVEP speller	Yin et al. 2013	12	56.44 bits/min	93.85
DTU BCI speller	Vilic et al. 2013	9	21.94 bits/min	90.81
Flash-type speller	Nezamfar et al. 2016	3	6.2–11 s/char	95.5–97
SSVEP + EMG	Lin et al. 2016	10	90.9 bits/min	85.8
MI + P300	Yu et al. 2016	11	41.23 bits/min	92.93
Oct-O-spell	Cao et al. 2017	3	69.16 bits/min	98.3
SSVEP + Eye tracking	Stawicki et al. 2017	32	10.6 char/min	93.87
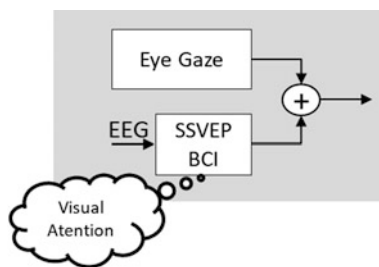
Fig. 2 Proposed hBCI on this work that uses data from two interfaces: SSVEP and eye gaze to generate a result

occur. On the other hand, interfaces based purely on SSVEP another problem may occur when multiple consecutive commands are executed in a sequence, as the user needs to shift his/her concentration between the targets and the data captured in that interval are not relevant to the classification of any stimulus.

Having these premises, the system was composed of the association of two interfaces, one that uses SSVEP, generated by three modulated light sources, for a higher rate stimuli classification [11], captured by an EEG acquisition system, and another that performs eye tracking in real time.

This way, according to Stawicky [11], some problems were mitigated:

- Eye tracking data is not used for letter selection.
- SSVEP data is only collected when the focus reaches a defined area.

This work presents the evaluation of a Brazilian Portuguese word speller based on a simultaneous hBCI (see Fig. 2) with a T9 variant graphic interface (nine-key text) [1], such as those used on phones keyboards.

The results obtained from the use of the system by volunteers are promising, since all individuals were able to conclude their tasks, and at each test an improvement in performance was observed. The system used for the speller

can be extrapolated to other applications such as the movement orientation of a motorized wheelchair.

2 Method

2.1 Data Acquisition System

The data acquisition system of the Speller consists of the following devices:

1. EEG signal acquisition device (Emotiv Epoc +) capable of collecting signals from 14 distributed channels obeying the 10–20 system with wet electrodes positioned on the regions AF3, F7, F3, FC5, T7, P7, O1, O2, P8, T8, FC6, F4, F8, and AF4. The sampling frequency used is 128 Hz. The device uses a high pass filter at 0.2 Hz and a low pass filter at 43 Hz. The passband signals are then collected from the user's head and sent to a PC via a wireless point-to-point communication. The channels used in the speller were: O1, O2 located in the back region of the skull (see Fig. 3). From these channels raw data are used and a feature extractor algorithm is applied.

2. Eye Tracking device (Tobii Eye Tracker 4C) with 60 Hz data acquisition rate with PC via USB (https://tobiigaming.com/eye-tracker-4c/) (see Fig. 4), using a toolbox developed for interaction between the Eyex Tobii integrated controller and MATLAB, allowing the device to be employed to measure the fixation, saccade and smooth pursuit of eye movements [4].

Flashing stimulators were used at 8, 11 and 13 Hz, consisting of three LEDs one for each frequency (see Fig. 5), each positioned in a box with a diffusing light film and their flickering controlled by a microcontroller [14].

The data analysis of the Speller was developed in MATLAB by integrating the aforementioned devices with their respective libraries and a specific toolbox for

Fig. 3 Name and position of the Emotiv EPOC + channels according to 10–20 system (**a**) and how the headset is weared (**b**)
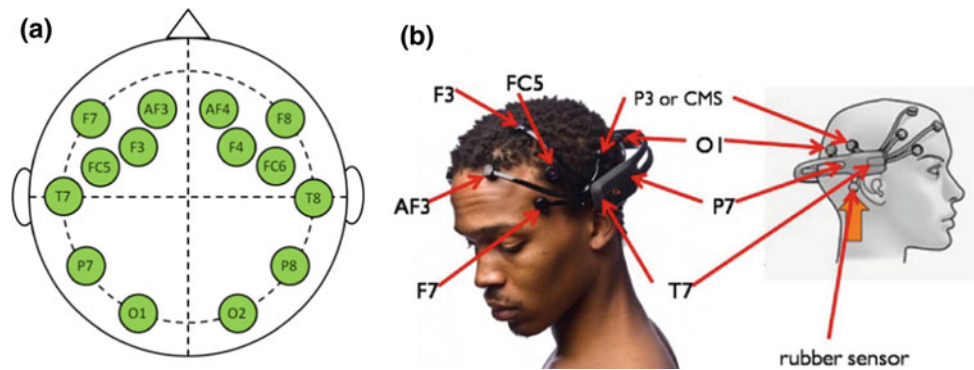
Fig. 4 Eye tracker and some components (**a**) and how they are mounted under the screen (**b**)
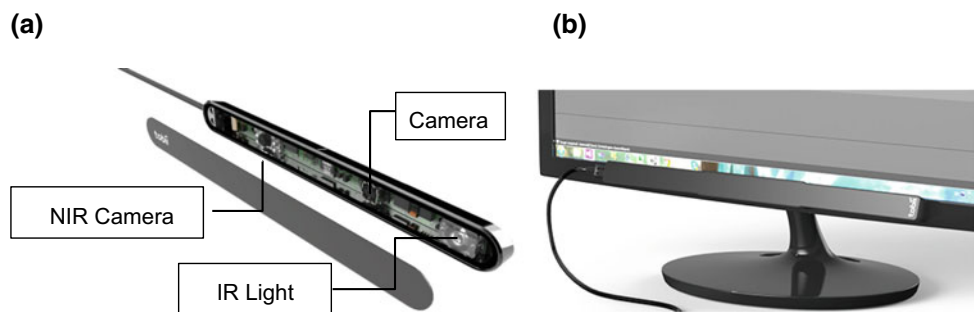
Fig. 5 **a** Position of the subject and the stimulator system. **b** A user experiencing the speller
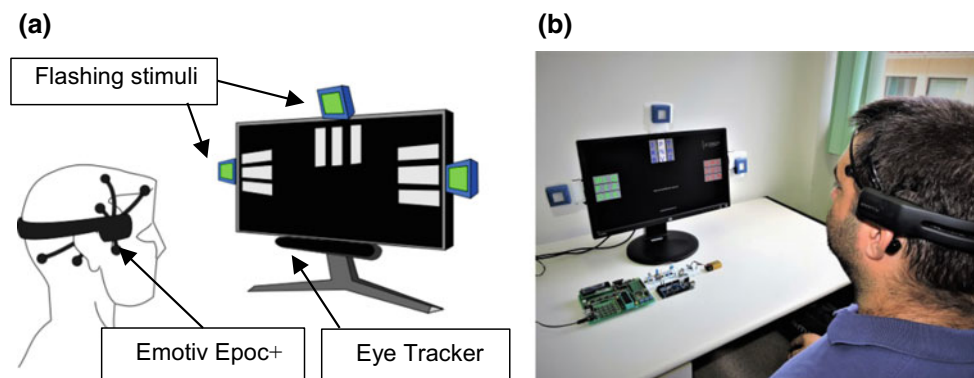
applications involving audiovisual stimuli. Psychtoolbox 3 was used to develop the graphical interface.

2.2 Data Acquisition Protocol

The protocol used by the Speller works as follows: at the start of the application the user is presented to a screen with the letters of the alphabet arranged in groups of three distributed in three zones of the computer screen (see Fig. 6).

Based on data sent by the Eye tracker, a circle is shown on the screen in the position the user is gazing on. The color of this circle varies between green and red, where green indicates that the distance between the screen and the user's eyes is ideal and red when this distance is too large. The red circle condition may compromise the precision of the

pointing by the application. Fixed to the edges of the monitor, near the lettered areas, are three boxes with LEDs in green color. The color of these LEDs is based on the studies on comfort and accuracy in SSVEP performed by Tello et al. [15]. The visual stimulation was controlled by a PIC18F4550 microcontroller, Microchip Technology Inc., at frequencies with a 50% duty cycle, distributed as follows: 11 Hz on the left edge, 8 Hz on the upper edge and 13 Hz on the right edge, based on previous studies conducted by [14–16]. This arrangement was chosen to prevent two adjacent frequency signals, as they are close to the user's field of view.

When the user gazes at a group of letters in the left region, for example, the speller starts capturing the EEG signal for four seconds, generating a total of 512 data samples, then correlates the signals collected on the Occipital

Fig. 6 Speller letter selection screen (**a**) and word selection screen (**b**)
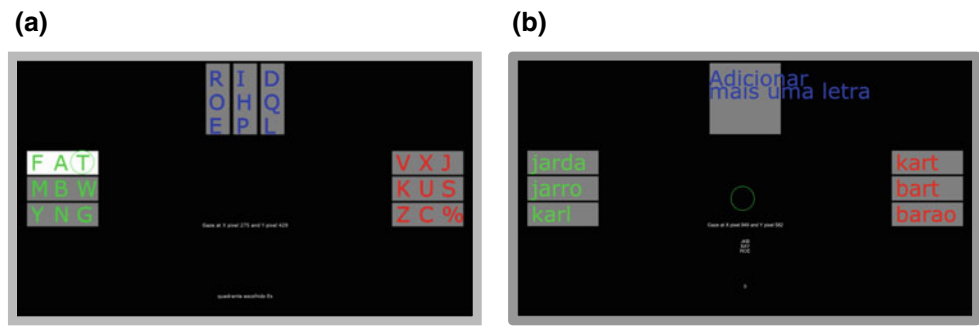
Fig. 7 Speller Eye tracking and EEG acquisition interaction
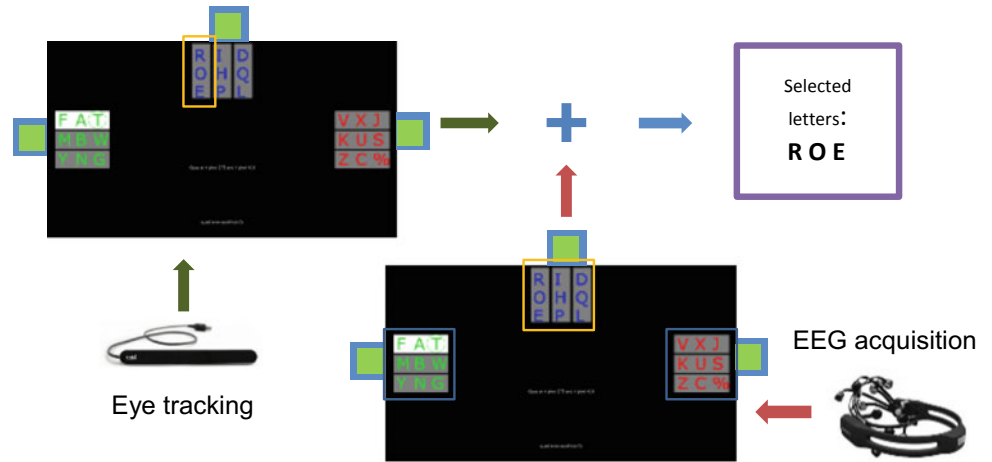
channels O1, O2, with the known frequencies previously quoted through a classifier algorithm based on canonical correlation analysis (CCA) [5, 7]. If the EEG signal is analyzed three times as 11 Hz (left corner stimuli), the speller stores the respectively group of letters and starts a new collection (see Figs. 7 and 8).

At each collection a word stack is formed containing the possible relationships between the chosen letters. After three sets of selected letters the speller presents to the user a group of possible words (see Fig. 6). If the desired word is between them, it is enough for the user to select it, otherwise he/she can choose to select another letter, and so, the word stack is updated since the previously displayed words are discarded, so that they are not displayed again (see Fig. 8).

The application finishes when the user selects a word from those presented on the screen.

2.3 The Speller Tests Protocol

The Speller experiments were performed with three volunteers, two male and one female, aged 35 ± 2 years, of whom two subjects did not require the use of corrective lenses. Meanwhile, they were in good health and had normal sleep time. According to the standards of the Declaration of Helsinki, the experiment was approved by the Academic Ethics Committee of the Federal Institute of Espirito Santo/Brazil with registration (CAEE: 57695716.9.0000.5072). Each volunteer was positioned at a distance of about one meter from the monitor; external light was blocked so that it would not interfere with the experiment. The user wore the EEG Emotiv Epoc + helmet with the wetted electrodes as recommended by the manufacturer, then the contact impedance of the Emotiv EPOC + electrodes with the scalp was verified using the CortexUI® software. After confirming that the quality of the contacts was 100%, the Speller was started.

Each participant received four words to spell, respectively: *apartamento* (apartment), *banheiro* (bathroom), quarto (bedroom) and *jardim* (garden). They should spell them in three repetitions each. The objective was to verify the operation of the application as well as if by the repetition the user could reach the goal in less time.

The data collected for the study were: EEG Raw signals provided by Emotiv Epoc + via Bluetooth from which channels 10 and 11 (respectively O1 and O2) were

Fig. 8 Block flux representing the steps needed for typing one letter (**a**), and the main flux off the speller (**b**)
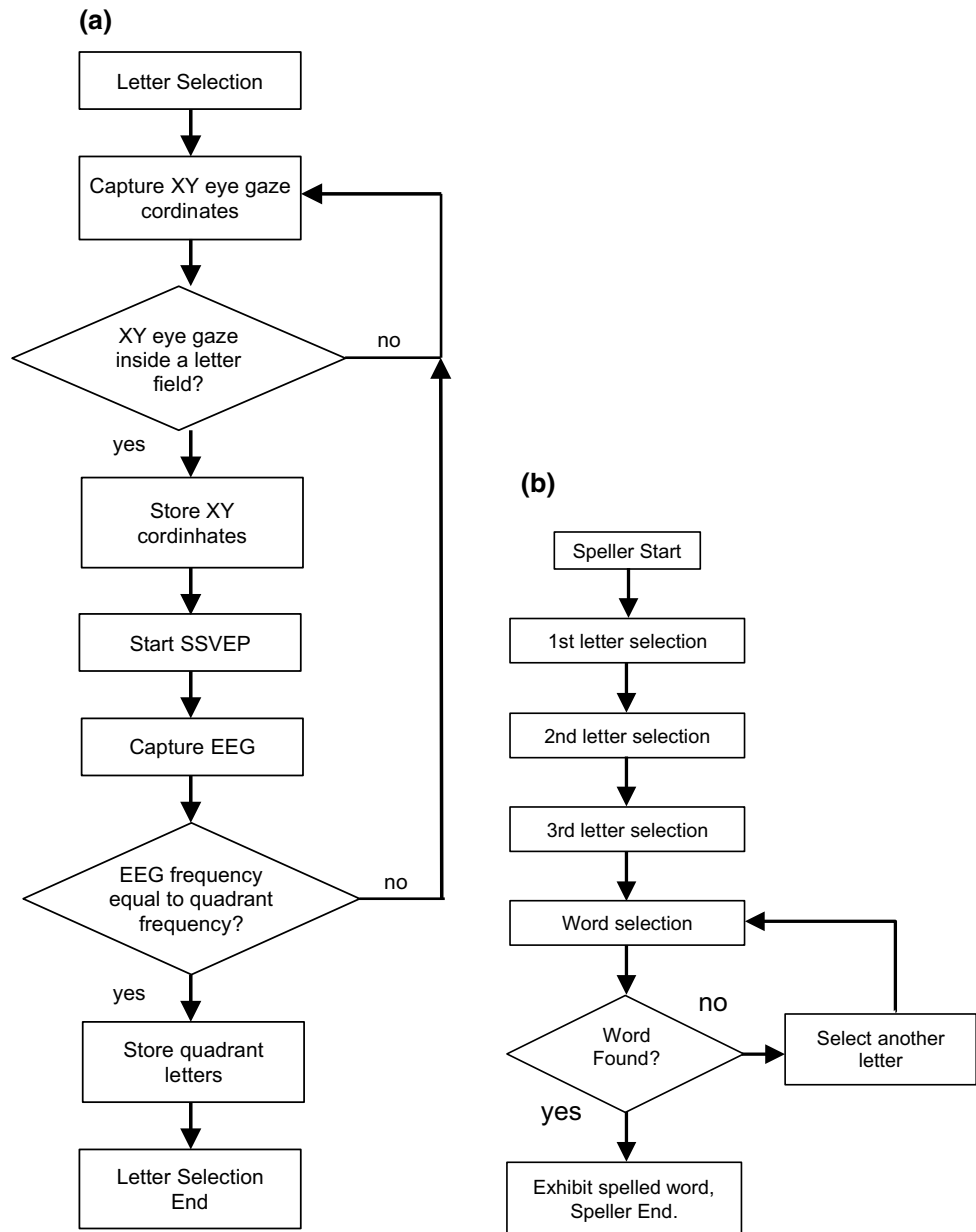
segregated. A bandpass filter was applied to these signals in order to eliminate frequencies lower than 3 Hz and higher than 60 Hz, and the filtered signal was subjected to a canonical correlation analysis, where a series of linear combinations were applied between the signal under analysis X and another signal consisting of Fourier series with the same frequencies of the stimuli and one of its harmonics Y. Assuming that there are K targets with stimulus frequencies $f_1, f_2, \ldots, f_k$, respectively. A pair of linear combinations $x = X^T W_x$ and $y = Y^T W_y$, called canonical variables, is found by using CCA between the two sets, such that the correlation is maximized [14].

The reference signals Y are set as:

$$Y = \begin{bmatrix} \sin(2\pi f_k t) \\ \cos(2\pi f_k t) \\ \vdots \\ \sin(2\pi N_h f_k t) \\ \cos(2\pi N_h f_k t) \end{bmatrix}, t = \frac{1}{F_s}, \frac{2}{F_s}, \ldots, \frac{T}{F_s} \qquad (1)$$

where f_k is the stimulus frequency, N_h is the number of harmonics, T is the number of sampling points (NFFT), and Fs is the sampling rate. CCA method needs to find the weight vectors, Wx and Wy that maximize the correlation

Table 3 CCA example of the user 1 data when spelling *apartamento* (apartment)

SSVEP	Gaze direction	Classification sequence	Canonical correlation analysis results			Classified stimuli frequency
			8 Hz (%)	11 Hz (%)	13 Hz (%)	
1ª	↑ A	0 2 3	0	33	33	Non classified
2ª	↑ A	0 0 3	0	0	33	Non classified
3ª	↑ A	1 1 1	100	0	0	8 Hz
4ª	→ AP	1 2 0	33	33	0	Non classified
5ª	→ AP	1 3 3	33	0	66.7	13 Hz
6ª	↑ APA	1 1 2	66.7	33	0	8 Hz
7ª	→ APAR	3 3 0	0	0	66.7	13 Hz
8ª	← APART	2 0 2	0	66.7	0	11 Hz
9ª	↑ APARTA	1 1 1	100	0	0	8 Hz
10ª	← APARTA	0 3 0	0	0	33	Non classified
11ª	← APARTA	0 0 1	33	0	0	Non classified
12ª	← APARTAMENTO	2 2 3	0	66.7	33	11 Hz

between x and y, i.e., it constrains and limits conditions established by (2) and (3).

$$E[xx^T] = E[x^T x] = E[W_x^T XX^T W_x] = 1 \quad (2)$$

$$E[yy^T] = E[y^T y] = E[W_y^T YY^T W_y] = 1 \quad (3)$$

CCA measures the linear association between two sets of variables using its autocorrelation and crosscorrelation [14], i.e., in mathematical terms, the total correlations calculated as the ratio between the autocorrelation and crosscorrelation of the input and output vectors, as shown in (4).

$$\rho k = \rho(x, y) = \frac{E[x^T y]}{\sqrt{E[x^T x]E[y^T y]}}$$
$$= \frac{E[W_x^T XY^T W_y]}{\sqrt{E[W_x^T XX^T W_x]E[W_y^T YY^T W_y]}} \quad (4)$$

These resulted canonical coefficients, that serve to classify the collected signal, define the highest coefficient as the frequency of the SSVEP stimulus [12, 17].
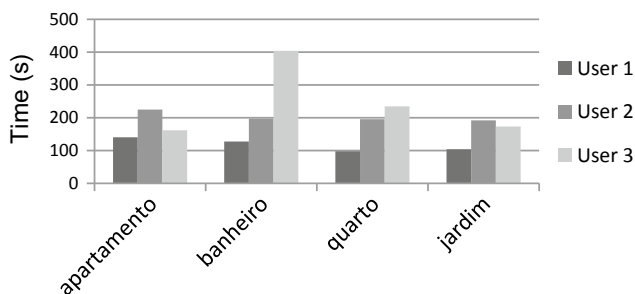
Fig. 9 Average results of each word spelled by volunteer
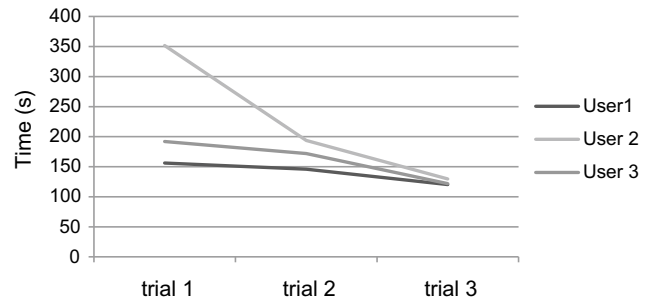
Fig. 10 Sequential results of each user when spelling *apartamento* (apartment)

At the end of each test a new off-line check of the data was performed to confirm the results. Table 3 shows that during the trials, more than one frequency was classified in the same EEG signal, but only those with a percentage greater than or equal to 66.7% generated a valid selection. In some cases the treatment of the EEG signals could not classify any frequency compatible with those of the stimuli; in those cases the speller ignored the attempt and started a new one.

The eye movements were stored to verify that the user was able to perform the path between the letters at each test (see Fig. 11). In order to qualify the spelling performance, we compared: the total time to spell each word in each attempt, (with this information we could evaluate the evolution of the user to each test), and the number of attempts to select one certain letter (see Figs. 9 and 10). It is noticeable that the time each user used to spell a word reduced along the use of the speller.
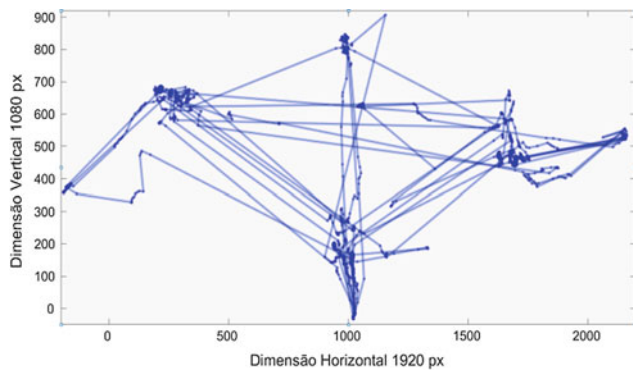
Fig. 11 Graphic of the eye track over the screen from user 1 when spelling the word: *apartamento* (apartment)

3   Conclusion

The results presented by the tests with this Speller demonstrated that this can be a promising communication tool for people with severe paralysis that are unable to speak. The tests were successful for the three volunteers; all were able to spell the words without errors. It was possible to observe that the performance of the user increases as they uses the system and concentrates on the task, nevertheless in some cases the posterior result was worse; in these cases the volunteers complained of fatigue and dry eyes due to being a long time concentrating on the stimulus. Improvements can be implemented by using more robust classifiers [14], and recursions can be reduced to classify an EEG signal stimuli and thus shorten the time to spell a word. Another way of reducing the time to spell may be the prediction of the word being spelled, using Convolutional Neural Networks (CNNs) with Deep Learning techniques and evolutionary algorithms, allowing the speller to present the desired word with a smaller number of selected letters [8].

References

1. Akram, F., Han, S.M., Kim, T.S.: An efficient word typing P300-BCI system using a modified T9 interface and random forest classifier. Comput. Biol. Med. **56**, 30–36 (2015)
2. Arthur, K.C., Calvo, A., Price, T.R., Geiger, J.T., Chiò, A., Traynor, B.J.: Projected increase in amyotrophic lateral sclerosis from 2015 to 2040. Nat. Commun. **7**, 12408 (2016). https://doi.org/10.1038/ncomms12408
3. Dornhege, G., et al.: Toward Brain-Computer Interfacing. The MIT Press Cambridge, Massachusetts London, England (2007)
4. Gibaldi, A., Vanegas, M., Bex, P.J., Maiello, G.: Evaluation of the Tobii EyeX Eye tracking controller and Matlab toolkit for research. Behav. Res. Methods (2016). https://doi.org/10.3758/s13428-016-0762-9
5. Islam, M.R., Tanaka, T., Nakanishi, M., Molla, M.K.I.: Frequency recognition of steady-state visually evoked potentials using binary subband canonical correlation analysis with reduced dimension of reference signals. In: 2016 IEEE International Conference on Acoustics, Speech and Signal Processing (ICASSP), Shanghai, pp. 769–773 (2016). https://doi.org/10.1109/icassp.2016.7471779
6. Kumar, D.K., Arjunan, S.P.: Human–Computer Interface Technologies for the Motor Impaired. CRC Press is an imprint of the Taylor & Francis Group, An Informa Business (2016)
7. Lin, Z., Zhang, C., Wu, W., Gao, X.: Frequency recognition based on canonical correlation analysis for SSVEP-based BCIs. IEEE Trans. Biomed. Eng. **54**(6), 1172–1176 (2007). https://doi.org/10.1109/tbme.2006.889197
8. Nejja, M., Yousfi, A.: The context in automatic spell correction. Procedia Comput. Sci. (Elsevier) **73**, 109–114 (2015)
9. Pfurtscheller, G., et al.: The hybrid BCI. Front. Neurosci. **4**, 3 (2010). ISSN: 1662-453X. https://www.frontiersin.org/article/10.3389/fnpro.2010.00003
10. Rezeika, A., Benda, M., Stawicki, P., Gembler, F., Saboor, A., Volosyak, I.: Brain-computer interface spellers: a review. Brain Sci. **8**, 57 (2018)
11. Stawicki, P., et al.: A novel hybrid mental spelling application based on eye tracking and SSVEP-based BCI. Brain Sci. **7**(4) (2017). ISSN: 2076-3425. Disponível em. http://www.mdpi.com/2076-3425/7/4/35
12. Tanaka, T., Zhang, C., Higashi, H.: SSVEP frequency detection methods considering background EEG. In: Joint 6th International Conference on Soft Computing and Intelligent Systems (SCIS) and 13th International Symposium on Advanced Intelligent Systems (ISIS), pp. 1138–1143 (2012)
13. Tang, Z., et al.: Learning to control an SSVEP-based BCI speller in naïve subjects. In: IEEE. Engineering in Medicine and Biology Society (EMBC), 2017 39th Annual International Conference of the IEEE, pp. 1934–1937 (2017)
14. Tello, R.J.M.G., Muller, S.M.T., Bastos Filho, T.F., Ferreira, A.: A comparison of techniques and technologies for SSVEP classification. In: IEEE-ISSNIP Biosignals and Biorobotics Conference: Biosignals and Robotics for Better and Safer Living (BRC), Salvador (Brazil) 2014
15. Tello, R.M.G., et al.: A comparison of techniques and technologies for SSVEP classification. In: 5th ISSNIP-IEEE Biosignals and Biorobotics Conference (2014): Biosignals and Robotics for Better and Safer Living (BRC), pp. 1–6 (2014). ISSN: 2326-7771
16. Tello, R.J.M.G., Muller, S.M.T., Bastos Filho, T.F., Ferreira, A.: Comparison between wire and wireless EEG acquisition systems based on SSVEP in an independent-BCI. In: 36th Annual International Conference of the IEEE Engineering in Medicine and Biology Society (EMBC 14). Chicago (USA) (2014)
17. Tello, R.J.M.G., Pouryazdian, S., Ferreira, A., Beheshti, S., Krishnan, S., Bastos Filho, T.F.: A new approach for SSVEP detection using PARAFAC and canonical correlation analysis. In: 37th Annual International Conference of the IEEE Engineering in Medicine and Biology Society (EMBC 15), Milano (Italy) (2015)
18. Tello, R.J.M.G., Muller, S.M.T., Ferreira, A., Bastos Filho, T.F.: Comparison of the influence of stimuli color on steady-state visual evoked potentials. Res. Biomed. Eng. **31**(3) (2015). online ISSN: 2446-4740, print ISSN: 2446-4732
19. Tello, R.J.M.G., Valadao, C., Muller, S.M.T., Ferreira, A., Bissoli, A., Carelli, R., Bastos Filho, T.F.: Performance improvements for navigation of a robotic wheelchair based on SSVEP-BCI. In: XII

SBAI—Simpósio Brasileiro de Automação Inteligente 2015, Natal (Brazil) (2015)

20. Tello, R.J.M.G., Muller, S.M.T., Hasan, M.A., Ferreira, A., Krishnan, S., Bastos Filho, T.F.: An independent-BCI based on SSVEP using figure-ground perception (FGP). Biomed. Signal Process. Control (Elsevier) (2016)

21. Vialatte, F.-B., et al.: Analyzing steady state visual evoked potentials using blind source separation. In: Proceedings of the Second APSIPA Annual Summit and Conference, pp. 578–582. Singapore (2010)

Adapted Computer Mouse for Cerebral Palsy Users

Antônio A. F. Quevedo and Thiago Bruschi Martins

Abstract

There are many computer pointing devices (mice) in the market for enabling people with motor impairment to use the computer. One popular system uses big push-buttons that are pressed by the user, each one corresponding to a cursor movement or a button click. However, the mechanical switches demand some force to be exerted on the buttons, which can be difficult with users with movement limitations. Also, they are prone to wearing and breaking. To overcome these problems, a system using capacitive touch sensors was designed. It uses a microcontroller which handles all hardware and firmware for touch sensing and USB mouse emulation. Sensors were made using square double-faced PCB pieces of 5 cm side, but they can be made with almost any size and shape. The system has 4 cursor movements, 4 button actions (left, right, left double-click, and left hold down/release), and a cursor speed setting. The device behaves as expected, and its design is quite simple, keeping costs at a reasonable range.

Keywords

Cerebral palsy • Assistive technology • Computer

1 Introduction

In developed countries, it is estimated that 2 or 3 out of 100 children are born or develop Cerebral Palsy (CP), and this number may double in underdeveloped countries [1]. Approximately 90% of the CP cases are spastic [2]. For these individuals, motor functions are hindered to extents that depend on many variables. Many of them cannot use a computer mouse or keyboard due to motor impairment.

There are several commercial versions of adapted keyboards and mice for motor impaired users, including special contoured mice trackballs and joysticks [3]. One of the simplest, cheapest and most common adapted mice uses a row of big push-button switches, each one for a different mouse displacement direction or button click [4]. Thus, if the user is capable of at least moving his or her hand and place it on the top of the switch, mouse control is possible.

This device has some limitations. The use of mechanical switches demands the user to exert an amount of force that can be beyond limits for some individuals with CP. Also, mechanical switches are prone to wearing and breaking. This increases maintainance costs, and also limits the number of users who can benefit from the device.

To overcome these limitations, we developed a mouse emulator system that uses capacitive touch sensors, keeping costs low through the use of a microcontroller with embedded touch sensing and USB communication capabilities, which reduces the number of electronic components.

2 Materials and Methods

2.1 Mechanical Structure

As a first step in this project, the design of the mechanical placement of touch sensors was defined, according to common CP user's limitations and abilities. Each sensor is made of a piece of a double-faced printed circuit board (PCB). The bottom side is electrically connected to the system ground, while the top side is connected to the active sensor input, thus forming a capacitor. When a body segment is placed close to the active electrode, its capacitance to ground increases, and these changes can be measured using a specific hardware.

The advantages of this type of sensor are its low cost, and the facility to customize size and shape. For this prototype,

A. A. F. Quevedo (✉) · T. B. Martins
Department of Biomedical Engineering, School of Electrical and Computer Engineering, UNICAMP, São Paulo, Brazil
e-mail: quevedo@ceb.unicamp.br

A. A. F. Quevedo
Center of Biomedical Engineering, UNICAMP, São Paulo, Brazil

we decided to use square boards measuring 5 cm each side. These dimensions are big enough to allow the user to target the sensor easily, keeping its size set at a reasonable range.

Using the current market models as a reference, we designed the structure of the sensor set using a wooden board measuring 500 × 80 mm, with a thickness of 22 mm. Eight sensors are lined in a single row, avoiding the onset of a sensor in the second row during reaching a sensor in the first row. Each sensor was fit into a square groove engraved into the board, with 2 mm depth. Each sensor slot has a hole (12.7 mm diameter) in the middle of the groove for passing the ground wire, and a small hole outside the slot (0.75 mm diameter), next to its edge, for passing the active electrode wire. Figure 1 shows the dimensions of the sensor set and Fig. 2 shows the partial assembly of the sensors into the wooden board. All bottom sides of the boards were
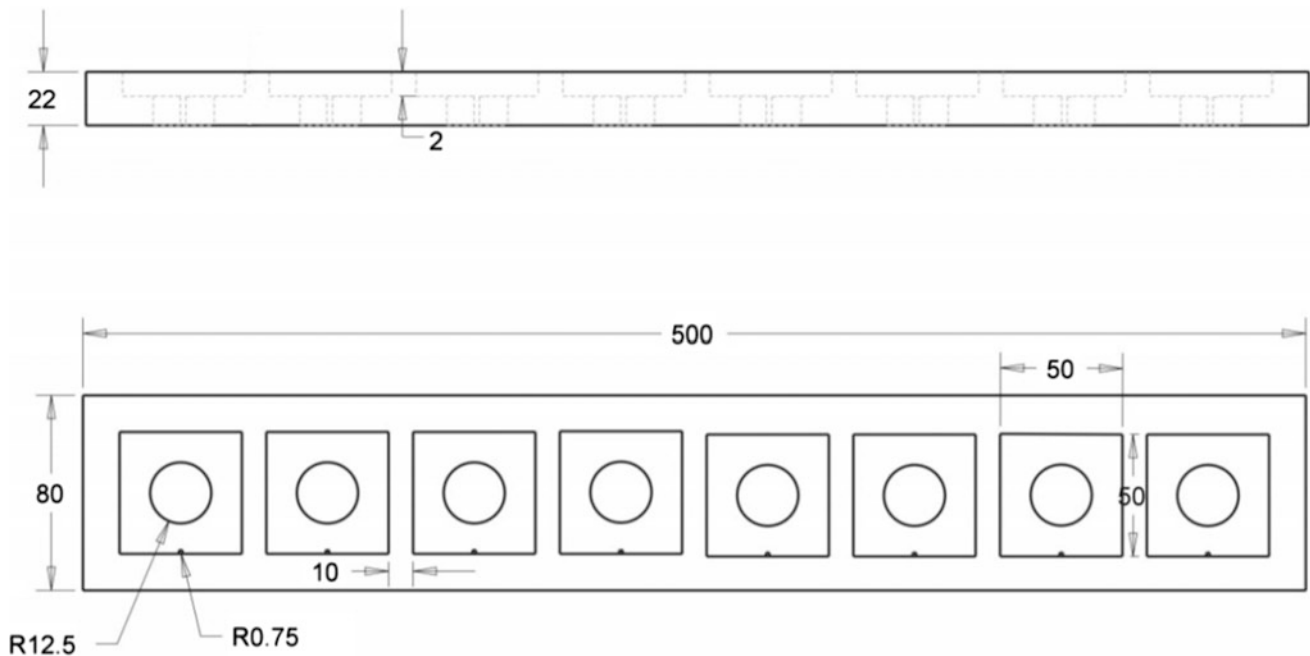
Fig. 1 Physical dimensions of the sensor set. All dimensions are in millimeters (mm)

Fig. 2 Partial assembly of the sensors into the wooden board. Notice the big hole in the middle of the sensor groove for passing the ground wire and the small hole next to the groove's edge for passing the active sensor wire

interconnected, and a total of 9 wires (8 active plus one general ground) connect the sensor set to the electronic control system.

2.2 Electronic Control

For touch detection and mouse command emulation, we selected the NXP® microcontroller KL25 [5], from the manufacturer's Kinetis® family. This microcontroller has ARM-M0 architecture, and has several hardware interfaces and modules embedded into its chip, including an USB OTG controller, an Analog-to-Digital Converter (ADC), and a multichannel capacitive touch sensor detector. Thus, the component count can be limited to the microcontroller itself, a potentiometer (for speed control), an USB connector (for power supply and mouse emulation), and a voltage regulator to drop the USB 5 V power to 3.3 V, which is the voltage used by the microcontroller. In the prototype, a FRDM-KL25 development board [6] was used. A shield board was used to connect the sensor wires and the potentiometer to the development board (Fig. 3). The sensors were connected to the eight FRDM pins available in the board for touch sensors, and the potentiometer was connected as a voltage divider, providing a voltage in the range 0–3.3 V to one of the Analog-to-Digital input of the board.

Power was provided from the PC computer through the onboard Mini-USB connector, which also provides communication with the target processor for mouse emulation.

This USB connector can provide 5 V power from a computer to the FRDM board, and is also connected to the USB OTG pins of the KL25 processor. Another mini-USB connector is available, for debugging purposes.

2.3 Final Assembly

For better identification of each sensor function by the user, we covered each sensor with a squared piece of paper, each one with a different color and with a figure representing its function. Table 1 shows the colors and functions for each sensor. Then each sensor was covered by transparent plastic tape to protect the sensor set from humidity. This can be done because there is no need for electrical contact between the user and the sensor active area. The system is configured to detect a sensor onset only when the user's hand is resting on the insulating layers of the sensor (paper and plastic tape). Figure 4 shows the final assembly.

2.4 System Firmware

The system firmware was developed using an IDE (Integrated Development Environment) customized to the microcontrollers of the Kinetis® family from NXP®, named CodeWarrior®. This IDE is based on Eclipse, a popular open-source customizable IDE, and has a custom plug-in named Processor Expert®, which speeds up the development
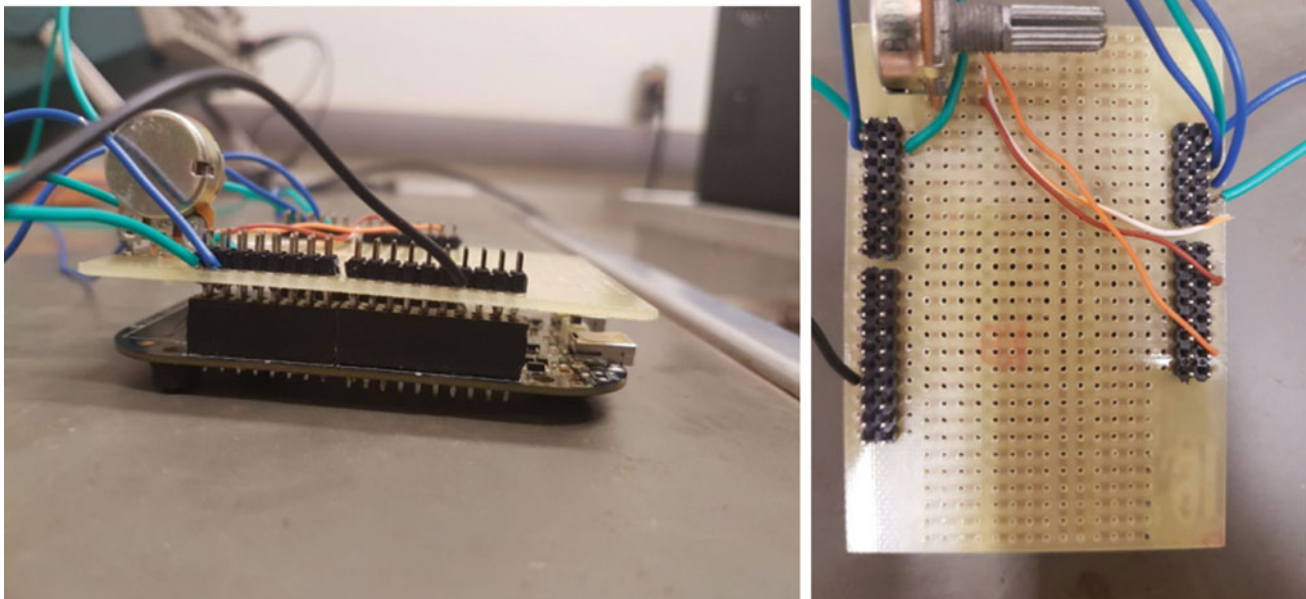
Fig. 3 FRDM-KL25 board and its shield

Table 1 Colors and functions for each sensor

Color	Function
Blue	Move left
Yellow	Move right
Green	Move up
Red	Move down
White	Left-click
Black	Right-click
Orange	Left double-click
Pink	Toggle left button (hold down)
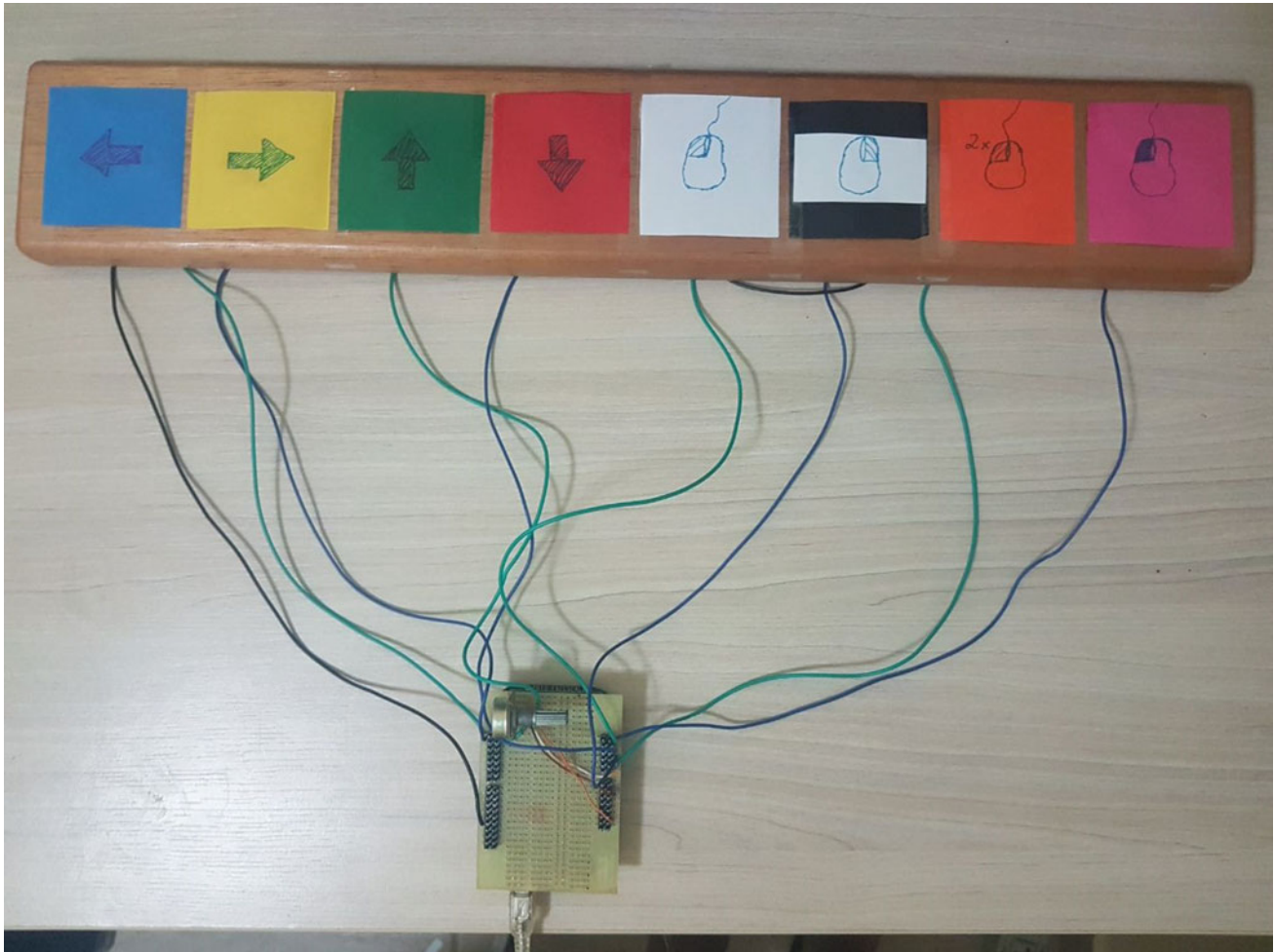
Fig. 4 Final assembly

process through scripts for code generation of initialization and service functions for all internal hardware modules. For example, one can setup one UART interface using a Graphic User Interface (GUI) for a *component*, providing the parameters (i.e. baud rate, pins to be used, etc.), and the plugin will generate code for initializing the interface, as well as a library for common functions (like sending characters or receiving characters). It also allows generating Interrupt Service Routines for the hardware modules that allow interruptions.

Three Processor Expert components were used: *USB HID Mouse Device* for emulating mouse commands through the USB controller; *TSS_Library* for detecting sensor touches; and *ADC* for reading the analog input.

The *USB HID Mouse Device* component [7] initializes the USB OTG controller so it behaves as an USB device,

which enumerates as a *Human Interface Device* (HID) when connected to a computer. Other devices can be emulated, but for this system the component was configured to emulate a mouse. Three functions generated through this component are used: *Move*, which moves the cursor in x and y axes by relative steps from current position; *Click*, which sends button click commands to the computer; and *Send*, which sends a raw command, used for the "click and hold" function (toggle left). The "toggle" sensor/function sends a "left button press" command the first time the sensor is touched, and a "left button release" when the sensor is touched again. This function allows dragging objects in the computer desktop.

The *TSS_Library* component [8] initializes the capacitive touch sensing hardware. This hardware measures the capacitance of each electrode. Thus, there is no need of electric contact between the electrode and the user's body. The program can be calibrated to detect a touch only when the user's body is very close to the electrode, when almost touching it. The library executes an auto-callibration when initialized, thus compensating for any sensor size or shape. This component was configured for 8 single electrodes, each one behaving as an independent key. The programmer has to call a callback function periodically to check for touches. The *BUFFER_READ* function inside the callback reads the status of the sensors and stores it in a variable. Thus, the programmer can check which sensor has changed state, and if it was touched or released.

The *ADC* component initializes the Analog-to-Digital Converter (ADC), and is configured for 1 single input, 16-bit resolution, and fast conversion. We used two functions from this component: *Measure*, which triggers the conversion and waits for its ending; and *GetValue16*, which places the result into a variable. The resulting value (which depends on the potentiometer position) is used to define the time interval between successive touch sensor callbacks, and eventual mouse commands. Thus, the potentiometer position sets the speed of cursor movement. It has to be used by another person to set up the best cursor speed for the user, depending on his or her motor reaction times.

3 Results

The system easily enumerates itself as a generic mouse when plugged into a computer. The authors tested the touch sensors, verifying that they respond adequately. No false positives or false negatives were noticed. The speed control can be set to values into a wide range, allowing it to be used by users with different degrees of motor impairment.

4 Conclusion

The system worked as expected. Results were satisfactory and the system can surely become a commercial product. All mouse functions were adequately reproduced, and the cursor speed can be adjusted according to the user's limitations.

We believe that the size and shape of the sensors are adequate for most users, but they can be changed if needed, without changes in performance, since the touch sensing firmware has an auto-calibration routine during initialization.

The number of components for the system is quite low, and a custom design for a final version is easy to be performed. Due to the reduced number of components, and their low prices, the final production cost should be quite low.

References

1. Bersch, R.: Introdução à Tecnologia Assistiva, pp. 1–7. Porto Alegre, RS (2013) http://www.assistiva.com.br/Introducao_Tecnologia_Assistiva.pdf. Last accessed 06 Oct 2017
2. Frazão, A.: Entenda o que é Paralisia Cerebral. Tua Saúde. https://www.tuasaude.com/paralisia-cerebral/. Last accessed 11 July 2017
3. National Health Services UK: Keyboard and Mouse Alternatives (2018). https://www.nhs.uk/accessibilityhelp/Factsheets/Keyboard-and-mouse-alternatives.pdf. Last accessed 12 June 2018
4. Vanzetti, C.: Mouse e Teclado Especial RCT-Barban (2018). http://catalogosp.vanzetti.com.br/index.php/mouse-e-teclado-especial-rct-barban/. Last accessed 12 June 2018
5. Freescale Semiconductor, Inc.: KL25 Sub-Family Reference Manual (2012). http://www.nxp.com/docs/en/reference-manual/KL25P80M48SF0RM.pdf. Last accessed 13 July 2017
6. Freescale Semiconductor, Inc.: FRDM-KL25Z User's Manual (2012). http://www.nxp.com/docs/en/user-guide/FRDMKL25ZUM.zip. Last accessed 13 July 2017
7. Styger, E.: Using the FRDM-KL25Z as a USB Mouse Device (2013). https://mcuoneclipse.com/2013/08/01/using-the-frdm-kl25z-as-a-usb-mouse-device/. Last accessed 03 Nov 2017
8. Styger, E.: Tutorial: Touching the Freedom KL25Z Board (2012). https://mcuoneclipse.com/2012/09/30/tutorial-touching-the-freedom-kl25z-board/. Last accessed 13 Oct 2017

Design and Development of Hardware and Software to Command a Motorized Exercise Static Bike

M. A. Romero-Laiseca, L. S. Morelato, K. A. Hernandez-Ossa, A. Frizera, and T. F. Bastos-Filho

Abstract

Previous works in literature have indicated that pedaling movements are safe, effective and accessible to patients with a wide range of motor impairments. Recent research in the field of rehabilitation has shown that patients with stroke and cerebral palsy may improve their motor and balance abilities after an early short duration of pedaling training. In this work, a novel low-cost Motor Exercise Static Bike (MESB) has been enhanced by incorporating a Raspberry Pi 3B. The enhanced MESB includes custom-made hardware and software for allowing a user to command it, in addition, to monitor its operation through a Graphical User Interface (GUI). The GUI was programmed in Python 3.5 and was tested on Ubuntu 16.04 and Raspbian (rel. 2017-09-08) operating system. An Inertial Movement Unit (IMU) was selected in order to acquire both bike's angular velocity and position data. The angular velocity was measured in degrees per second (DPS) directly from the IMU's gyroscope z-axis, and the angular position was calculated by integrating the angular velocity over time.

1 Introduction

Pedaling is a repetitive, functional activity that has been proposed to provide potential benefits for patients when it is used as an addition to therapy after stroke. Pedaling exercise has the potential to provide high number of repetitions of lower limb flexion and extension in reasonable therapeutic time frames. It is able to improve muscle activity, muscle strength, balance, and functional independence in post-stroke survivors [1]. Pedaling is considered similar as walking since the completion of this action also requires that agonistic and antagonistic muscles be alternately activated in coordination with a time sequence [2]. For patients with poor coordination and balance control, a pedaling ergometer bicycle can provide more adequate support for the trunk and help patients stretch their legs [3]. Previous works in literature have indicated that pedaling movements are safe, effective and accessible to patients with a wide range of motor impairments [4]. Recent research in the field of rehabilitation has shown that patients with stroke and cerebral palsy may improve their motor and balance abilities after an early short-duration pedaling training [5, 6].

Nowadays, there are many motorized single-rider stationary exercise bikes that are commercially available and that can provide a pre-programmed velocity for a rider [7]. Motorized pedaling exercise has been used in [7] where a smart motorized bicycle was designed and built for assisting Parkinson patients in improving their motor function. In other research studies such as [8–12] non-motorized single-rider stationary exercise bike, was used in order to detect pedaling intention in post-stroke survivors through Electroencephalography (EEG), stimulate individual's lower limbs in spinal cord injured patients (SCI) with Functional Electrical Stimulation (FES) and, build a rehabilitation system that allows a clinician to remotely monitor and manage the use of cycling exercise (for lower or upper limbs) equipment at home. The main objective of this work is to create hardware and a Graphical User Interface (GUI) to command and monitor a Motorized Exercise Static Bike (MESB).

M. A. Romero-Laiseca (✉) · L. S. Morelato ·
K. A. Hernandez-Ossa · A. Frizera · T. F. Bastos-Filho
Assistive Technology Center - NTA (Núcleo de Tecnologias Assistivas), Federal University of Espirito Santo (UFES),
Vitória, Brazil
e-mail: alejandralaiseca@gmail.com

2　System Architecture

A commercially available MESB from brand Exerpeutic (ACTIVCycle Motorized Mini Exercise Bike model 7101) was used in this work. The pre-assembled LCD display and remote control with an on/off switch and adjustable velocity potentiometer, were removed from the bike and replaced by a command system based on Raspberry Pi 3B (RPi3) and custom-made hardware. The system allows the user to turn on/off and change the velocity of the MESB through a GUI programmed in Python 3.5 which ran on an RPi3. Figure 1 shows the general diagram of the command system.

The MESB has three pairs of wires available: velocity pair (VP), sensor pair (SP) and power pair (PP). VP and PP wires come from the built-in motor driver and were originally connected to the remote control. The resistance value between VP wires determines how fast the motor turns. The MESB commanded by the remote control, reaches velocities from 15 to 75 rpm. In the case of PP wires, they turn on the MESB when they are connected together and turn it off when they are not. Finally, the SP wires come from a magnetic switch placed on the motor shaft, which has one wire always in 0 V (low wire) and the other one pulled to 5 V (high wire). The voltage of this last wire, changes to 0 V when the magnetic switch detects a magnet placed on the left side of the bottom bracket. The MESB's revolutions were counted by this magnetic switch.

2.1　Hardware: Electrical and Electronics

In order to command the MESB from a GUI, a command board was designed and developed to be able to turn on/off, count revolutions and control velocity changes in the MESB, through digital outputs from General Purpose Inputs/Outputs (GPIO) pins of the RPi3. The DC motor, motor drive, magnetic switch for counting revolutions and plug for power supply from the MESB were maintained in the original hardware design. A GPIO pin set in input mode, was used to count the revolutions of the MESB. The low wire of the SP

was connected directly to the RPi3 ground node, and the high wire was connected to an input pin of the RPi3. Counting revolutions was done by detecting the changes of the high wire.

Figure 2 shows the command board schematic circuit designed for communicating the RPi3 and the MESB. To transfer signals from the RPi3 to the VP and PP wires of the MESB, a commercial eight-channel analog demultiplexer (DEMUX) model MC14051B, two optocouplers model PC847 (4 channel type) and one relay model AX1RC-5 V, were used. The relay was used to turn the MESB on/off through a GPIO pin of the RPi3, in output mode, by changing its state between high or low, respectively. When the GPIO was set in high, it sent 3.3 V for activating the transistor's base, and when it was set in low, it sent 0 V, deactivating the transistor's base. After activating the transistor, the relay´s contacts were closed, allowing the PP wires to be electrically connected, therefore, turning on the MESB.

On the other hand, the DEMUX and the optocouplers were in charge of changing the velocity of the MESB selecting and setting only one specific resistance into the VP wires, such as the bike's original potentiometer did. Due to the DEMUX having 8 outputs, the number of control pins is 3. Each pin was connected to a GPIO of the RPi3 and encoded a sequence to select between 8 different resistance values, shown in Table 1.

Table 1 describes 8 discretized velocity values and their related resistors. These values were determined by measuring the resistance in 8 different positions of the original potentiometer and the corresponding MESB velocity.

2.2　Velocity Monitoring System

A wireless Inertial Measurement Unit (IMU) was used in this work to measure the angular velocity and the angular position of the MESB. These measurements will be used in a future work to verify what is the effect of the user's weight on the real MESB's velocity. The IMU selected was a

Fig. 1 General diagram of the command system designed for the MESB
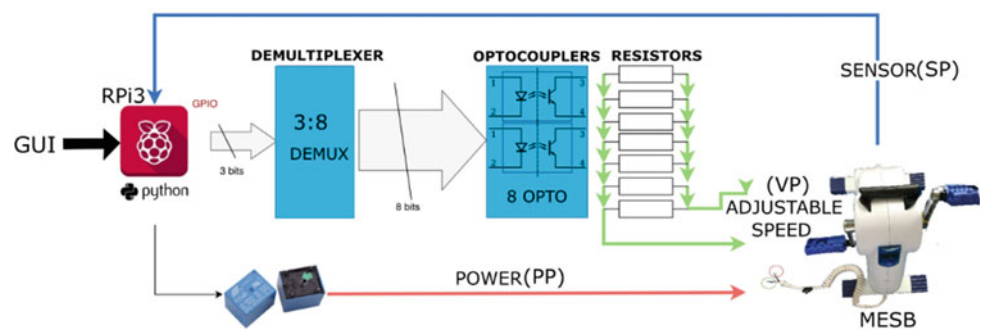
Fig. 2 Schematic circuit diagram of the command board designed for the MESB
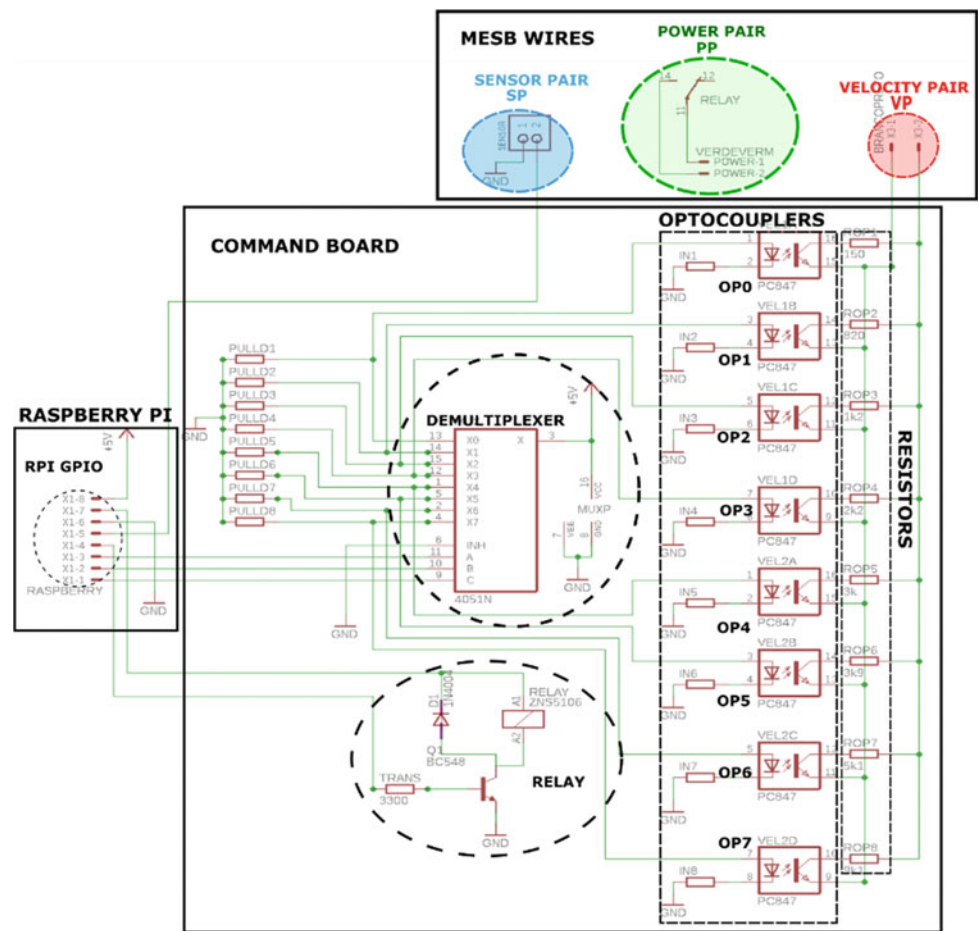
Table 1 3-bit signal from RPi3, optocouplers, resistors and velocity

Code	Active optocoupler	Resistor value (Ω)	Velocity (rpm)
000	0	150	30
001	1	820	35
010	2	1200	40
011	3	2200	45
100	4	3000	50
101	5	3900	55
110	6	5100	60
111	7	9100	70

prototype implemented in our research group, which was used previously in [13, 14]. This IMU was placed on the right crank arm of the MESB, such as shown in Fig. 3, and it communicates with the RPi3 through a Bluetooth connection.

The minimum sample frequency required to obtain an error lower than 1° is 420 Hz since the maximum velocity reached by the enhanced MESB is 70 rpm or 420 degrees per second (DPS). As result, a sampling frequency of 500 Hz was used and the gyroscope's z-axis data were
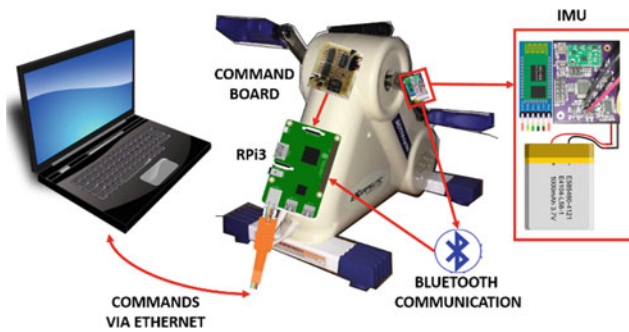
Fig. 3 Complete system architecture of the enhanced MESB

collected to measure angular velocity and angular position. In order to calculate the angular position, the angular velocity was integrated online.

3 User Graphical Interface (GUI) and Data Logging

Python was the programming language selected to implement the GUI and the data interpretation software for the IMU. It was chosen because it is already installed on the RPi3 operating system (OS), in addition to having an extensive library that allows easy communication and processing. It is important to mention that this GUI built was tested on Ubuntu 16.04 and Raspbian (release 2017-09-08) OS. Figure 4 depicts the methodology of the developed GUI
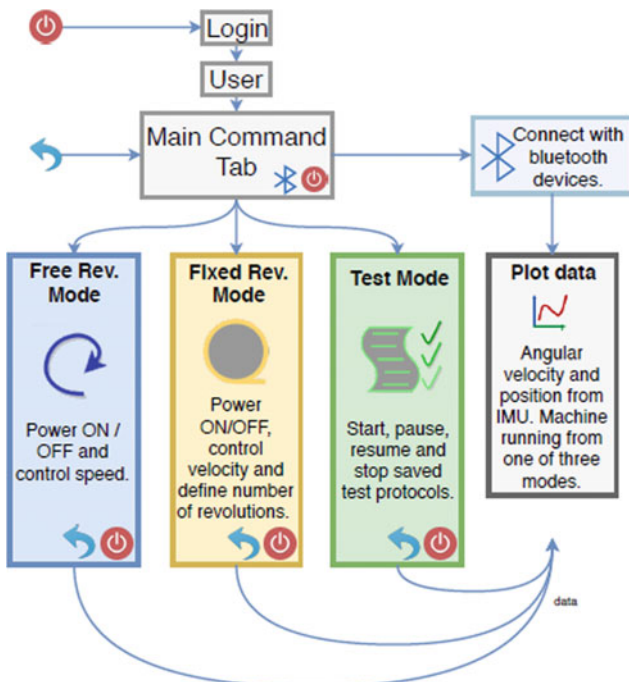
Fig. 4 Graphical user interface (GUI) diagram

to control the enhanced MESB. This GUI has a *Login Window* where the user is identified to access the main window called *Minibike Command*. The main window has three different modes of operation: *free revolutions mode*, *fixed revolutions mode*, and *test mode*. The GUI has also a Bluetooth window, which allows the user to connect with the IMU and watch the data received in an online plot window.

When the software is started, it displays the login window called *Minibike Login, such* as shown in Fig. 5a. It is an authorization window that enables users to access the program by typing their Username (label 1) and Password (label 2). Clicking on "Login" button (label 3), the software looks for users stored in a MySQL database to verify which of them match with the given information. The GUI is closed when "Exit" button (label 4) is clicked. After login, the main window (Fig. 5b) is open providing three buttons (labels 8, 9 and 10) that allow access to the *Free mode* tab (label 5), *Fixed mode* tab (label 6) and *Test mode* tab (label 7) respectively. On the lower left corner, the button indicated by the label 11 log out to the login window, and the button with the label 12 (Bluetooth icon) opens the *Bluetooth window*.

In the *free revolutions mode* and *fixed revolutions mode*, the user can turn the enhanced MESB on/off and change its velocity. The label 13 in Fig. 6a, and label 18 in Fig. 6b, describe instructions to command the enhanced MESB. To start, the user must choose one velocity in the drop-down list on label 15 and label 19 (default: 30 rpm) and then click on "Turn On" button. While running, it is also possible to increase or decrease the velocity by clicking on "speed up" and "speed down" buttons. All of these actions apply for both modes except for how to start the enhanced MESB in *fixed revolution mode*. The only difference is that the user must also specify the desired number of revolutions (there is no default value) by typing an integer value on "desired revolutions" entry. Information regarding the status (on/off), velocity and revolutions are shown on boxes label 16 and label 20. The boxes represented by label 17 and label 21 are used to log out to login window (red icon) or return to main command tab (blue arrow).

The third mode *test mode* tab (Fig. 7a) provides three recorded test protocols to be executed when clicked on "Teste 1", "Teste 2" or "Teste 3" buttons. "Teste 1" runs a specified revolution sequence; between revolutions, the enhanced MESB is stopped for 0.5–2 s. In "Teste 2" the enhanced MESB does 60 revolutions, and between revolutions, it also stops in intervals of 0.5–2 s. The last protocol is "Teste 3", which turns on the enhanced MESB around 2 min and then stops. The box in label 24 allows the user to pause, resume or stop a running test. Information such as target, progress, velocity, revolutions and status of the running test is displayed on the box correspondent to label 25. Since

Fig. 5 **a** Login window; **b** main window

some of the protocols follow a sequence of successive revolutions, the next number of revolutions to be performed by the enhanced MESB is presented in the green box named "Next Rev".

Returning to the main window or *Minibike Command* tab, the *Bluetooth window* in Fig. 7b can be opened, such as aforementioned, by clicking on the "Bluetooth icon" button in Fig. 5b. This window allows the user to search (label 28), select and connect to nearby available Bluetooth devices. As an IMU is connected to the software, there are two types of sample frequencies used to transfer data: 100 Hz (label 29) and 500 Hz (label 30). The Bluetooth device can be disconnected by clicking on "Disconnect" button at any time.

Lastly, there is a *Plot window* in Fig. 8 that displays online velocity and angular position taken from the IMU. This window can be opened by clicking on "magnifying glass icon" button on the box indicated by label 31 in *Bluetooth window*. Angular velocity (label 32) and angular
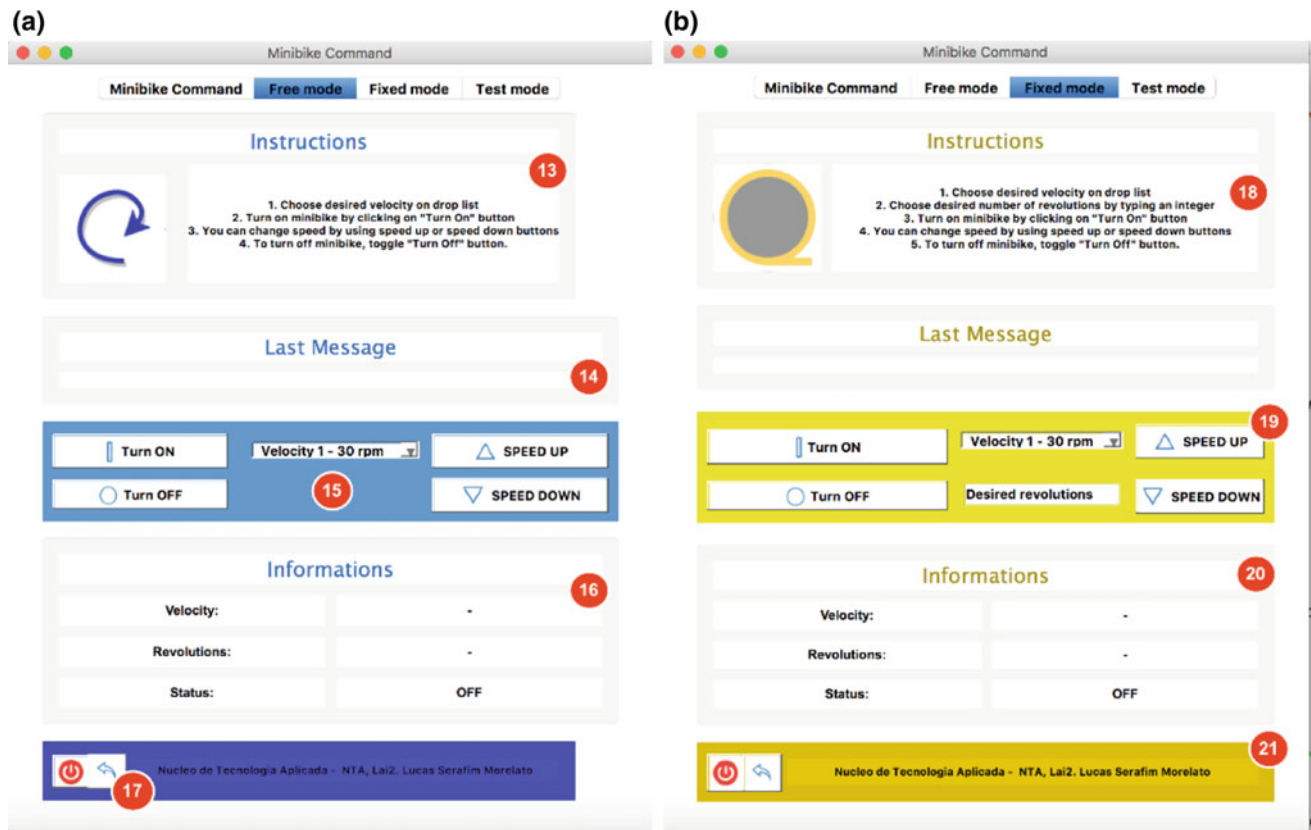
Fig. 6 a Free revolution mode tab; **b** fixed revolution mode tab

position (label 33) graphics are online plotted and updated according to data received from the IMU (label 34). After clicking on "Start" (label 35) button, the data acquisition is started and the obtained data are plotted. In addition, the plot can be stopped by clicking on "Stop" (label 36) button and then analyzed by clicking on "Analyze" (label 37) button. *Analyze window* (Fig. 8b) has some visualization tools, such as pan axis to drag into the graph, zoom in/out the graph and save the graph.

4 Conclusions

A novel low-cost Motor Exercise Static Bike (MESB) has been enhanced by incorporating a Raspberry Pi 3B. The MESB's chassis is a commercial bike unit and a currently available equipment for physical exercises. This innovative enhanced MESB allows monitoring of lower or upper extremity pedaling exercise in real-time. Monitoring is made
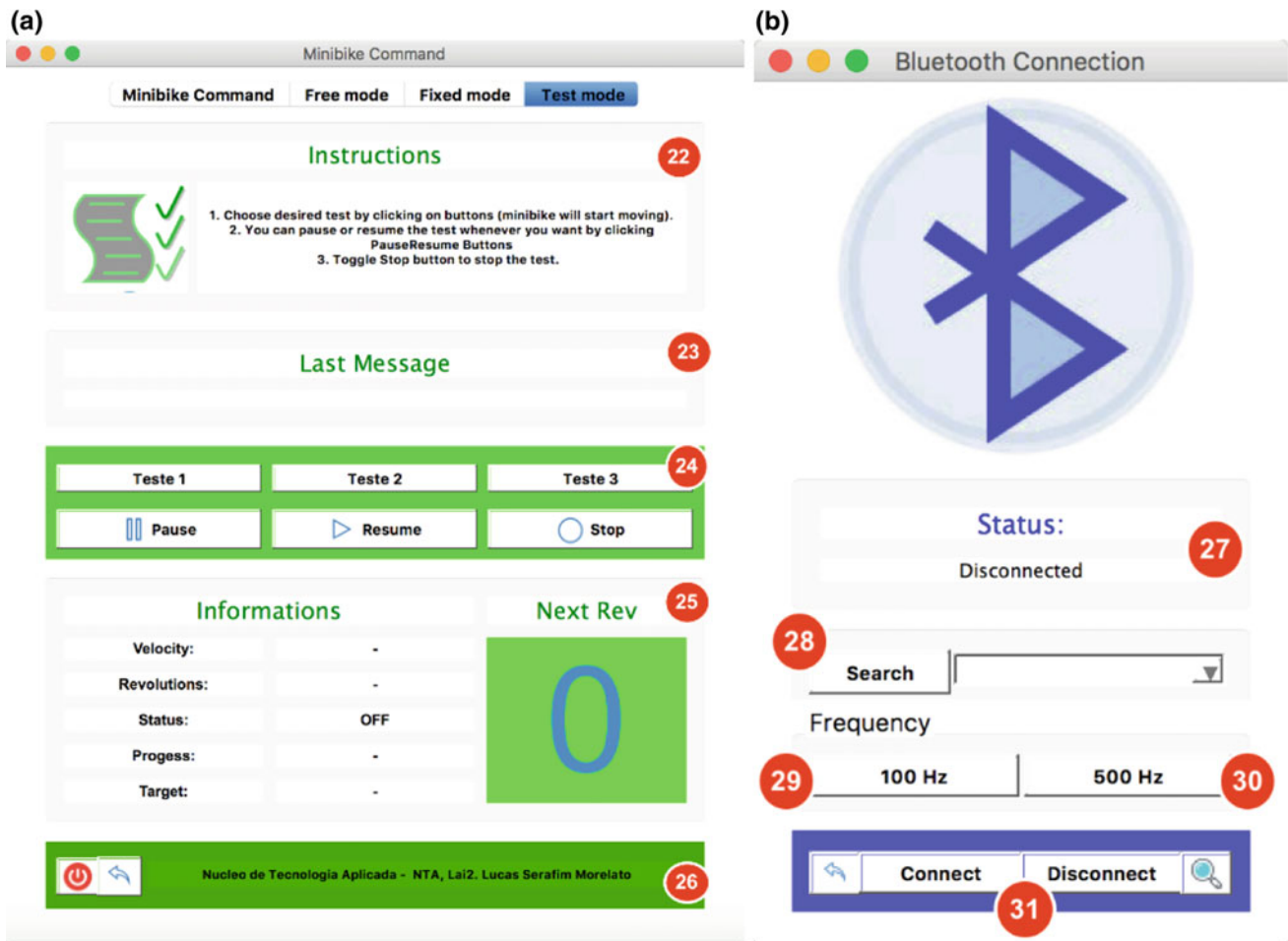
Fig. 7 **a** Test mode tab; **b** bluetooth window

through a user-friendly graphical interface on a computer screen that displays the main exercise parameters, such as angular velocity, angular position, current revolutions number, next revolutions number and status of the enhanced MESB.

This enhanced MESB can be used to improve motor and balance abilities during an early short-duration pedaling training, in a wide range of patients with motor impairments.

Furthermore, a new accessible methodology for rehabilitation therapies can be included.

(a)

(b)
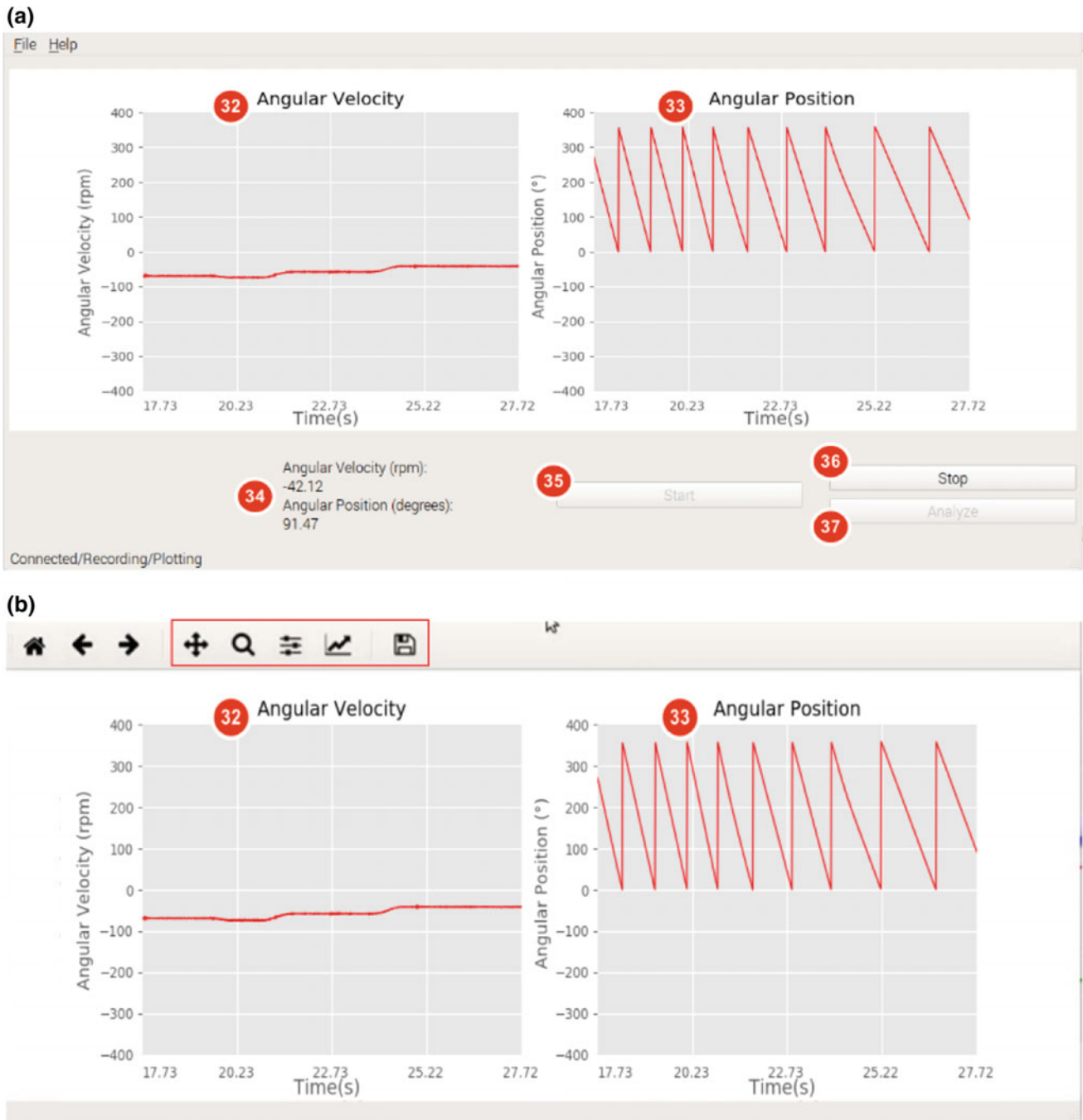
Fig. 8 **a** Online plot window; **b** analysis window

References

1. Hancock, N.J., Shepstone, L., Winterbotham, W., Pomeroy, V.: Effects of lower limb reciprocal pedalling exercise on motor function after stroke: a systematic review of randomized and nonrandomized studies. Int. J. Stroke **7**(1), 47–60 (2012)
2. Chen, S.W., Liaw, J.W., Chan, H.L., Chang, Y.J., Ku, C.H.: A real-time fatigue monitoring and analysis system for lower extremity muscles with cycling movement. Sensors (Switzerland) **14**(7), 12410–12424 (2014)
3. Chen, H.Y., Chen, S.C., Chen, J.J.J., Fu, L.L., Wang, Y.L.: Kinesiological and kinematical analysis for stroke subjects with asymmetrical cycling movement patterns. J. Electromyogr. Kinesiol. **15**(6), 587–595 (2005)
4. Rosecrance, J.C., Giuliani, C.A.: Kinematic analysis of lower-limb movement during ergometer pedaling in hemiplegic and nonhemiplegic subjects. Phys. Ther. **71**(4), 334–343 (1991)
5. Katz-Leurer, M., Sender, I., Keren, O., Dvir, Z.: The influence of early cycling training on balance in stroke patients at the subacute stage. Results of a preliminary trial. Clin. Rehabil. **20**(5), 398–405 (2006)

6. Clinical, C.H., County, K., Education, C.: Effects of a static bicycling programme on the functional ability of young people with cerebral palsy who are. Dev. Med. Child Neurol. **49**, 522–527 (2007)

7. Mohammadi-abdar, H., Ridgel, A.L., Discenzo, F.M., Loparo, K.A.: Design and development of a smart exercise bike for motor rehabilitation in individuals with parkinson's disease. IEEE/ASME Trans. Mechatron. **21**(3), 1650–1658 (2014)

8. Rodríguez-Ugarte, M., Iáñez, E., Ortíz, M., Azorín, J.M.: Personalized offline and pseudo-online BCI models to detect pedaling intent. Front. Neuroinform. **11**(July), 1–12 (2017)

9. Da Fonseca, L.O.: Instrumentação e Controle em Ciclismo Assistido por Estimulação Elétrica para Indivíduos com Lesão Medular. Universidade de Brasilia (2015)

10. Dorado, M.C.N.: Force Acquisition System and Control in Cycling Aided by Functional Electrical Stimulation. Universidade de Brasilia (2017)

11. Jeong, I., Finkelstein, J.: Interactive biking exercise (iBikE) platform to facilitate lower extremity cycling exercise: system design and feasibility. In: 2012 5th International Conference Biomedical Engineering and Informatics, BMEI 2012, pp. 1091–1095 (2012)

12. Jeong, I.C., Finkelstein, J.: Computer-assisted upper extremity training using interactive biking exercise (iBikE) platform. In: Proceedings of the Annual International Conference of the IEEE Engineering in Medicine and Biology Society EMBS, pp. 6095–6099 (2012)

13. Romero-Laiseca, M.A., et al.: Software interface for online monitoring of pedaling on an exercise bike. In: The 6th Brazilian Meeting of Biomechanical Engineering-ENEBI (2018)

14. Schneider, F.B.A., Vargas-Valencia, L.S., Frizera, A., Bastos-Filho, T.F., Ciarelli, P.: Automated time up and go test with redundant IMU system. In: The 6th Brazilian Meeting of Biomechanical Engineering (2018)

Development of a Toolkit for Online Analysis of Facial Emotion

Hamilton Rivera, Carlos Valadão, Eliete Caldeira, Sridhar Krishnan, and Teodiano Freire Bastos-Filho

Abstract

Facial emotion recognition is an important topic in the fields of computer vision and artificial intelligence, since has the potential to be a powerful tool to develop a wide variety of academic and commercial applications, such as human-computer interaction systems. Facial expression communication is especially effective because visual expressions are one of the main information channels in interpersonal communication. This work presents the development of a toolkit for Matlab, which allows online analysis of facial emotion. To facilitate the design of this system, four modules are implemented, which allow: data acquisition, feature extraction, expression classifier and graphic report of analysis. The results show that the six basic emotion classes were recognized by the computational system, with accuracy of 63.0% and 68.8% for LDA and KNN classifiers, respectively. These results are close to the success rates of other systems found in the literature that have an average of 63.2% accuracy. The use of the platform and the methods implemented in this work can benefit automatic emotion recognition applications, which require online processing and evaluation of human emotion objectively and non-intrusively.

1 Introduction

The motivation for many researchers to study the automatic analysis of human affective behavior is the potential wide variety of applications, such as human-computer interaction, health-care, anomalous event detection, computer assisted learning, and interactive computer games (see Fig. 1). Among various cues that express human emotion, nonverbal information like facial cues plays an important role in analyzing human behavior. Human emotion recognition, usually combined with speech, gaze and standard interactions, like mouse movements and keystrokes, can be used to build adaptive environments by detecting the user's affective states [1]. Similarly, one can build socially aware systems [2], or robots with social skills like Sony's AIBO and ATR's [3]. In addition, detecting students' frustration can help improve e-learning experiences [4], and gaming experience can also be improved by adapting difficulty, music, characters or mission according to the player's emotional responses [5]. Other examples of the importance of emotion recognition are pain detection used for monitoring patient progress in clinical settings [6], detection of truthfulness or potential deception used during police interrogations or job interviews [7], monitoring drowsiness or attentive state and emotional status of the driver, for the safety and comfort of driving [8], depression recognition from facial expressions for analysis of psychological distress [9], finally, in recent years, successful commercial applications like Emotient, Affectiva, RealEyes and Kairos to perform large scale internet-based assessments of viewer reactions to ads and related material for predicting buying behavior.

There are different ways of communication, verbal and non-verbal, such as body gestures, speech, facial expressions and hand gestures [10]. According to different surveys [11], verbal components convey one-third of human communication, and nonverbal components convey two-thirds. Among several nonverbal components, by carrying emotional meaning, facial expressions are one of the main

H. Rivera (✉) · C. Valadão · E. Caldeira · T. F. Bastos-Filho
Postgraduate Program in Electrical Engineering, Federal University of Espirito Santo, Vitoria, 29075-910, Brazil
e-mail: hamriver@gmail.com

H. Rivera · S. Krishnan
Department of Electrical and Computer Engineering, Ryerson University, Toronto, Canada

Fig. 1 Applications for automatic emotion recognition: **a** integration of emotion recognition with robotic rehabilitation [26], **b** emotion recognition with computer serious games into a rehabilitation scenario [19]
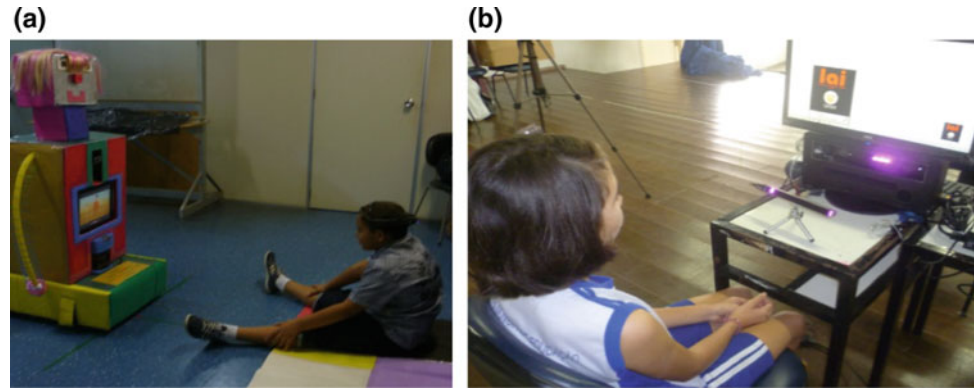
information channels in interpersonal communication and it is especially effective because there are some emotions (called basic emotions), whose expressions are the same over the entire population, in contrast to communication by body gestures, speech or hand gestures, whose elements are different among the cultures throughout the world. Therefore, it is natural that research of facial emotion has been gaining lot of attention over the past decades, with applications not only in the perceptual and cognitive sciences, but also in affective computing and computer animations [11].

Ekman and Fiesen developed a Facial Action Coding System (FACS) that describes all possible perceivable facial muscle movements in terms of predefined Action Units (AU) [12]. All AUs are numerically coded and facial expressions correspond to one or more AU. Although FACS is primarily employed to detect emotions, it can be used to describe facial muscle activation, regardless of the underlying cause. FACS presented by Ekman and Fiesen [12] provides a method for objective measurement of facial expressions.

Automatic recognition of FACS-AU is a difficult problem because AUs have no quantitative definitions and, as noted, they can appear in complex combinations. Essa [13] describe patterns of optical flow that correspond to several AUs, although did not attempt to recognize them [13]. Bartlett et al. report some of the most extensive experimental results of upper and lower face AUs recognition [14].

An automated facial expression analysis system must solve two problems: facial feature extraction and facial expression classification. The main problem of the systems for automatic expression recognition is that this often processes image offline, requires licensed hardware or software. Due to high cost of toolkits, this kind of system cannot be used in low cost applications. Furthermore, systems that require online analysis such as serious games and therapy cannot benefit from the aforementioned system, since it processes the image offline.

The goal of this work contemplates the development of an automated system for online analysis of emotion and

expression recognition, using different means of data acquisition, both online (Kinect, camera or webcam) and offline (image or video files). The facial feature extraction is based on OpenFace (open source facial behavior analysis toolkit) [15], and facial expression classification uses online classifiers (KNN and LDA). Additional a module for data analysis and report of results online and offline was developed.

2 Materials and Methods

The experimental platform implemented in this work is composed of one color camera (webcam, Kinect and other color cameras with image resolution greater than VGA 800×600 pixels), which provides high quality color to obtain facial points FACS-AU, and a computer for image and data processing. For the operation platform, different software are used. The programming languages used in this work are: Matlab 2017 and Visual Studio 2015, which allows building desktop applications for Windows. In addition, it is also used the OpenFace toolkit, an open source facial behavior analysis toolkit (15). To facilitate the design of this system, four modules were implemented (see Fig. 2), which consist of data acquisition module for acquiring and managing image and video data online and offline, feature extraction module, to allow facial AU recognition, and expression recognition modules, for automatic expression detection and classification using training classifier, and a data analysis and report module. This work had the approval of the Ethics Committee of UFES, number 1.121.638 (July 2015).

2.1 Data Acquisition Module

This module allows connecting the online system to different sensors (Kinect, color camera or webcam) using the appropriate driver and configuration, and use those image or video
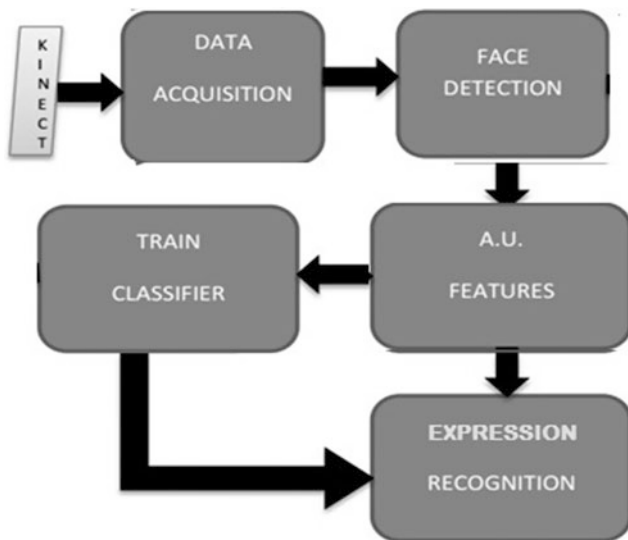
Fig. 2 Block diagram of the proposed system for online emotion recognition

files for offline processing. The system was tested with Extended Cohn-Kanade International Dataset (CK+), and the UFES dataset acquired using the Kinect device. For online experimental test a VGA webcam was used.

The Extended Cohn-Kanade Dataset (CK+) [16]: CK + contains 593 video sequences on both posed and non-posed (spontaneous) emotions, along with additional types of metadata. The age range of these 123 subjects is from 18 to 30 years, most of who are female. Image sequences may be analyzed for both action units and prototypic emotions. It provides protocols and baseline results for facial feature tracking, AUs, and emotion recognition.

The images have pixel resolutions of 640×480 and 640×490 with 8-bit precision for gray-scale values.

UFES Data Set: This research proposes a database focused on aspects of posed and induced emotion recognition and inference. The procedure in each test consist in asking each volunteer to sit comfortably in a chair positioned in front of a 19-inches computer screen and the Kinect sensor, with his/her eyes at 90 cm away from the screen and the sensor (see Fig. 3). The screen displays the six pictures relative to human facial expressions for 10 s. The volunteer is asked to imitate each emotional expression three times. The Kinect device records images of each emotional facial expression performed by the volunteer, and an algorithm identifies the set of features related to expressions of each emotion, based on the AUs. The test involves the participation of eight healthy adults, aged between 24 and 33 years (M: 26, SD: ±3.81).

OnLine Test: The procedure in each test consist of asking each volunteer to sit comfortably in a chair positioned in front of a 19-inches computer screen and the Kinect sensor, with his/her eyes at 90 cm away from the screen and the sensor (see Fig. 3). The screen exhibits six emotion-inducing videos to evoke certain emotions (surprise, sadness, disgust, fear and happiness).

2.2 Features Extraction Module

For features extraction, OpenFace was used, which is an open source tool for facial behavior analysis (facial landmark detection, head pose tracking, AU recognition and eye

Fig. 3 Experimental procedure. Set up for the experimental tests
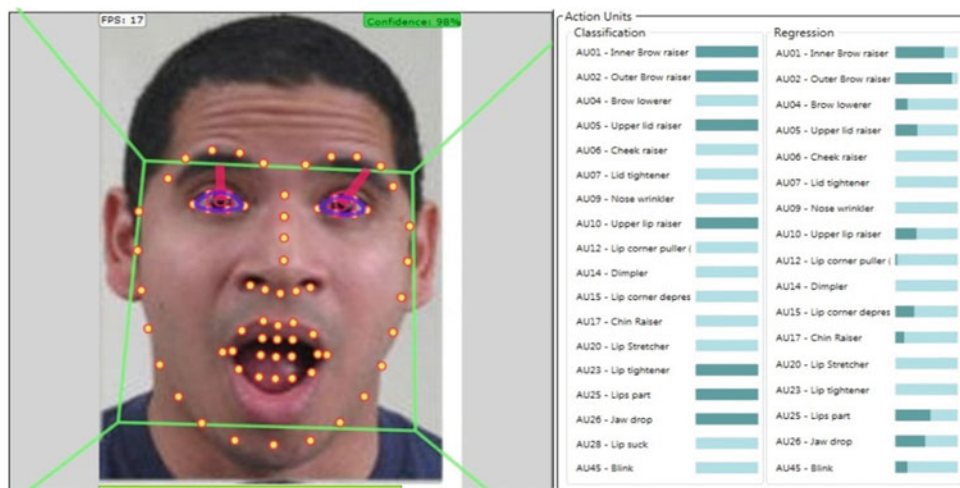
gaze estimation). It is also able to perform all of these tasks together in real-time [15].

Facial Action Coding System (FACS) is a system to taxonomize human facial movements by their appearance on the face. Movements of individual facial muscles are encoded by FACS from slight different instant changes in facial appearance. Using FACS it is possible to code nearly any anatomically possible facial expression, deconstructing it into the specific Action Units (AU) that produced the expression. It is a common standard to objectively describe facial expressions. OpenFace is able to recognize a subset of AUs (see Fig. 4), specifically: 1, 2, 4, 5, 6, 7, 9, 10, 12, 14, 15, 17, 20, 23, 25, 26, 28, and 45. OpenFace allows real-time Facial Action Unit intensity estimation and occurrence detection system based on appearance (Histograms of Oriented Gradients) and geometry features (shape parameters and landmark) [17].

2.3 Emotion Recognition Module

In the emotion detector module, in order to classify the user emotion based on AU, K-Nearest Neighbors (KNN) and Linear Discriminant Analysis (LDA) algorithms were used, based on the work of Jiawei [18].

K–Nearest Neighbors (KNN) algorithm allows predicting a value of variables (20-dimentional AU vector), classifying them into different classes (six basic facial expressions).

The training set was always created by learning process. In this case, this process is based on all previous observations. A very interesting issue in this algorithm is how to find

a similarity between two objects based on their features. KNN emotion detector is used to compute the emotion using Euclidean distance, the emotion features (which are the value of 20 AUs) are represented as set of value between 1 and −1 [19].

Linear Discriminant Analysis (LDA) algorithm or Fisherfaces method overcomes the limitations of the eigenfaces method by applying the Fisher's linear discriminant criterion. This criterion tries to maximize the ratio of the determinant of the between-class scatter matrix of the projected samples to the determinant of the within-class scatter matrix of the projected samples. The LDA method tries to find the subspace that best discriminates different facial expressions classes. The within-class scatter matrix, also called intra-personal, represents variations in appearance of the same individual due to different lighting and face expression, while the between-class scatter matrix, also called the extra-personal, represents variations in classes. In this research, one method maximizes the distance between the face AU of different classes, while other minimizes the distance between the face AU of the same class. In a previous work, a complete implementation of this module was presented [19].

2.4 Analysis and Graphic Report Module

The module for analysis and graphic reports (see Fig. 5) was developed to analyze and display different types of graphics: online to show the emotion detected for the classifiers, and offline to calculate the percentage of each emotion detected throughout the test or in a selected time range.
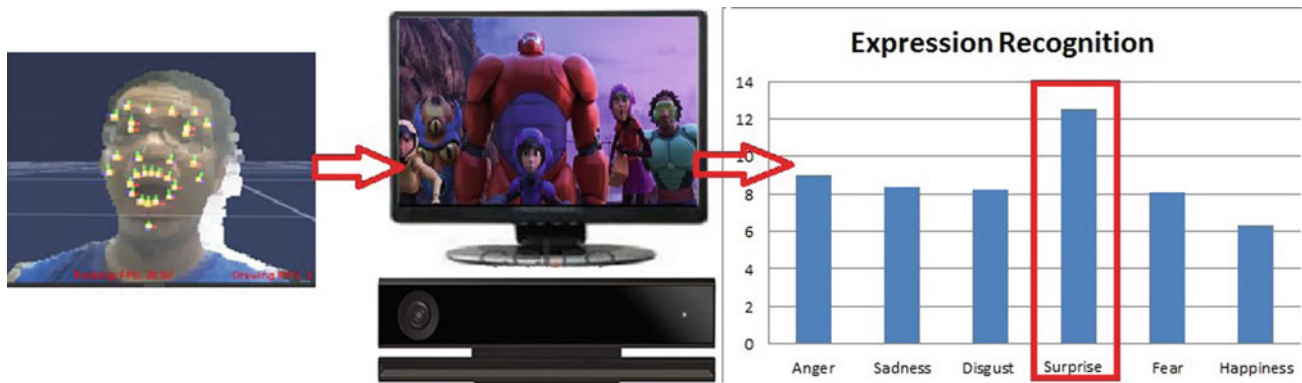
Fig. 5 Module for data analysis and report of results

3 Results

The number of samples per class was 100, and the data was split in 60% for training sets and 40% for test sets. For KNN, different k were evaluated (3, 5, 7, 9), with the best accuracy found for k = 7. Tests were carried out using classifiers LDA (Table 1) and KNN (Table 2), then the system was compared with the different tested dataset (Table 3) and finally compared with other works found in the literature of the state of the art (Table 4).

The expression recognition module is based on trained classifiers (LDA or KNN). Facial expressions using CK+ dataset (for six classes) were recognized by the

Table 1 Confusion matrix for recognition of six emotion using LDA

Expression	Anger	Fear	Sadness	Happiness	Surprise	Disgust
Anger	**49**	12	15	15	2	17
Fear	6	**55**	12	1	12	2
Sadness	3	4	**48**	3	1	0
Happiness	24	3	7	**70**	5	9
Surprise	7	25	6	5	**80**	0
Disgust	11	1	12	6	0	**72**

Table 2 Confusion matrix for recognition of six emotion using KNN

Expression	Anger	Fear	Sadness	Happiness	Surprise	Disgust
Anger	**58**	6	11	12	3	11
Fear	7	**64**	15	0	5	3
Sadness	2	5	**50**	4	0	2
Happiness	21	4	6	**89**	3	5
Surprise	8	20	8	3	**85**	4
Disgust	4	1	10	2	4	**75**

Table 3 Comparison of the system response for the different dataset tested

Dataset	Accuracy KNN (%)	Accuracy LDA (%)
CK+	65.1	69.9
Own dataset	62.3	70.1
Online	61.5	66.4
Average	63.0	68.8

Table 4 Comparison of the system with other in the literature

Brief description of main algorithms	Accuracy (%)
Sparse representation classifier with LBP features [20]	59.18
Sparse representation classifier with local phase quantization features [21]	62.72
SVM with Gabor wavelet features [22]	61.89
Sparse representation classifier with LBP from three orthogonal planes [23]	61.19
Sparse representation classifier with local phase quantization feature from three orthogonal planes [24]	64.11
Collaborative expression representation CER [25]	70.12

computational system, with accuracy rates of 65.1% and 69.9% for LDA and KNN classifiers, respectively. Using our own dataset (for six classes), the accuracy rates for LDA were 62.3 and 70.1% for KNN. For online acquisition the accuracy rates were 63.0 and 68.98% for LDA and KNN. The system have average accuracy rates of 63.0% for LDA and 68.8% for KNN, these results are close to the success rates of other systems found in the literature that have an average accuracy of 63.2%.

4 Conclusions

This work shows the development of an automated system for online analysis of emotion and expression recognition based on the FACS-AU system to classify six basic expressions. The developed system allows: image acquisition, both online (Kinect, camera or webcam) and offline (image or video files) and facial feature extraction (18 AU) based on OpenFace toolkit, for facial expression classification was implemented classifiers KNN and LDA (posed, expontaneous and online emotion recognition), and a module for data analysis and report of result online and offline was developed.

The data acquisition module allows connecting the OpenFace application using a Matlab interface with a webcam or other color cameras or Kinect for on-line feature extraction. The feature extraction module allows using image or video dataset to train AU predictors, which is very useful to calibrate the system to work with different cameras, different levels of lighting, different environments or recognize emotion in persons of different age ranges. The quality of the AUs depends on the camera, the illumination, head movements, distance to the sensor, facial characteristics and accessories (hair length, bangs, beard, mustache, glasses).

The expression recognition module is based on trained classifiers (LDA or KNN). Facial expressions for six classes (negative, neutral and positive) using posed image from CK + dataset were recognized by the computational system, with accuracy rates of 65.1% and 69.9% for LDA and KNN classifiers, respectively. For our own dataset test, the

accuracy rate for LDA was 62.3% and for KNN, it was 70.1%. In on-line test, the accuracy rate for LDA was 61.5% and for KNN, it was 66.4%. The results show that the system is close to the success rates of other systems found in the literature that have an average of 63.2% accuracy.

The tool developed will be integrated into the project Development of a multisensory system for recognition of emotions [26], which allowed exploring different emotional aspects, as the eye tracking, helped conducting studies about visual social attention [27, 28], the facial expression, allowed developing a tool for emotion recognition [19], and the facial thermal variation, was employed for valence and arousal recognition [26]. When performing the multisensorial integration of the system, it was possible to obtain a more complete and varied analysis of the emotional aspects [26].

In the healthcare field, this system can be useful, specially for socially interactive robots, since once they can infer emotions based on the images captured by the camera, they can interact better with humans. Using this system, the device could module its own behavior towards the human, bringing a more realistic experience, based on the probable emotion the human is feeling. Companion robots and even those that could be used for psychological and behavioral therapy can benefit from this algorithm, since emotion information can be inferred and, thus, more precise forms of acting can be applied to the robot controller leading to a better human robot experience, with the emotion content being captured unobtrusively and entering in the control algorithm as an important variable. Acting more precisely, the robot would not make people afraid and will allow them to comfortably interact with the machines and recognizing emotions is an important task for a robot that is built with the intention to have a friendly interaction with humans.

The next steps for future works are to implement a graphic user interface GUI to allow easy use of the tool, implement deep-learning-based facial emotion recognition approaches that could highly reduce the dependence on face-physics-based models, and use feature extraction and pre-processing techniques based on NMF (Non-negative Matrix Factorization) by enabling "end-to-end" learning to occur in the pipeline directly from the input images [29].

General approach goes towards machine learning, yielding state-of-the-art results in many computer vision studies with the availability of big data [30].

References

1. Maat, L., Pantic, M.: Gaze-x: adaptive, affective, multimodal interface for single-user office scenarios. In: Artifical Intelligence for Human Computing. Springer (2007)
2. Devault, D., Artstein, R., Benn, G., Dey, T., Fast, E., Gainer, A., Morency, L.: Virtual human interviewer for healthcare decisión support. AAMAS (2014)
3. Ishiguro, H., Ono, T., Imai, M., Maeda, T., Kanda, T., Nakatsu, R.: Robovie: an interactive humanoid robot. Ind. Robot. Int. J. **28**(6), 498–504 (2001)
4. Kapoor, A., Burleson, W., Picard, R.W.: Automatic prediction of frustration. IJHCS **65**(8), 724–736 (2007)
5. Blom, P.M., Bakkes, S., Tan, C.T., Whiteson, S., Roijers, D., Valenti, R., Gevers, T.: Towards personalised gaming via facial expression recognition. AIIDE (2014)
6. Irani, R., Nasrollahi, K., Simon, M.O., Corneanu, C.A., Escalera, S., Bahnsen, C., Lundtoft, D.H., Moeslund, T.B., Pedersen, T., Klitgaard, M.: Spatiotemporal analysis of rgb-dt facial images for multimodal pain level recognition. CVPR Workshops (2015)
7. Ryan, A., Cohn, J., Lucey, S., Saragih, J., Lucey, P., Torre, F., Ross, A.: Automated facial expression recognition system. ICCST (2009)
8. Vural, E., Cetin, M., Ercil, A., Littlewort, G., Bartlett, M., Movellan, J.: Drowsy driver detection through facial movement analysis. In: Human–Computer Interaction (2007)
9. Scherer, S., Stratou, G., Mahmoud, M., Boberg, J., Gratch, J., Rizzo, A., Morency, L.: Automatic behavior descriptors for psychological disorder analysis. In: 10th IEEE International Conference and Workshops on Automatic Face and Gesture Recognition (FG). IEEE (2013)
10. Koesltra, S., Mühl, C., Soleyman, M., Lee, J. S., Yazdani, A., Ebrahimi, T., Pun, T., Nijholt, A., Patras, I.: DEAP: a database for emotion analysis using physiological signals. Trans. Affect. Comput. **3**(1) (2012)
11. Kaulard, K., Cunningham, D.W., Bülthoff, H.H., Wallraven, C.: The MPI facial expression database: a validated database of emotional and conversational facial expressions. PLoS ONE **7**, e32321 (2012)
12. Ekman, P., Friesen, W.: The Facial Action Coding System: A Technique For The Measurement of Facial Movement. Consulting Psychologists Press, Inc., San Francisco, CA (1978)
13. Essa, I., Pentland, A.: Coding, analysis, interpretation, and recognition of facial expressions. IEEE Trans. Pattern Anal. Mach. Intell. **19**(7), 757–763 (1997)
14. Bartlett, M., Hager, J., Ekman, P., Sejnowski, T.: Measuring facial expressions by computer image analysis. Psychophysiology **36**, 253–264 (1999)
15. Tadas, B., Peter, R., Louis-Philippe, M.: OpenFace: an open source facial behavior analysis toolkit. In: IEEE Winter Conference on Applications of Computer Vision (2016)
16. Lucey, P., Cohn, J.F., Kanade, T., Saragih, J., Ambadar, Z., Matthews, I.: The extended Cohn-Kanade dataset (CK+): a complete dataset for action unit and emotion-specified expression. In: Proceedings of the IEEE Conference on Computer Vision and Pattern Recognition Workshops. San Francisco, CA, USA, pp. 94–101 (2010)
17. Tadas, B., Marwa, M., Peter, R.: Cross-dataset learning and person-specific normalisation for automatic action unit detection in facial expression recognition and analysis challenge. In: IEEE International Conference on Automatic Face and Gesture Recognition (2015)
18. Jiawei, H., Micheline, K., Jian, P.: Data Mining: Concepts and Techniques. Elsevier, USA, Third edition (2012)
19. Rivera, H., Goulart, C., Favarato, A., Valadão, C., Caldeira, E., Bastos, T.: Development of an automatic expression recognition system based on facial action coding system. In: Simpósio Brasileiro de Automação Inteligente (SBAI2017) (2017)
20. Huang, M.H., Wang, Z.W., Ying, Z.L.: A new method for facial expression recognition based on sparse representation plus LBP. In: Proceedings of the International Congress on Image and Signal Processing, pp. 1750–1754. Yantai, China. Sensors 2018, 18, 401 20 of 20 (2010)
21. Zhen, W., Zilu, Y.: Facial expression recognition based on local phase quantization and sparse representation. In: Proceedings of the IEEE International Conference on Natural Computation, pp. 222–225. Chongqing, China (2012)
22. Zhang, S., Zhao, X., Lei, B.: Robust facial expression recognition via compressive sensing. Sensors 3747–3761 (2012)
23. Zhao, G., Pietikainen, M.: Dynamic texture recognition using local binary patterns with an application to facial expressions. IEEE Trans. Pattern Anal. Mach. Intell. **29**, 915–928 (2007)
24. Jiang, B., Valstar, M.F., Pantic, M.: Action unit detection using sparse appearance descriptors in space-time video volumes. In: Proceedings of the IEEE International Conference and Workshops on Automatic Face & Gesture Recognition, pp. 314–321. Santa Barbara, CA, USA (2011)
25. Lee, S.H., Baddar, W.J., Ro, Y.M.: Collaborative expression representation using peak expression and intra class variation face images for practical subject-independent emotion recognition in videos. Pattern Recognit. **54**, 52–67 (2016)
26. Rivera, H., Bastos, T.: Development of a Multisensorial System for Emotion Recognition. Universidade Federal do Espírito Santo, Coordenação de Aperfeiçoamento de Pessoal de Nível Superior (2017)
27. Rivera, H., Goulart, C., Caldeira, E., Bastos, T.: Using eye-tracking for study about valence and emotional facial expressions. In: Congresso Brasileiro de Engenharia Biomédica, 2016, Foz de Iguaçu. Anais do Congresso Brasileiro de Engenharia Biomédica (2016)
28. Rivera, H., Bissoli, A., Goulart, C., Caldeira, E., Bastos, T.: Development of matlab toolbox for eye tracking systems. In: Congresso Brasileiro de Automática, 2016, Vitória. Anais do Congresso Brasileiro de Automática (2016)
29. Walecki, R., Rudovic, O.: Deep structured learning for facial expression intensity esti-mation. Image Vis. Comput. **259**, 143–154 (2017)
30. Kahou, S.E., Michalski, V., Konda, K.: Recurrent neural networks for emotion recognition in video. In: Proceedings of the ACM on International Conference on Multi-modal Interaction, pp. 467–474. Seattle, WD, USA (2015)

Development of Game-Based System for Improvement of the Left-Right Recognition Ability in Children with Down Syndrome

Thalyssa Rodrigues, Nicolás Valencia, Dayse Santos, Anselmo Frizera, and Teodiano Bastos

Abstract

Down Syndrome (DS) is one of the most common genetic disorder worldwide and the most common cause of intellectual disability, which generates problems regarding the functionality and independence to perform Activities of Daily Living (ADLs). This work proposes the development of a serious game-based system motivated by the results of a study concerning children with Down Syndrome (DS) and their laterality (left-right recognition) difficulty. This preliminary study was carried out using a system designed with the purpose to evaluate the children's functional performance through data acquired using an RGB-D camera Kinect v2. This system uses a performance assessment protocol to analyze the laterality ability in children, providing a mirror-type visual feedback to the user. Thirteen participants (twelve with DS and one without DS) with ages between nine and ten years old were evaluated. In this evaluation, the children's success percentage in distinguishing left from right was only 30.0%, confirming their laterality issue. Based on this preliminary validation, the serious game-based system was implemented as a proposal of an intelligent environment for the development of the right and left recognition. In general, children with DS are not able to pay attention for as much time as typical children. Thus, this game was designed to keep children interested and therefore focused on the task assigned, accelerating the learning. The game system acquires and processes parameters acquired by the Kinect and it aims to function as an intervention system that complements conventional therapies in helping the children to more efficiently develop their skills.

1 Introduction

Down syndrome (DS) is the most common non-inherited cause of cognitive deficit as a result of the presence of all or a portion of an extra copy of chromosome 21 [1]. According to 2010 Census of the Brazilian Institute of Geography and Statistics (IBGE), in Brazil there are more than 300 thousand people with DS [2].

Many medical and health-related complications are associated with DS, including cardiac and respiratory problems [3]. Dynamic motor dysfunction is also widespread among individuals with DS, which includes extended motion and reaction times, balance and postural deficits and co-contraction of agonist and antagonist muscle pairs [4, 5]. Noticeable in children, these deficits may have a causal link to delays in achieving motor development milestones [6]. In fact, the motor development of infants and children with DS is delayed, due to generalized muscle hypotonia and ligament laxity that is characteristic of DS [7]. The neuropathological basis for motor dysfunction in DS is unknown, but cerebellar dysfunction, delayed myelination and proprioceptive and vestibular deficits have been invoked as potential contributors [5, 8].

Other complications faced by individuals with DS, and perhaps the most noticeable ones, are related to the cognitive

T. Rodrigues (✉) · N. Valencia · A. Frizera · T. Bastos
Electrical Engineering, Universidade Federal do Espírito Santo, Vitória, ES, Brazil
e-mail: thalyssabaiocco123@gmail.com

N. Valencia
e-mail: valenciaj@ieee.org

A. Frizera
e-mail: frizera@ieee.org

T. Bastos
e-mail: teodiano.bastos@ufes.br

D. Santos
Psychology, Universidade Federal do Espírito Santo, Vitória, ES, Brazil
e-mail: daysekaroline@hotmail.com

development. Some studies have highlighted the existence of a relation between difficulty in motor abilities acquisition and delayed cognitive development, the latter being negatively influenced by the first [9].

Most of children with DS show a mild to moderate level of intellectual development difficulty, meaning that their learning process takes a longer time when compared to typical children [10]. The cognitive delay in children with DS arises within just a year from their birth and it narrows their capacity to pay attention, concentrate, communicate and memorize, as well as observe, analyze and deal with abstract concepts [11].

Therefore, individuals with DS usually show lower perception and discrimination skills [11]. The perception is associated with the ability to pay attention and depends on the proper functioning of the brain's large cortical areas of association; the discrimination is the ability to detect and tell the differences and similarities between distinct things [12].

An example of that impairment is the fact that people with DS have a considerably higher difficulty in identifying "left" and "right" than typical people, as shown in the study of Souza and Bruschi [13]. In this study, children with DS at the age of 10–14 were demanded to complete tasks concerning laterality: 60% of the children performed the tasks with interruptions and in an uncertain way (even after new verbal orientation); 20% were not able to perform the requested movements at all or used the wrong limbs; and the other 20% showed insecurity in performing the tasks, but were able to perform it correctly after a few trials.

The difficulty that individuals with DS show in acquiring motor and cognitive skills have been motivating scientists to study and develop means of intervention. The application of technology has improved the traditional way to handle therapies, especially with the development of Virtual Realities (VR). In this regard, serious games can create an immersive environment from recreational resources to aid in physical and motor rehabilitation and training [14]. Game technologies can assist the user in the correct execution of movements through stimulation from interactive elements of digital games, offering a broad scope of possible assistance to health and health-care [15]. Games can also generate motor skills, spatial skills, shape identification, and curiosity to the player [16].

Virtual reality-based therapy is one of the most innovative and promising recent developments in rehabilitation technology [17], which allows users to interact with a computer-generated scenario (a virtual world), making corrections and increasing intensity of training while providing feedback [18]. Users can interact with displayed images, move and manipulate virtual objects and perform other actions in a way that attempts to "immerse" them within the simulated environment [19].

However, these systems, although able to provide solutions and assist in the recovery of the users, should be designed carefully so as not to bring adverse effects [20]. Thus, for the development of these games, a domain analysis of the topic and studies of the playful elements to integrate serious goals and motivational resources are needed [21–23].

For instance, mirror-type interfaces play 0 a considerable motivational role [24], which is used here to generate a feedback to the children while evaluating their performance. The evaluation software should be interesting for the users, thus designing it as a game may serve as an encouragement to performance improvement, especially if the user can observe his/her movements on the screen.

Devices that capture the user's movements, combined with game systems that verify their correctness, can improve the experience of rehabilitation [25]. For tracking the user, previous systems have applied markers [26, 27] or required the user to wear a shirt with a rectangular highly textured region [28].

In order to build efficient systems, however, it is necessary to identify their functionalities and requirements to contribute to the user's necessities effectively [29]. Differently from the previously mentioned systems, a desired characteristic is to free the user from the obligation to wear/use an external tool. Several studies have explored this possibility by applying devices such as RGB-D cameras, IMUs and other sensors for physical training and therapy systems [30–32].

This present work considers the functionalities of game systems with RGB-D cameras (Microsoft Kinect v2) and how they can be used to help in the medical field, exploring reports in the literature, as well as practical needs and requirements raised by psychologists and physical therapists. In Sect. 2, the preliminary study carried out concerning the laterality in children with DS is presented, detailing the investigation of the user's needs. Section 3 presents and explains the serious game-based system developed for the improvement of the left-right recognition ability in children with DS, motivated by the results of the preliminary study. The game, proposed as a complement to conventional therapy, aims to provide support to professionals in the area and to generate objective performance reports for further analysis. Section 4 holds a discussion concerning the work developed and the possibilities for improvement in future works.

2 Methodology

A diagnosis study was firstly carried out to identify how children with DS responded to commands concerning laterality (left-right recognition). This factor was analyzed based on tasks that can reveal functional deficits in

psychomotor terms, covering sensory and perceptual integration, which are related to the child's learning potential.

More specifically, to evaluate the ability to distinguish left from right, the child was asked to point at a specific body part of a specific hemisphere of the body, such as left hand, right foot, left eye, right hand, and his/her movements were acquired using a RGB-D camera.

Details of the study, its participants, the inclusion and exclusion criteria and the preliminary results are given in the following sections.

2.1 Participants of the Diagnosis Study

The sample was composed of 12 children with DS and one typical child, aged 9–10 years. These children were non-probabilistically chosen from two rehabilitation centers (Associations of Parents and Friends of Exceptional Children—APAE), located in Vila Velha and Serra, Espírito Santo State, Brazil.

Inclusion criteria were as follows: children classified at level I of the Gross Motor Function Classification System (GMFCS) [33] and able to walk without personal assistance and/or assistive devices/orthesis; without any other neurological alterations, or associated respiratory or osteomyoarticular pathologies (not due to DS); and ability to understand and obey simple verbal commands. Exclusion criteria are children who did not follow correctly the instructions given by the therapist, i.e., that refused to cooperate with the therapist (even after several attempts).

The study was approved by the Research Ethics Committee of Federal University of Espirito Santo, Brazil (number 1.629.376), and all parents or legal guardians signed an informed consent form, authorizing their children to participate of the study.

2.2 Mirror Virtual Environment for Diagnosis Study

A virtual environment (VE) with visual feedback was developed to evaluate the functional performance of children with DS. The purpose of this VE is to discover which motor and cognitive abilities need training in these children, serving as basis for posterior intervention. A computer vision system based on Kinect was used to obtain kinematic parameters and to generate a kinematic evaluation interface with a virtual immersion system to detect and quantify the movements. The system has a graphical interface that allows body recognition and obtaining parameters, such as range of motion, velocities, and positions of each body articulation in three dimensions.

The system environment is set up with an RGB-D camera Kinect v2, used to acquire the user's articulations positions and orientations. The Microsoft Kinect consists of a 3D depth sensor, a color camera and a four-microphone array. It uses corporal segments parametrization sensors to identify human silhouettes and therefore the user's postures and movements.

The test with that environment begins by having the child positioned in front of the RGB-D camera; then the measuring device captures his/her position parameters and corporal patterns necessary to generate the information established by the VE. With these data, feedback is made in real time for the child, as well as quantitative values for the evaluator that accompanies the kinematic evaluation protocol. The system configuration can be seen in Fig. 1.

The feedback delivered to the children is due to the "mirror" characteristic of the virtual environment. This characteristic allows the child to see his/her movements and achieved activities. The system provides to the evaluator a tool that can measure and analyze movements of the child when performing requested tasks, while rewards the child for performing them.

The interface developed for analysis of the functionality of the ADLs is shown in Fig. 2. This tool provides the evaluator with the necessary information of the child (left side) and buttons to control the beginning and the end of the data capture ("Start" and "Stop" buttons, respectively). In the upper right corner, a 3D reconstruction of the skeleton of the child under test is shown, generating a perspective of the movements. Similarly, an on-line estimation of the angles of the shoulder and elbow joints of each arm of the child is presented. It is important to highlight that the parameters of each joint (position and orientation) are saved for further analysis.
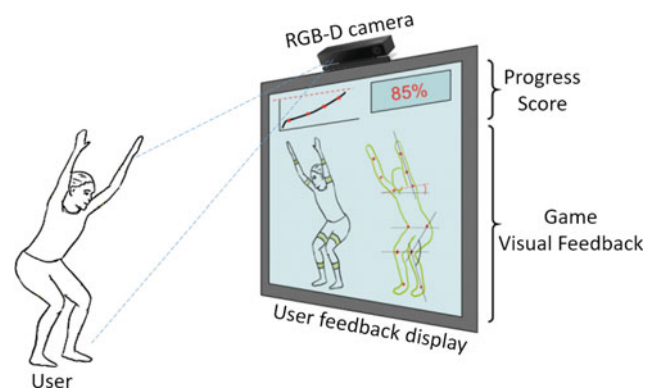
Fig. 1 Implemented system for motor evaluation with visual feedback for analysis of functional performance of children with DS
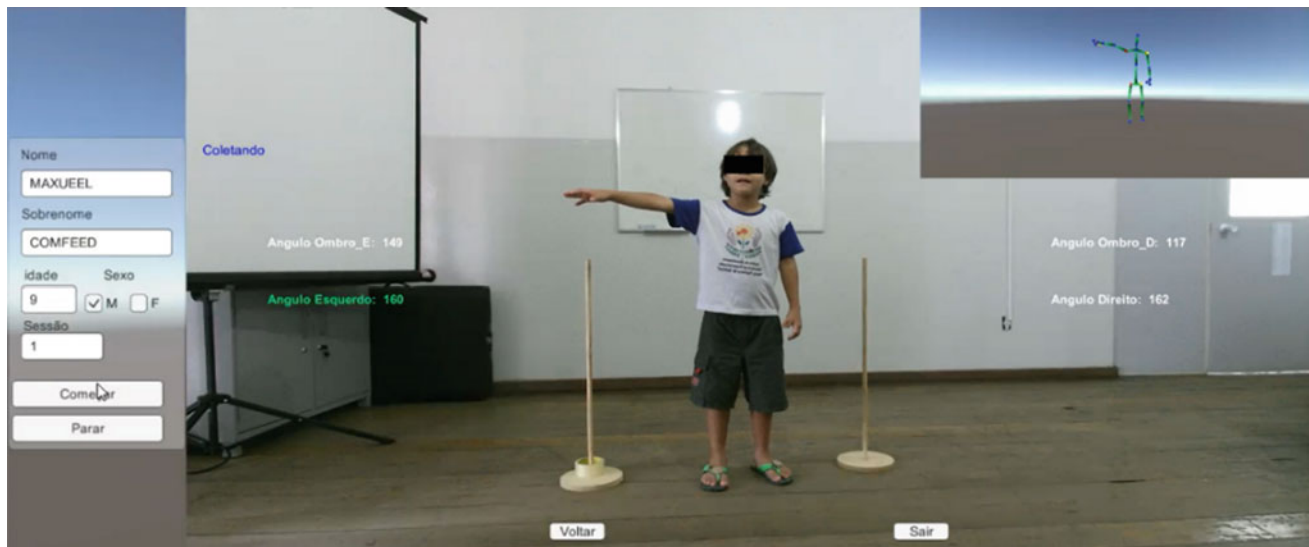
Fig. 2 Virtual environment interface developed for children with DS

2.3 Preliminary Results

The application of the game-based system in the diagnosis study has made explicit the laterality deficit on the children with DS that participated on the tests. As far as right-left recognition is concerned, they showed difficulty in distinguishing the sides, primarily when they were asked to relate it to a specific body part.

None of the children with DS was able to make a complete distinction between the two hemispheres of the body, as opposed to the only typical child, who performed all the tasks correctly. In Table 1, the tasks demanded and the percentage of children with DS that accomplished them are explicit.

It is not explicit in Table 1, but in only 30% of the times the children performed the task correctly and some children did not perform the task at all in 5.0% of the total amount of tasks assigned to all children. Figure 3 shows a test done with a child in which he had to identify a specific body part, following the tasks described in Table 1.

Analyzing these preliminary results and considering the pedagogical and psychological knowledges, a serious game

was developed for intervention. Details of the game implementation are given in Sect. 3.

3 Development of Serious Game for Intervention

The aim of this work is to offer a mean of clinical intervention for children with DS through a serious game. The importance of the diagnosis study previously detailed relies on the fact that it is important to identify the needs of the users before developing any type of intervention. Since the study carried out confirmed the children's difficulty in distinguishing left from right, a serious game was designed as an intervention interface proposal to teach and train this ability.

Games in general are appealing to children, therefore the development of serious games is appropriate for the improvement of skills in children, since they provide training at the same time that instigate the child's curiosity [34]. This aspect is of great interest especially when dealing with individuals with DS, given their concentration difficulty [11].

Table 1 Percentages of children with DS that manage to perform each task correctly

Task assigned	Percentage of children to perform correctly (%)
Task 1—show right hand	41.67
Task 2—point at left eye	33.33
Task 3—show right foot	25.00
Task 4—show left hand	33.33
Task 5—cross right leg over the left leg	16.67
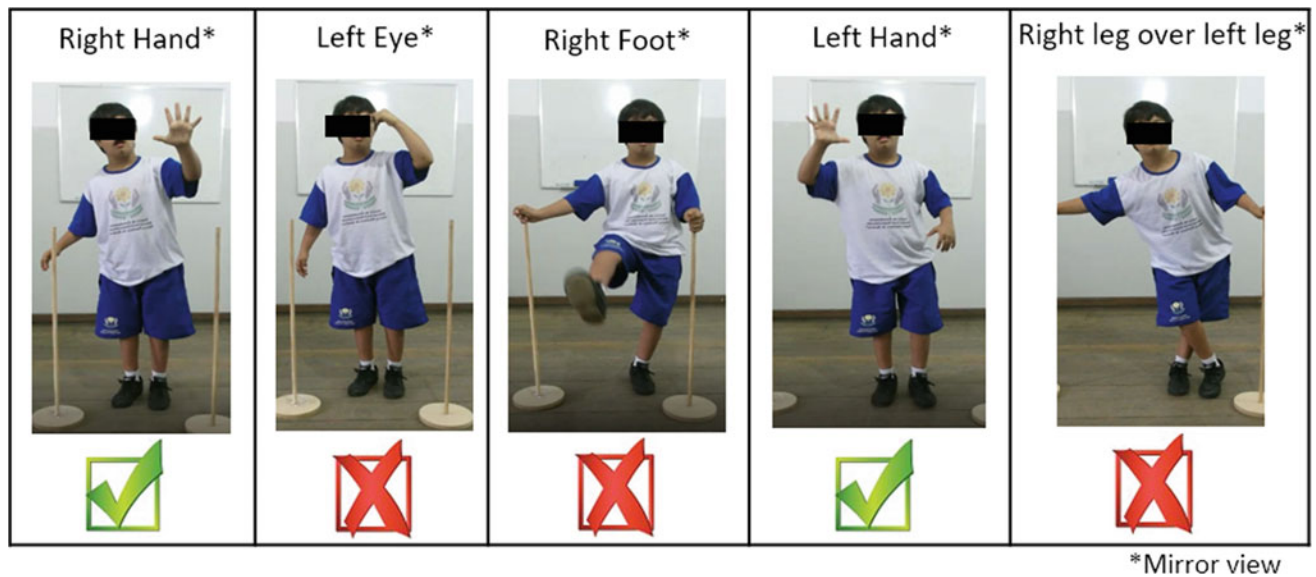
Fig. 3 Hits and misses of a child with DS during a test evaluating his capability of recognizing the hemispheres of the body

For the purpose of this game, the movements of interest are the ones corresponding to the user's hands. Once again, the Kinect v2 is used to capture the child's joints information and the correspondent movements. The advantage to use Kinect relies on the fact that it is less intrusive, in the sense that it does not require the use of sensors attached to the body. Therefore, besides being a low cost sensor, it is easy to interact with through the perspective of the user.

The game consists of six different stages, the first being an introductory concept presentation, clearly showing the child which of each side is the left one and which is the right one. The game starts when the child is placed in front of the Kinect. A voice command determines which object/side the child must choose, e.g. "select the star on the right side", "select the balloon on the left side". The child has to move his/her hand to select the correct object in the correct side, using the right hand to select objects on the right side and the left hand to select objects on the left side. If the child selects the correct side with the correct hand, he/she earns a point. If the wrong hand is used, a voice command reminds the child to switch hands, saying for instance "use the left hand instead". The game interprets as a mistake one of the two situations: the child selects the wrong side or the child uses the wrong hand twice. For both cases, the score is not affected, unless he/she makes five consecutive mistakes, in which case a point is debited. The flow chart shown in Fig. 4 explains how the game works.

The game process is designed to identify if the child is doing well in a level through his/her score. If the system detects that he/she is having a good performance in the current level, the child advances to a higher one. On the contrary, if it is detected that the child is having trouble, he/she moves back to a lower level. The game ends automatically when the child finishes the last level (level 6), but the therapist that accompanies the child can interrupt it at any time he/she finds necessary, for instance if a child is returning to the same level repeatedly.

To help the child to choose the correct side, there are a variety of visual stimuli in the game. Those stimuli are removed one by one, as the child moves to a higher level. The stimuli are: colored "right" and "left" identification tags, different color for each side, different object to be selected, a blink behind the object that should be chosen and right and left hand drawings in each side. The idea is that the child associates those images and colors with the correspondent side, serving as guides through the levels. The distribution of the stimuli along the game levels is shown in Table 2.

Those stimuli can be checked in Fig. 5a, b, in which the game interface is illustrated. Since all the stimuli are present in those pictures, they both correspond to level 1 and 2. It is possible to see in both figures that the user was moving the correct hand to select the assigned object. In Fig. 5a, the user had to select the balloon on the left side and he/she was moving the left hand, while in Fig. 5b, the hand used was the right one and the user had to select the star on the right side.

As shown in Table 2, the last stimulus to be removed is the colored tags. The idea behind it is that the child associates a color with each side and that this association remains the main guide through the levels.

The instruction for what the child has to do is given by the game through a voice command. The advantage to do so

Fig. 4 Game process flow chart
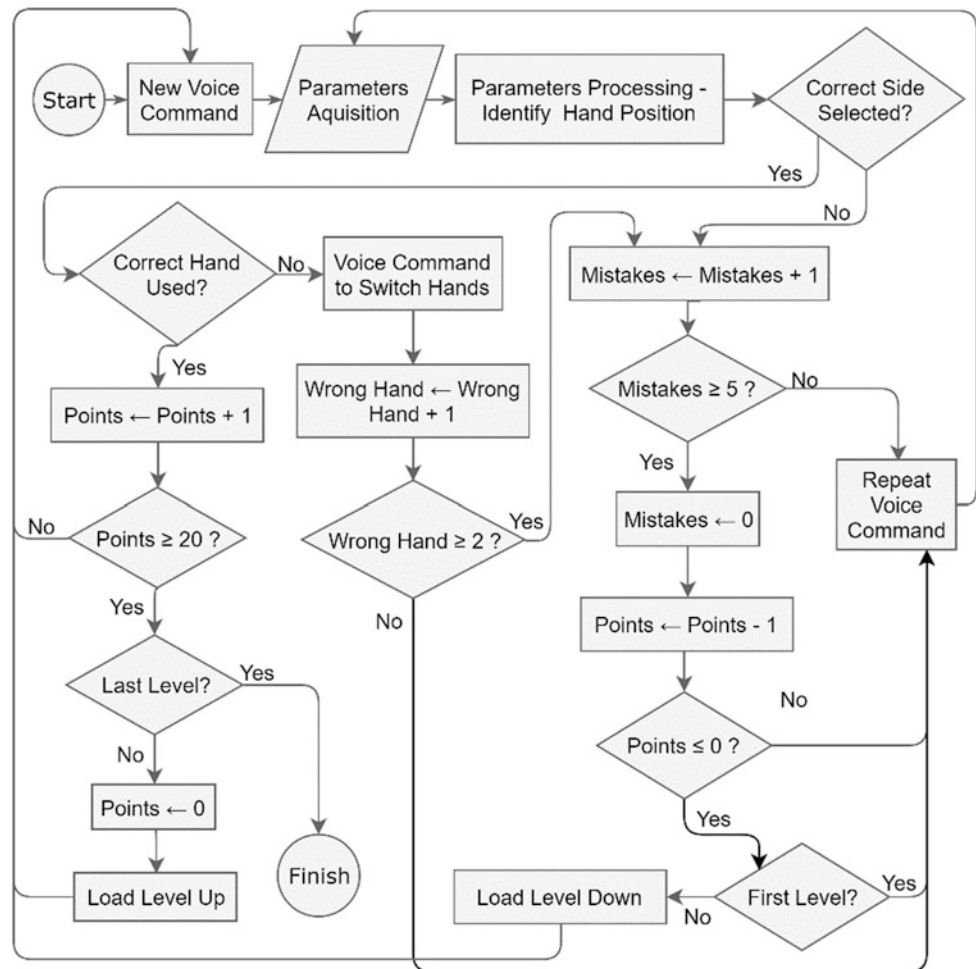
Table 2 Distribution of visual and sound stimuli through the game levels

Game level	Hands drawings	"Right" and "Left" tags	Blink	Different colors	Different objects
Level 1–presentation	Yes	Yes	Yes	Yes	Yes
Level 2	Yes	Yes	Yes	Yes	Yes
Level 3	Yes	Yes	Yes	Yes	–
Level 4	Yes	Yes (colored tags)	Yes	–	–
Level 5	Yes	Yes (colored tags)	–	–	–
Level 6	Yes	–	–	–	–

is that when people are asked to carry out a task in real life that involves distinguishing left from right, that request is almost always done verbally. This occurs, for instance, when a person is giving directions to someone else or wants to ask the other person whether he/she is left-handed or right-handed.

At the end of the game, whether the child finishes the last level or the therapist chooses to stop the training, a report is generated, showing the child's performance through percentage of hits and misses. This is important for keeping

record of the child's improvement, since they will have to play the game several times.

4 Discussion and Future Work

Previous studies from our research group pointed towards a decreased capacity in children with DS in recognizing left and right. The global percentage of success was only 30% among the participants, confirming their laterality difficulty

(a) Right hand on the right side.   (b) Left hand on the left side.
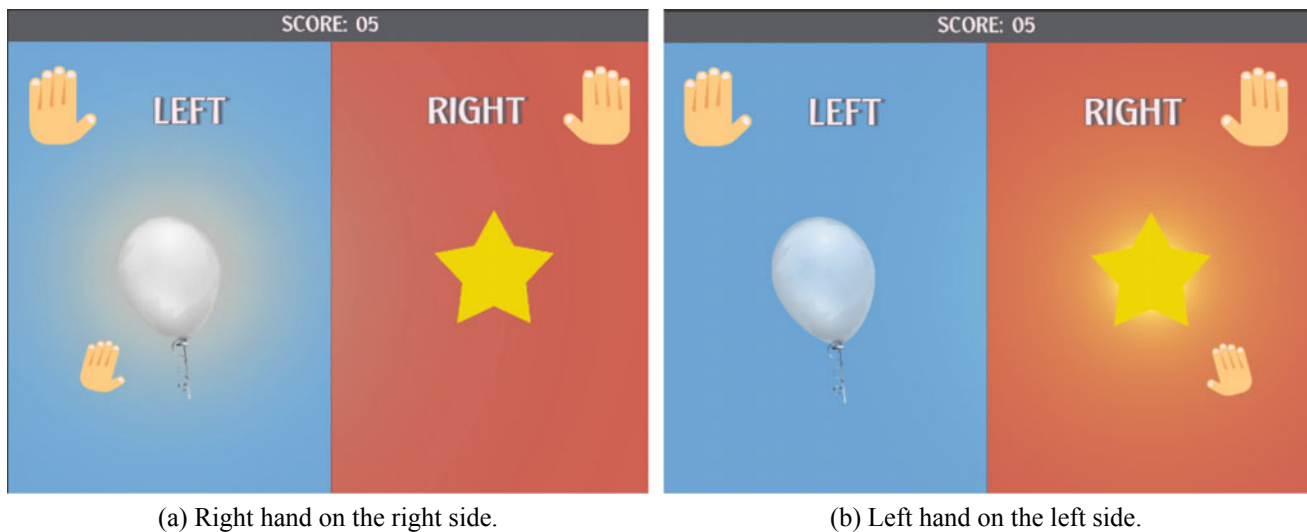
Fig. 5 Game interface corresponding to level 1 and 2, in which all visual stimuli are present. **a** Moment in which the task is to choose the balloon on the left side. **b** Moment in which the task is to choose the star on the right side

and giving the impression that they might have based their decisions on guessing.

These previous studies led to the development of the serious game explained in Sect. 3, which is the focus of this paper. One of the game's most important advantages is that it can be applied to a wide range of children, since the instructions are given through voice commands, not requiring the child to be alphabetized. Although there are the "left" and "right" identification tags, it is not expected that the children are able to read them. The intention is that they associate those letters with the correspondent side, just like they do in levels 1 and 2, when they are expected to associate the star with the right side and the balloon with the left side (Fig. 5).

The next step of this research is to test the developed game for the training of the right-left recognition in children with DS. Given that it evaluates the performance of the child to determine whether the level of difficulty should be increased or decreased, the game has the characteristic of adaptability, fitting the child's individuality. Therefore, it is expected to be a suitable tool for improving the laterality in children.

However, the laterality issue is just one of the cognitive abilities that need to be trained in children with DS in order for them to grow into more independent individuals. In this regard, other games aiming the development of different abilities are in the process of being developed, based on recommendations from the clinical staff. The plan is to create an interface that displays all these games to be used by therapists in cognitive training.

In order to improve the game robustness, another goal is to make the children's movement data acquisition through a multi-camera system. This will reduce the joint occlusion, allowing a higher range of movements. The system can also be used with augmented reality using video beams, projecting images and generating interactivity.

References

1. Arya, R., Kabra, M., Gulati, S.: Epilepsy in children with down syndrome. In: Epileptic. Disord. **13**(1), 1–7 (2011). http://www.ncbi.nlm.nih.gov/pubmed/21398208. Accessed 3 Apr 2018
2. B. I. o. G. IBGE and Statistics, Censo Demográfico 2010, 2013, vol. 55, no. 11. http://www.bcb.gov.br/pec/GCI/PORT/readout/readout.asp. Accessed 3 Apr 2018
3. Malak, R., Kostiukow, A., Krawczyk-Wasielewska, A., Mojs, E., Samborski, W.: Delays in motor development in children with Down Syndrome. Med. Sci. Monit. **21**, 1904–1910 (2015). http://www.medscimonit.com/abstract/index/idArt/893377. Accessed 3 Apr 2018
4. Mazurek, D., Wyka, J., Mazurek, D., Wyka, J.: Down syndrome—genetic and nutritional aspects of accompanying disorders. In: Rocz Panstw Zakl Hig **66**(3), 189–194 (2015). http://wydawnictwa.pzh.gov.pl/rocznikipzh/. Accessed 3 Apr 2018
5. Galli, M., Rigoldi, C., Mainardi, L., Tenore, N., Onorati, P., Albertini, G.: Postural control in patients with down syndrome. Disabil. Rehabil. **30**(17), 1274–1278 (2008)
6. Sacks, B., Buckley, S.: What do we know about the movement abilities of children with down syndrome? Down Syndr. Educ. Down Trust. Syndr. News Updat. **2**(4), 131–141 (2003)
7. Naito, M., Aoki, S., Kamide, A., Miyamura, K., Honda, M., Nagai, A., Mezawa, H., Hashimoto, K.: Gait analysis in down syndrome pediatric patients using a sheet-type gait analyzer: pilot study. Pediatr. Int. **57**(5), 860–863 (2015)
8. Tovar, Á.E., Westermann, G., Torres, A.: From altered synaptic plasticity to atypical learning: a computational model of down syndrome. In: Cognition, vol. 171, pp. 15–24, Oct 2017. http://dx.doi.org/10.1016/j.cognition.2017.10.021. Accessed 03 Apr 2018

9. Ciccheti, D., Beeghly, M.: An organizational approach to the study of down syndrome: contributions to an integrative theory of development. In: Ciccheti, D., Beeghly, M. (eds.) Children with Down's Syndrome: A Developmental Perspective. Cambridge University Press, Cambridge (1990)

10. Mcconnaughey, F., Quinnn, P.O.: O desenvolvimento da criança com síndrome de Down. In: Stray-Gundersen, K. (org) Crianças com Síndrome de Down guia para pais e educadores (Second edition), cap.1, pp. 134–159. Artmed—Porto Alegre (2007)

11. Marques, J.: Síndrome de Down, psicomotricidade, leitura e escrita—uma intervenção simultânea. Tese (Mestrado em Educação Especial—Área de Cognição e Motricidade)–Instituto Politécnico de Coimbra, Escola Superior de Educação (ESEC). Coimbra, Portugal (2012)

12. Toncoso, M.V., Cerro, M. M.: Síndrome de Down: Leitura e Escrita. In: Um guia para pais, educadores e professores. Porto: Porto Editora (2004)

13. Souza, L.H., Bruschi, M.: Análise do equilíbrio estático, lateralidade e força de membros inferiores em crianças com Síndrome de Down. In: EFDeportes.com, Revista Digital, ano 16, no. 157. Buenos Aires (2011). http://www.efdeportes.com/efd157/equilibrio-estatico-em-criancas-com-sindrome-de-down.htm. Accessed 03 Apr 2018

14. Abellard, A., Abellard, P., A. H.: Applications: serious games adapted to children with profound intellectual and multiple disabilities. In: 9th International Conference on Virtual Worlds and Games for Serious Applications (VS-Games), pp. 183–184 (2017)

15. Bernardini, S., Porayska-Pomsta, K., Smith, T.J.: ECHOES: an intelligent serious game for fostering social communication in children with autism. Inf. Sci. **264**, 41–60 (2014)

16. Glegg, S.: Virtual rehabilitation with children: challenges for clinical adoption [From the Field]. In: IEEE Pulse, vol. 8, no. 6, pp. 3–5 (2017). http://ieeexplore.ieee.org/document/8110871/. Accessed 03 Apr 2018

17. De Troyer, O.: Towards effective serious games. In: 9th International Conference on Virtual Worlds and Games for Serious Applications (VS-Games), pp. 284–289 (2017). http://ieeexplore.ieee.org/document/8056615/. Accessed 03 Apr 2018

18. Cameirao, M.S., Bermudez i Badia, S., Duarte Oller, E., Verschure, P.F.: Neurorehabilitation using the virtual reality based rehabilitation gaming system: methodology, design, psychometrics, usability and validation. J. NeuroEng. Rehabil. **7**(1), 48 (2010). http://jneuroengrehab.biomedcentral.com/articles/10.1186/1743-0003-7-48. Accessed 03 Apr 2018

19. Covaci, A., Kramer, D., Augusto, J. C., Rus, S., Braun, A.: Assessing real world imagery in virtual environments for people with cognitive disabilities. In: Proceedings—2015 International Conference on Intelligent Environments, IE 2015, pp. 41–48 (2015)

20. Konstantinidis, E.I., Billis, A.S., Paraskevopoulos, I.T., Bamidis, P.D.: The interplay between IoT and serious games towards personalised healthcare. In: 9th International Conference on Virtual Worlds and Games for Serious Applications (VS-Games), pp. 249–252 (2017). http://ieeexplore.ieee.org/document/8056609/. Accessed 03 Apr 2018

21. Toffalini, E., Meneghetti, C., Carretti, B., Lanfranchi, S.: Environment learning from virtual exploration in individuals with down syndrome: the role of perspective and sketch maps. J. Intellect. Disabil. Res. **8276017**, 1–11 (2017). http://doi.wiley.com/10.1111/jir.12445. Accessed 3 Apr 2018

22. Menezes, R.C., Batista, P.K., Ramos, A.Q., Medeiros, A.F.: Development of a complete game based system for physical therapy with Kinect. In: SeGAH 2014—IEEE 3rd International Conference on Serious Games and Applications for Health, Books of Proceedings, pp. 1–6 (2014)

23. Abdel Rahman, S.: Efficacy of virtual reality-based therapy on balance in children with down syndrome. World Appl. Sci. J. **10**(3), 254–261 (2010)

24. Ding, J., Huang, C., Lin, J., Yang, J., Wu, C.: Interactive multimedia mirror system design. IEEE Trans. Consum. Electron. **54**(3), 972–980 (2008)

25. Wuang, Y.P., Chiang, C.S., Su, C.Y., Wang, C.C.: Effectiveness of virtual reality using Wii gaming technology in children with down syndrome. Res. Dev. Disabil. **32**(1), 312–321 (2011)

26. Fiala, M.: Magic mirror system with hand-held and wearable augmentations. In: Virtual Reality (VR), pp. 251–254 (2007)

27. Ehara, J., Saito, H.: Texture overlay for virtual clothing based on PCA of silhouettes. In: International Symposium on Mixed and Augmented Reality (ISMAR), pp. 139–142 (2006)

28. Hilsmann, A., Eisert, P.: Tracking and retexturing cloth for real-time virtual clothing applications. In: Computer Vision/Computer Graphics Collaboration Techniques (MIRAGE), pp. 94 (2009)

29. Bork, F., Barmaki, R., Eck, U., Yu, K., Sandor, C., Navab, N.: Empirical study of non-reversing magic mirrors for augmented reality anatomy learning. In: 2017 IEEE International Symposium on Mixed and Augmented Reality (ISMAR), pp. 169–176 (2017). http://ieeexplore.ieee.org/document/8115415/. Accessed 03 Apr 2018

30. Alesii, R., Graziosi, F., Marchesani, S., Rinaldi, C., Santic, M., Tarquini, F.: Short range wireless solutions enabling ambient assisted living to support people affected by the down syndrome. IEEE EuroCon. **2013**(July), 340–346 (2013)

31. Svendsen, J., Albu, A.B., Virji-Babul, N.: Analysis of patterns of motor behavior in gamers with down syndrome. In: IEEE Computer Society Conference on Computer Vision and Pattern Recognition Workshops (2011)

32. Brandão, A., Trevisan, D. G., Brandão, L., Moreira, B., Nascimento, G., Vasconcelos, C. N., Clua, E., Mourão, P. T.: Semiotic inspection of a game for children with Down syndrome. In: Proceedings—2010 Brazilian Symposium on Games and Digital Entertainment, SBGames 2010, pp. 199–210 (2011)

33. Palisano, R., Rosenbaum, P., Walter, S., Russell, D., Wood, E., Galuppi, B.: Development and reliability of a system to classify gross motor function in children with cerebral palsy. In: Developmental Medicine and Child Neurology, pp. 214–223 (1997)

34. Bourazeri, A., Bellamy-Wood, T., Arnab, S.: EnCity: A serious game for empowering young people with down's syndrome. In: IEEE 5th International Conference on Serious Games and Applications for Health (SeGAH), 2017. Perth, Australia (2017)

Ergonomic Evaluation of an Active Wrist Orthosis for the Treatment of Muscular Rigidity in Individuals with Parkinson's Disease

Samila Costa, Julien Bourget, Gabriel Jablonski, Luiza Maire, Amanda Rabelo, Michael I. Okereke, Luciene Chagas, Adriano Pereira, and Adriano Andrade

Abstract

Muscular stiffness is one of the main symptoms of Parkinson's disease. This symptom can manifest in different areas of the body, being more common in the upper limbs, which makes it difficult to perform activities involving the use of hands. This study presents results obtained from the ergonomic evaluation of an active wrist orthosis for the rehabilitation of wrist flexion and extension movements of individuals with Parkinson's disease who have symptoms of muscular rigidity. The study focused on assessing the muscular strength required to initiate wrist flexion and extension in healthy subjects. In order to evaluate this strength, electromyographic signals of each subject were acquired during Maximum Voluntary Contraction while the subjects executed wrist flexion and extension movements with and without the use of the orthosis. The mean of peaks of the maximum envelop of the EMG signals was used as an indicator of the muscular strength. The results suggest that the use of the device does not negatively influence the subject's movement, opening thus, opportunity to further larger scale study involving subjects with Parkinson's disease.

Keywords

Ergonomics evaluation • Active wrist orthosis • Parkinson's disease

S. Costa (✉) · G. Jablonski · L. Maire · A. Rabelo · L. Chagas · A. Pereira · A. Andrade
Centre for Innovation and Technology Assessment in Health, Postgraduate Program in Electrical and Biomedical Engineering, Faculty of Electrical Engineering, Federal University of Uberlândia, Uberlândia, Brazil
e-mail: samilac.costa@gmail.com

G. Jablonski
e-mail: gabriel.jablonski.ufu@gmail.com

L. Maire
e-mail: luizamaire@gmail.com

A. Rabelo
e-mail: amandagomesrabelo@gmail.com

L. Chagas
e-mail: lchagasoliveira@gmail.com

A. Pereira
e-mail: a.alves.prereira@uol.com.br

A. Andrade
e-mail: adriano@ufu.br

J. Bourget
Biomedical Engineering, University Claude Bernard Lyon 1, Polytech Lyon, Lyon, France
e-mail: julien.bourget@etu.univ-lyon1.fr

M. I. Okereke
Department of Engineering Science, University of Greenwich, London, UK
e-mail: m.i.okereke@gre.ac.uk

1 Introduction

Parkinson's disease (PD) is a neurodegenerative disorder of the central nervous system (CNS), which leads to the loss of dopaminergic neurons of the substantia nigra [1]. Loss of neurons causes dopamine deficiency, which produces a severe non-extrapyramidal system effect, resulting in decreased strength, problems in posture and gait maintenance, muscle hardening, and others, which influence motion [2, 3]. These pathophysiological changes generate typical neurological symptoms or cardinal signs found in patients with PD, such as bradykinesia, rest and postural tremor, postural instability, and muscular stiffness [4, 5].

All these problems cause the individual affected by PD to experience functional limitations and physical dependence, which can lead to depression and isolation. Consequently, there is need to carry out research that improves the patients' quality of life by providing individual and group physical activity, psychological and physical therapy, all aimed at providing greater independence in daily tasks [1, 4].

The provision of physiotherapeutic aid can improve the outcomes of treatments employed for PD patients. This requires deploying robotic devices for safe and intensive

rehabilitation of individuals with light to severe motor deficits. Such use of robotic devices has been shown to partially restore the function of the upper limb of individuals affected by PD [6, 7]. Other recent studies demonstrate benefits of assisted physiotherapy by robotic devices in the recovery of upper limb movement [8, 9].

The work described by Sangha et al. [10] is an example of intervention that may help physiotherapists and caregivers implement several rehabilitation protocols for patients who have suffered neurological deficits. However, a limitation of that study was the negligence of ergonomic considerations of orthotic devices. Such considerations are essential for PD patients who have suffered the loss of muscular strength, experience limited mobility of limbs and consequently are unable to perform simple tasks.

The study of the ergonomics of any orthotic device is extremely important to enable the effective adoption of such a solution in physical therapy. In this preliminary study, we present the evaluation of the muscle effect arising from the use of the active orthosis for the execution of wrist flexion and extension movements. Based on this assessment, it is possible to suggest ergonomic modifications in the current design so that it can be improved.

2 Materials and Methods

The actual active wrist orthosis, used in this study is shown in Fig. 1. It was developed in the Centre for Innovation and Technology Assessment in Health (NIATS) of the Federal University of Uberlandia, Brazil. The current design of the orthosis has been patented with the Brazilian National Institute of Industrial Property (BR10 2014 023282 6). The developed wrist orthosis is made of aluminum and its total weight is of approximately 900 g. It has a linear actuator capable of generating forces that can modulate the muscular force necessary for executing flexion and extension of the wrist. From a functional perspective the orthosis provides a range of motion enough for carrying out the rotation, flexion and extension of the wrist without great interference upon the natural motion of the hand. In this study, we aimed to better understand the required muscular activity while the user was using the orthosis without the presence of any active force generated by the linear actuator. By understanding this aspect, we can improve the design of the orthosis if it is necessary.

2.1 Participants

Five healthy subjects, three men and two women, aged between 19 and 42 years, participated in this study. After written informed consent has been obtained, the participants were submitted to protocols previously approved by the local Research Ethics Committee (CAAE 65165416.4.0000.5152 approved on 29 May, 2017) of the host university.

2.2 Description of the Experimental Protocol

Data collection was carried out in an experimental cabin available in the laboratory. To establish the adequacy of the experimental protocol for an extensive future study involving patients with PD, this study developed and tested the protocol with 5 healthy subjects, representing the study group. To quantify the maximal strength of the subjects, the Maximum Voluntary Contraction (MVC) was acquired and analyzed. Data from the MVC served as baseline data for comparison.

In this study, the MVC was acquired during resistive active movement of wrist flexion and extension. Figure 1 shows the rest and contraction periods adopted for the MVC acquisition. The task was repeated three times with a two-minute interval between each repetition to allow adequate relaxation of muscle fibers (Fig. 2).

Fig. 1 Active wrist orthosis used in this study
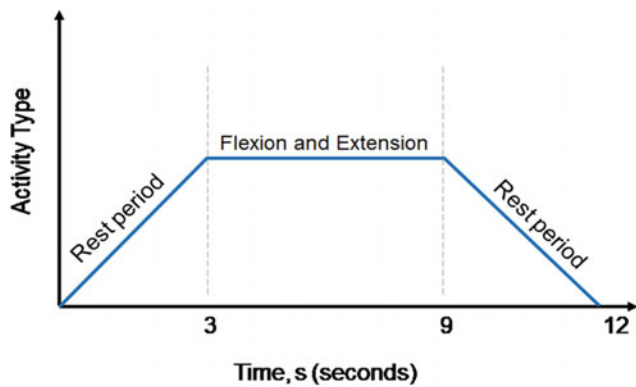
Fig. 2 Timeline of the active movement of the wrist flexion and extension

To acquire electromyographic signals, the study employed the Biological Signal Acquisition System (SASBio), a device developed at NIATS, which is based on the Intan Tech's RHD2000 Evaluation System technology. Electromyography (EMG) was collected simultaneously from the flexor and extensor muscles of the subject's dominant forearm and the electrodes were positioned according to Fig. 3.

Two types of experiments were carried out. First, the participant completed the task while not wearing the orthosis, and secondly, while wearing the device. Figure 4 shows the experimental setup with and without the orthosis.

In these experiments, the EMG signals of the flexor and extensor muscles were acquired during wrist flexion and extension. The participant's arm was supported by using an adjustable arm rest. Eight wrist flexion and extension repeats were carried out by the subject at four different angles of an arm-rest support (see Fig. 4). The angles were 0, 18, 45 and 90°, chosen based on increasing level of gravitational pull on the arm due to the weight of the orthosis. The angular-variation study was designed to investigate an ergonomic variable of *position of arm* while wearing the orthosis. From these tests, it was expected that a correlation can be established between arm position and ergonomic impact of the orthosis.

2.3 Signal Processing

For data processing and signal analysis, a MATLAB (Mathworks, USA) script was developed and used. EMG signals were filtered by a zero-phase high-pass Butterworth digital filter (6th order, 30 Hz cut-off frequency). The envelope of the signal was estimated by means of the root mean square value (RMS). The mean of its main peaks detected using on a predefined threshold (the minimum value from which the peaks are to be detected) was obtained as the main feature extracted from EMG signals: a measure of the muscular effect of using the orthosis device.

Fig. 3 Positioning of the sensors on the flexor and extensor muscles of the forearm
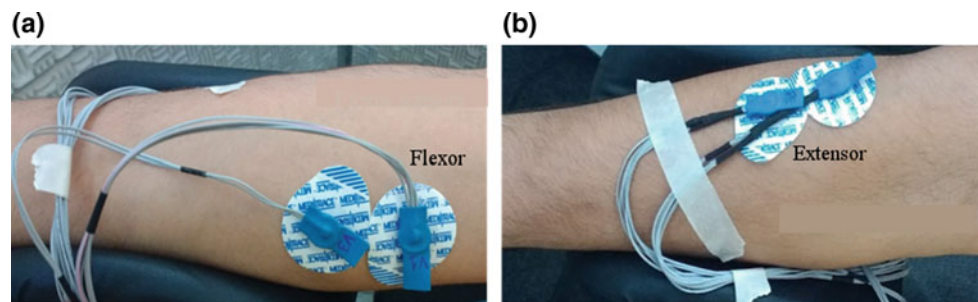
Fig. 4 Illustration of the experimental setup **a** with orthosis and **b** without the orthosis
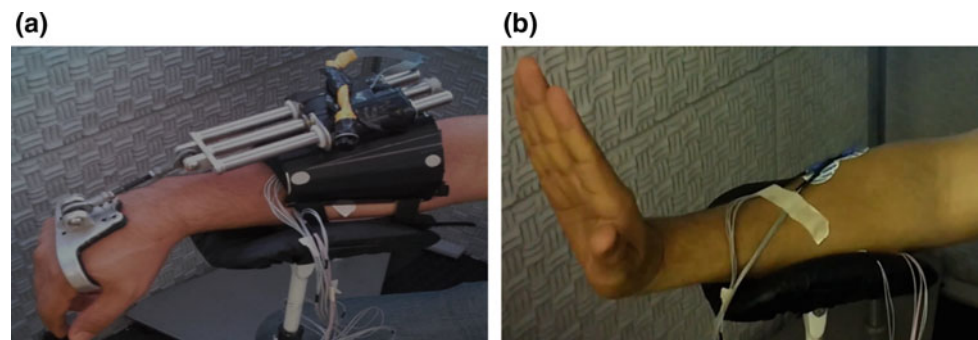
3 Results

Figure 5 shows a comparative analysis of all the subject's EMG signal-processed data, based on the mean muscular load due to the orthosis use (% MVC). The data used to calculate the mean were obtained during the flexion-extension movements of the wrist, for different angular orientations of the orthosis device. To distinguish between the results obtained with and without the use of the orthosis, the legend identifier O and NO, respectively, were used.

To illustrate the influence of the use of the active orthosis, an Ergonomic Index (EI) was proposed. This index is associated with wrist flexion and extension for each angle with and without the use of the orthosis and it is defined by Eq. 1,

$$Ergonomic\,Index\,(EI) = 1 - \frac{\%MVC_{with\,orthosis}}{\%MVC_{without\,orthosis}} \qquad (1)$$

where $\%MVC_{with\,orthosis}$ is the percentage of muscular activation when compared to MVC with the use of the orthosis and $\%MVC_{without\,orthosis}$ is the percentage of activation without the use of the orthosis. Figure 6 shows the results of the EI for the wrist flexion and extension.

4 Discussion

This study focused on the ergonomic evaluation of the impact in wrist flexion and extension during the use of an active wrist orthosis using EMG. Similar studies, such as those performed in [11–13], also use surface electromyography for ergonomic assessments of upper limb devices.

The results reported in this study were based on a convenience sample, which is a type of non-probability sampling method. This type of approach is often employed when information about the evaluated parameters are not available. Considering the high variability of the ergonomic index (> 17%) it should be noted that an increase in the sample size is necessary so that the obtained results can be representative and generalized. Despite of this limitation it is relevant to highlight the impact of the presented results as they introduce an objective evaluation of the usability of an orthotic device.

Figure 5 shows how the orthotic device influences the wrist flexion and extension at different angles. At 0 and 18°, it is possible to verify that the flexor and extensor muscles have lower %MVC during the use of the orthotic device. However, when repeating the task related to the protocol at 45 and 90°, it is noticeable that the flexors have lower % MVC without the use of the orthosis, while the extensors continue to present lower %MVC with the use of the device. The greater activation of the wrist flexor and extensor muscles of the wrist at 45 and 90° was expected, although this study allows us to verify how the weight of the orthosis, combined with the gravitational force, creates resistance to the wrist flexion, while the wrist extension is favored, which can be observed at 90°, where the extensors have the lowest value of %MVC.

Figure 6 shows an increase in the value of the EI value for the wrist extension as the angle increases. This result was expected because at 90°, the weight of the device helps the movement. For the wrist flexion, the EI decreases and presents negative values for 45 and 90°, which indicates greater effort to perform the movement. This was also expected because, at 90°, the weight of the device offers movement resistance.

Fig. 5 Comparison between % MVC for flexor and extensor muscles at different angles. The overall means and standard deviations are presented
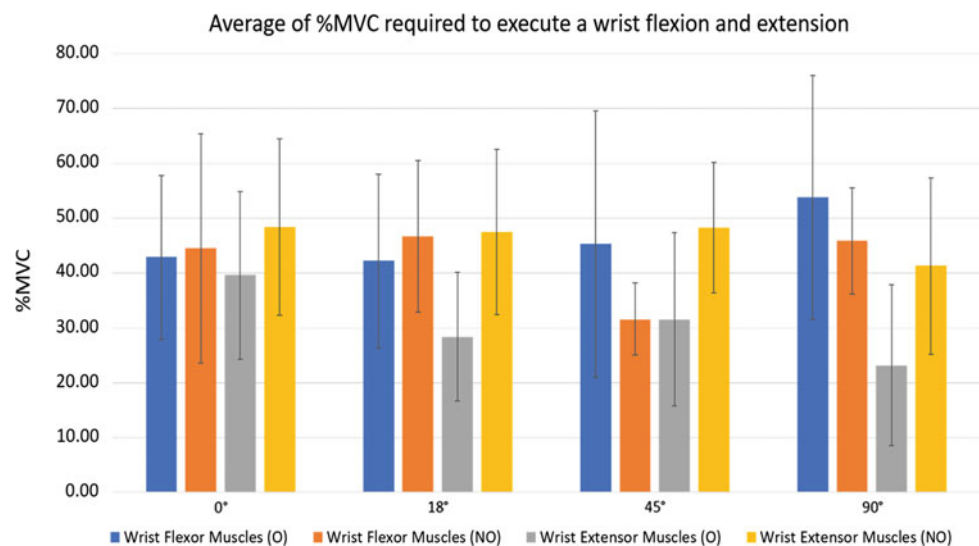
Fig. 6 Ergonomic Index from the WF and WE at distinct angles acquired from Eq. 1. The overall mean and standard deviation are presented
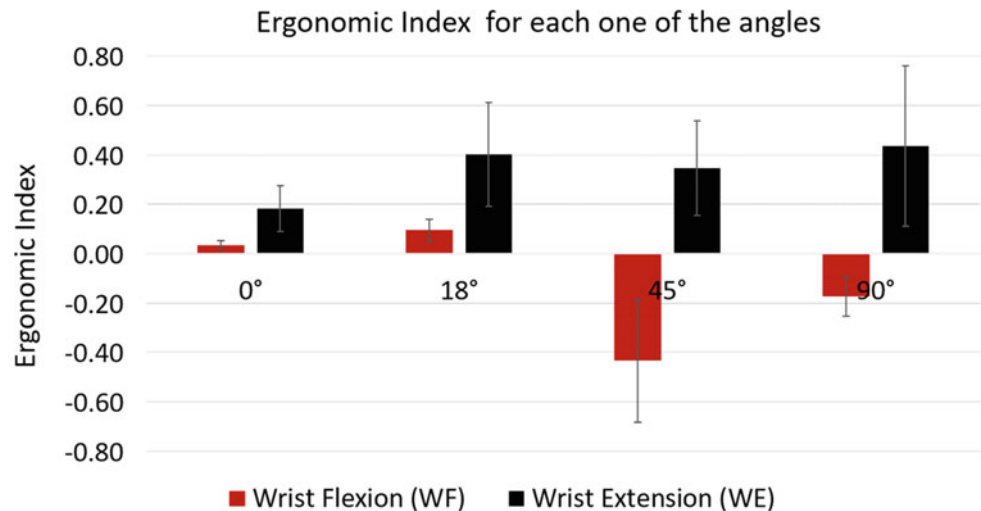
Based on the found results it was possible to identify the most suitable angulations (0 and 18°) for the adjustment of the support for future use of the orthosis. However, as already mentioned these findings cannot be generalized because of the relative high variance of the data, which was collected from a convenience sample of five subjects. Another limitation of this study is the difficulty in the positioning of the orthosis, since the variation in the size (in cm) of the forearm, wrist and hand of the volunteer, causes variation in the positioning of the orthosis from subject to subject, which directly influences the results.

The orthosis used in this study allows adjustments in the positioning of the actuator fixed to the structure that attaches to the forearm, the diameter of this structure and the length of the connection between the glove that is attached by hand and the structure that attaches to the forearm. However, in this study a standard positioning was adopted for all volunteers, being this another limitation (in terms of usability assessment) of this research.

5 Conclusion

This was a preliminary study that aimed to verify the influence of the use of an active wrist orthosis developed for the treatment of muscular stiffness symptom in subjects affected by Parkinson's disease. The results show that the use of the orthosis does not negatively interfere in the wrist flexion and extension, when compared to the same movements performed without the use of the device.

These results open up opportunities for a larger scale study with a larger group of healthy subjects and individuals with PD. During the data acquisition, it was possible to identify aspects of the experimental protocol that can be improved before further larger scale studies can be executed.

In the future the implementation of an interface where the subject can visually monitor the speed at which the wrist flexion and extension can be performed may contribute to the standardization of the experimental protocol, as it is known from the literature that very fast movements can induce movement artifacts to the signal.

Conflicts of Interest   The authors declare no conflict of interest.

References

1. Christofoletti, G., Cândido, E.R., Olmedo, L., et al.: Effects of a cognitive-motor intervention on depressive symptoms in patients with Parkinson's disease| Efeito de uma intervenção cognitivomotora sobre os sintomas depressivos de pacientes com doença de Parkinson. J. Bras. Psiquiatr. **61**, 78–83 (2012). https://doi.org/10.1590/S0047-20852012000200004
2. Hallett, M.: Overview of human tremor physiology. Mov. Disord. **13**, 43–48 (2008). https://doi.org/10.1002/mds.870131308
3. Galvan, A., Devergnas, A., Wichmann, T.: Alterations in neuronal activity in basal ganglia-thalamocortical circuits in the parkinsonian state. Front Neuroanat **9**, 1–21 (2015). https://doi.org/10.3389/fnana.2015.00005
4. Dickson, J.M., Grünewald, R.A.: Somatic symptom progression in idiopathic Parkinson's disease. Park Relat Disord **10**, 487–492 (2004). https://doi.org/10.1016/j.parkreldis.2004.05.005
5. Morris, M.E., Iansek, R.: Characteristics of motor disturbance in Parkinson's disease and strategies for movement rehabilitation. Hum. Mov. Sci. **15**, 649–669 (1996). https://doi.org/10.1016/0167-9457(96)00020-6

6. Fasoli, S.E., Krebs, H.I., Stein, J., et al.: Effects of robotic therapy on motor impairment and recovery in chronic stroke. Arch. Phys. Med. Rehabil. **84**, 477–482 (2003). https://doi.org/10.1053/apmr.2003.50110

7. Stefano, M., Patrizia, P., Mario, A., et al.: Robotic upper limb rehabilitation after acute stroke by NeReBot: evaluation of treatment costs. Biomed. Res. Int. **2014**, 1–5 (2014). https://doi.org/10.1155/2014/265634

8. Aisen, M.L., Volpe, B.T.: The effect of robot-assisted therapy and rehabilitative training on motor recovery following stroke robot-aided sensorimotor arm training. JAMA Neurol. **54**, 443–446 (1997). https://doi.org/10.1001/archneur.1997.00550160075019

9. Volpe, B.T., Krebs, H.I., Hogan, N.: Robot-aided sensorimotor training in stroke rehabilitation. Adv. Neurol. **92**, 429–433 (2003)

10. Sangha, S., Elnady, A.M., Menon, C.: A compact robotic orthosis for wrist assistance. Proc .IEEE RAS EMBS Int. Conf. Biomed. Robot. Biomechatronics 1080–1085 (2016) https://doi.org/10.1109/biorob.2016.7523775

11. Novais Van Petten, A.M.V., Ávila, A.F.: Effect of using wrist orthoses on forearm flexor and extensor muscle activation. Rev. Bras. Ortop. English Ed 45:72–78 (2010). http://dx.doi.org/10.1016/S2255-4971(15)30220-2

12. Gomes, A.D., Ricci, F.P.F.M., Zampar, A.C., et al.: Influence of static wrist orthosis on muscle activity and shoulder and elbow range of motion during a functional task: a biomechanical study. Fisioter e Pesqui **25**, 56–64 (2018). https://doi.org/10.1590/1809-2950/17016425012018

13. Johansson, L., Björing, G., Hägg, G.M.: The effect of wrist orthoses on forearm muscle activity. Appl. Ergon. **35**, 129–136 (2004). https://doi.org/10.1016/j.apergo.2003.11.004

Fall Detection Using Accelerometer on the User's Wrist and Artificial Neural Networks

Javier Alexis Urresty Sanchez and Daniel M. Muñoz

Abstract

Falls can occur during daily activities, being one of the primary sources of morbidity and mortality in the elderly population. Real-time detection of falls and their communication to an emergency center can enable rapid medical care, increasing the sense of security for the elderly and reducing some of the negative consequences of falls. This work presents an artificial neural network based algorithm for fall detection using a three-axis accelerometer wrist-wearable device. Samples were filtered and discretized in time domain allowing a multilayer perceptron neural network to classify the events. The training process was performed using 792 signals acquired by 22 volunteers. Validation results point-out that the proposed solution obtains a sensitivity of 98.10%, a specificity of 98.10% and an accuracy of 98.10%, concluding that the neural network generalization capacity allows the fall detection without the necessity of complex feature extraction algorithms.

Keywords

Fall detection • Artificial neural network • Embedded systems

1 Introduction

According to the World Health Organization, 646.000 people worldwide die every year due to falls. Falls are caused by a lack of balance or inability to regain balance, causing the person to hit the ground or other firm surfaces. Falls injuries

J. A. Urresty Sanchez (✉) · D. M. Muñoz
Department of Mechanical Engineering, University of Brasilia, Brasilia, DF, Brazil
e-mail: javierur10@gmail.com

D. M. Muñoz
Electronics Engineering Program, University of Brasilia, Gama, DF, Brazil

can be fatal, being the second cause of death from accidental or unintentional injuries worldwide. The risk and frequency of falls increases with age and fragility, being the population over 65 years the one which most suffers from morbidity and mortality due to falls [22].

The main hospital admissions related to falls are surface injuries, hip fracture, spinal cord injuries, cranioencephalic trauma and upper and lower limb injuries [4, 21]. Even in the absence of injury, falls can produce long-term psychological consequences, such as depression and loss of confidence, that can lead to restrictions in daily and social activities, and subsequently, will decrease health and increase the risk of future falls [1, 18].

The increase in the elderly population during the last decades is reflected in the rapid increment in the number of injuries caused by falls, becoming a relevant health problem [10, 22]. In this context, real-time fall detection and rapid communication to an emergency center is a technological challenge, and developments on automatic fall detection systems have been increased in the last 20 years [2].

In the scientific literature, there are several proposals for developing monitoring systems which allow the identification of different falls events. Some of these systems also ensure effective communication to medical care, minimizing the fatal consequences. Most of the current proposals make use of portable sensors such as accelerometers, gyroscopes, and magnetometers, enabling data acquisition of the monitored person's inertial information [9]. In addition, most of the previous works place the inertial systems in the waist or chest. However, this fact creates discomfort for users, making it difficult the acceptance of this technology. In this context, a fall detection system that facilitates usability must be studied from the technological feasibility perspective.

The main contribution of this work is the development of a fall detection system based on the acceleration measurements using a wrist-wearable device. A processing algorithm based on an artificial multilayer perceptron (MLP) neural network was developed to perform the classification of movements, including the detection of falls. Numerical

comparisons were made to select the best topology of the neural network and validation results point-out that daily living activities can be distinguished from falls with a sensitivity of 98.10%, specificity of 98.10% and accuracy of 98.10%. Experimental results demonstrate that it is possible to achieve high accuracy fall detection using only one sensor (accelerometer), directly processing the signals using an MLP neural network, avoiding complex pre-processing algorithms for features extraction.

The remainder of this paper is organized as follows: Sect. 2 presents the theoretical basis for understanding the proposed solution. Section 3 shows the related works. Section 4 describes the system architecture for data acquisition. Section 5 presents the proposed artificial neural network for fall detection and, before concluding, Sect. 6 presents several validation results.

2 Theoretical Background

2.1 Artificial Neural Networks

Artificial neural networks are used in a variety of engineering fields, such as signal processing, control systems, time series analysis, and pattern recognition. According to Haykin, a neural network is a parallel distributed processor composed of simple and interconnected processing units and has the natural ability to store knowledge and make it available for use. It resembles the brain in two main aspects: (a) the knowledge from the environment is acquired by the network through a learning process and (b) the connecting forces between neurons, known as synaptic weights, are used to store knowledge [7].

2.2 Neuron

The neuron is the fundamental processing unit of neural networks. The *perceptron* is an artificial neuron which consists of a set of inputs (representing synapses from previous neurons) which are weighted and then accumulated. The output of the neuron is modified by the bias which has the effect of applying an offset, depending on whether the bias polarization is positive or negative. The new result is called *induced local field*, which is applied to an activation function that restricts the amplitude of the output signal [6]. In mathematical terms, a perceptron neuron can be described with the following equations

$$u_k = \sum_{j=1}^{m} w_{kj} x_j \tag{1}$$

$$v_k = u_k + b_k \tag{2}$$

$$y_k = \varphi(v_k) \tag{3}$$

where in Eq. 1, $w_{k1}, w_{k2}, \ldots, w_{km}$ are the synaptic weights of neuron k. $x_1, x_2, \ldots x_i$ are the input signals and u_k is the result of the linear combination of the weighted inputs. In Eq. 2 the bias b is added to u_k thus obtaining the induced local field v_k. In Eq. 3, v_k is evaluated in the activation function φ resulting in the output signal of the neuron y_k.

The activation function is chosen during the design phase according to the type of output [3]. In this work, a hyperbolic tangent function was used (see Eq. 4), limiting the output values of the neuron and consequently the output of the neural network between −1 and 1 [7].

$$tanh(x) = \frac{e^x - e^{-x}}{e^x + e^{-x}} \tag{4}$$

2.3 Multilayer Perceptron Neural Network

This network, also called multilayer feedforward network, have a set of source nodes that constitute the input layer, one or more hidden layers, and an output layer [6]. Multilayer perceptron networks are used to solve many complex problems, such as those that are not linearly separable [7]. Supervised training algorithms are generally used for this type of network, for instance, the backpropagation algorithm which is based on the error correction learning rule, also considered as a generalization of the least mean squares (LMS) algorithm used in networks of a single linear neuron [7].

Figure 1 shows a multilayer perceptron neural network, with m neurons in the input layer, a hidden layer with n neurons and three neurons in the output layer.
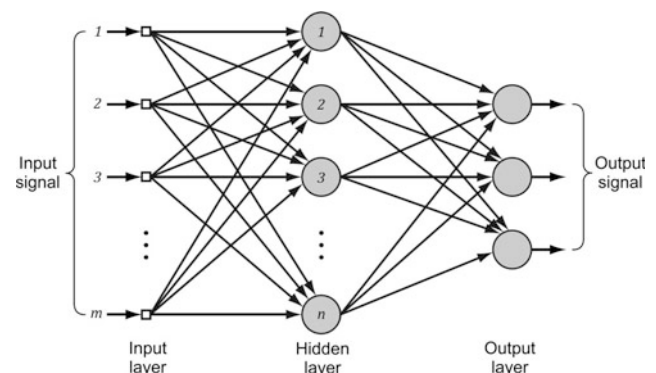

Fig. 1 Structure of a multilayer perceptron neural network [7]

2.4 Backpropagation Algorithm

The learning process by backpropagation of error is divided into two steps: one step forward called propagation and another backward the backpropagation. During propagation, a vector belonging to the environment is inserted into the network, it propagates through the network producing an output response. Throughout this step, the network's synaptic weights are fixed [6]. During backpropagation, the synaptic weights of the network are adjusted according to the error correction rule, where the error signal is obtained from the subtraction of the actual network response and the expected response. This error signal propagates backwards, adjusting the synaptic weights so that the network response is close to the desired response. After reaching a number of iterations or a previously established error value it is possible to obtain optimized synaptic weights [7].

3 Related Works

Fall detection systems employing wearable devices are most preferred because users can be monitored in indoor and outdoor environments [9]. In general, most of the developed systems make use of triaxial accelerometers and peak detection methods for data processing. This section presents an analysis of the previous works that make use of artificial neural networks for fall detection. Yuwono et al. [24] proposes a fall detection algorithm, with a single triaxial accelerometer placed on the user's waist and using two different classifiers: A multilayer perceptron network and an increased radial base neural network (RBF) achieving a promising result. Vidigal et al. [20] presents an implementation and performance comparison of MLP, RBF and Kohonen neural networks for the detection of falls, using the data provided by the triaxial accelerometer present in smartphones. Sengto and Leauhatong [17] suggests an algorithm with two processes: firstly, a simple threshold analysis, which is used to distinguish slow movements and other activities from a person's daily life. Secondly, if the values of the signals are greater than the thresholds, a back-propagation neural is used to classify eight different activities, including falls. Vallejo et al. [19] presents a fall detection system composed of an MLP neural network, which aims to improve detection accuracy with respect to traditional threshold-based methods. The network was implemented on a device placed on the user's waist and used the integral of the acceleration of each axis.

Kerdegari et al. [11] proposes a fall detection system using acceleration, angular velocity, speed and position measurements as well as different time domain characteristics, such as minimum, maximum, mean, interval, variance and standard deviation. These characteristics constitute the inputs of a multi-layer perceptron neural network which allow the classification of daily activities and falls. Yodpijit et al. [23] uses an accelerometer and a gyroscope placed on the user's waist to detect the orientation and the movement of the body. They implemented a threshold-based algorithm in conjunction with a multilayer perceptron neural network, decreasing the number of false positives and improving the accuracy of the fall detection system. Quadros et al. [15] proposes a movement decomposition feature extraction and machine learning method for a fall detection system using a wrist-wearable device with accelerometer, gyroscope and magnetometer.

Dinh and Struck [5] describes a fall detection system where the acceleration data is transformed from Cartesian coordinates to spherical coordinates. The system is based on Fuzzy logic and an MLP neural network. The achieved results show that it is single accelerometer measurements and the methods based on the neuro-fuzzy systems are feasible solutions in comparison with standard pattern recognition methods. Qingbin et al. [14] proposes a sensor fusion between accelerometer, gyroscope and magnetometer, by means of an extended Kalman filter in order to determine the attitudes of the pitch and roll angles that, together with the mean square of the acceleration, generating the entries of an MLP neural network. Nukala et al. [12] implemented an MLP neural network and a support vector machine (SVM) based on six features extracted from angular velocity measurements and accelerations on the three axes, achieving a fall detection system that is placed on the back and waist of the user. Nuttaitanakul et al. [13] proposes a Wavelet transform combined with an MLP neural network algorithm to detect falls from the acceleration signals of a sensor placed on the user's waist.

The proposal presented in this work makes use of a triaxial accelerometer placed in the user's wrist, improving usability and the sensation of comfort; however, representing a challenge to treat movements that generate false positives. In addition, low computational cost preprocessing methods and MLP neural networks were used allowing for filtering such movements.

4 Data Acquisition System

4.1 Data Acquisition Architecture

The data acquisition system was developed using a microcontroller, a three-axis accelerometer and a data storage device. All the subsystems are powered up by a 9 V battery as can be seen in Fig. 2.

A six-axis movement detection sensor (MPU650 from InvenSense) was used. It is a low cost and low power consumption device which includes a 3-axis accelerometer and a

Fig. 2 General system architecture
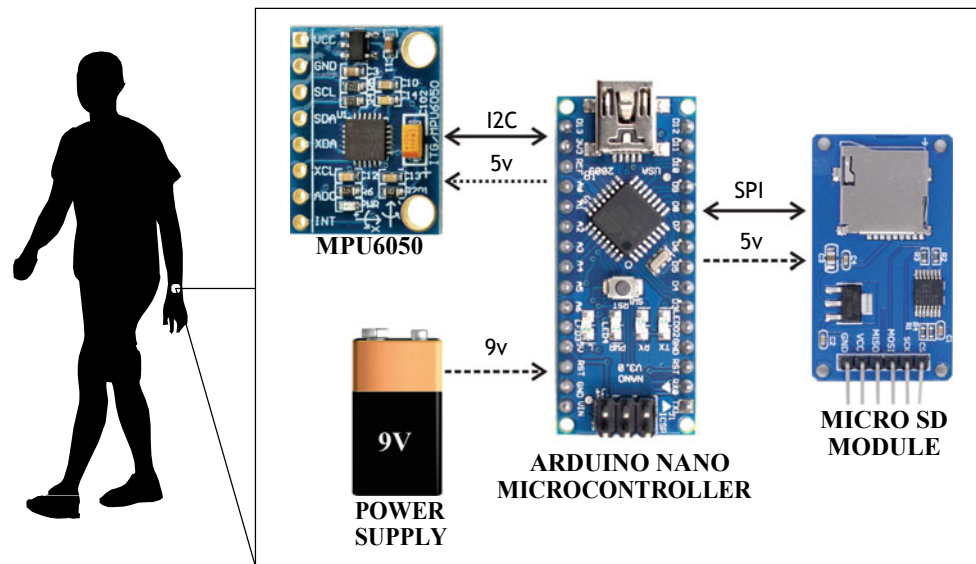
3-axis gyroscope and operates at 3.3 or 5 V. An *InterIntegrated Circuit* (I2C) communication was used to connect the sensor to a microcontroller. It is important to highlight that in the proposed system only the acceleration is used for fall detection.

An Arduino Nano microcontroller was used to control the data acquisition system. It is based on an ATMega328P processor, which uses a 32 KB flash memory and operates at 16 MHz clock frequency. The data captured by the accelerometer sensor are stored in a micro SD memory and then analyzed and classified by the MLP neural network. A *Serial Peripheral Interface* (SPI) communication was used to send the data from the microcontroller to the micro SD memory.

4.2 Data Acquisition Procedure

In this work, we have used the data set reported in [15]. This database is composed of acceleration, gyroscope and magnetometer signals acquired at 100 Hz by 22 volunteers which performed for six falls and six non-falls activities. A total of 792 signals are available including, forward falls, backward falls, sideways falls and falls after rotating the waist. The non-falls includes movements clapping hands, walking, opening and closing doors, moving an object, tying shoes and sitting on a chair. The volunteers have an average age of 26 years, an height of 1.68 m and weight of 67.82 kg. It is important to highlight that the data acquisition system used in [15] is similar to the one proposed in this work. A first analysis of the experimental data determined that taking into account the data acquisition rate all the falls can be represented using 138 samples. Therefore, we adapted the data set to the maximum range value supported by our data

acquisition architecture and manually extracted windows with 138 samples for each movement signal.

All the falls movements were simulated using a proper soft mattress. If compared with real falls, this controlled environment minimizes the intensity of the signal and generate oscillating movements after striking the mattress. However, the shape of the signal into the window of 138 samples is well preserved.

In order to analyze the action of the gravity on the user's wrist, the magnitude of the acceleration vector was computed. Figure 3 depicts the magnitude of the acceleration for walking, clapping and falling movements, respectively. In the latter, a deceleration from 1 to 0.5 g followed by a rapid acceleration from 0.5 to 3.5 g can be observed. This pattern was observed in almost all the 396 fall samples. Vallejo et al. [19] point-outs that the threshold-based analysis algorithms present several faults when the accelerometer is placed in the wrist, producing constant changes in the acceleration signal. However, our experimental observations allow us to verify that all the falls have repetitive patterns that can be interpreted and classified by ANNs.

5 Fall Detection Using MLP Neural Networks

The data set was divided into training and validation data. The training data are composed of 288 falls and 288 samples with daily living movements. The validation data set is composed of 108 falls and 108 daily living activities collected from users that do not belong to the training and testing data set.

In order to minimize the number of inputs, a mean filter was applied to the signals using windows composed of 32, 23, 16 and 13 samples, obtaining signals with 4, 6, 8 and 10
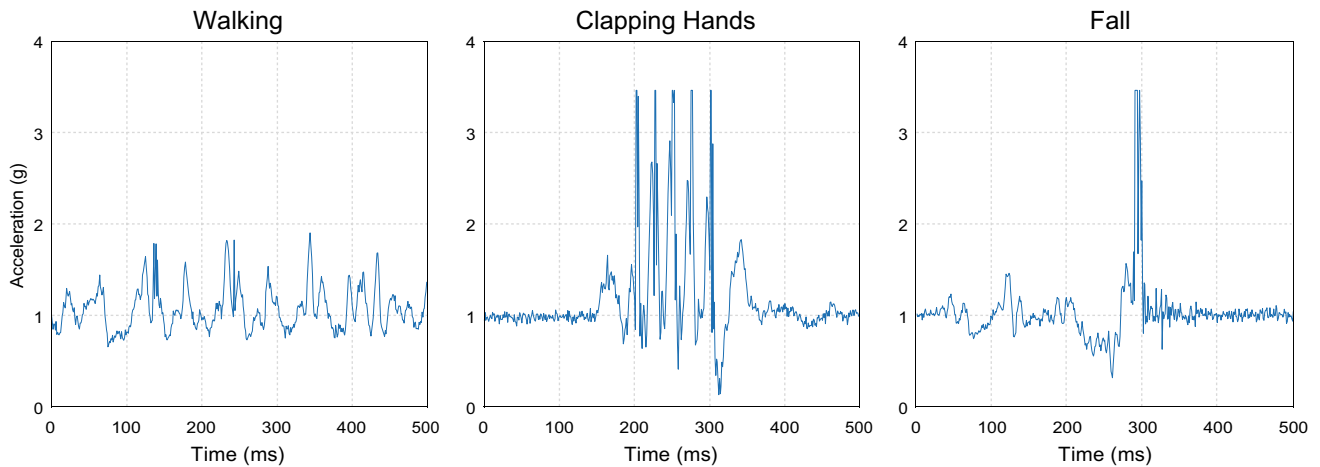
Fig. 3 Magnitude of acceleration for walking, clapping hands and falling movements

levels, respectively. Afterward, the signal was discretized in time using one sample per level, minimizing the number of inputs to 4, 6, 8 and 10 inputs. Figure 4 represents the above mentioned process for a 16 samples window.

The neural network process was performed in the *NNtool* from Matlab using the *Levenberg-Marquardt* backpropagation algorithm. Different MLP neural networks with 4, 6, 8 and 10 inputs, each with 2, 4, 6, 8, 15 and 20 neurons in the hidden layer, were trained and tested using the method known as *k*-fold cross validation. This method divides the training data set into *k* subsets of size n/k, where $n = 4165$. The network is then trained and validated *k*-fold, always leaving a subset for validation and $k - 1$ for training [8]. In this work, the most common validation with $k = 10$ was implemented, which allowed statistical comparisons to determine the best network topology [16]. Table 1 shows the performance results for each topology using the 416 samples of the testing data set.

According to the performance results, the best classification was obtained by the topology composed of 10 inputs, 20 neurons in the hidden layer and one output neuron. However, the topology composed of 8 inputs, 8 neurons in the hidden layer and one output neuron achieved the second best performance and has a lower computational complexity. Therefore, this topology was selected to validate the neural network, as presented in the next section.

6 Results

To evaluate the proposed fall detection algorithm we used the method reported in [5, 12, 19, 24]. Four possible situations can be observed: true negative (TN), movement without a fall classified correctly; false positive (FP), movement of daily living detected as a fall; true positive (TP), fall movement correctly classified; and false negative (FN), non
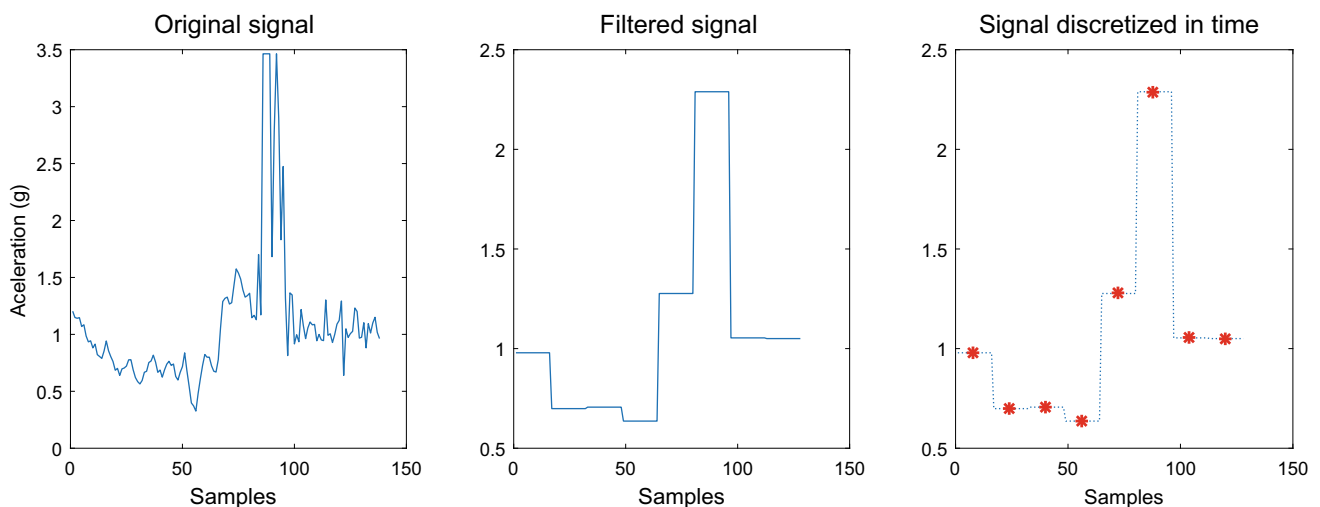
Fig. 4 Data preprocessing in the case of 16 samples window

Table 1 Percentage of hits for different network topologies

	Neurons						
Inputs	2	4	6	8	10	15	20
4	97.25	97.89	98.38	98.42	98.49	98.49	98.52
6	98.40	96.45	98.52	98.08	98.54	98.11	98.15
8	98.26	98.27	97.93	98.55	98.41	98.55	98.04
10	97.26	98.52	97.92	98.24	98.33	98.35	98.57

detected falls. Three commonly performance metrics are estimated using these situations, namely sensitivity, specificity, accuracy.

Sensitivity (SE) is the ability to detect real falls and is defined as the ratio between the number of properly detected falls (true positives) and the falls that actually occurred (true positives and false negatives), as shown in Eq. 5.

$$SE = \frac{TP}{TP + FN} \times 100\% \qquad (5)$$

Specificity (SP), see Eq. 6, it is the ability to filter false alarms and corresponds to the ratio between the movement without a fall classified correctly (true negatives) and the total number of movements without a fall (true negatives and false positives).

$$SP = \frac{TN}{TN + FP} \times 100\% \qquad (6)$$

Accuracy (AC) is the ratio of true results in the data set, as presented in Eq. 7.

$$AC = \frac{TP + TN}{TP + FP + FN + TN} \times 100\% \qquad (7)$$

In the data set, 108 falls and 108 non-falls were used to validate the network. The performance metrics of the fall detection system were calculated and shown in Table 2.

One can conclude that, based on the validation process using 216 samples, falls can be distinguished from normal activities with a sensitivity of 98.10%, specificity of 98.10%, and accuracy of 98.10%.

Table 3 shows a comparison with several related works in which the acceleration sensor was placed on the user's waist

and only [15] uses the sensor on the wrist. It can be observed that the results are within the range of previous studies, indicating that the proposed algorithm is feasible to classify falls with the sensor placed on the user's wrist.

7　Conclusions

This work proposed a fall detection algorithm, based on the data acquisition of an acceleration sensor placed on the user's wrist, the time discretization of the signals and a multilayer perceptron neural network.

Different neural network topologies were tested, and numerical comparisons demonstrate that the best MLP network topology is composed of 8 inputs, 8 neurons in the hidden layer and 1 neuron in the output layer, achieving a classification performance of 100% using the testing data set. During validation phase 108 falls and 108 daily living activities were collected from new users and results demonstrates the feasibility of the proposed MLP network to distinguish daily living movements from falls, achieving a sensitivity of 98.10%, specificity of 98.10% and accuracy of 98.10%. It is important to point-out that the proposed solution allows the classification of fall patterns regardless of the person's physical structure.

The achieved results are similar to those reported in related works in which one or more sensors were placed on the chest and/or waist. Therefore, one can conclude that the proposed fall detection system using the sensor on the user's wrist improves the acceptability and usability of the solution. For future works, we intend to use sensor fusion techniques in order to combine information from embedded heartbeat and microphone sensors.

Table 2 Results of the network validation

Positives	108	TP	106	FN	2
Negatives	108	FP	2	TN	106
Samples	216				
Sensitivity	98.10%	Specificity	98.10%	Accuracy	98.10%

Table 3 Numerical comparisons with related works

Author	Accuracy (%)	Sensitivity (%)	Specificity (%)
Dinh and Struck [5]	–	99,64	96,00
Yuwono et al. [24]	–	99,56	97,65
Sengto and Leauhatong [17]	–	99,50	96,25
Vallejo et al. [19]	–	98,60	98,40
Kerdegari et al. [11]	91,60	91,07	92,03
Qingbin et al. [14]	98,20	–	–
Nukala et al. [12]	98,80	100,00	94,10
Vidigal et al. [20]	96,40	98,30	85,00
Nuttaitanakul and Leauhatong [13]	85,60	–	–
Yodpijit et al. [23]	99,23	99,37	99,00
Quadros et al. [15]	99,00	100,00	97,90
This work	98,10	98,10	98,10

References

1. Abbate, S., Avvenuti, M., Bonatesta, F., Cola, G., Corsini, P., Vecchio, A.: A smartphone-based fall detection system. Perv. Mob. Comput. 883–899 (2012)
2. Bagalá, F., Becker, C., Cappello, A., Chiari, L., Aminian, K., Hausdorff, J. M., Zijlstra, W., Klenk, J.: Evaluation of accelerometer-based fall detection algorithms on real-world falls. PloS One (2012)
3. Caicedo, E., Lopez, J.: Redes neuronales artificiales, vol. 1. Programa editorial universidad del Valle (2010)
4. De Carvalho, E.M., Delani, T.C. D.O., Ferreira, A.A.: Atenção à saúde no idoso no Brasil relacionada ao trauma. Revista Uningá Review (2018)
5. Dinh, C., Struck, M.: A new real-time fall detection approach using fuzzy logic and a neural network. In: International Workshop on Wearable Micro and Nano Technologies for Personalized Health, pp. 57–60 (2009)
6. Haykin, S.: Redes neurais: princípios e prática. Bookman (2007)
7. Haykin, S.: Neural Networks and Learning Machines, vol. 3. Pearson, NY, USA (2009)
8. Joanneum, F.: Cross-validation Explained. Graz University of Technology, Institute for Genomics and Bioinformatics (2005)
9. Kangas, M.: Development of accelerometry-based fall detection. Technical Report, University of Oulu (2011)
10. Kannus, P., Palvanen, M., Niemi, S., Parkkari, J.: Alarming rise in the number and incidence of fall-induced cervical spine injuries among older adults. J. Gerontol. Ser. A Biol. Sci. Med. Sci. 180–183 (2007)
11. Kerdegari, H., Samsudin, K., Rahman Ramli, A., Mokaram, S.: Development of wearable human fall detection system using multilayer perceptron neural network. Int. J. Comput. Intell. Syst. 127–136 (2013)
12. Nukala, B.T., Shibuya, N., Rodriguez, A., Tsay, J., Lopez, J., Nguyen, T., Zupancic, S., Lie, D.Y.-C.: An efficient and robust fall detection system using wireless gait analysis sensor with artificial neural network (ann) and support vector machine (SVM) algorithms. Open J. Appl. Biosens. 29–39 (2014)
13. Nuttaitanakul, N., Leauhatong, T.: A novel algorithm for detection human falling from accelerometer signal using wavelet transform and neural network. In: 2015 7th International Conference on Information Technology and Electrical Engineering (ICITEE). IEEE, pp. 215–220 (2015)
14. Qingbin, Z., Guohui, T., Nana, D., Yanru, Z.: A fall detection study based on neural network algorithm using AHRS, pp. 773–779
15. Quadros, T., Lazzaretti, A., Schneider, F.: A movement decomposition and machine learning-based fall detection system using wrist wearable device. IEEE Sens. **18**, 5082–5089 (2018)
16. Refaeilzadeh, P., Tang, L., Liu, H.: Cross-validation. In: Encyclopedia of Database Systems, pp. 1–7 (2016)
17. Sengto, A., Leauhatong, T.: Human falling detection algorithm using back propagation neural network. In: Proceedings of Biomedical Engineering International Conference (BMEiCON), pp. 1–5 (2012)
18. Stel, V.S., Smit, J.H., Pluijm, S.M., Lips, P.: Consequences of falling in older men and women and risk factors for health service use and functional decline. Age Ageing 58–65 (2004)
19. Vallejo, M., Isaza, C.V., Lopez, J. D.: Artificial neural networks as an alternative to traditional fall detection methods. In: IEEE International Conference in Medicine and Biology Society, pp. 1648–1651 (2013)
20. Vidigal, M., Lima, M., Neto, A.D.A.: Elder falls detection based on artificial neural networks. In: Mexican International Conference on Artificial Intelligence (MICAI), pp. 226–230 (2015)
21. World Health, O. W.H.O. global report on falls prevention in older age. World Health Organization (2017)
22. World Health, O: Caidas. World Health Organization, Augusto (2017)
23. Yodpijit, N., Sittiwanchai, T., Jongprasithporn, M.: The development of artificial neural networks (ANN) for falls detection. In: 3rd International Conference on Control, Automation and Robotics, ICCAR, pp. 547–550 (2017)
24. Yuwono, M., Su, S.W., Moulton, B.: Fall detection using a Gaussian distribution of clustered knowledge, augmented radial basis neural-network, and multilayer perceptron. In: 6th International Conference on Broadband Communications and Biomedical Applications, pp. 145–150 (2011)

Fuzzy Neonatal Death Risk Assessment Based on the Determinants of Birth Weight and Gestational Age

C. M. D. Xesquevixos and E. Araujo

Abstract

A fuzzy system for assessing the risk of neonatal death based on the determinants of birth weight and gestational age is proposed in this paper. Such a fuzzy neonatal death risk assessment aims at identifying and evaluating the neonates at high risk of death to improve the survival rate. The birth weight and the gestational age correspond to the input linguistic variables that are mapped into the risk of death output linguistic variables by employing the Mamdani inference system. Results demonstrate that the proposed approach can both stratify (quality) and score (quantify) the risk of death of newborns. The fuzzy set theory and fuzzy system enable to design a neonatal death risk system for supporting the complementary clinical assessment to be used in the evaluation of newborns.

1 Introduction

The World Health Organization estimates that 5.9 million children under 5 years of age will die by 2015, of which 45% would be newborns, yielding a worldwide neonatal mortality rate of 19 per 1,000 births [1]. For neonatal mortality is understood the deaths occurring in the first 27 days of life [2]. The prevalence of neonatal mortality in Brazil is high, being the main element of the infant mortality rate since 1990.

In most circumstances, however, neonatal death is considered avoidable using health policies that include access to qualified health assistance to prenatal, baby birth, and newborn care [3]. Further, there are neonatal risk scores proposed in the literature to support predicting neonatal mortality. For example, there are the Score for Neonatal Acute Physiology (SNAP) [4], Score for Neonatal Acute Physiology-Perinatal Extension (SNAP-PE) [4], Clinical Risk for Babies (CRIB) [5], SNAP II and SNAP-PE II [6] only to mention few. Nonetheless, most of them use invasive biological samples, are costly and/or complex methods, and are composed of independent dichotomous (present or absent, yes or no) diagnosing input variables and outcomes.

Neonatal mortality may be related to several biological determinants. The socioeconomic consequences of mortality and morbidity of newborns and mothers compose the aspects that influence the risk of newborn deaths, as well. When interested in the biological determinants, they are exemplified by the use of surfactant, bradycardia, trauma, respiratory disorders, need for mechanical ventilation, macrosomia, intrauterine growth restriction, convulsion, polyhydramnios, oligohydramnios, abnormal heart rate pattern, hyperthermia, isoimmunization, cord prolapse, birth weight and gestational age. Moreover, it is worth mentioning that some of these risk factors are subjective, while others present uncertainty and/or imprecision in the analysis for the determination of the risk of neonatal death. Dealing with this type of imperfect information requires the use of techniques that incorporate the subjectiveness of analysis and assessment [7].

The fuzzy logic and the fuzzy sets theory are alternatives to address the biological-based newborn and the mother aspects, as well economical characteristics that influence the risk of death, enabling a rigorous and systematic use of these uncertain and imprecise factors. Fuzzy systems have been investigated in the literature for estimating the newborn

C. M. D. Xesquevixos (✉) · E. Araujo
Universidade Anhembi Morumbi – UAM - Centro de Engenharia Biomédica Parque Tecnológico, São José dos Campos, SP, Brazil
e-mail: carolinexesquevixos@gmail.com

E. Araujo
CITÉ - Centro de Inovação, Tecnologia e Educação Parque Tecnológico, São José dos Campos, SP, Brazil
e-mail: ernesto.araujo@dr.com

E. Araujo
IAMED – Inteligência Artificial em Medicina e Saúde, São José dos Campos, SP, Brazil

death risk. For instance, there is a fuzzy model which uses the birth and gestational age input variables to compute the risk of death of the newborn [8]. Another approach employs the gestational age and maternal age input variables aiming at evaluating the maternal age range that influence the risk of neonatal death [9]. In turn, a fuzzy model mapped the birth weight, gestational age, stillbirth and Apgar score into the newborn death risk output variable [10].

This paper proposes a fuzzy system for assessing the risk of neonatal death based on the determinants of birth weight and gestational age aiming at identifying and evaluating the neonates to improve the survival rate of newborn. Preterm birth can cause serious deficiencies in the newborn, the care provided generates loss of family income, thus damaging the well-being of the whole family and leading to a reinforcement of the cycle of poverty [11, 12]. There is, thus, a consensus in the scientific literature, that emphasizes birth weight and gestational age as the predominant factors for neonatal death [1–3, 13].

The proposed approach maps the birth-weight and gestational-age two-dimensional Cartesian input premise space into five class of risk of neonatal death output variable, as depicted in Fig. 1. In so doing, such an approach aims at investigating the use of fuzzy systems to infer and to achieve a stratification and a measure to support or be employed for complementary severity assessment and thus translate the perception of healthcare professionals to qualify and quantify the risk and severity concerning of neonatal.
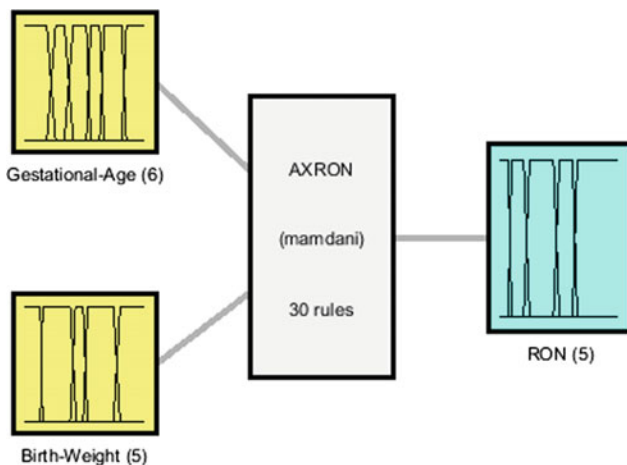
Fig. 1 The diagram of the fuzzy neonatal death risk system based on birth weight and gestational age for complementary severity assessment

2 Method

Most of the risk assessment systems are dichotomic, i.e., based on the principle of bivalence, where a statement is true or false, also understood as an element that belongs, or not, to a set. When interested in using the fuzzy logic and fuzzy set theory, it is possible to deal with elements that belong, does not belong, and partially belong to set in such a way to represent multivalued levels of truth or certainty. A fuzzy system is also an alternative when interested in decisions in environments with imperfect information since it enables modeling the knowledge of experts and the human approximate reasoning [14]. The modeling employed in this paper is based on the Mamdani inference system since it enables to imitate and to represent knowledge concerning the experience de experts.

2.1 Fuzzy Input-Output Inference Mapping

The fuzzy modeling employed in this paper uses the Mamdani type inference, characterized as a set of fuzzy IF–THEN rules [15], a non-linear mapping of an input space, Xn, into an output space Y. The antecedent part, IF $\langle proposition \rangle$, defines the premise while the consequent part, THEN $\langle proposition \rangle$, defines the conclusion, both described by linguistic expressions in the proposition form, $P = \langle x \text{ is } M \rangle$. The ith rule for $i = 1, 2, …, M$, such that m represents the total number of rules is given by:

$$IF \langle x_1 \text{ is } M_1(x_1) \rangle \text{ AND } … \text{ AND } \langle x_i \text{ is } M_i(x_i) \rangle \text{ AND} …$$
$$AND \langle x_n \text{ is } M_n(x_n) \rangle \text{ THEN } \langle y \text{ is } N \rangle$$

$$(1)$$

where $\langle x_1 \text{ is } M_1(x_1) \rangle$, is the set of input fuzzy propositions, $P_i \forall i = 1, …, n$, where n is the number of input universe of discourse and represents the dimensionality of the premises; and $\langle y \text{ is } N \rangle$, the inferred fuzzy proposition, Q. The elements x_1 and y refer, respectively, to the ith input and the output concerning objects inserted in distinct classes (sets) named *universe of discourse*, $x_i \in X_i$ and $y \in Y$, also assigned linguistic variables. The input vector, $x = [x_1, …, x_n]^T$, is related to the *premises* (antecedent of the rule) while the output, y, is associated to the *conclusion* (consequent of the rule). The linguistic expressions "AND" corresponds to the *set operation, intersection, ∩, logic operation, conjunction, ∧, and Triangular norm operation (T-norm),*

$t(x, y)$, ⊤. An operator ⊤: $[0, 1]^2 \rightarrow [0, 1]$ is called a *T-norm* if it is commutative, associative, monotonic and has 1 as neutral element. The defuzzication process is the center area method.

2.2 Input and Output Fuzzy Sets

Low birth weight and prematurity are universally recognized as important risk factors for neonatal mortality [16]. Many of these factors have socioeconomic correlations and can be prevented with good coverage by health services and pre-natal care. The proposed system is based on the biological determinants of the newborn encompassing the input linguistic variables of birth weight and gestational age. The input fuzzy sets *MBirth-Weith,* and *MGestational-Age,* for *jBirth-Weith* = 1, …, 5 and *jGestational-Age* = 1, …, 6, and the output fuzzy sets *MRON-Severity* for *jRON-risk* = 1, …, 5, that partition their respective universe of discourse have their membership functions defined according to the general description as follows. Consider a membership function, μ_M: $X_i \rightarrow [0, 1]$, defined upon an universe of discourse, X_i, to which is associated a set of terms $T = \{M_1, M_2, M_3\}$; a linguistic term $M_j \in T$, where $c(M_j) = \{x_0 \in X_i | \mu M_j (x_0) = 1\}$ and $s(M_j) = \{x_0 \in X_i | \mu M_j (x_0) > 0\}$, respectively, denote the core and support of M_j. In this paper, each linguistic term $M_j \in T$ is shaped according to a trapezoidal membership function $\mu_{M_{ij}} (x_i; a, b, c, d) = \max (\min ((x - a) (b - a), 1, (d - x) (d - c)))$, where $a < b \leq c < d$, represented by a 4-tuple (s_1, c_1, c_2, s_2), with $s(M) = [s_1, s_2]$ and $c(M) = [c_1, c_2]$ is the core (center). The system is designed by employing the Ruspini partitions.

2.3 Input Linguistic Variable

Birth Weight

The prevalence of low birth weight is associated with unfavorable socioeconomic conditions, insufficient prenatal care, mothers at the extremes of age, high parity, reduced newborn childbirth interval, presence of maternal malnutrition and smoking [17, 18]. In addition, it is possible to observe an association between the increase in the low birth weight frequency in multiparous mothers, generally due to the small newborn childbirth interval [19]. Having low birth weight makes the newborn vulnerable to conditions such as prematurity. For the variable Birth Weight, the linguistic terms are: Extreme Low Weight (ELW), Low Weight (LW), Insufficient Weight (IW), Regular Weight (RW) and High Weight (HW) (Fig. 2a).
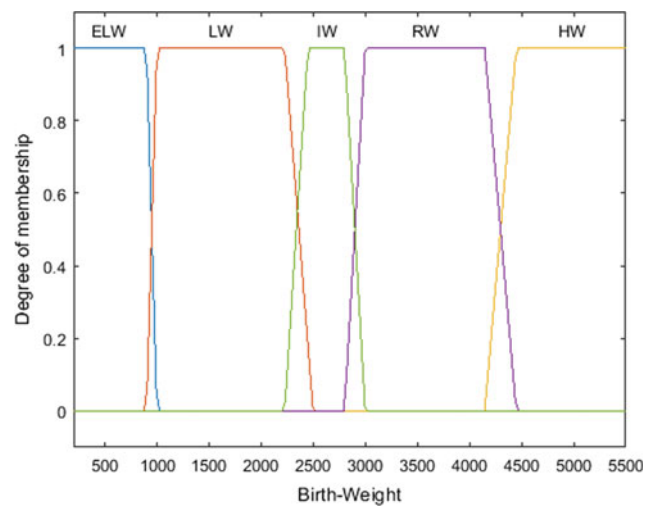
(a) $X_{Birth-Weight}$: Fuzzy partition of the birth weight diagnosing variable.
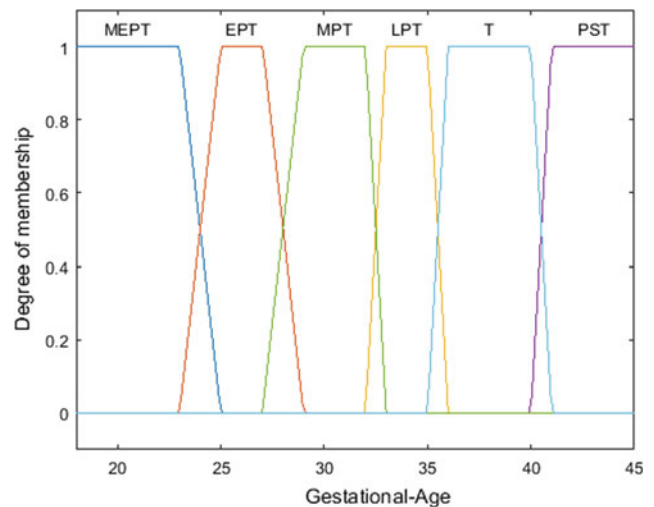
(b) $X_{Gestational-Age}$: Fuzzy partition of the gestational age diagnosing variable.

Fig. 2 Input linguistic variables for fuzzy neonatal death risk assessment

Gestational Age

Gestational age is defined by WHO as the time from conception to birth, being represented in full days or weeks. The current classifications are preterm newborn (PRT), term (T) and post-term (PST). For instance, preterm infants present diverse risks due to physiological immaturity [20]. The proposed approach considers the gestational age linguistic variable partitioned by the linguistic terms of Very Extreme Preterm (VEPT), Extreme Preterm (EPT), Moderate Preterm (MPT), Light Preterm (LPT), Term (T), and Postterm (PST), as shown in Fig. 2b.
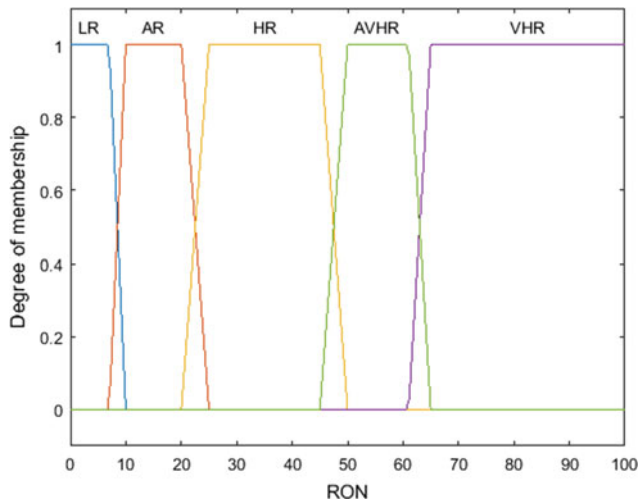
Fig. 3 Y_{RON}: fuzzy partition of the risk of neonatal death output diagnosing variable

Fig. 4 Risk of neonatal death surface derived from the proposed fuzzy model

2.4 Output Linguistic Variable: Risk of Neonatal Death

The risk of neonatal death is the output linguistic variable partitioned by the linguistic terms of Low Risk (LR), Average Risk (AR), High Risk (HR), Average Very High Risk (AVHR) and Very High Risk (VHR). The universe of discourse is from 0 to 100 (Fig. 3).

2.5 Fuzzy Neonatal Death Risk Rules

The resulting Mamdani-based fuzzy neonatal death risk system[1] is given as:

R1 :   IF ($X_{Gestational-Age}$ is *Very Extreme Preterm*) AND ($X_{Birth-Weight}$ is *Extreme Low*)
        THEN (Y_{RON} is *Very High*)

R2 :   IF ($X_{Gestational-Age}$ is *Extreme Preterm*) AND ($X_{Birth-Weight}$ is *Extreme Low*)
        THEN (Y_{RON} is *Very High*)
        . . .

R15 : IF ($X_{Gestational-Age}$ is *Light Preterm*) AND ($X_{Birth-Weight}$ is *High*)
        THEN (Y_{RON} is *High Risk*)
        . . .

R29 : IF ($X_{Gestational-Age}$ is *Term*) AND ($X_{Birth-Weight}$ is *Regular*)
        THEN (Y_{RON} is *Low*)

R30 : IF ($X_{Gestational-Age}$ is *Term*) AND ($X_{Birth-Weight}$ is *Insufficient*)
        THEN (Y_{RON} is *Average*)

$$\tag{2}$$

The severity surfaces for the diagnosing risk of neonatal death accomplished by using the proposed fuzzy decision support system for clinical assessment is shown in Fig. 4. The knowledge base of the fuzzy system is build up with

data from the literature. It is worth mentioning that such a system may be employed with any shape of fuzzy sets available in literature. Trapezoidal membership functions are employed to illustrate the proposed approach.

3 Discussion and Illustrative Example

The resulting surface as depicted in Fig. 4 represents the human reasoning concerning an input–output evaluation model about newborns with the risk of death. The interrelation between the gestational age and the weight of a newborn reflects the adequacy of the intrauterine growth, inducing the anticipation of the risk of neonatal death, anticipating not only the necessity of therapeutic measures but also preventive approaches to be taken in a timely manner. On the other hand, intrauterine growth also translates into population and socioeconomic characteristics of the population's life, be nutritional, environmental habits, and/or lifestyle [21].

Further, at a glance, the outcome risk surface worsens as both the gestational age and the birth weight achieves high and low values (Fig. 4). Such a feature excels a central region in the surface in which the risk of neonatal death is reduced. According to the surface, it can be observed that the gestational age ranging from 37 to 39 weeks presents a lower risk for neonatal death. On the other hand, the extremes of gestational age increase the risk of neonatal death, that is, from 20 to 36 weeks the fetus is not yet adequately complete. In contrary, from 41 weeks, the permanence of the fetus in the uterus can trigger meconial aspiration [22], chorioamnionitis [23], asphyxia, neurological problems and other well-established complications in the literature [22–24].

---

[1]Disclaimer: The fuzzy rules listed should not be used in clinical diagnosis without consulting experienced physicians.

Table 1 Comparison of the risk of neonatal death outcomes obtained with neonatologist experts and the proposed fuzzy model

Birth weight (grams)	Gestational age (week)	Neonatologist expert (%)	Fuzzy model (%)
800	29	88.8	81.7
1,200	28	77.5	73.5
1,500	34	60.3	35.0
1,500	32	68.8	55.2
1,600	37	38.4	35.0
2,000	38	38.4	35.0
2,000	34	52.5	35.0
2,200	36	33.6	35.0
2,300	39	30.0	31.1
2,500	38	18.3	15.5
2,900	39	4.3	11.6
2,900	35	25.0	27.0
3,000	40	3.8	4.04
3,500	40	4.0	4.04
3,500	42	40.0	35.0

In turn, the fetal weight gain during pregnancy is the result of regular consumption of various foods. It promotes a healthy nutritional intake and optimize fetal development and growth [22, 25]. When the nutrition state of the fetus is not adequate, there are risks for the fetus. It is possible to observe that birth weight values below 2500 g excerpt a great influence on the risk of neonatal death. Moreover, the extremely low birth weight lower than 1000 g strongly influences neonatal death, even with the increased of gestational age, consistent with the literature that detaches the high association with low birth weight and neonatal death [22, 23].

The proposed fuzzy inference model is compared with the evaluation of the expert professionals through 15 clinical conditions to estimate the risk of neonatal mortality, as shown in Table 1. The fuzzy neonatal death risk assessment based on the determinants of birth weight and gestational age achieved a Pearson's correlation coefficient of 0.96 (Fig. 5). The comparison between the model and the specialists outcomes work very well in extreme situations, for example in cases where gestational age and birth weight are not optimal or when these variables are critical. Despite the divergences in some cases, the correlation is shown to be strongly positive linear. In this sense, the application of fuzzy set theory in neonatology has presented promising results.

It is worth mentioning that, care for the newborn may differ depending on the hospital (small or big) and its location (for example, rural or urban areas). In small

hospitals, the neonatologist is not always present at the time of birth, i.e., other professionals have the function of evaluating the newborn. The fuzzy model can help in the evaluation of the risk of neonatal death by offering relevant information to anticipate situations of clinical complications of newborns [26]. The system is easy to use and is non-invasive, unlike the main systems used as CRIB and SNAP-PE, therefore, it offers no risk to the newborn and can be easily used. The proposed model can support the complementary clinical assessment to estimate neonatal mortality, becoming an important tool in the evaluation of neonates.
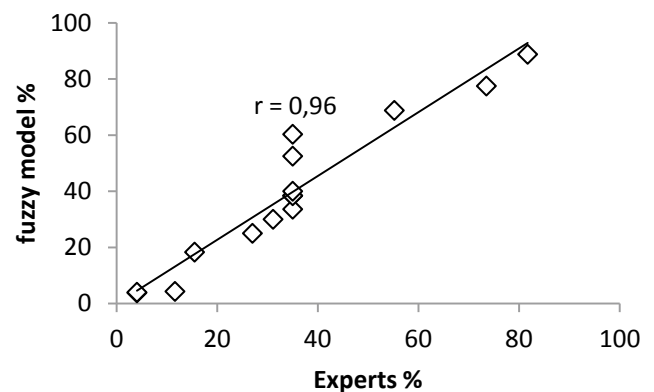
Fig. 5 Linear and positive Pearson correlation coefficient of 0.96 between the fuzzy model and the experts

4 Conclusion

This paper proposes a fuzzy inference linguistic model to evaluate the risk of neonatal death based on birth weight and gestational age. The model is easy to apply and non-invasive and safe for the newborn. The resulting model achieved a linear and positive Pearson correlation coefficient of 0.96 when compared to the opinion of neonatologists. The model can be used for the reallocation of resources and professionals, as well as therapeutic behavior for the female patient and then for the newborn.

References

1. WHO, World Health Organization. World Health Statistics 2016: Monitoring Health for the SDGS, sustainable development goals, Geneva (2016)
2. Ministério da Saúde. Agenda de compromissos para a saúde integral da criança e redução da mortalidade infantil. Brasília (DF): o Ministério (2004)
3. Millennium Development Goals Indicators. MDG country progress snapshot. Brazil. http://mdgs.un.org/unsd/mdg/resources/static/products/progress2015/snapshots/bra.pdf (2015)
4. Richardson, D.K., Gray, J.E., Mccormick, M.C., Workman, K., Goldmann, D.A.: Score for neonatal acute physiology: a physiologic severity index for neonatal intensive care. Pediatrics 91, 617–623 (1993)
5. International Neonatal Network: The CRIB (Clinical Risk Index For Babies) score: a tool for assessing initial neonatal risk and comparing performance of neonatal intensive care units. Lancet 342, 193–198 (1993)
6. Richardson, D.K., Corcoran, J.D., Escobar, G.J., Lee, S.K.: SNAP-II and SNAPPE-II: simplified newborn illness severity and mortality risk scores. J. Pediatr. 138, 92–100 (2001)
7. Lansky, S., et al.: Pesquisa nascer no Brasil: perfil da mortalidade neonatal e avaliação da assistência à gestante e ao recém-nascido, pp. 192–207. In Caderno Saúde Pública, Rio De Janeiro (2014)
8. Nascimento, L.F.C., Ortega, N.R.S.: Modelo linguístico fuzzy para estimação do risco de morte neonatal. Revista Saúde Pública 36 (36), 686–692 (2002)
9. Xesquevixos, C.M.D., Araujo, E.: Sistema difuso de suporte a decisão do risco de óbito neonatal pela avaliação da idade gestacional e idade da mãe. Congresso Brasileiro de Informática em Saúde, Campos do Jordão (2008)
10. Nascimento, L.F.C., Rizol, P.M.S., Abiuzi, L.B.: Establishing the risk of neonatal mortality using a fuzzy predictive model. Cad. Saúde Pública, Rio de Janeiro 25(9), 2043–2052 (2009)
11. Ramos, H.A.C., Cuman, R.K.N.: Fatores de risco para prematuridade: pesquisa documental. Escola Anna Nery Revista de Enfermagem, Rio de Janeiro 2(13), 297–304 (2009)
12. Belsey, M.: Global overview of newborn health. Summary of oral report to director-general of WHO at 89. WHO Executive Board, pp. 87–89 (1992)
13. Xesquevixos, C.M., Araujo, E.: Avaliação da importância dos fatores de risco para óbito neonatal. In: XIII Encontro Científico e de Iniciação Científica Anhembi Morumbi, São Paulo (2017)
14. Shaw, I.S., Simões, M.G.: Controle e modelagem fuzzy. São Paulo: Editora Edgard Blücher Ltda, 1ª Edição, (1999)
15. Mamdani, E.H., Assilan, S.: An experiment in linguistic synthesis with a fuzzy logic controller. Int. J. Man Mach. Stud. 7, 1–13 (1975)
16. Paiva, J.P., Feitosa, F.E.L.: Rotura prematura de membranas. Maternidade-Escola, Assis Chateaubriand—Diretrizes Assistenciais (2007)
17. Morais Neto, O.L., Barros, M.B.A.: Fatores de risco para mortalidade neonatal e pós neonatal na região centro-oeste do Brasil: linkage entre bancos de dados de nascidos vivos e óbitos infantis. Cadernos de Saúde Pública 16(2), 477–485 (2000)
18. Horta, B.L., Barros, F.C., Halpern, R., Victora, C.G.: Baixo peso ao nascer em duas coortes de base populacional no sul do Brasil. Cad Saúde Pública 12(Suppl 1), 27–31 (1996)
19. Araujo, B.F.: Mortalidade neonatal precoce no município de Caxias do Sul: Um estudo de coorte. Jornal De Pediatria 76(3) (2000)
20. Reis, M.A.M., Ortega, N.R.S., Silveira, P.S.P.: Fuzzy expert system in the prediction of neonatal resuscitation. Braz. J. Med. Biol. Res. 37(5) (2003)
21. Pittard, W.B.: Classification of the low-birth-weight infant. In: Klaus, M.H., Aa, Fanaroff (eds.) Care of the High-Risk Neonate, 4th edn, pp. 86–113. Wb Saunders, Philadelphia (1993)
22. Jwc, Jonhson, Mk, Yancey: A critique of the new recommendations for weight gain in pregnancy. Am. J. Obstet. Gynecol. 174, 254–258 (1996)
23. Wyllie, J., Bruinenberg, J., Roehr, C.C., Rüdiger, M, Trevisanuto, D., Urlesberger, B. European resuscitation council guidelines for resuscitation 2015: Section 7. Resuscitation and Support of Transition of Babies at Birth. Resuscitation 95, 249–63 (2015)
24. Fishman, S.G., Gelber, S.E.: Evidence for the clinical management of chorioamnionitis. Semin. Fetal. Neonatal Med. 17(1), 46–50 (2012)
25. Sa, Lederman: Pregnancy weight gain not excessive. Letter. Am J Obstet Gynecol 175, 1395–1396 (1996)
26. Nascimento, L.F.C., Rizol, P.M.S.R., Abiuzi, L.B.: Laptec: Fuzzy approach to establish the risk of neonatal death. In: Vi Congress of logic applied to technology. Santos/SP, Brasil (2007)

Identification and Compression Ratios of Standards for Recording Time-Series Resulting from Biomedical Signals

João Paulo Folador and Adriano O. Andrade

Abstract

Over the years, the development of technologies in the healthcare sector has been fundamental for the identification of diseases, time reduction of clinical assessments and patient monitoring. The main implication of this is an increase in the quality of care provided to patients. However, the use of technology has some relevant side effects, being the increase in the amount of produced information one of the most important. Currently, there is a large volume of medical devices able to collect vital signs from patients, and this diversity generated by different equipment manufacturers, originates a variety of file formats. This factor complicates the sharing of data between research centers. In this context, this study identified the main file formats existing for the storage of time-series resulting from biomedical signals. The distinct file formats were assessed by using a benchmark, which was biomedical data publicly available. It was found that the file format EDF is the one which requires less memory storage capacity and the possibility of accounting for embedding structured information relevant for the description of the data (e.g., annotation of events, patient and device information). Considering the increase in the amount of digital information and the eminent necessity of sharing data among researchers these results suggest that researchers should adopt available solutions, for instance the use of the EDF file format, for dealing with the problem of data compression and dissemination.

Keywords

Health data management • Biomedical signal • File format • EDF

J. P. Folador (✉) · A. O. Andrade
Centre for Innovation and Technology Assessment in Health,
Postgraduate Program in Electrical and Biomedical Engineering,
Faculty of Electrical Engineering, Federal University of
Uberlândia, Uberlândia, Brazil
e-mail: jpfolador@gmail.com

1 Introduction

The evolution of technologies in the medical field has greatly benefited patient care, by easing the recording of biological signals such as blood pressure, body temperature, oxygenation of blood, cardiac and cerebral activities [3]. Technological evolution has also allowed for continuous monitoring of patients at home and in intensive care unit.

According to [13], the primary purpose of biomedical data acquisition is monitoring, diagnosis or research, and its recording depends on these goals. Thus, monitoring of vital signs in a surgery requires immediate analysis and visualization, whereas data collection for research or diagnosis needs to store the data in the first place, dispensing real-time visualization.

These biomedical signals can be continuously measured in different ways depending on the underlying physiological phenomenon responsible for its generation. Bioelectric signals, generated by nerve and muscle cells, are one of the most used in the field of Biomedical Engineering and Medicine. Other signal types include: bioimpedance signals (where tissue impedance is measured), bioacoustic signals (sounds produced by the human body) and biomagnetic signals (magnetic fields produced by living organisms) [3]. In accordance with [13], in any approach related to biomedical signal collection it is necessary to verify memory occupancy and the quality of stored information for avoiding data loss.

A large amount of biomedical data is generated by the recording of time varying signals from different parts of the body, for instance, the electroencephalogram (EEG), electrocardiogram (ECG), electromyogram (EMG), electrooculogram (EOG) and inertial activity. In this context, over the years the medical industry and research consortiums have been addressing the issue of establishing the most suitable data format for the storage of biomedical time-series [15].

The search for standardization and its adoption can reduce costs, optimize joint work, and increase the quality of

research results [17]. For instance, the authors of the European project called SIESTA [13] reported problems in multimodal data (e.g., ECG, EEG, EMG, EOG, body temperature and pressure) acquisition and processing because device incompatibility due to different types of file format, filtering, sensor and amplifier specifications. This has motivated the development of standards such as the European Data Format (EDF) [11] and its extension EDF+ [10].

Guerrero et al. [7] developed an educational tool called BioLab to assist in the understanding and processing of different file formats. It was created in MatLab, and it provides support for data conversion of files. Another tool is the BioSignal software, which is open source, and it was developed in Matlab, Octave, C/C++ and Python, allowing the use of more than 30 different biomedical file formats [16]. These initiatives illustrate the relevance of data format in research.

Our research group has been working on the development of the architecture and implementation of a database for the management of biomedical data [6, 12]. One of the aims of the system is to allow for the organization and analysis of data. For this, it was necessary to define standards for input file formats considering the current literature. This was the main motivation of the research presented in this paper.

The first objective of this work was to identify the most used types of file formats employed for storage of time-series resulting from biomedical data. The second purpose was to compare distinct file formats by verifying data compression rates and suitability.

2 Materials and Methods

2.1 Search Criteria

In order to understand the file formats used in the recording of biomedical signals and their context today, some questions were raised:

- What are the file formats used to collect biomedical signals?
- What are the features and information available in these formats?
- Is there a file format that is widely used and supports different biomedical signals?
- Do commonly used files take up a lot of storage space?

A list of the types of biomedical file formats available published in Wikipedia (https://goo.gl/8Qiczm) guided the first steps of the research. Subsequently, the type of each file (GDF, EDF, OpenXDF, HL7, etc.) and the key terms "biomedical signal", i.e. EDF AND "biomedical signal", were searched in the different databases provided by CAPES

(Web of Science, Pubmed, Scopus, Science Direct and Bireme), without temporal limit and considering the name of the file extension in the title, abstract and key words. Another used string of search in the databases was "biomedical time-series" AND "file format" to try to answer the objectives. All results were analyzed by reading the abstract and its correspondence with the research objectives.

For each identified file format, it was sought information about the characteristics of the files, the type of encoding of the header and the collected signal, the kind of biomedical signals possible to be recorded by the type of file, the type of documentation used as a guide or whether the format was open source or not. File formats that were not found were searched on the internet in attempt to find their manufacturers and/or developers.

2.2 Test File Database

The data used for analysis was obtained from Physionet [14]. These data are about sleep recordings and hypnograms stored in the European Data Format (EDF). Sixty one files in EDF format were used (22 files had occupied between 20 and 30 Megabytes (MB) of space in disk and 39 files between 45 and 50 MB) and each file was converted to GDF, BDF by BioSignal [16] and plain text (ASCII CSV–Comma-Separated Values) by EDFBrowser [2]. After that, each file was compressed by WinRar 5.40 64-bits software, installed on the Windows 7 64-bits operating system, using its default settings.

3 Results

Table 1 summarizes information from the distinct types of file format that were identified. Most of files in Table 1 that deals with time-series storage has a header specifying relevant parameters of data collection and then the time-series of the collected signal, except for ecgML, which is based on the eXtensible Markup Language (XML) structure, which separates the information into 3 basic files, and other additional, non-mandatory, for different forms of data visualization (graphics, audios, images) [18].

The Institute of Science and Technology of Austria maintains a page with information guiding biomedical file formats [9]. The EDF+ and GDF format have similar characteristics, great compatibility between the file formats of different biomedical signals and, accept other formats converted directly without losses [10, 16].

The second objective of this research was to compare some of the most used file standards for time-series storage. The aim of the comparison was to identify which file type occupies less memory in disk.

Table 1 Identified file standards and their characteristics

References	Format	Characteristics description	Documentation	Developer
[8]	ACQ	Proprietary file format for Biopac systems. It has an API for developers to obtain information from data collections. It supports the storage of biomedical signals: ECG, EEG, EOG and others. It uses the ASCII standard	Proprietary	*Biopac Systems*
[9]	ADICHT	Company specific format ADInstruments for use in the software called LabChart for Windows or Mac	Proprietary	*ADInstruments*
[9]	BCI2000	General-purpose software platform for brain-computer interface that can be used freely for research and studies. It provides recording information from the brain such as EEG, Electrocorticography (ECoG), Magnetoencephalography (MEG), etc. It uses the ASCII standard	BCI2000 framework	*Wadsworth Center*
[9]	BDF	This format is used in BioSemi systems and supports 24-bits sampling based on the 16-bit EDF format. Commonly used for EEG, ECG and EMG signal storage. It is based on ASCII encoding. It has drivers and software for Windows, Mac and Linux	Proprietary	*BioSemi Instrumentation*
[9]	BKR	A specific EEG data format developed by EEG Processing Software (EPS). It has a header of 1024 bytes and the size of the data collection area varies with the number of channels	Proprietary	*EPS*
[9]	CFWB	A simple binary format for exporting and importing graphical data. It has some C/C ++ libraries for extracting information	Proprietary	ADInstruments
[9]	DICOM	It constitutes a standard that structures a protocol for transmission, storage and treatment of medical images, such as: resonance, X-ray, tomography and others	DICOM; ISO/IEC. 2016/05	*DICOM Standards Committee*
[18]	ecgML	This format was proposed by Food and Drug Administration agency (FDA) and it is XML-based for data acquisition, sharing, and ECG mining. It has hierarchical configuration by addressed attributes and it is flexible to changes	FDA XML format; DICOM; CEN/TC251	*FDA*
[10]	EDF+	EDF is widely accepted in the research community for data exchange and many suppliers provide import and export filters. The maintenance of the format aims at the backwards compatibility of previous versions. It uses the ASCII standard and supports the storage of files such as EEG, ECG, EMG, MEG, EOG, etc	European data format (EDF)	*European Community*
[9]	FEF	The purpose of this format was to share vital signs. It was built based on the ASN.1 protocol that defines its structure. It has parts based on ASCII and binary coding	CEN/TC251	*Project CEN/TC251/PT-40*
[16]	GDF	This format provides a large set of compatibility across multiple formats. The GDF structure is similar to EDF. It has configurable header, ASCII and binary based parts. The data type is configurable to support EEG, ECG, MEG, EMG, EOG, etc	BCI2000	*IST Áustria*
[1]	HL7	A framework that standardizes the exchange, integration and retrieval of files by the community and not for profit. Its current version uses the XML format. It is based on Electronic Health Record (EHR), focused on web applications	ANSI/ISO/HITSP; HL7 framework	*Health Level 7 International (HL7)*
[9]	MFER	Format developed by Medical Waveform Format Encoding Rules (MFER). It has been applied to store EEG, ECG, etc. Records can be of short or long duration. It is based on ASCII coding	ISO/TS 11073/92001	*MFER*
[4]	Open XDF	Format based on XML and UTF-8 and UTF-16 encoding. It is possible to associated videos in the recording. It is used to exchange EEG, ECG, oximetry files, etc	OpenXDF	*Neurotronics*
[15]	SCP	International self-documented standard for the digital exchange of ECG signals and related metadata. It is used for short term recording. It was developed by European Project of the Advanced Informatics in Medicine Program (AIM)	EN1064:2007; ISO 11073/91064	*AIM*
[5]	SIGIF	Format created by the Institute of Electronics and Informatics Engineering of Aveiro (IEETA). It has an ASCII-based header and binary data. It supports EEG, oxygen saturation (SaO2), EMG and others. There is library available in C/C++	ASTM e EDF	*IEETA*
[9]	WFDB	A Waveform data used for ECG files. It supports 8 to 16 bits. ASCII-based header file and binary data. It is open source and supports several platforms (Windows, Mac, Linux, Solaris, etc.)	PhysioBank softwares	*PhysioBank*
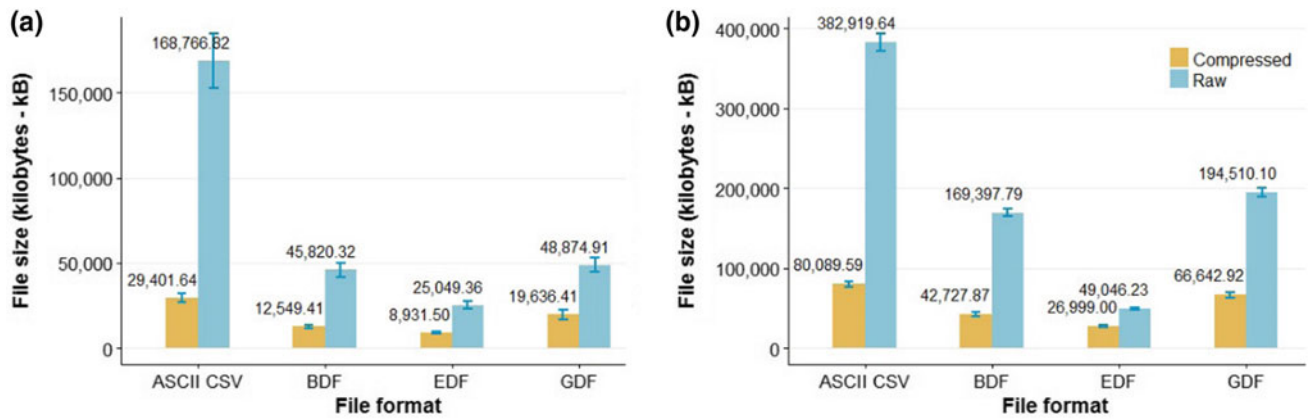
Fig. 1 Mean and standard deviation of the file size for raw and compressed files, for each file format. **a** Raw files of 20–30 MB and **b** raw files of 45–50 MB

Figure 1 presents the mean and standard deviation of the file size. The raw and compressed files for the formats EDF, GDF, BDF and ASCII (CSV) were analyzed. The results take into account two scenarios: (a) raw files between 20 and 30 MB, and (b) raw files between 45 and 50 MB.

Figure 1a, which presents the results for raw files of 20 to 30 MB, shows that the ASCII (CSV), BDF, EDF and GDF file formats yielded a mean compression ratio of approximately 82.58%, 72.61%, 64.34% and 59.02%, respectively. Figure 1b, which presents the results for raw files of 45 to 50 MB, yielded compression rates of 79.08%, 74.78%, 44.95% and 65.74% respectively.

It was verified that the EDF file yielded the best mean raw and compressed sizes. The BDF, EDF and GDF file formats (without further compression) yielded files at least 30% smaller than the text files without compression, which illustrates good quality for storage, transmission and sharing.

4 Discussion and Conclusion

There are several file formats for a variety of different devices that manage distinct biomedical signals. This diversity of file formats hampers the exchange of data between research centers around the world, makes it difficult to store, process and analyze information, since it requires specific software for each file format, and consequently, quality of data analysis decreases and the costs with hospital management and health care centers increase.

The BDF format was created based on EDF, but BDF supports 24-bit resolution. In this sense, if there is a need to convert a BDF file to a more widely used format such as the EDF, there may be loss of information. The GDF format allows several other formats to be converted to it without loss [16].

In the analysis considering file formats and the space occupied in the disk, the EDF yielded the best compression

capability, and the GDF occupies the largest disk space, which may not only be impacted by the standard compression of the format, but also by maintaining structures that make it compatible with most other formats. Although the GDF standard may imply in increase of physical space, digital storage has become cheaper [13], and the compatibility between distinct formats may be more relevant in future.

The XML-based formats (ecgML, HL7, OpenXDF) follow a pattern in which there is a hierarchical structure with attributes addressing the characteristics and configurations of the file, unlike the others, whose information is based on a sequence of data controlled by the positioning of the characters. In this context, XML allows for flexible changes without causing problems in the structure. In addition, XML-based formats are ready to be exchanged in web environments and across multiple applications.

For information sharing, there is a list of formats shown in [9], which attempts to group important features from distinct types of biomedical signal formats. It would be interesting to have a tool capable of providing information to manufacturers, developers, researchers of these formats, to keep their information and the characteristics updated, helping thus, future researches, problem corrections and better implementations.

In order to better understand and optimize the space occupied by different file formats, a future study can be carried out on all available file formats (Table 1) to verify which one produces better compression ratios, considering the compatibility among distinct standards.

References

1. Al-Enazi, T., El-Masri, S.: HL7 engine module for healthcare information systems. J. Med. Syst. **37**, 1–8 (2013)
2. Beelen, T.: EDF Browser. https://www.teuniz.net/edfbrowser/, Accessed 28 Feb 2018
3. Bronzino, J.D.: Medical Devices and Systems: The Biomedical Engineering Handbook, 3rd edn. CRC Press, Hartford, Connecticut, U.S.A (2006)
4. OpenXDF Consortium. Open eXchange Data Format Specification. pp. 1–49 (2008)
5. Cunha, M.B., Cunha, J.P.S., Silva, T.O.: SIGIF: a digital signal interchange format with application in neurophysiology. IEEE Trans. Biomed. Eng. **44**, 413–418 (1997)
6. Folador, J.P., Chagas, L., Fraga, M., Andrade, A.O.: Architecture and organization of a computational system for the management of data from individuals with Parkinson's disease. In: Proceedings of the World Congress on Medical Physics and Biomedical Engineering. p accepted (2018)
7. Guerrero, J.F., Bataller, M., Soria, E., Magdalena, R.: BioLab: an educational tool for signal processing training in biomedical engineering. IEEE Trans. Educ. **50**, 34–40 (2007)
8. Acqknowledge file formats for PC. In: BIOPAC Syst. https://www.biopac.com/application-note/acqknowledge-file-formats-windows/. Last accessed 05 Feb 2018
9. Institute of Science and Technology: Scientific data formats. http://pub.ist.ac.at/~schloegl/matlab/eeg/. Accessed 30 Jan 2018
10. Kemp, B., Olivan, J.: European data format "plus" (EDF+), an EDF alike standard format for the exchange of physiological data. Clin. Neurophysiol. **114**, 1755–1761 (2003)
11. Kemp, B., et al.: A simple format for exchange of digitized polygraphic recordings. Electroencephalogr. Clin. Neurophysiol. **82**, 391–393 (1992)
12. Folador, J.P., Andrade, A.O.: Mineração de dados aplicada à séries temporais resultantes de sinais motores da doença de parkinson. In: Anais do V Congresso Brasileiro de Eletromiografia e Cinesiologia e X Simpósio de Engenharia Biomédica. Even3, Uberlândia, Minas Gerais (2018)
13. Penzel, T.: Acquisition of biomedical signals databases. IEEE Eng. Med. Biol. Mag. **20**, 25–32 (2001)
14. PhysioNet, The Sleep-EDF Database. https://physionet.nlm.nih.gov/pn4/sleep-edfx/. Last accessed 20 Jan 2018
15. Rubel, P.: SCP: ECG V3.0: An enhanced standard communication protocol for computer:assisted electrocardiography. In: Computing in Cardiology Conference (CinC), 1–4 (2016)
16. Schlögl, A.: GDF—A general dataformat for biosignals. Cornell Univ Libr, 1–15 (2006)
17. Värri, A., Kemp, B., Penzel, T., Schlögl, A.: Standards for biomedical signal databases. IEEE Eng. Med. Biol. Mag. **20**, 33–37 (2001)
18. Wang, H., Azuaje, F., Jung, B., Black, N.: A markup language for electrocardiogram data acquisition and analysis (ecgML). BMC Med. Inform. Decis. Mak. **3**, 1–13 (2003)

Investigating Dynamic Grip Force Control During Object Manipulation to Design Improved Control Schemes of Prosthetic Hands

Ana Carolina Torres Cresto, Andrei Nakagawa Silva, and Alcimar Barbosa Soares

Abstract

Prosthetic devices are capable of restoring motor functions that were lost due to amputations caused by diseases, traumas or injuries. Advanced prosthetic hands are greatly desired since manipulating objects are a great part of daily life. Research have focused on developing enhanced robotic hands with many degrees of freedom and different control mechanisms that makes use of Electromyography (EMG) or Electroencephalography (EEG) signals, for example. Restoring proprioceptive and tactile feedback of prosthetic devices, however, is still a major challenge to the field. Object manipulation consists of complex interactions between the hand and the object and sensory feedback is crucial for proper scaling grip force to avoid slip and excessive force. Therefore, studying how grip forces are adjusted under different conditions can provide insights for developing control schemes that can be added to prosthetic devices in order to make them easier to use and more reliable. In this paper, we investigated how grip force is modulated during pronation and supination movements. We found that changes in force occur in parallel to changes in object orientation, suggesting that it is not a feedback based control scheme where force is adjusted gradually after a change in the orientation is detected. Furthermore, there is a synergism between the forces generated by the thumb and the index finger to maintain grasp stability.

Keywords

Grip force control • Object manipulation • Prosthetic devices

A. C. T. Cresto (✉) · A. N. Silva · A. B. Soares
Biomedical Engineering Lab, Federal University of Uberlândia, Uberlândia, Brazil
e-mail: anatcresto@gmail.com

A. C. T. Cresto
PET Engenharia Biomédica, Federal University of Uberlândia, Uberlândia, Brazil

1 Introduction

Skilled object manipulation in humans heavily depends on somatosensory feedback. Touch feedback is provided by mechanoreceptors in the glabrous skin [1]. These sensors respond in a distinct manner to different kinds of forces, pressures and vibrations. Meissner and Pacinian corpuscles are fast-adapting sensors while Merkel cells and Ruffini endings are slow-adapting sensors. The population response of these mechanoreceptors encodes information such as object texture, shape and weight [1–3].

Studies on the control of grip forces during object manipulation have demonstrated that such forces are produced largely in parallel to changes in load force [2, 3]. This sensorimotor control scheme is largely feedforward where an internal model of object dynamics is used to predict what kind of forces has to be produced to maintain grasp stability during manipulation. Reactive or feedback-based control takes place when unexpected perturbations or forces are applied, changing the dynamics of the task. Such internal model is formed and calibrated with experience and is shaped by the information encoded by the mechanoreceptors [4].

Considering the importance that sensory feedback plays on sensorimotor control, it is possible to imagine that amputees would improve their usage of prosthetic devices if they were equipped with tactile sensors. However, most commercial devices do not have any kind of sensory feedback and amputees have to rely solely on vision to control them. Interestingly, the lack of feedback is one of the reported reasons for myoelectric prosthesis rejection [5]. Thus, some works have been trying to restore sensory feedback by means of sensory augmentation or sensory substitution [6, 7]. This approach delivers sensory feedback from the prosthesis to the subjects and let them control grasping based on the perceived sensory feedback. An alternative is to include some level of intelligence in the prosthetic hands and let them take actions autonomously,

such as independently scaling grip force, to avoid excessive force or prevent slip [8, 9].

Here, we investigate how grip forces are modulated during pronation and supination movements that cause changes in the orientation of the object being grasped. We hypothesize that future motor commands can be used by an internal model and, therefore, grip forces would change in parallel to changes in object orientation and that different level of forces would be applied by the fingers under different positions.

2 Materials and Methods

2.1 Apparatus

The test object used during the experiment was a tube of cylindrical shape with 13.4 × 3 cm, weighting 90 g and, as for the experiment, the tube was filled with a 310 g weight, making it a total of 400 g. Two force resistive sensors (FSRs) were placed at symmetrical positions on both sides of the tube at its center of mass. The size of the FSRs is compatible with the fingers and the reading circuitry was developed so it is sensitive enough to smaller forces (Force Sensitivity Range ~ 0.2–20 N) The force sensors were fixated using velcro to avoid direct contact with the sensor while providing additional friction. An inertial measurement unit (IMU: MPU6050, 6 axis accelerometer + gyroscope) was placed at the low side surface of the object to measure changes in object orientation during the manipulation task with its y-axis aligned with gravity. The FSRs signals were digitized with an Arduino Uno board using two 12-bit ADC channels. Communication with the MPU6050 was made via I2C to read the raw values from the accelerometer and the gyroscope. All the signals were sampled at 100 Hz.

A custom-made software received data from the Arduino board and saved them to a text file for further processing. Figure 1 presents the apparatus and experimental setup.

A calibration process of both sensors was made. It was placed different weights over the sensors and this procedure lasted for one minute for each weight. The values of the different weights used were: 20, 50, 100, 200, 300, 400, and 500 g. A polynomial regression was applied in order to find the value of the signal in kilogram force (kgf).

2.2 Subjects

Four participants (all man, aged 21–23) were enlisted to participate in the experiment. All participants were right-handed and naive to the object manipulation task. This research has been approved by the Ethical Commitee of the Federal University of Uberlândia in December 2016 (CAAE: 60910916.0.0000.5152) and all participants provided a formal written consent prior to the experiment.

2.3 Experimental Procedures

Participants sat comfortably and were positioned beside table with their forearm resting over the table in a comfort position. Prior to the beginning of the experiment, participants were informed about the manipulation task as they observed an instructor performing the task. The manipulation task consisted on grasping the tube and performing pronation and supination movements with a precision grasp (using the thumb and the index finger). The other fingers should be closed, touching the palm of the hand and should not be involved in the manipulation task. Subjects were carefully instructed to place their fingers over the sensors, to

Fig. 1 Experimental setup
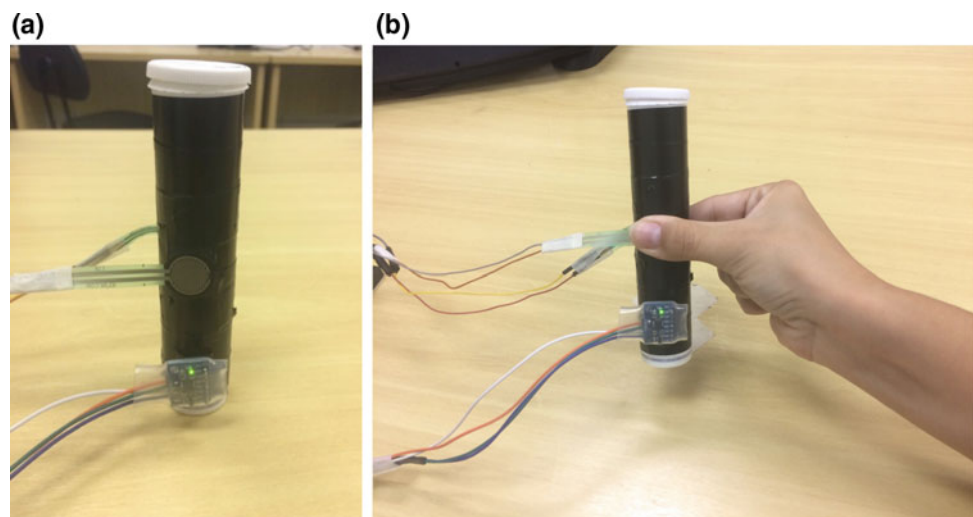
Fig. 2 Experimental segment positions

apply natural forces and were given oral commands to perform the movements.

The experiment consisted of 3 trials of 35 s each and was divided into 3 segments (Fig. 2) with different time durations: (A) subjects are required to grasp and lift the object and hold for 10 s. The hand should be aligned with the shoulder in height; (B) subjects perform a 90° pronation movement and hold the object for 10 s in the new position and (C) subjects perform a 90° supination to return the object to its original orientation and hold for 10 s. In the end of the trial, participants are instructed to relax for 2 min before another trial begins.

2.4 Data Analysis

The experiment results were analyzed in order to elucidate how grip force is dynamically modulated during object manipulation. First, we averaged the signals from all subjects across all trials. Then, we analyzed the mean grip force profile in the resulting signals during the three hold phases: (a) previous to pronation, (b) holding the object rotated and (c) after supination. Measures of the mean forces would demonstrate the steady-state forces generated by each finger to stabilize and hold the object at different orientations. We separated each phase in the following time intervals, respectively: (a) 8–13 s, (b) 18–22 s and (c) 30–35 s.

We have also measured the correlation coefficient between the accelerometer signal (the z-component of the accelerometer was chosen as reference since it was facing up at rest, measuring close to 1 g) and the forces produced by the thumb and the index finger. We separated the transition parts of the pronation and supination movements (14–17 and 24–27 s respectively). Correlation between the aforementioned signals would indicate how grip force is adjusted with respect to the changes in the object orientation. Higher correlations would indicate that the produced forces are being generated in parallel in order to stabilize the object.

3 Results

Figure 3 presents the averaged accelerometer and grip force signals. Tilting the object with pronation and supination movements cause a change in the accelerometer signal. Grip force is shown as individual force signals for the thumb and index fingers. Here we see that changes in grip force occur in parallel to changes in object orientation. Furthermore, during and after pronation, the thumb is the contact point responsible for stabilizing the object. Thus, its force should be higher than the ones produced by the index finger whose role in these conditions is to provide another contact point for holding the object.

Figure 4 presents the mean force values measured for each finger during the three distinct hold phases. During initial grasp and lift, the index finger applies more force. As the tube is tilted during the horizontal grip phase, the thumb applies more force to stabilize the object. Also, if the index finger applies force, it will become an unstabilizing force by itself, potentially causing a rotational slip and triggering large responses from the thumb. Thus, its force should be lower than the thumb so it does not interfere with stability. After the tube returns to its original orientation, there is a tendency of the forces stabilizing around the same values from before the movement.

Figure 5 presents the changes in grip force during the pronation and supination movements in greater detail. During pronation, there is a decrease in the force applied by the index finger and an increase in the force produced by the thumb. During supination, the index finger increases its applied force again while the thumb force decreases. Interestingly, it is possible to observe that during pronation, the faster decrease in the index finger force is followed by a peak in force for the thumb. In a similar manner, during supination, thumb force decreases only after some amount of force from the index finger is produced. These slight delayed mechanisms highlight the synchronization of forces in order

Fig. 3 Grip force is dynamically modulated according to changes in object orientation. Pronation begins short after 15 s and supination starts at 25 s. Top: Z-axis accelerometer response during the object manipulation task demonstrating the change in orientation of the tube. Bottom: Changes in the force profile of the thumb and the index finger. The thumb applies more force after pronation since it is the one more responsible for stabilizing the object
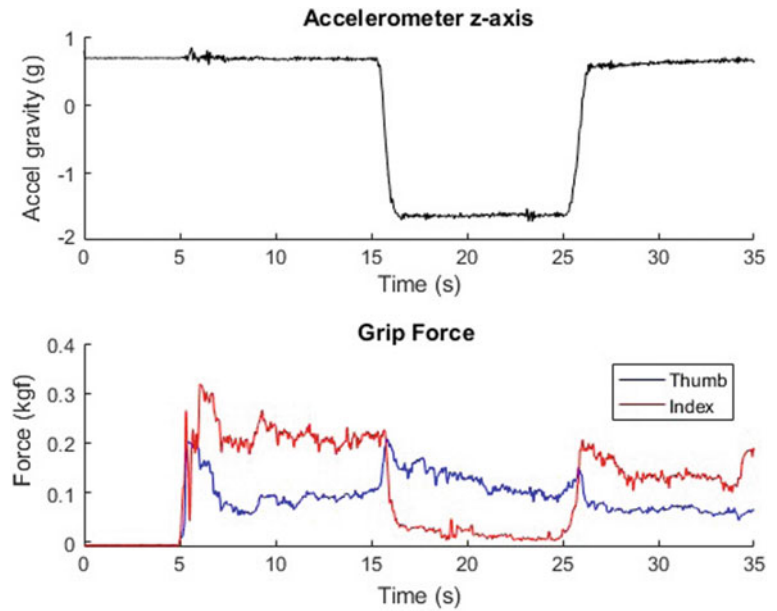
Fig. 4 Average force applied by the thumb and the index finger during the three hold phases. Notice how the force applied by the thumb is larger than that of the index finger after pronation for stability purposes
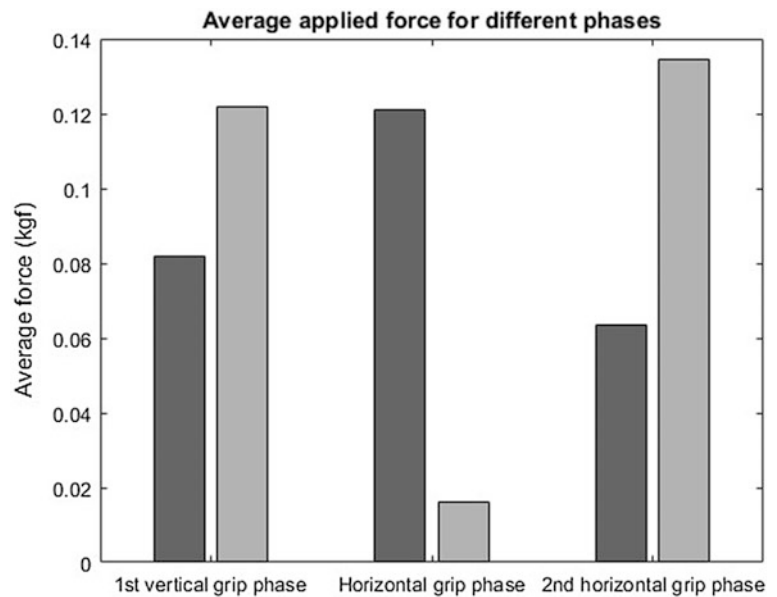
to maintain optimal stability. If one force suddenly increases or decreases, it is harder to stabilize the object. However, if there is a synergism between them, then stabilization can be achieved with less overall forces.

The interaction between grip force and object orientation were analyzed by estimating the correlation coefficient between the accelerometer signal and the forces produced by the thumb and the index finger. During both pronation and supination we found high correlations between the accelerometer signal and the force produced by the index finger. For the former, a positive correlation (0.95) for the index finger and a negative correlation (−0.77) for the thumb were found. For the latter, a positive correlation of (0.97) for

the index and a negative correlation (−0.32) for the thumb were found. These values indicate a close relationship between grip force and object orientation for the index finger while the thumb is less correlated due to its role in stabilization.

4 Discussion

In this paper we investigated how grip force control is modulated during an object manipulation task. We studied how changing the orientation of an object would affect the forces applied by the thumb and the index finger in a
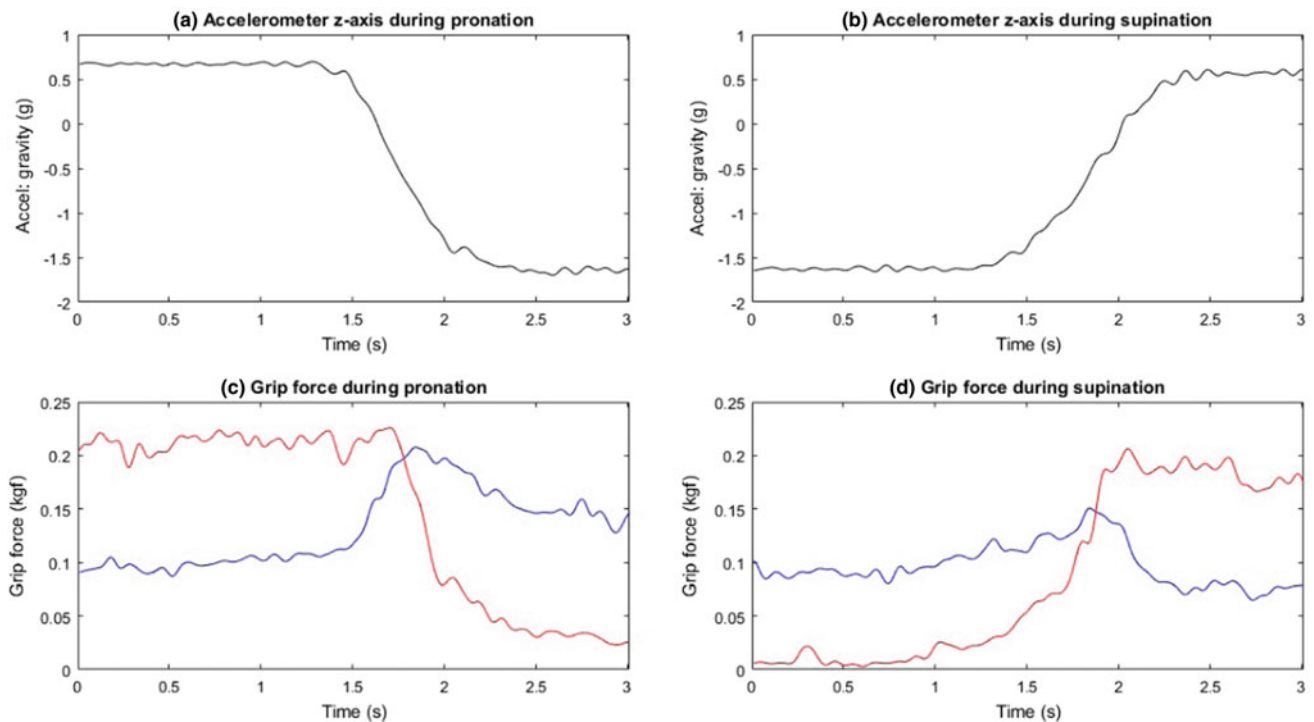
Fig. 5 Dynamic grip force modulation during pronation and supination movements that cause changes in object orientation. **a** and **b**: Z-axis accelerometer readings demonstrating the change in orientation of the object. **c** During pronation, there is an increase in the applied force by the thumb (in blue) to stabilize the object while the index finger (in red) force decreases. **d** During supination, there is an increase in the force produced by the index finger (in red) and a decrease in thumb force (in blue)

precision pinch grasp. Changes in orientation of the objects are challenging because the field of gravity changes, making the necessary forces to avoid slip for example to be different from those required in its original orientation.

Our work is similar to the experiment conducted by Johansson et al. [10]. However, we tried to find a simplified approach to study the same problem. While the authors used a more sophisticated device that allowed changing the center of mass of the object and to apply external perturbations, we used a single, usual object to conduct our studies. More importantly, we defined the pinch grasp to be aligned with the center of mass of the object, different from their approach. This change brings a fundamental difference to the production of forces for stabilizing the object.

When a base support is placed at the center of mass, if the area is large enough, then it should be capable of stabilizing the load or object. If the area is not large enough, then it is possible to have another support on the other side of the object so it can be grasped and stabilized. However, if the base support is placed away from the center of mass, then a rotational force will appear and it is essential to have another support to stabilize the object. This illustration serves to

explain the main difference between our results and the ones obtained by Johansson et al. [10]. In their work, they found that grip force increased both in the thumb and in the index finger. This is necessary to stabilize the object since the grip is not positioned at the center of mass. Both fingers need to apply force to prevent the object from rotating.

In contrast, in our experiments the thumb could act as a base support and the index finger needs to apply just a slight force to maintain the center of mass of the object in contact with the thumb. In this scenario, the thumb is the main responsible for stabilizing the object and, if the index finger applies more force than necessary, as a response, the thumb would produce even more force to counterbalance the object and the opposing force. This explains why in our results the force produced by the thumb is larger than the index during the hold phase with the object tilted.

Furthermore, the correlations found between the accelerometer signals and the force signals suggest that grip force might be dynamically modulated in parallel in order to maintain grasp stability. Our work can be improved with further temporal analysis of the dynamics of these signals to investigate whether the changes are feedback based or not.

Such analysis can be used to explore the idea of internal models. The concept of internal models is interesting for developing novel control methods to prosthetic devices where such intelligent behavior can be used in order to alleviate the users to send many commands to the prosthesis.

References

1. Johansson, R.S., Flanagan, J.R.: Coding and use of tactile signals from the fingertips in object manipulation tasks. Nat. Rev. Neurosci. **10**(5), 345–359 (2009)
2. Johansson, R.S., Westling, G.: Roles of glabrous skin receptors and sensorimotor memory in automatic control of precision grip when lifting rougher or more slippery objects. Exp. Brain Res. **56** (3), 550–564 (1984)
3. Westling, G., Johansson, R.S.: Factors influencing the force control during precision grip. Exp. Brain Res. **53**(2), 277–284 (1984)
4. Flanagan, J.R., Bowman, M.C., Johansson, R.S.: Control strategies in object manipulation tasks. Curr. Opin. Neurobiol. **16**(6), 650–659 (2006)
5. Biddiss, E., Chau, T.: Upper limb prosthesis use and abandonment: a survey of the last 25 years. Prosthet. Orthot. Int. **31**(3), 236–257 (2007)
6. Antfolk, C., D'Alonzo, M., Rosén, B., Lundborg, G., Sebelius, F., Cipriani, C.: Sensory feedback in upper limb prosthetics. Expert Rev. Med. Devices **10**(1), 45–54 (2013)
7. Schweisfurth, M.A., Markovic, M., Dosen, S., Teich, F., Graimann, B., Farina, D.: Electrotactile EMG feedback improves the control of prosthesis grasping force. J. Neural Eng. **13**(5), 56010 (2016)
8. Romano, J.M., Hsiao, K., Niemeyer, G., Chitta, S., Kuchenbecker, K.J.: Human-inspired robotic grasp control with tactile sensing. IEEE Trans. Robot. **27**(6), 1067–1079 (2011)
9. Osborn, L., Kaliki, R.R., Soares, A.B., Thakor, N.V.: Neuromimetic event-based detection for closed-loop tactile feedback control of upper limb prostheses. IEEE Trans. Haptics **9**(2) (2016)
10. Johansson, R.S., Backlin, J.L., Burstedt, M.K.O.: Control of grasp stability during pronation and supination movements. Exp. Brain Res. **128**, 20–30 (1999)
11. Gibo, T.L., Bastian, A.J., Okamura, A.M.: Grip force control during virtual object interaction: effect of force feedback, accuracy demands, and training. IEEE Trans. Haptics **7**(1), 37–47 (2014)
12. Johansson, R.S.: How Is Grasping Modified by—Somatosensory Input Department of Physiology, University of UmeA, 901 87 UmeA, Sweden
13. Johansson, R.S., Cole, K.J.: Sensory-motor coordination during grasping and manipulative actions. Curr. Opin. Neurobiol. **2**, 815–823 (1992)
14. Macefield, V.G., Johansson, R.S.: Control of grip force during restraint of an object held between finger and thumb: responses of muscle and joint afferents from the digits. Exp. Brain Res. **108**, 172–184 (1996)
15. Johansson, R.S., Vallbo, Å.B.: Tactile coding in the glabrous skin of the human hand. Trends Neurosci. **6**, 27–31 (1983)
16. Flanagan, J.R., Tresilian, J.R.: Grip load force coupling: a general control strategy for transporting objects. J. Exp. Psychol. Hum. Percept. Perform. **20**, 944–957 (1994)
17. Birznieks, I., Burstedt, M.K.O., Edin, B.B., Johansson, R.S.: Mechanisms for force adjustments to unpredictable frictional changes at individual digits during two-fingered manipulation. J. Neurophysiol. **80**, 1989–2002 (1998)
18. Jenmalm, P., Johansson, R.S.: Visual and somatosensory information about object shape control manipulative finger tip forces. J. Neurosci. **17**, 4486–4499 (1997)

Knowledge Acquisition of Expert for Structuring Healthcare Data and Information

Douglas Rocha, Henderson Sanches, Janice Lamas, Liana Matheus, and Lourdes Brasil

Abstract

In recent times, information technology has been undergoing a considerable degree of development, especially with the massive use of the healthcare information. Thus, the importance of storing healthcare data and information in a way that can be retrieved and studied and the need to create computational tools to support disease prevention and medical diagnosis, suggests this proposal for structuring the data and information contained in the scope of healthcare. The acquisition of the Expert Knowledge is one of the main stages of the ontologies creation and of structuring data and information in healthcare as in any domain, but its complexity makes it one of the most difficult tasks to perform. In this context, considering the large volume of data generated in the healthcare area and the value they have in the treatment of patients and for future research, there is a need to treat the information generated in an ontologically structured way, based on a knowledge acquisition of expert well-founded. The knowledge engineer can adapt among the several existing methodologies for acquiring knowledge using the techniques and strategies that best apply to a research area, developing a methodology that meets his specific needs. This article proposes to demonstrate techniques and strategies for the knowledge acquisition of expert in healthcare, showing some peculiarities of this domain.

1 Introduction

Notably, in recent times, a great advance in technology has been observed, especially with the massive use of computer science in healthcare, allowing large amounts of data to be stored and processed in a relatively short time, and still with employment of computational tools, favoring the extraction of information to facilitate solving complex problems [1, 2].

Thus, with the advances in information technology [3], comes the need to store healthcare data and information in a way that can be retrieved and studied, and to create computational tools for support in disease prevention and medical diagnosis, comes up the proposed structuring of the data and information contained in the scope of healthcare arises [4]. This structuring of these data takes place through a pre-defined, standardized and restricted set of terminologies, facilitating the visibility of data and information [5, 6].

Transforming data without structuring into computable information is not a trivial task, according to Barbosa et al. [7]. A broad solution for such questions is the elicitation of domain knowledge and the processing and interpretation of healthcare data and information, transporting them to an ontological computational structure, formalizing the knowledge [7–9].

Knowledge Acquisition (KA) of Expert is one of the main steps in structuring data and information in healthcare and any domain, but its complexity makes it one of the most difficult tasks to perform [3]. This difficulty is due to the lack of an efficient, reliable and standard methodology for extracting and organizing knowledge from the various sources [10]. KA of expert assists directly in raising requirements for the construction of an Expert System (ES) or for structuring data and information through

D. Rocha (✉) · H. Sanches · L. Brasil
Postgraduate Program in Biomedical Engineering at Gama (FGA), University of Brasilia (UnB), Distrito Federal, Brasilia, Brazil
e-mail: dmr.meb@gmail.com

J. Lamas
Janice Lamas Clinic of Radiology, Distrito Federal, Brasilia, Brazil

L. Matheus
University Hospital of Brasilia (HUB), Distrito Federal, Brasilia, Brazil

ontology, since it abstracts all the expertise of the expert in the area in question, in order to elucidate the entire process of development [11].

This paper proposes to demonstrate some research, techniques and strategies for KA of expert in healthcare, showing the peculiarities that this domain brings in relation to the others because there is no standard methodology.

2 Knowledge Acquisition of Expert

The KA of expert and a stage involving several tasks such as: interviews/questionnaires/consultations with specialists from a specific area; study of norms, manuals, reports, legislation, books, scientific articles, theses, case studies, literary reviews; observation of scenario; database analysis; data mining, etc. [1, 6, 12]. Knowledge can be classified as specific to the domain of a problem or to problem-solving procedures, or it may be knowledge in a general scope or a specific meta-knowledge. Meta-knowledge can be understood through information about how experts use their knowledge to solve difficult problems in their professional work [12].

Turban et al. [12] state in their book that the KA is the critical point in the development of the ES. This can be explained because all the final results of this system development are conditional on the quality in the KA of expert experience that fosters the leverage of requirements, a crucial point for the successful development of any systems [6]. There are many factors that generate problems in the KA when one tries to abstract the knowledge of Specialists [3, 10]. An initial problem is the communication between the Specialist and the Knowledge Engineer [12]. Other related problems often follow the lack of time available by the specialist to be interviewed/questioned/consulted: the variation and standardization between different sources of knowledge, the refinement of the knowledge gathered, and the lack of a methodology addressing each type of domain, etc. [3, 12, 13]

In the KA of expert there are processes that must be executed in order to obtain the expected product. Among these processes we can describe in a first level the knowledge elicitation, in which the knowledge engineer uses a variety of techniques to abstract the expertise of the expert. After the elicitation of knowledge, the process of merging the acquired knowledge is carried out, in which the different sources and means of knowledge are integrated, dissolving controversies, contradictions and ambiguities that exist. In the coding or representation of the knowledge base everything is converted into rules and standards and stored in a structured way in a knowledge base, which can be a cluster of data or an ontology facilitating its manipulation. At the end, all the knowledge elicited, integrated and represented goes through the process of testing and validation, starting from entrance tests and observation of the results verifying their origin as to the knowledge acquired, all with the supervision of the expert in the related area [3, 6, 12, 14, 15].

3 Structuring Healthcare Data and Information

In the structuring of healthcare data and information, each item has its unit of measurement and its uniform format, facilitating the learning and understanding of the terminologies used because they are restricted and standardized [6, 16]. In addition, healthcare professionals can obtain the information they always need in the same visual space, because they are standardized as well as data and information can be retrieved when needed [2, 17].

The structures are constructed so as to allow complex queries to the database in a fast and precise way, in order to find relationships or correlations existing in the information contained in the structures, besides being able to apply artificial intelligence techniques for identification of patterns and to assist in the early diagnosis of pathologies [17, 18].

In this context, considering the large volume of data generated and the value they have in the treatment of patients and for future research, the need arises to treat the storage and retrieval of the information generated in a faster, reliable and safe way [1]. Figure 1 shows how the structuring of a radiological report of breast ultrasound.

The KA is a fundamental step in the construction of ontologies and in the structuring of data and healthcare information [6, 19]. Each area within the healthcare domain has peculiarities that must be treated with caution and observation, since not always a methodology used to acquire knowledge in one may not be well used for another [6].

In Fig. 2, Weng [16] demonstrates three different processes for structuring free text within healthcare, and for each there is a different KA method, which is best applied to each situation, transforming data and free text information to structured form.

4 Techniques and Strategies for Acquiring Healthcare Knowledge

When we deal with KA in healthcare, we deal with knowledge extraction through numerous sources guided by an expert of the desired area. Techniques and strategies can be adjusted and improved based on the difficulties mentioned earlier in this paper in order to narrow the bottlenecks and errors that may result from the process [6, 10, 20].

In general, the first step for a knowledge engineer in acquiring knowledge in the field of healthcare is to

Fig. 1 Structured data and report information [6]
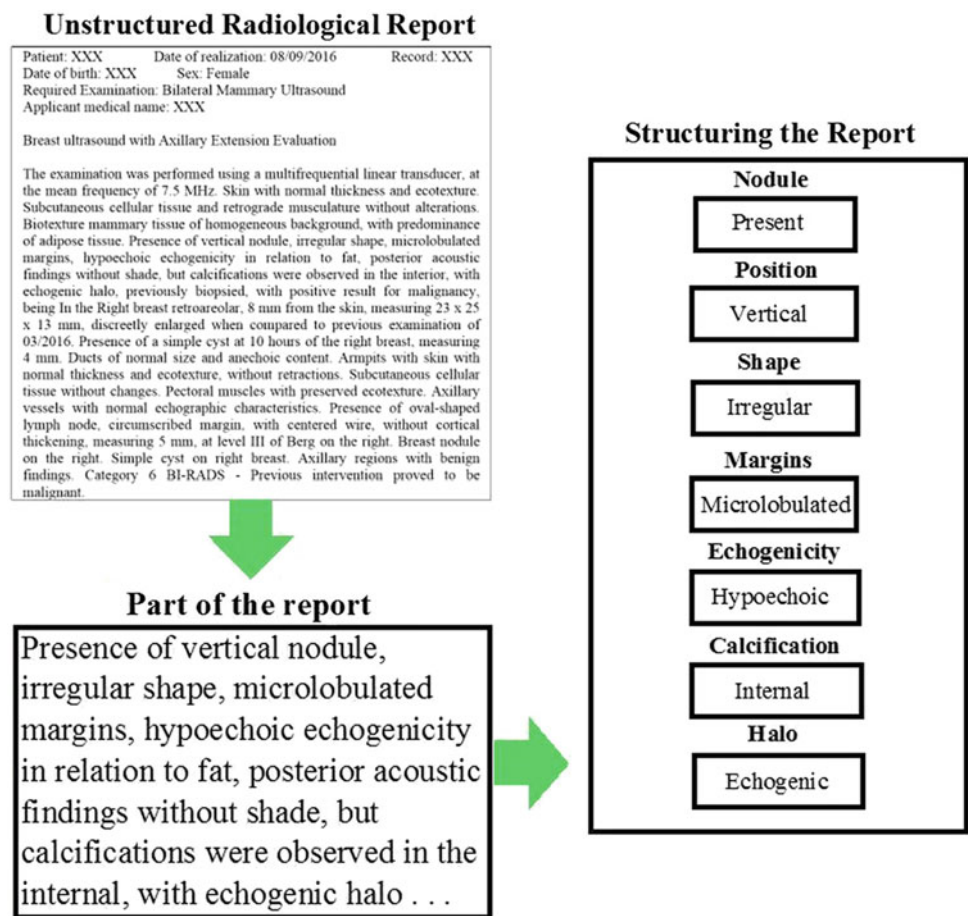
Fig. 2 A comparison of three approaches to structuring free-text [16]
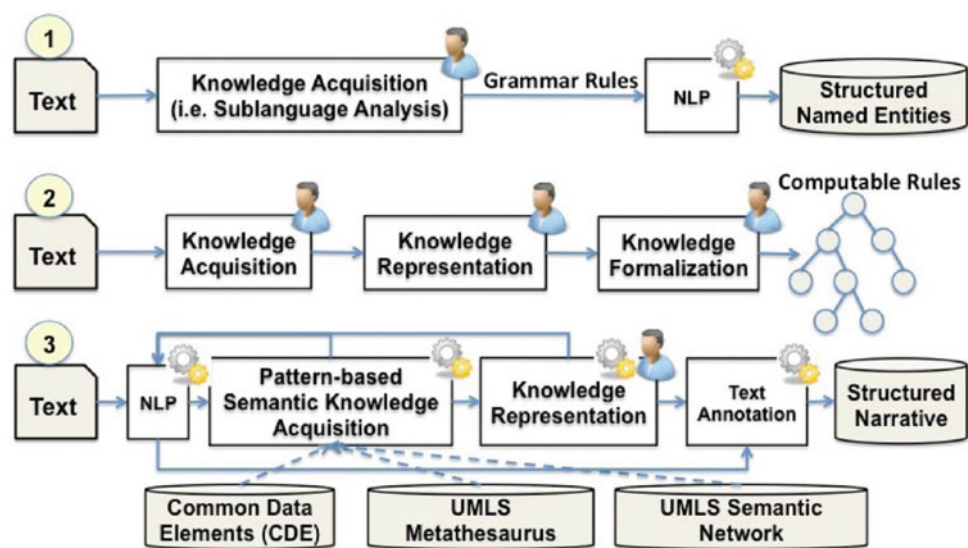
reasonably understand the domain to be addressed through a conceptual study (concepts, meanings, terms, symbols, structures, etc.). That is, to have a good idea of the subject to facilitate communication and interaction with the expert, reducing barriers and constraints [10, 20].

Often the unavailability of time can be a present factor on the part of the expert, since he has his duties and obligations and the KA can only be performed between work shifts or in his rest times. In this way the knowledge engineer must have

common sense and always check with the expert for the best times to interview [3].

Another important factor, that the knowledge engineer cannot fail to take into account and the possible difficulty of the specialist to pass on his knowledge or that the information passed on is not correctly understood/abstracted, negatively impacting the final result. One solution to the case is to carry out revisions of the collected knowledge and always interview several experts, thus having material for analysis and refinement [15].

During the KA there may be several sources for research, and during the studies, there may be variations among these sources, which can generate conflicts and ambiguities that harm and hamper the work of the knowledge engineer. An alternative to avoid these divergences is always to be guided by the most modern documentation, that uses the greatest methodological rigor for its design, optimising KA with most modern and developed aspects. In the case of divergences between specialists in the same area, the knowledge engineer must observe what the latest documentation informs and so question the specialist who has a different view, so that he can carry out an evaluation of the reliability of the information passed, performing the refinement of the collected knowledge [21].

The knowledge engineer can adapt among the several existent methodologies for the KA using the techniques and strategies that best apply to the context researched, developing his own methodology that meets his specific needs. What is important is always to carry out a background study

and planning for the KA of expert, so that it can fill all the existing gaps.

5 Related Searches

The ONTO-MAMA, a project originated in the Informatics Laboratory in Health (ILH) at the University of Brasília (UnB) at Gama (FGA), presents a process of elaboration of an ontology to describe the anatomy of the female breast. At the KA stage, three glossaries of terms for the female breast anatomy were elaborated, as well as diagrams that define the ontological model structure. The steps of formalization and implementation of the model were concluded with software Protégé, which generated as the final result of the study the ontology model of breast anatomy in format Web Ontology Language (OWL) [22]. In Fig. 3 is illustrated the Infrastructure of ONTO-MAMA.

ANAMAMA, Female Breast Anatomy System, an ILH project at UnB/FGA, is a content manager for the area of female breast anatomy, built with the help of the Methontology methodology, to read the OWL language of ONTO-MAMA. The acquisition of ANAMAMA knowledge was carried out through a questionnaire with bad, regular, good and optimal results, with the following results; questionnaire, related to the information of the mammary anatomy in the application, the following distribution was obtained: 50% Great, 43% Good, 7% Regular and none of the students considered the application bad; questionnaire,

Fig. 3 Infrastructure of ONTO-MAMA [22]
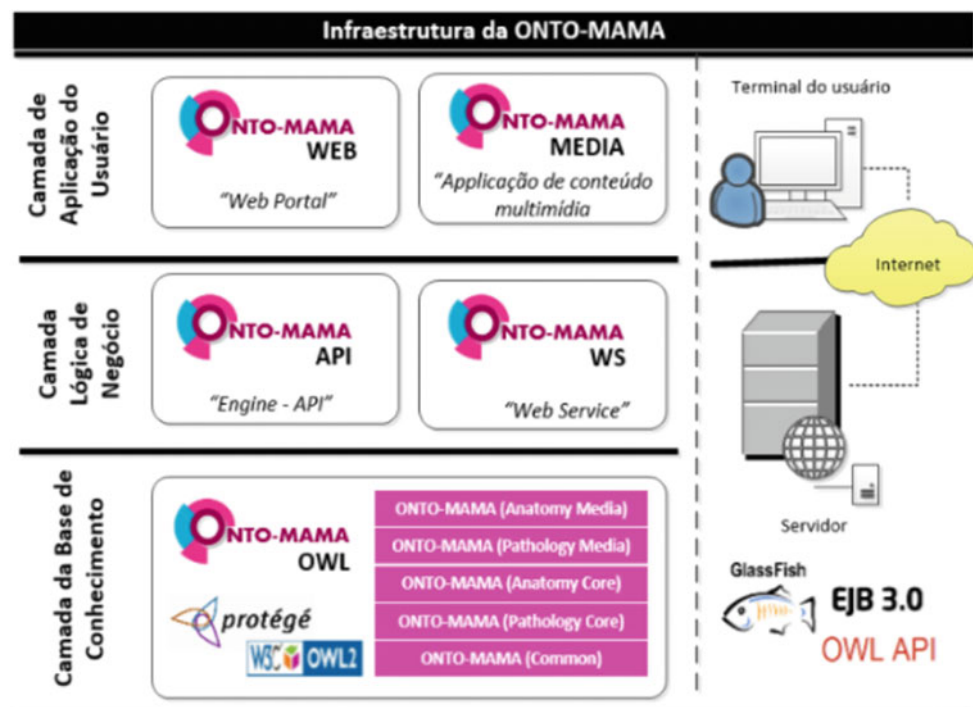
related to the organization of breast anatomy information in the application, the distribution was 4% between Bad and Regular and 96% for Good and Great; With the application of the questionnaire, the students' interest in the content with Videos (37%), Images (33%), 3D (19%) and Texts (11%) and Diseases (33%) related to Female Breast [23]. The Fig. 4 we can see how the Process macro of the navigation in the ANAMAMA application.

ONTO-MAMA-NM is the second version of the LHI ONTO-MAMA project at UnB/FGA, a tool developed to assist healthcare experts and students in the treatment of breast cancer. Its main advantage is the facility to express meanings and semantics and applicability in the information process in an automated way. The ONTO-MANA-NM developed in OWL is compatible with the Digital Imaging and Communications in Medicine (DICOM) and Health Level Seven International (HL7) standard, in order to preserve interoperability of information from patients in hospital settings. The entire development process was described, from the KA through interviews with experts in the field, analysis of documentation (theses, articles, norms and legislations), creation of sequence and block diagrams, abbreviations list, types of surgeries in the breast, the hierarchy of the treatment, until the final validation of the model with the

expert. As a result, we obtained a detailed ontology developed and implemented in the Protégé 5.1 software with the support of the methodology called Methontology. At the end of the ONTO-MAMA-NM validation process, the first ontological model for the treatment of mammary neoplasia was generated, as can be seen in the Fig. 5 [19].

LaudExUltra, a project also carried out at HIL at UnB/FGA based on the projects referenced above, presents a process for the elaboration of an ontology for structuring the report of the breast ultrasonography examination and the creation of a formwork manipulation system structured. The purpose of this project was to structure the data and information contained in the report so that they could be effectively used in clinical and scientific research through the use of computational tools such as Artificial Neural Networks for recognition of pathological patterns, Specialist Systems for medical diagnostic assistance, among others. The KA was done through interviews with experts in the field, analysis of documentation (theses, articles, reports, standards, manuals, and legislation), the creation of block and sequence diagrams, list of standardized terminologies, hierarchy of classes, until the final validation of the ontology and the system with the expert. In the end, the research resulted in the creation of the structuring ontology of breast
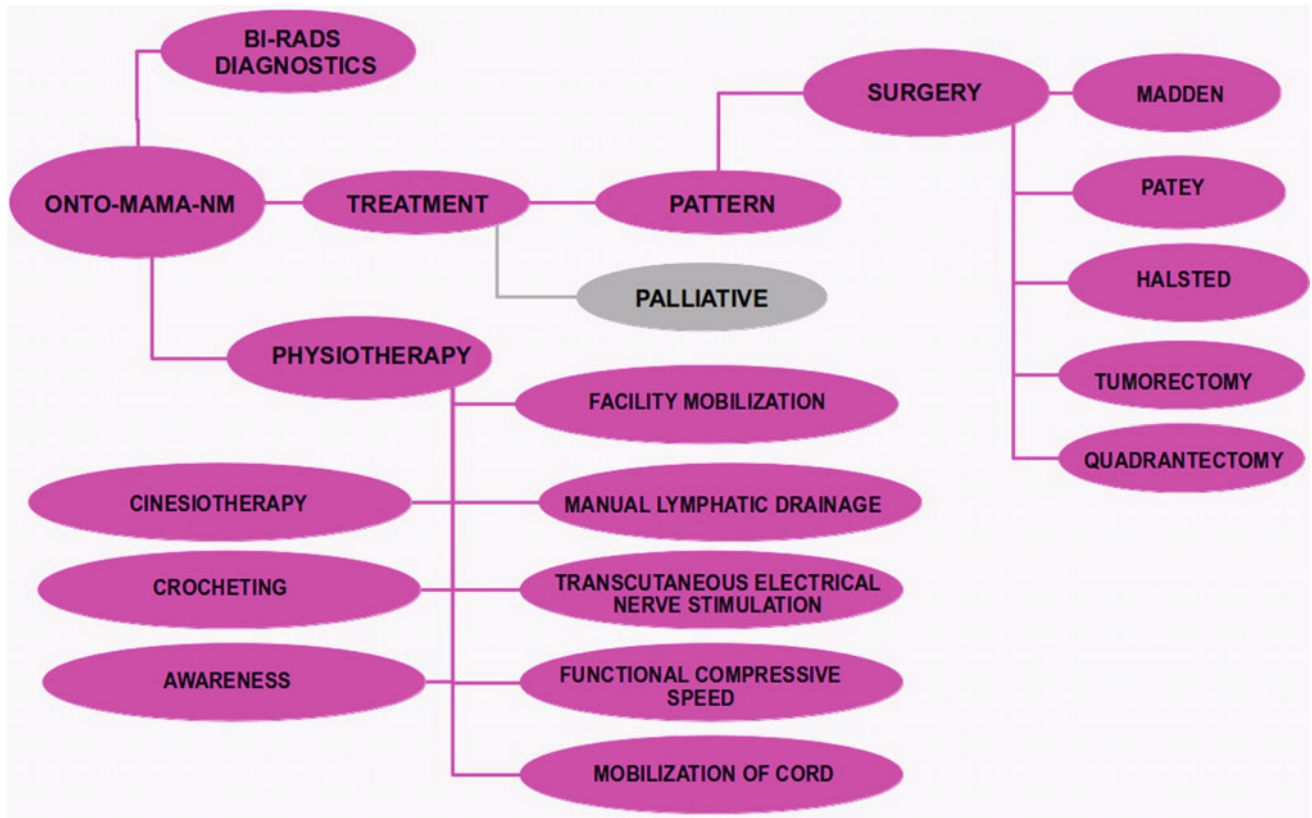
Fig. 5 Ontological model ONTO-MAMA-NM [19]
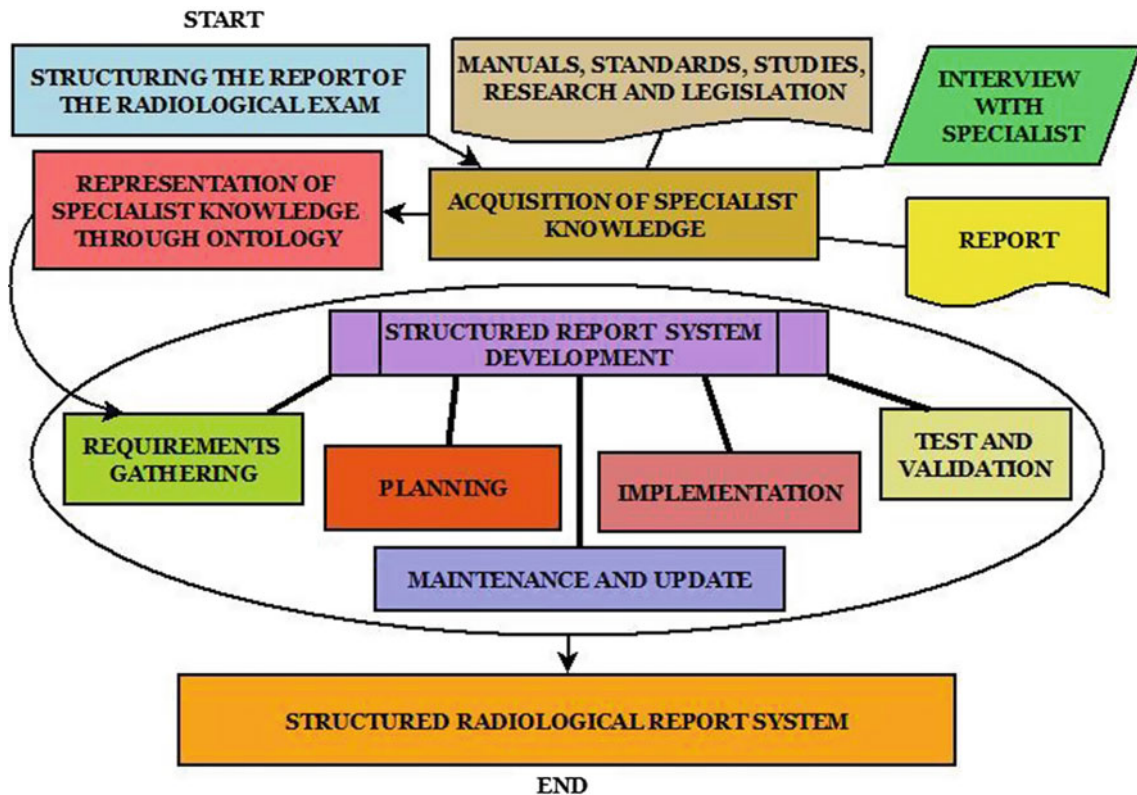
Fig. 6 Flowchart of structuring a radiological report [6]
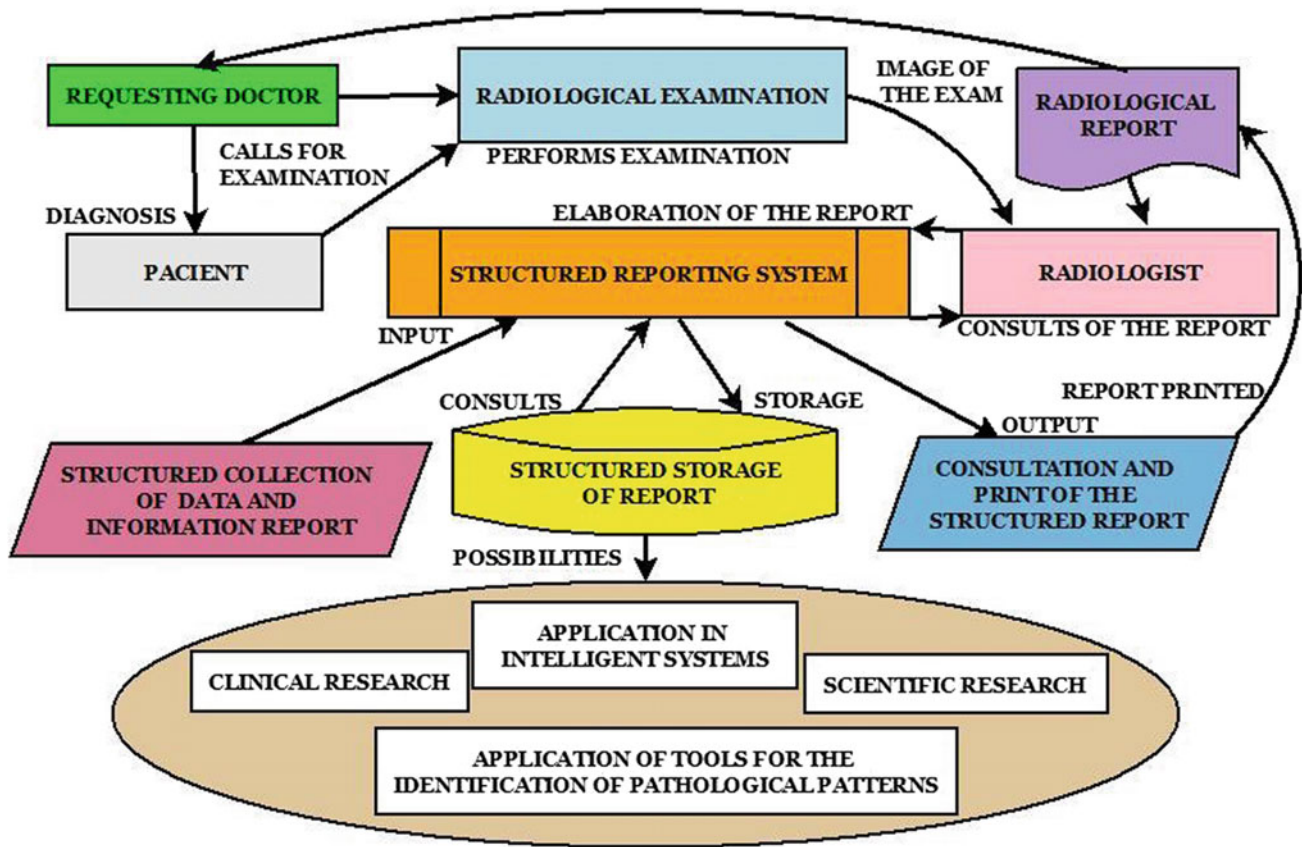
Fig. 7 Design of a structured radiological report system [6]

ultrasound examinations and the development of the structured report system for the examination of the breast ultrasound [6], as shown in Figs. 6 and 7.

6 Discussion

The Structuring healthcare data and information is a rising trend, which enables clinical and scientific research to benefit the patient [1, 6]. Ontology is commonly used to formalize data structure and healthcare information, with several methodologies for its creation/maintenance, with *Methontology* being the most used [19]. The KA is a necessary step towards the creation of ontologies and the structuring of data and information in general, fostering the survey of requirements for the development of expert systems [16].

Several studies are being carried out to structure data and information in healthcare. Among these studies, the ONTO-MAMA-NM [19], projects stand out, created in the ILH of the UnB/FGA, that structure the data and information on the treatment of female breast neoplasia and the

structuring of the report of the breast ultrasound examination [6] through the ontology. All of these inform the massive use of the KA OF EXPERT for its development and completion.

In conclusion, in this paper we provide a brief overview of the KA of expert for structuring healthcare data and information, of some techniques and strategies for better employment of this process.

Conflict of Interests The authors deny that there are other interests besides the dissemination of the scientific knowledge contained in the present research.

References

1. Rocha, D.M., Lamas, J.M., Brasil, L.M.: Formulation of a checklist for structuring the report on abdominal ultrasound. Brazilian Congr. Biomed. Eng. **XXV**, 1 (2016)

2. Oliva, J.T.: Automation of the Process of Mapping Medical Reports to a Structured Representation. State University of Western Paraná (2014)

3. Gaines, B.: Knowledge acquisition: Past, present and future. Int. J. Hum Comput Stud. **2011**, 1–37 (2013)

4. Travis, A.R., et al.: Preferences for structured reporting of measurement data. an institutional survey of medical oncologists, oncology registrars, and radiologists. Acad. Radiol. **21**, 785–796 (2014)

5. Barbosa, F.: Radiological Report: Comparison of the Efficiency of the Transmission of Information between the Free Text and the Structured Report. University of São Paulo (2009)

6. Rocha, D.M. et al.: Structuring the Radiological Report. In: A. do V Congr. Bras. Eletromiografia e Cinesiologia e X Simpósio Eng. Biomédica. Uberlandia, pp. 839–842 (2018)

7. Barbosa, F., Traina, A.J., Muglia, V.F.: Meta-generalis: a novel method for structuring information from radiology reports. Appl. Clin. Inform. **7**, 803–816 (2016)

8. Sabino, A.R., Heinzle, R.: Tool for ontology construction from non-structured data. Comput. Beach 141–150 (2015)

9. Gregory, G., Pretto, F.: Data mining for knowledge discovery in health promotion data. Rev. Destaques Acadêmicos **8**, 51–65 (2016)

10. Hidalgo, E.M.P.: Knowledge Acquisition Method for Specialist Systems for Fault Diagnosis: Application of Reliability and Risk Analysis Techniques. University of São Paulo

11. Coelho, K.C., Almeida, M.B.: Knowledge acquisition method for specialist systems for fault diagnosis: application of reliability and risk analysis techniques. Encontros Bibli Rev. eletrônica Bibliotecon e ciência da informação **17**, 47–74 (2012)

12. Turban, E., Aronson, J.E., Liang, T.-P.: Knowledge Acquisition, Representation, Reasoning. Decis, pp. 174–253. Support Syst. Intell. Syst, Opening Vi (2007)

13. Council, S.S.S.: Knowledge Acquisition A study of Knowledge Acquisition Methods Currently Used to Support Candidates Taking SVQ Social Services and Healthcare at SCVF level 7and/ or in SVQ Social. Scottish Soc. Serv. Council Compass 76

14. Payne, P.R.O., et al.: Conceptual knowledge acquisition in biomedicine: a methodological review. J. Biomed. Inform. **40**, 582–602 (2007)

15. Mendes, D.: Clinical Practice Knowledge Acquisition and Interrogation using Natural Language. University of Evora (2014)

16. Weng, C., et al.: Towards symbiosis in knowledge representation and natural language processing for structuring clinical practice guidelines. Stud. Heal. Technol. Inf. **1343**, 113–119 (2014)

17. Barbosa, F.: Methodology for Structuring Information of the Radiological Reports. University of São Paulo (2013)

18. Warren, L., et al.: A model of knowledge acquisition in early stage breast cancer patients **18**, 69–72 (2013)

19. Sanches, H.M.: ONTO-MAMA-NM: An Ontological Model of Treatment of Mammary Neoplasia. University of Brasilia

20. Peruzzo, D.M., Silveira, S.R., Parreira FJ (2013) Specialist System to Assist in the Diagnosis of Depression. University of Fed St Maria. pp. 1–32

21. Santos, G.S.: A strategy based on knowledge acquisition for risk management in the requirements in a distributed XP development. Iber. Mag. Inf. Syst. Technol (2016). https://doi.org/10.17013/risti.20.18-33

22. Klavdianos, P.B.L., et al.: ONTO-MAMA: an ontology of the female breast anatomy applicable to a virtual learning environment. Pan. Am. Health Care Exch **2011**, 315 (2011)

23. Braga, D.S.: Female Mammary Anatomy Tutoring Using an Artificial Neural Network Service-Oriented Interactive Activation and Competition. University of Brasilia (2015)

Logistic Regression Classifiers in the Analysis of HIV-1 Use of CCR5 and CXCR4 Coreceptors

Cesar Barros, Letícia Raposo, and Flavio Nobre

Abstract

The development of HIV coreceptor antagonists—such as maraviroc—has made coreceptor use diagnosis mandatory for each patient in the clinical setting. Technical issues presented by Trofile™, the gold standard phenotypic assay, hindered its use as a routine diagnostic tool. This issue has lead to the development of genotypic algorithms, whose evaluations are based on V3 region sequences of the viral envelope. These algorithms proved to be cheaper, easier to use, and less time consuming than the phenotypic method. One of them, geno2pheno has also gained widespread use since it showed 86.5% concordance with the gold-standard phenotypic assay. In this regard, the present project aims to develop accurate predictive models based on V3 sequence information. For this, 2,109 DNA sequences from HIV-1 subtype B were used. Data labeled with geno2pheno's results were used to construct and evaluate the logistic regression models. Three parsimonious models were obtained, and their evaluations showed promising results. These outcomes encourage us to continue the project of an easy to use and more accurate alternative for HIV coreceptor use diagnosis, capable of guiding clinical decision making regarding the use of CCR5 antagonists in HIV treatment.

Keywords

HIV • Coreceptor use diagnosis • Logistic regression

1 Introduction

AIDS has become a devastating pandemic, and this fact has stimulated the continuous improvement of anti-HIV therapies and diagnostic tools. In 1996, studies verified the HIV requirement of a second cellular coreceptor—CCR5 or CXCR4—to infect target cells [1, 2]. Since then, drugs that antagonize these molecules and act by blocking HIV from entering host cells have been studied [3, 4]. The approval for use of maraviroc—the first CCR5 antagonist—has made the HIV coreceptor usage diagnosis mandatory for each patient in the clinical setting [5, 6].

The gold standard phenotypic assay, Trofile™, has presented technical aspects that hinder its use as a routine diagnostic tool. Conversely, genotypic algorithms, whose evaluations are based on V3 region sequences of the viral envelope, proved to be cheaper, easier to use, and less time consuming than the phenotypic method [6, 7]. In this sense, different HIV European guidelines have recently recommended the use of validated genotypic algorithms to manage the use of CCR5 antagonists in clinical setting [6]. Among them, geno2pheno is one of the most widely used algorithms for HIV coreceptor use diagnosis [6, 7]. Its operational mode is based on phenotype-genotype paired database, and relies on the use of support vector machine and decision trees to obtain the predictive outputs [6–9].

Based on the use of HIV sequences labeled with geno2-pheno's results, this study presents logistic regression models and evaluates their abilities to predict viral coreceptor use. In this regard, the project aims to develop models with potential to be used in routine clinical decision-making as an easy to use and more accurate alternative for clinical management of HIV treatment.

2 Methods

This study used DNA sequences from HIV-1 subtype B. These sequences were relative to V3 variable region of the viral envelope, with 105 nucleotides encoding for 35 amino acid peptides. In this regard, 2,333 DNA sequences were retrieved from the Los Alamos database (https://www.hiv.lanl.gov/content/index) and downloaded in January 2018. DNA sequence alignment and coreceptor use diagnosis were

C. Barros (✉) · L. Raposo · F. Nobre
Biomedical Engineering Program, Federal University of Rio de Janeiro - UFRJ, Ilha do Fundão, Rio de Janeiro, RJ, Brazil
e-mail: cesar.barros@peb.ufrj.br

performed by geno2pheno coreceptor 'original method' (http://coreceptor.bioinf.mpi-inf.mpg.de/). The predictions were realized under a false positive rate of 10%, and then used in the modeling as response variables.

Those peptide sequences obtained by geno2pheno, that presented ambiguities in their amino acid composition, were removed from the dataset. The remaining 2,109 sequences (1,541 from CCR5-tropic virus, or R5 virus, and 568 from CXCR4-tropic virus and CCR5/CXCR4 dual-tropic virus, or non-R5 virus) contained 35 amino acid positions. The categorical data was constructed using the international code for each amino acid, combined to its respective position P1 to P35. Then, this categorical data was converted into numerical variables using the amino acid values of hydrophobicity established by Eisenberg's scale [10].

The 2,109 sequences were randomly split into groups according to the proportion of 0.7:0.3. The train set contained 1,477 sequences, 398 from non-R5 virus, and the test set contained 632 sequences, 170 from non-R5 virus. Balanced train data was obtained by random splitting of the 1,079 R5 sequences into three subsets, containing respectively, 360, 360, and 359 R5 sequences. Each subset was combined to the same 398 non-R5 sequences, showing a final proportion of 0.53:0.47. Those amino acid positions with Eisenberg's values that were invariant in more than 95% of the training data were excluded from the modeling. Within the 35 sequence positions, the excluded ones were P1, P3, P4, P6, P7, P8, P17, P26, P28, P30, P31, P33, and P35. The positive class was represented by the non-R5 (NR5) sequences.

The three balanced training sets presenting 22 sequence positions that remained in the analysis were used to obtain three logistic regression models. Then, the models were submitted to variable selection by the backward stepwise method, employing the Akaike information criterion (AIC) [11]. The resulting three parsimonious models (A, B and C) were evaluated for prediction performance, according to accuracy, sensitivity, specificity, Kappa index, and area under the ROC curve (AUC) using the test data. Analyses were performed using R software, version 3.4.3.

3   Results

Train and test data were used to respectively obtain and evaluate logistic regression models for HIV-1 coreceptor use diagnosis. The trained models showed the following equations and AICs:

$$\text{Model A} = 2.74 + 1.20P9 + 0.64P10 - 0.80P11 - 2.04P12 + 1.32P13 - 0.74P14$$
$$- 3.58P15 + 1.17P16 + 0.44P18 + 0.85P19 + 2.89P20 + 0.47P21$$
$$+ 0.58P22 - 1.38P23 - 2.64P24 - 1.03P25 - 0.66P27 - 2.50P29$$
$$- 1.50P32 - 0.69P34, \text{ and AIC of } 636.6.$$

$$\text{Model B} = 1.49 + 1.33P9 + 0.59P10 - 0.66P11 - 3.26P12 + 1.29P13 - 0.90P14$$
$$+ 1.50P16 + 0.47P18 + 1.34P19 + 3.43P20 + 0.60P21 - 1.41P23$$
$$- 3.08P24 - 1.17P25 - 0.76P27 - 3.69P29 - 1.77P32, \text{ and AIC of } 614.2.$$

$$\text{Model C} = 1.50 + 0.77P9 + 0.84P10 - 0.68P11 - 3.94P12 + 1.13P13 - 1.11P14$$
$$+ 1.09P16 + 0.67P18 + 1.45P19 + 3.36P20 + 1.07P21 - 1.40P23$$
$$- 3.59P24 - 1.06P25 - 2.52P29 - 2.01P32 - 1.52P34,$$
$$\text{and AIC of } 610.4.$$

The performance measures including accuracy, sensitivity and specificity confidence intervals (95%) are presented in Table 1. The ROC curves with their respective threshold values are illustrated in Fig. 1.

4   Discussion

Beyond its technical, cost-benefit and time-consuming advantages over phenotypic assays, geno2pheno has also gained widespread use since it showed 86.5% concordance with

Table 1 Performances of the three parsimonious models

Measure\Model	A	B	C
Accuracy (%) [CI95%]	87.7 [84.8–90.1]	81.8 [78.6–84.7]	84.2 [81.1–86.9]
Sensitivity (%) [CI95%]	81.2 [75.3–87.1]	84.1 [78.2–89.4]	86.5 [81.2–91.2]
Specificity (%) [CI95%]	90.0 [87.2–92.6]	81.0 [77.1–84.4]	83.3 [79.9–86.6]
Kappa index	0.694	0.584	0.634
AUC	0.880	0.886	0.887
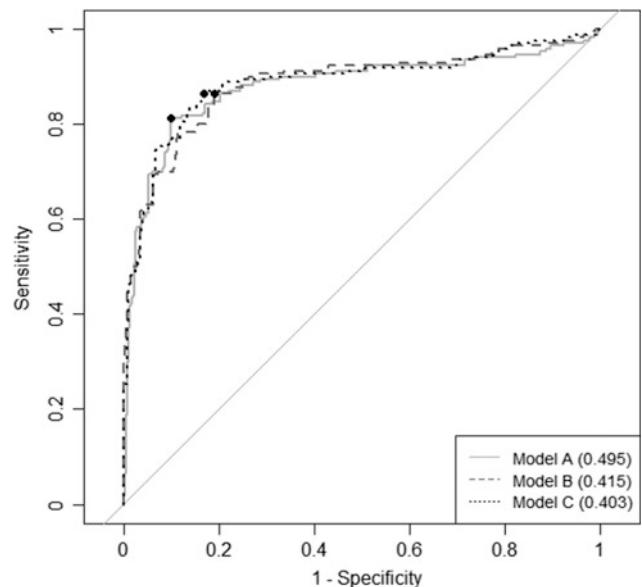
Fig. 1 ROC curves. The cut-off points are shown in parentheses and indicated in the curves by circles

Trofile™ in the analysis of clinically derived HIV-1 samples [12]. Although the algorithm is trained mainly by sequences from HIV-1 subtype B, it recently showed a high accuracy in the prediction of sequences from subtype C virus [13].

In our study, the logistic regression models showed a good concordance with geno2pheno's results. The less parsimonious Model A presented the best accuracy (87.7%) and specificity (90.0%). These results were statistically different compared to the models B and C. Otherwise, the sensibility results showed no statistically significant difference within the models, presenting a mean of 83.9%.

Concerning the input data, the models were trained with 758 (Models A and B) and 757 (Model C) sequences paired with geno2pheno's outputs. The eventual increase of this data may improve the performance measures and, consequently, the concordance between the predictive methods. It should be also noted that the use of unbalanced training data can lead to loss of robustness and generalization capacity, both considered important characteristics in effective predictive analysis [14]. In this sense, balanced data was used to control this risk and avoid the generation of models that could perform better in favor of a larger class present in the training data.

Among the explanatory variables, nine were associated with positive regression coefficients, and eight of them were shared by the three models. Of these, five had a p-value < 0.001 (0.1%), demonstrating a very strong and positive association with the NR5 outcome. Eleven variables were associated with negative coefficients, and eight of them were shared by the models. Of these, five had also a p-value < 0.001, demonstrating a very strong but negative association with the NR5 outcome.

Interestingly, within the variables with negative coefficients and p-value < 0.001, three—P11, P24 and P25—are the explanatory variables used for the predictions of two early algorithms: rules 11/25 and 11/24/25 [15, 16]. However, as previously mentioned, other seven variables had a p-value < 0.001. Moreover, other variables also showed real associations with the NR5 outcome, as demonstrated by a p-value < 0.01 (1%). This information reinforces the existence of an intrinsic and functional V3 region variability, a fact that has been confirmed in the last years [6]. In this context, there are evidences that various genetic clusters within the V3 region act as stronger determinants in HIV coreceptor use compared to specific changes, such as those associated to rules 11/25 and 11/24/25 [6]. The discriminative power of the newer algorithms is positively correlated with their capacity to properly interpret the genetic variability of the V3 region [6]. As a consequence, the less discriminative algorithms were gradually replaced by more sophisticated ones, like geno2pheno.

Clinical demand associated with HIV coreceptor use diagnosis by genotypic tools has attracted a great deal of research to this scientific field. The development of an algorithm with good accuracy for the diagnosis of subtype A viral sequences is an very recent example of this ongoing effort [17]. This demand encourages us to improve the modeling by including other techniques and predictors to increment the predictive analysis of HIV-1 subtype B sequences, and by expanding the diagnosis to other viral subtypes. In addition, the consolidation of a phenotypic database will allow a direct comparison of our models to the main genotypic algorithms, including geno2pheno.

5 Conclusion

In summary, the logistic regression models showed promising results in HIV-1 subtype B coreceptor use diagnosis. These outcomes encourage us to continue the development of an easy to use and more accurate genotypic alternative for this diagnosis, with the potential to guide clinical decision making regarding the use of CCR5 antagonists in HIV treatment.

References

1. Deng, H., Liu, R., Ellmeier, W., et al.: Identification of a major co-receptor for primary isolates of HIV-1. Nature **381**(6584), 661–666 (1996)
2. Dragic, T., Litwin, V., Allaway, G., et al.: HIV-1 entry into CD4R cells is mediated by the chemokine receptor CC-CKR-5. Nature **381**(6584), 667–673 (1996)
3. Maeda, K., Nakata, H., Ogata, H., et al.: The current status of, and challenges in, the development of CCR5 inhibitors as therapeutics for HIV-1 infection. Curr. Opin. Pharmacol. **4**(5), 447–452 (2004)
4. Seibert, C., Sakmar, T.: Small-molecule antagonists of CCR5 and CXCR4: a promising new class of anti-HIV drugs. Curr. Pharm. Des. **10**(17), 2041–2062 (2004)
5. Anonymous: FDA approves maraviroc tablets. AIDS Patient Care STDS **21**(9), 702 (2007)
6. Poveda, E., Alcaní, J., Paredes, R., et al.: Genotypic determination of HIV tropism—clinical and methodological recommendations to guide the therapeutic use of CCR5 antagonists. AIDS Rev. **12**(3), 135–148 (2010)
7. Aiamkitsumrit, B., Dampier, W., Antell, G., et al.: Bioinformatic analysis of HIV-1 entry and pathogenesis. Curr. HIV Res. **12**(2), 132–161 (2014)
8. Beerenwinkel, N., Daumer, M., Oette, M., et al.: Geno2pheno: estimating phenotypic drug resistance from HIV-1 genotypes. Nucleic Acids Res. **31**(13), 3850–3855 (2003)
9. Soulie, C., Derache, A., Aime, C., et al.: Comparison of two genotypic algorithms to determine HIV-1 tropism. HIV Med. **9**(1), 1–5 (2008)
10. Eisenberg, D., Weiss, R.M., Terwilliger, T.C.: The hydrophobic moment detects periodicity in protein. Proc. Natl. Acad. Sci. U.S. A. **81**(1), 140–144 (1984)

11. Akaike, H.: A new look at the statistical model identification. IEEE Trans. Autom. Control **19**(6), 716–723 (1974)

12. Skrabal, K., Low, A.J., Dong, W., et al.: Determining human immunodeficiency virus coreceptor use in a clinical setting: degree of correlation between two phenotypic assays and a bioinformatic model. J. Clin. Microbiol. **45**(2), 279–284 (2007)

13. Riemenschneider, M., Cashin, K.Y., Budeus, B., et al.: Genotypic prediction of coreceptor tropism of HIV-1 subtypes A and C. Sci. Rep. **6**(24883), 1–9 (2016)

14. He, H., Garcia, E.: Learning from imbalanced data. IEEE Trans. Knowl. Data Eng. **21**(9), 1263–1284 (2009)

15. Cardozo, T., Kimura, T., Philpott, S., et al.: Structural basis for coreceptor selectivity by the HIV type 1 V3 loop. AIDS Res. Hum. Retroviruses **23**(3), 415–426 (2007)

16. Isaka, Y., Sato, A., Miki, S., et al.: Small amino acid changes in the V3 loop of HIV type 2 determines the coreceptor usage for CXCR4 and CCR5. Virology **264**(1), 237–243 (1999)

17. Lochel, H.F., Riemenschneider, M., Frishman, D., Heider, D.: Scotch: subtype A coreceptor tropism classification in HIV-1. Bioinformatics **1**, 1–6 (2018)

Performance of Two Types of Motors in Robotic Hands Made by Additive Manufacturing

Ana Beatriz Simões Fontana, Mariana Sêda Cunha,
Roberto Luiz Assad Pinheiro, Elisa Rennó Carneiro Déster,
and Rani de Souza Alves

Abstract

This paper presents the development and comparison of two robotic hands printed on 3D, which will be used in the future as prosthetic hands. Both models were created through the scanning of real hands. These robotic hands are different due to specific motors and sensors which are part of each one. Prototype A has a mini high-power servo motor with metallic gears, in comparison with prototype B, which uses linear stepper motor actuators. They were made by using printer 3D technology and black and blue ABS filaments were used in the process. After assembling, the motors and the sensors were adapted, both are responsible for the movement and perception of touch, respectively. Through the resistance tests, it was concluded that prototype B is more effective, because it supported 20 kg, whilst the other supported 11 kg.

Keywords

Additive manufacturing • Motor • Robotic hand

1 Introduction

Assistive technology is a field dedicated to the study and development of projects aimed at helping disabled people and enabling them to have a better quality of life [1].

An example of assistive technology is the prosthesis used to contribute to the needs caused by amputation [2]. Amputation can be defined as the removal of body parts and it can be led to by several factors, as trauma from accidents

and tumors [3]. Nowadays, it is not possible to specify the incidence of amputation. However, as the registers in military hospitals are more specific, there is more occurrence in war periods [4]. Therefore, the development of prosthesis reached a larger scale in order to help the war-wounded as a result of amputation [5, 6].

Nonetheless, there are failures in prosthesis manufacturing. High price, weight and little functionality are amongst them [7]. Thus, the studies about this device must be consistent and new projects have to be proposed and developed. It is possible to obtain prosthetic models that meet the needs of patients in a more effectively way and allow more autonomy, functionality and a better quality of life.

Through 3D printing technology, a new alternative to building prosthesis was revealed [8]. There are many open-source projects on the internet. One example is the humanoid robot INMOOV [9]. This model was chosen to adapt a humanoid robotic arm to be used as a sensory prosthesis [10]. However, it was necessary to improve this project, by virtue of the anatomy and the technology selected. Hence, the aim of this current project was the development of a better anatomical robotic hand, which can be used as a hand prosthesis in the future.

2 Materials and Methods

2.1 Prototypes

The robotic hand was developed by using a model obtained through a partnership between CDTTA and the Federal University of Goias. The model was made by scanning a real hand. The prototypes were 3D printed by using a prt1(B3D) printer. The materials used were black and blue acrylonitrile butadiene styrene (ABS) filaments. The density used in the printing was 70% and it were applied two 0.42 mm layers.

After completing the printings, the pieces were manually adapted to fit the robotic hands. Furthermore, in order to fit the sensor wires and the motors, the parts' perforation had to

A. B. S. Fontana · M. S. Cunha · R. L. A. Pinheiro ·
E. R. C. Déster · R. de Souza Alves (✉)
Centro de Desenvolvimento de Tecnologia Assistiva (CDTTA),
Instituto Nacional de Telecomunicações (INATEL), Av. João de
Camargo, 510, Centro, Santa Rita do Sapucaí, MG 37540-000,
Brazil
e-mail: rani@inatel.br

be adapted. Firstly, they were opened with the help of soldering iron, drill and a grinder. Thermo retractable tubes were inserted to enable wire fitting. Finally, to close the additional holes and to improve the finishing, a solution containing ABS filament immersed in acetone was used and applied where needed.

Subsequently, the dimensioning of motors responsible for individual movement of each finger was started. Two prototypes, called A and B, were printed and different motors and sensors were placed in each one so that it was possible to verify their efficiency. Five mini high-power, high-force and metal-geared Adafruit servo motors were used in prototype A [11]. For prototype B, five motors were also used, but 20DBMXXD1B-K linear stepper motor actuators [12] and they were provided by Portescap. The motors were fixed inside the hands' palmar region by using a thermal blower and a soldering iron to customize the inner part.

In order to do the finger flexion, twisted multifilament wires are attached to the motors. To perform the extension movement, elastic filaments were put in the internal part of the fingers. They exert the motor opposite force to return the fingers to the extended position. The mini servo motors are configured to 0° and 160° in order to move. On the other hand, the linear actuators execute 835 steps until the end of their linear course and they move the axis by 20 mm horizontally. To perform the flexion, the axis are returned to first position.

Other robotic hands' technology was the pressure sensors which are used to identify touch. Prototype A has 0.2″ and 0.5″ resistive force sensors, while B has *Velostat*, a resistive polymer. Both are able to vary the resistance according to the pressure applied on them. They were positioned on the surface of distal and medial phalanges. On prototype A, the sensors were coated with silicone and attached to the finger tips like a cape. On B, *Velostat* was sewn on the tip of a glove with a conductive thread to prevent wire breaks, and the glove had the tips cut

The robotic hand general control is done by a bracelet, which has four buttons made with *Velostat*, the resistive polymer. The buttons' functions are: fingers flexion and extension, a random preprogrammed movement and a safety lock, activated to prevent the other buttons from working. This lock was designed for people who do physical activities or move the arm often. All the required softwares for movement and prototype control were developed on Arduino IDE.

2.2 Mechanical and Energy Consumption Tests

In order to test the functional parameters of both A and B prototypes two different analysis were conducted: the movement test and the resistance test. For the two tests,

voltage and current were measured to calculate energy consumption (power) and the temperatures from inside the hands and from the motors' surface.

The robotic hands were positioned orthogonally to the ground with fingers down in both tests (Fig. 1). All measures were performed in triplicate.

A LM35 [13] sensor inside the rear end was used to measure the internal temperature (Fig. 2). The temperature monitoring on motor surfaces were performed with the help of a Type k thermocouple [14] in direct contact with the metal housing of one motor for each prototype.

On the other hand, an ammeter and voltmeter were used to measure energy consumption, which were connected to the motor power supply. During the tests, data was collected every minute and inserted on the Excel spreadsheet.

Movement Test

This first test was important to observe the behavior of the models in real situations, where the prototypes can be submitted to continuous movements, so it can be possible to analyze their performances. Therefore, both prototypes were programmed to perform a 10-s flexion loop 10-s extension loop to move the fingers during 5 min. Data was collected initially and at every minute. After 5 min, the prototype stayed stationary for 2 min with the fingers completely open. This process was repeated three times.
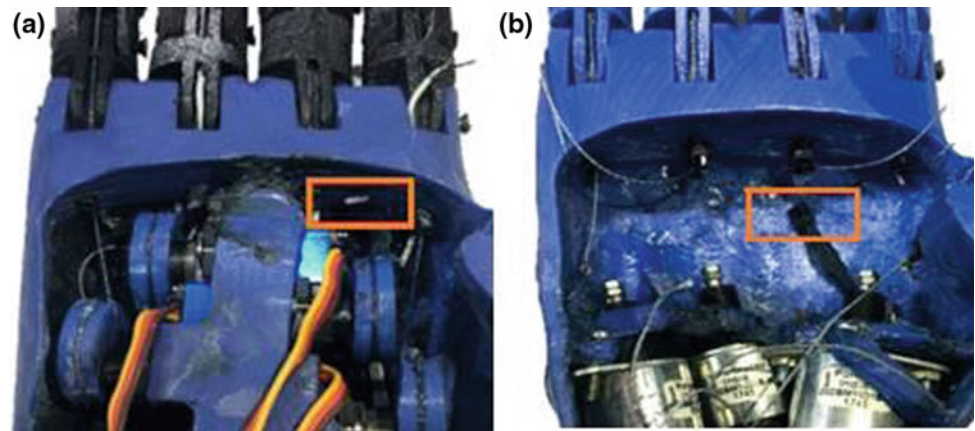
Resistance Test

The robotic hands were closed and supporting weights for 5 min, which were added gradually until the hands were not

Fig. 1 Positioning of the robotic hand to perform movement and resistance tests

Fig. 2 Positioning the temperature sensor. **a** Prototype A. **b** Prototype B

Fig. 3 Weights used in the resistance test to combine the load supported

able to support them anymore. After 5 min, the hands were opened and stayed in rest for 2 min. The measurement variables were verified and noted three times for each weight. In total, the hands supported each weight for 15 min and the 1-kg ones were added every nineteen minutes. Weights Corre Corre were used in the process (Fig. 3). When the load reached 6 kg, a 20-min break was needed for both models.

2.3 Statistical Analysis

The data was organized in tables and descriptive statistics was done. The data were submitted to the test of normality, and then the comparisons between the both prototypes were performed by using Mann–Whitney test with 0.05 significance.

The prototypes were compared to each test separately (movement and resistance). In the movement test, the instant from 0 to 5 of all values were compared. Moreover, the values which were generated during the 5 min of the test were used in the calculation of the resistance test.

3 Results

3.1 Prototype

The two prototypes and its dimensions are presented in Fig. 4. Prototype A weighs 300 g and B weighs 400 g. Prototype B has a 5 cm extra part to protect the linear actuators.

The picture also shows the pressure sensors. Prototype A presents the 0.2″ and 0.5″ resistive force sensors, and B has *Velostat*, a resistive polymer.

3.2 Movement Test

Energy Consumption

The voltage, current and power results for both prototypes are shown in Figs. 5, 6 and 7.

Significant differences were not found among the 3 tests for both prototypes. The voltage for the linear motors was significantly higher ($p < 0.0001$) than prototype 2 for all minutes measured in all tests. The average voltage for servo motors was 4.98 ± 0.15 V and for the linear actuators was 6.48 ± 0.36 V.

For the current consumption measurements, when comparing the values of all tests for each prototype, there were not significant differences. The average current for prototype A was 0.78 ± 0.30 A and 0.90 ± 0.07 A for prototype B.

When comparing the energy consumption data (power), prototype A (3.81 ± 2.99 W) was significantly different ($p < 0.05$) from prototype B (5.82 ± 1.35 W) for all test repetitions.

Fig. 4 **a** Dimensions of prototypes A. **b** Dimensions of prototype B
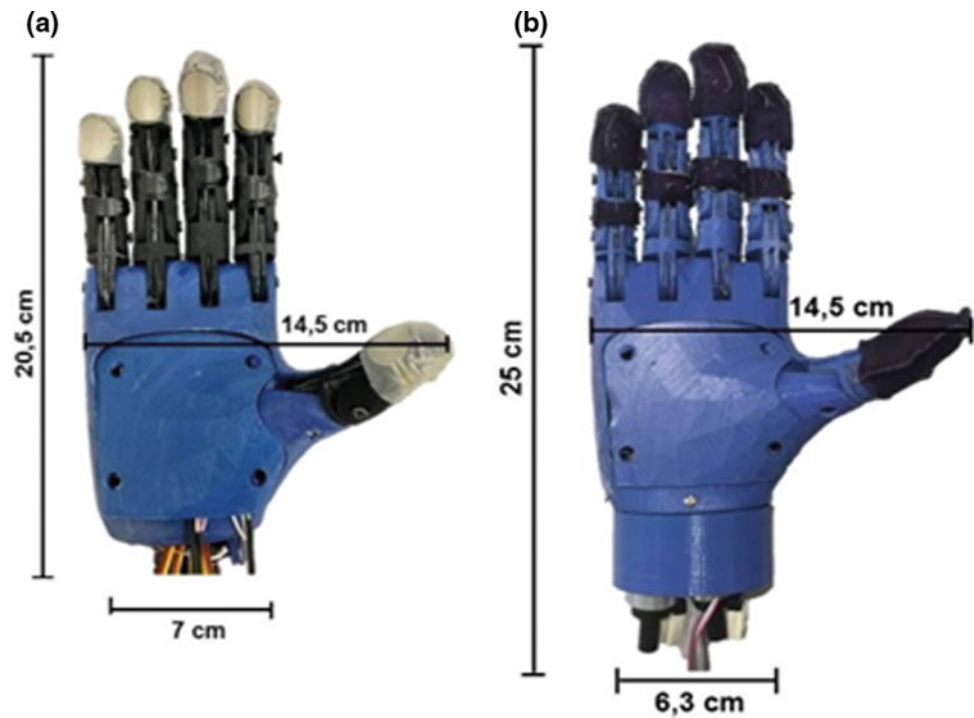
Fig. 5 Voltage movement test chart for both prototypes

Temperature

The results of internal temperature of the hands and temperature of the motors' surface for the movement tests are shown in Table 1.

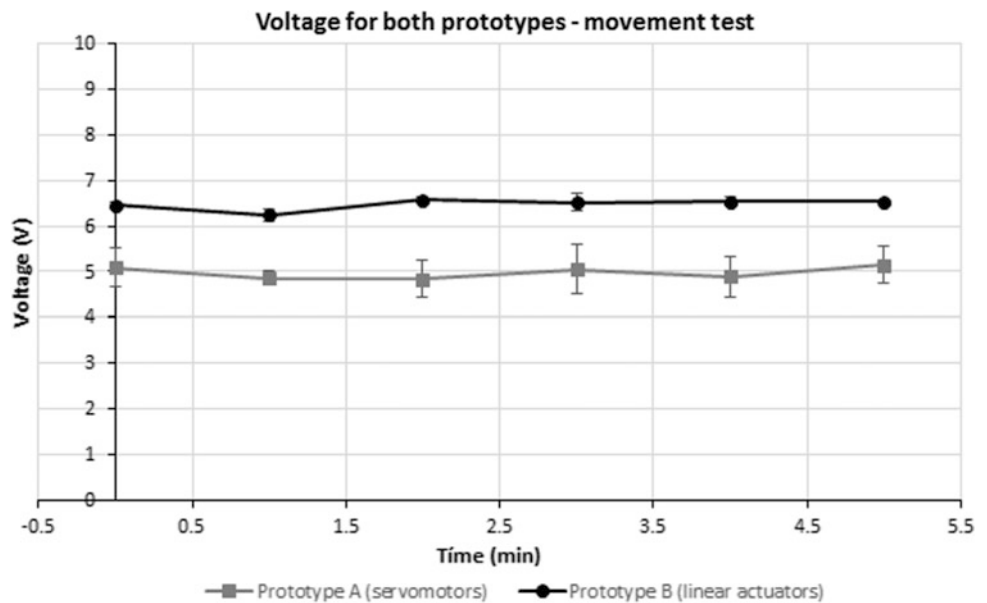The average internal temperature for prototype A significantly increased comparing the first test to the 2 and 3 tests. For prototype B, the significant increase on the internal temperature was observed between the test 1 and 2, between the test 1 and 3 and comparing the tests 2 and 3. When the motor temperatures were compared, the same results were found for prototype A and for prototype B, the temperatures of test 1 were significantly different from the others tests, also with significant differences between the test 2 and 3.

3.3 Resistance Test

The voltage, current, power and temperature results during the resistance test for both prototypes are presented in the Figs. 8, 9, 10 and 11. For prototype A, the second and fifth

Fig. 6 Current movement test chart for current for both prototypes

Current for both prototypes - movement test
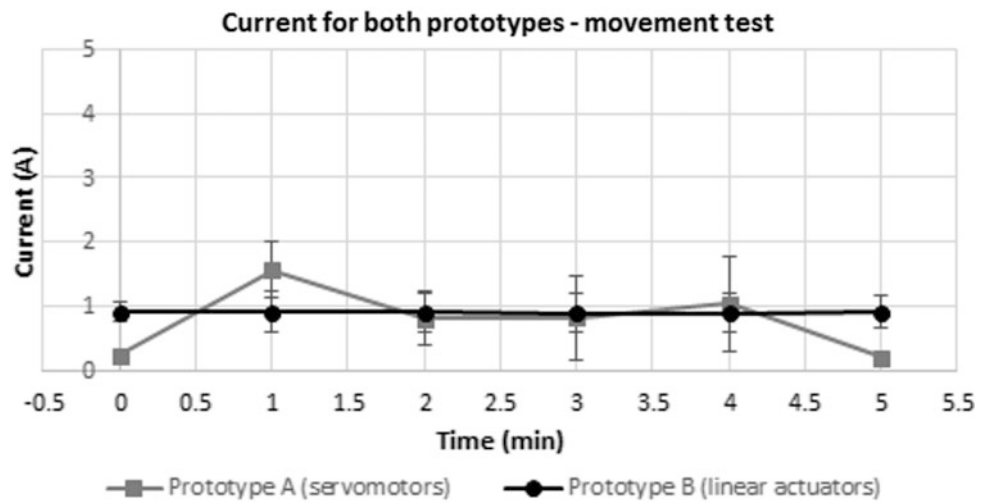
Fig. 7 Power movement test chart for both prototypes

Power for both prototypes - movement test
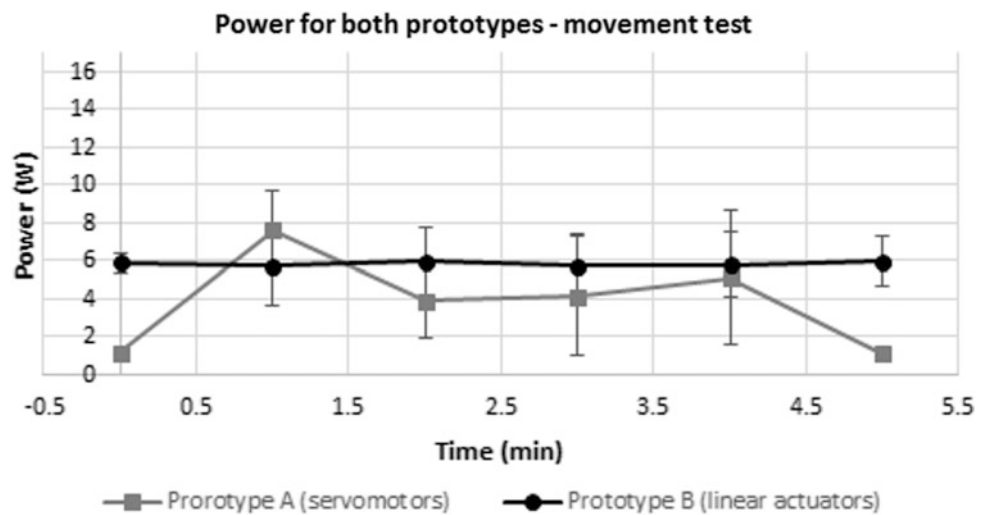
Table 1 Results of internal temperatures and temperatures of the motors for both prototypes

Prototype	Internal temperatures (°C)		Motor temperatures (°C)	
	A	B	A	B
Test 1	27.04 ± 0.60	26.04 ± 0.25	27.67 ± 3.14	37.33 ± 3.01
Test 2	27.20 ± 0.40	26.94 ± 0.64*	32.00 ± 0.89*	44.00 ± 3.16*
Test 3	28.58 ± 0.40*+	28.08 ± 0.41*+	32.33 ± 1.03*	47.83 ± 2.14*+

*Significant differences related to test 1 (p = 0.03)
+Significant difference between tests 2 and 3 (p = 0.03)

fingers stopped its function at 6 kg. Nevertheless, the prototype would not support more weight at 11 kg anymore. For prototype B, the fingers supported weight until the 20 kg.

For the voltage analysis, prototype A has an average value (4.66 ± 0.06 V) significantly lower (p < 0.0001) than prototype B (6.56 ± 0.13 V). There were no major variations among the data for each mass of each prototype.

For current, the consumption of prototype A (2.02 ± 0.09) was significantly higher (p < 0.0001) than prototype B (1.14 ± 0.04). It is possible to notice that the prototype B had a linear behavior than the prototype A for the current consumption for all masses supported.

For the power during the resistance test, the average value for prototype A (9.38 ± 0.38) was higher than the one for prototype B (7.50 ± 0.37), significantly (p < 0.0001).
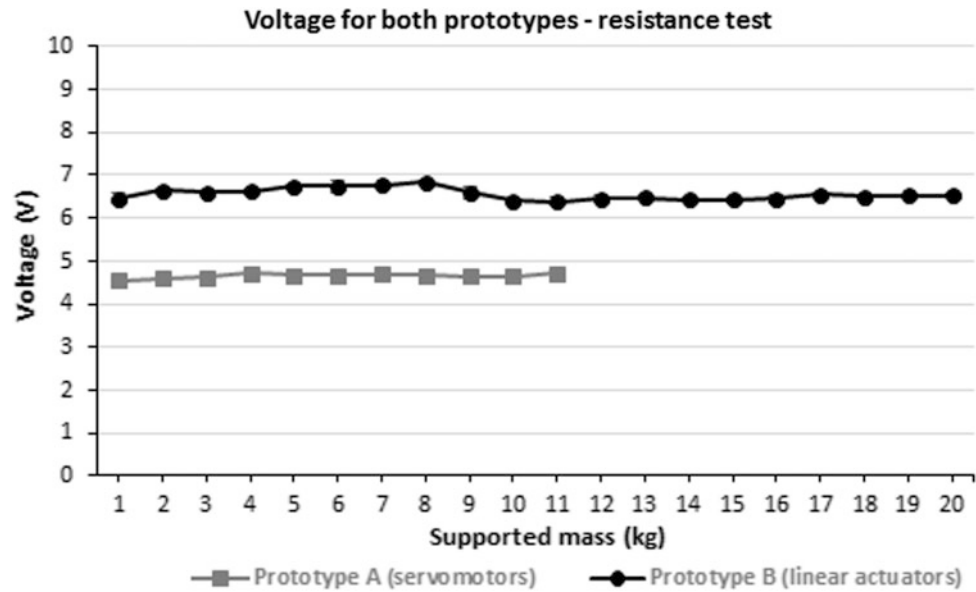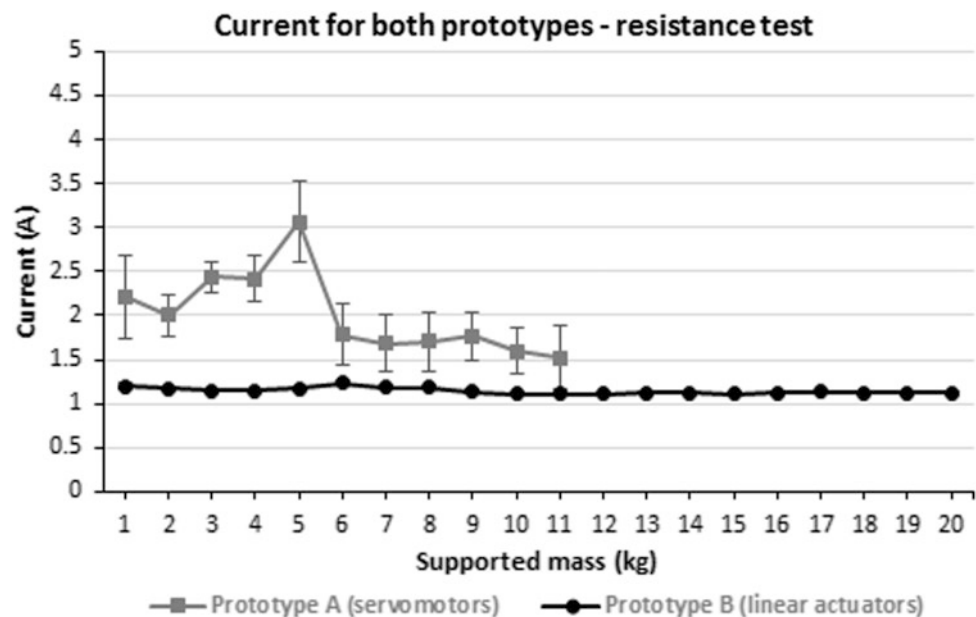
The behavior for the power was similar to the consumption of the current and the prototype A showed more variations during the tests comparing with the prototype B.

Due to the twenty-minute pause at 6 kg, the internal and motor temperatures for both prototypes presented a decay, which can be observed in Fig. 11. The internal average temperature for prototype A from 1 to 5 kg was 34.50 ± 2.90 °C and 31.90 ± 0.76 °C from 6 to 11 kg. The motor temperatures were 87.82 ± 11.44 °C (from 1 to 5 kg) and 68.58 ± 12.18 °C (from 6 to 11 kg). For prototype B, the internal temperature was 29.32 ± 2.79 °C (from 1 to

5 kg) and 31.13 ± 0.92 °C (from 6 to 20 kg). The motor temperatures were 65.78 ± 11.60 °C (from 1 to 5 kg) and 67.54 ± 5.23 °C (from 6 to 20 kg).

4 Discussion

During the printing and development of prototypes, several challenges were tackled. In order to succeed in the completion of the robotic hands, some pieces were printed a few times as a reflect of faulty parts. These problems occurred

Fig. 10 Power resistance test chart for both prototypes
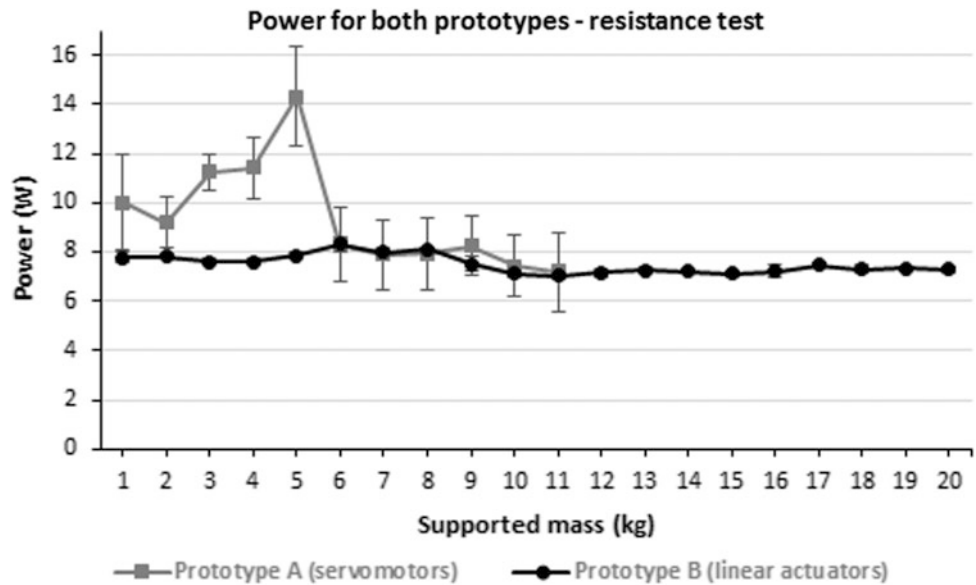
Fig. 11 Internal temperature resistance test chart for both prototypes
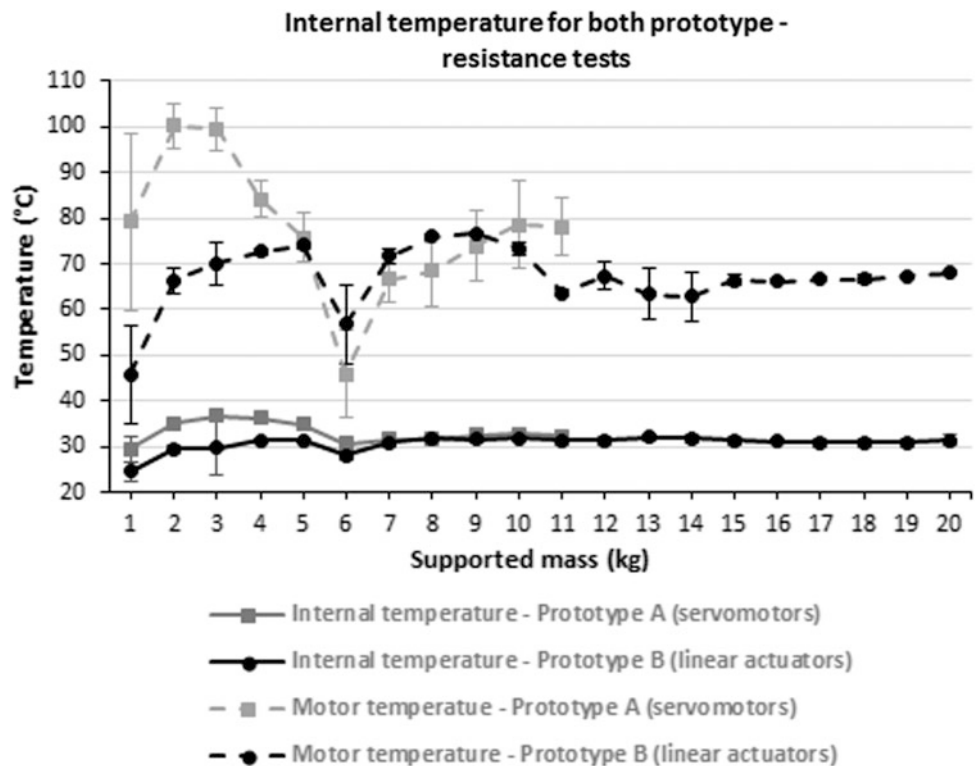
due to several factors, for instance: temperature changes in the environment in which printing is being performed, which causes fissures on the pieces; lack of adherence of the piece to the table, which makes the pieces move or be poorly formed; blackout that interrupts the printing process.

As reported, the first prototype of this study [10] was adapted from one humanoid robotic arm. Therefore, the anatomy and distribution of pressure points were an issue, so a new model was required. After the tests, it was possible to

compare the first device, adapted from INMOOV [9], with those robotic hands. The main differences concern the anatomy. The prosthesis has hand and forearm, the weight is 902 g, whilst the robotic hands are only the hands and the weight are 300 g (A) and 400 g (B).

This difference between the weights of the two prototypes is caused by the 5.0 cm extra part printed for prototype B. This was necessary because the linear actuators are bigger than servo motors and they need a 20 mm gap to move the

horizontal axis and perform the movement. This fact might be a nuisance when considering using the robotic hand as prosthesis. In this scenario, a prosthesis using prototype B (with linear actuators) will be recommended for forearm amputation, while prototype A model can be used in a more distal amputation.

Through the tests, it was noticed that prototype B is the most effective one. With regard to energy consumption, high loads were supported with a stable consumption. The maximum temperature reached was 78 °C on the motor surface and 32 °C on the inside. Prototype A reached 100 °C on the motor surface and 38 °C on the inner parts.

The tests were conducted with the wrist opened, allowing the heat to be extinguished partially. If exposed to complete closure to be fixed to the user, the temperature will tend to rise internally and externally. This increase in temperature can cause burns to the user, because the fixation structure will be rather close to the motor, apart from causing the melting of the plastic or damaging the lines of movement. Through the results gathered, it can be concluded that prototype B has seemed to be more acceptable. A study concerning the dissipation of the heat and how to minimize overheating must be conducted.

The results with prototype B shows that this robotic hand is ready to be adapted as a prosthesis and presents that it will have many usability possibilities because its sturdiness.

The sensors were damaged as a result of the resistant tests. Thus, a better way to fix these sensors is being designed. One of them would be the use of a polyurethane resin. Following tests will be conducted in order to identify the most effective sensor. Others tests will be performed after fixing the new sensors so it may verify the impact resistance.

Regarding the performance of the motors, it was noticed that the linear actuators used in prototype B have all the features expected for project efficiency, but their high cost is the disadvantage compared to the servo motor used in prototype A. The linear motor costs roughly U$287.50 and the servo motors, U$59.75. The high cost makes the project unfeasible to design a more accessible hand prosthesis.

5 Conclusion

The project began with the choice of the model that would be printed and several challenges were dealt with due to it. During the printing process, some nuisances were found, sometimes caused by printing failures, others by power outages or part settings, and this is the reason why printing was done repeatedly.

Once the printings were completed, the development process of the robotics hands started and manual work was performed in order to allow better adhesion between the pieces.

After having the prototypes assembled, the motors were dimensioned and the servo motors (prototype A) and linear actuators (prototype B) were defined, being fixed and tested subsequently.

Through the analysis of the tests conducted, it is clear that prototype B has more significant results compared to prototype A. However, when it comes to the value, prototype B presents very high cost to be used as a robotic hand.

More effective methods for sensor fixation will be studied as future improvements. Another point to deal with is to obtain the cost and benefit of the robotic hand, combining the efficiency of prototype B and the cost of prototype A.

Therefore, it will be possible to continue the process and adapt the prototype to a prosthesis and thus, achieving the goal of helping people with physical disabilities have more autonomy and better life conditions.

References

1. Brasil. DECRETO N° 13.146, DE 6 DE JULHO DE 2015. Lei Brasileira de Inclusão de pessoas com deficiência. http://www.planalto.gov.br/ccivil_03/_ato2015-2018/2015/lei/l13146.htm. Accessed 15 Dec 2017
2. Polis, J.E.: Projeto e Construção de Parte Estrutural de Prótese de Mão Humana com Movimentos. Accessed 24 Feb 2018
3. Bolth, J.L., Badke, M.R., Hepp, D.R., Santos, A.M.: Acompanhamento de paciente com amputação de membro superior: Um estudo de caso 612–615 (2011)
4. Gabarra, L.M., Crepaldi, M.A.: The psychological aspects of amputation surgery, pp. 2–14 (2009)
5. Goellner, P., Paiva, L.L., Goellner, S.V.: Reinventing life: a qualitative study on the cultural meanings attributed by amputees to body reconstruction through implantation of prosthetics. Interface—Comunic. Saúde Educ. **12**, 485–497 (2008)
6. Carvalho, F.S., et al.: Prevalência de amputação em membros inferiores de causa vascular: análise de prontuários. Arq. Ciênc. Saúde Unipar 23–30 (2005)
7. Carvalho, G.L.: Proposta de um método de projeto de prótese de membros superiores com a utilização da engenharia e análise do valor, pp. 2–166 (2004)
8. Ribeiro, W.C., Miyadaira, A.N., Ferruzzi, Y.: Development of low-cost robotic hand. Accessed 15 Mar 2018

9. Langevin, G.: Hand and Forarm—InMoov Open Source 3D Printed Life-Size Robot. http://www.inmoov.fr/hand-and-forarm. Accessed 18 Feb 2018

10. Celani, G., Silvério, M.B., Pinheiro, R.L.A., Alves, R.S., Dester, E.R.C., Carvalho, F.V., Costa, F.E.C.: Adaptação de um projeto de robô humanoid impresso em 3D emu ma prótese sensorial de mebro superior. Accessed 18 Feb 2018

11. Adafruit®. https://www.adafruit.com/product/2307. Accessed 18 Jan 2018

12. Portescap. http://www.portescap.com/sites/default/files/20dbm_k_specifications.pdf. Accessed 12 Jan 2018

13. Texas Instruments. http://www.ti.com/lit/ds/symlink/lm3519.pdf. Accessed 18 Feb 2018

14. Ecil Temperatura Industrial. www.ecil.com.br/upload/produto/pdf/termopares.pdf. Accessed 18 Feb 2018

Recognition of Navigation Commands for a Smart Walker Through Force Sensors

Mario F. Jiménez, Anselmo Frizera, and Teodiano Bastos

Abstract

Smart Walkers are robotic devices that may be used to improve physical stability and sensorial support for people with lower-limb weakness or poor balance. Even though such devices may offer support to people who cannot safely use conventional walkers, their interaction strategy with the user still needs to be improved. In this context, this work presents a strategy to obtain navigation commands of a smart walker based on multi-axial force sensors. It also shows how to obtain the user's motion intention from the interaction between his/her arms and the robotic walker. An admittance controller and an adaptive filter are used to obtain the user's cadence. To validate the proposed strategy, a lemniscate curve marked on the floor is used to be followed by both the user and the smart walker. The parameters of the admittance controller are adjusted to find the more suitable values that allow a natural locomotion. As a result, the user can command the smart walker and establish a natural speed for his/her locomotion (around 0.3 m/s) using the admittance control.

1 Introduction

Mobility is fundamental to the independence and daily living of people, consequently, it is essential to quality of life, wellbeing, and overall functional independence [1]. After 60 years of life, disabilities related to hearing, sight and movement, in addition to diseases such as heart failure, stroke, chronic respiratory disorders and dementia often appear [2]. These can cause mobility impairments and a reduction in the quality of life in elderly population, which is increasing around the world [3].

Due to these mobility impairments, several studies have been conducted to develop assistive mobility devices that aid people with gait disabilities to allow them to improve balance and increase independence during locomotion [4].

Conventional assistive devices for mobility, such as walkers, canes, and crutches can be used to improve balance and weight support [5], however, they may not be enough to offer different functional domains (i.e. physical support, sensorial and cognitive assistance) that elderly need to navigate independently and functionally.

Advances in robotics allowed the incorporation of actuators and sensors in conventional walkers to turn them in Smart Walkers (SWs) able to provide users with support for guidance, orientation and localization, in addition to a better physical support, sensorial and cognitive assistance, and also to be used for health monitoring, through the use of advanced human-machine interfaces [6]. In this context, it is necessary to develop interaction strategies and interfaces to detect the human motion intention in order to obtain a natural and safety human-robot interaction (HRI).

According to the literature, the human motion intention in robotic walker can be measured or estimated through the use of force sensor and/or laser sensor. For example, PAMM [7] employs a six-axis force/torque sensor mounted under the user's handle to serve as the main HRI. MAR [8] integrates two force/torque sensors mounted at the handles of the SW, which are used to drive the device and for motion control. In

M. F. Jiménez (✉) · A. Frizera · T. Bastos
Federal University of Espírito Santo, Vitória, 29075-910, Brazil
e-mail: mariof.jimenez@gmail.com; mario.hernandez@aluno.ufes.br

A. Frizera
e-mail: anselmo@ele.ufes.br

T. Bastos
e-mail: teodiano.bastos@ufes.br

ISR-AIWALKER [9] and in *i-Walker* [10], force sensors at the handlebar are used to detect the user intention. In other works, force sensor resistors (FSR) and laser ranger finder (LFR) are used in a multi-sensor fusion method to detect the human walking intention [11]. In [12], the human movement intention is captured by force sensors on the arm support. Regarding the SW control, a control strategy commonly used to develop a natural interaction between the human and the SW is the admittance control [7, 8]. This control strategy depends on the users' force/torque sensing, and allows detecting the user's motion intention in a natural way, without the need for external sensors in either the user or the environment.

Using an admittance control strategy and force sensors localized under the forearm support on the SW, this work presents the development of a strategy to detect the human motion intention to command a SW. The user's cadence oscillation and others noise present in the force signals are filtered by both Fourier Linear Combiner (FLC) and Weighted-Frequency Fourier Linear Combiner (WFLC) filters [12]. This way, taking advantage the physical contact between the user and the SW, an interface to detect the human motion intention in a natural and intuitive way is also presented.

This work is organized as follows. Section 2 describes the smart walker and the physical interaction interface, presenting also the admittance control strategy and the adaptive filters. Section 3 describes the experimental setup and the strategy of interaction. Section 4 shows and discusses the experimental results. Finally, conclusions and future works are presented in Sect. 5.

2 Materials and Methods

The SW used in this work was developed at UFES/Brazil (Fig. 1a). This SW consists of a pair of differential rear wheels driven by DC motors and a front caster wheel. The wheel velocities are measured with optical shaft encoders H1 (US Digital, USA). An inertial sensor BNO055 with 9 DOF is used to provide the robot orientation, and an embedded computer (PC/104-Plus standard) is used for control and processing tasks, which are integrated into a real-time architecture based on Matlab-Simulink Real-Time xPC Target Toolbox. The SW provides assistance during gait based on two 3D force sensors MTA400 (Futek, US) located under the handle support (see Fig. 1b) and an LRF sensor (Hokuyo URG-04LX) used to detect the user's legs' position. Information from both sensors are used to determine the user's motion intention [12], and also as safety
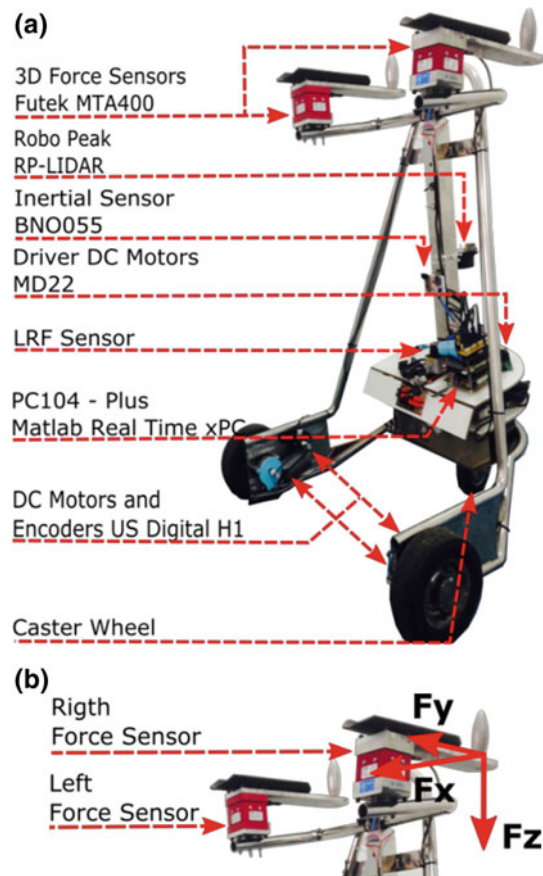
Fig. 1 **a** UFES Smart Walker; **b** Physical human-robot interface based on force sensor

parameters for the user. Obstacle avoidance, SW localization and environment maps are carried out by an RP-LIDAR laser sensor located on the SW front (Fig. 1a).

2.1 Admittance Control Strategy

The UFES's SW employs an impedance controller [8] to relate linear and angular velocities with the force signals that are produced naturally on the forearms when the user is assisted by the SW, thus recognizing the human motion intention. In this case, the force signals on the y axis captured by each force sensor are used to generate a force $F(t)$ and torque $\tau(t)$ signal on the SW, defined as

$$F = -\frac{F_{LY}(t) + F_{RY}(t)}{2}, \qquad (1)$$

$$\tau = -\frac{F_{LY}(t) + F_{RY}(t)}{2} \cdot d, \qquad (2)$$

where F_{LY} is the force on the left arm, F_{RY} is the force on the right arm, and d is the distance between both sensors.

$F(t)$ and $\tau(t)$ signals are used by the admittance controller to generate the desired linear $v_c(t)$ and angular $\omega_c(t)$ velocities for the SW, defined as

$$v_c(t) = \frac{F(t) - m_v \dot{v}(t)}{d_v} \qquad (3)$$

$$\omega_c(t) = \frac{\tau(t) - m_\omega \dot{\omega}(t)}{d_\omega}, \qquad (4)$$

where the masses m_v and m_ω, and the damping d_v and d_ω are parameters that have to be adjusted, as they have a direct influence on the HRI.

Both velocities are also used to impose not only the start and end of the locomotion with the SW, but also a comfortable gait speed.

2.2 Navigation Command Recognition

When the user is walking assisted by the SW, the natural cadence oscillation is transmitted to the velocity commands of the SW through both force sensors, due to the user has a physical contact with the SW. This oscillation and other mechanical vibrations of the SW structure make necessary the use of a filter to obtain the user's motion intention, and thus produce a natural locomotion without increasing or decreasing the SW speed, which may be a consequence of the cadence.

The algorithm to extract the motion intention is an adaptive filter proposed in [13], which uses a Fourier Linear Combiner (FLC) algorithm to estimate and cancel cadence components of each input signal (F_{LY} and F_{RY}), and a Weighted-Frequency Fourier Linear Combiner (WFLC) algorithm to perform the filtering of the force sensors signals, and thus obtain the force $F(t)$ and the torque $\tau(t)$ (see Eqs. 1 and 2).

The FLC algorithm allows canceling quasi-periodic signals with a low computational cost, hence, it may be implemented in real time [12]. The model is based on harmonics of the dynamic Fourier model given by

$$S_r = \sum_{r=1}^{M} [w_r \sin(r\omega_0) + w_{r+M}\cos(r\omega_0)], \qquad (5)$$

where S_r is composed of a set of M harmonics of the sine and cosine signals with frequency $f_0 = \omega_0/2\pi$, and frequency weight w_r [13]. The Least Mean Square (LMS) algorithm is used to estimate the amplitude coefficients of w_r. Then, the weights ω_0 and w are adapted through (ε_k), which

is the result of the subtraction of the input signal (y_k) and the estimate of the oscillatory component (S_r), i.e.:

$$\varepsilon_k = y_k - S_r \qquad (6)$$

On the other hand, the WFLC algorithm is an adaptive signal processing technique that forms a truncated Fourier series model of a periodic signal of unknown frequency and amplitude [13]. This algorithm minimizes the error ε_k between S_k, which is the component of input y_k without oscillatory component, with the following harmonic model

$$\hat{\varepsilon}_k = S_k - \widehat{W}_k^T X_k, \qquad (7)$$

where X_k is the reference input vector of S_r that consists of M harmonics of sines and cosines, and W_k are the amplitude adaptive weights. Thus, Eq. 7 can be written as

$$\hat{\varepsilon}_k = S_k - \sum_{r=1}^{M} [w_{rk} \sin(r\omega_{0k}k) + w_{rk+M}\cos(r\omega_{0k}k)]. \qquad (8)$$

Using the LMS algorithm, the frequency and amplitude can be updated as

$$\omega_{0k+1} = \omega_{0k} + 2\mu_0 \hat{\varepsilon}_k \sum_{r=1}^{M} r(w_r x_{M+r} - w_{M+r} x_r), \qquad (9)$$

$$W_{k+1} = W_k + 2\mu_1 \varepsilon_k X_k. \qquad (10)$$

Finally, the algorithm WFLC must set four parameters: M, which is the number of harmonics of the model; $\omega_{0,0}$, the instantaneous frequency at initialization; μ_0, the frequency update weight; and μ_1, the amplitude update weight. It is necessary to take into account that the correct selection of μ_0 and μ_1 parameters can be a complex task [12].

Figure 2 shows the algorithm to eliminate the cadence from the force signals (F_{RY} and F_{LY}). In the first instance, the force signals are filtered through a low pass filter to eliminate the mechanical vibrations of the SW. Then, the WFLC estimates the user's gait cadence using the user's legs position, which is measured with the LRF sensor. With the cadence and force signals after applying the low-pass filter (F_{LPF}), the FLC algorithm estimates the cadence frequency (F_{cad}). After, F_{cad} is used to filter the F_{LPF} signal, and finally, the filtered force signals are used to detect the user's motion intention.

3 Experimental Setup

Twenty subjects without previous training with the SW participated in the experiments. A computer was used to record both the SW velocities and the user's data, such as

Fig. 2 Block diagram to eliminate the cadence from force signals
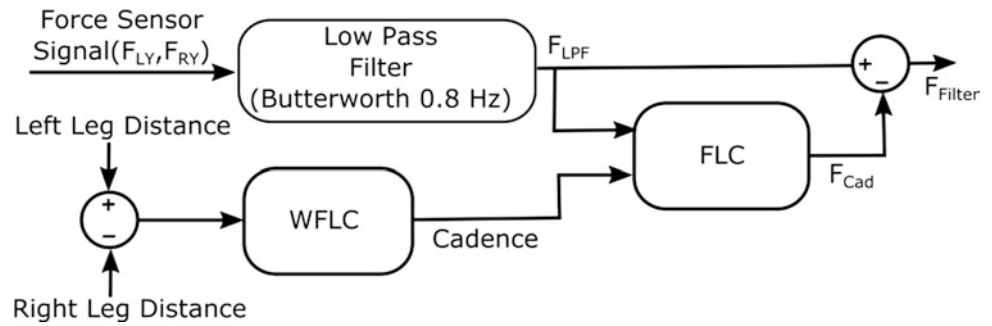
Fig. 3 Experiment where the subjects were asked to follow a lemniscate curve indicated on the floor

Fig. 4 Following the lemniscate curve

force and torque applied to the SW. The mean weight of the participants was 66.72 ± 13.63 kg, and their mean height was 1.66 ± 0.075 m. At the first part of the experiment, the user was asked to follow a straight line. Once the user was able to move the SW without any extra effort on his/her lower-limbs or hip, i.e., only applying natural effort for the gait, the values of the admittance control parameters were assigned. It is necessary to take into account that the mass values vary according to the user's discharge force on t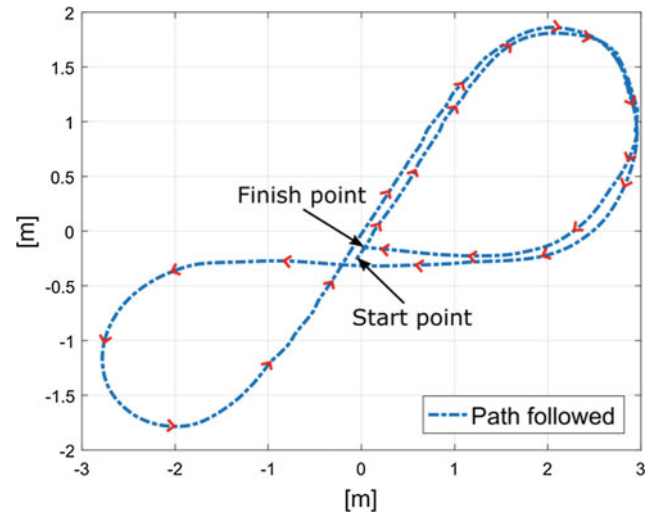he SW, which have m_v of 16.35 ± 5.21 and m_ω of 0.234 ± 0.063. Regarding the damping parameters, it was noticed that they only influenced the comfort of the gait speed, which have d_v of 10, and d_ω of 20. The adjustment of the adaptive filter was empirically obtained, which are: $M = 2$, $\omega_{0,0} = 1$, $\mu_0 = 0.02$ and $\mu_1 = 0.1$.

One experiment was proposed to validate the strategy presented in this work, in which the user was asked to follow a path performing a lemniscate curve (see Fig. 3). Each participant was asked to do one and a half curve, starting from the middle of the path indicated on the floor, and implementing his/her wished speed for locomotion.

4 Results and Discussion

Once the parameters of the admittance controller were adjusted, it was verified that the users did not put any additional effort on their lower-limbs or on their hip. Figure 4 shows one of the paths traveled by the user. It is possible to observe that the user was able to follow the lemniscate curve without any inconvenience, as the traveled path does not show any oscillations (which implied a hard maneuverability of the SW).

Figure 5 shows the behavior of the adaptive filter. It can be observed that the oscillations detected by the force sensors, caused by the user's cadence and mechanical vibrations of the SW, were eliminated. Also, the adaptive filter estimates the user motion intention and allows establishing a natural speed for his/her locomotion (see Fig. 6).

The user's cadence was filtered from the force signal on the y axis, and the locomotion velocity of the SW did not show any oscillation (see Fig. 6), which could be a

Fig. 5 Adaptive filter behavior
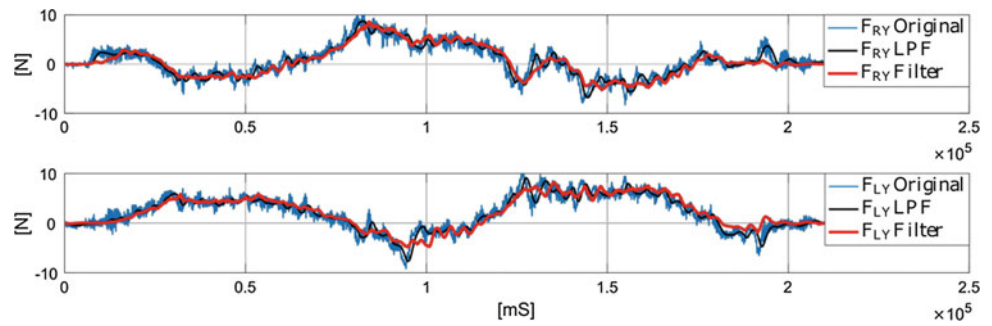
Fig. 6 Controller and UFES's SW behavior
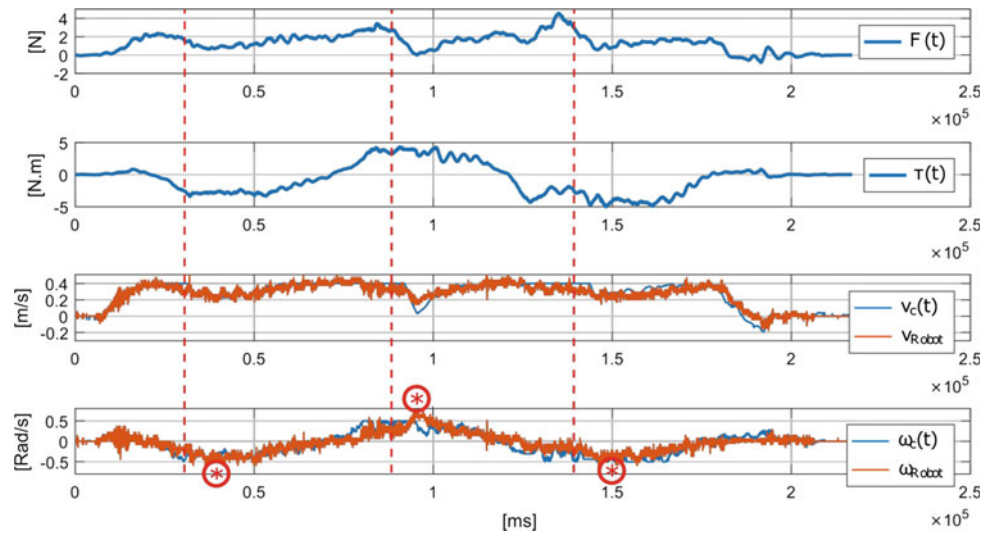
consequence of the continuous oscillation during the walking. Furthermore, the linear and angular velocities of the SW correspond to the commands of the control strategy and the user's motion intention detected, as shown in the $\tau(t)$ signal at Fig. 6. It can be noticed that there are three wave crests that correspond to the traveled path of one and a half curve (see red asterisks at Fig. 6). Also, the linear velocity was limited to 0.4 m/s as a safety factor for the user. It can be also observed that the user reduces the force signal $F(t)$ when he/she is on the curves (see the red dotted line at Fig. 6).

5   Conclusions and Future Works

The admittance control strategy proposed here allows a natural locomotion with the UFES's SW. Also, it was shown that with this control strategy the user can regulate a comfortable gait speed. In addition, the use of only force sensors to define a natural HRI is reflected on the computational efficiency and low processing of the control algorithm in real time. This experimental study allowed obtaining good results in terms of user's locomotion performance, according to his/her motion intention. This way, the interface developed here allowed a natural interaction between the user and the SW without the need of external sensors on either the user and/or the environment.

A good set of filter parameters allowed correctly detecting the human motion intention, and through the use of an admittance control strategy, the SW attended to such motion intention. Once established the suitable filter, this work showed that the motion intention was executed in real time, and the signal oscillations and noise were canceled.

In the future, new strategies will be evaluated to improve the HRI developed here. Also, we want to study new strategies to involve the environment in a natural and intuitive way into the HRI. Furthermore, using the RP-LIDAR sensor, we will be able to obtain more information about the environment, which may be used in probabilistic techniques, such as SLAM and path planning.

References

1. Davis, J.C., et al.: Mobility and cognition are associated with wellbeing and health related quality of life among older adults: a cross-sectional analysis of the Vancouver Falls Prevention Cohort. BMC Geriatr. **15**, 75 (2015)
2. WHO: World Report on Ageing and Health (2015)
3. P. D. United Nations, Department of Economic and Social Affairs: World Population Ageing 2015 (2015)
4. Werner, C., Ullrich, P., Geravand, M., Peer, A., Bauer, J.M., Hauer, K.: A systematic review of study results reported for the evaluation of robotic rollators from the perspective of users. Disabil. Rehabil. Assist. Technol. 1–12 (2017)
5. Bradley, S.M., Hernandez, C.R.: Geriatric assistive devices. Am. Fam. Physician **84**(4), 405–411 (2011)
6. Martins, M.M., Santos, C.P., Frizera-neto, A., Ceres, R.: Assistive mobility devices focusing on Smart Walkers: classification and review. Robot. Auton. Syst. **60**(4), 548–562 (2011)
7. Yu, H., Spenko, M., Dubowsky, S.: An adaptive shared control system for an intelligent mobility aid for the elderly. Auton. Robots **15**, 53–66 (2003)
8. Geravand, M., Werner, C., Hauer, K., Peer, A.: An integrated decision making approach for adaptive shared control of mobility assistance robots. Int. J. Soc. Robot. **8**(5), 631–648 (2016)
9. Paulo, J., Peixoto, P., Nunes, U.J.: ISR-AIWALKER: robotic walker for intuitive and safe mobility assistance and gait analysis. IEEE Trans. Hum.-Mach. Syst. 1–13 (2017)
10. Morone, G., et al.: Overground walking training with the i - Walker, a robotic servo-assistive device, enhances balance in patients with subacute stroke: a randomized controlled trial. J. Neuroeng. Rehabil. **13**, 1–10 (2016)
11. Xu, W., Huang, J., Yan, Q.: Multi-sensor based human motion intention recognition algorithm for walking-aid robot. In: 2015 IEEE International Conference on Robotics Biomimetics, IEEE-ROBIO 2015, pp. 2041–2046 (2015)
12. Cifuentes, C.A., Frizera, A.: Human-Robot Interaction Strategies for Locomotion. Springer International Publishing Switzerland (2016)
13. Riviere, C.N., Reich, S.G., Thakor, N.V.: Adaptive Fourier modeling for quantification of tremor. J. Neurosci. Methods **74**(1), 77–87 (1997)

Remote Monitoring of Temperature and Humidity—A Reliable and Inexpensive Device Development Applied in Neonatal Incubators

Severino Peixoto Nunes Netto, Pablo Filipe Santana Chacon,
Amauri Marcos C. de Morais Junior,
Clara Luísa Bezerra de Rubim Costa, and Fabrício Lima Brasil

Abstract

Neonatal incubator is a medical technology responsible for providing thermoneutral environments to newborn, especially those with low weight. This population requires specific levels of temperature and air humidity to decrease metabolic intake and avoid developmental impairements. Based on that, the present work aims to build up an inexpensive and reliable device that monitors mentioned variables and notify via web or mobile when a critical variation is detected. According to the data obtained, we conclude that the project succeed with a good refresh rate and proper functioning of alarms and notifications. The device, build up with inexpensive components, could be broadly used in any space that requires monitored temperature and humidity, resulting in safer environments.

S. P. N. Netto (✉) · P. F. S. Chacon · A. M. C. de Morais Junior · F. L. Brasil
Edmond and Lily Safra International Institute of Neuroscience, Santos Dumont Institute. Rod. RN 160, Km 3, n. 3003, Macaiba, RN 59280-000, Brazil
e-mail: severino@edu.isd.org.br

P. F. S. Chacon
Department of Biomedical Engineering, Federal University of Rio Grande do Norte, Natal, RN 59064-741, Brazil

C. L. B. de Rubim Costa
Department of Textile Engineering, Federal University of Rio Grande do Norte, Natal, RN 59064-741, Brazil

1 Introduction

Low weight newborns represent a serious public health problem due to the high mortality rate. According to the World Health Organization (WHO) it is estimated that more than one in ten babies are underweight, resulting in about 1 million deaths in 2015 [1], this population requires special cares [2]. According to the Computer Department of Brazilian Public Health System (DATASUS), in 2015 the majority of child deaths that occurred before the first year happened until the first 27 days of life. In order to minimize this problem, it's necessary to provide an environment where the newborn has the lowest energy expenditure as possible, in other words, a thermoneutral environment. In this context, the incubators are one of the most important tools to reduce the mortality and disease risks [3]. Neonatal incubators are used to provide a more suitable environment to infant survivals, with a compartment filled with distilled water, the incubators use the steam produced by heating this water to both heat and moisten the environment.

With this need to ensure a specific environment to newborns, the Clinical Engineering is presented as the sector that provides technological support to health institutions and guarantees safety to patients and clinical staffs [4]. Moreover, this sector is responsible for cost control in operational activities related to medical devices, such as purchase, contract, repair and maintenance [5, 6]. The incentive to Clinical Engineering occurred in about 1960 in the United States, when engineers were encouraged to join clinics and hospitals with the increase of quantity and complexity of hospital equipments [4].

The Clinical Engineering can be integrated with other fields like Internet of Things (IoT), enhancing management and technology associated with health services. The IoT refers to give objects representation in the digital realm through giving them an unique ID and connecting them in a network [7]. The union between these two areas is ongoing, creating Health-IoT ecosystems that are based on a network

of devices that connect directly with each other to capture and share vital data and significant context information [8].

Many studies already used IoT in health. Some works applied IoT combined with telemedicine [9] or with neuroengineering and rehabilitation [10–12]. Others focused on remote monitoring of patient [13–15]. There are also works that link IoT and Clinical Engineering [16, 17].

Combining the vast areas of IoT and Clinical Engineering, the present work aims to develop a low cost device which monitors temperature and humidity in neonatal incubators. The device exhibits in web platform the monitored values in predetermined time intervals, with notifications and visual alarms for health professionals. It should be emphasized that the project does not intend to replace the original sensors of the incubator, but to provide a new feature to assist health establishments, allowing remote access to data and increasing patient safety.

2   Methods

According to the Brazilian Ministry of Health, the minimum humidity value in a neonatal incubator is supposed to be 75%, and the temperature depends on the weight and age. If considered only the low weight newborns (under 1200 g), the values should follow the ones presented in Table 1.

Table 1 Relationship between age, ideal temperature and temperature range allowed in incubators in order to ensure an adequate survival environment for newborns

Age	Ideal temperature (°C)	Allowed range (°C)
0–12h	35.0	34.0–35.4
12–24h	34.0	34.0–35.4
24–72h	34.0	34.0–35.0

Adapted from [18]

Aware of these characteristics and aiming to develop a new device, maintaining the low cost, we opted to use the following components:

- 1 ESP8266 NodeMcu
- 1 DHT22 Digital Temperature and Humidity Sensor
- 1 Red and Yellow Light Emitting Diodes (LEDs)
- 8 Jumper Wires
- 1 Cellphone Charger

All the device was controlled by the ESP8266 NodeMcu, which is an opensource IoT platform. Widely used, the ESP8266 contains an embedded Wi-Fi module, which requires appropriate infrastructure to this technology and brings benefits and convenience to the healthcare institution in question of remote monitoring. It is programmed in C++ through the Arduino's IDE and supplied by 3.3–5 V with USB cable.

DHT22 was the temperature and humidity sensor used, with operating range of −40 to 80 °C for temperature and 0–100% for humidity, and a resolution of 0.1 °C for temperature and 2–5% for humidity. The product is widely disseminated in temperature monitoring projects with low cost. The sensor has 4 pins, but only three are necessary (Power Supply, Ground and Data pin).

The LEDs are needed to warn if the parameters exceed the limits. Yellow LED is used when the parameters may be out of ideal range due to resolution, while the red LED is used when it is out of range for sure independent of resolution. Audible alarms were not used due to the silence required in this specific environment. The Fig. 1 presents a schematic of the circuit which was done in Fritzing™ Software (Interaction Design Lab Potsdam, Brandenburg, Germany) using the listed components to optimize the electronic prototyping process.

Monitoring is done using the ThingSpeak™ Web Service Platform, which is a robust open API service that acts as a

Fig. 1 Device schematics in breadboard
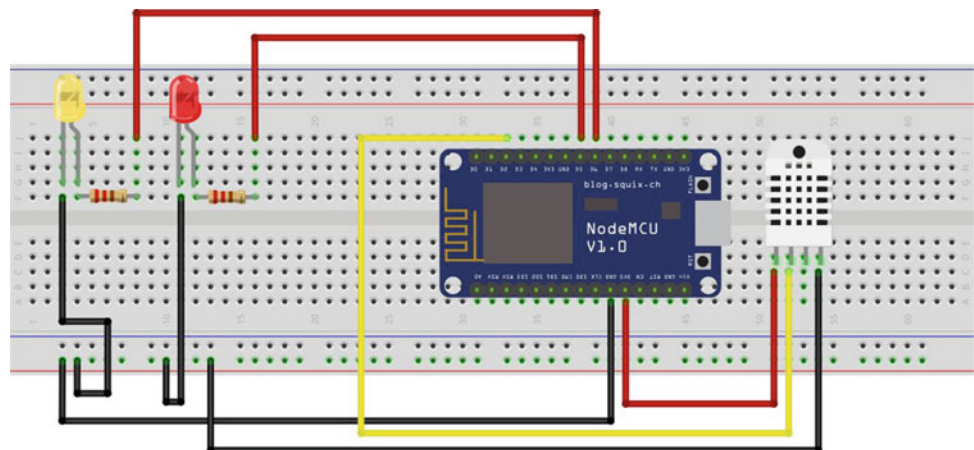
Table 2 Project costs

Component	Cost (R$)
ESP8266	22.00
DHT22	16.50
LEDS	1.00
Jumpers	10.00
Power charger	20.00
Total	69.50

host for a variety of data sent to cloud level [19]. Authentication occurs through read and write keys called String APIkeys in order to establish a TCP connection with the host. This demands a good internet connection from the health institution, ensuring reliability and speed of data transmission.

After the electronic prototyping was finished, the developing of control software was started. By the Arduino IDE C ++ based and using the string APIkeys, the data was transmitted to the server and displayed graphically over time. The code is available on the GitHubTM Platform via the link: https://github.com/SeverinoNetto/IoT-Monitoring-Temperature-and-Humidity. As shown in Table 2, total value of the system was quoted at R$69.50 (approximately U$18).

Initially, tests were performed to ensure proper operation of the sensor, analyzing the behavior under sudden changes of temperature, such as inside of refrigerator or close of flames. In a second moment, the device was tested in a functioning Vision 2286 incubator (Fanem, SP, Brazil) (Fig. 2), considering the parameters for the first day of life shown in the Table 1. This last test was carried out at Onofre

Lopes University Hospital (HUOL) of the Federal University of Rio Grande do Norte (UFRN). The main aspect analyzed with the supervision of the clinical engineer and a nurse of the HUOL was the web application refresh rate of temperature and humidity variation.

3 Results and Discussion

Considering the constant improvement of hospital environment along with the need to maintain controlled temperatures in the neonatal incubators, the system presented here was idealized and developed. Thereby, a low cost device was built up to monitor the temperature and relative humidity variables of a neonatal incubator in the neonatal and pediatric intensive care sector. The system offers a high monitoring precision and triggers visual alerts if the monitored variables undergo undesired oscillations.

In relation to the tests performed and their functionality, it could be verified that the project here presented is a low-cost innovation with precision. With the resolution presented, it was observed that the data were always among those established by the ministry of health described in the Table 1. One of the advantages of this device is the monitoring via wifi system that provides remote information over the internet, along with the visual alarms used to alert health professionals about possible intercurrences. It is a web application and therefore it facilitates the user adherence, considering that the professional do not have to download or install any program.

The proposed solution uses the interface provided by ThingSpeak™. The system interface is updated every 20 s,
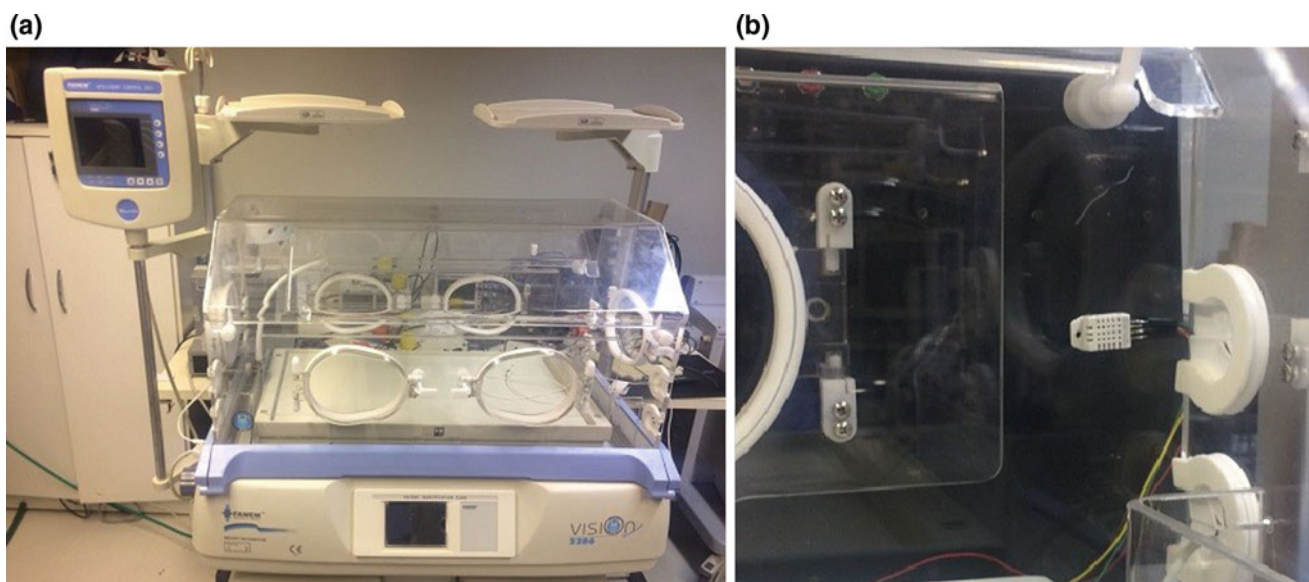
Fig. 2 Device in operation in the incubator. **a** External view of the incubator with the device. **b** Approximate view of the internal sensor
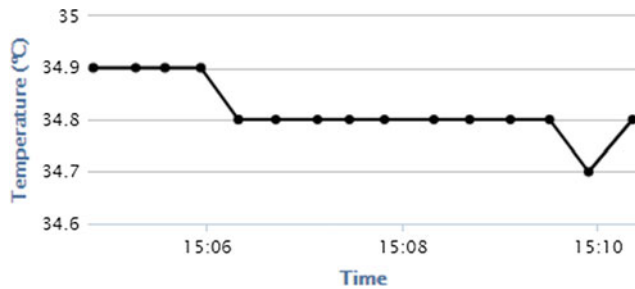
Fig. 3 Temperature monitoring in ThingSpeak
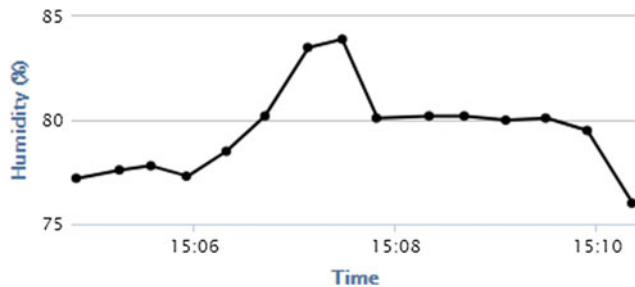
Fig. 4 Humidity monitoring in ThingSpeak

allowing the monitoring of variables from anywhere in the world by internet access. The developed format is very useful, enabling the observer analyze the behavior of previous sensor readings. Furthermore, ThingSpeak™ is a free platform, not generating new expenses to the hospital, besides having friendly and intuitive interface.

Temperature and humidity were plotted separately on a single screen where they were updated every 20 s, but the activation of the LEDs happened instantly since internet communication is not required to this feature. The Figs. 3 and 4 show 5 min of a total of 20 min data collection in a functioning incubator, displaying the variables within the allowed limits.

In order to test the accuracy of the device, two samples were obtained with 35 values collected every 10 min for 6 h. With this data, it was conducted an independent-samples t-test which showed no significant difference between the readings of the incubator (M = 34.997, SD = 0.0382) and the proposed device (M = 34.974, SD = 0.0611), p = 0.066. It is important to note the small difference observed between the averages of the samples, approximately 0.023 °C, proving proper measurement.

Aiming to increase patient's safety, the network installations and the power source of the system are connected to a no-break with energy autonomy around 45 min. This is necessary in cases of power failure, keeping the system working while the repair is performed.

4 Conclusion

The work here presented shows the development of a low-cost air temperature and humidity monitoring system, which allows more innovation to hospitals, clinics and establishments in general that require monitoring of these variables in order to provide more safety for patients in neonatal incubators. This work is an example of how to impact the processes and technologies of a health institution in a beneficial and innovative way, at same time that allocates few resources. The device was tested in a conventional incubator and the desired result was achieved by monitoring and displaying the data in small time intervals.

In this context, Clinical Engineering has to be seen as a tool for continuous improvement of the services provided to the patients and modernization of the institution internal processes. To do this, engineers need to be always upto-date on technological innovations and have critical thinking to develop new applications in health. This continuous improvement brings more quality and effectiveness to health services, reflecting a better quality of life for the population served.

As future perspectives of the work, two aspects can be emphasized. One is the data monitoring via smartphone, offering a more informative and accessible information, portable and easily accessed by the health team. Another aspect for improving the work would be to use the same system but with different parameters for the application in other sectors, such as the hospital engine room, blood banks, operating boxes used in animal training [20–22] or any other location that requires a monitoring of the temperature and humidity variables.

Finally, it is important to indicate that this work is a proof of concept, in other words, a demonstration of the applicability of the IoT in clinical engineering. This way, costs related to the development of the prototype (hardware and software) did not consider final product costs. As a prototype we noted that a simple implementation can be used in many applications different from the proposed here, increasing safety and control of temperature and humidity.

References

1. Care of the preterm and low-birth-weight newborn, World Prematurity Day. http://www.who.int/maternalchildadolescent/newborns/prematurity/en/. Accessed 21 Mar 2018
2. Oliveira, M.: Sistema De Ensaio De Desempenho De Incubadora Neonatal, 112 (2007)
3. Barbosa, A.: O advento das incubadoras no exterior e no Brasil: um ensaio histórico. Pediatria Atual **15**(6) (2002)
4. Brozino, J.: Clinical engineering: evolution of a discipline. In: Dyro, J. (ed.) Clinical Engineering Handbook. Elsevier Academic Press, Burlington, vol. 1, pp. 3–7

5. David, Y.: Planning hospital medical technology management. IEEE Eng. Med. Biol. Mag. 73–79 (2004)
6. Lenel A.: Guide 1: how to organize a system of healthcare technology management. In: "How to Manage" Series of Health-care Technology, p. 167 (2005)
7. Ashton, K.: That "Internet of Things" thing. RFiD J. 4986 (2009)
8. Fernandez, F.: Opportunities and challenges of the Internet of Things for healthcare. In: Proceedings of the 4th International Conference on Wireless Mobile Communication and Healthcare —"Transforming Healthcare through Innovations in Mobile and Wireless Technologies," pp. 263–266 (2014)
9. Zhang, X.: An open, secure and flexible platform based on internet of things and cloud computing for ambient aiding living and telemedicine. In: 2011 International Conference on Computer and Management, CAMAN 2011, pp. 1–4 (2011)
10. Akash, S.: A novel strategy for controlling the movement of a smart wheelchair using Internet of Things. In: 2014 IEEE Global Humanitarian Technology Conference—South Asia Satellite GHTC-SAS 2014, pp. 154–158 (2014). https://doi.org/10.1109/ghtc-sas.2014.6967575
11. Domingo, M.: An overview of the Internet of Things for people with disabilities. J. Netw. Comput. Appl. 35(2), 584–596 (2012)
12. Simplicio, H.: Neurociência aplicada as práticas tecnológicas. In: Hugo Saba, Eduardo Manuel de Freitas Jorge, Claudio Reynaldo B. de Souza (Org.) Pesquisa aplicada & inovaçao, 1 ed., vol. 1, pp. 15–32. Edifba, Salvador (2016)
13. Hassanalieragh, M.: Health monitoring and management using Internet-of-Things (IoT) sensing with cloud-based processing: opportunities and challenges. In: Proceedings—2015 IEEE International Conference on Services Computing, SCC 2015, pp. 285–292 (2015)
14. Gope, P.: BSN-Care: a secure IoT-based modern healthcare system using body sensor network. IEEE Sens. J. 16(5), 1368–1376 (2016)
15. Istepanian, R.: The potential of Internet of m-health Things m-IoT for non-invasive glucose level sensing. In: Proceedings of the Annual International Conference of the IEEE Engineering in Medicine and Biology Society, EMBS, pp. 5264–5266 (2011)
16. Kanase, P.: Smart hospitals using Internet of Things (IoT). Int. Res. J. Eng. Technol. (IRJET) 3(3), 1735–1737 (2016)
17. Yu, L.: Smart hospital based on Internet of Things. JNW 7(10), 1654–1661 (2012)
18. Calil, S.: Equipamentos Médico-Hospitalares e o Gerenciamento da Manutenção. Ministério da Saúde (2002)
19. Pasha, S.: Thingspeak based sensing and monitoring system for IoT with Matlab analysis. Int. J. New Technol. Res. (IJNTR) 2(6), 19–23 (2016)
20. Ribeiro, M.: OBAT: an open-source and low-cost operant box for auditory discriminative tasks. Behav. Res. (2017)
21. Ribeiro, M.W.: An open-source and low-cost operant conditioning equipment for studying auditory discrimination in common marmosets. In: 45th Society for Neuroscience Meeting, Chicago. 45th Society for Neuroscience Meeting (2015)
22. Rodrigues Neto: Condicionamento operante em saguis (Callithrix jacchus) para discriminaçao de estímulos auditivos. In: II Simpósio de Neuroengenharia do ISD, Macaíba (2015)

Serious Game Based on Myo Armband for Upper-Limb Rehabilitation Exercises

Berthil Borges Longo, Mariana Midori Sime, and Teodiano Bastos-Filho

Abstract

The purpose of a rehabilitation processes is to restore a person to a state of optimal functioning. A wide variety of rehabilitation processes consist of repetition tasks. Thus, Serious Games (SG) can be used as a technology to assist in this process by motivating patients to perform the exercises during rehabilitation sessions using a variety of devices, with goals or scores to be achieved during sessions. This work addresses the development and usage of SG based on the Myo Armband, an affordable-access device, which is used to build an Assistive Technology for upper-limb rehabilitation. This SG has a circus target shooting as theme, in which the individuals must make the selected upper-limb rehabilitation exercise (the full fist position), in order to shoot with the gun and hit the targets. To test these SG, five healthy volunteers used them during 3 sessions of 10 repetitions each. To evaluate this SG, the volunteers answered a System Usability Scale (SUS) questionnaire and a free questionnaire with questions about the structure of the SG. Results showed that these SG have good potential to be used as a rehabilitation tool, and the suggestions of the free form questionnaire will be useful to make the necessary changes before its usage with impaired patients.

Keywords

Myo Armband • Serious games • Upper limbs rehabilitation

B. B. Longo (✉) · M. M. Sime · T. Bastos-Filho
RENORBIO, Universidade Federal do Espírito Santo, Vitória, Brazil
e-mail: berthilbl@gmail.com

T. Bastos-Filho
Programa de Pós-Graduação em Engenharia Elétrica,
Universidade Federal do Espírito Santo, Vitória, Brazil

1 Introduction

The speed of the emergence of innovations developed for the health area in this early century is unparalleled with other moments in human history. According to the WHO, 50% of all therapeutic advances available today did not exist until the beginning of this century [1], which includes new equipment, drugs, biomedical and surgical procedures to prevent, diagnose and treat diseases. In this context, Assistive Technology (AT) is also benefited by technological advances. In 2006, a committee was established in Brazil, aiming to improve, give transparency and legitimacy to the development of AT. The number of people with any kind of disabilities in Brazil is about 43.5% of the population [2]. According to results of the 2010 census released by the Brazilian Institute of Geography and Statistics (Instituto Brasileiro de Geografia e Estatística —IBGE), the country has approximately 13.3 million people with physical disabilities, which 5 million are men and 8.3 million are women [3].

Physical disabilities include a broad range of disabilities that affect motor skills, causing problems at person's limbs, muscles or nerves, which may be acquired congenital or during life, from physical injury or disease [4]. People affected by physical disability can make use of AT to restore fully or partially their movements by making rehabilitation sessions accompanied by a specialist when physical restoration is possible.

Thanks to the different potential of video games and their positive aspects, medical and rehabilitation field has been using these positive effects and become interested in the gamification of some interventions [5]. Also, the popularization of video games in the last decades helped to increase Serious Games (SG) usage, acceptance and development. SG are games designed to intentionally stimulate other characteristics rather than pure amusement as first objective, like healthcare, rehabilitation, education, training, prevention of injuries and others [6]. In this context, SG can be used as AT to help in rehabilitation sessions, which, in many cases,

consist of task repetition exercises [7], and can be adapted to the condition of each patient [8]. Thus, SG can be used in this process, assisting both patients and clinicians, and motivating patients to execute the exercise movements during the rehabilitation sessions, using a variety of devices with goals or scores to reach during the gameplay. The objective of this work is to evaluate a SG designed for upper-limb rehabilitation based on the Myo Armband with the goal of improving its usability before its usage with the impaired patients.

2 Materials and Methods

Myo Armband (Fig. 1) is a device to be worn on the forearm, which uses a set of eight surface electromyography (sEMG) sensors to capture electrical activity in the forearm muscles to recognize hand gestures. It has wireless connection with the computer and built-in gyroscope, accelerometer and magnetometer [9]. It also has vibration to deliver haptic feedback to the user, when a preestablished movement is recognized. The SG developed here is based on this Myo Armband as input/output device, which is to be used by patients who need to execute upper-limb rehabilitation exercises. To trigger an action inside the SG, the Full Fist (FF) position exercise

(Fig. 1), a commonly executed exercise in upper-limb rehabilitation process developed in [10], is used.

The designed SG has a circus target shooting as theme, and the patient must make the rehabilitation exercise in order to shoot with the gun and hit the targets (Fig. 2). The number of bullets of the gun, which is the same as the number of repetitions of the rehabilitation exercise of each session, is set by the health professional responsible for the patient's rehabilitation. This can be set before the beginning of each session. Each target hit by the patient has a value of 10 points, and the score, which is the sum of all hit objects, is shown on a corner of the SG screen. The game screen moves to the right, with the gun always in the center while the targets passes through the screen going to the left. The difficulty increases with time, making objects smaller or moving. This change in difficulty follows the increase of bullets, which is the numbers of repetitions, and it keeps a good level of challenge while the patient evolves in therapy, that is, makes more exercises in the following sessions. It is extremely important that the game played during the rehabilitation, its repetition and movement complexity match the skill level of the patient, in order to prevent frustration, boredom, and fatigue. Also, to keep attention and motivation, the task difficulties may be increased as the patient improves [11].

Fig. 1 Myo Armband device worn on a user's forearm executing relaxed to Full Fist position exercise

Fig. 2 Designed SG with circus target shooting as theme. In the middle of the image is the gun controlled by the user, and in front of it the hit object and its score. On the right corner the left bullets are shown, and on the left corner the total score is shown

The game engine used to develop this SG was Unity 3D Personal Edition, which, according to Silva and Silva [12], is one of the most suitable programs for this purpose and considered by Hjorungdal et al. [13] as an efficient integration platform, which is important when working with a commercial input/output device [14]. The structure of the objects, animations and texturing process were done using Blender, a professional free and open-source 3D computer graphics software [15]. To make textures and other images, Gimp, a free and open-source raster graphics editor, was used [16].

This SG is part of Virtual-R, a rehabilitation platform under development, which uses SG and affordable access devices. Each SG has, including the one here described, a patient registration menu to store patient's data, like name, session number, repetitions done and score of each session. This data is shown on screen, on a scoreboard, before and after each session. This is important to keep the user motivated, trying to acquire better results on each session.

Before the implementation of the designed SG with patients, they were tested with healthy volunteers to verify their usability and acceptance. Five healthy volunteers participated of the study. Before the usage, the structure and functioning of the device and SG were explained to the participants. After the registration, each participant tried the SG with a free time, so they were able to adapt to it. They were instructed to indicate when they feel comfortable enough to start the first session, and the adaptation time was registered. Each participant made 3 sessions with 10 repetitions each (or 10 bullets to shot). To test the usability and acceptance of the developed SG, the participants answered a System Usability Scale (SUS) questionnaire. SUS is a ten-item, five-point scale and it takes in account three different aspects: effectiveness, efficiency, satisfaction [17]. A free form with four questions about the SG structure was also answered by each participant. It includes questions about the color scheme, game speed, number of targets on
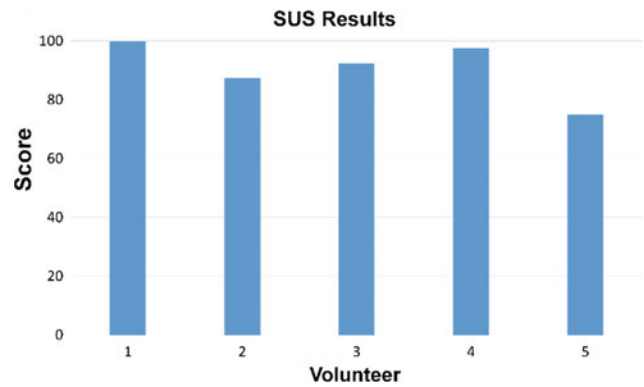
Fig. 3 SUS results for the five volunteers

screen and size of the targets. Also, the participants were asked to leave comments and recommendation of any aspect after their experience with the SG.

This research was previously approved by the Ethical Committee of Federal University of Espírito Santo— UFES/Brazil (CAAE: 64797816.7.0000.5542), and all the volunteers signed the Free and Informed Consent Form.

3 Results

SUS results show that the system was well evaluated by the volunteers, with all scores above 70 (Fig. 3). According to Bangor and colleagues, products with score above 90 are exceptional, products with score above 80 are good, and products with score above 70 are acceptable; anything below a 70 has usability issues that must be reviewed [18].

The session results show that the users were able to use the Myo Armband properly, and all the users reached a score over 60, which means they hit, at least 6 objects over 10. The user number 4 hit all objects, reaching a score of 100 for all sessions (Fig. 4).

Fig. 4 Session results for the five volunteers
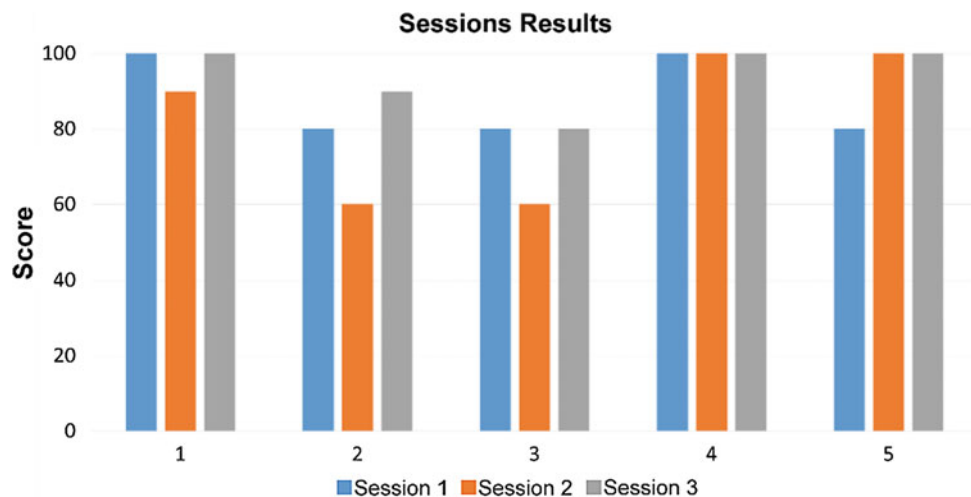
The free form questions helped to point out some potential changes to improve the user experience. All the users answered it positively, and some left comments to improve some aspects. One of the users highlighted that the color of the gun was confused with the background in the color scheme question. Another one highlighted that the speed of the screen could increase to change difficulty over the time in order to keep the challenge in the same level of patients with more residual skills, who can make more repetitions.

4 Conclusion

The development of a SG passes through a sequence of design, implementation, tests and modifications, till reaching its final version. These changes are made based on the evaluative method results and opinions from users and patients, in addition to requests from the health professional responsible for these patients.

The first test of the developed SG showed that they have good potential to be used as a rehabilitation tool, increasing users' interest and motivation, however, some changes must be made to improve user's usability. As future works, after the implementation of the proposed changes, these SG might be tested again with a higher number of healthy users and health professionals before its usage with patients with tendon/nerve injuries or forearm/wrist fractures.

References

1. Brasil. A Coleção Progestores – Para entender a gestão do SUS. Ciência e Tecnologia em Saúde, 1 ed. Brasília (2007)
2. Brasil. Subsecretaria Nacional de Promoção dos Direitos da Pessoa com Deficiência. Comitê de Ajudas Técnicas. Tecnologia Assistiva. CORDE, 138 pp. Brasília (2009)
3. Brasil. Ministério do Planejamento, Orçamento e Gestão. Instituto Brasileiro de Geografia e Estatística - IBGE. Censo demográfico 2010: características gerais da população, religião e pessoas com deficiência, pp. 1–215. Rio de Janeiro (2010)
4. Robitaille, S.: The Illustrated Guide to Assistive Technology and Devices: Tools and Gadgets for Living Independently. Demos Medical Publishing, New York (2010)
5. Ritterfeld, U., Cody, M., Vorderer, P.: Serious Games: Mechanisms and Effects. Taylor & Francis, New York (2009)
6. Bonnechère, B.: Serious Games in Physical Rehabilitation. Springer International Publishing, Brussels (2018)
7. Delisa, A., Gans, M., Walsh, E.: Physical Medicine and Rehabilitation: Principles and Practice, 15th edn. Lippincott Williams & Wilkins, Philadelphia (2005)
8. Monteiro, C.B.D.M.: Realidade virtual e jogos eletrônicos: uma proposta para deficientes. Realidade virtual na paralisia cerebral, pp. 68–87. São Paulo (2011)
9. Masson, S., Fortuna, F., Moura, F., Soriano, D.: Integrating Myo Armband for the control of myoelectric upper limb prosthesis. In: Proceedings of the XXV Congresso Brasileiro de Engenharia Biomédica. Foz do Iguaçu (2016)
10. Kisner, C., Colby, L.A.: Therapeutic Exercise: Foundations and Techniques, 6th edn. Fa Davis, Philadelphia (2012)
11. Levin, F., Weiss, L., Keshner, A.: Emergence of virtual reality as a tool for upper limb rehabilitation: incorporation of motor control and motor learning principles. Phys. Ther. **95**(3), 415–425 (2015)
12. Silva, R., Silva, A.: Tecnologias para Construção de Mundos Virtuais: Um Comparativo Entre as Opções Existentes no Mercado, FAZU em Revista, pp. 211–215 (2012)
13. Hjorungdal, R.M., Sanfilippo, F., Osen, O.L., Rutle, A., Bye, R.T.: A. game-based learning framework for controlling brain-actuated wheelchairs. In: ECMS, pp. 554–563 (2016)
14. Unity Technologies: Unity. http://unity3d.com/ (2018). Accessed 18 Feb 2018
15. Blender Foundation: Blender. https://www.blender.org/ (2018). Accessed 18 Feb 2018
16. Gimp: Gimp. https://www.gimp.org/ (2018). Accessed 18 Feb 2018
17. Finstad, K.: The system usability scale and non-native english speakers. J. Usability Stud. **1**(4), 185–188 (2006)
18. Bangor, A., Kortum, P., Miller, J.: Determining what individual SUS scores mean: adding an adjective rating scale. J. Usability Stud. **4**(3), 114–123 (2009)

Simulation of Human Hands Movements Using Forward Kinematics

Ingrid Miranda de Sousa, Joel Lucas de Jesus Trindade,
and Gerardo Antônio Idrobo Pizo

Abstract

The human hand is one of the human body extremities that allows to perform numerous movements to accomplish tasks. This paper presents the mathematical model of forward kinematics and the first results of the human hand simulation using computational tools as Matlab, which allows to represent of the movements in 3D. The equations used are based on Denavit-Hartenberg convention, where a homogeneous transformation matrix is determined that relates position values of the end ends of the fingers with the angular position values of the phalanges. The results provide a series of information and recommendations that can be used in the biomechanical study of the hand. The mathematical model serves as complementary information in the gesture recognition process. Helping to solve diverse singularities of possible positions of the fingers when they are not clearly identified in images of intensity for recognition of gestures translated into text or voice.

Keywords

Human hand • Simulation • Forward kinematics • Denavit-Hartenberg

1 Introduction

The knowledge of the kinematics model of the human hand allows to predict gestural behavior, that can be mathematically fused with other models to fully describe the configuration of human hand position. There are some programs that allow simulation the biomechanics of the human body as: Anybody [3], MSMN [4, 7], BoB [9], openSim and SIMM [5, 6]. The programs are authorship registered and have as limits to perform tasks for which it was developed. The idea of this research work is to present the mathematical and practical development to virtually move the phalanges of the hands. The future expectation is to fuse the kinematic model with the gesture detection model using digital image processing.

The structure of this work is as follows: In item (2) the skeletal model of the hand is described using biomechanical parameters such as: degrees of freedom (DoFs), motion bands, metrical dimensions of the phalanges. Also the parameters of the Denavit-Hartenberg matrix are described. In item (3) it describes the mathematical model that involves the forward kinematics of movement to locate the position of each of the fingers according to the angle value selected for each phalanges. In item (4) is presented validation of the kinematic model and the three-dimensional simulation of different movements of the human hand. Finally, in item (5) the conclusions.

2 Geometric Parameters of the Human Hand

The human hand has 17 rotating joints [4] that are connected through links. The joints described in this work are: metacarpal (MC), proximal (P), medial (M) and distal (D) phalanges, and distal interphalangeal (DIP), proximal interphalangeal (PIP), metacarpophalangeal (MCP), carpometacarpal (CMC), interphalangeal (IP) e trapeziometacarpal (TMC).

The kinematic chain of spatial representation of the hand is calculated on the basis of the Denavit-Hartenberg model [1, 2] and uses four input parameters (θ, α, d, r). Where θ is the angle of folding between the joints, α is the angle between the fingers, d is the size of each phalanx and r is the distance between the fingers.

I. M. de Sousa · J. L. de Jesus Trindade · G. A. I. Pizo (✉)
Faculty of Gama, Department of Electronic Engineering,
University of Brasília, Brasília, Brazil
e-mail: gerardo.idrobo@gmail.com

I. M. de Sousa
e-mail: ingridmsousa0@gmail.com

J. L. de Jesus Trindade
e-mail: joelucasjoel@gmail.com

Table 1 Denavit-Hartenberg parameters for ring finger

Ring finger	
$d_{Rin,P}$	34
$d_{Rin,M}$	25
$d_{Rin,D}$	26
$r_{Rin,W}$	62
$r_{Rin,MC}$	75
$r_{Rin,P}$	−75
$\alpha_{Rin,MC}$	−0.0152
$\alpha_{Rin,P}$	−0.0105

Table 2 Denavit-Hartenberg parameters for thumb

Thumb finger	
$d_{Thu,P}$	29
$d_{Thu,D}$	27.5
$r_{Thu,W}$	−304
$r_{Thu,MC}$	−383
$r_{Thu,P}$	42
$\alpha_{Thu,MC}$	0.0532
$\alpha_{Thu,P}$	0.0127

Table 3 Denavit-Hartenberg parameters for index finger

Index finger	
$d_{Ind,P}$	32.5
$d_{Ind,M}$	22
$d_{Ind,D}$	24
$r_{Ind,W}$	70
$r_{Ind,MC}$	40
$\alpha_{Ind,MC}$	−0.0289

Table 4 Denavit-Hartenberg parameters for middle finger

Middle finger	
$d_{Mid,P}$	36
$d_{Mid,M}$	28
$d_{Mid,D}$	25.5
$r_{Mid,W}$	86
$r_{Mid,MC}$	3
$\alpha_{Mid,MC}$	−0.0286

Table 5 Denavit-Hartenberg parameters for the little finger

Little finger	
$d_{Lit,P}$	22.5
$d_{Lit,M}$	18.5
$d_{Lit,D}$	23
$r_{Lit,W}$	55
$r_{Lit,MC}$	49
$r_{Lit,P}$	−74
$\alpha_{Lit,MC}$	−0.0118
$\alpha_{Lit,P}$	−0.0113

the position of the joints. And the second works in the opposite way. Through the position and speed of the end effector is obtained the positions and velocities equivalent to the joints.

In this work its used the forward kinematics which is used to spatially locate the fingertips as a function of the value of the angle of the joints.

3.1 Mathematical Model

The forward kinematics equations are formed by a multiplication of matrices, which represent translational and/or rotational movements of each joint. The general model of matrices can be seen in (Eq. 1) and (Eq. 2). Where (x) represents the finger type e (y) the type of joint.

$$P_x = {}^{\omega}_0 T_{x,y} \cdot {}^0_1 T_{x,y} \cdot {}^1_2 T_{x,y} \cdot {}^2_3 T_{x,y} \cdot {}^3_4 T_{x,y} \tag{1}$$

$$T_{x,y} = \begin{bmatrix} \cos\theta_{i,j} & -\sin\theta_{i,j} & 0 & d_{i,j} \\ \sin\theta_{i,j}\cos\alpha_{i,j} & \cos\theta_{i,j}\cos\alpha_{i,j} & -\sin\alpha_{i,j} & -r_{i,j}\sin\alpha_{i,j} \\ \sin\theta_{i,j}\sin\alpha_{i,j} & \cos\theta_{i,j} & \cos\alpha_{i,j} & r_{i,j}\cos\alpha_{i,j} \\ 0 & 0 & 0 & 1 \end{bmatrix} \tag{2}$$

(a) **Index finger and middle finger**

The forwards kinetic matrix is described in Eq. (3) using the parameters of Table 6. Since IM a variable that can be assigned to the middle finger or index finger. The matrix

The α, **d** and **r** parameters are conventionally fixed and θ is the parameter that change.

Therefore, the system effects only the folding movement of the joints. The values assigned to the variables (θ, α, **d**, **r**) can be seen at Tables 1, 2, 3, 4 and 5. Where the angles θ and α are given in radians and **r** in millimeters. Such measures were chosen based on real values of a human hand.

3 Kinematic Model

According to [8], the kinematics of manipulator robot consists in a study of position and velocity of its effector and its links. There are two types of kinematics, which are: forward and Inverse kinematics. The first one is used to obtain the position and velocity of the end effector, depending on

Table 6 Denavit-Hartenberg parameters

Junta	$\theta_{i,j}$	$d_{i,j}$	$r_{i,j}$	$\alpha_{i,j}$
ω	0	0	$r_{IM,\omega}$	0
1	$\theta_{IM,MCP}$	0	$r_{IM,MC}$	$\alpha_{IM,MC}$
2	$\theta_{IM,PIP}$	$d_{IM,P}$	0	0
3	$\theta_{IM,DIP}$	$d_{IM,M}$	0	0
4	0	$d_{IM,D}$	0	0

Table 8 Denavit-Hartenberg parameters

Junta	$\theta_{i,j}$	$d_{i,j}$	$r_{i,j}$	$\alpha_{i,j}$
ω	0	0	$r_{Thu,\omega}$	0
1	$\theta_{Thu,MCP}$	0	$r_{Thu,MC}$	$\alpha_{Thu,MC}$
2	$\theta_{Thu,PIP}$	$d_{Thu,P}$	0	0
3	$\theta_{Thu,DIP}$	$d_{Thu,M}$	0	0
4	0	$d_{Thu,D}$	0	0

containing the position and orientation of the fingertip is formed by (Eq. 4).

$$T_{IM,y} = \begin{bmatrix} \cos\theta_{i,j} & -\sin\theta_{i,j} & 0 & d_{i,j} \\ \sin\theta_{i,j}\cos\alpha_{i,j} & \cos\theta_{i,j}\cos\alpha_{i,j} & -\sin\alpha_{i,j} & -r_{i,j}\sin\alpha_{i,j} \\ \sin\theta_{i,j}\sin\alpha_{i,j} & \cos\theta_{i,j}\sin\alpha_{i,j} & \cos\alpha_{i,j} & r_{i,j}\cos\alpha_{i,j} \\ 0 & 0 & 0 & 1 \end{bmatrix}$$
(3)

$$P_{IM} = {}^{\omega}_{0}T_{IM,y} \cdot {}^{0}_{1}T_{IM,y} \cdot {}^{1}_{2}T_{IM,y} \cdot {}^{2}_{3}T_{IM,y} \cdot {}^{3}_{4}T_{IM,y} \quad (4)$$

(b) Little finger and ring finger

The forwards kinetic matrix is described in Eq. (5) using the parameters of Table 7. Note that the variable AM corresponds to the chosen finger. The nomenclature defined for the little finger and ring finger is Ane or Min, respectively.

$$T_{AM,y} = \begin{bmatrix} \cos\theta_{i,j} & -\sin\theta_{i,j} & 0 & d_{i,j} \\ \sin\theta_{i,j}\cos\alpha_{i,j} & \cos\theta_{i,j}\cos\alpha_{i,j} & -\sin\alpha_{i,j} & -r_{i,j}\sin\alpha_{i,j} \\ \sin\theta_{i,j}\sin\alpha_{i,j} & \cos\theta_{i,j}\sin\alpha_{i,j} & \cos\alpha_{i,j} & r_{i,j}\cos\alpha_{i,j} \\ 0 & 0 & 0 & 1 \end{bmatrix}$$
(5)

$$P_{AM} = {}^{\omega}_{0}T_{AM,y} \cdot {}^{0}_{1}T_{AM,y} \cdot {}^{1}_{2}T_{AM,y} \cdot {}^{2}_{3}T_{AM,y} \cdot {}^{3}_{4}T_{AM,y} \cdot {}^{4}_{5}T_{AM,y}$$
(6)

(c) Thumb

For the thumb, the general form of the matrix consists of the equation seen in (Eq. 7). Thus, by assigning the values in

Table 7 Denavit-Hartenberg parameters

Junta	$\theta_{i,j}$	$d_{i,j}$	$r_{i,j}$	$\alpha_{i,j}$
ω	0	0	$r_{AM,\omega}$	0
1	$\theta_{AM,CMC}$	0	$r_{AM,MC}$	$\alpha_{AM,MC}$
2	$\theta_{AM,MCP}$	0	$r_{AM,MC}$	$\alpha_{AM,P}$
3	$\theta_{AM,PIP}$	$d_{AM,P}$	0	0
4	$\theta_{AM,DIP}$	$d_{AM,M}$	0	0
5	0	$d_{AM,D}$	0	0

Table 8 in this equation it is possible to find each one of the matrices that are part of (Eq. 8). And so, map the position and orientation of the thumb.

$$T_{Thu,y} = \begin{bmatrix} \cos\theta_{i,j} & -\sin\theta_{i,j} & 0 & d_{i,j} \\ \sin\theta_{i,j}\cos\alpha_{i,j} & \cos\theta_{i,j}\cos\alpha_{i,j} & -\sin\alpha_{i,j} & -r_{i,j}\sin\alpha_{i,j} \\ \sin\theta_{i,j}\sin\alpha_{i,j} & \cos\theta_{i,j}\sin\alpha_{i,j} & -\cos\alpha_{i,j} & -r_{i,j}\cos\alpha_{i,j} \\ 0 & 0 & 0 & 1 \end{bmatrix}$$
(7)

3.2 Kinematic Model Solution

The kinematic solution matrix contains a rotation matrix, a position vector, a perspective effect, and a scale factor, as can be seen in Eqs. (8–10).

$$P_{Thu} = {}^{\omega}_{0}T_{Thu,y} \cdot {}^{0}_{1}T_{Thu,y} \cdot {}^{1}_{2}T_{Thu,y} \cdot {}^{2}_{3}T_{Thu,y} \cdot {}^{3}_{4}T_{Thu,y} \quad (8)$$

$$T = \begin{bmatrix} R_{3x3} & p_{3x1} \\ f_{1x3} & 1 \end{bmatrix} \quad (9)$$

$$T = \begin{bmatrix} rotation\,matrix\,(3 \times 3) & position\,vector\,(3 \times 1) \\ perspective\,effect\,(1 \times 3) & scale\,factor\,(1) \end{bmatrix}$$
(10)

4 Simulation

To validate the mathematical model was used the MATLAB program that allowed to imitate hand movements and to know ranges of angular displacements to produce realistic movements.

4.1 Graphics

The figures represent the skeletal simulation of a hand and the results are similar to real human hand placements (Figs. 1, 2, 3, 4, 5 and 6).

The simulations show that the model can perform some common hand movements.
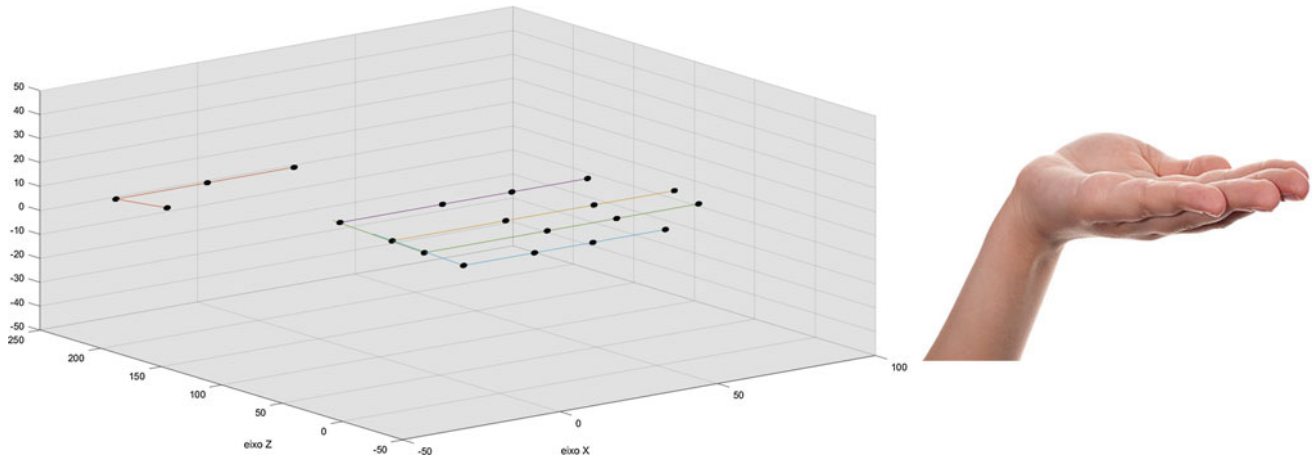
Fig. 1 Simulation of an open hand. Graph in the plane [XYZ]
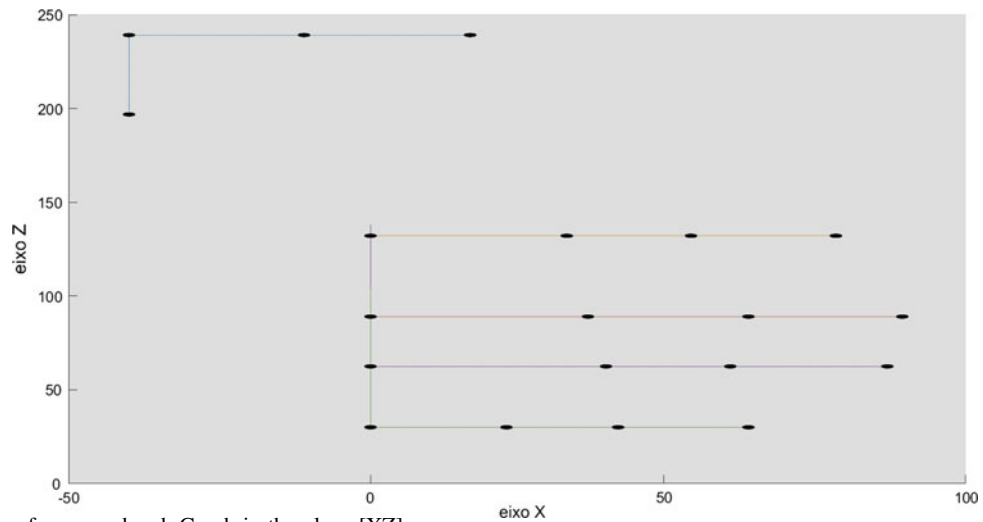
Fig. 2 Simulation of an open hand. Graph in the plane [XZ]
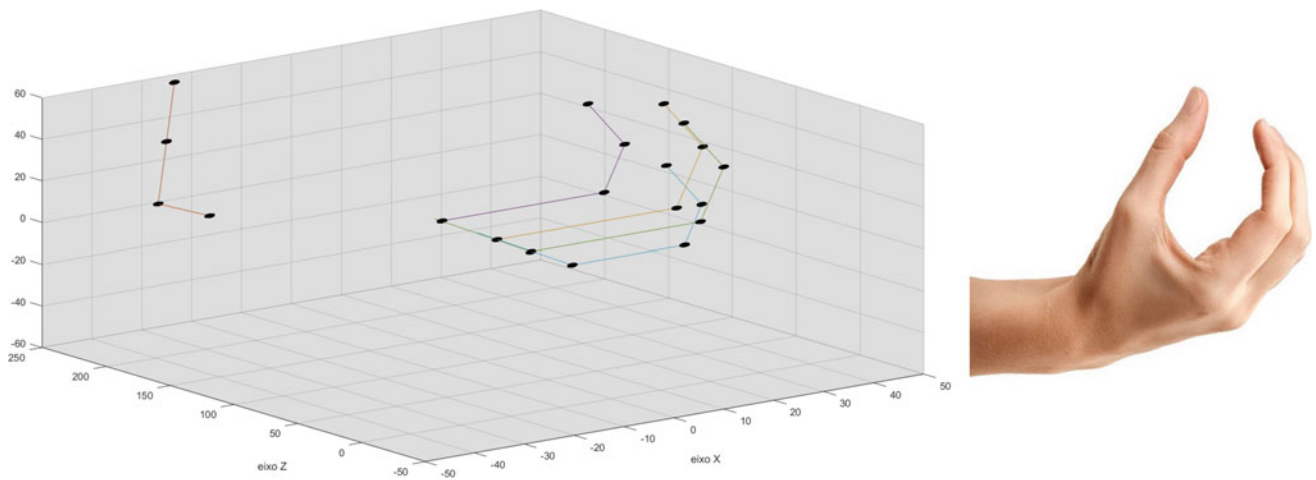
Fig. 3 Simulation of left hand movement

Fig. 4 Simulation of a pointing finger

Fig. 5 Simulation of a closed hand

Fig. 6 Simulation of two fingers touching

5 Conclusions

In this paper is present the forward kinematics of the human hand and the first important results on the validation of the mathematical model, running on a simulator that represent the basic movements. The control of the hand will allow as future work to reveal some solution of singularities of gesture recognition systems.
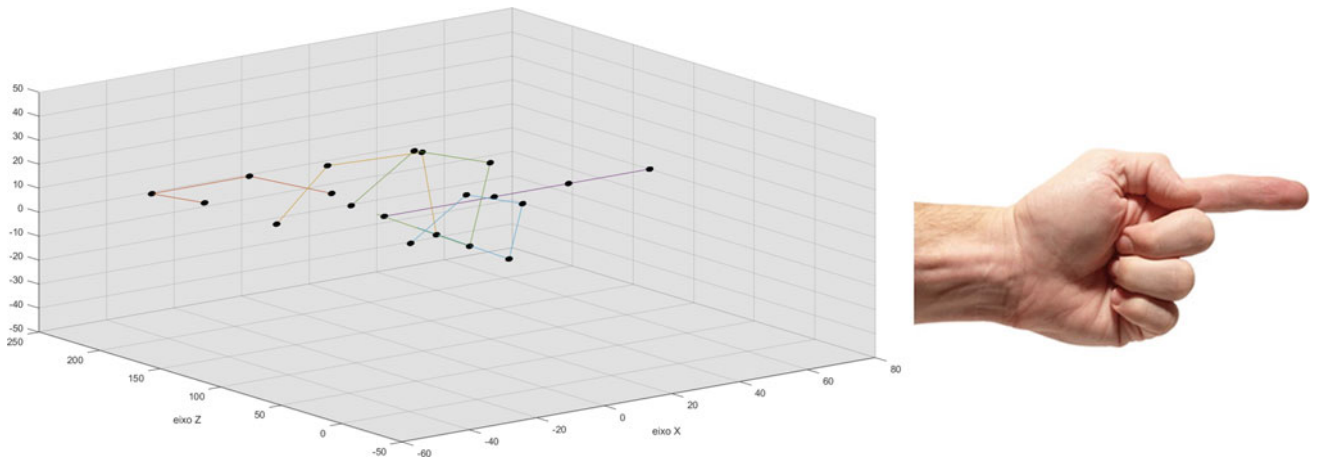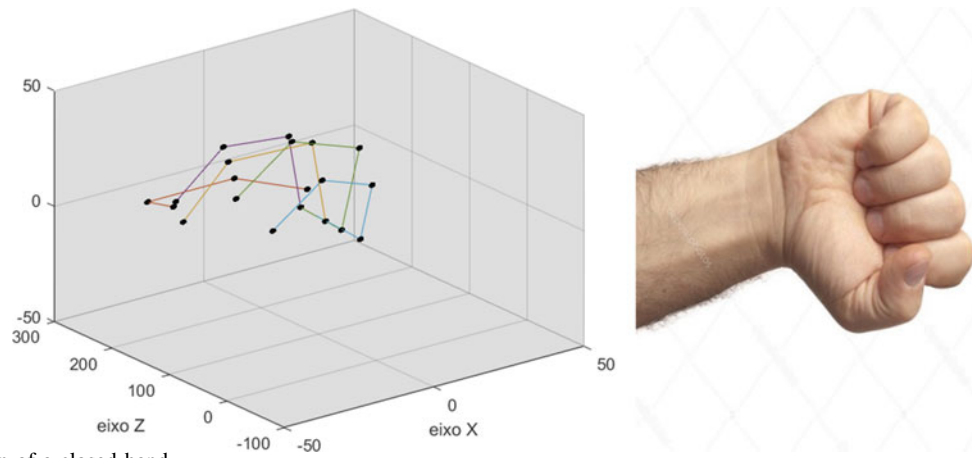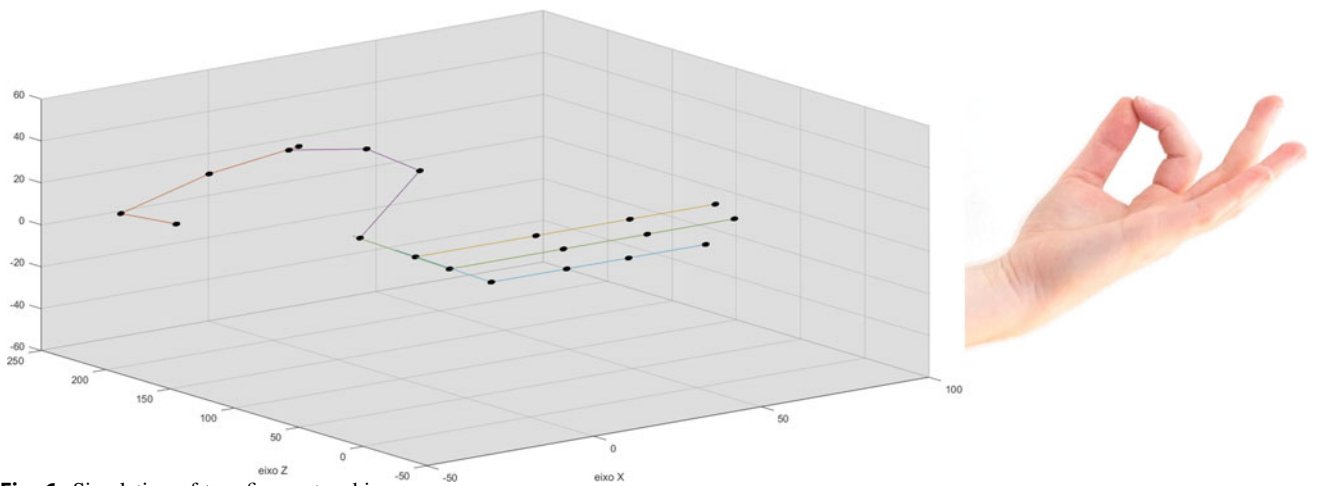
References

1. Cabral, E.L.L.: Análise de Robôs, ch. 5. Disponível em: http://sites.poli.usp.br/p/eduardo.cabral/Cinem%C3%A1tica%20Direta.pdf. Acesso em 18/03/2018
2. Craig, J.J.: Introduction to Robotics: Mechanics and Control, vol. 3, pp. 48–70. Pearson/Prentice Hall, Upper Saddle River, NJ, USA (2005)
3. Damsgaard, M., Rasmussen, J., Christensen, S.T., Surma, E., de Zee, M.: Analysis of musculoskeletal systems in the AnyBody modeling system. Simul. Modell. Pract. Theory **14**(8), 1100–1111 (2006)
4. Davoodi, R., Urata, C., Todorov, E., Loeb, G.E.: Development of clinician friendly software for musculoskeletal modeling and control engineering. Med. Biol. Soc. (2004). https://doi.org/10.1109/iembs.2004.1404281
5. Delp, S.L., Anderson, F.C., Arnold, A.S., Loan, P., Habib, A., John, C.T., Guendelman, E., Thelen, D.G.: OpenSim: open-source software to create and analyze dynamic simulations of movement. IEEE Trans. Biomed. Eng. **54**, 1940–1950 (2007)
6. Delp, S.L., Loan, P.: A graphics-based software system to develop and analyze models of musculoskeletal structures. Comput. Biol. Med. **25**, 21–34 (1995)
7. Khachani, M., Davoodi, R., Loeb, G.: Musculo-skeletal modeling software (MSMS) for biomechanics and virtual rehabilitation. IEEE Trans. Biomed. (2000)
8. Lopes, A.M.: Modelação Cinemática e Dinâmica de Manipuladores de Estrutura em Série. FEUP, Porto (2001)
9. Stoppa, M.H., Carvalho, J.C.M.: Modelagem cinemática, simulação de movimento, construção e controle de prótese de mão para tarefas de manipulação. In: Matemática aplicada à indústria: problemas e métodos de solução, pp. 183–208. Blucher, São Paulo (2016)

Social Robot for Interaction with Children

Christiane Goulart, Carlos Valadão, Vinícius Binotte, Alvaro Favaratto,
Douglas Funayama, Eliete Caldeira, and Teodiano Bastos-Filho

Abstract

Assistive robotics is a field that has gained more visibility recently due to the social impacts it can provide. Currently, robots can be used to assist people in mobility, healthcare and even in behavioral issues, and thus, they are also known as social robots. This work shows the first contact of typically developing children with a robot, which will be used for interaction with children with Autism Spectrum Disorder further. The first contact with typically developed children is important to know if the robot is able to catch their interests and, which improvements the children would recommend about the robot shape and behavior. In total, 36 typically developing children had a first contact with the social robot and the experiment took place in elementary schools. Social skills, such as eye gaze, tactile interaction, communication, proximity and social engagement were evaluated. Surveys asked about the facial expressions of the robot and children's likes, dislikes and feelings. The results showed that the children performed the social abilities satisfactorily, understood the robot emotional facial expressions easily, liked the robot and suggested improvements.

Keywords

Autism spectrum disorder • Social robot • Social skills

C. Goulart · T. Bastos-Filho
Postgraduate Program in Biotechnology, Assistive Technology Group, Federal University of Espirito Santo, Vitória, ES, Brazil
e-mail: christiane.ufes@gmail.com

T. Bastos-Filho
e-mail: teodiano.bastos@ufes.br

C. Valadão (✉) · V. Binotte · E. Caldeira · T. Bastos-Filho
Postgraduate Program in Electrical Engineering, Assistive Technology Group, Federal University of Espirito Santo, Vitória, ES, Brazil
e-mail: carlostvaladao@gmail.com

V. Binotte
e-mail: vbinotte@gmail.com

E. Caldeira
e-mail: eliete.caldeira@ufes.br

A. Favaratto
Department of Mechanical Engineering, Assistive Technology Group, Federal University of Espirito Santo, Vitória, ES, Brazil
e-mail: alvarofavarato@gmail.com

D. Funayama
Department of Computer Engineering, Assistive Technology Group, Federal University of Espirito Santo, Vitória, ES, Brazil
e-mail: douglasfunay@gmail.com

1 Introduction

Robotics has a wide field of applications that ranges from industry to daily life applications, including healthcare. This latter can be subdivided in subgroups, such as social assistive robotics, which can aid human-robot interaction by stimulating some human behaviors [1]. This can benefit both patient and caregiver or therapist, once they can monitor several data about the individual and try to establish some level of interaction with the patient [2].

Social robots have been shown as a promising tool in therapies for children with Autism Spectrum Disorder (ASD), since these tend to accept the robots and machines more than other humans, because they are easier to predict and understand [3, 4]. Therefore, in the therapeutic treatments these children usually undergo, the robot can stimulate them to have contact with the surrounding environment [5, 6].

According to [7], the emphasis given to socially assistive robots are related to the human-robot interaction and includes social skills, as eye contact, verbal and non-verbal communication, imitative game, joint attention, among other social kinds of interaction. Such social skills are very relevant to the socializing and relationships. To cope with this interaction, the robot can be designed in different shapes, including anthropomorphic (humanoid shapes), non-anthropomorphic (only biomimetic, i.e., resembling

animals or biological creatures) and non-biomimetic (not resemble humans or biological creatures) [8].

Some of these robots are mobile robots, which mean they can move in the space. This is an attractive to catch the children's attention, for both typically developed and those with ASD [8], making possible new capabilities of interaction with the children when compared with a standing only robot [8, 9].

Other functionalities such as human recognition and machine emotional intelligence can create a better environment for a human-robot interaction experience with the children [8–10]. Studies such as presented in [11] and [12] present some research in the development of robots to interact socially with people, including the use of external movies, robot expressions [11] and tactile strategies [12]. In [11], it is shown that a multimodal robot, called ALICE, that includes gestures and voice synthesis can help adult people understand emotion content better in cases when there are less affective cues. Furthermore, it is also presented in [12] that tactile sensors in robot KASPAR, could help children with ASD to interact better with the robot, enhancing the way they interact with the robot in the proposed scenarios, including a "cause and effect" game that needed to have tactile interaction. These authors also suggest that, although a log-term therapeutic study should be conducted for more information about the children's development, they may have benefits with a tactile robot, including by participating of therapeutic games that can use the robot tactile sensors to help children improve their focus and concentration.

In our work, we present a robot called N-MARIA, acronym for New Mobile Autonomous Robot for Interaction with Autistics, with an anthropomorphic shape and some machine-like elements that make it highly identified as a robot, not as humanoid. Besides, an evaluation of social skills (tactile interaction, eye gaze, proximity and social engagement) is performed during the interaction between typically developing children and the social robot, and analysis of surveys are conducted about robot facial expressions, structure and function.

2 Methodology and Materials

2.1 The Social Robot

A design of an assistive robot is introduced here in which some features of the aforementioned robots were considered to build a new version of the previous robot called MARIA, acronym for Mobile Autonomous Robot for Interaction with Autistics. The new version is called N-MARIA, with the word "New" added before the acronym. Essentially, N-MARIA main features (Fig. 1) are presented as follows:

- Dynamic face, running in a tablet, that supports animations for seven emotional expressions: happiness, sadness, anger, disgust, fear and surprise (which are the six basic ones) added to the neutral expression;
- Speaking ability, which allows it to make preprogrammed speeches;
- Mobility, that includes both autonomous and supervised movement, which counts with safety support and supervision;
- Multiple sensors, to be able to better interact with the environment and children, such as thermal and color cameras, laser, in addition touch sensors;
- Height: 141 cm, close to a 9-year-old child's height to allow a face to face interaction.

Fig. 1 Robot N-MARIA built with ideas taken from a survey with children and from the literature
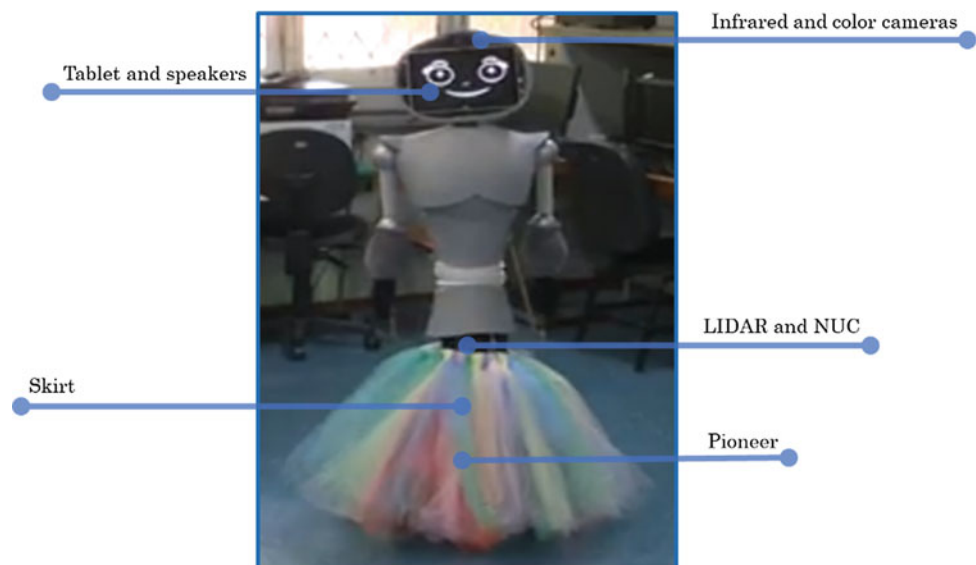
2.2 Experiments with N-MARIA

Tests were conducted in two elementary schools of Vitoria, Brazil. Both schools accepted to participate in the tests, and volunteered students (their parents gave informed consent), allowing their participation on the tests. Thirty-six children took part of the test, being 18 boys and 18 girls, aged from 8 to 13 years old. The test planning and protocol were previously submitted and approved by the Ethical Committee of the Federal University of Espirito Santo (number 1,121,638).

The tests were conducted in the school room where temperature was held about 22 °C. Individually, each child participated of the tests. Inside the room, initially, the robot was still and covered with a black mantle, while the child remained sit in a relax state for about 10 min, to stabilize the body temperature with the room temperature, in order to ensure appropriate thermal image acquisition. Analysis of the facial thermal images will be conducted further to evaluate the emotions expressed by the children when seeing the robot for the first time. As it was the first contact with children, it was decided to keep the robot stopped.

The child was positioned in front of the covered robot at a 70 cm distance. However, the cameras on the top of the robot head were discovered to allow the recording of facial images before the display of the robot. 70 cm away from the robot is an appropriate distance for recording facial images and visualizing the robot; in addition, it is inside the personal zone, with basis on proxemics concepts that define this zone between 45 and 120 cm [13], distances previously marked on the floor. Proxemics quantifies the spatial distances that individuals maintain in various social and interpersonal situations and was used here to classify the children's proximity in relation to the robot.

The experiment that evaluates the interaction with the robot N-MARIA was conducted in two short parts with 2-min duration each one, where social skills, as tactile interaction, shared engagement, eye gaze and proximity were evaluated through analysis of images obtained by external and internal-to-the-robot video camera and touch sensors. In the first part, the black sheet that covered the robot was removed, and a self-presentation was made by it through dialogues displayed during the experiment, encouraging the child to approximate the robot, have eye contact and communication. This part is important to help the child lose possible fear and feel comfortable with it. During the second part, the child was encouraged to interact freely with the robot, touching and dialoguing with it and with the mediator. If the child wished, he/she could approximate to the robot, stare at its structure, touch its

structure and even talk to it. In the whole experiment the robot does not move, images of the experiment and child's facial images were acquired and a Bluetooth keyboard was used to manual change of the dialogue playing.

After four minutes, the cameras were turned off and the child was invited to fill up a questionnaire, under structured interview, applied the same way to all participants. A first questionnaire was related to emotions exhibited by the robot face, which could be one of the six basic emotions (happiness, sadness, fear, disgust, anger or surprise). Another questionnaire was related to the child's perception in relation to the robot, about things the child liked or not. The questionnaire consisted of a mix of questions for objective and free answers and was based on a previous questionnaire developed with the aim of evaluating the structure of the robot MARIA (first robot prototype) [14]. After accomplishing the questionnaires, the test was ended.

3 Results

During the first part of the interaction, where the robot performs a self-presentation, the analysis of the images showed an intense eye gaze with the robot and communication, by answering questions made by the robot about their names and preferred tasks. In addition to these two social skills identified, the children did not distance from it, when the robot was discovered, keeping proximity in relation to the robot, inside personal zone. In the second part of the interaction, tactile interaction (Table 1) and shared engagement with the mediator (when children asked about the robot structure) was evaluated.

After the test, the children answered a second survey about the robot emotions (Table 2) and shapes and functions (Table 3). This last survey, basically, contains questions about the robot shape, size, aesthetics and the functions, in addition to questions about how the child felt before and after the test with the robot.

Table 1 Robot touched areas

Touches by region		
Region	Touches	Percentage (%)
Arms and Hands	186	44.5
Trunk	169	40.4
Skirt	48	11.5
Head	14	3.3
Base platform	1	0.2
Total	418	100.0

Table 2 Recognition of the robot emotion expressions by typically developing children

Emotions	Happiness	Sadness	Surprise	Disgust	Fear	Anger	General
Success rate	100	94	92	100	94	100	97

Table 3 Answers from the survey about the robot made by typically developing children

#	Question	Answers			
1	How did you feel before seeing the robot?	**Normal** 20	**Happy** 9	**Surprised** 6	**Afraid** 1
2	What is your opinion about the robot's appearance?	**Beautiful** 23	**Different** 12		
3	What did you like in the robot?	**Functions** 17	**Shape** 8	**Face** 7	**Height** 3
4	What did you dislike in the robot?	**Color** 10	**Clothes (skirt)** 9	**Shape** 3	**Height** 3
5	Did you like to see the robot?	**Liked** 36	**Dislike** 0		
6	How did you feel after seeing the robot?	**Surprised** 17	**Happy** 14	**Normal** 5	
7	What would you change in the robot?	Suggestions: put hair on the robot and change it in color, clothes, voice, shape and body ornaments			

4 Discussion and Conclusions

Results obtained in the first contact of typically developing children with the robot N-MARIA were mostly positive. Through a 4-min experimental protocol, children could see, communicate and touch the structure of the robot, in addition to understand most of its functions. In general, they had curiosities and did not presented repulsion, staying at a distance classified as personal zone, according to proxemics.

Emotional expressions of the robot were successfully identified by children with accuracy rate higher than 90%, and the answers of the questionnaire about the shape and functions of the robot were evaluated to improve the robot (mainly in its appearance). Additionally, touch sensors were properly used, recording the number of touches performed by children in the robot structure. The parts of the robot structure most touched were arms and hands, which also could be observed in [15].

The major limitation of this work was the external noise, a variable hard to be controlled since the tests were performed in schools. On the other hand, as contributions, the study was able to get information about children behavior towards the robot using contact free sensors, based on imaging and touching. This may be especially useful for children who have ASD diagnosis, since they are sensitive to any kind of sensor attached to their bodies.

4.1 Future Works

This first set of tests was conducted with typically developing children, i.e., without ASD, to collect information about how children would react to the robot. Findings obtained up to now give a clue about possible children's behaviors during the interaction with the robot. This will help the N-MARIA developers to implement improvements for future tests with children with ASD.

At first, the same protocol conducted here will be applied for children with ASD with the help of the therapist who works with them. Posteriorly, these children will be exposed to the robot actions for a five-week term in order to evaluate increase of social skills. Thus, it will be possible to analyze statistically if the child could have their social skill and behavior stimulated by the robot or not. Scales such as System Usability Scale, known as SUS [16], will give a quantitative measurement of the robot usage. Parallelly, thermal image acquisition will be recorded for further analysis of emotions in the child-robot interaction.

Conflict of Interest The authors declare that they have no conflict of interest.

References

1. Kim, E.S., et al.: Social robots as embedded reinforcers of social behavior in children with autism. J. Autism Dev. Disord. **43**(5), 1038–1049 (2013)
2. Feil-Seifer, D., Mataric, M.: Automated detection and classification of positive vs. negative robot interactions with children with autism using distance-based features. In: Proceedings of the 6th International Conference on Human-Robot Interaction—HRI '11, p. 323 (2011)
3. Duquette, A., Michaud, F., Mercier, H.: Exploring the use of a mobile robot as an imitation agent with children with low-functioning autism. Auton. Robots **24**(2), 147–157 (2008)
4. Robins, B., Amirabdollahian, F., Ji, Z., Dautenhahn, K.: Tactile interaction with a humanoid robot for children with autism: a case study analysis involving user requirements and results of an initial implementation. In: Proceedings—IEEE International Workshop on Robot and Human Interactive Communication, pp. 704–711 (2010)
5. Robins, B., et al.: Human-centred design methods: developing scenarios for robot assisted play informed by user panels and field trials. Int. J. Hum. Comput. Stud. **68**(12), 873–898 (2010)
6. Scassellati, B., Admoni, H., Matarić, M.: Robots for use in autism research. Annu. Rev. Biomed. Eng. **14**(1), 275–294 (2012)
7. Boccanfuso, L., Scarborough, S., Abramson, R.K., Hall, A.V., Wright, H.H., O'Kane, J.M.: A low-cost socially assistive robot and robot-assisted intervention for children with autism spectrum disorder: field trials and lessons learned. Auton. Robots **41**(3), 637–655 (2017)
8. Cabibihan, J.-J., Javed, H., Ang, M., Aljunied, S.M.: Why robots? a survey on the roles and benefits of social robots in the therapy of children with autism. Int. J. Soc. Robot. **5**(4), 593–618 (2013)
9. Salter, T., Dautenhahn, K., Te Boekhorst, R.: Learning about natural human-robot interaction styles. Robot. Auton. Syst. **54**(2), 127–134 (2006)
10. Picard, R.W., Vyzas, E., Healey, J.: Toward machine emotional intelligence: analysis of affective physiological state. IEEE Trans. Pattern Anal. Mach. Intell. **23**(10), 1175–1191 (2001)
11. Aly, A., Tapus, A.: Multimodal adapted robot behavior synthesis within a narrative human-robot interaction. In: IEEE International Conference on Intelligent Robots and Systems, vol. 2015, December, pp. 2986–2993 (2015)
12. Robins, B., Dautenhahn, K.: Tactile interactions with a humanoid robot: novel play scenario implementations with children with autism. Int. J. Soc. Robot. **6**(3), 397–415 (2014)
13. Hall, E.T.: The Hidden Dimension: Man's Use of Space in Public and Private, 201 pp.. The Bodley Head Lts, London (1966)
14. Goulart, C.: Uma Contribuição ao Estudo de Sinais de EEG para Avaliar Estados Emocionais e Mentais de Crianças com Autismo na Interação com Robô Móvel (2015)
15. Valadão, C.T., et al.: Analysis of the use of a robot to improve social skills in children with autism spectrum disorder. Res. Biomed. Eng. **32**(2), 161–175 (2016)
16. Brooke, J.: SUS: a retrospective. J. Usability Stud. **8**(2), 29–40 (2013)

Structural Analysis with Finite Element Method of a Child Electric Wheelchair Built with PVC and Arduino

Filipe Loyola Lopes, Henrique Alves de Amorim, and Maria Elizete Kunkel

Abstract

The electric wheelchair allows people with severe motor disabilities, such as cerebral palsy, to be more independent, to have more quality of life and to be included in society. In the world 20 million people with motor disabilities do not have access to manual or electric wheelchair due to high costs of this technology. In Brazil, the Unified Health System does not grant electric wheelchairs for children under 12 years old and its costs about R$13,000.00. This is a relevant factor for these children that do not have access to formal education. The aim of this research was evaluate, through mechanical simulation by the finite element method, a low-cost child electric wheelchair built with PVC Pipes and Arduino. The evaluation indicates that the PVC material is suitable for the mechanical structure of an electric wheelchair. To avoid the wheelchair frame deformation, the loading mechanical limits was defined with a safety margin of 50% (141 kg for the PVC structure and 46 kg for the medium density fiberboard seat). Future modifications can be made, so that the wheelchair can withstand higher weight, such as adult. Furthermore, the results of this research can help future studies about smart electric wheelchair interfaces that require a low-cost wheelchair framework for tests.

F. L. Lopes (✉) · M. E. Kunkel
Federal University of ABC - UFABC, São Bernardo do Campo, SP, Brazil
e-mail: loyolafilipe@gmail.com

F. L. Lopes
National Institute of Telecommunications - INATEL, Santa Rita do Sapucaí, MG, Brazil

H. A. de Amorim · M. E. Kunkel
Federal University of São Paulo - UNIFESP, São José dos Campos, SP, Brazil

1 Introduction

Societies in many countries have organized themselves to provide resources for social inclusion, such as wheelchairs for people with motor disabilities [1]. Nowadays, about 1% of the world population needs a wheelchair, it represents 70 million people [2]. However, due to high costs of technology and the high rate of low-income people, 20 million do not have access to a manual or electrical wheelchair (EWC) and this lack of access has been a complex problem in countries in development [3]. This is even more severe for children than adults, because the problem may represent the lack of access to formal education. Most of the out-of-school population consists of children and adolescents with disabilities, and the greater the degree of disability, the more impaired is access to education [4]. In addition, the lack of wheelchair access impairs psychosocial development, as it makes it difficult for children with disabilities to participate in games and have contact with other children. Therefore, it is hindering the development of emotional and social skills that depend on contact with other children. The use of EWC for small children is a medical necessity to promote integration, psychosocial development, independence and functionalities of the child [5]. In Brazil, due to high costs of technology, the Brazilian Unified Health System (SUS) does not provide EWC for children under 12 years old [6].

Until the 1980s, materials such as wood, leather, iron and aluminum were used for the development of assistive devices [7]. From the 1990s, new materials such as polyvinyl chloride (PVC) began to be used to produce low cost assistive technology. PVC has peculiar characteristics such as lightness, ease of cleaning, durability, good mechanical resistance, modularity and low cost. This thermoplastic was applied in some studies to construction of wheelchair [8–11]. However, there has been a lack of researches that quantitatively verifies the mechanical strength of a wheelchair frame constructed by PVC pipes.

The finite element method (FEM) is a way of evaluate the mechanical resistance of a materials system. This method is used in structural engineering and helps in stress and strain analysis of solids with varied geometries, such as the wheelchair structure. The FEM works through differential equations that represents the physical integration of elements of a 3D mesh. Graphics, animations and representations on the stress and deformation of materials system can be generated through means of a computer simulation program [9, 12–14]. In an earlier study, a model of child EWC was built with PVC and Arduino [15, 16]. The aim of the present study was to perform static mechanical simulation through FEM in order to measure how much weight the PVC structure can withstand.

2 Materials and Methods

The research was developed in four phases: (1) Study of PVC child's EWC model; (2) Creation of 3D model; (3) Static mechanical simulation by FEM; (4) Math analysis. The PVC child's EWC frame used in this study was assembled with reference to an Open Wheelchair Foundation (OWF) [9]. However, the design was reconfigured to be assembled with parts available in Brazil (1/4″ PVC tubes and connections for cold water (Tigre, Joinville, Brazil). Anthropometric measurements concerning a 5-year-old child were used to define the dimensions of the EWC frame: (a) back height of 36 cm; (b) hip width of 25 cm; (c) length of thighs of 30 cm; (d) length of legs of 28 cm; (e) height of arms of 14 cm; and (f) length of forearm of 25 cm [15]. The wheelchair frame was built with 55 PVC connectors and 68 segments of PVC pipe (Fig. 1).

The electronic system has nine functional blocks (Fig. 2). The parts of EWC cost approximately R$1,830.00, considering electronic and mechanical structural parts.

Fig. 1 3D rendering of child's electric wheelchair frame made by PVC pipes and Arduino

The 3D model and static mechanical simulation by FEM were made with the SolidWorks program (Dassault Systèmes, Vélizy-Villacoublay, France). A simplified frame was modeled as a single piece built by beams and the medium density fiberboard (MDF) seat was modeled as solid mesh, made by tetrahedrons with 4.82 μm maximum edges. The simulation was performed with different mechanical loading

Fig. 2 Blocks diagram of child's electric wheelchair circuit. Adapted from [16]
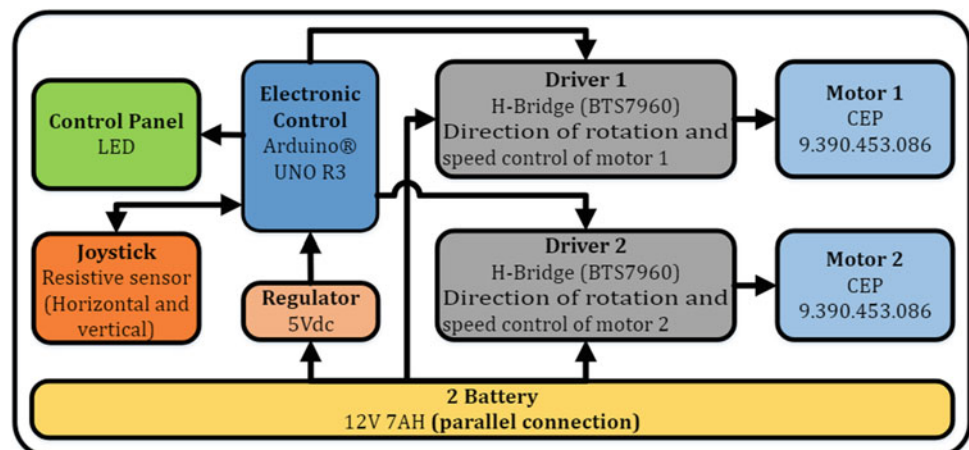
from 15 to 100 kg. The material properties used in the frame were rigid PVC, available from the Solidworks simulation library. However, the elasticity modulus (3061.2 MPa) and the flow limit (34.8 MPa) used were based on literature [17]. The material used in the 3D mesh of the seat was MDF. This material does not exist in the SolidWorks library, so, the characteristics of the wood barsa available in the program were used and the modulus of elasticity was modified (2934 MPa) [18]. The results obtained in the simulations were used to create scatter plots with Excel 2016 program (Microsoft Corporation, Redmond, USA). A simple regression was performed to obtain a mathematical model that represented the interaction between the applied load and the mechanical stress obtained.

3 Results

A simplified 3D model of the EWC frame was created to FEM simulation. It was created by beams mesh with the dimensions of 1/4″ PVC tubes. The seat was created by MDF (solid mesh) (Fig. 3).

Four fixed points were inserted in the 3D mesh, at the same points where the EWC frame is trapped by the wheels. In addition, for the simulation, vertical forces were applied to the surface of the seat. The simulations were performed with different loads: 15, 30, 45, 60, 75 and 100 kg. For each simulation five parameters were obtained: von Mises stress in the beam mesh, axial stress in the solid mesh, maximum sprain, maximum deformation and safety factor (Table 1).

The safety factor is automatically generated by the Solidworks program. It considers the maximum material stress in relation to its flow limit. If the safety factor is greater than 1 there is a safety margin of 50% [13]. The flow limit considered to the frame material (PVC) was 34.8 MPa and the flow limit considered to the seat material (MDF) was
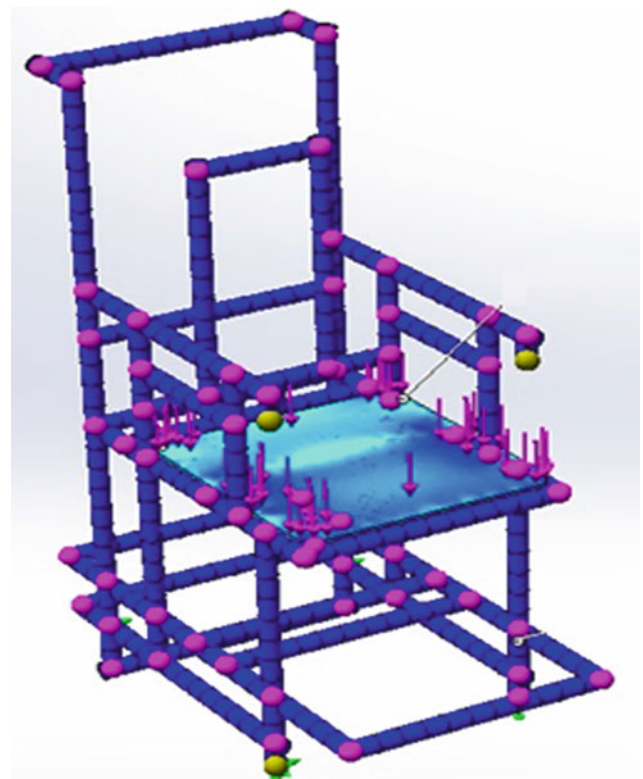
Fig. 3 Mechanical static simulation of child electric wheelchair with a PVC frame. The purple arrows indicate the application of the loading force (Color figure online)

19.99 MPa. Considering solid mesh (MDF seat) the maximum weight supported by the materials is 45.54 kg. A simple dispersion and regression graphs were performed to relate the von Mises (beam mesh) values as a function of the applied load. The correlation coefficients (R^2) were 100% (Fig. 4).

With 50% safety margin, the mathematical models generated by the regressions were used to estimate that the maximum weight supported by PVC structure is 141.25 kg.

Table 1 Results obtained in the mechanical simulation by the finite element method. The bold values are outside the safety margin of 50%

Applied load (kg)	Maximum von Mises stress to the beam mesh (MPa)	Maximum axial stress to the solid mesh (MPa)	Maximum sprain (mm)	Maximum deformation (%)	Safety factor
15	2.04	3.52	1.05	0.1	2.56
30	4.08	6.78	2.06	0.2	1.51
45	6.12	**10.17**	3.08	0.3	**1.00**
60	8.16	**13.56**	4.11	0.4	**0.75**
75	10.20	**33.18**	5.14	0.5	**0.60**
100	13.59	**44.25**	6.85	0.7	**0.45**

Fig. 4 Von Mises stress in the PVC structure as a function of the applied load

Function:
y = 0,1359x + 0,0035

Correlation coefficients:
$R^2 = 1$
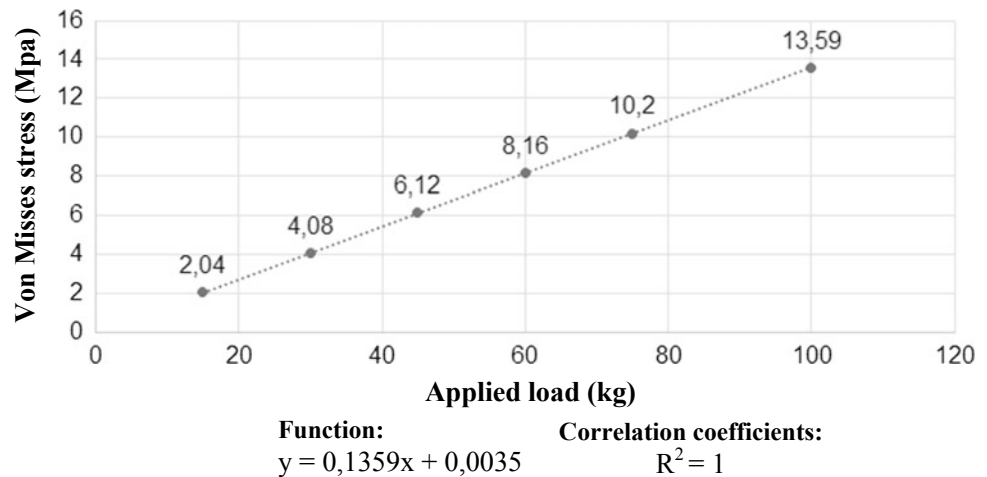
4 Discussion

This research showed that it is possible to construct a child EWC with PVC pipes for water, with a 3/4″ outside diameter, one of the low-cost and easy to find PVC pipe types in Brazil. Other studies have also approached the PVC for the construction of wheelchair [8–11]. However, only the present research and OWF have approached the PVC for the construction of EWC [10]. OWF used a special type of PVC pipe by 1/2″ of diameter, which is a suitable material for the construction of planned furniture (https://formufit.com/). This type of pipe is not easily found in Brazil and the USA imports cost is high. In this research, the PVC pipe used was PVC for conducting cold water in civil construction, so, it is the low-cost easier to acquire.

Through the mechanical simulations and mathematical analysis performed in this research it was verified that the wheelchair model constructed with PVC pipes can sustain a person up to 141.25 kg without deformation in the structure of his frame. However, the MDF seat has a lower weight limit: 45.54 kg. It can be seen by analyzing the deformation image of the material that the tension limit on the MDF seat can be increased if the design is modified, with more PVC pipes being inserted below the seat. Since there will be greater contact between the seat and the beam mesh, there will be better weight distribution. In the present study it was verified that PVC is a strong enough material to build an EWC frame. This result agrees with another study that compared the structures of aluminum wheelchair frame with PVC wheelchair frame and concluded that PVC has enough mechanical resistance to support a person of 81.5 kg and has the advantage of lower cost [9].

5 Conclusion

In this study a computational static simulations by FEM were performed in order to verify the maximum weight load supported by the PVC structure without plastic deformation of the material. The PVC was satisfactory for a mechanically resistant and functional for infant child EWC structure. This research has the potential to help the low income population access EWC and provide new possibilities about different sizes and designs of PVC wheelchairs.

References

1. WHO: Word Report on Disability, p. 350. Genebra, Suiça (2011)
2. WHO: Guidelines on the Provision of Manual Wheelchairs in Less-Resourced Settings, p. 131 (2008)
3. WHO: Wheelchair Service Training Package: Basic Level, p. 90 (2012)
4. UNICEF: O direito de aprender: Potencializar avanços e reduzir desigualdades. Situação da infância e da adolescência brasileira, p. 131. Fundo das Nações Unidas para a Infância (UNICEF), Brasília (2009)
5. Rosen, L., et al.: RESNA position on the application of power mobility devices for pediatric users. Assist. Technol. (1), 22 (2017)
6. DATASUS homepage. http://sigtap.datasus.gov.br/tabela-unificada/app/sec/inicio.jsp. Accessed 15 June 2017
7. Dallegrave, C.P.M., et al.: Proposta de unidade terapêutica domiciliar de baixo custo baseada no protocolo Pediasuit. Revista Brasileira de Inovação Tecnológica em Saúde, Online **3**(2), 1–8 (2013)

8. Pettit, D.J., Cooper, R.A., Bennet, P.: Design and evaluation of a simple, inexpensive, ultralight wheelchair. In: 14th Annual International Conference of the IEEE Engineering in Medicine and Biology Society, pp. 1515–1516. IEEE, Paris, France (1992)

9. Teymori, M., et al.: Assessment of a newly designed PVC standing wheelchair by finite element method. In: 21st Iranian Conference on Biomedical Engineering (ICBME 2014), pp. 44–48. Biomedical Engineering Faculty, Amirkabir University of Technology (Tehran Polytechnic), Tehran, Iran (2014)

10. OWF homepage. http://www.openwheelchair.org/Gallery. Accessed 19 June 2017

11. Picart, J., et al.: Wheelchair for disabled children in Haiti. In: IEEE Systems and Information Engineering Design Symposium, pp. 252–254. IEEE Conference Publications, Charlottesville, VA, USA (2015)

12. Cota, F.D.P., et al.: Estudo numérico comparativo do emprego de materiais alternativos na construção de uma cadeira de rodas. Ciência e tecnologia: Fatec-JB, Jaboticabal **3**(1), 50–69 (2011)

13. Souza, L.R.D.S., et al.: Simulação computacional por elementos finitos e validação experimental de tubos de PVC solicitados à flexão. Congresso Nacional de Matemática Aplicada à Industria, pp. 1–8. CNMAI, Caldas Novas - GO (2014)

14. Dassault Systemes homepage. http://help.solidworks.com/2016/portuguese-brazilian/SolidWorks/cworks/c_Element_Types.htm?id=fc303328a5f546de87a3ebd1499bfc3a. Accessed 15 Jan 2018

15. Lopes, F.L., Kunkel, M.E., Amorim, H.A.: Design and testing of a low-cost electric wheelchair with PVC pipes and Arduino. In: 8th World Congress of Biomechanics. World Council for Biomechanics, Dublin, Ireland (2018)

16. Kunkel, M.E., Lopes, F.L., Amorim, H.A.D.: Low-cost electronic control with resistive joystick and Arduino for children electric wheelchair. Int. J. Biosens. Bioelectron. **3**(2), 00058 (2017). https://doi.org/10.15406/ijbsbe.2017.03.00058

17. Junior, L.C.G.P., Silva, F.R.D., Deus, E.P.D.: Avaliação e caracterização de tubos fabricados com PVC reciclado. Polímeros Ciência e Tecnologia **23**(4), 547–551 (2013)

18. Eleotério, J.R., Filho, M.T., Júnior, G.B.: Mechanical and physical properties of MDF panels of different. Ciência florestal **10**(2), 75–90 (2000)

Upper Limb Prosthesis for Patients with Congenital or Acquired Deformity

Ricardo Taoni Xavier, Aparecido Augusto de Carvalho, Eric Rohmer,
Fabian Castro, Fabio Agostinho Boris, José Paulo Codinhoto,
Erica Regina Marani Daruichi Machado,
and Marcelo Augusto Assunção Sanches

Abstract

A prototype of an upper limb prosthesis with a single control is presented in this paper. The prosthesis has 16 degrees of freedom, five fingers with independent joints and articulations in the hand's palm, being able to reproduce movements of anthropomorphic and anthropometric joints and holds. A sensorized glove was used to generate a database for the bionic hand, with different types of movements. Tests were performed on volunteers with congenital and acquired deformities. The results showed that the upper limb prosthesis works adequately with both types of patients.

Keywords

Upper limb prosthesis • Social inclusion • Electromyography • Grasps

1 Introduction

The hand is the main motor organ of the human body, being present in most everyday activities [1]. It should be borne in mind that bionic hands, in addition to providing better living conditions, also help to reinsert the individual into the social environment, improving their self-esteem and mental health.

A special issue in the upper limbs prosthesis field is the development of low cost bionic hands. Often, low cost bionic hands with many degrees of freedom, tactile sensors, electromyography driven mechanism and also using 3D printing technology are found in the specialized literature [2–6].

Polisiero et al. [7] developed a low-cost bionic hand to serve people of underdeveloped countries. The mechanism was developed in aluminum, with structure like a claw, driven by a single DC motor performing only the pincer movement.

Simmons and Welsh [8] developed a prototype of upper limb prosthesis operated by a low-cost electronic system using electromyographic signals, aiming the implementation of a reduced circuit, making viable the electromyography technology for the activation of upper limb prostheses.

Abid et al. [9] used low-cost technologies to analyze and develop a real-time bionic hand manipulation algorithm. They also used hand anthropomorphic mechanisms to perform the tests. The mechanism was developed in 3D printer, using the concept of the Inmoov platform arm.

Villoslada et al. [10] developed a mechanism with flexible sensors to analyze and study systems of dynamic mechanisms, and the mechanism applied to the reproduction of the robotic hand of the Inmoov platform. To control and develop a control method, they used sensors directly attached to each finger of the mechanism. This configuration allowed developers to analyze and qualify the movements performed by the engine.

O'neill [11] developed a low-cost upper limb prosthesis with anthropomorphic design and including all-finger joints. The bionic hand was made in 3D printing, and for stump fitting was adapted a PET bottle. A commercial electromyographic capture circuit was used as communication interface between user and bionic hand.

Fajardo et al. [12] developed a low-cost hand prosthesis with anthropomorphic design in 3D printing. Communication between patient and prosthesis was performed through processed electromyographic signals and pattern recognition using Artificial Neural Networks. For the system's activation, they developed a software with the 3D model of the mechanism, then dynamic analysis of the movements realized by the bionic hand was studied.

Xavier et al. [13] developed a low-cost upper limb prosthesis, made of recyclable material and commanded by

R. T. Xavier (✉) · A. A. de Carvalho · F. Castro · F. A. Boris · J. P. Codinhoto · E. R. M. D. Machado · M. A. A. Sanches
UNESP – São Paulo State University, Ilha Solteira, Brazil
e-mail: rtaoni@gmail.com

E. Rohmer
UNICAMP – Campinas State University, Campinas, Brazil

voice. It had five fingers with joints that simulate anatomical movements.

Hunold et al. [14] developed a low cost bionic hand using a smartphone as controller and a LEGO® platform as mechanical structure.

Stoppa and Carvalho [15] developed a mathematical modeling to analyze the degrees of freedom of the Inmoov platform, in order to develop and apply a low cost upper limb prosthesis.

Anthropomorphic projects of bionic hands have been gaining recognition and increased acceptance by users, however 80% of prosthesis are abandoned and discarded by users because they do not have the desired utility, are not very functional and have a high cost.

With analysis in the bibliographical references acquired, we contacted two fundamental aspects for the development of this work, being the first, the importance of developing an efficient and anthropomorphic prosthesis to reduce the current signs of abandonment. And the second is the implementation of low cost prosthetics, essential need in underdeveloped countries. The objective of this work is to implement a low-cost prosthesis for people with congenital and acquired physical disabilities, guaranteeing functionality and anthropomorphism.

2 Methodology

A prototype of upper limb prosthesis was built by using the mechanical structure from the free hardware and software Inmoov® platform, that is a humanoid structure constructed for human-like robotic interactions [16]. The mechanism has five fingers with independent joints, articulation in the hand's palm and 16 degrees of freedom.

Each finger is driven by a mechanical tendon that is attached to a servomotor; this system represents the anatomical structure of the organic tendons in the upper human limb [17]. Adaptations were made to improve the mechanical drive of the prosthesis. Originally, two tendons extended and flexed the fingers. Then, only one tendon of flexion was used in each finger, the extension movement is being carried out using springs adapted to the internal structure of the mechanism.

Force sensing resistors (FSR) were used to monitor the force applied to objects. The electronic system provides visual feedback through LEDs, which are used both to control the force applied to the object and to select the type of gripping motion. For recognition of the desired movement patterns in the bionic hand, a glove was used to monitor movements performed by the hand of a healthy individual. This information was later transferred to drive the prosthesis.

For analog and digital signals processing, as well as for communication between the user and the prosthesis,

a printed circuit board was developed, designed as a shield for the hardware platform and free software Arduino, based on the microcontroller Atmega 2560. This one is responsible for data processing and commanding the prosthesis.

The shield, called EMGLieb, has two acquisition channels for electromyographic signals, SD module for storage, and a connector for an electronic system. The electromyography (EMG) signal is picked up by surface electrodes and sent to the analog processing circuit. After being properly amplified and filtered, the EMG is sent to an analog-to-digital converter. The converted values are stored on the SD card through the SPI protocol.

The filtered signal is amplified about 500 times, reaching the amplitude of approximately 3 V. A variable gain inverter amplifier is used to better take advantage of the resolution of the 10-bit A/D converter, characteristic of the Atmega 2560 microcontroller.

A special methodology was implemented to correctly operate the prosthesis. This methodology begins with the formation of a database generated by a sensorized glove capable of storing the movements in real time. For this storage we dress the glove in a healthy hand and some motion is done and record the data. After this, it is necessary to store electromyography signals using EMGLieb. For parameterization and recognition of captured values, an algorithm containing the RMS value of the signal was used in the source code. This algorithm counts the number of pulses generated by the user and relates this amount to the desired movement that was programmed.

Calculating the RMS value causes the microcontroller to recognize only the necessary signals, eliminating possible false positives. The RMS, for a collection of N values $\{x_1, x_2, \ldots, x_N\}$ is given by Eq. (1):

$$x_{rms} = \sqrt{\frac{1}{N}\sum_{i=1}^{N} x_i^2} = \sqrt{\frac{x_1^2 + x_2^2 + \cdots + x_N^2}{N}} \qquad (1)$$

The RMS value of the signal picked up at each electrode is calculated and stored according to the need of the drive and the number of pulses to be counted within the same period.

The protocols and the interface used will be presented, for application of the codes of each command. As will be shown in Table 1, the command protocol is divided into three groups, being 100, 200 and 300. These groups have sub-groups that are responsible for activating the required command. Group commands 100 are used to start the bionic hand operation.

The commands of group 200 are used to store and acquire the electromyographic signals. The commands in group 300 are used for parameterizing the movements of the sensorized glove and for the ligament of movement performed with the glove and the number of pulses captured by the EMGLieb.

Table 1 Activation codes for the bionic hand command parameters

Code	Command
100	In this mode the hand must operate by positioning the hand according to the sEMG commands
120	Displays the positioning and the respective connected controls
130	Displays positioning and commands relative to stored sensor glove data
200	Configuration of sEMG commands for a given command file. In this mode you can enter myoelectric commands in different ways, and you can delete and view them Ex1: 200 1 (start command 1 settings)
210	Start an indefinite collection
211	Start a timed collection Ex1: 211 1000 (initiates a collection for 1 s) Ex2: 211 (starts a collection with TMP_PADRAO)
212	Start a collection by number of samples Ex1: 212 500 (starts a collection with 500 samples) Ex2: 212 (inicia uma coleta com QTD_PADRAO de amostras)
220	Appeal to stop the collection of undetermined time
230	Display data collected in the current command
240	Calculate and display number of pulses and RMS
290	Deletes the current command file
300	Configuration of movement positions. In this mode, the bionic hand must mimic all movements of the sensor glove automatically
310	Display the current values reported by the glove on the console
320	Store the current values entered by the glove in the current position file
330	Store values specified in the terminal in the current position file Ex: 330 10 20 30 40 50 (store the values 10, 20, 30, 40 and 50 as positions (minimum, annular, mean, pointer and thumb)
340	Display data stored in the current file
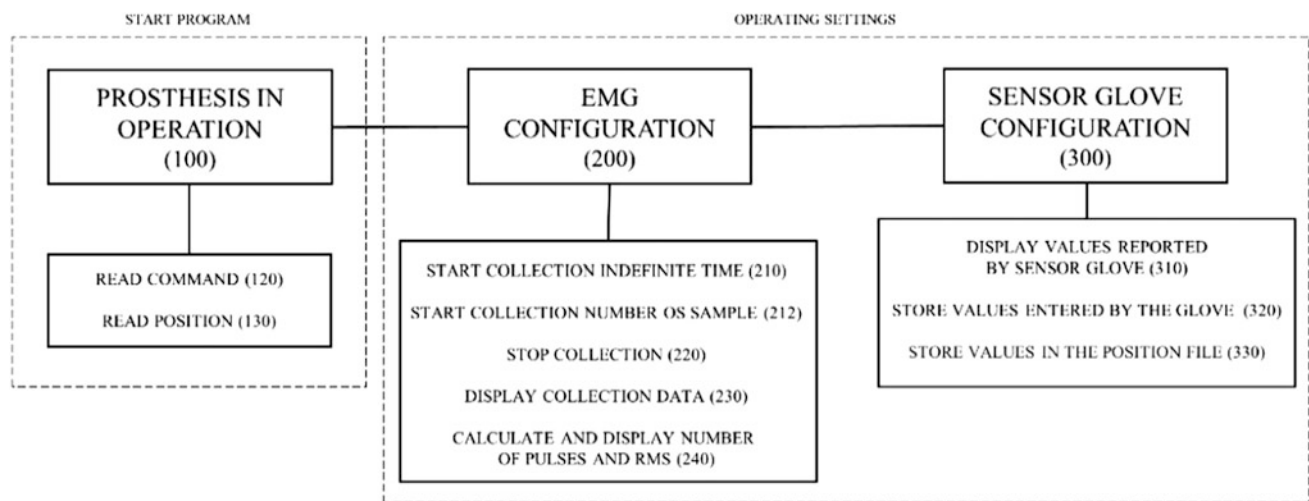
Fig. 1 Diagram of the codes for display in the IDE of stored general data

To exemplify the operation of the protocol, the diagram in Fig. 1 shows the activation of the commands in order. To include a command code, just write it at the Arduino IDE command prompt, since the source code is already properly programmed into the microcontroller.

Initial tests were performed with healthy volunteers, with congenital deformity, and with acquired deformity. Tests with volunteers were approved by the Brazilian National Research Ethics Committee (Process No. 15283613.0000).

3 Results and Discussions

Figure 2 shows some types of gripping motions performed by the prosthesis implemented. With the use of an accelerometer, the system can identify the position of the prosthesis in the pre-activation moment and, in this way, better perform some gripping motions. The preliminary results were positive, because with the prosthesis it was possible to perform gripping motions limiting the applied force.

The results showed that the correct application of the gripping motion is important for the use and adaptation of the user with the bionic system and that this prototype has functionalities that can aid in the rehabilitation of people. Considering that the electronic system of the bionic hand is capable of storing a database with several movements, it is at the discretion of the user to modify or add new movements.

The algorithm developed for characterization and recognition of pulses using the RMS value of the electromyography signal was able to identify and consider pulses valid for both people with congenital or acquired deformity.

Figure 3 shows tests performed with volunteers with congenital and acquired deformities.

So that the tests are not very tiring for the volunteers, the test protocol presents the action with only four muscle contractions. Considering that EMGLieb has two acquisition channels, the number of pulses per activation doubles, providing a greater amount of functional movements in the bionic prosthesis.

The EMG captured is sufficient for recognition in the algorithm responsible for the activation of the prosthetic system. Figure 4 shows the signals produced by three muscle contractions. After acquiring the signals, the algorithm was able to quantify and parameterize the pulses coming from muscle contraction performed by the healthy volunteer.

The generated signal was acquired by EMGLieb and processed by Arduino, where it was digitized and parameterized at a resolution of 10 bits, with the calculation of the RMS value quantifying each pulse. Figure 5 shows the discretized signals with the calculation of the RMS value in the time of five seconds.


Fig. 2 Spherical palmar grip (I); Bidigital grip (II); Open hand, total extension of fingers (III); Symbol of victory, representing gestural expressions (IV); Closed hand (V), total flexion of the fingers (VI); Cylindrical palmar grip (VII); Pluridigital grip; Extension of the indicator (VIII)
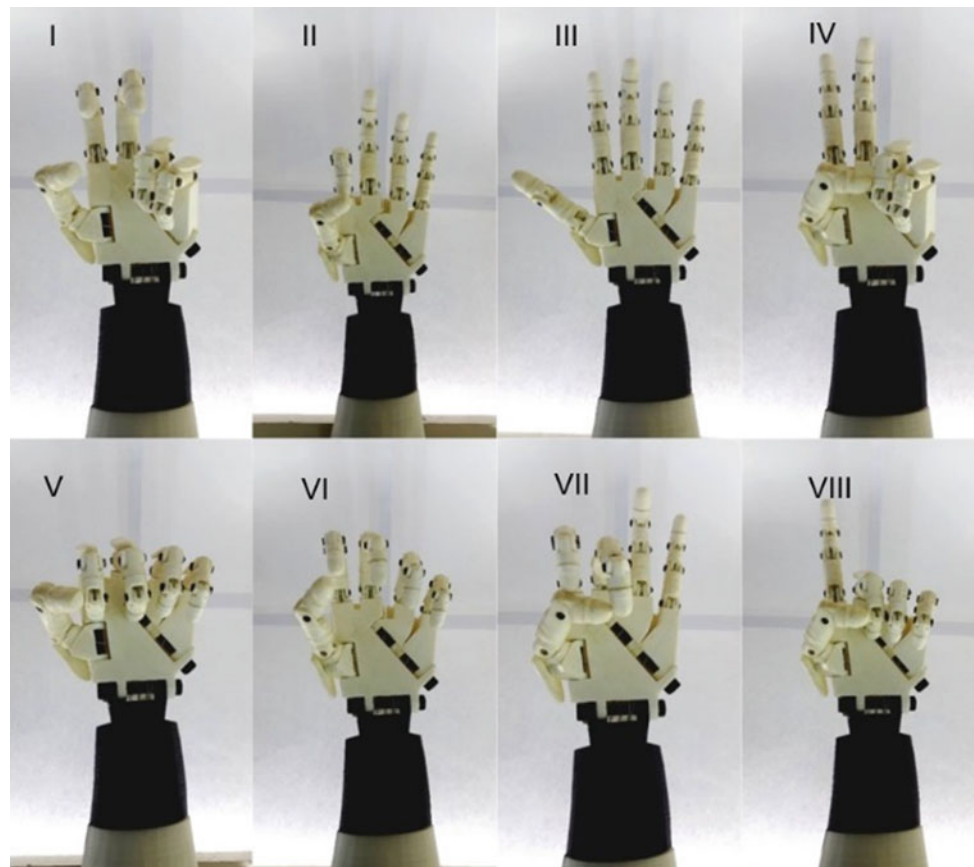
Fig. 3 Volunteers with congenital deformity (a) and with acquired deformity (b)
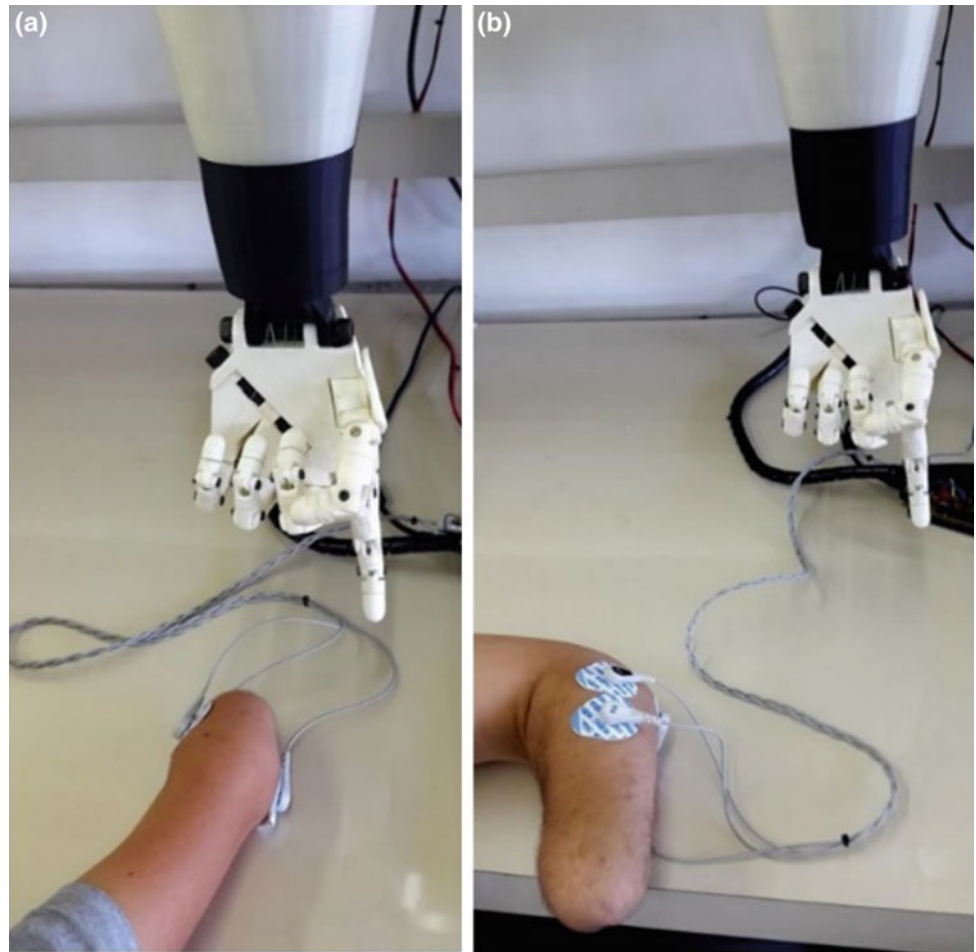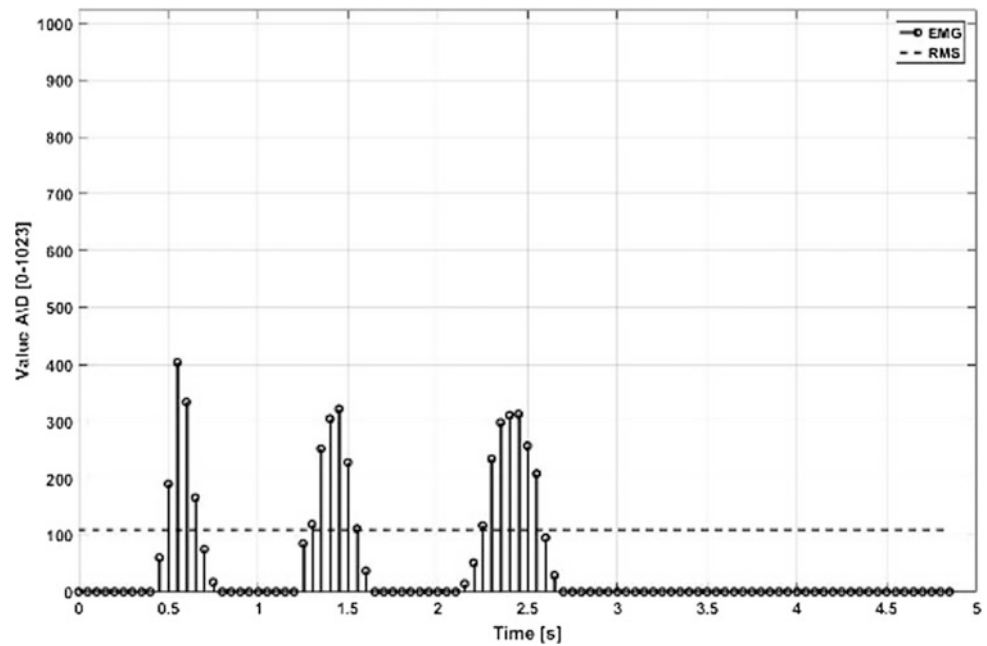

Fig. 4 Three EMG pulses resulted from a contraction processed by EMGlieb
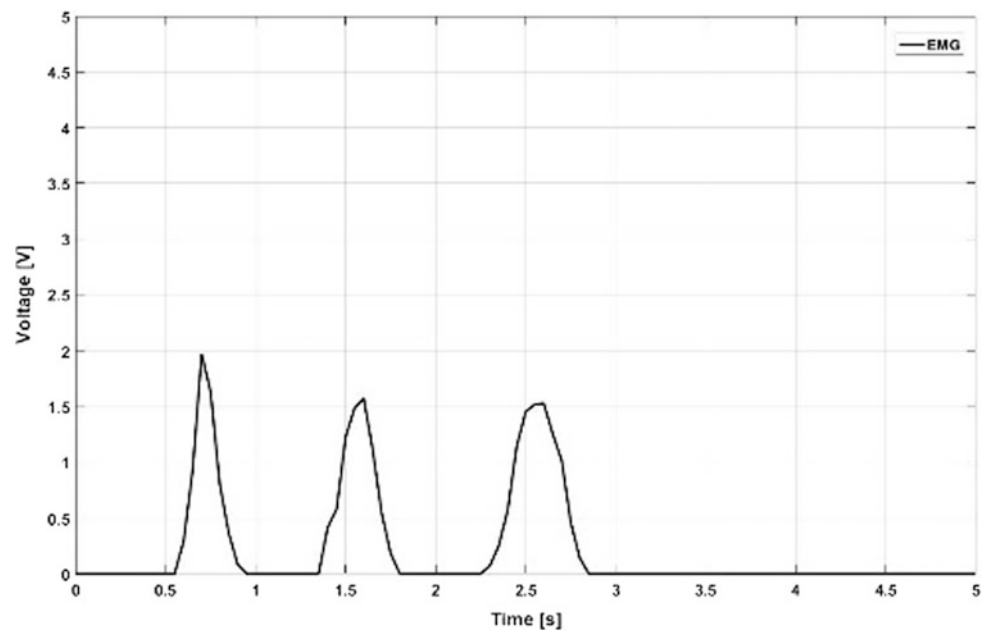
Fig. 5 Three pulses of digitized EMG result from three consecutive contractions processed with RMS value

4 Conclusions

The results show that the bionic hand prototype worked well for volunteers with congenital and acquired deformities. There is no need to modify the programming of the electronic system when changing the patient, making its use simpler compared to other prosthesis. Being a device built with low cost, open source technology, and functional applications, it is a viable product for the production of low cost upper limb prosthesis. The value of the implemented prosthesis was approximately US$200.

References

1. Aires, M.M.: Fisiologia, 4th edn. Guanabara Koogan, Rio de Janeiro (1991)
2. Tanrikulu, S., et al.: Anatomy and biomechanics of the wrist and hand. In: Sports Injuries: Prevention, Diagnosis, Treatment and Rehabilitation, 2nd edn., pp. 441–447. Springer, Berlin (2014)
3. Pylatiuk, C., Schulz, S., Döderlein, L.: Results of an Internet survey of myoelectric prosthetic hand users. Prosthet. Orthot. Int. **34**(4), 362–370 (2008)
4. Sureshbabu, A.V., Metta, G., Parmiggiani, A.: A new cost effective robot hand for the iCub humanoid. In: 2015 IEEE-RAS 15th International Conference on Humanoid Robots (Humanoids), pp. 750–757. Seoul (2015)
5. Nguyen, H.: Perceptual and comparative analyses of a passive, linear, multiple degree-of-freedom skin stretch device for proprioceptive substitution. M.S. dissertation, Dept. Aerospace Eng., Univ. of Illinois at Urbana-Champaign, Champaign, Illinois (2015)
6. Zuniga, J., et al.: Cyborg beast: a low-cost 3D-printed prosthetic. BMC Res. Notes **8**(10) (2015)
7. Polisiero, M., et al.: Design and assessment of a low-cost, electromyographically controlled, prosthetic hand. Med. Dev.: Evid. Res. **6**(4), 97–104 (2013)
8. Simmons, L.P., Welsh, J.S.: Compact human-machine interface using surface electromyography. In: IEEE/ASME International Conference on Advanced Intelligent Mechatronics (AIM), pp. 206–211. Wollongong (2013)
9. Abid, M.R., et al.: Dynamic hand gesture recognition for human-robot and inter-robot communication. In: IEEE International Conference on Computational Intelligence and Virtual Environments for Measurement Systems and Applications (CIVEMSA), pp. 12–17. Ottawa (2014)
10. Villoslada, A., et al.: High-displacement fast-cooling flexible Shape Memory Alloy actuator: Application to an anthropomorphic robotic hand. In: 14th IEEE-RAS International Conference on Humanoid Robots (Humanoids), pp. 27–32. Madrid (2014)
11. O'neill, C.: An advanced, low cost prosthetic arm. In: IEEE SENSORS 2014 Proceedings, pp. 494–498. Valencia (2014)
12. Fajardo, J., Lemus, A., Rohmer, E.: Galileo bionic hand: sEMG activated approaches for a multifunction upper-limb prosthetic. In: 2015 IEEE Thirty Fifth Central American and Panama Convention (CONCAPAN XXXV), pp. 1–6. Tegucigalpa (2015)
13. Xavier, R.T., Xavier, P.T., Souza, R.M.: Aplicações com Arduino em eletrodinâmica e biomecânica para comunicação de um mecanismo biônico por comando de voz: protótipo para prótese de membro superior. In: XIII Congresso Nacional de Iniciação Científica, p. 6. Campinas (2013)
14. Hunold, M., et al.: Protótipo de Prótese de Mão Robótica de Lego Controlada por Sistema Android para Bi-Amputado. In: XXIV Congresso Brasileiro de Engenharia Biomédica, pp. 2452–2455. Uberlândia (2014)
15. Stoppa, M.H., Carvalho, J.C.M.: Kinematic modeling of a multi-fingered hand prosthesis. In: Congresso Nacional de Matemática Aplicada à Industria, p. 10. Caldas Novas (2015)
16. Langevin, G.: InMoov Open Source 3D Printed Life-Size Robot. http://inmoov.fr/. Accessed 25 Apr 2018
17. Xavier, R.T., et al.: Desenvolvimento de uma Mão Biônica e de um Sistema Eletrônico para Estudo dos Movimentos da Mão. In: VIII Congreso Iberoamericano de Tecnologias de Apoyo a la Discapacidad (IBERDISCAP), pp. 211–214. Punta Arenas (2015)

Virtual Reality Simulator for Electric Powered Wheelchairs Using a Joystick

K. A. Hernandez-Ossa, E. H. Montenegro-Couto, B. Longo,
A. Frizera-Neto, and T. Bastos-Filho

Abstract

For some people with severe physical impairments, the main assistive device to improve their independence in activities of daily living and to enhance overall well-being is an electric powered wheelchair (EPW). However, a large number of wheelchair users find nearly impossible to drive with conventional EPW interfaces, so there is a necessity to offer users EPW training. In this work the SimCadRoM is presented. It is a virtual reality simulator for EPW safe driving learning purposes, testing of driving skills and performance, and testing of input interfaces. At this research stage, some tests were conducted to validate this version of the SimCadRoM as a reliable simulator capable of providing a training experience close to reality. The SimCadRoM was, in general, well accepted by the volunteers and proved to be a system that simulates, very realistically, the usability, kinematics, and dynamics of an EPW in a virtual environment (VE) using a standard EPW's joystick as input interface. The level of sense of presence in the VE generated by the simulator revealed a great potential for training and transferring skills to a real environment (RE).

K. A. Hernandez-Ossa (✉) · E. H. Montenegro-Couto ·
B. Longo · A. Frizera-Neto · T. Bastos-Filho
Assistive Technology Center of the Federal University
of Espirito Santo (NTA-UFES), Vitória, Brazil
e-mail: kahoss@live.com

E. H. Montenegro-Couto
e-mail: eduardo.hmc1@gmail.com

B. Longo
e-mail: berthilbl@gmail.com

A. Frizera-Neto
e-mail: frizera@ieee.org

T. Bastos-Filho
e-mail: teodiano.bastos@ufes.br

1 Introduction

Diseases like spinal cord injury, traumatic brain injury, multiple sclerosis, quadriplegia, cerebral palsy, stroke and some congenital problems can lead to movement disorders that significantly reduce the quality of life. For reference purposes, there were approximately 13 million people with physical disabilities in Brazil, according to the last census from the Brazilian Federal Institute of Geography and Statistics (IBGE) in 2010, reaching almost 7% of the total population [1], with a growing population tendency of people with disabilities in last decades [2].

For some people with severe physical impairments, the main assistive device to improve their independence in activities of daily living and to enhance overall well-being is an electric powered wheelchair (EPW), even so, a large number of wheelchair users find nearly impossible to drive with conventional EPW interfaces [3].

A wide variety of alternative approaches has been proposed for EPW guidance [4], among special joysticks [5], EEG [6], EMG [7], gaze tracking [8, 9] and hybrid EEG/EMG [10]. Additionally, to prevent any safety risks when driving EPW, several algorithms have been developed, including obstacle avoidance technics and autonomous navigation [11]. However, there is still a necessity to offer interfaces customization to new EPW's users and EPW training [12].

The use of systems that provide training in virtual reality (VR) scenarios is becoming a potential tool to support and improve rehabilitation outcomes and physical therapies [13], due to its wide variety of benefits including safe controlled environments, low costs, and flexibility. There are several of these VR environments approaches on the literature applied to EPWs, including: proposal of joysticks to improve virtual EPW driving in individuals with tremor [5], virtual wheelchair simulator with hand motion controller as an interface for reaching tasks [14], and a cost-effective prototype

Fig. 1 Participant testing the real EPW (left) and the virtual one in the SimCadRoM (right)

wheelchair simulator [15] designed to allow children with disabilities to familiarize themselves with a real wheelchair.

In this paper we present the SimCadRoM (Portuguese acronym for *Simulador de Cadeiras de Rodas Motorizadas*). It is a VR simulator for EPW safe driving learning purposes [16], testing of driving skills and performance [17], aiding in the customization and test of new functionalities and methods in a safe environment [18], and testing of input interfaces. This work is a continuation of a previous pilot study [19] that is also part of a cooperation project between the Federal Universities of Uberlândia (UFU), Espirito Santo (UFES) and Amazonas (UFAM), Brazil [12]. Some tests were conducted to evaluate the simulator when comparing participants' VR experience and driving performance with a real EPW driving experience and performance (see Fig. 1). The driving performance rates for this simulator are estimated based on measurements: time spent executing a given task, number of movement commands made with the input interface [17], spectral analysis of the movements [20], average speed, number of collisions and path following error, although for this part of the project, the performance is based only on time measurements.

2 Materials and Methods

The main components of the SimCadRoM are shown in Fig. 2. This VR system for training and testing of EPW input interfaces has an Oculus Rift DK2 VR headset running on a PC with Windows 10, 8 GB of RAM, Intel i7 processor and an MSI GeForce GTX 1060 graphics card.

Conventional EPWs regularly use proportional standard movement sensing joysticks. Therefore, at this research stage, a real Freedom LP20 EPW (with no movement while

Fig. 2 Main components of the SimCadRoM
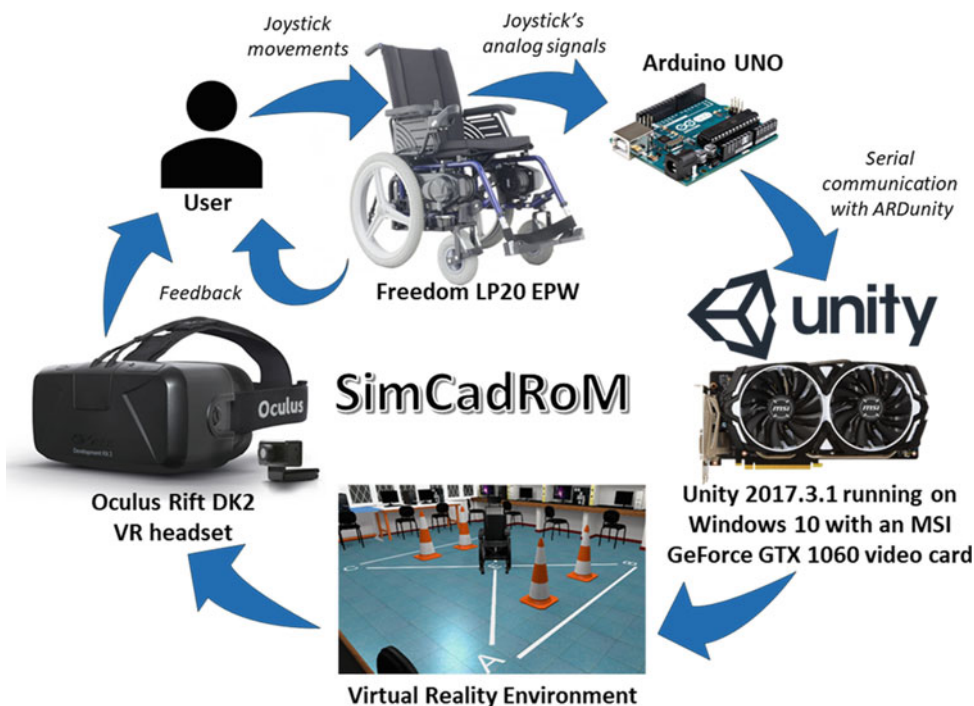
Fig. 3 Real (left) and virtual (right) NTA Research Group Laboratory

using the VE) and its joystick (the input device for the virtual training system), were selected to offer a greater immersive VR user experience. So, the performance reliability of this VE for wheelchair guidance tasks can be compared to the driving in a real environment (RE) [5].

The VE of the SimCadRoM was created with the Unity 3D game engine, from Unity Technologies. In accordance to [21], it is one of the most adequate software used to create VE, and in [22] it has been considered as an efficient integration platform for training with a virtual EPW.

The VE selected as the testing scenario was the NTA Research Group Laboratory (Assistive Technology Center) of UFES. This scenario and the virtual EPW were made in Unity for Windows (see Fig. 3). An Arduino UNO board acquires the analog signals from the joystick of the Freedom LP20 EPW and send them to the VE in the PC, by serial communication using ARDunity Basics libraries. Finally, the VR environment is displayed in the Oculus Rift headset used by the user, to allow a better immersion and realistic experience controlling the virtual EPW.

Proportional joysticks are commonly used to change EPW's velocity in proportion to the amount of deflection (typically 0°–18°) of the spring-loaded joystick post, and the wheelchair moves approximately in the direction the handle is pointed. Additionally, features such as dead zone, gain and axes rotation are also mechanically defined. Considering all this, some tests with a joystick as input device were conducted in order to acquire its analog voltage signals with the Arduino board and associate them with the joystick deflections. Then, various EPW's velocities were obtained by emulating the analog voltage input with the Arduino's analog output (PWM values from 0 to 255, equivalent to a duty cycle from 0 to 100%). Finally, the EPW's velocities were registered for different loads, since the linear and angular velocities of the real EPW are affected by the wheelchair user's mass and the analog voltage signals generated by the joystick at different deflections, which were emulated with different PWM values. The obtained data were interpolated in three dimensions (see Fig. 4a, b) to represent better the real EPW's velocity considering dynamic effects into the VE.

3 Experiment Setup

Before validating the SimCadRoM for EPW training purposes, it was tested to validate it as a reliable VR simulator, thus, the protocol used for the test aids in finding how real the simulator is when comparing the real EPW behavior and user experience with the virtual EPW behavior and virtual experience, using the same joystick and driving in the NTA Research Group Laboratory and its virtual equivalent. This test involving VR was approved by the Federal University of Espirito Santo Ethics Committee (protocol number 2264126 of September 7, 2017).

Participants for this pilot test were five healthy people (n = 5) recruited from UFES, without any physical impairments and without any previous experience with EPWs. Inclusion criteria consisted of being between 18 and 36 years old, weight between 45 and 120 kg, having normal or corrected vision, being right-handed and having their right arm and right hand able to control the EPW with its joystick; participants also required proprioception and dexterity at joints to efficiently use the proportional control [23].

The participants were asked if they could perform the tests on both real and virtual scenarios and were told they could leave at any time. The proposed protocol contains a path that the participants needed to follow with the EPW, starting at point E, in the middle, and then passing through points A, B, C, D and then returning to E as indicated by the marks on the floor shown in Fig. 3. The participants were asked first to drive the real EPW six times and then the virtual EPW once in the SimCadRoM to compare them and find out how similar was the simulator to the real experience. The participants were also instructed to drive the real EPW by keeping the chair along the center of each path segment of the path and to complete it as quickly and as accurately as possible. During this task, the participant's elapsed times for going from each point to the next one were registered.

After completing the task, the participants were asked to fulfill an Igroup Presence Questionnaire (IPQ) in Portuguese (instrument properly validated in different cultural context) [24, 25] to measure their sense of presence in the VE and

Fig. 4 a Experimental linear velocities of the real EPW for different masses and different joystick's Y-axis deflections, **b** experimental angular velocities of the real EPW for different mass and different joystick's X-axis deflections
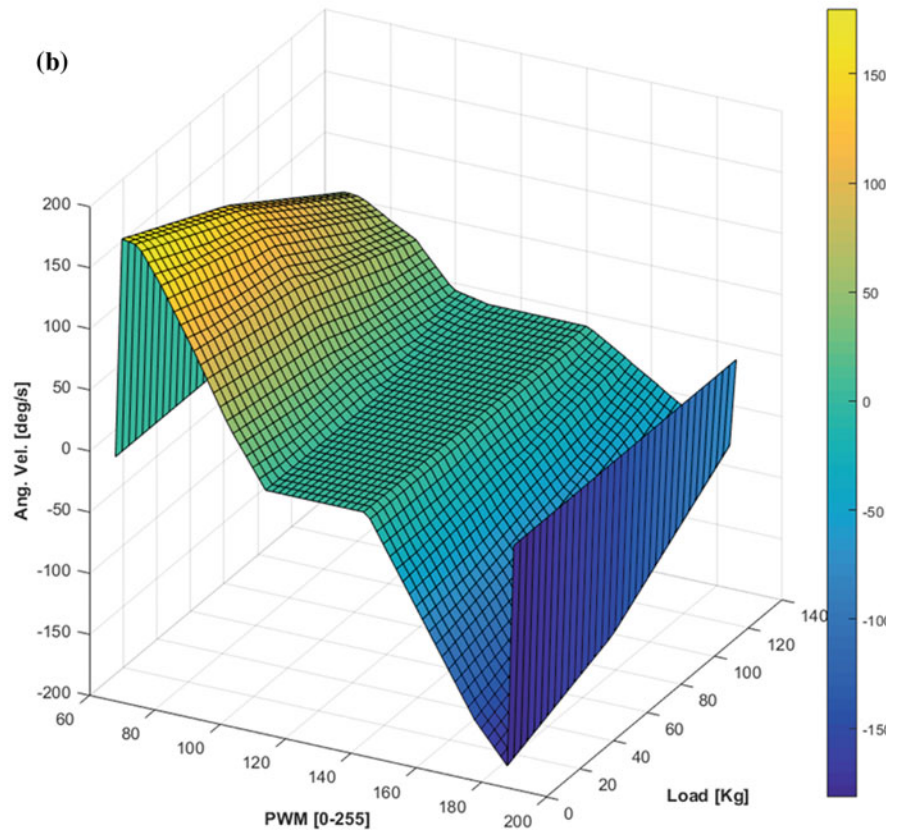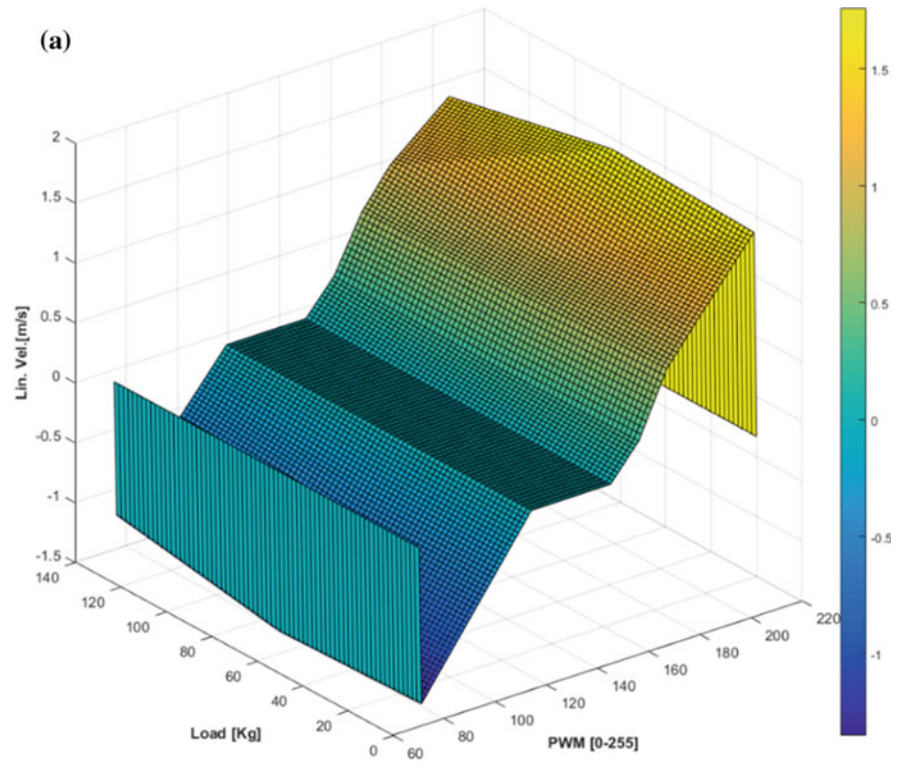
Table 1 t-Test: Paired two-sample performed for real and virtual mean times of participants P

t-Test: paired two-sample for means

P	Total elapsed time (s)		t critical two-tail	t-value	p-value α = 0.05
	Real EPW	Virtual EPW			
1	24.04	30.27	2.77645	2.05242	0.10939
2	31.84	44.03			
3	36.40	71.84			
4	33.76	28.40			
5	34.49	58.37			

another questionnaire (5-point Likert scale) about their experience using the SimCadRoM.

4 Results and Discussion

In this section, main results from the above-mentioned tests were analyzed as quantitative and qualitative criteria to find out how similar is the SimCadRoM experience to a real EPW driving experience.

The elapsed time to drive along the real path, going from point E to A, B, C, D and E again, was registered per trial and the total elapsed time mean was calculated for each participant, which is presented along with each total elapsed time for the virtual path in Table 1.

According to Shapiro-Wilk test, the elapsed times along the real and virtual paths have a normal distribution for $\alpha = 0.05$, with $p = 0.201933$ for the real path and $p = 0.537087$ for the virtual path.

A paired two-sample Student's t-Test assuming unequal variances was performed to determine whether a statistically significant time difference exists or not between the participants' total elapsed times when they drove the real EPW along the real path, and their total elapsed times when they drove the virtual EPW along the virtual path. The results show enough evidence to accept the null hypothesis, $t(4) = 2.05242$, $p = 0.10939$. Therefore, we can conclude there is no statistically significant difference between the mean of total elapsed times along the real and virtual paths.

Right after finishing the task in the VE, the participants answered the questions from the IPQ shown in Table 2. The items used in the survey split into distinct factors, describing either presence experiences (SP), emphasizing the importance of actions in the VE; global presence (G1) as the highest-loading item in the IPQ; evaluations of the immersive technology or interaction (INV) as manifestation of the attention component of the presence experience, and judgments of realness (REAL) [25] as a comparison between

Table 2 Results for each IPQ item

Item name	English question
G1	In the computer-generated world, I had a sense of "being there"
SP1	Somehow I felt that the virtual world surrounded me
SP2	I felt like I was just perceiving pictures
SP3	I did not feel present in the virtual space
SP4	I had a sense of acting in the virtual space, rather than operating something from outside
SP5	I felt present in the virtual space
INV1	How aware were you of the real world surrounding while navigating in the virtual world? (i.e. sounds, room temperature, other people, etc.)?
INV2	I was not aware of my real environment
INV3	I still paid attention to the real environment
INV4	I was completely captivated by the virtual world
REAL1	How real did the virtual world seem to you?
REAL2	How much did your experience in the virtual environment seem consistent with your real-world experience?
REAL3	How real did the virtual world seem to you?
REAL4	The virtual world seemed more realistic than the real world

Fig. 5 Results for each IPQ item
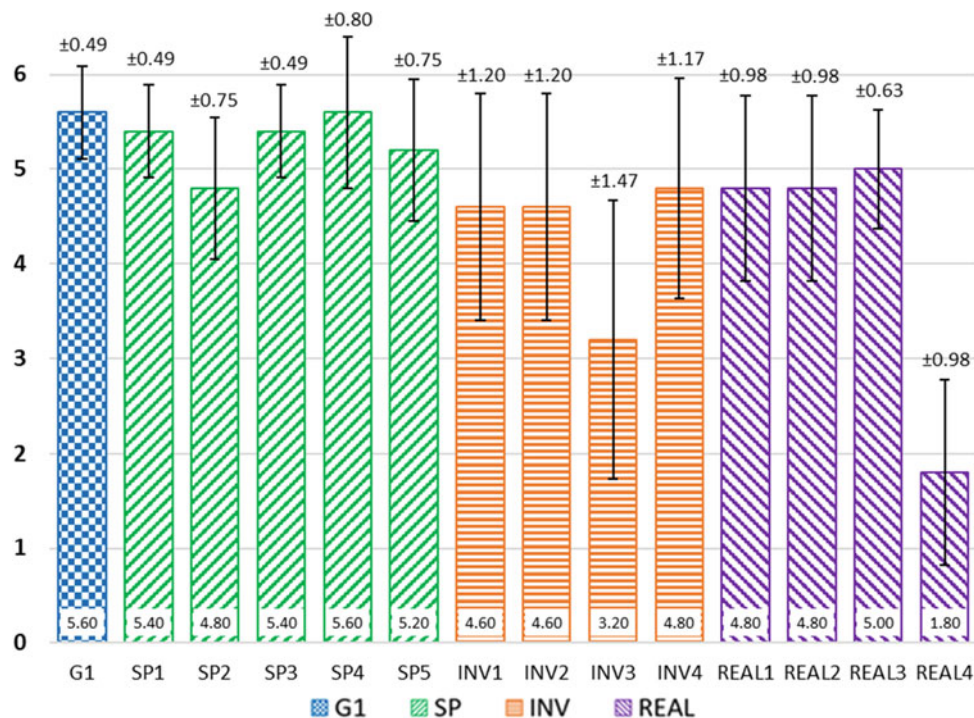
driving the virtual EPW and the real one. Figure 5 shows the obtained mean score with its corresponding standard deviation for each IPQ item. All items are rated from 0 to 6; the greater the score, the greater the overall sense of presence using the SimCadRoM. Questions related to items in bold (SP2, INV3, and REAL1) have reversed wording; therefore its score had to be reversed as well in order to work with means. The overall results per factors are presented in Fig. 6.

The overall scores for each IPQ factor and most of the IPQ items show satisfactory results (mean above 4 in a 0 to 6 scale). Because of the state of current available VR technology, it is not really expected to have high scores in the REAL4 item, and although the INV3 item presents the

highest dispersion and a mean of 3.2, it is still considered an acceptable score. We believe that sitting in a real EPW while performing some tasks in the VE increases the sense of immersion associated with the INV factor, however, external noises from our lab could have been enough distraction for the participants to make them maintaining part of their attention in the real world. Perhaps, the inclusion of isolating headphones for the participants could lead to higher INV factor results.

After completing the IPQ, a user experience test of eight questions was performed, in which the participants had to specify their level of agreement or disagreement on a symmetric agree-disagree 5-point Likert scale. Results are shown in Fig. 7 in a diverging stacked bar chart, such as suggested by [26].

These user experience questions in Fig. 7 show satisfactory results in users' acceptance of the SimCadRoM as an EPW simulator. Also, most of the participants agreed that using the real EPW previously helped them complete the task in the VE. This tells us about the learning effect that training before in the RE has, which will be studied in the opposite order with more detail in a future work.

In general, the participants were not afraid of performing the tests with the real or virtual EPW and they felt that the real EPW was easy to use. Most of them indicated agreement with the idea that "the virtual experience is similar to the real one", which is consistent with the IPQ results, and they also agreed on the easiness of "completing the task in the VE", nevertheless, some participants did not feel that way, mainly
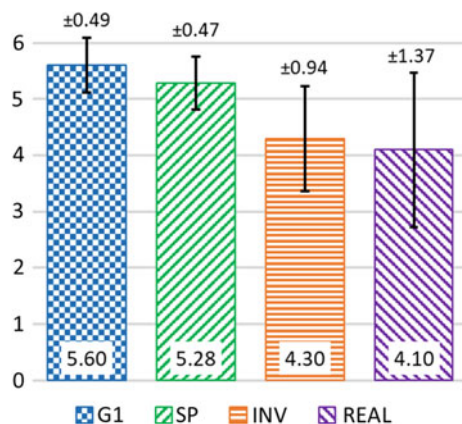
Fig. 6 Mean and standard deviation of each IPQ factor

Fig. 7 Results of participants' agreement-disagreement level for each user experience question
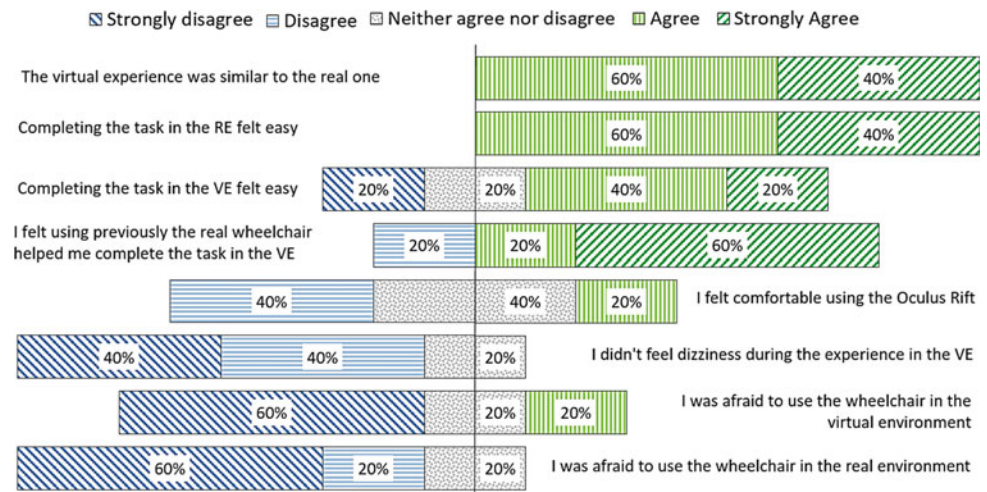
because they experienced some dizziness symptoms while using the simulator with the Oculus Rift.

This last result is independent of the VR headset technology. As long as the users perceive the illusion of movement just with their eyes, with almost no participation of their vestibular system, is likely for them to feel some level of dizziness, and although not everyone felt dizzy, this could represent a big setback for long training sessions. Moreover, the dizziness associated with the use of the VR headset also explains why not everyone "felt comfortable using the Oculus Rift".

5 Conclusions

This work presented the SimCadRoM, a virtual reality simulator to command a virtual EPW for testing of input interfaces and driving training purposes. This system uses a real EPW, a standard proportional joystick as the main input interface and a VR headset to make the system more immersive.

At this research stage, some tests were conducted to validate this version of the SimCadRoM as a reliable simulator capable of providing a training experience close to reality. A t-Test (Table 1) was used as a quantitative criterion, showing that there is no statistically significant difference between the mean of total elapsed times along the real and virtual paths ($t(4) = 2.05242$, $p = 0.10939$). This gives us an idea of how similar the virtual EPW's kinematics is in comparison with the real one considering also dynamic effects of the wheelchair and user's mass.

The overall results for each IPQ factor and most of the IPQ items (Figs. 5 and 6) show satisfactory results (mean above 4 in a 0 to 6 scale), consequently, there is a clear manifestation of general presence (G1), spatial presence (SP), involvement (INV) and realism (REAL) in the VE of

the SimCadRoM. Although there is still room for improvements in the immersion factor, the current version of this simulator is capable of inducing a cognitive process in the users, in order to create a mental model of their bodies and let them experience the sense of being in the VE training with the EPW and its joystick.

The acquired training skills proved to be transferable from the RE to the VE as reported by the participants in Fig. 7. This could influence the outcome effects using the virtual EPW, thus, further tests with the opposite order are needed and proposed for future work. The user experience questions showed satisfactory results in users' approval of the SimCadRoM as an EPW simulator and of its easiness to use. Still, some participants experienced dizziness while using the simulator with the VR headset. This should be solved or at least avoided in future versions of the simulator for long training sessions.

The SimCadRoM was, in general, well accepted by the users and proved to be a system that simulates the usability, kinematics and dynamics of an EPW, in a very realistic way, in a VE using a standard EPW's joystick as input interface. The level of sense of presence in the VE generated by the simulator revealed great potential for training and transferring skills to a RE.

References

1. Censo: IBGE Censo 2010. Instituto Brasileiro de Geografia e Estatística (2010)
2. Lenzi, M.B.: Os dados sobre Deficiência nos Censos Demográficos Brasileiros. XVIII Encontro Nac. Estud. Popul. - Transform. na Popul. Bras. complexidades, Incert. e Perspect., vol. XVIII, pp. 1–20 (2012)
3. Fehr, L., Langbein, W.E., Skaar, S.B.: Adequacy of power wheelchair control interfaces for persons with severe disabilities: a clinical survey. J. Rehabil. Res. Dev. **37**(3), 353–360 (2000)

4. Bastos-Filho, T.F., Kumar, D.K., Arjunan, S.P.: Devices for Mobility and Manipulation for People with Reduced Abilities. Rehabilitation Science in Practice Series. CRC Press, Hardcover (2014)

5. Dicianno, B.E., Sibenaller, S., Kimmich, C., Cooper, R.A., Pyo, J.: Joystick use for virtual power wheelchair driving in individuals with tremor: pilot study. J. Rehabil. Res. Dev. 46(2), 269–275 (2009)

6. Huang, D., Qian, K., Fei, D.Y., Jia, W., Chen, X., Bai, O.: Electroencephalography (EEG)-based brain-computer interface (BCI): a 2-D virtual wheelchair control based on event-related desynchronization/synchronization and state control. IEEE Trans. Neural Syst. Rehabil. Eng. 20(3), 379–388 (2012)

7. Kaiser, M.S., Iqbal, Z., Shamim, C., Mamun, A.: A neuro-fuzzy control system based on feature extraction of surface electromyogram signal for solar-powered wheelchair. Cogn. Comput. (2016)

8. Purwanto, D., Mardiyanto, R., Arai, K.: Electric wheelchair control with gaze direction and eye blinking. Artif. Life Robot. 14 (3), 397–400 (2009)

9. Montenegro-Couto, E.H., Hernandez-Ossa, K.A., Bissoli, A.L.C., Sime, M., Bastos-Filho, T.F.: Towards an assistive interface to command robotic wheelchairs and interact with environment through eye gaze. In: Anais do V Congresso Brasileiro de Eletromiografia e Cinesiologia e X Simpósio de Engenharia Biomédica (2018)

10. Leeb, R., Sagha, H., Chavarriaga, R., Millán, J.D.R.: A hybrid brain-computer interface based on the fusion of electroencephalographic and electromyographic activities. J. Neural Eng. 8(2), 25011 (2011)

11. Martins, F.N., Celeste, W.C., Carelli, R., Sarcinelli-Filho, M., Bastos-Filho, T.F.: An adaptive dynamic controller for autonomous mobile robot trajectory tracking. Control Eng. Pract. 16(11), 1354–1363 (2008)

12. Borges, L.R., Martins, F.R., Naves, E.L.M., Bastos, T.F., Jr, V.F. L.: Multimodal system for training at distance in a virtual or augmented reality environment for users of electric-powered wheelchairs. IFAC-PapersOnLine 49(30), 156–160 (2016)

13. Song, Z., Guo, S., Yazid, M.: Development of a potential system for upper limb rehabilitation training based on virtual reality. In: 4th International Conference on Human System Interaction, HSI 2011, pp. 352–356 (2011)

14. Tao, G., Archambault, P.S.: Powered wheelchair simulator development: implementing combined navigation-reaching tasks with a 3D hand motion controller. J. Neuroeng. Rehabil. 13(1), 1–13 (2016)

15. Headleand, C.J., Day, T., Pop, S.R., Ritsos, P.D., John, N.W.: A cost-effective virtual environment for simulating and training powered wheelchairs manoeuvres. Stud. Health Technol. Inform. 220, 134–141 (2016)

16. Adelola, I.A., Cox, S.L., Rahman, A.: Virtual environments for powered wheelchair learner drivers: case studies. Technol. Disabil. 21(3), 97–106 (2009)

17. Archambault, P.S., Tremblay, S., Cachecho, S., Routhier, F., Boissy, P.: Driving performance in a power wheelchair simulator. Disabil. Rehabil. Assist. Technol. 7(3), 226–233 (2012)

18. Braga, R.A.M., Petry, M., Moreira, A.P., Reis, L.P.: Intellwheels —a development platform for intelligent wheelchairs for disabled people. In: ICINCO 2008—Proceedings of the 5th International Conference on Informatics in Control, Automation and Robotics, 2008, vol. 1, RA, pp. 115–121

19. Hernandez-Ossa, K.A., Longo, B., Montenegro-Couto, E., Romero-Laiseca, M.A., Frizera-Neto, A., Bastos-Filho, T.: Development and pilot test of a virtual reality system for electric powered wheelchair simulation. In: 2017 IEEE International Conference on Systems, Man, and Cybernetics (SMC), Banff, AB, pp. 2355–2360 (2017)

20. Niniss, H., Inoue, T.: Assessment of driving skills using virtual reality: comparative survey on experts and unskilled users of electric wheelchairs. Technol. Disabil. 18(4), 217–226 (2006)

21. Silva, R., Silva, A.: Tecnologias para Construção de Mundos Virtuais: Um Comparativo Entre as Opções Existentes no Mercado. FAZU em Rev. 8, 211–215 (2011)

22. Hjorungdal, R.-M., Sanfilippo, F., Osen, O.L., Rutle, A., Bye, R. T.: A game-based learning framework for controlling brain-actuated wheelchairs. In: Claus, T., Herrmann, F., Manitz, M., Rose, O. (eds.) ECMS 2016 Proceedings, May 2016, pp. 554–563

23. Mahajan, H., Spaeth, D.M., Dicianno, B.E., Collins, D.M., Boninger, M.L., Cooper, R.A.: Comparison of virtual wheelchair driving performance of people with TBI using an isometric and a conventional joystick. Arch. Phys. Med. Rehabil. 92(8), 1298–1304 (2012)

24. Vasconcelos-Raposo, J., et al.: Adaptation and validation of the Igroup Presence Questionnaire (IPQ) in a Portuguese sample. Presence Teleoperators Virtual Environ. 25(3), 191–203 (2016)

25. Schubert, T., Friedmann, F., Regenbrecht, H.: The experience of presence: factor analytic insights. Presence Teleoperators Virtual Environ. 10(3), 266–281 (2001)

26. Robbins, N.B., Heiberger, R.M.: Plotting Likert and other rating scales. JSM 2011, 1058–1066 (2011)

Virtual Reality Simulator for Laparoscopic Procedures Performed with a Robotic Endoscope Holder

Fernanda Amaral Melo and Mariana C. Bernardes

Abstract

The use of virtual reality (VR) simulators for training novice laparoscopic surgeons has the potential of improving psychomotor skills and reducing the learning curve on real laparoscopies. This paper refers to a VR simulator to be used with CLARA system, which is a robotic endoscope holder developed at University of Brasilia for abdominal laparoscopic procedures. It aims to train CLARA's future users at handling the robotic device, besides presenting the product in an innovative approach. The simulator was evaluated by ten students from UnB Health College which were asked to perform a simple task on the CLARA simulator twice. The total time needed for each user to complete the task for the second time was measured and compared to their first trial. The verified improvement is on average 70% in the mean response time and 37% in the mean time to complete the task for all the subjects.

1 Introduction

Most traditional surgeries performed currently on SUS (Brazilian Health System) require a long incision, which implies an increased risk of infection and a long recovery time on public hospital beds. The incoming of minimally invasive surgery (MIS) introduced many benefits over traditional surgeries including reduced blood loss (about 47% of traditional method mean rate) and smaller recovery time (about 67% of traditional method length of hospital stay) [1], besides less postoperative pain [2] and smaller scars, since the whole procedure is made through small incisions with the aid of a camera.

Laparoscopy is a type of MIS commonly used to execute procedures performed in the abdomen and pelvis region such as Cholecystectomy, Colectomy and Nephrectomy. Usually, it requires at least two doctors to be accomplished: one to perform the surgery itself and another one to guide the endoscope, which is a major disadvantage of laparoscopy, specially in SUS that has a shortage of health professionals, making the use of two doctors in the accomplishment of a simple procedure highly costly and inefficient.

Some alternatives have been developed worldwide to overcome this laparoscopy drawback. The Da Vinci Surgical System, for instance, contains three robotic arms holding medical tools and another one to control an endoscope, and can be commanded by a single surgeon from a console. However, the system costs on average US$2 million, which is too expensive for the Brazilian government to fund for public surgical rooms.

Therefore, a robotic endoscope holder is being developed by University of Brasília so that a single doctor can control the camera through a joystick attached to the surgical tool while performing a laparoscopic procedure. The award-winning CLARA Project (honorable mention in Prêmio de Incentivo em Ciência, Tecnologia e Inovação para o SUS 2017, na categoria Produtos e Inovação em Saúde) has had encouraging results so far, but the conclusion of its first functional prototype is expected only for 2018. Since the device is still in testing stage, it was also necessary to have a software for testing, training and presenting the product, promoting an easier and faster integration of CLARA System to the national health system.

This paper presents a virtual reality simulation software in which a virtual prototype of the endoscope holder CLARA can be controlled through the real joystick of the system. It also contains an immersive 3D model of the surgical room and proposes a simple task to measure the user's handling of

F. A. Melo (✉) · M. C. Bernardes
Laboratório de Automação e Robótica (LARA), Universidade de Brasília, Brasília, Brazil
e-mail: fernanda.amaral.melo@gmail.com

M. C. Bernardes
e-mail: bernardes@unb.br

the virtual endoscope, so the surgeons are able to adapt to CLARA's displacement steps and endoscope motion velocities before actually performing surgeries.

2 Methods

Training of laparoscopic surgery in a simulated environment has been proved as an effective step before clinical practice [3, 4]. The main approaches for simulations include the use of phantoms and surgical models [5], Augmented Reality (AR) simulators [6], and Virtual Reality (VR) simulators [7].

While good phantoms and surgical models can provide the most realistic simulations, they are very costly, and highly dedicated to an specific clinical situation. The use of computational tools instead of physical trainers allow surgical simulators to emulate many aspects of a real surgery, while providing the user with valuable training opportunities by having lifelike graphics, various scenarios, and repeatable training modules.

AR simulators superimpose three-dimensional images over images provided by cameras, which are obtained from a real world environment that must be properly prepared for the simulation to take place. On the other hand, VR simulators create an artificial environment which can be fully controlled by the programmer. For the CLARA surgical simulator, the VR option was chosen since it provides most flexibility and less dependence on infrastructure conditions, which can be a challenge in Brazilian SUS reality.

To improve the engagement and sensorial responses of the users, we have proposed an immersive 3D virtual reality which is obtained by the use of stereo vision with the aid of a smartphone combined to a VR Headset as a low-cost alternative to an Oculus RIFT, with proved efficiency without any obvious loss of performance [8].

Hence, the CLARA simulator is composed of a VR Headset to be attached to the user's smartphone, the original joystick used to control the CLARA robot, and a smartphone application that provides the immersive 3D reality and controls the virtual CLARA robot from joystick commands. As requirements, the smartphone must be equipped with bluetooth communication and a built-in IMU, besides using Operational Systems Android 4.4 or IOS 8.0 (or higher).

2.1 Development of a 3D Model

Immersion into virtual reality is a perception of being physically present in a non-physical world; it can be reached by surrounding the user with sensorial stimuli. This sensation can enhance education by increasing the interest and absorption of the content, reducing the learning curve [9, 10]. Therefore, the first step in the development of CLARA simulator was the creation of the environment 3D model shown in Fig. 1c. The software *Autodesk Maya* was used to create an immersive surgical room and a virtual patient.

The organs from the abdominal region of Fig. 1a were modeled based on the illustrations from Netter's Atlas of Human Anatomy [11] and the endoscope holder of Fig.1b was imported from Solidworks® model used for the real CLARA robotic arm manufacturing.

Fig. 1 3D Models developed: **a** Abdomen anatomy organs; **b** CLARA robotic arm; **c** Immersive surgical room
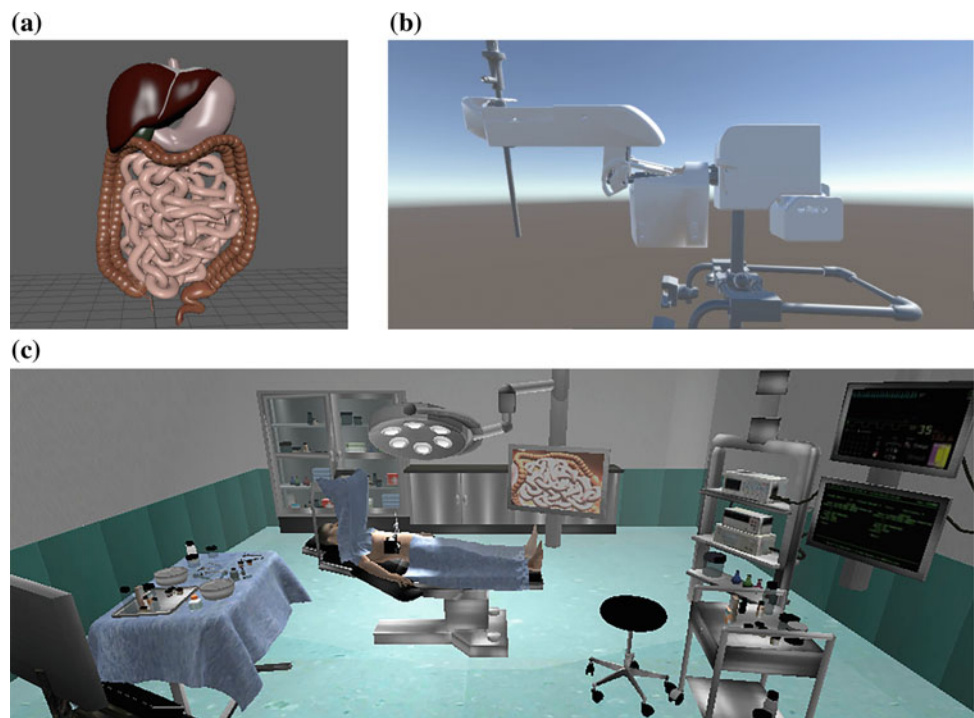
2.2 Virtual Simulation

Simulation is the reproduction of a real-world process or system and it can be reached by using the developed 3D model to interact with the user. Thus the model, still completely static, was exported to another software called *Unity3D* which is a cross-platform game engine that supports C# scripting for implementing the desired behaviour on each virtual object of the model. Besides that, *Unity* supports building to many different platforms including IOS and Android, chosen platforms for CLARA aiming to use a smartphone attached to a low-cost VR Headset.

Virtual Reality on smartphone. The first step on the simulation development was attaching a virtual reality script to the simulated camera view, thus the screen splits in two parts, for left and right eyes, which makes 3D vision sensation possible. Since the smartphone contains a 6 axis Inertial Measurement Unit (IMU) which can sense accelerations in all 3 translational axes and all 3 rotational axes, the script also integrates these accelerations to find position and velocity variation of the device, using this information to rotate the camera view to properly follow the user's head movement.

The VR script is a native package from *Unity3D* to be used with *Google Cardboard headset*, which is a low-cost head mount for smartphones developed by Google. The two splitted views shown in Fig. 2a are displaced precisely so that the distance between two 45 mm focal lenses and the smartphone screen creates the 3D perspective in a pleasant way for the human eyes. The chosen VR Headset for CLARA simulator was not *Google Cardboard* due to its low material resistance, but a similar plastic model displayed in Fig. 2b, that presents the same dimensions so that the Unity VR package can be used without adaptations.

CLARA endoscope holder simulator. The mathematical model that describes the robotic arm motion must regard two important features of the real CLARA robot: the parallelogram rule and the mechanical link of the pieces.

Parallelogram Rule: During the laparoscopy, the endoscope is inserted through orifice on a small incision on the patient's abdominal wall and only moves around this pivoting point until the end of the procedure. Thus, it is indispensable that the endoscope holder can keep this entry point constant to prevent the endoscope shaft to injure patient's tissue. Aiming for it, the CLARA mechanism was projected to keep the position of the endoscope zone aligned to the lower rod of the robotic arm, as illustrated in points A and B from Fig. 3b. This is achieved through a parallelogram mechanism, in which all the opposite rods must be parallel, as illustrated in Fig. 3a, so that backward and forward movements will change the angle of the vertical rod and the position of the upper horizontal rod, but never change the distance between points A and B.
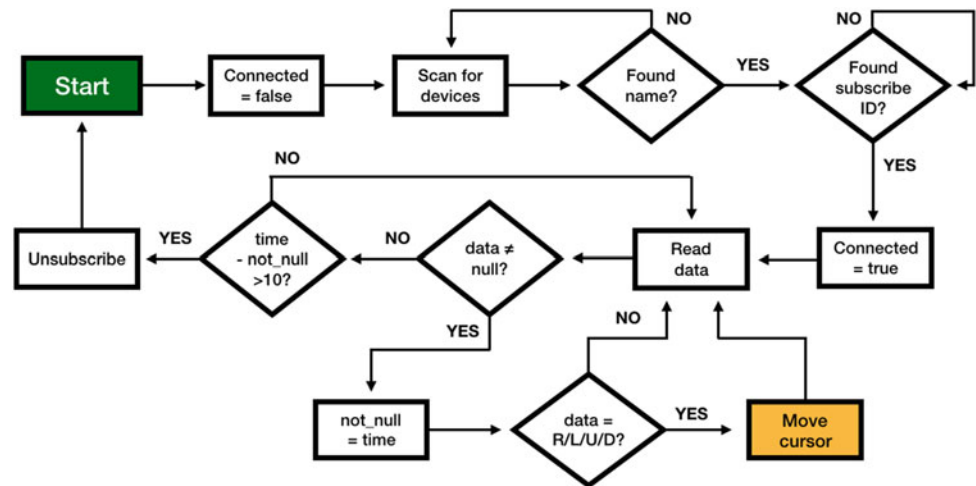

Fig. 2 **a** Simulation screen divided into right and left eye; **b** Virtual reality headset used for CLARA simulator
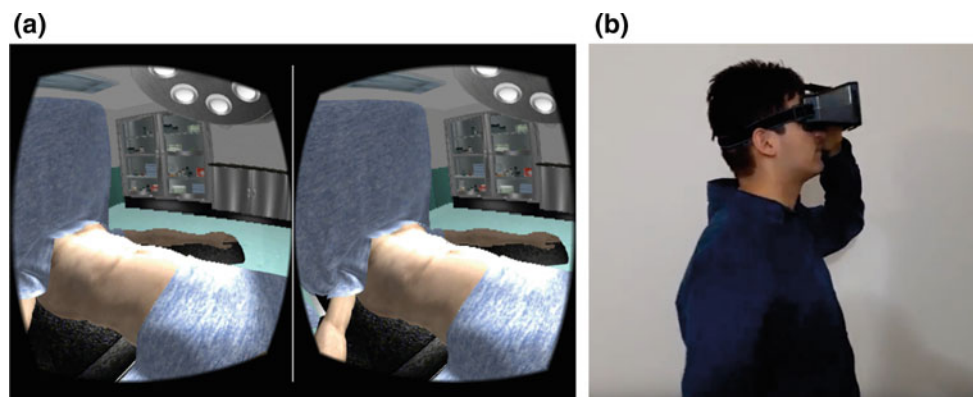
Fig. 3 **a** Real robotic arm illustrating the parallelogram rule; **b** 3D model of the robotic arm illustrating incision spot 'A' and the fixed reference of the mechanism 'B'
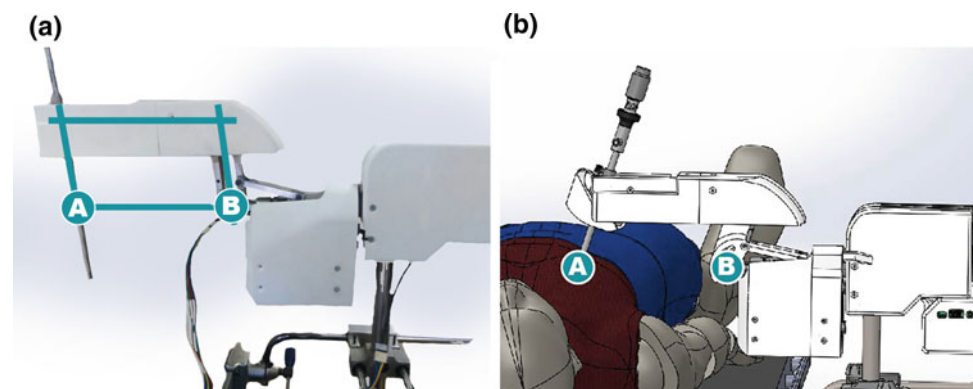
Fig. 4 Fluxogram of the bluetooth script used to receive joystick data and move the cursor

Mechanical link: The mechanical behaviour simulation of each piece of the robotic arm was set individually so that the entire virtual system can operate identically to the real endoscope holder, since its position and rotation in all axis are calculated and external forces are considered, such as gravity and friction. In practice, there is a cursor being controlled by the joystick commands and all other pieces are adjusted at each frame to geometrically fit the cursor new position and the parallelogram rule.

Receiving Joystick Commands. The device attached to the medical tool contains a Bluetooth 4.0 chip associated to a microcontroller which sends a data bundle containing the data read from joystick at each time instant. Figure 4 illustrates the implemented script for receiving this data through the smartphone bluetooth and using it to move the virtual cursor.

The command script consists in finding the name and subscribe ID of CLARA joystick and wait for it to send data.

When data arrives, if it is a recognized command (Right, Left, Up or Down) the cursor position is updated based on the pointed direction. If elapsed time without incoming data exceeds 10 s, it is supposed that joystick has disconnected and the whole process is restarted.

2.3 Task for Training Evaluation and Simulator Validation

In order to evaluate the real improvement of the psychomotor skills of the users, a quantitative study was made with ten students from UnB Health College in which a simple task should be completed using the CLARA simulator.
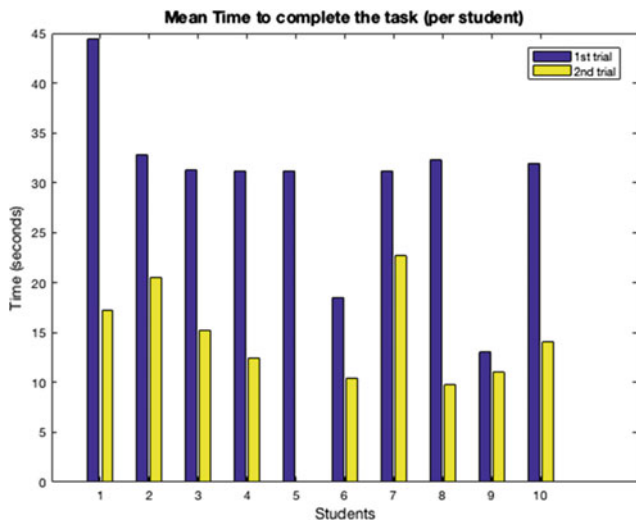
The task consists in moving the virtual endoscope while attempting to reach a goal, which is positioning the small sphere shown in Fig. 5a, at the center of the virtual monitor, such as illustrated in Fig. 5b.
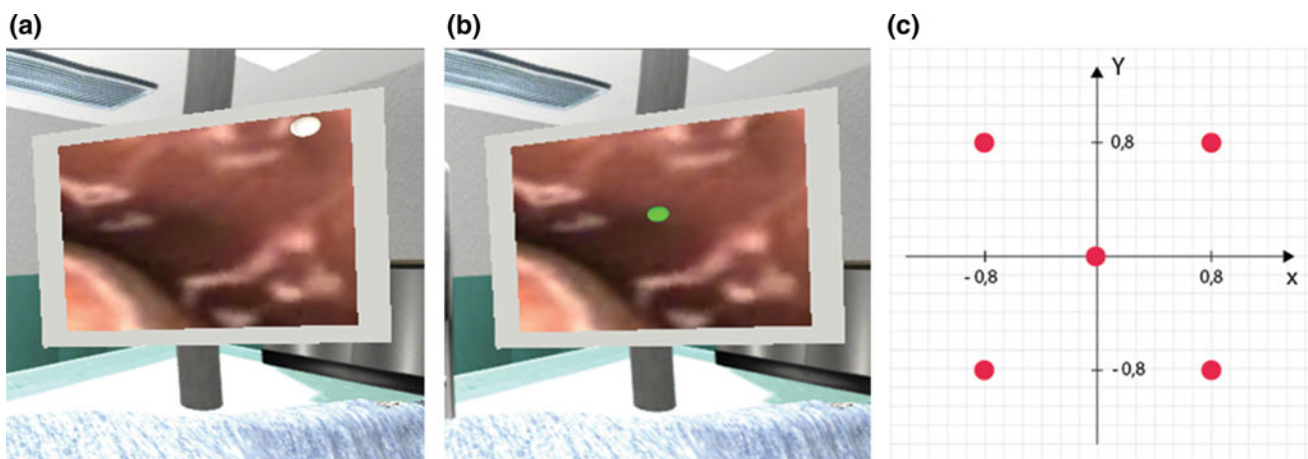
Fig. 5 **a** Sphere of the task; **b** Target reached on the middle of virtual screen; **c** Central point, four possible positions and its distances from each other on local units reference
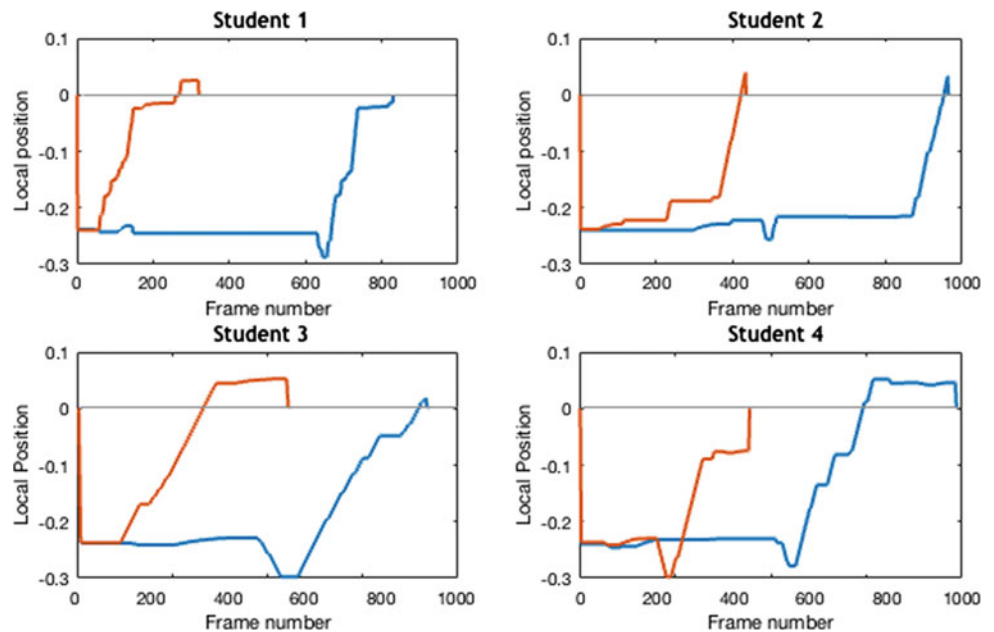
During a setup phase, the sphere is positioned close to the center, and the user has the opportunity to test the joystick operation before the task time is accounted for user performance. Once the center is reached, the task begins and a starting position for the sphere is initialized.

The sphere admits 4 different initial positions, as shown in Fig. 5c, that alternate between each other and must be moved around by the user to reach the central point. After a success, another initial position is randomly selected and the user is asked to reposition the sphere, repeating the task for 4 times in total per trial.

To determine whether the target is reached or not, the central position of the virtual screen and the center of the sphere are compared. If its difference is smaller than a threshold $\Delta = 0.05$ (on local units reference) the hit is accounted. Also, the sphere must be held at this position for 500 ms before the achievement is validated.

At each simulation frame, the position and time are saved to be compared to previous trials in order to generate quantitative data to be analyzed. Besides that, all the subjects who took part on the test filled a form evaluating the simulator and the task, generating also qualitative data from possible future users of CLARA. Such feedback aims for forthcoming improvements of the system.
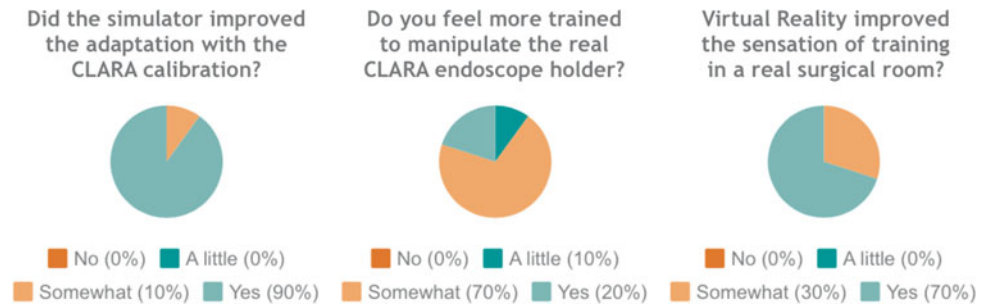
3 Results

The mean time to reach the target was computed for the ten testing subjects and then compared to the previous trial, presenting an increase of up to 60% (for the first subject) and a mean of 37% of improvement to all subjects, except for the fifth subject whose data of the second trial was corrupted and could not be compared. The individual mean time of each subject is shown in the bar graph of Fig. 6.

All data recorded during setup phase was discarded so that the period for VR Headset adjusting, securing the joystick and finding the virtual screen the on 3D environment does not affect the results.

Figure 7 illustrates the mean distance to target of subjects 1–4. The grey line delimits the desired position of the target in the horizontal image axis. It can be seen that the response time

Fig. 6 Bar graph illustrating the mean time of each subject to complete the task on the first and second trials. The second trial data of the fifth subject was corrupted, thus it is not represented

Fig. 7 Mean distance to target (on the horizontal image axis) for first (blue) and second (red) trials of subjects 1–4. The grey line delimits the desired position of the target (Color figure online)

Fig. 8 Qualitative results of the form

Did the simulator improved the adaptation with the CLARA calibration?

■ No (0%) ■ A little (0%)
■ Somewhat (10%) ■ Yes (90%)

Do you feel more trained to manipulate the real CLARA endoscope holder?

■ No (0%) ■ A little (10%)
■ Somewhat (70%) ■ Yes (20%)

Virtual Reality improved the sensation of training in a real surgical room?

■ No (0%) ■ A little (0%)
■ Somewhat (30%) ■ Yes (70%)

increases substantially on the second trial, on up to 90% for the first subject and 72% on average for all testing subjects.

Figure 8 shows the results of the form filled by all the subjects who took part on this research. It illustrates the qualitative perception of them about the simulator and the learning process associated to it. The majority of our test subjects considered the CLARA simulator was helpful in their familiarization with the endoscope holder and the surgical procedure.

4   Conclusion

The obtained quantitative results suggest that virtual reality training is a good method for improving the learning curvature and response time of the CLARA joystick users, besides increasing the mean time to complete a simple task, which implies an advance on their psychomotor skills. Qualitative data indicates that the subjects felt acquainted with the device calibration after the first trial and became more confident about manipulating the real endoscope holder.

Since the real CLARA System is still in testing phase of its first functional prototype, there is no research comparing the performance of the users on the real device after the simulator training. Hence, it is still not possible to conclude that the simulator indeed improves the handling of the system on real surgeries. However, the presented results indicate that the proposed simulator has great potential as a training tool for the users of the real CLARA robot.

This leads to possible future work, which include not only comparison of user performance on the real CLARA robot before and after simulation training, but also the validation of the virtual reality training with residents and surgeons with different experience levels in laparoscopies. Future work also encloses the development a desktop version of the simulator so that the people who do not get used to the virtual reality sensation (e.g. sight problems) will still be able to use the CLARA simulator.

References

1. Magrina, J.F., Kho, R.M.: Robotic radical hysterectomy: comparison with laparoscopy and laparotomy. Gynecol. Oncol. **109**, 86–91 (2008)
2. Mais, V., Ajossa, S.: Treatment of nonendometriotic benign adnexal cysts: a randomized comparison of laparoscopy and laparotomy. Obstet. Gynecol. 770–774 (1995)
3. Taffinder, N., Sutton, C.: Validation of virtual reality to teach and assess psychomotor skills in laparoscopic surgery: results from randomised controlled studies using the MIST VR laparoscopic simulator. Stud. Health Technol. Inform. **50**
4. Aggarwal, R., Grantcharov, T.P.: An evidence-based virtual reality training program for novice laparoscopic surgeons. Ann. Surg. 310–314 (2006)
5. Nigicser, I., et al.: Anatomically relevant pelvic phantom for surgical simulation. In: Proceedings 7th IEEE International Conference on Cognitive Infocommunications, pp. 427–432 (2016)
6. Larrarte, E.A., Alban, E.V.: Virtual markers in virtual laparoscopy surgery. In: Proceedings XXI Symposium on Signal Processing, Images and Artificial Vision, pp. 1–6 (2016)
7. Owlia, M., Khabbazan, M., Mirbagheri, M.M., Mirbagheri, A.: Real-time tracking of laparoscopic instruments using kinect for training in virtual reality. In: Proceedings 38th Annual International Conference of the IEEE Engineering in Medicine and Biology Society (EMBC), Orlando, pp. 3945–3948 (2016)
8. Papachristos, N.M., Vrellis, I., Mikropoulos, T.A.: A comparison between oculus rift and a low-cost smartphone VR headset: immersive user experience and learning. In: Proceedings IEEE 17th International Conference on Advanced Learning Technologies, pp. 477–481 (2017)
9. Gallagher, A.G., Ritter, E.M.: Virtual reality simulation for the operating room. Ann. Surg. 364–372 (2005)
10. Seymour, N.E., Gallagher, A.G.: Virtual reality training improves operating room performance. Ann. Surg. 458–464 (2002)
11. Netter, F.H.: Atlas of Human Anatomy, 6th edn. Elsevier (2014)
12. Choi, C., Han, H., An, B., Kim, J.: Development of a surgical simulator for laparoscopic esophageal procedures. In: Proceedings 28th IEEE Annual International Conference of the IEEE Engineering in Medicine and Biology Society (EMBC), New York City, pp. 819–822 (2006)

Virtual Surgical Planning: Patient-Specific Imaging Segmentation

F. W. Grillo, C. Rondinoni, A. C. S. S. Filho, F. H. Simozo, J. A. Farina Jr., T. Z. Pavan, H. R. Machado, and A. A. O. Carneiro

Abstract

Medical errors cause death of thousands of people around the world each year. From common to complex procedures, medical training can be one method to reduce these alarming numbers. The medical simulation is a technique aimed at enhancing structured and guided experiences for learning and rehearsal of technical procedures. Computed tomography and magnetic resonance imaging can be used to reconstruct the patient's morphology and create a three-dimensional virtual environment to assists medical teaching and surgical planning. In this study we developed a virtual patient-specific model for surgical planning of a rare case of total craniopagus twins. Using the software 3D Slicer we created an environment which enables medical team studies and surgical planning using models that represents surgical steps and patient morphology. Images and videos were used by the medical team for discussions and explanations. The virtual models were considered by the medical team as useful tools to reliably represent the target patient's anatomy. Consequently, a patient-specific virtual environment became an important tool for surgical planning and medical training. Pipelines which enable the faster imaging segmentations and 3D model's reconstructions will become more common. In future work, we intend to develop a dedicated platform, which enables any user to access many visualization functions without programming experience.

1 Introduction

According to the 2017 Hospital Assistance Security Yearbook by "*Instituto de Estudo de Saúde Complementar* (IESS)", in 2006 were registered between 170,000 and 430,000 deaths related to hospital issues, described as deaths by "acquired conditions" [1]. Preventable medical errors are not restricted to one country, as it causes the death of up to 98,000 Americans annually [2, 3]. Medical errors can be considered common and a serious health problem, most of them involving the whole health care team [4]. This can be even more critical when teams need to handle extremely complex cases, like the separation of craniopagus twins [5].

The medical simulation is a technique aimed to replace or amplify clinical procedures with structured and guided practices [6]. It is expected that a simulated procedure evokes aspects of the medical routine by offering an interactive environment. In neurosurgery, for instance, a common mistake leads to believe that medical training should be a solo activity. However, simulation can include the whole team of surgeons and nurses, training their individual and intrapersonal capabilities. Simulation as a medical training technique has grown in the last ten years. Diagnostic imaging, using computed tomography (CT) and magnetic resonance imaging (MRI), contributed to surgical planning and boosts the three-dimensional (3D) reconstructions as a visualization method.

In this study we developed a virtual patient-specific model for surgical planning of a rare case of total vertical

F. W. Grillo (✉) · C. Rondinoni · T. Z. Pavan · A. A. O. Carneiro
FFCLRP - Physics Department, University of Sao Paulo, São Paulo, Brazil
e-mail: fwgrillo@usp.br

A. C. S. S. Filho · F. H. Simozo
FFCLRP - Computation Department, University of Sao Paulo, São Paulo, Brazil

J. A. Farina Jr. · H. R. Machado
FMRP – Neurosurgery Department, University of Sao Paulo, São Paulo, Brazil

C. Rondinoni
InRad-FMUSP – Radiology Department, University of Sao Paulo, São Paulo, Brazil

Type-III craniopagus. Surgical steps were simulated using 3D virtual models, such as craniotomy window opening and vessels division. At this point, the model must be detailed enough to accommodate the need of the surgical team regarding procedures like skin incisions, bone craniotomy, vascular management (either selective embolization or venous clipping), or tissue expanders for the plastic surgery procedure [7]. Future development of this study include comparing all the four surgical steps within a single virtual planning environment.

2   Methodology

The computed tomography and magnetic resonance images from the 19 months old craniopagus twins were acquired using a Brilliance Big Bore scanner (Philips Medical Systems, Cleveland, USA) and Achieva 3T (Philips, The Netherlands), respectively. The images were exported to DICOM files and imported and segmented using the software 3D Slicer (version 4.8.0) [8].

2.1   Threshold Segmentation

A simple segmentation using threshold tool was made based on CT image as master volume. Therefore, the images were initially segmented into two distinct models: bone and soft tissue. Fusion and editing of these two segmentation labels were used to study the relationship between the superficial landmarks (i.e. ears, eye lids and orbits) and the underlying traits of the bone and deeper soft tissues.

2.2   Complex Segmentation

Soft tissue segmentation: To define the brain tissues in MRI images and its virtual representation, a hybrid segmentation procedure was adopted. Firstly, the intracavity volume space was obtained from a surface-based inflation procedure, proposed in BET algorithm [9]. Secondly, with the brain volume being defined, both N4 [10] and anisotropic anomalous diffusion (AAD) [11] filters were applied, which complies with bias field and Rician noise image artefacts reduction [12], respectively. In addition, the Expectation-Maximization segmentation model [13] with anatomical regularization was used, resulting in the final compartments for the major brain tissues, i.e. cerebrospinal fluid (CSF), white matter (WM) and gray matter (GM). The anatomical constraint used in this case was driven by a canonical brain atlas provided by Gousias et al. [14], which offers a case-specific brain structural modulation with neonate's brains. Finally, a label propagation procedure using

elastic brain registration methods, proposed in ANTs tools [15], was also applied in order to overlay the cortical label representation [13] in the native space. This procedure assisted us to locate several brain cortical regions in the case-specific virtual model.

Angiography. A complex segmentation using *vesselness* tool was made based on CT and MRI data as master volumes. Therefore, the images were initially separated into three distinct models: CT angiography twin 1, CT angiography twin 2, MRA (magnetic resonance angiography). An interactive scripted module in 3D Slicer was used to execute enhanced vessel segmentation of tubular structures. The initial deformable model was inflated to match the contours of the target volume.

2.3   Co-registration and Presenting

A co-registration of CT and MRI data was initially done using fiducials points; fine-tuning was done using the BRAINS module. The final images were presented to the medical team as support for the surgery planning. The users had access to the 3D viewport using the interface actions to rotate, zoom and pan the models. Any individual structure could have its visibility turned on or off and its opacity changed to semi-transparent. All images, animations and videos were prepared using the 3D Slicer publication modules.

3   Results and Discussion

Neurosurgeons often learn anatomy and surgical procedures based on books containing bi-dimensional images and representations. However, during the patients-specific studies, the time necessary to create the relationship between generic illustrations and patient images is not optimized. Elastic brain registration methods were used to obtain cortical regions, as proposed in ANTS tools. Figure 1 shows anatomical regularization and representation of the cortical overlay in twin 2's native space. The inset on the right shows a medial sagittal slice and helps to locate the several slices along the craniocaudal axis.

The bone and skin virtual models were segmented from CT images using the threshold tool. To remove all non-connected segments, the "island effect" tool was also used (Fig. 2).

Among surgical planning steps, one of the most complex understanding for this surgical case was blood vessels connections. A non-usual morphology should change the location of structures, such as the basilar artery or internal carotid artery. Figure 3 shows three different visualization methods used to illustrate the main arteries distribution. Transparency

Fig. 1 Result of the label propagation procedure using elastic brain registration methods, proposed in ANTs tools. **a** Representation of the anatomical regularization used, resulting in the final compartments for the major brain tissues. **b** Overlay the cortical label representation in the native space
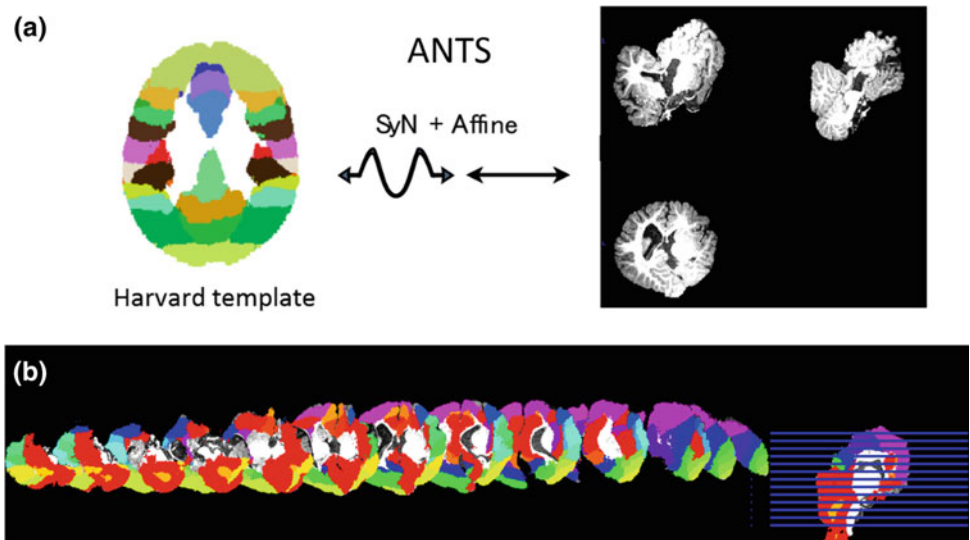

Fig. 2 Virtual models segmented from CT and MRI images. **a** Skin. **b** Bone. **c** Bone with first surgery opened window
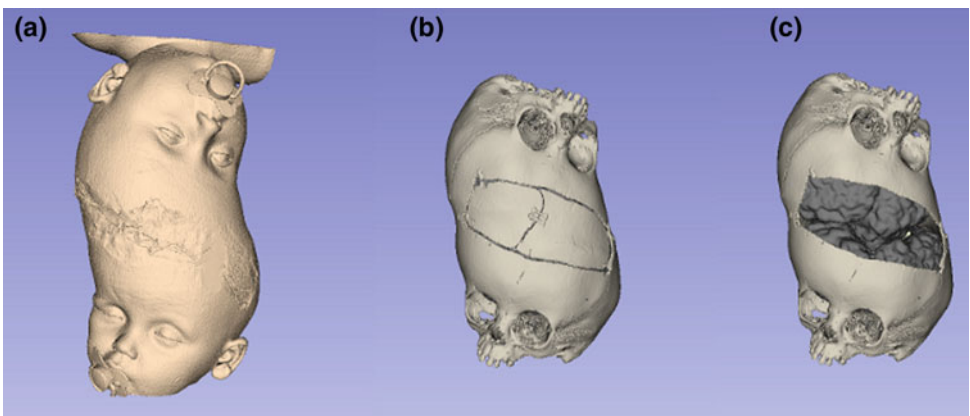
tool is a helpful method, which enables surgical team to create external references from internal structures. However, it is important to note that the pipeline to create a virtual environment can change from a patient to another. Therefore, automatic segmentation must be revised to avoid missing structures and do not represent the patient in virtual models.

In regard to the 3D environment, the use of a non specific software, as 3D slicer, turns the access to various tools somehow difficult normal users. It is still required a dedicated software to present, easily, the complete combinations of transparency and structures modeling. However, according to medical team, the 3D visualization has contributed to

Fig. 3 Virtual twin's blood vessels visualization. **a** Red (upper) and green (bottom) identify each twin's brain circulation. **b** The transparent skull was added to assists the structures localization. **c** Brain segmentation was added to increase realism of surgical planning (Color figure online)
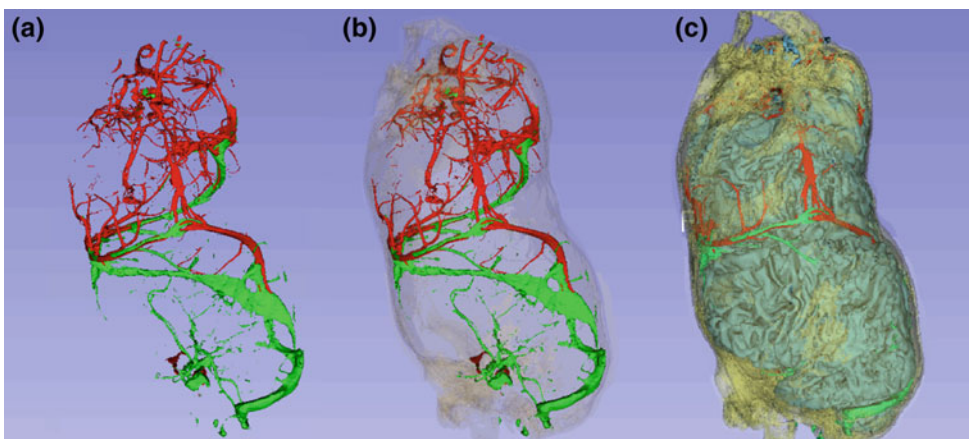
a better understanding the MRI and CT images during the team meetings.

4 Conclusion

In this work, we developed an imaging segmentation pipeline for patient specific surgical planning. The result was evaluated by the satisfaction of the surgical team. In this special case of the craniopagus twins, the virtual phantom and segmentation were designed to guide surgery on the pathway and the connectivity of the vein and arteries between the twin's heads. This specific virtual phantom was also used for 3D printing of parts of the head according to the need for training requested by the surgical team during the surgical planning

Pipelines which enable the faster imaging segmentations and 3D model's reconstructions will become more common. In future works we intend to develop a dedicated platform, which enables any user to access many visualization functions without programming experience.

References

1. Couto, R.C., Grillo Pedrosa, T.M., Duarte Roberto, B.A., Daibert, P.B.: Hospital Assistance Security in Brazil Yearbook. Instituto de Estudos de Saúde Suplementar, Belo Horizonte (2017)

2. Van Den Bos, J., Rustagi, K., Gray, T., Halford, M., Ziemkiewicz, E., Shreve, J.: The $17.1 billion problem: the annual cost of measurable medical errors. Health Aff. Proj. Hope **30**(4), 596–603 (2011)

3. Rolston, J.D., Zygourakis, C.C., Han, S.J., Lau, C.Y., Berger, M.S., Parsa, A.T.: Medical errors in neurosurgery. Surg. Neurol. Int. **5**(Suppl 10), S435–S440 (2014)

4. Rolston, J.D., Bernstein, M.: Errors in neurosurgery. Neurosurg. Clin. N. Am. **26**(2), 149–155 (2015)

5. Stone, J.L., Goodrich, J.T.: The craniopagus malformation: classification and implications for surgical separation. Brain J. Neurol. **129**(Pt 5), 1084–1095 (2006)

6. Gaba, D.M.: The future vision of simulation in health care. Qual. Saf. Health Care **13**(Suppl 1), i2–10 (2004)

7. Alokaili, R.N., Ahmed, M.E., Al, A.F., Goodrich, J.T., Aloraidi, A.: Neurointerventional participation in craniopagus separation. Neurointerventional participation in craniopagus separation. Interv. Neuroradiol. J. Peritherapeutic Neuroradiol. Surg. Proced. Relat. Neurosci. Interv. Neuroradiol. **21**(4), 552–557 (2015)

8. Pieper, S., Halle, M., Kikinis, R.: 3D slicer. In: IEEE International Symposium on Biomedical Imaging: Nano to Macro, 2004, vol. 1, pp. 632–635 (2004)

9. Smith, Stephen M.: Fast robust automated brain extraction. Hum. Brain Mapp. **17**(3), 143–155 (2002)

10. Tustison, N.J., et al.: N4ITK: improved N3 bias correction. IEEE Trans. Med. Imaging **29**(6), 1310–1320 (2010)

11. da S. Senra Filho, A.C., Salmon, C.E.G., Murta Junior, L.O.: Anomalous diffusion process applied to magnetic resonance image enhancement. Phys. Med. Biol. **60**(6), 2355–2373 (2015)

12. Dietrich, O., Raya, J.G., Reeder, S.B., Reiser, M.F., Schoenberg, S.O.: Measurement of signal-to-noise ratios in MR images: Influence of multichannel coils, parallel imaging, and reconstruction filters. J. Magn. Reson. Imaging **26**(2), 375–385 (2007)

13. Devi, C.N., Chandrasekharan, A., Sundararaman, V.K., Alex, Z.C.: Neonatal brain MRI segmentation: a review. Comput. Biol. Med. **64**, 163–178 (2015)

14. Gousias, I.S., et al.: Magnetic resonance imaging of the newborn brain: manual segmentation of labelled atlases in term-born and preterm infants. NeuroImage **62**(3), 1499–1509 (2012)

15. Avants, B.B., Tustison, N.J., Stauffer, M., Song, G., Wu, B., Gee, J.C.: The insight ToolKit image registration framework. Front. Neuroinform. **8** (2014)

A Descriptive Comparative Observational Study About the Quality and Preservation at the Hospital Furniture

Lígia Reis Nóbrega, Selma Terezinha Milagre, and Adriano Alves Pereira

Abstract

Hospital furniture is the furniture used as support to specific services at the hospital. The quality and the conservation state of this furniture influence on security and performance of the health professionals and the patient's recover. Thereby, this study carries on an evaluation of the quality and the conservational state of the furniture used at general inpatient rooms from different inpatient units of three hospitals, aiming to detect the factors that can influence on patient care or compromising the attendance. The furniture included in this study are hospital bed, meal table, companion armchair, locker, bedside table, serum support, and two-step stairs. Two methods were used for this evaluation: checklist and questionnaire. This research was approved for the Ethics committee with de CAAE: 65008617.1.0000.5152 and was fullfilled on Inpatient Units of Health Care Facility (HCF) Public, Private and maintained by a Non-governmental Organization (NGO), for comparison. The Private HCF got mostly positive results. Followed by the HCF maintained by a NGO and, for last, the Public HCF. The characteristics of demand, economy and exposure that influence these results were discussed.

Keywords

Hospital furniture • Furniture quality • Furniture preservation

1 Introduction

Hospital furniture are the furniture used on Health Care Facilities (HCF) to help the patient's attendance. Quality hospital furniture are not related to luxury but rather to comfort, security and good condition in providing services.

Adequate furniture contributes with the well-being of the patient and the efficiency in performing tasks by health professionals. While improper or inappropriate furniture can harm the patient or the companion during hospitalization, it hampers the health professional's performance, offers ergonomic risks and corroborates for the occurrence of adverse events.

Adverse events in hospitals are the occurrences of an unwanted complication resulting from the care provided to the patients, not attributed to the natural evolution of the base disease. They are associated with intrinsic factors, which are linked to the patient (old age and reduced mobility), and extrinsic factors that are linked to the physical environment (inadequate height of furniture, obsolete and poorly maintained furniture, high beds and/or no grilles), and other organizational characteristics [1, 2].

Some hospital furniture can cause adverse events like falls, fractures and bruises, and these accidents can be avoided when its original cause is detected and previously treated.

Similar to the fact that the environment influences patient safety, it also influences the performance of the HCF staff. The ergonomics of health professionals is a topic that deserves attention. The health professionals live an intense rut, innumerous complaints can be reduced with equipment and furniture ergonomically correct designed, that support and guarantee a safe handling of the patient [3].

Hospital Furniture, as well as Medical Assistance Equipment (EMAs), also has a phase of obsolescence, need for maintenance and adaptation to the environment, but this care is often neglected by the hospital administrators. Therefore, evaluate the hospital furniture's quality and state

L. R. Nóbrega (✉) · S. T. Milagre · A. A. Pereira
Federal University of Uberlândia, Uberlândia, MG, Brazil
e-mail: Rn.ligia@hotmail.com

of conservation to verify questions of ergonomics, performance, safety, and usability is necessary.

Based on this, the main objective of this study was evaluate the quality and the state of conservation of the hospital furniture present in general rooms of different Hospitalization Units of three hospitals in order to detect factors that may influence the health professional's performance, offer ergonomic risks, and compromise the efficiency and effectiveness of patient care. There are no Interest Conflict in this study.

This study considered the furniture present in the inpatient room, that is the hospital bed, meal table, companion armchair, personal storage locker, bedside table, serum support and two-step auxiliary stairs.

This work was carry out in Hospitalization Units of a Public HCF, a Private HCF and a HCF maintained by a NGO, in order to compare the results. At the end a report containing all the data collected and the pertinent observations to the work's scope was written and presented for the hospitals' administrators.

2 Methods

The evaluation of quality and state of conservation was carried out using two methods: a checklist to document the researcher's general view and a questionnaire applied for the professionals who most use the inpatient room's furniture (nursing and physiotherapy staff).

This descriptive comparative observational study was performed between August 2016 and August 2017 at three HCFs: Public, Private and maintained by NGO, authorized by the Ethics Committee in Research from Federal University of Uberlândia with the CAAE number 65008617.1.0000.5152.

The checklist, elaborated to better organize information, consider all the furniture included in the research and allows all the researcher's observations to be written down. It enabled the registration of the furniture present in each room, defining quantities, specific characteristics and preservation.

All Inpatient Units were observed from Monday to Friday considering the movement and routine of the patients' care from each HCF.

The second part of the research was applying the questionnaire. The questionnaire was developed by the author and has questions about quality and state of conservation. Its answers follow the Linkert scale, which measure the agreement's intensity between five points [4].

The participants' approach to answered the questionnaire was in the Inpatient Units. The invitation to participate in the research was made personally respecting the availability offered, it means that only those who were in the moment of pause of activities were approached.

To participate in this study the person should be part of the nursing or physiotherapy staff. Also they should work at least for six months in the hospital, because they are the ones that most operate/use the hospital furniture daily.

In order not to harm the participants, identification codes were used to replace their names, keeping them anonymous and preserving their identities.

The Cochran's Principle defined the number of respondents required in each HCF. This principle says that by specifying the error margins of the items considered most important to the research it is possible to determine the size of the sample. It is based on the Eq. 1 [5].

$$n = \frac{N * Z^2 * r * (r-1)}{(N-1) * t^2 + Z^2 * r * (r-1)} \qquad (1)$$

where:

N   Population's size: 104 for the Public HCF, 29 for de Private HCF and 14 for the HCF maintained by NGO;
Z   Z value for the confidence percent: 1.645 for 90% of confidence level;
r   proportion of expected answers: 0.5 for 50%;
t   maximum error margin: 0.05 for 5%.

The results for the Public HCF was n = 75.32, for the Private HCF was n = 26.28, and for the HCF maintained by NGO was n = 13.35.

The data collected with the checklist and the questionnaire were organized in tables. They show the quantity, the state of conservation using percent of obsolete or inadequate furniture, and the ergonomics and security's factors, as the percent of furniture with rounded corners, rubber protection and height adjustment. Finally the data collected using both methods were compared.

3 Results

The checklist was applied in seven Hospitalization Units, five of them from the Public HCF.

Table 1 shows the Hospitalization Units included in the survey with the number of general rooms and the number of inpatient room, because some general rooms are shared. And also shows the quantity of each furniture. SC is the abbreviation for Surgical Clinic. The quantity of furniture should be equal to the number of inpatient room.

The checklist's outcomes are in Table 2, which shows the percentage of furniture with low quality and bad state of conservation in each HCF. In this moment is important to emphasize the difference between quality and state of conservation: quality is the property that determines the essence of something, if it is good/bad or its negative/positive degree of excellence. The state of conservation is the status of the

Table 1 Inpatient Units where the research was carried on with the respective quantity of rooms, inpatient's room, and each furniture included in the study

Evaluated HCF	Inpatient unit	Rooms	Inpatient room	Beds	Armchair	Lockers
Public HCF	Maternity	11	25	26	24	19
	Pediatrics	13	26	26	26	52
	SC I	13	31	31	18	31
	SC II	11	30	30	30	60
	SC III	8	20	20	12	20
Private HCF	Unique	4	4	4	4	4
NGO HCF	Unique	15	21	21	21	21
Evaluated HCF	Inpatient unit	Serum support	Food table	Bed-side table	2s stairs	–
Public HCF	Maternity	26	10	0	21	–
	Pediatrics	25	26	26	3	–
	SC I	31	31	10	0	–
	SC II	27	30	0	0	–
	SC III	35	20	2	1	–
Private HCF	Unique	4	4	4	0	–
NGO HCF	Unique	32	20	30	6	–

Table 2 Percentage of low quality and bad state of conservation furniture in each HCF evaluated. Data collected in March, 2017

Outcome	Furniture						
	Bed (%)	Arm-chair (%)	Locker (%)	Serum support (%)	Food table (%)	Bed-side table (%)	2s stairs (%)
Public HCF							
Quality	23.08	0	3.9	27.3	0	2.6	91.7
State of conservation	19.23	49.1	8.7	0	0	44.7	95.8
Private HCF							
Quality	0	0	0	0	0	0	0
State of conservation	0	0	0	0	0	0	0
HCF maintained by NGO							
Quality	0	0	0	0	0	0	16.6
State of conservation	0	9.52	0	0	90.5	6.7	0

preservation against damage, a set of permanent actions to prevent something from deteriorating over time or use [6].

The author considered defective and with no preservation the hospital beds with broken bed crank, beds without height adjustment or without grid security locks. Also the armchairs with broken or missing parts, such as footrest, armrest, backrest and seat; armchairs with no inclination, compromised structure or upholstered torn or damaged. The lockers without door handle or with doors that did not close and without wheel security locks or no rubber protection were considered defective and with no preservation too.

Others characteristics that marks no preservation and defectiveness of the furniture were the serum support with broken parts and the food tables with stuck wheel, loose top or alive corners. It was considered defective and with no preservation the bedside tables with alive corners, broken parts or the ones positioned incorrectly, like over the patient head or far from the bed.

Table 3 The quality of the hospital furniture from each HCF according to the research participants. Data collected in April, 2017

Furniture	Quality		Public HCF (%)		Private HCF (%)		HCF NGO (%)	
Bed	SP	P	37.33	42.66	84.61	15.38	46.15	53.84
	Regular		17.33		0		0	
	N	SN	2.66	0	0	0	0	0
Arm-Chair	SP	P	0	17.33	76.92	19.23	0	0
	Regular		32		3.84		61.53	
	N	SN	21.33	29.33	0	0	15.38	23.07
Locker	SP	P	1.33	33.33	73.07	23.07	0	69.23
	Regular		41.33		0		30.76	
	N	SN	20	4	0	0	0	0
Serum support	SP	P	1.33	20	61.53	34.61	0	61.53
	Regular		41.33		3.84		38.46	
	N	SN	24	13.33	0	0	0	0
Food Table	SP	P	4	45.33	65.38	34.61	0	46.15
	Regular		29.33		0		46.15	
	N	SN	10.66	9.33	0	0	7.69	0
Bedside table	SP	P	0	37.33	53.84	23.07	0	30.76
	Regular		32		0		53.84	
	N	SN	17.33	10.66	3.84	3.84	15.38	0
Stairs	SP	P	0	20	0	0	0	30.76
	Regular		25.33		0		69.23	
	N	SN	22.66	20	0	0	0	0

SP is strong positive, *P* is positive, *N* is negative and *SN* is strong negative

Finally, broken and inclined stairs and two-step stairs with alive corners are considered defective and with no preservation.

Using the Cochran Equation (Eq. 1) the sample size was defined and the questionnaire was applied to 114 participants, 75 from the Public HCF, 26 from the Private HCF and 13 from the HCF maintained by NGO.

Table 3 refers to the question "What is the quality of this hospital furniture used in this Unit?" and Table 4 refers to the question "What is the state of conservation of this hospital furniture used in this Unit?". There were five options: strong positive (SP), positive (P), regular, negative (N), strong negative (SN). For each furniture there is three lines showing the results (if positives, regular or negatives) and three columns (one column for each HCF).

Some items did not complete 100% because some questions were not answered in the questionnaire. The perceptual of no answers were the bedside table and two-step stairs from the Public HCF with 2.68% and 12.01%, respectively. Also the bedside from the Private HCF, which the no answers was 13.41% and the two-step stairs nobody answered.

4 Discussion

It is not possible to evaluate the Hospital Furniture without consider the hospital's structure. The use of manuals hospital beds at the Maternity of the Public HCF happens because it's an old building and does not offer good structural conditions. Electric beds don't go through the inpatient rooms' door.

The furniture's quality depends on the economic spends availability offered by the hospital. A Private HCF has more purchasing power than a Public HCF, that depends on bidding.

But this research shows the quality of the hospital furniture in a Public HCF is good and the author observations and the questionnaire's bad results is related more to the furniture's preservation there.

The questionnaire's negative results, which appears mainly at the Public HCF, agree with the collected data of Mahlmeister [7], with which he states that the furniture is

Table 4 The state of conservation of the hospital furniture from each HCF according to the research participants. Data collected in April, 2017

Furniture	State of conserv.		Public HCF (%)		Private HCF (%)		HCF NGO (%)	
Bed	SP	P	21.33	48	80.76	19.23	30.76	53.84
	Regular		24		0		15.38	
	N	SN	5.33	1.33	0	0	0	0
Arm-Chair	SP	P	0	10.66	80.76	19.23	0	15.38
	Regular		24		0		36.76	
	N	SN	37.33	26.66	0	0	30.76	23.07
Locker	SP	P	0	28	76.92	19.23	0	38.46
	Regular		50.66		0		30.76	
	N	SN	16	5.33	0	0	30.76	0
Serum support	SP	P	0	16	61.53	38.46	0	53.84
	Regular		40		0		46.15	
	N	SN	28	16	0	0	0	0
Food Table	SP	P	2.66	41.33	69.23	26.92	0	0
	Regular		37.33		0		53.84	
	N	SN	13.33	1.33	3.84	0	38.46	7.69
Bedside table	SP	P	0	30.66	53.84	15.38	0	38.46
	Regular		37.77		0		61.53	
	N	SN	24	5.33	3.84	3.84	0	0
Stairs	SP	P	0	21.33	0	0	0	23.07
	Regular		29.33		0		69.23	
	N	SN	21.33	17.33	0	0	7.69	0

one of the most reasons dissatisfaction between the public hospital's professionals he evaluated in 2010.

At the Public HCF, the majority of the health professionals classify the armchair conservation state as "negative" or "strong negative". And this confirm the checklist results, which showed that several armchairs in the Public HCF, mainly at de Maternity and Surgical 1 and 3, are inappropriate for use, with broken or missing parts and damage upholstered.

The same way the Hospital Furniture can not be evaluated separately from the HCF structure, it is also not possible to evaluate disregarding the people that uses it. The turn over of people in a public hospital receives is much greater then a private hospital, and some are not careful about public assets. This explains the armchair results.

This discourages the Public HCF buying more comfortable and better quality armchairs and carry out the maintenance frequently. The maintenance issue is a reason that contributes to the negative or strong negative state of the armchairs. As there is no preventive or corrective maintenance program for the Hospital Furniture, the armchairs are unattended.

The stainless locker design leaves everybody susceptible to any adverse events, such as stumbles that can lead to falls or injuries.

The existence time of the hospitals also influences in the state of conservation. The Public HCF exists for about 50 years, the Private HCF exists for 3 years and the HCF maintained by NGOs less than 20 years. Therefore, it is pertinent that the Private HCF's furniture is newer and well maintained than he others. Likewise, the furniture of the HCF maintained by an NGO have a well-cared maintenance than the Public HCF.

In the NGO-maintained HCF the food table status was assessed as regular, negative and strong negative. And this results also agree with the check-list, which showed that the food tables are inadequate, as most are with the wheels stuck and make noise to get around, and some have a broken top.

This inadequate furniture represent extrinsic factors to the patient, and as defined by de Jesus et al. [1] and Zottis et al. [2], these factors directly influence the occurrence of adverse events.

5 Conclusion

Based on outcomes, a report was formulated informing the situation of the Inpatient Hospitalization's furniture about the quality and the state of conservation. The purpose of this report is to support the decisions of the HCF managers, in

order to increase the patient safety, improve the health professionals' working conditions, and turn the hospitalization environment more comfortable. Either improve the description of the furniture in the purchases or biddings or implement an efficient maintenance program in the HCF.

The used methods in this research allowed to collect the characteristics of the environment and its furniture, and to understand the several factors that influence on them. Such as demand, economics, turnover, and maintenance program for each HFC. And it was possible to obtain the opinion of health professionals from three different hospitals: Public, Private and maintained by NGO.

Knowing the problems and the advantages of the furniture can contribute to a better interactivity with the user and consequently, better performance. The recognition of difficulties faced by healthcare professionals or defects from the furniture itself in advance can prevent the occurrence of adverse events and increase patient safety.

The outcome showed the Private HCF excelled at the others with mostly positive results. Followed by the HCF maintained by NGO, which obtained relevant information on the food table, and, finally, the Public HCF, with disadvantages mainly in the companion armchair, but also the manual hospital bed, the serum support and the size of the locker. The factors of demand, economy and exposure were duly discussed.

Both applied methods helped to understand some of the needs of the users, this direct communication with them is essential for good human factor work.

References

1. de Jesus, J.B., Botelho, H.M.S.B., Aguiar, B.G.C., Pereira, G.L., Leite, J.L.: Avaliação do ambiente físico e mobiliário quanto ao risco de quedas: diagnóstico situacional. Revista ACRED-ISSN, 85–99 (2014)
2. Zottis, G.A., Ribeiro, M.L., de Moura, P.M.: Rotina de Prevenção de quedas, pp. 1–14. Grupo Hospitalar Conceição Hospital Cristo Redentor (2010)
3. Stichler, J.F.: Healthy work environments for the ageing nursing workforce. J. Nurs. Manag. **21**(7), 956–963 (2013)
4. Filardi, A.L., Traina, A.J.M.: Montando questionários para medir a satisfação do usuário: avaliação de interface de um sistema que utiliza técnicas de recuperação de imagens por conteúdo. In: Proceedings of the VIII Brazilian Symposium on Human Factors in Computing Systems, pp. 176–185. Sociedade Brasileira de Computação (2008)
5. Cochran, W.: Sampling Techniques, 3 edn. Wiley Series in Probability and Mathematical Statistics. Wiley, Nova Iorque (1977)
6. Ferreira, A.B.deH.: Dicionário da língua portuguesa, 5. ed. Positivo, Curitiba (2014)
7. Mahlmeister, L.R.: Human factors and error in perinatal care: the interplay between nurses, machines, and the work environment. J. Perinat. Neonatal Nurs. **24**(1), 12–21 (2010)

Analysis of the Resolution in Basic Health Units in the City of Curitiba Using Data Mining

W. H. Santos and G. Y. Sato

Abstract

The E-Saúde system manages data related to the health care provided to patients in the public health system in the city of Curitiba. We applied data mining in the public database derived from E-Saúde, in order to identify attributes that determine the resolution prescribed by physicians working in Basic Health Units, specifically with regard to the quantity of laboratory tests requested and referrals to specialized care. For this, the decision tree classification algorithms of rule generators were applied on the 15 thousand records generated during one month in one of the sanitary districts of the city. The decision tree algorithm used was J48, which displays the nodes with the weights of the predictive attributes. The rule generator algorithm used, the JRip, displays sets of rules that can be easily interpreted allowing basic unit managers to monitor and determine the training and recycling needs of the professionals working in their units.

Keywords

Data mining • Public database • Decision tree J4.8 • Rules generator JRip

1 Introduction

Considering health as a right of all and a duty of the State, one of the functions of the Brazilian Unified Health System (SUS) [1] is to promote the recovery of the health of individuals and communities, emphasizing the principles of universality, completeness and resolve. The population access to the health care system should be via primary care

services provided by a Basic Health Unit (UBS) in their locality.

UBS should be qualified to meet and solve about 80% of users' health problems [2]. Only unresolved cases, around 15%, would be referred to a secondary level, the Specialty Centers level. A minority of the cases, about 5%, would reach the tertiary level of care, the hospitals, that have at their disposal resources and competences to address unresolved issues at other levels.

The proper functioning of the health care system depends on the efficiency of the primary level care (UBS). It must solve most of the problems, in order to not overload Specialized Clinics and Hospitals. In this way, the system as a whole could fulfill its objectives, increase user satisfaction, as well as use resources more efficiently.

The branch of the SUS in Curitiba serves the population of 1,848,943 inhabitants, in 2013, according to the Brazilian Institute of Geography and Statistics (IBGE) [3]. It has 141 units, among which 109 are Health Units and nine are Emergency Care Units, as well as other specialized units [4].

The objective of this paper is to describe the application of mining algorithms in the public database derived from the E-Saúde system to find attributes that show the resoluteness of health care at health units (UBS), as well as to evaluate the accuracy of the found attributes.

2 Theoretical Framework

2.1 Medical Data Mining

Applying data mining to medical data is a challenging process [5]. Operators feed incomplete information in computer systems, producing sparse databases, with highly varied data. Using such data demands the application of different techniques and tools in order to exploit the databases in a way that it produces some effective result.

There are still ethical, legal and social restrictions regarding privacy and clinical validation of the findings. So,

W. H. Santos (✉) · G. Y. Sato
Graduate Program in Biomedical Engineering, Federal University of Technology - Paraná, Curitiba, Brazil
e-mail: williamsantos@gmail.com

G. Y. Sato
e-mail: sato@utfpr.edu.br

most of the time, the data that is actually being analyzed contains a subset of the original data.

However, data mining has been gaining prominence in the health care area, helping health organizations make management decisions regarding users and their employees, such as nursing professionals and physicians [6].

One of the approaches to extracting useful information (knowledge) in the analysis of medical computational databases is the use of theories related to the field of Knowledge Discovery [7] called KDD.

KDD [8] is a non-trivial process that seeks to identify valid, unpublished, potentially useful and understandable patterns of data. Often, the term "Data Mining" is used broadly, as synonymous with KDD, for the application of specific algorithms to extract data patterns.

2.2 Classifiers

Classification can be understood as the systematic distribution of data in different categories, according to analogies and common characteristics [9]. The classifier algorithms used in this work were chosen according to the characteristics of the output data of each one, so we used a decision tree classifier and a rule-based classifier.

A decision tree is a set of conditions arranged in a hierarchical structure. It is a model in which an example is sorted by following the path of satisfied conditions from the root until it reaches a leaf, which will correspond to a class label [10].

Decision trees are considered easy-to-understand models because a reasoning process can be given for each conclusion. They have many advantages: they are simple, easy to understand and can handle numerical or categorical variables.

The model works by recursively partitioning a training set until each subset obtained from this partitioning contains cases of a single class. The initial set of generated nodes is very large and redundant, since it is generated from a decision tree. The overall optimization process is done by applying a greedy criterion to choose better partitions and better attributes [11].

In a rule-based classifier, the learned model is displayed in the form of a set of if-then rules. Rules are a convenient way to represent information or bits of knowledge [12]. An example of a rule-based classifier is the JRip algorithm, which implements Repeated Incremental Pruning to Produce Error Reduction, or RIPPER [13].

The model operates in two stages. In the first stage, using heuristic techniques, it picks up a set of initial classes and then makes adjustments in these classes. This strategy determines which class is the best to characterize the segmentation of rule sets. In the second stage, this procedure is repeated for each of the subsets generated in the iterations. The goal of the overall optimization process is to increase the accuracy of the rule set by replacing or revising individual rules [14].

3 Materials and Methods

3.1 Open Data

In its Internet portal, Curitiba government provides public domain documents and information, guaranteeing access to primary data that can be used to produce new information for society [15].

Among the 20 databases available, four are from the Department of Health, via the E-Saúde system. This system stores data about the care provided in the health care system. The four available databases are: Medical, Nursing, Dental and Other Higher Level Professionals.

For this work we selected the database regarding the care provided by the medical professionals of the Basic Health Units (Medical database). This database is a file in .csv format that can be downloaded directly from the open data portal.

The data from all units covering the first quarter of 2017 has a size of 280 Mb, with a total of 730,738 records. Along with it, a database dictionary is provided. This dictionary contains the description of each field in the database and, other technical details. In the Medical database, 37 fields are available for each instance (or record).

3.2 Database

The MySQL database [16] was used to create a table called MEDICO containing the original attributes of the database. The table fields have been created according to the database dictionary description.

Also, 10 new attributes were created in the MEDICO table and populated with values calculated or inferred from the original fields, to allow the optimization of the classifier algorithms.

For example, the CAP_CID attribute was created. It grouped in 21 values the 5.000 occurrences of the original cod_CID attribute, improving the convergence of the results when submitted to the algorithms. Table 1 presents the eight new attributes used in this work, and two new attributes are not shown because they are descriptive.

Then, a selection of the attributes that have a connection with the theme of the work was made, all descriptive attributes were removed, leaving the original codes, reducing the dimensionality to a total of 26 (Table 2). The attributes in low case are original attributes of the base, and those in the upper case are the ones we created.

Table 1 New attributes created

Cod	New attribute	Original attribute
1	CAP_CID	Diagnostic Code (CID)
2	DAY_OF_THE_WEEK	Date of service (patient)
3	AGE_RANGE	Date of birth (patient)
4	PHARM_PRESCR	Prescribed Qty Pharmacy Curitiba
5	PHARM_DISPEN	Dispensed Qty Pharmacy Curitiba
6	PHARM_NO_PATT	Non-Standardized Drug Qty
7	ROOM_RANGE	Room at home (number)
8	ORIGIN_CURITIBA	City of origin (patient)

Table 2 Attributes used in data analysis

Cod	MEDICO table attribute name	Description
1	DAY_OF_THE_WEEK	Day of the week (appointment)
2	AGE_RANGE	Age Range (patient)
3	sex	Sex (patient)
4	descr_unit	Customer Service Unit
5	descr_proced	Procedure Performed
6	descr_CBO	Occupation description (professional)
7	cod_CID	Diagnostic Code (CID)
8	CAP_CID	Chapter of the CID
9	solicit_exam	Indicates if an exam was request
10	PHARM_PRESCR	Prescription of drugs from the Pharmacy Curitibana
11	PHARM_DISPEN	Dispensing of drugs from the Pharmacy Curitibana
12	PHARM_NO_PATT	Non-standardized medication
13	enc_specialist	Indicates if there was referral to expert
14	admission	Indicates if hospitalization has occurred
15	water_treat	Type of Water Treatment at Home
16	water_supply	Type of Water Supply at Home
17	electric_power	Indicates whether there is electric power at home
18	house_type	Type of housing
19	waste_destin	Destination of household waste at home
20	feces_urine_dest	Destination of feces/urine at home
21	ROOM_RANGE	Number of rooms at home (range)
22	in_illness_case	Services sought in case of illness
23	community_group	Community group in which the patient participates
24	communication	Means of communication used at home
25	transport	Means of transportation used at home
26	ORIGIN_CURITIBA	If patient lives in Curitiba

3.3 Environment Weka

We generated the .arff (Attribute-Relation File Format) files, the standard input for the WEKA (Waikato Environment for Knowledge Analysis) environment [17]. The Weka was developed by the University of Waikato, New Zealand, in JAVA language, and has as main objective to solve problems of data mining based on machine learning, using analysis methods in data sets, in a fast and flexible way [18].

In WEKA, one of the decision tree inductors is the J.48 version of the C4.5 algorithm available in the package weka.classifiers.trees.J48. One of the algorithms that induces the available RIPPER classification rules is JRip, which is an optimized version of IREP available in the package weka.-classifiers.rules.JRip.

4 Results and Discussion

The WEKA was fed by an .arff file with 19,926 instances corresponding to the data from 14 Basic Health Units and the Emergency Care Unit of the Boqueirão sanitary district, with medical records for the month of March 2017.

The three attributes related to the expectation of a health system user to have their case resolved, in access to the health system, are solicit_exam, enc_specialist and admission. A negative response to each indicates that he will not have to return at a later time to continue his original care.

Submitting the three variables to the classifier J4.8, the one with the highest prevalence was solicit_exam. For this reason, solicit_exam was applied to the algorithms J4.8 and JRip, chosen in this work.

For both algorithms, cross-validation was used, which consisted in dividing the total data set in 10 subsets. For the cross-validation, the 10 subsets were mutually exclusive and of the same size. We used nine subsets, in each cycle, to train the model and the remaining dataset to test the model. The accuracy values obtained for the two classifiers are the results of the averages of the accuracies found in each of the 10 rounds to which each subset was submitted.

4.1 Classifier J.48

The decision tree obtained has the total size of 35 and number of leaves equal to 28 (Fig. 1). Of the total of 26 attributes (Fig. 1), the J4.8 algorithm identified as root, that is, as preponderant when requesting exams, the attribute enc_specialist (Indicates if there was referral to expert), and in the second level of the tree, the algorithm identified the Follow CBO Description attribute. The accuracy presented by the algorithm J4.8 was 74.66%.

```
Scheme:          weka.classifiers.rules.JRip -F 3 -N 2.0 -O 2 -S 1

enc_specialist = No: No (15442/3473)
enc_specialist = Yes
|   descr_CBO = MED_CLINICAL
|   |   PHARM_NO_PATT = NO_PATT_NO
|   |   |   CAP_CID = 10:CapX: Yes (25/11)
|   |   |   CAP_CID = 11:CapXI: Yes (40/10)
|   |   |   CAP_CID = 12:CapXII: Yes (16/7)
|   |   |   CAP_CID = 13:CapXIII: Yes (237/84)
|   |   |   CAP_CID = 14:CapXIV: Yes (34/12)
|   |   |   CAP_CID = 18:CapXVIII: Yes (165/57)
|   |   |   CAP_CID = 19:CapXIX: No (4/0)
|   |   |   CAP_CID = 1:CapI: No (4/1)
|   |   |   CAP_CID = 21:CapXXI: No (571/254)
|   |   |   CAP_CID = 3:CapII: Yes (2/0)
|   |   |   CAP_CID = 4:CapIV
|   |   |   |   sex = F: Yes (67/26)
|   |   |   |   sex = M: No (32/13)
|   |   |   CAP_CID = 5:CapV
|   |   |   |   sex = F: Yes (47/21)
|   |   |   |   sex = M: No (28/11)
|   |   |   CAP_CID = 6:CapVI: Yes (6/3)
|   |   |   CAP_CID = 7:CapVII: No (1/0)
|   |   |   CAP_CID = 8:CapVIII: No (4/0)
|   |   |   CAP_CID = 9:CapIX: Yes (128/57)
|   |   PHARM_NO_PATT = NO_PATT_YES: Yes (168/51)
|   descr_CBO = MED_FAMILY_HEALTH_STRAT
|   |   AGE_RANGE = 1:Baby: No (59/20)
|   |   AGE_RANGE = 2:Child: No (143/59)
|   |   AGE_RANGE = 3:Teenager: Yes (84/38)
|   |   AGE_RANGE = 4:YoungAdult: Yes (399/146)
|   |   AGE_RANGE = 5:Adult: Yes (577/177)
|   |   AGE_RANGE = 6:OldMan: Yes (522/209)
|   descr_CBO = MED_GYNECOLOGIST_AND_OBSTETRIC: Yes (834/103)
|   descr_CBO = MED_PEDIATR: No (281/91)

Number of Leaves:      28
Size of the tree:      35
```

An important feature in the generated tree is the two numbers displayed next to each leaf. The first shows the total of classifications performed, and the second the total of classifications performed incorrectly within the total, thus giving an idea of the effectiveness of the classification performed.

4.2 JRIP Classifier

The JRip Classifier generate 13 rules. Twelve of these rules indicate a request for exams ("YES"). In Table 3, the obtained rules were placed in descending order of occurrences.

From the total of 26 attributes, which the JRip algorithm identified as preponderant at the moment of requesting exams, was the attribute `enc_specialist` (Indicates if there was referral to expert) with 3,572 occurrences equal to "YES" within a total of 19,926 occurrences.

The fact that the generated output is a text with the attributes with their respective values connected by the logical operator facilitates the interpretation of the rule. Thus it is possible to identify that the attribute `enc_specialist` equal to "YES" is prevalent in the found rules.

Similar to the decision tree, in the last column of Table 2 two numbers are displayed. The first presents the total of classifications carried out, and the second the total of classifications performed incorrectly. The JRip classifier, globally, obtained a 74.80% of accuracy.

The percentage of correctly sorted instances for the J4.8 and JRip classifiers were 74.66% and 74.80%, respectively, thus showing that the performance of the two classification algorithms was practically the same. Both classifiers converged in the `enc_specialist` attribute as the main one to be considered when considering the request of examinations of a patient from a Basic Health Unit of the care network.

Table 3 Rules generated with the JRip classifier of the `solicit_exam` attribute

N.	Rules with solicit_exam=Yes	Occurrences Total/Errors
1	`(enc_specialist=Yes)` and `(descr_CBO=GYNECOLOGIST_AND_OBSTETRIC)`	834/103
2	`(enc_specialist=Yes)` and `(AGE_RANGE=4:YoungAdult)`	610/259
3	`(enc_specialist=Yes)` and `(descr_CBO=MED_FAMILY_HEALTH_STRAT)` and `(AGE_RANGE=5:Adult)`	514/165
4	`(enc_specialist=Yes)` and `(AGE_RANGE=5:Adult)`	504/240
5	`(enc_specialist=Yes)` and `(AGE_RANGE=6:OldMan)` and `(sex=F)` and `(community_group=participate_no)`	359/151
6	`(descr_CBO=MED_CLINICAL)` and `(CAP_CID=4:CapIV)`	356/174
7	`(enc_specialist=Yes)` and `(CAP_CID=13:CapXIII)`	355/77
8	`(enc_specialist=Yes)` and `(descr_CBO=MED_FAMILY_HEALTH_STRAT)` and `(AGE_RANGE=6:OldMan)`	266/115
9	`(enc_specialist=Yes)` and `(sex=F)` and `(CAP_CID=18:CapXVIII)` and `(PHARM_NO_PATT=NO)` and `(transport=Bus)`	85/11
10	`(enc_specialist=Yes)` and `(CAP_CID=18:CapXVIII)` and `(DAY_OF_THE_WEEK=5-Thursday)`	45/9
11	`(descr_CBO=MED_CLINICAL)` and `(CAP_CID=9:CapIX)` and `(descr_unit=UMS_MENONITAS)`	36/12
12	`(descr_CBO=MED_CLINICAL)` and `(CAP_CID=9:CapIX)` and `(PHARM_NO_PATT=Yes)`	20/6
13	**`solicit_exam=No`**	15942/3601

5 Conclusions

Using the decision tree J4.8 classifier and the JRip - rule generator, it was possible to highlight the attributes that contribute to the request for exams, especially the attribute `enc_specialist` (Indicates if there was referral to expert), in the Basic Health Units (UBS) of the Boqueirão health district.

Both classifiers presented accuracy close to 75% in the classification of instances, even with almost identical percentages. The combination of both outputs facilitates the interpretation of the results. The decision tree format and the rules in textual form could be interpreted by a person with some training. For example, a manager of one of the UBS could act on the information to improve the management of human resources available in health district units using the result of the classifiers.

Another result of our work was the web tool created in PHP language that makes possible to import the database available on the city's website to a MySQL database. Also, this tool provides the generation of .arff files for WEKA, which allowed us to analyze the data using the classifiers. Such a tool is a first step to allow managers of the Heath System analyze the data from E-Saúde and improve their decision-making process. This analyze would not demand programming or database manipulation skills.

With the case studied, we could conclude that the E-Saúde database is exploitable and could potentially improve the decision-making process in the Curitiba's Health Care System.

References

1. Sistema Único de Saúde. http://portalms.saude.gov.br/sistema-unico-de-saude/sistema-unico-de-saude. Accessed 28 Mar 2018
2. Ministério da Saúde. O SUS de A a Z: Garantindo saúde nos municípios. Série Comunicação e Educação em Saúde 3. ed. Brasília. http://bvsms.saude.gov.br/bvs/publicacoes/sus_az_garantindo_saude_municipios_3ed_p1.pdf. Accessed 01 Mar 2018
3. Histórico da Secretaria Municipal de Saúde de Curitiba. http://www.saude.curitiba.pr.gov.br/a-secretaria/historico-da-secretaria.html. Accessed 25 Feb 2018
4. Distritos Sanitários da Secretaria Municipal de Saúde de Curitiba. http://www.saude.curitiba.pr.gov.br/a-secretaria/equipe/distritos-sanitarios.html. Accessed 25 Feb 2018
5. Ferreira, E.L.: Mineração de Dados Aplicada à dados médicos. 68f Dissertação – UFMG, p. 3, Belo Horizonte (2015)
6. Ferreira, E.L., Rausch, H., Campos, S.: Medical data mining: a case study of a paracoccidioidomycosis patient's database. In: IEEE 16th International Conference on e-Health Networking, Applications and Services (2014)

7. de Oliveira Júnior, J.G.: Identificação de Padrões para a Análise da Evasão em Cursos de Graduação Usando Mineração de Dados Educacionais. 86 f. Dissertação – UTFPR, p. 15, Curitiba (2015)

8. Fayyad, U.M., Gregory, P.-S., Padhraic, S.: Advances in Knowledge Discovery and Data Mining, pp. 1–34. American Association for Artificial Intelligence, Menlo Park, USA (1996)

9. Librelotto, S.R., Mozzaquatro, P.M.: Análise dos Algoritmos de Mineração J48 e Apriori Aplicados na Detecção de Indicadores da Qualidade de Vida e Saúde. Revista Interdisciplinar de ensino Pesquisa e Extensão, vol. 1 (2013)

10. Romero, C., Ventura, S., Espejo, P.G., Hervás, C.: Data mining algorithms to classify students. In: The First International Conference on Educational Data Mining, pp. 8–17 (2008)

11. Socek, F., Orlovski, R.: Mineração de Dados: Conceitos e Aplicação de Al-gortimos em Uma Base de Dados na Área da Saúde. Revista Científica Semana Acadêmica. Fortaleza, ano MMXIV, nº 50 (2014)

12. Han, J., Kamber, M., Pei, J.: Data Mining: Concepts and Techniques, 3rd edn. Morgan Kaufmann Publishers Inc., San Francisco, USA (2011)

13. Souza, J.W.daC., Di Felippo, A.: Caracterização da Complementariedade Temporal: Subsídios Para Sumarização Automática Multidocumento Facebook Twitter Alfa: Revista de Linguística (São José do Rio Preto), 2018-3, vol. 62, nº 1, pp. 125–150 (2018)

14. Franca, G.E.F., Carvalho, D.R., Tsunoda, D.F.: Descoberta de Padrões em Ordens de serviço de Tecnologia da Informação em Hospital Revista de Gestão em Sistemas de Saúde, vol. 5 (2016)

15. Portal de Dados Abertos de Curitiba. http://www.curitiba.pr.gov.br/dadosabertos/. Accessed 05 Feb 2018

16. MySQL. The world's most advanced open source database. http://www.postgresql.org. Accessed 25 Feb 2018

17. Hall, M., Frank, E., Holmes, G., Pfahringer, B., Reutemann, P., Witten, I.H.: The weka data mining software: an update. ACM-SIGKDD Explor. Newslett. **11**, 10–18 (2009)

18. Weka 3—Data Mining with Open Source Machine Learning Software in Java. http://www.cs.waikato.ac.nz/ml/weka/. Accessed 05 Feb 2018

Computer Simulation as a Tool in the Definition of Computed Tomography Acquisition Characteristics

Rogerio Santos, Andrei Pires, Wagner Pereira, and Renan Almeida

Abstract

A careful planning of equipment acquisition is important for both private and public health services. Computed Tomography (CT) is one of the most important tools in diagnostic imaging. In Brazil, among medical imaging devices, 4.7% were CTs, representing eighth place in exam numbers and first in costs. The aim of this study was to simulate the installation of a new CT service with 1, 4, 16 or 128-slice devices, determining its profit after 3 years in a general hospital. To this end, exams were divided into six steps. Models were created in the MedModel® software and three years were simulated for a hospital operating 24 h/day. Two scenarios were simulated for four CT types with two values of exam increase rates (*scenario 1* starting with 50 exams/month, with a small growth rate in the number of exams; and *scenario 2* also starting with 50 exams/month, but with a greater growth rate). The costs for acquisition (new and used equipment), installation and operation were estimated, together with overall exam reimbursement values. None of the simulated CT models achieved profit after 36 months in scenario 1. In scenario 2, all simulated equipment were profitable after 36 months, except for the new 128-slice. In conclusion, the results indicate the need for a study of the expected number exams. The study shows the importance of knowing the real potential of a new medical service and the value of computer simulation tools in the design of a medical-hospital service.

1 Introduction

The careful planning of equipment acquisition is fundamental for both private and public health services. In fact, one of the most important tasks for Clinical Engineers is the management of the technological resources available for hospital medical units, from acquisition to retirement, and including operator training, maintenance and management. For instance, during acquisition, a Clinical Engineer should give input on installation feasibility and model specification according to the needs of the health unit, thus avoiding super or under-sizing [1].

Computed Tomography (CT) is one of the most important diagnostic tools in medicine, with a wide scope of clinical use [2]. Of all medical imaging devices in Brazil in 2009, 4.7% were CTs, ranking eighth in the number of installed devices [3–5]. In the US, the percentage of patients using CTs in emergency departments increased from 2.4% in 1992 to 13.9% in 2007 and only 0.7% of these patients used magnetic resonance imaging [6, 7], underscoring the importance of CT availability.

Computer simulation is as an important tool for the study the characteristics of computed tomography sectors, and it has been successfully applied in decision making in many areas. For instance, in the health sector it allowed for the optimization of physical, financial and human resources in many hospital settings [8–12].

Therefore, the objective of the present study was to simulate the installation of a new CT service with 1, 4, 16 or 128-slice devices, determining its profit after a pre-defined period. Two scenarios in a general hospital were considered.

R. Santos (✉)
CEFET "CSF" - RJ, Rio de Janeiro, RJ, Brazil
e-mail: rogeriopires1@uol.com.br

A. Pires · W. Pereira · R. Almeida
Programa de Engenharia Biomédica, COPPE/UFRJ,
Rio de Janeiro, RJ, Brazil
e-mail: andreilenine@uol.com.br

W. Pereira
e-mail: wcap58@gmail.com

R. Almeida
e-mail: renan.m.v.r.almeida@gmail.com

2　Materials and Methods

2.1　Studied Devices

To provide a broad overview of equipment use, and considering that even single-slice models are still used in many countries [2], models with 1, 4, 16 and 128 slices were studied here, in six private health facilities located in Rio de Janeiro, Brazil. Three single-slice CTs, one 4-slice, one 16-slice and 128-slice were studied (a convenience sample of six devices). All studied technologies are used in Brazil and remain in production in several countries [13]; and all studied equipment are still in use. The market prices were used for both new and used models.

2.2　Process, Exam Stages and Times

In the studied units, the process of obtaining a CT exam was characterized as follows:

- The operator of the CT scanner receives the exam request form and takes the patient from the waiting room to the examination room (first stage of the process: time between the exam request arrival and the patient entry into the room);
- The patient changes clothes for examination (second stage);
- The operator positions the patient in the CT (third stage);
- The operator inputs the patient data and sets the exam protocol into the CT console (fourth step: data entry);
- The CT acquires the images (fifth stage: image acquisition). If the exam needs a radiopaque contrast, the operator applies a venous access to the patient and injects the contrast, and two more image acquisitions are made (the sum of these times characterizes the acquisition stage for contrast exams);
- The operator removes the patient from the examination couch; the patient changes the clothes and exits the examination room (last stage of the process).

Therefore, exam procedures are divided into the six stages described below (process times). Times were measured by two researchers in the analyzed units, and these measures characterized the probability distributions used in the models (distribution of times in each process stage). The Easyfit® software was used to this end.

2.3　The Simulation

Discrete event simulation models were used in the present study. These models allow for the representation of real processes in a short period of time, and allow for the inclusion of non-linear effects in an analysis. These characteristics are especially interesting in the simulation of health system processes, in which effects may take a long time to appear and involve non-linear interactions among agents (e.g. exams cost, number and duration) [8]. The Models were created in the MedModel® software using as parameters:

- **Locations**: Entrance/Exit point, Waiting room, Dressing room, CT Scanner and Console (CT's command);
- **Entities**: Patients (scheduled consults, emergency and scheduled with radiocontrast);
- **Arrival cycles**: 60% of patients were defined as scheduled without radiocontrast, 30% were emergency patients (non-scheduled) and 10% were scheduled patients using radiocontrast. Two scenarios were simulated (described below);
- **Resource**: Only models with one operator were considered; and
- **Process times**: 1. Arrival of patient and patient records to the examination room; 2. Patient changing clothes; 3. Patient positioning; 4. Data input prior to exam; 5. Image acquisition; and 6. Patient departure. Steps 1, 3, 4 and 5 use one resource.

As mentioned, for exams using radiocontrast, two more data acquisition stages (with the same duration of "Image acquisition") and venous access placement/removing times are needed; these processes also use one resource each. Priority of care was defined as higher for emergency patients. The simulation focused on the profit (difference between revenues and expenditures) of the analyzed CT sectors; with no attempt to analyze patient treatment protocols or aspects concerning clinical routine.

Three years of a CT sector operation located inside a fictitious hospital operating 24 h/day were simulated with the following scenarios:

- **Scenario 1**: operation starts with 50 exams/month with a monthly growth rate in exams of 10% (first year), 5% (second) and 2% (third year);
- **Scenario 2**: also starts with 50 exams/month but with a monthly growth rate of 15, 7 and 3%.

Only the second scenario was simulated for the 128-slice model.

It was considered that no increase of electrical power would be necessary for the installation of the CT and that its placement area only would needs small structural changes, such as radiological protection, refrigeration and electrical installation.

Costs of installation and operation were inferred using as an example a similar operating unit in the city of Rio de Janeiro. All values were calculated in Brazilian Reais and converted to US Dollars at the rate of 1 Dollar = R\$3.30, and then rounded.

3 Results

3.1 The Stages Duration

The average times calculated from the measurements were as follows:

1. **Patient entrance to the examination room**		6.47e-002 + L(0.62, 0.82);
2. **Patient clothes change**		0.13 + E(1.04);
3. **Patient positioning at the CT scanner**		1.13e-002 + L(1.13, 0.62);
4. **Patient data input into the CT computer**		−1.21 + L(2.27, 0.48);
5. **Image acquisition**	Single-slice	1.4 + E(1.95)
	4-slice	0.13 + L(1.75, 0.55)
	16-slice	0.202 + L(2.6, 1.24)
	128-slice	0.37 + E(0.60)
6. **Patient departure**		−0.11 + L(2.08, 1.4)

Above, "L" and "E" are the Lognormal and Exponential probability distributions, and times are reported as "minimum + L((Mean − minimum), SD)" and "minimum + E (SD)"; all times in decimal minutes.

3.2 Costs, Reimbursements and Profit

Taking into account the assumptions above, an installation cost of US\$11,515.00 was considered, and CT acquisition costs were: 1-Slice: US\$90,909.00 for a new and US\$54,545.00 for a used one; 4-Slice: US\$175,758.00 new and US\$106,060.00 used; 16-Slice: US\$242,424.00 new and US\$151,515.00 used; 128-Slice: US\$484,848.00 new and US\$333,333.00 used.

The suggested monthly fixed cost (covering 7 operator wages and standby electrical power) during the CT contract warranty was US\$9,090.00; and, after the warranty period (1 year for new models and 3 months for used equipment), US\$909.00/month was added for a basic maintenance contract. The supposed cost for each exam was US\$21.00, including wear of the X-ray tube, power consumption and miscellaneous expenses. Exams with radiocontrast had an extra US\$26.00 cost. The reimbursement for each exam was defined as US\$72.00 without radiocontrast and US\$109.00 with radiocontrast after (20%) taxes. Table 1 shows profits after the defined 36 months period of operation and the necessary time to pay the initial investments for the four CT technologies studied in the two simulated scenarios.

None of the simulated CT models achieved profit after 36 months in scenario 1. In scenario 2, all simulated equipment became profitable after 36 months, except for the new 128-slice. Only the single-slice models were profitable after 24 months.

Table 1 Profit after 36 months (in dollar) and time needed (in months) to pay for initial investment; four CT technologies and two simulated scenarios

Equipment	Return of investment	New device, Scenario 1	New device, Scenario 2	New device, Scenario 1	New device, Scenario 2
1-Slice	Time to profit	–	24	–	22
	Profit 36 months	−91,312	268,998	−62,230	299,119
4-Slice	Time to profit	–	28	–	25
	Profit 36 months	−176,169	185,180	−113,745	247,604
16-Slice	Time to profit	–	32	–	28
	Profit 36 months	−242,836	118,513	−159,200	202,150
128-Slice	Time to profit	–	–	–	35
	Profit 36 months	–	−131,162	–	11,262

The number of patients attended were: without radio-contrast 4011 in Scenario 1 and 8136 in Scenario 2; with radiocontrast 668 in Scenario 1 and 1357 in Scenario 2; emergency (non-scheduled) 1999 in Scenario 1 and 4058 in Scenario 2.

4 Discussion

The aim of this study was to simulate and compare scenarios to determine how long the investment in a new CT sector facility would become profitable; and what profit would be achieved after 3 years using the types of studied CTs. Since the focus was specifically on CT sector facility cost, image quality and aspects related to clinical routine and protocol were not evaluated here.

The results indicate the need for a realist analysis of the expected number exams prior to equipment acquisition. A careful specification of equipment characteristics for acquisition is important for both private and public health services. In the latter, waiting lists sometimes may extend for months in Brazil [14]. Although faster exams may represent more exams/time, costs may become prohibitive and the productivity gains unnecessary [7]. In addition, CT manufacturers increasingly introduce new models and try to convince buyers of their need, but both acquisition and maintenance costs are also greater in these new models, and the correct equipment specification becomes even more important to avoid the effects of marketing advertising.

Exam reimbursements in this study are in an intermediate range between those paid by the Brazilian public health system (SUS) and those paid for more expensive private health insurances. This shows how much expensive CT services can be, even making their implementation unfeasible.

As mentioned, maintenance costs were also considered, and were incorporated into fixed monthly costs after a warranty period. However, the analysis clearly indicated that the most important factors in cost determination were acquisition costs, which were, therefore, the most important in the definition of times for return of investment.

Despite their slower speed, even simpler models still allow for most types of exams (except heart exams that demand 128-slice and angiographic exams that demand 16-slices for ideal quality) [2]. Therefore, choosing simpler and/or used equipment may adequately suit the needs of a health unit, especially for those with a small number of simple exams. In this case, the option for simpler and cheaper models could mean, for example, a greater access to the CT equipment, decreasing waiting queues without extra expenses [12, 13, 15].

On the other hand, health units that attend to specific needs, as angiographic and cardiologic exams, should opt for faster models. The same applies to units that have a high demand for exams and work with more expensive exam reimbursements. For a large demand of simple exams or a mix of complex/simple exams, a solution comprising two equipment (a simple CT model and a faster one) could be considered.

Scheduled and unscheduled stops for preventive and/or corrective maintenance could also be incorporated into more sophisticated models. These analyses, however, would demand more specific information about CT operation, such as their MTBF (Mean Time Between Failures) and MTTF (Mean Time to Failure).

5 Conclusion

This study indicated the importance of knowing the real exam demand of a new medical service (here, the CT sector), and also showed the importance of avoiding market "impositions", since more sophisticated/faster CTs should be reserved for services with a higher demand (e.g. scenario 2 in the present study), thus guaranteeing return on investment.

On the other hand, the importance of the availability of new cheaper CT devices such as single-slice for low-demand units (Scenario 1) should be noted.

References

1. Enderle, J.D., Bronzino, J.D.: Introduction to Biomedical Engineering. Academic Press (2012)
2. Seeram, E.: Computed Tomography: Physical Principles, Clinical Applications, and Quality Control, 4th edn. Elsevier Health Sciences, St Louis, MO (2015)
3. Instituto Brasileiro de Geografia e Estatística (IBGE). Estatísticas da Saúde - Assistência Médico-Sanitária-2009. IBGE, Rio de Janeiro (2009)
4. World Health Organization (WHO). Density of Computed Tomography Units. http://tinyurl.com/j33eh9a (2011). Accessed 14 Aug 2016
5. Organization for Economic Co-operation and Development (OECD). http://www.oecd-ilibrary.org (2011). Accessed 14 Aug 2016
6. Ginde, A.A., Foianini, A., Renner, D.M., Valley, M., Camargo Jr., C.A.: Availability and quality of computed tomography and magnetic resonance imaging equipment in US Emergency Departments. Acad. Emerg. Med. 15(8), 780–783 (2008)
7. Niska, R., Bhuiya, F., Xu, J.: National hospital ambulatory medical care survey: 2007 emergency department summary. Natl. Health Stat. Rep. 26(26), 1–31 (2010)
8. Jacobson, S.H., Hall, S.N., Swisher, J.R.: Discrete-event simulation of health care systems. Int. Ser. Oper. Res. Manag. Sci. 91, 211–252 (2006)
9. Ferreira, R.B., Coelli, F.C., Almeida, R.M.V.R., Pereira, W.C.A.: Optimizing patient flow in a large hospital surgical centre. J. Eval. Clin. Pract. 14, 1031–1037 (2008)

10. Coelli, F.C., Almeida, R.M.V.R., Pereira, W.C.A.: A cost simulation for mammography examinations taking into account equipment failures and resource utilization characteristics. J. Eval. Clin. Pract. **16**, 1198–1202 (2010)

11. Villamizar, J.R., Coelli, F.C., Pereira, W.C.A., Almeida, R.M.V.R.: Discrete-event computer simulation methods in the optimization of a physiotherapy clinic. Physiotherapy **97**, 71–77 (2011)

12. Santos, R.P., Pires, A.L.A., Pereira, W.C.A., Almeida, R.M.V.R.: Computer simulation in the analysis of computed tomography exam times. In: World Congress on Medical Physics and Biomedical Engineering, 3–8 June 2018, Prague, Czech Republic. Springer (2018)

13. Santos, R.P., Pires, A.L.A., Pereira, W.C.A., Almeida, R.M.V.R.: Computed tomography scanner productivity and entry-level models in the global market. J. Healthc. Eng. **2017**, Article ID 1304960, 5 pp. (2017). https://doi.org/10.1155/2017/1304960

14. Oliveira, J., Girard, A.C., Medeiros, A.A., Nascimento, N.F.S.: Satisfação e percepção dos usuários de uma unidade básica de saúde da família sobre o SUS. Cadernos de Educação, Saúde e Fisioterapia, vol. 1.1 (2014)

15. Jhaveri, K.S., Saini, S., Levine, L.A., Piazzo, D.J., Doncaster, R.J., Halpern, E.F., et al.: Effect of multislice CT technology on scanner productivity. Am. J. Roentgenol. **177**(4), 769–772 (2001)

Distribution of Mammographs by Minas Gerais Macroregions of Health

Sarah Mansur Resende de Miranda, Ana Claudia Patrocinio, and Hendrill Humberto da Silveira Urzêdo

Abstract

Breast cancer represents the second most frequent type of cancer in the world population and the most common among women, being in Brazil, the first cause of cancer death among ladies. The estimate for Minas Gerais for the 2018 and 2019 indicates the occurrence of 5,360 new cases of breast cancer in women. The main method to breast cancer screening is the mammography. At the nacional, state and macroregional levels, the number of mammographs, existing and in use, is larger than what is recommended by the legislation Brazilian. However, generally, these equipments are poorly distributed, with the majority concentrated in the metropolitan regions and with a higher socioeconomic standard, in the lag of peripheral and lower income regions. The quantity and qualification of health professionals, and the mechanisms such as financial resources, maintenance and calibration of mammographs also affect the population's access to mammography.

Keywords

Mammograph • Geographical distribution • Breast cancer

1 Introduction

The occurrence of the cancer is of multifactorial origin and may originate in the combination of several factors: genetic, environmental and lifestyle [1]. According to research conducted by the International Agency for Research on Cancer (IARC) of the World Health Organization (WHO), this disease is one of the major public health problems, especially among developing countries, where it is expected that the impact of cancer on their populations will account for 80% of the more than 20 million new cases estimated by 2025 [2].

Breast cancer represents the second most common type of cancer in the general world population and the most common among women [3]. In Brazil, the disease is the leading cause of cancer death among ladies [4].

The primary method of screening for breast cancer is the mammography. The mammography consists of the radiography of breast and allows the early diagnosis of the disease, when detecting lesions in their initial phase, of the order of millimeters [5]. Ordinance No. 1101/GM of 2002 determine that in Brazil, one mammograph must be available for use, for every 240 thousand inhabitants [6].

Regarding mammography exams, inequalities related to age groups, income brackets and access to medical appointments and equipments, persist in the Brazilian states. These inequalities in access, in general, are reflected in the existence of women who have never performed this type of examination [7].

The estimate of Brazil, for the years 2018 and 2019, indicates the occurrence of about 600 thousand new cases of cancer, for each year. Except for non-melanoma skin cancer (about 180,000 new events), these will be about 420,000 new cancer events. In women, breast cancer accounts for 29.5% of the new cases, corresponding to 59,700 occurrences, with an estimates risk of 56.33 events per 100,000 women. The estimate for the same period in Minas Gerais is 5,360 new cases of breast cancer in women, being the third state with the highest number of predicted diagnoses of this type of neoplasia in the country [8].

In order to obtain standardized, updated, good quality and representative information in a research that analyzes the distribution of mammographs in Minas Gerais state, it is fundamental to consider their regional differences, be they in geographic, cultural, social and economic aspects [9].

The actions of the Minas Gerais government are guided by the Minas Gerais Integrated Development Plan (PDMI). The strategic map of the State Department of Health of the

S. M. R. de Miranda (✉) · A. C. Patrocinio · H. H. da Silveira Urzêdo
Federal University of Uberlândia, Uberlândia, MG, Brazil
e-mail: sarahmansurrm@hotmail.com

state, developed in agreement with the PDMI, opts for the social construction of health care networks, requiring articulation of the different points of health care in health territories, so that care is provided with efficiency, effectiveness and quality. To achieve this goal, a Regionalization Master Plan of Minas Gerais State (PDR-MG) was created, based on the population and population flows of the demand for health services [10].

The state of Minas Gerais is composed for 853 municipalities, which were grouped into 77 micros and 13 macroregions of health, according to the PDR-MG (last updated in March 2011) and Deliberation CIB-SUS/ MG no. 1,979 of November 2014 [10].

The PDR-MG created the territorial basis for an optimal distribution of health equipments. According to this document, primary health care should be present in all municipalities and close to the households, while the health units with the highest technological density, as well as support systems, should be relatively concentrated: the secondary units (medium complexity) in the microregions and the tertiary units (high complexity) in the macroregions, in order to constitute health care networks that are efficient and of high quality [10].

A macroregion of health is defined as the territorial base of health care planning in the state of Minas Gerais, which encompasses regions and microregions of health due to the possibility of offering and access to health services of greater complexity, presenting a high technological level complexity and macroregional scope [11].

As tool, the PDR-MG was institutionalized by the Operational Standard for Health Care (NOAS 01/02) and has been used to guide the organization of health care networks, to provide the basis for calculating resources and monitoring health indicators, equity and wholeness. Therefore, the PDR-MG can be considered a health planning tool that establishes a territorial and population base for calculating needs, priority for resources allocation, programmatic and managerial decentralization [10].

Thus, the main objective of this work is to analyze the territorial distribution of the mammographs into the 13 Minas Gerais macroregions of health.

2 Methods

In this work, was analyzed the quantities of mammographs, existing and in use, considering simple-command, stereotaxic and computerized equipments, by macroregion of health and throughout the state of Minas Gerais, in April 2017. This information was collected, separately and manually, for each of the 853 municipalities of Minas Gerais, from the database of the National Registry of Health Establishments (CNES), available on the website of the Department of Informatics of the Unified Health System (DATASUS), which provides information on the equipments belonging to the Unified Health System (SUS), and those owned by the private health care system [12].

In addition, estimates of the number of inhabitants of each of the 853 municipalities in the state of Minas Gerais were collected, separately and manually, on the website of the Brazilian Institute of Geography and Statistics (IBGE) to estimate the population of the Minas Gerais macroregions of health.

Then, the information from the 853 municipalities, was manually grouped into 77 microregions, and later, in 13 macroregions of health, so that the calculations could be made.

Based on ordinance No. 1101/GM of 2002, the number of mammographs needed and the percentage of surplus equipments that are in full operation were calculated for Minas Gerais and its macroregions of health, through Eqs. 1 and 2, respectively.

$$Mammographs\,Needed = \frac{POPULATION}{240,000} \qquad (1)$$

$$Surplus\,Mammographs\,(\%) = \left(\frac{MAMMOGRAPHS\,IN\,USE}{MAMMOGRAPHS\,NEEDED} \right) - 1 \qquad (2)$$

The percentage of surplus equipments represents the percentage of equipments that is in use more than the number of mammographs that is determined by the legislation.

Subsequently, the distribution of inhabitants by equipment in use, which corresponds to the division of the total number of inhabitants of each macrorregion by the number of mammographs in operation in that locality, was calculated through Eq. 3:

$$Distribution\,of\,inhabitants\,by\,mammograph\,in\,use = \frac{POPULATION}{MAMMOGRAPHS\,IN\,USE} \qquad (3)$$

3 Results

Information collected on CNES and IBGE database, reference to the state of Minas Gerais and its macroregions of health is presented in Table 1, which contains the following data: population; number of inhabitants for each mammograph available for use; percentage of surplus mammographs, considering the determination of Brazilian legislation, which are in full operation. In all cases, we considered the mammographs belonging to SUS and the equipments of the private health system.

Table 1 Mammographs data from Minas Gerais and its macroregions of health

Macroregions of health/State	Population	Number of inhabitants by Mammograph in use	Surplus Mammographs (%)
Centro	6,579,816	30,891	660.71
Centro Sul	789,827	32,909	500
Jequitinhonha	298,645	37,331	300
Leste	1,527,436	52,670	314.29
Leste do Sul	702,449	50,175	366.67
Nordeste	932,573	186,515	25
Noroeste	626,457	52,205	300
Norte	1,678,938	54,159	342,86
Oeste	1,276,312	58,014	266.67
Sudeste	1,666,997	32,686	628.57
Sul	2,787,614	42,886	441.67
Triângulo do Norte	1,281,989	34,648	516.67
Triângulo do Sul	768,771	38,439	400
Minas Gerais state	20,917,824	39,393	503.4

Figure 1 presents: quantity of mammographs needed as determined by Brazilian legislation, total number of existing mammographs and quantity of mammographs in use, in Brazil. These data were obtained from another study [13].

Figure 2 presents the same informations as in Fig. 1, but the data refer to the Minas Gerais state.

Figure 3 presents the quantity of mammographs that are distributed by Minas Gerais macroregions of health.

In Fig. 3, the numbers 1–13 presented in the X-axis of the graph, represent, respectively, the 13 Minas Gerais macroregions of health: Centro, Centro-Sul, Jequitinhonha, Leste, Leste do Sul, Nordeste, Noroeste, Norte, Oeste, Sudeste, Sul, Triângulo do Norte e Triângulo do Sul.

Fig. 2 Quantity of mammographs in Minas Gerais state
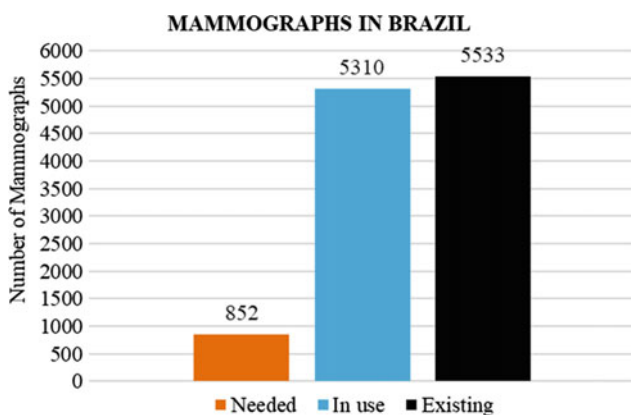
Fig. 1 Quantity of mammographs in Brazil
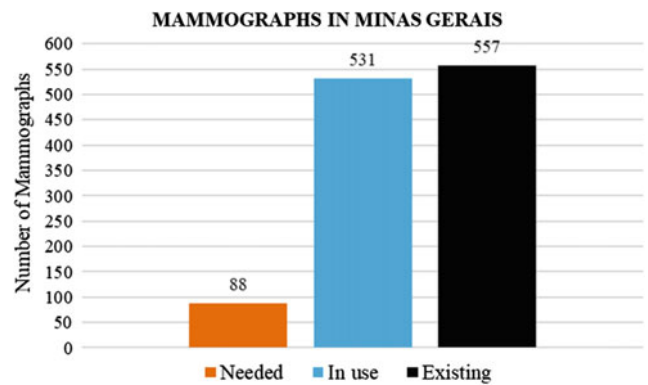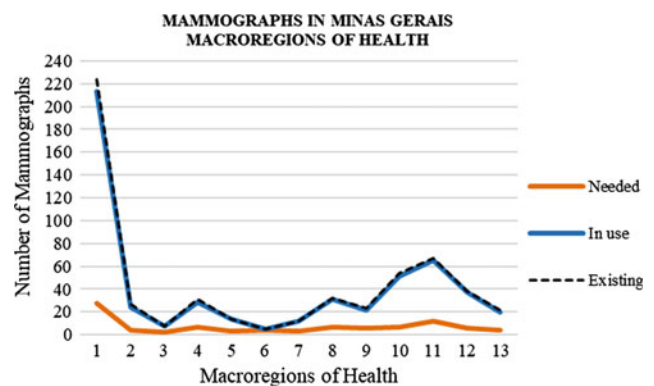
Fig. 3 Quantity of mammographs in Minas Gerais macroregions of health

4 Discussion

Analyzing the informations in Table 1, we can see considerable inequalities between the Minas Gerais macroregions of health, in the three aspects presented. An example that reflects well some of these inequalities is a comparison between the Centro Sul and Nordeste macroregions, where it is observed that even with the Nordeste region having a larger number of inhabitants than the Centro Sul region, their number of surplus mammographs is lower, even when compared to all other macroregions, which consequently generates a larger number of people for each equipment in use.

Brazilian legislation determines that, for every 240 thousand inhabitants, one mammograph must be available for use. According to Table 1, it can be observed that the percentage of surplus mammographs, which is in full operation, in Minas Gerais and in its macroregions of health, is high, and the number of inhabitants for each equipment in use is less than the determined value.

From the analysis of Fig. 1, it is noted that in Brazil the majority of existing mammographs is actually in full operation. In addition, the number of equipments available for use is larger than necessary required by legislation to meet the needs of the population, as well as in Minas Gerais state (Fig. 2) and its macroregions (Fig. 3).

Analyzing the data of Fig. 3, it is possible to observe the inequality in the distribution of mammographs among the 13 Minas Gerais macroregions of health.

Studies have found that access to mammography is generally larger and easier for people with higher incomes, who live in areas of better socioeconomic status and who are covered by private health insurance. Moreover, the geographic distribution of equipments, quantity and qualification of health professionals, and the mechanisms capable of guaranteeing the use of these services, such as financial resources, maintenance and calibration, also influence the population's access to the mammography exams [14, 15].

5 Conclusion

In this study, it was necessary to consider the limitations arising from the quality of data obtained from CNES and IBGE. The CNES, although an official source of the SUS, has limited information due to the fact that the Health Care Facilities (EAS) are responsible for updating the informations, without any type of inspection regarding the veracity of updating these data. The IBGE data also have limitations, because they are estimated information. However, it is worth mentioning that these are free access data and are used in decision-making processes, especially for health planning in Brazil.

At the nacional, state and macroregional levels, the number of mammographs, existing and in use, is larger than what is recommended by the legislation Brazilian. In addition, this research suggest that the number of equipments that are not fully functioning is small. However, despite the existence of a satisfactory number of mammographs, generally these devices are poorly distributed, with the majority concentrated in the metropolitan regions, than in periphery. Thus, it can be said that there are localities that concentrate more mammographs than necessary, while a large part of the population still does not have access to mammography [5].

The next step of this study is to analyze the distribution of mammographs and the population's access to mammography exams in the state of Minas Gerais and its macro and microregions of health, considering the time of displacement of patients and the distance between the poles municipalities, macro and microregional, which offer health services of a higher level of complexity, municipalities that have mammographs available for use (even though they are not designated as poles), and municipalities that do not offer this type of equipment.

References

1. Ministério da Saúde. Situação do Câncer no Brasil. Secretaria de Atenção à Saúde, Instituto Nacional de Câncer, Coordenação de Prevenção e Vigilância, pp. 48. Rio de Janeiro, Brasil (2006)
2. Stewart, B.W., Wild, C.P. (eds.): World Cancer Report: 2014. Lyon, IARC (2014)
3. Parkin, D.M., Bray, F.I., Devesa, S.S.: Cancer burden in the year 2000. The global picture. Eur. J. Cancer **37**, 4–66 (2011)
4. Boing, F., Vargas, L., Crispim-boing, A.: A carga das neoplasias no Brasil: mortalidade e morbidade hospitalar entre 2002–2004. Rev. Assoc. Med. Bras. **53**(4), 317–322 (2007)
5. Amaral, P., et al.: Distribuição Espacial de Equipamentos de Mamografia no Brasil. XVI Seminário sobre a Economia Mineira, p. 11. Diamantina., Brasil (2014)
6. Ministério da Saúde. Portaria nº 1101/GM. Brasil (1996)
7. Villar, V., et al.: Distribution of mammography equipment and mammographies in Rio de Janeiro State, Brazil, 2012 and 2013. Distribuição geográfica e acesso ao mamógrafo no estado da Bahia. Revista do Sistema de Saúde Publica do Brasil: Epidemiologia e Serviços de Saúde, vol. 24, no. 1, pp. 105–114 (2015)
8. da Saúde, Ministério: Estimativa 2018: Incidência de Câncer no Brasil. Brasil, Rio de Janeiro (2017)
9. da Saúde, Ministério: Estimativa 2012: Incidência de Câncer no Brasil. Brasil, Rio de Janeiro (2011)
10. Malachias, I., Leles, F., Pinto, M.: Plano Diretor de Regionalização da Saúde de Minas Gerais. Secretaria de Estado de Saúde de Minas Gerais, Belo Horizonte (2010)
11. Pinto, M., et al.: Plano Diretor de Regionalização da Saúde de Minas Gerais. Secretaria de Estado de Saúde de Minas Gerais, Belo Horizonte (2002)

12. Cadastro Nacional de Estabelecimentos de Saúde. http://cnes2.datasus.gov.br. Accessed 07 Apr 2017

13. Miranda, S., Patrocinio, A.: Distribuição de mamógrafos por macrorregião do Brasil. V Congresso Brasileiro de Eletromiografia e Cinesiologia e X Simpósio de Engenharia Biomédica, pp. 433–436. Uberlândia, Brasil (2017)

14. Coughlin, S., Uhler, R., Blackman, D.: Breast and cervical cancer screening practices among American Indian and Alaska Native women in the United States, 1992–1997. Prev. Med. **29**(4), 287–295 (1999)

15. Oliveira, E., et al.: Condicionantes socioeconômicos e geográficos do acesso à mamografia no Brasil, 2003–2008. Revista Ciência e Saúde Coletiva **16**(9), 3649–3664 (2011)

Health Information Systems Applied
to Maternity Hospitals: A Systematic Review

Gustavo R. da Costa, Adriana M. W. Stadnik, Rita C. G. Berardi,
and Rodrigo G. M. de Souza

Abstract

The computerized medical record systems have been
applied to enable the standardization and obtaining of
data related to the follow-up of pregnant women during
prenatal care, delivery and postpartum, emerging as an
important tool for better maternity data management
services. Thus, this study aims to identify how informa-
tion systems are being used in the workflows of maternity
hospitals. For that, a systematic review was carried out
based on studies from the period of 2012 to 2017, in
which 25 publications related to the use of information
systems in maternity wards or in hospitals were selected,
specifically when it was possible to care for pregnant
women. Recidivism of themes were observed in papers
and classified by thematic axes: costs; paper data
collection; workflows; admission and discharge of
patients; open data; computerized medical record sys-
tems; and semi-structured interviews. In the same way
that it was possible to identify the contributions of the
computerized medical record systems in the improvement
of health services and alignment of workflows between
the multi-professional team.

1 Introduction

Computerized medical record systems (CMRS) are emerg-
ing as important tool for better efficiency of hospital work-
flows, given the proposition of standards for data collection

[1]. Successfully deployed in referral hospitals in different
countries, they present as results the containment of costs
and the reduction of absence of records, communication
failures and loss of information [1–3]. Data provided in
individual or collective information systems (IS) can be
applied to the modeling and deployment of centralized
CMRS [3, 4].

In Australia, researchers have developed CMRS called
the Australasian Maternity Outcomes Surveillance System
(AMOSS), with the aim of correcting problems related to
insufficient records in more than 300 maternities, including
those of high complexity in that country and New Zealand. It
is open data SI, which provides invaluable contribution to
the scientific community and health professionals. It allows
entry and rapid data search and automated control, from
information based on mobility for use in clinical care, such
as access to the different protocols applied to the admissions
of high-risk pregnant women [5].

In this perspective, the existence of information that oper-
ates in a systematized manner has been identified as an
important tool for assessing the scope and quality of obstet-
rical care [4]. Thus, health IS are being applied both for
monitoring and for improving care during the gestational,
delivery and postpartum period [5–7]. The effectiveness of this
practice has been validated by pregnant women, who report a
preference for care in hospitals that practice them [8, 9].

Thus, the IS have been proposed to integrate the pro-
cesses inherent in workflows, contributing to the access to
databases, by health professionals, in the search for the best
intervention [10]. Likewise, CMRS can be used as an
important tool applied to verify if the professional assign-
ments established in the workflows are being fulfilled [11].

In view of the above, the present review aims to identify
how the information systems are being used in the mater-
nities workflows.

G. R. da Costa (✉) · A. M. W. Stadnik · R. C. G. Berardi ·
R. G. M. de Souza
Federal University of Technology, Paraná, Brazil
e-mail: guresend@gmail.com

2 Materials and Methods

It is a systematic review carried out from search engines that access different bibliographic databases, these being "BVS" (Virtual Health Library), Capes Journals, PubMed, ScienceDirect, and searches in the IEEE (Institute of Electrical and Electronics Engineers) digital library and annals of "CBEB" (Brazilian Congress of Biomedical Engineering) and "CBIS" (Brazilian Congress of Health Informatics).

For the initial analysis, the following keywords were crossed: Computerized Medical Record Systems (*Sistemas Computadorizados de Registros Médicos*) AND Workflow (*Fluxos de trabalho*); Information Systems (*Sistemas de Informação*) AND Hospitals, Maternity (*Maternidades*); Information Systems (*Sistemas de Informação*) AND Pregnancy, High-Risk (*Gravidez de Alto Risco*).

Inclusion criteria were the selection of original papers, experience reports, case reports and annals in congresses published between 2012 and 2017, available in full and online, in Portuguese, English or Spanish. The key words were searched in the title, abstract and descriptors, when this search option was available, in the English and Portuguese languages. As for the exclusion criteria, the elimination of redundant publications and of secondary articles was established.

3 Study Results

From the application of the inclusion criteria, 279 publications were found. After exclusion of the duplicate records, 246 publications were selected; of which 7 publications were excluded because they were secondary articles. The abstracts of the 239 selected publications were read, those in which the use of information systems in maternity or hospitals was not identified and were not available in full and online were excluded, totaling 198 exclusions.

After reading in full the 41 publications evaluated for eligibility, 25 publications were selected that had their own relation with the use of information systems in maternities or
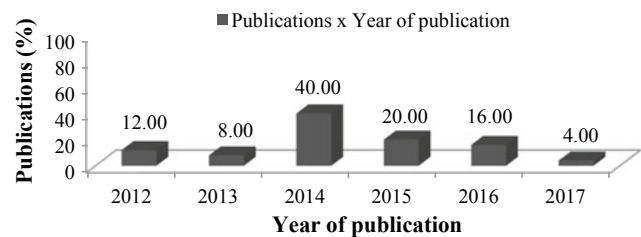
Fig. 1 Publications in periodicals and annals of congress between 2012 and 2017

in hospitals, specifically when there was the possibility of attending to the pregnant women.

Considering the number of publications, it was verified that the highest percentage, 40.00%, occurred in 2014, as represented in Fig. 1. Regarding the language, 19 papers were published in English and six in Portuguese.

Most of the scientific works, 48.00%, is from the American continent. Specifically, South America corresponds to 24.00% of all publications, as described in Table 1.

In Table 2, it is possible to identify the *Qualis* of the publications. It is observed that 40.00% are classified as *Qualis* B1 or higher, by area of greater impact, according to Periodicals *Qualis* evaluation [12]. Referring to the publications held in conferences, 24.00% were classified as *Qualis* B1 or higher, in Conferences *Qualis* evaluation [12].

The variables with the highest number of incidence in the publications are available in Table 3, they being classified by thematic axes: costs; paper data collection; workflows; admission and discharge of patients; open data; computerized medical record systems (CMRS); and semi-structured interviews.

4 Discussion

The computerized medical record systems (CMRS) are present in 92.00% of publications, either through the implantation process or concerning their use. According to

Table 1 Publications by mainland between 2012 and 2017

Mainland	Publication (%)
Africa	16.00
Central America	4.00
North America	20.00
South America	24.00
Asia	16.00
Europe	8.00
Oceania	8.00
Uninformed	4.00

Table 2 Classification of publications carried between 2012 and 2017 considering the *Qualis*

Qualis	Publications (%)	Qualification area	Evaluation
A1	8.00	Biotechnology or Computer Science	Periodicals *Qualis*
A2	16.00	Administration, Engineering IV or Dentistry	
B1	16.00	Nursing or Dentistry	
B2	8.00	Education, Medicine I or III	
Others	4.00	Computer Science	
A1	12.00	Conferences	Conferences *Qualis*
B1	12.00		
Others	24.00		

Table 3 Recurring themes in publications between 2012 and 2017

Themes	Incidence (%)
Costs	40.00
Paper data collection	44.00
Workflows	56.00
Admission and discharge of patients	20.00
Open data	20.00
CMRS	92.00
Semi-structured interviews	24.00

researchers, the CMRS have contributed to align the workflow among the multi-professional team, making possible the standardization and simplification of existing processes [1, 10].

From the analysis of the publications, it was verified that the CMRS have been frequently applied to replace the records made on paper [11, 13, 14]. Noteboom et al. (2014) report that the slightest use of the CMRS lead to interference of patient care and affect productivity of the professional team. Despite these problems, this team expresses that it would not trade the CMRS through the use of paper forms [14].

According to Parka et al. (2012), the CMRS can intervene in the interaction between team and patient. As an example, the researchers cite the case of medical residents who were notified of situations in which CMRS data were not properly filled. In view of this, residents had to dedicate longer period of time to filling out the electronic records, which caused shortage of time for other activities, such as visits to patients and collaboration with the medical staff.

In another context, Jalil et al. (2014) suggest that the CMRS application makes it possible to improve the execution of health services, increasing the capacity of information storage, availability and cooperation among the multi-professional team. In this perspective, researchers observed that CMRS enabled immediate data collection, and could also act strategically and identify legal issues related to the safety of pregnant women [13, 15, 16].

Regarding workflows, 56.00% of the publications presented reports correlating them with the processes related to the use of CMRS or collect paper data. For Fouzi et al. (2012), the workflows can be applied both in the detailing and in the investigation of the activities performed in hospitals. Mundim et al. [17] define workflows as the ways that exist in the execution of the processes, adding that for the adequate functioning of information systems (IS), it is necessary that the workflows are properly documented and well structured.

In this context, Yli-Kauhaluoma and Pantzar (2014) have identified that the use of IS can lead to interruptions in workflows, causing their execution to become unsuccessful. According to the researchers, the IS makes the professionals perform different tasks simultaneously, discontinuing the execution of something to perform another function [18]. However, such bottlenecks may stem from possible inappropriate division of activities.

Besides that, it was identified that 24.00% of the publications had application of semi-structured interviews for the collection of data. It is mentioned, for example, the study accomplished by Militello et al. [19] in eight American hospitals, in which semi-structured interviews were conducted to characterize the professionals' perceptions regarding the use of IS applied to health. Most of the professionals reported that the IS were seen as being of little benefit to the patients; which provided statistical and

informational reports, generally used for the punishment of medical staff.

In another context, in hospitals in Malaysia, information related to prenatal follow-up is recorded in a 44-page book, which stays in the possession and responsibility of the pregnant woman [20]. If the patient does not present it during the medical consultation, the hospitals will not have access to another type of clinical record. For this reason, the E-Maternity, first dynamic IS of that country's open data, is being implemented [20].

Developed as alternative to improve maternities ward management services of data, the E-Maternity allows the monitoring of prenatal to postpartum. It enables the user to record the development of gestation, notifying her about consultations and medications, as well as transmitting information about her gestational state to doctors [20].

Issues regarding paper data records were observed in 44.00% of publications. Likewise, the concern with costs was reported in 40.00% of scientific works. Regarding costs, it is important to highlight that these will be directly proportional to the volume of data administered [21]. Thus, for the modeling of IS applied to health, it is suggested to observe a minimum set of requirements necessary for its proper functioning [21].

The workflows related to admission and medical discharges are present in 20.00% of the publications. In summary, the IS have been used also to record the gestational period from admission and interventions to discharge of the patient [22, 23]. On the other hand, in a university hospital located in the southeastern region of Brazil, IS called SISMater-Gis was implanted to record birth data [24].

As application, this system has worked in the control of cesarean sections and maternal and neonatal information, helping to diagnose certain morbidities, such as *zica* virus, in addition to generating electronic clinical data on births, generating them in a standardized way with the data in health [24]. Similar challenges are observed in 20.00% of the publications, which reported on the implementation of IS of open data in health.

On the other hand, it has been observed that, in countries with high HIV prevalence IS have been applied in an attempt to reduce the maternal mortality rate [25]. It is the example of Southern Africa, whose use of IS has been shown to contribute to the promotion of interconnected and multifactorial network, which enabled the management of data for the provision of services in health [25].

In another context, the IS have allowed collaboration between different users during the execution of given task, simultaneously. Citing an analogous case, in Algeria the IS entitled CPlan made it possible for users to be notified whenever certain action was registered [16].

In addition, researchers from Romania implemented IS called OGD IS. This system allowed access, by means of computers and mobile, to the medical team, assisting it in the resolution of patients' complaints based on data from previously registered information. Thus, OGD IS stores data about new pregnant women in the cloud, comparing them with the records of 410 pregnant women who had their babies prematurely [26].

5 Conclusion

This paper found that information systems (IS) have been important for the standardization of health data, have improved workflows efficiency and have enabled the integration of records with the development of healthcare practices.

Also, changes regarding the substitution of records made on paper by computerized medical record systems were observed. Considering the positive aspects, the IS made it possible to improve the communication between the user team, access to the data immediately and the intervention, with the patient being the main focus. The negative aspects are related to the high time, used for the accomplishment of the registries, culminating in less time for assistance to the patient.

Despite the difficulties in the processes of change, health professionals were interested in the insertion of IS in their work processes. Next, we suggest new studies on the subject, which show the contribution of IS to workflows aimed at the care of high-risk pregnant women.

References

1. Gassert, G., et al.: Interventional radiology workflow management in the electronic medical record. J. Digit. Imaging **27**, 314–320 (2014)
2. Poba-Nzaou, P., et al.: Governance of open source electronic health record projects: a successful case of a hybrid model. In: 47th Hawaii International Conference on System Sciences (HICSS-IEEE) (2014)
3. Marcelin, A., et al.: Developing an electronic medical record for interlinked care services in Haiti. Stud. Health Technol. Inform. **216**(883) (2015)
4. Gaspar, J., et al.: Sistema de informação em saúde para o monitoramento da qualidade da assistência obstétrica e neonatal: SISMater. In: 8th Iberian Conference on Information Systems and Technologies (CISTI-IEEE) (2013)
5. Halliday, L., et al.: The Australasian maternity outcomes surveillance system: an evaluation of stakeholder engagement, usefulness, simplicity, acceptability, data quality and stability. Aust. N. Z. J. Obstet. Gynaecol. **53**(2), 152–157 (2013)
6. Feitosa, A., Ávila, A.: Uso do prontuário eletrônico na assistência pré-natal às portadoras de diabetes na gestação. Revista Brasileira de Ginecologia e Obstetrícia **38**(1), 9–19 (2016)
7. Lam, J., et al.: Ontology driven knowledge base for high risk pregnancy management. In: 4th Instrumentation, Communications,

Information Technology, and Biomedical Engineering (ICICI-BME-IEEE), pp. 2–3 (2015)

8. Gaspar, J., et al.: Improving health care access using geographic information systems. In: IEEE 27th International Symposium on Computer-Based Medical Systems (2014)

9. Willcox, J., et al.: Views of women and health professionals on mHealth lifestyle interventions in pregnancy: a qualitative investigation. JMIR mHealth uHealth **3**(4), e99 (2015)

10. Reiner, B.: Strategies for medical data extraction and presentation. Part 2: Creating a customizable context and user-specific patient reference database. J. Digit. Imaging **28**, 249–255 (2015)

11. Parka, S., et al.: The effects of EMR deployment on doctors' work practices: a qualitative study in the emergency department of a teaching hospital. Int. J. Med. Inform. **81**, 204–217 (2012)

12. CAPES: Coordenação de Aperfeiçoamento de Pessoal de Nível Superior. http://www.capes.gov.br. Accessed 19 Feb 2018

13. Jalil, N., et al.: Design and implementation of a Telehealth platform for pre-natal management in rural and remote areas. In: IEEE Conference on Biomedical Engineering and Sciences (2014)

14. Noteboom, C., et al.: Meaningful use of electronic health records for physician collaboration: a patient centered health care perspective. In: 47th Hawaii International Conference on System Science (2014)

15. Inokuchi, R., et al.: Motivations and barriers to implementing electronic health records and ED information systems in Japan. Am. J. Emerg. Med. **32**, 725–730 (2014)

16. Fouzi, L., et al.: A web application for supporting health care tasks with a groupware planning approach. In: International Conference on Information Technology and e-Services (ICITeS-IEEE) (2012)

17. Mundim, M., et al.: Prontuário eletrônico do paciente: mapeamento dos fluxos de trabalho. XV Congresso Brasileiro de Informática em Saúde (CBIS) (2016)

18. Yli-Kauhaluoma, S., Pantzar, M.: Technology-related interruptions and paper-based documents in back-office knowledge work. In: 47th Hawaii International Conference on System Sciences (HICSS-IEEE) (2014)

19. Militello, L., et al.: Sources of variation in primary care clinical workflow: implications for the design of cognitive support. Health Inform. J. **20**(1), 35–49 (2014)

20. San, O., Husain, W.: Maternity data management utilizing cloud computing. In: International Conference on Computer and Information Sciences (2014)

21. Laing, G., et al.: Development, implementation, and evaluation of a hybrid electronic medical record system specifically designed for a developing world surgical service. World J. Surg. **38**, 1388–1397 (2014)

22. Phiri, S., et al.: Rural-urban inequity in unmet obstetric needs and functionality of emergency obstetric care services in a Zambian District. PLoS ONE (2016)

23. Reis, Z., et al.: Análise do conteúdo do sumário de alta obstétrica em maternidade de referência. Revista Médica de Minas Gerais **25**(4), 476–483 (2015)

24. Cazorla, L., et al.: Avaliação do impacto da informatização dos registros sobre o parto na produção do conhecimento científico, em um hospital universitário. XV Congresso Brasileiro de Informática em Saúde (CBIS) (2016)

25. Madzimbamuto, F., et al.: Integration of HIV care into maternal health services: a crucial change required in improving quality of obstetric care in countries with high HIV prevalence. BMC Int. Health Hum. Rights **13**(27) (2013)

26. Crişan-Vida, M., et al.: ICT supporting treatment for high risk situations in obstetrics. In: The 6th IEEE International Conference on E-Health and Bioengineering-EHB (2017)

Incorporation of a DIRECT ACTING ANTIVIRAL Treatment for HEPATITIS C in the Brazilian Public Health System

Mayra Braga Lemos, Milene Rangel da Costa, and Rosimary Terezinha de Almeida

Abstract

Hepatitis C (HC) is a public health problem that affects 2% of the world population. Its chronification leads to chronic liver disease, cancer and advanced cirrhosis. In Brazil, HC prevalence ranges from 1% to 2% and free treatment is granted by the Unified National Health System (SUS). The direct acting antivirals (DAA) sofosbuvir, daclatasvir and simeprevir, recently made available in SUS, are considered a new promise towards HC virus (HCV) eradication. However, despite the greater DAA efficacy compared to previous drugs, their higher cost demands a continuous utilization assessment. The objective of this study was to characterize the utilization profile of DAA for HC treatment by SUS. Data from the Ambulatory Care Information System (SIA-SUS) were used. Between September 2015 and December 2016, 69,551 DAA dispensations occurred in SUS (45.2% for daclatasvir, 35.2% for sofosbuvir and 19.6% for simeprevir). There were differences in DAA utilization among the regions. Initially, sofosbuvir was the most frequently used DAA in the North (51.0%), Northeast (47.1%) and South (64%) regions, whilst daclatasvir was most used in the Center-West (55.9%) and Southeast (58.9%) regions. In 2016 the number of dispensations for sofosbuvir and daclatasvir became similar in Center-West region. Simeprevir was the least frequently used drug in all regions in both years. These differences in the DAA utilization could be justified by epidemiologic or clinical practice variations. Further studies are necessary to elucidate the factors implicated in those differences and their consequences in the quality of health assistance and resource allocation.

1 Introduction

Hepatitis C (HC) is a liver disease caused by HC virus (HCV). Its clinical manifestations vary from mild to severe, possibly resulting in chronic liver disease [1]. HC chronification is considered a public health problem and occurs in 80% of reported cases [2, 3]. From 20 to 25% of chronic patients may develop hepatic cirrhosis after 20–25 years from the onset of the disease, of which 1–4% can develop hepatocellular carcinoma [3].

In Brazil, the prevalence of HCV is 1–2% and there are approximately 657,000 people chronically infected with HCV [3, 4]. Between 1999 and 2016, 155,032 cases of HC were detected in Brazil, of which 64.1% were observed in the Southeast, 24.5% in the South, 5.5% in the Northeast, 3.3% in the Center-West and 2.5% in the North regions. Detection rates per 100,000 inhabitants were 12.0 cases in the South, 9.6 in the Southeast, 3.9 in the Center-West, 1.6 in the Northeast and 1.0 in the North regions [5].

According to the 2015 Brazilian national clinical guideline on HC treatment [6], which was the one in force during the analysis of the current study, chronic HC (HCC) can be treated through Response-Guided Therapy (RGT) or according to the HCV genotype. The treatment aims to eradicate HCV, increase life expectation and quality, reduce hepatic complications and virus transmissibility and prevent infection progression to cirrhosis, hepatocellular carcinoma and death [6].

In June 2015, the direct acting antivirals (DAA)—sofosbuvir, daclatasvir and simeprevir—were incorporated into the Unified National Health System (SUS) for the HCC

M. B. Lemos (✉) · M. R. da Costa · R. T. de Almeida
Universidade Federal do Rio de Janeiro, Rio de Janeiro, RJ, Brazil
e-mail: mayralemos@peb.ufrj.br

treatment, mainly for patients with advanced hepatic fibrosis. Treatment was also indicated in cases of HIV coinfection, regardless of fibrosis degree; hepatic cirrhosis and chronic or hepatic renal failure in the absence of hepatocellular carcinoma [7]. The advantages of these new drugs compared to interferon-based therapy include higher efficacy, more comfortable posology, shorter period of treatment and lower incidence of adverse events. Additionally, patients treated with the new DAA will require a lower number of molecular biology tests during therapy and the management of patients will occur similarly whether HIV coinfected or not [7].

The DAA sofosbuvir, daclatasvir and simeprevir are purchased by the Brazilian Ministry of Health and distributed to all country regions where local governments manage their dispensation to HCC patients. To have access to these drugs, patients must attend all the requirements established in the national clinical guideline. If so, they are granted a special authorization to receive the drugs monthly [8]. Despite the greater efficacy of DAA compared to previous drugs, their higher cost demands a continuous assessment of their utilization. Therefore, the present study aimed to evaluate the utilization profile of sofosbuvir, daclatasvir and simeprevir to treat HCC patients in SUS and to discuss it in light of the recommendations of the national clinical guideline for HC treatment.

2 Methods

An observational, retrospective, and descriptive study on the utilization of DAA sofosbuvir, daclatasvir and simeprevir for the treatment of HCC patients in Brazil was conducted from January 2015 to December 2016.

Data were obtained from the SUS Ambulatory Care Information System (SIA-SUS) which comprises, among others, all records about DAA dispensations. This database was available by the Ministry of Health Informatics Department [13]. Data were available as compressed files for each month and patient identity was encrypted to protect their privacy [9, 10].

The monthly data files of all Brazilian regions, in the study period, were downloaded and expanded using the software TABWIN 4.14. These files were united in order to obtain a single database comprising all dispensation records. Subsequently, only the records referring to DAA dispensation for HC patients from January 2015 to December 2016 were selected.

An exploratory data analysis was performed aiming to verify the diffusion patterns of DAA utilization for each Brazilian region using SPSS Software version 22.

3 Results

From September 2015 to December 2016, 69,551 DAA dispensations were recorded, of which 31,426 (45.2%) for daclatasvir, 24,465 (35.2%) for sofosbuvir and 13,660 (19.6%) for simeprevir. In the Northeast and South regions, the first dispensation record occurred in September 2015 whereas in the North and Center-West regions it occurred in October 2015 and in the Southeast region in November 2015.

The relative frequency distribution of dispensation according to the type of drug varied among the Brazilian regions (Fig. 1 a–e). In 2015, the proportion of daclatasvir dispensation records was the highest in the Center-West and Southeast regions (55.9 and 58.9%, respectively) whereas sofosbuvir was the most frequent drug in the other regions (46.9% in the Northeast region; 51.0% in the North region; 63.8% in the South region). In the South region, the relative frequency of daclatasvir dispensation was extremely low, approximately 0.2%. This region also presented the highest relative frequency for simeprevir dispensation.

In 2016, the Center-West, Northeast and South regions presented similar profiles. The relative frequencies of sofosbuvir and daclatasvir dispensation in these regions were very similar (39.8 and 40.4% in the Center-West, 42.7 and 41.0% in the Northeast, and 41.9 and 41.6% in the South, respectively). In the Southeast, the proportion of daclatasvir dispensation decreased in comparison to 2015 but it remained the highest one.

4 Discussion

This study aimed to evaluate the utilization profile of sofosbuvir, daclatasvir and simeprevir on HCC patient's treatment in SUS. The incorporation of these drugs occurred in June 2015 [7] and their distribution began in September 2015.

The utilization profiles of DAA showed different patterns among the Brazilian regions. These differences were more pronounced in 2015, as expected, considering that these were the first months of the incorporation process of these drugs. It is known that the initial phase of the incorporation is subject to several obstacles, such as changes in activity flow and infrastructure, adherence to the clinical protocol and staff learning curve.

As shown in Fig. 1, in 2016, the DAA utilization profiles changed compared to 2015. It is possible to note that the variations in terms of the DAA utilization decreased, especially among the Center-West, Northeast and South regions. In these regions, the relative frequency of sofosbuvir and
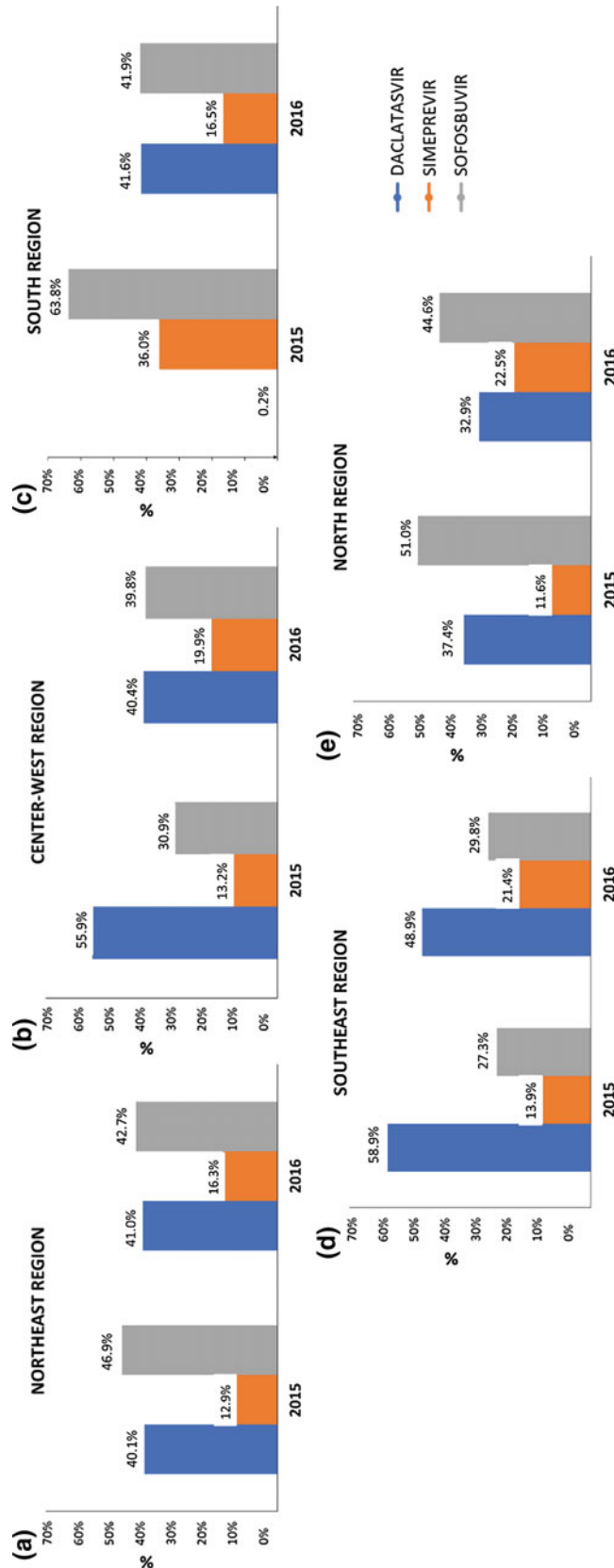
Fig. 1 Relative frequency distribution of DAA dispensation for patients with chronic hepatitis C in Brazil in 2015 and 2016 according to type of drug and region. *Source* SIA/SUS

daclatasvir dispensation became very similar. However, this was not the case for the North and Southeast regions where significant variations were still present.

At first, such variations in DAA utilization profiles could be explained by epidemiological differences between the regions. According to HC national clinical guideline [6], the therapeutic rationale depends on the patient genotype, if they are co-infected with HIV or not and previous treatments. Therefore, it would be reasonable to suppose that if there were epidemiological and clinical differences among the regions, the DAA utilization profiles should also vary. Although recent studies have shown that genotype 1 is the most prevalent in all regions followed by genotype 3 [11], there is still lack of data about the HCV-HIV co-infection prevalence across the Brazilian regions.

Nevertheless, if the DAA utilization profiles are analyzed considering the different therapeutic regimens stated in the HC national clinical guideline, some questions arise. According to the last, the use of a DAA is always in combination with a second DAA or other drugs such as ribavirin or pegylated interferon. Actually, sofosbuvir is present in all therapeutic regimens (except those intended for some patients with genotype 4) and the possible combinations of DAA regimes are: sofosbuvir+daclatasvir, sofosbuvir+simeprevir or sofosbuvir+ribavirin and/or interferon [6]. Hence, considering the predominance of genotypes 1 and 3 in all Brazilian regions, it would be expected that sofosbuvir dispensations were the most frequent in all scenarios. Additionally, it is reasonable to suppose that the relative frequency of sofosbuvir dispensations should at least equals to the sum of the relative frequencies for daclatasvir and simeprevir.

However, the relative frequency distributions observed in this study are not in agreement with the assumptions above. It is worth noting that there is evidence of data inconsistency in some of the Brazilian public health information systems such as the Mortality Information System (SIM) and the Information System of Notifiable Diseases (SINAN-AT) [12]. Perhaps such inconsistencies could also occur in SIA-SUS which could explain, at least in part, the variations observed among the regions. Moreover, the lack of trained professionals and of critical data input mechanisms could also contribute for faulty drug dispensation data recording. These issues combined could compromise the quality of the data and could be considered a limitation for the use of the SIA-SUS data file to monitor the utilization of the DAA in the treatment of HCC patients.

5 Conclusion

This study showed that there was variation in the drug utilization profile of DAA sofosbuvir, daclatasvir and simeprevir for the treatment of HCC patients in SUS. Further studies are necessary to verify whether the observed differences could be explained by regional variation in epidemiological and clinical profiles or if they are a result of inconsistency of the data on dispensation of these drugs in SUS.

References

1. Kretzer, I.F., Livramento, A., Cunha, J., Gonçalves, S., Tosin, I., Spada, C., et al.: Hepatitis C worldwide and in Brazil: silent epidemic - data on disease including incidence, transmission, prevention, and treatment. Sci. World J2014(827849), 1–10 (2014)
2. Tafarel, J.R.: Tratamento Da Hepatite C Crônica. Rev. Médica UFPR 2(4), 189–195 (2015)
3. Morais, A., Magno, L.A., Gomide, G.P.M.: Impact of hepatitis C on resource use and costs of patients with liver cirrhosis in the Brazilian public healthcare system (SUS). J. Bras. Econ. Saúde 7(2), 116–121 (2015)
4. Hanus, J.S., Ceretta, L.B., Simões, P.W., Tuon, L.: Incidence of hepatitis C in Brazil. Rev. Soc. Bras. Med. Trop. 48(6), 665–673 (2015)
5. Ministério da Saúde, Secretaria de Vigilância em Saúde, Hepatites virais, Boletim Epidemiológico. Ministério da Saúde, Brasília (2017)
6. Ministério da Saúde, Secretaria de Vigilância em Saúde, Protocolo Clínico e Diretriz Terapêutica para Hepatite C e Coinfecções. Ministério da Saúde, Brasília (2015)
7. Ministério da Saúde, Secretaria de Ciência Tecnologia e Insumos Estratégicos, Comissão Nacional de Incorporação de Tecnologias no SUS (CONITEC). Relatório de recomendação: Simeprevir, sofosbuvir e daclatasvir no tratamento da hepatite crônica tipo C e coinfecções, Ministério da Saúde, Brasília (2015)
8. Ministério da Saúde, Conselho Nacional de Secretários de Saúde (CONASS), Para entender a gestão do Programa de Medicamentos de dispensação em caráter excepcional. CONASS Documenta, Brasília (2004)
9. Imprensa Nacional, Resolução n° 510, de 07 de abril de 2016. Diário Oficial da União, Brasília (2016)
10. Imprensa Nacional, Resolução n°466, de 12 de dezembro de 2012. Diário Oficial da União, Brasília (2012)
11. Nutini, M.F.R., Hunter, J., Giron, L., Pires, A.F.N., Kohiyama, I.M., Camargo, M., et al.: HCV genotype profile in Brazil: a survey truly representative of an entire country. In: 9th IAS Conference on HIV Science, p. 4658 (2017)
12. Galdino, A., Sousa, V., Ii, S., Iii, S.F.: Quality of the record of data on fatal workplace injuries in Brazil. Rev. Saúde Pública 51, 1–9 (2017)
13. Ministry of Health Informatics Department Homepage. http://www2.datasus.gov.br/DATASUS/index.php?area=0901&item=1&acao=22. Last accessed 5 April 2018

Infusion Pump Training: from Course to Evaluation

Alice de Suassuna, Emanuel Vieira Mendes,
Cayo Eduardo Leal de Menezes, and Beatriz Stransky

Abstract

The Infusion Pump (IP) is a Medical-Hospital Equipment (MHE) that is used to regulate the passage of liquids that will be infused into the patient due to the positive pressure generated by the pump. There are three main types of failure causes that can occur in MHE: human error, technology failure, and external phenomena. At the Maternidade Escola Januário Cicco (MEJC), located at Natal, RN, most of the maintenance events in the IPs came from de lack of information from the professionals who handled the equipment, as well as from human error. The present study describes the training in IPs to the medical staff (nurses, nursing technician, and physician), elaborated and performed during the curriculum internship of one of the authors and aims to compare the number of maintenance calls in IPs before and after training to assess the impact of training. For this, the occurrence numbers were obtained before and after training, and a comparison was made between the results. There was a drop of more than 70% in the number of internal maintenance services, showing that the training is very important within the hospital environment.

A. de Suassuna (✉)
Edmond and Lily Safra International Institute of Neuroscience (ELS-IIN), Santos Dumont Institute RN, Macaíba-RN, 59280-000, Brazil
e-mail: alice.suassuna@hotmail.com

C. E. L. de Menezes
Maternidade Escola Januário Cicco (MEJC), Natal RN, 59012-300, Brazil

A. de Suassuna · E. V. Mendes · B. Stransky
Federal University of Rio Grande Do Norte (UFRN), Natal RN, 59084-100, Brazil

1 Introduction

Infusion Pump (IP) is a type of Medical-Hospital Equipment (MHEs) that is used to deliver fluids into a patient's body in a controlled manner. Infusion pumps can deliver fluids in large or small amounts and are used to deliver nutrients or medications – such as insulin or other hormones, antibiotics, chemotherapy drugs, and pain relievers [1]. It is present in many sectors of the hospital, such as Intensive Care Units (ICUs), oncology, and emergency, among others [2].

In the 1970 and 1980s, infusion pumps started to be used in the United Kingdom and were basic, mechanical devices with limited functions. Today, infusion pumps have a plethora of functions and features and a range of alarms to help alert the user and the patient that infusions are nearing completion, have ended, or their range of sensors has detected that the infusion pump, or patient, requires attention [3].

Three main types of failure causes occur in MHE: human error, technology failure, and external phenomena [4]. A study carried out at the Local Clinical Engineering Center of Carmela Dutra Maternity Hospital (Florianópolis, SC, Brazil) between 2001 and 2002 showed that 48.41% of the problems in corrective maintenance orders in infusion pumps are related to misuse of equipment [5]. Among other works that show that most cause of failures in MHE occurs due to human error [4, 6, 7]. Thus, to prevent any harm that comes from misuse, it is necessary to carry out training to the staffs that operate the MHE.

Operational errors of the infusion pumps and procedure failures may cause the equipment to malfunction, causing the non-fulfillment of the requested doctor's prescription. Moreover, such failures can cause the equipment to be removed to the maintenance sector unnecessarily [5].

At the Maternidade Escola Januário Cicco (MEJC), Natal/RN, the infusion pumps are plenty used, mainly in the Neonatal ICU, Maternal ICU, Kangaroo Ward, and Surgical Center. During a curriculum internship at the MEJC, it was

observed that most of the maintenance orders in IPs came from lack of information from professionals, mainly related to the drip sensor, as well as human error, for example, falls and failures when programming the equipment.

Thinking about that, this study aims to assess the impact of training within the hospital environment by comparing the number of maintenance calls in IPs before and after training. The training was provided to the medical staff operating the IPs (nurses, nursing technicians, physicians) at the Maternidade Escola Januário Cicco. Since most failures are due to the lack of information from the professionals who handle them we hope that a practical course will help to reduce the number of occurrences related to the infusion pumps.

2 Methodology

2.1 Data Collection Before Training

The data related to the corrective maintenance orders of the infusion pumps (Infusomat Compact, B|Braun) were obtained from the Clinical Engineering sector of the Maternidade Escola Januário Cicco. The control of the maintenance orders was done in an online spreadsheet where it is informed: (i) the equipment, (ii) the requesting sector, (iii) the defect, (iv) if the service was performed, (v) the procedure performed. The calls for maintenance were reported by the heads nurses of each sector, by means of phone calls or through daily visits performed in each sector. Data of occurrences of failures in infusion pumps were collected from February to March 2017. The data also included the information: defect presented and whether this defect was true or was just a "false call", i.e., the equipment works normally after the tests, showing that there is no real defect in the equipment.

2.2 Training Implementation

After the data collection, the "Infusion Pump Training" course was elaborated. The course was based on the manual's equipment and some videos, and it was presented orally and in person for all health staff (nurses, nursing technicians, physicians), from the following sectors: Kangaroo Ward, Neonatal ICU, Maternal ICU, and Surgical Center. These sectors are the ones that most use this type of equipment. The course was offered to each sector in the morning, together with professionals from other shifts, except for kangaroo ward, because it is a sector with no history of training of the infusion pumps, needed of greater attention, having received training in the morning and the afternoon.

Table 1 Sectors that received the course and topics covered in each sector

Sector	Historic of training	Subjects addressed in training
Kangaroo Ward	It has never received previously infusion pump training	• Cleaning • Intravenous administration set installation • Drip sensor installation • Functions of infusion pump programming • Troubleshooting related to the drip sensor alarm • How to disable the drip sensor • Clarification of doubts on the part of the professionals
Maternal ICU	It has received previously infusion pump training	• Troubleshooting related to the drip sensor alarm • How to disable the drip sensor • Clarification of doubts on the part of the professionals
Neonatal ICU	It has received previously infusion pump training	• Troubleshooting related to the drip sensor alarm • How to disable the drip sensor • Clarification of doubts on the part of the professionals
Surgical Center	It has received previously infusion pump training	• Functions of infusion pump programming • Troubleshooting related to the drip sensor • How to disable the drip sensor. • Clarification of doubts on the part of the professionals

For each sector, the focus of the course was given according to the specific demands and the training's history because there was a sector that had never received training in IPs. Table 1 shows the course and topics addressed to each sector.

The number of trainings varied from sector to sector, due to the demand and the difficulty to assemble the professionals in the sectors. In the kangaroo ward, four trainings were performed on different days, two in the morning and two in the afternoon, in order to contemplate a larger and more diversified number of professionals, being nurses, nursing technicians and physicians, with a total of 14 participants in all training. In the other sectors (Surgical Center,

Maternal and Neonatal ICU), only one training was performed in the morning for each sector. In the surgical center 5 professionals participated, in the Neonatal ICU 12 professionals and in the Maternal ICU 5 professionals participated, including nurses, nursing technicians and physicians. However, only 3 physicians have been present in all the trainings, highlighting the presence of nurses and nursing technicians. All training had an average duration of 30 min, varying according to participants' doubts.

2.3 Data Collection After Training and Course Evaluation

To evaluate the course effectiveness, the data referring to maintenance orders of infusion pumps after training were collected, from April to June 2017. This period (two months) were practically the same as the one used to collect data before training. A survey was also carried out for the participants, with the purpose of evaluating the course and inquire about other equipment courses that they would be interested in receiving training.

3 Results

3.1 Data Collection

The maintenance orders of IPs were recorded from February to March 2017. The maintenance orders are shown in Table 2, addressing the defects reported by the sector that requested the maintenance, the number of occurrences and whether the maintenance call was true or false.

Table 2 Occurrence and failures identification in IPs from February to March 2017 (before training)

Type of problem	Number of occurrences	Failure classification
Obstructed sensor	16	False
Broken cover	04	True
With defect/not work	03	False
Problem in the power supply	02	True
Keyboard with defect	02	True
Problem in the battery	02	True
It does not program the full volume	01	False
Alarming no drops	01	False
It does not turn on	01	False
Alarm "minimal drops"	01	False
Problem in the alarm	01	True
Structure of the infusion pump broken	01	True

In total, there were 35 occurrences in IPs in the period, of which 23 are "false calls" and 12 are true ones. Among the problems reported, the most frequent was related to the drip detect sensor (45% of the time), identified as "Obstructed Sensor". This type of fault is an alarm shown on the display that lights up when the detect drip sensor is not properly connected to the infusion pump. Thus, we can infer that this 'failure' comes from the lack of information or attention from the ones that handle the equipment, so it is considered a false call.

The Fig. 1 shows a case of this false call, but when proceeding the test, it was verified that the equipment was functioning normally.

3.2 Training and Evaluation

As reported in Table 1, each sector received the training and the main points addressed were the same as those described in it. After the training was implemented in these sectors of the hospital, the professionals who received the course answered a questionnaire to carry out a course evaluation. Considering that only the professionals in the kangaroo ward received the complete course, the questionnaire was answered by the health staff of this sector, having a total of 14 people, including morning and afternoon staff.

The responses analysis showed that 65% of the staff had never received training in MHE before and no professional had previously received training in infusion pumps.

Regarding the effectiveness of the course, among the answers to the question "Was the training satisfactory?", 13 people (92.9%) reported that they fully agree that the course was fully satisfactory, and one person agreed in parts that the course was satisfactory (7.1%) (Fig. 2). Regarding the question "Did the training bring you any news about the use of the equipment?", 12 people (85.7%) fully agreed that the course brought something they did not know about and two people (14.3%) agreed in part (Fig. 2).

The survey also showed that over 70% of professionals would like training to occur every three months (Fig. 3). Moreover, they would like to receive training whenever new equipment arrives in the sector.

Also, the professionals mentioned some suggestions and criticisms, among them the preparation of quick guides to facilitate the handling of the equipment in possible doubts that appear and periodic training.

3.3 Occurrences in IPs After Training

The failures in IPs occurred after the implementation of the course were registered following the same specifications as the ones occurred before the training (see Table 3).

Fig. 1 Arrow pointing a label that indicates "broken equipment - sensor obstructed", but the equipment works normally when being tested

Training evaluation

■ Question 1: "Was the training satisfactory?"

■ Question 2: "Did the training bring you any news about the use of IPs?"
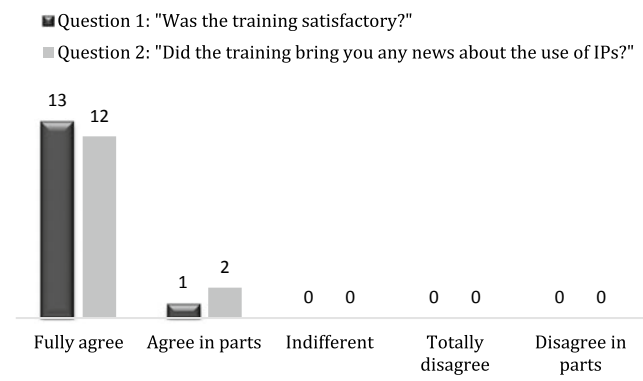
Fig. 2 Evaluation about the satisfaction (black) and new knowledge (gray) brought by the training

It is observed a total of 10 occurrences of IPs failures, in the two months analyzed, where 6 of these problems are false calls and 4 are true. Comparing the results before and after the training, it is possible to notice a great reduction in these maintenance services (Fig. 4a). It can also be observed that there was a decrease in both the false calls and the true ones (Fig. 4b).

4 Discussion

The completion of this course reinforces the data found in the literature on MHE training. The training is an essential factor for hospital equipment operation to occur within the normality and efficiency indicated by the manufacturers.

How often would you like the trainings happened?
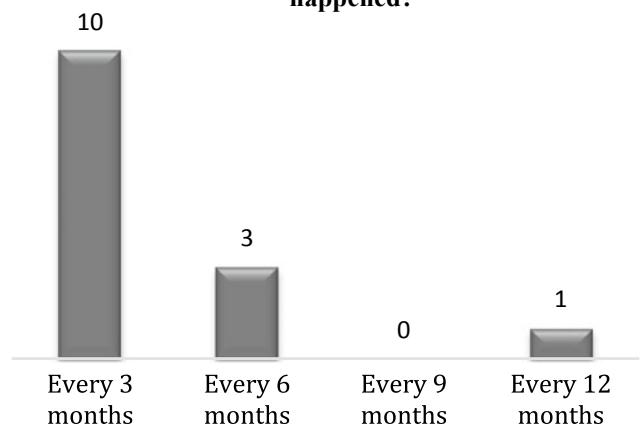
Fig. 3 Frequency of MHE training the health staff would like to receive

According to studies, one of the major problems that occur in EMH is due to operational error or misuse, as some studies have shown [4–7]. Reinforcing that one of the ways to reduce these incidents is training the health staff.

Moreover, other study analyzed the National Health Surveillance Agency data between the years 2006 to 2011, where there were 1.971 reports of medical equipment notification, and 251 of these reports on IP (12.6%). This percentage was the highest among all equipment reported, which can say that the professionals who operate the IP often denote lack of knowledge and/or lack of commitment to the activity [8].

Table 3 Occurrence and failures identification in IPs from April to May 2017 (after training)

Type of problem	Number of occurrences	Failure classification
Problem in the power supply	02	True
Obstructed sensor	02	False
It does not turn on	01	False
Alarming	01	False
Turning off	01	False
With defect	01	False
Broken cover	01	True
Flashing display	01	True

that was given in all sectors considering that this was a problem that occurred due to lack of staff information.

These data show the importance of training the health staff in the hospital environment. A well-trained staff provides greater safety for both patients and professionals, especially this type of equipment that is widely used in the neonatal ICU in newborns who are many times premature babies, who need the infusion of very delicate and controlled diets. Also, it provided a reduction in the number of corrective maintenance, which consequently reduces costs.

The evaluation is also fundamental to improve the professional growth of employees, and it is critical to keep up with and monitor the results to obtain control of the changes that have taken place.

5 Conclusion

Based on the data presented, the result successfully achieved the objective proposed by the study, since there was a considerable reduction (71%) in the occurrences of failures in infusion pumps. Reinforcing the power and importance of training, in addition to the benefits for everyone, especially for patients who can have greater safety within the hospital environment that has a well-trained and prepared staff.

As future work, it is possible to suggest the elaboration of forms and the realization of a survey about the equipment that the health staff needs training so that the Clinical Engineering staff helps to organize and promote the continuing qualification of the employees, as well as to improve the services of the health establishment.

Fig. 4 Comparation of IP maintenance calls before and after training. (**a**) Comparison in total number of IP maintenance calls before and after training. (**b**) Comparison of the number of false and true IP maintenance calls before and after training

In addition, lack of knowledge and training are factors that contribute to the occurrence of medication administration errors (MAEs), which can bring serious risks to patients [9, 10].

In the hospital in which this work was developed, although some health staffs had already received training in this type of IP before, the maintenance calling was constant in all sectors, bringing the need for a frequency in these training and not only during their installation.

The results showed that in total, the number of occurrences of infusion pumps failures decreased by 71%. The training did not reduce only what is called a "false call", but also the true ones, which can be concluded that it took greater care by the professionals in handling the BI, also reducing the problems related to the damages caused by falls. Regarding the false calls, this reduction was of 17 occurrences (approximately 74%), especially about the obstructed sensor, one of the topics covered in the course

References

1. FDA Homepage. https://www.fda.gov. Last accessed 27 Feb 2018
2. Button, V.: Dispositivos de Infusão. In: Calil, J.S. (org.). Equipamentos médico-hospitalares e o gerenciamento da manutenção, vol. 11, pp. 303–330. MS, Brasília (2002)
3. Lee, P.: Infusion pump development and implications for nurses. Br. J. Nurs. **24**(19), 30–37 (2015)
4. Lima, M.: Taxonomia dos modos e causas de falhas aplicadas na tecnovigilância de equipamentos médico-hospitalares. Revista Brasileira de Inovação Tecnológica em Saúde **4**(4), 32–41 (2011)
5. Alves, M.: Bomba de Infusão: Operação, Funcionalidade e Segurança. In: Congresso Brasileira de Engenharia Biomédica, pp. 260–261. São José dos Campos (2002)
6. Cooper, J.: Preventable anesthesia mishaps: a study of human factors. Anesthesiology **49**(6), 399–406 (1978)

7. Donchin, Y.: A look into the nature and causes of human errors in the intensive care unit. Crit. Care Med. **23**(2), 294–300 (1995)

8. Holsbach, L.: Use of an instrument to identify knowledge for safe administration of medications using automatic infusion. Rev. Bras. Eng. Biomédica **29**(4), 353–362 (2013)

9. Taxis, K.: Causes of intravenous medication errors: an ethnographic study. BMJ Qual. Saf. **12**(5), 343–347 (2003)

10. Taxis, K.: Causes of intravenous medication errors - observation of nurses in a German hospital. J. Public Health **12**(2), 132–138 (2004)

Occupancy Rate of Hospital Beds in Maternity of High-Risk

Gustavo R. da Costa, Adriana M. W. Stadnik, Frieda S. Barros, and Marcelo Maldaner

Abstract

Gestation is a physiological phenomenon, which encompasses physical, social and emotional changes, susceptible to risks to the pregnant and the fetus. Thus, this study aimed to identify the occupancy rate of hospital beds in high-risk maternity in the city of Curitiba, Brazil, during five years. For that, we analyzed data on: number of patients-day in the month, permanence of patients on days, occupancy rate of obstetric beds monthly and the obstetric beds available in the month, through cross-sectional retrospective documentary study with quantitative approach in maternity referential for care for high-complexity patients. It was observed that the overall stay-day in the period was 58,064; the average occupancy rate in the Joint Accommodation was 90.60% (SD: ± 11.98); in the Obstetric Emergency the average occupancy rate was 120.91% (SD: ± 16.15). Occupancy rate was higher than the limit recommended by the National Supplementary Health Agency to ensure the safety of the patient and of the multi-professional team.

Keywords

Bed occupancy • Health management • Hospitals, maternity • Pregnancy, high-risk

1 Introduction

Gestation is a physiological phenomenon, reflecting a healthy life experience, encompassing physical, social and emotional changes. The pregnancy period is in a borderline situation, which may involve risks to the mother and fetus binomial. Thus, there is certain contingent of pregnant women who present pre-existing pathologies and consequently, greater probabilities of unfavorable evolution, these are denominated "high-risk pregnant women" [1, 2].

The Ministry of Health of Brazil, based on the principles of Brazilian Health Care System (*SUS - Sistema Único de Saúde*), by means of Ordinance number 1459, established in 2011 program called *Rede Cegonha* (Stork Network). Considered as innovative strategy, the package of actions aims to ensure assistance to women, the right to reproductive planning humanized care during pregnancy, childbirth and the puerperium; equally, it guarantees children the right to be born with safe, healthy growth and development [3].

Thus, the *Rede Cegonha* encompasses concepts of the *Mãe Curitibana* Program (Curitiba's Mother), which was created in 1999, the year in which the live birth rate was 29,520. Its success attributed to Curitiba in 2010 the first place among the Brazilian capitals with the lowest infant mortality rate, 8.97 cases per thousand live births. Among the several actions of the program, the integral attention to pregnant women and the prevention of vertical transmission of HIV, syphilis, toxoplasmosis, hepatitis B, among other pathologies are highlighted, which when diagnosed are classified and linked to high-risk care [1, 4].

According to demographic data from 2016, Curitiba has a population of 1,893,997 people, being composed of 49.10% female, 23,160 live births and 4 maternal deaths [5]. In order to serve this population, the municipal public health network counts, in addition to the 10 Health Districts, nine Emergency Care Units, 109 Basic Health Units and a clinical analysis laboratory, with four hospitals for the pregnant woman who needs maternal and child care, whose classification is of habitual risk. However, when pregnant women present with comorbidities, giving them the high-risk classification, there are currently two maternity hospitals of reference in the city [4].

In view of this scenario, the present study was conceived with the objective of: identifying occupancy rate of hospital beds in the maternity of high risk in the city of Curitiba in the period from 2012 to 2016.

G. R. da Costa (✉) · A. M. W. Stadnik · F. S. Barros · M. Maldaner
Federal University of Technology – Paraná, Paraná, Brazil
e-mail: guresend@gmail.com

2 Materials and Methods

A cross-sectional retrospective study with quantitative approach, carried out in high-complexity maternity hospital in the city of Curitiba, Brazil. The objective of this study was to analyze the occupancy rate of the exclusively obstetrical beds.

At the institution in which the present study was developed, there were 38 exclusive beds for obstetric hospitalization, of which 28 beds were located in the Joint Accommodation (JA), which in turn were subdivided into: 16 beds for the hospitalization of postpartum (puerperal) patients with Newborn (NB), six beds for high-risk pregnant women needing treatment and six beds for NB who were admitted to the Neonatal Intensive Care Unit. Additionally, there were 10 beds of Obstetric Emergency (OE) located in the Obstetric Center, which were subdivided into: four beds for the treatment and six beds for prepartum, delivery and postpartum.

For the analysis we used descriptive statistics, through the distribution of absolute and relative frequency, mean and standard deviation, and minimum and maximum values. The data collection took place between August 15th and 30th, 2017, based on the descriptive analysis of primary data available through the local manager's information system. The information collected were stored in Excel® spreadsheet (2010) and transported to the statistical software R, which was processed for the calculation of descriptive statistic and its presentation.

2.1 Equations

Equation (1) shows the calculation of the mean number of day-beds of the month (MLd) by means of the daily sum of the total beds available for hospitalization divided by the total days of the month.

$$MLd = \frac{\sum Number\ of\ day\ beds\ in\ the\ time\ period}{Same\ time\ period} \quad (1)$$

Equation (2) represents the hospital occupancy rate (TOH), which was determined by dividing the sum of the number of patients-day of the month by the sum of the number of bed-days of the same month, multiplying the quotient by 100.

$$TOH = \frac{\sum Number\ of\ patients-day\ in\ the\ time\ period}{\sum Number\ of\ day\ beds\ in\ the\ same\ time} \times 100 \quad (2)$$

Equation (3) reproduces the total number of hospitalized patients (QPi), which was calculated by counting patients who are hospitalized for the day, adding up the amount of each day to accumulate these values throughout the month.

$$QPi = Number\ of\ patients-day\ in\ the\ time\ period \quad (3)$$

Equation (4) shows the mean permanence (MPe), which was calculated from the sum of patients-day in the month divided by the sum of exits (discharge, transfers and deaths) of the same month.

$$MPe = \frac{\sum Number\ of\ patients-day\ in\ the\ time\ period}{\sum Number\ of\ exits\ in\ the\ same\ time} \quad (4)$$

3 Study Results

Based on data analysis, there was variability of the availability of obstetric beds in the JA and OE sectors of this high-complexity maternity hospital, located in the city of Curitiba, Brazil. According to the values observed in Fig. 1, at the mean annual level, there was a decrease of 27.70% in the numbers of beds located in the JA in the years of 2015 and 2016, compared to the year of 2012. In the OE, despite of observed reduction in the number of beds in 2014, the year in which the average number of obstetric beds available was equal to eight beds compared to ten beds available in 2012, the sector resumed in 2015 the number of beds found in the initial year of this study.

The occupancy rates of obstetric beds of the JA and OE, from the period from 2012 to 2016, are represented in Fig. 2. From the analysis of the JA data, it was observed that in 63.33% of the months of the five years investigated, the occupancy rate was higher than 85.00%. It is noteworthy that in 28.33% of the months this rate was higher than 100.00%. In OE beds, only in 5.00% of the months did the occupancy rate not exceed the limit of 100.00%, and this rate reached its peak in 2014, with mean of 129.86% occupancy of the beds.

It should be noted that in periods when the occupancy rate exceeded 100.00%, in order to accommodate the patients, it was necessary to unblock beds, hospitalization
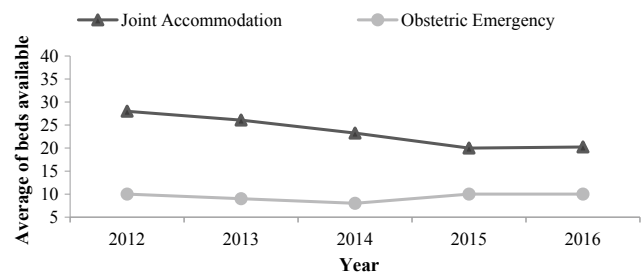
Fig. 1 Average number of available obstetric beds
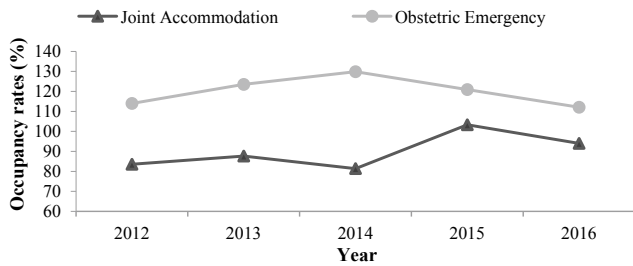
Fig. 2 Occupancy rates for obstetric beds
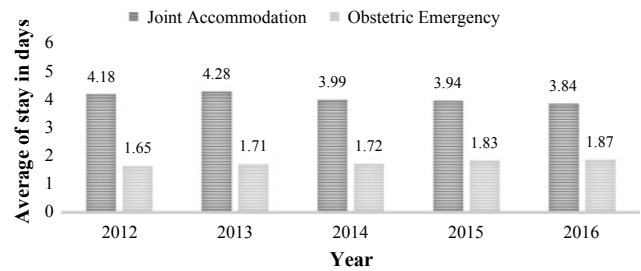
Fig. 4 Average in days of patients' stay
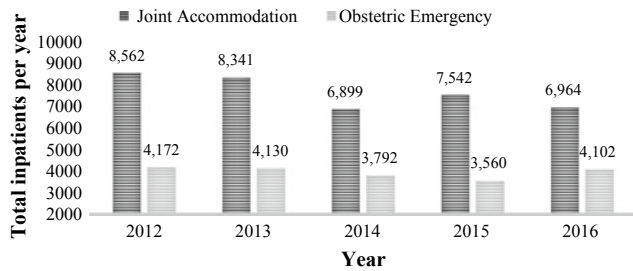
Fig. 3 Total inpatients per year
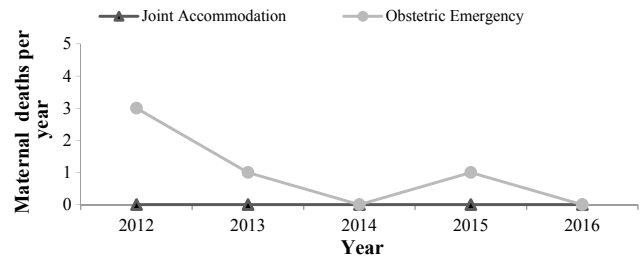
Fig. 5 Total maternal deaths per year

them in other beds available in the maternity ward or to suspend elective surgeries.

The Fig. 3 summarizes the total number of pregnant women hospitalized at the JA and OE between 2012 and 2016. In the year of 2012 there were 8,562 hospitalizations in the JA, being that the sector had its lowest annual hospitalization rate in 2014, with 6,899 hospitalizations. A total of 4,172 patients hospitalized in the year 2012 were registered in the OE; the admission rates had a notable variability in the years 2014 and 2015, with respectively 3,792 and 3,560 hospitalizations per year, increasing to 4,102 in the year 2016.

The average stay in days of patients in the JA decreased from 4.18 days in 2012 to 3.84 days in 2016. In OE, it was observed that the average length of stay in days increased

from 1.65 days in 2012 to 1.87 days in 2016, values which are shown in the Fig. 4.

Regarding maternal mortality, there were no deaths in JA between 2012 and 2016. In OE, there were three deaths in 2012, one in 2013 and one in 2015. These values are shown in Fig. 5.

The variables average and standard deviation (SD), in addition to the minimum (MIN) and maximum (MAX) values, of the total number of patients-day in the month, permanence of patients on days, occupancy rate of obstetric beds monthly, the obstetric beds available in the month and maternal deaths in the month, which were the objective of this study and analyzed by means of the monthly data obtained from the period between 2012 and 2016 of the JA and OE of high-complexity maternity hospital investigated are described in Table 1.

Table 1 Permanence, beds and maternal deaths in JA and OE at maternity of high-risk

Situation	Average	SD	MIN	MAX	Sector
Patients-day in the month	638.47	75.04	450.00	801.00	JA
Permanence of patients on days	4.06	0.30	3.61	5.03	
Occupancy rate of obstetric beds monthly	90.60	11.98	63.57	115.97	
Obstetric beds available in the month	23.52	3.87	18.00	28.00	
Maternal deaths in the month	0.00	0.00	0.00	0.00	
Patients-day in the month	329.27	35.49	248.00	396.00	OE
Permanence of patients on days	1.75	0.12	1.52	2.04	
Occupancy rate of obstetric beds monthly	120.91	16.15	84.52	174.73	
Obstetric beds available in the month	9.38	1.05	6.00	10.00	
Maternal deaths in the month	0.08	0.33	0.00	2.00	

4 Discussion

The occupancy rate of hospital beds are indicators that reflect the limits of the hospital to adequately serve its patients. In the United Kingdom, the ideal rate of occupancy of hospital beds was set at 82.00%, aiming to promote quality care [6]. In Brazil, the National Agency for Supplementary Health (ANS) recommends that the maternity rates should be between 75.00 and 85.00%, and never exceeds 100.00% [7].

Occupancy rates of 90.60% (SD: ±11.98) and 120.91 (SD: ±16.15), respectively of the JA and OE, were observed in the referential maternity of this study. These values were higher than the study performed in the obstetrics sector of university hospital in Sao Paulo, between 2003 and 2009, which presented occupancy rate between 70.50 and 85.90% [8].

It is observed that overcrowding is recurrent factor in the two hospitalization sec-tors. It is also noted that in the year of 2013 the occupancy rate of the OE reached average of 174.73% in the month of October, fluctuating to 174.44% in November.

Recent studies identified that factors such as overcrowded in hospital beds and the reduction of professional staff have impact on the quality of services, such hygiene and inadequate medication, that corroborate to increase the risks of hospital and care infections inappropriate to health [9, 10]. This way Boden et al. [11] have associated reduction in hospital bed occupancy rate with reduction in patient mortality in 32-month study in the United Kingdom [10]. Similar studies had already been carried out in other countries, such Canada and Australia, pointing to similar results [12, 13].

Between 2012 and 2016 in the maternity of this study, 5 maternal deaths occurred in the EO, place that presented higher occupancy rates. In the JA there were not cases of maternal deaths, since more complex patients are transferred to OE.

Curitiba had in 2016 the total of 68 obstetrical beds destined exclusively for high-complexity care, distributed in two hospitals. Of these, 38 beds authorized by the Municipal Health Department are located in the referential maternity of this study, what represents 55.88% of city's high-complexity obstetric beds [14].

The high occupancy rates in this maternity hospital suggest that the number of licensed high-risk obstetric beds is insufficient. In addition, there was a decline in the number of hospital beds

The high occupancy rates in this maternity unit suggest that the number of authorized high-risk obstetric beds is insufficient. Besides there was decline in the number of hospital beds in the JA in the years of 2015 and 2016, while there were higher occupancy rates in the respective years.

Such condition conveys that the reduction in the number of obstetric beds did not cause decrease in the occupancy rates of JA. This analysis is similar to the results of study carried out in hospitals in the United Kingdom, in which there was increase in the demand for emergencies due to reduction in the number of hospital beds [15].

Faiz and Dahl [16] warn that when there is imbalance between demand, resources and supply, such as rising bed occupancy rate over time, the multi-professional team feels pressure to solve the patient's problem and gets more prone to making mistakes. Factors these that confirm Allen's [17] study on the need to balance demand with resources.

The decrease in demand for obstetric care observed in JA between 2012 and 2016 coincides with the number of births in Curitiba, which decreased from 25,079 births in 2012 to 23,214 births in 2016 [4]. However, they did not indicate, in the sector, reduction and, consequently, normalization of the occupancy rate of hospital beds.

Among the variables investigated, the average permanence of patients on days was the one with the lowest dispersion. Although it is important to add that the average occupancy between the two hospitalization units is cumulative - it occurs that the patients admitted to the OE on discharge are transferred to the JA.

The high time of permanence, consequently, causes problems in the sector. In the JA, the mean hospitalization in days between 2012 and 2016 was 4.06 days (SD: ±0.30), 35.33% higher than that recommended by the ANS, which is three days [6]. This theme has been of interest to recent studies in Brazil and beyond the national sphere [18, 19].

In this context, Werle et al. [20] propose to carry out studies with workflows related to hospital discharge. Thus, it will be possible to identify existing problems in the sector, which may contribute to the reduction of bed overcrowding [20].

Moreover, it is suggested that factors that may have influenced the time excess length of hospital stay in this maternity are related to the complications of the patients, such as broad-spectrum antibiotic therapy, waiting for expert evaluation, diagnostic tests, social issues, such as transportation to home and even the puerperal having discharge from the hospital and the newborn still needing hospitalization - thus the patient remains in bed, raising the occupancy rate, depriving the possibility of occupation by other puerperal women.

In this context, researchers have illustrated how long-term patients can influence the increase in the mean number of hospitalized days. As example, if 20 patients stay on average two days hospitalized each, and two patients stay on average 20 days hospitalized each, these two long-term patients occupy, during the period in which they were hospitalized, the same hospitalization demand as that of the first example, of 20 patients of short duration [21].

5 Conclusion

The present study has retrospectively identified the occupancy rate of high-complexity maternity beds, whose annual average ranged from 81.39 to 103.32% in JA and from 112.08 to 129.86% in OE. It also contributed to the reflection about the effects that overcrowding entails in the hospital environment and in its users.

Considering the growing number of the population residing in Curitiba, it seems that there is imminent need of attention of the municipal managers of the SUS to establish new strategies in health, with the objective of minimizing the overcrowding of high-complexity beds, through actions that focus the basic attention with investments in the prevention and consequently, providing better service to the users of these services.

Next, we suggest new studies on the subject, which show the occupancy rates of hospital beds. Regarding the maternity of this study, it is suggested to investigate the reasons that could cause overcrowding in its sectors, through management methods, evidencing the impact of this overcrowding on the service to the users and on the activities of the professionals involved.

References

1. Brasil. Ministério da Saúde. Secretaria de Atenção à Saúde: Gestação de alto risco: manual técnico. 5th edn. Brasília (2012)
2. San, O.h., Husain, W.: Maternity data management utilizing cloud computing. In: International Conference on Computer and Information Sciences (2014)
3. Brasil. Diário Oficial [da] República Federativa do Brasil: Institui no âmbito do Sistema Único de Saúde - SUS - a Rede Cegonha. Portaria 1.459, 2011/6/24
4. Brasil. Secretaria Municipal de Saúde de Curitiba: Pré-Natal, Parto, Puerpério e Atenção ao Recém-Nascido. Curitiba (2017)
5. Brasil. Ministério da Saúde. DATASUS: Nascidos Vivos, Brasil. Last accessed 6 Nov 2017
6. Keegan, A.: Hospital bed occupancy: more than queuing for a bed. Med. J. Aust. **193**(5), 291–293 (2010)
7. Brasil. Ministério da Saúde. Agência Nacional de Saúde Suplementar: Taxa de Ocupação Operacional Maternidade. 1.01 (2012)
8. Brasil. Divisão de Enfermagem. Relatório: Hospital de Clínicas da Faculdade de Medicina de Ribeirão Preto – USP. Ribeirão Preto (2011)
9. Kaier, K., et al.: Bed occupancy rates and hospital - acquired infections-should beds be kept empty? Clin. Microbiol. Infect. **18** (10), 941–945 (2012)
10. Clements, A., et al.: Overcrowding and understaffing in modern health-care systems: key determinants in meticillin-resistant Staphylococcus aureus transmission. Lancet Infect. Dis. **8**(7), 427–434 (2008)
11. Boden, D., et al.: Lowering levels of bed occupancy is associated with decreased in hospital mortality and improved performance on the 4-hour target in a UK District General Hospital. Emerg. Med. J. **33**(2), 85–90 (2016)
12. Guttmann, A., et al.: Association between waiting times and short term mortality and hospital admission after departure from emergency department: population based cohort study from Ontario. Can. Br. Med. J. **342**, d2983 (2011)
13. Sprivulis, P., et al.: The association between hospital overcrowding and mortality among patients admitted via Western Australia emergency departments. Med. J. Aust. **184**(5), 208–212 (2006)
14. Brasil. Ministério da Saúde. DATASUS: CNES, Recursos Físicos, Hospitalar, Leitos de Internação. Last accessed 5 Oct 2017
15. Oliver, D.: Acutely ill patients on trolleys and beds - why not chairs? Br. Med. J. **352**, i1684 (2016)
16. Faiz, K., Dahl, F.: Overbelegg og faregrense for dødelighet. Tidsskr Nem Legeforen. **136**, 14–15 (2016)
17. Allen, D.: Inside 'bed management': ethnographic insights from the vantage point of UK hospital nurses. Sociol. Health lln. **37**(3), 370–384 (2015)
18. Silva, S., et al.: Fatores de atraso na alta hospitalar em hospitais de ensino. Revista de Saúde Pública **48**(2), 314–321 (2014)
19. Costa, A., et al.: Acute care inpatients with long-term delayed-discharge: evidence from a Canadian health region. BMC Health Serv. Res. **12**, 172 (2012)
20. Werle, N.B., et al.: Identifying opportunities for improvement in a maternity through Lean Thinking. Ingeniería Industrial. Actualidad y Nuevas Tendencias **5**(18), 71–82 (2017)
21. Papi, M., et al.: A new model for the length of stay of hospital patients. Health Care Manag. Sci. **19**, 58–65 (2016)

Sepsis Patient Outcome Prediction Using Machine Learning

José Lucas de Alencar Saraiva⬤, Marcus Henrique Victor Júnior⬤,
Otávio Monteiro Becker Júnior, Visakan Kadirkamanathan⬤,
Eliezer Silva, and Karl Heinz Kienitz⬤

Abstract

Sepsis is a life-threatening response of the body to infection that often leads to death. In Brazil, hundreds of thousands of deaths occur every year, with a mortality rate higher than the world average. In this context, it is important to develop tools for decision support and training of healthcare professionals. This work discusses a modelling for sepsis that may be instrumental for achieving such goals. Machine learning is used to train a model for prognosis of outcome of septic patients. The inputs of the model include information about the patient sepsis, previous clinical records and treatment variables. The results show that high accuracy can be achieved and that the network is able to really map patients in two highly distinct groups of risk (survival and fatal outcome), under certain conditions.

Keywords

Sepsis prediction • Neural networks • Machine learning

1 Introduction

Sepsis represents a set of serious manifestations produced by an infection, affecting the whole organism. Although the infection is normally present in only one organ, a systemic inflammatory response is established in the body in an attempt to combat the infectious agent. Systemic inflammation can have harmful effects and compromise other organs, rapidly deteriorating the clinical condition, which can lead to multiple organ failure and death.

In Brazil, sepsis is responsible for about 25% of bed occupancy in intensive care units (ICU), being the leading cause of death in these units and overcoming heart attack and cancer as causes of late hospital mortality [1]. Sepsis mortality in Brazil is about 65%, higher than the world average (30–40%) and in countries such as India and Argentina [2, 3]. Treatment for this condition is costly [4], as sophisticated equipment and expensive drugs are needed.

Since sepsis is a frequent and widely spread condition worldwide, advances in its understanding can have high impact on its treatment. Some past research was geared towards the onset of sepsis detection and predict mortality based on patient vital signs using machine learning techniques [5, 6] and clinical scores [7].

Using machine learning to build a model to make prognosis based on data from the patient record has achieved good results in individual survival prediction of septic patients. Accuracy of 77.1% was reported, along with sensitivity (true positive detection rate) of 95.8%, specificity (true negative detection rate) of 34.1% and area under sensitivity versus specificity curve (AUC) of 0.768 [8]. The high accuracy and sensitivity of such technique motivated further investigation of its performance.

The present study addressed the modeling of sepsis using the neural network design proposed in [8] using a dataset made available by Instituto Latino Americano de Sepse (ILAS). This is done by adapting that design to a new dataset (made available by a major Brazilian hospital) and reanalyzing the performance of the network on the first dataset without some variables which were not available in the new dataset. Once the model can handle different datasets, maintaining outcomes quality, it would be possible to build both a clinical decision support system and a tool for training of healthcare professionals. Both applications could significantly improve the treatment of sepsis.

J. L. de Alencar Saraiva (✉) · M. H. V. Júnior · K. H. Kienitz
Instituto Tecnológico de Aeronáutica, São Paulo, Brazil
e-mail: jlucas.saraiva@gmail.com

O. M. B. Júnior
Transplant Hospital Euryclides de Jesus Zerbini, São Paulo, Brazil

V. Kadirkamanathan
University of Sheffield, Sheffield, UK

E. Silva
Albert Einstein Israel Institute of Teaching and Research,
São Paulo, Brazil

2 Materials and Methods

2.1 Datasets

A neural network was designed and trained with the first dataset. Following, the used dataset variables and their types are enumerated: location prior ICU (categorical from 1 to 9); beginning of sepsis (categorical from 1 to 4); clinical or surgical (binary); respiratory failure (binary); heart failure (binary); renal failure (binary); hematologic failure (binary); metabolic failure (binary); hepatic failure (binary); neurologic failure (binary); clinical suspicion (binary); chronic obstructive pulmonary disease (binary); usage of antibiotics (binary); usage of vasopressors (binary); chronic heart disease (binary); AIDS (binary); use of sedative (binary); type of ICU (categorical from 1 to 8); SOFA Score (integer from 0 to 24); APACHE II score (integer from 0 to 71); age (integer); spot of infection (categorical from 1 to 11); Diabetes (categorical from 1 to 4); origin of infection (categorical from 1 to 3); active cancer (categorical from 1 to 4); chronic hepatic disease (binary); resuscitation volume (integer); resuscitation volume on ICU (integer); time of mechanical ventilation (days); time on mechanical ventilation on ICU (days); time on vasopressors (days); time of vasopressors on ICU (days); type of infection (categorical from 1 to 5).

The first dataset was comprised of information on over 12,000 patients, but any patient with a missing value for a feature was not used. The second dataset had over 1,100 patients, but some of them had missing labels as well as other features, which prevented them from being used. All the used data were anonymous and were used in retrospective.

2.2 Neural Network

From the enumerated variables, some possibilities of topology, cost functions and training for a neural network were tested, to predict septic patient outcomes. The chosen cost function was the cross entropy (1), as it is less affected by outliers than the root mean square cost function. In (1), y represents the actual outcome, N represents the total cases, and $\hat{y}$ represents the output of the final layer before the threshold. In [8] a feed forward neural network of one hidden layer, with 16 neurons of hyperbolic tangent activation function was trained. In this work, the number of neurons was reevaluated, and it did not seem to have a big impact on the performance, as shown in Fig. 1. Nevertheless, to establish a better comparison with the results in that work, the neural networks trained in this work had 16 hidden neurons. To investigate if there is any sizeable performance improvement in using 16 hidden neurons a logistic regression was trained in the second dataset.

$$C = -\frac{1}{N} \sum\nolimits_{n=1}^{N} \left(y_n \log \hat{y}_n + (1 - y_n)\log(1 - \hat{y}_n) \right) \quad (1)$$

Figure 1 presents the mean and the standard deviation of the cross entropy on test set for each number of neurons in the respective layers. For each topology, there were 10 repetitions of training and tests. In each trial, the dataset was split randomly in a training set (70% of the data), a validation set (15%, used to implement early stopping) and a test set (15%). The performance on the test set of each design is presented in Fig. 1. The experiments with a second hidden layer were performed with 16 neurons in the first hidden layer. Figure 1 (right), shows that adding a second layer did not make the overall performance better, while Fig. 1. (left) shows that using a single hidden layer with more than 16 neurons also did not lead to improvements.

Subsequently, for better generalization, an L2 penalty (i.e., the addition of a term related to the square norm of the weight vector to the cost function) was used. The cost function including the penalty is shown in (2), where K represents the number of weights of the network, W is the weight vector and $(1 - \lambda)$ the regularization parameter, which has been set to 0.55 as in [8].

$$C_{Reg} = \lambda C + (1 - \lambda) \sum\nolimits_{i=1}^{K} W_i^2 \quad (2)$$

The output of the neural network is the hyperbolic tangent function (normalized between 0 and 1) applied to a linear combination of the outputs of the hidden layer neurons and a decision of the prognosis comparing the final value with a threshold, i.e., a limit value for the output. If the output is greater than this threshold, a fatal outcome is considered more likely. Otherwise, patient survival is predicted. The training method was resilient backpropagation, as it was found to speed up the training in comparison to other tested algorithms.

In this work, two neural networks were trained: one using the patients from the second dataset and other using the first dataset, but excluding the variables indicated in Sect. 2.3.

2.3 Removal of Neural Network Inputs

Some enumerated variables were chosen for the study of neural network performance in the absence of them. The last five enumerated variables or some similar information had not been recorded for the patients in the second dataset, and therefore the performance of the network in the absence of such variables would be an indication of how well the network would perform on the new dataset.

Fig. 1 Cross entropy against number of neurons in each layer
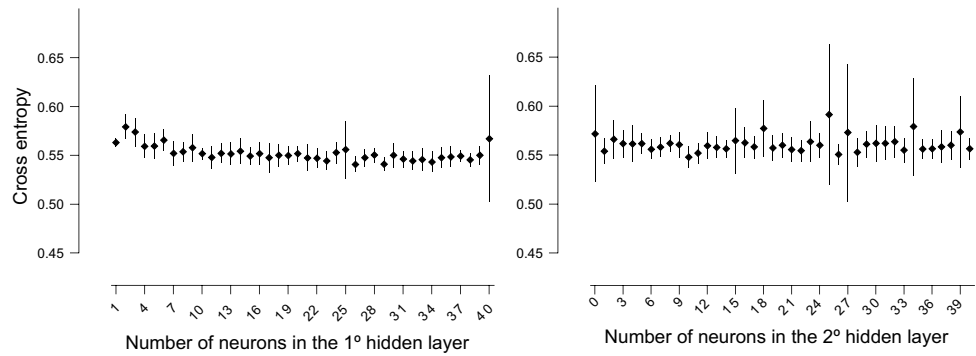
It is also interesting to study the importance of these variables considering the potential uses of the network since they are usually unknown by the medical team at the time of the patient's arrival in the hospital and should be preferentially excluded if the network would be used for a decision support system. However, it should be noted that if the network is used in a training system, then those variables should possibly remain, as, in this context, the overall scenario is needed for hypothesis testing.

3 Results

The outcomes obtained from the two different datasets will be shown below. Table 1 shows the performance of the trained neural network with the first dataset as reported in [8]. The confusion matrix allows observing the occurrence of errors and their types on a classification system. In the matrix columns, the patients are separated by the class to which they belong: survival or fatal outcome. In the rows, they are divided according to the prediction of the networks. In the parentheses are shown the percentages of each combination of prediction and outcome. This network was trained with a training set of 1796 patients, along with 406 patients in the validation set.

Furthermore, Tables 2 and 3 show the confusion matrices for the second dataset and for the first dataset, in the absence

Table 1 Results on test set for the neural network on the first dataset

	True negative	True positive
Predicted negative	42 (10.3%)	12 (3.0%)
Predicted positive	81 (20.0%)	271 (66.7%)

Table 2 Results on test set for the Neural Network on the second dataset

	True negative	True positive
Predicted negative	82 (82.0%)	7 (7.0%)
Predicted positive	5 (5.0%)	6 (6.0%)

Table 3 Results on test set for the Neural Network on the first dataset excluding the last five enumerated variables

	True negative	True positive
Predicted negative	128 (12.6%)	51 (5.0%)
Predicted positive	305 (30.1%)	528 (52.2%)

of the last five enumerated variables, respectively. For the results presented in Tables 2 and 3, the used threshold was 0.44 as this led to the best result with the original network. Figure 2 shows the plots for their accuracies against the threshold. Finally, Table 4 presents the result of a logistic regression in the second dataset.

Figure 2 shows that the threshold of 0.44 is close to the optimal value for both networks, but a slightly higher accuracy could be attained with other thresholds. The network which has its performance presented in Table 2 was trained with a training set of 468 patients, and 101 were used as a validation set. The network in Table 3 was trained with a training set of 4723 patients and had a validation set of 1012 patients. Finally, the logistic regression was trained with 567 patients.
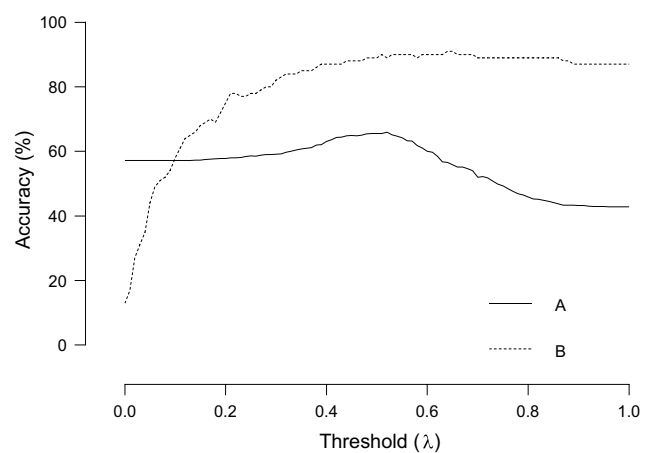
Fig. 2 Accuracy on test set versus Threshold for the trained networks. A stands for the network trained on the second dataset, and B for the network trained on the data from the first dataset without the excluded variables

Table 4 Results on test set for the Logistic Regression on the second dataset

	True negative	True positive
Predicted negative	77 (76.2%)	10 (9.9%)
Predicted positive	7 (6.9%)	7 (6.9%)

4 Discussion

From Table 1, the accuracy was 77.1% with the first dataset. Table 1 also shows that the neural network can classify well the patients who died because, in 95.8% of the cases in which the patient died, the network predicted such outcome. However, for patients who survived, performance decreased to 34.1%. In this context, it was verified that cross entropy does not present significant decrease from a certain point of the training, and also that the performance remained the same using smaller fractions of the datasets as training sets, indicating that lack of data is not a limitation for the learning. The observed result may be due to a combination of the following reasons:

1. The chosen variables contain more useful information to predict fatalities, but do not present any real pattern on survivors. If this was the case, more variables should be added as inputs;
2. The built model is not complex enough to extract information about surviving patients. This could be overcome changing the neural network design. In this case, a topology with more hidden layers and an appropriate training method could improve network performance. However, given Fig. 1, this seems unlikely;
3. The imbalance of the used dataset, which contains significantly more cases of fatal outcomes than survivals, has made the network inefficient in identifying cases of survival.

Figure 2 and Table 2 show the outcomes for the second dataset. The accuracy was greater than that verified in the first dataset, reaching 88%. One of the reasons is that the second dataset is highly unbalanced (as shown in the percentages of Table 2), with much more survivors than fatal outcomes. The network classified well patients of the predominant class in the database (in the case of this dataset, most patients survived), while the performance in the other patients was poor, achieving only 46.2% of sensitivity. This signs that the performance pattern on the second dataset was close to that of Tables 1 and 3, in the sense that the network classified patients belonging to the most common class in

each set well, but could not predict the least prevalent outcome efficiently

Table 4 shows a result slightly below that of Table 2, as the accuracy in this table is 83.2%. The associated specificity and sensitivity are 91.7 and 41.2%, respectively. This indicates that the regression is just slightly less sensitive than the network. However, the results in Tables 2 and 4 need to be further studied, as in both situations the test set had a small number of patients and in particular a tiny number of fatalities.

The neural network performance trained without the last five enumerated variables is shown in Fig. 2 and Table 3. First, it should be noted that accuracy decreased from 77.1% to 64.8%. However, the discrepancy between the precision in the analysis of survival and non-survival cases continues to exist, as the sensitivity is 91.2%, but the specificity is only 29.6%. This is evidence that although the accuracy dipped a lot, the discrimination ability of the network remained close to what it was, but on a test set that was more balanced (as shown by the percentages in Tables 1 and 3), it produced smaller accuracy.

These results seem to suggest that the discussed network should not be used for prognosis unless it is known that the dataset is unbalanced, as in the set from this major Brazilian hospital. In this case, provided that the performance of the network can be validated on a larger set, its output can be used for splitting patients in 2 groups of risk, as 92.1% of the patients predicted to survive do survive and 55% of the patients predicted to die actually died. In fact, even in the more balanced test set of Table 3, 71.5% of the patients predicted to survive survived, and 63.4% of the patients predicted to die, died, meaning that the network could still separate patients in two groups of different risks of having a fatal outcome.

A particular problem that seems to prevent the network of achieving better performances is the nature of the data being used in training: many features are categorical and since neural networks training through backpropagation relies on derivatives of cost function to the weights, this kind of data is not ideal for neural networks. The type of data used is probably holding the performance of the network down, as Table 4 presents a result that nearly matches that of Table 2.

This is evidenced by the fact that [6] managed to get a neural network for sepsis prognosis which had AUC of 0.878 using as inputs some vital signs and 2 binary variables, well above the 0.752 AUC of a logistic regression reported in the same contribution. It is likely that better performance would have been achieved if the network had been trained to make prognosis based on non-categorical data.

However, vital signs of patients, such as temperature and concentration of lactate in the blood, are not available on the first dataset. Another alternative would be to use one hot encoding for the categorical features, converting each of these inputs to a set of binary variables, as this would allow the network to perform learning without presuming any order between each value of the categorical inputs. In this work, the categorical variables were encoded as integers, as preliminary tests with one-hot encoding did not seem to raise the accuracy despite increasing the dimensionality of the input space.

5 Future Work

Future work with the modeling of sepsis with the network should address a better analysis of the robustness of the network modeling with regard to disturbances on selected variables. In particular, an investigation of the influence of perturbations on the categorical variables seems relevant, as it could show which of the categorical variables are relevant for the outcomes. It is also intended to study the influence of using other features as inputs to the network.

References

1. Silva, E., et al.: Brazilian sepsis epidemiological study (BASES study). Crit. Care **8**, 251–260 (2004)
2. Angus, D.C., Pereira, C.A., Silva, E.: Epidemiology of severe sepsis around the world. Endocr. Metab. Immune Disord. Drug Targets **6**, 207–212 (2006)
3. Beale, R., Reinhart, K., Brunkhorst, F.M., Dobb, G., Levy, M., et al.: Promoting global research excellence in severe sepsis (PROGRESS): lessons from an international sepsis registry. Infection **37**, 222–232 (2009)
4. Sogayar, A.M., Machado, F.R., Rea-Neto, A., Dornas, A., Grion, C.M., et al.: A multicentre, prospective study to evaluate costs of septic patients in Brazilian intensive care units. Pharmacoeconomics **26**, 425–434 (2008)
5. Kam, H.J., Kim, H.Y.: Learning representations for the early detection of sepsis with deep neural networks. Comput. Biol. Med. **89**, 248–255 (2017). ISSN 0010-4825
6. Jaimes, F., Farbiarz, J., Alvarez, D., Martínez, C.: Comparison between logistic regression and neural networks to predict death in patients with suspected sepsis in the emergency room. Crit. Care **9**(2), R150 (2005)
7. Kam, H.J.: Validation of predisposition, infection, response and organ dysfunction score compared with standard severity scores in predicting hospital outcome in septic shock patients. Minerva Anestesiologica **79**(3), 257–263 (2013)
8. Okuyama, I.F., et al.: REDES NEURAIS PARA PREDICÃO DE SEPSE. In: Anais do XXI Encontro de Iniciação Científica e Pós-Graduação do ITA - XXI ENCITA/2015, Instituto Tecnológico de Aeronáutica, São José dos Campos, SP, Brasil (2015)
9. Okuyama, I.F.: Avaliação preliminar do uso de redes neurais na predição de sepse. Poster presentation, XI Fórum Internacional de Sepse (2014)
10. Instituto Latino Americano de Sepse (ILAS). Homepage. http://www.ilas.org.br. Last accessed 21 March 2018

The Impact of Health Technology Management for the National Policy on Technological Innovation in Health – PNITS

F. S. Toscas, V. G. B. Júnior, T. R. Santos, and M. A. C. Nascimento

Abstract

The objectives of PNITS are, among others, to promote the SUS's (Brazilian Unified Health System) technological and economic sustainability, with the definition of structural conditions to increase the country's productive and innovation capacity, aiming to contribute to the expansion of access to health. It seeks to encourage innovation and scientific and technological research in the productive environment and promote technological capacity building, technological autonomy and the development of the national and regional productive system in the health area. The main challenge is to reduce the country's external dependence and productive and technological vulnerability related to strategic products and services for SUS. The PNITS establishes the criteria for the use of state purchasing power in order to rationalize health expenditures and induce scientific, technological and industrial development, trying to reach SUS sustainability and the consolidation of the CIS (Industrial Health Complex) in Brazil. The public administration lacks subsidies that Clinical Engineering and Biomedical Engineering are able to provide, in order to avoid an asymmetric dynamic of negotiations between State and market.

Keywords

Technological development • Industrial development • Biomedical technology

1 Objective

The study aims to highlight the challenges and efforts of the Ministry of Health in formulation and implementation of Public Policies to strengthen technological sovereignty and increase access to the Unified Health System (SUS). From this context on identify the opportunities of Clinical and Biomedical Engineering on subsiding essential technological information for the effective implementation of these policies, especially to reduce the healthcare gaps and technological gaps still observed in an inclusive health system and minimize the asymmetry of negotiations between State and market. It is worth noting that Brazil is the only Country in the world, with more than 100 million inhabitants, that accepted the challenge of establishing a public, universal and free health system.

2 Methodology of the Study

This article was based on a qualitative approach, based on exploratory research in official documents of the SCTIE Secretariat of Science, Technology and Strategic Inputs of the Ministry of Health related to Public Policies relevant to Health Technologies Management and to the strengthening the Industrial Health Complex (CIS). The methodology used research with a bibliographic survey and revision of the regulatory framework through the official website of the Ministry of Health.

F. S. Toscas (✉) · T. R. Santos
Department of Industrial Complex and Innovation
in Health - DECIIS/SCTIE/MS, Brasília, 70058-900, Brazil
e-mail: fotini.toscas@saude.gov.br

T. R. Santos
e-mail: thiago.rodrigues@saude.gov.br

V. G. B. Júnior
Senai Cimatec, Av. Orlando Gomes, 1845, Piatã, Salvador,
41659-010, Brazil
e-mail: valdir.junior@fieb.org.br

M. A. C. Nascimento
Oswaldo Cruz Foundation, Prédio da Expansão da Fiocruz,
Avenida Brasil, 4036, Manguinhos, Rio de Janeiro, 21.040-361,
Brazil
e-mail: marco.nascimento@fiocruz.br

3 Results and Discussion

The research considered the governmental main efforts to consolidate and expand the regulatory framework, which allow the State to act more strongly in the CIS: (i) National Policy on Health Technology Management (PNGTS); (ii) National Policy on Science, Technology and Innovation in Health of the Ministry of Health (PNCTIS); (iii) National Policy on Technological Innovation (PNITS).

The State's action in the CIS is based on the incorporation of the new development model, which considers the health sector essential for the country's development. Within this development model, it became possible for the Ministry of Health to give relevance and objectivity to the initiatives in the scope of the CIS and, especially, articulate the actions of the sector with the other public policies developed in Brazil, in order to end the enormous gap between assistance to the population and the activities related to productive and innovative base in products and services required for health.

The CIS is currently a key element for the development of the country, since it contemplates the economic and social dimensions of development and is configured as a production and innovation system with high potential for generating knowledge. The CIS is based on the systemic relation between the productive segments of health, among them, the subsystem of the equipment and health products industry.

With the responsibility of evaluating health technologies to be incorporated, excluded or altered in the public health system, stimulated by the existed dynamism to offer new technologies and exponential growth of health spending, the Ministry of Health published the National Policy on Technology Management in Health (PNGTS). The PNGTS, published in 2011, defines the management of health technologies as a set of management activities related to the processes of evaluation, incorporation, diffusion, management related to use and exclude of technologies from the health system. This process should have as reference the health needs, the public budget, the responsibilities of the three levels of government and social control, as well as the principles of equity, universality and integrality, which underpin health care in Brazil [1].

In 2008, the Ministry of Health had already published its own the National Policy on Science, Technology and Innovation in Health (PNCTIS). This Policy emphasizes the importance of the State acting in a prominent way as regulator of the flows of production and incorporation of technologies. Otherwise it also worked acting as an incentive for the innovation process, guiding and financing R & D activities, in line with the National Agenda for Priorities in Health Research and with the epidemiological indicators of each region.

The PNCTIS pointed out that "among the actions in the field of technological policy in which state participation is essential, we must highlight industrial modernization, the diffusion of technical progress and support for innovation. Considering the last mentioned point, it is relevant to emphasize the important role of using the state's purchasing power as a tool to induce technological development. "This policy emphasizes the role of the State in the promotion and regulation of the health industrial complex (CIS), through convergent actions to support competitiveness, financing and incentive to R&D in public enterprises; purchasing policy; defense of intellectual property; incentive to partnerships and investments in infrastructure. Finally, PNCTIS reinforces that it is essential to use the purchasing power of the State and its companies in different areas, in order to preserve jobs and achieve competitiveness in the national production of technologies, with social control [2].

Considering the need to consolidate the Policy instruments used by the Ministry of Health in recent years to strengthen the CIS, a National Policy on Technological Innovation in Health (PNITS) was instituted, launched after the signing of Decree 9.245 of 20 December 2017, which "regulates the use of state purchasing power in contracting and acquisitions involving strategic products and services for the Unified Health System - SUS" [3].

This Policy also aims to reinforce the parameters of the PNCTIS that have been maintained over the years, but which require more specific approaches and regulations considering currently CIS's demands. It is still waiting for specific regulation called Interministerial Ordinances. The construction of the regulation of this document is being carried out in a collegial manner, with the participation of the Ministry of Science, Technology, Innovations and Communications; Ministry of Industry, Foreign Trade and Services; and the Ministry of Planning, Budget and Management.

In this context, it is intended to understand how the management of health technologies, derived from clinical engineering activities, can support the policy instruments elucidated in PNITS. Thus, it is intended to present the elements of the PNGTS that can be consolidated into important tools so that the newly launched PNITS can achieve the greater goal of increasing the population's access to strategic products for the SUS.

3.1 The Objectives and Instruments of PNITS Policy

The PNITS aims to promote the SUS's technological and economic sustainability, with the definition of structural conditions to increase the country's productive and innovation capacity, and also to contribute to broader access to health.

It seeks to encourage innovation and scientific and technological research in the productive environment and promote technological capacity building, technological autonomy and the development of the national and regional productive system in the health area. Its challenge is to reduce the country's external dependence and productive and technological vulnerability in relation to strategic products and services for SUS. PNITS establishes the criteria for the use of state purchasing power with the purpose of rationalizing health expenditures and inducing scientific, technological and industrial development, in order to promote SUS's sustainability and the consolidation of the CIS in Brazil.

The strategic instruments of PNITS are the Productive Development Partnerships (PDP), the Technological Orders - ETECS; and the Technological Compensation Mechanisms - MECS.

The Productive Development Partnerships promote the establishment of technology transfer contracts between private companies, national or foreign, that have the domain of production and commercialization of strategic products for public laboratories. This tool seeks the induction of the technological domain, by national public institutions, of the production of strategic products for the SUS. A relevant change brought by PNITS is contained in the sole paragraph of article 7 of the decree: "specific act of the Minister of Health will define the strategic products for SUS that could be object of PDP, after hearing the Executive Group of the Industrial Health Complex (GECIS)". Previously, the definition of the list of strategic products was exclusive responsibility of the Ministry of Health.

The Technological Orders have the objective of contracting a Scientific, Technological and Innovation Institution (ICT), private non-profit entities or private companies, either alone or in consortiums, focused on research activities and with recognized technological qualification in the sector, to carry out research, development and innovation activities involving technological risk, to solve a specific technical problem or to obtain an innovative product, service or process in the health area. It is a direct expression of the State's purchase power in the direction of reaching specific society needs. The Technological Orders constitute an important sign of an intention to change the paradigm of the technology push system to demand pull, that is, an environment in which what fails the Brazilian social fabric is likely to convert and define the direction of technological development in order to correct the problem. In other words, instead of the public agent being only subject to the dynamics of the offer of technologies proposed by the developers, it is configured the possibility of directing the financing instruments to remedy a specific question. Instead of a plethora of unsolicited offers of solution to a particular problem, you have the specific order to solve it.

The Technological Compensation Mechanisms (MECS) includes "commercial, industrial and technological compensation or access to advantageous financing conditions" (as provided for in §11 of article 3 of Law 8,666 of 1993). This instrument takes advantage of the strong bargaining power of large government purchases to provide compensation of various kinds that may be decisive for the choice of particular supplier. A variant of the offset agreements is that this modality is particularly relevant because it associates the commercial advantage of the large-scale purchase with the compensation resulting from the size of the purchase, that is, the purchase of dozens of technologies gives to the buyer a much superior negotiating capacity. This is particularly important in business environments often subject to monopolies and oligopolies with asymmetric market power.

It should be noted that in both cases, the decree clarifies that specific acts cancelled by GEGIS and signed by the Ministers of Health, Science, Technology, Innovation and Communications, Industry, Foreign Trade and Services and Planning, Development and Management will be used to define the implementation of the latter two instruments.

3.2 The Importance of Clinical Engineering in the Implementation of PNITS

Clinical Engineering is crucial for any Public Policy initiative in the area of health technology management. Technological progress is nowadays not only marked by the operational aspect, but also by the repeated acceleration in ever-decreasing technological intervals. The impact of managing the tools available for health systems, from management to direct care, is critical to the efficiency of these services, and tends to grow dramatically in importance.

In a scenario of marked technological enhancement in which they appear on the horizon, not as distant promises, but as imminent realities, systems of interconnected devices (internet of things), high customization of manufacturing (advanced manufacture), miniaturization (nanotechnology), autonomous learning artificial intelligence or large data processing, the importance of disciplines capable of ensuring the interoperability and effectiveness of these innovations in the health promotion environment can not be underestimated.

It is up to clinical engineering, therefore, to ensure a smooth interface between the universe of care and the technological potential of our times.

It is in this scenario that the new mechanisms of promotion of the technological development in health are configured. As can be seen, the decree indicates that the implementation of the three instruments presents the need to establish the strategic products and services that can be contracted and purchased using government purchasing power. This can occur through the definition of the strategic product list for the SUS, in the case of PDPs, or of acts of

Ministers of State previously chancelled by GECIS, in the cases of ETECS and MECS.

Therefore, considering the particularities of the medical devices sector, it is necessary to consider the tools of Health Technology Management to support the Ministry of Health with information necessary for the formation of the strategic product list and for the definition of the products subject to ETECS and MECS. The tools of Health Technologies Management can offer strategic subsidies for health policies, such as:

- Identification of technology roadmaps for competitive intelligence and technological information;
- Market analysis with timeline of values practiced, risks and vulnerabilities;
- Identification of suppliers, productive chain, regional productive arrangements, mergers and acquisitions;
- Predictability for acquisitions, supplies, replacements and repairs;
- Supply, demand and distribution;
- Technical assistance parameters to cover care and regionality; and
- Post-market evaluation and performance of technologies in the real scenario with data from the operational domain.

4   Conclusion

It is evident the importance of Clinical Engineering as a field of improvement of technology management tools to accelerate the achievement of more effective and efficient results in health services, especially in maximizing available resources with the best possible clinical outcomes. Among the attributions of Clinical Engineering, it is worth mentioning the application of managerial and engineering knowledge to the management of health technologies, support and even intervention in health services, with the aim of achieving well-being, safety, costs and quality in the services available to patients and the multidisciplinary team.

The data obtained through the Health Technology Management instruments contribute to rationalization of the use and supply of technologies, efficiency in public spending, maximization of available resources with increased access, and provide future vision for the formulation and implementation of policies in health.

There are important gaps in the development of tools to strengthen Health Technology Management. Among these activities, it is relevant mentioning the establishment of a global standard of nomenclatures for medical devices with the objective of promoting the exchange of technical and economic information that reduces asymmetry of information that causes practices and abusive prices. It is also important to expand the use of health technology assessment throughout the technological life cycle, from research, development, diffusion, post-market to disinvestment and/or abandonment. Clinical engineering contributes to these issues since the sophistication of production creates a high level of information asymmetry, making it difficult for public managers to make decisions. It is important to emphasize that the choice for a particular health device is rarely subject to the patient's decision, but usually to the professional who will indicate them. They are called, therefore, "credential goods" and, because of this condition, are particularly subject to market failures. State action to prevent opportunistic behavior in these cases is vital.

However, it depends on the capacity of Clinical Engineering to generate sufficient data and information to formulate adequate public policies to prevent the abuse of any perverse actors. It is also crucial to subsidize structuring decisions of the SUS, for example, which equipment should be incorporated into the National List of Equipment and Permanent Materials that can be financed for SUS (RENEM).

The establishment of mechanisms that fill these gaps and allow public managers access to information regarding the development and use of medical devices will allow the Ministry of Health and the members of GECIS a reliable parameter of the healthcare demands presented under the SUS, in order to subsidize them in the definitions set out in the decree that indicate the need to define the products and services that can implement the policy instruments defined by PNITS.

Conflicts of Interest Declaration   The authors declare that there is no conflict of interest.

References

1. Brasil. Ministério da Saúde. Secretaria de Ciência, Tecnologia e Insumos Estratégicos. Departamento de Ciência e Tecnologia. Política Nacional de Gestão de Tecnologias em Saúde/ Ministério da Saúde, Secretaria de Ciência, Tecnologia e Insumos Estratégicos, Departamento de Ciência e Tecnologia. – 1. ed., 1. reimpr. – Brasília: Ministério da Saúde, 2011. 48 pp.
2. Brasil. Ministério da Saúde. Secretaria de Ciência, Tecnologia e Insumos Estratégicos. Departamento de Ciência e Tecnologia. Política nacional de ciência, tecnologia e inovação em saúde/Ministério da Saúde, Secretaria de Ciência, Tecnologia e Insumos Estratégicos, Departamento de Ciência e Tecnologia – 2. ed.– Brasília: Editora do Ministério da Saúde, 2008. 44 pp.
3. Brasil. Decreto nº 9.245, de 20 de dezembro de 2017 que institui a Política Nacional de Inovação Tecnológica na Saúde

Attenuation Coefficient Variation as a Function of Temperature in a Cortical Bone Phantom

Rebeca M. Souza, R. P. B. Costa-Felix, and André V. Alvarenga

Abstract

The ultrasonic properties vary depending on the temperature, thus the complete characterization of the material must include its behavior in function of this magnitude. The present article reports an experimental study that estimates the attenuation coefficient of ultrasound in a cortical bone phantom for the temperature range varying between 19 and 37 °C. This study performs a metrological approach, which presents the measurement uncertainty estimates of the measured attenuation coefficients for each temperature. The uncertainty model was proposed based on the Measurement Uncertainty Expression Guide. The results of the attenuation coefficient indicate a tendency to increase linearly as a function of the temperature increase. Hence, different values of attenuation coefficient should be considered when temperature varies in simulations or experimental procedures, and this has important implications for the research results carried out in bone phantoms.

Keywords

Ultrasound • Attenuation coefficient • Cortical bone phantom

1 Introduction

Ultrasonic phantoms are specimens used to mimic acoustic properties of biological tissues and play a relevant role in the study of their interactions with ultrasound [1, 2]. Thus, they can be used for performance testing of ultrasound equipment and studies of the application of therapeutic and diagnostic ultrasound in biological tissues [3]. The ultrasonic properties vary depending on the temperature, so that the complete characterization of the material must include its behavior in function of this magnitude. Hence, it is important to know and consider how their acoustic properties vary with different temperatures. In addition, no studies were found in the literature concerning to measuring attenuation from a metrological approach. In this way, this work assesses the attenuation coefficient variation of a cortical bone phantom for temperature ranging from 19 to 37 °C, and respective measurement uncertainty.

2 Materials and Methods

2.1 Cortical Bone Phantom

For this study, a 10 mm-thick epoxy block with short fibers (Sawbones™, USA) that simulates the acoustical and mechanical properties of the cortical bone was used. The phantom thickness is estimated by the pulse/echo technique as 10.302 mm (U = 0.018 mm; p = 0.95).

2.2 Experimental Setup

The experimental setup consists on a 5 MHz nominal frequency, 12.7-mm-diameter single-crystal circular unfocused ultrasonic transducer acting as transmitter and receiver (model V303, Olympus, USA) [6]; an arbitrary waveform generator (model 33250 A, Agilent Technologies, USA) set to 20 V peak-to-peak amplitude, sine burst of 30 cycles, at 5 MHz to excite the transducer; an oscilloscope (model DSO 5012 A, Agilent Technologies, USA) to acquire the echo-signals; a water bath (Fisatom, Brazil) to heat the cortical bone phantom (Sawbones®, USA); a thermometer (Thermo-Schneider, Germany) to measure temperature throughout the measurement process. Despite the transducer is typically used in non-destructive testing, its construction

R. M. Souza (✉) · R. P. B. Costa-Felix · A. V. Alvarenga
Institute of Metrology, Quality and Technology (Inmetro), Duque de Caxias, RJ, Brazil
e-mail: rebecasouzam@gmail.com

A. V. Alvarenga
e-mail: avalvarenga@inmetro.gov.br

characteristics are robust enough to be used in such kind of research.

2.3 Measurement Procedure

The attenuation coefficient can be determined as the ratio of ultrasonic pressure values. The implemented measurement system is the same one that was used to determine the longitudinal propagation velocity by [4]. However, in addition to times of flight, different RMS amplitude voltages are also measured using the oscilloscope, which express the ultrasonic pressure of different echoes reaching the transducer.

After aligning the system for signal maximization, the system remains at rest for 40 min to achieve a thermal equilibrium. Thereafter, the times of flight and amplitudes of the reflected echo signals are measured, as shown in Fig. 1. First, the time of flight in the water (t_w) and the amplitude of the signal (V_{in1}), without the sample, are measured. Then, the sample is inserted and the time of flight at the sample surface (t_{w1}) is measured, as well as the amplitude of the echo signals reflected on the sample surface (V_{in2}), and the reflected echo at the opposite face of the phantom, passing through the sample (V_{in3}) (Fig. 2).

This experiment was performed under repeatability conditions. All values were measured at six different temperature values between 19 and 37 °C. At each temperature change, four repetitions of the measurements were carried out. After the temperature rise for a new measurement, a new thermal equilibrium was required for at least 30 min.

2.4 Measurement Uncertainty

The whole procedure was repeated three times and the uncertainties were estimated based on the Guide to Expression of Uncertainty in Measurement [5].

Fig. 1 a Experimental setup where one can observe the thermal bath, the thermometer, the signal generator and the oscilloscope. **b** Detail inside the thermal bath where it is possible to observe the transducer, the phantom and the steel reflecting target
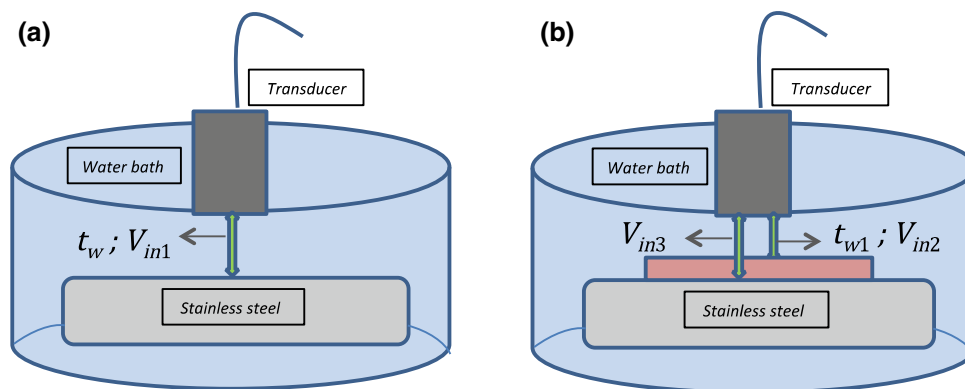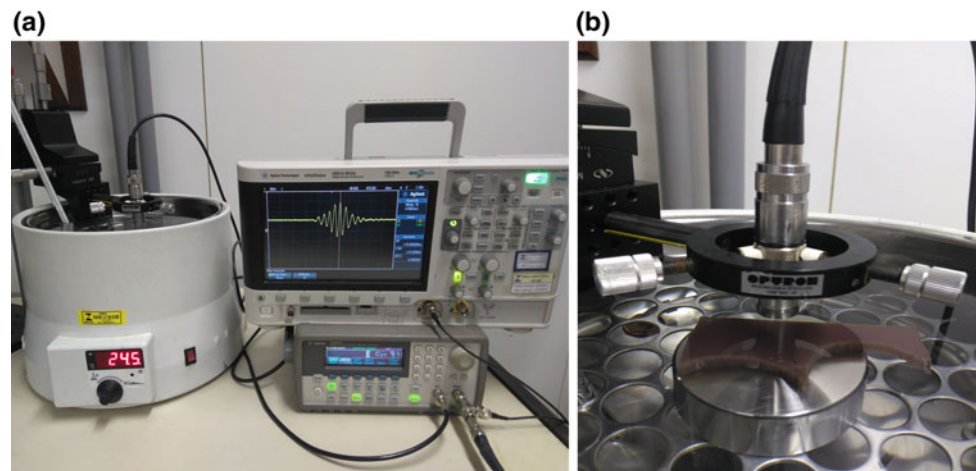
Fig. 2 Experimental Setup. **a** t_w: time of flight in the water; V_{in1}: amplitude of the signal without the sample; **b** t_{w1}: time of flight at the sample surface; V_{in2}: amplitude of the echo signals reflected on the sample surface; V_{in3}: the reflected echo at the opposite face of the phantom, passing through the sample

To determine the measurement uncertainty of the attenuation coefficient in the cortical bone phantom, the following sources of uncertainty were considered: the uncertainty of the calibration certificate of the thermometer (0.01 °C), the uncertainty of the time base of the oscilloscope (0.04% of measured time [s]), the uncertainty of the vertical amplitude scale of the oscilloscope (0.3% of the measured amplitude [V]), the uncertainty of the measurement of the thickness of the phantom $(0.018 \times 10^{-3} \, \text{m})$, the uncertainty of the calibration coefficient of the reflection coefficient in the steel (3.0×10^{-4}), the uncertainty regarding the water attenuation coefficient $(1.5 \text{dB} \cdot \text{m}^{-1})$, the uncertainty related to the correction due to diffraction (2.5%) [6] and the dispersion of the attenuation coefficient measurements.

3 Results

Tables 1, 2 and 3 present the results of attenuation coefficient measured at each temperature, their respective expanded uncertainties (U) and coverage factors (k), from three repetitions of the complete measurement procedure carried out in three different days.

Figure 3 presents the attenuation coefficient results from the three repetitions of the measurement procedure all together. One can observe that attenuation coefficient tends to increase linearly as temperature increase in the range of 19–37 °C.

4 Discussions and Conclusion

Many works have been assessing the attenuation coefficient on bone phantoms and samples, but none of them presents the results of the estimated measurement uncertainties. Nicholson and Bouxsein [7] evaluated the quantitative ultrasound dependency (QUS) at calcaneal temperature of five cadavers in situ in a temperature range of 25–40 °C. The velocity decreased linearly with the temperature rise, with an average thermal coefficient of −2.2 m/s/°C. Broadband ultrasonic attenuation increased with temperature, with an average thermal coefficient of +0.75 dB/MHz/°C. Kubo et al. [8] measured the propagation velocity and the attenuation coefficient in six bone marrow samples from different parts (proximal, middle and distal) of the femur of two bovine females, using a frequency range of 3–10 MHz, and

Table 1 Results of attenuation coefficient measured at each temperature, their respective expanded uncertainties (U) and coverage factors (k) for the first repetition of the measurement procedure

Temperature [°C]	Attenuation coefficient [dB/cm]	U [dB/cm]	k
20.7	6.71	0.26	1.96
24.6	7.28	0.22	1.96
26.9	7.83	0.19	1.96
30.0	8.41	0.23	2.03
33.0	8.95	0.20	1.98
37.2	9.61	0.20	1.96

Table 2 Results of attenuation coefficient measured at each temperature, their respective expanded uncertainties (U) and coverage factors (k) for the second repetition of the measurement procedure

Temperature [°C]	Attenuation coefficient [dB/cm]	U [dB/cm]	k
20.0	6.80	0.23	1.96
25.0	7.41	0.25	1.96
27.0	7.89	0.25	1.96
30.8	8.40	0.25	1.96
33.2	8.96	0.23	1.96
36.1	9.30	0.24	1.96

Table 3 Results of attenuation coefficient measured at each temperature, their respective expanded uncertainties (U) and coverage factors (k) for the third repetition of the measurement procedure

Temperature [°C]	Attenuation coefficient [dB/cm]	U [dB/cm]	k
20.2	6.97	0.24	1.96
24.7	7.67	0.21	1.97
27.0	7.97	0.23	1.98
30.0	8.45	0.26	2.00
33.1	9.15	0.20	1.96
36.5	9.63	0.21	1.96
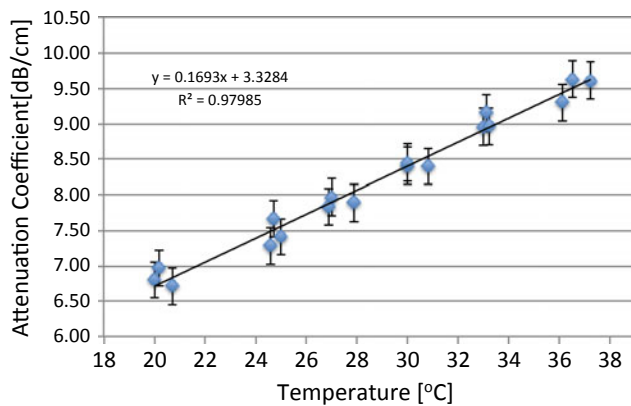
Fig. 3 The attenuation coefficient results from the three repetitions of the measurement procedure together

the temperature range was 15–40 °C. Both the wave velocity and the attenuation coefficient in the bone marrow always decreased as the temperature increased.

In this work, we observe that the attenuation coefficient on a cortical bone phantom tends to increase as temperature increase. Moreover, the uncertainty calculation was useful to help assessing the differences in attenuation coefficient for different temperatures. Thus, based on the uncertainty values obtained in this study, it can be stated that the measurement system produces results with uncertainties in the order of magnitude of those practiced in the literature for estimating the range of ultrasound propagation [9]. Finally, we conclude that different values of attenuation coefficient should be considered when temperature varies in simulations or experimental procedures, and this has important implications for the research results carried out in bone phantoms.

References

1. Souza, R., Santos, T., Oliveira, D., Souza, R., Alvarenga, A., Costa-Felix, R.: Standard operating procedure to prepare agar Phantoms. J. Phys. Conf. Ser. **733**(1), 012044 (2016)
2. Petrella, L., Maggi, L., Souza, R., Alvarenga, A., Costa-Felix, R.: Influence of subcutaneous fat in surface heating of ultrasonic diagnostic transducers. Ultrasonics **54**(6), 1476–1479 (2014)
3. Sellani, G., Fernandes, D., Nahari, A., Fabrício, M., Valois, C., Pereira, W., Machado, C.: Assessing heating distribution by therapeutic ultrasound on bone Phantoms and in vitro human samples using infrared thermography. J. Ther. Ultrasound **4**, 13 (2016)
4. Souza, R., Alvarenga, A., Costa-Felix, R.: The influence of temperature on the speed of sound of cortical bone phantom: a metrological view. J. Phys. Conf. Ser. **975**, 012021 (2018)
5. Inmetro. Avaliação de dados de medição: Guia para a expressão de incerteza de medição.: INMETRO/CICMA/SEPIN, Duque de Caxias, RJ (2008)
6. Zeqiri B., Lee N.: Comparison of 1 mm hydrophone calibrations in the frequency range 1 MHz to 15 MHz – Final Report. National Physical Laboratory-NPL (2005)
7. Nicholson, P., Bouxsein, M.: Effect of temperature on ultrasonic properties of the calcaneus in situ. Osteoporos. Int. **13**, 888–892 (2002)
8. Kubo, T., Fujimori, K., Cazier, N., Saeki, N., Matsukawa, M.: Properties of ultrasonic waves in bovine bone marrow. Ultrasound Med. Biol. **37**(11), 1923–1929 (2011)
9. Santos, T., Alvarenga, A., Oliveira, D., Costa-Felix, R.: Metrological validation of a measurement procedure for the characterization of a biological ultrasound tissue-mimicking material. Ultrasound Med. Biol. **43**, 323–331 (2016)

Calibration of Defibrillator Analyzer by Voltage Square Method

Fabrício Gonçalves Torres, Felipe Santiago Apolinário,
Regis Renato Dias, and Tiago Lopes Santos

Abstract

Defibrillator is an electromedical equipment used to rescue patients with cardiac arrhythmias. The success rate in the use of the equipment is high, however, it is necessary that the defibrillator is in good condition and, therefore, must be tested by means of a defibrillator analyzer. There is a need for the defibrillator analyzers to be calibrated and their measurements have metrological traceability. The measurements carried out by the analyzers must not exceed the tolerances determined by the medical standards and therefore the equipment used in the calibration of these devices must have an uncertainty lower than the required tolerances. The present work has the purpose of presenting a calibration method of defibrillator analyzer by means of the integration of voltage square level, which has an uncertainty lower than the tolerance required by the standards of electromedical. The uncertainty components that are relevant for calibration are described. The proposed method was tested in the calibration of a defibrillator analyzer and the results obtained from the calibration are presented.

Keywords

Analyzer defibrillator • Calibration • Metrology

1 Introduction

Defibrillator is an electromedical equipment that has the purpose of reverting cardiac arrhythmias of patients, through the application of electric energy on the patient's chest, being able to reach levels up to 360 J. The practice of defibrillation is highly recommended in emergency situations, as in cases of ventricular fibrillation, because a great chance of saving the patient's life is obtained, especially if used early [1].

The first experiments with defibrillation began in 1899 and until the 1960s, alternating current signals (60 Hz) were used. Subsequently, studies showed better results in defibrillation by means of direct current. Presently, two types of defibrillators are more common: monophasic and biphasic, the latter, more recently developed, represents greater patient safety and efficiency [1].

Monophasic defibrillation is a technique which involved charging of a bank of capacitors to the energy desired then delivering the charge through an inductance such as to produce a heavily damped sinusoidal wave of short duration, approximately 5 ms, to the heart by way of paddle electrodes, having a mainly uniphasic characteristic. On the other hand, biphasic defibrillation alternates the direction of the pulses, completing one cycle in approximately 12 ms (Fig. 1).

Like any electronic equipment, a defibrillator can cause failures over time, including applying energy levels with errors greater than the tolerances determined by the standards, such as ABNT NBR IEC 60601 (2016). Therefore, these devices must be tested regularly by means of a defibrillator analyzer. In turn, a defibrillator analyzer must be calibrated periodically, by means of standards that can guarantee the chain of metrological traceability of the measurements.

According to [2], to comply with the standards ABNT NBR IEC 60601-2-4: 2005 and ANSI/AAMI DF80: 2003 the energy measurement of a defibrillator analyzer must have a tolerance of $\pm 5\%$ of the measured energy or ± 1 J, whichever is greater, and therefore it is recommended that the measuring system used to perform the calibration has lower uncertainties than the recommended tolerances.

In the literature, several calibration methodologies for defibrillator analyzers can be found. In [3], it is recommended that the calibration of the analyzer be performed on each block of the equipment separately: internal attenuator, filter and A/D converter block. However, in order to perform

F. G. Torres (✉) · F. S. Apolinário · R. R. Dias · T. L. Santos
Instituto de Pesquisas Tecnológicas do Estado de São Paulo – IPT,
São Paulo, Brazil
e-mail: fabrigt@ipt.br
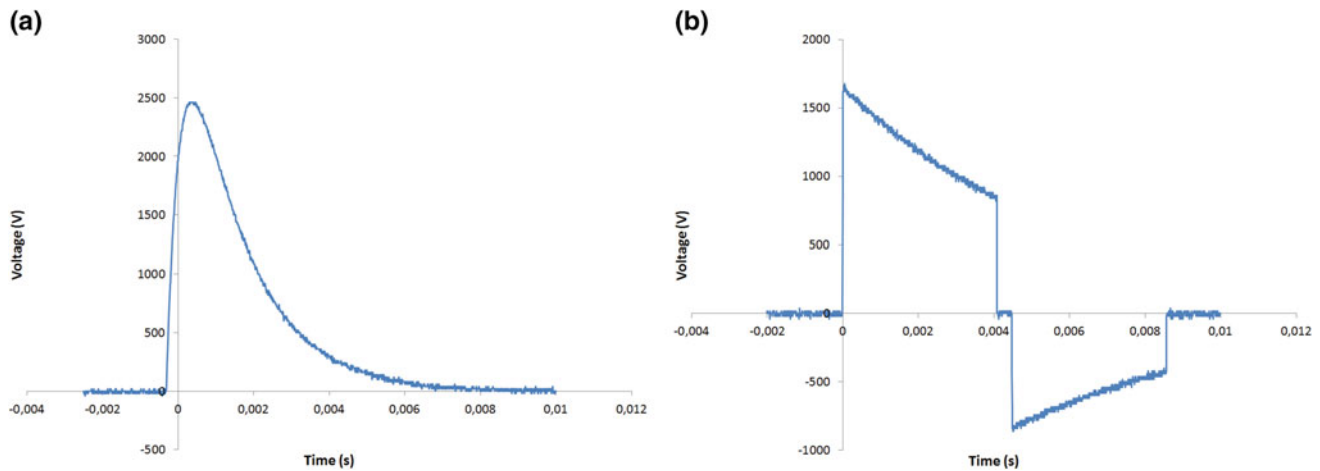
Fig. 1 Monophasic waveform (**a**) and biphasic waveform (**b**)

it, it is necessary to open the equipment and identify its main parts. This practice becomes difficult to perform by calibration laboratories since there is a need to have information about equipment that is not normally available by manufacturers. Another relevant issue is about the fact of the calibration being performed under different circumstances of the use of the item under calibration may present risks in the reliability of the results obtained. Finally, we don't recommend opening physically any instrument to calibrate it.

In [4], there are at least two ways of calibrating the energy range of a defibrillator analyzer: by simultaneously measuring the current and voltage applied by a defibrillator, or by measuring the resistance of the load and the voltage applied. The second case was the method adopted in this work. According to [4], the difference between the two methods is of the order of 0.05%, a negligible value as compared with the other uncertainty components of the calibration set.

2 Description of Materials and Method

The method adopted for this work consisted in measuring the resistance of the defibrillator analyzer by means of a high accuracy resistance meter and in the plot of the voltage curve as a function of time by means of a high voltage probe coupled to a digital oscilloscope. A commercial defibrillator with monopolar waveform was used as a transfer device and the energy points of 12, 25, 90, 180, 275 and 345 J were

available and adopted, since they are values typically applied by any defibrillator for adult treatment.

From the plotted curve, the square voltage values were integrated, according to Eq. 1.

$$Energy\ (J) = \int \frac{V_t^2}{R} dt = \left(\sum_{T_i}^{T_F} V_t^2 \right) \times \left(\frac{\Delta T}{R} \right) \quad (1)$$

where,

V_t peak voltage measured by the probe coupled to an oscilloscope

R resistance of the defibrillator analyzer

T_i and initial and final time of the plotted curve (record
T_F length)

ΔT quantization interval of the plotted curve.

For the quantization of the waveform, the oscilloscope function was used to measure the area. It was also developed, through LabVIEW®, a system that allowed presenting the results directly in Joule (Fig. 2). These results were considered as Reference Values, and were used to compare with the values indicated by the defibrillator analyzer under calibration.

It was also necessary to characterize the high voltage probe and the oscilloscope set by means of low uncertainty standards to obtain a calibration system with sufficient uncertainty for the calibration of the defibrillator analyzer. The characterization consisted basically in the determination of the nonlinearity of the high voltage probe and in the
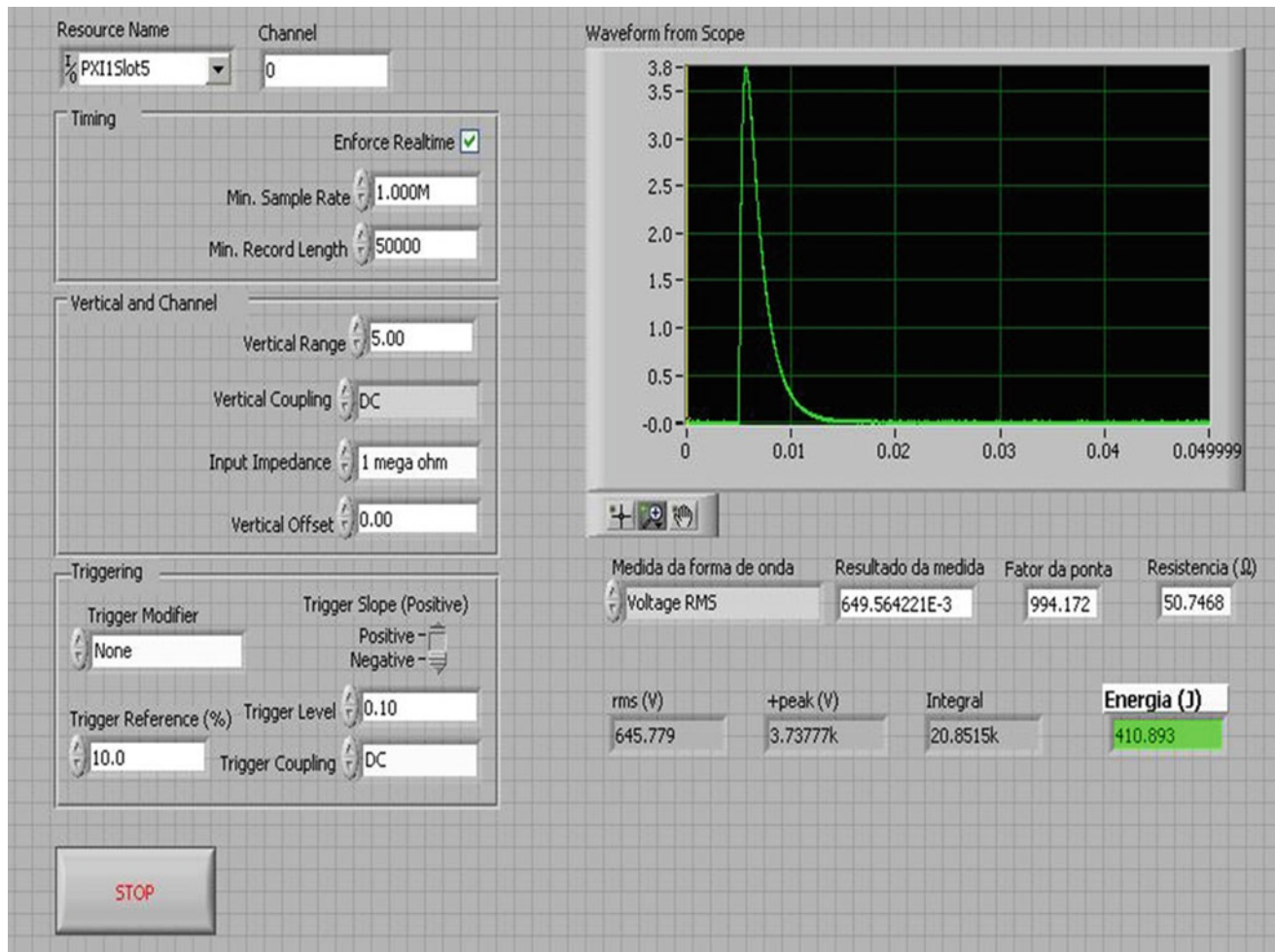
Fig. 2 Software developed for energy measurement

determination of the systematic and random error of the probe oscilloscope set.

2.1 Determination of the High Voltage Probe Nonlinearity

This method consists of the calibration of the Tektronix P6015A probe, whose output impedance is 1 MΩ, coupled to the National Instruments High Speed Digitizer PXI-5124 board, using the standard Fluke 5700A calibrator, thus determinating the uncertainty of the set.

To ensure the conditions of use of the equipment involved, the warm-up was met and the standards were self-adjusted, according to the manufacturers recommendations.

Typically, high voltage probe has accuracy specifications as high as some defibrillator analyzer, so it was necessary to study and characterize individual components of uncertainty to be able to use in this calibration.

For a complete analysis of the linearity of the set, DC voltage values (500, 1000, 3000 and 5000 V; negative and positive) and AC voltage (500, 1000, 3000 and 5000 V; with 60 Hz) were applied at the input of the high voltage probe. This values were choosed because any voltage generated by a defibrillator (biphasic waveform or monophasic waveform) was included in this interval.

The data acquisition software LabVIEW® was used for the acquisition of 4 readings of each value applied. The results were analyzed and the uncertainty due to the non-linearity of the set probe and high speed digitizer was determined.

2.2 Characterization of the Probe and Oscilloscope Set

Characterization of the probe and oscilloscope set is performed by means of Fluke 5700A multifunction calibrator, applying a 1000 V AC sinusoidal waveform with frequency

60 Hz. Measurements are performed before and after calibration of the defibrillator analyzer, in order to detect any variation of the set during the calibration.

The systematic and random error values obtained in the characterization was assigned as components of uncertainty and included in the final calibration uncertainty of the defibrillator analyzer.

3 Estimation of Uncertainty

The Table 1 summarizes the distribution assignments made for each input quantity of the measurement model.

From Eq. 1, in relative values, the combined standard uncertainty is calculated according to Eq. 2.

$$\left(\frac{u_E}{E}\right)^2 = \frac{\left(\frac{-E}{T}\right)^2 u_T^2 + \left(\frac{E}{R}\right)^2 u_R^2 + 2\left(\frac{E}{V}\right)^2 u_V^2}{E^2} \qquad (2)$$

Table 1 Components of energy measurement uncertainty

Quantity	Probability distribution function
Uncertainty due to variability	Gaussian
Resolution of the defibrillator analyzer	Rectangular
Uncertainty due to load resistance	Gaussian
Uncertainty due to probe and oscilloscope set for time interval	Gaussian
Uncertainty due to probe and oscilloscope set for voltage measurement	Gaussian
Resolution of the probe and oscilloscope set	Rectangular
Voltage probe nonlinearity	Rectangular

where,

u_E combined standard uncertainty of the energy measurement

u_T standard uncertainty due to probe and oscilloscope set for time interval

u_R standard uncertainty due to load resistance

u_V standard uncertainty due to probe nonlinearity and probe and oscilloscope set for measuring voltage.

The u_R uncertainty was obtained by measuring the internal resistance of the defibrillator analyzer under calibration using a digital multimeter. The uncertainty components taken into consideration for the u_R calculation were: uncertainty and resolution of the standard multimeter and variability from four resistance readings.

For the u_T uncertainty, the component was considered due to time base of the oscilloscope on the sampling rate of the oscilloscope (1 MS/s) resulting in the time interval of 1 μs.

The uncertainty u_V was calculated by means of the following uncertainty components: nonlinearity (described in Sect. 2.1) and characterization of the probe and oscilloscope set (described in Sect. 2.2).

The expanded uncertainty was obtained by multiplying the combined standard uncertainty with the coverage factor to a confidence level of approximately 95%.

4 Results

The results of the calibration of the defibrillator analyzer are shown in Fig. 3. For each point of the graph, there was its respective expanded uncertainty of the measurement represented by means of the vertical bars. The dotted lines of red color represent the tolerance of ±5% of the measured energy

Fig. 3 Results of the defibrillator analyzer calibration
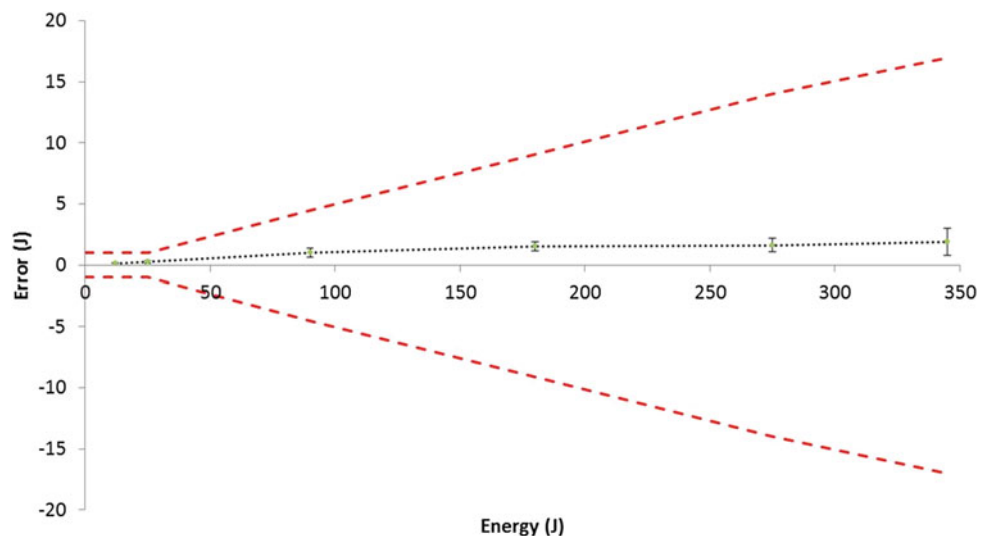
Table 2 Detailed defibrillator analyzer calibration values

Value (J)	Error (%)	U (%)	k	ν_{eff}
12	1.29	0.53	2.00	∞
25	0.96	0.52	2.25	12
90	1.14	0.42	2.25	11
180	0.84	0.21	2.01	209
275	0.60	0.20	2.01	189
345	0.55	0.32	2.28	11

or ± 1 J, whichever was greater, complied with the standards ABNT NBR IEC 60601-2-4: 2005 and ANSI/AAMI DF80: 2003.

Table 2 contains the most detailed information on calibrated points. For each point, the following information was reported: measurement error, expanded uncertainty (U), coverage factor (k) and degrees of freedom (ν_{eff}).

5 Analysis of Results

For the defibrillator analyzer, the maximum permissible measurement error is defined by the main reference standards for electromedical [2]. In the Fig. 3, it can be verified that the proposed calibration method was adequate, since the uncertainty obtained resulted in a value 10 times lower than the tolerance for this equipment.

According to Table 2, it was verified that the expanded uncertainty of the measurement was proportionally higher for the smaller values. This feature was due to the resolution of the defibrillator analyzer under calibration, which ends up contributing significantly to the low energy values. For the higher values, the uncertainty of the standards set is the most significant portion for the expanded uncertainty.

6 Conclusion

This work presented a method of calibration of the energy range of defibrillator analyzers that could be feasible its application to calibration laboratories, and that allowed obtaining, in its results, low enough uncertainties to meet the determinations of electromedical standards.

Although it is not the scope of the work, it can also be verified that the method can be used to calibrate any type of waveform (monophasic or biphasic, for example), since the developed system is versatile enough to perform the measurement of the energy for any waveform.

Perhaps the only disadvantage of the proposed calibration method could be the need to use a defibrillator as the transfer device. However, it is verified that it is the most reliable means to carry out the calibration, since it uses a signal with the same characteristics whose defibrillator analyzer must be able to measure with the best accuracy. Calibrating the equipment by applying another type of waveform may mask some type of error that is detectable only with the waveform of a defibrillator.

References

1. Fornazier, C., Melchior, S.C., Buss, G., Trindade, E., Pereira, A.A., Barbieri, D.X., Silva, J.E.L., Holsbach, L.R., Perlato, M.T., Glowacki, L.A., Almeida, A.P., Cruz, C.J.F.: Abordagem de Vigilância Sanitária de Produtos para Saúde Comercializados no Brasil: Desfibrilador Externo. Boletim Informativo de Tecnovigilância, Nº 01, Brasília, (2011)
2. Moraes, J.C.T.B., Oliveira, C.A.: Especificações mínimas aceitáveis de um analisador de desfibriladores e cardioversores. Braz. J. Biomed. Eng. **28**(2), 179–189 (2012)
3. Oliveira, C.A., Moraes, J.C.T.B.: Metodologia de avaliação metrológica da medição de energia para analisadores de desfibriladores e cardioversores. Braz. J. Biomed. Eng. **28**(3), 205–216 (2012)
4. Wei, Z., Haiming, S., Feipeng, L., Bo, L., Jiandong, D.: Energy calibration technique of defibrillator analyzer. In: IEEE 12th International Conference on Electronic Measurement and Instruments (2015)

Development and Validation of a Device for Mechanical Bend Test in Cardiac Defibrillators Electrodes Cables in Accordance with ABNT NBR IEC 60601-2-4:2014

Felipe Fava de Lima and José Carlos Teixeira de Barros Moraes

Abstract

The reliability and safety in electromedical equipment identified by certification tests mainly depend on the use of measuring instruments and appropriate testing devices. According to the subclause 201.15.4.101 of the Technical Standard ABNT NBR IEC 60601-2-4:2014, cardiac defibrillators cables and electrodes must be tested to mechanical bend endurance using a suitable electromechanical device. The present article describes the development and validation of a device to be employed in a Tests Laboratory accredited by CGCRE/INMETRO to perform this conformity test.

1 Introduction

The ABNT NBR ISO 601 series of Technical Standards are used in the certification process of electromedical equipments in Brazil. These normative documents prescribe various essential safety and performance tests to be executed on electromedical equipments and systems to ensure quality.

The particular Technical Standard ABNT NBR IEC 60601-2-4:2014 [1] defines a set of requirements for basic safety and essential performance applicable to cardiac defibrillators. The subclause 201.15.4.101 of this Standard defines a bend test to the defibrillator cable electrode. This test must be performed using a device similar to the one shown in Fig. 1. This device must perform 5.000 bend cycles on the connection point between the defibrillator

F. F. de Lima (✉) · J. C. T. de Barros Moraes
DEC-LEB-EPUSP - University of São Paulo, São Paulo, SP, Brazil
e-mail: felipe@leb.usp.br; felipefavadelima@gmail.com

electrode handhold and the defibrillator electrode cable (see Fig. 1), with bend angles of $\pm 45°$ or $\pm 90°$, depending on the electrode type, in a rate of 30 cpm (cycles per minute). Similar test is also requested on [2–6].

Some commercial cable bend devices are available to perform this kind of test as GT-7062-A (GoTech, Taichung City, Taiwan), Mattke D-79108(Mattke, Freiburg, Germany) and RS-810B (Infinity Machine, China), but for what is know so far does not exist any published work detailing the development and validation of such type of device.

In order to capacitate the infrastructure of the accredited tests laboratory DEC-LEB/EPUSP to perform this type of test and to contribute with the literature in this area, the development and validation of an device, as outlined in Fig. 2, is describe in this work.

2 Materials and Methods

2.1 Mechanical Project

The electrode holder is responsible to support the defibrillator handhold and allows cable bending when rotated (See Fig. 1). The bend action can be driven by an electric, pneumatic or hydraulic actuator. For the sake of simplicity an electric motor was chosen to drive the electrode holder. To actuate the electrode holder, the electric motor shaft can be directly coupled to the electrode holder, being necessary an electronic circuit to switch the motor direction (Fig. 3 left side), or connected to a rotating wheel (Fig. 3 right side). In this work was chosen the direct couple between the electric motor shaft and electrode holder allowing a smaller mechanical structure design.

The electric motor could be able to rotate both clockwise and counterclockwise with a minimum speed of 30 rpm (rotations per minute), following the Standard requirements. This actuator also should produce a minimum torque of 1.5 Nm. This torque was estimated assuming a maximum load of 1 kg and a rotation arm of 15 cm, based on a worst
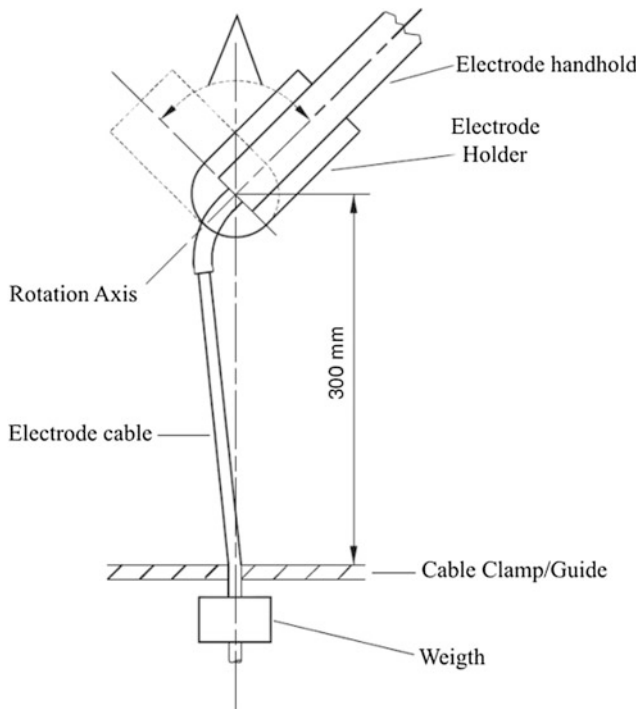
Fig. 1 Device to be used on the defibrillator electrode cable mechanical bend test as suggested by ABNT IEC 60601-2-4:2014 (Image copied and translated from ABNT IEC 60601-2-4:2014)

test case. Given the actuator specifications, a D.C. (Direct Current) electric motor (Bosh F006B20145, Bosh, Gerlingen, Germany) was selected for this finality.

A mechanical structural design was elaborated on a CAD (Computer Aided Design) tool (OnShape, OnShape Inc., EUA) (See Fig. 4 left side). This structure was designed to support the DC motor at a minimum height that would allow a distance of 300 mm between the electrode holder and the cable Clamp/Guide as the Standard Requirement (See Fig. 1) and also to give support to all electronic parts, as power supply and PCBs (Printed Circuit Boards).

The CAD project was used in a water jet cutter (Omax 55100, Omax, Kent, Washington, USA) to cut a 1050 aluminum sheet 3 mm thick. The cut parts were folded in a manual folder (Imag 2050, Imag, Limeira, São Paulo, Brasil) and hand sanded to eliminate all sharp edges. The assembled mechanical structure is shown on the right side of Fig. 4.

2.2 Hardware Project

An electronic circuit to control the D.C. motor and to interface with an operator through a personal computer, as schematized in Fig. 5, was developed.
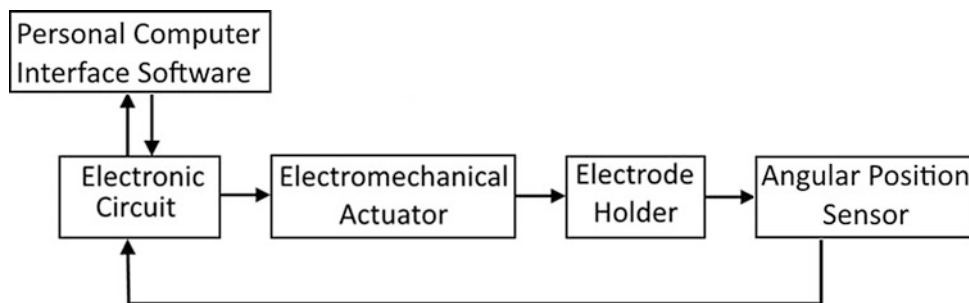
Fig. 2 Scheme of the developed device to perform the required test
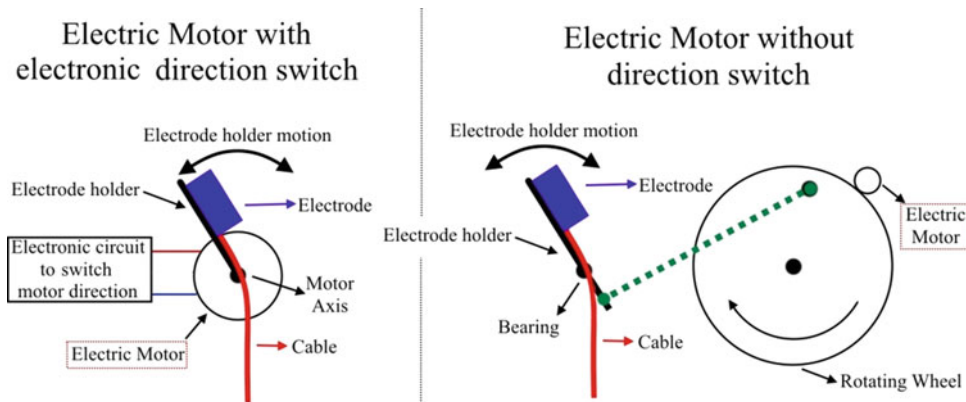
Fig. 3 Electrode holder actuation schemes. Left side: Electric motor shaft directly coupled to the electrode holder and electric motor driven by an electronic direction switcher. Right side: Electric motor, driven without electronic direction switcher, connected to a rotating wheel producing the bend motion of the electrode holder
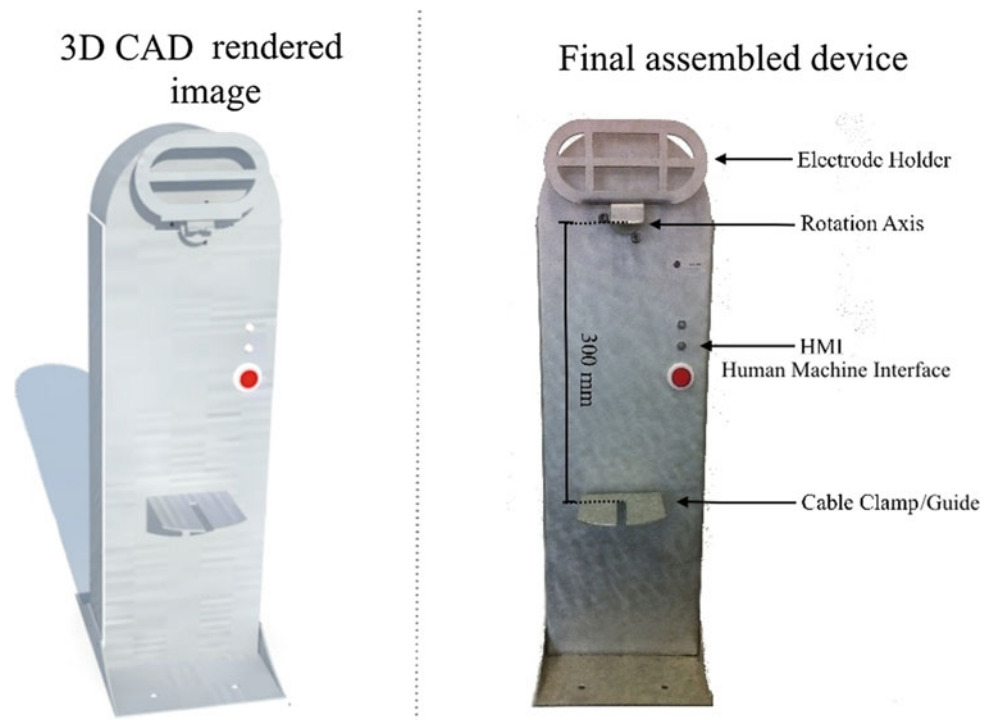
Fig. 4 Left side: Rendered 3D CAD image of developed mechanical structure. Right side: Final assembled mechanical structure
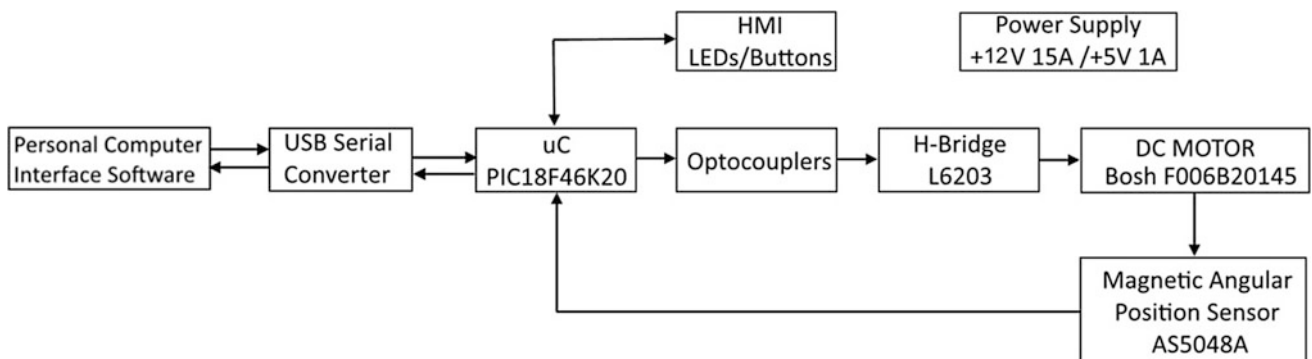
Fig. 5 Electronic circuit scheme

A magnetic rotary sensor (AS5048A, AMS AG, Austria) I.C. (Integrated Circuit) was selected as angular position sensor to measure the electrode holder angular position. This integrated circuit allows determining angular position without any mechanical contact between the rotating part and the sensor. Two cylindrical 6 mm × 5 mm N42 neodymium magnets were fixed to the motor shaft to produce a magnetic field detected by the sensor, placed 3 mm apart from these magnets (See Fig. 6). This assembly allowed the measurement of the angular position of the motor shaft and consequently of the electrode holder.

A fully integrated H-bridge I.C. (L6203, STMicroelectronics, Schiphol, Amsterdam, Netherlands) was employed to drive the D.C. motor. This I.C. can withstand an electric
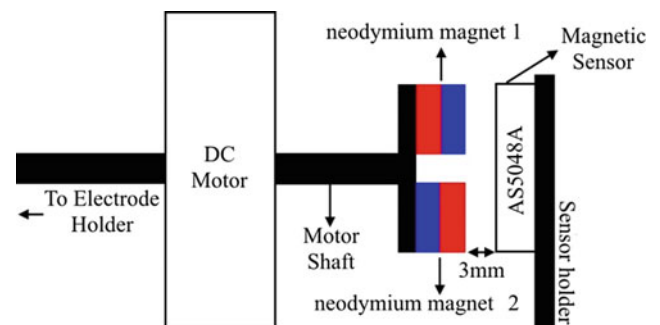
Fig. 6 Magnetic rotary sensor assembly

current up to 4 A and a maximum working voltage of 48 V, specifications higher than those required to drive the motor.

Both magnetic rotary sensor and H-bridge I.C.s are read and controlled by a µC (Microcontroller) (PIC18F46K20, Microchip, EUA). The µC drives the H-bridge I.C. controlling the motor direction and speed based on the angular information provided by the sensor. The rotation speed is controlled by PWM (pulse width modulation) regulated by a P.I. (proportional integrative) controller firmware implemented. This P.I. controller allows keep the same rate of 30 cpm, as specified by the Standard, for different adjusted bend angles. The coefficients of the P.I. controller were adjusted through empirical tests.

The logical part of the circuit is isolated from the H-bridge I.C. by optocouplers preventing that electrical surges, emanated from motor switching, reaches and damages any digital component, mainly those which are part of the connected personal computer.

The µC is also responsible to count the number of bends and stop the mechanical endurance test after a specified target number has been reached. An operator can interface with the device through a software executed on a personal computer. The communication between the computer and the µC is accomplished by means of an USB (Universal Serial Bus) to Serial converter I.C. (FT232R, FTDI, Glasgow, Scotland).

Two LEDs (Light-emitting Diodes) and one emergency button, also driven by the µC, enable a simple HMI (human machine interface) between an operator and device. The LEDs show the device status, and the emergency button can be pressed to stop a running test.

The µC firmware was developed in C programming language using the IDE (Integrated Development Environment) supplied by the µC manufacturer (Mplab X, Microchip, USA).

A generic 500 W ATX power supply was employed to supply all necessary electrical energy to the device.

Two PCBs were designed on an EDA (Electronics Design Automation) software (KiCad4.0, www.kicad-pcb.org). One PCB was designed to support the magnetic sensor close to the neodymium magnets installed on the motor shaft

(See Fig. 6) and one to the remaining components. PCBs and electronic components soldering were handmade.

2.3 Software Project

A LabView visual language (LabView 2014, National Instruments, USA) software was developed to allow the device interface with an human operator through a personal computer. This software allows the operator to configure some test parameters, as number of bends to be done and bending angle and speed (See Fig. 7). Also is provided a gauge indicating current bend angle, and some text boxes showing the number of bends executed and the elapsed time. Through four buttons is possible to start, stop, pause or continue an endurance test.

2.4 Device Validation

Before the developed device be used in bend tests of cardiac defibrillators cables electrodes in the accredited Laboratory DEC-LEB/EPUSP, it had to be validated. The instruments used on the validation process of the device were verified or calibrated in some Laboratory that participates of the Brazilian network of calibration, RBC (Rede Brasileira de Calibração).

A generic 5 mm thick test cable was used to simulate a cardiac defibrillator electrode cable. A mass was tied, as required by the Standard, to one cable end and the other cable extremity was tied to the electrode holder (See Fig. 8). A 1 kg mass was chosen to simulate a worst case weight defibrillator electrode.

The validation was performed by a previously verified accelerometer (ADXL05, Analog Devices, USA) connected to an Arduino Uno R3 board (Arduino, Italy) analog input port and a calibrated chronometer.

The accelerometer was fixed to the device electrode holder measuring the resulting gravitational force actuating
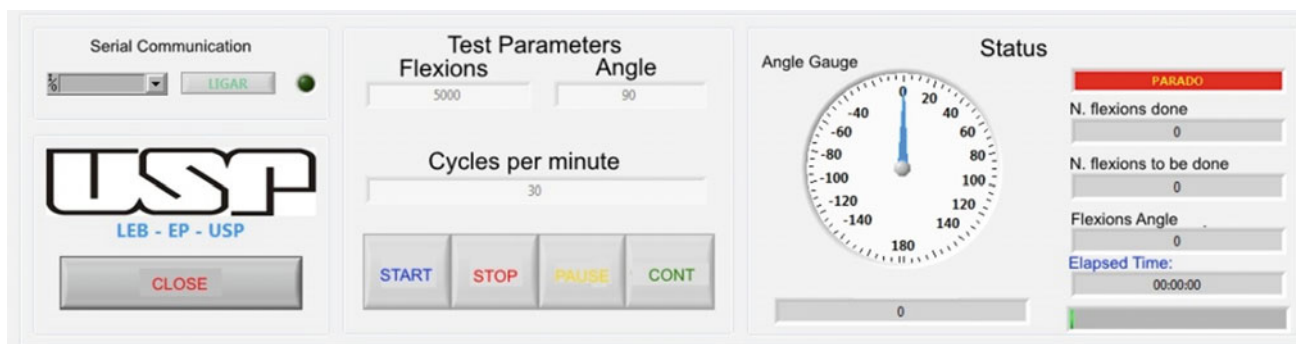
Fig. 7 Developed software to interface with a human operator
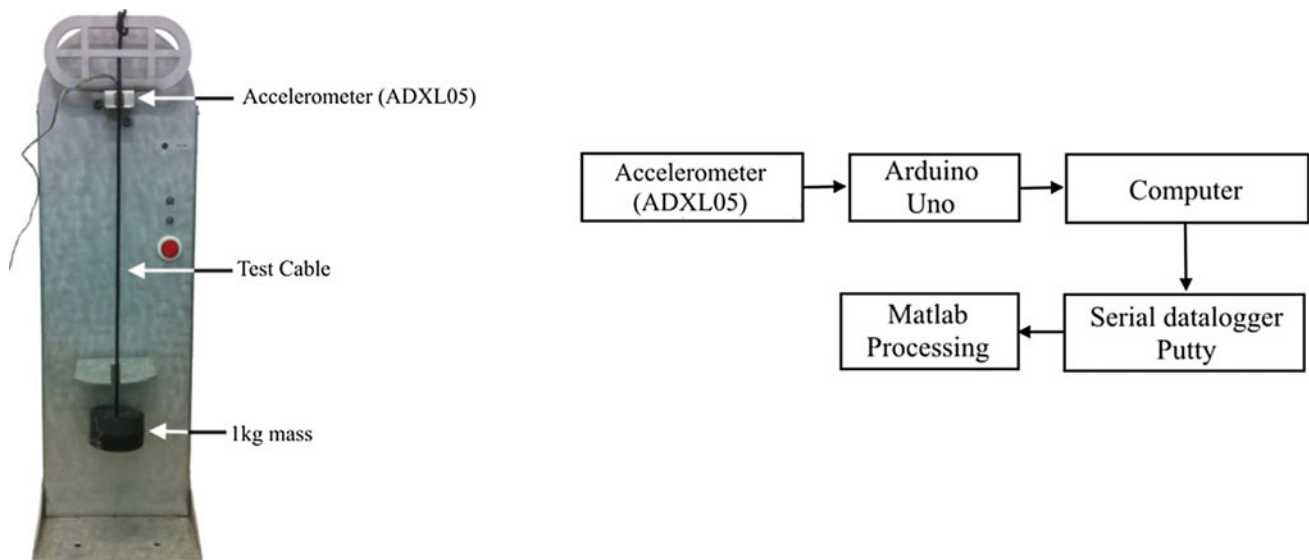
Fig. 8 Validation scheme
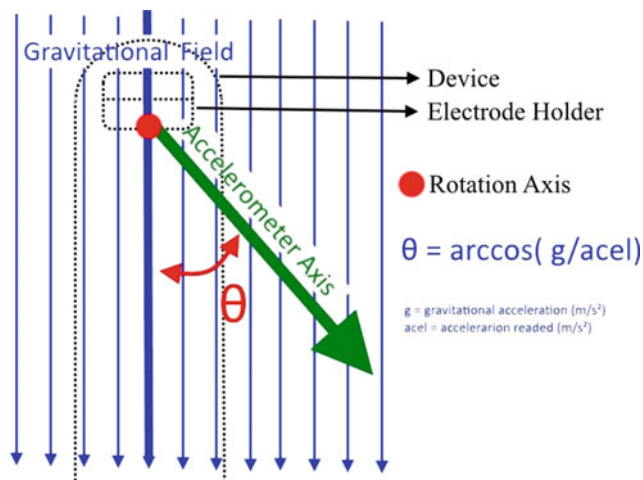
Fig. 9 Bend angle measurement of the electrode holder using an accelerometer

on its main axis, allowing the measurement of the electrode holder rotation angle in relation to the vertical axis (See Fig. 9). The accelerometer output was connected to one of the Arduino 10-bit analog inputs. The Arduino was programmed to convert the measured analog data in a digital value with sample frequency of 100 Hz and to send this value to a personal computer by the serial port. Also an elapsed time stamp was sent by the Arduino at every sent data. A serial datalogger software (Putty, www.putty.org) was used to record all data sent by the Arduino to a digital

file (See Fig. 8). The time stamps sent by the Arduino were validated using the calibrated chronometer. The final digital file recorded was analyzed in a numerical analysis software (MatLab 2014, MathWorks, USA). The number of blend cycles, cable blend angle and blend rate were estimated in the numerical analyses.

As the Standard for this test doesn't specify the acceptable values for a valid device, it was adopted that the device would be considered valid if it could execute exactly 5000 bend cycles, with angles bends with mean error lesser than 5° and standard deviation lesser than 10°, both for ±45° and ±90°, and rotation speed with mean error lesser than 1 cpm and standard deviation lesser than 1 cpm.

3 Results

For bends of 90° (±45°) the device showed a mean angle bend of 91.6°, resulting in a mean error of 1.6°, with a standard deviation of 1.3°. The mean rate of bend in this situation was 29.8 cpm, resulting in a mean error of 0.2 cpm, with a standard deviation of 0.7 cpm (See Fig. 10).

For bends of 180° (±90°) the device showed a mean angle bend of 179.9°, resulting in a mean error of 0.1°, with a standard deviation of 6.1°. The mean rate of bend in this situation was 30.1 cpm, resulting in a mean error of 0.1 cpm, with a standard deviation of 0.2 cpm (See Fig. 11).

The device performed exactly 5000 bend cycles on both situations.
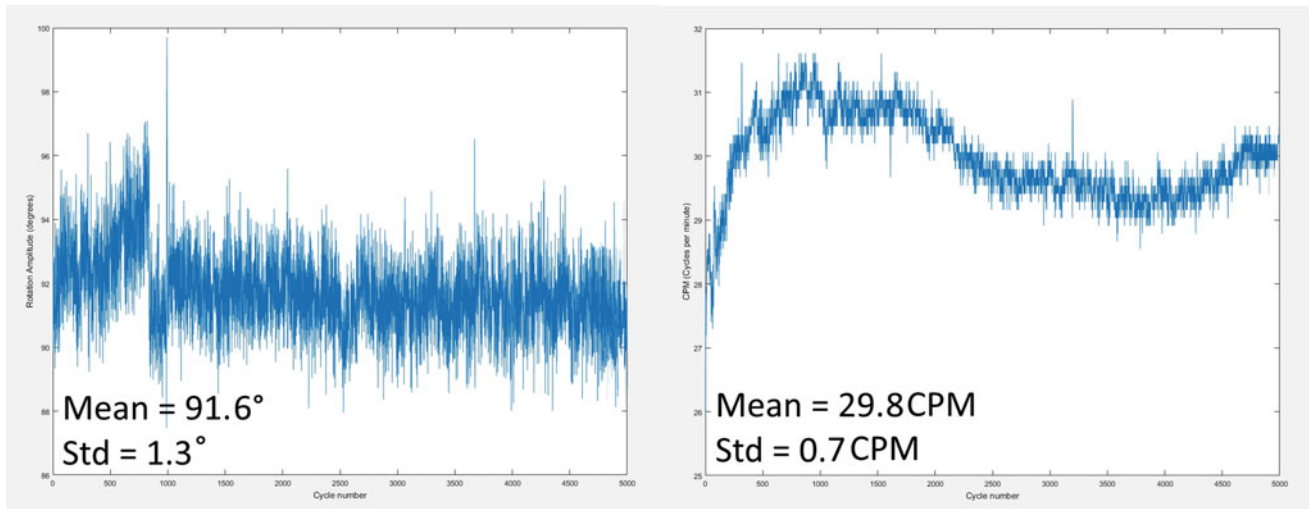
Fig. 10 90° (±45°) bend validation data and results
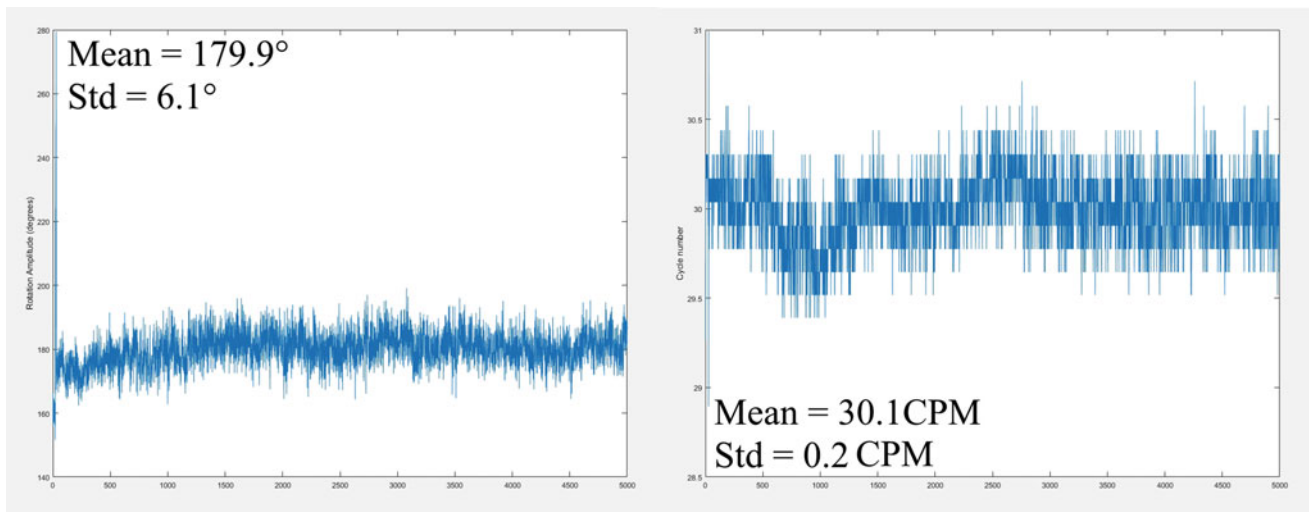
Fig. 11 180° (±90°) bend validation data and results

4   Discussion

The device developed was considerate valid to be used in electromedical certification tests by the accredited Laboratory DEC-LEB/EPUSP since during the validation process it executed exactly 5000 bend cycles, with angles bends with mean error lesser than 5° and standard deviation lesser than 10°, and rotation speeds with mean error lesser than 1 cpm standard deviation lesser than 1 cpm, for ±45° and ±90°.

The criterion used for acceptance of the device in the validation process is questionable since it is not defined by the Standard. But it is considered that the adopted criterion does not affect any quality test.

During the first use of the device was noticed excessive heating of the D.C. motor. In order to solve this problem an 80 × 80 mm fan was installed on the device cabinet.

Also it was noted excessive heating of a resistor used as snubber of the switching circuit of the D.C. motor. The original 1 W resistor was replace by one of 10 W, solving the problem.

The software code part responsible for the serial communication between the computer and the μC did not prove to be reliable, causing software freezing, fortunately, without losing test continuity. This problem has not been solved but for a next version of this device it would be a solution if all system control would be done without using a personal computer, probably increasing system reliability.

As the device must perform 5.000 bend cycles, a test has duration of approximately 2.5 h. As the device loses all test information if de-energized, it is recommended to plug it to a no-break system when performing a test, avoiding an unexpected power fail. Another solution, for a future version, should be to keep in an EEPROM memory the test status, preserving the test condition even in a power loss situation.

Comparing Figs. 9 and 10 right sides is noticed that the device control has a better performance for the 180 ($\pm90°$) degrees situation, evidenced by the obtained standard deviation values. This is not considerable an unacceptable behavior, but for a future version a better study of the PWM motor control system should be done to try to find a better control algorithm, since the adopted one was developed by empirical tests.

An Arduino Board Uno R3 connected to a serial Data logger, as used in the described validation process, proved to be an effective tool to simple data acquisitions that can replace expansive systems in these simple situations.

Despite the suggested modifications to be made in a future version, the developed device shown to be capable of being used in the certification process of electromedical equipments.

5 Conclusion

A mechanical and electronic project was developed in order to assembly a device to perform the bend test described on the subclause 201.15.4.101 of the particular Technical Standard ABNT NBR IEC 60601-2-4:2014 [1] in cardiac defibrillators electrode cables.

A validation process using calibrated instruments by Laboratories that participates of the Brazilian network of calibration was designed and evaluated on the device. This process validated the device to be used in electromedical equipment certifications tests in the Test Laboratory, accredited by CGCRE/INMETRO, DEC-LEB/EPUSP.

The development described in this work can help other test Laboratories or electromedical manufactures, who want test your own equipment before a real certification process, to assembly a similar device.

References

1. Associação Brasileira de Normas Técnicas (ABNT): ABNT NBR IEC 60601-2-4: Equipamento eletromédico Parte 2–4: Requisitos particulares para a segurança básica e o desempenho essencial de desfibriladores cardíacos (2014)
2. International Electrotechnical Commission (IEC): IEC 60601-2-4: Medical electrical equipment—Part 2–4: Particular requirements for the basic safety and essential performance of cardiac defibrillators (2010)
3. Associação Brasileira de Normas Técnicas (ABNT): ABNT NBR NM 60335-1: Segurança de aparelhos eletrodomésticos e similares Parte 1:Requisitos gerais (2010)
4. International Electrotechnical Commission (IEC): IEC 60335-1: Household and similar electrical appliances—Safety—Part 1: General requirements (2010)
5. Associação Brasileira de Normas Técnicas (ABNT): ABNT NBR NM 247-3: Cabos isolados com policloreto de vinila (PVC) para tensões nominais até 450/750 V, inclusive. Parte 3: Condutores isolado (sem cobertura) para instalações fixas (IEC 60227-3, MOD) (2002)
6. International Electrotechnical Commission (IEC): IEC 60227-2: Polyvinyl chloride insulated cables of rated voltages up to and including 450/750 V—Part 2: Test methods (1997)

Evaluating the Reliability and Validity of a Questionnaire Used to Collect Data About the Periodic Evaluation of Ultrasound Therapy Equipment

Jessyca Gomes da Silva, André Victor Alvarenga,
and R. P. B. Costa-Felix

Abstract

The collection of primary data allows a closer approximation of reality as it is the most up-to-date information obtained directly from the target audience. The questionnaire is one of the instruments used to capture this data, which is the most used because its practicality and low application cost. Nevertheless, it should be considered that it is not enough to collect answers on questions of interest, but rather to know how to analyze them statistically to validate the results. This article presents and exemplifies the validation of consistency (reliability and validity) of a questionnaire-measuring instrument. A questionnaire was used to collect primary data for a survey related to the periodic evaluation of ultrasound therapy equipment. It was intended to know the experience of the physiotherapist in the application of ultrasound therapy, how equipment maintenance happens and if the professional has information about the equipment conditions of use. We required outlining the profile of the usage and maintenance of the equipment and of the professionals who use it in clinical practice. This study demonstrated the use of Cronbach's alpha coefficient to determine the reliability of a questionnaire aimed at obtaining primary data related to professionals using ultrasound therapy equipment.

Keywords

Questionnaire • Primary data • Metrology

1 Introduction

1.1 Primary Data Collection

The collection of primary data allows a closer approximation of reality as it is the most up-to-date information obtained directly from the target audience. The questionnaire is one of the instruments used to capture this data, which is the most used for its practicality and low application cost [1]. The use of a questionnaire is an advantageous technique also because it allows reaching a large number of respondents and in remote geographic areas [2].

However, gathering data for surveys by means of questionnaires requires special care. It should be considered that it is not enough to collect answers on questions of interest, but rather to know how to analyze them statistically to validate the results. To ensure that a given questionnaire is effective and accurate, two measurement characteristics should be considered in its development: validity and reliability [3].

1.2 Reliability and Validity

Reliability and validity are requirements applicable to measurements derived from the physical phenomena, for example the measurement of velocity of a body, as well as from an instrument of data collection, such as the questionnaire [4–6].

The reliability is related to the regularity of the obtained results, from the repetition of the measurements maintaining the same conditions. Reliable measures are replicable and consistent, that is, they generate the same results. The reliability of a questionnaire is its coherence, determined by the constancy of the results [7, 8]. Instruments that measure physical phenomena, offer a high degree of reliability due to the stability of the phenomena, the variance associated with random errors is small. In the social universe, the continuous

J. G. da Silva (✉) · A. V. Alvarenga ·
R. P. B. Costa-Felix
Laboratory of Ultrasound, Directory of Scientific and Industrial
Metrology (DIMCI), National Institute of Metrology, Quality and
Technology (Inmetro), Av. Nossa Sra. das Graças, 50 (Prédio 1),
Duque de Caxias, RJ 25250-020, Brazil
e-mail: jgsilva@inmetro.gov.br

modifications, instability of the observed phenomena and facts make difficult to obtain a high degree of reliability. As the variance associated with random errors increases, the variance of the observed values distances from the variance of the true values [9]. This represents a lower reliability in the measurements (and consequently less reliability attributed to the data collection instrument used). Conceptually, reliability reflects how much the observed values are correlated to true value [10].

The validity refers to the instrument's ability to measure what it intends to measure accurately. The determination of validity apparently is the simplest technique to evaluate the validity. An apparent validity is evaluated by group of evaluators who examine a measurement technique and decide whether it measures what it suggested to measure. It is a subjective process, but of high importance. If the instrument of measures seems, in the eyes of the respondents, irrelevant, inadequate or difficult, the lack of apparent validity may compromise the whole study.

1.3 Influence Factors

Some factors may positively or negatively influence the reliability of a questionnaire. The number of questions and the sample of evaluators are one of the most striking facts.

The more items contained in a questionnaire, the greater is its reliability, because the sampling error decreases as the sample increases. However, the issues should be relevant and should not overlap or interfere with each other. And there must be precaution not to exaggerate the number of items, as it can lead respondents to fatigue, generating relapsing or impulsive responses.

A sample of evaluators made up of similar people may result in a questionnaire of low reliability. For example, if in the evaluation of an item all people in the sample indicate a true value 5 (considering a scale of absolute values ranging from 1 to 5), there is no variance in this item, and the calculated reliability will have zero value. Considering a significant sample of evaluators, it is very unlikely that there is an absolute agreement about the value of an item. However, when the evaluators are similar in their nature and professional training (experts), there may possibly be less variability in the judgments, which may lead to lower reliability values of the questionnaire [9].

1.4 Cronbach Alpha

Several techniques can determine the reliability of an instrument. In this article, we will discuss the application of the Cronbach alpha coefficient [11].

Cronbach's Alpha Coefficient (α) is a commonly used measure of reliability. Coefficient α proved to be useful for at least three reasons. First, it provides a reasonable measure of reliability in a single test, in a way that repetitions or applications of parallel forms of a test are not necessary to estimate the consistency of the test. Second, its general formula allows its application, for example, to multiple-choice questionnaires of dichotomous scales or attitudinal scales of categorical variables. And third, it is easily calculable by basic statistical principles, even at a time when the use of computers was not the rule. The direct interpretation of the coefficient is also pointed out as an advantage.

The alpha value is the average of all correlation coefficients. The item-total correlations and the Cronbach alpha value are revealing because they provide information about each individual item. Items that are not correlated with the others can be eliminated from the measure to increase reliability.

It is understood that the internal consistency of a questionnaire is the greater the closer to 1 is the value of the statistic. In general, acceptable alpha value range from 0.65 to a 0.95.

2 Application of a Questionnaire as an Instrument of Measurement

2.1 Research Objective

A questionnaire will be used to collect the physiotherapist's opinion about the periodic evaluation of ultrasound therapy equipment (USTE) and to draw the professional profile of the user of this type of equipment. It is intended to know the experience of the physiotherapist in the application of ultrasound therapy, how is the maintenance of the equipment and if the professional is informed about the equipment conditions of use. The questionnaire will help to identify the profile of the usage and maintenance of USTE and the professionals' profile whose use it in clinical practice.

Literature reports that USTEs used in clinics do not meet current metrological requirements [12], presenting disadvantages as ineffective treatment and being able to cause burns due to high temperatures. In addition, the development of a low-cost, qualitative method to periodically evaluate this type of equipment [13] was recently included as an annex to the international technical specification IEC TS 62462:2016 Ultrasonics—output test—Guide for the maintenance of ultrasound—Physiotherapy systems, which describes methods to assist users in checking their ultrasound devices therapeutic.

2.2 Questionnaire Development

An online questionnaire was developed with 15 items, composed of three cores, each with a specific objective:

- Core 1. Training and professional experience: to trace the professional profile of USTE's users based on the group age, the level of academic training, the time of professional performance and the time of experience with the application of therapeutic ultrasound.
- Core 2. Periodic evaluation of the USET: to know how the equipment is maintained and the perception of the importance of this maintenance by the physiotherapist. It was asked whether the ultrasound emission of the equipment is verified, by whom this verification is performed, the methodology used and the periodicity of the verification.
- Core 3. Interest in the developed technology: to understand the physiotherapist's conception about the periodic evaluation methods that exist in the market, whether they are complex, reliable, expensive or not. Finally, it is asked if there is any interest in a new evaluation method and what attributes are expected concerning cost, reliability and complexity.

The answers are multiple choices and at the end of the questionnaire the respondent could, optionally, add some comment that he considered pertinent.

2.3 Evaluation of the Questionnaire

The questionnaire, as a research instrument, had its consistency evaluated in order to test its coherence, clarity and if it is general objective is being reached.

In order to test the validity, the questionnaire was sent to a group of eight specialists in physical therapy linked to clinical practice in hospitals, academia and in the market as liberal professionals. Six answers were received and considered sufficient for validation. The apparent validity strategy was used. Each specialist evaluated whether the questions were pertinent to the research's objective, whether the statement was complete and whether the response options were adequate. Adding three questions to each item of the questionnaire, then each specialist answered 45 questions.

These evaluations were also performed through an online questionnaire and had its reliability tested. The degree of concordance between the responses was verified using the calculation of Cronbach's alpha coefficient. The response options for each item were dichotomous, "Yes" and "No". For the calculation of Cronbach's alpha, each response was converted into scores. Considering the questionnaire with k items, answered by n respondents, to calculate the Cronbach's alpha coefficient, the Eq. (1) was applied:

$$\alpha = \frac{k}{k-1}\left(1 - \frac{\sum_{i=1}^{k} S_i^2}{S_{sum}^2}\right) \tag{1}$$

in which k is the number of items, n is the number of respondents, S_i^2 is the variance of the n scores of the i-th respondent ($i = 1, …, k$), S_{sum}^2 is the variance of the totals of each respondent's scores. The variances are calculated by the Eq. (2):

$$S^2 = \frac{\sum (x - \bar{x})^2}{n} \tag{2}$$

2.4 Evaluation Result

The Cronbach's alpha calculated for questionnaire validation was 0.64. This result was considered sufficient for the purpose of the applied questionnaire, as the evaluators had similar professional profiles and the questions for questionnaire evaluation were the same for all items of judgment. Hence, the reliability found was satisfactory.

Regarding validity, the contribution of the experts was unanimous in agreeing that most of the questions were adequate to capture the information one wanted to know.

After analyzing the experts' suggestions, the questionnaire underwent minor modifications, such as improving the clarity of some questions, before being effectively sent to the target audience. In addition, a presentation on the objectives of the survey and instruction on how to fill out the questionnaire was made in the header to familiarize the respondent with the questionnaire.

One must be aware that for a questionnaire validation using a questionnaire, as it was the case for this experiment, the Cronbach's alpha is typically lower. The reason is that for the validation, specialists in the field are the respondents, and as so a more uniform response is expected.

3 Final Consideration

This study demonstrated the use of Cronbach's alpha coefficient to determine the degree of reliability of a questionnaire aimed at obtaining primary data related to professionals using ultrasound therapy equipment. The results obtained led to the validation of the measuring instrument, what was the main goal.

References

1. Manzato, A.J., Santos, A.B.: A elaboração de questionários na pesquisa quantitativa. Departamento de Ciência de Computação e Estatística – IBILCE – UNESP. http://www.inf.ufsc.br/~verav/Ensino_2012_1/ELABORACAO_QUESTIONARIOS_PESQUISA_QUANTITATIVA.pdf. Accessed 20 Apr 2018

2. Günther, H.: Como Elaborar um Questionário. Série: Planejamento de Pesquisa nas Ciências Sociais, Nº 01 (2003)

3. Freitas, A.L.P, Rodrigues, S.G.: A avaliação da confiabilidade de questionários: uma análise utilizando o coeficiente alfa de Cronbach. XII SIMPEP - Bauru, SP, Brasil, 7 a 9 de Novembro de 2005

4. Araújo, N.R.S., Laburú, C.E.: Uma análise da validação e confiabilidade da escala de opiniões da seleção de experimentos de química (EOSEQ). Ensaio – Pesq. Educ. Ciênc. **11**(2) (2009)

5. Torres, C., Fermam, R.K.S.: Avaliação da competição no mercado de carbono: elaboração e validação de questionário. Revista Internacional de Ciências **06**(02), 199. https://doi.org/10.12957/ric.2016.23501

6. Del Siegle, Developing an Attitude Instrument. https://researchbasics.education.uconn.edu/developing_an_attitude_instrument/. Accessed 20 Apr 2018

7. Brown, J.D.: Can we use the Spearrman-Brown prophecy formula to defend low reliability? Shiken: JALT Test. Eval. SIG Newslett. **4**(3), 17–18 (2001)

8. Brown, J.D.: The Cronbach alpha reliability estimate. Shiken: JALT Test. Eval. SIG Newslett. **6**(1), 17–18 (2002)

9. Del Siegle: Instrument Reliability. https://researchbasics.education.uconn.edu/instrument_reliability/. Accessed 20 Apr 2018

10. Hora, H.R.M., Monteiro, G.T.R., Arica, J.: Confiabilidade em Questionários para Qualidade: Um Estudo com o Coeficiente Alfa de Cronbach. Produto & Produção **11**(2), 85–103 (2010)

11. Cronbach, L.J.: Coefficient alpha and the internal structure of tests. Psychometrika **16**(3) (1951)

12. Ferrari, C.B., Andrade, M.A.B., Adamowski, J.C., Guirro, R.R.J.: Evaluation of therapeutic ultrasound equipments performance. Ultrasonics **50**(7), 704–709 (2010)

13. Costa, R.M.: Protocolo de Medição Para Análise Qualitativa de Equipamentos de Ultrassom Fisioterapêuticos Utilizando Um Corpo de Prova Termocromático, p. 95. Tese de Doutorado, Programa de Engenharia Biomédica (COPPE/UFRJ), Rio de Janeiro (2015)

International Overview of Eye Tracking Technologies Using Patent Bases

Alexandre Bissoli, Cesar Moreira Jr., Lucas Encarnação,
and Teodiano Bastos-Filho

Abstract

This work presents an international overview on eye tracking technology from the perspective of Industrial Property, more specifically of Patents. In this sense, a methodology of Technological Prospection using the Derwent Innovation patent base is addressed. The results show the growth in the number of patent requirements about eye tracking technology from 1998 to 2018, which is more accelerated from 2010. The results also show the United States (US) as the international leader in the development of this technology, both in the number of patent requirements in the country, which is an indicator of interest in protecting this technology, and in the number of companies involved. On the other hand, the results also indicate that, since 2015, the Chinese Office is the international leader in the number of patent requirements, leaving the US Office in second place. International data were stratified in different areas of technological development, with the aid of the International Patent Classification (IPC), with emphasis on the area of eye tracking for surgery and eye diagnosis, followed by eye tracking for human-machine interface purposes.

Keywords

Eye tracking • Industrial property • Patents • Technological prospection • International patent classification (IPC)

A. Bissoli (✉) · L. Encarnação · T. Bastos-Filho
Postgraduate Program in Electrical Engineering (PPGEE), Federal University of Espirito Santo (UFES), Vitória, Brazil
e-mail: alexandre-bissoli@hotmail.com;
alexandre.bissoli@inpi.gov.br

A. Bissoli · C. Moreira Jr.
Brazilian Patent Office (DIRPA), National Institute of Industrial Property (INPI), Rio de Janeiro, Brazil

1 Introduction

Eye tracking is a technique of measuring either the point of gaze (where someone is gazing) or the motion of an eye relative to the head. An eye tracker is a sensor/device for measuring either eye positions or eye movements. Eye tracking technology, used in eye trackers sensors/devices, has applications in industry and researches about visual system [1–4], psychology [5, 6], assistive technologies [7–10], marketing [11], as an input device for human-computer interaction [12–16], and in product and website design [17].

Eye trackers measure rotations of the eye in one of several ways, but principally they fall into three categories: (i) measurement of the movement of an object attached to the eye [15, 18]; (ii) optical tracking without direct contact to the eye [9, 14]; and (iii) measurement of electric potentials using electrodes placed around the eyes [19].

In view of the above, the objective of this work is to draw an overview of eye tracking technologies from the viewpoint of Industrial Property, through the accomplishment of a technological prospection using patent bases, seeking to highlight the main areas related to eye tracking.

1.1 Industrial Property Instruments—Patents

According to the Convention of the Union of Paris (CUP), Industrial Property is the set of rights comprising patents, utility models, trade names and indications of origin or designations of origin, and the suppression of unfair competition.

Created in 1970, the National Institute of Industrial Property (INPI/Brazil) is a federal autarchy linked to the Ministry of Industry, Foreign Trade and Services, responsible for the improvement, dissemination and management of the Brazilian system of granting, guaranteeing intellectual property rights for the industry.

829

A patent is a right conferred by the State, which gives the holder the exclusive right to exploit a technology. In return for the public's access to knowledge of the essential points of the invention, the law confers on the patentee a time-limited right, on the assumption that it is socially more productive to exchange the *de facto* exclusivity (that of the technology secret) for exclusivity of law [20]. It is patentable the invention that meets the requirements of novelty, inventive activity and industrial application.

It should be noted that the right to Priority is conferred to the signatory countries of the CUP. That is, after the first filling of a patent in a signatory country, the depositor has up to 12 months to make the deposit in another signatory country. Therefore, all search and analysis of patentability requirements must be performed based on the priority date of the application and, if there is no priority, the filling date of the application.

1.2 International Patent Classification (IPC)

The International Patent Classification (IPC) is a very important tool in conducting patent searches. This classification is the means of standardizing the documents of several countries with different language and technical expressions.

The Classification, according to the World Intellectual Property Organization (WIPO), plays an important role in the sense of being: (i) a tool for ordering patent documents in order to facilitate access to the technical and legal information presented therein; (ii) a basis for the selective dissemination of information to all who use patents as a reference and/or knowledge; (iii) a support to make a survey of the state of the art referring to some fields of technology; and (iv) support for the development of statistics on industrial property, allowing the analysis of technological advances in several areas [21].

The Classification of a technology is initially constructed by a section, represented by a letter (for example G), followed by two numbers, indicating the class (for example G06). Each class may involve one or more subclasses,

represented by a letter (for example G06F), each subclass having its subdivisions called groups, and may be main groups or subgroups. Each representation of the main group consists of the subclass symbol, followed by one to three numbers, the oblique bar and the number 00 (for example G06F 3/00). The subgroups form subdivisions under the main groups where the numbers after the oblique bar contain at least two digits other than 00 (for example G06F 3/01). This way, each section is subdivided by subcategories, until the final result of an IPC is presented as follows:

2 Materials and Methods

2.1 Patent Databases

Currently, the patent offices of each country provide the information they publish through its website. Documents published in Brazil can be accessed through the INPI database.

Some free databases are considered important, depending on the temporal and territorial coverage of publications, such as the European Patent Office (EPO) database (Espacenet), or depending on the country's relevance to the Intellectual Property system, such as the United States Patent and Trademark Office (USPTO) base and the Japanese Patent Office (JPO) base. However, such databases have limitations, and it is important that in using them, such limitations are considered, and the collection and processing of information are planned in order to avoid some problems they may cause.

There are other forms of access to information made available through the Intellectual Property system, which often have advantages over free bases, especially when the information will be used as a prospecting tool. These resources are made up of commercial databases and specific software for the retrieval and processing of data obtained through the patent system, such as Google Patents, Derwent Innovation (DWPI) and EPOQUE. Most of the time, these features enable the automation of many of the steps that, when using a free database, must be done manually.

Example: A61B 3/14
At where:
■ Section – represented by a letter between A and H: A – Human Necessities;
■ Class – represented by two numerical digits: 61 – Medical or Veterinary Science;
■ Subclass - represented by a letter ranging from A to Z: B – Diagnosis; Surgery; Identification;
■ Group - represented by one or more numerical digits: 3 – Apparatus for testing the eyes; Instruments for examining the eyes;
■ Subgroup - represented by at least two numerical digits: 14 – Objective types, i.e. instruments for examining the eyes independent of the patient perceptions or reactions; Arrangements specially adapted for eye photography.

Commercial bases have the disadvantage of being paid. This is the main impediment to use the base EPOQUE, in which each command sent is charged. In addition, EPOQUE does not edit or revise patent applications. In contrast, this is the main advantage observed in the Derwent Innovation database. DWPI has up-to-date and cross-country data. It has more than 900 professionals who edit and revise patent applications and has its own order classification, which improves the search results. The system has multiple search options, allowing compiling the results obtained into graphics, and is very simple to use. Thus, it was decided to use the Derwent Innovation (DWPI) in this work.

2.2 Search Strategy

Initially, a preliminary search was carried out at the IPC in order to obtain the classifications related to eye tracking technologies, in order to help in the delimitation of the scope of the subsequent searches. In this sense, to obtain international trends, the first adopted search strategy considered the following categories: delimitation of the scope of the request; use of keywords; classification (IPC) and time limit. Then, to obtain the country-specific data, the second search strategy considered, in addition to the above categories, the country or region of deposit. Table 1 illustrates the adopted and variable categories used in the search strategies.

With the time limit set for 1998–2018, the first international search was carried out. Thus, we identified the number of occurrences of deposits, priorities and publications each year, observing the behavior in this temporal cut. After this step, the search was carried out again and thus it was possible to obtain the main classifications used in this technology, the countries with more patent application fillings, and the main companies in the industry in number of patents and, finally, identify the world's technological area using eye tracking.

Table 1 Search Strategy

Categories adopted	Variables used
Scope delimitation	Title and abstract
Keywords	("eye" AND "tracking")
Classification (IPC)	A61B and A61F
Time limited	1998–2016/2000–2016
Application country	Brazil (BR), United States (US), China (CN) …

3 Results and Discussions

Figure 1 shows the international behavior of priority claims, patent applications and patents publications related to the eye tracking technology from 1998 to 2016. It can be observed that, although the growth in the period 1998–2010 is relatively small, from 2010 on it becomes quite high. Due to the so-called edge effect, the years 2017 and 2018 were suppressed. It was decided to keep the year 2016 on the chart, although it is still affected by the edge effect, which can be occasioned by the following reasons: (i) delay of publication of the applications by the patent offices; (ii) a period of secrecy of up to 18 months from the filling date until the publication of said patent application; (iii) delay of the commercial base in the updating of the data coming from the official bases of the patent offices. The years before 1998 were not presented, in order to highlight the latest technologies.

As expected, the profile of the three curves is similar. It can be noted that the number of priorities tends to be higher over time, since the same patent application may have more than one priority. It can be further noted that the publication curve is shifted by about one year from the application ones due to the confidentiality period of the patent application.

Figure 2 illustrates the international behavior of patents applications, related to eye tracking technology, at the world's largest patent offices in terms of number of fillings. The US leadership in the protection of these technologies over the years can be clearly observed, followed by China, Europe, Japan and South Korea, respectively, as the main markets of interest. It is worth mentioning that these five offices make up the so called IP5, which are the world's top five intellectual property offices. Again, due to the so-called edge effect, the years 2017 and 2018 were suppressed.

In analyzing Fig. 2, it can be seen that it can be divided into three blocks with similar characteristics. In block 1 are Australia (AU), Canada (CA), Taiwan (TW), Germany (DE), India (IN), United Kingdom (GB), Brazil (BR), Russia (UK) and Mexico (MX), although they are among the offices with the largest number of patent application fillings for eye tracking technology, this number is quite small and has remained approximately constant over the years. In block 2, there are Europe (EP), South Korea (KR) and Japan (JP), which stand out from the first group, mainly from 2010 on, when they achieved more relevant growth. Although they are in decline since 2014, they still have a number of patent fillings for eye tracking technology far superior to block 1.

Fig. 1 Comparison of international data on priority claims, patents applications and patents publications related to eye tracking technology per year
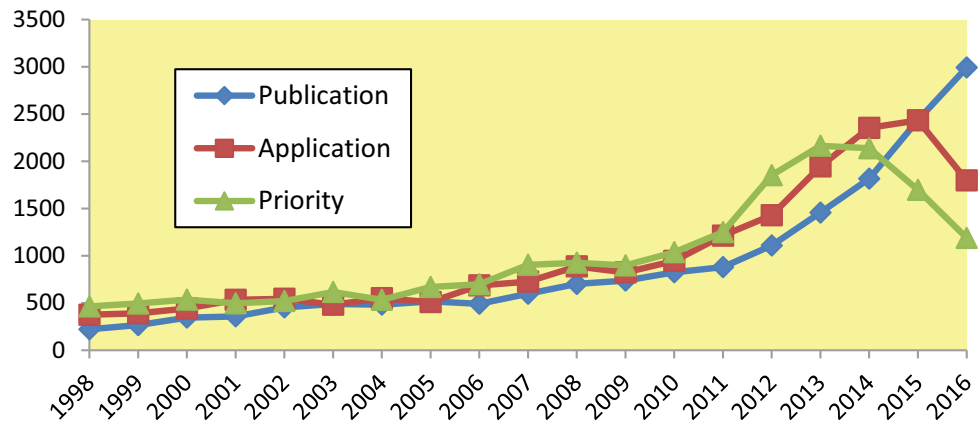
Fig. 2 Patent applications related to eye tracking technology per year in the international scope
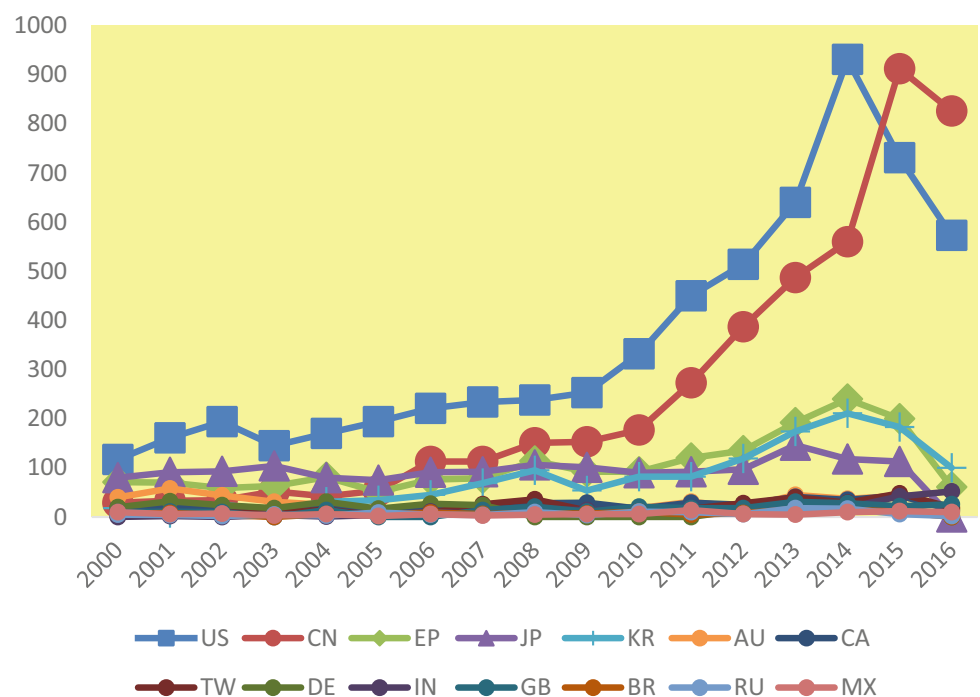
Finally, in block 3, there are United States (US) and China (CN) which receive the largest number of patent application fillings for eye tracking technology. Although the United States has the largest number of deposits over the years, it can be noted that China took the leadership from 2015. Both countries show a slight growth from 2000 to 2009 and become extremely sharp from 2010. The shift of about a year between the curves of the United States and China draws attention. One reason that may explain this fact is the right to Priority of the signatory countries of the CUP, since after the first filling of a patent in a signatory country, the depositor has up to 12 months to deposit in another signatory country. This corroborates the fact that the companies with the largest number of patent fillings are the US (Fig. 3).

Figure 3 shows the ranking of the companies with the highest number of patent applications fillings grouped by country of origin. Again, there is the leadership of the United States, both in number of companies and in number of fillings. It is noteworthy that Microsoft Corporation, which develops, manufactures, licenses, supports and sells computer software, electronic products, computers and personal services, was the first in the ranking with 668 patent deposits in total. Following are Canon Inc. (JP), Samsung Electronics (KR), Tobii Technology (SE), SeeReal Technologies (LU), Sony Corporation (JP), Intel Corporation (US), Google Inc. (US) and Zeiss Carl Meditec (DE), respectively. The companies are listed in order from bottom to top, from left to right, corresponding the caption from bottom to top.

Fig. 3 Ranking of the main companies in the number of patent applications grouped by country of origin
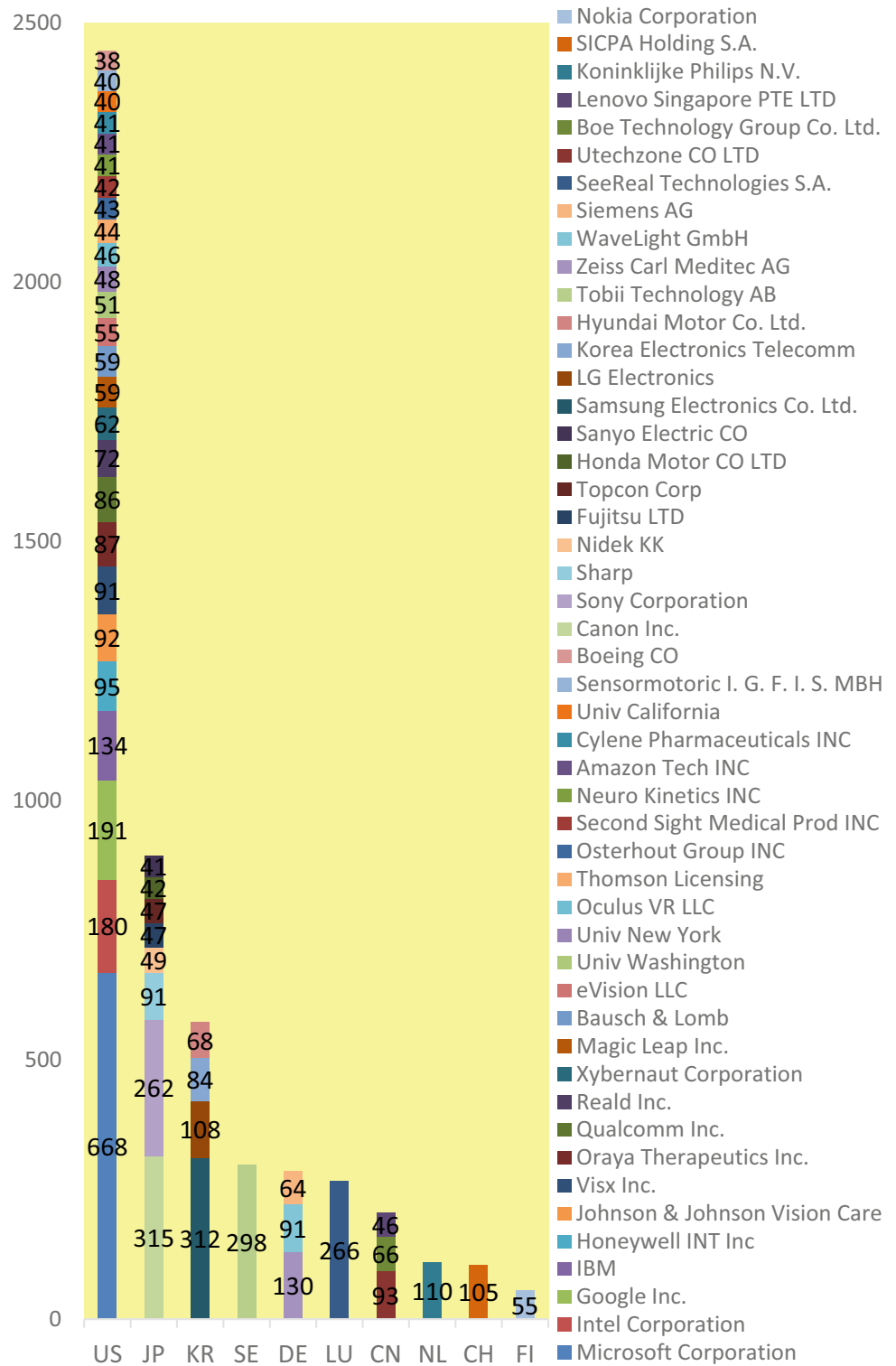
Figure 3, through the direct action of the companies, shows the leading countries in the protection of their developments and research of technology related to eye tracking. It shows clear leadership from the United States (US), followed by Japan (JP), South Korea (KR), Sweden (SE), Germany (DE), Luxembourg (LU), China (CN), Netherlands (NL), Switzerland (CH) and Finland (FI). Of note is Sweden and Luxembourg, which, even with only one company in each country, appear in the fourth and sixth positions, respectively.
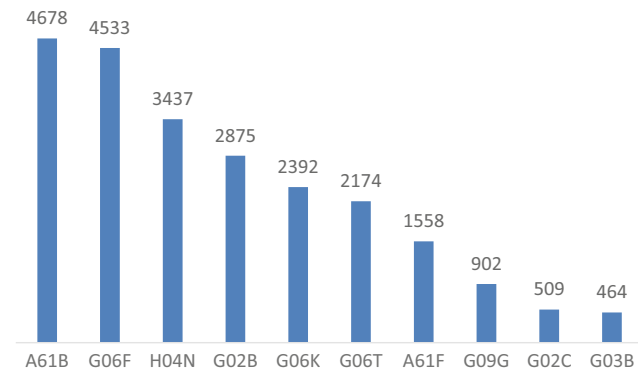
Fig. 4 Main subclasses of the IPC in descending order of occurrence

In addition, it is interesting to identify the main technological areas involved. In this sense, Fig. 4 shows the main IPC subclasses found in order of decreasing occurrence.

From the analysis of Fig. 4, it can be seen that the subclass A61B, referring to diagnosis and surgery appears with the highest number of occurrences, showing that the medical area is the main area related to eye tracking. Second is the subclass G06F, which is directly related to human-machine interfaces, referring to the digital processing of digital data. Then, representing the developments in the television area, we have the subclass H04N, referring to the communication of images. The next subclass found is G02B, which is also directly related to television technology, referring to optical systems or devices. G06K subclass, which is directly related to human-machine interfaces, refers to the identification,

presentation, support, manipulation and transport of data. G06T refers to image data processing or generation. A61F refers to treatment or protection of eyes. G09G refers to arrangements or circuits for control of indicating devices using static means to present variable information. G02C refers to spectacles, sunglasses or goggles insofar and contact lenses. G03B refers to apparatus or arrangements for taking photographs or for projecting or viewing them.

Based on the obtained classifications, it was possible to separate the protected technologies into six distinct groups, in descending order of filling of patent applications, as shown in Fig. 5.

From the analysis of Fig. 5, it can be observed that the area related to the identification, diagnosis and surgery of the eyes appears with the greatest number of occurrences, evidencing the importance of eye tracking for the health area. Secondly, there is the human-machine interface, based on eye movements, currently used in notebooks, tablets and smartphones, to improve user interaction with such devices, especially in games. Then, in third and fourth places, respectively, appear the areas of image communication and optical devices, both related to stereoscopic television (better known as three-dimensional or 3D). Fifth, the area of image analysis and processing appears, where eye tracking can be used to identify what attracts the most attention to the images. Finally, in the sixth position, the head-up displays used in cars and airplanes, which consist of displays designed on the glass of vehicles, in order for the user does not have to look elsewhere to have access to information from the car or plane.

Fig. 5 Main technological areas identified under the eye tracking technology
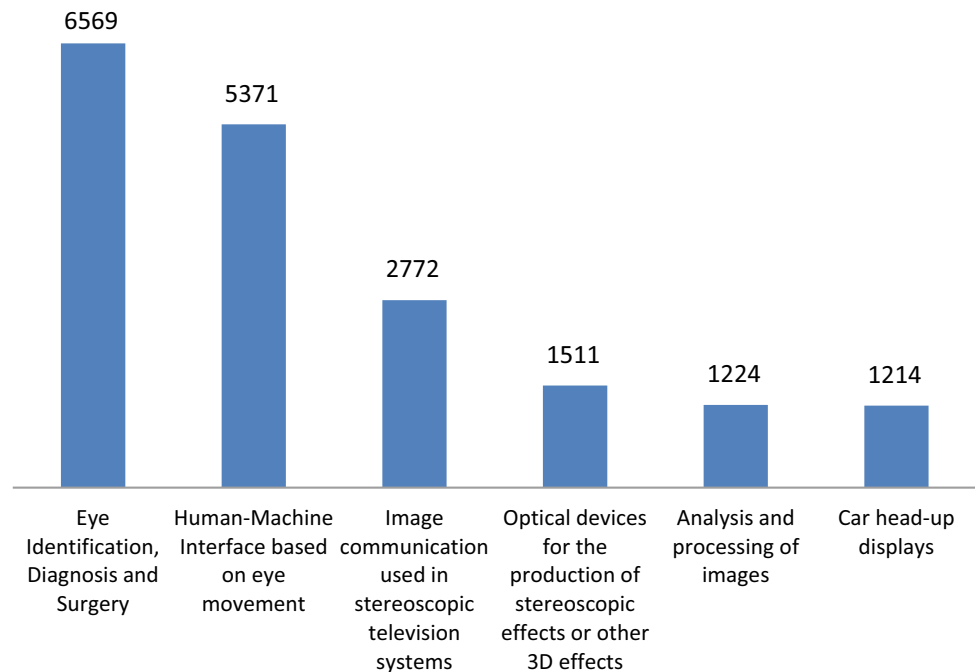
4 Conclusions

This work presented an overview of the technology of eye tracking from the point of view of Industrial Property, through the accomplishment of a technological prospection using patent bases. At the international level, the main areas of technological knowledge related to eye tracking were evidenced.

The patent base used was Derwent Innovation since it is simple to use, has updated data from several countries and still has peculiar characteristics, such as: professionals who edit and revise patent applications, develop a proper classification of the requests and rewriting of titles and abstracts, which greatly improves the search results.

The results obtained point to a growing trend regarding the number of patent fillings and patent applications for eye tracking, mainly from 2010. It should be noted that in the coming years a good increase is expected in the data obtained from 2015 onwards, due to the delay in the publication of patent applications.

It is worth noting the leadership of the United States in the development of eye tracking technology, both in the number of patent applications filled in the country, which is an indicator of the interest in protecting this technology, as well as in the number of companies involved and in the number of applications for patents of US companies. However, the results indicate that, since 2015, the Chinese office is the international leader in the number of patent applications filled, leaving the US office in second place.

International data were stratified in different areas of technological development, with the aid of the International Patent Classification (IPC), with emphasis on the area of eye tracking for surgery and eye diagnosis, which obtained the first place, followed by human-machine interface, showing that these are important and promising areas.

References

1. Khan, R., Tien, G., Atkins, et al.: Analysis of eye gaze: do novice surgeons look at the same location as expert surgeons during a laparoscopic operation. Surg. Endosc. **26**(12), 3536–3540 (2012)
2. Wilson, M., McGrath, J., Vine, et al.: Perceptual impairment and psychomotor control in virtual laparoscopic surgery. Surg. Endosc. **25**(7), 2268–2274 (2011)
3. Richstone, L., Schwartz, M., Seideman, et al.: Eye metrics as an objective assessment of surgical skill. Ann. Surg. **252**(1), 177–182 (2010)
4. Wilson, M., McGrath, J., Vine, S., Brewer, J., Defriend, D., et al.: Psychomotor control in a virtual laparoscopic surgery training environment: gaze control parameters differentiate novices from experts. Surg. Endosc. **24**(10), 2458–2464 (2010)
5. Moore, L., Vine, S., Cooke, A., et al.: Quiet eye training expedites motor learning and aids performance under heightened anxiety: the roles of response programming and external attention. Psychophysiology **49**(7), 1005–1015 (2012)
6. Sun, Q., Xia, J., Nadarajah, N., et al.: Assessing drivers' visual-motor coordination using eye tracking, GNSS and GIS: a spatial turn in driving psychology. J. Spat. Sci. **61**(2), 299–316 (2016)
7. Eid, M., Giakoumidis, N., Saddik, A.: A novel eye gaze-controlled wheelchair system for navigating unknown environments: case study with a person with ALS. IEEE Access **4**(1), 558–573 (2016)
8. Lupu, R., Ungureanu, F., Bozomitu, R.: Mobile embedded system for human computer communication in assistive technology. In: Proceedings of the 2012 IEEE 8th International Conference on Intelligent Computer Communication and Processing, pp. 209–212 (2012)
9. Lupu, R., Ungureanu, F., Siriteanu, V.: Eye tracking mouse for human computer interaction. In: Proceedings of the 4th IEEE International Conference on E-Health and Bioengineering, 4 pp. (2013)
10. Davis, F., Bagozzi, R., Warshaw, P.: User acceptance of computer technology: a comparison of two theoretical models. Manage. Sci. **35**(8), 982–1003 (1989)
11. Scott, N., Green, C., Fairley, S.: Investigation of the use of eye tracking to examine tourism advertising effectiveness. Curr. Issues Tour. **19**(7), 634–642 (2016)
12. Lewis, T., Pereira, T., Almeida, D.: Smart scrolling based on eye tracking. Design an eye tracking mouse. Int. J. Comput. Appl. **80**(10), 34–37 (2013)
13. Nehete, M., Lokhande, M., Ahire, K.: Design an eye tracking mouse. Int. J. Adv. Res. Comput. Commun. Eng. **2**(2), 1118–1121 (2013)
14. Pascual, M., Zapirain, B.: Assessing visual attention using eye tracking sensors in intelligent cognitive therapies based on serious games. Sensors **15**(5), 11092–11117 (2015)
15. Basterretxea, A., Zorrilla, A., Zapirain, B.: Eye/head tracking technology to improve HCI with iPad applications. Sensors **15**(1), 2244–2264 (2015)
16. Cecotti, H.: A multimodal gaze-controlled virtual keyboard. IEEE Trans. Hum.-Mach. Syst. **46**(4), 601–606 (2016)
17. Lee, S., Yoo, J., Han, G.: Gaze-assisted user intention prediction for initial delay reduction in web video access. Sensors (Basel) **15**(6), 14679–14700 (2015)
18. Takemura, K., Takahashi, K., Takamatsu, J., Ogasawara, T.: Estimating 3-D point-of-regard in a real environment using a head-mounted eye-tracking system. IEEE Trans. Hum.-Mach. Syst. **44**(4), 531–536 (2014)
19. Manabe, H., Fukumoto, M., Yagi, T.: Direct gaze estimation based on nonlinearity of EOG. IEEE Trans. Biomed. Eng. **62**(6), 1553–1562 (2015)
20. Barbosa, C.: Propriedade Intelectual: Introdução à Propriedade Intelectual como Informação. Elsevier (2009)
21. Delvizio, E.: Avaliação das estratégias da indústria para-petrolífera pelos respectivos depósitos de patentes. In: Rio Oil and Gas Expo and Conference (2010)

Reduction of *Pseudomonas* Inoculated into Whole Milk and Skin Milk by Ozonation

M. C. Munhõs, R. S. Navarro, S. C. Nunez, D. I. Kozusny-Andreani, and A. Baptista

Abstract

Milk is one of the most consumed foods in the world by owning in its composition carbohydrates, proteins, lipids, vitamins and minerals. However, these intrinsic characteristics make it an excellent substrate for microbial growth. The contaminating microbiota of milk is usually composed of psychrotrophic microorganisms, especially the species of *Pseudomonas* that multiply well at refrigeration temperatures and produce thermos-resistant enzymes, which compromise the quality of milk. The aim of this study was to evaluate the efficiency of ozonation of milk on the reduction on artificially inoculated *Pseudomonas*. The samples were divided in two groups: whole and skim milk. Five brands of whole milk and five brands of skim milk were tested, experimentally divided into control groups, contaminated groups and contaminated and exposed to ozonation groups. The time and concentration of ozonation in both assays were 5, 10 and 15 min and 28 mgL^{-1}. The results showed reduction of 1 log and 4 logs of Pseudomonas after 5 and 10 min of ozonation respectively, in both whole and skim milk ($p > 0.05$). After 15 min of ozonation the reduction of microorganisms was significantly higher for skim milk in relation to whole milk ($p < 0.05$). The results indicated that the effectiveness of the microbial reduction promoted by ozonation in samples of whole milk and skim milk contaminated with *Pseudomonas* is time and milk composition dependent. Therefore, according to our results the substrate composition interferes with the bactericidal action of the ozone.

Keywords

Ozone • *Pseudomonas* • Milk

1 Introduction

Humans are the only species that regularly drink milk from other species, but only a small proportion of humans have the lactase enzyme [1]. The first contact is with breast milk, rich in fats, vitamins and minerals essential for the development of the baby's immune system [2]. Milk is widely recognized as a nutritious drink for people of all ages. It's a good source of protein, calcium, vitamin D, potassium and other vitamins and minerals [3]. However, due to its high nutritional content, it can be a good substrate to support a rich microbiota growth, which in turn can cause milk spoilage leading to economic losses, especially for small producers [4, 5].

The contaminating microbiota in milk is usually composed of psychrotrophic thermoduric microorganisms, which multiply well at refrigeration temperatures, they survive pasteurization temperatures, produce thermo-resistant extracellular enzymes, which can compromise the quality and shelf life of milk and milk products [6]. Pseudomonas are commonly found in milk and is the most common cause of milk spoilage. These bacteria can become the predominant microorganism in raw milk stored at low temperatures promoting the production of extracellular enzymes, with lipases and proteases. These lipases degrade milk fat causing rancidity, while proteases degrade casein producing changes in the appearance, odor and taste of milk and dairy products [5].

The use of ozone for antimicrobial purpose is well established in the literature, acting over Gram-positive, Gram-negative bacteria, fungi and viruses, however, the level of microbial inactivation can vary according to low pH values, high temperature and amount of organic matter [7, 8]. The ozonation in the food industry has been the aim of

M. C. Munhõs · R. S. Navarro · S. C. Nunez · A. Baptista (✉)
Universidade Brasil, Bioengineering Postgraduation Program, São Paulo, Brazil
e-mail: alessandra.baptista@universidadebrasil.edu.br

D. I. Kozusny-Andreani
Universidade Brasil, Environmental Sciences Postgraduation Program, Fernandópolis, Brazil

researches since the compound was considered safe by international associations [9, 10]. Several studies have shown good results in the decontamination of fruits, meat, fish with ozone [10–12].

In addition, the use of ozone is gaining strength in the food processing industry as a safe, cost-effective technology for food disinfection [13, 14].

The objective of this study was to evaluate the effect of ozonation at different exposure times on the reduction of *Pseudomonas* inoculated into whole and skin milk.

2 Materials and Methods

An experimental quantitative study was carried out to evaluate the efficiency of different ozonation exposure times on the reduction of artificially inoculated *Pseudomonas aeruginosa* in samples of whole and skim milk. The experiments were carried out at the Central Laboratory of Microbiology of the Universidade Brasil - Campus Fernandópolis/SP.

2.1 Inoculum Preparation

P. aeruginosa CCCD P013 (CEFAR Diagnostica, Brasil) was subcultured from vial stock onto TSA (Tryptic Soy Agar) at 37 °C for 24 h. Bacteria inoculum was prepared from 24 h culture in TSB (Tryptic Soy Broth) incubated at 35 °C, under orbital shaking (200 rpm). The initial bacterial density was determined using the standard McFarland scale (0.5, BioMérieux, Marcy-l'Etiole, France) For the treatment with ozone the cell density was adjusted to an initial concentration of 10^6 cells mL^{-1} in saline solution.

2.2 Samples

UHT (ultra-high temperature) whole and skim milk were used to prepare the samples and divided into the following experimental groups:

- Whole Control Group – WCG
- Whole Contaminated Group – WCoG
- Ozonized Contaminated Whole Group – OCoWG
- Skim Control Group – SCG
- Skim Contaminated Group – SCoG
- Ozonized Contaminated Skim Group - OCoSG

2.3 Ozone

The ozone gas was obtained from an ozone generator (Ozon & Life® Corona, MODEL O & L 3.0 RM, São José dos Campos-SP). The gas concentration was limited by the equipment, calibrated O_3 at 28 mgL^{-1}. In the pilot study of this work, concentrations of 25 and 28 mgL^{-1} were used and the results showed more effectiveness with the higher concentration of ozone. Since the literature [15] shows studies using concentrations of ozone above 40 mgL^{-1}, we chose to use the 28 mgL^{-1} concentration. The O_2 pressure from the cylinder to the generator was regulated by a valve calibrated at 1 L of O_2/min. Ambient temperature was kept between 18 and 20 °C through the experiment. Each milk sample was transferred to a glass column with a capacity of 400 mL, sterilized in an autoclave at 121 °C and 1 ATM of pressure for 15 min. The glass columns were connected to the ozone generator directly through a diffuser. Initial samples of non-contaminated and artificially contaminated with Pseudomonas were collected in Falcon tubes and microbial load were calculated.

Three ozonation times were tested: 5, 10 and 15 min. Each assay was performed in triplicate.

2.4 Microbiological Analysis

To verify the effect of ozone over Pseudomonas reduction, 0.1 mL of each experimental and control group were collected, and were plated in TSA. Plates were incubated for 48 h at 37 °C. Bacterial colonies were counted and converted into colony-forming units per milliliter (cfu mL^{-1}). The survival fraction values were obtained by dividing the data for the mean of initial bacteria count. Shapiro-Wilk test showed normal distribution of the sample and statistical comparisons were performed using *Student T* test. Significance levels were established on $p < 0.05$.

3 Results

Initial bacterial load was the same for whole and skim milk. Microbiological analyzes showed a reduction of about 1 log of *Pseudomonas aeruginosa* after 5 min of ozonation compared to its initial value. This result was observed both in whole as well as in skim milk (see Fig. 1a, b).

After 10 min of ozonation, the results showed a microbial reduction of approximately 4 logs in both samples (see Fig. 1a, b).

Fig. 1 Effect of different ozonation exposure times on *Pseudomonas* in whole milk (**a**) and in skim milk (**b**). Data are mean values
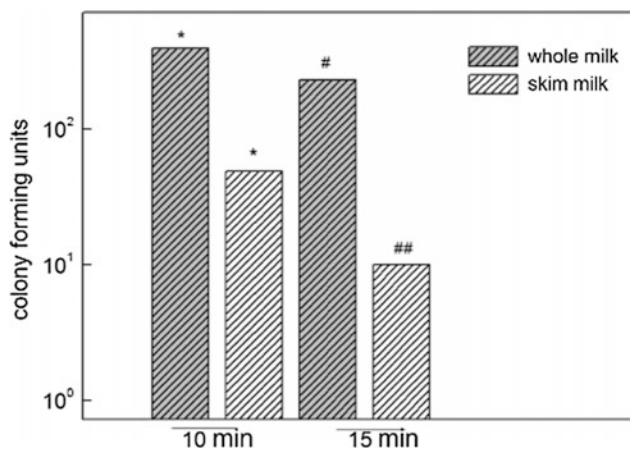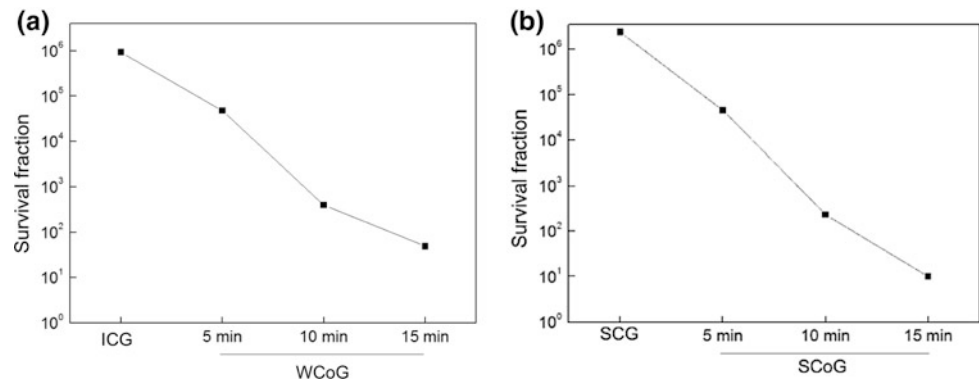
Fig. 2 Evaluation of microbial reduction in whole and skim milk in two different exposure times. Different symbols represent a statistically significant difference at each time (10 min - p = 0,09303 and 15 min - p = 0,00147). Data are mean values

The bacterial load calculated comparing reduction on whole and skim milk did not showed statistically significant difference after 10 min of ozonation. According to the results, after 15 min of ozonation we observed a higher reduction of microorganisms in skim milk than in whole milk (see Fig. 2).

4 Discussion

In this study, the ozonation process was applied to reduce *Pseudomonas* artificially inoculated in whole and skim milk. The results showed effectivity in both types of milk depending upon ozone exposure time. Longer exposure time promoted significantly higher microbial reduction. The same result can be found in the literature about ozone exposure and different microorganisms [16–18].

Study evaluated the effects of ozonation in sterile whole and skim milk after inoculation with *Staphylococcus aureus* [15]. They used two different concentrations of ozone (34.7 mg/L and 44.8 mg/L) and five exposure times of ozonation: 5, 10, 15, 20 and 25 min. The results showed that with 5 min of exposure there was no reduction of microbial load and that after 10 min of continuous exposure to O_3 they identify a significant decrease of the microbiota. This decrease was accentuated with the increase of exposure time up to 20 and 25 min that exterminate the sample. The result was the same for both whole and skim milk. The authors did not identify significant differences between ozone concentrations.

Our results showed that the reduction of *Pseudomonas* was more pronounced in skim than in whole milk. The same result was reported [19]. According to their study with two different microorganisms (*E. coli* and *Lb. Sakei*) the milk composition has a direct interference with ozone efficiency. The fat and protein content of the milk seems to serve as a target to ozone, preventing bacterial destruction, via ozone decomposition or substrate oxidation. The higher reductions of microorganisms on substrates containing organic matter were obtained for zero lactose skim milk, this milk have a maximum 0.5% fat and 0.5% of lactose. The second higher reduction occurred in homogenized skim milk, finally the lower reductions were observed in homogenized and non-homogenized whole milk with at least 3.0% fat content and 5.0% lactose [19]. Another factor to be considered is the homogenization process that promotes reduction on the size of the fat globules and the consequent increase of the contact surface, the junction of these two factors can influence on the decomposition process of the ozone and therefore it influences on inactivation of microorganisms by this process.

In addition, study evaluated the effectiveness of the ozonation process in the inactivation of Gram-negative bacteria, Gram positive bacteria, yeasts and molds in substrate formed by water with presence or absence of starch and bovine serum albumin [20]. The authors realized that the presence of organic matter affects significantly the inactivation of microorganisms.

Ozone is an unstable gas even when dissolved in water. However, in the presence of higher content of organic matter it is expected that the ozone decomposition occurs quickly and thus the effectiveness on microbial inactivation is

reduced [21]. Study demonstrated that consumption of ozone in aqueous media with organic matter is initially fast and with the degradation of the organic content, ozone decomposition occurs slowly as expected [22].

In the present study, the lower efficiency of ozonation in the reduction of *Pseudomonas* in whole milk compared to skim milk can be explained by ozone decomposition on substrates richer in organic matter, which as abovementioned occurs quickly.

Therefore, complex substrate deserves attention in regards of decontamination via O_3, since increasing the exposure time may not be enough due to ozone decomposition.

The results obtained in this study showed a significant reduction of microorganisms after 15 min of ozonation in both whole and skim milk, we encourage further research primarily about the nutritional content of whole and skim milk after ozonation to assure that all the dietary benefits of the milk are not affected by the process. The method can become viable mostly for small producers, and for organic milk production since the equipment can be produced with low cost and low operational conditions.

References

1. Haug, A., Høstmark, A.T., Harstad, O.M.: Bovine milk in human nutrition – a review. Lipids Health Dis. **6**, 25 (2007)
2. Pehrsson, P.R., Haytowitz, D.B., Holden, J.M., Perry, C.R., Beckler, D.G.: USDA's National Food and Nutrient Analysis Program: Food Sampling. J. Food Compos. Anal. **13**(4), 379–389 (2000)
3. Patton, S.: Milk: Its Remarkable Contribution to Human Health and Well-Being, 1st edn. Routledge, New York (2017)
4. Muehlhoff, E., Bennett, A., McMahon, D.: Milk and dairy products in human nutrition. Food and Agriculture Organization (2014)
5. Quigley, L., O'Sullivan, O., Stanton, C., Beresford, T.P., Ross, R. P., Fitzgerald, G.F., Cotter, P.D.: The complex microbiota of raw milk. FEMS Microbiol. Rev. **37**(5), 664–698 (2013)
6. Pinto, C.J.O., Martins, M.L., Vanetti, M.C.D.: Qualidade microbiológica de leite cru refrigerado e isolamento de bactérias psicrotróficas proteolíticas. Ciênc. Tecnol. Aliment. **26**(3), 645–651 (2006)
7. O'Donnell, C., Tiwari, B.K., Cullen, P.J., Rice, R.G.: Ozone in meat processing. In: Ozone in Food Processing, 1st edn. Blackwell Publishing, Chichester (2012)
8. Varga, L., Szigeti, J.: Use of ozone in the dairy industry: a review. Int. J. Dairy Technol. **69**(2), 15–17 (2016)
9. Mielcke, J., Ried, A.: Current state of application of ozone and UV for food processing. In: Proceedings of the Food Protection International Conference, Portugal, pp. 20–2 (2004)
10. Gonçalves, A.A.: Ozone - an emerging technology for the seafood industry. Braz. Arch. Biol. Technol. **52**(6), 1527–1539 (2009)
11. Tiwari, B.K., Muthukumarappan, k. Ozone in fruit and vegetable processing. In: Ozone in Food Processing, 1st edn. Blackwell Publishing, Chichester (2012)
12. Pohlman, F.W.: Ozone in meat processing. In: Ozone in Food Processing. 1st edn. Blackwell Publishing, Chichester (2012)
13. Vaz-Velho, M., Silva, M., Pessoa, J., Gibbs, P.: Inactivation by ozone of *Listeria innocua* on salmon-trout during cold-smoke processing. Food Control. **17**, 609–616 (2006)
14. Norton, T., Misiewicz, P.: Ozone for water treatment and its potential for process water reuse in the food industry. In: Ozone in Food Processing, 1st edn. Blackwell Publishing, Chichester (2012)
15. Couto, E.P., Ferreira, M.D.A., Alencar, E.R., Ribeiro, J.L.: Effect of ozonation on the *Staphylococcus Aureus* innoculated in milk. Semina: Ciencias Agrarias **37**(4), 1911–1918 (2014)
16. Lanita, C.S., Silva, S.B.: Uso de ozônio em câmara industrial para controle de bolores e leveduras durante a maturação de queijo tipo parmesão. Braz. J. Food Technol. **11**(3), 182–189 (2008)
17. Castillo, A., McKenzie, K.S., Lucia, L.M., Acuffi, G.R.: Ozone treatment for reduction of *Escherichia coli* 0157:H7 and *Salmonella serotype typhimurium* on beef carcass surfaces. J. Food Prot. **66**(5), 775–779 (2003)
18. Sheelamary, M., Muthukumar, M.: Effectiveness of Ozone in Inactivating *Listeria monocytogenes* from Milk Samples. WJYR **1** (3), 40–44 (2011)
19. Souza, S.M.O.: Estudo da interferência de substratos orgânicos na ação sobre microrganismos deteriorantes, benéficos e patogênicos. Tese de Doutorado em Ciências Ambientais – Universidade de Brasília (2016)
20. Restaino, L., Frampton, E.W., Hemphill, J.B., Palnikar, P.: Efficacy of ozonated water against various food-related microorganisms. Appl. Environ. Microbiol. **61**(9), 3471–3475 (1995)
21. Lullien-Pellerin, V.: Ozone in grain processing. In: Ozone in Food Processing, 1st edn. Blackwell Publishing, Chichester (2012)
22. Beltrán, F.J.: Ozone Reaction Kinetics for Water and Wastewater Systems. Lewis Publishers, Boca Raton (2004)

Samples Characterization of Commercial Regular and Lactose-Free Milk by Raman Spectroscopy

A. A. Ferreira, C. M. D. Xesquevixos, C. R. Franzini, C. F. Siqueira, E. B. Galvão, E. C. Luz, L. Silveira Jr., and M. K. Salomão

Abstract

The objective of this study was to verify the presence of lactose in whole and semi-skimmed bovine milk samples, and the absence of the same in samples of "lactose-free" milk by means of Raman spectroscopy. Samples of milk were obtained in local markets and divided into two groups: semi-skimmed milk and lactose-free milk. The samples were homogenized and an aliquot of 80 µl of milk was taken for reading on a Raman spectrophotometer (830 nm 250 mW) and the spectra were treated by principal component analysis (PCA). The Raman spectra presented peaks related to milk composition (proteins, lipids and carbohydrates) and particularly the zero lactose samples showed glucose and galactose peaks and showed no lactose peaks. It was also verified the different in the intensity of the fat peaks between the whole and semi-skimmed samples. The Raman technique associated with PCA was able to identify the presence of lactose due to its characteristic peak of glucose and galactose in lactose-free samples. It could be used as a fast, simple and non-reactive alternative for the identification of milk composition.

A. A. Ferreira · C. M. D. Xesquevixos (✉) · C. R. Franzini ·
C. F. Siqueira · E. B. Galvão · E. C. Luz · L. Silveira Jr. ·
M. K. Salomão
Universidade Anhembi Morumbi – UAM – Parque Tecnológico de São José dos Campos, São José dos Campos, SP, Brazil
e-mail: carolinexesquevixos@gmail.com

L. Silveira Jr.
e-mail: landulfo.silveira@gmail.com

L. Silveira Jr.
Center for Innovation Technology and Education - CITÉ - Parque Tecnológico de São José dos Campos, São José dos Campos, SP, Brazil

1 Introduction

The main carbohydrate present in milk and dairy products is lactose. Its molecule is composed of two monosaccharides, one molecule of D-glucose and one of D-galactose, being that human milk containing from 6% to 8% lactose, while milk from bovine provides from 4% to 6% lactose [1, 2]. The hydrolysis of lactose occurs through the enzyme lactase that catalyzes the β 1-4 glucosidic bond, converting the lactose into glucose and galactose that are absorbed by the intestine [3].

In spite of the nutritional importance of lactose present in milk, this carbohydrate can be a problem in the feeding of many people, since the activity of the enzyme lactase declines at some point in life, thus resulting in two groups of individuals: (i) with persistence of lactase (normolactase, lactose digestion) and (ii) non-persistence of lactase (hypolactasia, lactose maldigestion) [2–4].

The undigested lactose is fermented by the bacterial microbiota, producing hydrogen, methane, carbon dioxide and short chain fatty acids, which cause symptoms of lactose intolerance, such as flatulence, bloating, abdominal cramps and diarrhea, depending on the amount of lactose ingested [4–6]. The prevalence of hypolactasia in adults assorted among populations, in Denmark 4%, Great Britain 5% and Sweden 1–7% [7–9]. In Africa, Asia and Latin America the prevalence rates vary from 15% to 100% depending on the population studied [8], in Brazil it is 44.11% [2]. Against this background, the dairy industry performs hydrolysis of the lactose of the products, giving these individuals the consume of milk and its derivatives. There are two main methods: the chemical method is not used in the food industry because it depends on high temperatures and the use of very strong acids [1]. In the enzymatic method the addition of the enzimate lactase (β-galactosidase) is carried out in the milk. According to the National Agency for Sanitary Vigilance (ANVISA), lactose-free products, should be labeled with specific food regulations for special purposes.

The consumer with hypolactasia has the information stated by the manufacturer in the packaging, but if this information is not true, the consumption of these products can trigger the symptoms already mentioned, so the measurement of the lactose concentration in the milk should be part of the quality control performed by the industries.

The concentration of lactose in milk can be measured by gravimetric analysis, gas chromatography (GC-MS), liquid chromatography (HPLC) or by the dinitrosalicylic acid (DNS) method [10–12], and the concentration of glucose and galactose, is mostly determined by enzymatic methods (Table 1). These conventional methods are time-consuming, costly and complex [10, 13]. Thus, the development of fast, cheap and easy-to-perform methods is essential for the adequate quantification of lactose in milk.

Raman spectroscopy has been used as an alternative for the analysis of milk components and, therefore, as a possibility of use in the quality control. Its advantages include no need for sample preparation, measurements directly on the material without the need for reagents, speed, versatility, as well as being a non-invasive and non-destructive technique [14].

Raman spectroscopy is based on the interaction of a monochromatic light source, which upon reaching a sample, is scattered by the molecules, generating light with different energy from the incident light, this energy difference being related to the vibration energies of the material's chemical bonds. Raman (inelastic) scattering makes it possible to obtain information on the chemical composition of the sample [15, 16]. The Raman spectrum has peaks in the vibration frequencies of the chemical bonds and the intensity of the peaks is proportional to the concentration of the scattering molecules [17].

The objective of the study was to verify the possibility of using Raman spectroscopy to identify the presence of lactose in samples of semi-skimmed and "zero lactose" milk samples, identifying the lactose peaks in the samples of semi-skimmed milk and the peaks of glucose and galactose in the "zero lactose" samples, thus promoting an alternative methodology for the concentration of lactose and other macronutrients in the milk.

2 Materials and Methods

Samples of bovine milk were obtained in local store and were divided into two groups: semi-skimmed milk and "zero lactose" milk. The non-lactose group had two samples of different brands to certify the correctness of the labels indicating that the milk has no lactose in its composition.

The milk bottles were stirred for the homogenization of the liquid. An aliquot of milk was pipetted out and placed in an aluminum sample holder with wells of approximately 80 µL volume. Spectra were collected in triplicate.

The spectra were acquired using a dispersive Raman spectrometer (Dimension P-1, Lambda Solutions, Inc., MA, USA) composed of a diode laser (wavelength of 830 nm, output power of 350 mW), a Raman probe (Vector Probe, Lambda Solutions, Inc., MA, USA) coupled to laser and spectrometer, and a compact spectrometer with high sensitivity CCD camera. The laser power at the end of the Raman probe was set to 300 mW and the reading time of each spectrum adjusted to 30 s. The excitation laser beam has a diameter of about 180 µm at the focal point of the Raman probe.

The spectra were preprocessed for background removal (fluorescence and scattering from the sample) plotted in Excel software to better visualize the desired peaks and observation of spectral differences between milk types.

For analysis of the data, we used multivariate analysis based on principal component analysis (PCA). The PCA allows revealing the differences between samples with different characteristics, the variations between groups and the existence of anomalous samples, facilitating the grouping of samples that share certain spectral features.

Table 1 Methods used industrially for lactose removal and quality control of "lactose-free" products

Lactose removal			
Chemical method		Enzymatic method	
• High temperatures • Strong acids		• Addition of the enzyme β-galactosidase in milk • Average rest for 15 h at a temperature of 6 °C	
Quality control			
Gravimetric analysis	Gas chromatography	Liquid chromatography (HPLC)	Dinitrosalicylic acid (DNS)
• Delayed laboratory procedure • Bias in the precipitation process • Losses in the various steps	• Lower efficiency • Slow analysis	• Use of solvents • High maintenance cost of the equipment • Operator with experience is necessary	• Use of solvents • Complex method • Slow scan

Fig. 1 Mean Raman spectra of samples of semi-skimmed (low fat) milk and "zero lactose" milk of the same brands. The largest differences appear in the spectral regions between 400 and 600 cm^{-1} and between 1000 and 1200 cm^{-1}
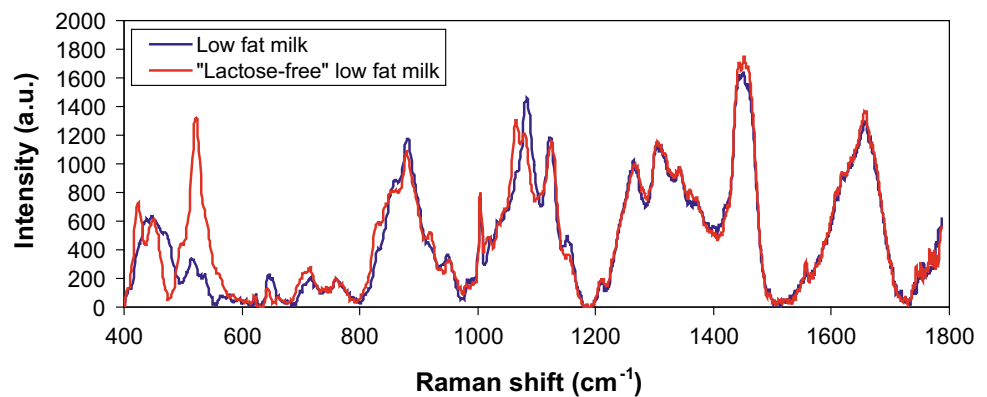
3 Results and Discussion

In the present study, Raman spectroscopy was used to verify the peaks related to the presence of lactose in semi-skimmed milk and the peaks corresponding to the products of lactase: glucose and galactose in the "zero lactose" samples. For so Raman spectra were taken from the semi-skimmed and "zero lactose" milk samples. Figure 1 presents the mean spectrum of each type of milk: semi-skimmed and "zero lactose". The main differences from milk samples can be observed in the spectral regions between 400 and 600 cm^{-1} evidencing a characteristic peak of glucose in the sample "lactose-free". Already in the regions between 1000 and 1200 cm^{-1} characterize the presence of lactose in low fat milk samples.

The PCA applied to the spectra resulted in principal components loadings (Scores) and intensities (PCs), which reveal the relevant spectral characteristics (Scores) that appear in the spectral data and the respective intensities (PCs) of each Score in each spectrum. Score 1 (Fig. 2) showed characteristic peaks that refer to the main components of milk: proteins (mainly casein), lipids (unsaturated and saturated fats) and carbohydrates (lactose, glucose and galactose) [18–20]. The similar intensity of PC1 suggests that the samples have similar macronutritional composition. Score 2 (Fig. 2) indicates a difference between milk types, where the positive peaks at 423, 452, 523, 842, 922, 1065 and 1136 cm^{-1} can be attributed to galactose and the negative peaks at 473, 855, 1087 and 1154 cm^{-1} can be attributed to lactose [20]. In fact, the samples from the semi-skimmed milk group have negative intensities for the negative peaks of lactose, while the samples from the group "zero lactose" milk have positive intensities for the positive peaks of glucose and galactose. Score 3 (Fig. 2) does not have relevant spectral characteristics.

The PCA analysis indicated that the difference in milk composition is characterized by peaks of glucose, galactose and lactose. This difference, which is quite evident in the analysis of PC2, can be used to characterize and validate the presence of monosaccharides glucose and galactose due to the action of the enzyme lactase in the "zero lactose" milk samples, and the presence of lactose in the samples of semi-skimmed milk. Therefore, according to the results presented, it can be confirmed that Raman spectroscopy can identify the presence of monosaccharides resulting from the lactose hydrolysis process and can be considered as a quick and precise methodology to identify the presence of lactose, glucose and galactose in milk samples.

In recent years, the technique has been presented in the literature as a resource for the analysis of the molecular components of different materials, being considered a "molecular fingerprint" [21]. In this sense, the research has demonstrated that it is possible to carry out the qualitative analysis of lactose or its hydrolysis, effectively discarding the presence of lactose in products that are characterized as "zero lactose".

There are methods of quality control on the market that promise to be effective in detecting the degree of lactose, however, they are slow and labor intensive processes, different from Raman spectroscopy, which can evaluate the presence of lactose with the ability to differentiate the samples of milk and possible adulterants.

The advantages of Raman spectroscopy, which can be applied independently of chemical reagents, are a quick and easy to use method, being a commercially viable alternative to verify the presence of lactose in bovine milk.
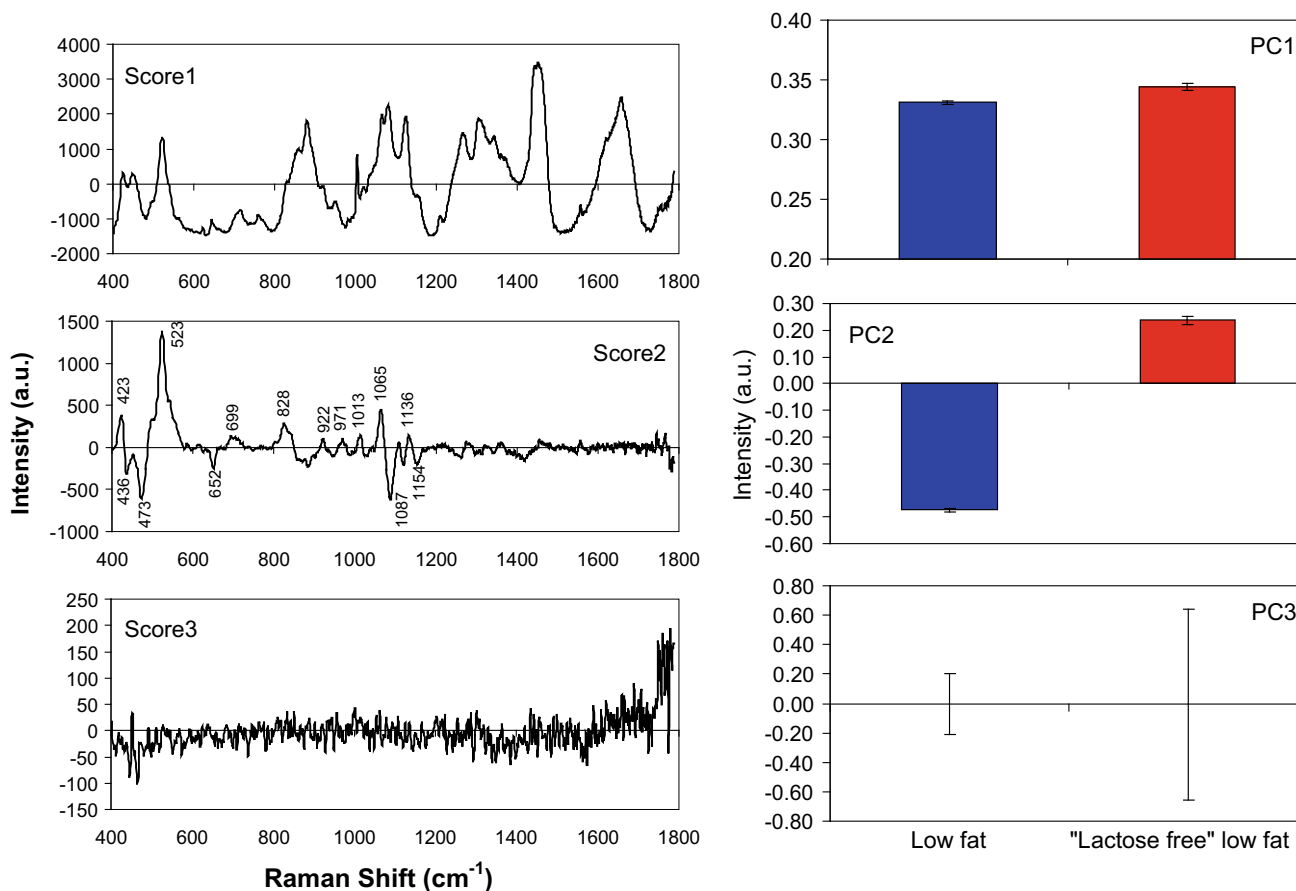
Fig. 2 Principal component loading vectors (Score 1 to Score 3) and intensities (PC1 to PC3)

4 Conclusions

Raman spectroscopy associated to PCA can be an efficient technique for the detection of lactose hydrolysis products in bovine milk due to the presence of specific peaks of each substance in the samples: lactose in samples of semi-skimmed milk and glucose and galactose in semi-skimmed "zero lactose" milk samples. Because it is a quick, simple and reagent-free alternative, its application to the quality control of "zero lactose" bovine milks may be advantageous compared to the techniques commonly used.

References

1. Longo, G.: Influência da adição de Lactase na produção de Iogurtes. Dissertação Mestrado. Universidade Federal do Paraná, Curitiba (2006)

2. Pereira, F.D., Furlan, S.A.: Prevalência de intolerância à lactose em função da faixa etária e do sexo: experiência do laboratório Dona Francisca, Joinville (SC). Revista Saúde e Ambiente, Joinville **5**(1), 24–30 (2004)

3. Toméi, M.C. D. M.: Lactose: Intolerância, Alergia e Rotulagem de Alimentos. Revista Científica Multidisciplinar Núcleo do Conhecimento. Ano 1. **9,** 99–110 (2016)

4. Mattar, R., et al.: Comparison of quick lactose intolerance test in duodenal biopsies of dyspeptic patients with single nucleotide polymorphism LCT-13910C > T associated with primary hypolactasia/lactase-persistence. Acta Cir. Bras. (São Paulo) **28** (supl. 1), 77–82 (2013)

5. Mattar, R., Mazo, D.F.C., Carrilho, F.J.: Lactose intolerance: diagnosis, genetic, and clinical factors. Clin. Exp. Gastroenterol. **5,** 113–121 (2012)

6. Cunha, L.R., et al.: Desenvolvimento e avaliação de embalagem ativa com incorporação de lactase. Ciência e Tecnologia de Alimentos, Campinas **27,** 23–26 (2007)

7. Mattar, R., Mazo, D.F.D.C.: Intolerância à lactose: mudança de paradigmas com a biologia molecular. Rev. Assoc. Med. Bras. (São Paulo) **56**(2), 230–236 (2010)

8. Lomer, M.C.E., et al.: Review article: lactose intolerance in clinical practice - myths and realities. Aliment. Pharmacol. Ther. **27**(2), 93–103 (2008)

9. Sahi, T.: Genetics and epidemiology of adult-type hypolactasia. Scand. J. Gastroenterol. **29,** 7–20 (1994)

10. Jasti, L.S., Dola, S.R., Fadnavis, N.W., et al.: Co-immobilized glucose oxidase and b-galactosidase on bovine serum albumin

coated allyl glycidyl ether (AGE)–ethylene glycol dimethacrylate (EGDM) copolymer as a biosensor for lactose determination in milk. Enzym. Microb. Technol. 64–65, 67–73 (2014). https://doi.org/10.1016/j.enzmictec

11. Sumner, J.B.: Dinitrosalicylic acid: a reagent for the estimation of sugar in normal and diabetic urine. J. Biol. Chem. **47**, 5–9 (1921)

12. Miller, G.L.: Use of dinitrosalicylic acid reagent for determination of reducing sugar. Anal. Chem. **31**, 426 (1959)

13. Barros, F., et al.: Evaluacion de ácido láctico intra-muscular através de espectroscopia Raman: novas perspectivas em medicina del deporte. Rev. Bras. Med. Esporte [online]. **9**(6), 388–395 (2003)

14. Silveira Jr., L., et al.: Characterization of nutritional parameters in bovine milk by Raman spectroscopy with least squares modeling. Instrum. Sci. Technol. **44**(1), 85–97 (2016)

15. Oliveira, M.X.: Efeitos da fototerapia de baixa intensidade em modelo experimental de tendinite em ratos. Tese de Doutorado, Universidade Camilo Castelo Branco, São José dos Campos (2013)

16. de Faria, D.L.A., et al.: Uma demonstração sobre o espalhamento inelástico de luz: repetindo o experimento de Raman. Química Nova **20**, 319 (1997)

17. Pelletier, M.J.: Quantitative analysis using Raman spectrometry. Appl. Spectrosc. **57**, 20A–42A (2003)

18. Stuart, B., Ando, D. J.: Biological Applications of Infrared Spectroscopy. Wiley, Chichester. Published on behalf of ACOL (University of Greenwich) (1997), 191 p.

19. Dekker, M.: Infrared and Raman Spectroscopy of Biological Materials. Marcel Dekker, New York: (2001), 581 p. (Practical spectroscopy; v. 24). ISBN 0824704096

20. Wells, H.A., Atalla, R.H.: An investigation of the vibrational spectra of glucose, galactose and mannose. J. Mol. Struct. **224**, 385–424 (1990)

21. Silveira, T.M.L., et al.: Comparação entre métodos de referência e análise eletrônica na determinação da composição do leite bovino. Arquivo Brasileiro de Medicina e Zootecnia **56**(6), 782–787 (2004)

Systematic Review: Metrology in Health- Failures, Limitations and Challenges

V. L. Goncalves, L. C. Mendes, A. C. Rosa, A. A. Pereira, and S. T. Milagre

Abstract

This work consists of a systematic review that aims identify and illustrate the various limita tions that health systems currently face regarding the metrological system reliability of medical equipment. Studies have been made in the search for scientific articles in databases chosen, and after the application of the criteria for inclusion and exclusion for articles, obtained 6 publications, that represented the base of the construction of this work. The metrological reliability of medical equipment is extremely important in health services, as it ensures, among other things, the safety of diagnostics and treatments. It was possible to observe that this is a matter of very little presence in the daily lives of the professionals of the health area, pointing to the need for evaluation of the reliability in most cases presented.

Keywords

Metrology • Healthy • Medical equipment

1 Introduction

The search for qualitative aspects, such as high performance and low rates of failure in the use of medical equipment, must be strict in order to avoid and reduce the rates of adverse events. The risk of using equipment without adequate metrological evaluation came to prominence only after 1990 with the publication of the results of the adverse events in Harvard Medical Practice Study, where it was found that 3.7% of patients who were hospitalize suffered adverse events and that 13.6% of the events led to death [1]. Thus, it is essential to use metrological tools that make sure the perfect operation of medical equipment.

Metrology is a word of Greek origin, in which *metron* meaning measures, and *logos* meaning science, being considered the science of measures and measurements. It covers all theoretical and practical aspects relating to measurement through a set of knowledge are they scientific and/or technological. Despite the breakthrough in scientific and industrial, metrology presents even incipient in healthcare [2].

Medical equipments are very important tool in order to have an accurate and effective diagnosis and treatment, which directly affects the results and practice of medical activities [2]. With the development of Science and Technology, in the twentieth century, the biomedical equipment went through an accelerated evolution in relation to the sophistication and complexity, making it difficult to detect possible failures by simple inspection. In addition, more and more doctors begin to trust their diagnoses and treatments on quantitative parameters offered by such instruments [3].

In Brazil the medical equipment must be registered with the National Health Surveillance Agency (ANVISA) before being made available for commercialization. To obtain this registry is made a certification of compliance with specific technical standards issued by Product Certification Organizations (OCP) and accredited by the National Institute of Metrology, Quality and Technology (INMETRO). However, there is no law or regulation in the Brazilian constitution that makes it essential to control and guarantee the metrological reliability of medical equipment, with the exception of mechanical sphygmomanometers of non-invasive measurement of type aneroid, equipment involving the use of ionizing radiation, and clinical thermometer mercury in glass [1].

In this context, accreditation becomes an important ally to health services, since it is a system that promotes evaluation and certification of quality. Accreditations can be carried out by national or international entities such as: the International Standardization Organization (ISO), the National

V. L. Goncalves (✉) · L. C. Mendes · A. C. Rosa
Postgraduate Program in Biomedical Engineering (PPGEB) - Federal University of Uberlândia (UFU), Uberlândia, Brazil
e-mail: veronica_lg@hotmail.com

A. A. Pereira · S. T. Milagre
Department of Biomedical Engineering, Federal University of Uberlândia (UFU), Uberlândia, Brazil

Accreditation Organization (ONA) and the Joint Commission for Accreditation on Health Organizations (JCAHO). These entities stipulate conditions and requirements in relation the guarantee of reliability of medical equipment, which must be followed by accredited establishments, especially in relation to the calibrations screened and preventive and corrective maintenance [1]. There are in Brazil currently 293 hospitals and several others are in the process of accreditation [1].

In order for the data obtained are trusted and accepted worldwide, the precision of the measurements is provided and must be evidenced by its traceability to certified and internationally recognized standards of measurement or reference materials. The metrological traceability is the result of a measurement or of the value of pattern be related to established references, usually to national or international standards, through a continuous chain of comparisons, all having uncertainties [3–5].

In this way, due to the importance and complexity commonly associated with the technology of medical equipment, it is evident the need of thorough follow-up to the good and correct operation of the same, thus avoiding the occurrence of possible adverse events [2].

The present work presents a systematic review of the failures, limitations and challenges of medical equipment metrology.

2   Methodology

For the development of this systematic review related to metrology in health research were made to search for scientific articles in BIREME, PUBMED, PORTAL CAPES, LILACS and GOOGLE ACADEMICO databases. The descriptors for the research were: metrology, health, medical equipment, calibration and adverse events.

The searches conducted in the databases were made with the intersection of descriptors, as follows: remained always the descriptors "metrology" and "health", changing only the other two last in each search, in addition to maintaining all descriptors. In each of the searches, all articles were selected and included in a spreadsheet made in Excel. It is important to note that all the descriptors were searched in three different languages: Portuguese, English and Spanish.

After the inclusion of all articles, the exclusion process using three criteria: repetition of articles; non-compliance with the theme; incomplete texts or who have not contributed significantly to the research.

The tool used for the identification, selection, eligibility, and inclusion of the articles was the call PRISM, which features favorite reports items for systematic analyzes and meta-analyzes. The research has resulted in 38 initial

articles, and after the exclusion of the same step by stage, obeying the criteria, this number reduced to 6. From this the articles were studied and evaluated.

3   Results

From the 38 articles, 25 were left after exclusion due to repetition. Then, with the removal of those who do not fit the theme, left 8. Two were excluded because they don't contain relevant information on the topic, and then 6 articles, which represented the basis of this work.

Figure 1 represents the step-by-step of each step of this process.

4   Discussion

Measurement set of activities aimed at determining the value of grandeur, presents significant relevance in a hospital environment, needing to be exact, real and comparable. The physical, chemical and biological measurements are critical in the assessment and risk characterization; in the diagnosis, prevention and treatment of diseases; and also, in the monitoring of patients [6, 7].

However, the measurements are subject to indication errors, which can occur by two factors: the first, by external factors linked to the environment, such as temperature, pressure, humidity, noise, dust, etc.; and the second, by the measuring instrument.

In this review were identified studies which highlight flaws and limitations found in health services in metrological reliability.

The first studies analyzed in this work dealing with blood pressure. Blood pressure is a physiological parameter risk indicator for cardiovascular and coronary diseases. Through a unique and simple measurement of blood pressure, hypertension can be diagnosed, and decisions related to the diagnosis, prognosis and therapy are adopted. For this reason, your correct and early detection is essential to the well-being of any patient.

The instrument used for the measurement of blood pressure is the sphygmomanometer, and for the mechanical sphygmomanometer non-invasive measurement of the aneroid type, is allowed a static error not exceeding ± 3 mmHg, according to the metrological technical regulations elaborated by INMETRO [1].

However, a study conducted in Australia, proved that, using a sphygmomanometer that overestimates the diastolic pressure in 3 mmHg, obtained an increase of 83% in the number of patients with diastolic blood pressure greater than 95 mmHg. This means that 4 of 5 diagnosed as hypertension, would have that diagnosis wrong, not being

Fig. 1 Preferred reporting items for systematic analyses (Prism)
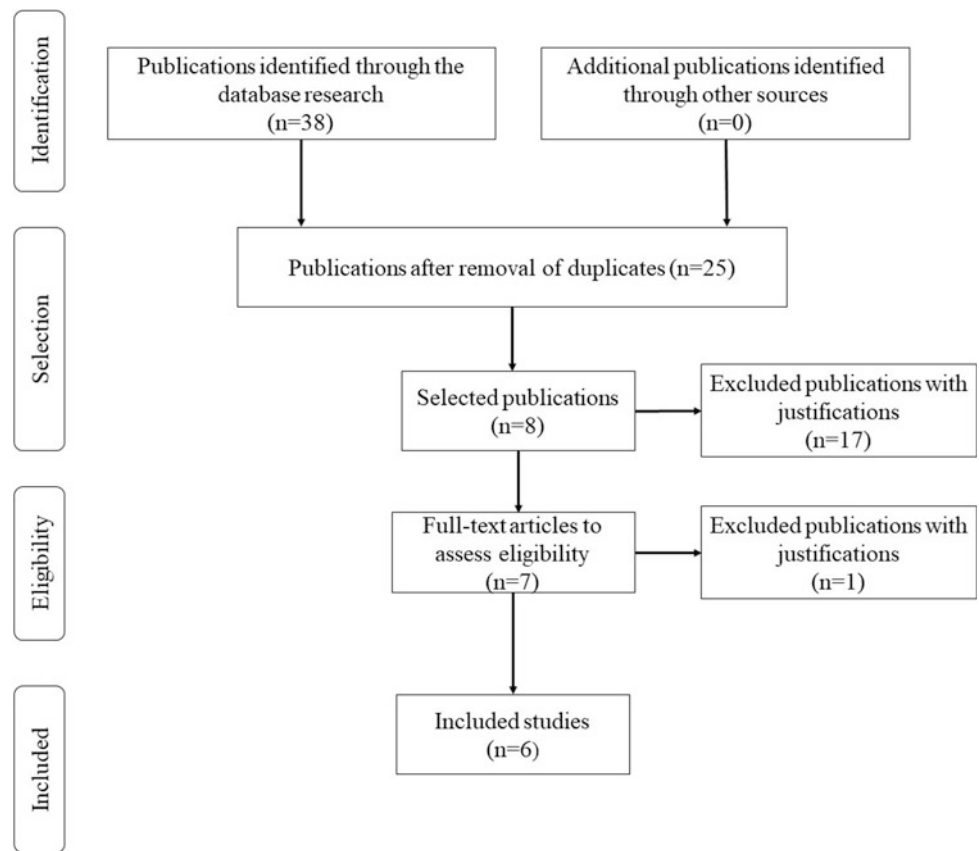
hypertensive. In contrast, using a sphygmomanometer that underestimates the diastolic pressure by 3 mmHg, it was found that 50% of patients with diastolic pressure greater than 95 mmHg would not be identified [1].

The results obtained by the researchers Rouse and Marshal (2001) reinforce this concern and suggest that the tolerance of ±3 mmHg is too wide for the realization of reliable diagnosis of diastolic arterial hypertension, indicating 1 mmHg as the ideal value for measurement uncertainty [1].

A research published in Research on Biomedical Engineering 2017 showed that 61.1% or 44 of the assessed sphygmomanometers to metrological conformities did not meet the specifications, and many of them were not suitable for hospital use and may lead to an inadequate diagnosis of hypertension. In addition, 26 of 72 devices evaluated exceeded their annual, periodic verification period, and that 15 of these 26 devices were not suitable for use [8].

In another study, from Mion et al., concluded that 72.0% of the sphygmomanometers evaluated had a problem related to several factors, such as: bladder integrity, manometer calibration, deflation valve, connection hose and hand pump [8].

According to Toledo et al., 12 of 57 evaluated sphygmomanometers presented physical defects and were then reproved for measurement. For accuracy, were assessed 45

devices, of which 35 were approved by INMETRO criteria and received the seal of accuracy. In short, this study found that 22 (38.5%) of all manometers evaluated were inadequate for clinical practice, 12 (21%) for physical defects and 10 (17.5%) for imprecision [9].

Another study published in the Journal of Physics: Conference Series 2018 assessed the relevance of metrological requirements in the process of acquiring medical equipment, both in public and private hospitals. The issue of greatest merit for private hospitals was performing maintenance of the equipment by the manufacturer, while the purchase price was the most important requirement for public hospitals. The hospitals that have acquired calibrated measuring instruments, only 50% performed the internal calibration. The methodology established by the hospitals for the acquisition of equipment not reflects in any way on metrological concerns. In addition, the relationship between maintenance and metrological operation was not well established every hospital, since metrological traceability was secondary to maintenance operations [10].

In this same study, were also evaluated the budgetary outcomes of hospitals that are applied to metrological operations and maintenance (preventive and corrective), calibrations and verifications of measuring instruments. The

corrective maintenance of measuring instruments was attributed by more than 30% of the overall budget in 13.6% of hospitals, while 75% of hospitals allocated less than 10% of the maintenance budget, evidencing the fact that a minority of hospitals invest in maintenance [10].

In the study by Reis et al., was rated a single infusion pump to uncertainty calculations for measurement, and for the estimation of the same, 15 flow samples were collected (50 ml/h), during the total period of the test, separated also in time. In no time the programmed value exceeds 50 ml/h. The results indicate that the bomb was inside the default suggested by manufacturer. However, it is undeniable the importance of analyzing of the uncertainty of measurement as a parameter evaluation tool, assisting in estimate the degree of reliability in the use of equipment [11].

In the study published by the magazine Technology and HealthCare, the tests were evaluated in 50 lung ventilators and 50 neonatal incubators. The tests were conducted in accordance with the safety and performance requirements laid down in the relevant international standards, guidelines and legal metrology policies. Of the 50 incubators inspected, 40% of them had measured values that were not within the limits indicated, and 48% of the mechanical ventilators were not within the limits indicated [12].

All these examples identify a decline in the effectiveness of the metrological control of medical equipment and management in a hospital environment.

5   Conclusion

Metrology in health is a condition to ensure that the results of measurements relevant medical diagnosis measurements are accurate, reliable and comparable. For this purpose, are absolutely necessary for the implementation of tools that ensure the metrological traceability of measurements and measuring instruments [6]. The reliability of health procedures, the accuracy and metrological traceability are contributions to promote patient safety in the hospital environment [13].

The absence of metrological control and calibration of medical equipment, leading to misdiagnoses due to measurement errors, endangering the health and life of people [14].

The correct execution of the metrological control in the health area allows: lower cost associated with the maintenance of medical equipment; increased productivity and availability of equipment; decrease in the misuse of medical technology by nonqualified personnel; deepen scientific and technical knowledge in medical equipment [2].

References

1. Monteiro, E.C., Lessa, M.L.: A metrologia na área de saúde: garantia da segurança e da qualidade dos equipamentos eletromédicos. ENGEVISTA **7**(2), 51–60 (2005)
2. Trujillo, M., Salazar, F.E., Andrade, M.E.: Politics for the integration of the activities of insurance metrological to the process of maintenance of biomedical equipments. Revista RevistaIngeniería Biomédica **9**, 33–40 (2015)
3. Inmetro, Vocabulário Internacional de Termos Fundamentais e Gerais de Metrologia, 3ª ed, INMETRO, Rio de Janeiro (2003)
4. International Organization for Standardization, Vocabulário Revision of the 1993 edition, International vocabulary of basic and general terms in metrology (VIM), 3rd edn. Draft April 2004
5. Santana, M.A.A.: Requisitos técnicos para competência de laboratórios de calibração e ensaios aplicados em P&D, ENQUALAB 2003, São Paulo-SP, julho de 2003
6. Ferreira, M.C.: A importância da metrologia na saúde **8**, 8–11 (2008)
7. Fernandes, W.D., COSTA, P.O., Silva, J.R.: Metrologia E Qualidade - Sua Importância como fatores de competitividade nos Processos Produtivos. XXIX Encontro Nacional de Engenharia de Produção (2009)
8. Faria, V.N.R., et al.: An investigative case study at local hospital into the current reliability of blood pressure sphygmomanometers. Revista Brasileira de Engenharia Biomédica **33**(1), 21–30 (2017)
9. Toledo, M.A., et al.: Validade Dos Esfigmomanômetros Utilizados Por Profissionais De Saúde Do Hospital Universitário Da Universidade De Brasília. Brasília Med. **53**(9), 5–9 (2002)
10. Ferreira, M., Matos, A.: Metrology in health: a pilot study. J. Phys. Conf. Ser. **588**, 12018 (2015)
11. Reis, R.B.S., et al.: Análise Metrológica e Incerteza de Medição com o auxílio na avaliação de qualidade de Bomba de Infusão, pp. 1–5 [s.d.]
12. Badnjevic, A., et al.: Testing of mechanical ventilators and infant incubators in healthcare institutions. Technol. Health Care **25**(2), 237–250 (2017)
13. Monteiro, E.C., Leon, L.F.: Metrological reliability of medical devices. J. Phys. Conf. Ser. **588**(1), 012032 (2015)
14. Paiva, M.R., et al.: Prospection for metrological control in medical scales and sphygmomanometers in the state of Santa Catarina-Brazil. J. Phys. Conf. Ser. **575**(1), 012047 (2013)

Ultrasonic Output Power Measurement According to IEC 61161:2013

P. A. Oliveira, A. V. Alvarenga, and R. P. B. Costa-Felix

Abstract

The ultrasound physiotherapy equipment must accomplish with the basic safety and essential performance requirements as ruled by the international standards. The technical standard IEC 61161:2013 specifies a measurement method to determining the total emitted acoustic power of ultrasonic transducers based on the use of a radiation force balance. In the present study, a metrological approach was adopted and the measurement system used in the ultrasonic output power calibration was evaluated through participation in the BIPM key-comparison. This work presents the measurement results, and the expanded uncertainty, of the emitted ultrasonic output power of two ultrasound physiotherapy equipment operating at 1 and 3 MHz and nominal power of 3.6, 5.4 and 7.2 W. The expanded uncertainty was calculated according to the Guide of the Expression of Uncertainty in Measurements. Measurement results are reported with remarkably low uncertainties. Thereof, it could be demonstrated that in both ultrasound therapy equipment there was a statistically significant difference between the nominal and the measured power. The metrological approach adopted could provide confidence to the experimental results.

1 Introduction

Therapeutic ultrasound (US) is frequently used by physiotherapists in applications such as treatment of chronic inflammation, degenerative rheumatic disorders, ankle distortions and post-traumatic diseases [1]. One of the advantages is that the absorption of ultrasound energy by tissues generates a temperature rise, which causes an increase in blood flow, reduction of the inflammation process, reduction of muscle spasm, and others [2]. The use of uncalibrated systems could result in inefficient treatments or even harm to patients [3]. Thus, the ultrasound physiotherapy equipment must be safe and effective to ensure the patient wellbeing, and it is fundamental that the ultrasonic output power delivered by the physiotherapy equipment is under safe levels.

The quantification of the ultrasonic output power generated by the equipment and delivered with the aid of a transducer is one of the ways to ensure its safety. Hence, the international standard IEC 61161:2013 [4] specifies a measurement method to determining the total emitted acoustic power of ultrasonic equipment based on the use of a radiation force balance. There are many studies in the literature that have evaluated physiotherapy equipment showing significant variations between nominal and measured ultrasonic output power. In the study performed by Guirro and Santos [5], forty-eight new ultrasound therapy equipment were evaluated operating in continuous mode. Although the ultrasound therapy equipment were new, a variation of more than 30% between the nominal and measured ultrasonic output power was observed in five of them. Ferrari [6] evaluated 24 ultrasound therapy equipment operating at the frequency of 1 MHz and 5 with frequency of 3 MHz. The author observed that 68% of the equipment presented variation between the nominal and the measured ultrasonic output power.

While there are studies in the literature that evaluate the emitted ultrasonic output power of ultrasonic therapy transducers [5–8], none of them present an estimate of the measurement uncertainty. In the present study, a metrological approach was adopted and the measurement system used in the ultrasonic output power calibration was evaluated through participation in the BIPM key-comparison CCAUV. U-K3.1 [9]. In this context, this study presents the

P. A. Oliveira (✉) · A. V. Alvarenga · R. P. B. Costa-Félix
Laboratory of Ultrasound, Institute of Metrology, Quality and Technology (Inmetro), Duque de Caxias, RJ, Brazil
e-mail: passuncaooliveira@gmail.com

Fig. 1 **a** Experimental setup used for ultrasonic output power measurement. [a] Analytical balance, [b] positioning system, [c] support, and [d] transducer, **b** Detail of transducer and absorbing target
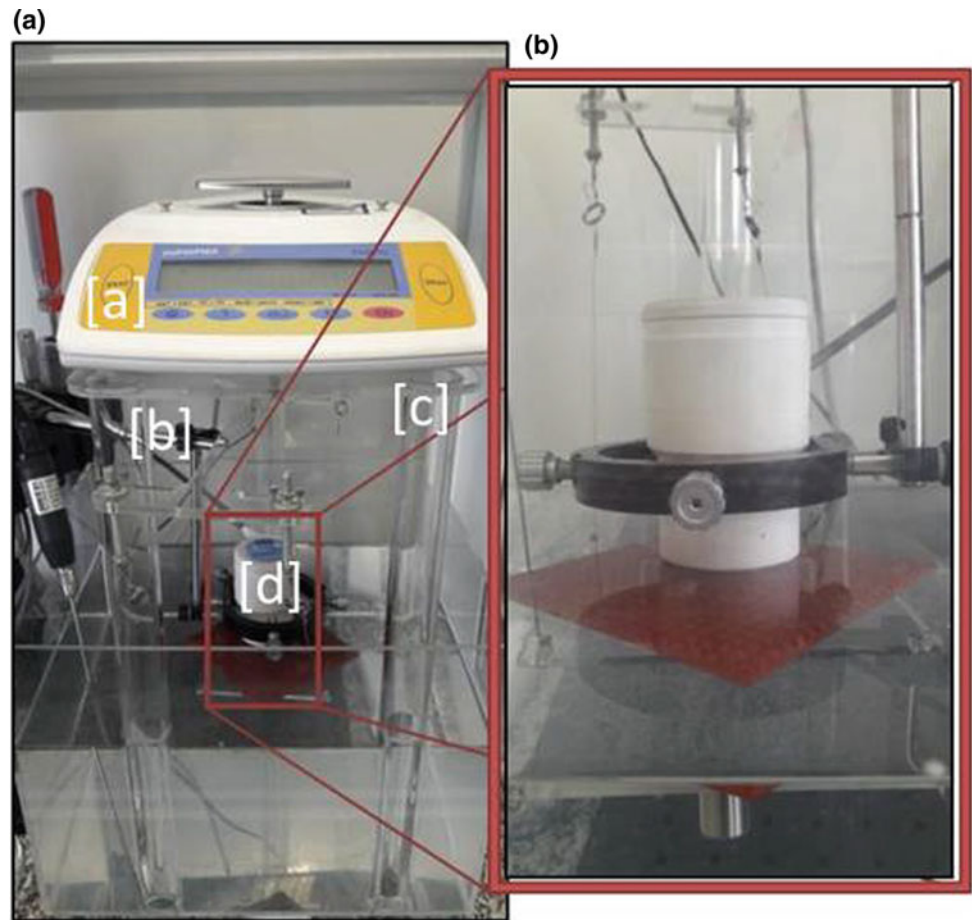
measurement results, and the expanded uncertainty (U), of the emitted ultrasonic output power of two ultrasound physiotherapy equipment operating at 1 and 3 MHz.

2 Materials and Methods

2.1 Ultrasonic Physiotherapy Equipment

Two ultrasonic physiotherapy equipment with their respective transducers were evaluated, operating in continuous mode at the nominal frequencies of 1 MHz (Equipment A) and 3 MHz (Equipment B) and nominal power of 3.6, 5.4 and 7.2 W.

2.2 Experimental Setup

A radiation force balance based on an absorber target was used to measure the ultrasonic output power emitted by ultrasound physiotherapy equipment. The experimental scheme was developed at Inmetro and consists in the following equipment and accessories: a tank containing distilled and deionized water; a calibrated analytical balance model CP224S (Sartorius, Germany); a 5 degrees of freedom positioning system (Newport Corporation, USA) to align the therapy transducer; a support in which the absorbing target is positioned; a dissolved oxygen meter model XL40 (Accumet Instruments, Singapore) to monitoring dissolved oxygen; a thermo-hygrometer model Hygropalm 3 (Rotronic, Switzerland) to monitoring the water temperature; and ultrasound physiotherapy equipment. The experimental setup is disclosed in Fig. 1.

2.3 Ultrasonic Output Power Measurement

The ultrasonic output power of the transducer can be determined by radiation force exerted by the ultrasonic field and the speed of sound in the water, according to Eq. 1.

$$P = c \cdot F = c(T) \cdot m \cdot g \, [\text{W}] \tag{1}$$

in which $c(T)$ is the speed of sound in a medium (distilled and deionized water) as a function of temperature, g is the gravitational acceleration, and m is the mass measured with the aid of the microbalance.

Table 1 Mains sources and contributions of type B uncertainty considered in the measurement of ultrasonic output power

Sources and contributions of type B uncertainty			
Balance (%)	Target (%)	Speed of sound (%)	Gravity (%)
Calibration 0.1	Imperfections 0.5	Equation 0.1	Calibration 0.001
Linearity 0.1	Transducer misalignments 0.5	Temperature 0.5	Resolution 0.1
Resolution 0.1	Target finite size 0.5	–	Position of the measurement system 0.01
Regression 0.01	–	–	

The ultrasonic output power measurement was performed according to the standard IEC 61161:2013 [4]. The transducer was fixed and aligned by the positioning system, and the measurements were performed at three different distances between the face of the transducer and the surface of the absorber target: 10, 15, and 20 mm. At each distance, two measurements were performed, slightly moving the transducer ¼ of a wavelength upwards. The whole procedure is repeated 3 times, and the measurements were performed under repeatability conditions. At each repetition the transducer was removed and reattached to the positioning system. The measurement system is automated by means of dedicated software developed in LabVIEW. Additional information on system automation is described in [10].

2.4 Measurement Uncertainty

The expanded uncertainty was calculated according to the Guide of the Expression of Uncertainty in Measurements [11], by a coverage factor k that takes into account a t-distribution with coverage probability of 0.95. Type A uncertainty was calculated considering the standard deviation for different distances within one repetition, and the standard deviation of different repetitions. Regarding to type B uncertainty, the main sources of uncertainty considered are described in Table 1.

3 Results

The results of measurement ultrasonic output power of the two ultrasound equipment operating in 1 and 3 MHz, and their respective expanded uncertainties and coverage factors, are shown in Tables 2 and 3.

The graphical representation of Tables 2 and 3 is shown in Fig. 2.

Table 2 Results of ultrasonic output power measurement for equipment A, operating at 1 MHz. **U [W]** is the expanded uncertainty for a confidence level of 0.95, resulting in the disclosed coverage factor **k**

Nominal power [W]	Measured power [W]	U [W]	Coverage factor k
3.6	4.22	0.14	2.09
5.4	6.51	0.19	2.01
7.2	9.06	0.56	2.45

Table 3 Results of ultrasonic output power measurement for equipment B, operating at 3 MHz. **U [W]** is the expanded uncertainty (p = 0.95)

Nominal power [W]	Measured power [W]	U [W]	Coverage factor k
3.6	2.80	0.19	2.45
5.4	4.11	0.22	2.36
7.2	5.36	0.25	2.26
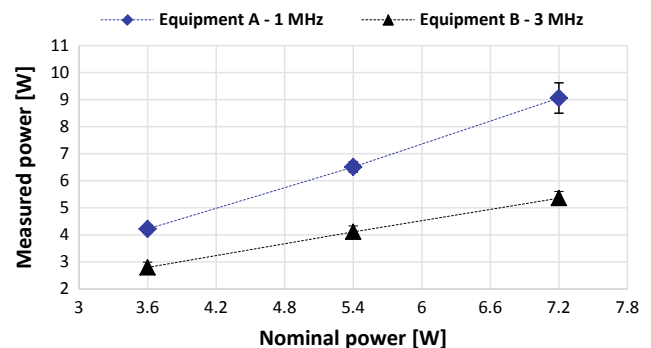
Fig. 2 Ultrasonic output power calibration curves for equipment A and B, operating at 1 and 3 MHz, respectively

4 Discussion and Conclusions

Considering the results obtained in this study, one can observe that in both ultrasound therapy equipment there was a significant difference between the nominal power and the measured power. In equipment A, the measured powers were greater than the nominal power, whilst in equipment B the measured power was lower than the nominal power. Measurement results are reported with low uncertainties, being 6.2% for equipment A and 4.6% for equipment B, providing confidence to the results found.

The results presented in this study are in agreement to the ones previously mentioned, which significant differences between nominal and measured ultrasonic output power was observed. Moreover, it is clear that the studies presented in literature still need a metrological approach, what is indispensable to allow comparability among the results achieved by different laboratories and research groups.

For biomedical engineers dealing with ultrasound therapy equipment, the research presented herein is valuable as they could be aware if a calibration certificate or a testing report from a competent laboratory are up to date with the regard of the best metrological practice worldwide. Furthermore, for a researcher who used ultrasound equipment, it is of utmost importance to assure their experimental results are based on the best metrology fundamentals.

References

1. Schabrun, S., Walker, H., Chipchase, L.: How accurate are therapeutic ultrasound machines? Hong Kong Physiother. J. **26**, 39–44 (2008)
2. Speed, C.A.: Therapeutic ultrasound in soft tissue lesion. Rheumatology **40**, 1331–1336 (2002)
3. Baker, K.G., Robertson, V.J., Duck, F.A.: A review of therapeutic ultrasound: biophysical effects. Phys. Ther. **81**, 1351–1358 (2001)
4. IEC 61161:2013 – Ultrasonics - power measurement - radiation force balances and performance requirements. IEC – The International Electrotechnical Commission
5. Guirro, R., Santos, S.C.B.: Evaluation of the acoustic intensity of new ultrasound therapy equipment. Ultrasonics **39**, 553–557 (2002)
6. Ferrari, C.B.: Avaliação do desempenho de equipamentos de ultrassom terapêutico [dissertação], Universidade Metodista de Piracicaba, São Paulo (2008)
7. Ferrari, C.B., Andrade, M.A.B., Adamowski, J.C., Guirro, R.R.J.: Evaluation of therapeutic ultrasound equipments performance. Ultrasonics **50**, 704–709 (2010)
8. Rocha, S.S., Nunes, L.S., Pereira, A.J.F., Omena, T.P., Costa, R.M., Von Kruger, M.A., Pereira, W.C.A.: Avaliação da potência ultrassônica durante um ano de um equipamento de ultrassom fisioterapêutico. In: XXIV Congresso Brasileiro de Engenharia Biomédica – CBEB, pp. 2727–2729 (2014)
9. Haller, J., Koch, C., Costa-Félix, R.P.B., Dubey, P.K., Durando, G., Kim, Y.T., Yoshioka, M.: Final report on key comparison CCAUV.U-K3.1. Metrologia **53**(Technical Supplement), 09002 (2016)
10. Costa-Félix, R.P.B., Alvarenga, A.V., Hekkenberg, R.: A fully automated system for ultrasonic power measurement and simulation accordingly to IEC 61161:2006. J. Phys. Conf. Ser. **279**, 012004 (2011)
11. GUM: Guia para a expressão de incerteza de medição. BIPM, JCGM:100 2008, Paris

Ultrasound Power Measurement with a Water-Based Calorimeter

G. Morgado, S. A. Miqueleti, and R. P. B. Costa-Felix

Abstract

Therapeutic ultrasound equipment typically employs frequency from 1 to 3 MHz and intensities ranging from 0.1 to 3.0 W cm^{-2} in continuous and pulsed modes. Ultrasound is among the physical resources most used by professional physiotherapists in the treatment in a wide diverse disorder of the musculoskeletal system. The intensity of the ultrasonic radiation is an essential factor for the success of any therapy, as well as its time of application. The ultrasound power should be calibrated to avoid lack of efficiency of the treatment. A fast and reliable ultrasonic power measurement is necessary to a rapidly assess the output of a physiotherapy equipment. This paper presents a comparison between an ultrasound power measurement based on a radiation force balance and a calorimeter. The ultrasound power source is a calibrated 3.5 MHz continuous-wave instrument, with a robust NDT transducer. The calorimeter was specially developed to assess ultrasonic power up to 1 W, using deionized and degassed pure water as sonication medium. The power measurement outcome from the calorimeter were equivalent to the power measurement undertaken with a calibrated radiation force balance. The expanded uncertainty (p = 0.95) achieved with the calorimeter was 60 mW, whilst with the calibrated microbalance the uncertainty was 32 mW. The results obtained so far indicates that the use of a calorimeter for ultrasonic power measurement is a fast and metrologically reliable way to assure the output power of ultrasonic physiotherapy equipment.

1 Introduction

Ultrasound is defined as an acoustic wave of frequencies higher than those can be detected by the human ear, or waves whose frequencies are greater than 20 kHz. Typical application of ultrasound can reach up to 100 MHz in some applications. Therapeutic ultrasound equipment typically use frequency from 1 to 3 MHz and intensities ranging from 0.1 to 3.0 W cm^{-2} in continuous or pulsed modes. Intensities less than 0.1 W cm^{-2} are used for diagnosis and greater than 10 W cm^{-2} for tissue ablation [1].

Ultrasonic waves are used in physiotherapy as a resource to generate heat, reduce inflammation and accelerate tissue healing [2]. According to [3], tissue heating occurs due to the absorption of the ultrasonic beam during its propagation throughout the treated tissue.

Ultrasound therapy depends basically on two factors: the adopted protocol of application and the performance of the equipment. When ultrasonic devices are calibrated, significant differences between nominal (manufacturer-supplied) and actual (estimated) values are verified for the effective radiation area (ERA), power and intensity [4–6].

The standard method for verifying the ultrasound therapy equipment (USTE) are standardized by the IEC 61689 [1], which defines general procedures for measuring and characterizing the ultrasonic beam of those devices. That technical standard defines the parameters for the calculation of the dose used in the treatment, as effective intensity, Effective Radiation Area (ERA), ultrasonic power, among others, in addition to defining its safety limits [4].

The standardized way to measure ultrasonic power is with the aid of a radiation force balance in accordance with the international technical standard 61161 [7, 8]. Nevertheless,

G. Morgado (✉) · S. A. Miqueleti · R. P. B. Costa-Felix
Laboratory of Ultrasound, National Institute of Metrology, Quality and Technology (Inmetro), Av. Nossa Sra das Graças 50, Duque de Caxias, RJ 25250-020, Brazil
e-mail: gisele.morgado@hotmail.com
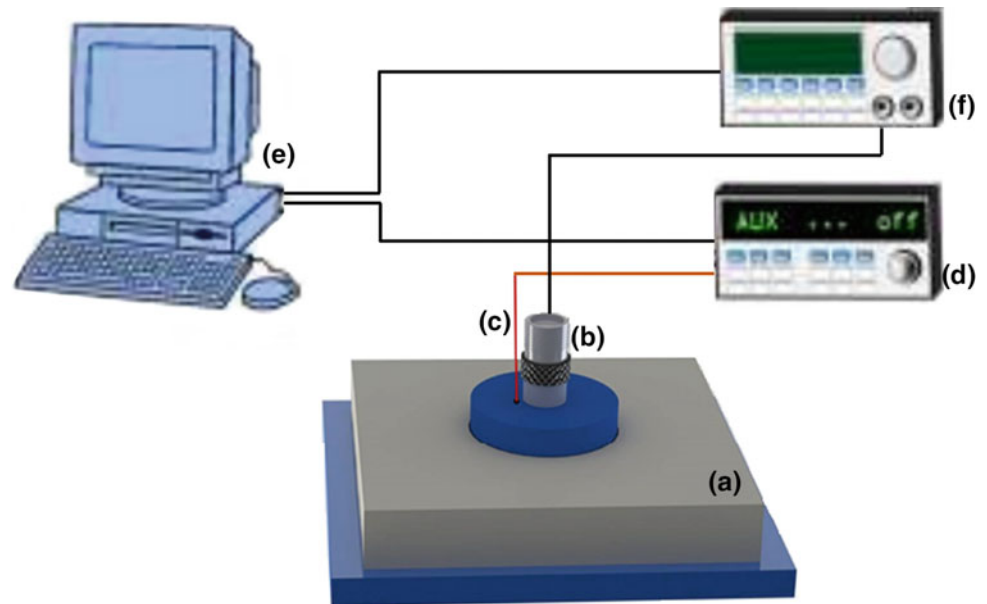
alternative ways are possible, as it is the case with a calorimeter. A thermal-sensitivity is the physical principle in a calorimeter, instead of the mechanical mass measurement principle applied with a radiation force balance [9–12].

This paper presents a simple but fully functional calibrated calorimeter for the measurement of the ultrasonic power. The experimental results found within this study were compared with the power measurement in a calibrated continuous wave ultrasound for 3.5 MHz. The gold standard was a radiation force balance internationally compared [13].

2 Methodology

2.1 Measuring of Ultrasonic Power

The ultrasonic power estimated from the thermal variation was determined based on three measurements under repeatability conditions. The ultrasonic power was in the range of 1 W. The ultrasonic power is given by the equation:

$$P = m \cdot c \cdot \left(\dot{\theta} \right) \tag{1}$$

in which m is the mass (in grams), c is the specific heat of water (equal to 4.1868 J g^{-1} °C), $\dot{\theta}$ is the rate of the temperature θ as function of the time t $\left(\dot{\theta} = \frac{\partial \theta}{\partial t} \right)$. A sample of pure water with 25.076 g was sonicated for 10 min with a calibrated continuous wave equipment. The power delivering transducer model A382S with 3.5 MHz as nominal centre frequency and 12.7 mm of nominal diameter (NDT-Panametrics, Olympus Corporation, Japan).

Figure 1 illustrates the experimental setup of the measuring system described as following: (a) a styrofoam recipient (120 mm X 70 mm X 25 mm) and (b) ultrasonic transducer. The sample temperature was monitored during the measurement process with the aid of a (c) calibrated thermocouple type K and a temperature measuring system model 34970A (Agilent Technologies, USA).

The temperature, for each repetition, was monitored and determined using a temperature measuring device (d) model 34970A (Agilent Technologies, USA) and transferred to a computer (e) through a program developed in LabView (National Instruments, TX, USA). The measurements were performed under repeatability conditions, with four measurements repetitions (Fig. 2). The ultrasonic transducer was excited through (f) a wave generator model 33250A (Agilent Technologies, USA). The time was calibrated with a chronometer and the LabView program.
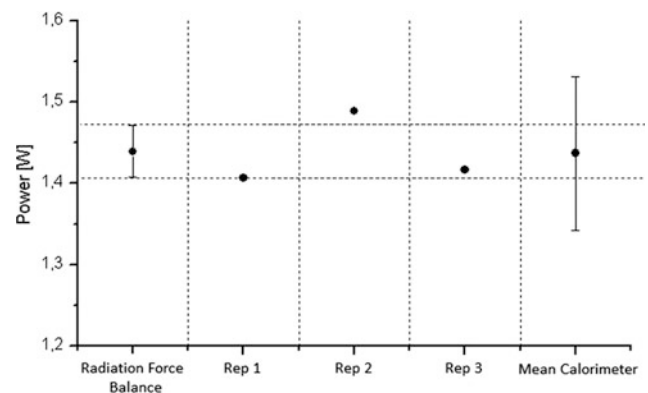
Fig. 2 Ultrasonic power measured with the calorimeter and the calibration value

As the recipient was made of styrofoam and the temperature rise was about 5 °C, it is reasonable to assume that an adiabatic process was under course. Another concern was to use a calibrated thermocouple smaller enough to minimize interference with the acoustic field (1.0 mm diameter). Uncertainties were assessed based on the GUM method [14, 15].

3 Results and Discursion

Three measurement results of ultrasonic power obtained with the calorimeter (P_{cal}), as well as the calibrated output power measured with a radiation force balance (P_{bal}), are shown in Table 1, with respective expanded uncertainties (p = 0.95).

Figure 3 discloses the calibrated results with its uncertainty as error bar ("radiation force balance"), the three repetition measuring values ("Rep1", "Rep2", and "Rep3"), and the average value for the three repetitions (Calorimeter mean) with the respective expanded uncertainty (p = 0.95) as error bar.

The calorimeter power measurement was undertaken after a temperature vs time measurement. Figure 3 discloses a typical curve, from which the temperature variation was assessed. The coefficient of determination (r^2) was used as the quality parameter for considering a good result. The coefficient of determination should be higher than 0.995 to configure as a reliable measurement result. The initial and the final time was chosen to avoid the thermal inertia of the medium, represented by the quasi-parallel behavior in the first 100 s. The output power was turned on somewhen between the 60 and the 70 s.

The coefficient of determination expresses the linear correlation relationship between the two variables
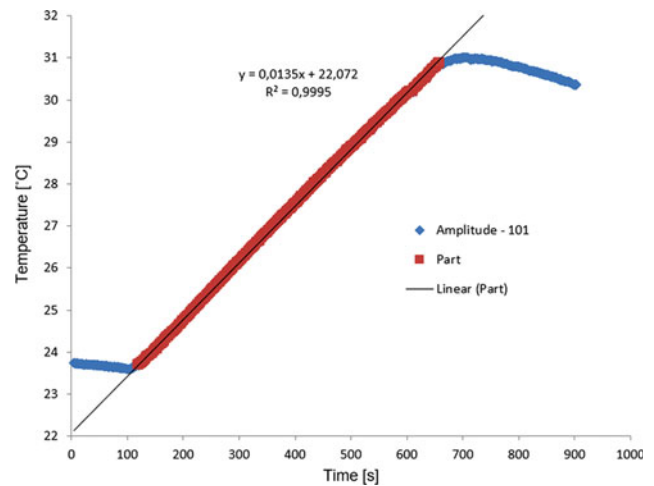
Fig. 3 The linear regression relating the time of exposure of the ultrasound and the temperature for one of the temperature acquisition. Thermal variation for 10 min of heating of 25.076 g of water

(temperature and time) and the result obtained for the three measurements is shown in Table 2. r^2 values close to 1 indicate a strong positive correlation between x and y.

4 Conclusion

In this work, we compared the results of the ultrasonic power measurements obtained from the radiation force balance and a calorimeter. The temperature rise as a function of time was plotted in triplicate, and for all cases the coefficient of determination was greater than 0.995, what was considered highly consistent.

The ultrasonic power measurement using the calorimetry approach was statistically equivalent to the standardized

Table 1 Measurement results of ultrasonic power obtained with the calorimeter and radiation force balance

Radiation Force balance P_{bal} (W)	Calorimeter P_{cal} (W)	$U_{0.95}$ (W)
1.439 ($U_{0.95}$ = 0.032)	1.400	0.095
	1.484	
	1.421	

Table 2 Coefficient of determination (r^2) for three temperature acquisitions

Measurement repetition	r^2
1	0.9984
2	0.9972
3	0.9995

method, as disclosed in [7] and in accordance with [13]. Those results are fundamental for a future development of an equipment joint with a proper procedure to be used in a final user establishment to evaluate the output power performance of a physiotherapy equipment.

References

1. IEC 61689:2013. Ultrasonics—physiotherap systems—field specifications and methods of measurement in the frequency range 0, 5 MHz to 5 MHz. IEC—The International Electrotechnical Commission, Geneva
2. Guirro, E.C.O., Guirro, R.R., Ultra-som. In: Guirro, E.C.O., Guirro, R.R. (eds.) Fisioterapia dermato-funcional: Fundamentos, recursos, patologias, 3rd edn., pp. 175–208. São Paulo, Manole (2004)
3. Fish, P.: Physics and Instrumentation of Diagnostic Medical Ultrasound, 2nd edn. Wiley, New York (1990)
4. Alvarenga, A.V., Machado, J.C., Pereira, W.C.A.: Implementação do protocolo para a obtenção de parâmetros do feixe acústico de transdutores ultra-sônicos usados em medicina. Revista Brasileira de Engenharia Biomédica. **17**(3), 151–163 (2001)
5. Johns, L.D., Straub, S.J., Howard, S.M.: Variability in effective radiating area and output power of new ultrasound transducers at 3 MHz. J. Athletic Train. **42**(1), 22–28 (2007)
6. Straub, S.J., Johns, L.D., Howard, S.M.: Variability in effective radiating area at 1 MHz affects ultrasound treatment intensity. Phys. Ther. **88**(1), 51–57 (2008)
7. IEC 61161:2013. Ultrasonics—power measurement—radiation force balances and performance requirements. IEC—The International Electrotechnical Commission, Geneva
8. Costa-Félix, R.P.B., Alvarenga, A.V., Hekkenberg, R.: A fully automated system for ultrasonic power measurement and simulation accordingly to IEC 61161:2006. J. Phys. Conf. Ser. **279**, 012004 (2011)
9. Morgado, G., Costa-Felix, R.P.B., Miqueleti, S.A.: Measurement of ultrasound power using a calorimeter. IOP Conf. Series J. Phys. Conf. Series 975. 012010 (2018)
10. Furtado, C.S.: Método calorimétrico para medição de campo térmico gerado por ultra-som empregado em Fisioterapia [dissertação]. Universidade Federal do Rio de Janeiro, Rio de Janeiro (2005)
11. Delchar, T.A., Melvin, R.J.: A calorimeter for ultrasound total power measurements. Meas. Sci. Technol. **5**(12), 1533–1537 UK (1994)
12. Ramos, C.B.Z.: Diseño de un sistema para la medición de potencia US por medio de calorimetría para transductores de terapia [thesis]. Centro de Investigación y de Estúdios Avanzados del Instituto Politécnico Nacional, México (2004)
13. Haller, J., Koch, C., Costa-Félix, R.P.B., Dubey, P.K., Durando, G., Kim, Y.T., Yoshioka, M. Final report on key comparison CCAUV.U-K3.1. Metrologia, vol. 53, Technical Supplement, 09002 (2016)
14. BIPM JCGM 100:2008: Evaluation of measurement data—Guide to the expression of uncertainty in measurement (2008)
15. Costa-Felix, R.P.B.: Measurement **39**, 169–175 (2006)

Uncertainty Model of the Temperature Rise Measurements in the Applied Part of Ultrasound Physiotherapy Equipment

Raquel Souza, R. P. B. Costa-Felix, and André Victor Alvarenga

Abstract

To guarantee the patient safety is necessary to evaluate the heating of the ultrasound physiotherapy equipment applied part. Besides, there is a gap in the literature concerning to metrology of ultrasonic physiotherapy equipment performance. This paper proposes a model to estimate the measurement uncertainty of the temperature rise in the applied part of the ultrasound physiotherapy equipment. It was used a test object as proposed by the ABNT NBR IEC 60601-2-5:2015, and it was applied the test criteria based upon temperature rise measurements presented by the same technical standard. The ultrasonic physiotherapy equipment assessed operated on intensity of 1 W cm^{-2}, in frequency of 1 MHz. It was used a calibrated thermocouple to measure the applied part temperature during the test. The measurement result was 8.26 °C $\pm$ 0.40 °C (p = 0.95), meeting the standard's requirements.

Keywords

Ultrasonic physiotherapy equipment • Temperature rise measurement • Measurement uncertainty

1 Introduction

The main aim of many therapeutic applications of ultrasound is tissue heating. Raising the temperature above normothermic levels by a few degrees may have a number of beneficial physiological effects, such as, for example, increasing the blood supply to the affected area [1]. There are many applications using therapeutic ultrasound, such as physiotherapy, which has been used since the 1950's [2]. The ultrasonic physiotherapy equipment has an electronic design, usually consisting of an electrical signal source, operating in a frequency range of 1–3 MHz. An unfocused piezoelectric transducer converts the electrical signals into acoustic energy producing biophysical changes in the tissue without damaging it [3].

To be effective, treatment using physiotherapy ultrasound should be performed safely and accurately, depending on the intensity, frequency and duration of the application [4]. Absorption is the property that increases the temperature [5]. When the rate of energy absorbed by a region of the tissue exceeds its ability to dissipate heat, the local temperature tends to increase. The heating of a transducer surface is dependent on the acoustic and thermal properties of the tissue that is in direct contact with it, as well as of its surrounding tissues [6]. The evaluation of this heating is essential to guarantee patient safety.

The standard IEC 60601-2-5:2015 [7] presents the particular requirements for the basic safety and essential performance of ultrasonic physiotherapy equipment that should be used including for manufacturing. More specifically, the basic conditions for evaluate the ultrasonic transducer heating are presented, and three measurement methods are proposed.

The first method is based on test object near human body temperatures. The applied part of the ultrasonic physiotherapy equipment (transducer) must be coupled acoustically to the test object, which must be at initial temperatures of at least 33 °C. To meet the requirements for this test, the temperature of the surface of the applied part shall not exceed 43 °C after 30 min of test. The second method is based upon temperature rise measurements. The initial temperature of the test object at the transducer interface shall be between 20 and 33 °C and the surface temperature rise shall not exceed 10 °C after 30 min of test. The third method is also based upon temperature rise measurements; however, the measurement must be carried out in still air without the employment of a test object. The initial temperature of the

R. Souza (✉) · R. P. B.Costa-Felix · A. V. Alvarenga
Institute of Metrology, Quality and Technology, Duque de Caxias, RJ, Brazil
e-mail: raquel.ms.eng@gmail.com

A. V. Alvarenga
e-mail: avalvarenga@inmetro.gov.br

applied part shall be 23 °C ± 3 °C and, after 30 min, the temperature rise shall not exceed 27 °C.

The IEC 60601-2-5 recommend three test object models that are tissue-mimicking materials intended to inhibit cooling by convection and to mimic the thermal and acoustical properties of a specific tissue: a bone-mimicking close to the surface of soft tissue; a skin-mimicking at the surface of soft tissue; and a soft-tissue mimic material. In addition, some authors use this standard to study new test object models [6, 8, 9].

It is noted that there is little concern about metrology in these studies. In 2014, Petrella et al. [8] presented an uncertainty model to diagnostic equipment performance measurements. On the other hand, the technical standard [7] does not present any measurements uncertainty model and there is a gap in the literature concerning to metrology of ultrasonic physiotherapy equipment performance.

Aiming to fill the metrological gap and to show the contribution of the metrology as a reliability tool, the proposal of this article is to present a model to estimate the measurement uncertainty of the temperature rise in the applied part.

2 Materials and Methods

2.1 Test Object Model

Among the models recommended by the standard [7], the one using a skin-mimicking material (SMM) at the surface of the soft tissue-mimicking material (TMM) was chosen for this work. To represent skin, it was used a SMM consisted of a layer of room temperature vulcanizing (RTV) silicone with a thickness of 2.814 mm ± 0.074.

For manufacturing the TMM, it was used the standard operating procedure described in [10]. The authors presented a detailed step-by-step procedure to develop an agar's material, according to the recipe disclosed at international standard [7].

The coupling between TMM and SMM was made of a conductive gel to avoid any air bubble. The TMM was covered by a polymer lamina to avoid water evaporation during the experiments. Moreover, the TMM rests over an acoustic absorber material in order to avoid reflections from the TMM bottom.

It is worth to remember that the TMM intended for these applications shall have the ultrasonic properties similar to human soft tissue. Therefore, the speed of sound and attenuation coefficient were measured (see Fig. 1) and compared to that proposed by [7] (see the reference values in Table 1). The measurement uncertainty was expressed based
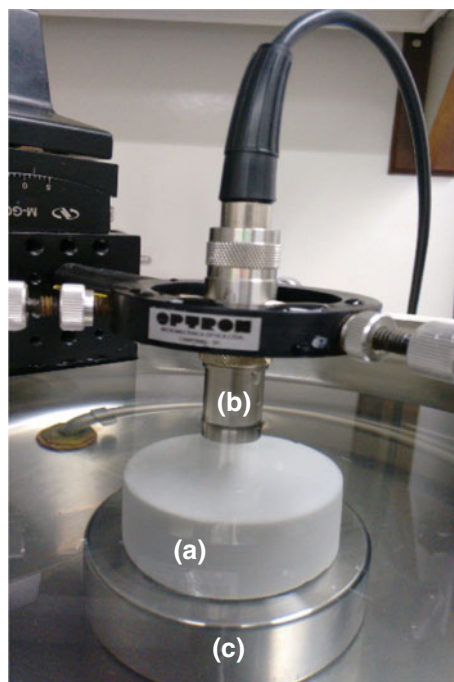
Fig. 1 Acoustic properties measurements—**a**: soft tissue-mimicking material (Ø 55 mm × 38 mm); **b**: transducer; **c**: stainless steel cylindrical reflector to acquire the reference signal

Table 1 TMM's ultrasonic properties manufactured and the reference values proposed in [7]

	Speed of sound (m s^{-1})	Uncertainty (m s^{-1})	Attenuation coefficient (dB cm^{-1})	Uncertainty (dB cm^{-1})
Reference values	1540	–	2.5	–
TMM's ultrasonic properties	1542.1	2.3	2.531	0.024

on the BIPM/JCGM:100 (GUM) [12]. The measurement procedure and the sources of uncertainty were the same presented by Souza et al. [11]. The t-test (see explanation in [11]) was applied to assess the statistical significance between the measurement results of the speed of sound and attenuation coefficient concerning the values presented in the international standard [7].

The mean value of the speed of sound measured in the TMM (Ø 55 mm × 38 mm) does not differ statistically from the reference value in the standard. In turn, the same occur with the attenuation coefficient, where t calculated (statistical test) was lower than t critic (extracted from Student's t-distribution table, on the basis of the degrees of freedom), indicating that the mean and the reference values do not differ significantly.

2.2 Ultrasonic Physiotherapy Equipment

To heat the test object model, it was used an ultrasonic physiotherapy equipment model 4144 (Sonomed, Brazil), operating in continuous mode at the frequency of 1 MHz and calibrated power of 4.22 W $\pm$ 0.14 W (p = 0.95), corresponding to an intensity of 1 W cm^{-2}.

2.3 Temperature Sensor

The temperature sensor used was a J type thermocouple model 34970A (Agilent, USA) and it was used a data acquisition unit (Agilent Technologies, CA) to monitor the temperature.

The IEC 60601-2-5 mentions that the temperature shall be measured on the surface of the applied part of the physiotherapy equipment in those areas that give the highest surface temperature. To meet this requirement, it was used an infrared camera (InfraCAMTM, FLIR Systems, Danderyd, Sweden) to verify if the thermocouple was in the region of maximum temperature.

2.4 Measurement Procedure

The measurements were made following the test criteria based upon temperature rise measurements presented by the standard IEC 60601-2-5 [7]. Although the standard mentions that the test duration shall be 30 min, this test was conducted for 15 min of exposure to preserve the physiotherapy equipment. The ambient temperature shall be 23 °C $\pm$ 3 °C.

The initial temperature of the test object surface shall be between 20 °C and 33 °C. To meet this requirement, the first step is to obtain the thermal equilibrium of the experimental setup, including the test object and the transducer. For this, the TMM (Ø 115 mm × 100 mm) was placed on an acoustic absorber layer and maintained for at least one hour, together with the ultrasonic transducer to be evaluated, the thermocouple and the IR camera. To avoid excessive air circulation, the measurements took place inside a polystyrene box.

The thermocouple junction and adjacent thermocouple lead wire should be securely held in good thermal contact with the surface being measured. The thermocouple was positioned and fixed in such a way that it has a negligible effect on the temperature rise of the area being measured.

After the setup reaches the thermal equilibrium, the transducer was positioned on the test object to provide a proper coupling with a conducting gel (see Fig. 2).

Then, the physiotherapy equipment was switched on and configured to work for 15 min at 1.0 W cm^{-2} in continuous
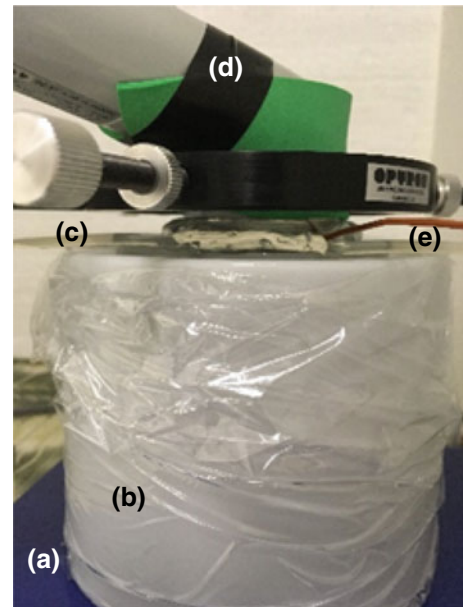
Fig. 2 Experimental Setup—**a**: acoustic absorber material; **b**: soft tissue-mimicking material (Ø 115 mm × 100 mm); **c**: skin-mimicking material (thickness of 2.814 mm $\pm$ 0.074); **d**: ultrasonic transducer and **e**: thermocouple

mode at 1 MHz. During this time, the thermocouple acquired the temperature values every 10 s. At the end of the procedure, an IR image was acquired from the TMM's surface, which was used to check the temperature distribution.

The increase on transducer surface temperature (ΔT) was obtained by Eq. 1.

$$\Delta T = T - T_0, \qquad (1)$$

where T and T_0 are the temperature values obtained by the thermocouple at the instants t = 15 min and t_0 = 0 min, respectively.

2.5 Uncertainty Model

The uncertainty of temperature rise measurement was calculated based on the Guide to the Expression of Uncertainty in Measurement [12]. It is worth to point out that the measurements were carried out under repeatability conditions. Following, the uncertainty model is presented.

Definition of mathematical model of measurement. The method for evaluating and expressing the uncertainty of the result measurement starts by defining the mathematical model of measurement, as seen in Eq. (1). In this case, the measurand is the temperature rise (ΔT).

Definition of uncertainty components. Two sources of uncertainties are considered:

Type A evaluation of standard uncertainty. For the estimate obtained from the statistical analysis of series from independent observations under the same conditions of measurements ($n = 3$), it is carried out the Type A evaluation of standard uncertainty (u_A), which is calculated by (2) and s is the experimental standard deviation.

$$u_A = \frac{s}{\sqrt{n}} \qquad (2)$$

Type B evaluation of standard uncertainty. This source of uncertainty is referent to components evaluated by other means. Here, the uncertainty of the temperature obtained from the calibration certificate of the thermocouple ($U_T = 0.033\,^\circ\text{C}; k = 2.0$) is used in the uncertainty budget.

Determining combined standard uncertainty. The combined standard uncertainty (u_c) can be obtained by combining the uncertainty components that characterize the measurand (ΔT), as can be seen in the Eq. (3).

$$u_C = \sqrt{(u_A^2 + u_B^2)} \qquad (3)$$

Calculation of expanded uncertainty. Then, the expanded uncertainty (U) is calculated by (4):

$$U = k \times u_C, \qquad (4)$$

in which k is the coverage factor determined by considering the effective degrees of freedom and a coverage probability of p = 0.95 (t-student distribution).

3 Results

As can be seen in Table 2, the measurement result was 8.26 °C ± 0.40 °C (p = 0.95). In Fig. 3, one can observe the behavior of the three measured carried out, as well as the calculated mean value.

As complementary information, Fig. 4 is an infrared image that shows the uniform temperature distribution in the

Table 2 The temperature rise of each measurement (ΔT), the mean of temperature rise measurements, the standard deviation (s), the combined uncertainty (u_c), the corresponding type A and B uncertainties (u_A) (u_B), the coverage factor (k) and the expanded uncertainty (U) for p = 0.95

n	ΔT (°C)	Mean (°C)	s (°C)	u_A (°C)	u_B (°C)	u_c (°C)	k	U (°C)
1	8.47	8.26	0.22	0.13	0.02	0.13	3.18	0.40
2	8.26							
3	8.04							

Fig. 3 The curves of the three measurements and the means of the observations are presented
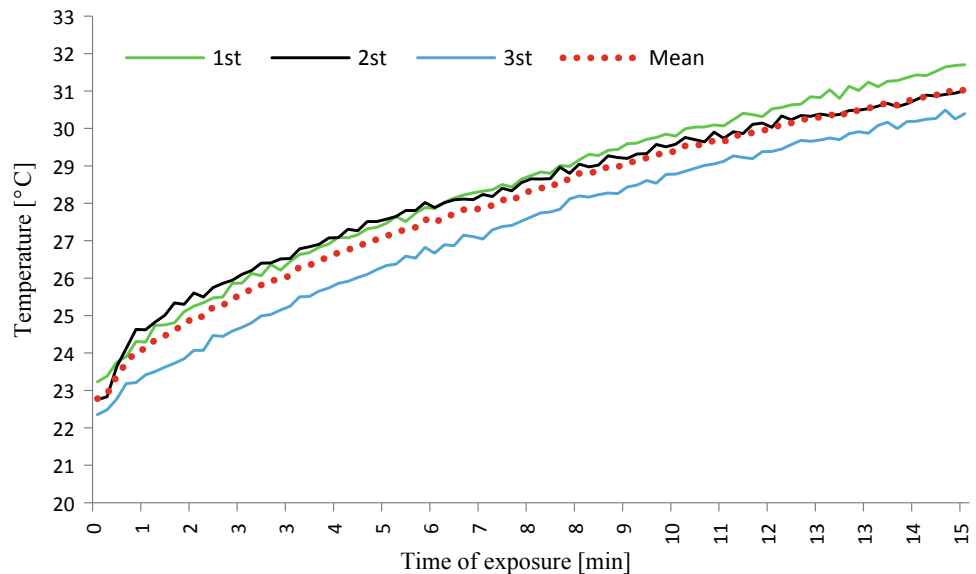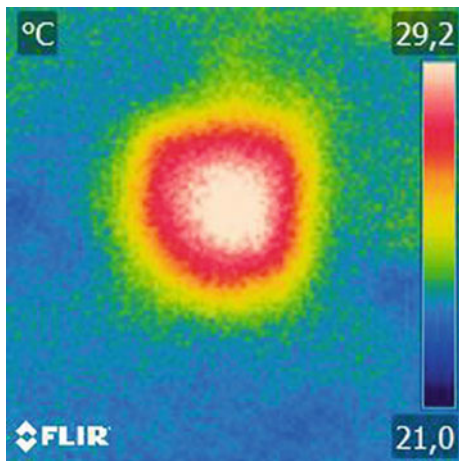
Fig. 4 Infrared image acquired from the test object's surface a few seconds later the transducer exposure

region where the thermocouple was located, right after the transducer exposure.

4   Discussions and Conclusion

This paper proposes a model for evaluating temperature rise measurements uncertainty. Test criteria based upon temperature rise measurements is described on the international standard [7] that presents the basic conditions for evaluate the ultrasonic physiotherapy transducer heating. However, the standard does not suggest any approach to evaluate the measurement uncertainty. In addition, concerning to performance of ultrasonic physiotherapy equipment, no studies were found in the literature reporting uncertainties for their measurements results.

Moreover, the uncertainty model presented here can be useful to metrological evaluate the temperature rise of the applied part of the physiotherapy transducer periodically. Hence, carrying out periodical tests and evaluating the measurement uncertainty, it is possible to estimate eventual variations in that value, which may indicate a possible change in transducer heating.

Variations on measurement conditions between different days were obtained from the standard deviation. Considering the three measurements results presented on Table 2, it was observed that the temperature increase did not exceed 10 °C. It is important to remember that the duration of the test carried out in this paper (15 min) was less than the duration required in the standard (30 min). Based on the behavior of the curves presented on Fig. 3, it is noticed that the trend was the temperature rise as a function of the transducer exposure time. Thus, if the test duration reached 30 min, the physiotherapy equipment evaluated in this study would not

meet the requirements of the protection against excessive temperatures test presented in the IEC 60601-2-5.

Petrella et al. [8] compared a test object model proposed by [7], the skin mimicking at the surface of soft tissue, with a new one using a layer of porcine subcutaneous. In turn, the authors used the requirements for the basic safety and essential performance of ultrasonic diagnostic equipment presented in the IEC 60601-2-37:2008 [13]. The authors carried out the test criteria based upon temperature rise measurements, which is the same in both standards [7, 13]. The temperature sensor used by Petrella et al. was an infrared camera. The result for the standard's test object model was 6.7 °C ± 1.7 °C and the diagnostic transducer exposure time was 30 min.

Thereby, it is realized that the heating in the applied part of the diagnostic equipment was less than the heating evaluated in the applied part of the physiotherapy equipment (8.26 °C ± 0.40 °C) operating in half the exposure time of the diagnostic transducer. This difference may be explained because the physiotherapy transducer is intended to cause tissue heating; on the other hand the same does not occur with the diagnostic transducer. However, both standards present the same tests criteria, including the test duration of 30 min.

Herein, as the main objective was to validate the proposed measurement uncertainty model, only one physiotherapy equipment was used and the test duration was 15 min to avoid equipment jeopardizing.

References

1. Haar, G.T.: Therapeutic of ultrasound. Prog. Biophys. Mol. Biol. **93**, 111–129 (2007)
2. Imig, C.J., Randall, B.F., Hines, H.M.: Effect of ultrasonic energy on bloodflow. Am. J. Phys. Med. **33**, 100–102 (1954)
3. Abrunhosa, V.M., da Costa-Félix, R.P.B., Von Kruger, M.A., Pereira, W.C.: Sensitivity determination of physiotherapy ultrasonic transducers by the self-reciprocity method. Revista Brasileira de Engenharia Biomédica **28**(1), 23–35 (2012)
4. Ishikawa, N.M., Alvarenga, A.V., Paes, L.F.C., Pereira, W.C.A., e Machado, J.C.: Analysis of the performance of ultrasound equipment for physiotherapy, operating in the city of Rio de Janeiro, according to the NBR/IEC 1689 standard of ABNT. Revista Brasileira de Fisioterapia **6**, 63–69 (2002)
5. Fish, P.: Physics and Instrumentation of Diagnostic Medical Ultrasound, 1st ed. Nova York, Ed. Wiley (1990)
6. Hekkenberg, R.T., Bezemer, R.A.: On the development of a method to measure the surface temperature of ultrasonic diagnostic transducers. J. Phys. **1**, 84–89 (2004)

7. Electrotechnical Commission. IEC 60601-2-5:2015: Medical electrical equipment Part 2-37: Particular requirements for the basic safety and essential performance of ultrasonic physiotherapy equipment, 2.0 ed. Genova (2015)

8. Petrella, L.I., Maggi, L.E., Souza, R.M., Alvarenga, A.V., Costa-félix, R.P.B.: Influence of subcutaneous fat in surface heating of ultrasonic diagnostic transducers. Ultrasonics **54**, 1476–1479 (2014)

9. Shaw, A., Pay, N.M., Preston, R.C., Bond, A.D.: Proposed standard thermal test object for medical ultrasound. Ultrasound Med. Biol. **25**, 121–132 (1999)

10. Souza, R.M., Santos, T.Q., Oliveira, D.P., Souza, R.M., Alvarenga, A.V., Costa-felix, R.P.B.: Standard operating procedure to prepare agar phantoms. J. Phys. Conf. Ser. (online) **733**, 120–124 (2016)

11. Souza, R.M., Monteiro, R.M., Costa-felix, R.P.B., Alvarenga, A. V.: Ultrasonic properties of a four years old tissue-mimicking material. J. Phys. Conf. Ser. (online) **975**, 120–125 (2018)

12. JCGM 2008 Evaluation of Measurement Data—Guide of the Expression of Uncertainty in Measurements JCGM 100 (2008)

13. Electrotechnical Commission. IEC 60601-2-37:2008: Medical electrical equipment Part 2-37: Particular requirements for the basic safety and essential performance of ultrasonic medical diagnostic and monitoring equipment, 2.0 ed. Genova (2008)

Author Index